All Text Search

K-1

NEW PNEUMATIC TECHNIQUES AND APPLICATIONS

Toshiharu KAGAWA*

* Precision and Intelligence Laboratory, Tokyo Institute of Technology, R2-45,
4259 Nagatsuta-chou, Midori-ku, Yokohama, 226-8503, Japan
(E-mail: kagawa.t.aa@m.titech.ac.jp)

ABSTRACT

In this paper, some new achievements of Kagawa's researches on pneumatic techniques and applications are introduced. One of them is concerned with a low noise pneumatic resistance. In regard to its basic principle, compressed air is blown out through a very thin radial slit structure to form laminar flow. By this means, aerodynamic noise caused by turbulence can be decreased to a much lower level comparing with other type resistances like orifice. The radial slit type resistance is applied to develop a new pressure regulator by making the gap thickness of radial slits adjustable, which is characterized by lower noise and less pressure fluctuation. Another proposal introduced in this paper is an unsteady mass flow generator which can continuously generate and control oscillatory flow at a frequency up to 50[Hz]. An important component of the generator is an isothermal chamber in which the essential isothermal condition is preserved. Utilizing the mass flow generator yields many practical applications, for example, the developments of air power meter. Recently, Kagawa's research interest extended to analysis and development of pneumatic non-contact handling device. A new non-contact handling method called vortex levitation by using swirling air flow is analyzed in Kagawa's laboratory. Swirling air flow can form a parabolic negative pressure distribution to pick up a work piece and keep it stably levitate with a considerably thin gap under the device. Furthermore, it is confirmed that a work piece will vibrate while being picked up and its vibration can be damped to zero due to a damping effect.

KEY WORDS

Radial Slit Type Regulator, Low Noise, Mass Flow Generator, Air Power Meter and Vortex Levitation

FOREWORD

Pneumatic technique is widely used because of its inherent advantages like generating little heat and magnetic free, etc. Though its researches and applications had been carried out for hundreds of years, more effort is obviously needed especially as the environmental problem and energy crisis become severe recently. The author is devoted to pursue the development of new pneumatic techniques to explore the possibility for the solutions of those problems. In this paper, some new achievements are introduced with key words of low noise, energy consumption assessment and energy-saving. First, low noise radial slit type regulator is developed and proven to be able to decrease aerodynamic noise to a much lower level than the orifice type regulator while depressurizing a high pressure. Next, unsteady mass flow generator is proposed and applied to the development of air power

meter. Finally, a new non-contact handling technique by using swirling air flow is introduced, which is characterized by its low air power consumption.

RADIAL SLIT TYPE REGULATOR

Usually, an orifice type regulator is widely used while depressurizing supply original pressure to a certain pressure that is often much lower than the original pressure. However, the orifice type regulator is always accompanied with problems of pressure fluctuation and considerable noise due to the turbulence flow. In order to solve those problems, a new pneumatic resistance is proposed by using radial slit structure, and is applied to develop a new pressure regulator by making the gap thickness of radial slits adjustable. In this section, the flow rate characteristics of the radial slit type regulator were investigated experimentally, and the noise level is confirmed to be decreased to approximately 40dB lower

than the orifice type one[1,2].

Structure of radial slit type regulator

Figure 1 shows a schematic drawing of the variable slit structure. The slit structure consists of three elements, a disk, a guiding bar and coned disk springs. The upper part of Figure 1 shows the cross section of the structure. The upper disk consists of a flow inlet and an upper surface of the radial slit. The inner diameter of upper disk is 8.5mm. The guiding bar guides the movement of the disk. Coned disk springs are installed between the disk structures and the height of them are precisely controlled. The compressed air enters from the center of the upper disk and is exhausted outward through the radial slits. The lower part of Figure 1 shows the top view of the lower disk. The lower disk consists of a lower surface of the radial slit and a groove for holding the disc springs. The outer diameter of upper disk is 50mm, and the depth of groove is 0.5mm. The structure of the coned disk spring is shown in the right part of Figure 1. Its material is SUS304, and the spring constant is 619.5N/mm. The diameter of the coned disk spring is 8mm. The thickness is 0.3mm, and height is 0.55mm. It is located on groove of disk. The height difference of groove and coned disk spring makes the 50μm slit. The height of it is precisely controlled with a control force.
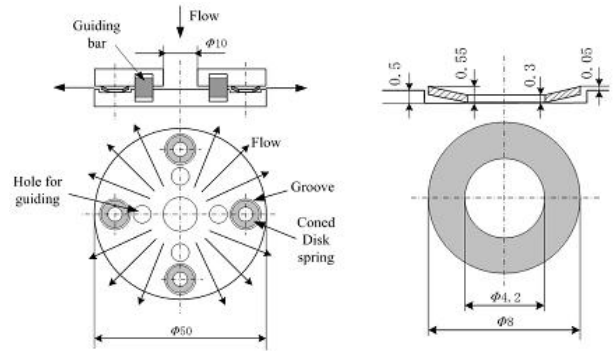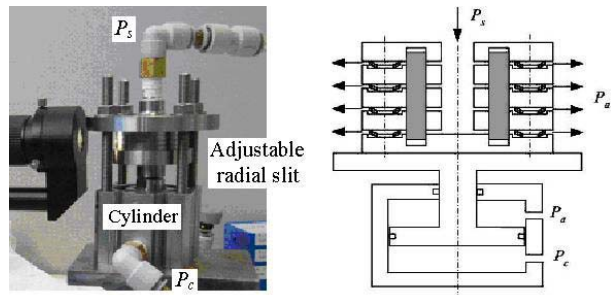
The picture and the structure of newly developed regulator are shown in Figure 2. In this study, we produced a new regulator which has four layers of slit as shown in the right side of Figure 2. The compressed air with supply pressure Ps enters from the center of the disks and is exhausted to atmosphere pressure through the slits. The pneumatic cylinder is set up below the disk, and its piston is connected with the disk. The control pressure Pc is supplied to the cylinder, and the cylinder moves the disk. Therefore, the gap thickness of slits is controlled with the pneumatic cylinder by changing the control pressure. The gap thickness of slit is measured by a microscope.

Flow rate characteristics

The flow characteristics were measured experimentally using the experimental apparatus shown in Figure 3. Buffer tank and two regulators are set up on the upstream side. Supply and control pressures were regulated by each regulator. The pressure and the flow rate were measured using a bourdon tube pressure gauge and a float-type area flow meter, respectively. The measured flow characteristic is shown in Figure 4. The supply pressure is set constant at 500kPa. The control pressure was increased from atmospheric pressure to 700kPa and then decreased to atmospheric pressure. The triangular symbols show the increased process of the control pressure and the rectangular show the decreased process.

When the control pressure was increased to 300kPa, the flow rate was decreased from 216Nl/min to 24Nl/min.

Figure 1 Adjustable radial slit
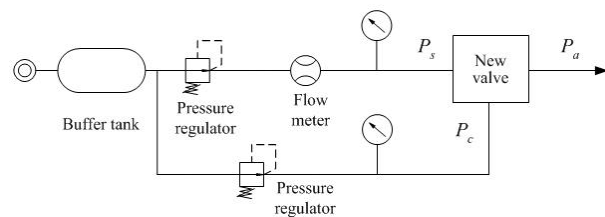

Figure 2 Radial slit type regulator

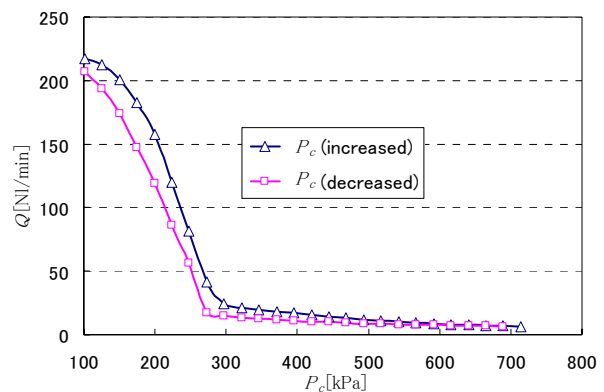Figure 3 Experimental apparatus for flow characteristics

Figure 4 Flow rate characteristics

The flow rate decreased at a rate of 1Nl/min in 1kPa, and a change of flow rate was large in this range. When the control pressure is beyond 300kPa, the flow rate decreased at a rate of 0.04Nl/min in 1kPa. In this range, a change of flow rate was small. The flow rate at 700kPa was close to 0Nl/min. When the control
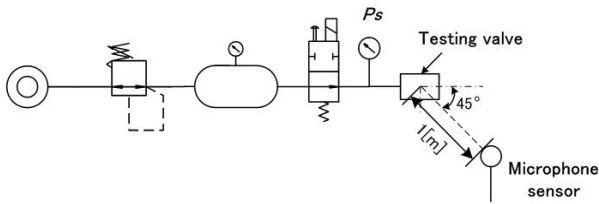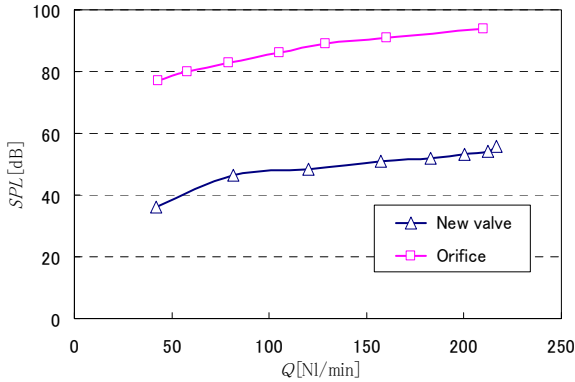
Figure .5 Experimental pneumatic circuit

Figure .6 Comparison of noise level between orifice type regulator and radial slit type regulator

pressure is decreased to atmospheric pressure, the flow rate is smaller compared with the increased process. This is considered to be caused by the hysteresis of the pneumatic cylinder and the coned disk springs.

Noise level

The noise level of the valve was measured using a microphone sensor. The background noise level of the room is at 30dB. Microphone was placed in the room at an angle of 45 degree from the center axis of the regulator as shown in Figure 5. The distance from the regulator to the microphone was 1.0m. The noise levels of the orifice and the newly developed regulator with the variable slit structure were compared. The experimental results are shown in Figure 6. The horizontal axis is flow rate, and the vertical axis is the noise level. We confirmed in advance that the flow characteristics of the orifice and the new regulator were approximately the same. The results indicated that the noise level decreased approximately 40dB in the new valve.

UNSTEADY MASS FLOW GENERATOR

There is no effective method to calibrate the dynamic characteristics of gaseous flow meters due to a fact that the density of those fluids changes largely with respect to both pressure and temperature. This section describes the development of an unsteady mass flow generator for gases. The generator mainly consists of an isothermal chamber and two spool-type servo valves. The heat

transfer area within the isothermal chamber is made sufficiently large by stuffing the copper wool materials to ensure that the essential isothermal conditions are preserved [3]. The calibration of the dynamic characteristics of the gaseous flow meters and the internal flows within such meters are achieved using the generator. Experimental tests reveal that the generator can control oscillatory flows at a frequency of up to 50 Hz with an uncertainty of 5.5%. In addition, the generator can generate flows for more than 30 min[4,5].

Principle

The unsteady mass flow is generated using an isothermal chamber and two servo valves, as shown in Figure 7. The state equation for compressible fluids in a chamber can be written as

$$PV = WR\theta \qquad (1)$$

The following equation can be derived by differentiating Equ.1, if the chamber volume is constant:

$$V\frac{P_c}{dt} = (G_{in} - G_{out})R\overline{\theta} + WR\frac{d\overline{\theta}}{dt} \qquad (2)$$

Here, the mass flow rate G_{in} is charged through the servo valve installed in the upstream of the isothermal chamber. The controlled mass flow G_{out}, which is the generated flow, is discharged through the servo valve installed in the downstream of the isothermal chamber. The generated flow G_{out} is given by the following equation by transforming Equ.2:

$$G_{out} = G_{in} - \frac{V}{R\overline{\theta}}\frac{dP_c}{dt} + \frac{W}{\overline{\theta}}\frac{d\overline{\theta}}{dt} \qquad (3)$$

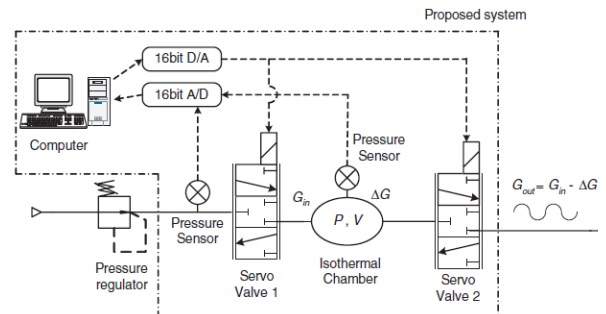If the state of the air in the chamber during charge or

Figure .7 Sketch of the unsteady mass flow generator

Figure .8 Photograph of the mass flow generator

discharge remains isothermal, the generated mass flow rate can be obtained from Equ.3 as

$$G_{out} = G_{in} - \frac{V}{R\overline{\theta}}\frac{dP_c}{dt} = G_{in} - \Delta G \qquad (4)$$

Since the condition remains isothermal, the average temperature in the chamber $\overline{\theta}$ is equal to the room temperature θ_a[3]. Equ.4 indicates that if the volume of the chamber V and the room temperature θ_a are known, then the generated mass flow rate can be controlled by the pressure difference in the isothermal chamber and the inlet mass flow rate. The inlet mass flow rate is controlled by servo valve 1, as shown in Figure 7, and the pressure change in the isothermal chamber is controlled by servo valve 2.

Apparatus
A schematic diagram and a photograph of the developed generator are shown in Figure 7 and 8, respectively. The apparatus consists of an isothermal chamber, two spool-type servo valves, two pressure sensors and a personal computer. Servo valve 1 controls the charged mass flow rate to the isothermal chamber, and servo valve 2 controls the generated unsteady flow from the chamber. A laminar flow meter having a high-speed response was arranged on the downstream side of the mass flow generator, as shown in Figure 9, and was used to verify the generated unsteady mass flow[6].

Experimental results
The target oscillatory mass flow rate is given as a sine wave. The low-pass filter was used for the processing of the measured data. The cut-off frequency of the filter was set at three times the frequency of the phenomenon. Figure 10 shows an experimental result at a frequency of 50Hz. In the Figure, the dashed line shows the target flow rate, the solid line shows the generated flow rate using the unsteady mass flow generator and the short-dotted line indicates the measured flow rate using the laminar flow meter. From Figure 10, it could be confirmed that the target flow rate and the generated flow rate show good agreement. And the flow is generated continuously for 30min. These results show that the maximum error between the target mass flow rate and the generated mass flow rate is less than approximately 5%.

Figure 11 shows a triangular wave at a frequency of 5 Hz. The maximum pressure change speed in the isothermal chamber is about 200 kPa/s that is the maximum value of the pressure control in the isothermal chamber. The proposed generator is thus proven to be capable of generating various flows.

Applications
The unsteady mass flow generator yields many practical applications. For example, the dynamic characteristics of an air power meter, which has an ability to measure instantaneous air power consumption and is shown in Figure 12, can be examined since an exact unsteady mass flow rate is available for test input. And the development of air power meter might contribute
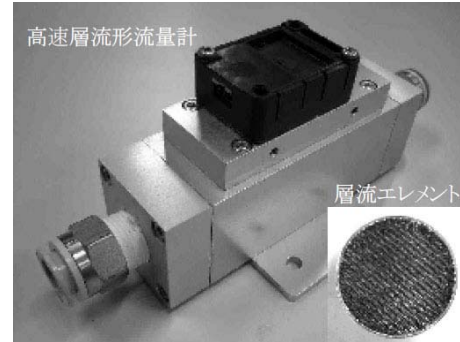

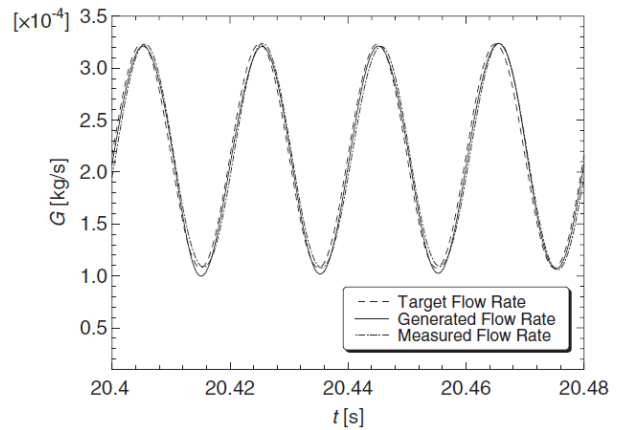Figure .9 Photograph of quick flow sensor

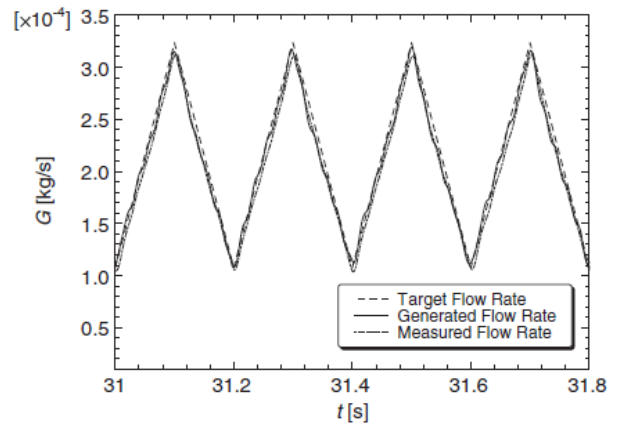
Figure .10 Oscillatory flow at a frequency of 50Hz

Figure .11 Triangular wave at a frequency of 5Hz

Figure .12 Photograph of air power meter

largely to energy-saving researches because of a proper measurement on pneumatic energy consumption[7].

NON-CONTACT HANDLING DEVICE USING SWIRLING AIR FLOW

Usually a work piece is brought into contact with a handling device in order to be picked up and moved. Such contact methods are often accompanied by surface scratching and static electricity. Therefore, many non-contact handling approaches had been proposed and have proven effective. In this section, a new pneumatic non-contacting handling approach named vortex levitation is introduced by the authors. Vortex levitation is characterized by its low air consumption. Comparing to Bernoulli levitation, it requires less air supply flow rate while generating the same lifting force. In our research, analysis is conducted on both its static and dynamic characteristics[8,9].

Mechanism of vortex levitation
A simple structure called the vortex cup (hereafter referred to as cup) is used to generate an air swirling flow. As can be seen in Figure 13, the cup is made up of a circular cylinder and a tangential nozzle inserted above. A fillet is cut at the bottom to direct air out of the cup. Compressed air is blown through the nozzle into the cup, and then spins along the circular wall to create a negative pressure in the central area by centrifugal force. This negative pressure will be applied as a lifting force to a work piece placed under the cup, which will then pick it up hold it at an equilibrium position where the weight is balanced by the lifting force. Because air is supplied continuously, the work piece will keep levitating with a gap of hundred micrometers from the cup, through which air can be discharged into the atmosphere. For this reason, the work piece never contacts the cup.

Pressure distribution
Figure 14 shows a sketch of the cup and indicates the coordinates. The lower of Figure 14 plots the radial pressure distribution at a certain gap thicknesses for the case in which the supply flow rate is set constant. It is observed from this figure that the pressure inside the cup is distributed along the radial direction, and the pressure distribution is quite similar to a parabolic curve. Moreover, because air flows relatively slowly toward the gap entrance and then is forced into the thin gap, it is observed that pressure drops through the gap.

One more important fact is that negative pressure inside the cup is dependent on the gap between the cup and the work piece. As the gap is enlarged, pressure at the gap drops to atmospheric pressure. At the same time, the parabolic pressure distribution shifts toward the vacuum with a uniform distribution. However, once pressure in the gap becomes nearly equal to zero, the negative pressure inside the cup slowly recovers toward atmospheric pressure.
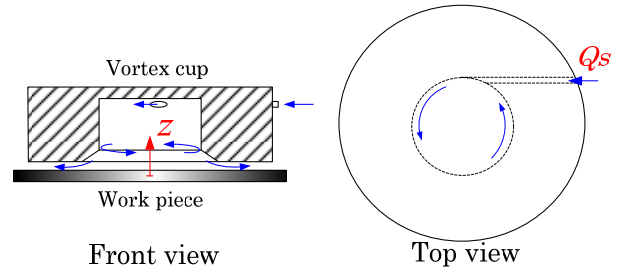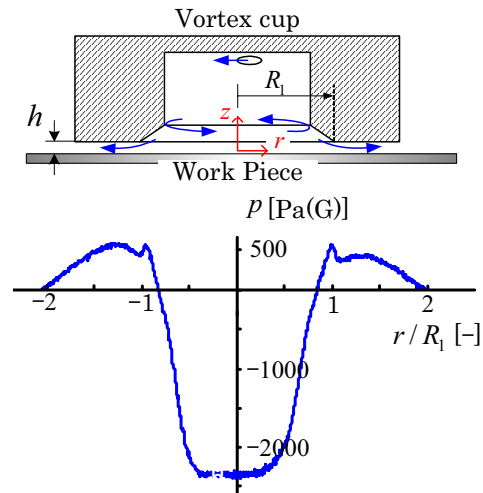

Figure .13 Sketch of vortex cup

Figure .14 Pressure distribution

Lifting force and stable levitation
According to the negative pressure distribution and its change with respect to the gap thickness between the cup and the work piece, the lifting force increases as the gap is enlarged, and decreases slowly after it reaches a maximum as the gap becomes bigger and bigger. The curve shown in Figure 15 indicates the lifting force and its change. From this result, it is known that the cup can handle a work piece whose weight is less than maximum lifting force. As an example, assume a 0.2 [N] work piece is handled by the cup, which is plotted by a broken line in Figure 15. This line intersects the lifting force line at two points A and B where the weight is balanced by the lifting force. If the work piece gets closer to the cup than A, it will obviously fall back to A because the lifting force is smaller than its weight. If it comes into the region between A and B, the lifting force becomes bigger than its weight to be able to pull it back to A. However, the work piece will fall down once it gets further away than B due to the insufficient lifting force. Therefore, A is defined as a stable levitation position and B is defined as the levitation boundary position. The region from the bottom of the cup to B is called the stable levitation region.

Dynamic levitation
The experiments and analysis as stated above were conducted only in the steady state conditions. Considering its practical uses, for example, in a

semiconductor production process where each wafer is handled frequently during repeated loading and unloading, efforts are obviously needed to investigate how the work piece behaves at the moments when it is picked up by the cup and when it is disturbed while levitating under the cup. Therefore, investigations on the dynamic characteristics of vortex levitation were conducted and reported. Figure 16 is an instantaneous movement of the work piece at the vertical direction when it is picked up by the cup. The vibration due to its inertia occurs and is damped to zero in several periods.

In order to clarify the reason of the damped vibration, a pressure response was measured while keeping the work piece to vibrate continuously under the cup. Pressure responses inside the cup and in the skirt are shown in Figure 16, respectively. A very thin air layer is formed between the surrounding skirt and the work piece. Air reaches a higher pressure when it approaches to the cup than when it gets away from the cup. Thus, by this means damping effect can be confirmed to result in the damped vibration.

AFTERWORD

Low noise, energy consumption assessment, energy saving non-contact handling technique, these achievements mentioned in this paper contribute toward improving environment and saving energy consumption. Their further applications can be expected in the future.

REFERENCES

1. C. Youn, H. Muramatsu, K. Kawashima and T. Kagawa, Research by visualization of low noise pressure reducing structure using slit flow, Journal of the Japan fluid power system society, Vol.36, No.3, 2005, pp. 59-65 (JPN).
2. K. Kawashima, C. Youn and T. Kagawa, Development of a nozzle-flapper-type servo valve using a slit structure, Journal of fluids engneering ASME, Vol.129, 2007, pp.573-578.
3. ISO 6358: Pneumatic fluid power – Components using compressible fluid - determination of flow rate characteristics, 1989.
4. K. Kawashima and T. Kagawa, Unsteady flow generator for gases using isothermal chamber, Meas. J. Int. Meas. Confed. (IMEKO) 33–34 333–40, 2003.
5. T. Funaki, K. Kawashima, S. Yamazaki and T. Kagawa, Generator of variable gas flows using an isothermal chamber, Measurement science and technology, Vol.18, 2007, pp.835-842.
6. T. Funaki, K. Kawashima and T. Kagawa, Characteristic analysis of laminar flow meter for gases with high speed response, T. SICE 40 1008-13 .
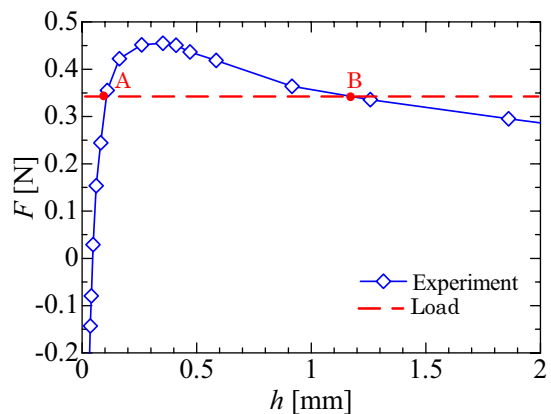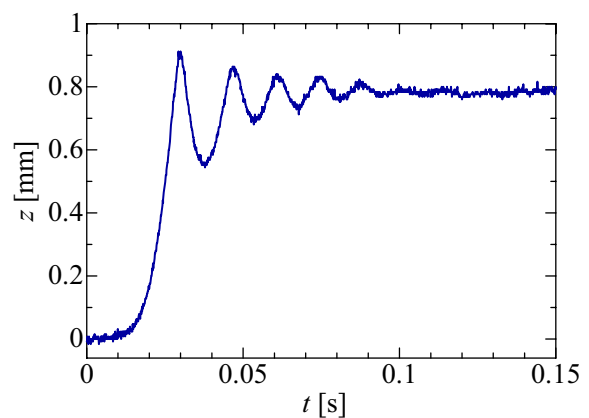7. M. Cai, T. Fujita and T. Kagawa, Energy consumption and assessment of pneumatic actuating systems, Journal of the Japan fluid power system society, Vol.32, No.5, 2001, pp.118-123 (JPN) .
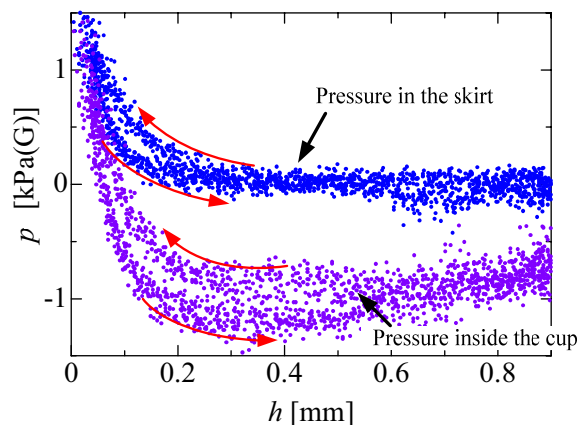8. X. Li, H. Tokunaga, M. Cai, T. Funaki, K. Kawashima and T. Kagawa, Research on non-contact handling device using swirling flow, Journal of the Japan fluid power system society, Vol.38, No.1, 2007, pp. 1-6 (JPN) .
9. X. Li, K. Kawashima and T. Kagawa, Analysis of vortex levitation, Experimental thermal and fluid science, 2008.

Figure .15 Lifting force

Figure .16 Instantaneous movement of work piece

Figure .17 Pressure response

K-2

SUSTAINABLE DEVELOPMENT WITH WATER HYDRAULICS – POSSIBILITIES AND CHALLENGES

Kari T. KOSKINEN, Timo LEINO, Hannu RIIPINEN

Department of Intelligent Hydraulics and Automation
Tampere University of Technology
Korkeakoulunkatu 6, PL 589, 33101 Tampere, Finland
(E-mail: kari.t.koskinen@tut.fi)

ABSTRACT

Water hydraulics is an old technology area, which has been used already hundreds of years. Earliest applications where water was used as power transmission medium are known already from 2000 years ago. Modern water hydraulics can be comprised as a technology area where new design, material and control technologies are applied to water hydraulic systems. In 1990's very much research and development of water hydraulic systems and components were carried out in several laboratories in many countries. During the new millennium the research efforts has been a little bit smaller, but the continuously rising concern about globe and global climate change has also increased the interest on water hydraulic applications. This paper describes the actual research activities related to development of water hydraulic components and systems. The main focus areas are discussed and the challenges and possible solutions of each subject are analyzed. Water quality aspects, component technology, control aspects and also applications are covered. Also some analysis about water hydraulics' possible role in climate change process and energy saving are presented.

KEY WORDS

Water hydraulics, Oil hydraulics, Sustainable development, Research, Component technology

NOMENCLATURE

CFD : computational fluid dynamics
DOC : dissolved organic carbon
$\beta(x)$: (Number of particles > (x) upstream) / (Number of particles > (x) downstream)

INTRODUCTION

Almost everybody agree that the use of not renewable energy and especially oil have to be decreased in the future. More emphasis have to be put on the use renewable sources like solar, wind and wave energy in the future. Even the consumption of hydraulic oil in the world is of course is much smaller than total oil consumption (over 80 million barrels per day [1]), the number of tons used in fluid power is still quite significant. By reducing this amount fluid power world and machine builders can do their share of global climate work.

The use of water hydraulics is one possibility to develop fluid power systems to more environmental friendly

direction. In this context water hydraulics can be understood as a technology, which is using water or water based fluids for transmission of energy and power.

Water hydraulics is the first fluid power technology, which is used already in 18th century. The modern water hydraulics technology is new application area, which has had strongly increasing trend since 1980's. Using different waters instead of oils in hydraulic systems brings the following benefits: environmental safe, fire safe, explosion safe, low cost fluid, good availability of the fluid, easy storage of the fluid etc.

IHA (Department of Intelligent Hydraulics and Automation, Tampere University of Technology) has put systematically efforts on developing water hydraulics technology during 1990's and during the new millenium. Research have been made in different projects in Finland and internationally.

ROLE OF HYDRAULIC PRESSURE MEDIUM IN SUSTAINABLE DEVELOPMENT

Pressure medium life cycle

If we are thinking about the lifecycle of hydraulic oil and the costs related to every phase, the total sum will grow quite very high. We have to take into account all the investments related to drilling the oil, transportation, refining, marketing, delivery, use and disposal. Naturally it is impossible to find out just costs focused on hydraulic oil, because also other oil products are produced always at the same time.

When comparing the supply of oil and water to each other, the difference is quite essential. Oil drilling is huge business, which needs big investments. For example the oil rigs have to be able to build in deeper water in the future. That means even bigger investments. Water is instead easily available and for example from sea water it is relatively easy to produce water for water hydraulic systems.

One important factor globally is the packages for oil products. All the oil products are packed to barrels, containers, cans etc. The production of these packages requires a lot more extra energy than taking the water from tap.

The use of water in hydraulic system needs extra care considering the water quality. Microbiological growth is a phenomenon, which causes extra costs for maintenance and service. Also when using some additives for preventing microbial growth, some extra costs are generated. On the other hand storage of water is much easier and normally, when tap water is used, no storage costs are generated. Also, water doesn't wear out, so the fluid replacement can be less frequent than with oil. That is also very much according to sustainable development, because less energy is used for fluid replacement and the disposal is every time easier than with oil, which have to be transported to special disposal plants.

Energy efficiency

Energy efficiency of machines and systems will be also very important aspect in the future. The consumption of energy during system building, system use and system disposal have to be minimized. So the whole life cycle of the whole systems have to be considered.

When thinking about water hydraulics, the situation is versatile. Due the material requirements of components, the system building costs are higher than oil hydraulics at present. The reasons for that are, for example, base materials and very small production quantities. In high pressure water hydraulics the price difference can be 3-5 times. However, in low pressures the price difference is decreasing. The energy consumption per system can be evaluated to be higher, because the materials used are requiring longer machining times and more complicated processing that in oil hydraulics.

The use of water instead of oil is offering benefits, when considering energy consumption. The pressure losses in pipes and components are smaller with water than oil, which is clear benefit, with large flows and long pipes. On the other hand the leakages could easily be higher with water. This, of course, leads to use of smaller clearances and seals, which can increase friction and that way energy consumption. However, the basic design and control principle of the system have very big role for the system energy consumption. If the basic design doesn't include relief function when needed, controllable pump rotation speed when needed or the control valve or block have to have small flow paths, the energy losses can rapidly increase. In accurate and fast control tasks with digital water hydraulics, also control algorithms can be optimized considering the minimizing of energy consumption.

When evaluating the system components disposal after the use, no significant differences between water and oil hydraulics can be found.

ACTUAL RESEARCH INTRESTS IN WATER HYDRAULICS

The Department of Intelligent Hydraulics and Automation (IHA) has a long history in water hydraulic research. The motion control has always been one of the most important research areas in both oil and water hydraulics research in IHA. The water hydraulics motion control research has been concentrated both on component research and system level research. In the beginning of new millennium a lot research was made with on/off-control in water hydraulics. On/off –control is very cost effective way to achieve relatively good characteristics, because the cost level of water hydraulic servo valves is very high. At present this work has been transferred to its own research team Digital Hydraulics, which also covers oil hydraulic on/off –systems.

Proportional technology is also an important part of water hydraulic motion control. Proportional valves are undeveloped except some exceptions and on the other hand the system and control technology has not been widely applied to water hydraulic motion control. Both areas are intensively researched in IHA.

Use of water in hydraulic has a great opportunity to cavitation in components where pressure gradients are large. One of these components is a seat valve where the pressure drops in relatively short length. The seat valve is, however, quite cost-effective valve type to water hydraulics, because it is possible to manufacture as non-leaky with reasonable tolerances that makes it interesting for industrial use. The research of cavitation in water hydraulic seat valves is one focus area. Also the leakage flows in water hydraulic spool valves have been studied.

Microbial growth is a problem in hydraulic systems, even though they are considered to be oligotrophic environments. Filtration is one of the possible methods to reduce microbial growth and particle contamination in water hydraulic systems. However, biofilm and particles can block the filter element very rapidly and prediction of the lifetime of the filter element of water hydraulic system is very challenging. IHA has made research in this area over 8 years.

Water quality aspects [2]

Growth and attachment of bacteria in water hydraulic systems is mainly a function of the nutrition concentration in the pressure medium. Hydraulic parameters and system materials have a slight effect on growth and attachment, but the best way to avoid problems with microbes is to maintain nutrition levels on a par with tap water (DOC 2-4 mg/l).

Lowering the nutrient concentration and increasing the system pressure have been reported as the most effective ways for controlling total bacterial numbers and counts of viable bacteria in the pressure medium. Low reductions have been obtained by adjusting the fluid flow velocity in the system. However, an increase in pressure resulted in enhanced microbial attachment on the reservoir as shown in figure 1.
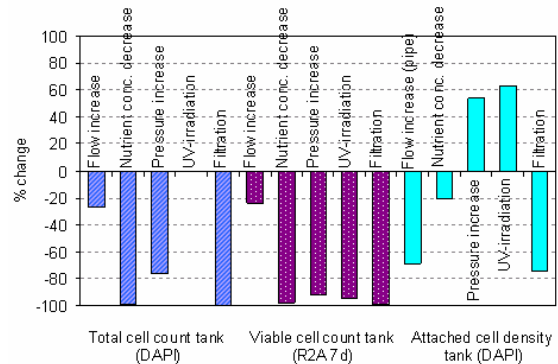

Figure 1. Changes in number of microbes in water hydraulic systems due to adjusted operational parameters and control treatments [3].

Experiments showed that biological or physical contamination can be reduced to acceptable levels in water to secure machine operation, when they are not simultaneously present in significant amounts. Based on the experiments, it is challenging to determine exactly the combined effect of particles and biofilm on a filter. Parallel experiments might contribute to statistical analyses, but, definitely, statistical analyses do not work well in this case because of the nature of microbial growth. For example enhanced microbial growth causes problems with determination of β(microbe)-value because of its bioreactor effect in the filter (Figure 2). That is, biologically active material together with water and suitable temperature promotes an environment for microbes to reproduce in filter cartridge.
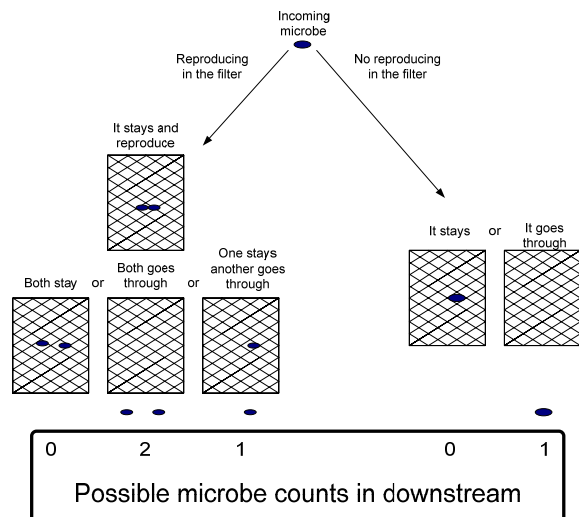

Figure 2. Bioreactor effect on a filter cartridge.

Because of the incomplete knowledge of both physical and biological system parameters, the working conditions of filters cannot be accurately predicted. Preventive maintenance requires more detailed data

about hydraulic systems than can be achieved even using pilot-scale systems in laboratory conditions.
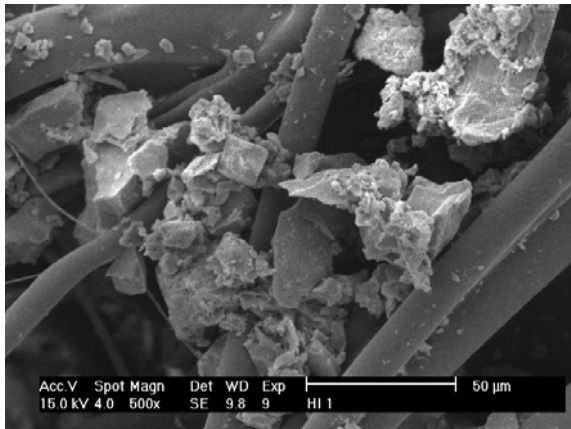

Figure 3. Particle and microbe contamination on filter fibres.

The best and only way to deal with filtering problems caused by both microbial growth and particles (Figure 3) is to use two-phased filtration and make sure that the system has minimum interface with the surrounding environment. A large filtering area ensures better long-term operation of filters, because abrupt malfunctions are more likely to happen with a filter system with a low dirt-holding capacity.

Water flow in valves [4]

Valve is a basic component in a hydraulics system. Its role is to control flow from a volume to another. It is therefore the place where lot of energy is dissipated to heat and makes the field worth of investigation. A seat valve is a good selection for water hydraulics, because low viscosity makes it essential to avoid leakage gaps in the valve structure. Seat valve is easy and cost-effective to manufacture to meet this requirement. Another challenge in water hydraulics is cavitation, which easily occurs in narrow channels of seat valve. Optimisation of the structure is the cure to solve this problem. The traditional method for the optimization, i.e. the product development, is to use prototypes, that however, is laborious and time- and energy-consuming process. The more effective expedient is to calculate flow through a structure and in a case of a complicated geometry, the method of computational fluid dynamics is usually used for this purpose.

The appropriateness and reliability of CFD for simulating flow of water in cavitating conditions in different seat valve structures are investigated with experimental measurements of flow rate, pressure distribution and cavitation occurrence. The experiments show the appearance location and path of travelling vapour produced by the cavitation phenomenon. The place, where cavitation is originated from, may be very minor and the process of the bubble growth is unsteady.

This makes the pressure measurement challenging, but in addition, increases risks of simulation errors. For instance, a corner in the seat, which is absolutely sharp in the model, causes the results not to show local pressure drop around the corner, whereas any chamfer on the corner brings it out. Figure 4 represents well the time dependency of the vapour cloud behaviour and the very local origin where the vapour is produced. At one moment, the chamber can full of vapour and at another, full of liquid.

Figure 4. Unsteady situation of cavitating flow.

The differences in the flow characteristics are diverse. Cavitation occurs with the smallest pressure drop over the orifice in valve of chamfered seat. On the other hand, the discharge coefficient of chamfered valve structure is bigger than that of sharp valve structure, which leads to conclusion that the cavitation sensitivity between these two valve types depends more on flow rate than just on pressure drop. The cavitation affects the chamfered seat valve lowering its discharge coefficient, but the performance of the valve with the sharp seat endures despite of vapour in the orifice.

Shape of poppet in a seat valve is mostly effecting on the direction and speed how the jet of vapour behaves in downstream side. This is meaningful considering the risk of damage caused by cavitation, if it can not be fully eliminated by the shape optimization.

Computational investigation of pressure distribution in the valve orifice shows the benefits of valve with multistage pressure drop. It reduces the risk of cavitation, but chamfer on a single corner of stage is still increasing it creating a local low pressure area. Figure 5 shows computational pressure distribution in a case of chamfered seat edge and figure 6 shows pressure distribution with correspondingly defined pressure boundaries when there are two edges instead of continuous chamfer. Clearly, there is no such a local small pressure area if the continuous chamfer surface is replaced with the separate edges. Thus, cavitation appearance is less probable in the latter case.
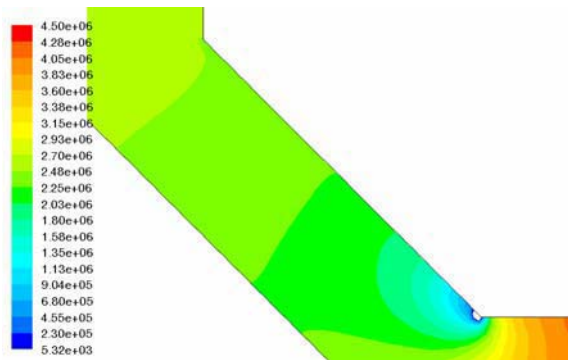
14

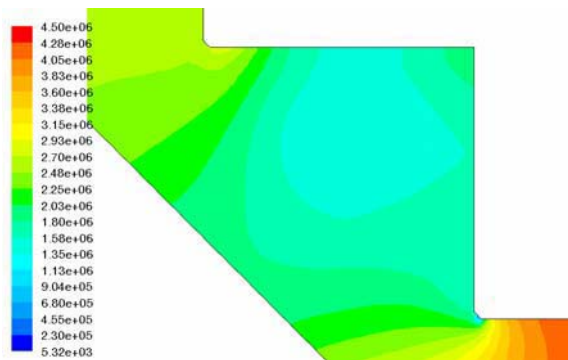Figure 5. Computational pressure distribution in chamfered orifice (Pa).

Figure 6. Computational pressure distribution in two-step orifice (Pa).

Even though there are uncertainties in the computational methods solving fluid flow in complicated valve structures, the benefits are undisputed. If thinking about hydraulics, its essence is basically interraction between fluid and solid parts. Combining the simulations of rigid body motions and the fluid dynamics (FSI, Fluid Structure Interaction) is a great opportunity to rise the modelling of hydraulics on to a new level. The availability of computational power is not anymore the limit. The only challenge is anymore the arrangement combinig of these two common modelling technologies in practice. Fortunately, the CDF software packages are developing to the direction making it possible.

Challenges with pumps [5]

The challenges of hydraulic pumps create a need for continued tribological research. One research area is the use of water hydraulics, particularly the use of variable displacement axial piston pumps, in the hydrostatic transmission of mobile machinery.

Axial piston pumps and motors are commonly used in hydraulic applications because of their compact size, wide operating range and controllability. On the other hand these types of pumps and motors are quite complex. To increase the overall efficiency of the system, variable displacement axial piston units are

widely used basic components in oil hydraulics nowadays. Axial piston type units are very competitive also in modern water hydraulic pumps and motors. In mobile machines most of the units are axial piston design at the moment. However, there are not commercial variable axial piston pumps or motors for water hydraulics, which is a significant problem in certain applications.

The aim of pump research is to study basic effects caused by the adjustment of the swashplate angle. At first, the attention is focused on measuring the water film thickness between the swashplate and the slipper pad and the forces affecting the piston while tilting the swashplate (Figure 7).
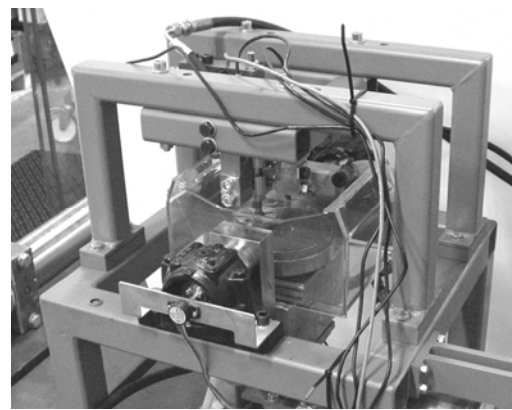

Figure 7. Water film thickness measurement test rig.

There are several different water hydraulic pumps on the market at the moment. Most of the pumps are oil lubricated piston pumps, which are driven by crankshaft mechanism. Only a few of the pumps are totally water lubricated. Water lubricated pumps are usually axial piston pumps with non-adjustable swashplate. Water as a pressure medium requires that all materials should be non-corrosive and all clearances are smaller than in oil hydraulic units.

Sliding pairs of the pumps are usually made of stainless steel and some type of reinforced industrial plastic, for example PEEK. All bearings are sliding because adequate ball or roller bearings are not yet available. Various materials have been tested in pumps in recent years and at least water hydraulic pumps with ceramic pistons are available. Because of the requirements of special design and materials, water hydraulic components, including pumps, are generally more expensive than oil hydraulic components. Costs are high also because of the amount of production is rather low. Usually maximum pressure level is 16 MPa but there is also at least one commercial pump with 21 MPa pressure level. Water flow of the pump varies from a few litres per minute to few hundred litres per minute. The pump body can be the same in pumps with different

displacements, the only difference being the angle of the swashplate. However, there is no variable displacement pump available on the market.

Control possibilities

Water hydraulic motion control is one of main focus points in research in TUT/IHA. The research of motion control means the research linear or rotary motion with components, control algorithms and controllers so, that the demanded steady state and dynamic characteristics are achieved. The control valves can be on/off –valves, proportional valves, servo valves or combination of any previously mentioned valves. The control algorithms needed are naturally very different in different system cases.

As an example of the water hydraulic controllability research, an on/off –control case can be mentioned (Figure 8). The idea is to use small, reliable and cheap mass production valves to implement a linear motion. There are several valves, which are controlled so that the best possible control accuracy and good dynamic characteristics can be achieved. The cost level of this kind of digital hydraulic system is only one fraction of a servo valve controlled system for handling the same operation.
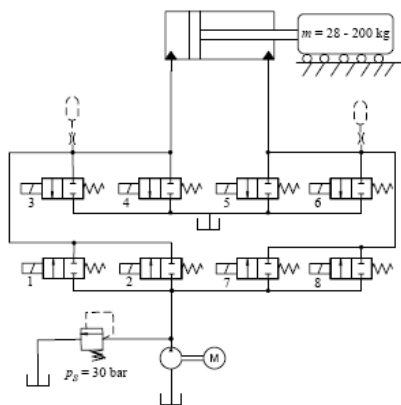

Figure 8. On/off –valve controlled water hydraulic cylinder [6].

New components are developed continuously in water hydraulics, because the variety of present components is still very small compared to oil hydraulics. During the last years, the development has concentrated on developing new control valves, but also some actuator and pump development projects can be found. As an example of resent development results, a new proportional valve presented in figure 9 can be mentioned [7]. The valve is developed by Finnish company Sitek-Palvelu Oy in cooperation with TUT/IHA. The valve enables to build accurate water hydraulic control systems cost-effectively.

Figure 9. New water hydraulic proportional valve for low pressures. (Sitek-Palvelu)

Control of water hydraulic manipulators and booms is also one research interest in IHA (Figure 10). In this work a hydraulic crane was equipped with water hydraulic components. A control system using two PID controllers plus a Feed Forward block (F-PID) was implemented, and in order to study the dynamic behaviour of this kind of system, a series of tests were performed. At first, a characterisation of the system (mechanical and hydraulic) was performed and then the different steps of the controllers design were analysed by means of various end-effector trajectories. The results show a very good behaviour of this kind of system with a low positioning error.

Figure 10. Water hydraulic boom with proportional control valves [8].

NEW APPLICATION AREAS

Mobile hydraulics

In the future mobile machines will also utilize water hydraulics more and more. At the moment there are only few commercial applications and some research projects related to the subject. One good practical example is Renova company in Gothenburg, Sweden [9], which is using water hydraulics in its waste packer lorry. Renova previously used 15,000 litres of hydraulic oil alone in a typical year which had to be purchased,

stored and disposed of. In contrast, water is literally 'on tap', doesn't create a slippery hazard when leaks occur (as hydraulic oil does) and is far easier to dispose of.

Forklift (reach truck) which is used as a research platform in this research is shown in figure 11 [10]. The work movements of the forklift are usually realized using oil hydraulics. In IHA's research forklift all the oil hydraulic components from the work hydraulics of the forklift have been replaced with water hydraulic ones and the main focus is in two work movements, which are lifting and reaching. In the original realization, there are also two other work movements which are shifting and tilting of the fork but lifting and reaching are the most significant and therefore those are chosen here. The driving transmission is electric. 10, 11)

Figure 11. Used research platform (forklift).

The goal of the study is to demonstrate how modern water hydraulics can be applied to mobile machines and to use this forklift as a research platform where developed condition monitoring system with different fault situations and different water hydraulic components with different material pairs and control systems are tested.

Very good future mobile application for water hydraulics is the lawn mover concept developed by Purdue University. For example the golf courses all over the world have very tight environmental regulations. The machines used in courses are creating great risk of leak of hot hydraulic oil.

Motion platform [11,12]

The motion platform developed in IHA will be used in real-time simulator construction that allows simulation of different vehicles with minimal changes. Figure 12 shows the construction of simulator. There are four standard PCs, one for simulation of vehicle (PC 1), one for control and position measurement of platform (PC 2), one for generating graphics (PC 4) and optional PC for main loop (PC 3). System is distributed through local

area network (LAN), using UDP (User Datagram Protocol) for communications. More detailed information about the simulator can be found in references 1) and 2).
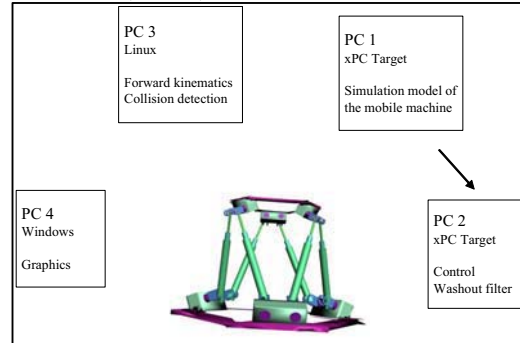

Figure 12: Structure of the simulator.

Commonly motion platforms of this type are used with either oil hydraulic or electric actuators. During the last ten years, water hydraulic control technology has been subject to an intensive research. The interest for an environmentally friendly technology with good controllability and high stiffness and force density has encouraged this development. The development of the water hydraulic motion platform combines water hydraulic research with the increasing interest of virtual technologies and virtual prototyping.

The structure of the platform is a common Stewart platform with six water hydraulic cylinder actuators. The diameter of the bottom plate is 1.2 meters and the diameter of the top plate is 1.0 meters. Actuators are 0.94 meters long on the shortest length. Distance between connection points is 0.16 meters and the mass of the top plate is about 100 kg without extra load.

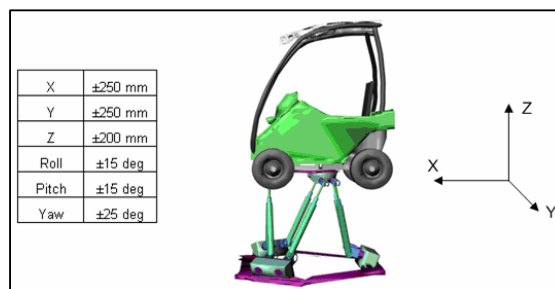Figure 13 shows the working area and the coordinate system of the platform.

Figure 13. Workspace and the coordinate system of the platform.

The working area of the platform in X and Y direction is ±0,25 m and in Z direction ±0,2 m. The rotating angles are ±15 deg and ±25 deg as shown in figure 13.

The platform is using low pressure proportional valves in the control of the platform. Due to characteristics of these valves, the performance of the platform is not as good as oil hydraulic one with servo valves.

CONCLUSION

It can be concluded that the main challenges for wider usability of water hydraulics are reliability, controllability and price level – and at the same time. Reliability means that the components have to be able to work longer periods without service and without big risk for brake. It includes the control of water quality so that the components can operate with optimal pressure fluid quality. It also includes the development of components' characteristics so that they are not sensitive for fluid quality, temperature, pressure peaks, cavitation, erosion and wear. And it also means having successful references, where water hydraulics is operation on demanding and long time tasks.

Controllability means that overall ability of water hydraulics to realize more accurate and dynamic control systems have to be improved. This can be done by developing better control valves, control methods and actuators. At the moment, fairly accurate position control systems can be achieved with low pressure by using servo valves or digital hydraulic controls. However, more challenges are in higher pressures (over 20 MPa), where the component supply is very limited. Also components and methods for realizing pressure controls are more needed in the future.

The price level of water hydraulic components is certainly one big challenge. Low pressure water hydraulics is offering one possibility to achieve cheaper costs by using cheaper materials like polymers. However, in general the biggest factors are more expensive materials and small production amounts. Even the components and systems are technically perfect, the price level still affects strongly to machine builders choices. Therefore increasing production amounts along with increasing practical applications, will slowly lead to decreasing price level of the components. And it is important that the machine builders remember always consider total costs for the whole system life cycle including purchase, use, disposal and fluid itself. In addition societal aspects like laws, environmental taxes, insurance costs etc. may also decrease water hydraulics' relative price level in fluid power market.

As a conclusion it can be stated that at present water hydraulics already have many possibilities for building motion control systems and in the future there will be even more, when technical level is still increasing. The major benefits – environmental friendliness and fire safety – are strong drivers for water hydraulics' future development.

REFERENCES

1. Web page, www.bp.com

2. Riipinen, H. 2008. *Life in the water hydraulics system.* DrTech dissertation. Tampere University of Technology. Tampere University of Technology Publications 716. 54 p.

3. Soini, S. M. (2002) *Microbial Ecology and Control in Water Hydraulic Systems.* DrTech Dissertation. Department of Environmental Technology, Tampere University of Technology. Tampere University of Technology Publications 361. 79 p.

4. Leino, T. 2008. *On the flow and cavitation characteristics of water hydraulic seat valve structures.* DrTech dissertation. Tampere University of Technology. Tampere University of Technology Publications 722. 131 p.

5. Rokala, M., Kalonius O., Koskinen K.T., Pietola M., *Tribological conditions between swashplate and slipper pad in water hydraulic axial piston unit test rig with variable swash angle.* 6th international fluid power conference, Dresden, 2008.

6. Linjama, M., Koskinen, K., Tammisto, J.& Vilenius, M. 2000. *On/off position control of low-pressure water hydraulic cylinder using low-cost valves.* In: Laneville, A. (ed.). Proceedings. Sixth Triennal International Symposium on Fluid Control, Measurement and Visualization, FLUCOME 2000, August 13-17, 2000, Sherbrooke, Canada 6 s.

7. Sairiala, H., Koskinen, K. T., Vilenius, M. 2004. Proportional Valves in Low-pressure Water Hydraulics. In: Codina Macia, E. et al. (Eds.). Proceedings of the 3rd FPNI-PhD Symposium on Fluid Power, Terrassa Spain, June 30-July 2, 2004 s. 501-508.

8. Bruno, S., Sairiala, H. & Koskinen, K.T. 2006. *Analysis of the behaviour of a water hydraulic crane.* International Journal of Fluid Power 7 2, pp.29-38

9. Waste management world, January 2007.

10. Krogerus T., Sairiala H., Koskinen K.T., *Water hydraulic fork lift with intelligent condition monitoring.* 51st National Conference on Fluid Power, Las Vegas, Nevada, 11-15 March 2008.

11. Rokala, M., Palonen T., Sairiala H., Koskinen K.T., *Control system development for the water hydraulic 6-dof motion platform.* 10th Scandinavian International Conference on Fluid Power, SICFP'07, Tampere, Finland, 2007.

12. Sairiala H., Rokala M., Koskinen K.T., *Control and Actuator Synchronization of Water Hydraulic 6-DOF Motion Platform.* 51st National Conference on Fluid Power, Las Vegas, Nevada, 11-15 March 2008.

K-3

BOSCH REXROTH AND BOSCH REXROTH JAPAN ACTIVITIES IN INDUSTRIAL HYDRAULIC SYSTEMS

Stefan Sacre, Dr,Eng.

President of Bosch Rexroth Corporation
5-1 Higashi-nakanuki Tsuchiura-shi, Ibaraki, 300-8588 Japan

ABSTRACT

Bosch Rexroth (BR) is worldwide player in hydraulics. And we are approaching each country to meet with local requirements. Japan is one of our target markets. Bosch Rexroth Corporation (BR-Japan) is strong position in Japan for mobile applications. In parallel, industrial is also our important profitable market. This paper presents BR and BR-Japan activities in industrial application, especially steel, press, test machine, marine, power generation. Additionally new products and system are introduced.

KEY WORDS

Innovative products, Open interfaces, electrohydraulics, multi-technology,

COMPANY   INTRODUCTION

Bosch Rexroth AG looks back across 200 years of tradition and has always successfully mastered its current challenges. Thus the company is among the oldest companies active worldwide. Bosch Rexroth sees in this the obligation to continue this history of success with innovations and customer orientation.

With approximately 33,000 employees, Bosch Rexroth AG earns approximately 5.5 billion Euros in revenue. For years, the company has been growing at above-market rates in Asia and Eastern Europe, and in the traditional industrial markets it has been gaining market share. For many years, the quotas for research & development and investments have been above the industry average and they have laid the foundation for further profitable growth.

As a global player, Bosch Rexroth is represented on location in more than 80 countries with production locations, sales and service offices, and dealers. In a worldwide manufacturing network, the control concept proved at Bosch guarantees reproducibly-high quality with local content. From an organizational standpoint and in its business processes, Bosch Rexroth combines user experience with expertise on location. 67 production locations in 25 countries, own sales and service in 39 countries

Rexroth brand combines a broad product portfolio that includes all essential drive and control technologies, from individual components through to system solutions, and the ability on this basis to offer integrated automation solutions with superior functions. In both individual technologies and for multi-technology solutions, Bosch Rexroth combines best-in-class products with extensive consulting expertise. Here Bosch Rexroth combines technological and economic benefits for the customer: supply from one source reduces interface costs and simplifies the customer's processes from project planning to purchasing, logistics, and start-up through to service. This reduces costs across the entire lifecycle. Bosch Rexroth is the technology and market leader for Drive & Control.

Bosch Rexroth offers automation solutions for industrial and factory automation, mobile applications, and individual projects (platform technology, steel

construction for hydraulic engineering, entertainment, offshore, etc.). Thus Bosch Rexroth is active in worldwide growth markets with high innovation potential. For its approximately 500,000 customers, Rexroth develops and produces standard components with high configurability and variance as well as complete system solutions with extensive software expertise

COMPANY   PRODUCTS

Bosch Rexroth's product range covers the entire spectrum of motion technology: hydraulics, electrics, pneumatics in conjunction with mechanics and the associated control technology. Only the specialist Rexroth offers all drive & control technologies and integrates them into complete automation solutions.

INNOVATIVE   PRODUCTS

Technology
For Bosch Rexroth, technology leadership in automation means shifting the boundaries of the technically-possible so that the user can be more productive. Best-in-class components form the basis. But the full customer benefit lies only in the combination of application experience and the modular design of the Bosch Rexroth automation system. Electrohydraulics in new dimensions are field bus-capable, highly-dynamic, and positioned with μm precision. Electropneumatics combine digital regulation technology with robust mechanical technologies. Integrated measuring systems and the ready-to-connect, pre-configured Cartesian motion system show how

much progress mechatronics has made. The open controls combine an extremely high motion quality consistently with an open SPS for scalable motion-logic integrations.

Figure 2   Innovative products
1) Digital regulation electronics with NC functionality HNC 100 2X
2) Roll rail guide with integrated measuring system
3) Electropneumatic pressure regulation valves
4) Bosch Rexroth IndraMotion with integrated motion control and SPS
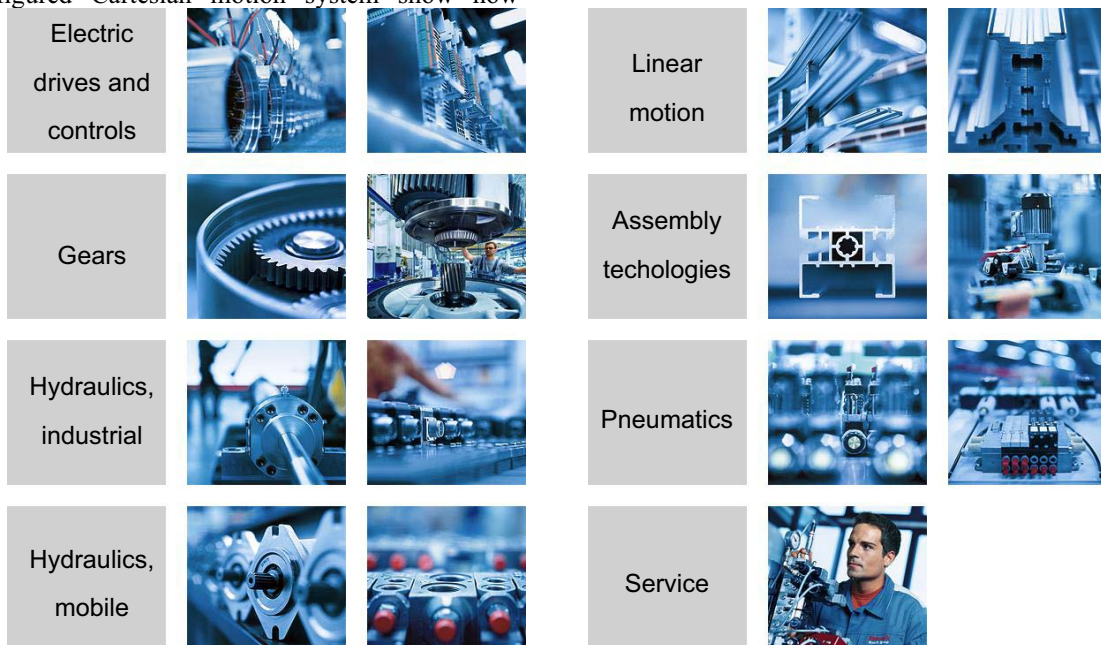
Figure1   BR products

Openness

Bosch Rexroth drive and control technology consistently supports open interfaces that are defined in international standards.

Both for application programming according to IEC61131-3 and for communication between control and drives via SERCOS, international standards are used.

Bosch Rexroth also continues this openness during the introduction of Ethernet-based communication in industrial automation with SERCOSIII according to IEC62410.

This allows easy incorporation into the end customer's IT systems as well as the hard real-time communication between controls and drives.

Figure 3   Digital controller with open interface

Industrial hydraulics: the key products
1) Pumps and motors
Axial pistons, interior gears, exterior gears, radial pistons, tendon cells, etc. Pump combinations and compact units (finished components)
2) Cylinders
Tie-rod cylinders, round cylinders, servo cylinders with hydrostatic bearings and special cylinders. Up to 45 m in length user-related systems for many industries
3) Compact hydraulics
Magnetically-operated globe valve and slide damper, proportional valve with customized electronics, block models in aluminum or steel blocks
4) Industrial controls
Control valves, continuous valves, control electronics, control and regulation systems as well as valve plates Product and system technology. Solutions for every conceivable use case
5) Assemblies and accessories
Small assemblies, customer-specific assemblies, and large assemblies for nearly all applications
6) Gears, pitch and azimuth drives for wind energy installations
Generator gears for systems with output ratings from 660 to 5,000 kW, plus pitch and azimuth gears.

Figure 4   Hydraulics, Industrial application

SUCCESS PROJECT IN THE MARKET

Dubai Maritime City, Dubai
Bosch Rexroth gives a new meaning to the term "ships of the desert". Since April 2007, an automation project in Dubai, planned and supplied by Bosch Rexroth, has been hoisting oceangoing ships weighting up to 3,000 tons from the sea and transporting them overland to the maintenance and repair docks. Construction work has already begun on a second ship lift for even larger ships measuring up to 130 meters in length and weighing up to 6,000 tons.

Fourteen electric winches work in the first lift. Working in unison, they raise a platform under the ships at a rate of 30 cm/min. Within 40 minutes, the raising process is completed and a powerful wheel tractor with hydrostatic drive then pulls the ships over a rail transfer system to a dry dock.

Figure 5   Ship maintenance and repair docks

Bosch Rexroth won the contract for the two automation projects in a global bid for tenders with a tailor-made concept, and accepted responsibility as prime contractor for the complete process of project planning, supply and commissioning. The climatic conditions encountered in Dubai placed extreme demands on the technology. Burning sun and temperatures up to 50 degrees Celsius, sandstorms and very high humidity.

For the 14 winches in the first ship lift, Bosch Rexroth employed IndraDrive frequency converters with a maximum current draw of 210 amperes. In Dubai, they work with a torque of 150 Nm and still have power reserves. The maintenance-free asynchronous servomotors have a very high power density. Two redundant brakes, a holding brake integrated into the motor and a brake on the winch are each capable of securely holding the maximum weight, enhancing operating safety. The second ship lift will use a total of 28 winches to raise ships weighing up to 6,000 tons.

Rexroth's Linux-based control system with its tailor-made user interface synchronizes the drives with extreme precision. The maximum deviation between any two winches is less than 0.1 mm, an important condition for preventing the ships from slipping. Before the start of operations, the automation solution technically approved by a Lloyd's certification in accordance with the internationally accepted rules and regulations of Lloyd's Register, EMEA.

The Three Gorges Dam, China

Behind these lock gates there is a man-made reservoir, 663 kilometers in length. The Three Gorges Dam in China, in the central section of the Yangtze River, exceeds all normal dimensions. As the world's largest water engineering project, it generates 88,700 gigawatts of current, effectively reducing CO_2 emissions by 100 million tons per year. The surface of the reservoir is twice as large as that of Lake Constance.

On the left flank of the 2,310 meter long dam, two separate waterways bridge the height difference of up to 101 meters in a series of five locks. The lock chambers, 208 meters long and 34 meters wide, are capable of taking ships weighing up to 10,000 tons.

Rexroth planned the drive and control technology for the lock gates at the top of the locks on the reservoir side. These are especially critical when it comes to safety. While the bottom gates only ever have to hold back the water in the chamber, the top gates have to reliably hold back the whole reservoir. Rexroth designed the drive cylinders for the gates with a corrosion-resistant steel structure. The CERAMAX coating reliably protects the piston rods against wear and corrosion for their entire service life.

All around the world, Bosch Rexroth has supplied automation for more than 200 locks and is unrivaled in its expertise in this field. This was impressively demonstrated by the commissioning of the Three Gorges Dam. The Drive and Control solution immediately worked with a maximum of reliability.

Airbus A380, France, Spain, UK, Germany

Size does matter! The Airbus A380, capable of carrying 555 passengers, is the world's largest passenger plane, and even on the ground it challenges for new records. France's TLD developed the TPX 500 S aircraft tractor with a Rexroth hydraulic power unit specifically for the flying giant.

The tractor has no towbar, which makes the job of coupling the aircraft to the tractor vastly easier. The vehicle has a U-shaped tail end. It reverses up to the nose landing gear of the A380 and encloses the front wheel. Hatches then lock into the framework of the front landing gear. The push blade then moves forward and fixes the wheels to the hatches. The towing tractor then lifts the nose landing gear - and as such the aircraft itself - to transport it. Even though Airbus engineers limited the weight of the new giant aircraft to a fully laden 600 tons, that is still some 50 percent more than today's long-haul aircraft.

In contrast to working with a towbar, the TPX 500 S can be operated by just a single person. The driver has a direct view of the aircraft's landing gear. Complex maneuvering with heavy towbars and couplings, always prone to accidents, is now completely redundant. With this "piggyback" technique, TLD has simplified and accelerated the whole process considerably. Moreover, the locking mechanism on the TPX 500 S has absolutely no play, protecting the nose landing gear and allowing it to assume all transport tasks. This innovative solution guarantees considerably smoother acceleration and

Figure 6   Dam gate

Figure 7   Airbus A380

braking maneuvers. This is appreciated by both the landing gear and the passengers.

In order to make the towbar-less aircraft tractor powerful enough for the A 380, TLD worked in close cooperation with Rexroth on the development and design of the hydraulic power unit. The hydraulic power unit reliably supplies the required power for the 600-ton giant by means of two axial piston double pumps and two axial piston variable displacement motors with a power rating of 583 kW. In addition, Rexroth also reduced the number of lifting cylinders. This allows the TPX 500 S to fulfill the constantly increasing demands of end users with regard to improved reliability and longer service life. Together with Rexroth specialists from France, TLD completed the development in less than 12 months from the start of the project to the first delivery.

Great Beijing Wheel, China

In China's capital city, a new ferris wheel will break all world records in 2008/2009. Up to 5,760 passengers per hour will be able to enjoy the view across Beijing from the 200 meter high glass cabins. The control and drive solutions were planned and supplied by Rexroth. As the exclusive partner for the operator, the Great Wheel Corporation, Rexroth has thus developed the blueprint for many more ferris wheels.

The Great Beijing Wheel has a total height of 208 meters. The diameter of the wheel is 198 meters. The drive hydraulics comprise four drive units, each with two double redundant motor/pump combinations. Each drive unit supplies a drive module, each with 8 hydraulic motors. A total of 32 special wheels press against the running surface on the ferris wheel. In addition, the hydraulics regulate the pressure of the wheels via variable cylinders. In rain and humid conditions, the cylinders increase the pressure to compensate for any slip of the wheels against the running wheel. Here, the force regulation system and the absolute measuring system integrated in the cylinders (CIMS) work together.

Besides the primary drive system, Rexroth also planned the fully automated boarding system that enables the passengers to board and disembark without the ferris wheel having to stop moving. Driverless electric feeder vehicles at the ground station move alongside the cabins. At the starting point, the doors open and within the space of 40 seconds, the passengers get out on the one side and after a short delay the new passengers get in on the other side. The higher-order control system synchronizes the feeder vehicles (which are driven by Rexroth's IndraDrive frequency converters) with the cabins.

In addition to the project planning, delivery and commissioning of the control and drive technology, Rexroth is also responsible for the entire maintenance of the ferris wheel. Here, Bosch Rexroth is basing its work on the processes employed in the aerospace industry. After 16 hours of operation, the maintenance staff have 8 hours to perform all maintenance operations. Here, the visual inspection of the construction elements of the ferris wheel is a major operation.

Figure 8   Great Wheel in Beijing

Bolshoi Theater, Moscow

The largest single contract in the history of Bosch Rexroth is associated with one of the most famous stages in the world. Rexroth is the general contractor modernizing the complete stage technology, including the steel structures, of the Bolshoi Theater in Moscow, a UNESCO-listed site.

Only the very latest in stage technology will be used. The hydraulic pressure station, with a capacity of 50,000 liters and an output rating of 700 kW for the understage machinery, is able to move 7 giant stage podiums at once − a solution found nowhere else on Earth. For the overstage machinery that moves the complete set, Bosch Rexroth is installing 72 electromechanical winches as stage suspension barrels and 81 electromechanical winches as point hoists. Each winch has a capacity of 1,000 kg. Numerous other drives move the curtain, the lighting bridges, microphones and take on the many minor tasks that are necessary for the perfect performance. All drives and motors work extremely quietly so as not to disturb the artistic enjoyment.

Safe operation of all the technical equipment on the stage is provided by the Rexroth SYB 2000 stage control system, which has proven itself to be extremely reliable and easy to operate in many of the world's opera houses. In addition, Rexroth supplies all the audio and video equipment - from the microphones to the
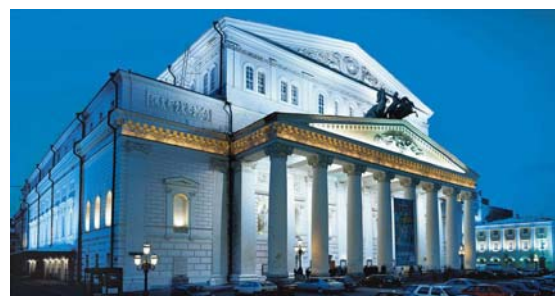

Figure 9   Bolshoi

complete television studio, and is responsible for the entire steel construction needed for the equipment. And then the Bolshoi will unite tradition with the latest technology.

renovation work is scheduled to be completed in 2008.

Environmental friendly application
For worldwide environmental friendly technologies, Bosch Rexroth also support for these application.

One of typical application is Wind energy. Bosch Rexroth makes wind turbines more efficient – thanks particularly to the technological advantages on hydraulics in terms of high power density in limited space, low-maintenance and rugged design and, not least, outstanding controllability. Bosch Rexroth offers Pitch control, drive train brake, yaw system and subassemblies of power units, motor-pump group, accumulators and filter and cooler.

Another technology is marine two cycle diesel engine control system. Marine application also should consider exhaust emission control and low consumption. One of the solution is electro-controlled engine by controlling of the fuel injection profile and exhaust valve lift. Bosch Rexroth can offer the electro-hydraulic control system for this kind of technology.

CONCLUSION

The Rexroth Automation System integrates hydraulic, electric, and pneumatic drive technology, scalable control technology, and high-performance engineering tools by Bosch Rexroth into an automation system. This reduces significantly the integration effort in our customers' systems and enables our customers to use the optimal drive and control technology for the process.
In addition, Bosch Rexroth products support all relevant communication systems for industrial automation worldwide, which enables the easy integration of Bosch Rexroth products into the systems of machine manufacturers in the triad.
We believe with best-in-class components and their easy but high-performance integration into our customers' machines and systems, Bosch Rexroth can offers the best solution in terms of both function and economy.

Figure 10   Wind power

Figure 11   Marine engine

K-4

E-DEFENSE AND ITS HYDRAULIC POWER SUPPLY SYSTEM

Keiichi OHTANI*

*Guest Researcher, National Research Institute for Earth Science and
Disaster Prevention
(Home) 3-20-13-501, Naka-Cyo, Koganei, Tokyo, 184-0012 Japan
(E-mail: keiichi_ohtani@yahoo.co.jp)

ABSTRACT

The Hanshin-Awaji Earthquake (January 17,1995) clearly demonstrated that the occurrence of very strong ground motion in the area near to the seismic faults is capable of causing severe structural damage beyond general estimation. It has emphasized the importance of earthquake engineering research into why and how structures collapse in real earthquake conditions. Considering the lessons learnt from recent earthquake disasters, National Research Institute for Earth Science and Disaster prevention (NIED) plan to construct the 3-D Full-Scale Earthquake Testing Facility (E-Defense is the nickname of this facility), which will be able to simulate the process of destruction of structures under the condition of real strong earthquake motions. The basic performances of E-Defense are maximum lording capacity 1,200 tons, maximum velocity 200 cm/s and maximum displacement 2 m p-p for two horizontal excitations and maximum velocity 70 cm/s, maximum displacement 1 m p-p for vertical excitation to realize destructive ground motion. The driving energies are mainly produced by the hydraulic power system, which is consisted 10 horizontal actuators, 14 vertical actuators, 20 main-accumulator units, 4 gas-engine units, oil supply system (include piping system) and others. The construction has begun at early 2000, five year after the Hanshin-Awaji Earthquake and was completed at the beginning 2005, ten year after that Earthquake.

KEY WORDS

Hanshin-Awaji Earthquake, 3-D Shaking Table, Structural Failure Mechanism
Hydraulic Power Supply System, Experimental Research

INTRODUCTION

The Hanshin-Awaji Earthquake (Hyogoken-Nanbu Earthquake, January 17, 1995) clearly demonstrated that the occurrence of very strong ground motion in the area near to the seismic fault is capable of causing severe structural damage beyond general estimation. The destructive earthquake occurred in the worldwide in the recent years.

In order to reduce the hazards associated with large earthquakes, it is essential to improve the reliability of earthquake resistance estimations and reinforcement methods in the construction of urban and major structures. For this purpose, failure mechanisms and collapse processes of various kinds of full-scale structures must be investigated. Many types of experimental apparatus have been used for such investigations, and some of them as large size as possible to alleviate any difficulties arising from limitation of the model. Considering the lessons learnt from recent earthquake disasters, the National Research Institute for Earth Science and Disaster Prevention

(NIED) planned to construct a new three-dimensional, full-scale, earthquake testing facility, which can carry large-size soil and structure models and reproduce the processes of structural failure. This facility is expected to become a powerful tool for international collaboration in earthquake engineering research. It also requires international cooperation to successfully complete the facility and to use it effectively for engineering purposes.

The construction of facility has begun at early 2000, five year after the Hanshin-Awaji Earthquake and was completed at the beginning 2005, ten year after that Earthquake.

E-DEFENSE (3-D FULL-SCALE EARTHQUAKE TESTING FACILITY)

Based on the lessons learnt from Hanshin-Awaji earthquake, the Minister of State for Science and Technology was inquired to the Council for Aeronautics, Electronics and Other Advanced Technology, which is the one inquire organization of the Minister, for the discussion of the effective arrangement or research bases for earthquake disaster mitigation at March 29, 1996. The Council was reported to the Minister at September 3, 1997.

The report clearly pointed out the arrangement of large-scale three-dimensional earthquake simulator facility as the core facility of research bases for earthquake disaster mitigation.

NIED initiated the project on the large-scale three-dimensional earthquake simulator facility just after the occurrence of Hanshin-Awaji earthquake. The research and development for core technology for this facility (E-Defense) was started on 1995. The fundamental concepts of this project were based on the report by the Council.

The E-Defense was constructed as the core facility of the research bases for earthquake disaster mitigation. Therefore, we need to clear the positions of the E-Defense.

1) Position of earthquake simulator for the main element of the "Time-Space Domain Simulation System for Earthquake Disaster".
2) Position of the clearly understanding of failure mechanism of structures.
3) Position of response mechanism for the request from major subject of earthquake engineering.

The importance of promoting the strengthening and rationalization of earthquake-proof structural design is just one of the lessons from Hanshin-Awaji earthquake. Because earthquake vibrations involve three-dimensional movement, it is necessary to set up a three-dimensional earthquake simulator facility to accurately reproduce earthquake motions. To perform tests on real-size objects or large-scale models of test structures and foundations, it is desirable to have the large-scale three-dimensional shaking table. If large-scale 3-dimensional shaking table is available, tests could be performed to shed new light on the mechanism of dynamic failure using real-size structures. If a stage reached whereby design based on such discovery can be performed, this will contribute immensely to reducing earthquake disasters.

The main specification of E-Defense is shown in Table 1. The limit performance for horizontal and vertical axes is shown in Fig. 1. The basic performances of E-Defense are maximum lording capacity 1,200 tons, maximum velocity 200 cm/s and maximum displacement 2 m p-p for two horizontal excitations and maximum velocity 70 cm/s, maximum displacement 1 m p-p for vertical excitation to realize destructive ground motion.

Table 1 Main Specification of E-Defense

3-D Full-Scale Earthquake Testing Facility		
Payload	12MN(1200tonf)	
Size	20m × 15m	
Driving Type	Accumulator Charge Electro-Hydraulic Servo Control	
Shaking Direction	X·Y – Horizontal	Z–Vertical
Maximum Acceleration (at Maximum Loading)	>900cm/s²	>1,500cm/s²
Maximum Velocity	200cm/s	70cm/s
Maximum Displacement	±100cm	±50cm
Maximum Allowable Moment	Overturning Momnet	Yawing Moment
	150MN·m	40MN·m
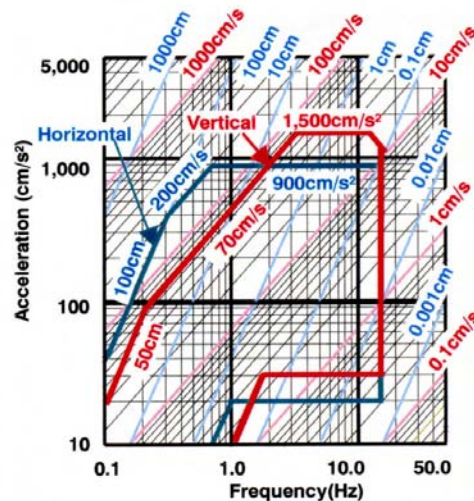
Fig. 1 Limit Performance of E-Defense

CONSTRUCTION AND MANUFACTURING OF E-DEFENSE

NIED have commenced the development work of shaking mechanism with very large size hydraulic actuators in fiscal year 1995 and completed

performance tests successfully in 1998. Following above technical development and surveys in earthquake engineering and related fields, NIED have began the design and construction of E-Defense in 1998.

Fig. 2 shows the drawing bird eye view of E-Defense.

Fig. 2 Layout of E-Defense

We were constructed several buildings, such as laboratory building, measurement and control building, hydraulic oil unit building, preparation building and so on. The 3-dimensional shaking table was installed in the laboratory building. Hydraulic oil will be supplied to shaking table by oil pipelines via underground culvert. The reaction foundation (shaking table foundation) has weight of about 2 GN (200,000 tonf) and set to the bedrock directly.

Following the construction of shaking table foundation, we constructed the laboratory building and other buildings. The laboratory building is 60 m X 85 m in plan and 45 m height and has two sets of 400 tons crane. For the construction of large space frame, we developed and applied new construction methods, such as the sliding construction method for roof members using permanent traveling crane structure, and the large panel method of external wall by steel frame and sandwiches panel.

The construction work has begun in 1998 and completed at the beginning of 2005. The E-Defense is constructed in "Miki Earthquake Disaster Memorial Park", which is being constructed in Miki city, on the north of Kobe city.

The manufacturing of the testing equipment, such as actuators, 3-D link joint, oil power pump unit, accumulator unit and so on, were also started in 1998. By the condition of construction site, where is located at the hill area, the weight and length of manufactured unit are limited some size by the condition of transportation. The set-up working will be done at the site.

HYDRAULIC POWER SUPPLY SYSTEM

The greater part of experimental equipment of E-Defense were composed by the hydraulic power supply system, such as shaking table, actuators (including servo-valves), 3-D link joint, oil piping, accumulator unit, main oil pressure pump unit, oil tank, oil filter and so on. We also installed the control system, measurement system and others. Here, we described the outline of hydraulic power supply system. The specifications of hydraulic power supply system were mentioned each equipments for the far side from shaking table. Fig. 3 shows the outline drawing of hydraulic power supply system.
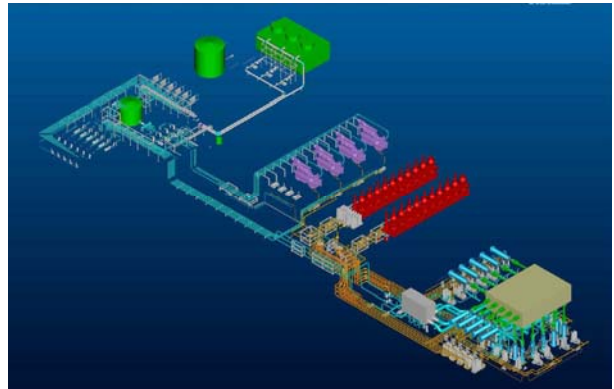
Fig. 3 Outline of Hydraulic Power Supply System

Oil Tank
Storage capacity 205 kL (This amount is only 30 % of total oil storage amount (750 kL). Remaining amount of oil was storage in the oil piping.)

Oil Piping
The total length and total weight of oil piping were 13 km and 1,200 ton, respectively. The maximum diameter of high pressure oil piping and low pressure oil piping were 350A and 1000A, respectively. By the advantage of flushing work of pipe inside, we used the non-welded flange method for the connection of these piping, which is consisted by the groove, retain ring and seal ring.

Main Oil Pressure Pump Unit
We installed 4 units of gas engine of 4000 Hp for the power-driven machinery of main oil pressure pump unit. These gas engines are derived 48 units of oil pressure pump and can generated 30,000 L/min (oil pressure: 20.6 MPa) of pressured oil. The reason of selection of gas engine was the consideration of environmental problem. We use the natural gas for minimize the nitrogen oxide and other noxious gas in exhaust fumes.

Accumulator Unit
This unit serve for the temporally storage of pressured oil. We installed 20 units, which storage capacity of each unit is 1,000 L, total capacity is 20,000 L. These 20,000 L of high pressured oil and oil from main oil pressure pump were combined and supplied to actuators

by the maximum flow late of 4,000 L/s.

Actuators

We installed 10 actuators for horizontal directions (5 actuators for X and Y axes, respectively) and 14 actuators for vertical direction. Each actuator has the driving force of 4,410 kN (450 tonf) and is derived by the electro-hydraulic servo control system. The maximum velocity 200 cm/s and maximum displacement 2 m p-p for tow horizontal excitations and maximum velocity 70 cm/s and maximum displacement 1 m p-p for vertical excitation to realize destructive ground motion by these actuators. The actuators were installed between the 3-D link joint and the shaking table foundation.

Servo Valves

The actuator was installed servo valve(s) for the control of the exciting movement. The maximum flow late of servo valve is 15,000 L/s. Each horizontal actuator has 3 units of servo valve (total maximum flow late: 45,000 L/s). Each vertical actuator has 1 unit of servo valve.

3-D Link Joint

Each 3-D link joint was installed between the shaking table and each actuator. The actuator should be move only on axial direction. The shaking table will be driven three-dimensional movement, therefore, we need to install the 3-D link joint.

Shaking Table

The size of shaking table is 20 m X 15 m X 5.5 m and the weight of itself is 775 tonf. It is impossible to transport such huge and heavy shaking table from the factory to construction site. Then, we made 32 blocks at the factory and transported them to the site. Next, we were conducted the assembling work at the site. Finally, the assembled shaking table was set in the pit by using the 2 sets of 400 tons crane.

CONCLUDING REMARKS

Based on the lessons learnt from Hanshin-Awaji earthquake, we, NIED, recognized to need more research to understand the failure mechanism of different kind of structures during earthquake. For this research needs, we conducted the construction project of E-Defense (3-D Full-Scale Earthquake Testing Facility) and completed on the beginning of 2005, just 10 years after the earthquake.

We already started the several research projects. Ministry of Education, Culture, Sport, Science and Technology (MEXT) was established the 5-year special project on "Seismic Hazard Mitigation in Megalopolis areas" in the fall of 2002. We started to the research program under this special project, which are (1) Experimental study on Reinforced Concrete Structures, (2) Experimental study on Liquefaction of Ground, (3) Experimental study on Wooden Structures and others. The large-scale model experiments for these 3 topics were conducted in 2005 and 2006.

In September 2006 NEES/ E-Defense meeting in Kyoto and Kobe built upon groundwork laid for collaboration. NEES is the special project for earthquake engineering sponsored by the US National Science Foundation (NSF). More than 100 attendees discussed the capabilities of NEES and E-Defense facilities in a program overview, and spoke of collaborative research in the area of steel buildings, bridge structures, wood structures, geotechnical study, and concluded the establishment of NEES/E-Defense Research Partnership.

We strongly hope that this tool is contributed to the dramatic progress of the earthquake engineering research, especially the understanding of structural failure mechanism, the progress of earthquake resistant design of structures and the evaluation/reevaluation of structural performance during earthquake, by the coordination and collaboration research works in the worldwide bases.

REFERENCES

1. Ogawa, N., Ohtani, K., Katayama, T., Shibata, H., World's Largest Shaking Table Takes Shapes in Japan – A Summary of Construction Plan and Technical Development-, SMiRT 15, 1999.
2. Ohtani, K., Ogawa, N., Katayama, T., Shibata, H., Nakagawa, O., Ohtomo, T., World's Largest Shaking Table Takes Shapes in Japan (The 2nd Report), SMiRT 16, 2001.
3. Ohtani, K., Ogawa, N., Katayama, T., Shibata, H., World's Largest Shaking Table Takes Shapes in Japan (The 3rd Report), SMiRT 17, 2003
4. Ogawa, N., Ohtani, K., Katayama, T., Shibata, H., Construction of a three-dimensional, large-scale shaking table and development of core technology, Bulletin of Phil. Trans. R. Soc. London, A(2001)359, pp.1725-1751.

K-5

ADVANCES IN MINING AND CONSTRUCTION MACHINERY THROUGH COMPUTERIZATION

Takao NAGAI*

*General Manager, Marketing and Support Department
AHS Division, Komatsu Ltd
2-3-6 Akasaka, Minato-ku, Tokyo, 107-8414 Japan
(E-mail: takao_nagai@komatsu.co.jp)

ABSTRACT

Recently developed construction machinery continues to advance from machines only capable of performing a stated task or function to machinery that provides automatic feedback regarding where and how the equipment is being used and the unit's current status. A number of such construction machines equipped with optional computerized construction features have even proved capable of interpreting construction designs and automatically regulating tools such as bulldozer blades. These new developments have led to conventional approaches to construction - such as continually interrupting operations in order to take measurements and check the project's finished status - no longer being necessary, thereby allowing for extremely effective and streamlined operations. In this study I will present specific examples of the application of this information technology to construction machinery and consider how such construction machinery will continue to advance.

KEY WORDS

Asset management, Remote operation, RTK-GPS, 3D-MC, Autonomous Haulage Sytstem

Use of IT in Construction and Mining Machinery

As shown in Figure 1., the increasing use of IT in construction and mining equipment can be viewed in terms of adding IT as part of electronic control of such machinery, and use of IT in support of this machinery or in aiding users' operating activities. Use of a core IT infrastructure allows for overall control to be brought to bear by working in close coordination, thereby differing markedly from conventional machines whose function is limited by only having access to onboard installed equipment. This paper will introduce a monitoring function that uses the internet and mobile communications, as well as mining and construction machinery that combine computerization and high accuracy GPS systems with automatic control functions. Due to these intelligent mining and construction machines operating in response to electronic signals and construction designs, they can even be referred to as robots in a broad sense of the meaning.
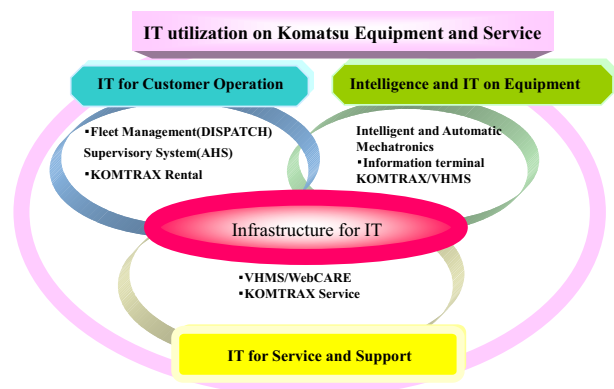
Figure 1 Use of IT in Construction and Mining Machinery

Remote Operating Control of Mining and Construction Machinery

Testing aimed at transmitting data regarding status and position of mining machinery equipped with onboard GPS and communication devices has been ongoing for several years now. In 1990 the U.S. company, Modular Mining Systems, successfully remotely operated a large capacity dump truck and loader within a mine from the company's offices using a computer and wireless LAN transmission system, with the computer sending optimized dispatch orders that were reflected on the truck's onboard monitoring screen with the operator being able to track the machine's status by viewing the data being transmitted back to the office's computer. Despite this success, however, as the use of construction machinery differs from that of mining machinery - such as the unrestricted nature of operating location - this means control by wireless LAN is an unrealistic option for the construction industry. This therefore required the development of a system with the ability to transmit wireless data at low cost while being capable of covering an extensive area.

As the use of mobile phones continued to expand, this heightened expectations for the development of such a data transmission service, leading to the drawing up of an initial concept for this system. At the time in 1995, however, in considering the high cost of mobile phones, usage fees, and poor coverage rate in areas of low population, it was decided that their use would be overly prohibitive, therefore requiring the adoption of an alternative service.

1999 saw the launch of a satellite-based data transmission service from ORBCOMM, and this was subsequently tested as part of an equipment monitoring system for construction machinery by Komatsu - marking the start of development of the KOMTRAX system. This study will introduce the KOMTRAX system and subsequent development of construction machinery that utilize the system.

Radio Controlled Unmanned Construction

Radio control is one of the earliest attempts to integrate information and communication technology with operation of construction machinery. In 1992 a high accuracy GPS and radio control device were integrated as part of an unmanned construction system used to prevent the spread of the Unzen-Fugen Dake eruption, with all operations being performed using radio controlled machinery. Figure 2 shows the remote operation control room used in this work. One of the challenges involved in using this system, however, was

that remote operation was relatively inefficient in comparison to operation using onboard systems installed on the machines themselves. Of the technical proposals floated as potential solutions to this problem, use of an economical video transmission system capable of sending high-resolution real time images from a wide spectrum of machinery, or automatization of radio-controlled finishing operations were both viewed favorably. As described below, the integration of the computerized construction system using high accuracy GPS was an integral part of this development.

Figure 2 Remote Operation Control Room

Computerized Construction

This area of operations also has a history of use stretching back decades, with a blade control system consisting of a laser emitter and receiver being used to ensure a finished horizontal surface in rice field construction dating from the 1970s. From 2000, the increasing use of high accuracy GPS together with a system known as 3D-MC that takes advantage of 3D geometry to automatically finish a project in line with the original design, meant that this marked the start of the spread of full-scale IT construction in civil engineering work. The installation of onboard high accuracy GPS on machines has allowed for easier operation and their use has continued to attract attention in recent years.

Equipment (Construction Machinery) Monitoring System

As shown in Figure 1., while construction equipment continues to advance intelligently through the use of technology such as mechatronics in developing independent products that are part of technical development, products that include services using new IT have become essential to any infrastructure, with the intended use of these being support and operations, meaning that providing information through mediums such as mobile wireless communication and internet are key. To apply this fast evolving technology to long-life machinery requires work on this product development. This will also require joint development between manufacturers with little knowledge of content development and long-term management by users.

System Overview

Komatsu refers to its equipment control system for construction machinery as KOMTRAX, and beginning in 2001 we launched this as a regional standard in the Japanese market as we planned for its gradual rollout. From 2004 the system was released as standard in China, and then in North America and Europe from 2005. Models in line to receive this system installation continued to expand, and by 2008 KOMTRAX had come to be installed in almost all Komatsu construction machines.

Calculating net growth of these new units by subtracting newly registered machines, gives an estimated net figure of 300,000 units expected to be in operation by 2010. Figure 3 shows an overview of this system.
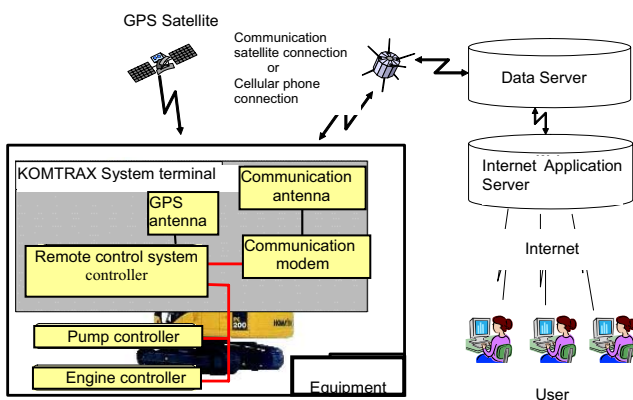
Figure 3 Overview of KOMTRAX System

Case Study Using the System

Using KOMTRAX allows information to be provided not only to the end user, but also to the sales and service outlet and other points, including the manufacturer.
Table 1 shows the main menu used for providing information with KOMTRAX.
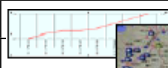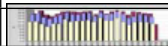
Key Information		Web Display, Report, Mail Forwarding Service
Service meter		Daily/Accumulated operating time
Equipment location		Current location; previous movement history
Operating history		Date / Operating Map Operating Time Daily log; equipment and operator monitoring
Error / Caution		Early warning of any abnormalities
Operating time		Analysis of work content
Fuel consumption rate		Provides fuel efficiency report
Handling		Monitors operating load (handling)
Remaining fuel		Daily display of remaining fuel
Radiator temperature		Displays radiator temperature

Table 1 Information Supplied by KOMTRAX

Use by End-Users

KOMTRAX's benefits to businesses with a large number of machines include daily collation and monitoring of operating performance information, allowing for optimal allocation of machines for improved efficiency in busy workplaces. Other benefits include control of planned maintenance - leading to lowered maintenance costs - and improving operator performance by monitoring operating costs for each operator. Anti-theft function and tracking function also come as standard.

Use by Sales and Service Outlets

Advantages for businesses who have installed KOMTRAX in service vehicles include the ability to integrate control of onsite repair personnel and construction machines. This also allows for effective planned servicing, with KOMTRAX receiving praise for ensuring a speedy and accurate response for dealing with emergency repair requests.
Information that is sent via KOMTRAX - including operating site details, operating times, errors and caution information, fuel costs, and hydraulic pressure frequency - are combined to calculate load factor

information for the machine. The system can also be used for machines that are sold under an installment plan to estimate return based on weekly or monthly operating time, and is useful for credit management purposes based on its ability to monitor any non-authorized resale.

Use by Manufacturers

This system's use by Komatsu is highly anticipated as bringing wide benefits in areas such as marketing, servicing, development, and manufacturing. KOMTRAX can also be used in rational stock and production management for products and spare parts based on monitoring operating status by region and machine type. Another effective point is the ability to significantly improve the accuracy of information regarding its use for product planning and development.

Computerized Construction System and Applicable Construction Machinery

The increasing accuracy of high accuracy GPS and reduction in time required for surveying have resulted in some eye-catching devices, with the RTK-GPS being able to capture data in real time up to 2 cm level of accuracy. Due to space limitations the theory behind RTK-GPS measurements is omitted here, but using this GPS technology in surveying allows for both construction and measurements to be performed simultaneously, while eliminating the need to redo any finished construction and providing for construction being carried out in a rapid and accurate manner using computerized construction. This also allows for integration of a design and construction database, and due to its ability to plan for visualization of construction control, both mining and construction machinery are being developed in response to this.

Overview of Mining System

Due to the high cost of applying high accuracy GPS to construction machinery, the system was first installed in mining machinery as part of large-scale mining operations. The system's use in mining machines is mainly focused on operator guidance. This is reflected in providing guidance for determining boring position for boring machines, monitoring earthwork quantity for bulldozers, regulating quality levels for loaders, and guidance for drilling sites for production control, when used in conjunction with mining control systems. Most mining control systems look to maximize allocation of

vehicles used in mines such as coordinating multiple ore transport dump trucks and loaders to ensure optimal drilling and transport of material, so that the use of GPS allows computerized calculation of such vehicles' position and speed - thereby sending programmed destinations to be displayed on the onboard display in each truck installed in the operator's cabin. An overview of this system is shown in Figure 4.
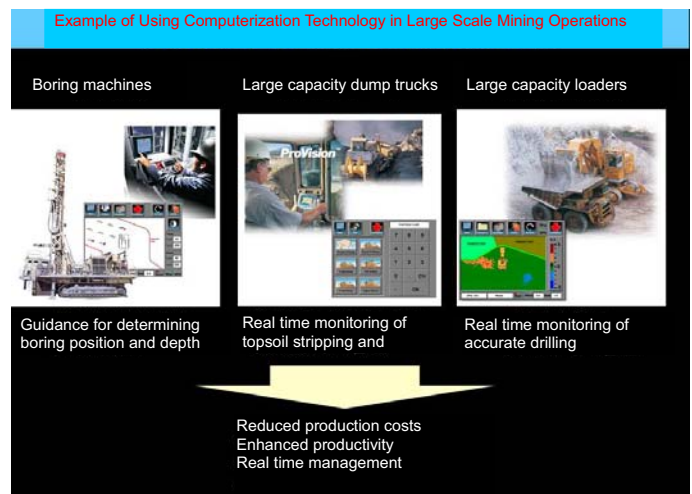
Figure 4 Computerized Construction System for Mining

Overview of System for Use in Civil Engineering

Following on from developments in the mining sector, from around 2000 an onboard GPS system debuted in construction machinery used in the civil engineering. Figure 5 provides an overview of this system. This was intended to be applied to use in construction and road building, and due to factors such as the automatic controlled blade requiring a more accurate GPS than that used in large scale mining operations, and need for integration with a 3D CAD system, this required some time before any commercial realization could be achieved.

Starting in 2003, a blade control system incorporating high accuracy GPS began to rapidly spread across the U.S. in use in bulldozers and graders. The significant effect this development had on the efficiency of finished work led to a reduction in construction period and improved operating rates. Despite being an expensive system to operate, its use has continued to spread in popularity. In Japan, however, this system is relatively expensive compared to the U.S., and the small scale of construction projects that are ordered within Japan has resulted in only a small number of projects capable of using the system and a low annual operating time, which means the system's depreciation cost is relatively

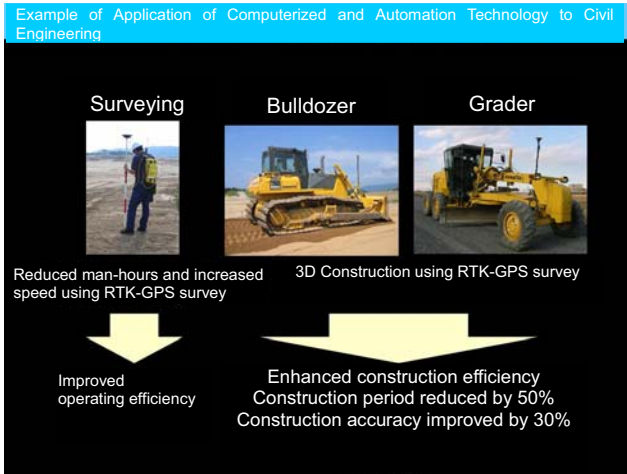high and it remains at an early stage of market penetration.

Figure 5 Overview of Computerized Construction System for Construction Machines

This section will provide an overview of the onboard installation of the system, using an example of its installation in a bulldozer. As shown in Figure 6., the GPS antenna - used to detect the horizontal and vertical position of the operating tool (the blade) - is directly attached to the blade through the pole. The reverse side of the blade has a tilt sensor attached to it, which detects the blade's tilt angle.
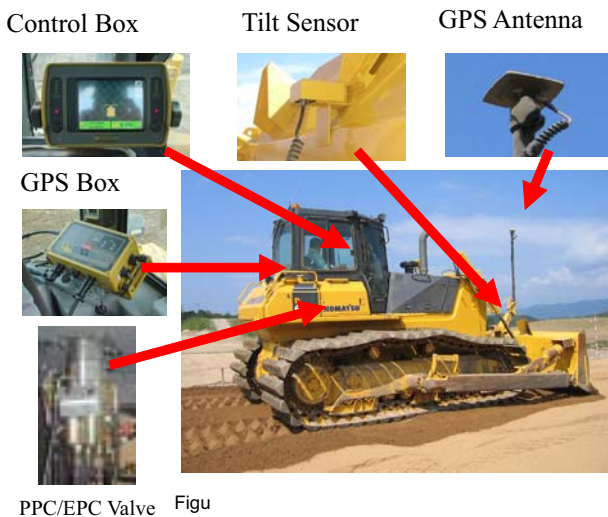
Figure 6 Computerized Construction System for Bulldozers

Construction plan data consisting of data created using

3D CAD is installed into the integrated control box consisting of the color indicator located in front of the operator's seat and control unit using compact flash memory that is also used in digital photography.

The control box color indicator constantly updates the display in real time of the machine's current position on the construction plan display, and this has been constructed so that the operator can confirm the operating status of the machine at any time (refer to Figure 6).

The control box can also be used to control the blade by comparing the actual position of the blade with the construction plan data in real time and manually operating and activating the valve.
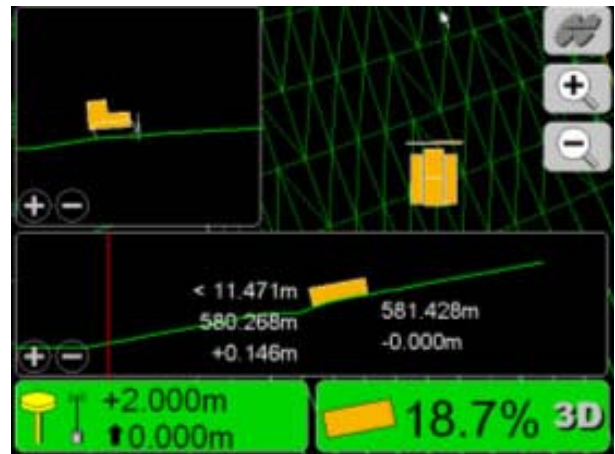
Figure 7 Insertion

Future Trends and Issues

One future direction for the development of mining and construction machinery lies in increasing robotization. Based on a combination of a computerized construction system and radio-controlled remote operating system, this will allow for future application of remote construction operating systems to mining machinery, in which integrated work can be performed from the comfort of a control room to direct drilling of mines and transport. Autonomous Haulage System in mining operations is already a reality, and there is a high possibility of drilling and material-handling operations in mine operations becoming a viable proposition in the near future. Areas that have to be overcome in order to make this a reality, however, include bringing effective

real-time wireless image broadcasting technology online. Also, in order to enable remote or automatic operation of such systems, it is essential to use external confirmation sensors (laser, radar, vision system) and confirmation technology to ensure the safety of the surrounding area. However, manual operation will still be required following the introduction of such systems and machinery, such as for maintenance and repair work, meaning that the realization of an actual unmanned system faces a considerable number of hurdles to become reality. Figure 8 shows an idea for Autonomous Haulage System
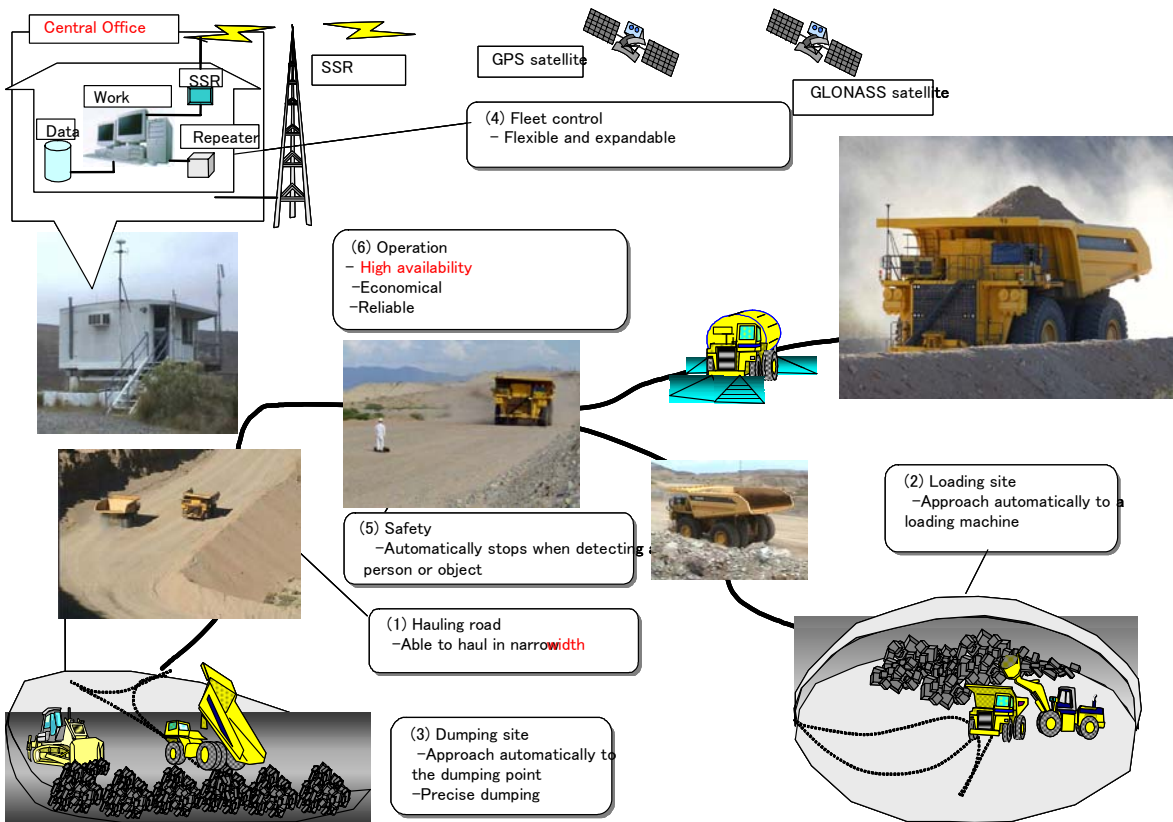
Figure 8 Autonomous Haulage System

K-6

HYBRID IN CONSTRUCTION MACHINERY

Masami Ochiai*, Shohei Ryu*

* Technical Research Laboratory, Hitachi Construction Machinery Co. Ltd
Kadatsu 650, Tsuchiura, Ibaraki 300-0013, Japan
(E-mail: m.ochiai.oq@hitachi-kenki.com)

ABSTRACT

After second oil shock in 1978, fuel consumption cost has become an important evaluation factor for construction machinery, many improvements have been made to increase machine efficiency[1]. Recent year, as the Kyoto Protocol get effective, further effort on fuel consumption cut or CO_2 cut is required for all machine makers. As the success of the hybrid system in automobile, construction machinery makers also put a lot of force on research to apply the hybrid concept in their own machines. This paper introduced the research and development of hybrid machinery in Hitachi Construction Machinery Co. Ltd , and also discussed the problems in this field.

KEY WORDS

Hybrid, Construction machinery, Excavator, Wheel loader

INTRODUCTION

Recently, for purpose of energy saving and green emission, various kinds of HYBRID vehicles are promoted in automobile industry. In construction machinery industry, makers also actively developed various kinds of machines based on hybrid concept[2]. This paper reviewed main features of construction machinery and problems on their hybridizations, and also introduced the development of hybrid wheel loader and hybrid excavator in our company.

HYBRID in CONSTRUCTION MACHINERY

Construction Machines and their Application Features

There are various kinds of machines in construction machinery, for example, crawler type machines as excavator in Figure 1(a), crane as Figure 1(b), and wheel type machines as excavator in Figure 1(c), wheel loader in Figure 1(d). When we want to apply the hybrid

(a) Excavator   (b) Crawler Crane

(c)Wheel excavator   (d) Wheel Loader

Figure 1 Various type of Construction Machinery

concept in each type of machines, the system has to be considered to fit its special working style. Compared with the automobile vehicle, construction machinery has two obvious features[3].

The first one is that the construction machines have multiple actuators. In automobile, a car has only one actuator for driving tires, and a large part of its engine power is prepared for its acceleration; A hybrid car can regenerates the moving energy in braking process, and re-used it for acceleration, so the engine size can be easily cut down, and the fuel consumption can be reduced. But for a hydraulic excavator, it has 6 actuators, e.g. swing, boom, arm, bucket, left and right travelers. According to its working content, sometimes the machine will share the total engine power to several actuators simultaneously, and sometimes, it needs to concentrate its full power to one actuator. The analysis of which actuator consumes more power, which actuator has more potential power to regenerate, and so to downsize the engine power is a quite difficult problem in hybridization of these machines.

Another feature is that the construction machine has to use hydraulic power. No matter what kind hybrid system, it needs a power storage component, such as accumulator, flywheel, battery, capacitor etc. Most machine makers prefer using electrical generator/motor as energy convention component, and battery or capacitor as energy storage component. The rotation actuators, says, motors are relatively easy to be substituted by electrical motors, but until now there is still no electrical device in the world which can substitute the hydraulic cylinder in same efficiency and same compacted size; So a well harmonized hydraulic and electric hybrid system is a practical way in current stage. But for Crawler Crane, all the actuators are in rotated motion, in this meaning, the hybrid based on electrical component will be easy to realize.

Figure 2 shows a simple comparison of power train efficiency for hydraulic and electrical systems. It can be found that for rotation movement, with the substitution of electrical system, at least 10% improvement in efficiency can be expected.
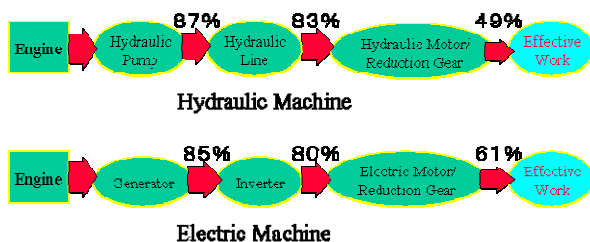
Figure 2　Comparison of the hydraulic and electric power systems

Example of Hybrid Systems

For wheel type machines as wheel loader, the power consumed in travel movement takes a large ratio in its total working process, and the wheel driving is easy to be driven by electric motor, the hybrid configure of the this type of machine is relatively clear. And it will be mentioned later in detail.

But for hydraulic excavator, there are multiple pumps to drive multiple actuators, various kinds of hybrid systems are possible. For different kind of hybrid systems, the energy saving effect is list up in Table 1 according to the system simulation.

Table 1 Fuel consumption for different system

System	Fuel Consumption Ratio
2-pump System (Conventional System)	1
Serial Hybrid 2-pump System	1.10
Parallel Hybrid 2-pump System	0.86
Serial Hybrid 4-pump System	0.46
Parallel Hybrid 4-pump System	0.40
Double-pump Regeneration System	0.43
4-pump Hydraulic System	0.41

Figure 3, 4, shows the concept figure of some typical systems. It can be found that comparing with standard machine, more than 50% energy saving effect can be expected in some conditions.
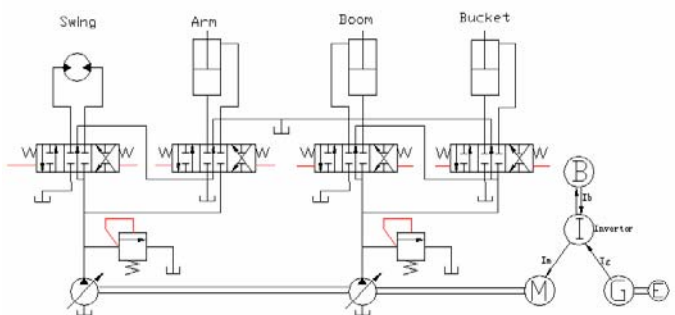
Figure 3 Two pumps serial system
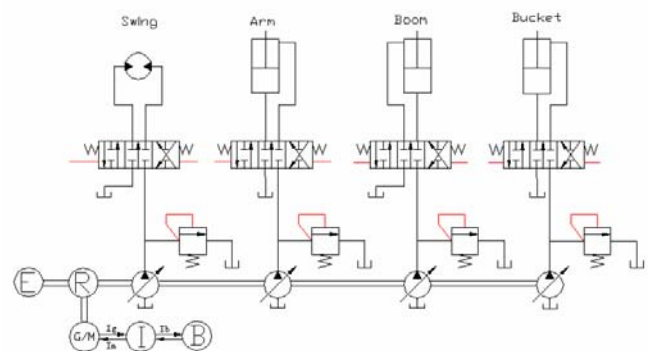
Figure 4　Four Pumps parallel

Problems in Hybrid Construction Machinery

Compared with the ordinary automobile, the load change rate and amplitude are much larger. For example, a 20 tons class excavator works in a 30 seconds typical working period, its total load power can be changed 2 or 3 times between 0kw to 60kw.

How to regenerate the energy in this kind of load change is an essential problem in hybrid construction machine. And so large and frequent changing of load power makes the battery or capacitor work in serious condition, how to extend their cycle life time is also a serious problem. And how to control the electrical actuator in quick and precise response under such a serious load process is also a difficult problem.

Construction machinery have to be applicable to all over the world, and all kind of environment condition, components need to have same or even higher capability than automobile on environment performance, for example, as to vibration and impact resistance, automobile need only to resist the vibration about 5-7G, but the construction machinery need to resist more than 10G.

HYBRID WHEEL LOADER

System Outline

Figure 5 shows the system outline of the hybrid wheel loader developed in our company[4]. Engine drives the hydraulic pump and electric generator in parallel, and the pump drives the hydraulic system for working front, and the generator drives electric motor and then the wheel movement. The working front driving uses the conventional hydraulic system, the wheel driving use serial hybrid system.
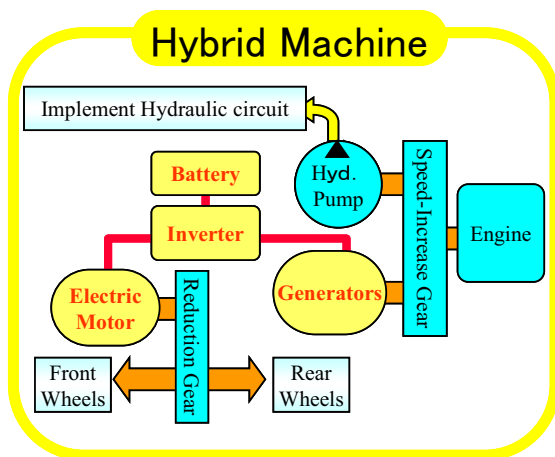
Figure 5 System outline of the Hybrid wheel loader

Since the ratio of traveling in total working process of the wheel loader is quite large, even so the system is simple, it has well effect on power saving

In practice, the hybrid system regenerates the braking energy into electric power and saves it in battery as the wheel loader is in deceleration, and use the power to assist the engine as it is in acceleration. The system can not only uses the braking energy effectively, but also improves engine efficiency in acceleration process. The most typical task of the wheel loader is V type loading, its working process is shown as Figure 6. In this process, acceleration and deceleration frequency is quite high, the fuel consumption can be largely cu-off with this hybrid system.
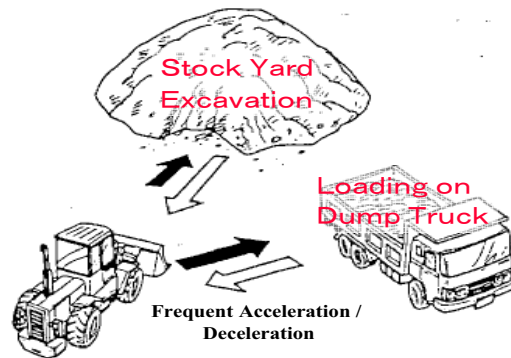
Figure 6 A typical working model of wheel loader

As it described above, the hybrid wheel loader can save the energy mainly in three aspects.
1) Increasing the efficiency of power train by the electrical driving.
2) Optical engine running by electric assistance
3) Power regeneration in deceleration

Experimental Performance

Figure 7 shows the picture of the hybrid wheel loader we developed. And Figure 8 shows the performance experiment records. It can be noticed that the energy regenerated in braking process well balanced the power needed in acceleration. And comparing with convention machine with HST system for wheel driving, in piston traveling process the fuel consumption can be cut down by 30-40%, and in total working process the fuel cost can save about 25-30%.

We did not take any changes for front working system in this case, if possible, better effect might be expected.

Figure 7 picture of the hybrid wheel loader
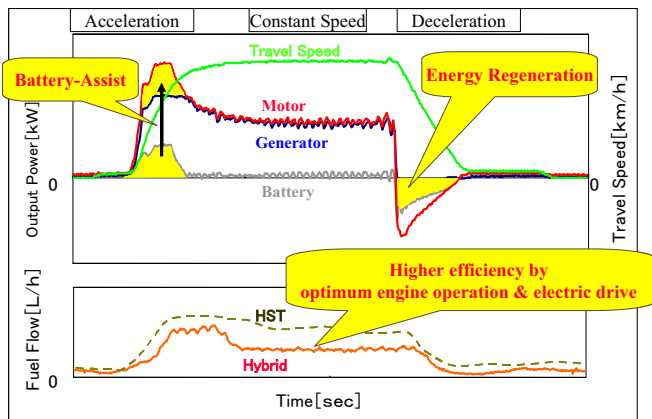
Figure 8 Running test results of hybrid wheel loader

HYBRID HYDRAULIC EXCAVATOR

System Outline

Figure 9 shows the system outline of the hybrid hydraulic excavator developed in our company[5].

The front working part, says the boom, arm, and bucket uses hydraulic system, swing uses electric motor to drive. When the swing is braking and boom is lowered down the energy is regenerated and saved in capacitor for assisting the engine on necessary.
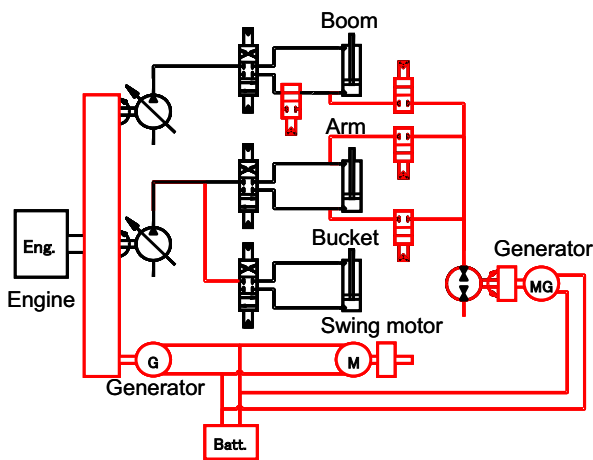

Figure 9 System outline of Hybrid excavator

Experimental performance

Figure 10 shows the state of machine for digging experiment. From the experiment we knew that compared with standard machine, the hybrid excavator can save the fuel consumption as much as 25%.

In this machine, to keep the total operation performance in same level with standard machine, engine size is not compacted. For some special used machine as its

working content is limited in some range, for example, the machine mainly used for handling or moving something, according to the load analysis, the engine size may be cut down, and so better fuel consumption result can be expected.

Figure 10 Picture of hybrid excavator

CONCLUSION

Since most of construction machines have multiple actuators and the hydraulic cylinder is difficult to be substituted by electric actuators, the hybridization of the machines is not an easy problem to answer. Even so in our practice, with electrical driving of partial system and well arranging of total system, the fuel consumption can be improved by 25-40%.

For reduction of CO_2 release, and stopping the earth warming process, we will continue to put effort on hybridization of the construction machinery.

REFERENCES

1. Sugiyama, G, et al, Reduction of fuel consumption in construction machinery, Construction Machinery, 2003,41-1,pp18-22
2. Ochiai, M, Technical Trend and Problem in Construction Machinery, Construction Machinery, 2002,38-4,pp20-24
3. Sugano,N,el al, Swing System Development of Construction Machinery, 2004,JSAE Annual Congress ISSN 0919-1364,pp7-12
4. Ochiai,M, Development for Environment Friendly Construction Machinery, Construction, Kenstsu-buka, 2003,No.9,pp24-28
5. Hitachi Construction Machinery, Co.Ltd, Development of Battery driven Construction Machinery for CO2 Reduction, Technical Report for Development of Technical Measure for Global Warming Control(Ministry of the Environment), 2005

OS1-1

DESIGN AND FUEL ECONOMY OF A SERIES HYDRAULIC HYBRID VEHICLE

Peter ACHTEN*, Georges VAEL*, Mohamed Ibrahim SOKAR** and Torsten KOHMÄSCHER**

* Innas BV
Nikkelstr. 15, 4823AE Breda, the Netherlands
(E-mail: pachten@innas.com)
** Institute for Fluid Power Drives and Controls (IFAS)
RWTH Aachen University
Steinbachstr. 53 B, 52074 Aachen, Germany

ABSTRACT

A series hydraulic hybrid drive train for application in a passenger car is described. This 'Hydrid' drive train features an in-wheel hydraulic motor in all four wheels, hydraulic transformers for power control and hydraulic-pneumatic accumulators for energy storage and power management. The hydrostatic components are based on the highly efficient floating cup principle. The result is an efficient all-wheel drive vehicle with variable traction control on the front and rear axis. The fuel economy and the CO_2-emission of the drive train are calculated for a mid-class sedan while driving the New European Driving Cycle (NEDC). The efficiency of the hydrostatic components is derived from efficiency measurements of the floating cup pump.

KEY WORDS

Series Hybrid Hydraulic Vehicle Efficiency

NOMENCLATURE

b_{NEDC}	specific fuel consumption [l/100km]
c	conversion constant [l/100km/Wh]
E_{drag}	cumulative rolling and aerodynamic resistance during the NEDC [Wh]
E_{kin}	cumulative kinetic energy during the NEDC [Wh]
η_{ICE}	average cycle efficiency of a diesel engine [-]
η_{recup}	degree of recuperated kinetic energy which is actually stored in the accumulator [-]
η_T	average cycle efficiency of a transmission component of a series hybrid [-]
φ	rotational position of the motor shaft [°]

INTRODUCTION

The fuel consumption of passenger cars could be strongly reduced if the engine would always be operated around the best point, where the engine has the highest efficiency. According to Breitfeld from BMW [1] the fuel consumption would then even be halved. To achieve this:

- a series hybrid drive train must be introduced
- the engine has to be operated in start-stop-operation
- low load operation of the engine should be avoided
- energy storage is needed for power management and energy recuperation.

This paper describes the 'Hydrid' [2, 3, 4], a full hydrostatic hybrid transmission that could fulfil the require-

ments for such a drive train. The IFAS-institute of RWTH Aachen University in Germany has determined the fuel consumption and CO_2-emission of the Hydrid. Starting point for the study is that the hybrid vehicle has the same performance, size and weight as the original non-hybrid vehicle. The study is performed for a mid-sized sedan driving the New European Driving Cycle (NEDC). The results of this study are summarized in this paper.

REQUIREMENTS FOR SERIES HYBRIDS

Series hybrid drive trains have several advantages compared to parallel systems. In parallel systems, an extra transmission is added to the mechanical transmission, which increases both the weight and the cost of the vehicle. In a series hybrid system, the mechanical transmission can be completely eliminated and replaced by an electric or hydraulic system, which allows power management and energy storage. The engine is no longer connected to the wheels but can now be optimized for producing energy in the most optimal way.
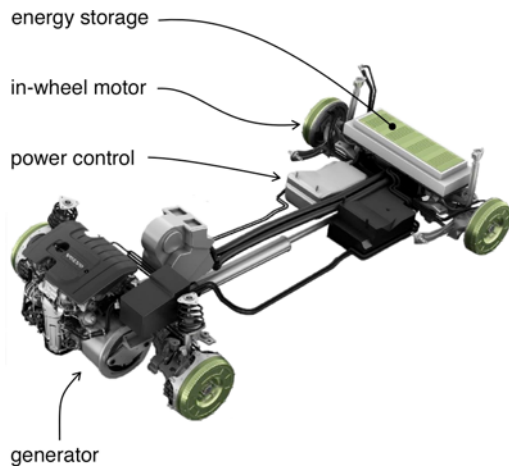
Figure 1: Transmission components of a series hybrid

This, however, is only an advantage if all transmission components (see figure 1) have a high efficiency, also at part load and low power operating points. If, for simplicity reasons, all the transmission components are assumed to have an equal average cycle efficiency η_T, then the specific fuel consumption can be calculated:

$$b_{NEDC} = c \cdot \frac{E_{drag} + E_{kin}\left(1 - \eta_T^6 \cdot \eta_{recup}\right)}{\eta_{ICE} \cdot \eta_T^4}$$

in which:

$$c = 9.25 \cdot 10^{-4} \left[\frac{l}{100\,km} \frac{1}{Wh}\right]$$

$$E_{drag} = 633 \text{ Wh}$$

$$E_{kin} = 397 \text{ Wh}$$

The amount of rolling and aerodynamic resistance (E_{drag}), and the amount of kinetic energy (E_{kin}) are calculated for a mid-sized sedan, while driving the NEDC. Since the engine can always be operated in the area with highest efficiency, the average (diesel) engine efficiency can be assumed to be quite high:

$$\eta_{ICE} = 0.37$$

The specific fuel consumption of the passenger car can now be calculated for various degrees of recuperation and various transmission component efficiencies:
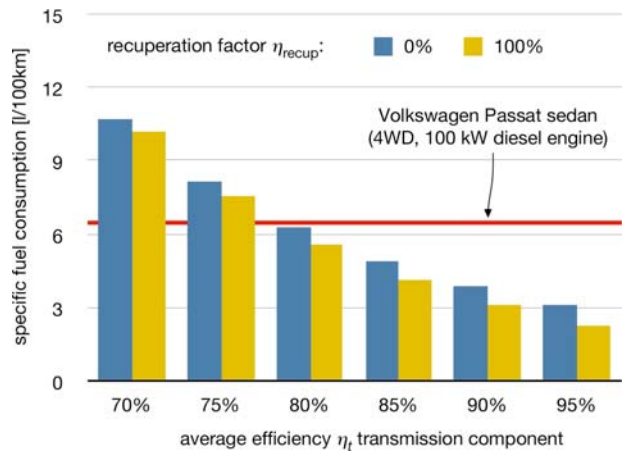
Figure 2: NEDC specific fuel consumption of a series hybrid vehicle, in comparison to the Volkswagen Passat benchmark.

This, rather simple analysis, shows the strong reduction of the specific fuel consumption that can be achieved with a series hybrid transmission. Compared to a vehicle with a conventional mechanical transmission, the fuel consumption can be reduced by more than 50%. Energy recuperation has a modest effect on the fuel consumption: for the NEDC 0.5 to 0.9 litres per 100km. The specific fuel consumption is first and foremost affected by the efficiency of the transmission components. The average cycle efficiency of the individual components has to be higher than 80% in order to achieve a substantial improvement of the fuel economy.

This demand cannot be fulfilled with current electric components [5]. Furthermore the electric transmission will substantially increase the weight and the cost of the transmission if the vehicle performance is not to be compromised.

The alternative for a series electric hybrid vehicle would be a full hydrostatic transmission, including hydraulic accumulators. Although accumulators have a rather low energy density, they are favoured for their high power density, much higher than of electric batteries. The torque control of the wheels can be realized by means of secondary controlled, variable displacement motors. As with the electric motors, the size of the hydraulic motors has to be chosen for maximum speed and maximum torque requirements. By reducing the swash-plate angle of the variable displacement motor, the torque to the wheels can be controlled. But this again results in a poor efficiency at low power demands, which are typical for average driving conditions, for instance as defined by the NEDC.

Another disadvantage of current variable displacement hydraulic motors is the reduced torque at start-up and low rotational speeds. This is for a part due to stick-slip friction. The start-up torque can further be reduced because of the strong torque variations caused by the limited number of pistons. The torque variation also creates concerns about the noise, vibration and harshness (NVH) of a hydrostatic drive train [6].

NEW HYDROSTATIC COMPONENTS

A series hydraulic hybrid transmission only makes sense, if all the transmission components have a high average cycle efficiency. Furthermore a solution for the NVH-issue has to be found.

Two recently developed hydrostatic principles are introduced to fulfil these demands:
- the Floating Cup Principle
- and the Innas Hydraulic Transformer.
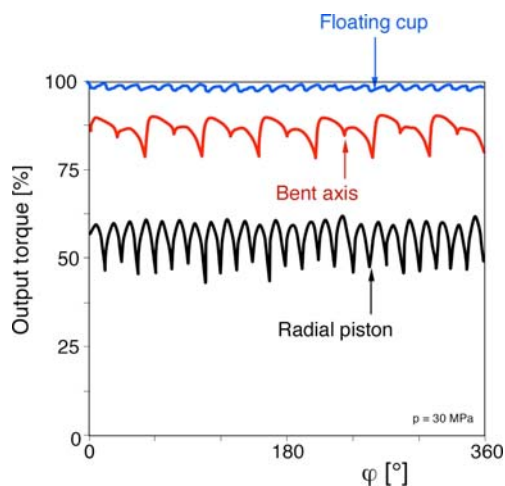
Figure 3: Low speed torque of three different hydraulic motors relative to the theoretical maximum torque

The Floating Cup Principle is a highly efficient positive displacement principle, which is developed for hydrostatic pumps, motors and transformers [7, 8]. Floating cup machines typically have around 24 pistons; 3 to 4 times as much as in conventional piston pumps and motors. This strongly reduces the noise, pulsation and vibration levels. Furthermore, the Floating Cup principle has extremely low friction losses. The effect of the low friction losses and the high number of pistons can be seen in the diagram of figure 3 which shows the torque output (relative to the maximum theoretical torque) measured at a low rotational speed (< 1 rpm) of a floating cup motor, compared to a bent axis and a radial piston motor.

The hydraulic transformer eliminates the need for variable displacement motors. Instead, each wheel will have its own constant displacement motor. The wheel torque is controlled by means of the hydraulic transformer, which controls the pressure level offered to the wheel motors, as well as the flow direction. The transformer is a continuously variable (hydraulic) transmission, converting the product of pressure and flow without any principle losses. The transformers can also act as pressure amplifiers, thereby creating a boost torque when needed.

THE HYDRID

On the basis of these new hydrostatic principles, a new series hydraulic hybrid, called the 'Hydrid', has been designed (figure 4). Each wheel has its own constant displacement motor. Due to the high power and torque density of the hydrostatic units, the increase of the unsprung wheel mass is limited. Alternatively, the hydraulic motors could be mounted on the chassis, driving the wheels by means of conventional constant-velocity joints. The motors act as pumps when braking, thereby recuperating the kinetic energy of the vehicle and storing it (as much as possible) in the high-pressure accumulator.

The backbone of the Hydrid is the Common Pressure Rail (CPR). This system collects and distributes all the power inside the vehicle. The accumulators determine the pressure levels in the system. On the high-pressure side, the pressure level varies between 200 and 400 bar.

The internal combustion engine delivers all its energy to a constant displacement pump. The torque demand of the pump is directly related to the pressure level in the high-pressure accumulator, and can consequently only vary between 50% (at 200 bar) and 100% (at 400 bar) of the maximum torque. Operation of the engine at low loads is therefore completely avoided.
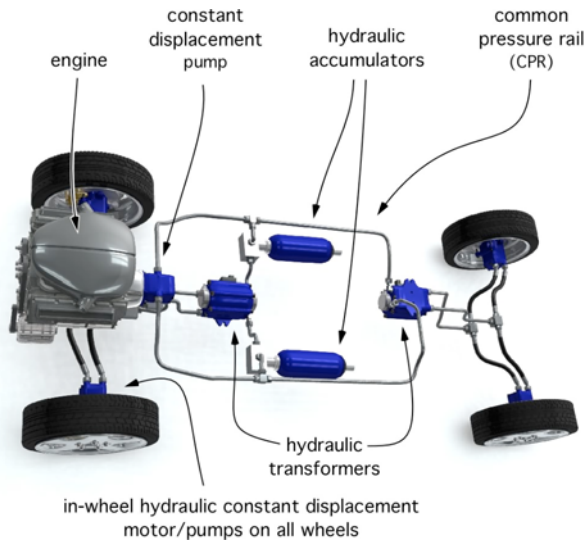
Figure 4: Main components of the Hydrid

Pump:	56 cc/rev constant displacement
Accumulators:	20 litres (high- and low-pressure)
Hydraulic transformers:	60 cc/rev (pump equivalent)
Wheel motors:	45 cc/ rev constant displacement

Table 2: Vehicle parameters

Vehicle:	Volkswagen Passat all-wheel drive Sedan (2007 Germany)
engine:	100 kW diesel engine
maximum traction:	4400 N
maximum vehicle speed:	190 km/h
empty curb weight:	1450 kg
frontal area:	2,26 m2
drag coefficient:	0,26
dynamic wheel diameter:	0,63 m
rolling resistance coefficient:	0,008

Table 1: Hydraulic components:

The hydraulic transformers are the power converters of the transmission, and control the traction and the speed of the vehicle in four quadrants. There are two transformers, one for each axis. The system offers a variable traction control for the front and the rear axis. At low torque demand, one of the axes can be shut-off completely. The differential function is created by means of a simple hydraulic T-joint. With hydraulic valves, a differential lock, or even torque vectoring can be realized, much more simple and less expensive than with mechanical systems.

MEASUREMENTS AND SIMULATIONS

The Institute for Fluid Power Drives and Controls (IFAS) of the RWTH Aachen University has built a simulation model of the Hydrid in order to calculate the specific fuel consumption and the related CO_2-emissions. For the pumps, motors and transformers, efficiency maps are used which are derived from recent efficiency measurements performed by IFAS on a 28 cc constant displacement floating cup pump. For the engine, the efficiency map of a Mercedes Benz diesel motor was applied [9], having a peak efficiency of 40%.

The size of the hydraulic components (see table 1) is chosen as such that the Hydrid has the same performance as the benchmark vehicle (a Volkswagen Passat sedan). Also the size (frontal area), aerodynamic resistance, rolling resistance, dynamic wheel diameter and vehicle weight have been chosen the same. Table 2 gives an overview of all the vehicle parameters. The test cycle used for the simulation was the NEDC specified by the European Community (directive 93/116/EC). According to this directive, some of the auxiliaries (like

the compressor for the air-conditioning) do not have to be taken into account. It is assumed that the energy for the water pump, the cooling fan, the generator and the fuel injection system are included in the efficiency map of the diesel engine. It is furthermore assumed that the power steering in the Hydrid does not consume any energy during the NEDC. Having a CPR hydraulic system, the steering system can now be a closed circuit system with no power consumption while driving straight on (as is the case in the NEDC).

FUEL CONSUMPTION

The first results of the simulations were published at the 6th International Fluid Power Conference (6.IFK) in April 2008 [4]. In the IFK-paper, a double engine concept was assumed, having two 50 kW diesel engines. In this paper the simulation has been run with a single 100 kW engine. Furthermore, the air density was adjusted from 1,29 to 1,2 kg/m^3, which is the correct value for an air temperature of 20°C.

Figure 5 shows the outcome of the simulation with respect to the fuel consumption. The result is compared to the fuel consumption and CO_2-emission of a Volkswagen Passat sedan having an all-wheel drive manual transmission and a 100 kW diesel engine. The data for this benchmark are provided by Volkswagen Germany and are valid for the NEDC test cycle.

The Hydrid strongly reduces the specific fuel consumption, on average with 58%. Contrary to conventional vehicles, driving in the city consumes less fuel (per km travelled) than driving on the highway. This is to be expected for any efficient drive train, since the aero-

dynamic drag is much less while driving in the city. The high efficiency of the Hydrid is the result of:
- the high average cycle efficiency of the hydrostatic components;
- recuperation of the kinetic energy while braking;
- operation of the internal combustion engine close to the best point.

The size of the 20 litres high-pressure accumulator is sufficient for recuperating about 90% of the kinetic energy during the city part of the NEDC. During the entire NEDC 58% of the kinetic energy is recuperated. The rest is dissipated by means of a pressure relief valve, especially during the final brake action of the NEDC, which is a full stop from 120 km/h. Including the recuperated energy, the total average efficiency of the hydraulic transmission is 95%. This is somewhat higher than the average cycle efficiency of the mechanical all-wheel drive transmission of the benchmark, which is estimated to be 91%.
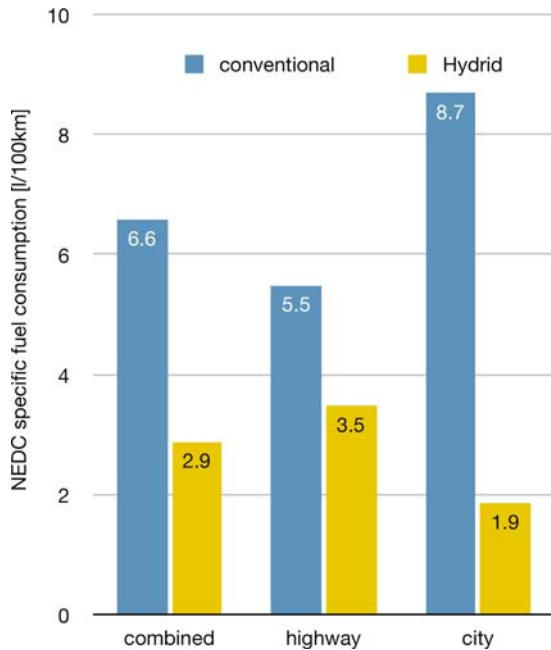
Figure 5: Specific fuel consumption for the Hydrid compared to the conventional benchmark (comparison based on a mid-sized 4WD sedan with a 100 kW diesel engine, driving the NEDC)

The most important advantage of the Hydrid is that it allows the engine to run at high loads and hence at a high efficiency. Figure 6 shows a Pareto-distribution of the propulsion power required by the vehicle at the wheels. During 40% of the cycle time the wheels don't require any propulsion power; this is when the vehicle is standing still (24%) or decelerating (16%). The maximum required propulsion power is 32 kW, which is much lower than the installed engine power. About 90%

of the time the required wheel propulsion power is even below 11 kW.
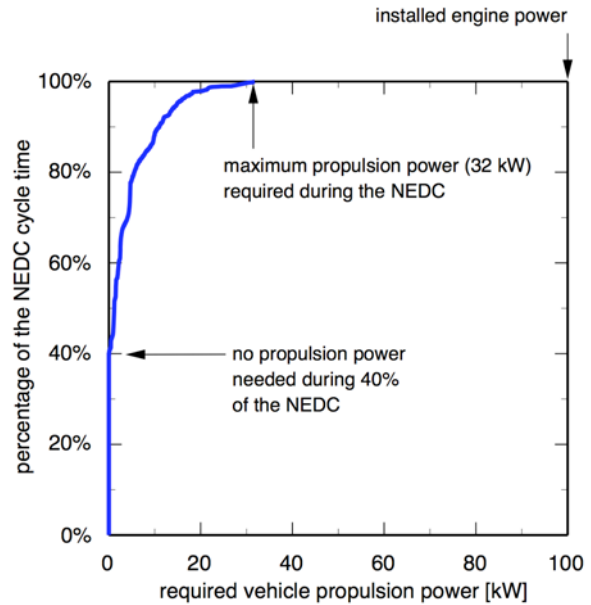
Figure 6: Pareto chart of the propulsion power required during the NEDC

In a conventional vehicle, there is no energy storage between the engine and the wheels. Consequently all the engine power has to be delivered directly to the wheels: the engine can't produce more mechanical power than the vehicle requires for propulsion. Since the engine can't be operated below a certain minimum speed, the engine has to be operated at low loads for the greater part of the cycle operation. Because the engine has a poor efficiency at these low load conditions (especially during city operation), the total drive train efficiency is strongly reduced and the specific fuel consumption is increased.

In the Hydrid, the engine is decoupled from the wheels. Instead the engine power is now completely converted to hydraulic power by means of a constant displacement pump. The pump delivers its pump flow to the high-pressure accumulator, having a pressure range of 200 - 400 bar. Having a constant displacement of 56 cc/rev, the pressure range of the accumulator requires a torque range of about 180 to 360 Nm. Consequently, the engine will only be operated between 50 and 100% load always having a nearly maximum efficiency.

CO_2-EMISSION

The CO_2-emission follows directly form the calculated specific fuel consumption. As before the CO_2-emission from the Hydrid is compared to the NEDC-data for the benchmark vehicle (as provided by the car manufactu-

rer).
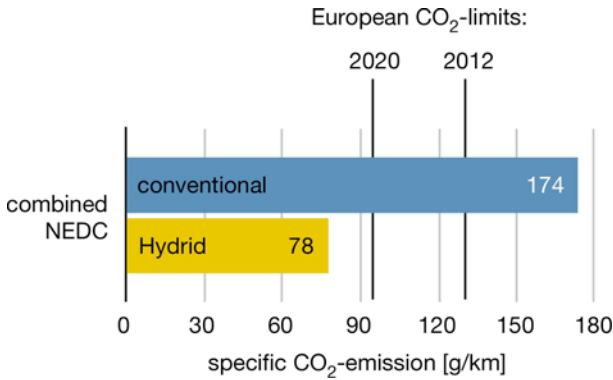
Figure 7: Specific CO_2-emission for the Hydrid compared to the conventional benchmark and the CO_2-emission limits expected for Europe (comparison based on a mid-sized 4WD sedan with a 100 kW diesel engine, driving the NEDC)

For the conventional vehicle, the specific CO_2-emission is 174 gr/km. This is much higher than the limits set by the European Community. The EU has agreed that by the year 2012, the average CO_2-emissions from new passenger cars should not exceed 130g CO_2 per km. By 2020, the limit is expected to be further reduced to 95 grammes CO_2 per km. Both limits can easily be met with the Hydrid.

ELECTRIC SYSTEM INTEGRATION

In the Hydrid, the hydraulic transmission competes with the mechanical transmission (which it eventually completely replaces), but it doesn't exclude electric systems and electric batteries.
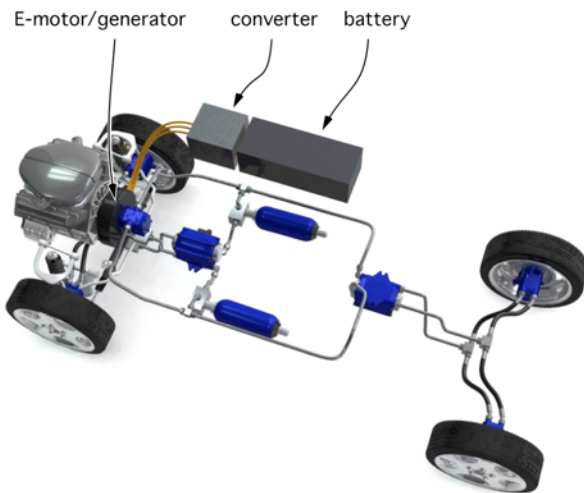
Figure 8: Electric system integration

On the contrary: the high power density of the accumulators can be very well combined with the high energy capacity of the batteries (figure 8). The hydraulic transmission handles all the power transients and peaks. Therefore, the electric system only needs to be designed for a base load of 5 to 10% of the installed engine power.

CONCLUSION

The fuel consumption and related CO_2-emissions of passenger cars can be strongly reduced by means of a series hybrid transmission. Series hybrid systems are however only successful if the individual transmission components are extremely efficient. This study has proven that the new floating cup principle and the hydraulic transformer fulfil this requirement. The specific fuel consumption can be reduced by more than 50%, without compromising the performance, size or weight of the vehicle.

REFERENCES

1. Breitfeld, C.(2007) The Efficiency-Optimised Drive – a Vision? Proc. 6th Int. CTI Symposium, Berlin
2. Achten, P.A.J. (2007) Changing the paradigm, Proc. of the 10th Scandinavian International Conference on Fluid Power (SICFP'07), May 21-23, 2007, Tampere Finland
3. Achten, P.A.J. (2007) The Hydrid transmission, Proc. SAE 2007 Commercial Vehicle Engineering Congress & Exhibition, October 2007, Rosemont USA, SAE 2007-01-4152
4. Achten, P.A.J. et al (2008) Energy efficiency of the Hydrid, Proc. Int. Fluid Power Conference 6.IFK, Dresden, Germany
5. Abthoff, J. et al (1998) The Mercedes-Benz C-class series hybrid, Proc. SAE Int. Congress and exhibition, 1998, SAE-paper 981123
6. Elahlnla, M.H. et al (2006) Noise and vibration control in hydraulic hybrid vehicles, SAE automotive dynamics, stability & controls conf. and exhibition 2006, SAE-paper 2006-01-1970
7. Achten, P.A.J. et al (2003) Design and testing of an axial piston pump based on the floating cup principle, Proc. of the 8th Scandinavian International Conference on Fluid Power, SICFP'03, Tampere, Finland, May 7-9, 2003
8. 20. Achten, P.A.J. (2003) Designing the impossible pump, Proc. Hydraulikdagarna 2003, Linköping, Sweden, June 3-4, 2003
9. Digeser, S. et al (2005) Der neue Dreizylinder-Dieselmotor von Mercedes-Benz fur Smart und Mitsubishi, MTZ 1/2005 Vol. 66

OS1-2

STEERING CONTROL SYSTEM FOR AUTONOMOUS TRACTOR

Keiichi INOUE*

* Lowland Crop Rotation Research Team,
National Agriculture Research Center for Hokkaido Region
1 Hitsujigaoka, Toyohira-ku, Sapporo, 062-8555 Japan
(E-mail: keich@affrc.go.jp)

ABSTRACT

An automatic power steering control system is modified to a tractor of 66kw engine power and using a navigation system of optical fiber gyroscope(IMU) and real-time kinematic GPS which are hybrid combined, the movement of the vehicle in the field is analyzed dynamically using a kinetic movement model of tractor to determine the parameters of the model. The tractor equipped with a planter was successfully controlled and was able to trace the target line correctly within 10cm by the method of adaptive travel control using the movement model of the vehicle considering the hydraulic time delay of the power steering mechanism.

KEY WORDS

Steering Control , Autonomous ,Tractor, , Vehicle modeling , Filtering,

NOMENCLATURE

ψ : Vehicle running direction
θ : Direction of vehicle body center line
φ : Steering angle
K_f : Cornering power of front wheel
K_f : Cornering power of rear wheael
v : velocity of vehicle
β : Slip angle λ
λ : Time rag of hydraulic operation
ω : Rotational rate
μ : Rolling resistance
$\square_w$: wheel base (suffices f:front, r:rear)
m : Mass of vehicle

INTRODUCTION

The speedup of the work is gradually highly required with the extension of the size of operational holdings per one farmer. However, the need for accurately controlling the implement becomes inevitable. Automatically steered farm equipment has many advantages of increasing agriculture accuracies at high speed operation including relieving the driver of the tedious task of accurately steering the vehicle, operation in low visibility circumstances such as at night. Many agricultural operations pull towed implements. It will become necessary to accurately control towed implements.

Tracked tractors are now used increasingly among farmers in Japan because of its soft compaction, strong fraction force, ability to work on the weak ground and stability in the high-speed field work. The operability and steering mechanism are constructed, and the running and turning performance is fairly improved nowadays. The operation is possible of the sense which is similar to the wheel tractor, and possible to work comfortable. However heading control of tracked vehicles at high speed is difficult for automatic driving or human driving with high accuracy because of the slippage between the crawlers and the ground. There has also been work done

on the control of wheel tractor implements, using GPS measurements, although there are no details on the model and control algorithms for the tracked tractors or semi-crawler tractor.

This paper describes a modeling of the steering actuation of a crawler tractor and a semi-crawler tractor and an extended Kalman filter to estimate the position, direction, attitude, speed of the tractor required for the state feedback algorithm and robustic adaptive control method of the electro-hydraulic system of the tractor. The linearization of the tractor-implement model is validated through a series of the line tracking experiments on a semi-crawler tractor and a planter.

METHOD

Vehicle Hardware and Control system

A semi-crawler tractor (front wheel drive, rear crawler drive tracked vehicles, KUBOTA Ltd.M90-PC FQ1BMAL) of 66kW(90PS) was converted to automatic controlled Tractor. The following functions are controlled by microcomputer through D/A converter: steering, throttle and tri-link. The following are controlled by microcomputer through digital parallel I/O interface: forward, reverse and idle; and PTO. Front wheels are actuated using a modified electro-hydraulic steering unit installed parallel to the power steering system. The wheel angle is sensed by encoder equipped front wheel shaft The microprocessor converts volt from the control computer into electro current , which are sent to the power circuits that control the steering servo valves. The steering valves are controlled by the method of PID control.

油圧クラッチへ
Hydraulic clutch .

Electro-hydraulic control unit .

ステアリング制御用油圧バルブ   70L/M
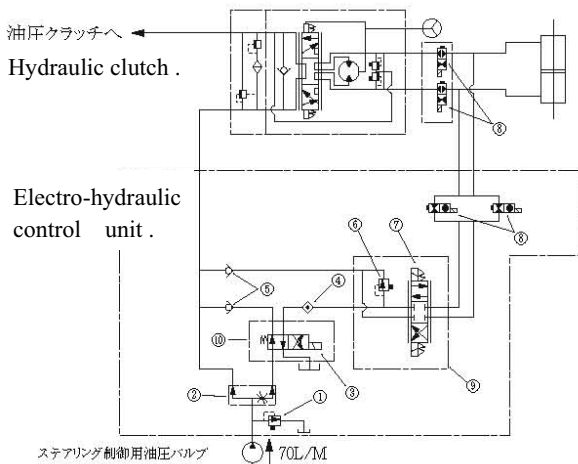
1 relief valve ,2 separate valve, 3 electromagnetic valve, 4 filer, 5 check valve, 6 relief valve, 7 servo valve, 8 stop valve, 9 manihold
Figure 1 Hydraulic system of the automatic power steering control

Throttle and lift link are controlled by potentiometer. A wire connected to a geared DC motor with a clutch

mechanism to maintain constant torque pulls the clutch or the brake pedal. PTO and other on-off switches are controlled by relay systems through parallel I/O interface board. The tractor is equipped with the IMU (JCS-7401A, Nihon Koukuu Denshi Co., Ltd.) which can output rotational   angle   and
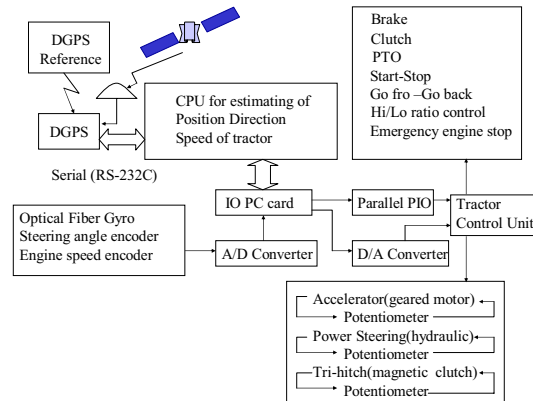
Figure 2 Schematic diagram of the computer control system of autonomous tractor.

velocity of each yaw, pitch, roll rates. The accuracy of the IMU is 0.2 degree of accuracy and drift of 5 degrees/hour. The RTK-GPS (SR530 , Leica Co., Ltd.) of accuracy within 2 cm and sampling rate 10Hz is also equipped with the tractor. The data of GPS are transferred through RS-232C interface to a notebook computer and the position, heading angle, attitude, speed of the tractor is calculated through a extended Kalman filter algorithm with the data of IMU.
equations.

Model of vehicle movement

In the flat field and hydraulic control time delay of front wheel of a tractor was made and the method of predictive motion control was applied to control the steering angle of an autonomous tractor by prediction of the motion of a vehicle in every 0.1 second based on the position, direction and velocity data from GPS and FOG. A X-Y coordinate axis is taken like Figure 3, then the running direction ψ and the direction of vehicle body center line θ equations are follows from the force ff,fr balance in the perpendicular direction to running direction of center of gravity and the moment balance in the circumference of center of gravity.

$$mv\,(d\phi/dt) = -2(K_f+K_r)\,\beta -2(K_f\ell_f -K_r\ell_r)\cdot (d\theta/dt)/v+2 K_f\phi \qquad (1)$$

$$I_z(d^2\theta/dt)= -\{2(K_f\ell_f - K_r\ell_r)+\mu_f mg\ell_r\}\beta - K_f\ell_f^2+ K_r\ell_r^2)(d\theta/dt)/v + 2K_f\ell_f\phi$$

The locus of vehicle center of gravity and the direction of the vehicle are calculated on the base eqn.(1),(2). When the velocity of vehicle is constant, then these equations are calculated as follows.

$$\beta = \left(1 - \frac{m\ell_f}{2 K_r\ell_w}v^2\right)\left(\frac{\ell_r}{\ell_w}\right)(\varphi/R) \qquad (2)$$

$$\omega = \left[1 - \frac{\mu_f mg\square_r}{2K_r\square_w\square_r}\square_w\right]\left[\frac{v}{}\right] \ (\varphi \diagup R) \qquad (3)$$

$$R = 1 - \{ (K_f\square_f - K_r\square_r)(mv^2 + \mu_{f} mg\square_r)$$
$$+ \mu_{f} m^2 g\square_r v^2 \diagup 2 \} \diagup (2\ K_f\ K_r\ \square_w^2) \qquad (4)$$

Steering control method

The steering angle $\varphi(k)$ is controlled so as to trace the target line Y-axis. The direction θ' and x' after short time λ second are estimated with the eqn .(6),(7). The $\varphi(k)$ is controlled so as to follow eqn.(5) relation. This eqn.'s relation means the direction of the vehicle is to proportional to the offset of the vehicle.

$$\theta' = f(x', v(k)\ ) = -K(\lambda)\cdot x' \qquad (5)$$

Where,

$$\theta' = \theta(k) + \omega(k)\cdot\lambda \qquad (6)$$
$$x' = x(k) + v(k)\cdot\lambda\cdot sin(\psi(k) + \omega(k)\diagup 2\cdot\lambda) \qquad (7)$$

$\psi(k)$ and $\omega(k)$ are small, so approximately replaced as follows eqn.

$$sin(\psi(k) + \omega(k)\diagup 2\cdot\lambda) = \psi(k) + \omega(k)\cdot\lambda/2 \qquad (8)$$

So, objective steering angle $\varphi i(k)$ is obtained from (5)-(8) eqn.

$$\varphi_i\ (k) = -R\cdot\square w \diagup Q\ \{(1 + K(\lambda)\ v(k)\ \lambda)\ \theta(k) +$$
$$K(\lambda)\ x(k)\} \diagup \{\ v(k)\ \lambda(1 + K(\lambda)\ v(k)\ \lambda\diagup 2)\} \qquad (9)$$

Where, $Q = (1 - \mu_f mg\square_r \diagup 2\ K_r\square_w) \qquad (10)$

Using a simulation model for a tractor mobile trace, after examining several functions f (x', v), determined when strait traveling,

$$f(x',v) = (1 + 3v)\cdot x'|x'| < \pi/2\cdot(1 + 3\ v)\ ) \qquad (11)$$

There is a relationship of dy / dx = 1 / tanθ, so if we suppose that Eq. (5) is satisfied, then the traveling trace is calculated by solving the differential equation of dy / dx = 1 / tan (f(x, v)). The relationship between offset x and vehicle direction θ' for vehicle control in strait traveling is expressed by Eq. (5). These parameters were fixed in the experiment.
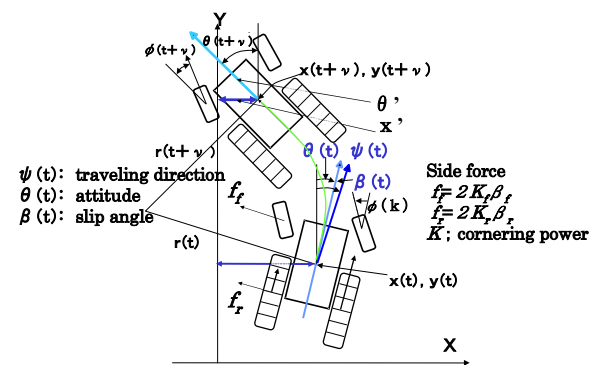
Figure 3 Schematic diagram of movement of tractor.

Experiment of automatic planting in the field

The semi-crawler tractor of 66kW(90 PS) was developed in our laboratory (Figure 4). After equipping this tractor with a planter for soybeans 2.52 m in work width, we conducted an experiment of automatic planting in the

field 10 × 385 m in area at 1.3 m/s in travel speed (engine: 1800 rpm). At the end of the field, the system calculated target steering angle and executed a turn to bring the tractor assembly to the next ridge. After directing the tractor to the next ridge, the system measured the position and direction by FOG, GPS and collected the direction offset of the fiber-optic gyro output.

Figure 4 Autonomous Semi-crawler tractor

RESULT and DISCUSSION

Responsibility of hydraulic steering control system

The response of the hydraulic power steering control system is shown in Figure 5 when the target steering angle is 10degree and initial steering angle is 0 degree. The steering angle is controlled linearly and controlled within 1 second. The idling time rag is about 0.2second.The process of the output volt from the computer PID control and measured steering angle is shown in Figure 6.
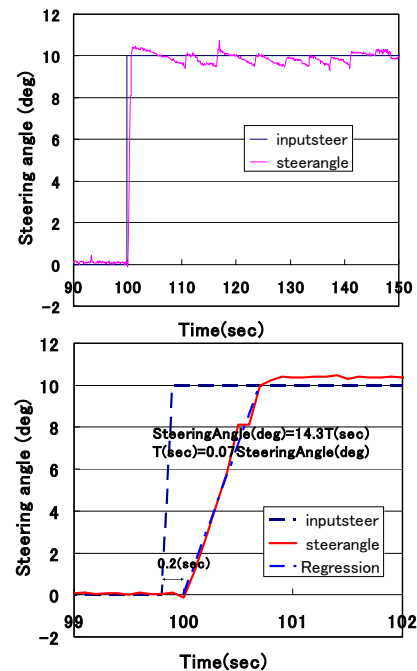
Figure 5 Response of electro-hydraulic power steering by PID control
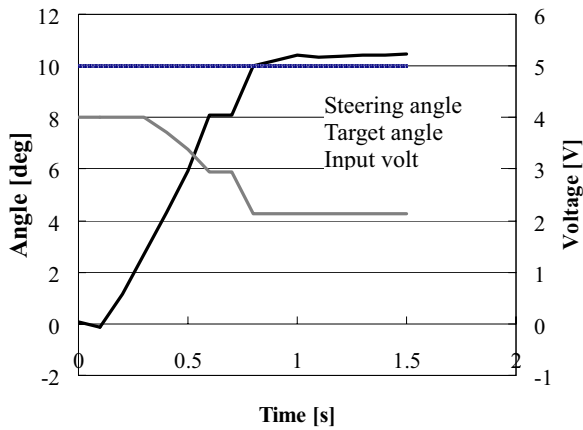
Figure 6 PID steering control

Characteristic of turning of the sem-crawler tractor

The tractor travel first straight 10m and next turn right on fixed steering angle by computer control as Figure 7 and the direction of the tractor is measured by FOG and the track is measured by RTK which's accuracy is 2 cm.

The relationship between the turning radius and the steering angle is examined in the field and the slip angle, the cornering power are calculated using these eqns..

$$\beta = \psi - \theta \tag{12}$$
$$Kf = \square_r mv\omega/(2Ca\square_w) \tag{13}$$
$$Kr = \square_f mv\omega/(2Cb\square_w) \tag{14}$$

When

$$Ca = \varphi - \square_f\omega/v - \beta, \quad Cb = \square_r\omega/v - \beta \tag{15}$$

The velocity of the vehicle is changed 0.5,0.75,1m/s and the steering angle is changed from 5 to 40degree every 5degree step. The relationship between the turning radius and the steering angle is shown in Figure 8. The turning radius is revealed as exponential function of steering angle with high correlation .
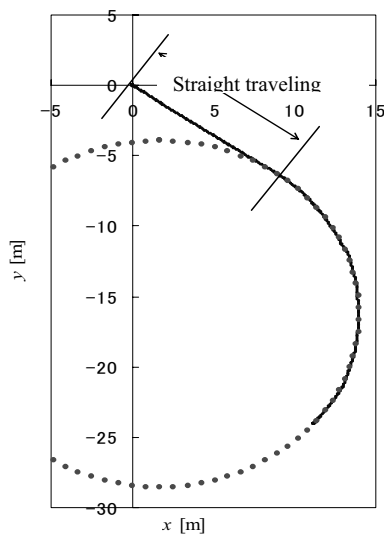
Figure 7   Turning trace of semi-crawler tractor

The cornering power Kf,Kr is calculated by eqn.(13),(14) as Figure 10.The cornering power of the rear track Kr increase with the steering angle grow while Kf decrease. By using this factor, turning radius is esteemed correctly with in 6 cm accuracy.
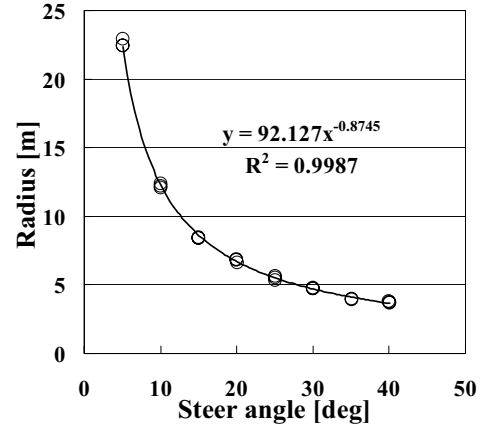
Figure 8 Relationship between steering angle and turning radius(V=0.75m/s)
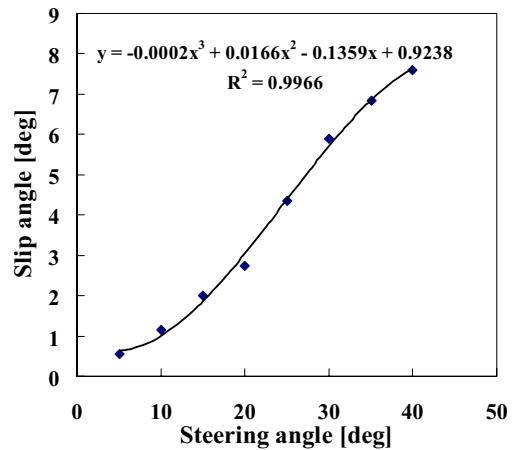
Figure 9 Relationship between steering angle and slip angle
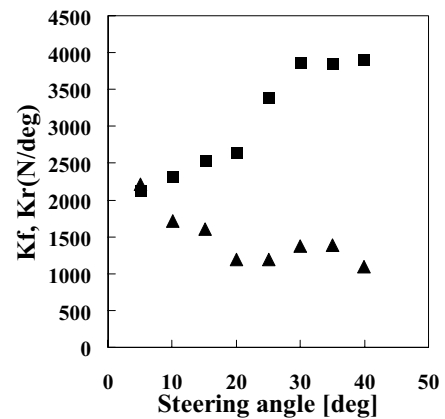
Figure 10 Cornering power Kf(front wheel;▲),Kr(rear track;■)(V=1m/s)

Simulation of the steering control and movement of vehicle

The result of simulation of the movement of the semi-crawler tractor by the predictive steering control method is shown in Figure 8. The steering angle is calculated considering the hydraulic cylinder's operational time lag and direction swinging which is supposed to occur by inequalities of the ground. Figure 11 show steering angle, direction of vehicle, x-position difference from the target line by adjusting predicting time lag. The tractor is more adequately controlled by predictive time 1s than 0.5s7s.
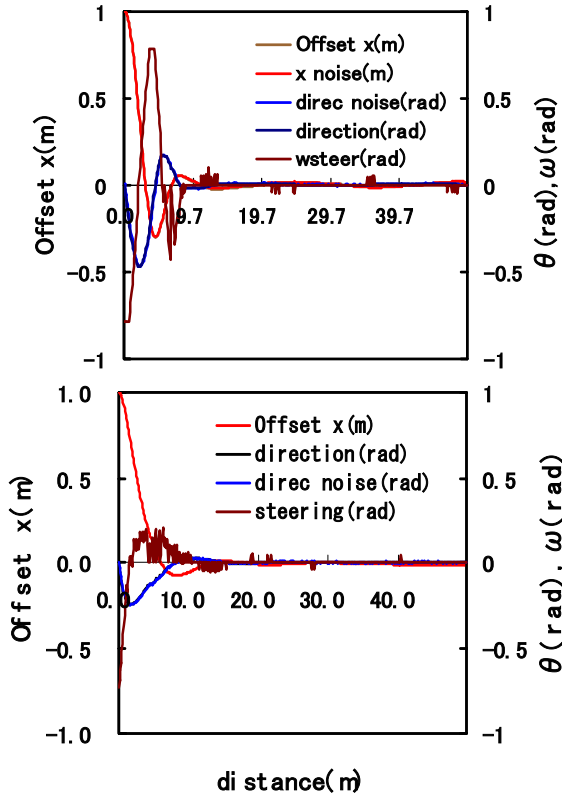
Figure 11 Comparison of dynamics for path tracking of vehicle between the predictive time o.5s(upper) and 1s(lower)

Automatic planting in the field

The tractor plant soybeans automatically by the round trip work of the straight distance 380m without the trouble at 1.3m/s speed for more than 30 minutes (experiment time).

Each lines is parallel and almost straight with equal interval. The tractor was controlled within 10 cm (RMS 5.2cm)of accuracy(Figure12-14). The tractor raise up planter and turn to next line automatically at the end of the operation area and select next target line which is generated by computer, and adjust the position and direction, after entering operational area, down planter and raise up engine revolution, and go forth. There is no meandering under the method of forecasting a position and direction of tractor. The traces of the seeding were

parallel and equal to the target line and the edge of the trace was almost same.
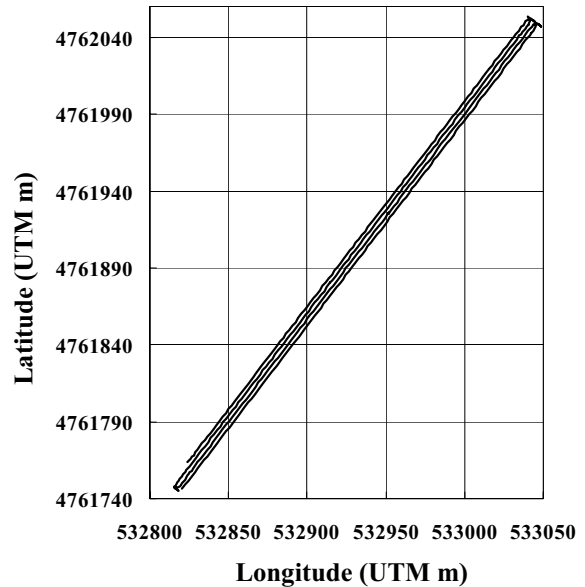
Figure 12 Track of autonomous tractor working on planting
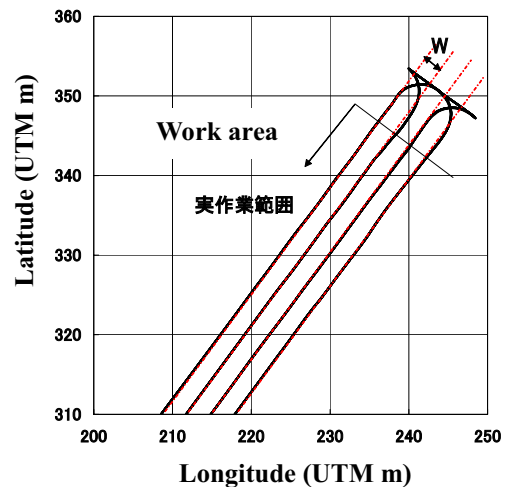
Figure 13 Track of the autonomous tractor working of planting(target line and actual track)
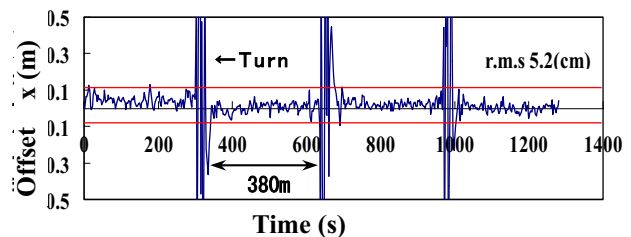
Figure 14 Offset x track of autonomous semi-crawler tractor

Figure 15 Planting soybeans by autonomous semi-crawler tractor (2007.5.29)

Automatic Manual

Figure 16 Comparison of plant raw (soybean) by automatic and manual operation

7. Kazutaka TAKAHASHI Minoru MUTO, Masamitsu KURISU, A Consideration about Estimation of The Slippage for Running Tracked Vehicles, Proceeding of JSME Conference on Robotics and Mechatronics, 2A1-L1-68,2004

REFERENCES

1. Kobayashi, K. et al. Accurate Navigation via Differential GPS and Vehicle Local Sensors. Proceeding of the IEEE International Conf.on MFI, 9-16,1994
2. Kise.M,Noguchi.N,Ishii.K,Terao.H,The development of the Autonomous Tractor with Steering Control Applied by Optimal Control, Proceeding of the ATOE conference,367-363,2002
3. Keiich,Inoue.,K.Otsuka, M.Sugimoto,N.Murakami,Wen Li, Sensor fusion Techniques for Automatic Guidance by the method of Kalman filter using DGPS and Gyrocompass(Part1),Vol61,No.4,103-113,JSAM
4. M. Ahmadi, V. Polotski and R. Hurteau:"Path Tracking Control of Tracked Vehicles.", In proc IEEE Int. Conf. On Robotics and Automation, pp. 2938-2943, 2000.
5. Z. Janosi and B. Hanamoto,The analytical determination of drawbar pull as a function of slip for tracked vehicles", In proc. 1st Int. Conf. On Terrain-Vehicle Systems, pp.707-736, 1961.
6. G. Bekker, Introduction to Terrain-Vehicle Systems, University of Michigan Press, 1969.

OS1-3

INNOVATIONS IN PUMP DESIGN – WHAT ARE FUTURE DIRECTIONS?

Monika IVANTYSYNOVA

Department of Agricultural and Biological Engineering, College of Engineering
Purdue University
225 S. University Street, West Lafaeytte, IN 47905, USA
(E-mail: mivantys@purdue.edu)

ABSTRACT

Displacement-controlled actuators, advanced continuously variable transmissions and hydraulic hybrid power trains represent new technologies for mobile hydraulic machines, off road and on road vehicles. These new technologies allow major fuel savings and reduced emissions, but they change the performance requirements of positive displacement pumps and motors. Additionally, the market demand for positive displacement machines will increase. This paper briefly discusses these technology trends and the impact on existing pump and motor designs. The three major challenges are efficiency improvements, noise reduction and advancements in pump and motor control. Examples from the author's research team documenting the progress in computer modeling of piston pumps and motors will be given.

KEY WORDS

Displacement controlled actuators, pump design, pump efficiency, pump model

NOMENCLATURE

A : piston area
R : pitch radius
Δp: differential pressure
V_0 : volume of displacement chamber at ODC
V_D : dead volume
β : swash plate angle
ΔV : volume to be compressed

INTRODUCTION

High power density is one of the greatest strengths of fluid power technology. This makes fluid power especially advantageous for mobile applications where part of the consumed energy is required to move the installed actuators and transmissions. Fluid power is the best choice for actuators and drives in agricultural, mining and construction machinery as well as other automotive and aerospace applications. However, the efficiency of fluid power systems is relatively low compared to electromechanical actuators and transmissions. This fact is becoming distressing due to rising fuel prices and stringent emissions requirements. The current use of metering valves (hydraulic resistances) in nearly all hydraulically powered actuation systems is one of the main reasons for low overall system efficiency. Another problem is the relatively low efficiency of most of the currently used pumps and motors. This paper will briefly discuss the potential of displacement controlled systems and other major trends in mobile machines like power split drive and hydraulic hybrids. These new technologies allow major fuel savings and reduced emissions, but they change the performance requirements of positive displacement pumps and motors. Furthermore, the market demand for positive displacement machines will increase.

TRENDS IN MOBILE HYDRAULICS

Displacement control for working hydraulics
Displacement controlled actuators avoid throttling losses and allow energy recovery. Berbuer [1] studied the performance of displacement controlled actuation introducing a hydraulic transformer 20 years ago. Since then many others have contributed to new circuit solutions for displacement controlled actuators. An overview of early pump controlled actuation concepts can be found in Ivantysynova [2]. Figure 1 shows the circuit solution proposed by Rahmfeld and Ivantysynova [3] for displacement controlled linear actuators with single road cylinder. Several advantages make this concept attractive:

- Throttling losses are eliminated
- Relief and check valves can be integrated into the pump case, thereby reducing the number of discrete components and fluid connectors
- Multiple cylinders can share a single low pressure line
- Recovery of potential and kinetic energy is possible since the pump automatically runs in motoring mode when the cylinder is driven by an aiding load

A similar solution has been studied by Lawrence et al [4]. An open circuit solution for displacement controlled actuators has been introduced by Haybroek, Larsen and Palmberg [5].
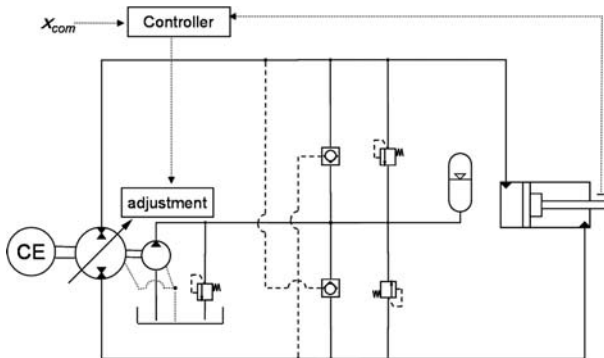
Figure 1 Displacement controlled actuator with single rod cylinder

Although much research effort has been spent over the last 20 years and impressive fuel savings have been reported displacement controlled actuators are still not on the market[10]. The author's research group continues its effort on introducing displacement controlled actuators to mobile machinery. Figure 2 shows a simplified circuit for an excavator with displacement controlled actuators for all functions. Detailed dynamic models of the standard LS excavator system and the proposed displacement controlled system were constructed, and a trench digging cycle was simulated for both. The displacement controlled excavator consumed 29% less total energy than the LS excavator for the simulated

operation, more details can be found in [6]. In displacement controlled actuators the pump becomes the main source of losses. In addition, more pumps need to be installed in each machine. Therefore the pump efficiency will determine the achievable energy savings. The impact of pump efficiency on total power consumption has been studied by the author's research group [7].
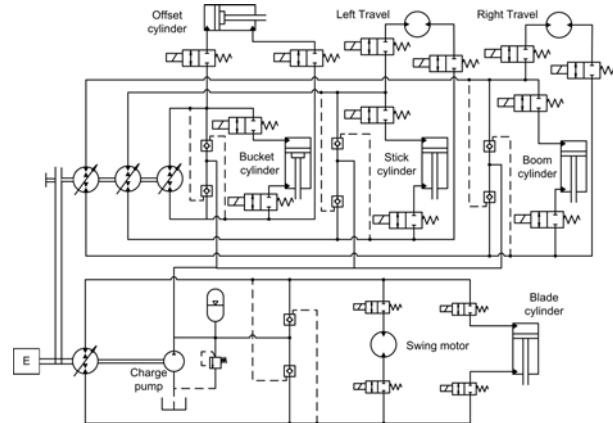
Figure 2 Simplified hydraulic circuit of a displacement controlled excavator

Figure 3 shows a simulated working cycle for a skeed-steer loader with displacement controlled boom and bucket functions, where two different pumps were used. Pump A had a maximum efficiency of 87% and pump B 90%. Although the difference in maximum efficiency is just 3% the system using type B pumps consumed 16% less energy for the same cycle. Thus improving efficiency in the entire range of operating parameters is very important for displacement controlled actuation.

Power Split & Hybrid Power Trains
The power train technology will also undergo major changes. Among the continuously variable transmission concepts (CVT) the power split transmission principle is the most efficient. It allows very effective engine management and can be used for a wide range of applications. Besides the current tractor applications power split and hydraulic hybrids will be introduced in different off road and on road vehicles [8],[9]. The transmission efficiency and ratio are strongly dependent on the efficiency of the pump and motor.

Closed loop control & Automation
A third clear trend is the introduction of more automatic functions and the development of small and large heavy-duty mobile robots or robot like machines. The replacement of human control by closed loop control will allow faster operation. The installation of necessary sensors to measure cylinder and pump displacement, system pressure, speed and machine acceleration will

60

allow the use of the installed actuator power for additional functions like active vibration damping [10].
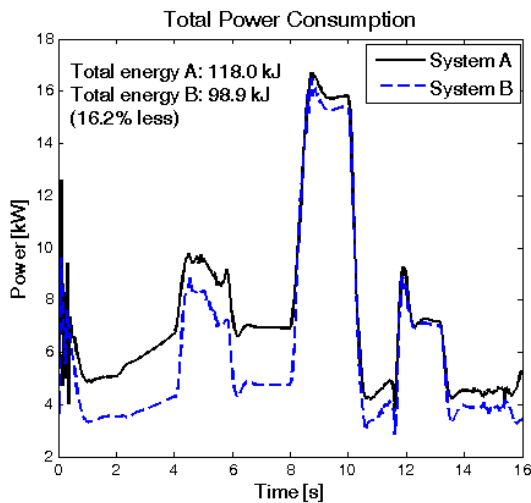
Figure 3 Total power consumption of displacement controlled skid steer loader

PUMP AND MOTOR REQUIREMENTS

The described new system technologies require major changes in pump and motor design. Highly efficient electrohydraulically controllable overcenter pumps are requested for the realization of displacement controlled linear and rotary actuators. The power split and hydraulic hybrid technology requires overcenter pumps and variable motors of the highest efficiency. The closed loop control of actuators and drives will require variable displacement pumps with installed sensors to measure the pump displacement. The integration of microcontrollers into the pump or motor will allow implementing many different control concepts and customer features by software, i.e. the design of smart pumps. Pumps for displacement controlled actuators usually require higher bandwidth of the pump controlled system. In addition pump noise will become a major challenge for mobile equipment when installing multiple pumps and motors in machines with quieter engines. The replacement of valve controlled systems by displacement control will increase the demand for smaller pumps. The future direction for pump and motor design need to address the following objectives:

- reduction of pump and motor power losses in the entire range of operating parameters
- increase of bandwidth of pump control
- reduction of pump and motor noise
- high operating pressures
- compact design and high power density

INNOVATIONS IN PUMP DESIGN

The first question to be answered is; do we need to in-

vent new pump principles to fulfill the above listed requirements? With gear, vane, screw and piston pumps and many different existing designs for each type the number of designs to choose from seems to be large enough. The current designs are usually much simpler than those developed 50 years ago [11]. The market share of variable units has continuously increased over the last 30 years and this trend will continue. That's why this paper focuses on trends in the area of variable displacement machines and will not include gear and screw pumps. Among the variable positive displacement machines only piston machines are applicable for high pressures, i.e. vane pumps are not suitable for the discussed new technologies. In mobile hydraulics radial piston pumps have not been used very often, except radial piston motors for high torque and low speed applications. Radial piston pumps with outer piston support are very similar to swash plate type axial piston pumps, thus both design allow high pressures, high efficiencies and comparable power density. However due to the radial piston arrangement the radial piston pump with outer piston support is much shorter than the swash plate type axial piston pump. This could be an advantage for the displacement controlled systems requiring the installation of a larger number of pumps in a single machine like the excavator shown in Fig. 2. One of the disadvantages of variable radial piston pump with outer piston support is the higher movable mass compared to swash plate type, thus for applications with high bandwidth of the pump control system the swash plate type is clearly the best solution. There are only two types of axial piston machines - bent axis axial piston and swash plate axial piston machines. The main difference between these two different designs is the generation of torque. In swash plate axial piston machines the torque generation takes place at the cylinder block. Therefore the piston is heavy loaded by a large radial pressure dependent force. This large force does not allow using piston rings to seal the displacement chamber better. The piston-cylinder pair requires a very good design to fulfill its double function (sealing and bearing). In bent axis axial piston machines the torque is generated on the driving flange. The lateral piston force is very small and therefore piston rings can be used to seal the displacement chamber. Consequently this principle allows achieving higher efficiencies than all other known designs. High starting torque and higher speed limit due to lighter pistons and the possibility to have very large tilt angles (45°and more) are further advantages of the bent axis principle. The main disadvantages are higher production costs, lower bandwidth and more complex design, which does not allow a through shaft in case of larger tilt angles. The swash plate type axial piston machine represents the simplest design. Unfortunately swash plate machines have a higher number of sealing and bearing gaps, which create a real challenge in achieving comparable high efficiencies. Computer

based design offers certain opportunities as will be discussed later in this paper. Another drawback of the swash plate unit is the limitation of maximum swash plate angle due to the high radial force exerted on the piston. This limits the power density of this design. Figure 4 shows a comparison of size of rotating group of different axial piston machines with different tilt angles, floating cup 10°, swash plate 18°, bent axis 45°. The dimensions shown are the main dimensions of the rotating group of a 125 cm³ unit.
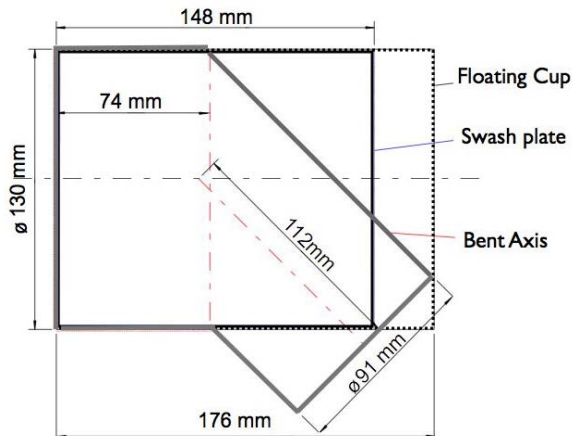
Figure 4 Comparison of main dimensions of rotating group of different piston machines

The floating cup design proposed by INNAS [12] is a bent axis machine with a limited tilting angle of 10°due to geometrical constraints [13]. The unit has 24 pistons and requires two valve plates and two cylinder blocks, i. e. the resulting number of parts of the rotating group is with 83 much higher compared to a 9 piston bent axis machine requiring 23 parts. Table 1 shows a comparison of power density of the three different designs. The swash plate unit and the bent axis have both 9 pistons. The high number of pistons (24) of the floating cup design allows reducing flow pulsation, but requires 50 gaps to be sealed. Compared to that, a bent axis with 9 pistons has only 19 gaps. Thus shows innovations in pump and motor design should rather focus on continuous improvement of well-known and well-understood principles, like bent axis, swash plate and radial piston units. Although decades of research many effects taking place in our current machines are not completely understood and models are still not accurate enough to reflect the complex nature of physical effects taking place in these machines. Sealing of the displacement chamber is the biggest challenge when designing a positives displacement machine for high pressure application. Therefore the design of the sealing and bearing gaps in the area of piston machines will offer many opportunities for innovations necessary to improve efficiency in the entire range of operating conditions. Surface shaping, surface texturing, the application of new materials and

coatings together with new manufacturing technologies will form the basis for further innovations to meet the described challenges.

Table 1: Rotating group power density comparison of 125 cm³ positive displacement units

DePorP	P owe PPwwD Po PP r	P owe ΔP Poorr	P owe Powwo Pow r	Pow PowPr	Power Powe	DePo
					Pow e owPr	Po r
PwoowPr PoP	Pooo	Poo	Poo	PPPe	oeww	woo
PwoPr Pwve	Pooo	Poo	PPw	woeP	oeve	woe
PePw owP	Pooo	Poo	Peo	weww	oePP	Poo

Figure 5 shows measured power loss and overall efficiency of a 75 cm³ variable swash plate unit for four different displacements and two operating pressures when running at 2000rpm. The power loss at lower swash plate angles is too high to keep the efficiency curve flat. In addition to that keeping the efficiency high also for lower pressures is very important for displacement controlled actuation and transmissions. Thus a further reduction of losses occurring at lower pressures is another challenge for the design of high pressure pumps and motors.
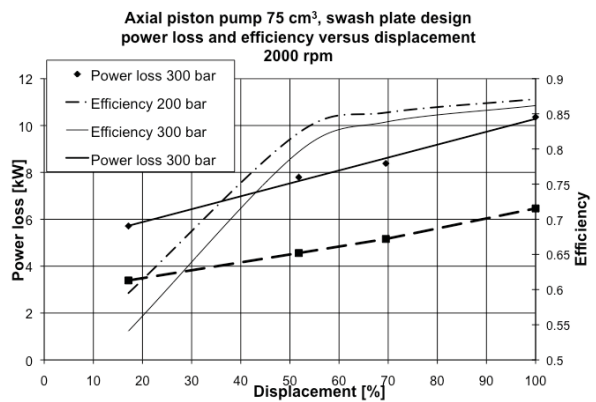
Figure 5 Measured power loss and overall efficiency of a 75 cm³ unit for different swash plate angles

The program CASPAR allows supporting pump design and optimization based on modeling non-isothermal gap flow in all three connected gaps of swash plate axial piston machines [12]. The model has been extended to consider fluid structure interaction, i.e. the hydrodynamic effects due to elastic surface deformation [15]. The CASPAR model considers micro-motion of all movable parts of the rotating group to determine the varying gap heights between highly loaded sealing and bearing surfaces over one shaft revolution. Based on the final gap heights the load carrying ability of the gap and

all other resulting parameters like viscous friction and leakage can be predicted. The program was used to optimize the piston shape for pumping and motoring conditions [16]. Recently the impact of a shaped valve plate has been studied [17]. Figure 6 shows the gap height between cylinder block and valve plate for the rotating angle φ=0°, i.e. the piston at the outer dead center. Changing external forces exerted on the cylinder block lead to a micro-motion of the cylinder block which causes varying gap height over one haft revolution while running the pump under steady state conditions. Figure 7 shows the impact of shaping on the fluid film thickness. The average maximum and minimum gap heights between valve plate and cylinder block are shown for different operating conditions (two speed settings, two different operating pressures and 100% and 20% swash plate angle). The gap heights for the standard design are shown in light gray and the gap heights obtained for the shaped surface in black. The investigated surface shape contributes to an increase of gap heights at lower operating pressures and lower displacements.
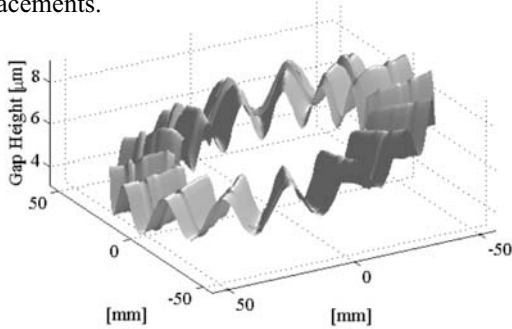
Figure 6 Gap height between valve plate and cylinder block using a shaped valve plate surface
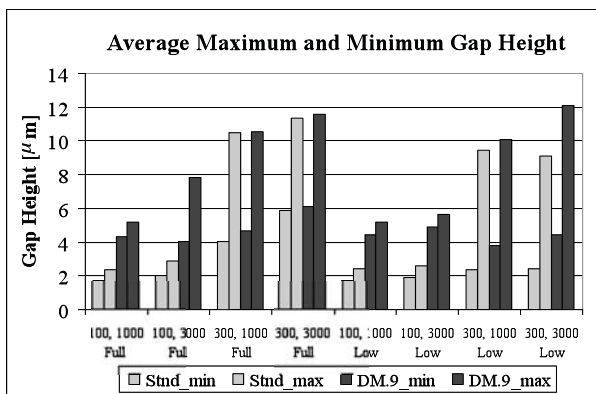
Figure 7 Maximum and minimum gap height between valve plate and cylinder block

The change in gap height leads to change in fluid flow conditions and consequently to a change of friction and leakage. Viscous friction and leakage determine the power losses generated in by the gap in case of full fluid film conditions. For all simulated eight operating condi-

tions a sufficient thickness of the fluid film has been obtained. The shaped valve plate surface reduces the power loss by more than 60% for lower operating pressures and low displacement. In case of high operating pressures the impact of the investigated shape is negligible.
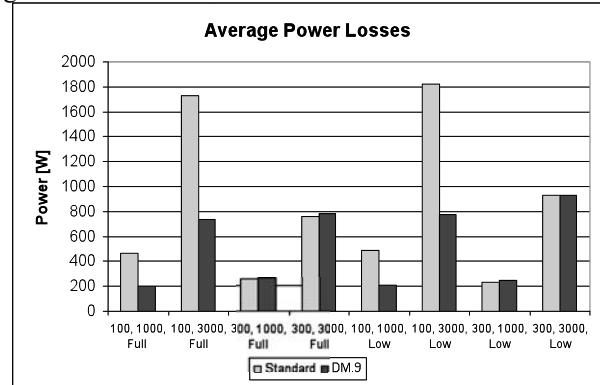
Figure 8 Average power loss of the gap between valve plate and cylinder block (standard & shaped valve plate)

Recently there has been an increasing trend of research on fast switching valves. The idea of creating a virtually variable displacement pump has been proposed and studied by different teams [18],[19]. Lumkes and Batdorff [19] investigated the losses associated with the use of fast switching valves, but did not consider that the fixed displacement pump will have in addition considerable losses. Fast electro-hydraulically operated switching valves could be used to reduce losses due to compressibility when integrating them in piston machines to connect each displacement chamber with the high pressure and low pressure port respectively. Figure 9 shows an example for a swash plate axial piston pump with rotating swash plate. By keeping the displacement chamber connected to suction during discharge for the required time the compression of the volume expressed by the second term in Eq. (1) will be avoided. Assuming that the switching valves are fast enough, for a 75 cm^3 pump running at 3000 rpm, 300 bar pressure and 20% displacement the theoretical increase in discharge flow rate is 1.34 l/min.

$$V_0 = V_D + R \cdot A \left(\tan \beta_{\max} + \tan \beta \right) \qquad (1)$$
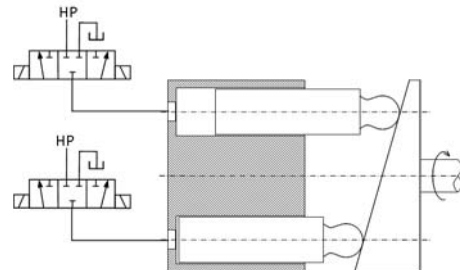
Figure 9 Swash plate axial piston pump with fast switching valves for individual chamber porting

CONCLUSION

Displacement controlled actuators, power trains based on power split transmission and hydraulic hybrids are the main emerging technologies, which can significantly reduce fuel consumption and emissions. These technologies require elctrohydraulically controllable variable displacement pumps with four-quadrant operation. Major challenges are high efficiency in the entire range of operating parameters; low noise and advancements in pump control. Surface shaping and texturing, the application of new materials and coatings together with new manufacturing technologies will form the basis for further innovations in pump and motor design. Due to the limited length of this paper only few examples for new directions in pump design are presented and the referenced work is very limited and does not reflect the amount of research accomplished in this field worldwide.

REFERENCES

1. Berbuer, J., NeuartigeServoantriebemitprimaererVerdraengersteuerung.PhD thesis RWTH Aachen, 1998.
2. Ivantysynova, M.,Pump Controlled Actuator - a Realistic Alternative for Heavy Duty Manipulators and Robots. Developments in Fluid Power Control of Machinery and Manipulators, Fluid Power Net Publication (2000), chapter 5, pp. 101 – 123.
3. Rahmfeld, R. and Ivantysynova, M. 1998. Energy saving hydraulic actuators for mobile machines. Proc.1st. Bratislavian Fluid Power Symposium, Casta-Pila, Slovakia, pp. 47 - 57.
4. Lawrence, P.D. ;Salcudean, S.E. ; Sepehri, N. ; Chan, D., Bachmann, S., Parker, N., Zhu, M. and Frenette, R., Coordinated and Force-Feedback Control of Hydraulic Excavators. 4th Intern. Symposium on Experimental Robotics, Stanford, USA, 1995.
5. Heybroek, K.; Larsson, J. and Palmberg, J.O., Open Circuit Solution for Pump Controlled Actuators. Proc. 4th FPNI PhD Symposium, pp. 27-40. Sarasota, Florida, USA, 2006.
6. Williamson, C., Zimmerman, J., Ivantysynova, M., Efficiency Study of an Excavator Hydraulic System Based on Displacement-Controlled Actuators. Bath/ASME Symposium on Fluid Power and Motion Control. Bath, UK, 2008.
7. Williamson, C. and Ivantysynova, M., The Effect of Pump Efficiency on Displacement Controlled Actuator Systems. Proceedings 10thSICFP '07, Tampere, Finland, Vol. 2, pp. 301-326, 2007.
8. Carl, B., Williams, K. and Ivantysynova, M., Comparison of Operational Characteristics in Power Split Continuously Variable Transmissions. SAE ComVec, Chicago, IL, USA, SAE Technical Paper 2006-01-3468.,2006.
9. Kumar, R.,Ivantysynova, M. and Williams, K.,Study of Energetic Characteristics in Power Split Drives for on Highway Trucks and Wheel Loaders. SAE ComVec, Chicago, IL, USA, SAE Technical Paper 2007-01-4193, 2007.
10. Eggers, B.,Rahmfeld, R. and Ivantysynova, M., An energetic comparison between valveless and valve controlled active vibration damping for off-road vehicles. 6th JFPS International Symposium on Fluid Power. Tsukuba, Japan. pp. 275-283, 2005.
11. Ivantysyn, J. and Ivantysynova, M., Hydrostatic pumps and motors, Akademia books international, New Delhi, 2001.
12. Achten, P. A. J., Power density of the floating cup axial piston principle. Proc. 2004 ASME ImechE Congress an Expo, IMECE 2004-59006 Anaheim, California, 2004.
13. Peter Aachten et al., Movement of the cups on the barrel plate of a floating cup axial piston machine. International Journal of Fluid Power 5 (2004) No. 2 pp. 25-33, 2004.
14. Wieczorek, U. and Ivantysynova, M., Computer Aided Optimization of Bearing and Sealing Gaps in Hydrostatic Machines - The Simulation Tool CASPAR. International Journal of Fluid Power, Vol. 3 (2002), No.1, pp. 7-20, 2002.
15. Huang, C. and Ivantysynova, M., A new approach to predict the load carrying ability of the gap between valve plate and cylinder block. PTMC 2003, Bath, UK, pp. 225 – 239, 2003.
16. Ivantysynova, M. and Lasaar, R., An investigation into Micro- and macro geometric design of piston/cylinder assembly of swash plate machines. International Journal of Fluid Power, Vol. 5 (2004), No.1, pp. 23- 36, 2004.
17. Baker, J. and Ivantysynova, M., Investigation of power losses in the lubricating gap between cylinder block and valve plate of axial piston machines. Proc.of 5thFPNI PhD Symposium, Cracow, Poland 2008.
18. Haink, C.T.,Rannow, M., Van de Van, J. Wang, M., Li, P., Chase, T., High speed rotary pulse width modulated on/off valve. Proc.of ASME-IMECE'07, Seattle, USA, IMECE 2007-42559, 2007.
19. Batdorff, M., Lumkes, J., Virtually variable displacement hydraulic pump including compressibility and switching losses. Proc.of ASME-IMECE'06, Chicago, USA, IMECE 2006-14838, 2006.

OS1-4

HYDRAULIC SYSTEMS AND COMPONENTS FOR MEDIUM－SIZED BULLDOZER

Seita HAYASHI*, Sadao NUNOTANI** and Masayuki MUKAINO***

* HST Development Group Hydraulic Equipment Technical Center
Komatsu Ltd
400 Yokokura Sinden , Oyama-Shi,Tochigi-ken, 323-8558 Japan
(E-mail: seita_hayashi@komatsu.co.jp)
** Development Division
Komatsu Ltd
2-3-62 Minatoku,akasaka, Tokyo, 107-8414 Japan
(E-mail: sadao_nunotani@komatsu.co.jp)
***Small Size Machine Development Group Construction Equipment Technical Center 1
Komatsu Ltd
23 Tsu,Futsumachi,Komatsu-Shi,Ishikawa-Ken 923-0392 Japan
(E-mail: masayuki_mukaino@komatsu.co.jp)

ABSTRACT

Introduce KOMATSU's newest hydraulic systems and components for medium-sized bulldozer, which includes electronic controlled HST (Hydro Static Transmission) and hydraulically drive fan system. Electronic controlled HST consists of tandem piston pumps and two inside-shoe type final drives. Inside-shoe type final drive consists of bent axis type piston motor and 2 stage planetary reduction gear. Hydraulically drive fan system consists of variable piston pump common with work equipment pump and in-fan type fixed motor. This system is also electronically controlled. By using these hydraulic systems and components, layout flexibility and vehicle design flexibility are drastically improved, therefore this bulldozer can get unrivaled blade visibility and productivity at the same time.

KEY WORDS

HST, Bulldozer, Electronic controlled HST, Inside-shoe type final drives, Hydraulically drive fan
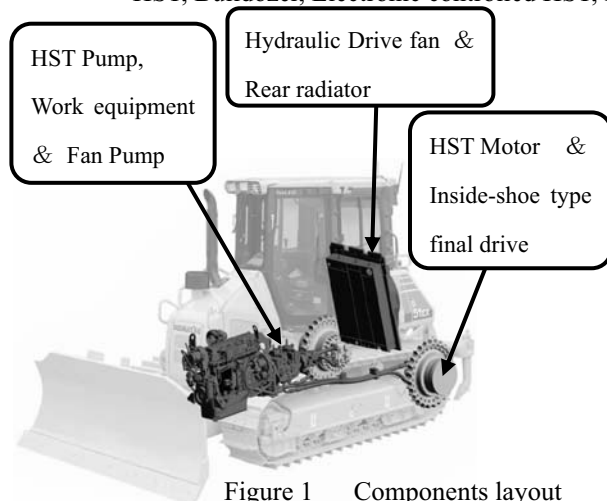
Figure 1   Components layout

Figure 2   Unrivaled blade visibility

1. TARGET AND ISSUES

To improve total performance by
①Create unrivaled blade visibility by super-slant nose.
②Increasing productivity and reducing hydraulic loss.

2. SOLUTION OF THE TARGET AND ISSUES

a) Change power train transmission with clutch and brake to HST.
b) Change front mount radiator with in-fan type motor to rear mount radiator with in-fan type motor.
By using HST drive and hydraulic drive fan systems, component's layout flexibility and vehicle design flexibility are drastically improved, therefore this bulldozer can get unrivaled blade visibility.
c) Seamless traction force and power turn by Electronic controlled HST with continuously variable pump and motor.

Speed sensor in both travel motors ensure straight tracking, even working on slopes and with uneven blade loads.
d) Change work equipment pump from two fixed gear pump to one variable pump and CLSS (Closed Center Load Sensing System) and change fan control system from surplus flow by-pass type in-fan type motor to fixed in-fan type motor and variable pump (common with work equipment pump) and CLSS.
This fan system is also electronically controlled by control valve with EPC valve.
Take out engine power efficiently at all speed range by electronic controlled HST.
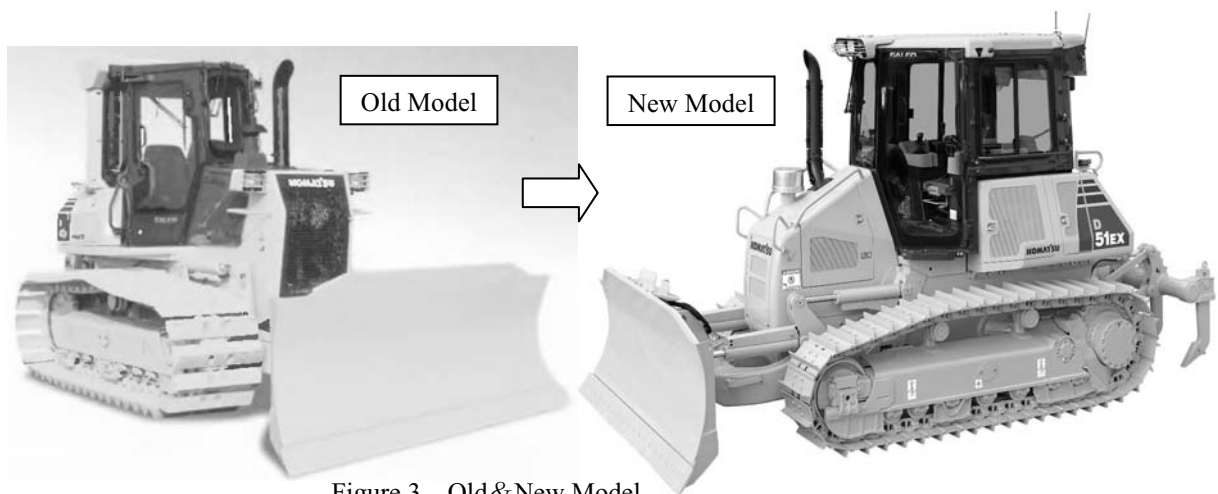
Figure 3   Old＆New Model
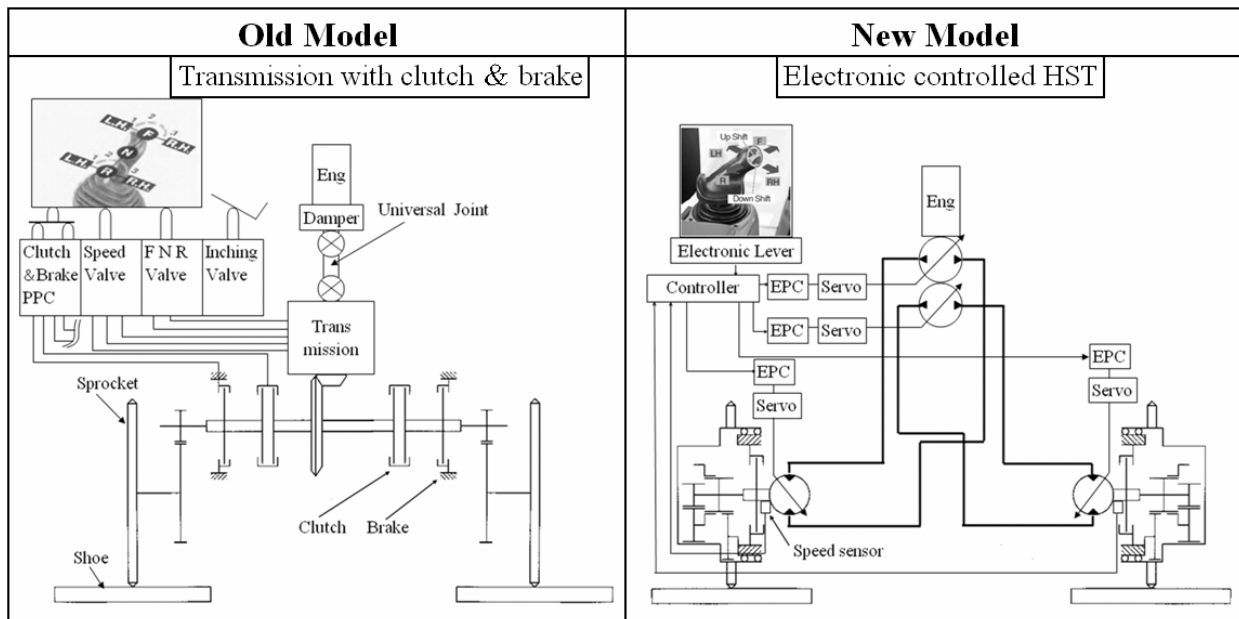
Figure 4   Comparison of power train

3. HYDRAULIC COMPONENTS

① HST Pump

 a) Superior Durability and Reliability
  ・ Variable displacement swash plate type piston pump using common internal parts with other KOMATSU made reliable construction machines.

 b) For electronic
  ・ Electronic controlled in-line servo structure with EPC Valve (Electronic Pressure Control Valve)

② HST Motor

 a) Superior Durability and Reliability
  ・ Variable bent axis piston motor same concept with other KOMATSU made reliable construction machines.
  ・ Free from attack by rock or soil owing to inside-shoe final drive layout.
  ・ Easy accessibility and maintainability by modular designed inside-shoe type final drive integrated with HST motor and reduction gear.

 b) For Electronic
  ・ Electronic controlled in-line servo structure by control pressure from frame mounted EPC Valve.

In-line servo   EPC Valve

Figure 5   HST Pump

In-line servo

Speed sensor

Figure 6   HST Motor

Old Model   New Model

Shoe width
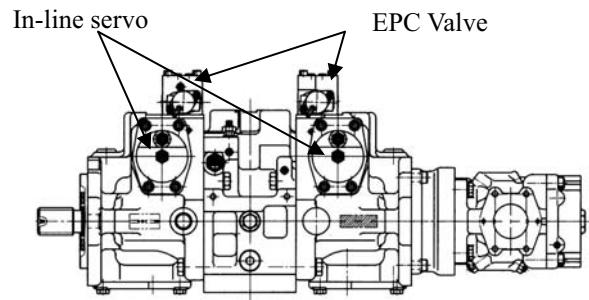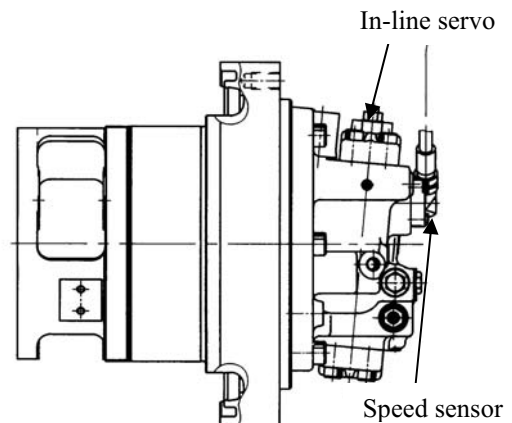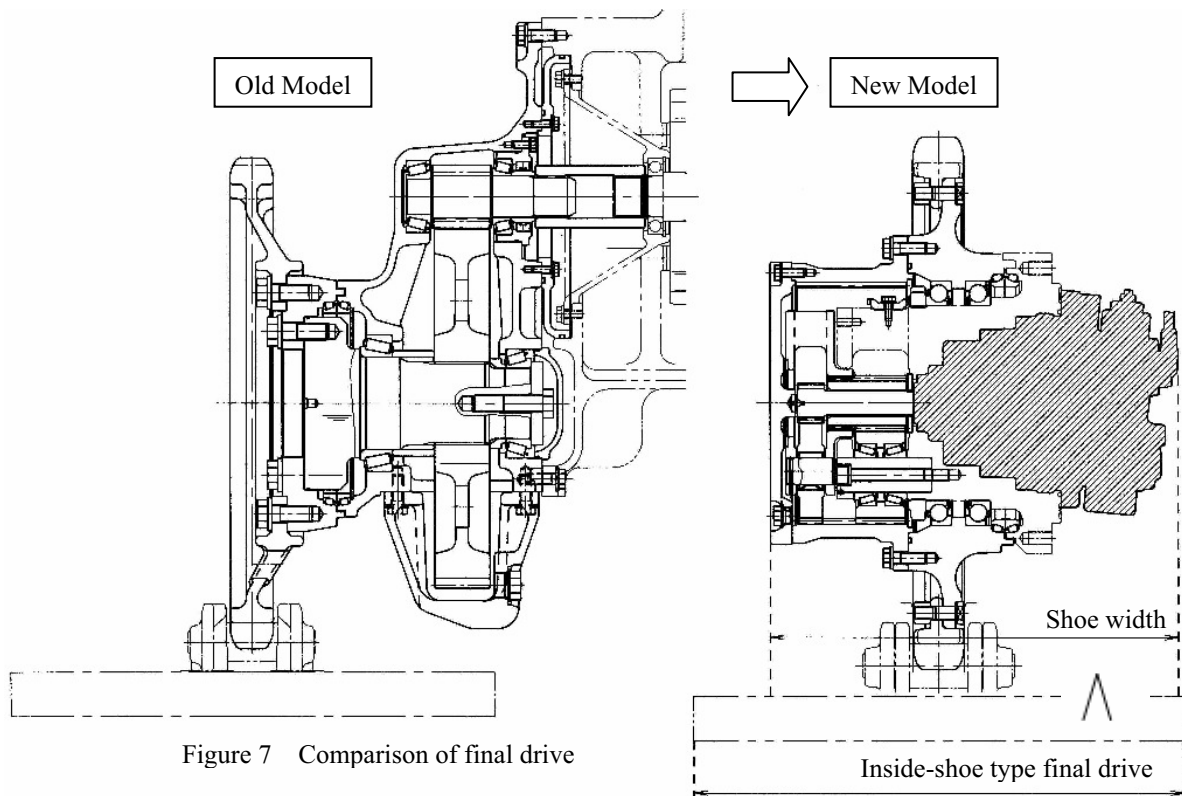
Figure 7   Comparison of final drive

Inside-shoe type final drive

67

4. CONCLUSION

KOMATSU's newest hydraulic systems and components for medium-sized bulldozer

①Create unrivaled blade visibility by super-slant nose.

②Increasing productivity and reducing hydraulic loss.

  a) Change power train transmission with clutch and brake to HST.

  b) Change front mount radiator with in-fan type motor to rear mount radiator with in-fan type motor.

  c) Seamless traction force and power turn by electronic controlled HST with continuously variable pump and motor.
  Speed sensor in both travel motors ensure straight tracking, even working on slopes and with uneven blade loads.

  d) Change work equipment pump from two fixed gear pump to one variable pump and CLSS and change fan control system from surplus flow by-pass type in-fan type motor to fixed in-fan type motor and variable pump (common with work equipment pump) and CLSS.
  This fan system is also electronically controlled by control valve with EPC valve.
  Take out engine power efficiently at all speed range by electronic controlled HST.

5. FUTURE PLAN

We will try to improve hydraulic systems and components day by day,
so as to achieve construction machine's selling point,
and to contribute to the customer's benefit

These concepts were adapted to 3 more models which will be launched soon.

6. REFERENCES

1. Masayuki Mukaino,Seita Hayashi and Osamu Takatori,
   Development of D39EX/PX-21 HST Machine,
   KOMATSU Technical report 2001 VOL.47 NO 1.

2. Toshihiko Fukasawa and Eiji Ishibashi,
   Development of Small-Sized Crawler Dozers "D31/37/39-21"with Electronically Controlled HST,
   KOMATSU Technical report 2004 VOL.50 NO 153.
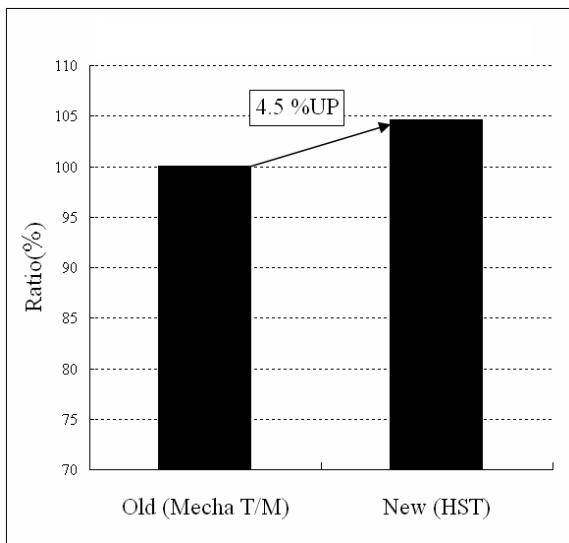
Figure 8   Comparison of productivity(m3/L)

OS2-1

TRENDS AND CONSTRAINTS FOR FLUID POWER IN MOBILE MACHINERY

Roberto PAOLUZZI*

Institute for Agricultural and Earthmoving Machinery – Italian National Research Council IMAMOTER –
C.N.R. Via Canal Bianco, 28 44100 Ferrara – Italy
E-mail r.paoluzzi@imamoter.cnr.it

ABSTRACT

The development of fluid power systems for use in agricultural and construction machinery faced in the last years a substantial contribution due to the increasing role played by electronics. The scenario of the next years in agricultural and construction will be very much influenced by legislation constraints in terms of environmental compatibility, noise emission, energy usage and recyclability. The new set of requirements in terms of safety level for machines, described in documents like ISO 15998:2008 will change the boundary conditions for machine design, requiring a deep investigation at system level, which will force a change in the design perspective for fluid power components. The new possibilities given by an extensive use of embedded electronics, advanced architectures and system level design of machines will be investigated and described trying to highlight threats and opportunities for next generation of products.

KEY WORDS

Hydraulic system, Mobile machinery, Electronic system, energy saving, sustainability

INTRODUCTION

The deep changes in hydraulic circuit layout due to the extensive use of electronics and distributed control is an unquestionable feature which characterized the evolution of high-end products over the last decade. However, the potential offered by the novel approach is not fully exploited since, with some remarkable exceptions, it affected mainly hydraulic components, seen as individual parts, performing local functions. The availability of a large amount of information on system variables, and the ability of control systems to react to abrupt changes in the operating environment, is one of the key features of fluid power systems coupled with electronic control. It can overcome the major limitations, in terms adaptation, shown by traditional hydro-mechanical approach.

On one hand, the mobile machinery industrial sector is one of the trailers in view of the reduced cost and improved flexibility of electronics, but on the other hand, the target of the efforts is strongly influenced by legislation constraints in machinery use. These constraints, after a long period of independent evolution, are now converging towards a global approach, where America, European and Asian markets tend to share a common objective. The paper tries to highlight these mid- or long-term objectives focusing on the way they can affect the development of fluid power systems for mobile use.

MAJOR CONSTRAINTS
NOISE EMITTED BY OUTDOOR EQUIPMENT

European Directive 2000/14/EC [1], amended by the Directive 2005/88/EC of the European Parliament and of the Council of 14 December 2005, corrected by Corrigendum to Directive 2005/88/EC (OJEU L 165,

17.6.2006, p. 35), concerning the noise emitted by equipment used outdoor, enforced strict limits on noise emission by mobile machinery, according to a long-term reduction strategy. Several machines (mainly earthmoving) were strongly affected by limits imposed and needed specific measures to be undertaken in order to improve their noise emission level. Apart from other side effects, which will be dealt with later, the first result of reduction in noise emissions from the main sources (engine and cooling fan) is the increased importance of hydraulic components as a noise source [2].

Research on noise reduction in fluid power components has always been a very active area, but in recent years a renewed attention revitalized the area, thanks to the pressure that machine manufacturers are exerting on hydraulic suppliers in order to get quieter components. Figure 1 shows the situation on noise emission values from hydraulic excavators as function of net engine power, prior to directive 2000/14/EC enforcement
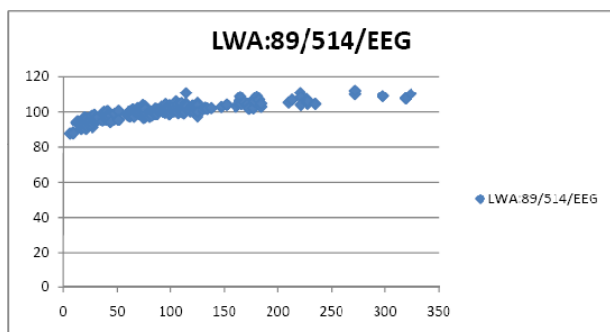
Figure 1 Emissions from off-road diesel engines in Europe

It is worth noting that emitted noise values are significantly above 100 dB(A) for a large part of installed power range.

Figure 2 shows the guaranteed noise levels admissible for excavators according to the requirements of the Directive 2000/14/EC.

A first comment is that the limits can be challenging for several machines, and according to several analysis of statistical data, in an excavator for example, the engine noise, fan noise and hydraulic noise can all be at a similar level, and in that case all need to be reduced together [13]. It is worth noting that at the time of switching from stage I levels (third column of figure 2) to stage II (last column), a remarkable 20% of the machines could not meet the requirement [13].

EMISSIONS FROM I.C. ENGINES

The topic of limitations to emissions of CO_2 and No_x from internal combustion engines used off-road, Directive 97/68/EC, amended by 2004/26/EC and

2006/105/EC is another of the environmental and legislation constraints able to change the overall scenario

Tracked dozers, tracked loaders, tracked excavator-loaders	$P \leq 55$	106	103 (²)
	$P > 55$	87 + 11 lg P	84 + 11 lg P (²)
Wheeled dozers, wheeled loaders, wheeled excavator-loaders, dumpers, graders, loader-type landfill compactors, combustion-engine driven counterbalanced lift trucks, mobile cranes, compaction machines (non-vibrating rollers), paver-finishers, hydraulic power packs	$P \leq 55$	104	101 (²) (³)
	$P > 55$	85 + 11 lg P	82 + 11 lg P (²) (³)
Excavators, builders' hoists for the transport of goods, construction winches, motor hoes	$P \leq 15$	96	93
	$P > 15$	83 + 11 lg P	80 + 11 lg P

Figure 2 permissible noise levels according to EC directive (dBA)

of boundary conditions that fluid power systems must comply with. If apparently this actions does not directly affect fluid power systems, when combined to noise emission limits it had, and will have, tremendous impact on design.

Figure 3 shows the evolution of limit emissions from I.C.engines according to European legislation, but the scenario does not change much if we refer to EPA in USA (figure 4) or Japan (Figure 5)

Mobile machinery are significantly impacted in the sense that up to 100% of the available power is transferred to implements or locomotion devices though hydraulic subsystems, and the coupling between demand and available power determines the engine working point and therefore its emissions.

The effect on machine constraints can be summarized as follows:

- Engine displacement becomes generally larger;
- Rated engine speed is generally reduced;
- Cooling system design is more stringent (also due to noise limitation)
- Electronic injection control is generalized

Stage III A Standards for Nonroad Engines

Cat.	Net Power	Date†	CO	NO_x+HC	PM
	kW			g/kWh	
H	$130 \leq P \leq 560$	2006.01	3.5	4.0	0.2
I	$75 \leq P < 130$	2007.01	5.0	4.0	0.3
J	$37 \leq P < 75$	2008.01	5.0	4.7	0.4
K	$19 \leq P < 37$	2007.01	5.5	7.5	0.6

† dates for constant speed engines are: 2011.01 for categories H, I and K; 2012.01 for category J.

Table 3
Stage III B Standards for Nonroad Engines

Cat.	Net Power	Date	CO	HC	NO_x	PM
	kW			g/kWh		
L	$130 \leq P \leq 560$	2011.01	3.5	0.19	2.0	0.025
M	$75 \leq P < 130$	2012.01	5.0	0.19	3.3	0.025
N	$56 \leq P < 75$	2012.01	5.0	0.19	3.3	0.025
P	$37 \leq P < 56$	2013.01	5.0	4.7†		0.025

† NO_x+HC

Figure 3 Emissions from off-road diesel engines in Europe

72

Engine Power	Year	CO	NMHC	NMHC+NO$_x$	NO$_x$	PM
kW < 8 (hp < 11)	2008	8.0 (6.0)	-	7.5 (5.6)	-	0.4[a] (0.3)
8 ≤ kW < 19 (11 ≤ hp < 25)	2008	6.6 (4.9)	-	7.5 (5.6)	-	0.4 (0.3)
19 ≤ kW < 37 (25 ≤ hp < 50)	2008	5.5 (4.1)	-	7.5 (5.6)	-	0.3 (0.22)
	2013	5.5 (4.1)	-	4.7 (3.5)	-	0.03 (0.022)
37 < kW < 56 (50 < hp < 75)	2008	5.0 (3.7)	-	4.7 (3.5)	-	0.3[b] (0.22)
	2013	5.0 (3.7)	-	4.7 (3.5)	-	0.03 (0.022)
56 ≤ kW < 130 (75 ≤ hp < 175)	2012-2014[c]	5.0 (3.7)	0.19 (0.14)	-	0.40 (0.30)	0.02 (0.015)
130 ≤ kW < 560 (175 ≤ hp ≤ 750)	2011-2014[d]	3.5 (2.6)	0.19 (0.14)	-	0.40 (0.30)	0.02 (0.015)

a - hand-startable, air-cooled, DI engines may be certified to Tier 2 standards through 2009 and to an optional PM standard of 0.6 g/kWh starting in 2010
b - 0.4 g/kWh (Tier 2) if manufacturer complies with the 0.03 g/kWh standard from 2012
c - PM/CO: full compliance from 2012; NOx/HC: Option 1 (if banked Tier 2 credits used)—50% engines must comply in 2012-2013; Option 2 (if no Tier 2 credits claimed)—25% engines must comply in 2012-2014, with full compliance from 2014.12.31
d - PM/CO: full compliance from 2011; NOx/HC: 50% engines must comply in 2011-2013

Figure 4 Emissions from off-road diesel engines in USA

Power (P)	CO	HC	NOx	PM	Smoke	Date	
kW	g/kWh				%	New Models	All Models†
19 ≤ P < 37	5.0	1.0	6.0	0.4	40	2007.10	2008.09
37 ≤ P < 56	5.0	0.7	4.0	0.3	35	2008.10	2009.09
56 ≤ P < 75	5.0	0.7	4.0	0.25	30	2008.10	2010.09
75 ≤ P < 130	5.0	0.4	3.6	0.2	25	2007.10	2008.09
130 ≤ P < 560	3.5	0.4	3.6	0.17	25	2006.10	2008.09

† Applies to continuously produced nonroad vehicles (but not special vehicles) and imported special/nonroad vehicles.

Figure 5 Emissions from off-road diesel engines in Japan

The effects on fluid power systems, to be considered additional to the noise effect already highlighted, are various:

- Increase of operating temperatures
- Variation in the torque-speed characteristic of i.c. engine
- Need to control the i.c. operating point shift due to load characteristic of fluid power subsystem
- Increased attention to overall efficiency and specific fuel consumption in actual operation
- Need for transparent interface between engine and fluid power systems electronic control

The above mentioned aspects more or less can be tackled with the system-wide approach to fluid power systems design, boosting the activity towards the development and adaptation of advanced system architectures also for small and medium size machinery [6, 7], with implications that will be discussed in the next paragraphs. A different effect is the increase of operating temperatures, which will rise beyond the traditionally considered threshold of 90° Celsius, to reach in most cases stable values above 100°. Most manufacturers already seek component and system qualification above those values, but design methods generally do not take into account the effects of this increase, both in terms of fluid performance and material compatibility. This temperature trends will influence fluid characteristics, material and component endurance and gathering of proper data on efficiency and service life of components.

ELECTRONICS AND SENSORS

The introduction of electronics in fluid power systems is not a new trend. It started in '90s and nowadays can be considered a settled achievement, widely accepted by the market.

However only in recent products the potential of this technology starts to be fully exploited. Notable examples in this field are the dedicated electronic control strategies for fluid power subsystems applied by more or less all the major earth moving machinery manufacturers and/or dedicated ranges of application optimized hydraulic components like the Electronic Flow Match (EFM) or Bodas by Bosch-Rexroth.

Also research is very active in this field and many new applications or strategies try to use electronics to find a best match between hydraulic subsystem and application [7,8]. In view of an exploitation of the perspectives in this field, some aspects are worth mentioning:

1. The number, location, precision and reliability of sensors will increase, as well as their degree of integration inside components;
2. Electro-hydraulic components will perform more and more complex actions, rather than receiving and applying an external command, being part of a common, distributed control system with increased need for data transfer throughput and reliable protocol;
3. Being a large amount of controls relying on electronic boards and programmable devices, safety issues require special treatment

The first two aspects have been broadly investigated by many authors and do not need special focus here; however the third is more impacting in the field of mobile off-road equipment [9,10,11].

The focus of new standards is on functional safety (much broader than component integrity), which will force functional analysis to become a common task, switching the focus from le component level to the system level, in evaluating a fluid power system. As an example, Figure 6 shows the flow chart for functional safety implied by the newly published ISO 15998 standard.

Most applications will need the certification of their Safety Integrity Level (SIL), according to EN 954 and EN 61508, and the impact of this requirement is much more extended than a trivial need for third party certification. The full approach to design of components and systems for mobile hydraulics must change, and concepts like reliability assessment, probabilistic design, risk management must become common practice for the fluid power component design.

A design can be completely scrambled by the switch from pure performance achievement to safe function certification, expecially when safety critical applications are concerned, like X-by-wire systems, lifting systems or travel control systems are concerned.

The evaluation of Safety Integrity Level (Figure 7) is a complex task, involving multidisciplinary approach, and which is best performed at early design stages of components and control boards. The close link to

application demand of this activity will boost the already generalized tendency to specialize fluid power components towards an integrated subsystem specifically tailored on application needs.

SUSTAINABILITY

The ever increasing attention to environmental and energy issues is having a great impact on standardization activity in the field of off-road machinery.
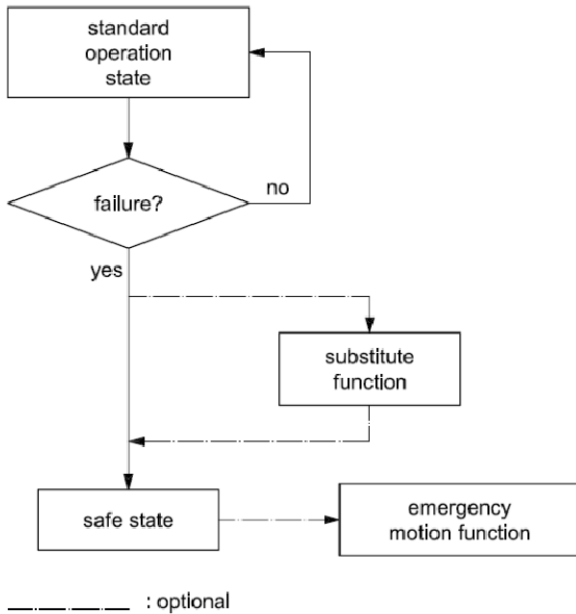

Figure 6 functional safety evaluation chart

ISO/FDIS 16714 is close to final publication, and will introduce a criterion for recyclability assessment of material used in earthmoving machinery. The final target is an ambitious amount of 95% recyclability in mass, with a significant part of the standard dealing with recyclability of fluid power components. Table 1 gives a snapshot of the breakdown of machine mass fractions which are subject to different (pre)treatment.

Table 1 Mass definition for recyclability matrix (adapted from ISO/FDIS 16714)

Symbol	Description
m_P	mass of materials taken into account at the pre-treatment step
m_D	mass of materials taken into account at the dismantling step
m_M	mass of metals taken into account at the metal separation step
m_{Tr}	mass of materials taken into account at the non-metallic residue treatment step and which can be considered as recyclable
m_{Te}	mass of materials taken into account at the non-metallic residue treatment step and which can be considered for energy recovery
SM	shipping mass (ISO 6016)

Fluid power components and hydraulic fluids will play a non marginal role, and their ability to be easily dismantled, recycled and possibly handled with a minimum energy usage will ease the application in off-road machinery. All of them are listed as components to be considered for pre-treatment, with the relevant
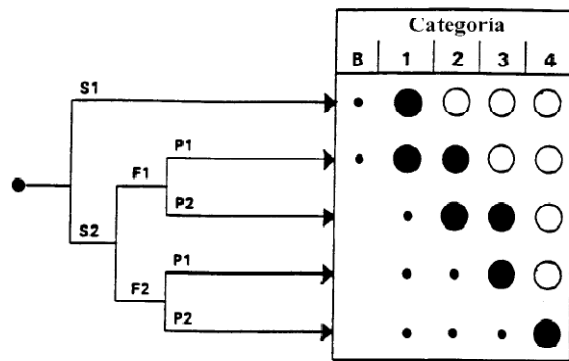
Figure 7 evaluation of Safety Integrity Level

exception of flexible hoses, filter cartridges and accumulators, which are to be accounted as non-metallic residue for which the availability of a proven technology for separation, recycling or energy recovery must be shown. The machine recyclability rate is defined in the standard as

$$R_{cyc} = \frac{m_P + m_D + m_M + m_{Tr}}{SM} \times 100$$

And the recoverability rate (which includes energy recovery) is given as

$$R_{COV} = \frac{m_P + m_D + m_M + m_{Tr} + m_{Te}}{SM} \times 100$$

The details are not relevant at this stage, but the content of the standard clearly shows a general trend in material life cycle assessment which is further amplified by recent attention in terms of sustainability of the entire life cycle of the machine.

A mobile machine, as far as sustainability is concerned, is an "energy consuming product" in the sense of the existing legislation. It is a shared opinion that for off-road operating machinery more than 80% of sustainability is in the efficiency of energy use by the machine (i.e. fuel specific consumption). This consideration is only apparently trivial. It means that most of the efforts in developing new products, systems and controls must be in the direction to induce energy savings in the machines during actual operation.

ENERGY USE

The concept of energy use automatically calls for efficiency. The concept of efficiency, however, apart from its apparent simplicity, as a ratio between energy or power output and input of a system or component can be tricky. Evaluation of efficiency depends on placement of the boundary of the domain where efficiency is computed, and on choice of the duty cycle of the component. In case of steady state operation, does not matter if power ratio or energy ratio is evaluated, as in this case instant efficiency, work cycle efficiency and lifetime efficiency are equal. Unfortunately this situation is far from being a real life case in off-road machinery. CVT (power-split) transmissions, introduced in the early '50s have been considered a little more than a curiosity for a long time, just because their steady state efficiency was significantly lower than mechanical or powershift transmissions. Only in recent years their intrinsic capability to adapt to different working conditions has been recognized as a key factor to get better efficiency in complex working cycles, with high and unpredictable load changes.

A similar approach applies if we look at the concept of efficient energy use of earth moving or agricultural machinery. Prime mover, hydraulic pumps and motors, transmissions, locomotion gears and implements have individual efficiency which depends on the operating point, with variations in the range of operation as high as 60-70%. Efficiency maps of the different parts of the energy path from prime mover to implements do not match to each other, and therefore the quest for optimal efficiency is a continuous struggle to find the best compromise among different needs.

This aspect is evident not only in many research papers and new products from leading manufacturers, but also in the international standardization activity. ISO/TC 127, Earthmoving machinery, recently started a high priority new work item on *test methods for efficient energy use*, with the objective to make a reference procedure available to rate machine energy consumption in working conditions as representative of actual usage as practicable. Japan government have been promoting to establish the specific and effective "Measures to Prevent Global Warming". As one of measures in the area of
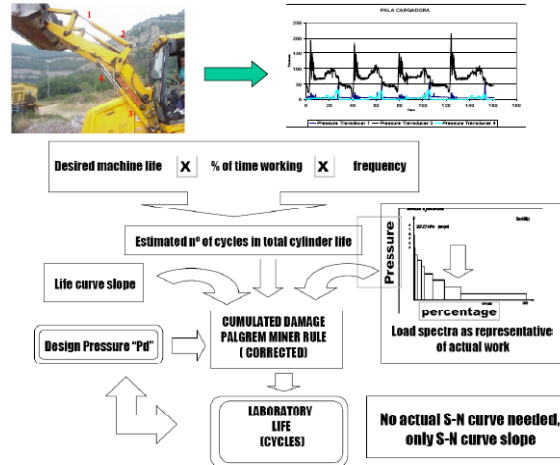
Figure 8 From field data to component qualification - PROHIPP design approach (Courtesy of Pedro Roquet SA – Spain)

construction method, it would be required to improve fuel consumption of construction machinery and to be able to select more "fuel-efficient" machines. Three test procedures about hydraulic excavator, tractor-dozer and wheel loader were released as JCMA standards(JCMAS) in May 2004. Afterwards, Revision of the standard has been advanced to improve accuracy, repeatability, reproducibility, and variance. This work is being used as a starting point for ISO activity.

Fluid power industry must take the opportunity offered by this expected boost in efficiency, with a deeper consideration of actual duty cycles of components in different applications and an improved control of the two main interfaces affecting efficiency: pump(s)-engine and soil-implement(s).
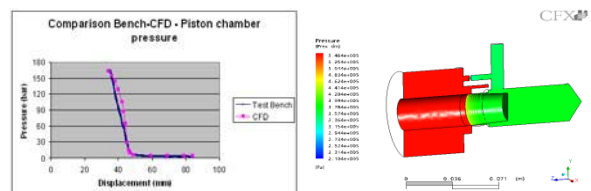
Figure 9 Example of advanced use of Computational Fluid Dynamics for cylinder cushioning design (IMAMOTER - PROHIPP project [12])

Advanced simulation tools are also a great opportunity, with their increased ability to perform multi-physics simulations and to include control systems analysis and synthesis. Application of virtual reality (VR) tools to machine design is already a common practice for many machine manufacturers, in view of ergonomics, visibility and maintenance optimization. However advanced simulation tools allow a better insight also to fluid power components, in order to get the information needed to improve design methods and system reliability. The EU funded project PROHIPP is such an example. It is aimed

at developing a novel, category based, probabilistic design applied to hydraulic cylinders, making an extensive use of advanced simulation tools for approach validation. Figure 8 is an example of the categories definition proposed, depicting a scenario which is consistent with a reliability evaluation approach in line with the already discussed SIL level for electronic subsystem.

An example of the level of insight made available by advanced simulation tools is the evaluation of cushioning device on hydraulic cylinders. The non-linear simulation and the CFD investigation gave full insight into the behavior, explaining and highlighting specific features such as oscillatory behavior and/or sealing damage due to the presence of unbalanced radial forces in cushioning stroke. Figure 9 shows the pressure field at a specific moment in time of the cushioning, and the comparison with the corresponding experimental results in one of the three specific designs investigated. The data reproduction is extremely good, validating the confidence on the set of parameters which can be derived by a numerical simulation and which cannot be measured in a physical experiment, such as discharge coefficients, turbulence parameters and surface pressure distribution. A full description of the findings of the project is beyond the scope of this paper, but they proof that the extensive, concurrent use, of advanced simulation tools, properly coordinated with experimental activity will make the probabilistic approach to design a feasible task for fluid power components with a significant improvement in machine reliability and efficiency, thanks to the reduced impact of oversized (or ill-sized) design usually implied by a traditional approach based on safety factors.

CONCLUSIONS

Future trends in fluid power will be highly constrained by the increasing demand by legislation and associated social concern about mobile machinery impact on environment and safety. However this situation should not be considered as a threat, but rather as an opportunity to improve performance and to drive the introductions of new technologies, materials and design approach. New approaches will be required in view of performance assessment and design practice and some of them could take advantage of technology transfer from more other sectors, such as automotive and aerospace. Nevertheless a significant possibility exist to develop original approaches in the field of system-wide approach to design and manufacture, application of integrated computer-assisted techniques and improvement of man-machine-environment interfaces. Building blocks of new achievements are already being developed and in the future, possibly, the overall appearance of machines will not change much, but their internal architecture will undergo a substantial change.

REFERENCE

1. Directive 2000/14/EC Of The European Parliament And Of The Council of 8 May 2000 on the approximation of the laws of the Member States relating to the noise emission in the environment by equipment for use outdoors, Official Journal of the European Communities, L 162/1, 3.7.2000.
2. Carletti, E., Casazza, C., Pedrielli, F., "Psychoacoustic characterisation of the noise at the operator position of a compact loader during real working conditions", Proc.s of 19th International Congress on Acoustics ICA2007, Madrid, Spain (2-7 Sept. 2007), pp. 1-6, ISBN 84-87985-12-2.
3. Carletti, E., "Outdoor Equipment: current situation on noise emissions and strategies for control", Noise/News International magazine, Vol.14, Nr.4, pp.152-154, December 2006
4. White, K. G., Green, B. and Brown, P. F.: Fluid Power Control, WWW Press, U.S.A (2001)
5. Koizumi J. and Yabu J. : New Challenges on Mechatronic Fluid Power, Proc. 55th JHPS Int. Symp. on Fluid Power Osaka '2000, 55/60 (2000)
6. Latour, C., Electrohydraulic flow Matching (EFM), the next generation of load sensing controls, Procs of Mobile 2006 Congress, Bosch-Rexroth AG
7. Marani, P., Ansaloni, G., Paoluzzi, R., Load Sensing With Active Regeneration System, Proc.s of the 7th IJFPS, in publication
8. Andruch, J., Lumkes, J., A Hydraulic system Topography with Integrated Energy Recovery and Reconfigurable Flow Paths Using High Speed Valves, Procs of 2008 NCFP, Las Vegas.
9. M. Hauke, M. Schaefer. Sicherheitsnorm mit neuem Konzept, o+p, 3/2006
10. J. Barg. Sicherheit in der Elektronik - Arbeitshydraulik von Telehandlern, o+p, 3/2005
11. Ruggeri, M., Il futuro dell'integrazione elettronica tra norme e tecnologie, Congresso Trasmissioni di Potenza, Assago (MI), Italy, 2007
12. PROHIPP - New Design And Manufacturing Processes For High Pressure Fluid Power Products, EU Integrated Research Project, NMP2-CT-2004-505466.
13. TNO report | MON-RPT-033-DTS-2007-03482 | v5.1b | December 12, 2007, European Commission

OS2-2

THE STATUS QUO AND DEVELOPMENT TENDENCY OF CONSTRUCTION MACHINERY AND ITS HYDRAULIC COMPONENTS IN CHINA

Chuanxin GUO *, Yaobao YIN **, Yangchun YE * and Xianghua CUI *

* Beijing Institute of Construction Mechanization
Beijing, 100007, P.R.China
** Institute of Mechatronics Engineering, Department of Mechanical Engineering,
Tongji University
Siping Road 1239, Shanghai, 200092, P.R.China
(E-mail: yinyaobao@hotmail.com)

ABSTRACT

The status and development tendency of construction machinery in china in recent years will be introduced; especially the outputs and performance level of the main products such as excavator, loader, crawler crane, truck crane, road roller and rotary drilling rig. Then the application of new products from internal corporation is analyzed and the research and development tendency of homemade hydraulic components of construction machinery field are also included. This paper introduces not only the national product standards of construction machinery but also the national policies and regulations for energy saving and pollution reduction in China.

KEY WORDS

Construction machinery, National product standards, Policy, Hydraulic component, China

GENERAL STATUS

With the development of 50 years, China construction machinery industry can provide products of 18 main kinds, more than 4500 species. It has been an important, large scale and flourished industry, which can meet the needs of home market. In 2006, there were about 1,000 large scale construction machinery factories, of which 130 were foreign-invested factories and joint ventures; 300 enterprises' annual sales over-passed 1,000 thousand dollars; 100 enterprises' annual sales over-passed 10,000 thousand dollars, and their total annual sales were 11.8 billion dollars, 75% that of whole industry's; 23 enterprises' annual sales over-passed 1,250 million dollars, and their total annual sales were 50% of whole industry's. In 2006, 420 thousand construction machines of all kinds were sold out, and the sales were 20 billion dollars, which grown up by 28% compared to that of the last years'. Based on

the sales statistics of the main enterprises and compared to the last year, sales of excavators (48021) grew up by 45.8%, and sales of loaders (126128) grew up by 13.3%, and sales of bulldozers (6063) grew up by16.2%, and sales of land scraper (2174) grew up by 31.3%, and sales of construction cranes (14081) grew up by 30.8%, and sales of road rollers (8470) grew up by 21.2%, and sales of forklifts (78709) grew up by 35.5%, and sales of rotary drilling rigs (368) grew up by 209%, and sales of long auger borings (479) grew up by 106.5%. As to concrete machines, concrete mixers (12000), concrete draw-pumps (4500), concrete pump vehicles (2500) and concrete mixing stations (1800), all grew up by more than 30%.

On the base of more than 20 billion dollars in 2006, total sales in 2007 was expected to be 25 billion dollars, and products of all kinds were exported to 197 countries and regions, which expectedly made Foreign exchange earnings more than 8 billion dollars, 70% more than 5

billion dollars in 2006. The product exports were about 25% of the total sales, and this tendency is still last yet. It is strongly expected to be 10 billion dollars next year. The situation of China construction machinery import and export showed that the total import increased every year, and it fell down slowly after the peak in 2004, and after increasing every year, the total export maintained general the same from 2005. Then, the structure of export has been improved, the proportion of whole machines rose from 45% in 2000 to 58.8% in 2005. The third, among the exporting enterprises, foreign-invested enterprises and joint ventures have been the main, whose exports taken up to 42% that of the total, state owned enterprises moved back to the second, who taken up 34% of the share, and not-state-owned firms also grew very fast, who have taken up 19% of the total export share. The last one, spare parts and fittings exported to American, Japan and South Korea increased, which shows that China construction machinery spare parts industry starts to enter the global industrial chain.

But compared with foreign colleague, the following questions exist in China: big gap in control technology, non standard of corresponding basic parts (spare parts and fittings, components) and shortage of R & D costs.

MINING MACHINERY

Production Development

Up to 2006, China's enterprises of hydraulic excavators have more than 30, producing a total of more than 150 kinds of the excavator with quality from 1.3 to 120.0 tons, including the state-owned enterprises, joint-stock enterprises, private enterprises, overseas-owned enterprises and Sino-foreign joint ventures[1].

In 2006, a total number of hydraulic excavators are 50,034 in China, the sales reach 48,021, and the exports sales reach 7887. In 2005 a total of hydraulic excavators (not including mining loader 211), is 34,511 in China, the sales reach 33,642, and the exports sales is 3617. China's excavator product and enterprises in 2005-2006 is shown in table 1 and table 2.

Table 1 Excavator product classification and China's main production enterprises

Product	Manufacturing Factory
Crawler excavator	Komatsu, Hitachi Construction Machinery, Chengdu Kobelco, Caterpillar, Guizhou Zhanyang, Doosan, Hyundai, Sichuan Bonny Heavy Machinery Co., Ltd., Liugong, Xuzhou Xuwa Excavator Machinery Co., Ltd., Sany, Changsha Sunward Construction Machinery Co., Ltd., Yuchai
Tire excavator	Guizhou Zhanyang, Doosan, Hyundai, Chengdu Kobelco Construction Machinery Co., Ltd., Hitachi Construction Machinery

Table 2 China's main products excavator production and sales from 2005 to 2006(unit)

Product Name	Production quantity		Sales (unit)	
	2005	2006	2005	2006
Crawler excavator	32289	47783	30899	45333
Tire excavator	2222	1865	2263	21687
Mining Loader	211	386	480	520
Total	34722	50034	33642	48021

Marketing and Sales

Since 2000, the Chinese excavator market has grown by the superior speed. In 2000, all the sales of excavators of China's domestic enterprises were 7926, it reached 34,800 in 2003 and it is 4.4 times larger than 2000. In 2003, National excavator sales grew 76% over the previous year. In 2004, the sales of the excavator, compared to 2003, drop a little. National excavator sales in 2006 reached 48,021, and grew 40% compared to 2005. In 2005, production of state-owned and private enterprises of various types of excavators in China's market share is 22 %. In 2006, it reached 26 %.

In the sales of excavators, crawler excavator is much higher than the tire excavator. The market share of 2005-2006 is shown in table 3.

In 2006, the largest sales of excavator between 20 and 22 ton is good, and it is 56% of total sales (64% for 2004). Small hydraulic excavators which quality is less than or equal to 6 ton, in 2006, is 30% of the total sales of the hydraulic excavator, and small excavators increase. In 2006, hydraulic excavators which quality is more than 30 t or equal to 30 t, also increase in sales.

Table 3 Crawler excavators and tire excavator of the market share from 2005 to 2006

Product Name	Market share (%)	
	2005	2006
Crawler excavator	96	94
Tire excavator	3	4.5

Product Imports and Exports

Exports of hydraulic excavator are 2561 in 2004, 3617 in 2005, and increases 42% than last year. In 2006, exports is 7887, increases 118% than 2005. From 2005 to 2006, China's import and export volume of excavator category in table 4.

EARTHMOVING MACHINERY

Production Development

Earthmoving machinery is composed of loader, bulldozer, grader, mine-used self-unloading truck. After many years continuous rapid development, the

development speed of the loader is still keeping. The growth of bulldozer and grader is fluctuant and is higher than loader in 2006. The growth of mine-used self-unloading truck is also high. Some results can be seen in Table 5 and 6.

Table 4 China's import and export volume of excavator category from 2005 to 2006

Product Name	Imports (unit)		Exports (unit)	
	2005	2006	2005	2006
Crawler excavator	17689	27857	3592	7781
Tire excavator	320	530	25	106
Mining Loader	5	3		
Total	18014	28390	3617	7887

Table 5 Product sales of earthmoving machinery in 2005-2006

Product classification	Yield		Sales		Export	
	2005	2006	2005	2006	2005	2006
Loader	111290	131600	105836	126128	2821	4621
Bulldozer	6031	5931	5237	6063	523	1063
Grader	1731	2871	1711	2174	581	706
Mine-used self-unloading truck	431	496	393	475	56	118

Table 6 Business income of China top 10 earthmoving machinery companies in 2006 (10000 dollar)

NO.	Enterprise name	Income
1	Guangxi Liugong Machinery Co. Ltd.	65127
2	China Longgong Holding Co. Ltd.	46474
3	Chengdu Shengang Construction Machinery Co. Ltd.	43092
4	Xiamen Construction Machinery Co Ltd	41387
5	Shantui Construction Machinery Co. Ltd	36508
6	Shantui Lingong Construction Machinery Co. Ltd.	35309
7	Xuzhou Construction Technology Machinery Co. Ltd.	32300
8	Changzhou Co. Ltd.	18912
9	Shandong Shangong Machinery Co. Ltd.	18254
10	Shandong Changlin Machinery Group Co. Ltd.	15560

CONCRETE MACHINERY

China totally produced about pump vehicles 2,500, towed pumps 4500, concrete mixing carriers 12,000, in 2006. From Concrete Machinery Branch of Chinese Constructional Machinery Industrial Association, products and sales in 2006 are shown in Table7 below.
Concrete Pump Vehicles
China has had rapid development on arm concrete pump vehicles in recent years, in aspects of stability and

process, though not as good as foreign products. In aspects of cost-effective and after services and others, our products have distinctive competitive advantages, and are more suitable for the actual constructional situation in China. For example, the research and development of concrete pump vehicles in Zhonglian and Sany. Zhonglian has made "concrete pump vehicle" standard, and developed a remote maintainable and positioning system for pump vehicles. Concrete pump vehicles from Sany, whatever in aspects of pumped pressure, pumped displacement or stability, reliability, can be compared to products of famous brands abroad, pump machinery products having had hot sales to the Middle East, North Africa, South Asia and etc.

Table 7 Products and sales of concrete machines in 2006

No.	Products	Enter-prises	Yields	Sales
1	Concrete mixers	19	18220	16984
2	Concrete mixing stations	25	1911	1882
3	Towed concrete pumps	15	3865	3686
4	Concrete Pump vehicles	6	1985	1890
5	Concrete Mixing carriers	10	5829	5626
6	Bulk cement carriers	1	1006	1040

The quality of hydraulic system, which is the core part of arm concrete pump vehicle, will directly affect the performance of the host. Hydraulic system of domestic arm concrete pump vehicle based on import of technology, has two kinds of control loops, one is closed-loop hydraulic system of Xuzhong, one is open-loop hydraulic system of Sany. Both open and closed loops with advantages and disadvantages, closed loop has little impact when reversing, little heat produced, simple structure; the most outstanding feature of open loop is that it can easily control the pump displacement according to load, especially when pumping in short distance, the pump capacity being big, taking full advantage of the engine power. Domestic concrete pump vehicles mainly choose hydraulic infrastructures from Europe and The United States, for example, hydraulic pumps and valves from REXROTH, PARKER, HAWE, while hydraulic components relatively seldom from Japan.
With the improvement of conditions, continuous development of arm manufacturing technology, the long-arm, high-efficiency arm concrete pump vehicles are favored by more and more users, and in the next three to five years, demand for arm long below 40-meter' pump vehicle being going to drop, arm long of 45-meter, 48-meter becoming the mainstream, for

example, Sany having developed a 65-meter long concrete pump vehicle, becoming the enterprise manufacturing the longest arm concrete pump vehicle in the world. In addition, intelligent control system technology will become universal accessories of arm concrete pump vehicles. The expansion of pumping capacity and application will also become trend of the concrete pump vehicle development [2].

CONSTRUCTION CRANE

Products Development
The construction crane in China includes mobile crane, such as truck crane, all-terrain crane, crawler crane, truck-mounted crane, tire mounted cranes and cross country tire mounted cranes. In the recent years, Chinese construction machinery industry has witnessed a rapid development, as the mobile crane is one of the fastest developing crane types. China construction crane industry in 2006 creates greater glories, and has the historical record of China.
Marketing and Sales
According to the statistics of the construction crane branch association, sale number of various kinds of the mobile cranes in 2006 is 17403, increased by 34.1% compared with the last year shown in table 8.

Table 8 Sales of the Construction Crane in 2006

Products Name	Sales			Percentage (%)	
	2006	2005	Growth rate(%)	2006	2005
Truck crane	14154	10805	31	81.3	83.2
Truck-mounted crane	2591	1768	46.5	14.9	13.6
Crawler crane	500	237	111	2.9	1.83
Tire mounted cranes	158	171	-7.6	0.9	1.31
Total	17403	12981	34.1	100	100

Note: The data in the column of the truck crane includes full road crane.

From table 8 we can find that the track crane takes the share of 81.3% of the four major cranes; we keep this product structure for many years. But the proportion assumes the declining tendency: 85.26% in 2004, 83.24% in 2005, in 2006 the percentage dropped by 1.94% compared with 2005. But the percentage of the track crane and the crawler crane in various kinds of the products continue to show an upward tendency.
Truck Crane
The major products of the construction crane of our country are truck cranes. The sale number exceeds 14000 in 2006, which increases by 31% compared with last year; continues exceeding ten thousand for 3 years. Also the production series improved constantly and

realized the marketing of 16 series of products from 8 to 130 tons. Minor tonnage truck crane increases slowly by the extent, while middle and big tonnage truck crane increases are prompt. Table 9 shows the truck crane sale in 2006.
The numbers of the all-terrain crane is small. With years of effort, Xugong and Changsha Zoomlion Co., Ltd, have developed the all-terrain cranes of 25t, 50t, 130t, 160t, 200t, 240t, 300t and have gradually opened the domestic market. The all-terrain crane products in Xugong have expanded into international market. But the production of the cross country tire mounted cranes of our country is almost blank [3].

Table 9 Sales of the truck crane in 2006 (units)

Type(tons)	2006	2005	Growth rate (%)
8-16	7042	6171	14.1
20-55	6671	4383	52.2
65-80	320	187	71.1
100-130	110	58	89.7

Truck-Mounted Crane
With the rapid development of the petrochemical industry, the petroleum, the chemical industry, the energy sources and large-scale municipal construction, the large truck-mounted crane market has been greatly stimulated. In the past, the large-tonnage truck-mounted cranes rely on imports. During the past two years, Chinese manufacturing enterprises have developed truck-mounted crane products actively. We have been able to produce a total number of 15 series such as 35t, 50t, 70t, 80t, 100t, 150t, 160t, 200t, 250t, 300t, 350t, 400t, 450t, 600t, 900t. The newly developed larger tonnage products have reached the advanced level of the similar products in the world. Also we get a number of independent intellectual property rights, the domestic brands was recognized by the vast numbers of customers. Also, the minor and middle tonnage of the products produced by our country has a competitive advantage with the brands abroad. We soled 500 in 2006, increased by 111% compared with 2005. Our countries' main production truck-Mounted Crane enterprises such as Fushun excavator manufacturers limited liability company, Xuzhou Heavy Machinery Co., Ltd., Zoomlion Heavy Industry Science & Technology Development Co., Ltd., and Shanghai Sany increases rapidly. Currently the entire industry tries to develop the 1600t scale truck-mounted Crane. More and more enterprises will join in the production of the truck-mounted crane. The top 4 enterprises of the truck-mounted crane can be seen from table 10.
Export of Products
The export of the construction crane had increased rapidly since 2005, and there was a decreasing tendency

of the imports. The entire industry export various of construction cranes and other construction machinery to a total number of 1022 in 2006, which increases about 138% compared with last year; the general amount of money reaches 164 million US dollars, increased by 237% compared with 2005. The Xuzhou Heavy Machinery Co., Ltd takes 61% of the general amount of money of the entire industry in 2006; 76% of the track crane exportation of the whole industry. The crane export in 2006 is shown in table 11.

Table 10 The top 4 enterprises of the truck-mounted crane producers in 2006

Name of the Enterprise	Sales	Export
Fushun Excavator Co. LTD	205	65
Xuzhou Heavy Machinery Co. Ltd	137	35
Shanghai SANY	122	18
Changsha Zoomlion Co., Ltd	32	5

Table 11 Export of construction crane exportation in 2006

Products	Numbers (units)	Sum (10000 US dollars)
Truck crane	770	12008
Truck-mounted crane	124	233.5
Crawler crane	123	4050.9

HYDRAULIC COMPONENTS OF CONST-RUCTION MACHINERY

Chinese construction machinery products were imitated from Soviet Union Products basically in 1960s. For example, both single-bucket excavators, bulldozers are mechanical transmission, manual manipulation. Equipment moves are all driven by the winch wire rope, ponderous machinery, low productivity, labor-intensive operator. In 1963, Japan displayed a new wheel loader 125A in China, and after the show, the machinery industry department is sent to the Tianjin Construction Machinery Research Institute to research imitation and stripped-down, and then gave the pattern to the Liugong, then Liugong manufactured the first wheel loaders in China. This is the first application of hydraulics in the field of construction machinery. Latter, a loader industry was gradually formed in 1970s, and up to now, the annual output has exceeded 100 thousand. Almost at the same time, fluid drive was applied in the field of bulldozer, grader and scraper, and make engineering machinery products look brand-new, technology have a qualitative leap.

Hydraulic Components of Construction Machinery
The development and the industry of the hydraulic components of construction machinery were mainly in the 1970s. After the reform and opening up, in order to shorten the gap between the advanced world level, Chinese construction machinery industry has introduced more than 170 items of advanced technology, in particular the new bulldozers, loaders key components through-train projects approved by the State Economic and Trade Commission, and 12 domestic enterprises jointly signed with U.S. Caterpillar company for an introduction of the Caterpillar bulldozers, wheel loaders, wheel skidding machinery, three categories of seven types of main manufacturing technology, which includes a hydraulic technology. Hydro-pneumatic and seal industry has also introduced into more than 40 foreign advanced technologies during the "7-5" and "8-5" plan. The formation of specialized production at that time gave a strong impetus to the development of China's hydraulic components, after digestion and absorption; we have fundamentally changed the blank of China Construction Machinery Hydraulic components, although the manufacturing technology level is not very high, but can basically keep up with the needs of the host development. In the 1990s, because of the entry of foreign brands of construction machinery, it further promotes the development of construction hydraulic machinery. Such as: Park Muke (high-pressure pump gear), Eaton (hydraulic steering gear, vane pump, etc.), Naboco, Rexroth (walking, Rotary, up from the motor and reducer), Komatsu Almighty (cylinder), the entry of these enterprises, increased competition in the industry, but also promote the development of the Chinese local hydraulic parts. China's local enterprises also raise their technology continuously, such as the Jinan Hydraulic Pump Factory's Asymmetric compensation radial-type gear pump and GBGJ series of gear pumps, Qingzhou Hydraulic Factory's floating coaxial gear pump, CBZb, CBAa, CBGg series gear pump, Linhai Haihong Factory's valve products are all patent product, and with independent intellectual property, as well as the Xuzhou-hydraulic factory's double-acting cylinder, and so on. All of them have taken a big step forward.

Status Quo and Gap
China's hydraulic parts of construction machinery have had a rapid development in recent years, and able to meet the needs of medium pressure and displacement host. For example: the largest sales wheel loader and the second sales forklifts and bulldozers, grader, tire cranes and other machines. At present, and even the hydraulic pilot valve and the corresponding distribution valve in G series of high-collocation loader's, local enterprises have been able to production, resolve instead of imports. However, the medium level hydraulic parts of construction machinery, the quality is not stability enough, leakage occur from time to time, valve locking, cylinder scoring also occur from time to time, problems. China's hydraulic parts of construction machinery is still blankness in the high-tech products, hydraulic components which used in excavators, large-tonnage

truck crane, crawler cranes, concrete pumps, concrete pump truck, rotary drilling rig are still dependent on Imports. Most of them import from German company as: Bosch-Rexroth, Linde, Kawasaki, Toshiba, KYB, Parker, Sawa, Eaton, and so on. Variable displacement pump and motor used in the variable hydraulic system of excavator, integral multi-way valve, high-pressure cylinder and other load-sensing and proportional control components are all urged to be developed.

The Next Work

To improve the overall quality of corollary parts, it is important to improve the parts of small excavator. One reason is that, the output of the excavators growth fast in recent years, market demand expand, the output growth 10 times in the past 10 years, annual sales is 34,000 sets in 2005, and 45,000 sets in 2006. Second, because excavator has a high technology, the corollary parts also have a high requirement. Third, because the key corollary parts almost dependence on foreign countries to offer, so the price is high, and delivery time can not be guaranteed. These restrict the development of excavator industry. Forth, if we make a breakthrough at the corollary parts of Excavator, the corollary parts of other machines would be solved easily.

The difficulty of corollary parts of excavator is variable hydraulic components. The pressure and flow are comparatively small in small excavators system. It is relatively easy to solve. Branch of Construction Machinery Organization have already held two seminars about corollary parts of small Excavator. In the meeting, corollary parts Branch have put forward the strategic objectives for conquer the small-scale hydraulic excavator: the first step, expect in three to five years, that is, during the 11th Five-Year Plan, conquering components used in 10t within 30 MPa variable system; in another three to five years to conquer the components used in more than 10t the system pressure more than 30 MPa system.

PROSPECT OF CONSTRUCTION MACHINERY

Construction machinery industry is investing-pulling type, which have closer relations with total fixed asset investment scale, especially infrastructure construction and real estate investment. China is still a developing country, and it should be sustained at least 15 to 20 years or more for large-scale infrastructure construction and urban development. During the "11th Five-Years Plan" (2006-2010), investments exceed that in the "tenth Five-Years Plan" (2001-2005) in transportation, water power, electric power, energy base construction, environmental protection, urban construction, national defense building, which will effectively drive the stable development of the construction machinery industry.

China's mechanization level of building operations is still far lower than developed countries, if it is counted by the number of engineering machinery per country's land area or per capita, the gap between developed countries and China will be father. For example, in 2005 China's market sales of earthmoving machinery was about 16 million units, 1.2 per 10,000 people; contrast to 7 per 10,000 people in North America; Germany 3; Sweden 3.1; Netherlands 2.8; Belgium 3.7 Taiwan; Denmark 8.

The country's land area of China is 25 times that of Japan's and Chinese population is 13 times that of Japan. In 2005 China's total sales of grabs, shovel loaders, cranes were only 2.3 times that of Japan. Now the number of grabs in use in Japan is about 570,000 units, which is about double that of China. So in the process of becoming the economic power of modernization, the market forecasting capacity of engineering machinery is quite large.

From the worldwide economic development, Japan's and the European engineering machinery market finishes years' hovering and goes to recovery, the development of North American market is strong, the markets grow fast in the Middle East, Latin America, Southeast Asia, Central Asia and other regions, it is forecasted that the world engineering machinery market will be the steadily increasing in the next five years, which will be a good opportunity for Chinese engineering machinery enterprises to expand overseas.

REFERENCES

1. Construction Machinery, China, 2005-2008; http://www.cm1981.com.cn/english/default.htm
2. Construction Machinery and Equipment, China 2005-2008; http://www.chinacme.com/shouye.asp
3. China Construction Machinery Industry Yearbook 2007, China Construction Machinery Association, 2007(Chinese)

OS3-1

NUMERICAL MODELING OF RECIPROCATING FLUID POWER SEALS

Richard F. SALANT* and Bo YANG*

* George W. Woodruff School of Mechanical Engineering
Georgia Institute of Technology
Atlanta, Georgia 30332-0405, USA
(E-mail: richard.salant@me.gatech.edu)

ABSTRACT

A numerical model of reciprocating fluid power seals has been developed. It has been applied to a variety of hydraulic rod seals, although it could also be used to simulate hydraulic piston seals as well as pneumatic seals. The model is soft elastohydrodynamic and consists of coupled fluid mechanics, contact mechanics, deformation mechanics and thermal analyses. Results for typical rod seals show that these seals operate with mixed lubrication between the rod and seal surfaces, and that the roughness of the seal plays a major role in determining the leakage characteristics of the seal. For a given seal design and set of operating conditions there is a critical seal roughness, below which there will be zero net leakage per cycle and above which the seal will leak.

KEY WORDS

Seals, Rod seals, Soft elastohydrodynamics

NOMENCLATURE

E elastic modulus
F cavitation index
H dimensionless average film thickness, h/σ
H_s static undeformed film thickness, h_s/σ
H_T dimensionless average truncated film thickness, h_T/σ
I_l influence coefficient for normal (radial) deformation
L length of solution domain in x-direction
P dimensionless fluid pressure, p/p_a
p_a ambient pressure
P_c dimensionless contact pressure for deformation analysis, p_c/E
P_{def} dimensionless fluid pressure for deformation analysis, $P(p_a)/E$
P_{sc} dimensionless static contact pressure, p_{sc}/E

P_{sealed} dimensionless sealed pressured, p_{sealed}/p_a
P_t dimensionless total pressure, $P_{def} + P_c$
$\hat{q}$ dimensionless flow rate per unit circumferential length, $12\mu_0 qL/[(p_a)\sigma^3]$
R asperity radius
U surface speed of rod
$\hat{x}$ dimensionless axial coordinate, x/L
$\hat{\alpha}$ dimensionless pressure-viscosity coefficient, αp_a
ϕ fluid pressure/density function, defined by Eqs. (2) and (3)
$\phi_{s,c,x}$ shear flow factor
ϕ_{xx} pressure flow factor
μ_0 viscosity at atmospheric pressure
$\hat{\rho}$ dimensionless density, Δ/Δ_l
Δ_l liquid density
$\hat{\sigma}$ dimensionless rms roughness of sealing element

v Poisson's ratio
ζ dimensionless rod speed, $(\mu_0 UL)/[(p_a)\sigma^2]$
η asperity density

INTRODUCTION

Fluid seals play important roles in fluid power systems, since excessive leakage can degrade performance and, most importantly, pollute the environment. The present paper is concerned with linear reciprocating seals, which are used in linear actuators as rod and piston seals. A significant amount of research on hydraulic reciprocating rod seals, both experimental and theoretical, has been performed since the 1960's, e.g. [1-13]. However, it is only in the last few years, with the advent of modern computational techniques, that it is possible to analyze the detailed behavior of these seals. While most previous theoretical studies assume that full film lubrication exists between the seal lip and the shaft, and the sealing surfaces are perfectly smooth, the present study shows that mixed lubrication occurs and the seal surface roughness plays an important role in determining whether or not a seal will leak. In the present study, a numerical model of reciprocating fluid power seals has been developed. It has been applied to a variety of hydraulic rod seals, although it could also be used to simulate hydraulic piston seals as well as pneumatic seals. In this paper, only a double lip U-cup seal is considered.

ANALYSIS

A typical double lip U-cup hydraulic rod seal is shown in Fig. 1. The rod is assumed to be perfectly smooth, while the seal lip is treated as rough. This is reasonable since during the run-in period, the rod is polished to a very smooth finish.
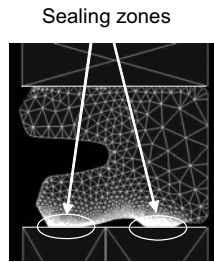
Sealing zones

Figure 1 Rod seal

The fluid mechanics of the sealing zone is governed by the Reynolds equation. Noting that the seal is axisymmetric, and that the film thickness is very small compared to the seal radius, the flow is modeled as one-dimensional in a Cartesian coordinate system. Since cavitation may occur, the following form of Reynolds equation is used [14].

$$\frac{d}{d\hat{x}}[\phi_{xx} H^3 e^{-\hat{\alpha}F\phi}\frac{dF\phi}{d\hat{x}}] = \quad (1)$$
$$6\zeta\left[\frac{d}{d\hat{x}}\left\{\left[1+(1-F)\phi\right]H_T\right\} + F\frac{d\phi_{s.c.x}}{d\hat{x}}\right]$$

In the liquid region,

$$\phi \geq 0 \quad F = 1 \text{ and } P = \phi \quad (2)$$

In the cavitated region,

$$\phi < 0 \quad F = 0 \text{ and } P = 0, \hat{\rho} = 1 + \phi \quad (3)$$

For the primary and secondary lips, the boundary conditions are,

$$\phi_{primary} = P_{sealed} \quad at \; \hat{x} = 0$$
$$= \phi_{interlip} \quad at \; \hat{x} = 1 \quad (4)$$
$$\phi_{secondary} = \phi_{interlip} \quad at \; \hat{x} = 0$$
$$= 1 \qquad at \; \hat{x} = 1$$

The flow factors ϕ_{xx} and $\phi_{s.c.x}$ are functions of the ratio of the film thickness to the roughness amplitude and the roughness geometry (aspect ratio and orientation of the asperities), and are obtained from [15, 16].

Equations (1)-(4) are solved for ϕ and F using a micro-control volume finite difference scheme, for given values of H, ϕ_{xx} and $\phi_{s.c.x}$, using the tri-diagonal matrix algorithm (TDMA). This yields the pressure distribution and the location of cavitation zones.

Once ϕ and F are obtained, the flow rate (per unit circumferential length) through the film (giving the instantaneous leakage rate) can be found from,

$$\hat{q} = -\phi_{xx} e^{-\hat{\alpha}F\phi}H^3\frac{dF\phi}{dx} + 6\zeta\left\{\left[1+(1-F)\phi\right]H_T + F\phi_{s.c.x}\right\} \quad (5)$$

The flow rates past the two lips must be equal.

Since significant asperity contact may occur (mixed lubrication), it is necessary to add an asperity contact pressure to the hydrodynamic pressure in computing the normal deformation and film thickness. This contact pressure is computed using the Greenwood and Williamson surface contact model [17]. Assuming a Gaussian distribution of asperities,

$$P_c = \frac{4}{3} \frac{1}{\left(1 - v^2\right)} \hat{\sigma}^{\frac{3}{2}} \frac{1}{\sqrt{2\pi}} \int_H^\infty (z - H)^{\frac{3}{2}} e^{-\frac{z^2}{2}} dz \qquad (6)$$

To compute the film thickness distribution, it is necessary to compute the radial (normal) deformation of the sealing element. Since this will be done within an iteration loop, it is necessary to use a computationally efficient method. The influence coefficient method has been chosen. With this method it is recognized that the deformation at any location is proportional to the forces applied at every location. Thus, in discretized form with n axial nodes across the sealing zone, the film thickness at the ith node can be expressed as,

$$H_i = H_s + \sum_{k=1}^{n} (I_1)_{ik} (P_t - P_{sc})_k \qquad (7)$$

The proportionality factors $(I_1)_{ik}$, the "influence coefficients," are computed off-line using a commercial finite element analysis code. Thus, the on-line model contains only linear algebraic equations. The pressure P_t is the sum of the fluid pressure and the contact pressure due to contacting asperities. P_{sc} is the static contact pressure distribution, also computed off-line with a commercial finite element analysis code.

The static film thickness, H_s, is computed by equating the static contact pressure obtained from the finite element analysis for smooth surfaces under pressurized conditions, P_{sc}, with the contact pressure distribution computed from Eq. (6) under static conditions [18].

In some computations, a thermal analysis is also included. It involves an analytical solution to the classical thermal conduction equation for a moving heat source, treating the rod as a semi-infinite body and neglecting heat transferred into the seal. Heat generation through both viscous friction and contact friction is accounted for. The computed interface temperature is used to evaluate the fluid viscosity in the sealing zone.

Since the equations discussed above are strongly coupled, it is necessary to use an iterative computational procedure, as shown in Fig. 2.

RESULTS

Injection Molding Application
Computations have been performed for a typical seal in an injection molding application, with base parameters of: E = 43 x 10^6 Pa, v = 0.49, p_{sealed} = 6.90 MPa (1000 psi), U = 0.635 m/s (25 in/s) outstroke, U = -0.813 m/s (-32 in/s) instroke, μ_0 = 0.043 Pa s, α = 20 x 10^{-9} Pa^{-1},
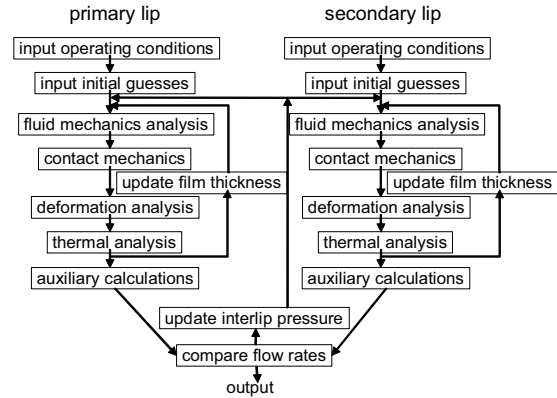
Figure 2 Computational procedure

R = 1.0 μm, η = 10^{14} m^{-2}, f = 0.25, rod diameter = 88.9 mm (3.5 in), stroke length = 1.93 m (76 in), seal width = 6.8 mm (0.27 in). The seal roughness is assumed to be isotropic. As pointed out in the Analysis section, the rod is treated as perfectly smooth.

Figure 3 contains a plot of the fluid transport during outstroke and instroke for the double lip seal. (The fluid transport past the secondary seal is the same as that past the primary seal, since this is a steady state analysis.) As can be seen, the difference between the fluid transport during outstroke and instroke, the net leakage per cycle, is strongly dependent on the seal roughness. For zero net leakage, the instroke fluid transport must exceed the outstroke transport. This occurs at values of rms seal roughness below a critical roughness of approximately 0.3 μm. For higher values of roughness, this seal will leak at the given operating conditions.
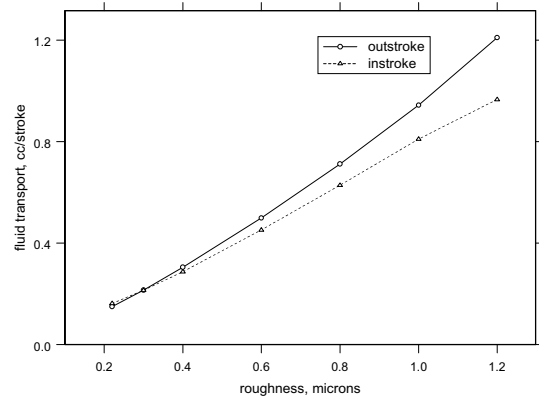
Figure 3 Fluid transport vs. seal roughness

From Fig. 3 it is seen that a seal with a roughness of 0.22 μm is non-leaking. Figure 4 shows the film thickness distributions under the primary lip during

outstroke and instroke, for such a seal. These indicate that mixed lubrication exist, since the film thickness is less than 3σ. It is also seen that the film thickness is larger during the instroke than during the outstroke. This promotes effective sealing, since it reduces the resistance to flow during the instroke compared to the outstroke.
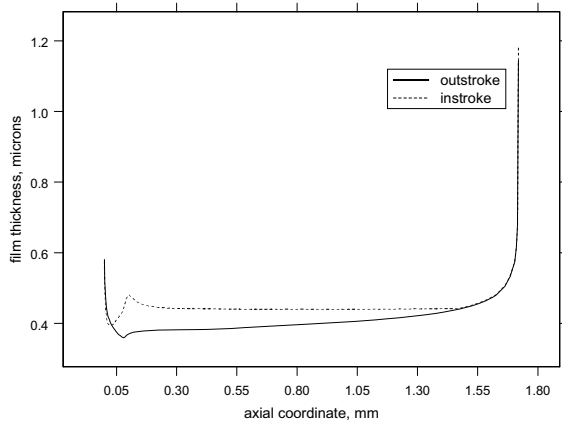
Figure 4 Film thickness distribution, primary lip, σ = 0.22 μm

The film thickness distribution under the primary lip for a leaking seal, with a roughness of 0.6 μm, is shown in Fig. 5. Here, again, mixed lubrication exists. However in this case the sealing zone is shorter during the outstroke than during the instroke (due to an elevated interlip pressure), and the film thickness during the instroke and outstroke have about the same values at
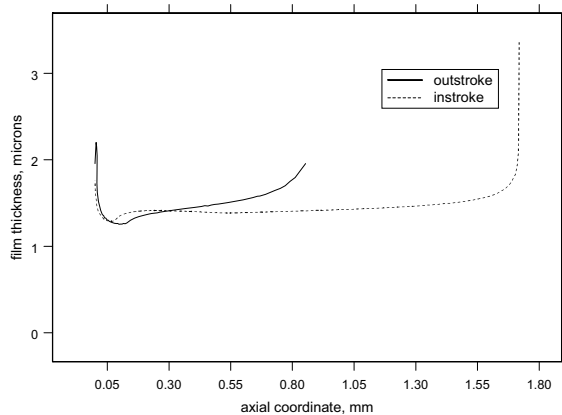
Figure 5 Film thickness distribution, primary lip, σ = 0.60 μm

corresponding locations. This is a less favorable characteristic, compared to the non-leaking seal.

Figure 6 shows the static contact pressure, dynamic contact pressure and fluid pressure distributions under the primary lip for the non-leaking seal during the outstroke. The fluid pressure is zero over a large portion of the sealing zone, indicating the occurrence of cavitation. This is a favorable characteristic, since cavitation restricts the flow of fluid out of the cylinder.
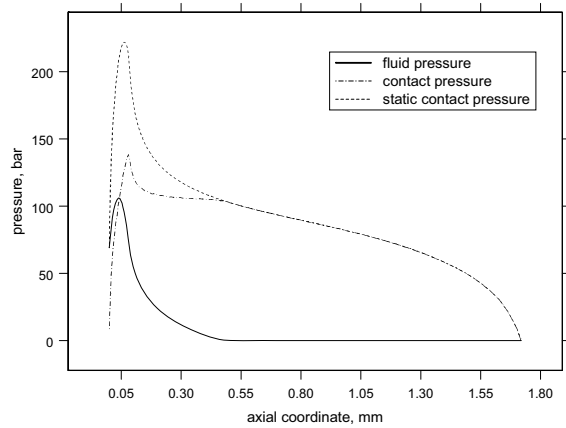
Figure 6 Pressure distributions, primary lip, σ = 0.22 μm, outstroke

The pressure distributions for the same seal during the instroke are shown in Fig. 7. Here it is seen that the extent of cavitation has been greatly reduced. This is favorable, since cavitation during the instroke tends to prevent fluid from being drawn back into the cylinder.
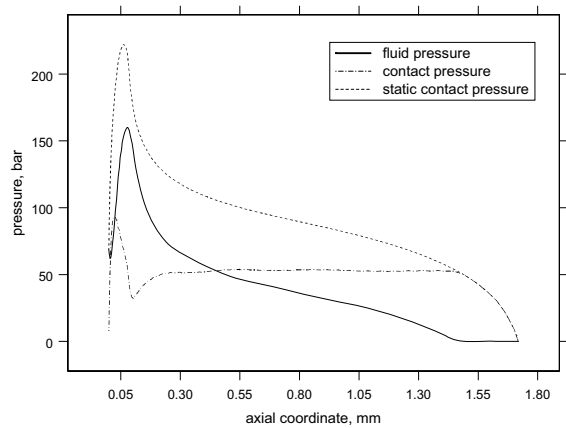
Figure 7 Pressure distributions, primary lip, σ = 0.22 μm, instroke

Figures 8 and 9 contain the corresponding outstroke and instroke pressure distributions for the leaking seal. The behavior is opposite to that of the non-leaking seal. During the outstroke there is no cavitation, allowing unrestrained flow out of the cylinder, while during the instroke there is extensive cavitation, tending to prevent fluid from being drawn back into the cylinder.
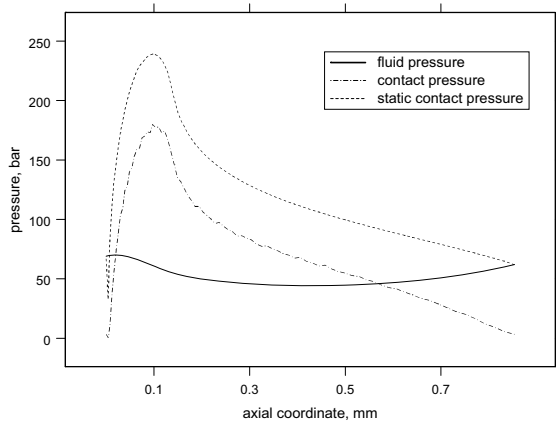
Figure 8 Pressure distributions, primary lip, σ = 0.60 μm, outstroke
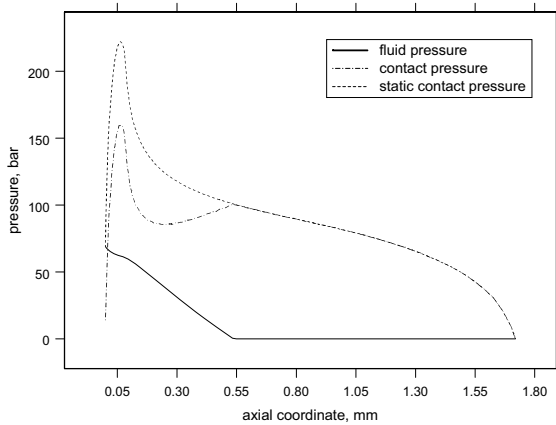
Figure 9 Pressure distributions, primary lip, σ = 0.60 μm, instroke

Conventional Actuator
In the above injection molding application, the sealed pressure is the same during the outstroke and the instroke (6.90 MPa). Computations have also been performed for a conventional actuator in which the sealed pressure is ambient during the outstroke and a range of specified values during the instroke. The seal has the same geometry as that in the injection molding application but is smaller, with a rod diameter of 44 mm (1.75 in) and a stroke length of 0.23 m (9 in).

The net leakage (per cycle) versus rod speed is shown in Fig. 10 for a sealed pressure of 6.90 MPa (1000 psi) and varying roughness. The leakage is highest at the lowest speeds; as the speed is increased the leakage decreases until the critical speed is reached, at which point there is zero leakage. At a given speed, the higher the seal roughness, the higher is the leakage.
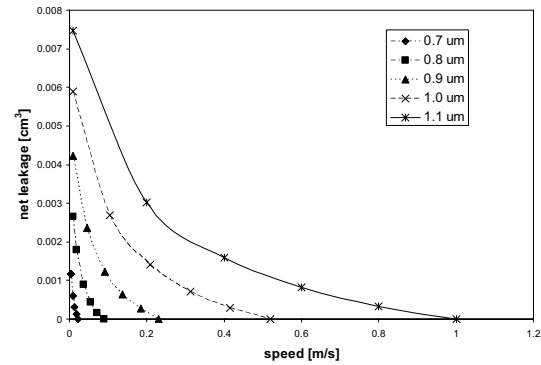
Figure 10 Leakage per cycle vs. rod speed, p_s = 6.9 MPa

Figure 11 shows a similar plot of net leakage versus rod speed, but for a seal roughness of 0.9 μm and varying sealed pressure. At a given speed, the higher the sealed pressure, the higher is the leakage. Similar to figure 4, at each sealed pressure, as the speed is increased the leakage decreases until the critical speed is reached, at which point there is zero leakage.
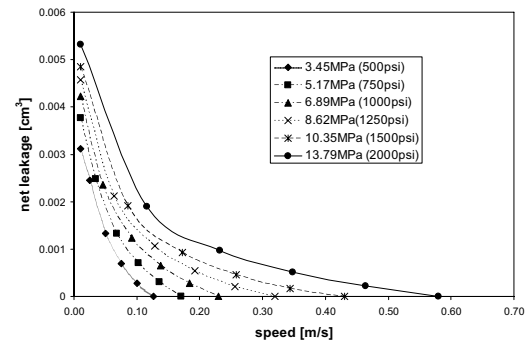
Figure 11 Leakage per cycle vs. rod speed, σ = 0.9 μm

The critical speed vs. seal roughness is shown in Fig. 12 for varying sealed pressure. It is seen that the critical speed increases with both increased roughness and increased sealed pressure.
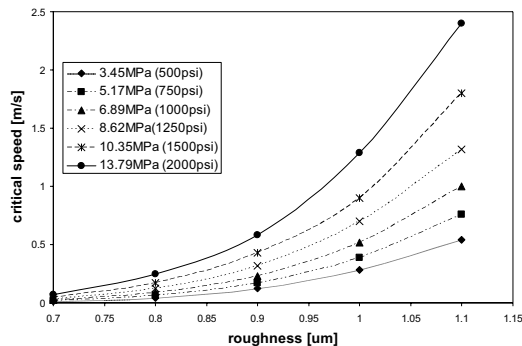
Figure 12 Critical speed vs. roughness

CONCLUSIONS

The results of this study indicate that typical rod seals operate with mixed lubrication in the interface between the rod and the seal, and the roughness of the seal surface plays a major role in determining the leakage characteristics. For a given seal design and set of operating conditions there is a critical roughness, below which there will be zero net leakage per cycle. For a given seal design, there is a critical rod speed, above which there will be zero net leakage per cycle. That critical speed is dependent on the seal roughness and sealed pressure.

The results also indicate that there are a number of characteristics that promote zero or reduced leakage in rod seals: small seal surface roughness, small lubricating film thickness, thicker film during outstroke than during instroke, cavitation in film during outstroke, and no cavitation or reduced cavitation during instroke.

ACKNOWLEDGMENTS

REFERENCES

1. Ishiwata, H. and Kambayashi, H., 1964, "A Study of Oil Seal for Reciprocating Motion," Proc. 2nd BHRA International Conference on Fluid Sealing, B3.
2. O'Donogue, J. P. and Lawrie, J. M., 1964, "The Mechanism of Lubrication in a Reciprocating Seal," Proc. 2nd BHRA International Conference on Fluid Sealing, B6.
3. Field, G. J. and Nau, B. S., 1974, "A Theoretical Study of the Elastohydrodynamic Lubrication of Reciprocating Rubber Seals," ASLE Transactions, 18, pp. 48-54.
4. Müller, H. K. and Nau, B. S., 1998, Fluid Sealing Technology, Marcel Dekker, New York.
5. Hirano, F. and Kaneta, M., 1971, "Theoretical Investigation of Friction and Sealing Characteristics of Flexible Seals for Reciprocating Motion," Proc. 5th BHRA International Conference on Fluid Sealing, G2.
6. Kanters, A. F. C., Verest, J. F. M. And Visscher, M., 1990, "On Reciprocating Elastomeric Seals: Calculation of Film Thicknesses Using the Inverse Hydrodynamic Lubrication Theory," Tribology Transactions, 33, pp. 301-306.
7. Field, G. J., and Nau, B. S., 1973 "Film Thickness and Friction Measurements During Reciprocation of a Rectangular Section Rubber Seal Ring," Proc. 6th BHRA International Conference on Fluid Sealing, C5.
8. Kawahara, Y., Ohtake, Y. and Hirabayashi, H., 1981, "Oil Film Formation of Oil Seals for Reciprocating Motion," Proc. 9th BHRA International Conference on Fluid Sealing, C2.
9. Kanters, A. F. C. and Visscher, M., 1988, "Lubrication of Reciprocating Seals: Experiments on the Influence of Surface Roughness on Friction and Leakage," Proc. 15th Leeds-Lyon Symposium on Tribology, pp. 69-77.
10. Nikas, G. K., 2003, "Elastohydrodynamics and Mechanics of Rectangular Elastomeric Seals for Reciprocating Piston Rods," J. of Tribology, 125, pp. 60-69.
11. Nikas, G. K, 2003, "Transient Elastohydrodynamic Lubrication of Rectangular Elastomeric Seals for Linear Hydraulic Actuators," J. of Engineering Tribology, 217, pp. 461-473.
12. Salant, R. F., Maser, N. and Yang, B. 2007, "Numerical Model of a Reciprocating Hydraulic Rod Seal," Journal of Tribology, 129, pp. 91-97.
13. Yang, B. and Salant, R. F. 2007, "A Numerical Model of a Reciprocating Rod Seal With a Secondary Lip," Tribology Transactions, 51, pp. 119-127.
14. Payvar, P. and Salant, R. F., 1992, "A Computational Method for Cavitation in a Wavy Mechanical Seal," Journal of Tribology, 114, pp. 199-204.
15. Patir, N. and Cheng, H. S., 1978, "An Average Flow Model for Determining Effects of Three-Dimensional Roughness on Partial Hydrodynamic Lubrication," J. of Lubrication Technology, 100, pp. 12-17.
16. Patir, N. and Cheng, H. S., 1979, "Application of Average Flow Model to Lubrication Between Rough Sliding Surfaces," J. of Lubrication Technology, 101, pp. 220-229.
17. Greenwood, J. A. and Williamson, J. B. P., 1966, "Contact of Nominally Flat Rough Surfaces," Proc. Royal Society (London), A295, pp. 300-319.
18. Streator, J. L., 2001, "A Model of Mixed Lubrication with Capillary Effects," Proc. 15th Leeds-Lyon Symposium on Tribology, pp. 121-128.

OS3-2

STUDY OF LUBRICATION CONDITIONS IN SLIPPER-SWASHPLATE CONTACT IN WATER HYDRAULIC AXIAL PISTON PUMP TEST RIG

Markus ROKALA*, Olof CALONIUS**, Kari T. KOSKINEN*, Matti PIETOLA**

* Department of Intelligent Hydraulics and Automation
Tampere University of Technology
P.O. Box 589, 33101 Tampere, Finland
(E-mail: markus.rokala@tut.fi)
** Department of Engineering Design and Production
Helsinki University of Technology
02150 Espoo, Finland

ABSTRACT

In water hydraulic systems, requirements for better energy efficiency call for the development of variable displacement axial piston pumps. Most axial piston units utilizing water as pressure medium lack the possibility of adjusting the swash plate tilt angle because of difficulties in constructing robust water compatible swash plate pivot bearings. Without smooth enough adjustment motion, the lubrication conditions between the swash plate and the piston slipper pads become disturbed and loss of fluid film may lead to early pump failure.

This study reports on measurements made with a test rig built for investigating tribological phenomena in variable displacement axial piston pumps. In the tests, the effects of changing the swash plate tilt angle were measured in a test setup with constant high pressure which loaded the piston. Lubricating film thickness and lateral force acting on the piston were measured together with changes in these quantities in response to changes in swash plate tilt angle.

KEY WORDS

Water hydraulics, Axial piston pump, Slipper-Swashplate contact

NOMENCLATURE

F_{piston} : total force acting in piston axis direction [N]
F_{sp} : force perpendicular to swashplate [N]
β : swashplate angle [deg]

INTRODUCTION

Modern water hydraulics should provide reliable fluid power components that operate with pure water and thus represent an environmentally friendly alternative to the oil hydraulics. Compared to mineral oil, water has lower viscosity and lower viscosity-pressure coefficient which makes good lubrication more difficult to achieve. The kinematic viscosity of oil is approximately 30 times that of water at representative operating temperatures. Consequently, clearances for sealing surfaces must be much smaller than for oil hydraulics to obtain sufficient volumetric efficiency. However, smaller clearances increase risk for direct contact between sliding surfaces,

higher friction and wear or component failure. [1]

In [2] water hydraulic pumps on the market are explored. Of the several different water hydraulic pumps that are on the market at the moment, most of them are oil lubricated piston pumps and only a few of the pumps are totally water lubricated. Water lubricated pumps are usually axial piston pumps with fixed swashplate angle.

To increase the overall efficiency of the system, variable displacement axial piston units are widely used basic components in oil hydraulics nowadays. Axial piston type units are very competitive also in modern water hydraulic pumps and motors. In mobile machines most of the units are axial piston design at the moment. However, there are not commercial variable axial piston pumps or motors for water hydraulics which is a significant problem in certain applications. [3]

Lubrication conditions between the swashplate and the slipper pad have been studied in many researches. Most of the researches were made using oil as pressure medium. Research has also been made with water based fluids. Li, Donders and Kazama have studied lubricating conditions using water or HFA-fluid in axial piston pumps [4,5,6]. All of these articles discuss pumps with constant swashplate angle.

The main objective of this study was to measure the water film thickness between the swashplate and the slipper pad and to record the basic effects caused by the adjustment of the swashplate angle.

TEST CONDITIONS

The structure of the test rig in this study allows changing the angle of the swashplate during measurements. The test rig that was used in measurements is shown in Figure 1. More information about the test rig is presented in [2].
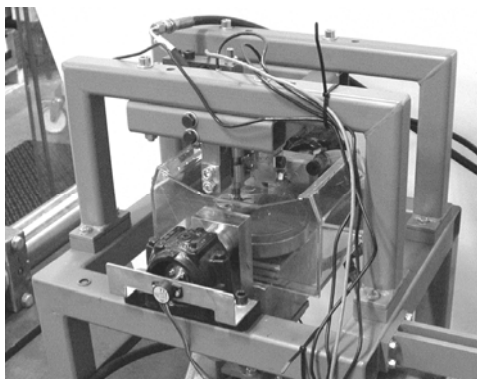
Figure 1 Test rig

The slipper pad is made of PEEK and the inner diameter of the sealing land is 9.90 mm and the outer diameter is

18.35 mm. The theoretical hydrostatic balance of the slipper is 0.729. Measured leakage for one piston-slipper pair is approximately 0.2 L/min with 10 MPa pressure difference. Surface roughness of the swashplate is R_a=0.22-0.24 µm.

Gap heights are measured outside of the slipper pad which makes changes of the water film more clear to see because of the geometric conditions. Measurements are made with three eddy current sensors with 1 mm measuring ranges (S1, S2, S3). Resolution of the sensors is 0.05 µm and static repeatability 0.1 µm. Dimensions of the test conditions are shown in Figure 2. Figure 2 also shows the locations of the sensors and the corresponding angular coordinates. The angular coordinate is used in reporting the results.
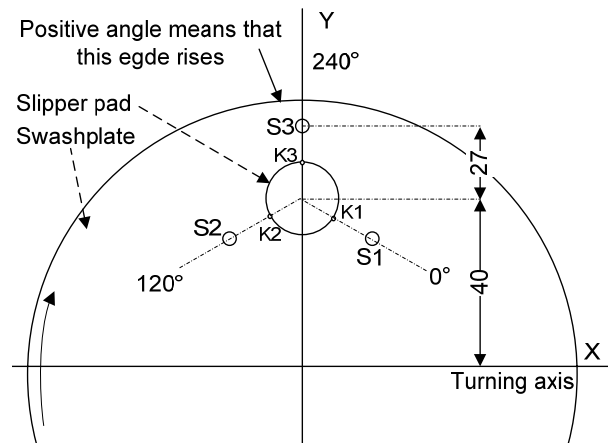
Figure 2 Dimensions of the test system and the slipper pad

Measured values are converted to the clearances between slipper pad and swashplate at points K1, K2, K3. With these points minimum gap height and location of the minimum gap can be calculated. Maximum gap located 180 degree clock wise from the minimum point.

EXPERIMENTAL RESULTS

The following figures show the computed gap between slipper pad and swashplate at the three clearance points (K1, K2, K3), at the center of the slipper (Av) and also the minimum value (Min). Figure 3 shows the reference measurements with 0 degree swashplate angle. The angular locations of the minimum and maximum values of the clearance during measurements are also plotted.

Measured gap heights can be compared to values computed assuming parallel gap flow [2]. With the present slipper dimensions and 10 MPa pressure difference, a leakage flow of 0.2 L/min corresponds to an average gap height of 7 µm.

$$F_{sp} = \frac{F_{piston}}{\cos(\beta)} \qquad (1)$$
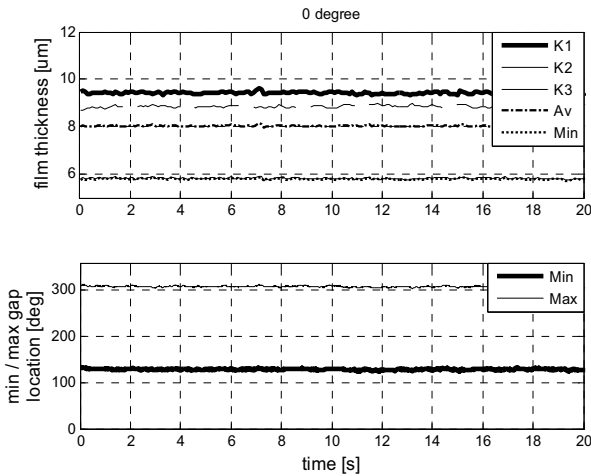
Figure 3 Gap heights of the slipper pad points with 1000 rpm, 0 degree swashplate angle and 10 MPa pressure difference

According to references [5] and [7] gap height is highest at inner edge and smallest at outer edge. Slipper is tilted backwards which means that gap height on the leading edge is higher than on the trailing edge. Measurements in this case show different kind of orientation as the Figure 3 shows. There could be some deformation at slipper pad or zero position is not exactly same as measured in 5 N load on dry circumstances. Minimum clearance is located about 129 degrees and maximum clearance located at 309 degrees (see Figure 2).

Orientation of the slipper pad is measured with four different constant swashplate angles: 0, 5, 10 and 15 degrees. Figure 4 shows the orientation of the slipper pad with 5, 10 and 15 degrees swashplate angle. Both measurements conditions are made in the following order: first adjustment of swashplate angle, then application of load pressure and finally setting the rotation speed.

Comparison between Figure 3 and curves at Figure 4 shows that there is not big difference at gap heights between different swashplate angles. Gap height changes are within 2 μm and at average gap height changes only under 1 μm. Also locations of the minimum and maximum points are almost same; difference is only a few degrees. That is obvious because contact between swashplate and slipper pad can carry only perpendicular load. Change at this perpendicular force is quite small. For example in our construction with 10 MPa, force change between 0 and 10 degrees angle is only 1.5 % (2084N → 2116 N) according to Eq. (1).
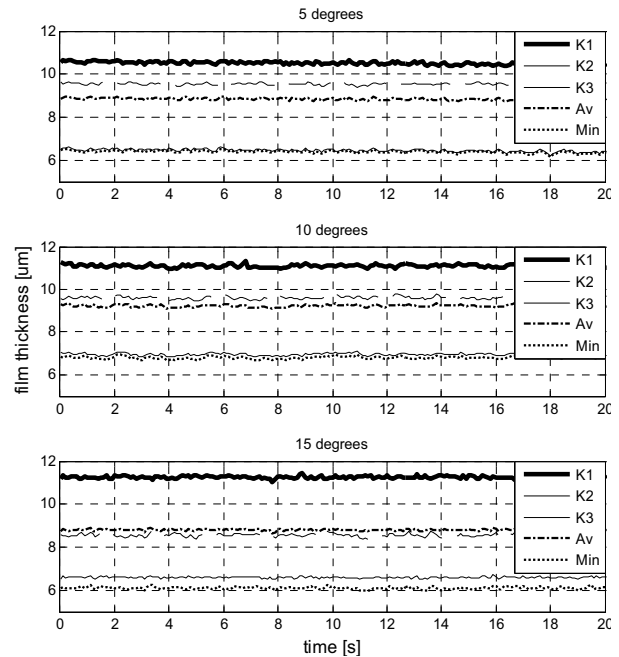
Figure 4 Gap heights of the slipper pad points with 1000 rpm, 5, 10 and 15 degrees swashplate angle and 10 MPa pressure difference

Situation is not exactly the same if 10 degrees is achieved during operation as Figure 5 and Figure 6 shows. Changes in gap heights are very smooth during turning process. Both for 0.2 MPa 10 MPa pressure orientation of the slipper pad is not exactly same before and after steps. Structure of the spherical joint is important for sliding conditions. Because of frictions of the spherical joint orientation of the slipper pad depends on turning direction and speed of the swashplate. In actual pumps the phenomenon is not significant because of low pressure area. It could be assumed that during the suction stroke orientation of the slipper pad is returned to the normal sliding position.

Figure 5 and Figure 6 shows the gap heights during swashplate turning with 0.2 MPa and with 10Mpa. Those figures also show that during step 0° to 10° average gap height reduces. During step to 10° to 0° gap height rises but overall changes are quite small. Friction force to X-direction is measured during swashplate change. Change of the friction force is about 30 N at 10 MPa pressure difference. Impact is of the same order as when pressure changes from 0.2 MPa to 10 MPa, which is about 40 N. Minimum and maximum gap height positions are almost same with both pressure levels, but location changes few degrees depending of swashplate angle.
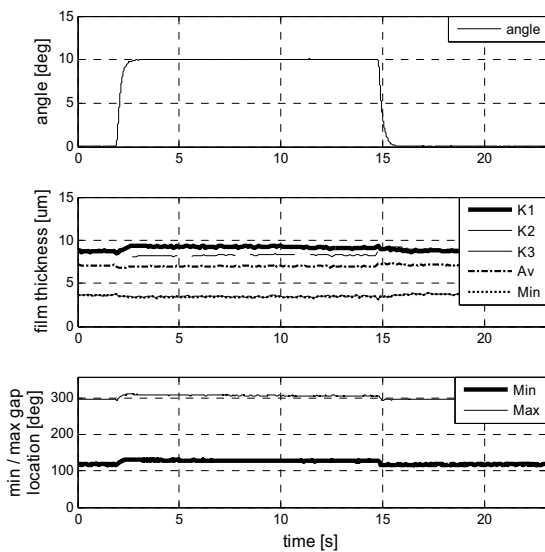
Figure 5 Gap heights during swashplate turning with 0.2 MPa load pressure. 1000 rpm
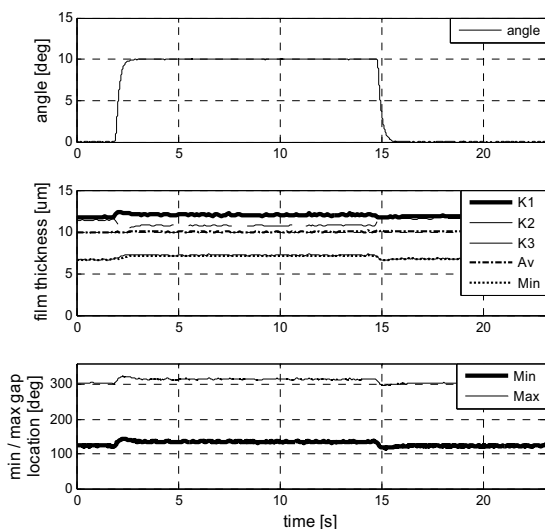
Figure 6 Gap heights during swashplate turning with 10 MPa load pressure. 1000 rpm
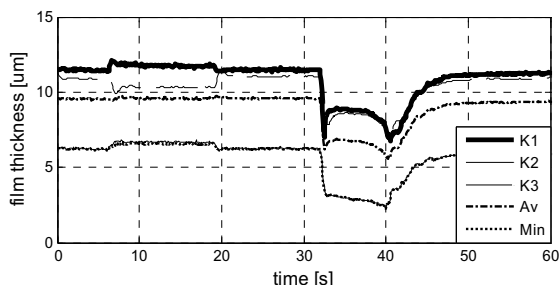
Figure 7 Gap heights during swashplate turning and pressure changes. 1000 rpm

Figure 7 shows changes during swashplate changes (from 10 degrees to 0 degree and back to 10 degrees) and after that during pressure changes from 10 MPa to 0.5 MPa and back to the 10 MPa. It could be seen that effect of pressure level is more significant than effect of the swashplate turning or effect of the swashplate angle.

CONCLUSION

In this paper experimental results on water film thickness measurements in an axial piston unit test rig were reported. It was shown how the swashplate angle affects the gap heights between swashplate and slipper pad. Constant angles in the range from 0 to 15 degrees have no big influence to the gap height or orientation of the slipper. Also effect of the 10 degrees step response of the swashplate angle is not significant for lubrication conditions. Pressure level of the pump is more important factor than swashplate angle.

Turning speed and turning direction of the swashplate under load pressure have an influence to the orientation of the slipper pad and more research in different conditions is needed to find that out. Also pressure cycle is interesting to research in future.

REFERENCES

1. Backé, W., Water- or oil-hydraulics in the future. 6th Scandinavian International Conference on Fluid Power, SICFP'99, Tampere, Finland, 1999
2. Rokala, M., Calonius O., Koskinen K.T. and Pietola M., Tribological Conditions Between Swashplate and Slipper pad in Variable Displacement Water hydraulic Axial Piston Unit, 6th International Fluid Power Conference Workshop Proceedings, 2008, pp.301-312.
3. Rydberg, K-E. Energy efficient water hydraulic systems. http://fluid.power.net/techbriefs/hanghzau/5_1_4.pdf. Accessed 2007-11-14.
4. Li, K.,Y., Hooke, C., J., A note on the lubrication of composite slippers in water-based axial piston pumps and motors. Wear, 147, 1991
5. Donders, S., Backé, W., Optimisation of high-pressure piston pumps for HFA-fluids. 5th Scandinavian International Conference on Fluid Power, SICFP'97, Sweden, 1997
6. Kazama, T., Numerical simulation of a slipper model for water hydraulic pumps/motors in mixed lubrication. Proceedings of the 6th JFPS International Symposium on Fluid Power, Tsukuba, Japan, 2005
7. Wieczoreck, U., Ivantysynova M., CASPAR – a computer-aided design tool for axial piston machines. PTMC 2000, Bath, United Kingdom.

OS3-3

WATER HYDRAULIC SYSTEM FOR HIGH SPEED CYLINDER DRIVE

Shigeru IKEO*, Hirotaka NAKASHIMA** and Kazuhisa ITO***

* Faculty of Science and Engineering, Sophia University
7-1 Kioicho, Chiyoda-ku, Tokyo, 102-8554 Japan
(E-mail: s_ikeo@sophia.ac.jp)

** Future Architect Co. Ltd

*** Faculty of Engineering, Tottori University

ABSTRACT

In order to apply the water hydraulic drive system to the precision die casting machine, the system with accumulator and logic valves are examined. As the pressure medium, water is environmental friendly, but it has disadvantage, e.g. leakage due to low viscosity, low lubricity and so on.
In this report, the friction force acting on logic valves were taken into account in the mathematical model, because for the purpose of prevention of leakage on logic valve two or three O-ring seals were used instead of labyrinth seal used in oil hydraulic logic valve. The validity of the mathematical model is assured by experimental results. Afterward the model is introduced into the mathematical model of whole high speed cylinder drive system and characteristics of the system is examined.

KEY WORDS

Key words; Water Hydraulics, High Speed Drive, Logic Valve, Mathematical Model, Friction Force

INTRODUCTION

Water hydraulics is a new power source having very high environmental friendliness that cannot achieved by conventional hydraulic systems while it has some technical problems to be solved. Japan Fluid Power System Society (JFPS) and Japan Fluid Power Association (JFPA) were and still are promoting its efficient application and supporting concerning projects. These several years are devoted to reveal the performance and the problems of conventional water hydraulic devices with practical experiments. In this project, the aim was 1) to know how high cylinder speed we can achieve, and 2) to clarify the obstacles which must to be solved in future.

In references [1], [2], we examined how to apply the water hydraulic technique for the injection and the dwelling processes of the hydraulic die casting machine. It was shown that the cylinder velocity is enhanced by three fold to seven fold by using the circuit combining the proper accumulator as auxiliary power source and logic valve than the case for using only directional control valve. Also we showed that the feasible highest cylinder velocity at medium supply pressure range up to 14MPa was 4.5m/s and at the water hydraulic cylinder stroke end the pressure rise was observed[3].
In this paper, our objectives are: 1) to establish the mathematical model of the water hydraulic system using

logic valves, 2) to investigate pressure response in circuit and 3) to estimate pressure rise which occurs at the stoppage of the cylinder by simulation.

SWITCHING CHARACTERISTICS OF LOGIC VALVE

Mathematical model

In this research two types of logic valve, as shown in Figure 1, are used. Figure 2 shows the experimental circuit for testing the switching characteristics of logic valve.

The mathematical model of water hydraulic logic valve. which consists of continuity equations, equation of motion and equations on the relation between flow rate and pressure drop across the orifice, is similar to one for oil hydraulic logic valve [4]. Only the model of friction force is deferent, because for the purpose of prevention of leakage in water hydraulic logic valve, two or three O-ring seals were used instead of labyrinth seal used in oil hydraulic logic valve. The friction model is given as follows;

$$F_{RN} = F_{RN1}(\dot{x}) - F_{RN2}(\dot{x}) \qquad (1)$$

$$(2)$$

$$F_{RN1} = \frac{\dot{x}}{|\dot{x}| + \mu} F_s$$

$$F_{RN2} = \begin{cases} 0 & for & |\dot{x}| \leq V_{fri} \\ \frac{\dot{x}}{|\dot{x}| + \mu}(F_s - F_d) & for & |\dot{x}| \geq V_{fri}: \end{cases}$$

where F_{RN1} is the static friction term, F_{RN2} the dynamic friction term, Fs the maximum static friction force, Fd the dynamic friction force and μ the connecting factor.

In water hydraulic logic valve, O-ring seals are used to prevent the leakage through the clearance between the valve body and the bush. Deformation of O–ring is influenced by pressures acting both sides of O–ring. During the opening operation, the pressure of one side of O-ring is high, while the other side pressure is tank pressure. On the other hand, during the closing operation pressures on both sides are high. In order to take into the consideration of this situation, different values of Fs and Fd are adopted as shown in Table 1.

Results of simulation and experiment

As a example of experimental result, the displacement of valve body and pressures are shown in Figure 3 for Form A valve with fixed orifice $Rx = Rt = 1.5$mm and load pressure 13MPa. From experimental results conducted under changing the valve shape, load

(a) Form A

(b) Form A
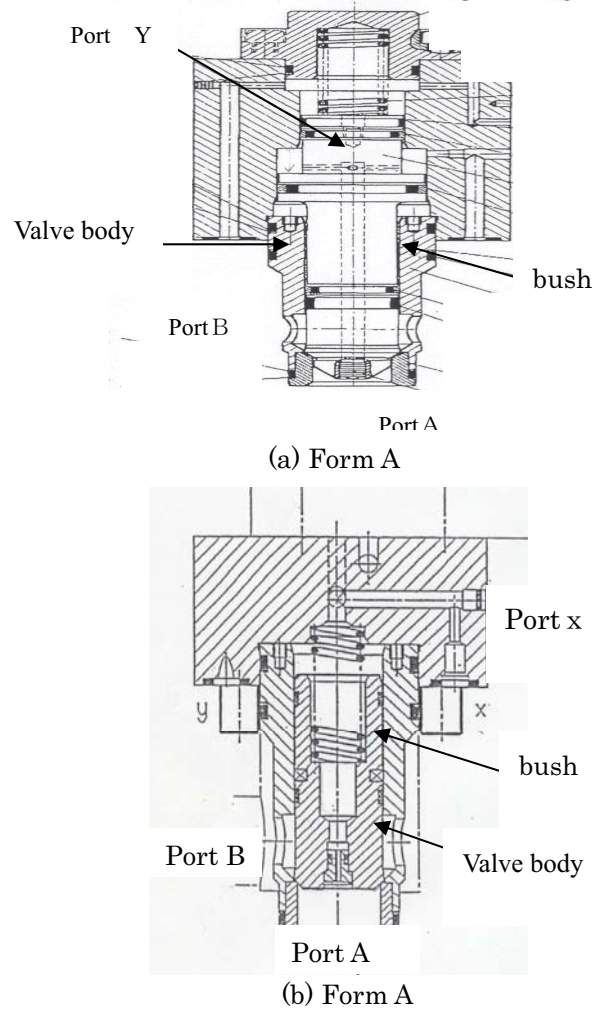
Figure 1 Water hydraulic logic valve
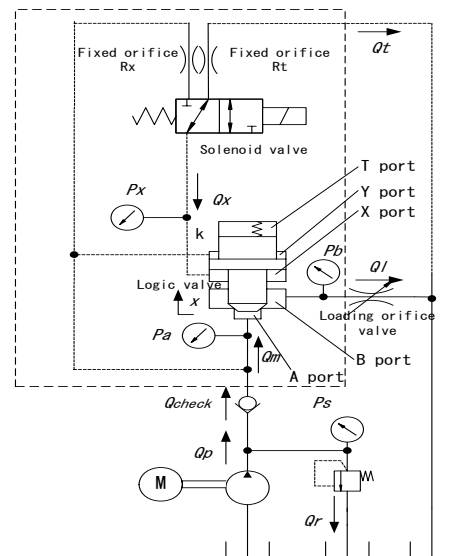
Figure 2 Experimental circuit

Table 1 Friction force vs. pressure

Pressure (MPa)	Friction force (N) (valve open)		Friction force (N) (valve close)	
	F_{s1}	F_{d1}	F_{s2}	F_{d2}
13	2600	1400	210	150
9	2200	1200	207	140
4	2000	800	207	130
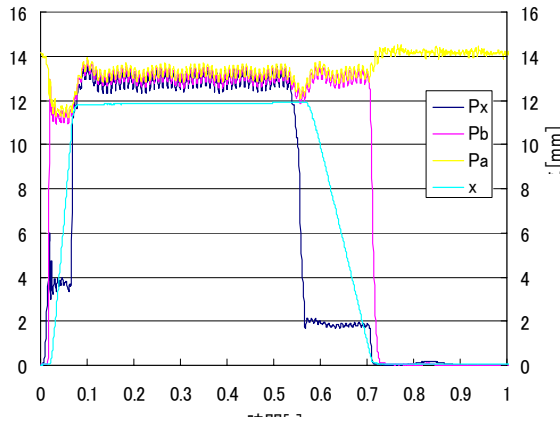
Figure 3 Experimental result
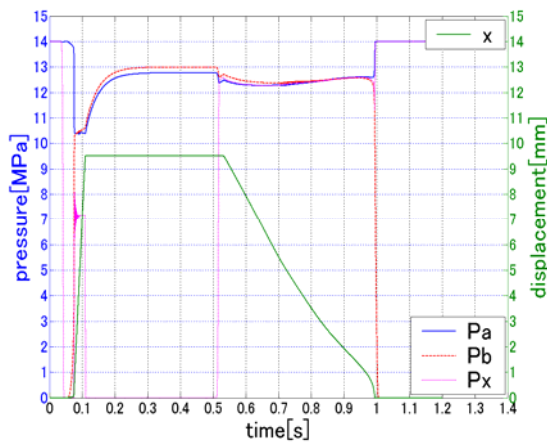
Figure 4 Resultsof simulation

2) the increase of load pressure make the closing time pressure and flow direction, it is seen that 1) the increase of load pressure make the opening time shorter, shorter in Form A valve and longer in Form B valve, 3) the opening and closing times for flow direction from A-port to B-port are shorter than ones for flow direction from B-port to A-port.

Figure 4 shows the result of simulation for Form B valve with fixed orifice $Rx = Rt$ = 1.5mm and load pressure 13MPa. Figure 5 shows the comparison of the experimental and simulated displacements.

From Figure 4, it is seen that the opening and closing
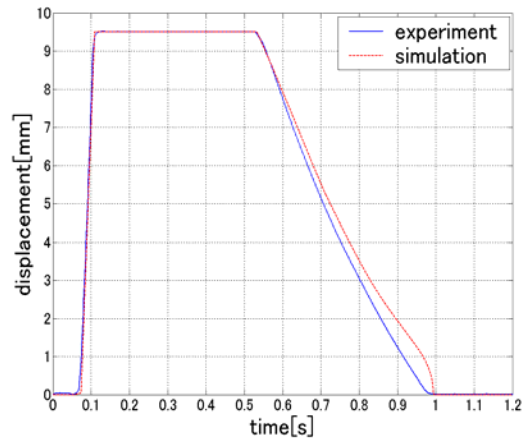
Figure 5 Comparison of experimental and simulated results

times given from simulation coincide with experimental results well. Experimental results on pressure variations are not shown here, they coincide well with results of simulation shown in Figure 4.

From these results the validity of the mathematical model is confirmed. Then, the dynamic characteristics of the water hydraulic system for high speed cylinder drive will be discussed in the next section.

CHARACTERISTICS OF WATER HYDRAULIC HIGH SPEED CYLINDER DRIVE SYSTEM

Experimental setup

Experimental apparatus and circuit are shown in Figure 6. This system is divided into three parts: the water supply unit, the water hydraulic cylinder and the load simulator unit. In the water supply unit, a fixed displacement axial piston pump is driven by the induction motor and 43.5L/min of flow is supplied at 1540rpm. The pressure rating of this circuit is 14MPa.

The high speed cylinder control circuit consisting of the accumulator and two logic valves is connected to the pump. The rod of the water hydraulic cylinder is connected to the same size oil hydraulic cylinder, which simulates the injection and the dwelling processes by loading the hydraulic cylinder. The load simulator is constructed with hydraulic cylinder and unload valve, and the PC controls the load/unload signal of this unit.

The experimental parameters are as follows(see Fig.6):
  ─discharge pressure of pump(no.3) are set by the relief valve(no.10)
  ─load pressure (no.29) by the relief valve (no.31)
  ─pilot flow of logic valve (no.15) by changing the orifice (no.14) in pilot valve (no.12)

The following items are measured :
  ─rod and head pressure of water hydraulic cylinder (P28C, P28D)
  ─cylinder displacement x
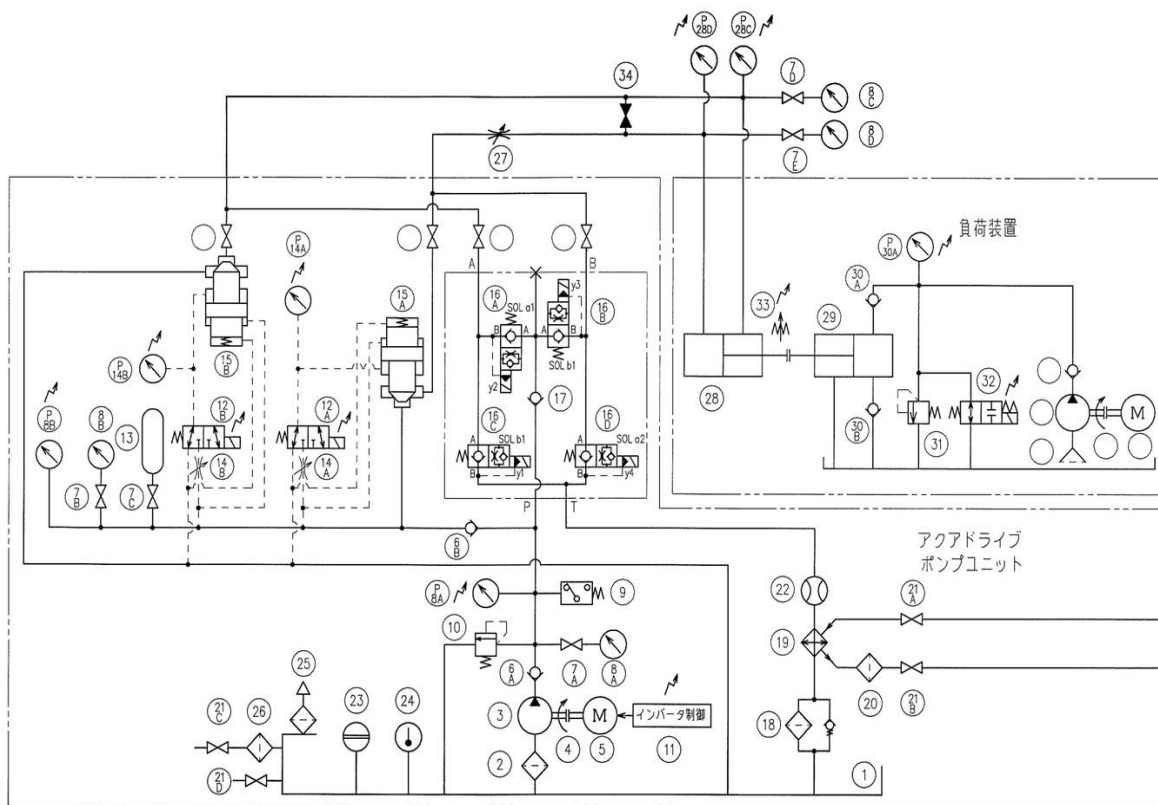
Figure 6   Water hydraulic high speed drive system

In this system, pressures acting two valves, 15A and 15B. For the logic valve 15A which delivers high pressure water to the cylinder head side port, high pressure in accumulator act at the port A and the load pressure in cylinder head side chamber at the port B. For the logic valve 15B which delivers the water from the cylinder rod side port to tank, the pressure in cylinder rod side chamber act at the port A and the tank pressure at the port B. Since B-port pressure (load pressure) of valve 15B is lower than the load pressure of valve 15A, valve 15B start moving later than valve 15A as explained before. Therefore pressure surge occurs in the cylinder head chamber. To avoid the pressure surge, it is necessary to operate the pilot valve 14B, which drives the logic valve 15B, some interval earlier than the pilot valve 14A, which drive the logic valve 15A.

In order to decide the proper time interval in the design stage, the mathematical model of the logic valve discussed before is used for the simulation of dynamic characteristic of whole water hydraulic high speed cylinder drive system

The rod of the water hydraulic cylinder is connected to the same size oil hydraulic cylinder, which simulates the injection and the dwelling processes by loading the hydraulic cylinder. The load simulator is constructed with hydraulic cylinder and unload valve, and the PC controls the load/unload signal of this unit.

Experimental results
Figure 7 shows the cylinder displacement and the pressure responses for 2.0mm orifice diameter and 14MPa supply pressure and Figure 8 its close-up.
From Fig.6, the cylinder velocity decreases and the head pressure in the cylinder increases rapidly at the end of cylinder stroke. This is the surge pressure. Another pressure rise can be also observed at the rod/head of the cylinder when the rod starts to move. This comes from the time delay between two logic valves. This is due to the difference of the forces acting both valve bodies. Before opening the logic valves, logic valve (no.15A) is pressured by the supply pressure while the other (no.15B) by the return pressure from the water hydraulic cylinder. The former is much higher than the latter. Therefore the pressure in cylinder head rises as the logic valve (no.15A) opens because the logic valve (no.15B) is still closed. To suppress this pressure rise, we opened the pilot solenoid valve (no.12B) earlier than the no.12A so that this time lag would be decrease
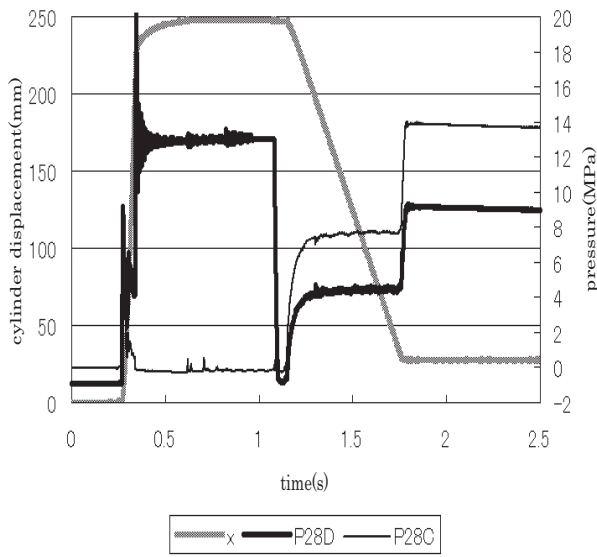
Figure 7   Cylinder displacement and pressure behavior
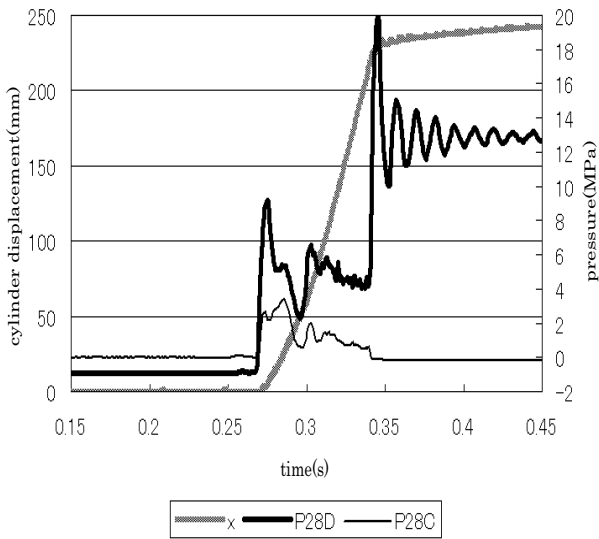
Figure 8   Cylinder displacement and pressure behavior (close-up)

Figure 10 Results of simulation
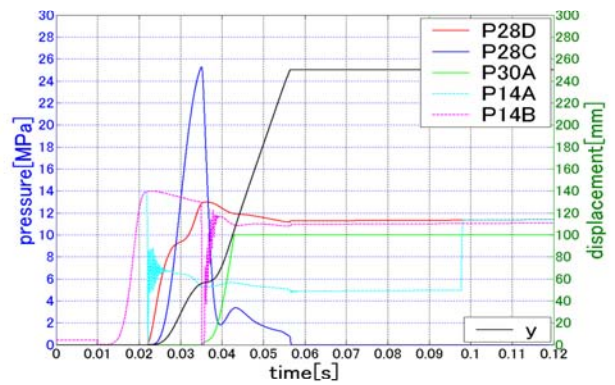
(a) displacement and pressures
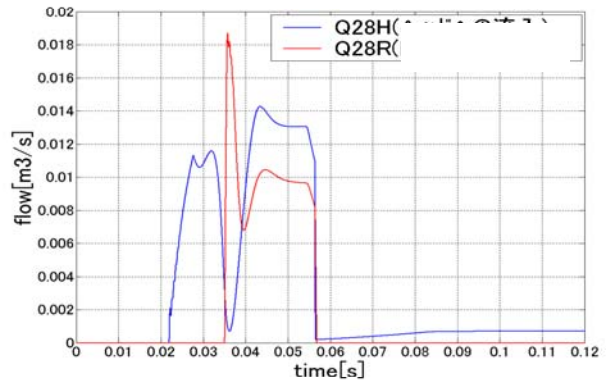
(b) Flow rates
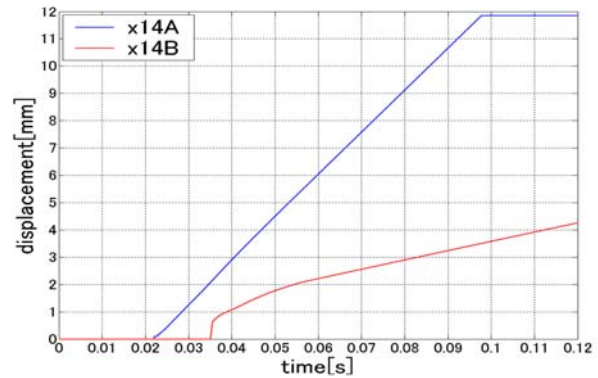
(c) Displacements of logic valves
Figure 9 Results of simulation

Discussion

Figure 9 shows the result of simulation when both pilot valves, 14A and 14B, operate simultaneously. Figure 9a shows pressures in cylinder head side chamber and rod side chamber P28D and P28C, pilot pressures P14A and P14B, load simulator pressure P30A and cylinder displacement y.   Figure 9b shows flow rates into cylinder head chamber Q28A and out of cylinder rod chamber. Figure 9c shows displacements of both logic valve x14A and x14B.
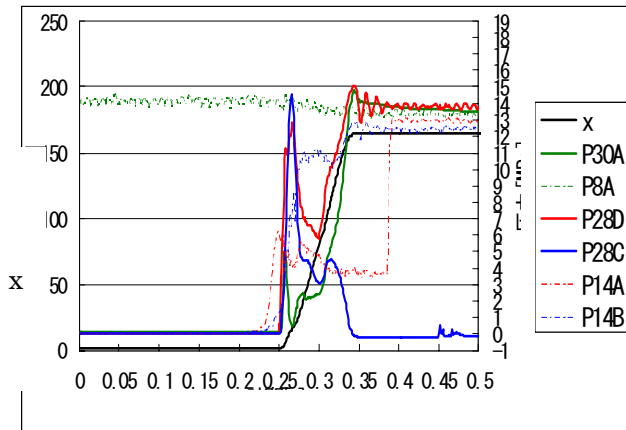
(a) without delay
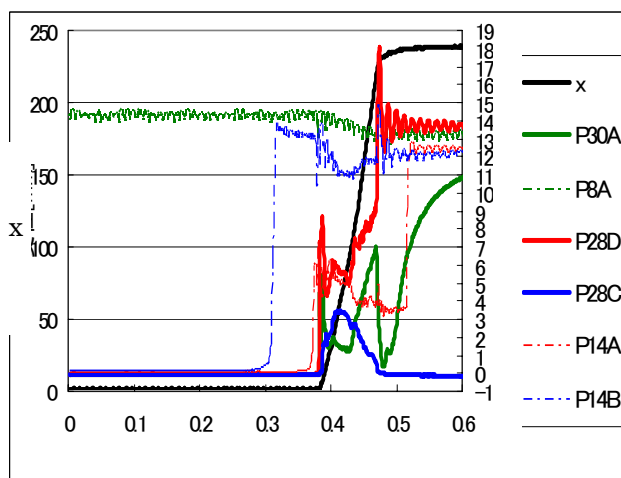
(b) with delay
Figure 11 Experimental Results

Discussion

Figure 9 shows the result of simulation when both pilot valves, 14A and 14B, operate simultaneously. Figure 9a shows pressures in cylinder head side chamber and rod side chamber P28D and P28C, pilot pressures P14A and P14B, load simulator pressure P30A and cylinder displacement y. Figure 9b shows flow rates into cylinder head chamber Q28A and out of cylinder rod chamber. Figure 9c shows displacements of both logic valve x14A and x14B.

Figure 10 shows the pressures and displacement of the logic valve from the simulation when the pilot valve 14A operates 35ms later than the pilot valve 14B. It is seen from this figure that the pressure surge can be depressed by operating the pilot valve 14A later than pilot valve 14B. The time interval 35ms was decided from

simulation by trial and error.

Figure 11a shows the experimental results when both pilot valves are operated simultaneously and Figure 11b when the pilot valve 14A operates 50ms later than the pilot valve 14B. From these results the effectiveness of operating time interval of both valves are confirmed.

CONCLUSION

In order to apply the water hydraulic drive system to the precision die casting machine, the system with accumulator and logic valves are examined. As the pressure medium, water is environmental friendly, but it has disadvantage, e.g. leakage due to low viscosity, low lubricity and so on.

(1) Mathematical model of water hydraulic logic valve is derived and its validity is assured experimentally. In the model, the friction force acting on logic valves were taken into account, because for the purpose of prevention of leakage on logic valve two or three O-ring seals were used instead of labyrinth seal used in oil hydraulic logic valve.

(2) The model is introduced into the mathematical model of whole high speed cylinder drive system and characteristics of the system is examined.

(3) In order to prevent the pressure surge which occurs when the cylinder rod starts to move, the method of operating the pilot valve 14A later than 14B is effective.

References

1. Japan Fluid Power Association: Annual Survey Research Report on Practical Application of Aqua Drive System Technique 2003, 2004(in Japanese)
2. Japan Fluid Power Association: Aqua Drive System -A Technical Guide II, 2002
3. Shigeru Ikeo, Kazuhisa Ito and Takashi Ochiai: Research on High Speed Drive of Water Hydraulic Cylinder, Proceedings of 6th International Conference on Fluid Power Transmission and Control, pp.208-211, Hangzhou, China, 2005.
4. Shigeru Ikeo, Koji Takahashi, Ryuji Miura and kunio Kanda: Switching Characteristics of Two-Way Cartridge Valve, Proceedings of 7th International Fluid Power Symposium, pp.245-252, Bath, UK, 1986

OS4-1

ANALYSING LOSSES IN HYDROSTATIC DRIVES

Hubertus MURRENHOFF*, Ulf PIEPENSTOCK* and Torsten KOHMÄSCHER*

* Institute for Fluid Power Drives and Controls (IFAS)
RWTH Aachen University
Steinbachstr. 53, 52074 Aachen, Germany
(E-mail: info@ifas.rwth-aachen.de)

ABSTRACT

The paper introduces three levels of details in the analysis of losses in hydrostatic drives which are carried out at IFAS of RWTH Aachen University (Germany). The first level of detail investigates the over-all system efficiency, the second level is focused on components while in the third level of detail the tribological contact in hydrostatic displacement machines are analyzed. Due to an increased environmental awareness and rising energy cost energy efficiency becomes a crucial factor in system design, components and single tribological contacts. Therefore the efficient conversion of mechanical into hydraulic energy and vice versa is the main objective when developing e.g. mobile construction machinery. An increase in the energy efficiency of hydraulic pumps, motors, valves and cylinders directly leads to significant reduction in energy consumption of hydrostatic drive lines and working kinematics. From the system point of view the power consumption of the diesel engine, as the power source of most mobile machinery, has to be reduced in order to increase tank-to-wheel efficiency. Modern management strategies for mobile machinery have to include diesel engine, drive line and working hydraulic with focus on an efficient operation of the engine.

KEY WORDS

System efficiency, volumetric losses, hydro-mechanical losses, work of friction, single-piston test stand

NOMENCLATURE

$F_{R, ax}$:	axial friction force	n:	revolution speed
$F_{S, ax}$:	axial friction force in suction stroke	s:	piston stroke
$F_{P, ax}$:	axial friction force in pump stroke	s_{max}:	max. piston stroke
M:	torque at pump shaft	Δp:	pressure difference
Q_1:	pump inlet flow	p_1:	pump inlet pressure
Q_2:	pump outlet flow	p_2:	pump outlet pressure
$Q_{L, ext}$:	leakage flow	p_L:	leakage pressure
V_i:	individual displacement	η_{tot}:	over-all energy efficiency of system
W_f:	work of friction	$\eta_{tot, C}$:	over-all energy efficiency of component
		η_{hm}:	hydro-mechanical efficiency
		η_{vol}:	volumetric efficiency
		ω:	angular speed
		ϑ:	temperature

INTRODUCTION

Due to the widely spread increased environmental awareness and rising energy costs the energy efficiency becomes a crucial factor in systems, components and the single tribological contact. Efficient conversion of mechanical into hydraulic energy and vice versa is one of the most important aspects when developing mobile construction machinery. Because of their high power density and flexible arrangement hydrostatic drives are used in most applications of mobile machinery. An increase in energy efficiency of hydrostatic pumps, motors and cylinders directly leads to significant reduction in energy consumption of hydrostatic drive lines and working kinematics.

In scope of this paper three different levels of detail in the analysis of hydrostatic drives which are carried out at IFAS of RWTH Aachen University are introduced:
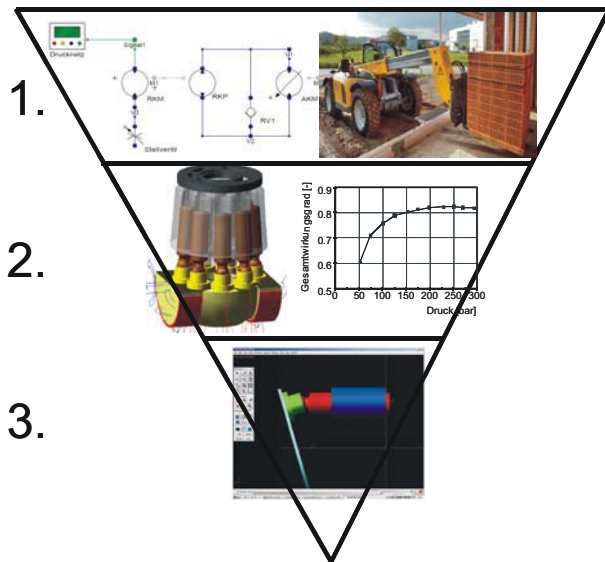
Figure 1 Three levels of detail

1. The first level of detail considers the over-all energy efficiency η_{tot} of the mobile machinery. The optimization of drive line concepts, working hydraulic and control algorithms is supported by dynamic system simulation (DSH*plus*) of the hydraulic circuits implementing all hydrostatic components. The detailed modeling of losses, systems and controls enables valuable information for the further development of hydrostatic drives.

2. The second level of detail is based on measurements of the hydraulic displacement units – pump and motor. Losses and component efficiency are investigated in dependency on speed n, pressure difference Δp, displacement V_i and temperature ϑ.

The results of these measurements on the one hand proof the results of the 3rd level and on the other hand serve as an input for the 1st level of detail.

3. The third level of detail aims at the optimization of the hydrostatic displacement machines. Single tribological contact surfaces, e.g. piston-bushing or slipper-swash- plate, are investigated in simulations and measurements. Measured friction forces on the piston result in a work of friction W_f for one revolution of the single piston. This work of friction can be seen as a benchmark of different types of pistons and bushings.

These three levels of detail contribute to the advantageous investigation of hydraulic system solutions. The system depends on components which imply various tribological contacts.

1st LEVEL OF DETAIL
→ Over-all system efficiency ←

Hydrostatic power supply systems for mobile machines are quite complex. Considering a typical hydrostatic transmission, it is a fluid power system with many active and passive components having interfaces to the internal combustion engine (ICE), electronics and mechanics. In the development phase, dynamic simulation of new system solutions allows for optimization in a short cycle time and reduces time for testing significantly. The over-all system efficiency of mobile machines results out of the required output power and losses in every single component, e.g. ICE and transmission (see equation 1). Thereby, a higher over-all efficiency results in lower fuel consumption as well as lower CO_2 and NO_x emissions.

$$\eta_{tot} = \eta_{ICE} \cdot \eta_{trans} \tag{1}$$

Figure 2 introduces a simple design for a driveline containing ICE, hydro-mechanical power split transmission and tire.
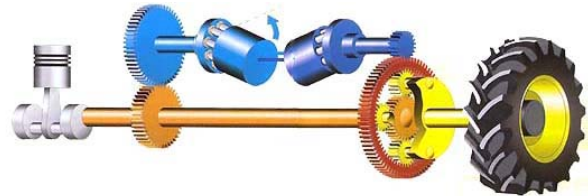
Figure 2 Exemplary drive line including engine, transmission and wheel

In order to achieve near-to- reality simulation results, precise loss modeling for changing operation conditions is required [5]. Modern drive line concepts are controlled by an electronic efficiency management

system (EMS) which is regarding best-point-operation of engine and transmission.

Accordingly, the total efficiency of the vehicle can be improved by:

1. implementation of high efficient transmissions, e.g. hydro-mechanical power split transmission (HMT).
2. implementation of high efficient ICE
3. rising the average efficiencies of transmission and ICE due to an advantageous control strategy.

A hydro-mechanical power split transmission (HMT) combines the advantages of mechanical and hydrostatic transmissions. The high efficiency of mechanical gears and the continuously variable transmission ratio of hydrostatic transmission result in a highly efficient continuously variable transmission (CVT). Conse-quently, vehicle velocity is decoupled from engine speed, which can result in best-point- operation of the ICE. Vehicle velocity can be increased at constant ICE speed or the ICE speed is varied without influence on the vehicle velocity.

In scope of a collaborative research project IFAS is developing a flexible tool for the investigation and further development of drive line concepts for off-highway machines. Based on a loss-based model of drive lines and ICE the fuel consumption and thereby the emissions are evaluated. Recent work shows the huge influence of the ICE operation on the fuel consumption [4]. Three different control concepts for the same drive line concept were investigated for one short and one long loading cycle of a 120 kW wheel loader:

- **Control concept 1 (CC1)** – ICE throttle is held in a constant percentage which results in a nearly constant ICE speed. Vehicle velocity is controlled by the ratio of the implemented HMT.
- **Control concept 2 (CC2)** – In modern wheel loaders the ICE speed governs transmission ratio and thereby vehicle velocity. This concept is adapted to a drive line including a HMT.
- **Control concept 3 (CC3)** – Aims on high torque loads on the ICE shaft and higher ICE efficiency. The current power demand of drive line and work hydraulic is determined and ICE speed is adapted to the required power.

Constantly high ICE speed for **CC1** results in low torque loads on the driving shaft, high fuel consumption and thereby low over-all efficiency. Due to **CC2** the ICE speed varies with vehicle velocity and torque loads as well as efficiency can be increased. Savings of 13% fuel consumption for the short loading cycle and 6% for the long cycle seem possible. The ICE speed adaption according to the determined power requirement of the

machine (**CC3**) results in saving of 15% for short and long loading cycle. ICE speed can be reduced for low power requirements and the efficiency is improved. Part of the improvement is also caused by the HMT. Advanced control strategies are therefore capable of increasing the average efficiencies of HMT and ICE.

For all simulations in scope of this paper DSH*plus* is used as the dynamic system simulation tool using an extended component library.

All these loss-based simulations of drive line concepts including the ICE rely on precise loss models of the implemented components. The losses of hydrostatic pumps, motors and transformers are essential for the investigation of partly and fully hydrostatic solutions. Additionally, the implemented control concept bears huge potential for reduced emissions and fuel consumptions. Precise measurements are required for the development of loss models for the flow and torque losses of hydrostatic units. These measurements are described in the 2nd level of detail.

2nd LEVEL OF DETAIL
→ Losses of hydrostatic displacement machines ←

Efficiency measurements of hydrostatic units – pumps and motors – require reliable sensor technology with high accuracy. In a first step, the real displacement of the hydrostatic units is determined. This can be done using different methods, as described in [3]. When running-in is completed, the machine is driven at chosen operating points and measurements are taken. Figure 4 shows the input and output power flows of a pump [6] and thereby the required measurement results.

Measured speed and torque result in the mechanical input power at the pump shaft which generates the hydraulic power in terms of flow and pressure (Figure 3).
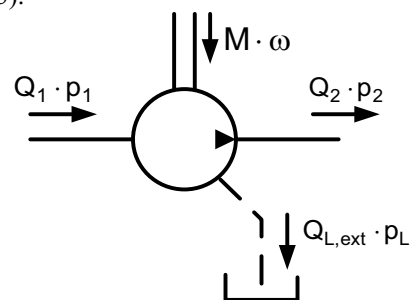
Figure 3 Input and output power of a pump [6]

Losses of the hydrostatic unit have to be separated into flow and torque losses by means of the real displace-ment for further detailed analysis. Flow and torque losses result in volumetric η_{vol} and hydro-mechanical efficiencies η_{hm}. These efficiencies are calculated according the following relations:

$$\eta_{hm} = \frac{V_i \cdot (p_2 - p_1)}{2 \cdot \pi \cdot M_{eff}} \qquad (2)$$

$$\eta_{vol} = \frac{Q_2}{n \cdot V_i} \qquad (3)$$

$$\eta_{tot,C} = \eta_{hm} \cdot \eta_{vol} \qquad (4)$$

The reliable determination of the real displacement V_i of the machines is essential for a precise separation into volumetric and hydro-mechanical efficiencies. The over-all efficiency is not dependent on V_i. Furthermore, fluid temperature ϑ is of huge influence and therefore has to remain constant during the measurements.

To allow for the testing of hydrostatic units in pumping and motoring mode on one test stand, the electric motor drive has two shaft extensions at IFAS. One is used for the test unit and the other one is connected to a variable displacement axial piston machine, which operates as a recovery and load unit. This provides an energy-efficient operation in pumping and motoring mode during testing. Only the occurring losses have to be overcome by the electric motor drive.

3rd LEVEL OF DETAIL
→ Individual friction at tribological contacts ←

For the optimization of hydrostatic units the step towards the investigation of single tribological contacts is required. At IFAS this investigation is performed by means of simulation and specialized single-piston test stands.

Within the Collaborative Research Center 442 and the additional transfer project "Axial piston machines with PVD-coated components" three different single-piston test stands for swash-plate unit were developed:

- low speed single-piston test stand
- high speed single-piston test stand
- dry-running single-piston test stand

All these realize an inversed kinematics, compared to axial piston swash-plate units. Accordingly, the bushing is housed by the measuring platform which is mounted to stiff force sensors while the piston is moving in axial direction. This principle is described in detail by Renius [7] and allows for measurements of friction forces between piston and bushing. The axial friction force is one of the most relevant losses for swash-plate units. Figure 4 shows the main assembly of the low speed single-piston test stand.
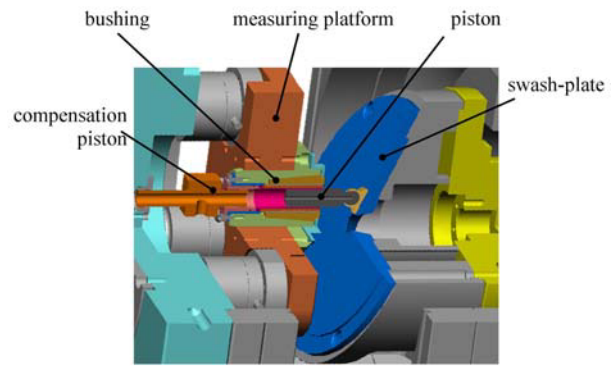
Figure 4 Low speed single-piston test stand

The axial movement of the piston is caused by a rotating wobble-plate and guided by the bushing in the measuring platform. All loads in terms of forces are taken up by four piezo-force sensors supporting the platform. All the lateral forces and the axial friction force are measured by the sensors [1, 2]. A specifically designed compensation piston is required to apply the hydraulic pressure to the back of the measured piston without disturbing the measurements. High and low pressure are varied in dependency of the rotating angle of the swash-plate by a control valve.

The test stand allows for speeds up to 10 rpm and aims at the optimization of the start-up torque of hydraulic motors. Normally, the hydro-mechanical efficiency is poor for low speeds of motors which results in torque ripples. This is mainly caused by the relatively high friction between piston and bushing while there is only little hydrodynamic lubrication in the gap. This low speed test stand is a suitable tool for analysis and optimization in order to rise start-up torque and lower the losses in swash-plate units.
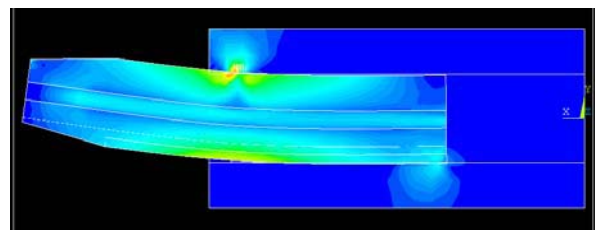
Figure 5 Calculation of stress and deformation

FEM-simulation models are implemented to learn about different influences on the losses and to determine stresses and deformations. Furthermore the design of the tribological contact between piston and bushing can be optimized by means of simulations. Figure 5 shows stresses and deformation of the piston caused by a lateral load force and the guiding bushing.

Especially when there is a hard/hard contact between the materials of piston and bushing the bending of the

106

piston and the local deformation of piston and bushing has to be regarded. The FEM-simulation help to find an appropriate contouring of the contact surfaces. This means e.g. choosing the radius at the front edge of the bushing and the piston-radius.

Looking at pumps, rotating speeds of more than 500 rpm are required. Therefore a high speed single-piston test stand was recently developed at IFAS. This test stand is capable of running at speeds of 500 rpm to 2,500 rpm. The friction forces are measured according to the same principle which was introduced for the low speed test stand. Certainly, all components were well optimized for this new purpose. Friction forces are much lower at high speeds of the hydrostatic unit than at low speeds. To maintain the high accuracy of the measurements at the low speed test stand, cross-talk of the piezo-force sensors is measured and subsequently compensated for.
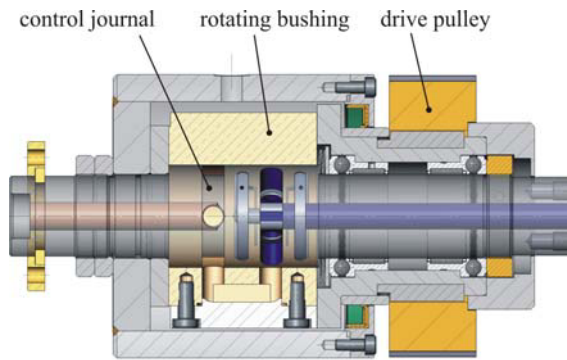
Figure 6 Sectional view of the control valve

Again, the hydraulic connection is realized via a compensation piston. While the commutation of pressure on the back of the piston can be performed by a simple electro-hydraulic valve at low speed, a new control valve was designed for high speeds. Figure 6 shows a cross-sectional view of the control valve.

Using the drive pulley, the rotating bushing is driven at operation speed and synchronized with the wobble-plate. The control journal has two ports: high pressure and low pressure. In the rotating bushing there is an integrated transfer port which realizes the commutation. The described control valve offers a reproducible pressure variation according to Figure 7.
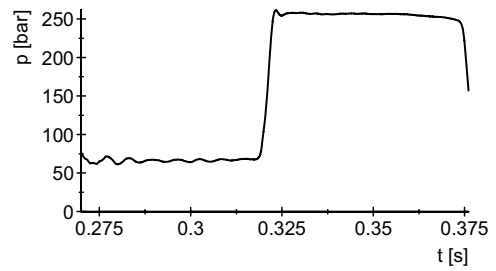
Figure 7 Pressure variation @ 500 rpm

The design and assembly of the third single-piston test stand is not yet completed. It is a simple construction with the purpose to measure dry friction between piston and bushing. Using two hydraulic cylinders a side force can be applied and the piston can be driven in axial direction, as Figure 8 shows.
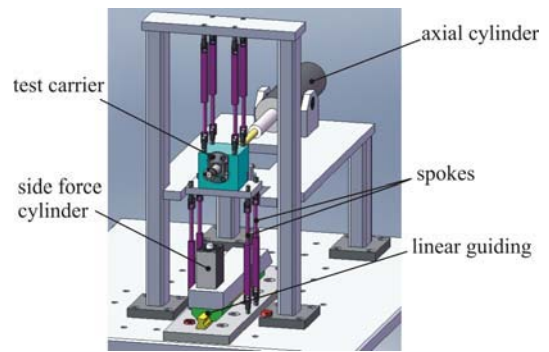
Figure 8 Dry-running single-piston test stand

Friction force is measured by one piezo-force sensor and the test carrier is fastened to the frame by spokes. When the piston is moved by the axial cylinder, the axially guided cylinder for the lateral force moves with the piston. Measuring the friction coefficient using this test stand is supposed to be better than using other principles like a disc/disc test stand for instance.
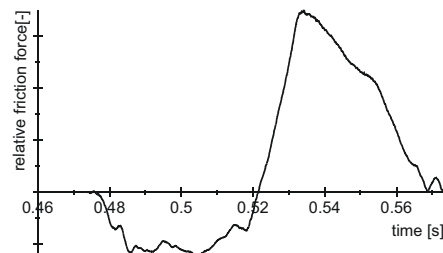
Figure 9 Friction force @ 500 rpm, 300 bar

The most interesting output of all the measurements with the presented single-piston test stands are the resulting friction force diagrams. Usually the friction force is plotted versus time or angle as shown in Figure 9.

107

With these friction force diagrams it is difficult to compare different designs of pistons and bushings. It is much better to have a close look on the losses which are caused by the friction force for one stroke of the piston. Consequently the friction force is plotted versus the working stroke of the piston (Figure 10).
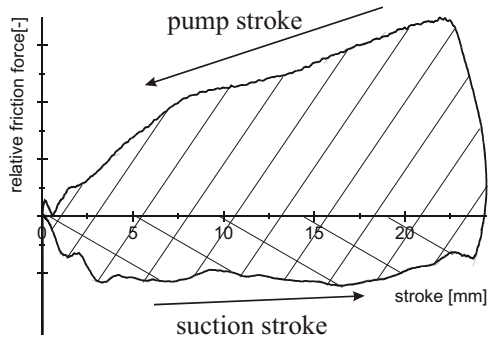
Figure 10 Work of friction @ 500 rpm, 300 bar

The work of friction W_f is calculated by the integration of force in dependency of the working stroke. It is indicated by the hatched area and calculated according to:

$$W_f = \int_0^{s_{max}} F_{P,ax} ds + \left| \int_0^{s_{max}} F_{S,ax} ds \right| \qquad (5)$$

Finally, the work of friction W_f is dedicated to be an appropriate benchmark for analysing and comparing axial friction losses between piston and bushing.

In addition to the measurements on single-piston test stands, the performance for most suitable piston-bushing combination can be analyzed on the component test stand at IFAS. Improvements in the single tribological contact will also lead to improvement in the component behaviour. Afterwards, the measured component performance can be integrated into system simulation tools and prove the functionality in the hydraulic system. Small changes on the contact side may result in huge improvements on the unit performance.

SUMMARY

In times of rising energy costs and tightened governmental restrictions regarding the emissions and fuel consumption of vehicles and mobile working machines, losses in hydrostatic units are to be reduced.

At IFAS three different level of detail are utilized to analyze and improve the performance of hydrostatic drives. Tribological contacts are the main loss source in hydrostatic units. FEM-simulation models and advanced measurements result in a good understanding of the origin of volumetric and hydro-mechanical losses in order to derive improvements by geometric changes.

Measurements on hydrostatic units, pumps and motors, are a major benchmark for the quality of improved components. Additionally, precise measurements can result in precise simulation models for the over-all system investigation. Beneath the improved efficiency of hydrostatic components the improvement of the over-all system efficiency will be the result of new structures. These structures, e.g. hybrid, motor controlled, will first be analyzed by state-of-the art system simulation tools.

In summary, the introduced tools are capable of improving the efficiency of hydrostatic system by means of simulation, measurement and system know-how.

REFERENCES

1. Breuer, D. (2007): Reibung am Arbeitskolben von Schrägscheibenmaschinen im Langsamlauf, Dissertation, Shaker, Aachen, Germany
2. Enekes, C., Murrenhoff, H., Verwendung beschichteter Bauteile im tribologischen System Kolben-Buchse in Axialkolbenmaschinen, 48. Tribologie-Fachtagung 2007, Goettingen, Germany, Vol. 2, pp. 41/1-41/11
3. Ivantysyn, J., Ivantysynova, M. (2001): Hydrostatic Pumps and Motors. Principles, Design, Performance, Modelling, Analysis, Control and Testing. First English Edition. New Delhi, India: Akademia Books International
4. Jähne, H. et al, Drive Line Simulation for Increased Energy Efficiency of Off-Highway Machines, 6th International Fluid Power Conference (IFK), April 1-2, 2008, Dresden, Germany, Vol. 1, pp. 49-64
5. Kohmäscher, T., Murrenhoff, H., Rahmfeld, R. and Skirde, E., Improved loss modeling of hydrostatic units – requirement for precise simulation of mobile working machine drivelines, Proc. ASME International Mechanical Engineering Congress, November 11-15, 2007, Seattle, WA, USA, IMECE2007-41803
6. Palmen, A., Murrenhoff, H. (2007): Experimentelle Wirkungsgraduntersuchungen – Am Beispiel einer Axialkolbenpumpe. In: Ölhydraulik und Pneumatik, Jg. 51, H. 5, S. 264– 268.
7. Renius, K. T. (1974): Untersuchungen zur Reibung zwischen Kolben und Zylinder bei Schrägscheiben-Axialkolbenmaschinen. Düsseldorf, Germany: VDI-Verlag (VDI-Forschungsheft, 561)

OS4-2

TELEOPERATION OF HYDRAULIC CONSTRUCTION ROBOT USING VIRTUAL REALITY

Hironao YAMADA*, Tatsuya Doi **

* Department of Human and Information Systems
Gifu University
Yanagido 1-1, Gifu 501-1193 Japan
(E-mail: yamada@gifu-u.ac.jp)
** Department of Mechanical and Systems Engineering,
Gifu University, 501-1193 Japan

ABSTRACT

This research deals with master-slave control of a teleoperated hydraulic construction robot. In this system, the master consists of two joysticks, and the slave is the hydraulic construction robot (including the fork glove, boom, arm, and swing, driven by hydraulic actuators). In a previous research, the authors proposed a force feedback method based on position-velocity control, in which the cylinder velocity is proportional to the position of the joystick. The purpose of this research is to confirm the effectiveness of the force feedback method using behavioral measures and subjective indexes. An experiment was conducted to evaluate operational performance, confirming the effectiveness of the force feedback control system.

KEY WORDS

Key words, Construction Machinery, Robot, Hydraulic Actuator, Master-slave control, Force feedback

INTRODUCTION

The remote operation systems for construction machinery in general use adopt methods that give the operator only visual feedback, which is obtained by cameras mounted on the construction equipment. Naturally, the amount of information regarding the site provided to the operator by such methods is inadequate, and it has been reported that work efficiency is significantly inferior to that in direct operation.[1] In this case, if the operator could grasp various situations to the detailed level from the general condition of the work area, safe, precise work would be possible.

In previous research, the authors studied a master-slave system in which the master consisted of a pair of joysticks and the slave comprised all four actuators (fork glove, swing, boom, arm) of a hydraulic excavator (hereinafter, construction robot), using a position-position control system, in which the cylinder position of the construction robot displayed one-to-one correspondence with positional commands to the joystick. However, general construction machinery employs position-velocity control, in which the cylinder velocity is proportional to the position of the joystick. Therefore, in a previous report [2], we proposed a new master-slave control method (hereinafter, this control method) based on position-velocity control in order to approximate more closely the operating system in actual equipment. In this position-velocity control method, the cylinder velocity is proportional to the position of the joystick. Tests confirmed that accurate force representation was possible by this method.

On the other hand, in ordinary remote operation, there are limits on the number of visual sensors that can be installed at the site and the volume of data that can be transmitted. Furthermore, various factors (attitude of construction robot, change in attitude of front part) which occur during work create dead angles for cameras, making operation difficult and hindering work. It is

considered possible to overcome the aforementioned problems of limits on the number of visual sensors and data transmission volume and camera dead angles by introducing an operation system mediated by virtual space constructed in a computer. However, the condition of the actual space and the work must be reflected satisfactorily in the virtual space. It can be assumed that work performed in a virtual space that does not satisfy this requirement will be difficult, like work in real space. Even when using a virtual space with these advantages and drawbacks as visual information, safe and precise work is expected to be possible if a feeling of force can be fed back to the operator, because the operator will be able to grasp the condition of the work intuitively.

Therefore, in this report, the position-velocity control type master-slave control system proposed by the authors was applied to a remote operation system mediated by virtual space constructed in a computer, and its effectiveness was verified from task efficiency, risk measurements, the success ratio, and subjective work load.

TELEOPERATED CONSTRUCTION ROBOT SYSTEM

Fig. 1 shows a schematic diagram of the experimental construction robot using the remote operation/virtual reality system which will be discussed in this paper. As shown in the figure, this system consists of two joysticks, which comprise the master, and a construction robot (Landy KID-EX5, manufactured by Hitachi Construction Machinery Co., Ltd.; weight: 0.5t), which is the slave. The joysticks form a bilateral pair, and can each be operated in the forward/back and right/left directions.
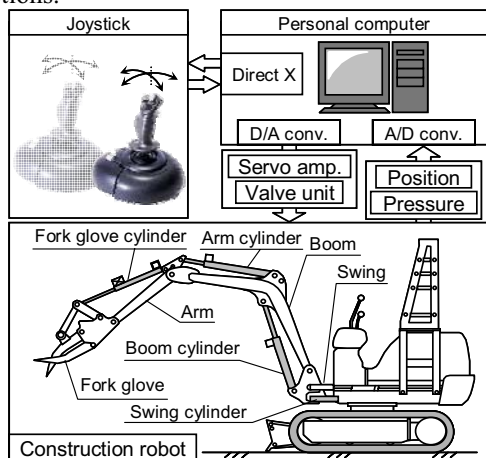
Figure 1 Schematic diagram of experimental apparatus

The mechanical system consists of a robot arm with four degrees of freedom. The hydraulic cylinders used as actuators for the fork glove (hereinafter, glove) at the end of the robot arm and the swing, boom, and arm are moved by operating the joysticks in these four directions. To give the operator a feeling of grasping objects with the glove and the work reaction force (force) generated during work by the swing, boom, and arm, two DC motors are incorporated in each of the joysticks. Feedback control by proportional control valves is used in the above-mentioned four cylinders (Stroke Sensing Cylinder, manufactured by KYB Co., Ltd.; resolution: 0.01mm). Force sensors are installed on the head side and cap side of each of the cylinders to detect load pressure. These pressure signals can be used as force signals, which are necessary on the master side.

POSITION-VELOCITY CONTROL IN MASTER-SLAVE SYSTEM

In this research, first, for the glove, a control method that enables satisfactory representation of grasping in a wide range of grasping tasks was proposed. The features of this control method are as follows[2].

① The threshold value f_{prei} for representing reaction force is variable, using measured velocity-drive force characteristics.

② Reaction force to the joystick comprises a term that depends on the position-velocity deviation of the master and slave, and a term that depends on piston drive force. (Symmetric positioning and force reflection control method are used in combination.)

The reaction force τ_{ri} on the joystick in this control method is given by Eq. (1). The subscript i in τ_{ri} and the other terms is $i = 1 \sim 2$, corresponding to the fork glove or boom, respectively.

$$\tau_{ri} = T_i \left\{ k_{pmi} \left(Y_{mi} - V_{si} \right) + k_{tmi} f_i \right\} \tag{1}$$

Gain T is given by the following equation:

$$T_i = \begin{cases} 0 \; ; & \left(|f_{si}| \leq |f_{prei}| \right) \\ \dfrac{f_{si} - f_{prei}}{f_{e\_max} - f_{prei}} ; & \left(f_{si} > 0 \cap f_{si} > f_{prei} \right) \\ \dfrac{f_{si} - f_{prei}}{f_{c\_max} - f_{prei}} ; & \left(f_{si} < 0 \cap f_{si} < f_{prei} \right) \end{cases} \tag{2}$$

Here, Y_m, V_s are nondimensional displacement of the master and nondimensional velocity of the slave, f is piston drive force, and k_{pm}, k_{tm} are gain of the master system. f_{e_max}, f_{c_max} denote the maximum drive force of the piston in expansion and contraction (f_{e_max}=11.7kN, f_{c_max}= -6.8kN).[2]

Application of this control method, composed as described above, to this system makes it possible to give the operator a satisfactory feeling of the task, not only when grasping hard objects or opening and closing the

glove without load, but also when grasping comparatively soft objects. In the case of the boom, external forces caused by gravity, etc. are included in the measured drive force. Therefore, when this control method is applied, the load force is estimated and subtracted from the measured drive force. In this research, the position-velocity control type master-slave control method was also applied to the boom for use in risk measurements, in addition to the fork glove. (In the previous report, application was limited to the glove.) Force feedback for the boom is expected to make it possible to avoid dangerous situations, such as overturning of the robot due to excessive pressure by the robot arm on the ground. In this report, this was also evaluated using the risk measurements.

EVALUATION OF OPERATIONAL PERFORMANCE

System Configuration

In this research, a system that displays CG of the work site to the operator was constructed assuming "block stacking by construction robot," which is frequently used in "mudslide countermeasure work by block stacking at disaster recovery sites." Fig. 2 shows the configuration of the object system used in an experiment to evaluate operational performance. The light gray arrows show the flow of signals for expressing the construction robot in virtual space; the dark gray arrows show the flow for the work object.
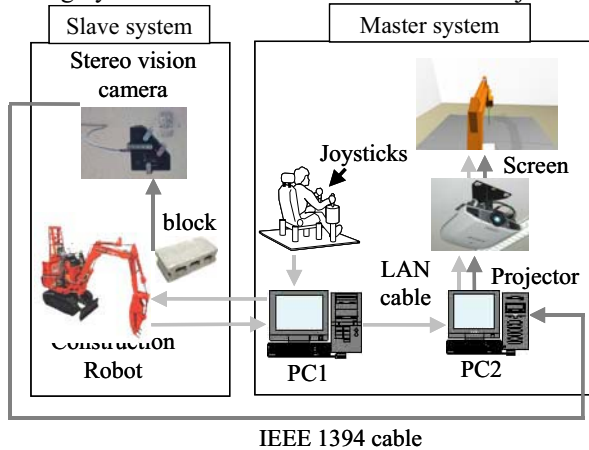
Figure 2   Experimental apparatus for evaluation of operational performance

PC1 is the computer which is used to control the construction robot. A master-slave system for feeding back the displacement of the joystick of the robot, which is the master, and the displacement of the piston of the robot, which is the slave, is configured using this computer. In addition to control of the construction robot, PC1 also transmits the cylinder displacement of the construction robot to PC2, which is the computer that creates the virtual space, using TCP/IP. Based on

this information, PC2 draws the construction robot on the virtual space. In addition, distance and color information on the work object are sent to PC2 from a 3-dimensional shape input device using an IEEE1394 cable, and this information is used to draw the work object on the virtual space. The video images of the virtual space drawn in this manner are displayed on a screen using a projector. The 3D shape input device used is a 3D digital camera Color DIGICLOPS (manufactured by Point Grey Research; hereinafter, simply DIGICLOPS), which makes it possible to obtain 3-dimensional images in the field of view of the sensor.
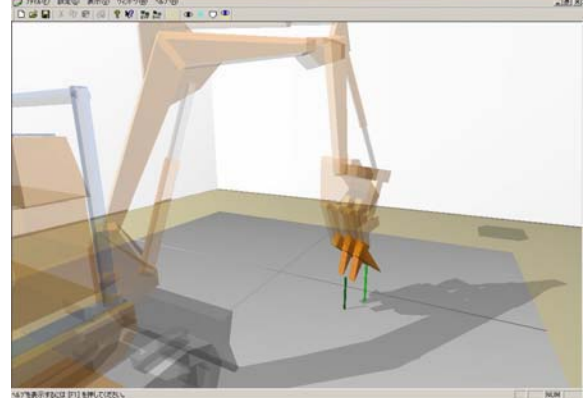
Figure 3   Example of created virtual space

The operator operates the robot while viewing the virtual space created by PC2. Fig. 3 shows an example of the virtual space displayed to the operator at this time. As illustrated here, the images displayed to the operator include the shadows of the construction robot and the object and a gauge showing the distance between the tip of the fork glove and the ground surface or object. The robot itself is semi-transparent. For easy operation with visual feedback using only one screen, an auto viewpoint move function is used. This function moves the viewpoint and reference point in response to the behavior of the swing and boom.

Content of Task

Two types of tasks (Task 1, 2) were adopted. These tasks involved sorting, movement, and stacking of blocks in the task area shown in Fig. 4, using four blocks with two different hardnesses (concrete blocks wrapped in sponge, hereinafter called hard blocks, and sponges, hereinafter called soft blocks). The contents of the respective tasks were as follows.

(1)   Task 1

In the initial condition, one block each was arranged at point A and point C in Fig. 4, and 2 blocks were arranged at point B. The task was to grasp each block in order, beginning from the left as seen from the robot, and reply verbally as to whether the block was a hard block or soft block.
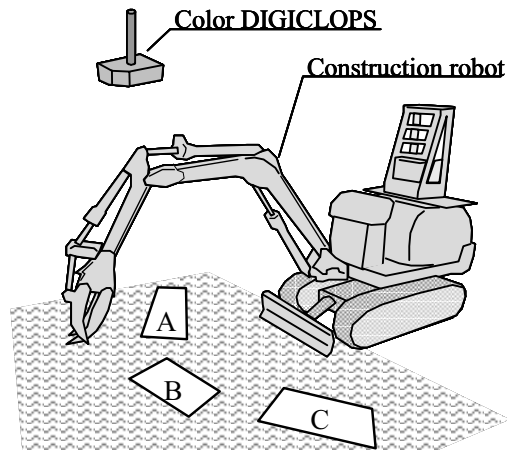
Figure 4 Task area for evaluation of operational performance

(2) Task 2

In the initial condition, two blocks each were arranged at point A and point C in Fig. 4. The task was to grasp each block in order, beginning from the left as seen from the robot, move the hard blocks to point B, and leave the soft blocks in the initial position. When two or more hard blocks were found, the operator was instructed to stack the blocks in accordance with the block arrangement plans in Fig. 5.

In case of 2 pieces	In case of 3 pieces	In case of 4 pieces
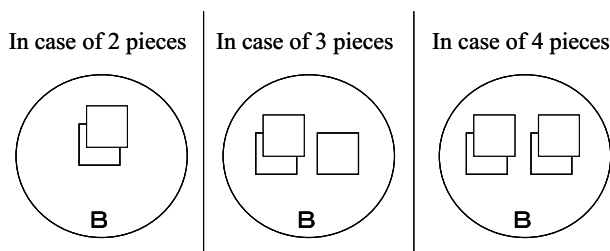
Figure 5 Block arrangement plans

Evaluation Indexes

A total of five evaluation methods were used. Three evaluation indexes were used to verify the effectiveness of the force feedback function by this control method, these being task efficiency, risk measurements, and success rate. These are objective behavioral measures. In addition, NASA-TLX and an evaluation questionnaire were also used as subjective indexes. The features of these various indexes are outlined below.

Behavioral measures refer primarily to objective task performance. These include the amount of work performed, error rate, etc. In the present research, task efficiency and risk measurements were used. The details of these items are as follows.

(1) Task efficiency

Task efficiency is an index that measures the number of blocks moved to the designated position and arranged in a unit of time [Obj./min].

(2) Risk measurements

The following two measures are used as indexes showing that the task is being performed irrespective of the fact that the robot is in an unstable condition.

① Time t_c during which the construction robot is in an unstable condition due to contact between the front part and the ground surface or object (hereinafter, contact time).

② Average value of force, F_c, generated in the boom, arm, and swing of the construction robot while the robot is in an unstable condition (hereinafter, average generated force).

Based on the action-reaction relationship, here, the excess force generated by the piston when in contact with the ground, etc. can be treated as equivalent to an external force acting on the piston. Introduction of the above-mentioned gain T enables nondimensional expression of the excess forces generated in each piston. The generated force Ft is obtained from the sum of these values. A threshold value is set for the generated force F_t obtained as described above, and conditions that exceed this value are considered unstable. Because the contact time tc shows the total time during which the generated force F_t exceeds the threshold value, the average generated force F_c is obtained by dividing the integrated value of Ft during this t_c counting time by the contact time t_c.

(3) Success rate

The success rate expresses the rate of success in correctly determining whether blocks are hard or soft. It is calculated by the percentage (%) of the number of blocks successfully judged among the total number of blocks.

SWAT (Subjective Workload Assessment Technique) and NASA-TLX (NASA Task Load Index) may be mentioned as psychological indexes in wide general use. In the present research, NASA-TLX was adopted as a subjective index, as there are many examples of application and it is easily introduced.

NASA-TLX consists of six measures, these being mental demand, physical demand, time demand, operational performance, effort, and frustration. The flow of evaluation by NASA-TLX consists mainly of three processes: ① paired comparisons of the various measures, ② work which is the object of the load evaluation (in this paper, block stacking work), and ③ evaluation of the load for each measure. Based on this procedure, it is possible to evaluate the size of the load for each measure, and to make an evaluation of the total load (WWL score: mean weighted workload score).

EXPERIMENTAL RESULTS
SYSTEM CONFIGURATION

This experiment was performed in order to verify the

effectiveness of applying the force feedback function using this control method to actual work. Therefore, this chapter presents the results for the behavioral measures, subjective index and evaluation questionnaire when the block sorting and stacking tasks described above were performed. The subjects were 6 persons (all male, average age: 23.5 years), three of whom were inexperienced persons who received an explanation of operation of the construction robot prior to the start of the experiment to evaluate operational performance. All subjects were allowed sufficient time to practice operation of the construction robot prior to the experiment.

Behavioral measures

(1) Task efficiency

As task efficiency results, Fig. 6 shows the actual task efficiency and standard deviation by subject.
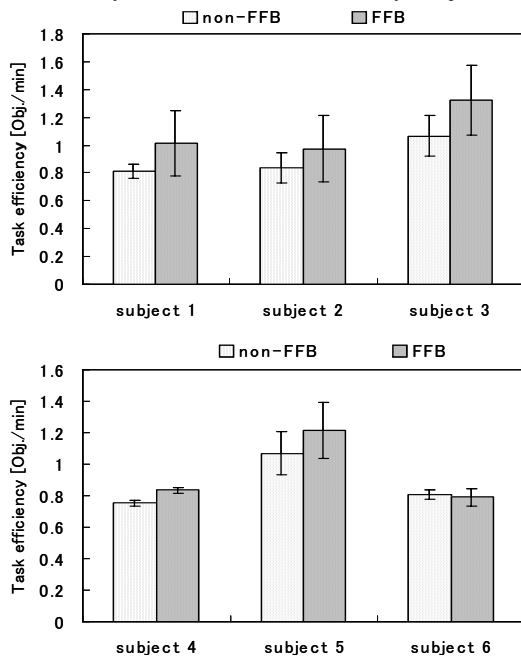
Figure 6 Task efficiency in behavioral measures

In this figure, "non-FFB" and "FFB" mean that operation was performed without or with force feedback, respectively. The x-axis shows the subjects, and the y-axis shows task efficiency [Obj./min]. Larger values on the y-axis mean higher task efficiency. Because the subjects were allowed to practice before the experiment, it was assumed that there would be little improvement in task efficiency as the subjects became more accustomed to operation of the robot. Therefore, no correction was made for this factor. According to Fig. 6, the task efficiency of almost all subjects as improved by using FFB. Accordingly, the results showed that the meaningful difference of force feedback in remote operation systems mediated by virtual space is not

insignificant.

(2) Risk measurement

As risk measurement results, Fig. 7 shows contact time t_c and average generated force F_c by subject. In this figure, the left y-axis shows contact time t_c, and the right y-axis shows average generated force F_c. In both cases, smaller values mean that work can be performed more safely.
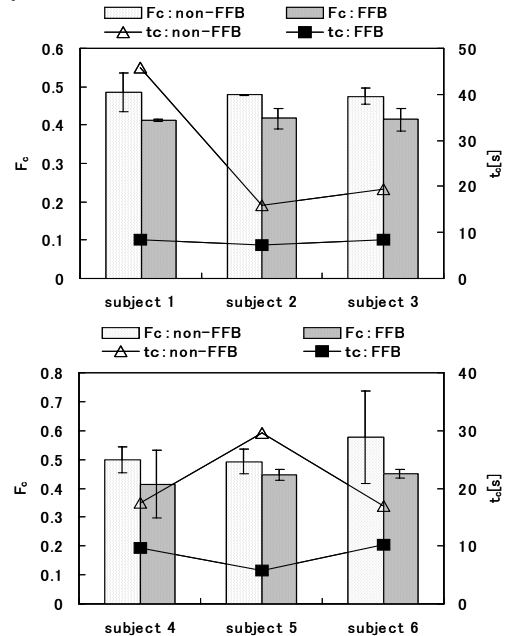
Figure 7 Risk measurement in behavioral measures

This figure shows that risk increases when force feedback is not provided. This is because the subjects could not judge contact with the floor due to the lack of reaction force. Conversely, with reaction force, the subjects could judge contact with the floor and move away immediately. These results confirmed that the condition of the construction robot can be grasped intuitively when force feedback is provided, and safer operation of the robot is possible.

(3) Success rate

Fig. 8 shows the results of the success rate by subject. In this figure, the x-axis shows the subjects, and the y-axis shows the success rate as a percentage. Because 8 blocks were used in all of the tasks in this experiment, the result is calculated as (number of blocks successfully judged) / 8. Larger values on the y-axis mean that a large number of blocks was judged successfully and errors were fewer.

According to Fig. 8, the success rate was higher when force feedback was provided. This is attributed to the fact that judgment is easier with force feedback because the task reaction force is communicated to the operator by way of the joystick. Conversely, when force feedback is not provided, judgments must be made based only on the CG, which does not show any change in the shape of the object. In this case, the operator must

depend on his intuition, based on the condition of deformation of the task object.
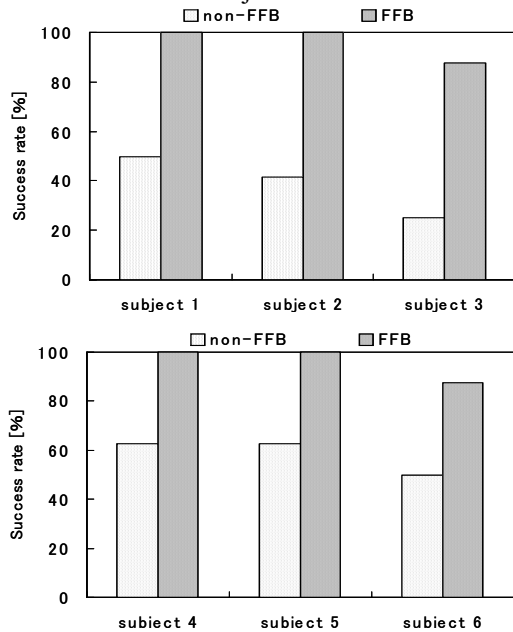
Figure 8 Success rate in behavioral measures

For this reason, there were considerable differences in the success rates of the subjects. The fact that in some cases the success rate was not 100% when force feedback was provided is attributed to locations where it was difficult to feel the reaction force due to the position where the block was grasped. Accordingly, it was found that accurate work is possible when force feedback is provided.

Subjective Index

Fig. 9 shows the results of NASA-TLX. It should be noted that, because NASA-TLX is a subjective evaluation method, the evaluation standard for each measure will differ depending on the habits and judgment standards of the respective subjects. For this reason, evaluation based on an average value for all subjects is difficult. Based on the results of the experiment, the results for the six subjects can be largely divided into two groups. Therefore, rather than showing the average values for all subjects, the figure shows the results for two subjects as representative examples. In this figure, the ■ mark shows the evaluation values for each measure without force feedback, while the Δ mark shows the case with force feedback. Smaller scores mean the load on the subject was lighter. Fig. 9 shows that both the respective evaluation values and the WWL score decreased when force feedback was provided. Accordingly, it can be understood that the mental load on subjects is reduced when force feedback is provided in comparison with the case where force feedback is not provided. Inferring from the tendencies of the two representative subjects, it

was found that the loads for the measures mental demand (MD), effort (EF), frustration (FR), and operational performance (OP) were reduced with force feedback. However, one subject showed a slight increase in physical demand (PD). This is attributed to the increased load on the hands in joystick operation due to feedback of work reaction force. This seems to indicate that some persons may find operation more physically demanding with force feedback.

The results described above confirmed that, in situations where it is difficult to grasp the condition of the construction robot based on visual information alone, it is possible to supplement the visual information by providing force feedback, and this can lighten the mental load on the operator.
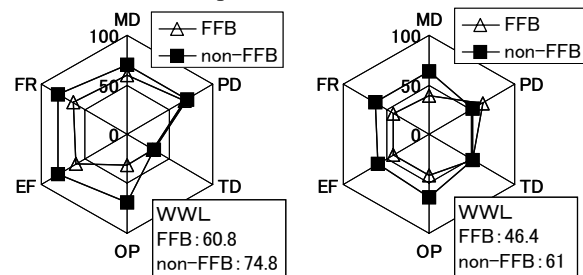
Figure 9 NASA-TLX in subjective measures

CONCLUSIONS

The objective of this research was to improve operational performance in work performed by teleoperation of construction robots. Using a general-purpose hydraulic excavator with a position-velocity control system proposed by the authors in previous work, force feedback was provided to operators and their operational performance was evaluated. These results show the effectiveness of the force feedback.

ACKNOWLEDGEMENT

REFERENCES

1. Kanno, S., Okada, T., Kitahara, S., Unmanned construction technology by remote control (in Japanese), The mechanization of construction,1994 ,**8**, pp.17-20.
2. Yamada, H., Gong M., Zhao, D., A Master-Slave Control for a Tele-Operation System for a Construction Robot(Application of a Velocity Control Method with a Force Feedback Model), Journal of Robotics and Mechatronics, **19**-1, pp.60-67, (2006).

OS5-1

ENERGY-SAVING HYBRID HYDRAULIC SYSTEM COMPRISING HIGHLY EFFICIENT IPM MOTOR AND INVERTER, FOR INJECTION MOLDING AND MANUFACTURING MACHINE

Takayuki IMAMURA, Yuzo SAWADA, Masashi ICHIKAWA and Hirokazu NAKAMURA

Oil Hydraulics Division, Daikin Industries, Ltd.
1-1 Nishihitotsuya, Settsu-shi, Osaka, 566-8585 Japan
(E-mail: takayuki.imamura@daikin.co.jp)

ABSTRACT

We have developed a novel energy-saving hydraulic pump system—Super Unit—that comprises a high-efficiency motor, low-inertia pump and an inverter controller (We call this type of system 'hybrid'). Compared with conventional hydraulic pumps each driven by a constant speed induction motor, our novel hydraulic pump system driven by a high-efficiency variable-speed IPMSM (Interior Permanent Magnet Synchronous Motor) features energy-saving of 40% or more when used for an injection molding machine which is a typical application of this new pump system.
By means of a pressure feedback control function and run speed control software on the controller, the pressure and flow rate of the hydraulic fluid are accurately controlled according to a command from the controller of the molding machine. This control software allows a high-torque high-precision motor to drive a low-inertia pump: as a result, high-speed high-response control of hydraulic actuators is realized, thereby the quality of molding products obtainable from injection machines controlled by our system is higher compared with quality resulting from conventional systems.
A series of our variable-speed pump system products adopting hybrid hydraulic pressure technology are available for NC lathes, machining centers and other industrial machines such as a press machine.

KEY WORDS

Inverter, Energy-saving, Hydraulic Pump, Molding, IPMSM

INTRODUCTION

In the technical field of industrial machinery, combinations of constant-speed induction motors and variable-displacement pumps have been often used on hydraulic power units. In the year 2000, we developed an energy-saving hydraulic unit product series, each hydraulic unit comprising a compact fixed-displacement pump and a variable speed inverter motor whose maximum speed is at least twice as high as that of conventional inverter motors.
Since then, this product line has been positively contributing to reducing energy consumption on machine tools. Furthermore, we have successfully developed a variable-speed energy-efficient hydraulic unit incorporating a highly efficient motor whose rotor has embedded rare earth magnets (IPMSM).
Currently, we are offering an unique line of products, each product type optimized for industrial machine application.

Figure 1 summarizes some examples of units we have so far developed and their typical features.
After development of the first product line intended for machine tools, we developed the next product line for general industrial machines such as a press machine, wherein the new hydraulic products incorporate the IPMSM in order to improve energy efficiency, feature increased pressure and flow rate so that they are more suitable for general industrial machines, and at the same time, they have enhanced functions for example in communication capability. We are further developing new line of products for molding machines: for this purpose, these new products feature not only improved response by way of an increased instantaneous motor torque but also an increased rated motor output capacity. Functionality of our hybrid hydraulic pump system contributing to energy-saving is described below. Also, its advantages, when it is compared with conventional hydraulic system and electric servo motor mechanisms with ball-screws for molding machines are presented.
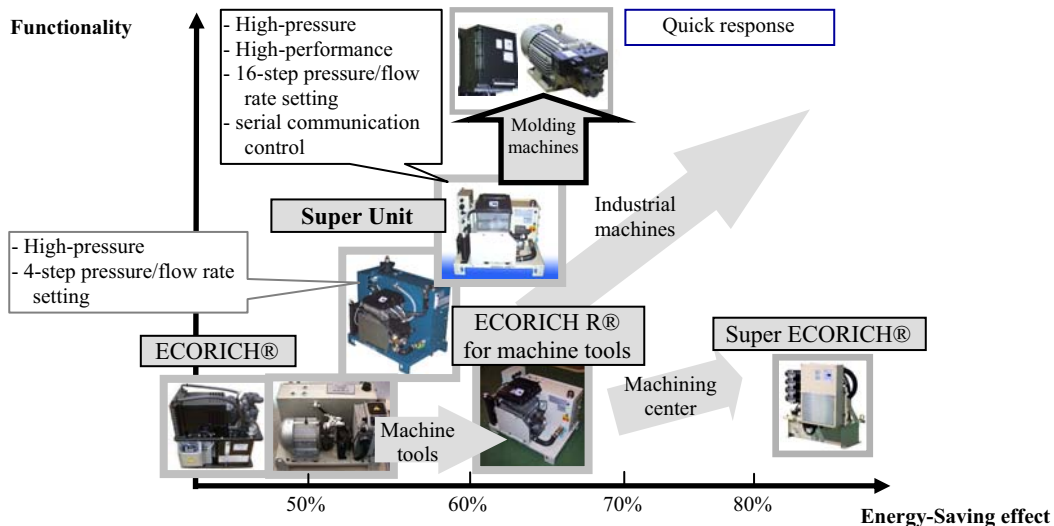
Figure 1 History of Daikin's development works for energy-saving hydraulic pump units

ENERGY-SAVING WITH HYDRAULIC PUMP SYSTEM FEATURING VARIABLE SPEED CONTROL

As shown in Figure2, in a pressure maintaining mode on a conventional hydraulic pump system, where the hydraulic actuator is not executing an effective work such as when the hydraulic cylinder is at its stroke end and is maintaining the hydraulic pressure, the motor remains running at a speed (usually, 1800 min^{-1}) same as in the situation where the cylinder is being actuated. Consequently, energy is wasted in this mode owing to mechanical frictional resistance and viscous friction resistance that results from stirring of the hydraulic fluid.

Since the cylinder velocity, which is proportional to the flow rate, on a conventional hydraulic system is usually controlled by varying the resistance of the valve flow passage, pressure loss, which is consumed as waste heat, will inevitably occur. In contrast, our "Super Unit" is a unique energy-saving hydraulic pump system, whose running speed is regulated by an inverter controller so that the hydraulic fluid is fed at a necessary flow rate only during an appropriate period according to the loading condition. (Arrows and a solid line in Figure 2)

Figure 3 schematically illustrates a control block for our hydraulic pump system. With this system, the pressure and flow rate of hydraulic fluid are regulated appropriately according to the following pressure feedback scheme:

[1] When the hydraulic actuator is operating, necessary amount of flow is supplied by high rotation.
[2] By monitoring the pressure, necessary amount of flow is supplied in accordance with load condition.
[3] While the pressure is maintained, the minimum amount of flow is supplied to compensate for the leakage from the circuit by low speed rotation.
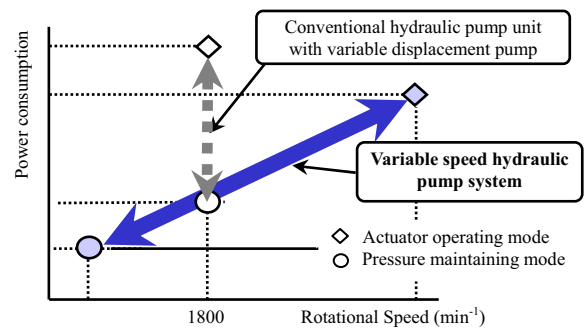
Figure 2 Difference between conventional hydraulic unit and variable speed hydraulic pump system
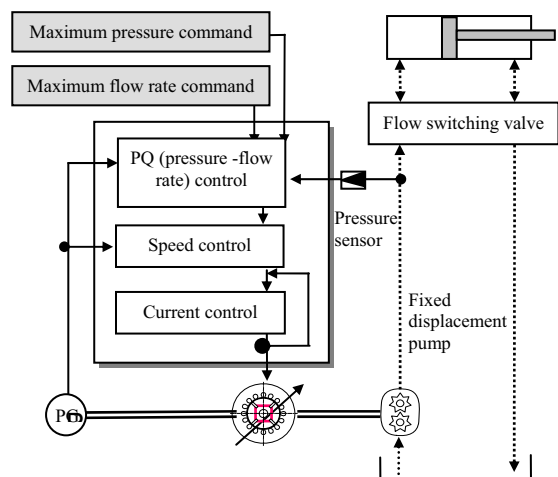
Figure 3 Control block for variable speed hydraulic unit

HIGH-EFFICIENCY HIGH-RESPONSE IPMSM

The IPMSM (Interior Permanent Magnet Synchronous Motor) was originally developed for energy-saving arrangement on Daikin's air-conditioning equipment, and its response and velocity control performance has been improved in order to adopt for our hydraulic pump system.

As shown in Figure 4, the rare earth magnets are embedded in the rotor. Through synchronous control that helps efficiently develop both a magnet torque and a reluctance torque, the synchronous motor attains a very high degree of efficiency as high as about 95%.
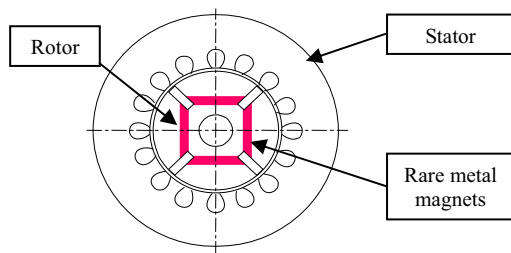
Figure 4 Cross-section of IPMSM rotor and stator

Response of conventional variable-displacement pumps falls in a range of about 0.1 second from the minimum flow rate to the maximum flow rate. In variable-speed pump system, the response time from the minimum running speed (100 min^{-1}) to the maximum running speed (3500 min^{-1}) must be not longer than approximately 0.1 second. In conjunction with an optimally designed inverter controller, our IPMSM satisfies this requirement.

ENERGY-SAVING PERFORMANCE OF SUPER UNIT FOR INDUSTRIAL MACHINES

Figure 5 graphically plots the energy-saving effect of 3.7 kW Super Unit for industrial machines, compared with conventional hydraulic system.
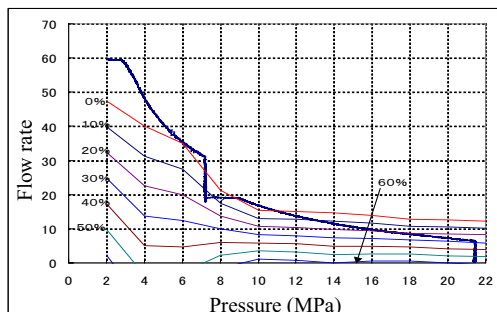
Figure 5 Energy-saving performance of 3.7 kW Super Unit

OTHER FEATURES OF OUR HYDRAULIC PUMP SYSTEM FOR INDUSTRIAL MACHINES

In addition to its energy-saving performance, our hydraulic pump system features lower loss on its hydraulic circuit, thereby increase in the hydraulic fluid temperature is inhibited and noise is kept at a low level.

Because the pressure and flow rate is regulated by the running speed of motor, our hydraulic pump system needs a smaller number of valves, thus its hydraulic circuit can be simplified.

Figure 6 illustrates a typical circuit for a conventional hydraulic circuit and that for our variable-speed hydraulic pump unit.

Conventional circuit   **Circuit of Variable-speed hydraulic pump unit**
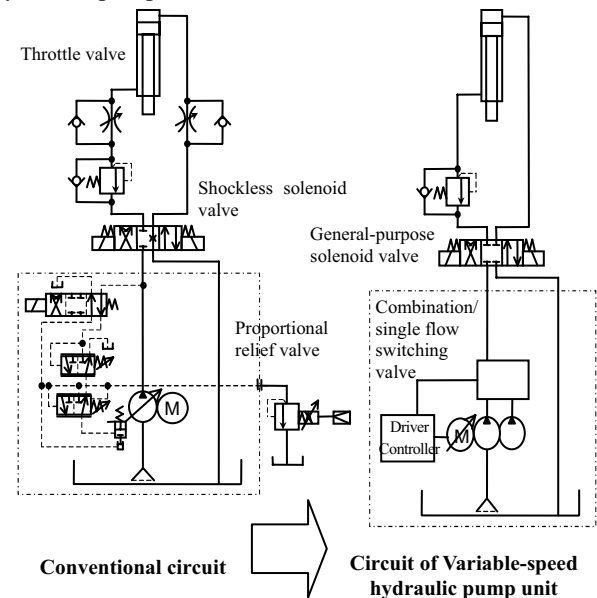
Figure 6 Simplification of hydraulic circuit with Super Unit

FEATURES OF SUPER UNIT FOR INJECTION MOLDING MACHINES

Figure 7 11 kW Super Unit for injection molding machines

Resent years, electric servomotors and ball-screws have been commonly used to drive the injection molding machines, particularly in Japan. Hybrid hydraulic drive molding machines, adopting hybrid hydraulic pump system has advantages over conventional hydraulic drive machines or electric servo drive machines.

Figure 7 shows a hydraulic pump system that incorporates an 11 kW IPMSM. By adopting a low-inertia geared pump and using an IPMSM whose

inertia moment is minimized for application to injection molding, our Super Unit achieves quick response—acceleration to maximum speed in 50 msec: previously, this level of response time was obtainable only with electric servo motor mechanisms with ball-screws.

Furthermore, compared with conventional hydraulic power units each comprising a piston pump and an induction motor, our hydraulic pump system features smaller degree of pulsation, and therefore, an injection molding machine with our system run at a lower speed stably and delivers quality moldings.

Like a result from our hydraulic pump system for industrial machine such as a press machine, our Super Unit for molding machines features smaller heat generation compared with conventional hydraulic pump systems, and therefore an oil cooler can be eliminated or downsized. Another advantage not available on an electric servomotor mechanism is that our Super Unit is free from the grease maintenance and a problem associated with a limited life of ball-screws.

ENERGY-SAVING PERFORMANCE OF SUPER UNIT FOR INJECTION MOLDING MACHINES

Figure 8 shows graphical plotting of comparison in terms of power consumption with injection molding machine in pressure maintaining mode.

Compared with power consumption with a conventional hydraulic drive system that comprises an induction motor and a piston pump, Super Unit apparently exhibits significant reduction of power consumption.
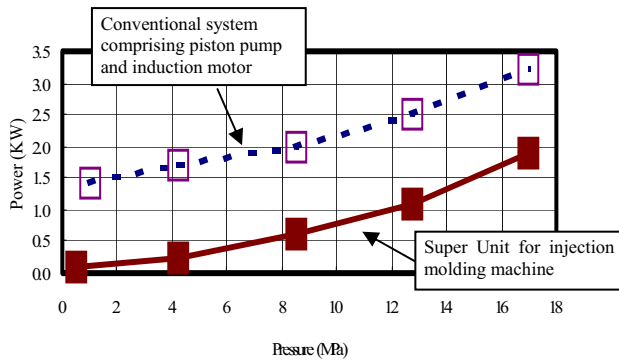
Figure 8 Energy-saving effect with Super Unit for injection molding machines (in pressure maintaining mode)

Figure 9-1 shows pressure-flow rate waveforms obtained from a run pattern (dry run) of an injection molding machine driven by the Super Unit, while Figure 9-2 provides those of the pressure-flow rate for the same run pattern of the machine driven by a conventional hydraulic pump unit. We can see that both pressure and flow rate can be reduced. Table 1

summarizes comparison in terms of average power consumption, resulting from these run patterns. Under this run pattern, our Super Unit exhibits 41.5% reduction in power consumption compared with conventional hydraulic system.

Table 1 Comparison in terms of average power consumption

		Super Unit	Conventional piston pump + induction motor
Power consumption	kW	**2.4**	**4.1**
Cycle	sec	14.4	14.4
Operating mode		Dry run	
Number of shots		248	248
Duration of measurement	hrs.	1.0	1.0
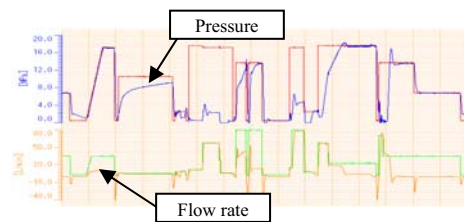
Figure 9-1 Pressure-flow rate waveforms with Super Unit (run cycle for injection molding machine)
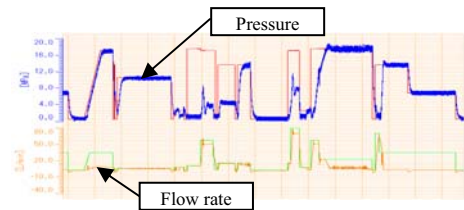
Figure 9-2 Pressure-flow rate waveforms with conventional hydraulic pump unit (run cycle for injection molding machine)

CONCLUSION

The features of the energy-saving hybrid hydraulic pump unit series—Super Unit—have been presented. As the needs for conservation of the global environment have been growing in the industrial fields including that for injection molding machines, we believe the role of Super Unit will be increasingly important. We will remain committed to further improved energy-saving effect and more diversification of its applications.

REFERENCES

1. Shigetoshi Simoo, Hitoshi Horiuchi, Tetsuo Nakata, Yoshiyuki Ochi, Energy saving High Pressure Duplex Pump System driven by IPMSM (Interior Permanent Magnet Synchronous Motor), 2003 Spring Lecture on Fluid Power System, theses, pp.86-88.
2. Shigetoshi Simoo, Hitoshi Horiuchi, Yoshiyuki Ochi, Energy saving and Time Sharing Proportional Pressure Control System for NC Lathe, 2004 Autumn Lecture on Fluid Power System, theses, pp.59-61.

OS5-2

MOTION CONTROL IN WAVES OF A 140M SES

Naoki OHBA*, Taketsune MATSUMURA*, Akihiko IMAKITA*

* Basic Design Department, Mitsui Engineering and Shipbuilding Co., Ltd.
6-4, Tsukiji 5-chome, Chuo-ku, Tokyo, 104-8439, Japan
(E-mail: ohba@mes.co.jp)

ABSTRACT

This paper introduces the air cushion pressure control of the 140m Techno Super Liner (TSL), which Mitsui Engineering & Shipbuilding Co., Ltd. (MES) has constructed. TSL is an air-supported catamaran ship, which contains pressurized air between rigid side hulls. The ship dynamic performance is investigated through simulations, for the first, which is based on 3DOF motion (Heave/Pitch/Roll) and air cushion dynamics. It was performed for both model and full scale in various wave headings. The scale effect is discussed through simulation results. Then, the results of towing model tests in both regular and irregular waves are described. The model is equipped with lift fans and all the tests are carried out under the on/cushion conditions. The results of model scale simulations and model tests are compared and verified. With these results from the simulations and model tests, the design of the air cushion control system is discussed in terms of the fan stability and ship vertical accelerations. The basic concept of air-vent louver control is presented. As for the sea trial of the ship, it was successfully completed on October 12, 2005. Some of her splendid performances were demonstrated. A brief introduction of the trial is also presented in this paper.

KEY WORDS

Motion Simulations, Model Tests, Scale Effect, Ride Control System, Air Suction

INTRODUCTION

In 2005, the new huge TSL was constructed as a cargo and passenger liner, and whose route was 1000km far away across the open sea.[1] Her photograph is given in Fig.1 and the outline is given in Table 1.

Figure 1 140m huge TSL

The TSL is categorized into Surface Effect Ship (SES) and it has an aluminum catamaran-type hull form which contains an air cushion with flexible structures called seals at the fore and aft ends of the air cushion. Pressurized air is supplied into the cushion by eight lift fans and is retained by rigid side-hulls and the flexible seals. Fig.2 shows a perspective view of the hull form of the TSL without seals.
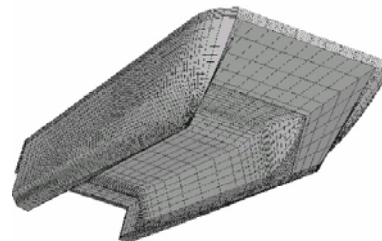
Figure 2 Perspective view of the hull form of the TSL

The major part of the ship weight is supported by the excess air cushion pressure, with the rest of its weight supported by the buoyancy of the side-hulls. The ratio of the weight supported by air-cushion system to the total weight is called cushion borne ratio. The lifted condition is called on/cushion, while the condition where it is fully in displacement mode is called off/cushion. Fig.3 illustrates these two conditions.

Table 1 Outline specification of the TSL

Length over all	140.00 m
Length of design waterline	126.83 m
Breadth, mld.	29.80 m
Depth, mld.	10.50 m
Draft, mld. (Off cushion)	5.00 m
(On cushion)	2.34 m
Gross tonnage	13,923 t
Dead weight	925 t
Maximum cargo payload	210 t
Maximum passenger number	740 p
Trial Maximum Speed	42.8 knot
Endurance	2,500 km
Propulsion machinery (2G/T & 2W/J)	
Maximum continuous output 25,180 kW/unit	
G/T : gas turbine (GE LM2500+)×2	
W/J：water-jet (Rolls Royce 235S2)×2	
Lift machinery (4D/E & 8L/F)	
Maximum continuous output 4,000 kW/unit	
D/E : diesel engine (Niigata 16V20FX)×4	
L/F : lift fan (centrifugal type fan)×8	
ETC (4B/T & RCS)	
B/T : bow thruster (Nakashima 5blade CPP)×4	
RCS：air vent louvers (MES)	
fin stabilizer (MDI)	

*RCS means ride control system
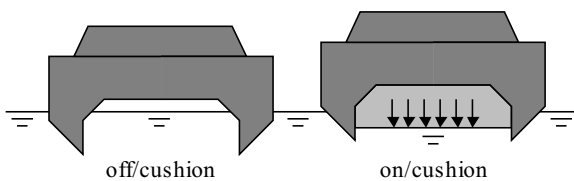
Figure 3 Conditions of on/cushion and off/cushion

Practical applications of SES have been so far limited to relatively small craft such as fast patrol craft, military craft, passenger craft, and so on. The length of these craft is around 40 meters and the cushion borne ratio is about 80%. Some of the main challenges related to hydrodynamics of such small SES are discussed by Steen[2].

Whereas, the developed TSL is far larger than those craft, in fact, it has the length of 140 meters indeed. It is

necessary to make the hull size large to some extent to cope with a longer voyage because of its large scale of the necessary accommodation, machinery, and dead weight including round-trip fuel oil. Besides, it is preferable to make the ship length long enough to achieve the tough seaworthiness in a seaway.

Fig.4 shows the frequency distribution of the wave height on the route of the TSL. The significant wave height of 5m is the worst intended conditions [4] of the TSL.
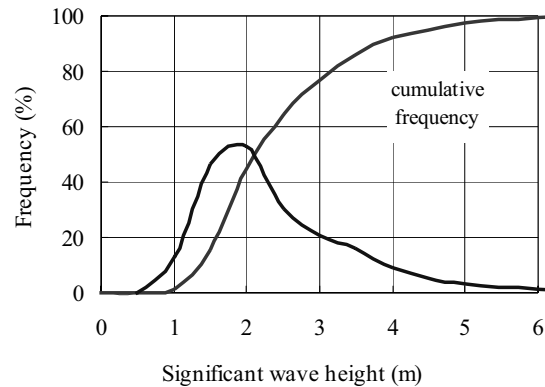
Figure 4 Frequency of the wave height on the route

SES is known to offer a better seaworthiness in heavy sea states compared with conventional catamarans, which often experience wet-deck slamming. However, shallow draft causes air suction to the water-jets and air leakage from the cushion in some cases. Besides, in low and moderate sea states, there are said to be such discomfort due to high-frequency vertical accelerations caused by resonant oscillation of the air pressure in the cushion. [2) 3)]

As a result of these considerations on typical features of SES, the TSL has been developed according to the concept of huge SES with the moderate speed and moderate cushion borne ratio. In fact, the speed range in terms of Froude number Fn is around 0.55 and its cushion borne ratio is about 70%. This new concept of the TSL has rather different effects on the hydrodynamics compared with the traditional fast small SES. Some of those dynamic features of the TSL were investigated through simulations and model experiments.

MOTION SIMULATIONS AND MODEL TESTS

Mathematical models in motion simulations
As for the mathematical model adopted in motion simulations presented here, coupled equations of motion (Heave/Pitch/Roll) and uniform cushion pressure are solved numerically with an aid of strip theory. The ship is assumed to be advancing in regular sea waves in any

oblique direction. Equations of motion (Surge/Sway/Yaw) and the spatially varying pressure are not taken into account. In the air cushion thermodynamics, adiabatic process is assumed. The volumetric airflow into the air cushion is given by linearization of the fan characteristic curve about the ship equilibrium operating point. The ride control system (RCS) of a pair of roll fin stabilizers and variable air vent louvers are taken into account. More explanation in detail is given by Sorensen [3] and Kaplan [5].

Model experiments in regular waves

The tests were conducted in regular head waves at a certain forward speed (corresponding to 34.2 knots), and in beam regular waves at rest condition. The lift fans were carefully adjusted to set a correct cushion pressure before towing. A set of motion, acceleration, and cushion pressure was measured. The test results are introduced in the following subsection with the simulation results. Fig.5 shows a photograph of the model advancing in head waves.

Figure 5 The model test in regular head sea

Motion simulations in model scale

As stated by Kaplan et al. [5], the natural frequency and damping of the heave-pressure mode of SES motion dynamics are not in accordance with the Froude's law of comparison. They are relatively higher in the model case than what would be indicated by the Froude scaling. This is the reason why it is difficult to predict the full-scale performance from the data obtained by model experiments according to the Froude scaling. To cope with this difficulty, it is necessary to validate the observed model data by means of simulation results for the same conditions, using the appropriate model scale parameters, and then to get the full-scale prediction with full-scale parameters by means of simulation.

A comparison between heave response amplitude operator (RAO) obtained by the simulation and the one from the model test is shown in Fig.6. The ship is advancing in head regular waves at corresponding ship speed of 34.2 knots (Fn=0.5). Similar comparisons for pitch, accelerations, and cushion pressure are also shown in Fig.7 through 9. All the simulation results are based on model scale parameters, but do not take any RCS into account.
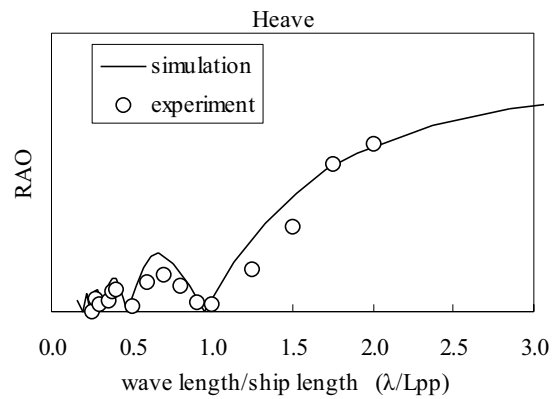
Figure 6 Heave RAO in head sea (Fn=0.5)
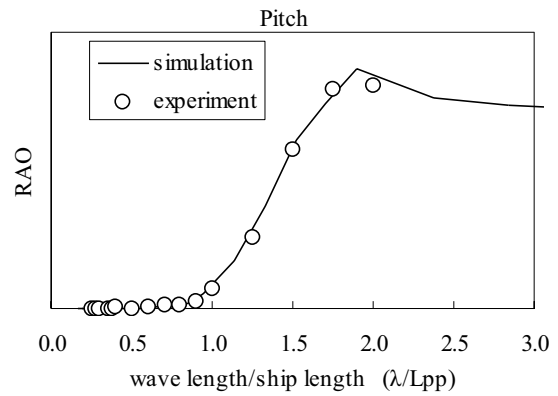
Figure 7 Pitch RAO in head sea (Fn=0.5)
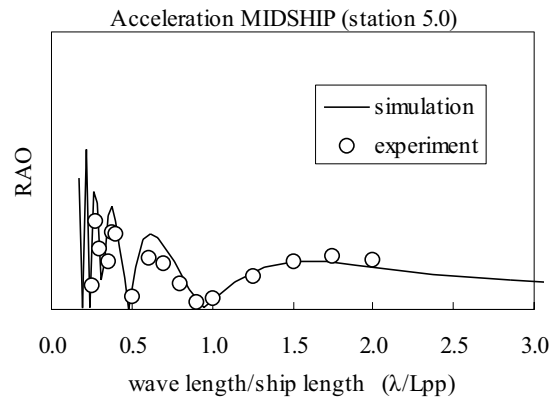
Figure 8 MIDSHIP acceleration RAO in head sea (Fn=0.5)

Non-dimensional uniform pressure variation
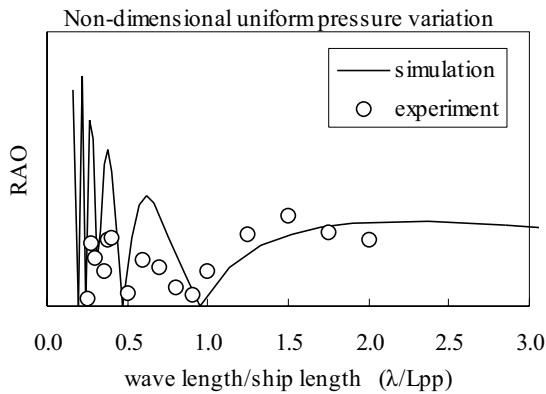
Figure 9 Non-dimensional uniform pressure variation
RAO in head sea (Fn=0.5)

Although some exaggerated humps in simulation results
are recognized around 0.4 and 0.7 of λ/Lpp, the
simulation results are in good agreement with the
experimental ones for the most part. Such humps are
caused by wave volume-pumping phenomena, and some
of the linearizing assumptions might induce an
exaggerative estimation in these λ/Lpp regions.
As long as the model scale parameters, the simulation is
valid on the whole.

Full –scale motion simulations
It is advisable to recognize the scale effect stated above
by means of the simulation before full-scale prediction.
Fig.10 shows a comparison between heave response
amplitude operators (RAO) obtained by the full-scale
simulation and the one by the model-scale simulation.
The ship is advancing in head regular waves at
corresponding speed of 34.2 knots (Fn=0.5). A simple
RCS of the air vent louver is taken into account in the
full-scale simulation to avoid a serious resonance in the
pressurized air cushion. Fig.10 also shows typical sea
spectra of significant wave height of 3m and 4m to
illustrate the power density distribution of the irregular
sea states.

HEAVE RAO & SEA SPECTRUM
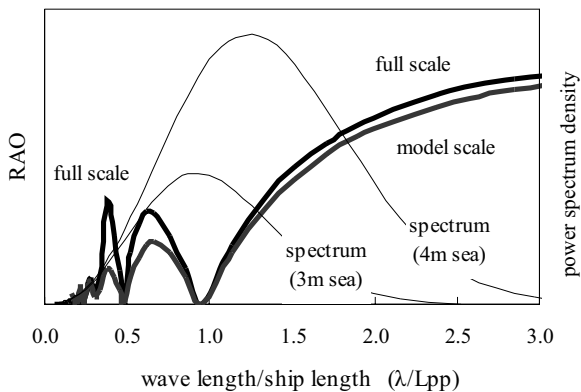
Figure 10 Heave RAO in head sea of model-scale and
full-scale, with the typical sea spectra

A sharp peak is recognized around 0.4 of λ/Lpp in the
full-scale simulation result. This is caused mainly by the
resonance with the natural frequency in the pressurized
air cushion and the lower damping of the heave-pressure
mode. The natural frequency of the uniform air cushion
pressure is about 0.5Hz, which induces certain vertical
accelerations in the high frequency region. This
phenomenon is not recognized in the model tests. This
is the reason why it is important to validate motion
simulations in design of huge SES.

Ride control systems (RCS)
The TSL has two ride control systems; a louver system
for air cushion pressure fluctuation control and a fin
stabilizer system for roll motion control.
Fig.11 shows the photograph of the fore louver system.

Figure 11 Photograph of the fore louver system

The louver opens or shuts the air vent automatically
according to the information from pressure sensors to
reduce the pressure variation. This control system is
effective to reduce the heave motion and vertical
accelerations mainly caused by the resonance of the
cushion pressure at high frequency region. Fig.12 shows
the vertical acceleration obtained by simulation and sea
trial at the head sea. It has been made clear that the
vertical accelerations with RCS/ON are about 20%
lower than those with RCS/OFF.
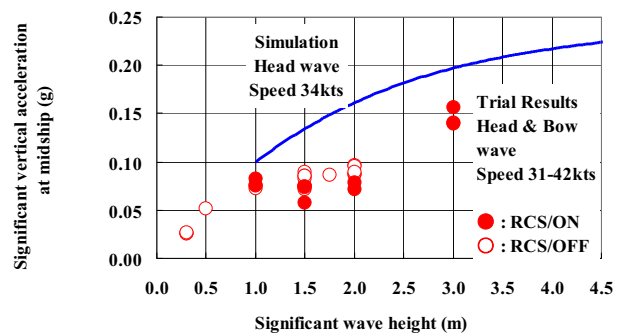
Figure 12 Vertical accelerations (single amplitude)
obtained by the simulation and sea trial of the TSL

Figure 13 Photograph of the fin stabilizer system

In addition, the TSL has one pair of the fin stabilizer to damp the roll motion. Fig.13 shows the photograph of the fin stabilizer system. Fig.14 shows the simulation results of the significant roll angle in beam sea with RCS/ON and RCS/OFF. The TSL is assumed to be advancing at 34.2 knots .The fin stabilizer system with advancing at high speed is very effective to reduce roll motion, so the horizontal accelerations are also reduced.
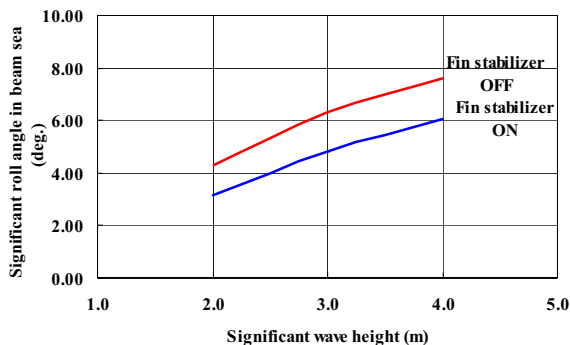
Figure 14 Significant roll angle (single amplitude) in beam sea   (34.2 knots)

AIR SUCTION TO WATER-JETS AND DESIGN OF THE INELT SHAPE

Air suction to water-jets
In the design about seakeeping performance, it is important to consider prevention of the air suction to water-jets in waves if the design draft is shallow like SES. The air suction often occurs when the water-jet inlet is close or above the sea surface[2].
The reason why the air suction is serious is that this phenomenon often leads to torque fluctuation or main engine trip.

Design of the inlet shape and model tests
One of the effective countermeasures to prevent the air suction is to design appropriate inlet shape for wave condition. In the design of TSL, scoop-type inlet was

developed to cope with this matter. Fig.15 shows the model of scoop-type inlet with conventional flush-type inlet.
The water-jets with scoop-type inlet draw deeper water than ones with flush-type inlet, so it is hard to suck up air with water. The added resistance due to protuberance by the inlet is also smaller than pod-type inlet.

Figure 15 Model of the flush-type inlet (above) and scoop-type inlet (below)

The model self-propulsion tests were carried out to investigate flow rate fluctuation in waves. In these tests, pressure at water-jet outlet was measured and the flow rate was calculated from the pressure. Eye observation around inlet and outlet is also effective to grasp this phenomenon. Fig.16 shows an example of the flow rate fluctuation with scoop-type inlet and flush-type inlet for comparison, where the TSL is advancing in head irregular waves ($H_{1/3}$=3.0m) at corresponding ship speed of 34.2knots (Fn=0.5).
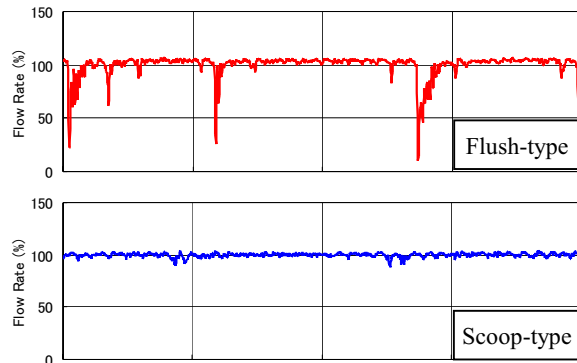
Figure 16 An example of the flow rate fluctuation with flush-type inlet (above) and scoop-type inlet (below) in head irregular waves (34.2knots, $H_{1/3}$=3.0m)

It has been made clear that the large-scale air suctions found with flush-type inlet doesn't occur with scoop-type inlet. A simple simulation about main engine revolution was also carried out with scoop-type inlet. The torque fluctuation was assumed to be in proportion to the flow rate fluctuation. An example of the simulation result is given in Fig.17, where the TSL is advancing in head irregular waves ($H_{1/3}$=3.5m).
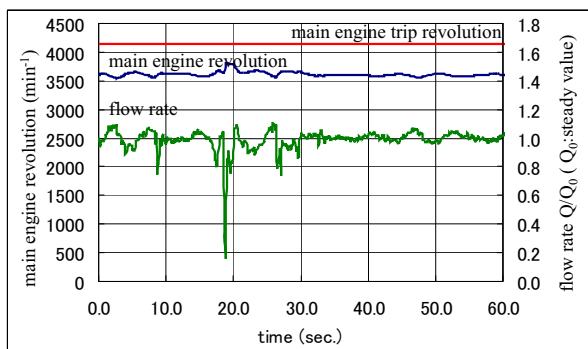
Figure 17 An example of the main engine revolution
and water-jet torque fluctuation in waves

The main engine revolution sometimes rises up corresponding to the water-jets torque deduction, but it is confirmed that the extent rise is low enough to avoid the trip phenomena.

In addition, the louver opening condition is also controlled to reduce the cushion borne ratio in waves. It makes the ship draft and water jet immersion deeper. This control is effective to not only the prevention of air suction but also the reduction of acceleration caused by the leakage of cushion air.

BRIEF REVIEW OF THE TRIAL RESULTS

MES successfully completed a sea trial of the 140m TSL on October 12, 2005. The sea trial has made it clear that the performance of the TSL exceeds design requirements in many respects. Especially, the speed of 42.8 knots (about 80km/h) was confirmed at the 92% MCO in spite of sea condition with the wave height of 2 meters.

As for the dynamic performance, it has been made clear that the significant vertical acceleration is below the estimated one and the maximum horizontal acceleration is far below the safety level 1 defined by 2000 HSC code in all conditions encountered in the sea trial.   .

CONCLUSIONS

The TSL was developed according to the concept of huge SES with moderate speed and cushion borne ratio, to achieve the tough seaworthiness for the long voyage. This new concept of the TSL has various unique dynamic features and they were investigated through simulations and model experiments.

As for the full-scale performance prediction, it is necessary to depend on not only model testing but also simulation because of the lack of applicability of Froude scaling. In terms of the model scale parameters, the present simulation is successfully verified being compared to the model test results.

It is only the well valid simulation that predicts the full-scale dynamic performance of the TSL. The simulation has made it clear that the vertical accelerations in the high frequency region are prominent when advancing in head waves.

The model test and simulation about air suction to the water-jet in waves were also carried out and effective scoop-type inlet was developed.

These investigations played an important part in realization of such a large TSL.

REFERENCES

1. Matsumura, T., Yamashita, S., Ohba, N., 2006, Dynamic performance of a 140m SES in simulations, model tests and sea trial: an introduction to recent development of the Techno Super Liner, Australian journal of mechanical engineering vol. 3 No2, pp91-101
2. Steen, S. and Strand, G., 2001, SES performance evaluation in model and full scale, FAST 2001
3. Sorensen, A.J., Steen, S., and Faltinsen, O.M., 1993, SES Dynamics in the Vertical Plane, Ship Technology Research, 40, pp.71-94.
4. IMO, 2001, 2000 HSC Code, pp.12
5. Kaplan, P. and Davis, S., 1974, A Simplified Representation of the Vertical Plane Dynamics of SES Craft, AIAA Paper, pp.74

APPLICATION OF THE "ASR SERIES" AC SERVO MOTOR DRIVEN HYDRAULIC PUMP TO INJECTION MOLDING MACHINES

Kenichi TAKAKU*, Hirokazu HIRAIDE**, Koichi OBA**

* International Sales Department, Yuken Kogyo Co., Ltd
4-8, Shiba-Daimon, 1-chome, Minato-ku, Tokyo, 105-0012 Japan
(E-mail: ke.takaku@yuken.co.jp)
** Research and Development Center, Yuken Kogyo Co., Ltd.
4-4-34, Kamitsuchidana-naka, Ayase-shi, Kanagawa Pref. 252-1113 Japan

ABSTRACT

Injection molding machines typically use hydraulic or electric systems, the selection of which depends on the performance, energy saving, investment cost, etc. Although hydraulic systems have the major disadvantage that they are less energy-efficient, it is well known that they have the advantage of high response and high thrust required for the control of pressurization and pressure holding. This paper introduces a control system and an AC servo motor driven hydraulic pump that are full-hydraulic and can achieve higher energy saving efficiency and performance. It also reports the current market trend toward the application of the system in Japan and overseas.

KEY WORDS

AC servo motor driven, Bidirectional hydraulic pump, Hybrid, Energy saving, Space saving

INTRODUCTION

As the need for energy saving has grown, hydraulic control and circuitry have evolved accordingly. The development and application of load sensing pumps and valves and electronically controlled variable displacement pumps have all contributed to improved performance and energy saving for injection molding machines. The advantages of hydraulic systems - simple structure, easy application to larger injection molding machines, long service life, and low lifetime cost - are offset by the energy cost.

As servo motors achieve higher thrust and smaller size, electric systems with high energy saving efficiency and cleanness compared with hydraulic systems have become a mainstream drive source for injection molding machines in Japan.

This paper introduces a hydraulic pump control system (also referred to as a hybrid system since it is driven by an AC servo motor). The system provides pressure and flow control to achieve a level of energy saving equivalent to electric systems, thus overcoming the major disadvantage related to hydraulic systems.

AIM OF THE DEVELOPMENT OF THE ASR SERIES

- Concept of the development of Yuken's rotational speed control system

The concept for development is to maximize the "advantage of hydraulic control" established over years, to achieve a level of energy saving equivalent to full-electric systems, and to provide higher performance than that of conventional injection molding machines. Based on this concept, the development of the ASR series aimed to provide higher performance than that of electronically controlled variable displacement swash plate type piston pumps and achieve a level of energy saving equivalent to

electric systems by directly controlling the rotational speed of a bidirectional hydraulic pump with an AC servo motor.
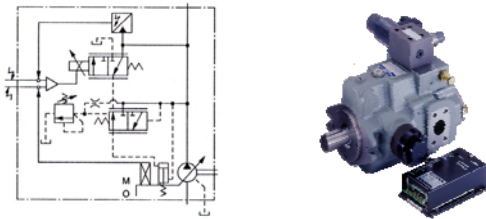
Figure 1 Proportional Electro-Hydraulic Variable
Displacement Piston Pump
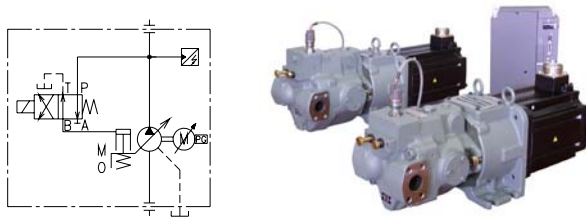
Figure 2 AC Servo Motor Driven Hydraulic Pump

- Specific goals of the development
(1) Energy saving: Achieving low power consumption equivalent to that of electric injection molding machines and/or half or less than half of that of variable displacement pump control
(2) Performance improvement: Providing higher response and improving stability during operation at low pressure and low speed
(3) Low noise: Achieving a lower noise level than that of electric injection molding machines
(4) Low heat generation: Significantly reducing the tank volume (space saving), eliminating the necessity of oil cooling, or allowing the natural radiation of heat
(5) Improvement of reliability and product quality
(6) Cost: Reducing the TCO of hydraulic molding machines (including initial investment, running cost, and maintenance cost)
(7) Full utilization of hydraulic technology: Regardless of whether the toggle type or the direct pressure type is used, maximizing the advantage of each molding machine manufacturer. Also, easily retrofitted onto existing hydraulic molding technology.

PRODUCTS AND SPECIFICATIONS

Following the A series, a well proven drive source for injection molding machines, the ASR series has a pump size (displacement) of 16 to 145 cc/rev. The ASR series also includes a dual displacement type for high speed injection or for operation with smaller motor capacity. The ASR series operates at 16 to 21 MPa, a typical range of operating pressures of injection molding machines determined based on experience.
A special motor and driver for pump driving have been developed with the characteristics of torque vs. rotational speed

appropriate for providing high speed and high load for the control of injection molding machines. The motor and driver also have an enhanced function for overload protection.
The ASR series has adopted a piston pump as the hydraulic pump and an AC servo motor as the driving motor for the following reasons.
- Piston pump
  Efficiency and leakage in a low speed range (pressure gain)
  Variable displacement
- AC servo motor
  High response and high torque for low speed operation

Table 1 ASR Series

Item	Series	ASR1	ASR2	ASR3	ASR5	ASR10
Power Capacity		C	C	E	G	J	M
Flow	Max. Flow L/min	40	55	90	130	200
	Hysteresis	1 % or less				
	Repeatability	1 % or less				
Pressur	Max. Operating Pres. MPa	21	16	21		
	Min. Adj. Pres. MPa	0.1				
	Hysteresis	1 % or less				
	Repeatability	1 % or less				
Motor	Rated Output kW	4.5	6	8	11	15
	Insulation	Class F				
	Cooling	Totally-enclosed self-cooling			Totally-enclosed fan-cooling	
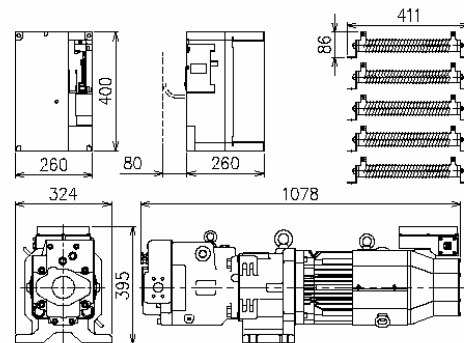
Figure 3 Appearance of ASR10
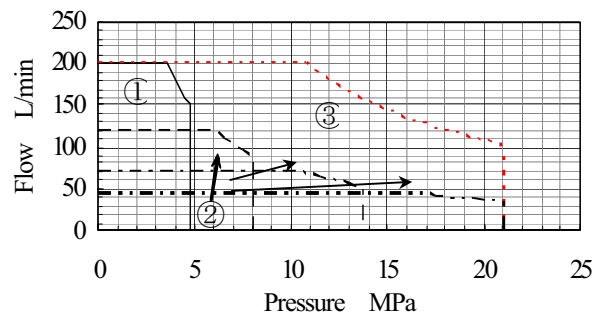
Figure 4 Pressure vs. Flow Characteristics of ASR10

APPLICATION EXAMPLES

(1) Configuration of hydraulic circuits and components for Injection molding machines (Figure 7)

(2) Data obtained from actual operation (torque, rotational speed, etc.) (Figure 8)

REQUIREMENTS FOR DRIVE SYSTEMS AND CAPABILITIES OF THE ASR SERIES

Generally, full-electric systems are regarded as high-precision and high-performance systems compared with hydraulic systems. However, full-electric systems are based on full-closed loop control unlike hydraulic systems that utilize open loop control; considering this difference in the basic principles, the comparison above may not be appropriate. The development of the ASR series has assumed that the open loop control method may be more appreciated in overseas markets, especially in China, Taiwan, and Korea. Based on this assumption, the focus of the development has been on the improvement of system performance. The major features of the ASR series are described below.

(1) Control range (pressure and flow rate)

The ASR series pump is driven by a servo motor, and it is advantageous to operate it with as high rotational speed as possible. Taking into account the pump's suction characteristics, the maximum rotational speed has been set at approximately 2500 rpm. This setting allows for a significant expansion of the flow control range.

In respect of pressure control, variable displacement swash plate type piston pumps operate with self pressure control, with a restriction on the minimum adjustment pressure. Our system, on the other hand, basically uses zero pressure as the minimum adjustment pressure. It should be noted that, for practical use, the minimum adjustment pressure is determined by tank pressure.

(2) Response characteristics (when compared with full-electric or valve-based systems)

Inertia load applied to pump rotors is generally lower than that applied to servo motors. Therefore, the start-up response largely depends on the capability of servo motors. In the development of the ASR series, a goal has been set to provide response characteristics that are superior to those of variable displacement swash plate type piston pumps and are equivalent/superior to those of full-electric systems. Our system has a flow start-up time of 40 to 60 ms.

If higher response is required for direct driving with a servo motor, it is feasible to increase the pump displacement and reduce the maximum rotational speed.

As the injection rate of injection molding machines increases, a shorter start-up time is demanded. The start-up time is 8 to 10 ms for systems using hydraulic servo valves, 40 to 60 ms for our system and full-electric systems, and 60 to 120 ms for variable displacement swash plate type piston pumps. Thus, there are definitive differences in response characteristics between these categories.
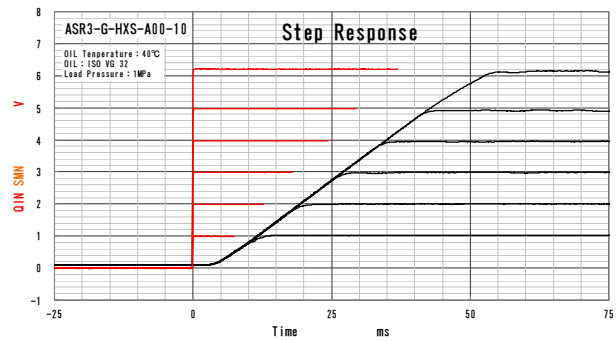
Figure 5   ASR3's Step Response

(3) Repeatability

A principle requirement of injection molding machines is that variations in the weight of molded products are stable. As a matter of course, the repeatability of speed and pressure is an important factor in terms of hydraulic control. The repeatability is especially important upon switching from speed control to pressure holding since it is related to load.

(4) Fluid temperature drift, LQC, Q-Comp

Conventionally, hydraulic systems have the major disadvantage that the flow rate varies due to fluid temperature drift, affecting the stability of products. However, as our system does not depend on valve control, it can significantly reduce this problem compared to conventional systems. In addition, our system eliminates the necessity of flow rate compensation during low pressure operation or due to load pressure variations, which has been the basis for conventional variable displacement swash plate type piston pumps.

(5) Energy saving

Most of energy consumption by injection molding machines is accounted for by driving power and electric power for nozzle heaters. A major concern has been to reduce driving power consumption. The hydraulic driving system presented in this paper basically "consumes power only when necessary" and is equivalent to electric systems in this respect. In addition, our system has been improved by replacing the control using an induction motor driven pump for conventional hydraulic driving systems with a control using an AC servo motor driven pump. There are many reports that the application of our system, which is driven by an AC servo motor, to injection molding machines may reduce power consumption by 70 to 80 % compared to fixed displacement pumps or by 40 to 60 % compared to variable displacement pumps, depending on the molding condition.

The data below shows pump efficiency based on total power consumption for each driving motor type. The data reveals a significant difference in efficiency between the AC servo motor driven pump and the induction motor driven pump.
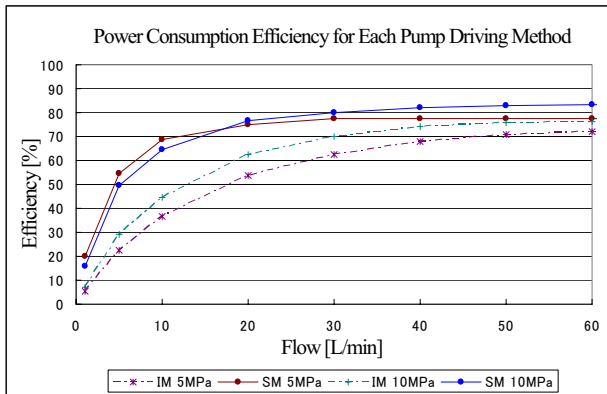
Figure 6 Power Consumption Efficiency for Each Pump Driving Type

FUTURE DEVELOPMENT

Japan has taken a technological lead in the market of injection molding machines. Particularly, great advancement has been made in the field of small/mid-size precision molding machines for IT and electronics parts and in the field of full-electric systems for large-size injection molding machines. Ten years have passed since full-electric systems appeared in the market, but our perspective is that hydraulic systems, particularly including the system introduced in this paper, are attracting attention and being rapidly adopted in Japan and worldwide because of their advantages, such as cost-effectiveness, reliability (failure tolerance), and application to larger-size injection molding machines.

Urgent challenges related to our system include achieving further higher response and developing high flow pumps and servo motors for supporting larger-size injection molding machines. At the same time, price reduction is a major issue since hydraulic systems are widespread in the market, and price competition has already become harsh. This trend is apparent in the development of systems focusing on the improvement of energy saving performance.

In respect of higher response, full-electric systems that achieve an injection rate of 800 mm/s in 15 ms are already available in the market. This fact means that the response provided by such systems is approaching the region covered by hydraulic servo valves. The future development for achieving higher response will be addressed considering this trend.

For large-size injection molding machine applications, the best development option may be total flow control, but this will need to be judged against cost.

To improve precision and performance, the modification of our system into a full-closed loop type will be looked at. This modification will entail the creation of a common view with overseas machine and control panel manufacturers.

Our system will be accepted in the field of both full-electric and full-hydraulic injection molding machines. The system was first marketed and adopted for injection molding machines in 2006 and started to prevail in 2007. One of the world-class injection molding machine manufacturers has announced a production plan for 2008, stating that its production mix will be 50 % full-hydraulic systems, 35 % hybrid systems (our ASR system), and 15 % full-electric systems. It can be said that this estimate predicts the share of each drive method in the future.
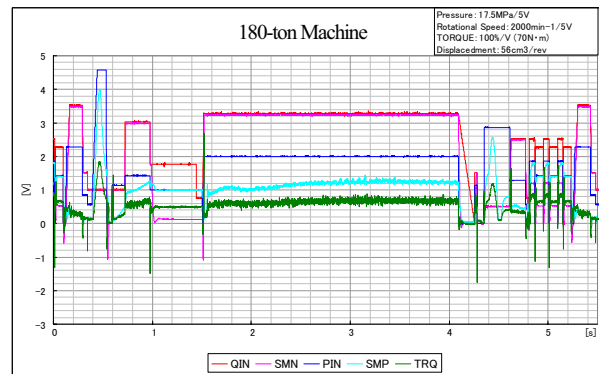
Figure 8 Operating Characteristics of Injection Molding Machines
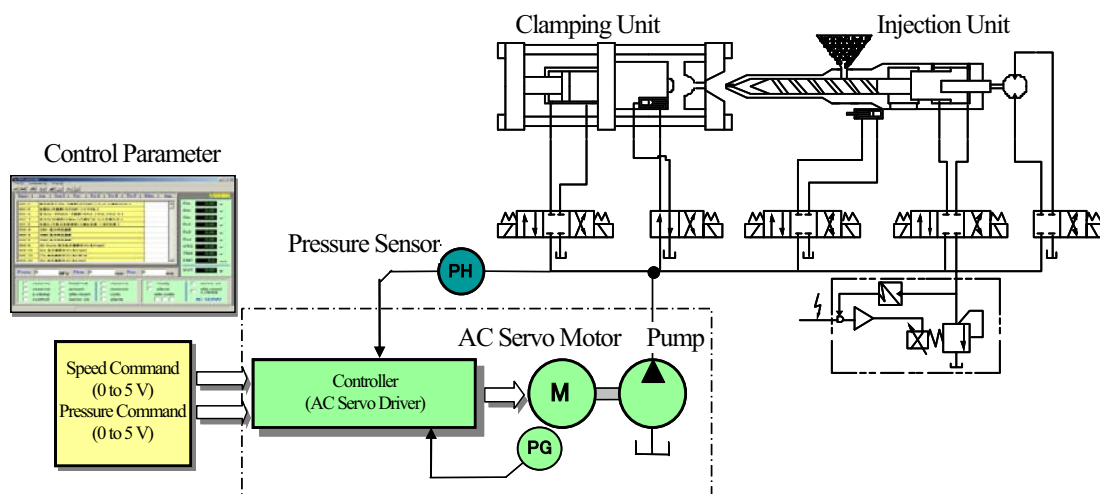
Figure 7 Basic Configuration of Injection Molding Machine

OS6-1

TECHNICAL TRENDS IN STEERING SYSTEMS

Hiroyuki MIYAZAKI

Engineering Planning Department
JTEKT Corporation
333, Toichi-cho, Kashihara, Nara 634-8555 Japan
(E-mail: hiroyuki_miyazaki@jtekt.co.jp)

ABSTRACT

Automotive steering systems have gone through the transitions from non-assisted type to hydraulic-assist type, and then, to electric-assist type for its assist.   Still, some issues are remaining to adopt the electric-assist type steering to heavier duty vehicles. Therefore, we are depending more on the technology of electrically controlled hydraulic power steering.

This paper covers the technical trends in regard to power steering (PS) energy saving, especially focuses on electronic control of hydraulic PS.

KEY WORDS
Electric Steering, Hydraulic Steering, Energy Saving

INTRODUCTION

Technologies in steering systems have been advancing since hydraulic PS (power steering) for automobiles started to be adopted in the 1950s. Steering systems that support a function of turning are recently facing rapid progress of electronic control in order to meet market needs such as improvements of energy efficiency and safety as well as comfort.

After 1980, an electronically controlled hydraulic PS, hydraulic PS with motor-driven pump, and electric PS have been developed and manufactured. Steering technologies have improved remarkably when compared with conventional hydraulic PS technologies[1]-[3].

The development of electric PS will continuously make progress. However, there still remain various issues such as adoption to heavier duty vehicles and global mass-production. With a background like that, saving energy of hydraulic PS is one of the main issues from an environmental viewpoint.

INFLUENCE ON STEERING ENERGY CONSUMPTION

Current hydraulic PS with constant flow accounts for 3% in the energy consumption of a car. Figure 1 shows the breakdown of the energy loss. The largest energy loss is the over flow loss of pump (1.4%), the second is loss by system weight and efficiency loss from belt & pulley (0.5% each), and the third is the over flow loss by the flow control valve (0.3%).
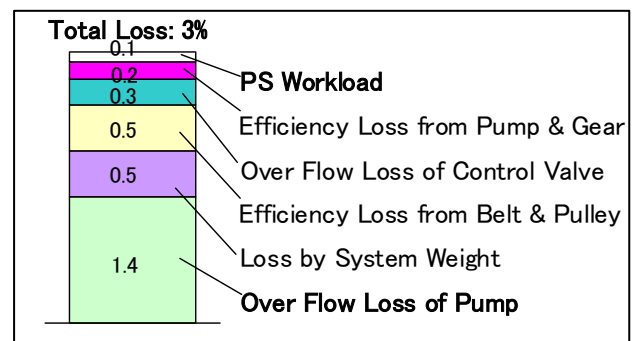
Figure 1 Steering System Energy Consumption

In this system, wasteful energy is consumed when driving straight or driving at high speed that do not require steering operations because the engine-driven hydraulic pump is constantly operating.

As a countermeasure for energy saving, we can provide the following steering systems.
1) Hydraulic type PS with low-flow high-pressure pump
2) Hydraulic-electric type power steering (H-EPS)
3) Electric power steering (EPS)

Figure 2 shows the ratio of energy consumption of these steering systems.
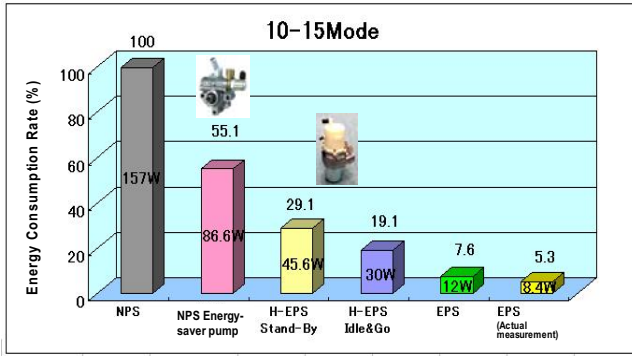
Figure 2 Energy Consumption Comparisons by Power Steering System

DEVELOPMENT TRENDS AND ISSUES OF ELECTRIC PS

Since electric power steering (EPS) was first adopted to mini-sized vehicles in 1988, the output power of EPS has been improved. And now it covers from passenger cars to SUV. The number of vehicles with EPS will increase year after year. The EPS is expected to take 40% of the steering market in 2010. (See Figure 3 and 4.)

There are three types of EPS depending on where the motor assist power is supplied (column-assist type, pinion-assist type and rack-assist type). Figure 5 shows a widely used column-type EPS[4].
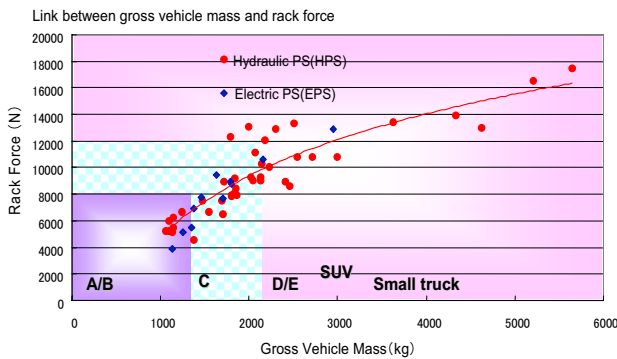
Figure 3 Steering System and Vehicle Segment
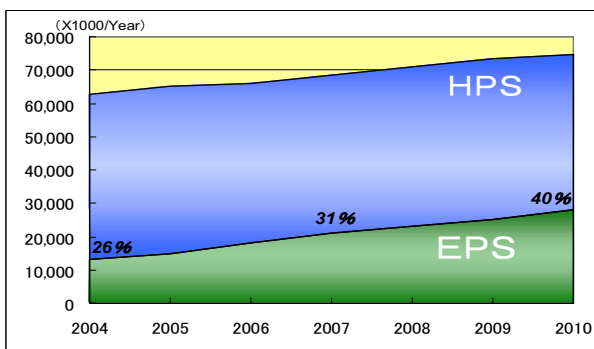
Figure 4 Steering Type Transition

Figure 5 Column Type Electric PS

The steering market will accelerate the shift to EPS for improvement of environment and safety. However, we still depend more on hydraulic PS.

The EPS has issues such as packaging, high power, steering feeling, cost, global supply and so on. When high power specifications are required, not all EPS can be installed. It depends on the motor size. The maximum output of EPS is limited by the mechanical strength of the structure. Therefore, it cannot cover all current hydraulic PS range. Regarding steering feeling, drivers have been familiar with the steering feeling of hydraulic PS for a few decades since it was released. Smooth and comfortable steering feeling was realized through fuzzy media, called hydraulic pressure, between a steering wheel and tires. Although the steering feeling of EPS has been improved and getting close to that of hydraulic PS thanks to advancements in electronic controlled technologies, we can say that it is not easy to receive benefit from hydraulic damping effect.

ENERGY SAVING TECHNOLOGY OF HYDRAILIC PS SYSTM

As mentioned above, we are depending more on hydraulic PS. Our energy-saving technologies with some examples are introduced.

1) Hydraulic type PS with low-flow high-pressure pump

As shown in Figure 6, the PS is in unloaded condition (non-steer) for most of the driving time (80 to 90%). Therefore, it is effective to reduce the energy loss. The equation below (1) is a pump consumption torque formula, based on the experiment. The consumption torque of PS pump can reduce its internal pump pressure by reducing the flow in non-steering conditions.
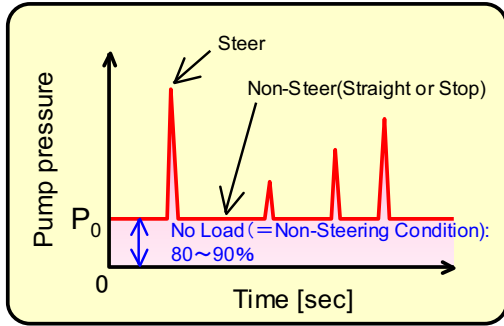
Figure 6   Steering Condition and Pump Pressure

$$T = \frac{Vth}{2\pi} \times (1 + Cf) \times P_{IN} + Cd \times \mu \times Vth \times N + Tc \quad (1)$$

Pressure term   Speed/Temperature Term   Fixed term

Vth : Pump Flow Rate
P_{IN} : Pump Internal Pressure
N : Pump Rotational Speed
μ : Oil Viscosity
Cf、Cd : Friction/Wear Factor
Tc : Friction Torque

The external outline of a Variable Flow Control pump is shown in Figure 7. It has a structure to receive signals of vehicle speed and steering angle into the ECU, and go through the compact electromagnetic valve to provide appropriate amount of flow into the pump.
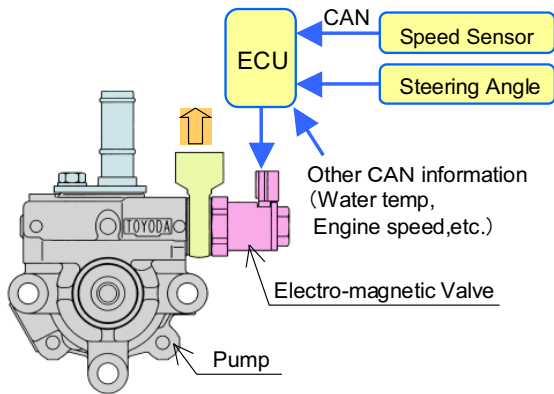
Figure 7   VFC Pump Outline
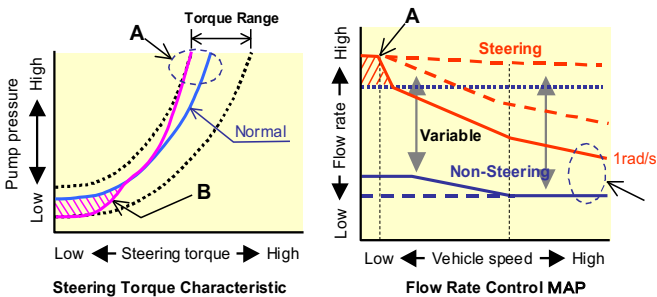
Figure 8 VFC Pump Control Methods

Figure 8 shows a relation between vehicle speed and PS pump flow. It provides comfortable and safe steering operations by reducing the flow in non-steering conditions, and by increasing the flow when driving at high speed or when turning the steering wheel fast.

2)   Hydraulic-electric type power steering (H-EPS)

H-EPS is an energy-saving PS, which does not have a pump driven by engine but has an electric pump. The system structure is shown in Figure 9. A pressure balanced gear pump (see Figure 10) has an advantage over a commonly used vane pump in efficiency[5]. It has a feature to rotate the motor appropriately based on the signals of vehicle speed and steering angle. Figure 11 shows the hydraulic control diagram.
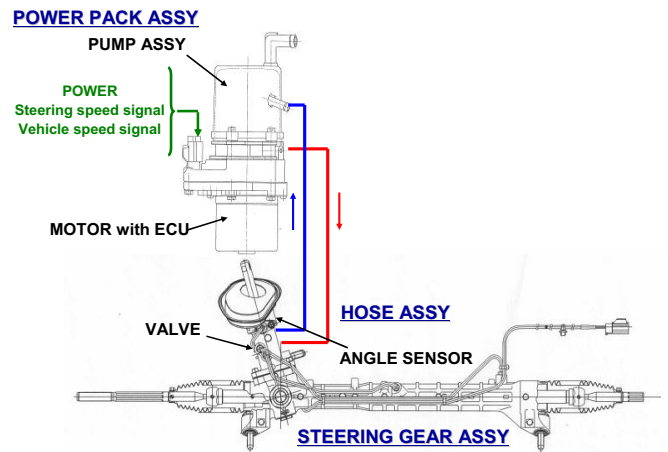
Figure 9 Hydraulic-Electric PS Outlines
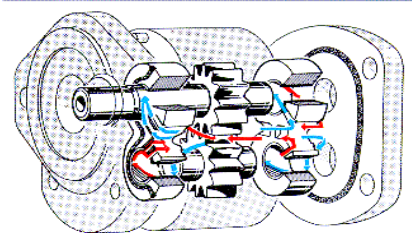
Figure 10 Gear Pump for H-EPS
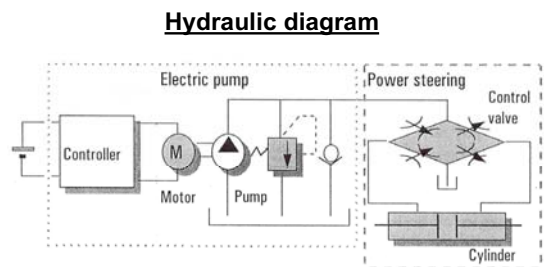
Hydraulic diagram

Figure 11 Hydraulic Diagrams of H-EPS

135

Figure 12 shows a relation between steering velocity and motor rotational speed.   It provides comfortable and safe steering operations by reducing the motor rotation in non-steering conditions, and by increasing the rotation when driving at high speed or when turning the steering wheel fast.
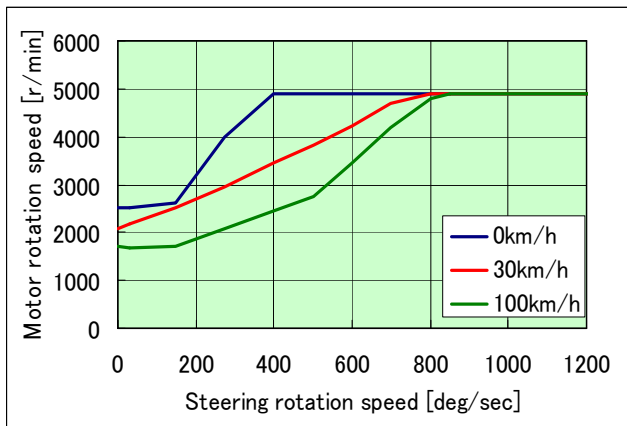
Figure 12 Control Map of H-EPS

The following is a control approach; stand-by type and stop-and-go type[6].

<Stand-by type control>
The simplified low cost controller, without using an external sensor, controls the electric pump efficiently to prevent loss of extra energy.   As shown in Figure 12, it puts the motor into low rotation when driving straight or making a stop and into high-speed rotation when power assist is needed.
<Stop-and-go type control>
By controlling the motor with a torque sensor or a steering angle sensor, it stops the rotation of motor while driving straight or making a stop to save energy.

SUMMARY

The steering systems are shifting from hydraulic type to electric type. However, hydraulic PS is a system expected to maintain its market share over 50% even after 2010. Considering the prospects of the market, hydraulic PS combined with electric control technologies that contribute to energy saving is an important technology to support the motorized society. It is expected to bring out the best of the hydraulic PS more and develop the technologies to make further contribution to the world.

REFERENCES

1. M.Noguchi, Trends and future views on steering system technology, Koyo Engineering Journal No.159(2001), pp.39-43 (in Japanese)
2. T.Taniguchi, Transition, trends and future prospects of steering technology, Automotive Technology, Vol.59, No.1(2005), pp63-68) (in Japanese)
3. Automotive technology 2006, JSAE, pp.63-65
4. JTEKT Engineering Journal No.1001(2006), pp.127-128 (in Japanese)
5. H.Jounokuchi, Technical trends of hydraulic-electric power steering system, Koyo Engineering Journal No.166(2004), pp13-18 (in Japanese)
6. A.Matsuda, Development of new energy saving power steering devices, Koyo Engineering Journal No.153(1998), pp.27-32 (in Japanese)

OS6-2

INTRODUCTION OF THE LATEST HYDRAULIC CONTROL SYSTEM FOR AUTOMATIC TRANSMISSION

Takashi SHIBAYAMA*, Hiroyuki YADA*, Yoshio MORITA* and Masumi FUJIKAWA*

*R&D Division , JATCO Ltd
BENEX S-3 , 3-20-8 Shin-Yokohama , Kohoku-ku , Yokohama City , Kanagawa 222-0033 Japan

ABSTRACT

From the social background of global warming issue, earth environment protection issue and the rise of oil price,the demand of the improvement of fuel economy and CO_2 reduction to a vehicle is very high nowadays. Continuously variable transmission (CVT) adoption has been recently increased to respond such social demand. JATCO is now also expanding the lineup of CVT as new solution for vehicle automatic transmission. In CVT, the shift control hydraulic pressure is a little bit higher than that of conventional stepwise shifting automatic transmission. So, unstable behavior of pressure is sometimes caused, for example, pressure oscillation. Such issue should be solved in early development stage. In this paper, we would like to introduce the feature and the techniques of oil pressure control system of CVT as an example of latest hydraulic control system for automatic transmission .And we would like to introduce our recent simulation for the optimal design of hydraulic control system.

KEYWORD

CVT , Fuel economy , Hydraulic simulation , Oil pressure stability

INTRODUCTION

The specific approach on the environmental problem is socially requested, for instance the Kyoto Protocol.

The technology for the improvement of fuel economy like the CO_2 emission control etc. is assumed to be an important strategy of technology for an auto sector, and many companies are accelerating development to achieve the fuel economy improvement target. (Figure 1.)

Especially, the efficiency improvement of the power train composed by engine & transmission greatly contributes to the improving fuel economy.

Regarding the transmission, the automatic transmission is a main current. And the share of it is 90 percent or more in Japan and the United States. Therefore, the further improvement as an environmental measure is expected to the automatic transmission.

By such background, continuously variable transmission (CVT) adoption has been increased recently. Compared with stepwise shifting automatic transmission (STEP AT), CVT can make more flexible speed ratio, not stepwise, but continuously. By the flexibility of the CVT,
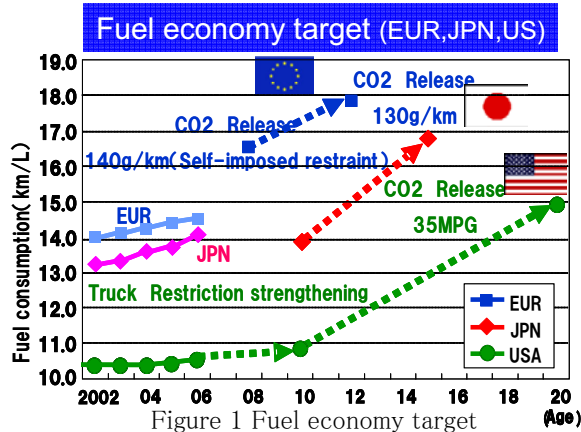
Figure 1 Fuel economy target

the engine operation condition can be maintained at optimal point for fuel economy. Moreover, CVT is very simple and that is good to adopt vehicle without greatly changing the system of the vehicle. It is simpler than the fuel cell vehicle system or the hybrid vehicle system. Therefore, recently, CVT adoption is expanding as a general technology for contribution to environment protection.

The torque capacity of CVT used to be small. It had started for the small, compact vehicle. But currently, CVT exists from the light vehicle to large vehicle with displacement volume 3.5L engine.

It shows that CVT has become very common, available technique for almost all vehicles which are general front wheel drive vehicle. By such background, as the one of main movement of transmission, automobile manufacturer has expanded the model equipped with CVT. （Figure 2）
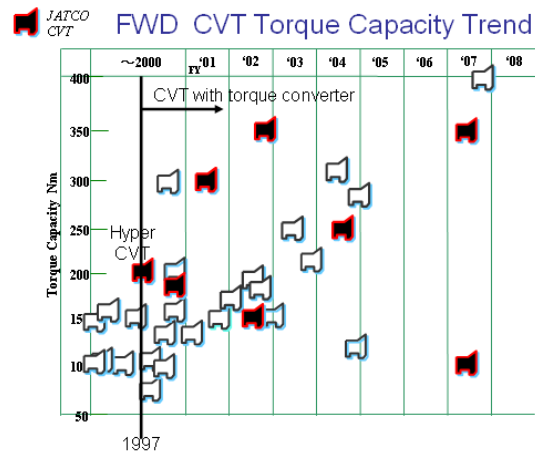
Figure 2 FWD CVT Torque Capacity Trend

CVT Unit structure

This chapter describes the belt CVT that is the main current in the CVT.

Regarding the structure of the CVT, several improvement has been developed. The big topic was adopting torque converter. Since "Hyper-CVT" that was released in 1997 by Nissan, torque converter starting system has become very common for CVT.

Figure.3 shows the torque flow of the CVT. Figure.4 shows the current typical CVT internal structure.

The torque input from the engine is input to the planet gear through the torque converter.

D range, R range, and the neutral are switched by a planet gear and multiple plate clutch combination.

The output torque from the planet gear is input to input pulley of the variator. And output from the output side pulley is transmitted to reduction gears. And, the torque is distributed by differential gear to right and left driveshaft and it is output to the tires finally.

The shift control is operated by pulley actuator.

138

Beside the input pulley, a hydraulic control piston
is equipped and also beside the output pulley another
hydraulic control piston is equipped.

In shifting, these two piston are actuated by hydraulic
pressure, and the two pulleys are moved
to adequate position to get targeted speed ratio.

The multiple plate clutch for obtaining forward and
reverse is also controlled by hydraulic pressure. Torque
converter inner pressure is also controlled by
same hydraulic control device. In such way, hydraulic
control system has many roles for CVT.

CVT Hydraulic Control System

Figure 5 shows the outline of the CVT hydraulic control
system.

Figure 6 shows the CVT hydraulic control unit.

The oil pump is driven by the drive chain (Refer to
Figure 4) that is set on the engine input shaft and the oil
pressure is generated.

The oil pressure from the oil pump is regulated by
Pressure Regulator Valve (P.Reg), and this regulated oil
pressure becomes supply pressure to the pulley.

The oil that remains by P.Reg flows to Clutch Regulator
Valve (CL.Reg.) that is in the downstream.

Figure 4 the current typical CVT internal structure

The oil pressure from P.Reg is regulated by CL.Reg
proportionately to the P.Reg pressure, and this oil
pressure becomes supply pressure of the clutch.

In addition, the oil that remains by CL.Reg flows to
Torque Converter Regulator Valve (T/C.Reg) that is in
the downstream. It is regulated to constant pressure in
T/C.Reg, and this oil pressure becomes supply pressure
to Torque Converter.

At each driving condition, an optimal oil pressure is
calculated by the CVT control unit(C/U). And, it is input
from C/U to each actuator (solenoid valve and Stepping
Motor (S/M)) as a output signal. Therefore, oil pressure
can be optimized proportionately to the torque. As a
result, the friction loss by an excessive oil pressure can
be reduced.

When changing the speed ratio, S/M is operated.

The speed ratio is changed by operating Shift Control
Valve (SC/V) connected with S/M. Primary pulley is set
on extension line of SC/V and S/M. The oil pressure is
adjusted physically detecting the pulley position by this
structure.

The pulley oil pressure is automatically adjusted by
physically controlling the position. An optimal changing
speed is achieved by this technology not being
influenced to differences of parts. In addition,   it
contributes to the reduction of the friction loss by the oil
pressure accuracy.

Figure 3 The torque flow of the CVT

This mechanism is a typical technology for CVT ratio

control. There is another technology, that has not have such mechanical link, with directly pulley pressure control system. Input pulley and output pulley actuator pressures are directly controlled by solenoid valves.

 The merit and the demerit of the two systems are exist. We cannot say which is better or not. Today, we would like to mention about the former system.

Recent trend for CVT oil pump is vane pump driven by chain. This system can reduce oil pump drive torque and is contributing to improve CVT efficiency.(Figure.7)

And further development is proceeding around pump technology. Variable displacement pump or part time operating pump, for example electric driven pump, will be the technique for near future. Because CVT control system needs a little bit higher pressure than that of STEP AT(CVT:5.7MPa MAX , STEP AT:1.8MPa MAX), the reduction of oil pump loss is very important for fuel economy. So that such new pump improvement technology is now eagerly waited.

Figure 5   Outline of the CVT hydraulic control system.
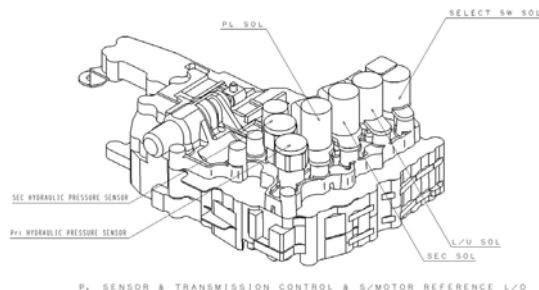
Figure 6   Hydraulic Control unit

Figure 7 O/P ASSY(vane pump)

And another issue caused by the little bit higher pressure utilization compared with STEP AT is system stability. If the pressure becomes higher, it is sometimes caused unstable issue, for example pressure oscillation. Such issue require long time for solve.

For the smooth development of new control system, a system stability analysis is very important.

It is necessary to predict such stability issue and to facilitate adequate countermeasure in early development stage.

With such back ground, JATCO has recently developed simulation system for predict hydraulic pressure behavior for CVT control hydraulic system.

In the next paragraph, we would like to mention about our hydraulic simulation system.

CVT HYDRAULIC SIMULATION

Figure 8 shows the control model of the CVT hydraulic control system.

Oil pressure stability

The simulation technique and the result concerning the stability of the valve are described.

For example, the simulation model of Torque Converter Pressure is assumed to be a model like Figure 9.

When oil flows from the upstream (solid line) and it reaches the given pressure, the port of spool valve is opened and the remaining oil is exhausted (short dashes line).

We confirmed the oil pressure stability at the moment of opening the port when SPOOL is operated. （Figure 10）
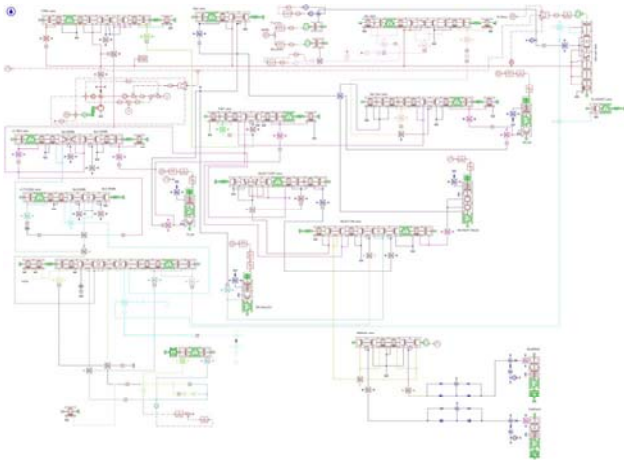
Figure 8 AME-Sim Full model
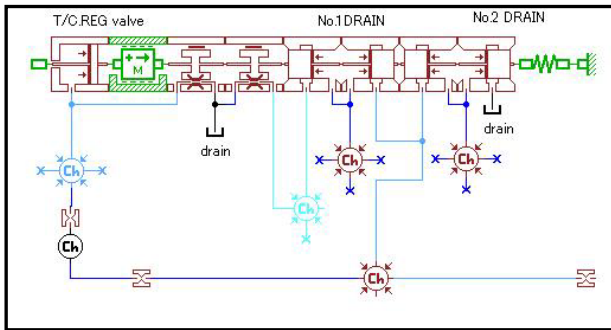
Figure 9   Simulation model (T/C Reg.)
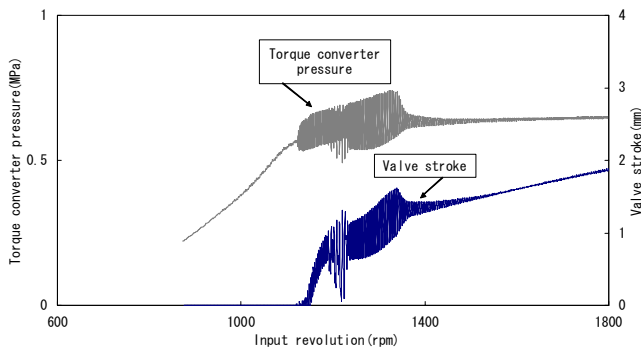
Figure 10 The behavior of T/C Reg pressure and T/C Reg stroke

In an initial setting, the problem about oil pressure stability turned out in the calculation.

Then, by confirmation of the sensitivity and the correlation between the feedback orifice area and Torque Converter Pressure, optimal orifice diameter was set.In addition, by experimenting, the validity of the simulation was confirmed.（Figure 12）

It shows that the experiment results correspond to the simulation results.
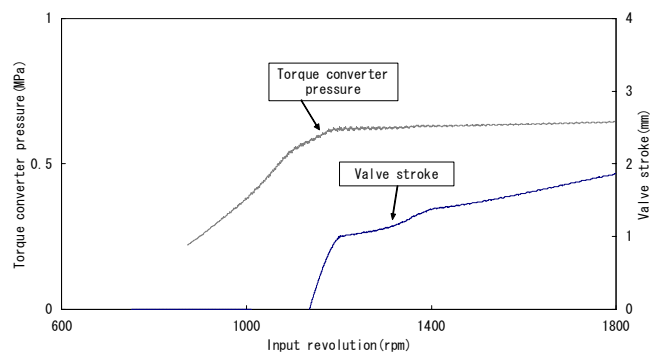
Figure 11 The behavior of the Torque Converter Pressure (The most suitable orifice diameter)
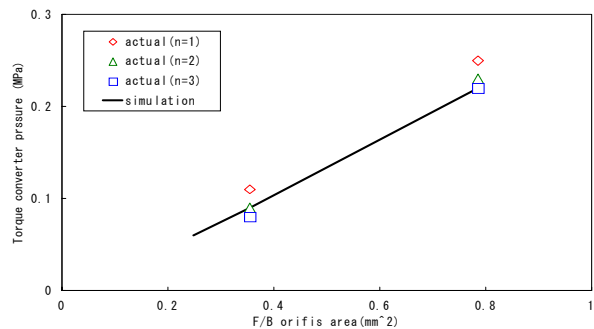
Figure 12 The correlation of the orifice diameter and the Torque Converter Pressure

SUMMARY

In this paper, the outline of latest hydraulic system of transmission, future direction of the technology, the typical concerning, and the solution technology with an example of CVT hydraulic system are described..

JATCO would like to continue to contribute to the social demand, progress oft transmission technology and the progress of fluid power technology.

REFERENCES

1. Tatsuo Wakahara et al: "Hydraulic System, Shift and Lockup Clutch Controls Developed for the Large torque Capacity CVT3", Jatco Technical Review No.5 ,2004.
2. K.Abo, "Development of New-Generation Belt CVTs with High Torque Capacity for Front-Drove Cars", SAE 2003-01-0593,2003
3. S.Segawa and K.Adachi , "Design method for the slip speed control system of a lockup clutch(II)", JSAE Lecture Series,20025528
4. K.Adachi ,T.Wakahara et al : "Robust control system for continuously variable belt transmission", JSAE Review, 9930036,1999
5. Tatsuo Wakahara and Hirohisa Tanaka: "Research of Hydro-Mechanical Shift system of Belt-CVT to improve both efficiency and performance", JFPS Review 2005.11
6. Oshita et al., "Hydraulic System, Shift and Lockup Clutch Controls Developed for a Large Torque Capacity CVT", 04CVT-7, Intl. CVT & Hybrid Congress 2004
7. Yamamoto, et al., "DEVELOPMENT OF A NEW-GENERATION STEEL-BELT CVT FOR USE WITH 3.5L ENGINES", F2004F446, FISITA World Congress 2004

OS6-3

OPTIMIZATION OF A PASSENGER HYDRAULIC HYBRID VEHICLE TO IMPROVE FUEL ECONOMY

Kim A. STELSON*, Jonathan J. MEYER*, Andrew G. ALLEYNE**, Brandon HENCEY**

*Department of Mechanical Engineering
University of Minnesota-Twin Cities
111 Church St. SE, Minneapolis, MN 55455 USA
(E-mail: kstelson@me.umn.edu)

**Department of Mechanical Engineering
University of Illinois-Urbana/Champaign
1206 W. Green St., Urbana, IL 61801 USA

ABSTRACT

This paper investigates power management strategies for hydraulic hybrid passenger vehicles. Parallel, series, and power-split architectures are modeled and explored in the Matlab environment using variable efficiency hydraulic pump/motor models. Results are presented using a rule-based strategy with ad hoc selection of engine on/off setpoints for the accumulator and transmission gear shifting. The dynamic programming algorithm is then used to determine the optimal trajectories for engine/hydraulics power splitting for each of the architectures over urban and highway drive cycles. Results are then compared to baseline simulation for improvement. Using the given vehicle parameters, the parallel architecture for both the urban and highway drive cycles was shown to be best. By decreasing the volumetric displacement of the hydraulic pump/motors for the power-split configuration, fuel economy can be improved with a corresponding decrease in acceleration.

KEY WORDS

Key words: Hydraulic Hybrid Vehicle, Power Management, Dynamic Programming, Optimization

NOMENCLATURE

L : Fuel consumption in one time step (g)
k : Time step index
N : Number of time steps in drive cycle
u : Control vector
x : State vector

INTRODUCTION

A major source of global energy consumption is transportation, which consumes approximately 4.8 billion barrels of crude oil per year in the United States, as of 2003. Passenger vehicles consume 2 billion barrels of the total with a value of over $200 billion at $100/barrel [1]. This significant usage of oil for passenger vehicles is the motivation for developing a vehicle that dramatically improves the fuel economy. A promising way to improve mileage is with a hybrid vehicle.

A hybrid vehicle is one that contains two sources of power, with one source most commonly being an internal combustion engine. The other power source can be mechanical in the form of a flywheel, electric in the form of motor/generators and batteries, or hydraulic in the form of pumps/motors and accumulators. The hybrid also allows energy storage during braking.

Currently, mass produced hybrid vehicles for passenger vehicles have been electric hybrids. One reason is the technological advances that have been made in electronics over the past few decades. Also, electric batteries have high energy density, allowing large energy storage. However, a disadvantage of

electric hybrids is the low power density of electric motors/generators and batteries.

To overcome this shortcoming, hydraulics should be used in passenger vehicles due to the large power density of hydraulic pumps/motors and accumulators. Also, hydraulic components are inexpensive when compared to their electrical counterparts, especially for state-of-the-art battery packs. Developments are also being made in the area of digital hydraulic valves and higher energy density accumulators, making hydraulic technology look promising for passenger vehicles.

Researchers have previously studied using hydraulics in hybrid vehicles, but most of these have been concentrated on large vehicles such as buses, delivery trucks, and military vehicles. As computing power increased, researchers began developing simulations and trying different control strategies for city buses to improve fuel economy [2]. Research has also been done using models of hydraulic hybrid military vehicles, optimal control theory, and numerical algorithms to determine drive train parameters to minimize fuel consumption [3]. Researchers have also used the dynamic programming technique to optimize the power management strategy for a delivery truck [4] and the design and power management strategy for military vehicles [5]. Very little research has been done on using hydraulics with optimal power management in passenger vehicles.

In this paper, the different types of architectures for hybrid vehicles are explained. The computer model used to obtain simulation results is briefly described, and baseline results using ad hoc parameters are presented. The dynamic programming optimization technique is explained as it relates to each architecture. Optimized results are presented and compared for each architecture for an urban and highway drive cycle. Finally, future modifications are studied.

HYBRID VEHICLE ARCHITECTURES

Regardless of the secondary power source of the hybrid vehicle, three main types of architectures exist: parallel, series, and power split. In this section, the overall operation of each will be described. Figure 1 shows a schematic of each type.

Parallel Hybrid Vehicle
In a parallel hybrid vehicle, the engine shaft is directly connected to a transmission, which is connected to a differential to provide power to each wheel. The hydraulic pump/motors are connected to the drive shaft between the engine and the
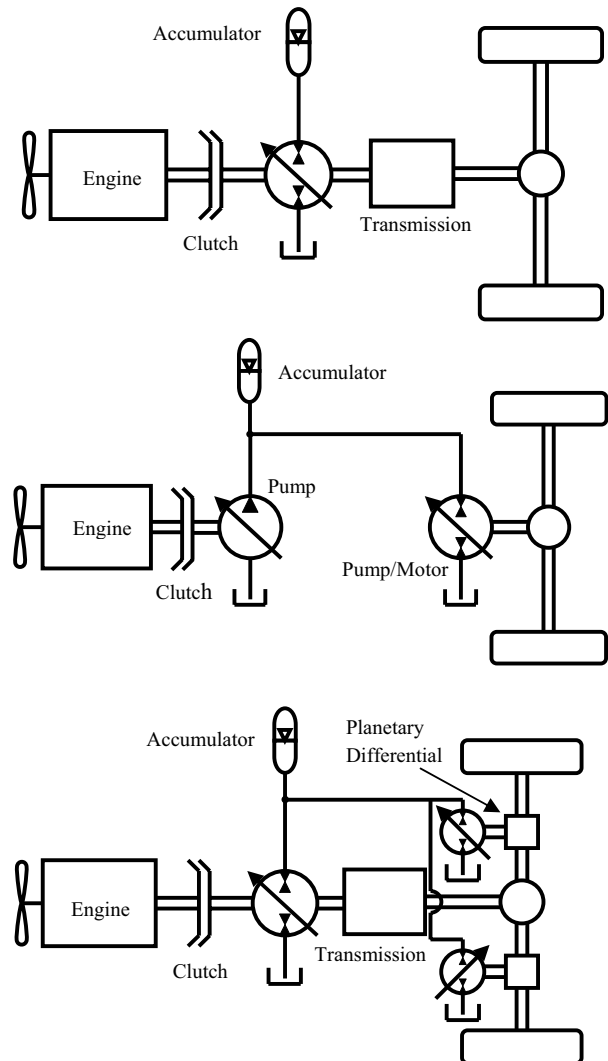
Figure 1 Schematic for the parallel hybrid (top), series hybrid (middle), and power-split hybrid (bottom) configurations

transmission to provide or absorb power from the accumulator as needed. A clutch is placed between the engine and hydraulic pump/motors so the engine can be decoupled from the road load and the vehicle powered entirely by hydraulics. This allows the engine to be turned off when not needed, and turned back on when the accumulator becomes low. While the engine power does not need to match the load, the engine speed is matched to the wheel speed by the transmission gear ratio, and optimal engine management is not possible.

Series Hybrid Vehicle
In a series hybrid vehicle, the mechanical drive train is removed, and the vehicle is powered purely from hydraulics. The engine shaft is directly connected to a hydraulic pump/motor, which is connected to an

144

accumulator to allow for energy storage. A hydraulic pump/motor is placed at each wheel to provide power and propel the vehicle. A clutch decouples the engine allowing on/off engine management. This architecture not only allows the engine output power to not match load demand, but also the engine speed does not need to match wheel speed, allowing for optimal engine management.

Power-split Hybrid Vehicle
The power-split configuration combines the parallel and series architectures into one. The mechanical drive train is still intact as in the parallel hybrid design, but hydraulic pump/motors are also connected to the drive wheel shafts as in the series hybrid design. This configuration allows for optimal engine management since, even though the engine is coupled mechanically to the drive wheels, the pump/motors at the wheels can be used to make up for the desired wheel speed. The clutch immediately downstream of the engine allows the engine to be decoupled completely from the load as in the parallel and series configurations. The power-split combines the advantages of both the parallel and series configurations: the mechanical drive train enables highly efficient power transfer from engine to wheels of the parallel architecture while maintaining the optimal engine management of the series architecture.

MODELING AND SIMULATION

A model of each type of vehicle architecture is needed to perform the power management optimization and compare results. The model used for the optimization was developed by Van de Ven et al [6], and is briefly explained here for completeness. The model is a backward-facing model with limited dynamics, meaning the power is calculated backwards through the drive train from the wheels to the engine. The model includes aerodynamic drag, rolling resistance, road grade, and inertial forces.

Hydraulic Pump/Motor Efficiency Model
Since optimization relies heavily on the efficiencies of the individual components, having an accurate hydraulic pump/motor efficiency model is essential. The hydraulic pumps/motors used in each configuration are variable displacement. Efficiency is characterized by displacement, operating pressure, angular velocity, and oil viscosity. The model developed by McCandlish and Dorey [7] is used to determine the efficiency at different operating parameters. This requires knowing the volumetric flow and torque data of the pump/motor at different operating conditions, which is mathematically fit to the equations. The volumetric and mechanical efficiency are calculated given the operating pressure, pump/motor angular speed, fractional displacement,

and oil viscosity, and the two are multiplied together to calculate the overall efficiency.

OPTIMIZATION VIA DYNAMIC PROGRAMMING

Once the system configuration, components, and drive cycle are fixed, the fuel economy of the vehicle depends only on the strategy for power splitting between the two sources and the transmission gear. The optimal control problem is formulated and solved by using the dynamic programming algorithm [8]. This is a powerful technique for solving optimal control problems for nonlinear, constrained dynamic problems since the true optimal solution is found.

The dynamic programming algorithm is based on Bellman's principle of optimality, which states that if a sequence of decisions is optimal, each subsequence must also be optimal. Using this principle, the algorithm can start at the end of the drive cycle, go one step back and find the optimal trajectory, go another step back and find the optimal trajectory, and continue this process until the beginning is reached.

The formulation of the problem for the hybrid vehicle is as follows. The objective is to find the optimal trajectory of control signals u(k), which include engine command and gear shifting, to minimize the fuel consumption of the vehicle over an entire drive cycle. Mathematically, this is given in Eq. (1).

$$\min_{u(k)} J = \sum_{k=0}^{N-1} L[x(k), u(k)] \qquad (1)$$

In Eq. (1), L is the fuel consumption in one time segment, N is the number of time segments, x is the state vector, which includes vehicle speed and accumulator state of charge, and u is the control vector, which includes engine command and transmission gear ratio.

The optimal cost at time step N-1 is:

$$J_{N-1}^*[x(N-1)] = \min_{u(N-1)} L[x(N-1), u(N-1)] \qquad (2)$$

For all other time steps, the optimal control is found by minimizing the total cost.

$$J_k^*[x(k)] = \min_{u(k)} \{ L[x(k), u(k)] + J_{k+1}^*[x(k+1)] \} \qquad (3)$$
$$0 \le k < N-1$$

Once the equation is solved backwards from step N-1 to 0, a lookup table is formed in which, given the state of charge of the accumulator at a time step, the

optimal control is found to minimize fuel consumption. Then, given the initial state, the optimal control can be found from the lookup table, the model is executed to find the state the next time step, and this can be propagated forward in time until the end of the drive cycle is reached. The resulting optimal control trajectory is then simulated to obtain the fuel economy result.

RESULTS

In this section, results are presented from the dynamic programming optimization for each type of architecture for an urban and highway drive cycle. To compare the optimization results to determine the amount of improvement in fuel economy, a baseline simulation is executed for each type of architecture.

Baseline Simulations

For the baseline simulation, control parameters were chosen using physical intuition about the system. For the parallel configuration, the control parameters are the engine state and the transmission gear ratio. To determine engine state, a constant lower and upper setpoint was determined based on the accumulator pressure. When the pressure falls below the lower setpoint, the engine will turn on to refill the accumulator, and above the upper setpoint the engine will turn off and run purely on hydraulics. For this simulation, the lower setpoint is 60% of the full pressure and the upper setpoint 90% of the full pressure. The gear shifting setpoints of the transmission were chosen to take advantage of the full speed range of the engine and hydraulic pump/motor. If the engine is on, the gear shifting point is when the engine speed equals 3000 rpm, corresponding to a vehicle speed of 12.9 m/s. If the engine is off, the gear shifting point is when the hydraulic pump/motor equals 3600 rpm, corresponding to a vehicle speed of 15.5 m/s. Using this strategy produced a fuel economy of 7.4 L/100km (31.8 mpg) for an urban drive cycle and 5.11 L/100km (46 mpg) for a highway drive cycle.

For the series configuration, the control parameters are the engine state and engine speed. The engine state is determined as described for the parallel configuration above. The engine speed is determined by operating at the most efficient point, corresponding to a speed of 2200 rpm. This can be done since the displacement of the hydraulic pump/motor attached to the engine can be varied as the operating pressure changes. The displacement of the hydraulic pump/motors at the wheels is fixed due to the specified wheel speed, operating pressure, oil viscosity, and efficiency, and therefore is not a decision variable. This strategy produced a fuel

economy of 4.42 L/100km (53.2 mpg) for an urban drive cycle and 5.6 L/100km (42 mpg) for a highway drive cycle.

Since the power-split configuration is a combination of the parallel and series architectures, the control parameters are a grouping from each and include engine state, engine speed, and transmission gear ratio. The engine state is the same as the parallel and series architectures, using the constant fixed lower and upper setpoints of accumulator pressure. The engine is also operated at its most efficient point as in the series configuration. However, the transmission gear ratio is chosen differently than in the parallel configuration. The transmission gear is chosen to minimize the speed of the hydraulic pump/motors connected to the drive wheels. This is done to maximize the power flow through the highly efficient mechanical drive train and minimize the power through the hydraulics. This strategy resulted in a fuel economy of 7.97 L/100km (29.5 mpg) for an urban drive cycle and 5.88 L/100km (40 mpg) for a highway drive cycle.

Optimization Results

The dynamic programming algorithm is now implemented for each type of architecture. For the parallel configuration, two control variables are used, engine state and transmission gear ratio. The equations given in section 4 are used to determine the optimal trajectories. The results for both the urban and highway drive cycles are shown in Figure. 2.
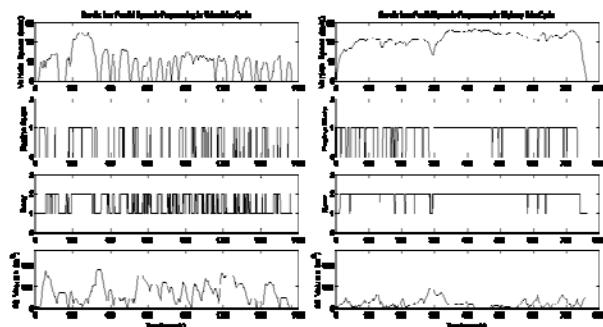
Figure 2 Dynamic programming results for the parallel hybrid configuration over an urban (left) and highway (right) drive cycle

The transmission gear ratio for the highway drive cycle is almost constant in 2nd gear, while for the urban drive cycle it fluctuates much more due to the higher vehicle speed during the highway drive cycle. Also, while both never reach a full accumulator state of charge, the highway drive cycle utilizes the accumulator less due to limited regenerative braking. The optimized results gave a fuel economy of 3.46

L/100km (68 mpg) for the urban drive cycle and 4.5 L/100km (52.3 mpg) over the highway drive cycle, a significant improvement over the baseline results.

For the series configuration, the two control variables are engine state and engine speed (if the engine is on). Applying the dynamic programming algorithm gives the results shown in Figure 3.

The results show when the engine is on, the engine speed is fairly constant around 2000 rpm, especially over the highway drive cycle. This is to utilize the efficient operating region of the engine. Also, the optimized results use the full volume of the accumulator for both drive cycles. This is due to the fact that the vehicle is a purely hydraulic drive train. The highway drive cycle does not fill the accumulator at the end of the cycle, however, since the optimization algorithm knows the end of the drive cycle is approaching. The optimized fuel economy for the urban drive cycle is 3.77 L/100km (62.3 mpg) and 5.10 L/100km (46.1 mpg) for the highway drive cycle, an improvement over the baseline result.
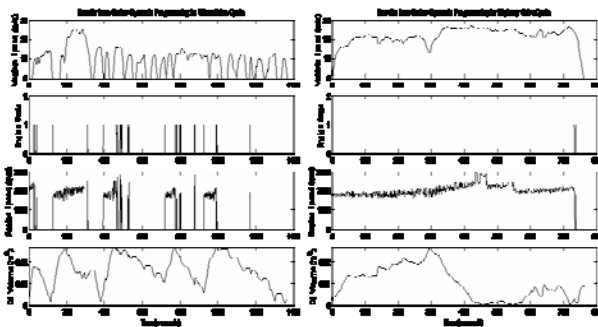
Figure 3 Dynamic programming results for the series hybrid configuration over an urban (left) and highway (right) drive cycle

Finally, the dynamic programming algorithm is applied to the power-split configuration, which has control variables of engine state, engine speed, and transmission gear ratio. The results are shown in Figure 4.
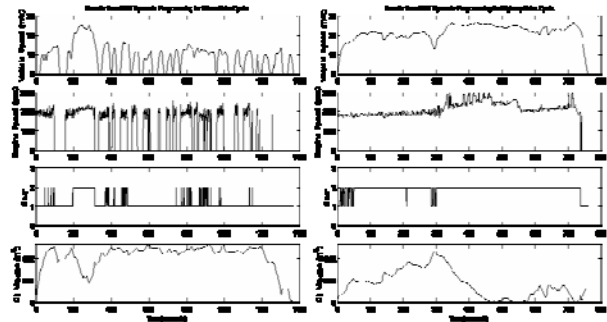
Figure 4 Dynamic programming results for power-split configuration over an urban (left) and highway (right) drive cycle

The results are very similar to those for the series hybrid, especially for the highway drive cycle. The engine speed is still operating near 2000 rpm, but more fluctuations exist in the transmission gear ratio. One interesting results is the high average state of charge of the accumulator over the urban drive cycle. The hydraulic pump/motors at the wheel are operating at a relatively slow angular velocity at low displacement, so the optimization forces the operating pressure higher to improve the efficiency of these pump/motors. The optimized fuel economy for the urban drive cycle is 7.17 L/100km (32.8 mpg) and 5.38 L/100km (43.7 mpg) for the highway drive cycle. The results for all architectures for the urban and highway drive cycles are shown in Table 1.

Improvements to power-split configuration

The optimized results show the power-split configuration being significantly worse for fuel economy than the parallel and series architectures. The main reason is that the hydraulic pump/motors are oversized for this application. Using the same coefficients for the loss terms in the pump/motor models, the maximum displacement of the pump/motors can be decreased, and the fuel economy over an urban drive cycle can be recalculated. These results are plotted in Figure 5. As the maximum pump displacement is decreased, the fuel economy improves.

Table 1 Summary of results for the urban and highway drive cycles

Configuration	Urban Drive Cycle			Highway Drive Cycle		
	Baseline (l/100km)	Optimized (l/100km)	Percent Improvement	Baseline (l/100km)	Optimized (l/100km)	Percent Improvement
Parallel	7.4	3.46	53.2%	5.11	4.5	11.9%
Series	4.42	3.77	14.7%	5.6	5.1	8.9%
Power-Split	7.97	7.17	10.0%	5.88	5.38	8.5%
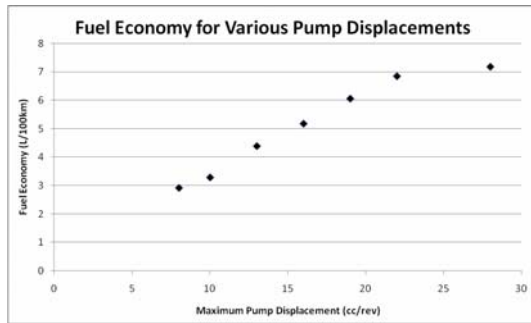
Figure 5 Plot showing fuel economy for various hydraulic pump/motor sizes

Figure 6 shows the time to accelerate to 100 km/h for the pump sizes above. As the maximum displacement decreases, the time to accelerate increases since the hydraulics are not able to add as much power to the drive train.
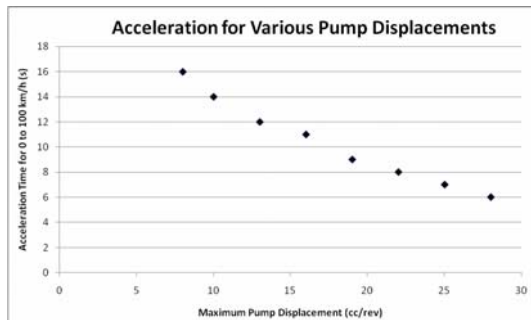
Figure 6 Plot showing acceleration performance for various hydraulic pump/motor sizes

To balance fuel economy and performance, the results above were used to determine two different sizes of the hydraulic pump/motors, one size at the engine and a smaller size at the wheels. A size of 19cc/rev was chosen at the engine since this gave the desired acceleration, while a size of 10 cc/rev was chosen at the wheels for the improved fuel economy. This led to a fuel economy of 4.2 L/100km using dynamic programming while maintaining a zero to 100 km/h acceleration time of 9.0 seconds.

CONCLUSION

By optimizing the control strategy used for hydraulic hybrid vehicles, improvements can be made in fuel economy. In this paper, three different configurations were studied over an urban and highway drive cycle. For each configuration and drive cycle, improvement was made in the fuel economy by optimizing the control strategy. The most significant improvement for both drive cycles was in the parallel configuration. The optimized results also showed that the parallel configuration obtains the best fuel economy for both

the urban and drive cycle, with the power-split being the least efficient. However, it should be noted that the hydraulic pumps/motors used are oversized for a passenger vehicle and therefore are operating at low, inefficient displacement, especially at the wheels. When lower displacement pump/motors are used, the fuel economy can be improved while maintaining performance.

ACKNOWLEDGEMENTS

REFERENCES

1. Department of Energy, Annual Energy Review 2003, Washington, D.C., Energy Information Administration (EIA), 2004.
2. Buchwald, P.; Christensen, G.; Larsen, H; Pedersen, P. S., Improvement of Citybus Fuel Economy Using a Hydraulic Hybrid Propulsion System - A Theoretical and Experimental Study. SAE Preprints (790305), 1979.
3. Matheson, P.; Stecki, J., Optimisation of a Hybrid Diesel-Hydraulic Automotive Powertrain Using ADVISOR, Matlab, and Simulink, Australian Journal of Mechanical Engineering , 2005, Vol. 2 (1), pp. 43-50.
4. Wu, B.; Lin, C.; Filipi, Z.; Peng, H.; Assanis, D., Optimal Power Management for a Hydraulic Hybrid Delivery Truck, Vehicle System Dynamics, 2004, Vol. 42 (1-2), pp. 23-40.
5. Filipi, Z., et al, Combined Optimisation of Design and Power Management of the Hydraulic Hybrid Propulsion System for the 6 x 6 Medium Truck, International Journal of Heavy Vehicle Systems, 2004, Vol. 11 (3-4), pp. 372-402.
6. Van de Ven, J. D.; Olson, M. W.; Li, P. Y., Development of a Hydro-Mechanical Hydraulic Hybrid Drive Train with Independent Wheel Torque Control for an Urban Passenger Vehicle, Proceedings of the International Fluid Power Exposition. Las Vegas, Nevada, 2008.
7. McCandlish, D.; Dorey, R. E., The Mathematical Modelling of Hydrostatic Pumps and Motors, Proceedings of the Institution of Mechanical Engineers, 1984, Vol. 198B (10), pp. 165-174.
8. Bertsekas, D. P., Dynamic Programming and Optimal Control (3rd ed.), 2005, Belmont, Massachusetts, Athena Scientific.
9. Wilson, W. E., Rotary-Pump Theory, Trans. ASME, 1946, Vol. 68, pp. 371-384.

OS6-4

PRECISION FLOW CONTROL COMPONENTS SUPPORTING THE EVOLUTION OF SPACECRAFT PROPULISON SYSTEMS

David Hodge

Moog Space and Defense Group
Nisseki Yokohama Bldg. 14F
1-1-8 Sakuragi-cho, Naka-ku, Yokohama, 231-0062 Japan
(E-mail: dhodge@moog.com)

ABSTRACT

A number of design and manufacturing techniques have been established over the years to ensure reliable products for spacecraft fluid control. Designs and processes originally intended for spacecraft chemical propulsion now have applications in electric propulsion as well as missile defense. The common element in each application is manufacturing processes that ensure assembly cleanliness, reliability, and repeatability.

KEY WORDS

Space, Propulsion, Contamination, Quality

INTRODUCTION

Moog is widely known for its contributions to the hydraulic fluid flow and pressure control field. Originally developed by Bill Moog 1951 to provide steering control for missiles, the design and core manufacturing techniques of the electro-hydraulic servovalve quickly spread to support aircraft and industrial automation applications.

A less obvious derivative of the hydraulic servovalve emerged in the 1980's as the need to reliably meter and seal propellants for orbiting spacecraft became apparent. The electro-magnetic circuit of torque motor thruster valves and latching valves are similar to those used in the first stage electro-hydraulic servovalves. However, precise flow control of gas in the vacuum environment of space required increased care in the preparation of sealing surfaces, cleaning parts of burrs and oils, creating assemblies without threaded fasteners, and handling assemblies in such as way as to avoid introduction of potential contaminants.

Enabling Technologies for Space Valves

One of the most critical, and often overlooked, elements to successful production of critical flow control components for space application is the rigorous application of component cleaning and careful handling. Contaminant as small as 5 micron can adversely affect the hardware and cause failure of mission critical subsystems. A comprehensive contamination control program includes a Class 1000 clean air environment, filtering of test fluids used on flight hardware, control of manufacturing processes to minimize the generation of contaminant, and a periodic inspection process to ensure compliance.

With the support of JAXA, Moog recently introduced this type of facility and process in Hiratsuka, Japan. The 59 m^2 clean room was designed and tested to conform to the requirements of JIS B9919 (ISO14644-4). In addition, a water flushing stand was designed and installed utilizing filtered de-ionized water and pressurized gaseous nitrogen. The resulting

turbulent flow effectively scrubs the flow paths of the unit, eliminating potential contaminant.

Figure 1 -- Clean Room for Space Valve Manufacturing in Hiratsuka, Japan

While a valve can be built without internal contaminants, traditional solenoid type valves have a potential to generate contamination over the spacecraft mission life due to sliding friction between the moving parts.

Moog's patented suspended armature solenoid valve eliminates this sliding fit by using a proprietary designed S-spring, shown below in both the valve open and closed positions.
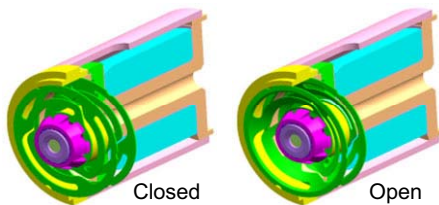
Figure 2 – Suspended Armature Valve Design

As shown in Figure 3, tests conducted at Moog's engineering facilities in East Aurora, New York demonstrate a substantial reduction in particulate generated by valves using this design feature when compared to conventional sliding fit solenoid valves.

The spring is designed for infinite fatigue life, which has been supported by multiple tests including a 2,000,000 cycle test.   The manufacture of the critical spring assembly is accomplished in a 10-step process, including:

- Precipitation Hardening

- Chemical Etching
- Lapping
- Electrochemical Polish
- In-Process Inspections

Each of these steps is performed to proprietary process control documents in accordance with an AS9100 Quality Control Plan.   The establishment and qualification of these processes for a particular configuration valve enables parametric applications for a wide variety of high reliability, contamination free flow control needs.
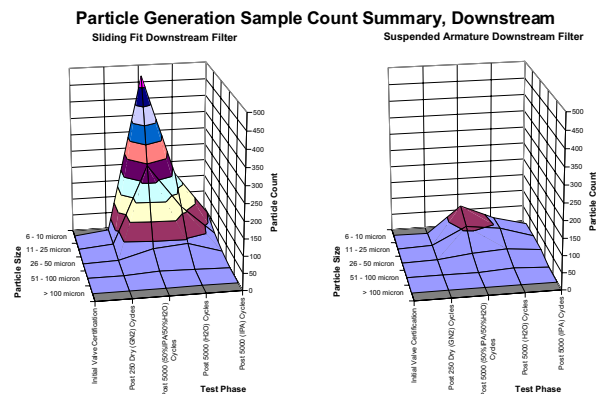
Figure 3 – Reduction in Generated Contaminant

Finally, the components and subassemblies of the propulsion valve are mechanically joined by electron beam welding.   This process is typically used for spacecraft propulsion systems for the following reasons:

- Minimum weight for the mechanical joint
- No contamination is generated during joining (as compared to threaded fasteners, for instance)
- Leak proof sealing to 2000 psi and beyond
- No deterioration in space environment (temperature extremes and radiation)

Electron beam processes have been commercially available for decades, and can be applied if sufficient care is taken in process control.   These processes are again controlled by quality control documentation and require a combination of non-destructive inspection as well as destructive sampling of weld coupons with each batch.

Potential Applications

The solenoid valve produced by Moog Japan demonstrates all of the necessary design and manufacturing elements to support various applications. The typical performance parameters of the 20N valve are shown in Table 1 below[4].

Table 1 – Typical Performance of 20N Thruster Valve

Property	Target value
Compatible fluid	N_2H_4,IPA,GN_2,GHe, (NTO/MON-3)
Pressure	
operating	0 to 2.76 MPa
proof	MEOP×1.5
burst	MEOP×2.5
Flow rate	10 gram/sec @ N_2H_4
Pressure drop	0.172 MPa(d)
Internal leakage	$< 1 \times 10^{-5}$ scc/sec
Operating voltage	24 to 32 VDC
Response time	Open: < 15 msec @MEOP Close: <10 msec @MEOP
Power consumption	< 30 W @28V/5℃
Cycle life	Wet: 1,000,000 cycle Dry: 50,000 cycle
Mechanical environment	
Random vibration	42 Grms
Shock	2,800G
Temperature range	5 to 149 ℃
Weight	< 300 gram

More importantly, the processes are documented, controlled, and scaleable to support a large variety of isolation valves for propulsion systems ranging in thrust from less than 1N to over 500N with only parametric modifications. The design can also evolve to support bipropellant applications with a simple change in seal material to ensure fluid compatibility.

Applications also exist beyond conventional monopropellant and bipropellant flow and isolation.

Minor design features can be added and simple changes made to parts in order to create proportionality within the valve. Thus, changes in flow rate would be initiated by changing the applied current to the coil. In one example, the valve remains in the closed position with input currents between 0 and ~90 mA, then starts to modulate flow between 90 mA and a maximum applied current of 125 mA. The 90 mA starting current may vary slightly from valve to valve due to build tolerances within the solenoid valve. This variation can be accommodated for within the control system.

Figure 4 – Propulsion Valve Manufactured in Japan

The proportional valve, when driven by a Proportional, Integral, Derivative (PID) controller, results in a proportional flow or pressure control subsystem. These subsystems have been demonstrated to provide throttling control for Ion propulsion systems, providing significantly increased efficiency for spacecraft propulsion[2].

Figure 5 – Typical PID Controller

Finally, the need for highly reliable, extreme environment capable valves is not limited to orbiting spacecraft. Similar propulsion valves are used in reaction control assemblies for launch vehicles. This technology has also recently been coupled with high speed computing in complex Divert and Attitude Control Systems (DACS). This systems support the national defense against intercontinental ballistic missiles by dynamically colliding with incoming weapons at extremely high speeds. The flow valves in the divert and attitude control thrusters are manufactured using similar or identical processes to the space propulsion valves discussed above.
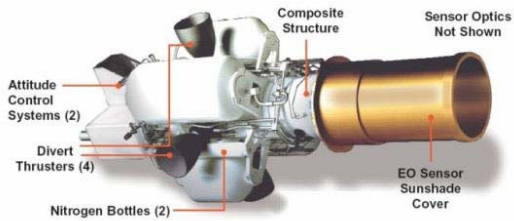
Figure 5 – Missile Defense
Divert and Attitude Control System

Conclusions

Moog has been a world leader in flow control for over five decades. Technology derivatives of the electro-hydraulic servovalve have led to flow control applications of a variety of spacecraft propellants. Careful process control is essential to the success of space missions, as there is no opportunity to repair or replace such components once on orbit. This level of process control supports growth to future applications, including advanced ion propulsion for spacecraft, as well as critical defense applications such as ballistic missile intercept. Moog has established and qualified these critical processes in facilities both in the United States as well as in Japan.

REFERENCES

1. Bushway III, E. and King P.T. et al, "A Xenon Flowrate Controller for Hall Current Thruster Applications" IEPC-01-315, October, 2001.
2. Bushway III, E. and Perini, "Proportional Flow Control Valve (PFCV) for Electric Propulsion Systems" AIAA-2000-3551, July, 2000.
3. Huftalen, Richard L, "Next Generation Propellant Isolation Valve Design and Development" AIAA, July 2006.
4. Kushiki, Kenichi and Kagiwara, Kenichi and Sugimura et al, "Development of a 20N Thuster Valve for Spacecraft Propulsion System" On-Board Energetic Equipment, 2004.

OS7-1

PERFORMANCE OF A POWER TRANSFER UNIT FOR AIRCRAFT APPLICATIONS

John WATTON

School of Engineering, Cardiff University UK
(E-mail: WattonJ@cardiff.ac.uk)

ABSTRACT

This paper considers power transfer between two fluid power circuits such that a failing pressure in one of them is improved by power transfer from the other circuit. The two coupled axial piston machines are effectively driven by the pressure differential across the two machines and particular features are required for the unit to operate successfully. Steady state theory is presented that may be used to select the relative displacement ratios and the range predicted is compared with those typically found in aircraft applications.

KEY WORDS

PTU, pump, motor, direct coupling

NOMENCLATURE

B_v	combined viscous friction coefficient
D_m, D_p	motor and pump displacements
P_1, P_2	pressure at load a and load b
P_{rv}	pressure relief valve setting
Q_1, Q_2	flow into and out of the PTU
Q_a, Q_b	flows to load a and load b
Q_{p1}, Q_{p2}	flows from supply pump 1 and pump 2
Q_{po}	ideal flows from both supply pumps
Q_{rv1}, Q_{rv2}	flows through PRV1 and PRV 2
R_{mp}	PTU motor and pump equal resistance
R_{ps}	supply pumps equal resistance
R_t	total resistance
R_v	PRV resistance for both valve
T_{sc}	total static/coulomb friction torque
ε	displacement ratio D_p /D_m
ω	PTU speed

INTRODUCTION

This approach is used to ensure that pressure is maintained in a circuit in the event of an unacceptable or unexplained drop in pressure, and is used in aircraft applications. Another existing healthy circuit is used to supply flow to the faulty circuit in a manner that attempts to restore the faulty pressure as close as possible to its normal healthy value. The approach is shown in figure 1. For the purpose of example, healthy circuit **a** provides make-up flow rate to faulty circuit **b** via the Power Transfer Unit (PTU), the left hand side of the PTU acting as a motor and the right hand side of the PTU acting as a pump. The PTU rotates due to the net pressure differential across the motor unit being greater than the net pressure differential across the pump unit. This creates a torque unbalance beyond the friction value when one circuit pressure changes due to a fault condition. In practice, a variable displacement axial piston machine is used together with a bent axis fixed displacement piston machine. The machine acting as a motor must have a displacement greater than the machine acting as a pump. As the direction of power transfer is changed then the swash-plate stroke of the
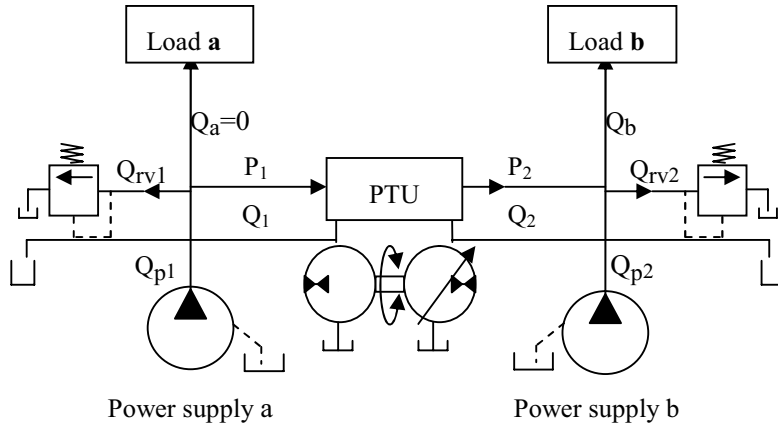
Figure 1 Power transfer using reversible axial piston units

variable displacement machine must also be changed. Power transfer is from left to right due to a pressure drop in supply line 2 relative to supply line 1. Therefore the machine at the left hand side is acting as a motor and the machine at the right hand side is acting as a pump.

There is little to no published information on PTUs and the following analysis is based upon well established steady state pump/motor theory. Some SAE and patent information may be found in [1-7]. It will be deduced for patent information that there are some complex mechanisms developed to create displacement ratio change, and the dynamic behaviour of a PTU is also complex. The steady state theory presented here has resulted from the author's involvement with a particular manufacturer, but precise details cannot be disclosed. The approach is therefore generalized, but results are compared with typical SAE data.

THEORY
Consider therefore the following theory [8-11] which is satisfactory for a first-estimate of performance :

PTU flow rates   Motor $Q_1 = D_m \omega + \dfrac{P_1}{R_{mp}}$ (1)

Pump $Q_2 = D_p \omega - \dfrac{P_2}{R_{mp}}$ (2)

PTU torque $D_m P_1 - D_p P_2 = B_v \omega + T_{sc}$ (3)

Here the viscous coefficient B_v and the friction torque T_{sc} is the sum for both machines. Considering each identical supply pump :

$Q_{p1} = Q_{po} - \dfrac{P_1}{R_{ps}}$ (4)

$Q_{p2} = Q_{po} - \dfrac{P_2}{R_{ps}}$ (5)

Assuming that both identical PRVs are in operation on both power supply sides then a linear flow rate/pressure drop characteristic may be used to give :

$Q_{rv1} = \dfrac{P_1 - P_{rv}}{R_v} \quad P_1 > P_{rv}$ (6)

$Q_{rv2} = \dfrac{P_2 - P_{rv}}{R_v} \quad P_2 > P_{rv}$ (7)

For the purpose of identifying unique features of a PTU performance, a suddenly-demanded flow rate Q_b at side 2 will be used while the load flow rate at side 1 is zero. Therefore, flow rate continuity on each side then gives :

$P_1 = R_t (Q_{po} - D_m \omega + \dfrac{P_{rv}}{R_v})$ (10)

$P_2 = R_t (Q_{po} + D_p \omega + \dfrac{P_{rv}}{R_v} - Q_b)$ (11)

$\dfrac{1}{R_t} = \dfrac{1}{R_{ps}} + \dfrac{1}{R_{mp}} + \dfrac{1}{R_v}$ (12)

It is well established that a PTU performs better if the pump displacement is less than the motor displacement, so let :

$D_p = \varepsilon D_m \quad \varepsilon < 1$ (13)

Combining the torque and flow equations and the displacement ratio equation then gives :

156

$$\bar{\omega} = \frac{(\bar{P}_{rv} + 1)(1 - \varepsilon) + \varepsilon \bar{Q}_b - \bar{T}_{sc}}{(1 + \varepsilon^2 + \bar{B}_v)} \qquad (14)$$

$$\frac{P_1}{P_{rv}} = \frac{R_t}{R_v}\left[\frac{(1 - \bar{\omega})}{\bar{P}_{rv}} + 1\right] \qquad (15)$$

$$\frac{P_2}{P_{rv}} = \frac{R_t}{R_v}\left[\frac{(1 + \varepsilon\bar{\omega} - \bar{Q}_b)}{\bar{P}_{rv}} + 1\right] \qquad (16)$$

where the non-dimensional term are :

$$\bar{\omega} = \frac{D_m \omega}{Q_{po}} \qquad \bar{T}_{sc} = \frac{T_{sc}}{D_m R_t Q_{po}}$$

$$\bar{P}_{rv} = \frac{P_{rv}}{R_v Q_{po}} \qquad \bar{Q}_b = \frac{Q_b}{Q_{po}} \qquad \bar{B}_v = \frac{B_v}{R_t D_m^2}$$

$$\frac{R_v}{R_t} = \frac{R_v}{R_{ps}} + \frac{R_v}{R_{ps}} + 1 \qquad (17)$$

where probably $R_v \cong R_t$

The individual pressures are defined with respect to the pressure relief valve cracking pressure P_{rv} so a check can be made on whether a particular design causes any pressure to fall below the pressure relief valve setting. The pressure differential must lie outside the friction dead-band for PTU motion to occur. This is given by :

$$\text{PTU friction dead-band} \quad \bar{P}_1 - \varepsilon\bar{P}_2 = \pm\frac{\bar{T}_{sc}}{\bar{P}_{rv}} \qquad (18)$$

Consider the following, real, data :

PTU machines $\qquad\qquad R_{mp} = 10^{12}$ Nm^{-2} /m^{3}s^{-1}

Supply pumps $\qquad\qquad R_{ps}$ $\quad = 10^{12}$ Nm^{-2} /m^{3}s^{-1}

PRVs $\qquad\qquad\qquad R_v = 0.25x10^{10}$ Nm^{-2} /m^{3}s^{-1}

PRV cracking pressure $\quad P_{rv} = 210$bar
Supply pumps no-load flow rate Qpo = 24litres/min
Fixed displacement machine displacement
$D_m = 4$x10^{-6} m^3/rad
PTU friction torque $T_{sc} = 12$Nm
PTU viscous friction coefficient $B_v = 0.04$ Nm/rad s^{-1}

$$\frac{1}{R_t} = \frac{1}{R_{ps}} + \frac{1}{R_{mp}} + \frac{1}{R_v} = 402\text{x}10^{-12}$$

$$R_t \cong R_v = 0.25\text{x}10^{10} \text{ Nm}^{-2}/\text{m}^3\text{s}^{-1}$$

The PRV resistance is clearly dominant. For no-load flows from each power supply the pressure increase across each PRV is given by :

$$R_v\, Q_{po} = (0.25\text{x}10^{10})(0.4\text{x}10^{-3}) = 10\text{bar}$$

The non-dimensional parameters are :

$$\bar{P}_{rv} = 21 \qquad \bar{B}_v = 1 \qquad \bar{T}_{sc} = 3$$

If the PRV cracking pressure is 210bar, then the operating pressure for no-load is not 220bar but ≈ 219bar when the PTU losses are included.

To fully understand how a PTU operates it is necessary to consider particular conditions of speed and pressure.

The condition for zero speed
From (14) this occurs when the following condition is satisfied :

$$\varepsilon = \frac{\bar{P}_{rv} + 1 - \bar{T}_{sc}}{\bar{P}_{rv} + 1 - \bar{Q}_b} \qquad (19)$$

The condition for pressures to fall to their PRV setting.
To understand the pressure behaviour, it is noted that since it is probable that $R_t \approx R_v$ then the pressures are given by:

$$\frac{P_1}{P_{rv}} \approx \frac{(1 - \bar{\omega})}{\bar{P}_{rv}} + 1 \qquad \frac{P_2}{P_{rv}} \approx \frac{(1 + \varepsilon\bar{\omega} - \bar{Q}_b)}{\bar{P}_{rv}} + 1 \qquad (20)$$

Therefore the condition for each pressure to fall to the PRV setting is given by :

$$\frac{P_1}{P_{rv}} = 1 \quad \text{when } \bar{\omega} = 1$$

$$\varepsilon^2 + \varepsilon(\bar{P}_{rv} + 1 - \bar{Q}_b) - (\bar{P}_{rv} - \bar{B}_v - \bar{T}_{sc}) = 0 \qquad (21)$$

Therefore the speed is at its maximum

$$\frac{P_2}{P_{rv}} = 1 \text{ when } 1 + \varepsilon\bar{\omega} = \bar{Q}_b \text{ and not possible} \qquad (22)$$

The example conditions are shown in figure 2 for various load flows and figure 3 for a particular load flow $\bar{Q}_b = 0.5$.
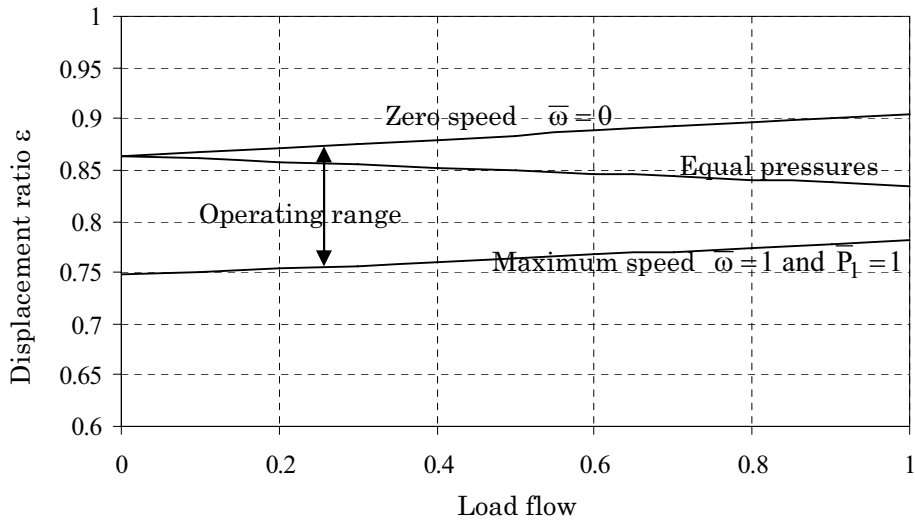
Figure 2   Determination of the PTU displacement ratio
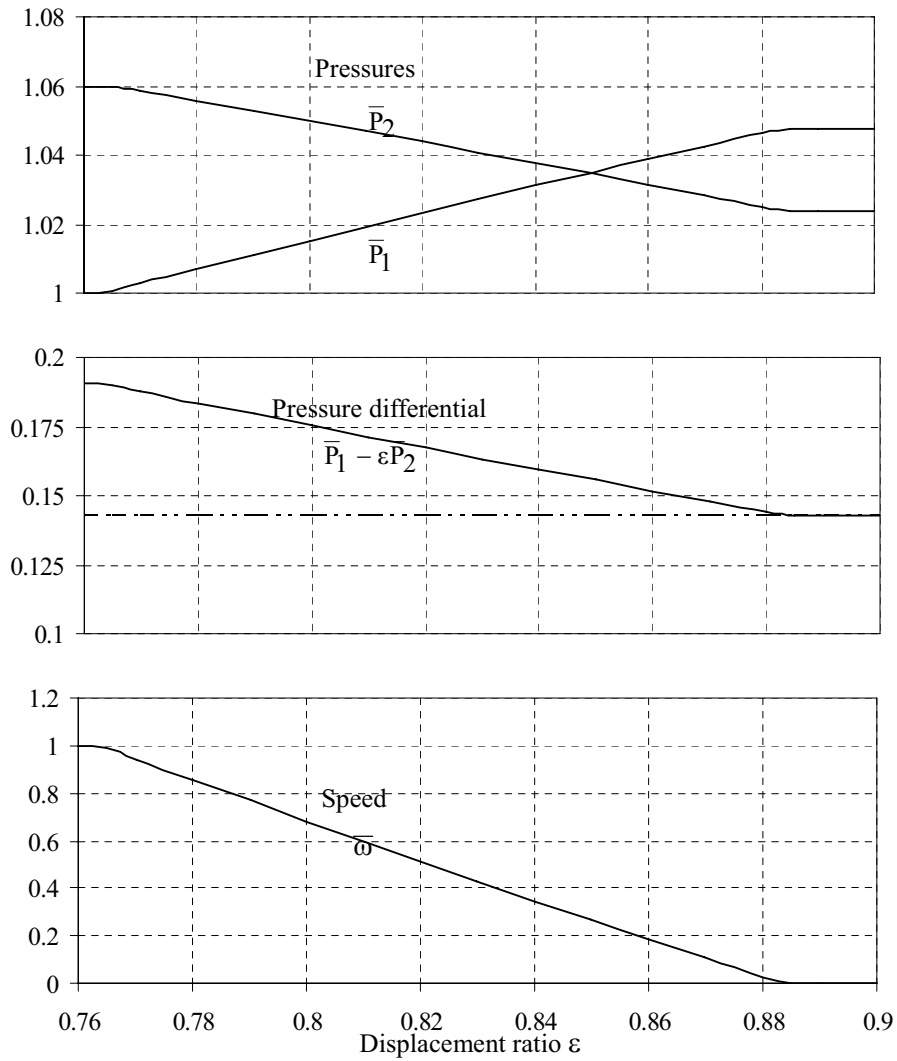
Figure 3   PTU performance for a specific undesirable load flow $\overline{Q}_b = 0.5$

The condition for equal pressures.
It seems reasonable to aim for equal pressures under PTU operation as a good design guide. This condition is achieved when :

$$\overline{P}_1 = \overline{P}_2 \quad \text{when} \quad \overline{\omega} = \frac{\overline{Q}_b}{(1+\varepsilon)}$$

$$\varepsilon^2(\overline{P}_{rv}+1) + \varepsilon(\overline{T}_{sc} - \overline{Q}_b)$$
$$+ \overline{T}_{sc} + \overline{Q}_b(1+\overline{B}_V) - \overline{P}_{rv} - 1 = 0 \qquad (23)$$

Considering figure 2 :

- It will be seen that the displacement ratio range is restricted overall to typically $0.75 < \varepsilon < 0.91$ but depends upon the load flow rate to be supplied.
- It will be preferable for the displacement ratio to be closed towards the lower end of the operating range.

Considering figure 3 for the specific load flow rate :

- A displacement ratio beyond 0.882 will not allow the PTU to rotate and power transfer will not exist.
- As the displacement ratio decreases below 0.882 the pressure differential increases and the PTU speed increases. The supply pressure P_1 continually decreases and the pressure to be compensated P_2 increases as required.
- As the displacement ratio decreases further the speed rises to its maximum when the supply pressure P_1 reaches the PRV setting and the equations then do not apply.
- A lower displacement ratio therefore ensures that the driving pressure differential lies beyond the friction dead-band.
- The PTU speed decreases linearly with increasing displacement ratio

Table 1   Data taken on PTUs used in different aircraft [7]

Aircraft	D_m $(10^{-6}\text{m}^3/\text{s})$	D_p $(10^{-6}\text{m}^3/\text{s})$	Displacement ratio ε	Motor pressure (bar)	Pump pressure (bar)
Uni-directional, fixed displacement					
DC-10/ND-11	1.23	1.13	0.92	200	179
757	4.00	3.65	0.91	172	150
Gulfstream 11	1.73	1.57	0.91	207	200
A-300	4.00	3.46	0.87	207	207
767	0.25	0.21	0.84	112	86
727, 747	0.25	0.21	0.84	207	207
737	0.81	0.63	0.78	169	166
Bi-directional, variable displacement					
DC-10/MD-11	5.00	4.46-5.50	0.89-(1)-1.10	207	193
C-17A	3.15	2.62-3.66	0.83-(1)-1.16	275	255
A-320	2.10	1.57-2.62	0.75-(1)-1.25	207	200

Considering data from aircraft applications, Aerospace recommended practice SAE ARP1280 [7], Table 1 shows actual data for a range of aircraft and for fixed displacement and variable displacement PTUs. The displacement ratio can vary between :

$$0.78 < \varepsilon < 0.92$$

for uni-directional operation with fixed displacements.

$$0.75 < \varepsilon < 0.89$$

for bi-directional operation with variable displacements.

$$0.76 < \varepsilon < 0.88$$

suggested from the theory presented.

For a variable displacement PTU, a swash-plate adjusting control system is required to change the displacement ratio of the in-line axial piston unit depending on the direction of power transfer, figure 4. The displacement ratio would be changed around the neutral position, when no PTU action is needed. Hydromechanical control system is normal practice, and integral with the variable displacement unit, to change swashplate position in the correct direction from neutral.

CONCLUSIONS

The approach presented has a qualitative synergy with the data from typical applications, the linear approximations giving a good first-order insight into PTU behaviour.

An understanding of the interaction between load flow and each pressure relief valve setting is crucial and the resulting design equations are not explicit. However the design only requires solution of quadratic equations.

It is clear that for a particular design the effect of increasing load flow results in a displacement range that increases slightly. It seems preferable to move towards the lower end of the displacement range. The pressure on the healthy side is then closer to its pressure relief valve setting and the speed moves towards a higher value. A good design will try to avoid the extremely high speeds that could occur in practice.

Further work on PTU dynamics is needed, and poses an interesting analysis problem when an actual PTU design is considered for variable displacement units.

Figure 4   Bi-directional operation of a PTU with displacement

REFERENCES

1. Heinrich Ebert. Hydrostatic axial piston fluid transmission, US patent 3,052,098, 1962
2. Boehringer WE et al, McDonnell Douglas Corporation. Reciprocating transfer pump, US patent 3,890,064, 1975
3. Bick DE, Dowty Rotol Ltd. Power transfer unit. US patent 4,168,652, 1979
4. Boehringer WE et al, McDonnell Douglas Corporation. Hydraulic power transfer unit, US patent 4,286,927, 1981
5. McGowan PT, The Garrett Corporation. Fluid motors and pumps, European patent 0,015,127, 1979
6. McGowan PT, Allied Signal Inc. Power transfer apparatus, European patent 0,280,532,B1 1987

7.   Aerospace recommended practice SAE ARP1280, reaffirmed 2002-07, SAE Int,Warrendale, USA
8. Zarotti GL and Nervegna N. Pump Efficiencies-Approximation and Modelling. Proc 6th BHRA Fluid Power Symposium, 1981
9. Chapple PJ and Dorey RE. The performance comparison of hydrostatic piston motors-factors affecting their application and use. Proc 7th BHRA Fluid Power Symposium, UK, 1986, 1-8
10. Watton J. Closed-loop design of an electrohydraulic motor drive using open-loop steady state characteristics. J Fluid Control, Vol 20, No 1, 1989
11. Watton J. An explicit design approach to determine the optimum steady state performance of axial piston motor speed drives. Proc IMechE, Journal of Systems and Control Engineering, Vol 220, 2006

OS7-2

THE TECHNOLOGY TREND AND PERSPECTIVE OF HYDRAULICS IN AIRCRAFT FLIGHT CONTROLS

Hirokazu YOSHIDA*, and Shinya SATO**

* Preliminary Designing Section, Defense Aircraft Engineering Department
Mitsubishi Heavy Industry, Nagoya Aerospace Systems
10 Oye-cho, Minato-ku, Nagoya 455-8515 Japan
(E-mail: hirokazu_yoshida@mhi.co.jp)
** Mechanical Systems Designing Section, Defense Aircraft Engineering Department
Mitsubishi Heavy Industry, Nagoya Aerospace Systems
10 Oye-cho, Minato-ku, Nagoya 455-8515 Japan

ABSTRACT

The recent technologies of hydraulics and flight controls have been progressing step by step. The research effort for establishing the technology to build 55.2MPa (8000psi) hydraulic system for practical use has begun to fruit around the world, and high-pressurizing is getting to be standardized, shifting from the conventional 20.7MPa (3000psi) system pressure. The system pressure is settling into 34.5MPa (5000psi), which is practical in both cost and performance with the appropriation of the existing parts and ground support equipment considered.
Also, ALL ELECTRIC AIRCRAFT (AEA) technologies proposed more than 20 years ago have begun to come into practical use, such as electric actuators for primary control surfaces, as improved are 270Vdc power source technology, the permanent magnet peformance for electric motors, the power transister capability for control device, and the reliabilities of mechanical parts such as ballscrews and bearings.
This paper discusses the application of new materials to aircraft such as piezoelectric, magnetostrictive, and shape-memory materials, which have recently become stabilized in production and begun to be applied in commercial fields other than aircraft industry.

KEY WORDS

Aircraft, Hydraulics, Actuator, Active, Material

INTRODUCTION

Aircraft have two kinds of power generation systems, "Hydraulic" and " Electrical," to drive various subsystems on board. These two power generation systems are used in proper combination with system functions well distributed over them, which gives the optimum redundancy to system functions in aircraft to secure the flight safty.
Hydraulic systems are mainly used to drive flight control systems and landing gear systems in aircraft. These systems consist of servo-actuators, servo valves, solenoid valves, power cylinders, hydraulic motors, check valves, orifices, and they are not so different from industrial hydraulic systems in terms of hydraulic compositions.
Then, this paper summarizes the technology trend of aircraft hydraulic generation systems and flight control servo-actuators, and gives information on the application of new materials to Electro Hydraulic Servo Valves.

AIRCRAFT HYDRAULIC SYSTEM

Aircraft hydraulic system pressure had been 20.7MPa (3000psi) for a long time, but the system evaluation tests and flight tests of 55.2MPa (8000psi) hydraulic system has been started around 1970 with the developments and testing of hydraulic components for 55.2MPa (8000psi) system conducted simultaneously. Then, now hydraulic product makers are learning from those efforts and commercializing high-pressure aircraft hydraulic components. The large aircraft and high maneuverability aircraft lately under development are applying 34.5MPa (5000psi) hydraulic systems in many cases, and 34.5MPa (5000psi) is becoming the standard for aircraft hydraulic systems.
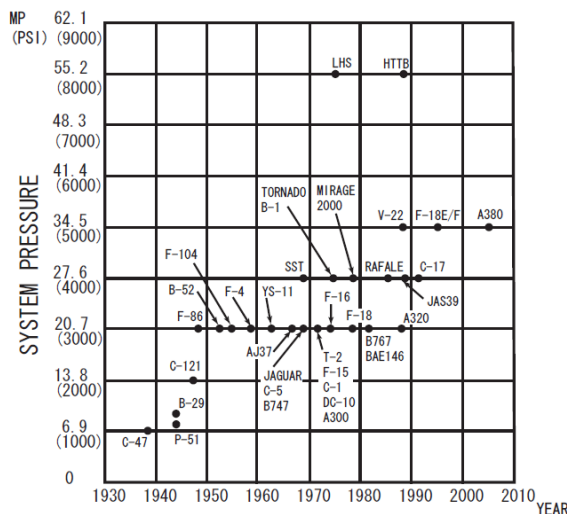
Figure 1 Hydraulic System Pressure Trend (Taki [1])

Some decades ago, mechanical signals from pilot commands were fed into manual valves to control flight control hydraulic servo-actuators. In around 1950, electrical computer controls became possible in aircraft controls, and since then, servo-actuators using Electrical Hydraulic Servo Valves (EHSV), which convert electrical signals into hydraulic signals which in turn amplify hydraulic power to control actuators, have been popular in aircraft flight controls.

Furthermore, since around 1990, direct drive valves (DDV), which use electric coil force motors to directly control main control valves, have been used as hydraulic servo valves, as electric magnets characteristics were improved. This DDV requires high cost to procure, and large aircraft still use EHSVs for servo-actuators, so the effort to reduce the production cost of DDV is required for the future.

HYDRAULIC AND ELECTRIC ACTUATORS

The system pressure becomes 34.5MPa (5000psi), and the reliability and maintenability of aircraft hydraulic systems have become quite stable. Also, aircraft electric power supply systems have been able to provide 270VDC power, and it has become possible to reduce the current in electric actuators and controllers by providing high-voltages in power supply systems. The production cost of electric actuators are getting low, and the reliability are being improved, as IPM (Interior Permanent Magnet) motor are started to be widely used such as in hybrid cars. As a result, replacing hydraulic actuators, electric actuators have started to be used in primary flight control systems in some new aircraft developments.

Table 1 shows the characteristics comparison between hydraulic and electric actuators.

As shown in Table 1, the performance of electric actuators matches for that of hydraulic actuators, so it is becoming possible to select two types of actuators according to power source redundancy (hydraulic and electric) and installation easiness of tubing or wiring.

However, electric actuators have to keep consuming electric current to hold an actuator position with aerodynamic load applied on when they are used in primary flight controls, while hydraulic actuators are capable of holding an actuator position against aerodynamic load with just control valve closed to maintain cylinder differential pressure. Also, hydraulic actuators are advantageous for flight control surfaces in that damping effect can be obtained in case of failures by utilizing bulk modulus of hydraulic fluid and flow restriction through orifices.

Sufficient considerations should be given to these characteristic differences and energy efficiency when hydraulic and electric actuators are applied.

Table 1 Characteristics Comparison Between Hydraulic and Electric Actuators

	Hydraulic	Electric
Speed	○	○
Frequency Response	○	○
Weight	unit:○　system:○	unit:△　system:○
Reliability	○	△
	Leakage is the most frequent failure, but not as critical as piston sticking	Weight penalty of adding mechanism to prevent mechanical load paths from sticking
Maintenability	△	○
	Frequent change due to leakage	Periodical lubrication required

NEW MATERILS TO HYDRAULICS

Flight control systems are now being high-pressurized and electricalized as above, and the electrical input (command) is converted to hydraulic command by motors or force motor.

Recently, researches for active materials, which convert electrical inputs directly into mechanical strokes, have been progressed. These active materials have mechanical strokes of about 10 to 100 micro meters, so they cannot simply replace hydraulic actuators which have mechanical strokes of about 10 to 100 milli meters. However, active materials are possible to be utilized as actuating devices in servo valves, shutoff valves, and very small hydraulic pumps.

Active materials such as piezoelectrics and electrostrictives respond well at high frequencies of the order of 1000Hz, and some efforts are being put into the researches to apply active materials to very small pumps and servo valves utilizing this characteristic. Also, shape-memory alloys can be applied to operate selector (on/off) valves for hydraulic components which do not require high response operations.

It is expected that these active materials are going to be applied to not only hydraulic components but also small moving products such as micro aircraft.

APPLIATION OF PEIZOELECTRIC STACKS

In this chapter, the application of piezoelectric stacks to electro-hydraulic servo valves (EHSV) generally used in aircraft hydraulics in large numbers is considered.

Figure 2 shows a typical EHSV. Coils (electric magnet) in the upper portion produce magnetic forces as currents are through them, and the force moves the flapper in the first stage. This flapper movement in turn changes pressures on both end of the valve spool in the second stage. In this way, control pressures are amplified in the second stage to move the main control valve of servo valve. The displacement of the flapper base produced by the electrical magnet is so small that it is possible to apply active materials to this part.

The reasons that piezoelectric stacks are selected for EHSV driving element from among several types of active materials such as magnetstrictives and shape-memory alloy are shown below.

(1) The frequency response of EHSV is 10 to 200 Hz.
(2) The electrical magnet part, which is the control portion of EHSV, is desired to be miniaturized.
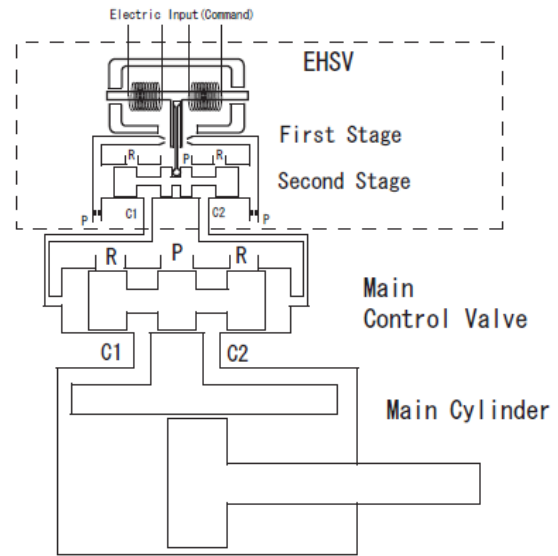
Figure 2 EHSV schematics
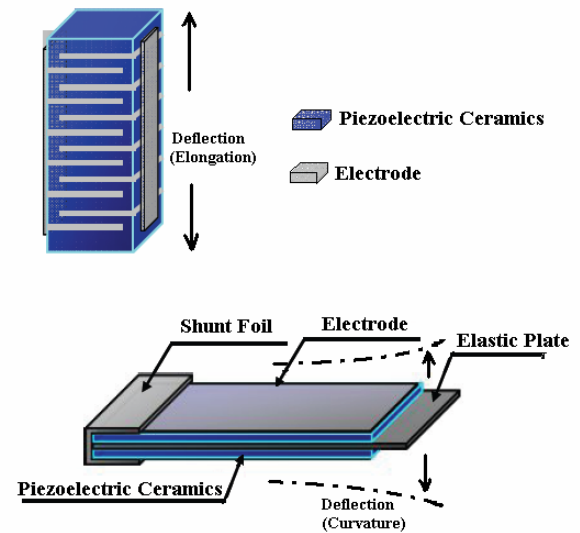
Figure 3 Piezoelectric Stacks(above) & Bimorph(below)

Also, although bimorph piezoelectric members can produce relatively large displacement, the generated force is not large enough to stably operate EHSV against hydraulic pressure fluctuation and flow forces. Thus, the stacked piezoelectric element type is selected, which is capable of producing both displacement and force enough for stable operations.

Table 2 Applicability of Active Materials to Servo Valves

	Piezoelectric	Megnetstrictives	Shape-memory	Electrical
Response	High	High	Low	High
Weight	Light	Heavy	Light	Very Heavy
Displacement	Small	Small	Large	Medium
Force	Large	Large	Small	Medium

163

Table 2 summarizes the applicability of active materials to servo valves.

Ref. 2. put together the experimental data collected for the stack piezoelectric element of 7mm by 7mm by 32mm size. The deflection is 30 to 50 micro-meters, which is enough for EHSV application.

Figure 4 shows that the Young's modulus to temperature is stable at -20 to 120 degree C. Since the usage temperature of EHSV in aircraft hydraulic system is from 0 to 80 degree C, the thermal compatibility will meet the requirement for practical uses. Also, the hysteresis characteristic shown in Figure 5 is as favorable as that of the electrical magnet is.

The piezoelectric stacks are vulnerable to tensile forces, and avulsion of stacks will be caused by tensile forces. Thus, it is required to be used with compressive forces pre-loaded. Conveniently, the deflection characteristic is little affected by compressive preload forces.

Therefore, it is possible to design with compressive preload forces so that piezoelectric stacks will have enough durability, and the design of the preload forces will have an impact on a product life. In conclusion, it is considered that the application of piezoelectric stacks to aircraft hydraulic EHSV will become practical by testing and evaluating power consumption, environmental condition requirement (vibration, high and low temperature, thermal shock, fluid compatibility,) and durability in the future.

POSTSCRIPT

The aircraft hydraulic system is making progresses step by step, and now, its reliability is well-established. It is required to make it more efficient, more reliable, and lighter in weight by studying the application of new materials in the future.

Also, The aircraft hydraulic and general industrial hydraulic systems are common in the base technology, so effort should be made to lower the system cost by making components tandardized as much as possible.

Figure 5 Hysteresis characteristic of piezoelectric stacks (Tanaka [2])
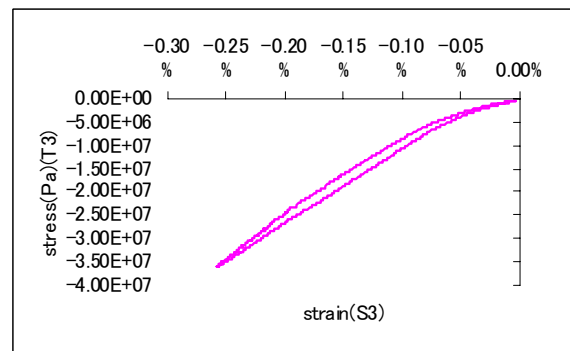
Figure 6 Displacement - compressive preloaded force relationship of piezoelectric stacks (Tanaka [2])

REFERENCES

1. Taki, H., High Pressurization of Aircraft Hydraulic System, Japan Hydraulics & Pneumatics Society, 1989, 20-1 p26-31.
2. Tanaka, N., et al. Effect of Temperature on Elastic and Piezoelectric Constants of PZT, Department of Aerospace Engineering, Nagoya University, Nagoya, Japan, 2007.

Figure 4 Young's modulus – temperature relationship of piezoelectric stacks (Tanaka [2])

OS7-3

DEVELOPMENT OF PROTOTYPE ELECTRO-HYDROSTATIC ACTUATOR FOR LANDING GEAR EXTENSION AND RETRACTION SYSTEM

Norio TAKAHASHI*, Taku KONDO**, Masayuki TAKADA**, Kazuhiro MASUTANI**,
Shingo OKANO**, Mitsuhiro TSUJITA**

* International Business Department – Aerospace
**Engineering Department - Aerospace
Sumitomo Precision Products Co., Ltd.
1-10 Fuso-Cho, Amagasaki, Hyogo, 660-0891, Japan
(E-mail: takah-no@spp.co.jp)

ABSTRACT

More Electric Aircraft (MEA) or All Electric Aircraft (AEA) is intensively researched and developed all over the world to reduce total Aircraft power consumption, and thus total operation cost. In MEA or AEA development, Aerospace Research and Technologies activity are focusing the area of Electrical Power system, Flight control, Engine system, Environmental Control System and Landing Gear System. [1] We are focusing the Landing Gear Actuation System and as our 1st step we have developed prototype ELECTRO-HYDROSTATIC ACTUATOR (EHA) for Landing Gear Extension and Retraction System (LGERS) application. The prototype EHA was designed and tested to evaluate the performance, weight and reliability to apply the future Aircraft application. From our prototype model development, we have clarified the technical issues to be improved or considered in the future MEA or AEA application.

KEY WORDS

EHA, LGERS, More Electric Aircraft

NOMENCLATURE

AEA : All Electric Aircraft
BIT : Built-in-Test
ECU : Electronic Control Unit
EHA : Electro-Hydrostatic Actuator
EMI : Electro Magnetic Interference
LGERS : Landing Gear Extension and Retraction System

MEA: More Electric Aircraft

INTRODUCTION

We are developing prototype ELECTRO-HYDROSTATIC ACTUATOR (EHA) for Landing Gear Extension and Retraction System. Our final target is to replace all of the conventional

hydraulic actuation system with electrical system to comply with future ALL ELECTRIC AIRCRAFT. The following system is our scope;

(1) Landing Gear Extension and Retraction System,(LGERS)
(2) Brake Control system.
(3) Nose Wheel Steering Control System.

This time, we have designed and developed the EHA for LGERS application. For our development study, the following Commercial Aircraft was targeted;

1   Passengers : 100～150 Seats
2   Aircraft Weight : 50 ton (MTOW)

Illustrations

1.   Function of EHA

To fully replace with the conventional hydraulic Retraction Actuators, the following LGERS functions were incorporated in the EHA functions;

(1) Normal Extension and normal Retraction
(2) Snubbing Mechanism (in Actuator)
(3) Emergency Extension via free fall extension
(4) Protection for Jamming/Over Load
(5) BIT(Built-in-Test) Function by Control Unit
(6) Failsafe Function by Control Unit

The items (4), (5) and (6) were incorporated only for EHA application.

2.   Structure of EHA and its Operation

System architecture is shown in Figure 1. The EHA consists of the Hydraulic Power Unit and Electronics Control Unit (ECU). Hydraulic Power Unit consists of the hydraulic linear actuator with snubber function, hydraulic manifold, pump and DC brush-less motor. DC brush-less motor rotates both directions under the control by the ECU. Pump generates the high pressure to the hydraulic manifold, and the hydraulic manifold controls the hydraulic flow to the Actuator. That is, when the Motor rotation is "CW", the actuator is extended and vice verse. To achieve the extension and

retraction time as same as the conventional LGERS system, the ECU controls the motor rotation speed and also monitors the extension and retraction time. When the ECU is powered off, the Bypass valve in the hydraulic manifold is always de-energized. In this status, the full area port in the Actuator is hydraulically connected to the annulus chamber. When the emergency extension is triggered, the bypass valve is de-energized and the Landing Gear can be extended by the free fall extension.

3.   Key Technology for EHA Development

Our key technology for compact Actuation Mechanism is Hydraulic Reservoir in the internal of Piston Rod. The most important purpose of prototype EHA is clarification of the function and performance of the Hydraulic Reservoir in the internal of Piston Rod as shown in Figure 2.

The EHA system generally equips a full-volume reservoir outside its cylinder that compensates the fluid volume caused by the difference of volume between annulus chamber and bore chamber. Our new concept EHA equips the reservoir built into the piston rod ("Dead space") as shown in Figure 2. It is possible to save its weight and space envelope. In the case of insufficient volume in the piston rod, an additional reservoir which is smaller than a full volume reservoir may be installed on the outside to compensate a lack of fluid. Effect of current prototype Actuator against Full Outside reservoir Actuator from our Study;

Weight:
6 % Weight Reduction by Full Outside Reservoir Actuator (About 3 kg Reduction Estimated)

Volume (Envelop):
 1250 cc Volume Reduction by Fully outside Reservoir Actuator (1250cc is nearly equal to the volume ofφ70mm×L300mm cylinder estimated)

4.   Design Specification and Performance

The following is our Prototype EHA design specification and performance;

Input Power :
1   MIL-STD-704E DC270V 180Amax
2   RTCA-DO-160D Section16 Category A
3   DC28V   6A max

Power Consumption :   9.33kW

Hydraulic Fluid: MIL-PRF-5606 for Prototype only

Regulated Pressure: 210 bar (3,000 PSIg)

Environmental Temperature
   EHA   -55 deg C to 70 deg C
   Controller   -55 deg C to 70 deg C

Pump:
Constant Displacement piston pump
   1   Rotation Bi-directional

   2   Output   Volume   of   rotation
         0.11cipr(1.8mL/rev)
   3   Target Revolution 14850rpm (Retraction)
         12000rpm (Extension)

Electric Motor:
   1   Type: DC BRUSHLESS MOTOR
   2   INPUT POWER: AC270V, 3 ϕ
   3   OUTPUT POWER: 9.33kW
   4   RATED SPEED: 14850rpm (Retraction)
                       12000rpm (Extension)
   5   RATED TORQUE: 6.0N-m

The prototype EHA is shown in Figure 3.
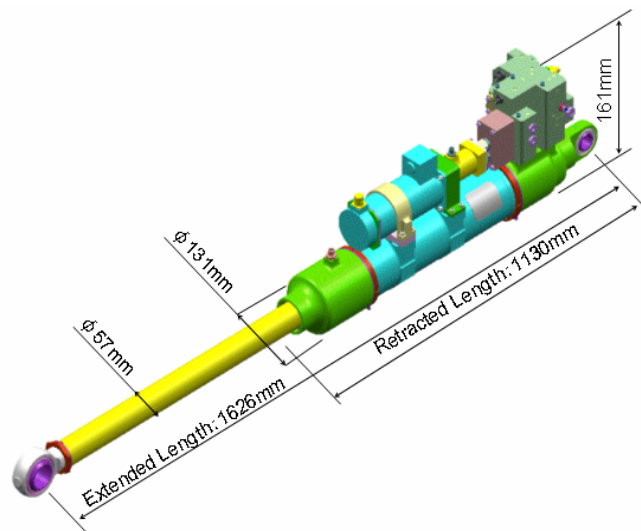
Figure 1. Three-dimensional View of prototype Landing Gear EHA
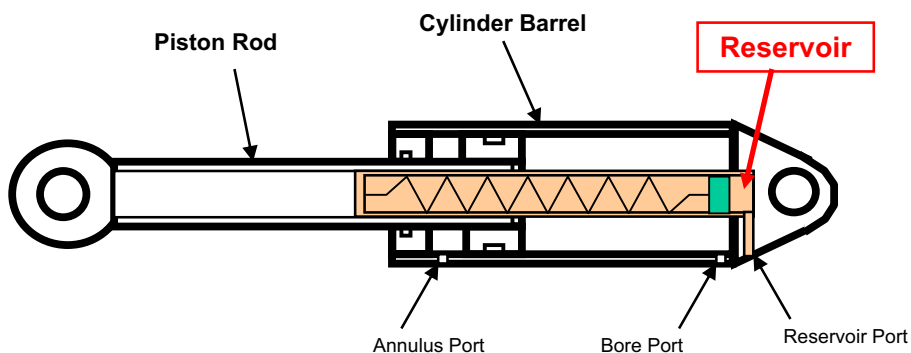
Figure 2. Internal Hydraulic Reservoir in Piston Rod bore Structure

5.   Engineering Validation Test

The following tests were carried out for our design

validation of the Prototype EHA;

(1) Normal Extension and Retraction Testing

to our design requirement

(2) Emergency Extension Test to our design requirement
(3) High and Low temperature test to RTCA DO-160D Section 4 Category D2
(4) Vibration test at Full retract position to RTCA DO-160D Section 8 Category T
(5) EMI test for Motor and ECU to RTCA DO-160D Section 21 Category H

From out Engineering Validation Test, we have got some feedback to improve our future design.

6. Lessens Learned

From our prototype design development of Landing Gear EHA for 100-150 seats class Commercial Aircraft application, we have some lessens learned as follows;

(1) We can not visually check the fluid volume in the in-Piston-Rod reservoir.
- To incorporate the Pressure Gauge to visually check the fluid volume.
(2) To increase the reliability to the actual Commercial aircraft application.
- To refine the hydraulic circuit. In addition, the detail reliability analysis should be carried out to optimize our design.
(3) To enhanced the anti-vibration performance.
- To optimize our design of hydraulic manifold to reduce the weight and volume, and installation to make the C.G. lower.

These lessons learned will be incorporated in our further development of the Landing Gear EHA to achieve the optimized EHA for the future MEA.
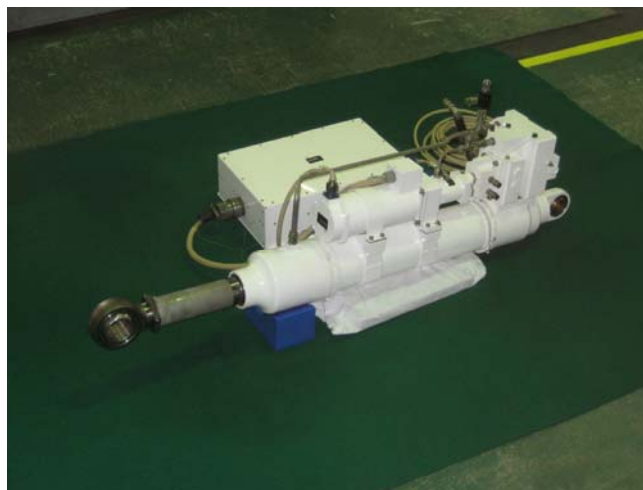
Figure 3. Overview of prototype Landing Gear EHA

Table 1 Design Specification of prototype Landing Gear EHA

Descriptions	Specifications		Remarks
Size	Full Extended Length	1626 mm (Nominal)	
	Full Retracted Length	1130mm (Nominal)	
Stroke		496mm (Nominal)	
Rate	Extending Rate	41mm/sec	496mm/12sec
	Retracting Rate	58mm/sec	496mm/8.5sec
Load (External)	Extension Case	54kN	
	Retraction Case	107.6kN	

REFERENCES

1. Power Optimized Aircraft R&T Website; http://www.poa-project.com/

OS7-4

DESIGNING ADVANCED RUDDER ROLL STABILIZATION SYSTEM
- Using High Power with Small Size Hydraulic System -

Hiroyuki ODA *, Kohei OHTSU**, Hiroshi SATO*** and Kazuhiko KANEHIRO****

* Akishima Laboratories (Mitsui Zosen) Inc.
1-1-50 Tsutsujiga-oka Akishima-city, Tokyo, 196-0012 Japan
(E-mail: oda@ak.mes.co.jp)
** Tokyo University of Marine Science and Technology
2-1-6 Etchujima Koto-ku, Tokyo, 135-8533 Japan
(E-mail: ohtsu@kaiyodai.ac.jp)
*** Daiichi Electric Co., LTD
1177 Aza Tobara Daigiri Fijisawa-shi, Kanagawa, 251-0002 Japan
(E-mail: fujisawa@daiichi-denki.co.jp)
**** Mitsui Engineering and Shipbuilding Co., LTD
3-1-1 Tama Tamano-shi, Okayama, 706-8651 Japan
(E-mail: kanehiro@mj.mes.co.jp)

ABSTRACT

This paper will outline the various stages in the design and development of advanced rudder roll stabilization system based high slew rate steering system. The slew rate means rudder angle change rate. First, this paper introduces a high slew rate steering system with Electric hydraulic system (EHS). The basic concept of EHS system is to combine the hydraulic power source system and actuator system with controlling the speed of electric motor of hydraulic pump depending on the condition required to the actuator. Next, this paper presents the adaptive rudder roll stabilization system based on a multivariate auto-regressive model that is called Multivariate Auto-regressive Rudder roll Control System (MARCS). Finally, conclusions and discussions based on full scales experiments are summarized.

KEY WORDS

Electric hydraulic system (EHS), Multivariate Auto-regressive Rudder roll Control System (MARCS), Adaptive control

INTRODUCTION

The purpose of rudder roll stabilization system is put on roll reduction as well as course keeping by appropriate steering using only rudder. This paper will outline the various stages in the design and development of advanced rudder roll stabilization system based high slew rate steering system and adaptive control. The slew rate means rudder angle change rate.

The approach to this control system is based on a multivariate auto-regressive model that is called Multivariate Auto-regressive Rudder roll Control System (MARCS) [1][2].
First, this paper introduces a high slew rate steering system with Electric hydraulic system (EHS). The basic concept of EHS is to combine the hydraulic power source system and actuator system with controlling the speed of electric motor of hydraulic pump depending on

the condition required to the actuator [3].

The effectiveness of any roll stabilization system depends on the magnitude of the stabilization moment that can be applied to the ship. For the MARCS to be effective, it is necessary to change faster in slew rate. In case of applying EHS to steering system which is one of the most typical hydraulic systems in ship's equipment and have good results with roll reduction.

Next, this paper presents application of the batch adaptive control based on a locally stationary auto-regressive model. The control gain of conventional MARCS does not change through the navigation at sea. However wind and wave can be regarded as stationary for a short time, it is necessary from a viewpoint of long-time observation to consider that the property of the stochastic process will be changed and be non-stationary [4].

Finally, conclusions and discussions based on full scales experiments are summarized. The EHS can save power consumption on average by over 80(%) in comparison with a conventional hydraulic steering system. The advanced MARCS using EHS reduced the roll motion in average with 30(%) -- 50(%) comparison with the conventional auto-pilot.

ELECTRIC HYDRAULIC SYSTEM (EHS)

In conventional hydraulic system, power source and actuator are separated as shown in Figure 1. The power source is designed to meet maximum required flow-rate of actuator. Electric motor of hydraulic pump is operated with constant speed all the time. This system should be controlled with servo-valve and remain is returned to oil tank through relief valve. In some conditions, a variable mechanism is applied to the pump and actuator, but the controllability is not sufficient to cover all condition. Also in those systems, the power source ant actuator are generally equipped separately and connected with piping complexity on the floor. In those piping, fluid vibration is a usual problem that causes to operate noise.
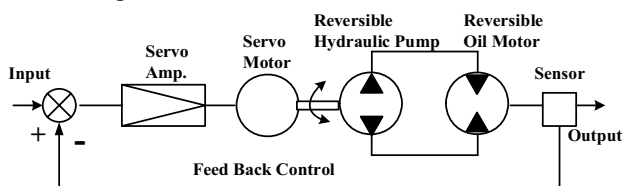
Figure 1 Servo Control of EHS

The basic concept of EHS is to combine the hydraulic power source and actuator with controlling the speed of electric motor of hydraulic pump depending on the condition required to the actuator. The EHS is developed as a new revolution control techniques for electric motor. The construction of EHS is shown in Figure 2. The concept of this system is that the speed of electric motor of hydraulic pump is controlled with inverter against the load change, so it can supply required volume of system oil to an actuator.

As the result, such components as servo-valve, relief valve would be able to be removed from hydraulic system. This system could improve the efficiency of system, because the hydraulic pump operates whenever the actuator is moving.
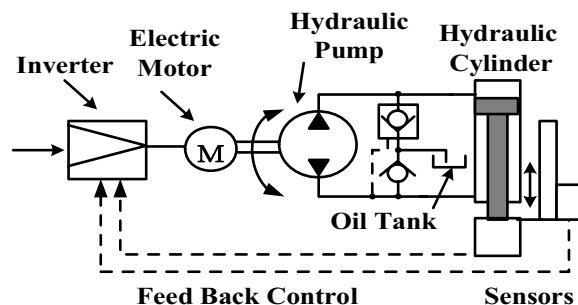
Figure 2 EHS Hydraulic System

The basic components of EHS are as follows [6],
a. Reversible Hydraulic Pump:
   Suction or discharge of hydraulic pump should be changed with the direction of revolution.
b. Servo motor or AC-motor with inverter:
   The motor for hydraulic pump should equip with speed control function.
c. Reversible motion actuator:
   The actuator should have the function of reversible motion.
d. Oil tank and piping:
   The volume of oil tank should cover total volume of components. Only supply line and return line to be equipped with.
e. Control system:
   The motion of the actuator should be controlled directly with the pump revolution.

DESIGN OF EHS STEERING SYSTEM

The conventional steering system is equipped with steering wheel, autopilot, rudder operating system, hydraulic source system and rudder. In case of applying EHS to steering system, the rudder operation system and hydraulic source system of conventional system are though to be replaced with it. Supposing that the pump characteristics using servo controlled servo-motor is proportional function, the design of EHS steering system is shown in Figure 3.

This system is composed of servo motor, servo pack, reversible hydraulic pump and can drive high slew rate not only the realization of small size reduction of weight of steering system. In case of applying EHS to steering, the rudder operation system and hydraulic power unit of conventional system are though to be replaced with it.

170
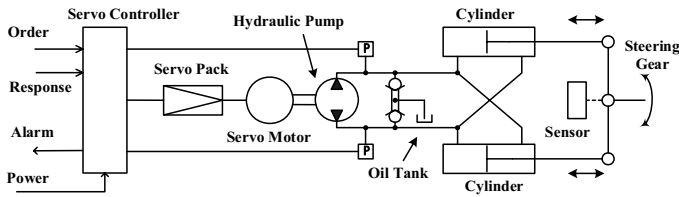
Figure 3 Design of EHS Steering System

CONVENTIONAL MARCS

As one of the authors, has demonstrated in paper [4], Multivariate Auto Regressive eXogenous (MARX) model expressed by

$$X(n) = \sum_{m=1}^{M} A(m)X(n-m) + \sum_{m=1}^{M} B(m)Y(n-m) + U(n) \quad (1)$$

is powerful stochastic model in designing a roll reducible autopilot system, where X(n) is 2 dimensional vector of controlled variable (r); yaw and roll. Y(n) is 1 dimensional vector of control variable(l): rudder angle. U(n) is Gaussian white noise. The order M of this model is obtained by AIC (Akaike's Information Criterion [5],

$$AIC(M) = N\log(\det(d_{r,M})) + 2r(r+l)M + r(r+l) \quad (2)$$

$d_{r,M}$ is the covariance matrix of the residual of the MARX model. N is number of data. The optimal order in the MARX model is determined by minimizing the value of AIC. Based on the modem control theory, this model can be transformed to state space representation.

$$Z(n) = \Phi Z(n-1) + \Gamma Y(n-1) + W(n) \quad (3)$$
$$X(n) = HZ(n)$$

where Z(n) is the state vector and Φ is the transfer matrix that controls the transition of the state Z(n). Y is the observation vector. In order to evaluate a performance of the control, quadratic criterion function optimal in the **I** suitable interval.

$$J_I = E\left\{\sum_{n=1}^{I}\left\{Z^T(n)Q(n)Z(n) + Y^T(n-1)R(n)Y(n-1)\right\}\right\} \quad (4)$$

Q and R are the weighting function for the controlled and the control variables, respectively. The optimal control law which minimizes J_I under constraint of the above state space equation is given by a feedback law with the stationary gain G. Then the optimal control law can be represented by

$$Y(n) = GZ(n) \quad (5)$$

PROTOTYPE EHS STEERING SYSTEM

To confirm the effectiveness of EHS, the prototype EHS is established to the conventional steering system. The actual ship for experiment is the training ship "SHIOJI

MARU" of Tokyo University of Marine Science and Technology. The principal particulars are shown in Table 1. The basic specification of steering system is shown in Table 2.

Table 1 Principal Particulars of "SHIOJI MARU"

Hull	Length (Lpp)	46.0 (m)	Propeller	Type	Cpp
	Breadth	10.0 (m)		Aspect Ratio	1.47
	Draft	3.8 (m)		No. of Blade	4
	Gross Ton	425.0 (ton)	Engine	Type	Diesel
	GM	1.48 (m)		HP	1400 (HP)
	KB	1.56 (m)		RPM	700 (rpm)
	Roll Period	6 – 7 (sec)		No.	1
Rudder	Area	4.25 (m^2)			
	Aspect Ratio	1.47			
	Slew rate	2.3 – 4.6(deg/s)			

Table 2 Basic Specification of Steering System

Actuator	Cylinder Bore	100 (ϕ)
	Rod Diameter	56 (ϕ)
Hydraulic Cylinder	Stroke (hard to hard)	427 (mm)
Power Unit	Power (pole)	3.7 (kw) / set * 2
Electric Motor	Performance	2.3 – 4.6 (deg/s) [1 set – 2 sets]
	Revolution	1500(rpm)
Hydraulic Pump	Type	Vane Pump
	Delivery min.	23 (l/m) at 12.3(MPa)

The hydraulic steering circuit of this ship is shown in Figure 4. Applying the conventional system, the flow rate becomes constant at its upper limit when the movement of rudder angle is large. It is ordinary as operating that the slew rate is 2.3 (deg/s) with one set of power unit and also using two sets of power units, it can drive 4.6 (deg/s).

Table 3 Comparison of Conventional and EHS Steering System

Item	Conventional	DDVC
Size (H * B * D)	0.8 * 1.2 * 0.6 (m)	0.3 * 0.7 * 0.25 (m)
Weight	600 (kgf)	60 (kgf)
Electric Motor	3.7 (kW) * 2	4 (kW)
Slew Rate	max. 4.6 (deg/s)	max. 10.2 (deg/s)
Oil Volume	500 (little)	20 (little)
Flux adjustment	Servo valve	Hydraulic pump
Power Consumption	-----------	90 (%) reduction
Noise Level	-----------	10 (dB) reduction
Installation & Maintenance	Dock & Difficult	Quay & Easy

The conventional steering system is equipped two sets of AC electric motor and servo valve with large oil tank. The EHS steering system is equipped only servo motor and hydraulic pumps with very small oil tank. The comparison of typical performances of conventional and EHS steering system are shown in Table 3.

171　　　　　　　　　　Copyright © 2008 by JFPS, ISBN 4-931070-07-X
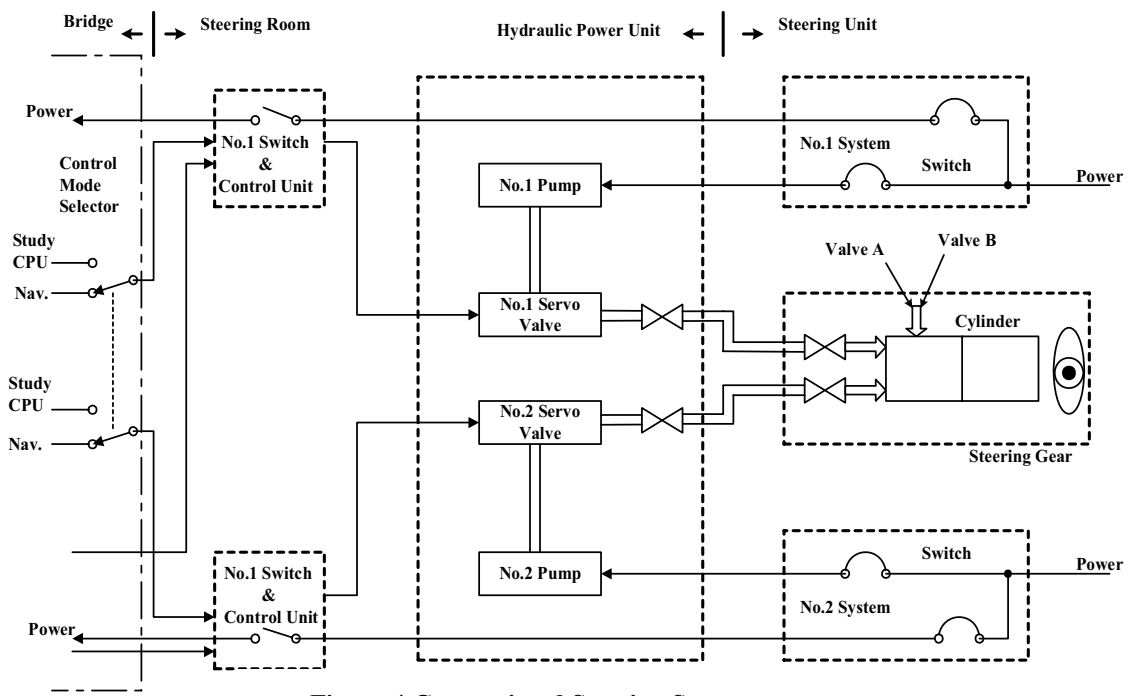
Figure 4 Conventional Steering System
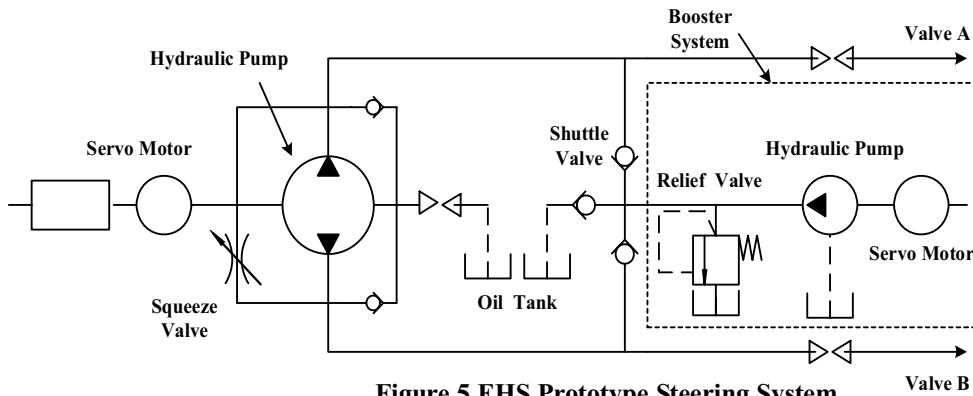
Figure 5 EHS Prototype Steering System

In order to utilize the ship's own steering system as much as possible, the EHS steering system was installed in the spare circuit of own steering system as shown in Figure 5. The valve A and B of EHS prototype are connected with valve A and B of conventional system.

Figure 6 Conventional and EHS Steering System

The overview of steering room is illustrated in Figure 6. The EHS steering system is more efficient regarding size, weight, electric motor and oil tank volume in comparison with conventional steering system. Especially it understands that EHS steering system is excellent in term of slew rate. It would appear reasonable to assume that the cost of increasing the size and complexity of procurement of conventional system.

PERFORMANCE OF EHS STEERING SYSTEM

The authors carried out actual experiments aboard the training ship "SHIOJI MARU". Figure 6 shows the results of experiments of the batch adaptive MARCS. Figures on the left are the time series of ship course, roll rate, and rudder angle with the conventional steering system. Figures on the right are the time series of ship course, roll rate, and rudder angle with the EHS steering system.
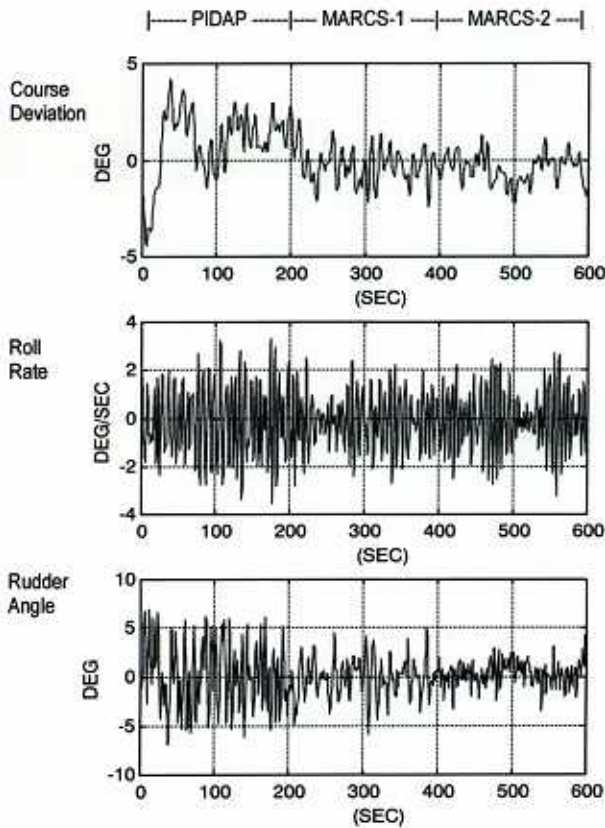
Conventional Steering System (Ju32)   EHS Steering System (Ju35)
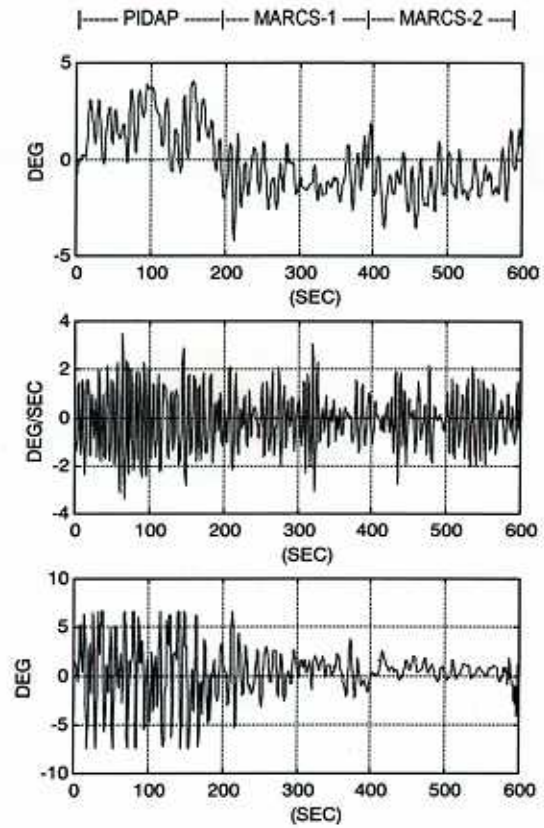
Figure 6 Results of Adaptive MARCS
【Conventional and EHS Steering System】

There are three batch periods, each of which length is 200(sec) and the sampling time is 1.0(sec). The first batch shows result of the digital PID-typed steering law with disturbance. Both the second and the third batch period are the results of the rudder roll stabilization steering with MARCS. The batch adaptive MARCS uses the optimal gains adapting MARX model, which are estimated from the former batch data [6][7].

Table 4 shows the variances of ship course, roll rate, rudder angle and reduction ratios. The reduction ratios of roll rate are calculated by ship's auto-pilot and MARCS-1, MARCS-2 in the batch adaptive MARCS.

The reduction in the case of using EHS steering system is larger than that in the case of the conventional steering gear.

According to Figure 7 and Table 4, the authors can conclude that:

a. The rolling in the case of the MARCS using EHS is reduced less than that in the case of the conventional one.

b. When the weight function changed, the roll rate is reduced and a change in rudder motion is occurred simultaneously.

Table 4 Results of full scale experiments

Test No	Control Mode	Ship Course (Variance)	Roll Rate (Variance)	Roll Rate Reduction(%)
Ju32 (Conventional)	PIDAP	3.178266	2.525148	——
	MARCS-1	0.885640	1.291034	48.87
	MARCS-2	0.547671	1.535240	39.20
Ju35 (DDVC)	PIDAP	1.907401	2.218735	——
	MARCS-1	1.100737	1.063286	52.07
	MARCS-2	1.166585	0.945265	55.67

CONCLUSIONS

This paper presents the various stages of the design and development of advanced rudder roll stabilization system based high slew rate steering system and adaptive control. The effectiveness of any roll stabilization system depends on the magnitude of stabilization moment that is applicable to the ship. In order to make the MARCS more effective, it is necessary to improve a slew rate (rudder speed) design.

First, this paper introduced a high slew rate steering system with EHS. The EHS steering system realizes the

slew rate over 10(deg/s). The EHS has the advantage to save energy consumption on average by over 80(%) in comparison with a conventional hydraulic steering system. It was reported that the EHS steering system reduced the noise level about 10(dB) in comparison with the conventional one.

Next, this paper presented the application of the batch adaptive control based on a locally stationary auto-regressive model. The advanced MARCS reduced the roll motion in average with 30~50(%) comparison with the conventional autopilot. Through these studies, it proved that the EHS steering system and batch adaptive MARCS have higher controllability than the conventional MARCS for the problem of reducing roll motion of ships with rudder control.

ACKNOWLEDGEMENTS

REFERNCES

1. H.Oda, K.0htsu, and T.Hotta
   Statistical Analysis and Design of a Rudder Roll Stabilization System. IFAC Control Eng. Practice, Vol.4. NO.3,1996.
2. H.Oda, KJgarashi, K.0htsu
   Simulation Study and Full Scale Experiment of Rudder Roll Stabilization System. llthSCSS,1996.
3. M.Ito, H.Sato, Y.Maeda
   Direct Drive Volume Control of Hydraulic System and its APplication to the Steering System of Ship. 5th Tech. Symp. on Fluid Control,1997.
4. K.0htsu, M.Horigome, G.Kitagawa
   A New Ship's Auto Pilot through a Stochastic'Model. Automatica, Vol.1, No.3, 1979.
5. H.Akaike
   On the use of a Linear Model for the Identification of Feedback systems. Ann. Inn. Statist. Math. Vol.20,1968.
6. T.Ozaki, H.Tong
   On the Fitting of NOn-Stationary Auto-regressive Models in Time Series Analysis. Proc. of 8th Hawaii Inter. Conference on System Science,1978.
7. K.0htsu, J.S.Park
   Batch Adaptive Rudder Roll Control System. J. Kansai Soc. N. A, Japan, NO.228,1997.

OS8-1

ENERGY SAVING MEANS AND EFFECT OF OIL HYDRAULIC UNIT FOR PRODUCTION MACHINE

Mitsuo KUBO

Department of Hydraulic Engineering, Essential Component Division
NACHI-FUJIKOSHI CORP.
3-2-1 Nakada, Toyamashi, Toyama, 931-8453 Japan
(E-mail: kubomi@nachi-fujikoshi.co.jp)

ABSTRACT

Environmental problems of global warming are common topics that relate to all people on the earth now. The effort of conservation of energy is already an obligation. The purpose is to reduce the amount of the CO_2 exhaust that occupies most of the heat-trapping gas that causes global warming. As for the oil hydraulic unit used for the production machine in the factory, the one of energy conservation or more is strongly requested.

In this paper, it proposes our two kinds of conservation of energy oil hydraulic units. After the problem for a current oil hydraulic unit is clarified, the applied technological means and the effect are shown with the application case such as machine tools and the press machines.

KEY WORDS

hydraulic power unit, electric power consumption, efficiency, trade-off

NOMENCLATURE

W : Electric power consumption [W]
N : Rotation speed [min-1]
T : Torque [Nm]
q : Displacement of Pump [cm^3/rev]
P : Pressure [MPa]
Q : Flow rate [l/min]
η_M : Motor efficiency
η_m : Mechanical efficiency of Pump
η_v : Volumetric efficiency of Pump

INTRODUCTION

Some of the chief merits of oil hydraulic system are it can output big power with compact system and easy force control - more precisely pressure control - . This grace enables a lot of hydraulic actuators to be widely used for the clamping device in machine tools.

Furthermore, a lot of hydraulic systems are used as driving system of the press machine that needs bigger power.

Now efforts to reduce the emission of the CO_2 which affects on global warming are made in the production machines of the factory. Therefore, the hydraulic equipment that decreases the consumption energy is needed in the production machine.

We have been working on developing and improving its hydraulic equipment that aims at Energy Saving, Safety, Compactness and High Quality. As for the hydraulic power unit, we take different energy saving means to each one, because all the required functions

differ depending on its usage. It is also because each acceptable cost is different according to how to use it.

This paper is organized as follows. In Section 2, power consumption of the hydraulic power unit is explained. In Section 3, a feature of usage in machine tools, past issues and best fit means to solve these issues are explained. Moreover, results which proved by actual applications are shown. In Section 4, same topics of the hydraulic power unit which mainly adopted by Press Machine are mentioned. Conclusions are summarized in Section 5.

Electric power consumption of the hydraulic power unit

Hydraulic power unit is constructed by Pump, Motor which drives the Pump and Tank. Now let's look at the electric power that the hydraulic power unit consumes.

Electric power consumption of Motor is below.

$$W = 2\pi \times N \times T / 60 / \eta_M \qquad (1)$$

And, the Torque needed for Pump is

$$T = q \times P / 2\pi / \eta_m \qquad (2)$$

Re-organizing equations (1) and (2), then electrical power consumed by the hydraulic power unit becomes equation (3).

$$W = N \times q \times P / (\eta_M \cdot \eta_m) \qquad (3)$$

On the other hand, flow rate discharged from the Pump is equation (4).

$$Q = q \times N / 1000 / \eta_v \qquad (4)$$

The role of hydraulic power unit is to supply the needed pressure (P) and flow rate (Q) according to the machine's movement.

What should be noted here is that the efficiency mentioned in equation (3) and (4) is not constant but is variable according to load condition and driving conditions.

It is difficult as a real problem, though it is an ideal to decrease the loss in all the areas to raising efficiency. Therefore, we paid attention to an actual way to use, and aimed at the efficiency improvement of the corresponding area. As a result, the consumption energy can be decreased while used actual.

Hydraulic power unit for machine tool

In the machine tool, the electric motor such as AC servo motor is used for the spindle and the table drive. These are axes that influence the processing accuracy directly. On the other hand, the hydraulic equipment is used for the part that supports work processing such as clamping and chucking. And, during the work processing, hydraulic unit is used in pressure keeping mode for a long time which doesn't require almost any flow rate Q.

Hydraulic power unit which equipped variable displacement pump is now generally used on machine tool. The pump is driven with an induction motor that turns in a constant rotation. However, the pump can reduce flow rate Q by reducing displacement q of the pump in equation (4).

Here, the problem and the improvement method are described about each of the pump and the electric motor that composes the hydraulic power unit. And, the operating method of the hydraulic power unit is similarly described.

Pumps

Volumetric efficiency η_v of the pump decreases by rising of pressure. This is because the amount of the leakage from internal sliding area increases.

In the variable displacement pump, displacement q becomes small when pressure is keeping. However, it is necessary to enlarge displacement q in equation (4) to keep pressure when the amount of an internal leakage is large. As a result, the electric power of equation (3) increases, too. Therefore, reducing the leakage contributes to the power consumption decrease.

On the other hand, it is understood that the mechanical friction increases when the leakage is decreased and mechanical efficiency η_m worsens.

Then, we did the design that took the trade-off of η_v and η_m so that the torque T of equation (2) might become small with pressure keeping mode.

Electric motors

A general electric motor is designed so that efficiency η_M at the load factor 100% may rise, and when the load factor lowers, becomes inefficient. The torque T is small in the variable displacement pump, while keeping pressure. So it will be used for a long time in the point where the electric motor efficiency is in a word low.

Then, even if some efficiency at the ratings load was sacrificed, the electric motor that improved efficiency in the point where the load factor was low was adopted.

Driving method

It is understood to be able to reduce power consumption by even reducing rotational speed N

from equation (3). In the variable displacement pump on keeping pressure, the pump axis input lowers as shown in Figure 1, when the rotational speed is lowered.
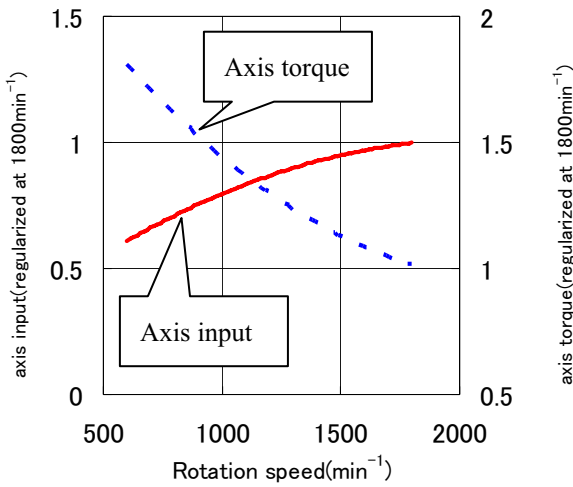
Figure 1 Pump axis input and torque

On the other hand, the efficiency η_M of the electric motor (driven by inverter) decreases oppositely when the rotational speed is lowered as shown in Figure 2, and efficiency changes in the same rotational speed according to the load torque.
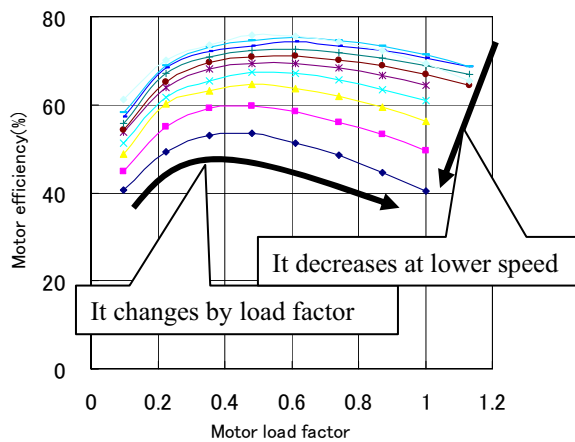
Figure 2 Motor efficiency

Although the user adds the inverter to an existing hydraulic power unit for saving energy, to lower the rotational speed, it is understood it is necessary not only to lower the rotational speed to do the best conservation of energy driving but also to make it to efficiency of the electric motor and the best rotational speed corresponding to the state of the load.

In the hydraulic power unit driven by inverter of Figure 3, the built-in controller calculates the load from the pressure sensor signal. And, it drives in the condition with better the entire efficiency.

The hydraulic power unit works by driving the variable displacement pump in a constant rotational speed. Or, the hydraulic power unit works by driving of changing the rotational speed the fixed displacement type pump by the inverter.

On the other hand, the hydraulic power unit of Figure 3 has two control degree of freedom of variable displacement of the pump and a changeable rotational speed. And, the control moved to an efficient operation point is done by using this one tedious degree of freedom.

Figure 3 Hydraulic power units driven by inverter
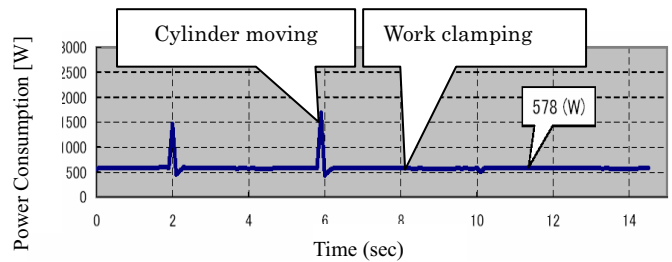
Figure 4 Power consumption of hydraulic unit (Conventional.)
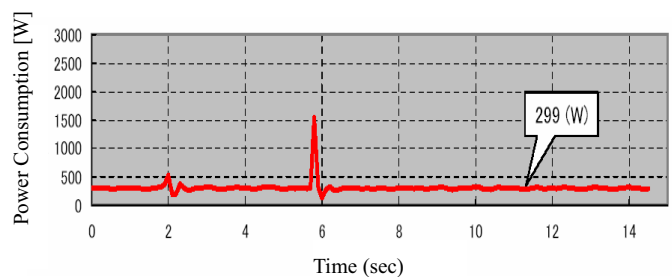
Figure 5 Power consumption of hydraulic unit (Driven by inverter)

Application and effect

The result of measuring the power consumption of the hydraulic power unit is shown in Figure 4 and Figure 5, in the machining centre where the hydraulic power unit

179

of conventional type and Figure 3 was installed.

The hydraulic power unit is used for clamping work, which electric motors are 2.2kW, flow rate at a no load is set to 28L/min, and the highest pressure is set to 6.0MPa. It is understood that most time is clamping work from the measurement result. The power consumption at this time is 578W in Figure 4, 299W in Figure 5, and it is decreased by about 48%.

Hydraulic power unit for press machine

The movement performance of the hydraulic actuator is related to the performance of the machine as it is in the press machine. Because it influences the processing accuracy of work, the hydraulic system with good control performance is requested. Moreover, a big difference with how with the machine tool to use it is that the hydraulic actuator works frequently.

Generally, the hydraulic power unit to which the variable displacement piston pump is driven with the induction motors is used. The movement direction switch and the speed control of the actuator are done with the valve. In this system, the pressure loss in the control valve is large. Within the range of the control, it is not good at control of a narrow, especially low side from about 1/10. Moreover, the electric motor keeps rotating when standing by, and the energy loss at this time is also large.

To solve these problems, the hydraulic system that drives both rotation piston pump with the AC servo motor has been commercialized. It is a system that does all the controls of pressure, the speed, and the position by only rotating the motor. And it can decrease the energy consumption that the pump operates only as for a necessary amount when it is necessary.

A fixed pump is used to avoid the complexity of the control without using the variable displacement pump.

The servo motor used with this system has the following feature. Efficiency is high from low speed to the high speed revolution. A torque that is even about 0 rotations bigger can be generated. Acceleration and the deceleration are made a high response, too. Thus, there are depend on the ability of the servo motor a lot of performances of this system.

On the other hand, the pump improved volumetric efficiency η_v when low-speed rotating. This is an important point to suppress pump rotational speed N low while keeping pressure.

In the vending machine of Figure 7[2], the positioning accuracy of each micron and a brilliant movement has been both achieved by combining the prefill circuit with this system. The comparison of power consumption with a past system is shown in Figure 8. Power consumption is decreased to about 1/4.

Figure 7 Vending machine
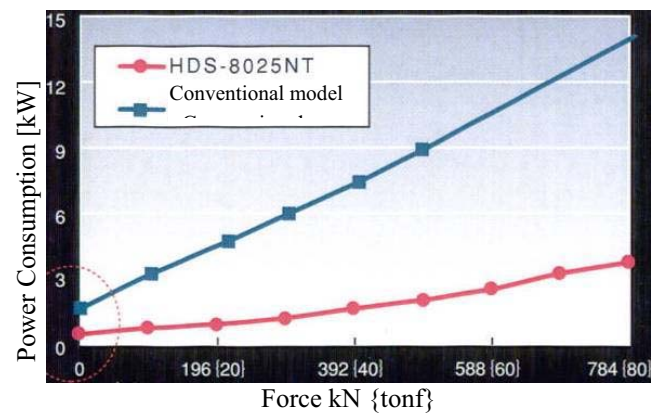
Figure 8 comparison of power consumption

CONCLUSION

We introduced two hydraulic power units for the machine tool and for the press machine that attempted conservation of energy. As for the system that uses the servo motor, the energy-saving effect is large though it costs. It is thought that application will increase in the future. Of course, this system is not a hydraulic system of almighty in the point of conservation of energy. It is necessary to be going to do the approach of the loss decrease of each equipment in the future, to ascertain an actual way to use, and to continue the approach that attempts conservation of energy in the effect.

REFERENCES
1. NACHI-FUJIKOSHI CORP., The hydraulic unit with variable displacement pump driven by inverter, Japan Machinery Federation, Outline of Excellence in Energy-Conserving equipments awarded in 2007 fiscal year, pp.46-49.
2. AMADA CO., LTD., Catalog of HDS NT series.

OS8-2

INTRODUCTION OF SERVO VALVE OF BOSCH REXROTH AND APPLICATION FOR TESTING MACHINE

Takahiro Urai

Industrial Application Engineering
Bosch Rexroth Corporation
5-1 Higashi-nakanuki Tsuchiura-shi, Ibaraki, 300-8588 Japan
(E-mail: takahiro.urai@boschrexroth.co.jp)

ABSTRACT

Bosch Rexroth (BR) has three categories control valves. One is the standard proportional valve, second is high response control valve and final one is servo valve. These three valves are applied to feed back control system for position, speed, force and acceleration. In this presentation, each valves design and performance are explained. And also applied applications for testing machine by Bosch Rexroth are introduced.
.

KEY WORDS

Servo control, Proportional valve, High response valve, Servo valve

COTROL VALVE CATEGORIES

Proportional valves

Many controls would hardly be conceivable without proportional valves with integral electronics (OBE). They reduce the cabling effort and simplify handling while offering exact reproducibility and low manufacturing tolerances.
-Performance profile
 < Pressure and flow control and directional valve variants in sizes 6 to 52
 < Maximum flow 2800 L/min
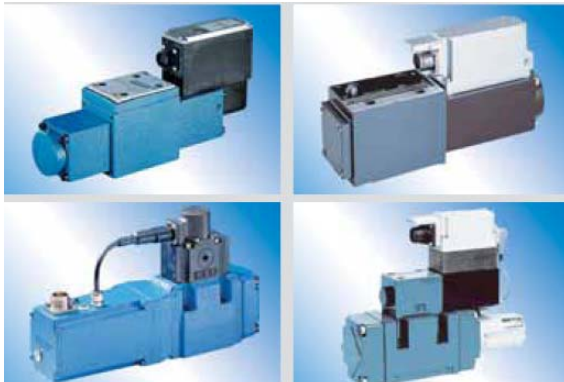
Figure 1   High response valve

Maximum operating pressure 350 bar
< Proportional solenoid with electrical closed-loop position control for high accuracies (> 1 %)
< Rugged electronics for stationary and mobile applications

High-response valves

High-response valves are compact and robust. They are convincing in their high dynamics and control accuracy. The core product of size 6 and size 10 can be combined with main stages of up to size 160 with a nominal flow of up to 18000 liters.
-Performance profile
 < Maximum flow 50000 L/min
 < Maximum operating pressure 420 bar
 < Sizes 6 to 160
 < Highly dynamic valves with zero overlap for use in closed control loops
 < Direct and pilot operated
 < For subplate mounting and block installation

Servo-valves

Servo-valves are hydraulically pilot operated 2- or 3-stage directional valves with porting pattern to DIN 24340 form A. They are mainly used for closed loop-controls of position, force or pressure and velocity.
They are characterized by:
– Compact build

– Low electrical power consumption
– High dynamics and
– Excellent quasi-steady-state values
-Performance profile
   < Maximum flow 1600 L/min
   < Maximum operating pressure 315 bar
   < Sizes 6 to 32

Figure 2   Servo valve

Cartridge Servo-valves
This is high response cartridge valve operated by pilot servo valve. Two way and three way is available. High flow and high response closed control is achieved.
-Performance profile
   < Size 32 to 160, Maximum flow 17,000 L/min
   < very short switching times, low hysteresis
   < Integrated control electronics type available

Figure 3   Cartridge servo valves

APPLICATION EXAMPLE

Testing equipment
Testing equipment for testing the durability of vehicles has a modular structure. The use of standardized subassemblies combined with intelligent engineering yields individual concepts, which can be integrated in the individual testing equipment in the form of self-contained overall systems.

Testing of functions and components
With the testing rigs in the form either of testing function rigs for hydraulic components/vehicle components or of testing component rigs for testing the durability of vehicle components, weak points are identified and eliminated, and product quality is documented.

Figure 4   Testing machine

Central hydraulic power station
Typical test centers of car manufacturers and OEM car part suppliers need to supply a wide range of hydraulic actuators of different testing and simulation equipment. For this purpose it is of high advantage to install a central hydraulic power station with a programmable controller to control the pressure supply. This comprises in house pipe work with a pressure, tank and leakage oil line, the shut-off valves and monitoring sensors.

Inverse crash facilities
The automotive industry continuously is facing demands for tougher safety standards which has been compelled to build high-precision test equipment. Real and inverse crash facilities are the answer to this question. They are used in the laboratory to investigate accident situations to get information about the passive safety of the vehicle and its components.

By converting deceleration into acceleration, it is possible to simulate a situation from standstill which would occur due to collision with an obstacle at high speed. Outstanding advantage is that the specimen does not get destroyed and the test can be performed several times for little costs to the user.

Figure 5   Inverse crash facilities

OS8-3

APPLICATIONS WITH A NEW 6-DOF BENDING MACHINE IN TUBE FORMING PROCESSES

Hiroyuki GOTO*, Ken ICHIRYU**, Hidenobu SAITO**, Yuu ISHIKURA**,
and Yutaka TANAKA***

* Technical Research Institute, Japan Society for the Promotion of Machine Industry
1-1-12- Hachiman-cho, Higashikurume-shi, Tokyo, 203-0042 Japan
(E-mail: goto@tri.jspmi.or.jp)
** Kikuchi Seisakusho
2161 Miyama-cho, Hachioji -shi, Tokyo, 192-0152 Japan
*** Faculty of Engineering & Design, Hosei University
2-17-1 Fujimi, Chiyoda-ku, Tokyo, 102-8160 Japan

ABSTRACT

This research presents a new flexible bending machine and its practical applications. The proposed machine uses a new method. When tubes are fed into the fixed and mobile dies, they are bent by shifting the relative position of the mobile die. The bending radius is controlled by the relative distance and orientation between the mobile die and the tube. The bending angle is controlled by the length of the fed tube. This forming process has a big advantage. A change of the expected bending shape will need no change in the tooling system but only a new definition of the motion of the active die and the length of the fed tube. The active die movements are controlled by a 6-DOF parallel kinematics mechanism (PKM) with hydraulic servo drive. Making use of the PKM serves not only to achieve a complete motion along six axes but also to obtain a high dynamic motion of the bending machine. Application examples show that the bending machine can be applied to designer's interiors, universal designed products, and automotive parts. Until now these processes have been difficult to achieve using a conventional bending machine.

KEY WORDS

Parallel kinematics mechanism, Hexapod, Hydraulic servo, Tube forming, Free-form bending,

NOMENCLATURE

R	:	Bend radius.
u	:	Offset .. .
L	:	Distance between dies...
F	:	Working load.
F_p	:	Pushing load.
α, β, γ	:	Euler angle of a moving die.
P	:	Point located at the canter of a moving platform.
O	:	Origin of the fixed platform.
A_i	:	i th ball point on the fixed base.
B_i	:	i th ball point on the moving platform.
$\mathbf{P}$	:	Position vector of a point P with respect to origin of the fixed platform.
$\mathbf{a}_i, \mathbf{b}_i$	:	the position vectors of points A_i and B_i.
$^A R_B$	:	Rotation matrix that describes the orientation of frame B with respect to frame A.
$\mathbf{u}, \mathbf{v}, \mathbf{w}$	:	Unit vector pointing along the u,v,w-axis of a moving frame.

INTRODUCTION

Bent tube products are employed in manufacturing many kinds of products such as fluid arrangements, furniture, transport apparatus, and mechanical parts, as required for reduction of production cost and weight.

For basic bending methods of tubes, (1) rotary-draw bending, (2) press bending, and (3) roll bending, have been commonly used. The rotary-draw bending is the most standard method used on rotary-type bending machines, which can be powered, manual, or numerically controlled. The draw bending consists of the rotating bending form, clamping die, and pressure die. The workpiece is secured to the bending form by a clamping die. As the bending die rotates, it draws the workpiece against the pressure die. These machines handle about 95% of tube bending operations [1]. The press bending method uses simple tooling and is quick and easy to set up. The major advantage of press bending is its high production capabilities but it has less accuracy. Roll benders use the basic principal of force applied between three rotating rolls. The material enters the rolls and roll pressure causes it to yield on the underside of the center roll.

Besides these conventional techniques, a new flexible CNC bending machine which is based on the MOS bending method [2] has been developed. MOS bending is a versatile and flexible method for a free-form circular tube. However, this method can not bend a square or rectangular tube. For the hydroforming of space frame components, there are the increasing needs for three-dimensional free-form bending profiles of non-circular tubes.

This paper, therefore, presents a new flexible bending machine for non-circular tubes and profiles that are difficult to bend using conventional bending machines.

BASIC CONCEPT

The applied basic concept [3] is shown in Figure 1. Two tooling dies are used for the bending process. One is fixed and the other one is actively moved forming the part to be bent. Both dies are shaped in accordance with the outside shape and parameters of the tube or profile. The tube or profile is pushed through the fixed die and is bent by the motion of the mobile die. Pusher movement and movement of the mobile die are synchronized. When the tubes are fed into the fixed and mobile die, they are bent by shifting the relative position of the tube. The bending radius R is controlled by the relative distance between the die and the tube. The bending angle is controlled by the length of fed tube.

This forming process has a big advantage. A change of the expected bending shape will need no change in the tooling system but only a new definition of the motion
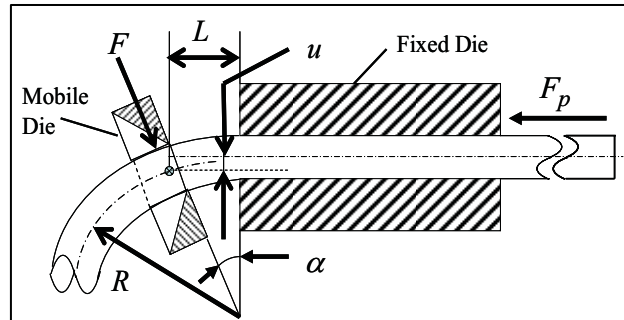
Figure 1 Basic concept
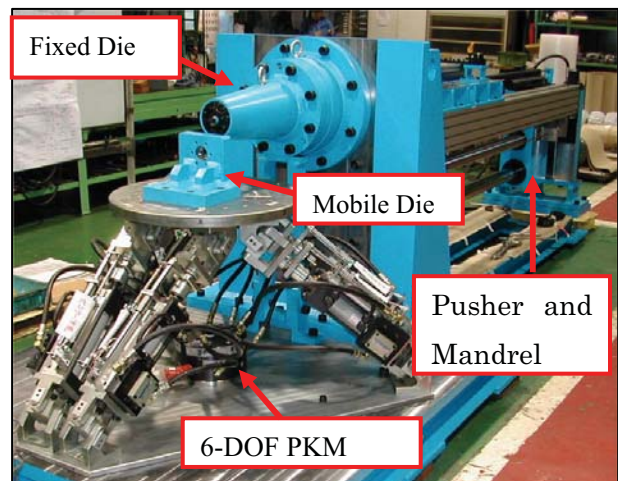
Figure 2 The proposed bending machine

of the active die and synchronization of the pusher.

MACHINE STRUCTURE AND DESIGN

Figure 2 shows the schematic of the proposed bending machine. This machine consists of a mobile die with a 6-DOF parallel kinematics mechanism, a fixed die, a pusher and a mandrel.

Mobile Die and 6-DOF PKM

The active die movements are controlled by a 6-DOF parallel kinematics mechanism (PKM). Making use of the PKM serves not only to achieve a complete motion along six axes but also to obtain a high dynamical motion of the bending machine.

Fixed Die

The mounting carries the rigid fixed die and must absorb the press force in conjunction with the frame components.

Pusher

The feeding or pusher module creates a controlled feeding motion of the workpiece in the bending zone to generate the bending geometry. The feeding motion is defined as a function of the corresponding forming procedure. The pusher is driven by a hydraulic servo

motor. The rotary motion is transformed into a translation one upon a ball screw. Within this module, feed forces up to 40kN and positioning accuracy of ±0.1mm can be achieved in this machine. In the prototype bending machine, profiles up to a length of 2300mm can be formed. In order to avoid buckling risk, the profile runs through a conduit which completely encapsulates it. This conduit depends upon the profile's cross-section and must be changed for another profile cross-section. The conduit is split into a right and left box in conjunction with an automatic profile feeding module. The conduit can be opened manually.

Mandrel

The mandrel is a tool inserted in a tube or pipe in the region of the bend tangent. This tool is not only to diminish the risk of buckling, but also to reduce wall thickness alterations, distortion and torsion of the cross-section. On the proposed machine, the mandrel is attached to a rod anchored at the rear of the machine. The rod incorporates lateral and longitudinal adjustment capability to position the mandrel in relation to the bend radius and at the point of the bend.

KINEMATIC MODELING

Figure 3 and 4 show this 6-DOF PKM known as a Stewart-Gough platform [4]. Six identical limbs connect the moving platform to the fixed based by spherical joints B_i and A_i, $i = 1,2,...,6$, respectively. Each limb consists of an upper member and lower member connected by a prismatic joint. Ball screws can be used to vary the lengths of the prismatic joints and therefore to control the location of the moving platform. For the purpose of analysis, two Cartesian coordinate systems, frames $A(x,y,z)$ and $B(u,v,w)$ as shown in Fig.4, are attached to the fixed based and moving platform, respectively. The transformation from the moving platform to the fixed base can be described by the position vector $\mathbf{p}$ of the centered P and the rotation matrix $^A R_B$ of the moving platform. Let $\mathbf{u}$, $\mathbf{v}$ and $\mathbf{w}$ be three unit vectors defined along the u , v and w axes of the moving coordinate system; then the rotation matrix can be written as:

$$^A R_B = \begin{bmatrix} u_x & v_x & w_x \\ u_y & v_y & w_y \\ u_z & v_z & w_z \end{bmatrix} \tag{1}$$

As shown Fig.4, let $\mathbf{a}_i = \left[a_{ix}, a_{iy}, a_{iz} \right]^T$ and $\mathbf{b}_i = \left[b_{iu}, b_{iv}, b_{iw} \right]^T$ be the position vectors of points A_i and B_i, respectively. We can write a vector-loop equation for the th limb of the manipulator as follows:
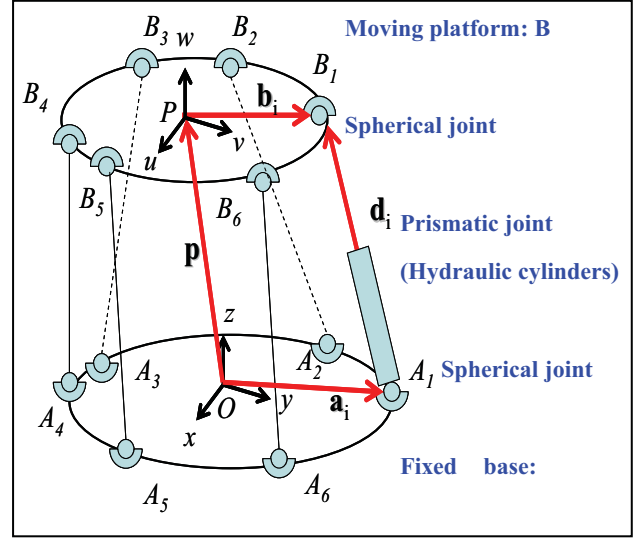
Figure 3 Kinematic modeling (Stewart-Gough platform)

$$\overline{A_i B_i} = \mathbf{p} + {}^A R_B \mathbf{b}_i - \mathbf{a}_i \tag{2}$$

The length of the i th limb is obtained by taking the dot product of the vector with itself:

$$d_i^2 = \mathbf{p}^T \mathbf{p} + \left[\mathbf{b}_i \right]^T \left[\mathbf{b}_i \right] + \mathbf{a}_i^T \mathbf{a}_i$$
$$+ 2\mathbf{p}^T \left[{}^A R_B \mathbf{b}_i \right] - 2\mathbf{p}^T \mathbf{a}_i - 2\left[{}^A R_B \mathbf{b}_i \right]^T - \mathbf{a}_i \tag{3}$$

where d_i denotes the length of the i th limb. Taking the square root of Eq. (3) we obtain:

$$d_i = \pm \left[\mathbf{p}^T \mathbf{p} + \left[\mathbf{b}_i \right]^T \left[\mathbf{b}_i \right] + \mathbf{a}_i^T \mathbf{a}_i \right.$$
$$\left. + 2\mathbf{p}^T \left[{}^A R_B \mathbf{b}_i \right] - 2\mathbf{p}^T \mathbf{a}_i - 2\left[{}^A R_B \mathbf{b}_i \right]^T - \mathbf{a}_i \right]^{1/2} \tag{4}$$

for $i = 1,2,...,6$. Hence, corresponding to each given location of the moving platform, there are generally two possible solutions for each limb. However, a negative limb length is physically not feasible. When the solution of becomes a complex number, the location of the moving platform is not reachable.

CONTROL SYSTEM

PKM with six degrees of freedom using six electro hydraulic servo cylinders has large rigidity and support power. This feature is widely used for a driving device with multi degrees of freedom that has a heavy load and needs a large driving force. These hydraulic PKM focusing on major acceleration forces are flight simulators, which requires a high degree of dynamics in
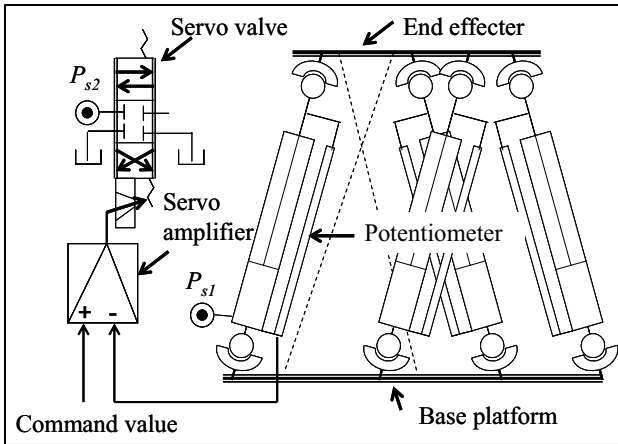
Figure 4 Hydraulic control system

their guidance behavior. On the other hand, for hydraulic PKM in the bending machine, the focus is on high positioning accuracy and load rigidity. Figure 4 shows the electro hydraulic servo control system for the proposed bending machine.

EXPERIMENTS

Basic Bending

In order to evaluate the performance of the proposed bending machine, basic bending was performed. Figure 5 ,6 and 7 show an overview of the basic bending.

The bending radius R of the tube is decided by the magnitude of offset u. The relationship between the offsets u and the bending curvature $1/R$ is shown in Figure 8 as a parameter of material shapes. The relationships can be obtained by bending experiments. The flexural rigidity, Young's modulus and other material properties vary with changes of materials and dimensions of the tubes. Therefore, the bending radius R fluctuates even though the offset u does not change. But this bending machine can bend the tubular workpiece into a certain bending radius by adopting a suitable relationship of u and R for the tube, even though the tubular material or dimensions change.

APPLICATIONS

Experimental results show that the bending machine can be applied to many kinds of products such as furniture, universal designed products, and automotive parts. Until now these manufacturing processes have been difficult to achieve using a conventional bending machine.

The designer interior

The new bending machine has no limit for the designers' request about shapes as compared with the conventional bending machine. Therefore, designers can display their ability to create a new design concept.

Figure 5 Results of the square tube bending (aluminum)

Figure 6 Results of the circular tube bending (aluminum)

Figure 7 Result of the circular tube bending (steel)
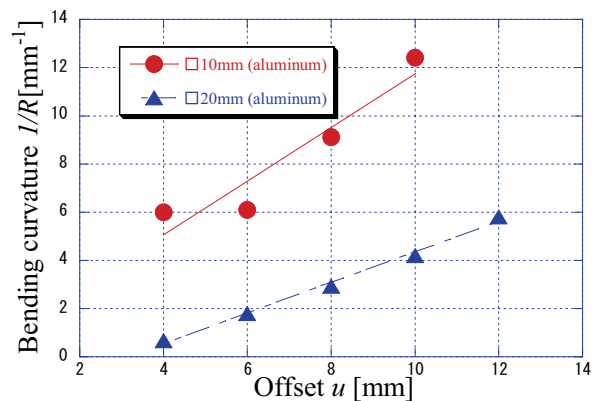
Figure 8 Relationships between u and $1/R$

Figure 9 The sketch of "STROKE vase"

Figure 10 the vase production

Figure 11 "STROKE vase"

Figure 12 The design of a handrail

Figure 13 The handrail with universal design

Figure 9,10 and 11 shows the designers' image sketch and the vase product as an example.

Universal Design

The human body has very complex and three dimensional shapes. Therefore, the medical equipment's parts such as a handrail should be made to fit for the complex and three dimensional human body shapes. When the handrail is made by a conventional bending machine, the bending process is very difficult and many days are needed for preparing the dies. But, if the new bending machine is used, the complex shaped handrail can be easily produced after a little trial bending.

Extrusion bending

Bent thin-walled aluminum extrusions (see Figure 14) have great potential for automotive parts. However, extrusion bending process has been difficult to achieve using a conventional bending machine. Figure 15 and 16 show the results of extrusion bending. Experimental results show that the bending machine can be applied to extrusion bending process.

Figure 14 An aluminum extrusion

Figure 15 An example of the extrusion bending
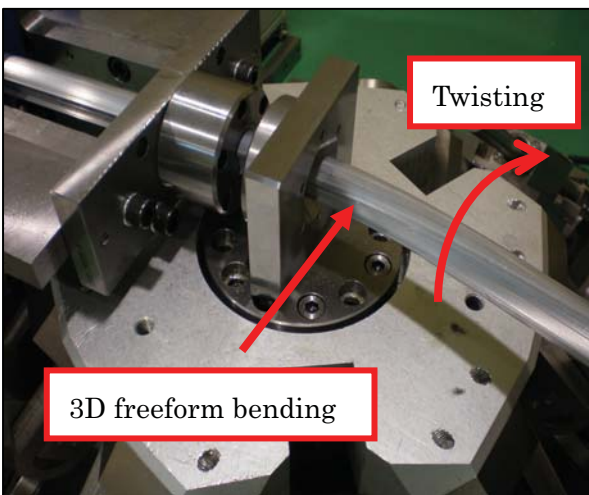
Figure 16 An example of the extrusion bending process

CONCLUSION

In this paper, a new flexible bending machine for tubes and profiles that are difficult to bend using a conventional bending machine was proposed. This system utilized the 6-DOF PKM as a controlling mobile die. The geometrical relationship between the moving platform and the length of six limbs of the PKM were formulated. The electro hydraulic servo control system for the bending machine was also proposed. The hydraulic PKM has been focusing on high positioning accuracy and load rigidity. Experimental results show that the bending machine can be applied to designer's interiors, universal designed products, and automotive parts. Until now this process has been difficult to achieve using a conventional bending machine.

ACKNOWLEDGEMENTS

REFERENCES

1. G.Miller, Tube Forming Processes: A Comprehensive Guide, 2003, Soc. Manuf. Eng., Michigan, pp.72.
2. S.Murata: Effects of Die and Material of Circular Tube in MOS Bending Method (in Japanese), Trans. of Japan Soc. Mech. Eng. Series C, Vol.62, No.601, 1996, pp. 292-297.
3. H.Goto, K.Ichiryu, Y.Tanaka: Development of a New Versatile Tube Bending Machine Using 6-DOF Parallel Kinematics, Proceedings of the 4th International Conference on Leading Edge Manufacturing in 21st Century (LEM21), 2007, pp.465-468
4. Lung-Wen TSAI, Robot Analysis: The Mechanics of Serial and Parallel Manipulators, 1999, John Wiley & Sons Inc. New York, pp.151-154.

OS8-4

DEVELOPMENT OF HYDRAULIC LOAD SIMULATOR FOR FORCE CONTROL WITH HIGH PRECISION

Kyoung Kwan AHN[*], Dinh Quang TRUONG[**], Ho Triet HUNG[**] and Jong Il Yoon[**]

[*] School of Mechanical and Automotive Engineering
University of Ulsan
San 29, Mugo 2 dong, Nam-gu, Ulsan 680-749, Republic of Korea
(E-mail: kkahn@ulsan.ac.kr)
[**] Graduate school of Mechanical and Automotive Engineering
University of Ulsan
San 29, Mugo 2 dong, Nam-gu, Ulsan 680-749, Republic of Korea
(E-mail: truongdq@mail.ulsan.ac.kr)

ABSTRACT

Nowadays, hydraulic actuators play an important role in a modern industry where controlled force or position with high accuracy is the most significant demand. This paper presents a new kind of hydraulic load simulator (HLS) for conducting performance and stability test in the bench system where force control is important. The system model consists of a hybrid hydro-electric actuator and another hydraulic circuit generating disturbances. For the purpose of improving force control performance of hybrid systems, a robust force controller using Quantitative Feedback Theory (QFT) technique applied to the HLS is also proposed in this paper. The controller is designed to satisfy the robust performance requirement, tracking performance specification, and disturbance attenuation despite uncertainties of HLS. Experiments are carried out to evaluate the effectiveness of the proposed control method applied for hydraulic systems even in the large varying perturbation.

KEY WORDS

Key words: Hydraulic system; Force control; Quantitative feedback theory (QFT)

NOMENCLATURE

$P(s)$: Transfer function of the nonlinear plants
$G(s)$: Cascade compensator - Controller
$F(s)$: Input filter transfer function
$y(t)$: Plant output
$r(t)$: Command input
V, D : Disturbances
$T(s)$: Closed-loop transfer function
$L(s)$: Opened-loop transfer function
$Dis(t)$: Disturbance source

ω : Frequency

INTRODUCTION

Hybrid actuation systems have a wide range of applications because of their advantages such as durability, high power, controllability, accuracy, reliability, etc ... To improve the stability and performance of the hybrid actuators, especially in dynamic loading process with unknown disturbances, some kinds of load simulator systems were presented. Su and Wang [1] presented a new kind of electro-hydraulic load simulator with high precision. The experiment results showed the effect on the way how to eliminate or reduce the disturbance torque and improve control performances of loading system. Li [2]

189

carried out the thorough analysis and research on torque load simulator using electro-hydraulic servo control. However the control problem is very complicated because of the dynamic characteristics of the hydraulic load actuation systems are basically nonlinear and uncertain. The nonlinearities and uncertainties mainly come from the unstableness of some hydraulic parameters such as bulk modulus, compressibility of oil or viscosity of oil.

The Quantitative Feedback Theory (QFT) is ideally suited to feedback design for systems with large parameter uncertainties. The concept was first introduced by Horowitz in the early 1960s and continuously developed by him and others into an efficient robust control design technique [3]. QFT technique has been successfully applied to solve many engineering problems, including robot position control, flight control actuators and manufacturing systems. In improving performance of variable-displacement hydraulic vane pump, Thompson and Kremer [4] developed a robust controller via QFT technique. The simulation results showed that the closed-loop system response remained stable under variation in fluid bulk modulus and linkage areas parameters. Niksefat and Sepehri [5] succeeded in using nonlinear QFT technique to design a robust force controller and overcame many of nonlinearities and uncertainties existed in the experimental industrial hydraulic actuators.

This paper proposes a new testing model of hybrid actuator – hydraulic load simulator (HLS) which contains a hybrid hydraulic-electric actuator and a disturbance generator. Moreover, a robust force controller is also designed for the (HLS) using QFT technique. Therefore, it contains two parts: derivation of a nominal plant model with the uncertain bounds for HLS dynamics and a force control loop design based QFT. The controller is designed to satisfy the robust performance requirement, tracking performance specification, and disturbance attenuation requirement.

EXPERIMENTAL APPARATUS

The schematic diagram of the new HLS is shown in Fig. 1. The system hardware consists of a hybrid hydraulic-electric actuator, a computer included PCI-bus multifunction cards and another hydraulic circuit generating disturbances simulating the noises in the hydraulic hybrid systems. In this model, the hybrid hydraulic-electric actuator is an intelligent hydraulic system. This is a combination of AC servo motor (SGMGH-30PCA21), piston pump, reservoir and hydraulic control circuit. The operation at the speed which meets the machine requirements (flow rate and pressure) reduces power loss, and provides energy savings. The pressure oil line from the pump without a control valve minimizes the pressure loss and substantially reduces the heat generation of hydraulic

fluid. About the operation of the hybrid actuator, the bidirectional rotational pump is used and driven by the AC servo motor so that the pump can supply pressured oil in both directions. The pump is well equipped as a hydraulic driving force. With the servo drive, the digital control parameter setting facilitates the operation of the system and its maintenance. In addition, to prove the effectiveness of the presented control method when the system operates in the real conditions, another hydraulic-electric circuit is applied for generating disturbance which is a combination of band-limited white noises and a sine wave noise. The simulink interface with compatible PCI cards is used to supply the noise signal for the AC servo motor (FMA-KN55), through a hydraulic control circuit and piston to generate the perturbation environment. A compression spring with 519 kN/m stiffness is used to connect the hybrid actuator and the disturbance generator. A load cell (YG38-T5) is used for obtaining the feedback force signal. The setting parameters for the HLS system are as shown in Table 1.

In the control strategy of the hybrid hydraulic-electric actuator, the deviation between the reference input signal and the force sensor signal is measured on the PC. Here, the proposed controller processes the data inputs and the control signal is sent from the PC to the servo drive to drive the AC servo motor (SGMGH-30PCA21) by using PCI cards, consequently forming a feedback control loop.
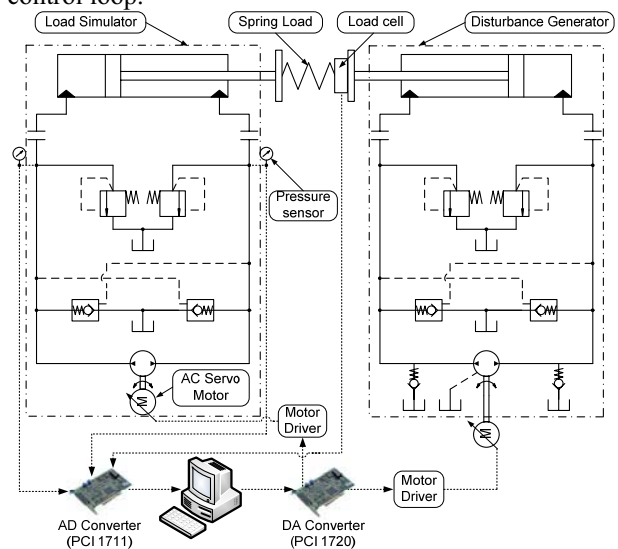
Figure 1 Schematic diagram of HLS

Table 1 Setting parameter for HLS System

| System parameters | Parts | | Meaning |
	Load simulator	Disturbance generation	
AC Servo Motor	200	200	Power supply (Volt)
	2.5	2.2	Power (kW)

	18.6	26.18	Rate torque (Nm)
Pump	2500	2200	Speed (rpm)
	15	10	Displacement (cc/rev)
M (kg)	1000		Load
Cylinder param eters	63 x 35 x 150	55 x 35 x 100	Piston diameter x Rod diameter x Length of stroke (mm)
Spring (kN/m)	519		Environment stiffness
Relief Pressure (bar)	175		Relief valve cracking pressure

A PC (AMD Athlon 1.9 GHz) included two PCI-bus data acquisition & control cards (Advantech cards, PCI 1711 and PCI 1720) is used to receive, process feedback signals and generate the output signals to control the motors. The control algorithm is built within Simulink environment combined with Real-time Windows Target Toolbox of Matlab. Fig. 2 displays the experimental apparatus.
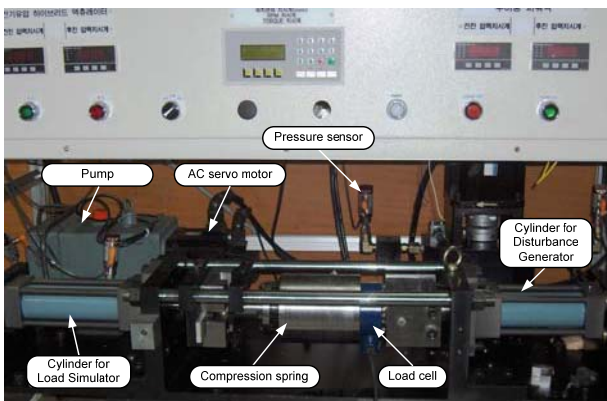
Figure 2 Photograph of HLS system

ROBUST CONTROLLER DESIGN

Quantitative Feedback Theory (QFT) is a unified theory that designs and implements robust control for a system with structure parametric uncertainty to satisfy the desired performance specifications, even when faced with the presence of disturbance, noise amplification or resonance.

The QFT method proposes as a general control strategy the two of freedom structure presented in Fig. 3. The output y(t) is required to track the command input r(t) and reject disturbances.
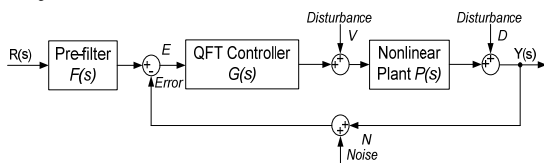
Figure 3 Structure of QFT algorithm

The controller $G(s)$ is to be designed so that the variation of $y(t)$ resulting from nonlinear plant uncertainties is within allowable tolerances and that the effects of the disturbances of $y(t)$ are acceptably small. Also, the filter $F(s)$ must be designed to achieve the desired tracking close-loop control ratio.

Model Identification

For the purpose of controller design, the derivation of linear time-invariant equivalent models is necessary. The first step in designing a robust QFT controller is thus to derive a family of uncertainties of the plant transfer function. An equivalent family of plants can be derived analytically, numerically from a plant model or directly from plant experimental input-output data.

In this study, a family of linear time invariant transfer functions for the HLS is obtained from experimental frequency responses of the system in the presence of significant uncertainty. Experimental frequency responses to a square input signal are carried out. The input signal is supplied to the driver of the AC servo motor in the load simulator part and then makes the cylinder impact on the spring-load sensing. Moreover, the maximum impact force to the load cell is 5 tonf. Therefore to avoid the damage to the load cell, the amplitude of the input signal is set to ± 4.2 V at which the acting force to the load sensing measured is more than 4 tonf.

In the identification process, the experiment was done many times to obtain the gathering of the input and output data. To identify a family of uncertainties of the plant transfer function, the estimation of simple process models in MATLAB was used with the sampling time is 0.01s.

One sample experimental result is shown in Fig. 4. This result corresponds to the case when the maximum allowable control signal is applied to AC servo driver. As shown in the upper part of Fig. 4, the simulation and experiment results closely agree.
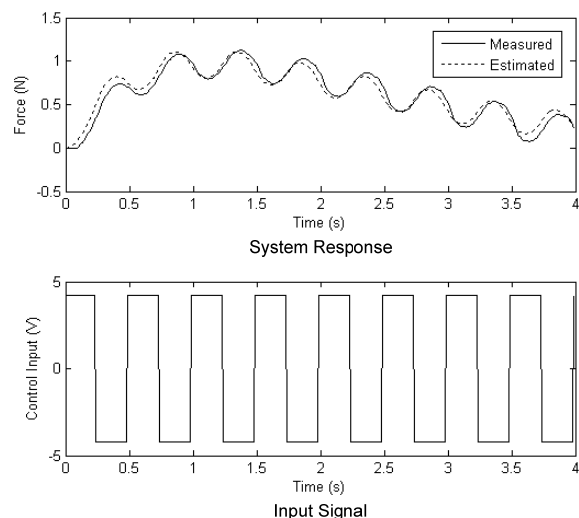
Figure 4 Identification of the system model

The HLS system can be presented by a family of second-order transfer functions as followings:

$$P(s) = \frac{k}{(1+as)(1+bs)} \quad (1)$$

here $k \in [3.97, 6.81]$; $a \in [0.75, 1.16]$; $b \in [0.75, 1.16]$;

QFT Controller Synthesis

The objective of this section is to design a robust force controller for the HLS that is represented by the uncertainty transfer function (1). In QFT, for tracking performance requirement, the strictly proper controller, $G(s)$, and a strictly proper pre-filter, $F(s)$, (Fig. 3) are to be designed base upon the stability and system performance's specifications. In this case, the HLS system should fulfil the following control criterions:

- Settling time = 1.5 [s]
- Maximum percentage of overshoot $\leq 2 [\%]$

In the case study, the bounds for tracking specifications correspond to the trajectory defined by the responses to the step input. The time responses $y_u(t)$ and $y_l(t)$ in Fig. 5 represent the upper and lower bounds, respectively. For a satisfactory design, an acceptable response $y(t)$ must lie between these bounds. The modeling of a desired transmittance $T(s)$ is discussed in detail by Horowitz [3].

After using an iteration process to find acceptable models, we have the following T_l and T_u functions:

$$T_u(s) = \left| \frac{3479s^2 + 6.737e004s + 2.384e005}{s^4 + 94.04s^3 + 5220s^2 + 7.017e004s + 2.396e005} \right| \quad (2)$$

$$T_l(s) = \left| \frac{26.54s^2 + 74.82s + 46.68}{s^4 + 17.67s^3 + 64.28s^2 + 96.76s + 47.11} \right|$$
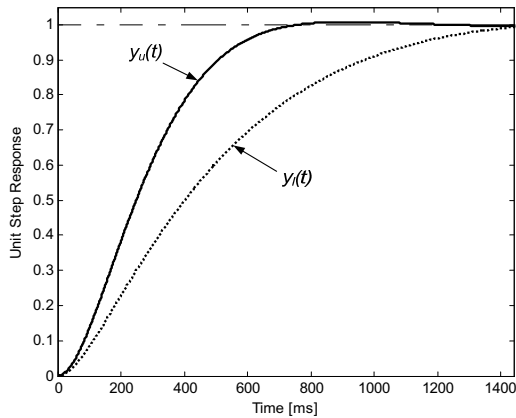
Figure 5 Tracking bounds in the time domains

Therefore, the QFT force control loop of the HLS system is designed how the signal robust tracking meet the acceptable range of variation with respect to a reference signal as follows:

$$\left| T_l(j\omega) \right| \leq \left| T(j\omega) \right| \leq \left| T_u(j\omega) \right|, \quad \omega \geq 0 \quad (3)$$

where $T(s)$ is the closed-loop transfer function:

$$T(s) = \frac{F(s)G(s)P(s)}{1 + G(s)P(s)} \quad (4)$$

In QFT approach, there are two control objectives. The first is the closed-loop robust stability which must be checked with reasonable margins. By the Nyquist criterion, closed-loop stability is retained as long as the loop gain does not cross the point -1 under uncertainty. The robust stability is presented by a forbidden region about the origin which is enclosed by an M-locus in the Nichols chart. Hence, an approximately of $M = 1.4$ (3 dB) gain margin for the closed-loop system is given by:

$$\left| \frac{L(j\omega)}{1 + L(j\omega)} \right| \leq M = 1.4, \quad \omega \geq 0 \quad (5)$$

where $L(s)$, the opened-loop transfer function, is defined

$$L(s) = P(s)G(s) \quad (6)$$

The second control objective is closed-loop disturbance attenuation. For disturbance rejection at plant output, the sensitive reduction problem has to be solved. Therefore, the upper tolerance is imposed on the sensitive function. Here, a constant upper bound to limit the peak value of disturbance amplification is considered as follows:

$$\left| \frac{1}{1 + L(j\omega)} \right|_{max} \leq M_D(\omega) = 1.2, \quad \omega \geq 0 \quad (7)$$

Inequalities (3), (5) and (7) impose constraints on nominal loop gain $\left| L_0(s) \right|$ (where $L_0(s) = P_0(s)G(s)$, and $P_0(s)$ denotes the nominal plant transfer function). These constraints are used to determine the tracking performance, robustness and output disturbance rejection boundaries on the Nichol chart at each critical frequency as $\omega = 0.01; 0.05; 0.1; 0.5; 1.5; 5; 10; 50; 100$ rad/s. A feedback design satisfies these bounds if for each critical frequency the corresponding value of the loop gain is on or above the performance boundary, output disturbance boundary and to the right of or on the robustness forbidden region.
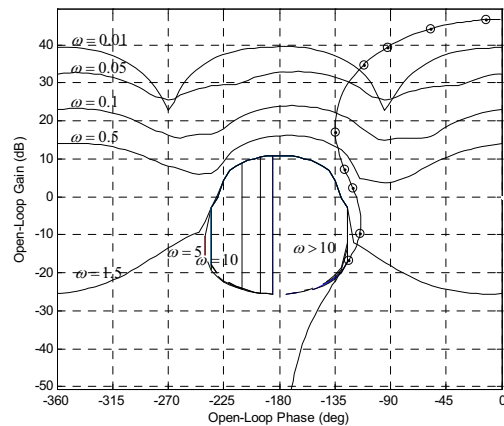
Figure 6 Superposition of all bounds

a) Robust tracking performance without filter

b) Robust tracking performance with filter F(s)
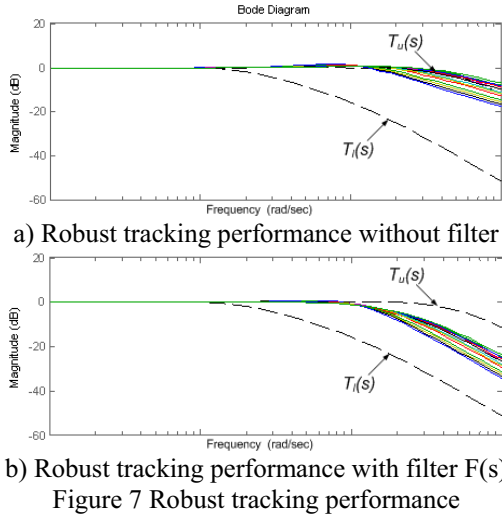
Figure 7 Robust tracking performance

The generated QFT bounds (by constrains (3), (5) and (7)) and the final loop shaping for the HLS are shown in Fig. 6. Based on the above analysis, the QFT robust controller is determined:

$$G(s) = \frac{621150.4154(s+7.528)}{s^2 + 583.7s + 1.475e005} \quad (8)$$

The final step in QFT design process is the selection of the pre-filter $F(s)$. Design of a proper function $L_o(s)$ guarantees only that the variation in $|T(j\omega)|$ is less than or equal to its constraint (3).

Fig. 7.a shows the closed-loop frequency response of the HLS system not lay between the upper and the lower tracking performance boundaries of $T_l(j\omega)$ and $T_u(j\omega)$. Therefore, the purpose of the pre-filter is to position $\ln T(j\omega)$ within the frequency domain specifications. The pre-filter was found:

$$F(s) = \frac{14.0425}{s+14.45} \quad (9)$$

The effect of the pre-filter is illustrated by comparing closed-loop frequency response both with and without a pre-filter. From Fig. 7, it is clear that all tracking specifications are satisfied in frequency domain.

EXPERIMENTAL RESULTS

The QFT control algorithm and the conventional PID controller which is used to control the HLS system is built by the combination of Simulink and Real-time Windows Target Toolbox of Matlab and connected to Advantech cards. Fig. 8 displays the proposed control scheme applied to the HLS. The sampling time was set to be 0.001s for all experiments. Furthermore, in order to prove the effectuality of the proposed controller, a disturbance source containing the band-limited white noises and the sine wave noise (Fig. 8) is generated real time during the system operation as given:

$$Dis(t) = A\sin(\omega t) + Rnd(t) \quad (10)$$

where: A, ω are amplitude, frequency parameters of the sine wave; $Rnd(t)$ is the random white noise signal.

All the disturbance parameters are changed to generate the small or large perturbation as shown in Table 2. The noise signal performed in (10) is sent from the computer to the AC servo drive of the disturbance generation part by the DA converter (PCI 1720). Then the controlled AC servo motor (FMA-KN55) with the hydraulic control circuit and piston are used to create the perturbation environment for the load simulator part in testing the control performance (see Fig. 1 and Fig. 8). Furthermore, the noise signal generated in (10) is added to the signal from the system output with a chosen gain to make a challenge for the force control problem.

At first, the small disturbance was generated to make comparisons of HLS using different controllers. The experiments were done with step reference input. In case of the HLS using traditional PID, the PID coefficients must be tuned by experience and trials to get the tracking performance in the acceptable range.

Table 2 Disturbance Parameters

Disturbance Kinds			Small Disturbance	Large Disturbance
Sine wave	Amplitude	Volt	0.4	0.8
	Frequency	Hz	5	2
White Noise	Power	Volt	0.00005	0.00015
Sampling time	T	sec	0.001	0.001
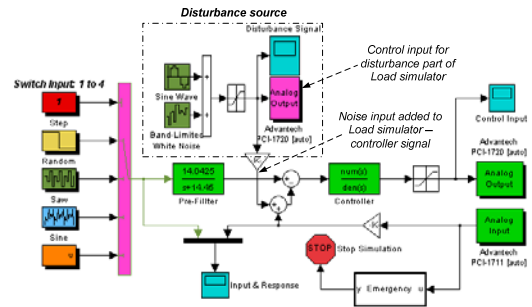
Figure 8 Simulink control diagram for HLS
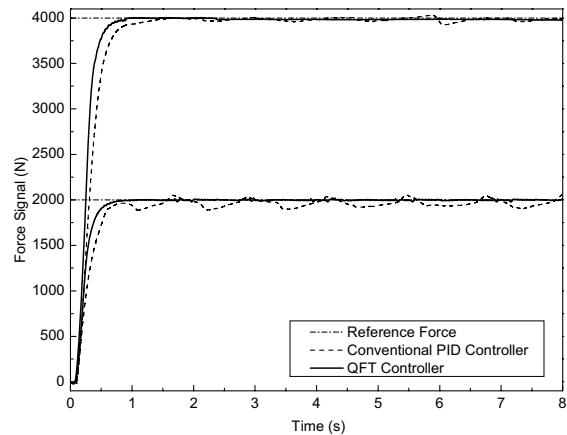
Figure 9 Step responses of HLS using PID and QFT – In case of small disturbance

Fig. 9 is the force responses with respect to step reference input. From the results, it shows that although the PID coefficients were tuned by trials, the control performance is worse than in case of using the QFT controller. Moreover, the effect of perturbation on the HLS makes the PID controller is unable to track the reference input with the allowable tolerance of error. It is shown clearly when the HLS operates in the large noise environment. Fig. 10 displays the control signals and the force response of HLS in case of step reference input and the working condition had large disturbance. These results show that conventional controller with fixed gains does not yield reasonable performance over a wide range of operating conditions. Hence, the robust force controller described in section 4 is implemented to overcome the above control problems.
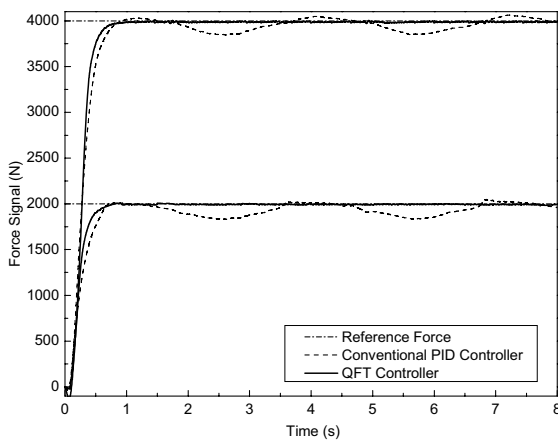
Figure 10 Step responses of HLS using PID and QFT
– In case of large disturbance
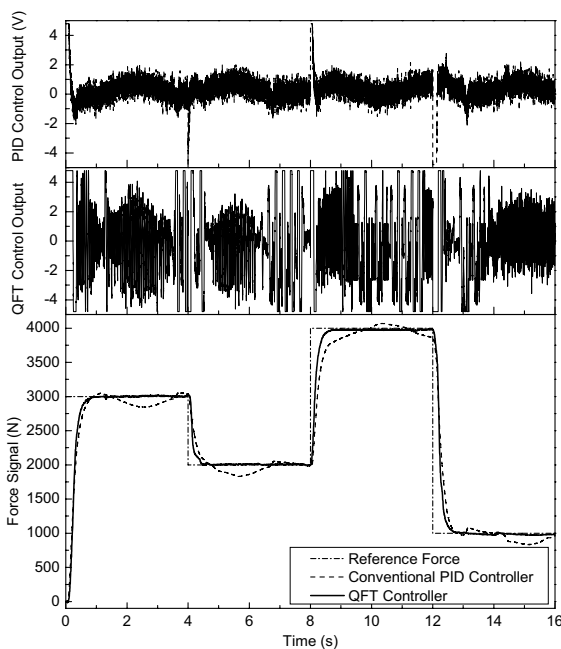
Figure 11 Multiple step responses of HLS
– In case of large disturbance

In order to make the comparison between the conventional PID and the QFT controller for different set-point reference inputs, the multiple step signals, is also investigated. Fig. 11 is the responses of the HLS between using the PID and the QFT controllers. The results prove that, in case of different setting-points, the responses of the system using proposed controller is more stable than the conventional one. It is clear that a good force regulation is realized in the case of using QFT to design a robust force controller.

CONCLUSIONS

This paper presents a new kind of HLS which is very convenient for conducting performance and stability test for control force of hydraulic hybrid systems. A robust force control using the QFT design technique was developed and successfully applied to the HLS. The input pre-filter transfer function F(s) and proper controller G(s) are designed to satisfy the required specifications of robust stability, robust tracking and disturbance attenuation.

The experimental evaluation compared with the conventional PID controller prove convincingly that the QFT controller could achieve good tracking with respect to different reference input signals and in case of variation of disturbances.

ACKNOWLEDGEMENTS

REFERENCES

1. Su, D.and Wang, Y., Development of electro-hydraulic load simulator with high precise, Proceeding ICFP 5th International Conference, Hangzhou, China, 2001, pp. 4-8.
2. Li, Y., Development of hybrid control of electro-hydraulic torque load simulator, ASME Journal of Dynamic Systems, Measurement and Control, 2002, **124**-3, pp. 415-419.
3. Horowitz,I.M., Quantitative Feedback Design Theory (QFT), Boulder, CO:QFT Publication, 1992, **1**.
4. Thompson, D.F. and Kremer, G.G., Quantitative feedback design for a variable-displacement hydraulic vane pump, Proceeding of the American Control Conference, 1997, pp. 1061-1065.
5. Niksefat, N. and Sepehri, N., Robust force controller design for a hydraulic actuator based on experimental input-output data, Proceeding of the American Control Conference, 1999, pp. 3718-3722.

OS9-1

NEW PNEUMATIC ACTUATORS PRODUCING BREAKTHROUGH IN MECHATRONICS

Koichi SUZUMORI

*Graduate School of Natural Science and Technology,
Okayama University
3-1-1, Tsushima-naka, Okayama, 700-8530 Japan
(E-mail: suzumori@sys.okayama-u.ac.jp)

ABSTRACT

New pneumatic actuators developed in the author's laboratory will be presented with their applications to new mechatronics. Examples of them are a pneumatic rubber actuator for compliant robots, a micro pneumatic tube actuator assisting the colonscope insertion, a pneumatic stepping motor with high torque and resolution, a pneumatic drive bicycle, an intelligent pneumatic cylinder which has encoder and micro CPU realizing local control and communication functions, and a new control method utilizing multiplex pneumatic transmission for pneumatic systems with multi-degrees of freedom.

KEY WORDS
pneumatic actuator, robot, mechatronics

INTRODUCTION

We have developed many kinds of actuators from nano positioning actuator using piezoelectric material to big force hydraulic actuator and their applications [1, 2]. In this report, our research activities on pneumatic actuators are introduced. They include 1) a small stepping pneumatic motor with high torque, 2) compliant pneumatic rubber actuators, 4) pneumatic drive bicycle, 5) intelligent pneumatic cylinder, and 6) a new control method for pneumatic system consisting of many cylinders.

NUTATION MOTOR

Figure 1 shows an example of the developed nutation motor [3, 4]. It consists of a pair of bevel gears; a cone-shaped bevel gear, shown as a fixed bevel gear in Fig.1 and a cup-shaped bevel gear, shown as a rotary bevel gear, which is supported by a spherical bearing. As the bevel gears have different numbers of tooth, gearing between two gears causes rotation of the rotary bevel gear, resulting in the rotation of the output shaft through the output bevel gears.

The rotary bevel gear is driven by a rubber diaphragm behind it, which has three pneumatic rooms. Driving each pneumatic room sequentially causes the
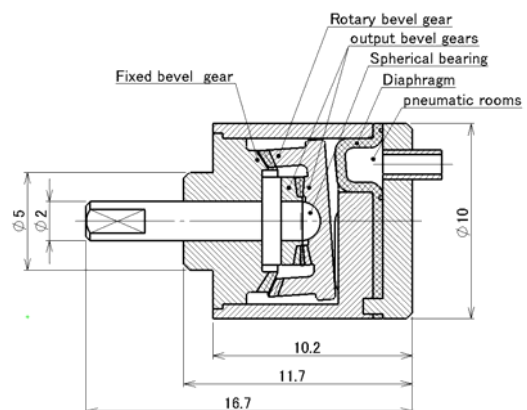
Fig.1 An Example of internal structure of nutation motor
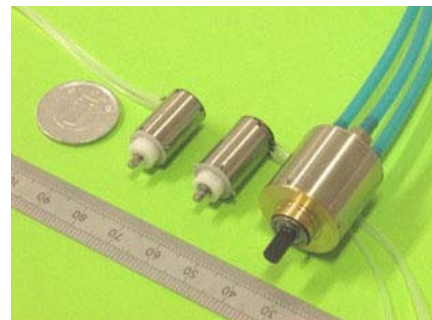
Fig.2 Developed nutation motors

nutation of the rotary bevel gear to drive the motor. As this gear mechanism works as a reduction gear, the motor works as a stepping motor generating big torque.

We have developed many prototypes as shown in Fig.2. The motor shown in Fig.1 has the bevel gears of 30 and 29 in tooth numbers, respectively, and generates the maximum torque of 5.5×10^{-3} [Nm] and 4 degree in stepping angle.

COMPLIANT ROBOTS

Manta robot

We developed a bending pneumatic rubber actuator named flexible microactuator, FMA [5] and applied it to various kinds of compliant robots. Figure 3 shows the FMA structure. It is made of rubber and has three internal chambers. Applying air pressure to each chamber causes the motion of three degrees of freedom; bending in any direction and stretching. It is designed based on non-linear FEM, where geometrical and material nonlinearities and contacting problems are analyzed. The analysis results agree well with the experimental results in general as shown in Fig.4 to make us design the actuators easily.

Pneumatic rubber actuators in general are suitable for underwater robots to move smoothly like living creatures because pneumatic rubber actuators have water-resistance, high power density, light weight, and high compliance to deform smoothly with interaction
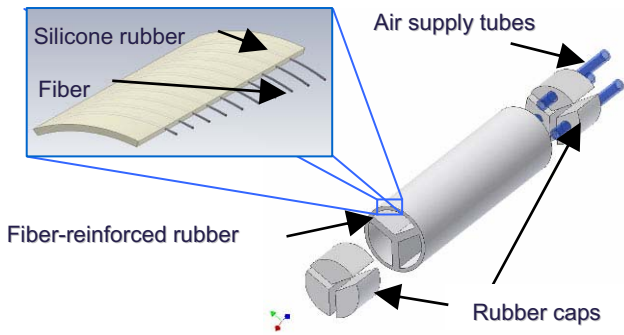
Fig.3 Structure of Flexible Ficroactuator
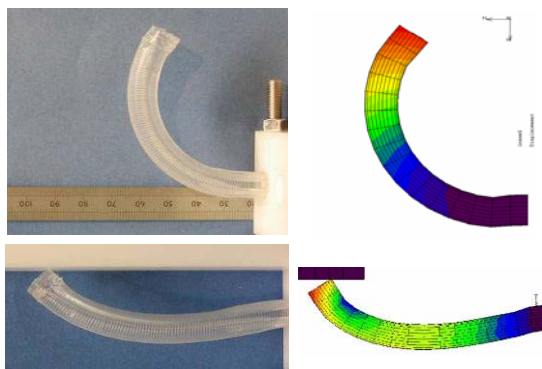
Fig.4 FMA design based on non-linear FEM analysis
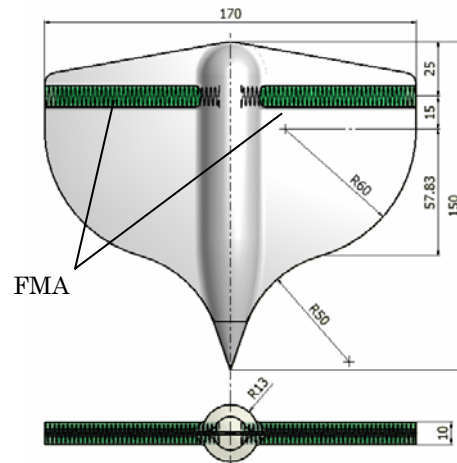
Fig.5 Manta swimming robot
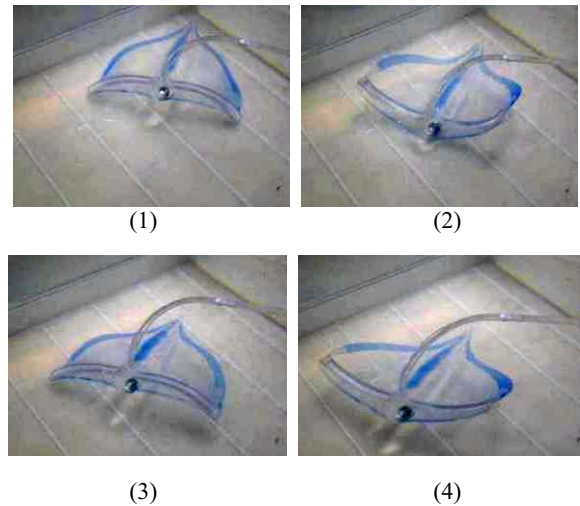
Fig.5 Experimental results of manta swimming motions

with water.

A manta type swimming robot is designed as shown in Fig.5 [6]. Two FMAs are embedded in the robot as shown in Fig. 5. The manta robot is 170 mm in width and 150 mm in length. It is made only of silicone rubber. Two flexible pneumatic tubes are connected to each actuator, resulting in four flexible pneumatic tubes in total to drive the robot. The developed manta robot works very well in water with the swimming speed of 100 mm/s and also steers in any desired direction.

Tube actuator assisting colonoscope insertion

Inserting an endoscope into the colon requires very technical procedure and it is difficult in some cases even for experienced doctors. Although active colonoscopes have been researched, these instruments are still in the development stage. Mechanisms for this application are required to be soft enough not to injure the colon wall and being deformable enough to adapt to the curves of the colon. In addition, the mechanisms must generate

5.8mm
0.2mm
φ 13mm
0.5mm
φ 16mm
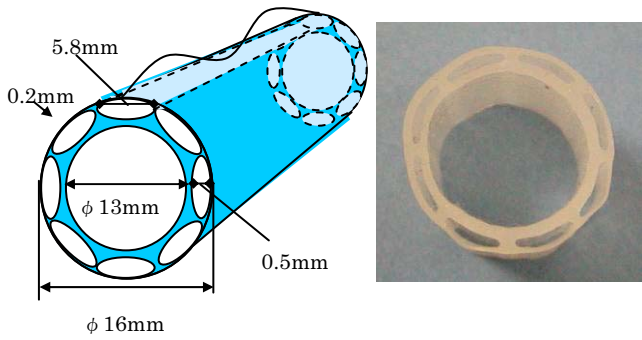
Fig.6 Multi-room rubber tube actuator applied to colonoscope

Fig.7 Simple insertion experiment using a dummy scope with force gauge

Fig.8 Experimental results of insertion force. The upper figure shows the force without driving the tube and the lower figure shows the force with driving the tube.

distributed force adequate for traveling. These requirements are difficult to be satisfied using conventional mechanisms and actuators. We have designed and developed two types of new driving mechanism using pneumatic rubber actuators and made their feasibility tests [7].

One mechanism is "Multi-room rubber tube actuator", shown in Fig.6: introducing pulse pneumatic flows to a thin rubber tube causes traveling deformation waves on the tube surface, which drives an object placed on the tube. A colonoscope is inserted in the 13 mm hall and applying pulse pneumatic flows generates progressing waves on the tube surface, which convey the colonoscope with the tube itself.

A basic insertion experiment was made using a dummy colonoscope equipped with a force gauge to detect the insertion force of the operator as shown in Fig.7. The path was made of a vinyl hose with the curvature of 17 to 26 cm. Figure 8 shows the force required to insert the dummy scope to the vinyl hose. The upper figure shows the required force without driving the tube while the lower figure shows the required force with driving the tube. Notes such as 60cm and 70 cm in the figure indicate the position of the head of the scope. The horizontal axis indicates time.

As shown in Fig.8, the results show the effectiveness of the thin tube wave generator very clearly; driving the tube enabled the insertion to 85 cm position in 1 sec, while it was difficult to insert the scope beyond 70 cm position without driving the tube because of the friction between the scope and the vinyl hose. It took 4 sec to insert the scope to 70 cm position without driving the tube [7].

The other mechanism is "Tetra Chamber Actuator"[9]: a rubber tube which has four chambers in it is wound around the colonoscope to cause traveling deformation waves on the scope surface by sending pneumatic pressures to each chamber sequentially. Its original idea comes from bubbler actuator [7, 8]. The designed cross section of the actuator and its deformation are shown in Fig.9. It generates the deformation six times larger than that of the conventional bubbler. More information in detail can be found in ref. [9].
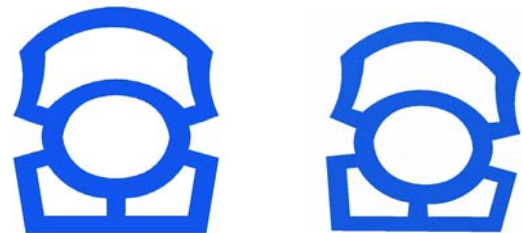
Fig. 9   Deformation of tetra chamber actuator

PNUMATIC BICYCLE
Although pneumatics is not suitable for the transmission of large amounts of power, this technology is suitable for the transmission of smaller amounts of power. By applying pneumatic transmission to bicycles, rather the

Fig.10 Prototype bicycle with pneumatic transmission

conventional chain transmission, two new functions may be realized: 54 gears and energy recovery.

The bicycle shown in Fig.10 has two cylinders connected to the pedals and two cylinders connected to the rear wheel. The cylinders near the pedals generate high pressure air, which is sent to the cylinders near the rear wheel through pneumatic valves to drive the wheel. Switching the valves enables an amazing 54 gears to be realized. During braking, the cylinders connected to the rear wheel work as pumps to generate pressurized air, which is stored in an air tank, enabling energy recovery. The experiments carried out in outside fields showed that that the energy efficiency is about 30% on flat road and the variable-speed function and the energy regeneration function works successfully [10].

INTELLIGENT CYLINDER

A goal of our research is to develop intelligent actuators for small mechatronic systems which have multi-degrees of freedom of motion such as micro robots.

An example of multi-DOF mechatronic systems is shown in Fig.11 [11, 12]. This example is developed for physical human-machine interface which makes the operators feel as if they actually touched
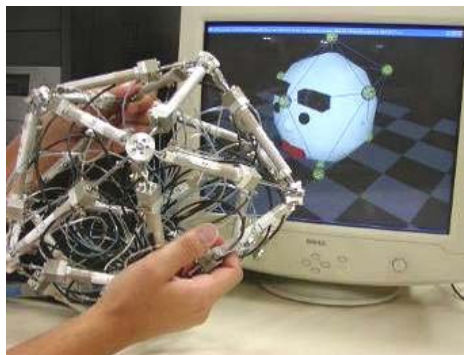
Fig.11 Active polyhedron with 30 cylinders working as a physical human/machine interface
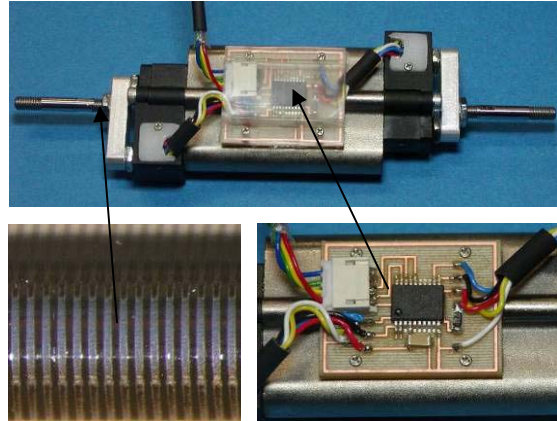
Fig.12 Intelligent pneumatic cylinder, micro CPU, and encoder built in the cylinder

three-dimensional continuous virtual objects in PC. The prototype shown in Fig.11 consists of thirty pneumatic cylinders, forming a linkage mechanism of icosahedron. The final goal of this research is to realize a virtual physical continuous object consisting of a great number of intelligent miniature actuators, and is expected to work as a pre/post processor for analysis of finite elements method.

The development of intelligent actuators is one of the biggest key points to realize these mechatronic systems. The intelligent actuators for these purposes are required to have sensing functions of motions and forces, control function with local signal processing, and communication functions between the other actuators and host computer, which reduces the numbers of electrical/pneumatic cables.

Figure 12 shows an intelligent pneumatic cylinder developed for this pneumatic active polyhedron with 120 degrees of freedom shown in Fig.12. The developed cylinder is almost same sized as conventional cylinder and is equipped with a micro optical encoder to detect position of the piston rod as shown in Fig. 12. In the optical encoder chip a micro LED and two pairs of micro optical lens and photo detector are fabricated. On the surface of the piston rod, 0.16mm stripe marker

Fig.13 Active polyhedron consisting of 120 intelligent cylinders
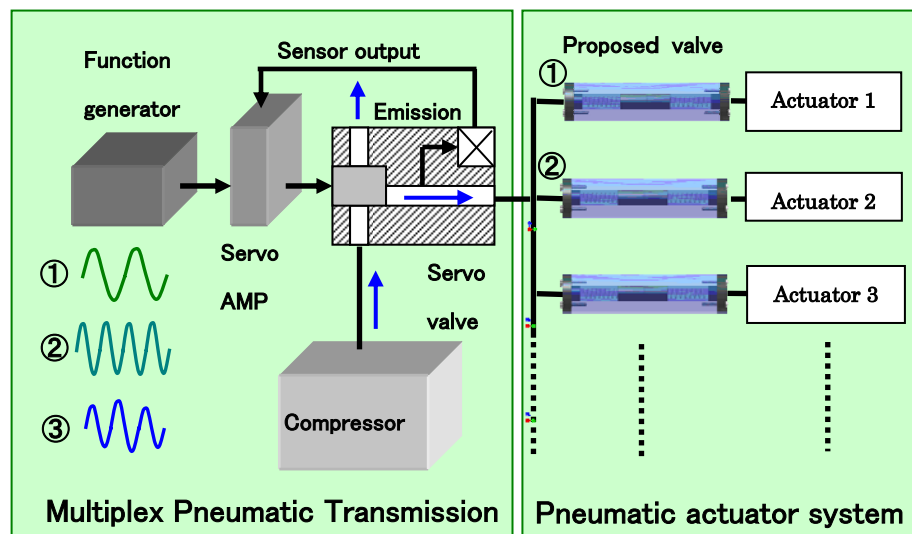
Fig.14 Proposed control system for pneumatic mechanical systems with multi-degree of freedom

(a) Non-resonance frequency   (b) Resonance frequency
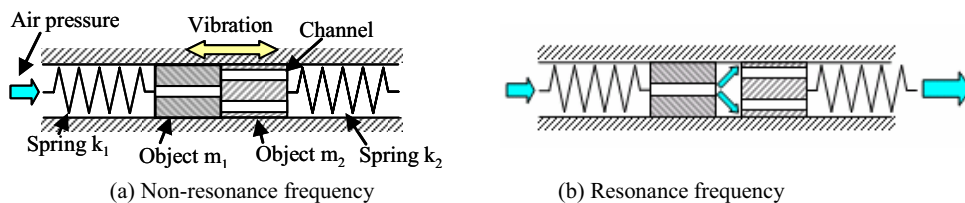
Fig.15 Basic structure of the pneumatic on/off valve which is activated when the pneumatic
vibration at the natural frequency is applied to the air supply line

lines are fabricated with oxidization of the stainless steel rod surface by YAG laser marker [12,13].

PNEUMATIC VALVE OPERATED MULTIPLEX PNEUMATIC TRANSMISSION

A new pneumatic valve for controlling pneumatic actuators and its operation system using air vibration in air supply line are newly proposed and being developed [14].

Driving mechanism of this valve and operation system is based on a novel idea: superimposing pneumatic waves into the air supply line drives any selected valve(s) which are connected to the air supply line. Each valve is designed to have different natural frequency to be driven and it is activated when pneumatic vibration at the natural frequency is applied to the air supply line.

Figure 14 shows the outline of pneumatic mechanism to which the proposed control system and the valves are applied. As shown in the figure, an oscillator built in the air supply line gives the supply air vibration.

Each actuator is equipped with the proposed pneumatic valve(s) which has a natural frequency for activation. Superimposing the pneumatic vibrations at

the frequency corresponding to the natural frequency of its valve causes mechanical resonance of the oscillating bodies in the valve to drive the actuator.

Since the superimposed pneumatic waves is transmitted in the air supply line as control signals and valve drive energy, electrical cables, which are needed to be connected to each valve in conventional pneumatic drive systems, are not needed in this system. This results in very simple pneumatic systems with multi-degree of freedom.

Figure 15 shows a structure and working principle of the proposed valve. The valve has two oscillating bodies, m_1 and m_2, which have through holes for air flow, and are supported elastically by two springs, k_1 and k_2, respectively. This mechanical system acts as a spring-mass vibration system. Without the pneumatic oscillation at the natural frequency, two bodies contact by the spring force and there is no air flow through the valve, while applying air oscillation of the natural frequency causes the bodies oscillate separately to cause air flow through the valve.

At current, we successfully control two cylinders independently using this system [15]. We are now trying to increase the number of the controlled cylinders.

REFERENCES

1. Koichi SUZUMORI，New Actuators and Their Applications --From Nano Actuators to Mega Actuators--, 004 International Symposium on Micro-Nano Mechatronics and Human Science, (2004-11)
2. http://www.act.sys.okayama-u.ac.jp
3. Koichi SUZUMORI, Tatsuya HASHIMOTO, Kazuo.UZUKA, Isao ENOMOTO, Pneumatic Direct-drive Stepping Motor for Robots, Proc. IEEE/RSJ Int'l Conf. on Intelligent Robots and Systems, (Oct., 2002),pp.2031-2036
4. Koichi Suzumori, Takashi Nagata, Takefumi Kanda, Kazuo Uzuka, and Isao Enomoto, Development of Electromagnetic Nutation Motor (Electromagnetic Investigation), Journal of Robotics and Mechatronics, Vol.16, No.3, (2004-6), pp.327-332.
5. Koichi SUZUMORI, Shoichi IIKURA and Hirohisa TANAKA, Applying A Flexible Microactuator to Robotic Mechanisms, IEEE Control Systems, vol.12, no.1, (Feb.1992), pp.21-27. Schlihiting, H., Boundary Layer Theory, McGraw Hill, New York, 1969, pp.350-363.
6. Koichi Suzumori, Satoshi Endo, Takefumi Kanda, Naomi Kato, Hiroyoshi Suzuki, A Bending Pneumatic Rubber Actuator Realizing Soft-bodied Manta Swimming Robot, 2007IEEE, International Conference on Robotics and Automation (ICRA 2007), FrE12.3, pp.4975-4980, (2007-4)
7. Koichi Suzumori, Takayuki Hama, Takefumi Kanda, New Pneumatic Rubber Actuators to Assist Colonoscope Insertion, 2006 IEEE International Conference on Robotics and Automation, 995，pp.1824-1829,（2006-5）
8. Koichi SUZUMORI, A Pneumatic Rubber Actuator Driven by Elastic Traveling Waves, Int'l Journal of Japan Society of Mechanical Engineers, Series C, Vol.42, No.2, (1999), pp.398-403.
9. Hisakazu Onoe, Koichi Suzumori, Takefumi Kanda, Development of Tetra Chamber Actuator, 2007 IEEE/RSJ International Conference on Intelligent Robots and Systems, Oct. 2007, pp.777-782.
10. Shinji GOTO, Koichi SUZUMORI, Takefumi KANDA, Pneumatic Transmission for Intelligent Bicycle, Proc. JSME ROBOMEC06, 1A1-C05, p.18, （2006-5）in Japanese.
11. Jumpei OCHI, Koichi SUZUMORI, Junichi TANAKA, Takefumi KANDA, Development of Active Links for Physical Man-Machine Interaction, Journal of Robotics and Mechatronics, Vol.17, No.3, (2005-6), pp.293-301.
12. H.Ogawa, K.Kosaka, K.Suzumori, T.Kanda, Force-Presentation Method for Active Polyhedron for Realizing Physical Human-Machine Interaction，2006 IEEE International Conference on Robotics and Automation, 347,pp.3941-3947,（2006-5）
13. Koichi Suzumori，Takefumi Kanda，Kazuyoshi Kosaka, Kodai Tsujino, Kenji Kure, Hiroshi Ogawa, Akina Kuwada，INTELLIGENT SERVO ACTUATORS FOR MULTIDEGREES OF FREEDOM MECHATRONICS，10th International conference on new actuators （ACTUATOR2006），A3.4, pp.128-131,（2006-6）
14. Yasutaka Nishioka, Koichi Suzumori, Takefumi Kanda, Pneumatic valve operated by multiplex pneumatic transmission, JSME-KSME Joint International Conference on Manufacturing, Machine Design and Tribology (ICMDT 2007), Jul.2007, CDROM.
15. Yasutaka Nishioka, Koichi SUZUMORI, Takefumi KANDA, and Shuichi WAKIMOTO, A new pneumatic control system using multiplex pneumatic transmission, 7th JFPS International Symposium on Fluid Power Toyama 2008 (to be presented).

OS9-2

WEARABLE FLUID POWER COMPOSED OF FLAT TUBES TO ACTIVATE THE BODY

Hideyuki TSUKAGOSHI*, Shumpei KASE*, Toshiyuki KATO*,
Takeaki SUZUKI *, Ato KITAGAWA*

* Department of Mechanical and Control Engineering,
Tokyo Institute of Technology
2-12-1-S5-19 Ohokayama, Meguro-ku, Tokyo, 152-8552 Japan
(E-mail: htsuka@cm.ctrl.titech.ac.jp)

ABSTRACT

A novel fluid power actuator called Flat Ring Tube (FRT) is introduced in this paper. The mechanism of FRT is so simple that it only needs a urethane flat tube and water pressure power source. No valves or switches are required. Applying constant water pressure results in periodic oscillation of the tube. The frequency is proportional to the flow rate of water and inversely proportional to the tube length. By contacting the tube with a passively supported shaft, it rotates due to the periodic tube oscillation. This principle can also generate the linear driving force, when FRT is mounted so as to kick the ground. Such kind of performance can be also expected to stimulate the blood flow rate, when FRT touches on the skin of the human body appropriately. The experimental results showed us the developed wearable massage device could effectively improve both the circulation of the blood flow and the density of oxygen in blood, which resulted in let the people feel more comfortable than conventional massage devices.

KEY WORDS

Wearable Fluid Power, Self-excited Oscillation, Massage Actuator, Water Hydraulics, Rehabilitation

INTRODUCTION

An actuator with the flexible structure and the pliant performance would be useful for the driving system which is assumed to come into contact with the human body, considering that the human muscle and the skin are composed of soft tissues.   To realize such kind of actuators, we have proposed a variety of fluid actuators based on a flat tube which was made of urethane with thermoplasticity. When the inside of the tube is pressurized, the cross sectional shape approaches a circle, while the circumference of the tube is almost kept constant. As a result, the tube becomes resistant to relatively high pressure so that large force is easy to be generated, even though the whole size is small. On the other hand, the structure piling up some tubes are required to increase the displacement, since that of each tube is small. A spiral shaped structure named Wound Tube Actuator and a zigzag shaped structure called Zigzag Tube Actuator are the examples to cope with it, which were designed to be applied to wearable actuators
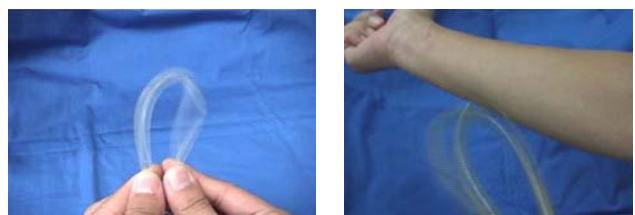
Figure 1 Overall view of the self-excited oscillation of FRT which stimulates the human skin

to stimulate the body motion[1-2] and rescue robots to go through small spaces to find survivors[3]. These actuators must have been operated by valves to switch from pressurized mode to decompressed one, which results in requiring at least a valve per an actuator.

In this study, a novel type of fluid power actuator with no use of valve to operate will be discussed, although it also takes advantage of the flat tube. It is based on the self-exited oscillation which occurs when the flat tube bent in the ring shape called Flat Ring Tube is pressurized by tap water pressure, as shown in Fig.1. This phenomenon is peculiar to a flat tube, which does not occur in the general pipe shaped tube. The oscillation discussed in this paper is basically different from that of Collapsible Tubes studied previously [4]. Then in this paper, after the oscillating principal and condition of FRT are illustrated, a couple of useful applications are introduced such as a novel water hydraulic motor and a wearable massage device.

BASIC PRINCIPLE

A fluid power actuator taking advantage of novel phenomenon will be introduced here. It is based on a flat tube whose cross sectional shape is flat and is made of urethane, as shown in Fig.2. When the inside of a flat tubes is pressurized by domestic tap water pressure of approximately 0.2 to 0.3 [MPa], and the tube is bent in the round shape, then the periodic self-excited oscillation occurs without using any valves to switch. This is the phenomenon peculiar to a flat tube bent in this form, which we call "Flat Ring Tube", abbreviated to "FRT" here.

(a) Top view of a flat tube.

(c) Overall view of Flat Ring Tube.

(b) Side view of a flat tube.
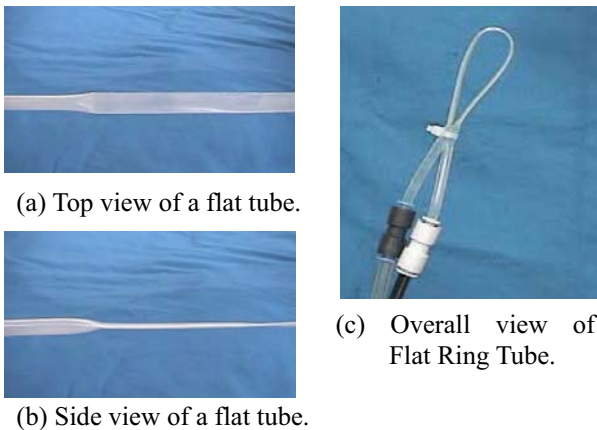
Figure 2 Composition of Flat Ring Tube

The principle of the oscillation can be illustrated as follows. As the inside of the FRT is pressurized, it curves more and more and then it buckles at some point reaching the curvature limit. Since the fluid passage is perfectly cut off at buckled point, this point is pushed from the upstream to the downstream as the tube continues to be pressurized, shown in Fig.3 i) and ii). At

the same time, a new buckled point is also generated at the side of upstream shown in Fig.3 iii), which slides to the downstream shown in Fig.3 iv). Finally, it returns to its original shape. This is a cycle of oscillation.

In order to make the tube oscillate in the above way, there are a couple of conditions. If you replace the flat tube with the pipe shaped one, the above oscillation does not occur all, because the buckled point on the pipe shaped tube is difficult to slide from the upstream to the down stream due to the tube resistance to deform and the flow leak at the sides of the flat tube. In this sense, the above oscillation is peculiar to the flat tube.

The experimental results showed the frequency of the oscillation by FRT is proportional to the flow rate, while it decreases as the tube becomes longer under the condition of the constant flow rate, shown in Fig.5. This is because the velocity of the buckled point is also proportional to the flow rate and the longer sliding period for a cycle is required as the tube becomes longer. If the tube is too short, it does not oscillate because the second buckled point is hard to be generated. If the tube is too long, it neither oscillates because the buckling point is not generated. Due to the same reason, the frequency decreases, as the tube diameter increases, as shown in Fig.6.
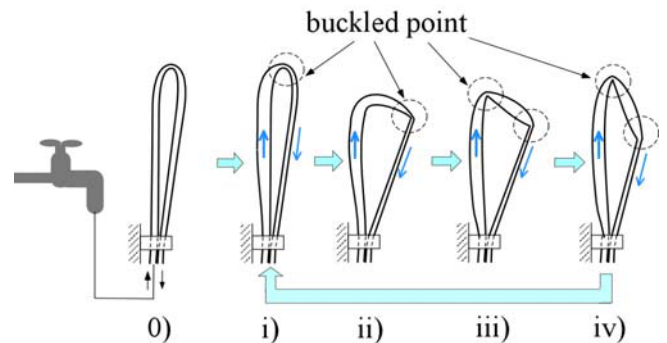
Figure 3 Principle of oscillation by FRT
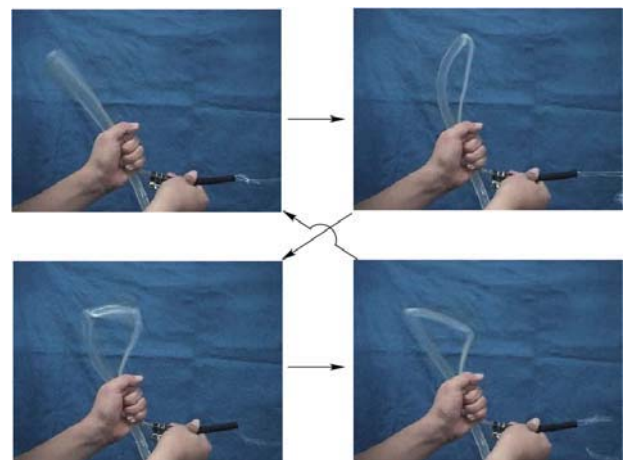
Figure 4 A cycle of oscillation by a developed FRT

204
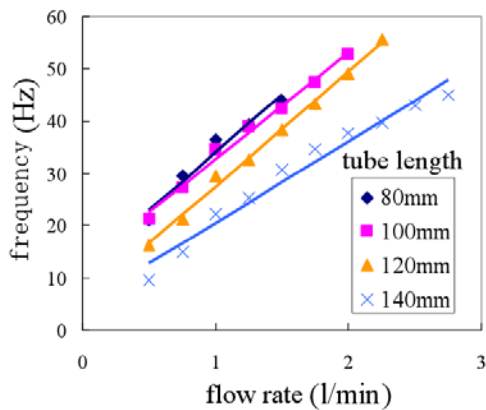
Figure 5 Experimental results of the frequency related to the tube length and the flow rate
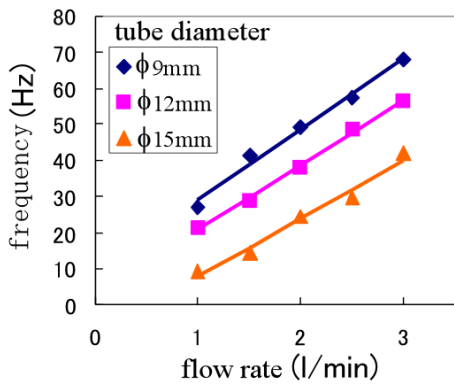
Figure 6 Experimental results of the frequency related to the tube diameter and the flow rate
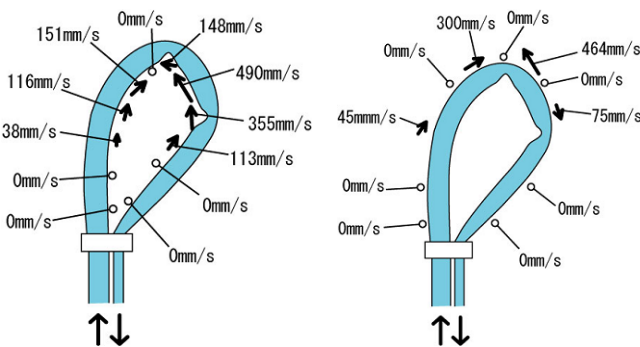
Figure 7 Tangent velocity of the contact point on FRT

To investigate the performance of FRT generating the infinite rotary motion, the tangent velocity of each contact point on FRT was experimentally examined by measuring the rotational speed of the shaft which was touched on FRT from both the inner side and the outer one. Here, the tube width and length was 9mm and 120mm respectively, while the oscillating frequency was 70Hz.

The experimental results in Fig.7 suggest us that there exists the turning point around the middle of FRT where the driving force direction changes inversely in both cases of the inner and outer touching. Furthermore, the fast point appears at the down stream side from the middle of FRT, which can be seen in any size of FRT. If the shaft touched from the outer side of FRT, two turning points appeared. In any cases, it was clear that there exists the optimal point in FRT to come into contact with the shaft to maximize the rotational speed.
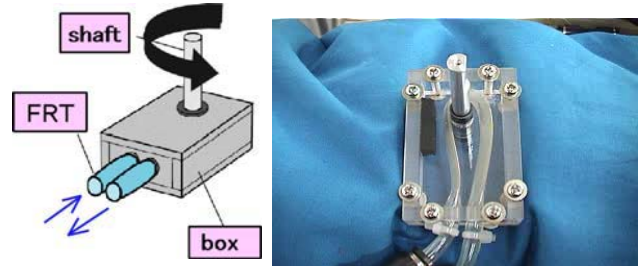
Figure 8 Application of FRT to a water hydraulic motor

Figure 8 shows a motor taking advantage of the above rotating drive function of FRT. It was designed for the shaft to touch on FRT at the optimal point. The developed motor, could generate 76[kg*cm] of torque and was 50g in weight with extremely simple mechanism composed of a flat ring tube and a shaft. The relationship between the rotational speed and the torque was as shown in Fig.11. Since the rotational speed increases monotonously as the flow rate is gained, it can be also applicable for a flow meter. Particularly, the mechanical driving part does not come into contact with the fluid directly, this kind of meter is useful for measuring the flow of the industrial waste water, for example.
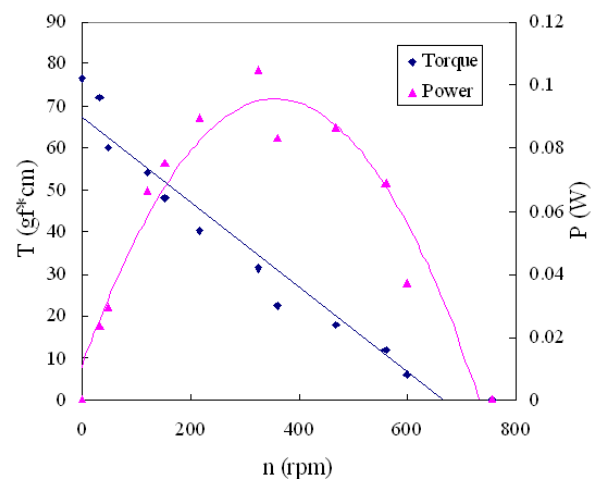
Figure 9 Relationship among the rotational speed, the torque and the power of the developed FRT motor.

APPLICATION TO A MASSAGE DEVICE

If you take advantage of this principle, it is expected to promote the blood flow. Then, we tried to apply it for massage devices, shown in Fig.7. Since it can generate the frequency of 0.5Hz～10Hz with soft touchiness to human body, it can let them feel comfortable. In addition to the good feeling, the muscle blood flow meter showed that the muscle blood flow increased at 12% after 5 minutes massage, and that the effect of its increasing continues after 30 minutes, shown in Fig.8. The thermography also showed that the body temperature of the skin surface rose at 10 % after 5 minutes massage by FRT. Unlike the conventional massage machine using the electricity, the FRT massage device does not generate the electromagnetic at all.

Figure10 Massage device by the handy type of FRT

Figure 11 Wearable massage device mounting two pairs of FRT on the jacket
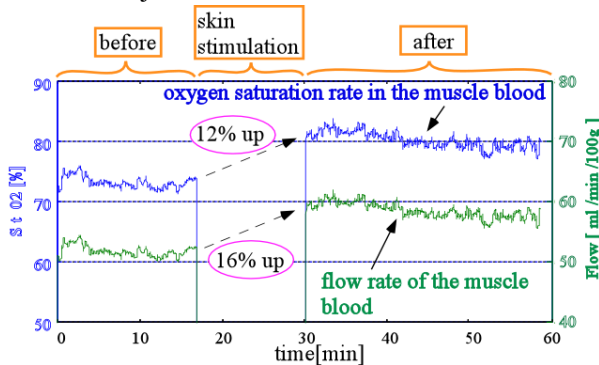
Figure 12 Effect of FRT on the human body

Therefore, this device can be also applicable for a pacemaker user without any fear. At present, a wearable massage device is being developed which can massage shoulder, back and waist so as to promote the muscle pressure around the whole body.
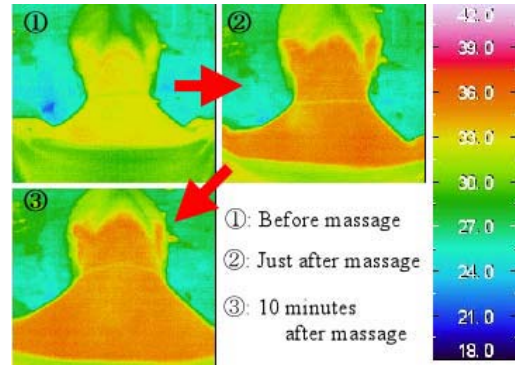
Figure 13 Transient of the skin temperature while taking massage of the wearable type of FRT massage device.

CONCLUSIONS

A novel fluid power actuator called Flat Ring Tube (FRT) was introduced in this paper, which was composed of a urethane flat tube pressurized by domestic tap water pressure and no valves or switches were required. Applying constant water pressure resulted in periodic oscillation of the tube. The applications of FRT for the water hydraulic motor and the massage device were introduced. The experimental results showed us the developed wearable massage device could effectively improve both the circulation of the blood flow and the density of oxygen in blood, which resulted in let the people feel comfortable.

REFERENCES

1 H.Tsukagoshi, A.Kitagawa, Y.Kamata, "Wearable Fluid Power Composed of Transformed Flat Tube Actuators," IEEE／RSJ International Conference on Intelligent Robots and Systems, 1178-1183(2002)
2 H.Tsukagoshi, S.Nozaki, A.Kitagawa : Versatile Water Hydraulic Motor Driven by Tap Water, IEEE／RSJ International Conference on Intelligent Robots and Systems,(CD-ROM:F-AII-2)(2000)
3 A.Kitagawa, H.Tsukagoshi, M.Igarashi, "Development of Active Hose with a Small Diameter for Search and Life-prolongation of Victims," Journal of Robotics and Mechatronics, 15-5, 474/481(2003)
4 Conrad, W.A., IEEE Trans. Bio-Med. Eng., BME-16, 284(1969)

OS9-3

PASSIVE CONTROL OF FLUID POWERED
HUMAN POWER AMPLIFIERS

Perry Y. Li and Venkat Durbha
Center for Compact and Efficient Fluid Power &
Department of Mechanical Engineering,
University of Minnesota,
Minneapolis, MN 55455, USA.
Email: `pli@me.umn.edu,  durbh002@umn.edu`

Abstract

A unified control framework is proposed for the control of fluid powered human power amplifiers. Human power amplifiers are mechanical tools that humans operate directly and the human force is amplified hydraulically or pneumatically. The tool and the environment forces would therefore appear to the human as having been scaled down. Ideally, the assistive force is transparent to the human such that the tool should feel haptically like any other passive mechanical tool to the human. To ensure safety and coupling stability, it is helpful that the controlled human power amplifier interacts with the human opeartor and other environments passively. In the proposed unified control framework, the hydraulic or pneumatic actuator is controlled to interact virtually with a fictitious inertia. The control problem then becomes one of coordinating the velocities between virtual inertia and the actuator. Both processes of augmentation with virtual inertia, and coordination can be done passively; the latter via the energy preserving passive decomposition approach into locked and shaped systems. The overall control system can be shown to possess the needed passivity property. The control schemes for both the hydraulic and pneumatic cases have been experimentally implemented.

Keywords:

Passivity, coupling stability, coordination, exoskeleton, virtual system.

INTRODUCTION

Human amplifiers, extenders or exoskeleton are tools that humans manipulate directly, but have the ability to attenuate or amplify the apparent power that the human exerts. By being physically connected to the task, the control is more intuitive for the human operator. In particular, the operator controls and is informed by the machine via physical quantities like power, forces and displacements, as in the use of common mechanical tools such as hammer, scissors etc. Hydraulics and pneumatics actuations have better power densities than electromagnetic actuation. However, we must consider the fluid compressibility and the fact that a hydraulic actuator is mainly a velocity source whereas an electromechanical actuator is typically treated as a torque/force source.

The control objective is to amplify the power that the human exerts on the machine. Since human power amplifiers interact physically with the work environment and the human, the interactive stability with a variety such environments are needed to ensure safety. For this reason, an additional requirement is that the human power amplifer can interact with the human operator at the handle as well as with its physical environment in an energetic passive manner. Since most physical environments and human dynamics are energetically passive or can be shown to behave nearly energetically passive, ensuring that the

human power amplifer behave passively can ensure the system can operate stably in a many situations. Even with active environments, infinite net external energy input is needed to make an energetically passive human power amplifier unstable.

The human power amplifier control problem can be posed simplistically as a force tracking problem [1] - i.e. the actuator force is controlled to be a scaled copy of the applied human force. However, this requires the use of velocity positive feedback which has a destabilizing effect in the presence of uncertainty, slow sampling or time delay. Without the velocity positive feedback, force tracking performance degrades especially during free-space operation. Passivity property cannot be easily ensured structurally.

An alternate passive control structure was proposed in [2] for hydraulically actuated human power amplifiers. Instead of using a force tracking paradiagm, the control problem becomes one of coordinating the velocity of the system with that of a fictitious passive mechanical system that is coupled to the human power amplifier via the measured force and the valve command input. In essence, the velocity feedforward term is now generated by the velocity of the fictitious mechanical system. The control law for achieving coordination is accomplished via a passive decomposition [3], [4], [5] into a shape
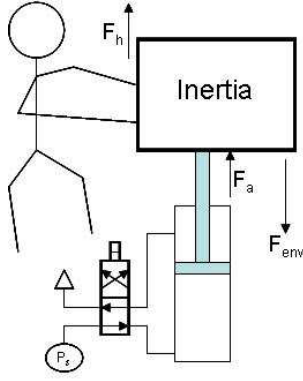
Figure 1.   1 DOF fluid powered human power amplifier setup

Figure 2.   Each hydraulic actuator is modeled as an ideal kinematic actuator and an equivalent fluid spring.

and a locked system, from which a plethora of control laws can be designed to stabilize the shape system. A significant advantage of the control is that the passivity property is enforced by the control structure itself, and is therfore more robust. In this paper, we show that this control structure can be generalized for pneumatic systems as well.

PROBLEM FORMULATION

For simplicity, we consider only one degree of freedom motion. Extension to fully coupled multi-DOFs dynamics can be done but will detract from the key concept. For each degree of freedom, the generalized inertia $M_p > 0$ is acted on by the generalized human input F_{human} and environment force F_{env}, as well as the hydraulic / pneumatic actuator force F_a:

$$M_p \ddot{x}_p = F_{human} + F_{env} + F_a \qquad (1)$$

We assume that the displacement of the human amplifier x_p is measured; and both the applied actuator force F_a and the applied human force F_{human} are measured by force sensors. The environment force F_{env} which includes interaction force with all environment other than the human operator as well as friction, is not measured. The actuator force is generated by a hydraulic/pneumatic actuator (or motor), controlled by a four-way proportional valve with a constant pressure supply. The valve bandwidth is sufficiently high so that the valve command corresponds statically to spool displacement. The models for the actuator force F_a will be considered in the next section.

It is desired that the closed loop system would enable the human operator and the work environment to interact via a rigid mechanical tool except that the human would feel as if he/she is $\rho + 1$ times stronger. Therefore, the target dynamics would be

$$M_L \ddot{x}_p = (\rho + 1)F_{human} + F_{env} \qquad (2)$$

where M_L is the inertia of the rigid mechanical tool, which in the proposed control structure will be slightly different from M_p in (1).

The human power amplifier interacts with both the human operator and the work environment via the effort and flow variables of $(F_{human}, \dot{x}_p)$ and $(F_{env}, \dot{x}_p)$. To ensure safety, it is also desired that this interaction satisfies an energetic passivity with power scaling condition. Let the supply rate be the sum of the mechanical power input from the environment and the scaled mechanical power input by the human:

$$P_{total}(F_{human}, F_{env}, \dot{x}_p) := \{(1 + \rho)F_{human} + F_{env}\} \dot{x}_p \qquad (3)$$

The desired passivity condition is that there exists $c^2 \geq 0$ such that for any human and environment input F_{human} and F_{env} and for any $t \geq 0$,

$$\int_0^t P_{total}((F_{human}, \dot{x}_p), (F_{env}, \dot{x}_p))d\tau \geq -c^2 \qquad (4)$$

This condition implies that the net amount of scaled energy that can be extracted from the system by the work environment and the human are limited by c^2 and $c^2/(1 + \rho)$ respectively.

MODELING OF ACTUATOR FORCE

We now model a fluid power actuator with capside and rodside areas of A_1, and A_2, area ratio of $r := A_1/A_2$. The actuator is controlled by a matched, symmetric and critically lapped four-way valve with fast spool dynamics so that the command input corresponds to the valve area opening. We consider the hydraulic and the pneumatic cases separately.

Hydraulic case

A useful way to account for the fluid compressibility in a hydraulic actuator is to model the actuator as consisting

of an ideal kinematic actuator (with displacement x_I) interacting with the system inertia (with displacement x_p) via an equivalent spring with a compression (Figure 2):

$$\Delta = x_I - x_p \qquad (5)$$

The position dependent spring force $F_a(x_I, \Delta)$ encompasses the compressibility of the fluid in the actuator and the fluid line, as well as other mechanical compressibility. Inclusion of the compressibility effect is essential for modeling the force exerted by the hydraulic actuator.

Let V_1 and V_2 be the chamber volumes that include dead volumes,

$$V_1 = V_{10} + A_1 x_I = A_1(L_{10} + x_I)$$
$$V_2 = V_{20} - A_2 x_I = A_2(L_{20} - x_I)$$

Using basic bulk modulus equation, we have:

$$F_a(x_I, \Delta) = \beta \left(\frac{A_1^2}{V_1} + \frac{A_2^2}{V_2} \right) \Delta \qquad (6)$$

$$= \beta \left(\frac{A_1}{L_{10} + x_I} + \frac{A_2}{L_{20} - x_I} \right) \Delta \qquad (7)$$

$$= K(x_I)\Delta \qquad (8)$$

where $K(x_I)$ is the position dependent linear spring stiffness.

The ideal actuator speed $\dot{x}_I$ would be the acuator speed when compressibility is neglected. For a four-way proportional control valve, it is related to the command u as follows:

$$\dot{x}_I = \gamma_q(\mathrm{sgn}(u), F_a) u \qquad (9)$$

$$\gamma_q(\mathrm{sgn}(u), F_a) = \begin{cases} \frac{w}{A_1} \left(\frac{r^3}{r^3+1} \right)^{\frac{1}{2}} \sqrt{P_s - F_a/A_1}, & u \geq 0 \\ \frac{w}{A_1} \left(\frac{r^2}{r^3+1} \right)^{\frac{1}{2}} \sqrt{P_s + r F_a/A_1}, & u < 0 \end{cases} \qquad (10)$$

where $\gamma_q(\mathrm{sgn}(u), F_a)$ is the loaded velocity gain, P_s is the supply pressure, and w is the area gradient.

Pneumatic case

In the pneumatic case, the definition and dynamics of x_I and of the equivalent spring are not as obvious. Suppose that the air mass and volume (including dead volume) in each actuator chamber are m_1, V_1 and m_2, V_2. Since

$$V_1 = V_{10} + A_1 x_p = A_1(L_{10} + x_p)$$
$$V_2 = V_{20} - A_2 x_p = A_2(L_{20} - x_p)$$

The force exerted by the actuator can be rewritten as,

$$F_a = P_1 A_1 - P_2 A_2 - P_{atm}(A_1 - A_2)$$

$$= RT \left[\frac{m_1 A_1}{V_1} - \frac{m_2 A_2}{V_2} \right] - P_{atm}(A_1 - A_2)$$

$$= RT \left[\frac{m_1}{L_{10} + x_p} - \frac{m_2}{L_{20} - x_p} \right] - P_{atm}(A_1 - A_2) \qquad (11)$$

The last term models the effect of the atmospheric pressure acting on piston rod area. Define x_I' to be the actuator position when $F_a = -P_{atm}(A_1 - A_2)$. Hence,

$$x_I' = \frac{m_1}{m_1 + m_2} L_o - L_{10} \qquad (12)$$

$$\Delta = x_I - x_p \qquad (13)$$

where $L_o = L_{10} + L_{20}$. Let $\mathbf{m} = (m_1, m_2)$. The force exerted by the actuator can then be written as

$$F_a = \bar{K}(\mathbf{m}, x_p)(x_I' - x_p) - P_{atm}(A_1 - A_2) \qquad (14)$$

$$\bar{K}(\mathbf{m}, x_p) := \frac{RT(m_1 + m_2)}{(L_{10} + x_p)(L_{20} - x_p)} \qquad (15)$$

We now define

$$x_I := x_I'(\mathbf{m}) - \frac{P_{atm}(A_1 - A_2)}{\bar{K}(\mathbf{m}, x_p)} \qquad (16)$$

$$\Delta := x_I - x_p \qquad (17)$$

We have

$$F_a(\mathbf{m}, x_p) = \bar{K}(\mathbf{m}, x_p)\Delta \qquad (18)$$

This defines a nonlinear and air mass dependent spring element.

For moderate actuator force, $x_I' - x_p$ is small compared to $L_{10} + x_I'$ and $L_{20} - x_I'$. Then

$$K(\mathbf{m}) := \bar{K}(\mathbf{m}, x_I') \approx \bar{K}(\mathbf{m}, x_p) \qquad (19)$$

Furthermore, if $L_{10} \approx L_{20}$, the error in the approximation is only second order in the compression. Eq.(19) is advantageous because, in the isothermal situation, x_p enters only through Δ but not the stiffness term, and x_I is a function of $\mathbf{m}$ only but not of x_p, similar to the hydraulics case. This assumption is made hence forth so that:

$$F_a(\mathbf{m}, \Delta) := K(\mathbf{m})\Delta \qquad (20)$$

$$\Delta := x_I(\mathbf{m}) - x_p \qquad (21)$$

which is a linear spring with stiffness being dependent on the amount of gas in the actuator chambers.

Mass flow rate through the valve to either chamber can be obtained by modeling it as flow through converging-diverging nozzle. Although highly nonlinear with respect to upstream and downstream pressures, they are linear with respect to valve opening and hence command u. Hence, $\dot{x}_I$ and $\dot{\mathbf{m}}$ are of the form:

$$\dot{x}_I = \gamma_I(\mathrm{sgn}(u), \mathbf{m}, F_a) u \qquad (22)$$

$$\dot{\mathbf{m}} = \gamma_q(\mathrm{sgn}(u), \mathbf{m}, F_a) u \qquad (23)$$

Passivity property of hydraulic / pneumatic actuator

Consider the storage function for the hydraulic actuator,

$$W_{hyd} = \int_0^\Delta F_a(x_I, \sigma) d\sigma = \frac{1}{2} K(x_I)\Delta^2 \qquad (24)$$
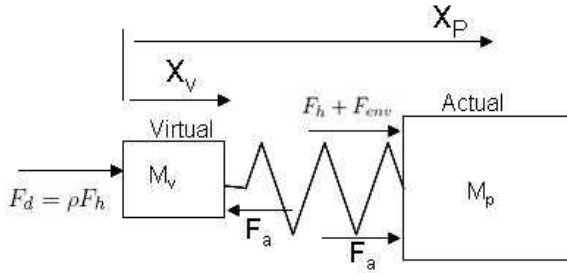
Figure 3. Virtual coordination control strategy

Figure 4. Bond graph of hydraulic human power amplifier with a virtual mechanical system. u_{loss} and w are dissipative term and extra control signal that are not considered in this paper.

Then,

$$\dot{W}_{hyd} = F_a(x_I, \Delta)(\dot{x}_I - \dot{x}_p) + \frac{1}{2}\frac{\partial K}{\partial x_I}\Delta^2 \dot{x}_I \quad (25)$$

$$= F_a(x_I, \Delta)\left\{-\dot{x}_p + \left[1 + \frac{\Delta}{2K(x_I, \Delta)}\frac{\partial K}{\partial x_I}\right]\dot{x}_I\right\} \quad (26)$$

$$= F_a(x_I, \Delta)\left\{-\dot{x}_p + \gamma_1(x_I, F_a, sgn(u))u\right\} \quad (27)$$

where

$$\gamma_1(x_I, F_a) = \left[1 + \frac{\Delta}{2K(x_I, \Delta)}\frac{\partial K}{\partial x_I}\right]\gamma_q(\text{sgn}(u), F_a)$$

Similar result is obtained for the pneumatic actuator with the storage function given by:

$$W_{pneu} = \int_0^\Delta F_a(\mathbf{m}, \sigma)d\sigma = \frac{1}{2}K(\mathbf{m})\Delta^2 \quad (28)$$

Then,

$$\dot{W}_{pneu} = F_a(\mathbf{m}, \Delta)(\dot{x}_I - \dot{x}_p) + \frac{1}{2}\frac{\partial K}{\partial \mathbf{m}}\Delta^2 \dot{\mathbf{m}} \quad (29)$$

$$= F_a(\mathbf{m}, \Delta)(-\dot{x}_p + \left[\frac{\partial x_I}{\partial \mathbf{m}} + \frac{\Delta}{2K(\mathbf{m}, \Delta)}\frac{\partial K}{\partial \mathbf{m}}\right]\dot{\mathbf{m}}) \quad (30)$$

$$= F_a(\mathbf{m}, \Delta)(-\dot{x}_p + \gamma_1(\mathbf{m}, F_a, \text{sgn}(u))u) \quad (31)$$

where

$$\gamma_1(\mathbf{m}, F_a, \text{sgn}(u))$$
$$= \left[\frac{\partial x_I}{\partial \mathbf{m}} + \frac{\Delta}{2K(\mathbf{m}, \Delta)}\frac{\partial K}{\partial \mathbf{m}}\right]\gamma_q(\text{sgn}(u), \mathbf{m}, F_a).$$

For either the hydraulic / pneumatic case, the compressibility is shown to be a passive 2-port capacitive field (like a spring), with a mechanical port via $(F_a, \dot{x}_p)$ that interacts with system inertia M_p in Eq.(1) and the valve command port via $(F_a, -\gamma_1 u)$.

VIRTUAL COORDINATION CONTROL FORMULATION

With the actuator compressibility shown to be a spring like object with one end interacting with inertia of the machine, the approach is to so control the valve so that the other end of the spring is interacting with a small virtual mass which is acted upon by the desired force $F_d = \rho F_h$

(Fig. 3). If the virtual mass (M_v) and the system inertia M_p are exactly coordinated, M_p and M_v become a single rigid inertia which is acted upon by the desired actuator force F_d and the human and environment forces F_h and F_{env}. We illustrate this process for the hydraulics case only. The pneumatic case can be obtained by substituting x_I by $\mathbf{m}$ for the most parts.

Consider the dynamics of a virtual mass and its coupling to the fluid power actuator given by:

$$M_v \ddot{x}_v = F_d - F_a(x_I, \Delta)$$
$$u = \frac{1}{\gamma_1}x_v + \frac{1}{\gamma_q}u_1 \quad (32)$$

where $F_d(t)$ is the desired actuator force typically given by $F_d(t) := \rho F_h(t)$. Notice that the coupling between the virtual inertia and the human power amplifier is similar to an integral controller ($u_1 = 0$). u_1 is the control term that will cause coordination $\dot{x}_v \rightarrow \dot{x}_p$.

The coupled system is given by:

$$M_p \ddot{x}_p = F_{human} + F_{env} + F_a(x_I, \Delta)$$
$$M_v \ddot{x}_v = F_d - F_a(x_I, \Delta)$$
$$\dot{\Delta} = \dot{x}_I - \dot{x}_p \quad (33)$$
$$\dot{x}_I = \frac{\gamma_q}{\gamma_1}\dot{x}_v + u_1$$

which has a bond graph representation shown in Fig. 4.

Using the storage function,

$$W_{total} = W_{hyd} + \frac{1}{2}M_p \dot{x}_p^2 + \frac{1}{2}M_v \dot{x}_v^2 \quad (34)$$

where W_{hyd} is the storage function for the capacitive field in (24). From this, it can be shown that the coupled system (33) satisfies the passivity property:

$$\int_0^t [F_d \dot{x}_v + (F_h + F_{env})\dot{x}_p]d\tau$$
$$+ \int_0^t [\frac{\gamma_1}{\gamma_q}F_a u_1 - F_d v_E]d\tau \geq -c_0^2 \quad (35)$$

for some c_0 and for all $t \geq 0$. Thus, if the control terms u_1 are designed such that for some c_1, and for all $t \geq 0$,

$$\int_0^t [\frac{\gamma_1}{\gamma_q}F_a u_1 - F_d(t)v_E]d\tau \leq c_1^2 \quad (36)$$

where $v_E = \dot{x}_v - \dot{x}_p$, then, for $F_d(t) = \rho F_h(t)$, the human power amplifier under control will satisfy the desired passivity property in (4).

Coordinate transformation into locked and shape systems

To see the effect of the control u_1 on the dynamically coupled system and the coordination error, consider the coordinate transformation:

$$\begin{pmatrix} v_L \\ v_E \end{pmatrix} = \begin{pmatrix} M_p/M_L & M_v/M_L \\ 1 & -1 \end{pmatrix} \begin{pmatrix} \dot{x}_p \\ \dot{x}_v \end{pmatrix} \quad (37)$$

$$M_L := M_v + M_p \quad (38)$$

$$M_E := \left(\frac{1}{M_p} + \frac{1}{M_v} \right)^{-1} = \frac{M_p M_v}{M_p + M_v} \quad (39)$$

(v_L, v_E) are referred to as the locked and shape system velocities, since v_E measures the difference between the speeds of the virtual and actuator manipulator, and $v_L = \dot{x}_v = \dot{x}_p$ when $v_E = 0$. Hence, v_L is the speed of the manipulator and the virtual manipulator when they are locked in place. M_L and M_E are respectively the locked system inertia, and the shape system inertia.

Eqs. (37)-(39) is an instance of decomposing the velocity space of the coupled system (i.e. $\Re^2 = \{(\dot{x}_p, \dot{x}_v)\}$) into a component given by the coordination error $v_E = \dot{x}_p - \dot{x}_v$ and its orthogonal complement v_L with respect to $\text{diag}(M_p, M_v)$ being the metric. This decomposition approach can be generalized to nonlinear multi-DOF mechanical systems as well [3], [4], [5].

The dynamics in the transformed coordinates are given by:

$$M_L \dot{v}_L = F_h + F_{env} + F_d \quad (40)$$

$$M_E \dot{v}_E = \underbrace{\frac{M_v}{M_L}(F_h + F_{env}) - \frac{M_p}{M_L} F_d(t)}_{F_E} + F_s(\Delta) \quad (41)$$

$$\dot{\Delta} = -v_E + u_2 \quad (42)$$

We can associate storage functions for the locked and shape systems respectively as,

$$W_L = \frac{1}{2} M_L v_L^2; \quad W_S = \frac{1}{2} M_E v_E^2 + \int_0^\Delta F_s(\delta) d\delta \quad (43)$$

Notice that the coordinate transformation Eqs.(37)-(39) preserves kinetic energies and storage functions in that the sum of the kinetic energies and storage functions, respectively, of the locked and shape systems are exactly those of the coupled system [6]

$$\kappa := \frac{1}{2} M_p \dot{x}_p^2 + \frac{1}{2} M_v \dot{x}_v^2 = \frac{1}{2} M_L v_L^2 + \frac{1}{2} M_E v_E^2 \quad (44)$$

$$W_c := W_L + W_S \quad (45)$$

This means that by ensuring that the shape and locked systems are passive, the coupled system in Eq.(33) will also be passive.

Shape system control

The shape system control objective is to make $v_E \to 0$ in:

$$M_E \dot{v}_E = F_E(t) + F_a(x_I, \Delta) \quad (46)$$

$$\dot{\Delta} = \dot{x}_I - \dot{x}_p \quad (47)$$

$$\dot{x}_I = \frac{\gamma_q}{\gamma_1} \dot{x}_v + u_1 \quad (48)$$

A variety of control algorithms can be designed for u_1 to ensure that $v_E \to 0$ exponentially. A backstepping control law is used to obtain the experimental results in this paper.

Locked system control

If $F_d := \rho F_h$, the locked system dynamics becomes

$$M_L \dot{v}_L = \underbrace{(\rho + 1)F_h + F_{env}}_{F_{total}} \quad (49)$$

which is the desired dynamics of a passive rigid mechanical tool.

When $v_E \to 0$, we also have the RHS in Eq.(41) being zero on average:

$$0 = F_E + F_s(\Delta)$$

$$0 = \frac{M_v}{M_L} F_{total} + F_a(x_I, \Delta) - F_d(t)$$

Since F_{total} is the total forcing term for the locked system (49) scaled by M_v/M_L (which is small if M_v is small), thus unless the locked system undergoes large acceleration, F_{total} is typically small. Therefore, we have the original force control objective being approximately satisfied:

$$F_a(x_I, \Delta) \approx F_d(t)$$

This is despite the specified objective (because of the dynamics of the added M_v inertia) being a coordination control problem.

EXPERIMENTAL RESULTS

Hydraulic case

The hydraulic human power amplifier has two DOF. The pitch motion is actuated by a linear actuator, and the reach motion actuated by a hydraulic motor and a rack-and-pinion drive. The reach direction has a range of 0.4m, and a range from 40° to 90° in the pitch direction. Load cells are used to measure force signals from the human and the actuator, along both the directions of motion. Experiments are performed at a supply pressure of $6894.75 N/m^2$. Moog series 7 servo valves are used to control both the actuator and motor.

With a torque amplification factor of 3, force tracking results are illustrated: when the system is suddenly loaded with a 9.7kg block (Fig. 5) in free motion, and when it is pushed against a rigid obstacle Fig. 6. In all cases, force tracking results are quite reasonable.
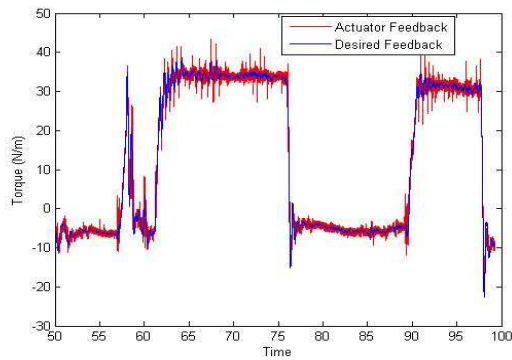
Figure 5.   Hydraulic force tracking in free motion with load added and removed.
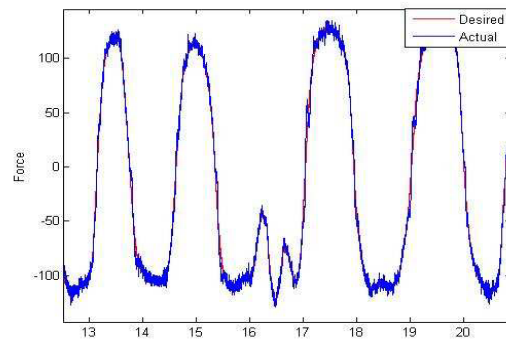
Figure 7.   Pneumatic force tracking in Free motion.
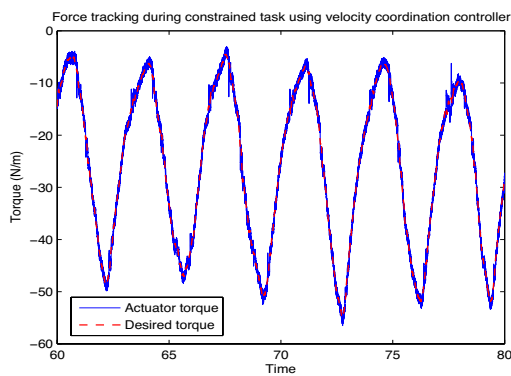
Figure 6.   Hydraulic force tracking during constrained task.
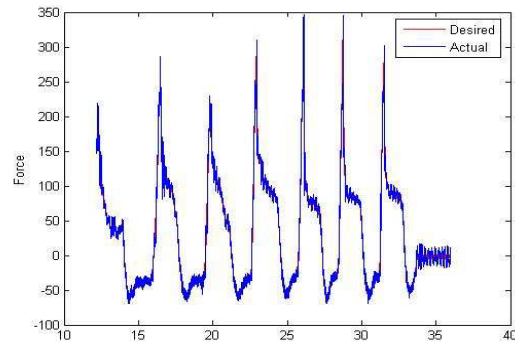
Figure 8.   Pneumatic force tracking during repeated hard contacts.

Pneumatic case

The pneumatic human power amplifier is a one degree of freedom setup consisting of a pneumatic actuator supporting a 4kg load. The human interacts with the setup through a load cell. The force exerted by the actuator is determined by measuring the pressure in the chambers on either side of the piston. The actuator has in-built position feedback sensor which is used to determine the piston position. All the experiments are done at a supply pressure of 5.7 bar (gauge). A Festo 5/3 proportional servo valves is used for controlling the air flow rate.

The amplification gain for pneumatic actuator is set at 5. Fig. 7 shows the force tracking result when moving a load, Fig. 8 shows the force tracking results when the actuator hits an obstacle. The system is not destabilized by sudden contact and is quite safe to use.

CONCLUSIONS

A unified control framework hydraulic and pneumatic human power amplifier is proposed. The control law converts a force control objective into a coordination control paradigm. The key aspect lies in modeling the compressibility effect and imposing a control structure that respects the power continuity. Experimental results demonstrate the usefulness of the framework.

REFERENCES

1 P. Y. Li, "Design and control of a hydraulic human power amplifier," in *Proceedings of the 2004 ASME IMECE. Paper #IMECE2006-14973. FPST Divisiion*, 2004.

2 P. Y. Li, "A new passive controller for a hydraulic human power amplifier," in *Proceeding of the 2006 ASME-IMECE*, no. 15056, November 2006, chicago, IL.

3 D. Lee and P. Y. Li, "Passive decomposition of multiple mechanical systems under coordination requirement," in *Proceedings of the IEEE CDC 2004*, vol. 2, 2004, pp. 1240–1245.

4 D. J. Lee, "Passive decomposition and control of interactive mechanical systems under motion coordination requirements," Ph.D. dissertation, Department of Mechanical Engineering, University of Minnesota, May 2004.

5 D. Lee and P. Y. Li, "Passive bilateral control and tool dynamics rendering for nonlinear mechanical teleoperators," *IEEE Transactions on Robotics*, vol. 21, no. 5, pp. 936–951, October 2005.

6 D. J. Lee and P. Y. Li, "Passive feedforward approach for linear dynamically similar bilateral teleoperated manipulators," *IEEE Transactions on Robotics and Automation*, vol. 19, no. 13, pp. 443–456, June 2003.

OS9-4

RESEARCH ON SPACE DOCKING HIL SIMULATION SYSTEM BASED ON STEWART 6-DOF MOTION SYSTEM

Han Junwei, Huang Qitao, Chang Tongli

Department of Mechatronic Engineering, Harbin Institute of Technology, Harbin, China
(E-mail: hjw@hit.edu.cn)

ABSTRACT

This paper presents the research on the experimental testing system of the space docking HIL (Hardware-In-the-Loop) simulation, which is based on a Stewart 6-DOF (Degree-Of-Freedom) motion system. First of all, spacecraft dynamics is analyzed. Because of the under-damping characteristic, stability of the HIL simulation system is analyzed, and control strategy of the 6-DOF-motion system, which is based on the phase compensation, is put forward to improve system stability. The influence created by the frequency characteristics of the 6-DOF-motion system on the accuracy and stability of the HIL simulation system is also analyzed. The characteristics of the spacecraft dynamics and the accuracy and feasibility of the HIL simulation system are verified with a non-damp collision device.

KEY WORDS

HIL simulation, On-orbit docking, 6-DOF Stewart platform, Dynamic simulation

INTRODUCTION

It is great signification to research HIL (Hardware-In-the-Loop) simulation technique for on-orbit docking, because that spacecraft docking technique play very important role in human space program. For the docking mechanism is very complex and the on-orbit docking is a complicated dynamics process, it is necessary to research spacecraft on-orbit docking process dependent on HIL simulation.

In 1964, Langley Research Center of American firstly established a docking simulator [1]; it is employed to test of Gemini-Agena. In March 16th, 1966, NASA accomplished the famous Gemini-Agena on orbit docking, which the first time on-orbit spacecraft docking activity is made by human beings.

In 1969, Langley Research Center established another docking simulator[2],[3], which is employed to research on the complex docking process between the Lunar Excursion Module and Command/Service Module of Apollo. The docking simulator had been made use of to training astronauts.

In 1971, former USSR designed a docking simulator that had been employed to the test of APAS-89 docking mechanism [4].

The docking simulators mentioned above are called physics simulation. With the development of computer technology, mathematics simulation and half-physics simulation has been played more and more important role in human space program. After the Apollo-13 Disaster in 1970, American and USSR began to cooperation in space program, and a new docking mechanism called APAS-75[5] was developed. The composition and dynamics of APAS-75 were much more complex than that of the docking mechanism developed before. To ensure the reliability in space and determine the dynamic parameters of the docking mechanism, an integrated testing system[6],[7] for docking mechanism, shown in Fig.1 and Fig.2, was developed by the American and Russian scientists. Then

Figure1 Integrated testing system for docking mechanism
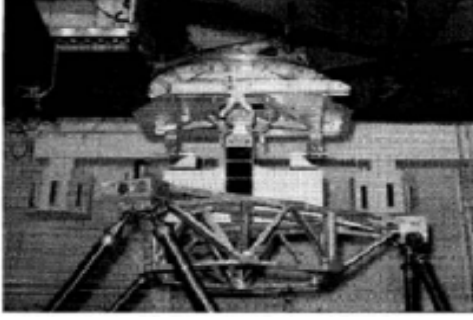
Figure 2 6-DOF contact dynamic simulator

Figure 4 Rendezvous and docking operation test system

Figure 3 European proximity operation simulator

the research on spacecraft docking simulation has come into the time of HIL simulation. Using APAS-75, Union-19 docking with Apollo was realized in July 17th 1975, which is the USA and USSR cooperation on-orbit docking for the first time.

In 1980s, Europe Space Bureau began to research on the unmanned spacecraft rendezvous and docking technology, and a docking mechanism for unmanned spacecraft is developed, which would be employed in Eureca A docking with Eureca B, and Hermes Shuttle docking with Columbus Space Station. Meanwhile, the spacecraft docking simulator[8], shown in Fig.3, was also developed. In the same time, the research on the spacecraft rendezvous and docking technology was put forward in Japan, and a rendezvous and docking operation test system, shown in Fig.4, was developed in NASDA[9], and the docking mechanism was developed too, which is employed in the on-orbit docking of ETS-7 Unmanned Spacecraft.

China began manned space program in 1992. In 2008, an integrated testing system for docking mechanism is developed by HIT and Shanghai Space Bureau. In this paper, firstly the compositions, and the model of system included dynamic model of the spacecraft are given, and secondly the characteristics of the system is analyzed, at last a simply verifying model is employed to research on the effect of 6-DOF Stewart platform frequency

characteristics on the system stability and accuracy of the docking dynamics.

SYSTEM DESCRIPTION

Docking mechanisms are employed for docking a spacecraft with another spacecraft. The on-orbit spacecraft is called passive spacecraft, and its docking mechanism name passive docking mechanism. The launched spacecraft is called active spacecraft, and its docking mechanism called active mechanism. To research the docking dynamics, coordinate frames are defined as shown in Fig.5, which includes inertial frame e (O-XYZ), a moving frame e_1 (O$_1$-X$_1$Y$_1$Z$_1$), a moving frame e_2 (O$_2$-X$_2$Y$_2$Z$_2$), a moving frame e_3 (O$_3$-X$_3$Y$_3$Z$_3$), a moving frame e_4 (O$_4$-X$_4$Y$_4$Z$_4$). The Euler angles are defined as yaw ψ, pitch θ, and Yaw φ, then the transfer matrix between inertial frame and moving frame is as follows:

$$A = \begin{bmatrix} c\theta \cdot c\psi & s\varphi \cdot s\theta - c\varphi \cdot c\theta \cdot s\psi & c\varphi \cdot s\theta + s\varphi \cdot c\theta \cdot s\psi \\ s\psi & c\varphi \cdot c\psi & -s\varphi \cdot c\psi \\ -s\theta \cdot c\psi & s\varphi \cdot c\theta + c\varphi \cdot s\theta \cdot s\psi & c\varphi \cdot c\theta - s\varphi \cdot s\theta \cdot s\psi \end{bmatrix}$$

(1)

where $s(\cdot) = \sin(\cdot)$, and $c(\cdot) = \cos(\cdot)$. A generalized coordinate vector $\mathbf{q}$ is defined as:

$$\mathbf{q} = [x, y, z, \varphi, \theta, \psi]^{\mathrm{T}} \qquad (2)$$

where x, y, z present the varying coordinates of moving frame from inertial frame.

According to Newton-Euler formula, if the mass of the docking mechanism is neglected, the dynamic formula of active spacecraft can be written as

$$\frac{^r \mathrm{d}^2}{\mathrm{d}t^2} \mathbf{r}_1 = \frac{\mathbf{F}_1 + \mathbf{F}_3}{m_1} \qquad (3)$$
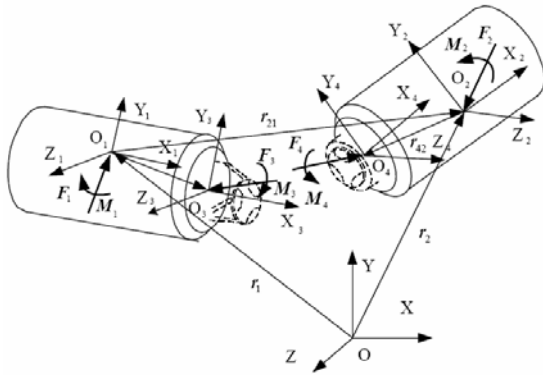
Figure 5 Two On-orbit Docking Spacecraft

$$\mathbf{J}_1 \cdot \frac{^r\mathrm{d}}{\mathrm{d}t}\boldsymbol{\omega}_1 + \boldsymbol{\omega}_1 \times \mathbf{J}_1 \cdot \boldsymbol{\omega}_1 = \mathbf{M}_1 + \mathbf{M}_3 + \mathbf{r}_{31} \times \mathbf{F}_3 \qquad (4)$$

and the passive spacecraft dynamic formula is

$$\frac{^r\mathrm{d}^2}{\mathrm{d}t^2}\boldsymbol{r}_2 = \frac{\boldsymbol{F}_2 + \boldsymbol{F}_4}{m_2} \qquad (5)$$

$$\mathbf{J}_2 \cdot \frac{^r\mathrm{d}}{\mathrm{d}t}\boldsymbol{\omega}_2 + \boldsymbol{\omega}_2 \times \mathbf{J}_2 \cdot \boldsymbol{\omega}_2 = \mathbf{M}_2 + \mathbf{M}_4 + \mathbf{r}_{42} \times \mathbf{F}_4 \qquad (6)$$

If the active spacecraft is defined as reference, and the relative movement $\boldsymbol{r}_{21}$ between active spacecraft and passive spacecraft is

$$\frac{^r\mathrm{d}}{\mathrm{d}t}\boldsymbol{r}_{21} = \frac{^b\mathrm{d}}{\mathrm{d}t}\boldsymbol{r}_{21} + \boldsymbol{\omega}_1 \times \boldsymbol{r}_{21} \qquad (7)$$

$$\frac{^r\mathrm{d}^2}{\mathrm{d}t^2}\boldsymbol{r}_{21} = \frac{^b\mathrm{d}^2}{\mathrm{d}t^2}\boldsymbol{r}_{21} + \frac{^r\mathrm{d}}{\mathrm{d}t}\boldsymbol{\omega}_1 \times \boldsymbol{r}_{21} + 2\boldsymbol{\omega}_1 \times \frac{^b\mathrm{d}}{\mathrm{d}t}\boldsymbol{r}_{21} + \boldsymbol{\omega}_1 \times (\boldsymbol{\omega}_1 \times \boldsymbol{r}_{21}) \qquad (8)$$

where $(\overset{\circ}{\ }) = \frac{^b\mathrm{d}}{\mathrm{d}t}(\ )$ is angular velocity in moving frame, $(\overset{\bullet}{\ }) = \frac{^r\mathrm{d}}{\mathrm{d}t}(\ )$ is angular velocity in inertial frame, $(\overset{\circ\circ}{\ }) = \frac{^b\mathrm{d}^2}{\mathrm{d}t^2}(\ )$ is angular acceleration in moving frame, $(\overset{\bullet\bullet}{\ }) = \frac{^r\mathrm{d}^2}{\mathrm{d}t^2}(\ )$ is angular acceleration in inertial frame.

Then on-orbit docking dynamics is shown in Fig.6.

To research on the docking dynamics, a docking simulator is built, and the overall docking simulator system developed by HIT is shown in Fig.7, the system is consisted of the dynamic simulation software, a 6-DOF Stewart platform, a 6-DOF force and torque sensor, and a docking mechanism. When the docking conditions that involves the relative position and relative velocity between active spacecraft and passive spacecraft are given, the passive mechanism driven by Stewart platform impacts the active mechanism that is fixed on the frame through 6-DOF force and torque sensor, the impacting forces and torques effects each other on the passive mechanism and the active mechanism is measured by 6-DOF force and torque sensor. The dynamic simulation software calculates the relative movement between the active spacecraft and the passive spacecraft according to the docking dynamics, the relative movement is replicated by 6-DOF Stewart
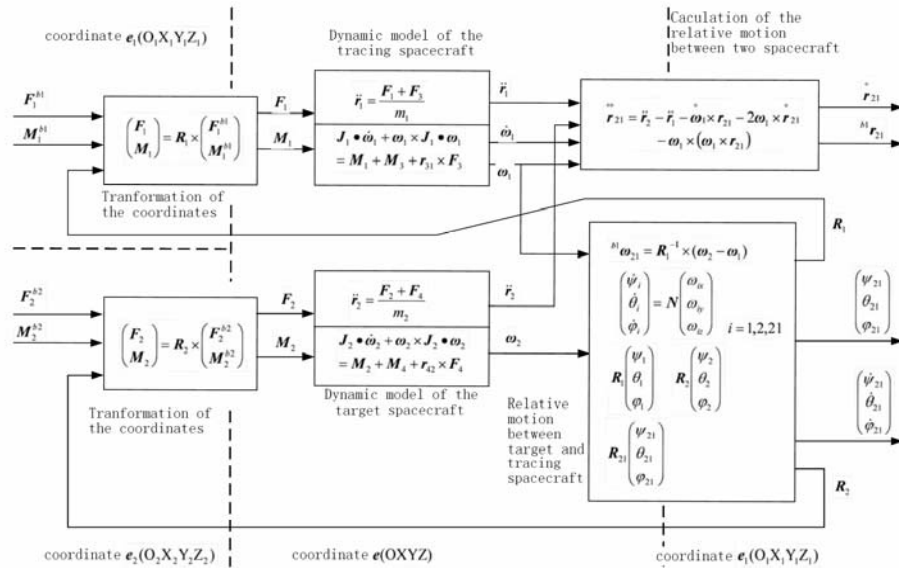
Figure 6 The diagram of docking dynamics

Figure 7 Integrated testing system

platform.

There are several problems for the docking simulation system:

(1) Stability. For the under-damping characteristic of the docking mechanism, the spacecraft dynamics performs under-damping oscillation. Stewart platform has phase lag, which may result in the unstable docking dynamics.

(2) Docking dynamics validation. The docking dynamics presented here is derived from the laws of physics. Where the parameter values were taken from design values or rough approximations of what could be expected in practice. The docking dynamics can be valuable for design and analysis of the spacecraft and docking mechanism. The strengths of the dynamics should, however, be proven by experimental validation.

SYSTEM ANALYSIS

The diagram of the docking simulator is shown in Fig.8, and its the transfer function can be written as

$$G_I(s) = G_M(s)G_D(s)G_S(s)G_T(s) \qquad (9)$$

where $G_M(s)$ is the transfer function of docking mechanism, $G_D(s)$ is that of spacecraft dynamics, $G_S(s)$ is that of Stewart platform, and $G_T(s)$ is that of other parts of the simulator. If the transfer functions of Stewart platform and other parts could be seen as

$$G_O(s) = G_S(s)G_T(s) = 1 \qquad (10)$$

The docking simulator may replicate the on-orbit docking process with no error. But in fact, $Go(s)$ is not equal to 1, and as result, the docking dynamics replication on the docking dynamics has error. In order to ensure the validation of the docking dynamics replication on the simulator, the attention must be paid to the design of $Go(s)$. Because the docking mechanism and docking dynamics is very complex, to simplifying
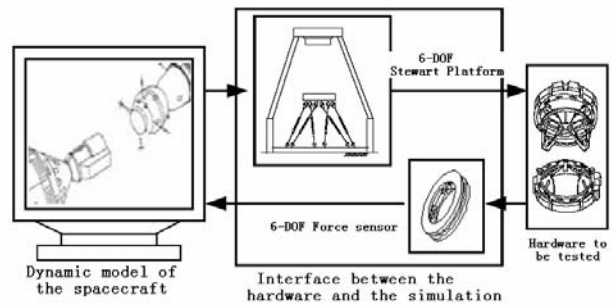
Figure 8 The Schematic diagram of the docking simulator
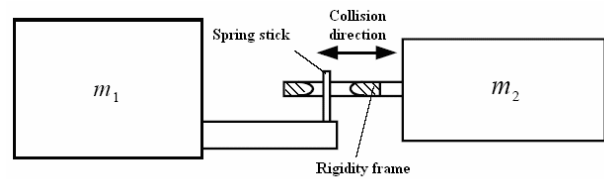
Figure 9 A simplified docking mechanism

the analysis, a simple non-damping collision-rebound device, shown in Fig.9 is employed to research on the parameters determination of $Go(s)$.

VERIFICATION

The simplified docking mechanism as show in Fig.9 is a non-damping collision-rebound oscillation system that is similar with the docking process, the nature frequency of the system is
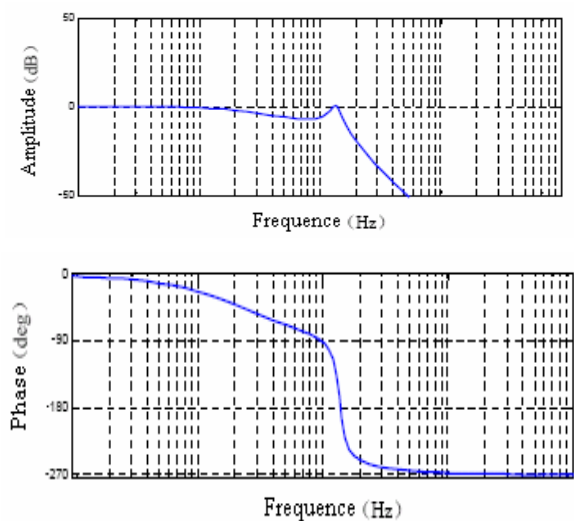
Figure 10 Frequency characteristics of the Stewart platform

$$\omega_n = \sqrt{\frac{K(m_1 + m_2)}{m_1 m_2}} \qquad (11)$$

and the rebound coefficient is defined as

$$R_v = \frac{v_i}{v_o} \qquad (12)$$

where v_i is input velocity, and the v_o is rebound velocity. If the mass m_1 has a muzzle velocity relative to the mass m_2, the system will oscillation in critical state, and the rebound coefficient is equal to 1. To prove the validation of docking simulator, the simulator is employed to simulation the non-damping collision-rebound oscillation device.
If the frequency error

$$e_f = \left| \frac{\omega_n - \omega_{nc}}{\omega_n} \right| \le 0.05 \qquad (13)$$

where ω_{nc} is simulation oscillation frequency, and the rebound coefficient error

$$e_r = 1 - R_{vc} \le 0.05 \qquad (14)$$

where R_{vc} is simulation rebound coefficient, the validity of docking simulator can be verified.

ANALYSIS AND EXPERIMENT

The 6-DOF Stewart platform frequent characteristics are shown in Fig. 10, which has phase lag. Without compensation of the phase lag of the Stewart platform, the outputs of non-damping collision-rebound dynamics simulation system are unstable as shown in Fig.11.
A phase compensation controller of Stewart platform is designed as

$$D(s) = k_p \frac{T(s)}{S(s)} \qquad (15)$$

Where k_p is the gain of the controller, generally, $k_p = 1$. With the phase compensation, the phase lag from Stewart platform to force sensor is zero, then the simulation outputs of non-damping collision-rebound dynamics, shown in Fig.12, is stabilized. The frequency of the output is greater than theory result, and the rebound coefficient is about 0.97. It is impossible that the damp of the overall system is zero, which result in the rebound velocity attenuation. But what causes the variation of the oscillation frequency?
When the gain k_p of the controller $D(s)$ is decreased, i.e. $k_p < 1$, the experiment results is shown in Fig.13, the frequency of the output becomes smaller.
When the gain k_p is increased, i.e. $k_p > 1$, the experiment results is shown in Fig.14, the frequency of the output becomes much greater.
From analysis above, it is known that the frequent characteristic of the Stewart platform has great effect on the replicating accuracy of the docking dynamics. The

phase lag of the transfer function may cause the docking simulator unstable, and the gain may change the nature frequency of the docking dynamics.

CONCLUSIONS

The docking simulator can be employed to analysis the on-orbit docking dynamics. For the complexity of the docking mechanism, it is difficult to analytically research on the docking dynamics, consequently, experiment research can play important pole on the research job. Then the on-orbit docking simulator is established to carry out the experiment research on docking dynamics. To simplify the research work, and do not lost the generality, a non-damping collision-rebound device that its characteristics is known analytically is employed to verify the validation of the docking simulator. Apart from the stability, two
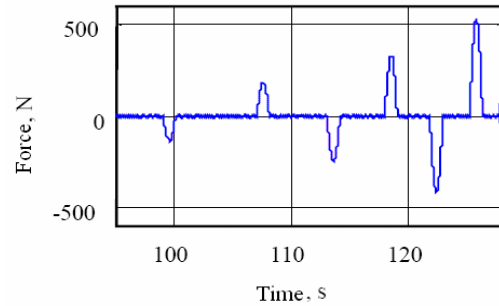
Figure 11 Dynamics output without compensation
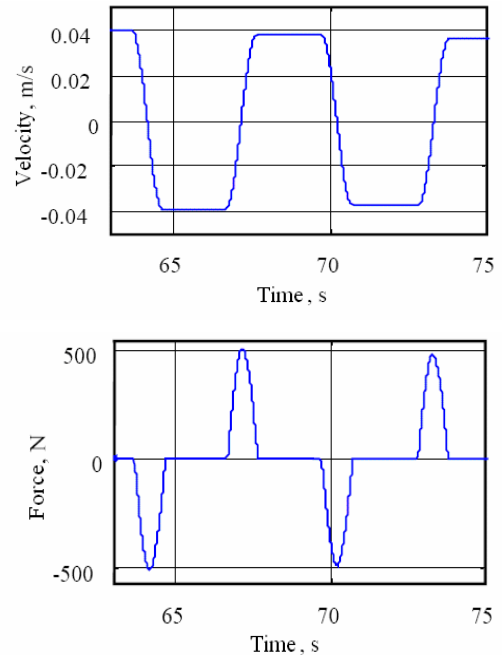
Figure 12 Dynamics output with phase compensation
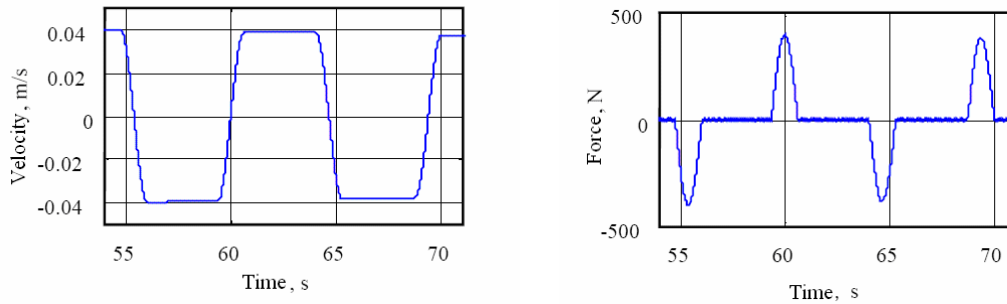
Figure 13 Dynamics output with phase compensation with greater gain
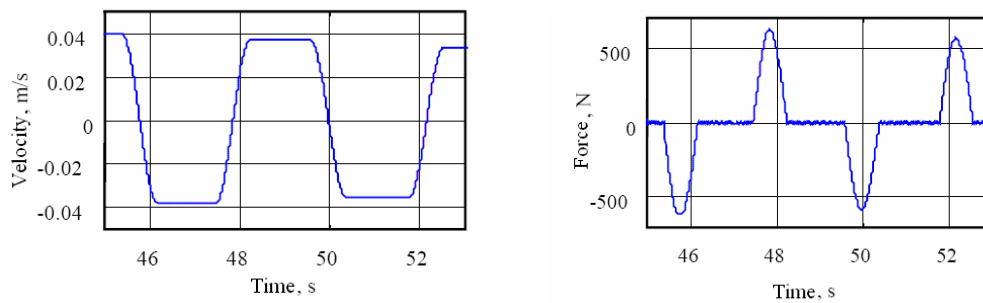
Figure 14 Dynamics output with phase compensation with less gain

other validation indexes are introduced, one is the frequency error, and another one is rebound coefficient. The 6-DOF Stewart platform is used of to replicate the relative movement of the spacecrafts. From the experiment research, it's known that the frequent characteristic of the Stewart platform has great effect on performances of the docking simulator, its phase lag has influence on the stability of the simulator, which will cause the docking dynamics unstable, and its gain may effect on the nature frequency of the docking dynamics. To ensure the validation of research work, a phase compensation controller on Stewart platform is designed. With the controller, the phase lag and the gain of the Stewart platform frequent characteristic is corrected, and the docking dynamics is well replicated consequently.

REFERENCES

1. Donald R. Riley, Byron M. Jaguet, Jack E. Pennington, et al, Comparison of Results of Two Simulations Employing Full-size Visual-cue for Pilot-controlled Gemini-Agena Docking. NASA TN D-3687,1966:1-35.
2. Robert D. Langley. Apollo Experience Report – the Docking System. NASA TN D-6854, 1972:1-45.
3. H. G. Hatch, J. E. Pennington, J. B. Cobb. Dynamic Simulation of Lunar Module Docking with Apollo Command Module in Lunar Orbit. NASA-Langley, NASA TD-3972, 1967:1-26.
4. U. S. Congress, Office of Technology Assessment. U. S. – Russian Cooperation in Space. OTA-ISS-618. U. S. Government Printing Office. 1995: 1-130.
5. David S. F. Portree. Mir Hardware Heritage. NASA-RP-1357. 1995:1-205.
6. S. Ananthakrishnan, R. Teders, K. Alder. Role of Estimation in Real-time Contact Dynamics Enhancement of Space Station Engineering Facility. IEEE Robotics & Automation Magazine, 1996, 9:20-28.
7. NASA. Johnson Space Center Inspection 2000 Exhibit Catalog. NASA Johnson Space Center. Houston, USA, 2000:122.
8. Toralf Boge, Erwin Schreutelkamp. A New Commanding and Control Enviroment for Rendezvous and docking Simulation at the EPOS-facility. 7th International Workshop on Simulation for European Space Programs – SESP 2002, ESTEC, Noordwijk, Netherlands 2002:1-8.
9. C. Lange, E. Martin. Towards Docking Emulation Using Hardware in the Loop Simulation with Parallel Platform. Proceedings of the Workshop on Fundamental Issue and Future Directions for Parallel Mechanism and Manipulators. Quebec, Canada, 2002:1-4.

OS10-1

DESIGNING AND EXPERIMENTAL INVESTIGATION OF AN IMMERSION UNIT WITH DOUBLE GAS-CURTAIN SEALING FOR IMMERSION LITHOGRAPHY

Xin Fu, Wenyu Chen, Ying Chen, Xiaodong Ruan, Huayong Yang

The State Key Lab of Fluid Power Transmission and Control, Zhejiang University
Hangzhou 310027, China
(e-mail: xfu@zju.edu.cn)

ABSTRACT

For most of the microelectronics industry history, optical lithography has been the backbone for continuing the trend of making features even smaller. The intention of immersion lithography is to increase the index of refraction in the space between the lens and wafer by introducing a high refractive index liquid in place of the low refractive index air that currently fills the gap. Because the liquid acts as a lens component during scan-step process, it must maintain a high and uniform optical quality. Thus, an immersion unit structure must be implemented to keep the flow field from leaking. After analyzing the mechanics of the flow-field in immersion lithography, an immersion unit structure with double gas-curtain sealing and gas-fluid mixing phase collecting was designed and implemented, featuring chemical surface characteristics. Experimental results were analyzed in terms of vacuum degree in collection antrum, input pressure for gas sealing, bubble-trap within flow field, double gas-curtain, double mixing-phase collection, surface characteristics of wafer.

KEYWORDS

Immersion lithography, Immersion unit, Gas sealing

INTRODUCTION

For most of the microelectronics industry history, optical lithography has been the backbone for continuing the trend of making features even smaller. However, as the apparent inability of optical lithography for future requirements, technology evolution to next-generation lithography (NGL) was becoming necessary.

Among all of the competing NGL technologies,

Immersion lithography has been proposed in the past as a method to improve the resolution of optical lithography, but more recently it has been gaining popularity due its potential for achieving resolution down to 50 nm and below. It has shown promise as a technology extending optical lithography without significant changes to the manufacturing infrastructure used for decades [1, 2, 3].

The intention of immersion lithography is to increase the index of refraction in the space between the lens and

wafer by introducing a high refractive index liquid in place of the low refractive index air that currently fills the gap. Because the liquid acts as a lens component during scan-step process, it must maintain a high and uniform optical quality. Thus, an immersion unit structure must be implemented to keep the flow field from leaking. Also, the immersion liquid within the gap has to be updated as substances unwrapped from chemical reacting may affect the optical quality of the liquid

IMMERSION UNIT MAIN STRUCTURE

Four generations of immersion unit structure have been developed up to present.

For the first generation of immersion unit, a basic liquid-transportation concept with double gas-curtain sealing and gas-fluid mixing phase collecting was designed and implemented

Improved porous medium processing was introduced for second generation, which has shown better performance with less vibration during gas-liquid phase mixing in liquid collection.

As for immersion unit generation three, continuous air sealing curtain along circumference direction within working area was implemented, providing enhanced air sealing performance, requiring smaller structure volume and less pressured air.

With inherited advantages from parental generation, No.4 generation of immersion unit was designed and implemented, aiming at integrated within an experiment platform for lithography scan-step moving and exposing.

Figure 1 Generation one of immersion unit.

Figure 2 Generation tow of immersion unit.
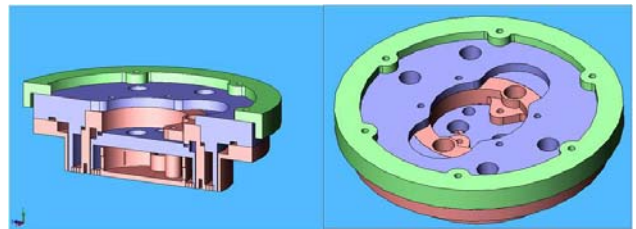
Figure 3 Generation three of immersion unit.
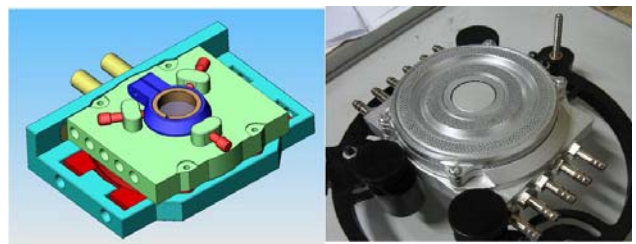
Figure 4 Generation four of immersion unit.

A schematic of the immersion unit implementation model is shown in Figure 5. Down-top and cross-sectional views of the lens/unit/gap/wafer system are illustrated [4].
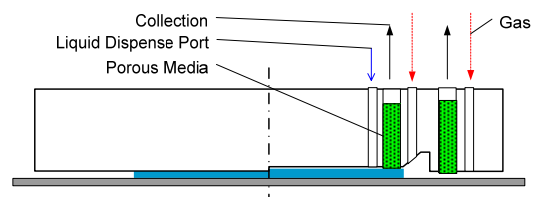
Figure 5 Schematic of the immersion unit structure implemented.

The immersion fluid is continuously injected through dispense ports that are located adjacent to the lens. Then the liquid is collected and removed from the wafer surface through collection ports that are located outboard of the dispense ports. Within the recovery channels, the porous media are applied to suppress vibration brought up by liquid/gas mixing phase collection. Certain negative

222

pressure is provided within collection antrum, leading fluid pass under the lens. The wafer motion is oscillatory and characterized by velocities as high as 200 mm/s and accelerations as high as twice the acceleration of gravity, which will also improving the liquid motion and collection.

VACUUM DEGREE IN COLLECTION ANTRUM

Negative pressure is provided within the collection antrum for recovering immersion liquid from wafer surface. The proper vacuum degree is significant for flow field's completeness and non- leakiness. The classic gauge pressure is -25kPa corresponding to the classic liquid pumping pressure of 6kPa. Figure 6 illustrates the gauge pressure in collection antrum rise as a function of the liquid with different injecting pressure.
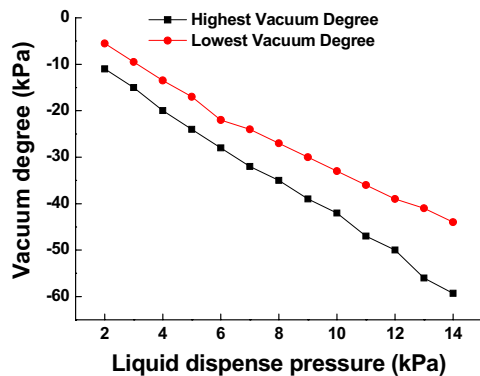
Figure 6 Collection antrum gauge pressure rise as a function of the liquid with different injecting pressure.

In terms of a specific liquid injecting pressure, the vacuum degree has a range of proper values. With the vacuum degree values lower than the range, recovering system will not be able to collect all the immersion liquid, leading to leakiness outboard immersion unit working area on the wafer. However, with the vacuum degree higher than the range, liquid from dispense ports will not be able to fill the gap flow field completely, destroying liquid phase continuity beneath the lens area. Experiment shows that increase the annular collection area offers wider range of vacuum degree acceptance region.

GAS SEALING PRESSURE

The wafer motion is oscillatory and characterized by velocities as high as 200 mm/s, and the immersion liquid leakiness is likely to occur as such relative motion between the contact line and the substrate. For higher scanning process speed, increasing the gas sealing pressure could maintain the intact gap flow field and avoid liquid leaking. Figure 7 illustrates the safe region with scanning speed rise as a function of gas sealing input pressure.

HYDROPHILIC AND HYDROPHOBIC SUBSTRATE

Wafers with different coating types are tested in scanning speed tolerance and vacuum degree threshold experiments. Figure 7 shows curves of acceptable scanning speeds as a function of gas sealing input pressure, with the substrate coating of titanium dioxide, silicon dioxide, and magnesium fluoride separately.
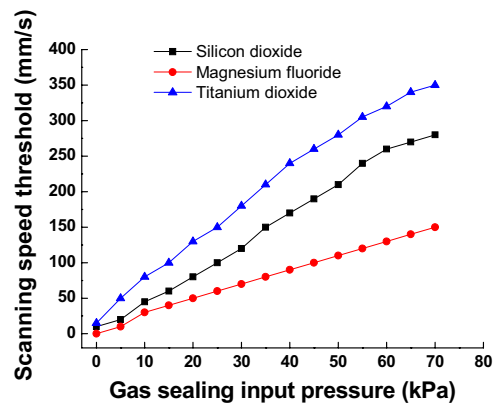
Figure 7 Acceptable scanning speeds as a function of gas sealing input pressure, with the substrate coating of titanium dioxide, silicon dioxide, and magnesium fluoride separately.

Titanium dioxide is extremely hydrophilic with a contact angle less than 10 degree, while magnesium fluoride is hydrophobic with a contact angle larger than 170 degree, and silicon dioxide coating in the middle of the range. Apparently, for an immersion unit structure with double gas-curtain sealing and gas-fluid mixing phase collecting, hydrophilic wafer surface supports higher speed threshold before gap flow field leaking.

VELOCITY DISTRIBUTION

The flow field velocity contours are investigated, by computational fluid dynamics modeling, which are annulated around within the gap flow field beneath the lens area with double dispense ports. Through high speed camera sampling random particles' position at particular interval, velocity magnitudes are calculated and gathered, as illustrated in Figure 8. The overall velocity distribution slightly goes up as liquid injecting pressure increases.
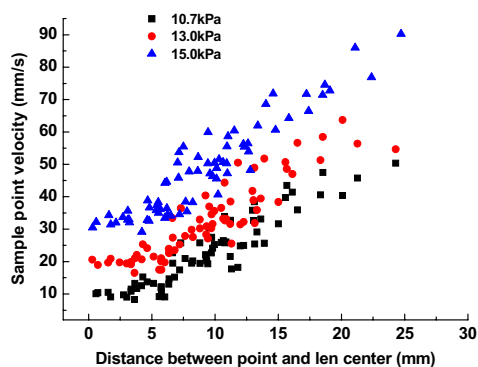
Figure 8 Random sample points velocity distribution as a function of point's center distance beneath lens area under different liquid injection pressure.

SUMMARY AND CONCLUSIONS

In this paper, the results of experiments on an immersion unit have been presented. Parametric studies have been carried out that analyze the important factors for improve the immersion unit working performance in terms of scanning speed tolerance and velocity distribution, including vacuum degree in collection antrum, input pressure for gas sealing, surface characteristics of wafer. Gas sealing pressures and vacuum degree in collection antrum that correspond to various liquid dispense pressure have been identified. Velocity distributions beneath lens area have also presented.

ACKNOWLEDGEMENTS

REFERENCES

1. M. Switkes, M. Rothschild, J. Microlith. Microfab. Microsyst.1 (2002) 225.

2. B. Lin, Microelectron. Eng. 6 (1987) 31.

3. Michael Quirk, Julian Serda. Semiconductor Manufacturing Techonology. Pearson Education, Inc. 2001.

4. Huayong Yang, State Intellectual Property Office of the P.R.C, PRC Patent No. ZL200720107284.X.

THERMAL MODEL OF A TANK FOR SIMULATION AND MASS FLOW RATE CHARACTERIZATION PURPOSES

Rosario de GIORGI*, Niazi KOBBI*, Sylvie SESMAT* and Eric BIDEAUX*

* Laboratoire AMPERE, INSA-Lyon (UMR CNRS 5005)
25 avenue Jean Capelle, 69621 Villeurbanne Cedex, France
(E-mail: eric.bideaux@insa-lyon.fr)

ABSTRACT

The paper focuses on the modeling of heat transfer in pneumatic systems. The main aim of this work is to represent these phenomena during the charge or the discharge of a tank for complex circuit simulation or for the identification of instantaneous mass flow rate.

In the first part, a macroscopic model will be proposed. It is based on the dimensional analysis theory. This approach enables the main heat transfer mechanisms to be identified according to flow conditions, pressure levels and tank shape. A relation between the corresponding dimensionless groups is then used to develop a general model for computing the heat exchange coefficient according to the system state and geometry. The identification procedure is presented and the first simulation results show good agreement between experimentation and theory.

KEY WORDS

Pneumatic systems, orifice modeling, thermal exchange model, identification procedures, experimentation

NOMENCLATURE

Physical constants

g	: acceleration of gravity	$[9.81\ m/s^2]$
c_v	: specific heat at constant volume	$[717\ J/(kg.K)]$
c_p	: specific heat at constant pressure	$[1004\ J/(kgK)]$
r	: gas constant	$[287\ J/(kg.K)]$
γ	: ratio of specific heat	$[1.4]$

Physical parameters

b	: critical pressure ratio	
C	: sonic conductance	$[m^3/(Pa.s)]$
D	: characteristic diameter	$[m]$
k	: conductivity	$[W/m]$
m	: mass	$[kg]$
n	: polytropic index	
P	: static pressure	$[barA]$

Q	: heat	$[J]$
q_m	: mass flow rate	$[kg/s]$
S	: surface of heat exchange	$[m^2]$
T	: static temperature	$[K]$
U	: internal energy	$[J/kg]$
V	: volume of the tank	$[m^3]$
$\delta_1, \delta_2, \zeta, \zeta'$:	heat exchange parameters	
λ	: heat exchange coefficient	$[W/m^2/K]$
μ	: viscosity	$[kg/(m.s)]$
ρ	: density	$[kg/m^3]$

Dimensionless groups

Nu	: Nusselt number
Gr	: Grashof number
Pr	: Prandtl number
Ra	: Rayleigh number
Re	: Reynolds number

Exponents and indices

d :   downstream
ext :   environnement
in :   inlet
out :   outlet
ref :   reference value
u :   upstream
V :   tank
W :   wall of the tank

INTRODUCTION

In pneumatic systems, temperature is a critical variable when modeling or characterizing pneumatic systems. It influences not only the fluid properties but also the system performances. It can be an important value to predict the dynamic behavior of a system or to determine the sizing of components such as compressor, cylinder chambers, tanks, etc. However it is still difficult to directly measure it in transient conditions. Indeed, thermocouples do not enable measurements at high frequencies due to their high time constant. Moreover, its measurement is punctual while a macroscopic model focuses rather on the equivalent homogeneous temperature than on its spatial distribution. This leads to many difficulties at the modeling stage and at the model validation or experimental phases. The study of an accurate macroscopic thermal model for a tank constitutes the main purpose of the proposed paper.

There are here two modeling objectives. The first one aims at implementing a model, which can be used to identified the mass flow rate characteristic according to the new proposal for characterizing orifices in transient conditions [1], but using standard tanks [2]. The second one is the simulation of complex circuits such as braking systems for railway or heavy vehicles, for which the sizing of energy storages (tanks) are depending on official safety requirements. The presented work investigates the discharge of a tank, and tries to analyze the heat transfer problem. As the success of our first objective is conditioning the applicability of the development to simulation of complex pneumatic circuits, the paper focuses mainly on the modelling of the temperature transient in a conventional tank during charge or discharge (Fig 1). The dynamic behaviour during the discharge process is then given by (3).
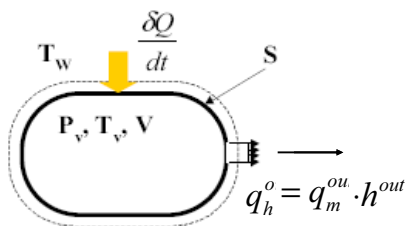
Figure 1: Charge or discharge process in a tank.

During the last decade, a method for characterizing the instantaneous mass flow rate of pneumatic components was developed by the Tokyo Institute of Technology and is based on the charge or discharge of a tank. In 1996, Kagawa and Kawashima [3] used an "isothermal" tank to identify the mass flow rate through an orifice, assuming the temperature variations are small and the mass flow the same anywhere in the circuit [4]. This method is the basis of the Japanese Standard (JISB8390) [5]. Assuming an isothermal process, the mass flow rate is directly given by the measurement of the pressure and its derivative according to (1).

$$q_{m_{out}} = -\frac{V}{r\gamma T_v}\frac{dP_v}{dt} \tag{1}$$

This interesting approach was then extended first to identify the mass flow rate characteristic of a servovalve in the frequency domain [6], second to introduce correction terms considering the influence of the circuit between the tank and the component to be characterized [7], and third to analyze the influence of a temperature correction term [8]. In fact, for an "isothermal" tank, the process cannot be exactly isothermal if the pressure gradient is over a certain value (about 1 bar/s). Due to this condition, the isothermal tank still shows some limitations but when the size is well-adapted to the circuit, it can efficiently be used for component characterization and as a mass flow generator [1].

These works show also that for conventional tanks the modelling of the heat exchange is essential in order to reach a good precision when identifying the mass flow rate characteristic of a component [9]. Polytropic models (2) and models with a constant heat exchange coefficient (4) do not enable the required precision to be reached.

$$q_{m_{out}} = -\frac{V}{rn(t)T_v(t)}\frac{dP_v}{dt} \tag{2}$$

Up to now, only a few works have tried to use conventional tanks for identifying mass flow characteristics. For example in 1989, assuming that the process is isentropic for very fast discharge, Wencan and de Las Hers proposed a first method [10, 11] but these approaches are only usable in sonic conditions. Benchabane was the first in 1994 to develop such a method [12]. His work constitutes the basis of a French standard NF E49-300 [13]. In this case, the polytropic index n is adjusted according to the temperature measured in the tank at any time. There were here important limitations due to the size of the tank in order to reach slow transient conditions and the need to equip the tank with a fan air for temperature homogeneity. In 2004, Kuroshita [14] defined a method still using the temperature measurement in the tank but enabling to adjust the polytropic index from the initial and final

values of the temperature.

However, all these approaches show some drawbacks such as the validation of the assumptions and their sensitivity to flow conditions. Figure 2 shows clearly the difficulty. It plots the instantaneous polytropic index and the heat exchange coefficient according to time during the discharge of a tank through the same circuit but starting from different initial pressures. Therefore it justifies the development presented here that uses a physical approach to properly model the heat exchange phenomena.
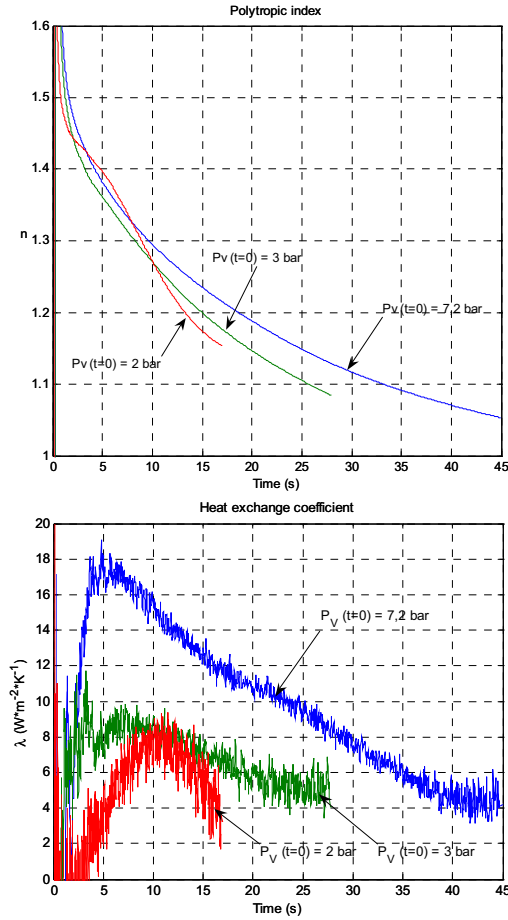
Figure 2: Polytropic index and heat exchange coefficient for different initial pressures in a discharge process.

In the first part, a macroscopic model will be proposed. It is based on the dimensional analysis theory. This approach enables the main heat transfer mechanisms to be identified according to flow conditions, pressure levels and tank shape. A relation between the corresponding dimensionless groups is then used to develop a general model for computing the heat exchange coefficient according to the system state and geometry. The identification procedure is presented and the first simulation results are compared with experimentation.

THERMAL EXCHANGE MODELING

Considering the discharge of a tank (Fig.1), if the chamber volume is large enough, the kinetic energy of the fluid in the chamber can be neglected. The mass conservation law and the energy conservation law enable the complete description of the dynamic behaviour of the gas in the chamber. Considering the heat exchanged with the environment, without any mechanical work, the first law of the thermodynamics can be applied to this opened system. With the hypothesis of a perfect gas, and assuming that, at any time, the pressure P_V, the temperature T_V and the density ρ_V of the gas are uniform in the chamber and equal to their mean value according to space, the state model of the system can be described by (3) using pressure and temperature in the volume as state variables.

$$\begin{cases} \dfrac{dP_V}{dt} = -\dfrac{r\gamma T_V}{V} q_{m_{out}} + \dfrac{\gamma-1}{V} \cdot \left(\dfrac{\delta Q}{dt}\right)_V \\ \dfrac{dT_V}{dt} = \dfrac{(\gamma-1)T_V}{P_V V}\left[-rT_V q_{m_{out}} + \left(\dfrac{\delta Q}{dt}\right)_V\right] \end{cases} \quad (3)$$
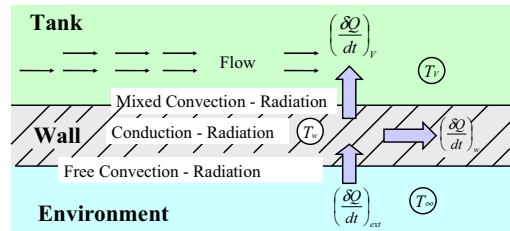
Figure 3: Thermal exchange between tank and gas.

Generally, 3 types of heat transfer are considered [15]:
- ✓ radiation: the transfer of thermal energy is due to absorption or emission of electromagnetic radiation (it is the only mechanism without a material medium);
- ✓ conduction: the heat transfer is due to molecular movement inside the medium;
- ✓ convection: the heat transfer occurs between a solid and a fluid in association with mass transfer.

It is thus necessary to study more precisely the heat exchanges taking place between the gas in the tank and the environment (Fig.3). Classical hypotheses used in pneumatic chambers rely on the assumption that the thermal conductivity and the heat capacity of the wall material are sufficiently large compared with those of air, the wall temperature is therefore considered as a constant and the heat exchanged (4) can be described by a convection heat transfer model expressed by the Newton's Law using a convection coefficient λ.

$$\left(\dfrac{\delta Q}{dt}\right)_V = \lambda S\left(T_V - T_W\right) \quad (4)$$

Benchabane [12] and Det [16] have tried different approaches to obtain an evaluation of the heat exchange coefficient λ according to flow conditions. For example, Det used the Eichelberg's model (5) [17], but this improves only slightly the precision and requires a calibration procedure for each circuit.

$$\lambda = \lambda^{ref} \sqrt{\frac{P_V T_V}{P_V^{ref} T_V^{ref}}} \tag{5}$$

CONVECTION PHENOMENA

The convection can be split in two phenomena according to the phenomena influencing mass transfer:
- ✓ natural convection: it occurs when the mass transfer is due to a temperature gradient;
- ✓ forced convection: the mass transfer is here imposed by a difference of pressure.

The dimensional analysis is used at the mascroscopic scale for modelling physical phenomena depending from several variables. For convection, it is shown that 3 dimensionless groups are required: Nusselt (Nu), Prandtl (Pr) and Grashof (Gr) numbers. According to the Buckingham's theorem [18], the relation between these groups is then given by (6):

$$Nu = \zeta Gr^{\delta_1} Pr^{\delta_2} \tag{6}$$

The parameters ζ, δ_1 and δ_2 are constants that can be obtained experimentally by varying characteristic values of the dimensionless groups defined as follows (7), (8), and (9):

$$Nu = \frac{\lambda D}{k} \tag{7}$$

$$Gr = g \frac{(T_W - T_V) D^3 P_V^2}{\mu^2 r^2 T_V^3} \tag{8}$$

$$Pr = \frac{c_p \mu}{k} \tag{9}$$

$$r_d = Gr / (Re)^2 \tag{10}$$

$$R_a = GrPr \tag{11}$$

The main advantage of this approach relies on the physical interpretation of the phenomena that are associated to the dimensionless groups [15]:
- ✓ the Nusselt number corresponds to the ratio between the heat power exchanged by convection and conduction;
- ✓ the Prandtl number characterizes the velocity distribution versus the temperature distribution;
- ✓ the Grashof number is the ratio between the product of Archimedes and inertial force, and viscous forces.

Combining these dimensionless groups, the main heat exchange mechanism can be determined:
- ✓ the ratio r_d (10) is used to determine the type of convection phenomena:

- if $r_d \ll 1$, natural convection can be neglected,
- if $r_d \gg 1$, forced convection can be neglected,
- if $r_d \approx 1$, both phenomena have about the same magnitude, it is called mixed convection.
- ✓ the Rayleigh number (eq.11) is also used for natural convection modelling in order to determine the transition between laminar ($Ra < 10^6$) and turbulent convection ($Ra > 10^{10}$).

In the case of the mass flow rate characterization [2] of a component by discharge of a tank (Fig.4), the heat exchange is essentially due to laminar natural convection because the flow velocity is low inside the tank (small Re number). Note that mixed convection may occur in specific conditions such as high initial pressure, high component sonic conductance, or small tank volume.
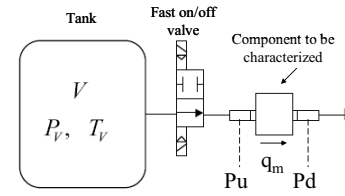
Figure 4: Experimental bench for mass flow rate characterization using tank discharge.

IDENTIFICATION OF CONVECTION COEFFICIENTS

The experimental bench (Fig.4) is used here for characterizing the heat exchange phenomena. The discharge of the tank is realized through a component with a known mass flow rate characteristic obtained from a direct mass flow rate measurement according to ISO6358:89 [19]. According to (12), deduced from (3), measuring the pressure and the temperature in the tank during the discharge allows the computation of the heat transfer. The instantaneous heat exchange coefficient λ is then computed from (13). Median filtering and under sampling is applied to pressure measurement before differentiation, and the temperature is obtain from partial discharges of the same circuit according to the stop method introduced by Kawashima [4].

$$\left(\frac{\delta Q}{dt}\right)_V = \frac{V}{\gamma - 1} \frac{dP_V}{dt} + c_p T_V q_{m_{out}} (P_V, T_V) \tag{12}$$

$$\lambda = \frac{\left(\dfrac{\delta Q}{dt}\right)_V}{S(T_V - T_W)} \tag{13}$$

The experimental results presented in the paper correspond to the discharge of a $45 \, \ell$ tank through a component with a critical pressure ratio $b = 0.41$ and a sonic conductance $C = 3.39 \, 10^{-8} \, kg / (Pa.s) \cdot$
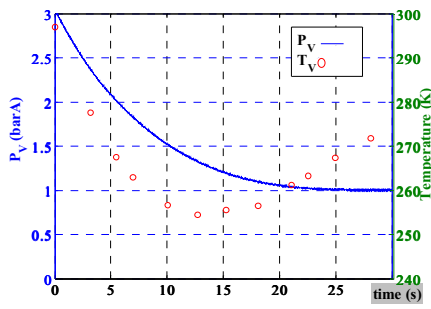
Figure 5: Pressure and temperature during the tank discharge.
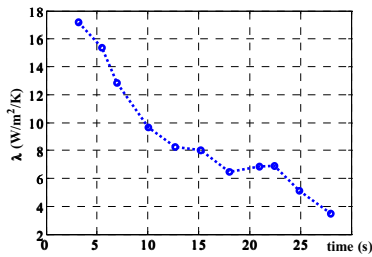
Figure 6: Heat exchange coefficient during tank discharge.

From the experimental data (Fig.5), the dimensionless groups (Nu, Gr, Pr, and Ra) can now be computed. Because the air viscosity shows low variations in the range of temperature observed in this kind of application, the Prandtl number can be considered as constant ($Pr \approx 0.715$) and according to (14) deduced from (6), the parameters δ_1 and ζ' can be identified.

$$\ln(Nu) = \ln(\zeta') + \delta_1 \ln(Gr) \qquad (14)$$
with $\zeta' = \zeta Pr^{\delta_2}$
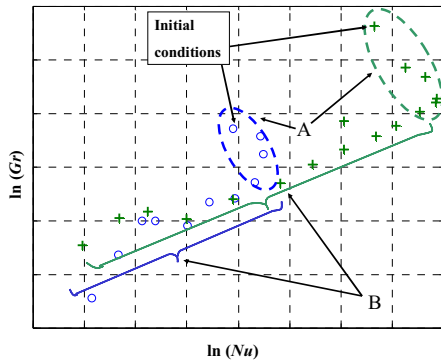
Figure 7: Nusselt number according to Grashof number.

Figure 7 presents the results obtained for several initial pressures. They show clearly two domains. When the

discharge starts, complex transitory phenomena occur for a few seconds (A), and the proposed approach can not be applied. However in zone (B), the results are in good agreement with (14) and this part is used to identify the parameters δ_1 and ζ' of relation (6).

VALIDATION AND MODEL ANALYSIS

The simulation model of the tank is consequently given by (15):

$$\begin{cases} \dfrac{dP_V}{dt} = -\dfrac{r\gamma T_V}{V} q_{m_{out}} + \dfrac{\gamma-1}{V} \cdot \dfrac{k}{D} \zeta' Gr^{\delta_1} S(T_V - T_W) \\ \dfrac{dT_V}{dt} = \dfrac{(\gamma-1)T_V}{P_V V}\left[-rT_V q_{m_{out}} + \dfrac{k}{D} \zeta' Gr^{\delta_1} S(T_V - T_W) \right] \end{cases} \quad (15)$$
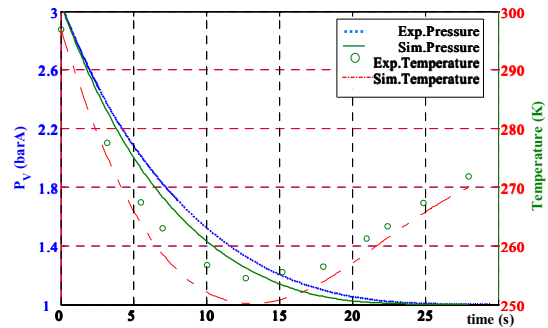
Figure 8: Simulation vs. experimentation when the initial transitory effect is neglected.
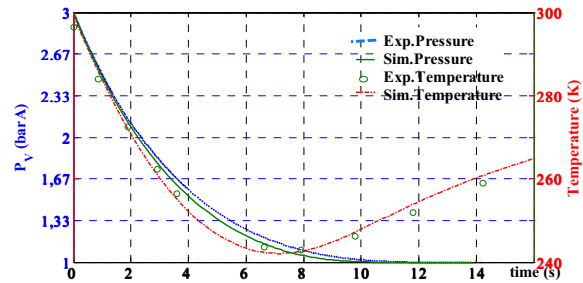
Figure 9: Simulation vs. experimentation when the component is changed.
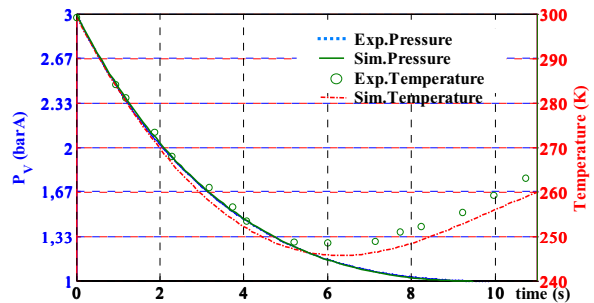
Figure 10: Simulation vs. experimentation when the tank volume is changed.

229

The simulation model is firstly validated for the same circuit as previously using the heat exchange parameters obtained from zone (B). Figure 8 shows a good agreement with experimental results. The modeling error resulting from the approximation of the heat exchange parameter when the discharge starts, has a low influence on the representation of the temperature and pressure change during the whole discharge.

Finally, if circuit (component) or tank is changed, the results (Fig.9 and 10) from the simulation model are still in good agreement with experimental data.

CONCLUSION

This paper has proposed a physical approach for modeling heat transfer phenomena during the discharge of a tank. The model is based on dimensional analysis. This approach allows firstly the main thermal effect to be characterized and the heat exchange parameters to be identified from experimentation.

However the simulation results presented here are only given for a single tank, the modeling approach has been extended to other tanks using a shape factor ξ that modify the effective heat exchange area s in order to take into account the tank shape changes (for example the ratio between tank length and diameter). Moreover a forced convection model has been now developed to reach a better approximation of the global convection phenomena (mixed convection) that are observed for high flow rate and pressure level.

One of the main advantages of this modeling approach is that it allows a proper evaluation of the heat exchange coefficient according to different factors such as pressure, temperature, flow conditions and tank shape.

Further works rely now on a rigorous model validation in order to verify the shape factor ξ and to evaluate the influence of other parameters such as tank material (conduction) and painting (radiation).

REFERENCES

1. K. Kawashima, T. Fujita, and T. Kagawa. Flow rate measurement of compressible fluid using pressure change in chamber. Trans. of the Soc. of Instrument and Control Engineers, E-1(1):252–258, 2001.
2. R. De Giorgi, E. Bideaux, and S. Sesmat. Using inverse model for determining orifice mass flow rate characteristics. 6th Int. Symp. on Fluid Power, pp. 380–385. Tsukuba, Japan, Nov.7-10 2005.
3. K. Kawashima, T. Fujita, T. Kagawa, and J. Jang. Characteristics measurement of pneumatic elements using isothermal chamber. 3rd Int. Symp. on Fluid Power, pp. 253–258. Yokohama, Japan, Nov.4-6 1996.
4. T. Kagawa, K. Kawashima, and T. Fujita. Effective area measurement method using isothermal chamber. Hydraulics and Pneumatics, Vol. 26(1):76–78, 1995.
5. JIS B 8390. Pneumatic Fluid Power Components using Compressible Fluids - Determination of Flow-rate Characteristics, 2000.
6. K. Kawashima, T. Fujuta, T. Kagawa, and J. Jang. Characteristic measurement of pneumatic flow control valves using isothermal chamber. 10th Int. Fluid Power Workshop, pp. 10–15. Bath, UK, Sept. 10-12 1997.
7. B. Han, T. Fujita, T. Kagawa, K. Kawashima, and M. Cai. Flow rate coefficient measurement by using pressure discharge velocity of pneumatic RC circuit. 4th JHPS Int. Symp. on Fluid Power, pp. 143–148. Tokyo, Japan, Nov. 15-17 1999.
8. T Kagawa, T. Wang, Y. Ishii, Y. Terashima, T. Morozumi, T. Mogami, and N. Oneyama. Determination of flow rate characteristics of small pneumatic valves using isothermal chamber by pressure reponse. 7th Symp. on Fluid Control, Measurement and Visualization. Sorrento, Italy, Aug. 25-28, 2003.
9. G. Peng, X. Chai, and W. Fan. A new measurement method of the flow rate characteristics of the regulator. 6th JFPS Int. Symp. on Fluid Power, pp. 776-770. Tsukuba, Japan, Nov. 7-10 2005.
10. X. Wencan. To measure the mass flow rate characteristic of pneumatic components in series-mounting using sonic velocity exhaust method. Int. Conf. on Fluid Power Transmission and Control, pp.708-711. Hangzhou, China, Mar. 20-22 1989.
11. S. de las Heras. A new experimental algorithm for the evaluation of the true sonic conductance of pneumatic components using the characteristic unloading time. Int. Journal of Fluid Power Vol 2(1):17–24, 2001.
12. S Benchabane, M. Bonis, and J.P. Lecerf. Economic measurement of isopneumatic coefficients. 11th IFK, volume 3, pp. 131–141, Aachen, Germany, 1994.
13. NF49-300:2000. Transmissions pneumatiques - Méthode de caractérisation des coefficients de débit pneumatique par vidange de réservoir, 2000. 22p.
14. K. Kuroshita, Y. Sekiguchi, K. Oshiki, and N. Oneyama. Development of new test method for flow-rate characteristics of pneumatic components. PTMC'04, pp. 243–256, Bath, UK, Sept. 2004.
15. F. Incropera and D. Dewitt. Fundamentals of heat and Mass Transfer. John Wiley and Sons, 2002.
16. F. Det, S. Scavarda, and E. Richard. Simulated and experimental study of charging and discharging of a cylinder using an electropneumatic servovalve. 1st JFPS Int. Symp. on Fluid Power, pp. 199–206. Tokyo, Japan, Mar.13-16 1989.
17. C. Eichelberg. Some new investigations of old combustion engine problems. Engineering, 148(27):463–466, 1939.
18. E.R.G. Eckert and R.M. Drake. Heat and Mass Transfer. McGraw-Hill Book Company, INC., 1959.
19. International Standard ISO 6358. Components using compressible fluids – Determination of flow-rate characteristics, 1989. 15p.

OS10-3

DESIGN AND NANOMETER POSITIONING OF A LOW FRICTION PNEUMATIC CYLINDER EMBEDDED WITH AEROSTATIC BEARINGS

Ming-Chang Shih and Kei-Ren Pai

Department of Mechanical Engineering,

National Cheng-Kung University,

No.1, Ta-Hsueh Road, Tainan 701, Taiwan (R.O.C.)
(E-mail:mcshih@mail.ncku.edu.tw)

ABSTRACT

In the paper, a low friction pneumatic cylinder and a sliding table, and both of them are embedded with aerostatic bearings are designed. A low friction pneumatic table is constructed by combining the pneumatic cylinder and the sliding table. The characteristics for the friction force versus velocity of the pneumatic cylinder and the pneumatic table are measured. Moreover, a hybrid self-tuning fuzzy sliding mode controller with dead zone and load compensation is designed to precisely control the position of the pneumatic table. The experimental results have shown that the pneumatic table has positioning accuracy of 20 nm, the resolution of the pulse scale.

KEY WORDS

Nanometer Positioning, Pneumatic Table, Aerostatic Bearing

INTRODUCTION

The development of the modern industry such as the semiconductor, communication and bio- medicine technology leads to the extensive study on the ultra-precision measurement and positioning technology of nanometer classes. Low friction elements and suitable control strategies are needed to be designed and developed to lower the friction force and thus to obtain better positioning accuracy. Compared to the hydraulic and electric driving system, the pneumatic driving system has the following advantages: low cost, clean, and easy in power transfer; therefore it can be applied in many industries. However, because of the compressibility and leakage of the air, the friction force, and the load disturbance, the pneumatic system is time variant and highly nonlinear [1-2]. Moreover, the

difficulty of the cylinder position control is mainly caused by the friction force between the cylinder and the piston as well as the stick slip effect phenomenon during the motion control of the pneumatic cylinder[3-4]. Recently, various nonlinearity compensation strategies such as dithering compensation and friction force compensation have been analyzed and designed according to the nonlinear characteristics of pneumatic components to overcome the nonlinear effects and thus to get a higher positioning accuracy. In the articles [5-7], the effective friction compensation methods are introduced and combined with the designed control approaches. Besides, the low friction force actuator is developed to reduce the system friction force. The friction force can be further reduced through the installation of the aerostatic bearings in the pneumatic cylinder. Because there are thus no seals in this

pneumatic actuator, the actuator becomes a low friction actuator. The compressed air flows to the small gap between the bearing and the sliding guide, and the cylinder can thus float around the air film and on the guide surface of the table. Due to the air film between the bearing and the sliding guide, the relative motion is almost free of friction. Moreover, because the air is used as the medium, it can be applied at very high or very low temperature environment. In the paper, the pneumatic cylinder and the sliding table embedded with aerostatic bearing are designed. Besides, a hybrid nonlinear self-tuning fuzzy sliding mode controller with deadzone and load compensation is designed for the system. The experimental results show that the nanometer accuracy control is successfully completed.
.

DESIGN OF A PNEUMATIC CYLINDER EMBEDDED WITH AEROSTATIC BEARINGS AND FRICTION MEASUREMENT ILLUSTRATIONS

The scheme of the designed pneumatic cylinder embedded with aerostatic bearings is shown in Figure 1. The air gap is found between the cylinder block and the piston, as well as between the piston rod and the right- and left- end covers of the cylinder. If the compressed air is supplied, the pneumatic piston rod and the piston tend to float in the air. The friction force becomes very small because there is not any contact between the cylinder and the piston rod.
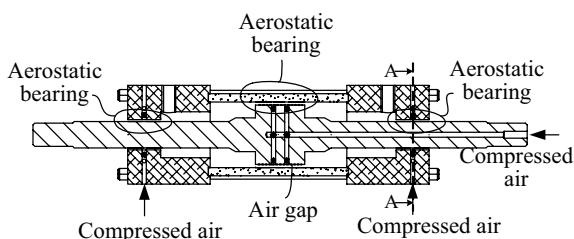
Figure 1 Scheme of the pneumatic cylinder embedded with aerostatic bearings.

Figure 2 shows the scheme of the measurement for the friction force of the pneumatic cylinder embedded with the aerostatic bearing. The compressed air flows through the pipes and the servo valve, and then flows into the pneumatic cylinder to drive the table, which is supported and guided by eight pieces of round aerostatic bearing pads. Moreover, a hydraulic cylinder is connected to this pneumatic cylinder to stabilize the motion of the pneumatic cylinder. The pulse scale is used to measure the position and the velocity by differentiating the position signals. The load cell is connected to the two pneumatic cylinders to indicate the friction force of the cylinder during motion. Figure 3 shows the experimental results of the relationship of the

friction force versus the moving velocity of the cylinder. The friction force is found to be a function of the compressed air pressure. One can see that the static friction force at pressure 2, 3 and 4 bar are found to be 0.5 N, 1.0 N and 1.2 N, respectively. Generally, the friction forces of the aerostatic bearing cylinders are very small, and the difference between the static and dynamic friction forces is also very small. In this figure, the differences between the static and dynamic friction forces are in the range between 0.3N and 0.5 N.
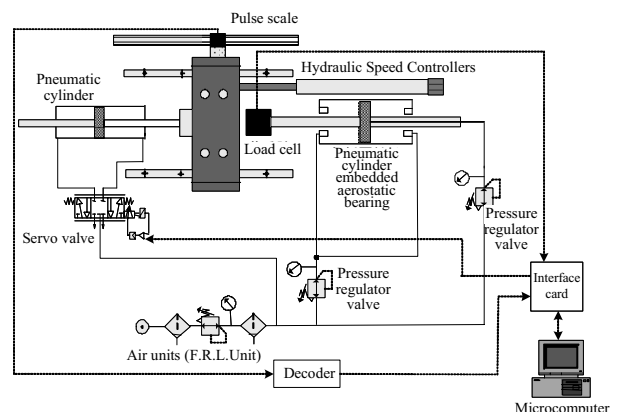
Figure 2 Scheme of friction force measurement.
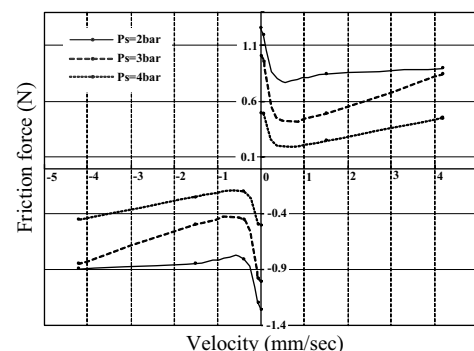
Figure 3 Friction force vs. velocity for a pneumatic cylinder with aerostatic bearing.

CONSTRUCTION OF A LOW FRICTION PNEUMATIC SERVO TABLE EMBEDDED WITH AEROSTATIC BEARINGS PADS AND FRICTION MEASUREMENT

A low friction table driven by the pneumatic cylinder embedded with the aerostatic bearing is constructed. Figure 4(a) shows the structure of the table. Four pieces of round aerostatic bearing pads are installed to support the weight of the table in order that the table can be floated and moved along the guide of the base seat. Another 4 pieces of the round aerostatic bearing pads are installed at the two sides of the base seats to ensure the table sliding in the fitted direction. Figure 4(b) is the photograph of the constructed table.
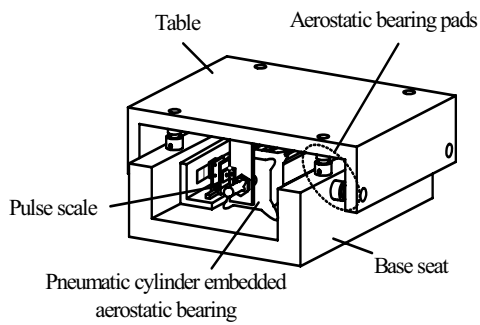
(a) Structure

(b) Photograph

Figure 4 Structure and photograph of the pneumatic table embedded with aerostatic bearings and pads.

Figure 5 shows the scheme of the friction force measurement of the table driven by the aerostatic bearing cylinder. The load cell is installed to measure the friction force. The pulse scale is used to measure the displacement and the velocity signal is obtained by the differentiation of the displacement. The pressure of the compressed air is 3 bar and the supply compressed air of the aerostatic bearing pad is 6 bar. The friction force versus the velocity is measured and shown in the Fig. 6. The maximum static friction force is about 3.144 N and the smallest dynamic friction force is 2.019 N. When the velocity of the cylinder is larger than 1.4 mm/sec, it is found that the friction force keeps almost the same. The viscous friction force tends to be constant even when the velocity is further increased to be 5 mm/sec.

PRECISE POSITION CONTROL OF THE PNEUMATIC TABLE EMBEDDED WITH AEROSTATIC BEARINGS

The scheme of the position control system of the low friction pneumatic driven servo table is shown in Figure 7. The actuator is the low friction pneumatic servo cylinder, and the table is guided by the round aerostatic bearings. The position is measured by a pulse scale with a resolution of 20 nm.
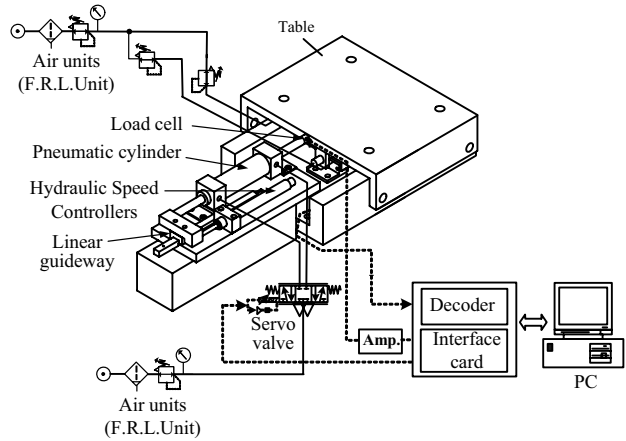
Figure 5 Scheme for measuring friction force vs. velocity of the table.
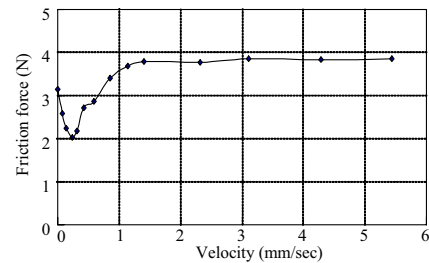
Figure 6 Friction force vs. velocity of the pneumatic cylinder driven table.
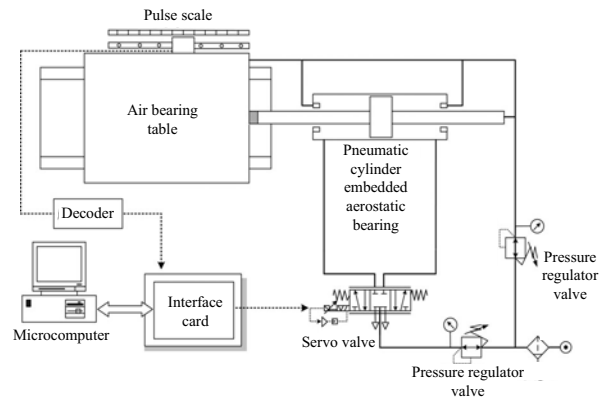
Figure 7 Scheme of the low friction pneumatic servo table.

Considering the nonlinear characteristic of the air flow through the servo valve and the compressibility of air, one knows that the system highly nonlinear and time variant. It is a great challenge for many researchers who have designed various nonlinear compensators to raise the accuracy of position control. In the paper, a self-tuning fuzzy sliding mode nonlinear controller compensated with the dead zone of valve and the variable load has been designed and implemented in the system to control the position of the table. The block diagram of the system is shown in Figure 8.
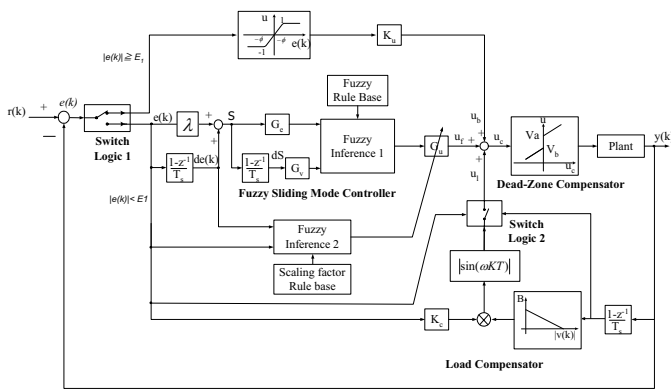
Figure 8 Block diagram of the pneumatic servo control system.

In the paper, a hybrid controller consisting of a hyperbolic tangent function and a self-tuning fuzzy sliding mode controller is designed to control the pneumatic table. One of them acts as a 'coarse' controller while the other acts as a 'fine' controller. A switching logic is applied to shift the control algorithm according to the error variable. The variable E_1 represents the boundary values of two mode control and $e(k)$ is the position error. The choice of the value E_1 is according to the requirement of the rise time and the limit of overshooting. If $|e(k)| \square E_1$, the positioning system performs speedily with its control signal designed by hyperbolic tangent algorithm at the start of control process. The positioning process tends to be decelerated near the boundary point. The algorithm of control signal in this stage is given by:

$$ u_b = f(e(k)) = k_u \times \tanh(\frac{e(k)}{\phi}), \qquad (1) $$

where k_u is the proportional gain and ø is the value of boundary layer. The proportional gain k_u is set to decide the response speed of the system at the start of control process. Increasing k_u, the transient response can be accelerated but the undesired overshoot will also happen. Because of the above reason, the value of boundary layer ø is designed to execute the deceleration task for the control system when the system is near the boundary point $E1$ so that the control system can smoothly go into the region of fine tuning and can avoid the appearance of overshoot.

As $|e(k)| < E1$, the switching logic is to shift the control algorithm and the self-tuning fuzzy sliding mode controller (SFSMC) is designed to execute the fine positioning control. The designed controller (SFSMC) includes the algorithm of the time variant gain factor ($\alpha(k)$) and the tuning of the scaling factors.

The fuzzy control theory was combined with the sliding mode control theory in the study to control the servo pneumatic system. The structure of the fuzzy control includes four parts: fuzzification inference, knowledge base, decision logic and defuzzification. In the article, Mamdani control rules and maximum-minimum algorithm are applied, and the "center of the gravity" method is used to defuzzify and to get the accurate control signal. For sliding mode control, the sliding surface S and the change of sliding surface dS are defined as

$$ S(k) = de(k) + \lambda \times e(k), \qquad (2) $$
$$ dS(k) = S(k) - S(k-1), \qquad (3) $$

where e(k) is the error, de(k) is the change of error and λ is the slop of sliding surface S. The variables $S'(k)$, $dS'(k)$ and $U(k)$ are chosen to be the two inputs and one output of the fuzzy controller, respectively. The variables $S'(k)$ and $dS'(k)$ are defined by

$$ S'(k) = S(k) \times Ge, \qquad (4) $$
$$ dS'(k) = dS(k) \times Gv, \qquad (5) $$

where *Ge* and *Gv* are the scaling factors of sliding surface and the change of sliding surface. The control output signal $u_f(k)$ is defined as:

$$ u_f(k) = U(k) \times Gu(k), \qquad (6) $$

where $U(k)$ and $Gu(k)$ denote the controller output and the output scaling factor of the controller at time instant *kT*. In this paper, the triangular membership function is applied to define the fuzzy sets of the inputs and the output, Figure 9 illustrated. Three linguistic fuzzy sets are applied for the input and output variables. The control rules are illustrated in Table 1. The "max-min" and "center of gravity" methods are adopted for fuzzy inference logic and defuzzification algorithm.
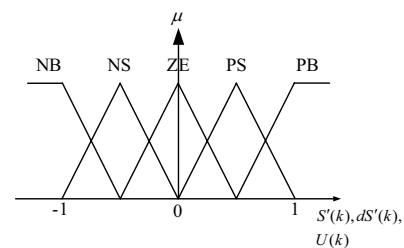
Figure 9 Membership function of $S'(k)$, $dS'(k)$ and $U(k)$.

234

Table 1 Fuzzy sliding mode control rules.

S'(k) / U(k) / dS'(k)	NB	NS	ZE	PS	PB
NB	NB	NB	NS	NS	ZE
NS	NB	NS	NS	ZE	PS
ZE	NS	NS	ZE	PS	PS
PS	NS	ZE	PS	PS	PB
PB	ZE	PS	PS	PB	PB

For the conventional fuzzy inference, its control parameters such as rules table, scaling factors and membership functions are usually obtained by trial-and-error method. The method is time- consuming and difficult to obtain the optimum parameters. Moreover, the conventional controller has not the adaptive resource to supervise and modify its control parameters to reject the disturbance. Therefore, in this paper the output scaling factor $Gu(k)$ of fuzzy sliding mode controller is tuned on-line by a real-time gain updating factor $\alpha(k)$ to raise the positioning precision and robustness of the control system. The new scaling factors are modified by

$$Gu(k+1) = Gu(k) \times (1 + \alpha(k)), \qquad (7)$$

where α(k) is the real-time gain factor. The value of real-time gain factor α(k) is computed on-line using a model independent fuzzy rule-base defined by error and change of error of the controlled variable. The most important point to note is that real-time gain factor is not dependent in any way on any process parameter. The value of real-time gain factor depends only on the input variable of controller at the sampling instant. The membership functions for input variables $e(k)$ and $de(k)$ and output variable $\alpha(k)$ are shown in Figure 10. The membership function for $\alpha(k)$ is also a triangular type and the rule-base in Table 2 is used for the computation of $\alpha(k)$.

When a loading is applied on the pneumatic control system, the control characteristic will be varied due to the variation of operating pressure, and caused a obvious effect on the positioning precision. Therefore the load compensator, which is similar to the dither signal, is designed according to the error $(e(k))$ and the velocity $(V(k))$ to overcome the variation in this paper. The algorithm of load compensator is expressed by the following equations:

$$u_l = \begin{cases} e(k) \times K_c \times B(k) \times |\sin(\omega kT)|, & for\ |V(k)| \le V_1\ and\ |e(k)| \ge E_2 \\ 0, & for\ |V(k)| > V_1\ or\ |e(k)| < E_2 \end{cases},$$

$$(8)$$
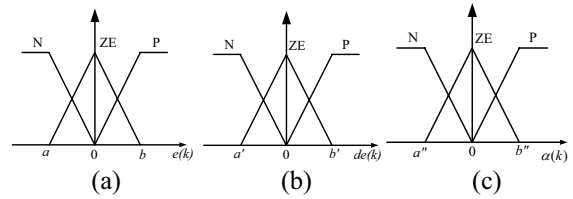
Figure 10 (a) Membership function of $e(k)$. (b) Membership function of $de(k)$. (c) Membership function of $\alpha(k)$.

Table 2 Fuzzy rules of real-time gain factor.

de(k) / α(k) / e(k)	N	ZE	P
N	ZE	N	ZE
ZE	P	ZE	P
P	ZE	N	ZE

where K_c is the gain of the amplitude and $B(k)$ is the variable amplitude. The algorithm of the variable amplitude $B(k)$ is expressed as:

$$B(k) = -\frac{\delta}{V_1} V(k) + \delta, \qquad (9)$$

where δ is the maximum peak value of variable amplitude $B(k)$. When the loading effect causes the control system to lie at the stop state and the error is bigger than the desired steady state error(E_2), the compensation signal is triggered and thus set to be the maximum value to ensure that the system never stops. As the control system is driven again from the stop state, the amplitude of load compensation signal is appropriately attenuated with the change of velocity to prevent the overshoot or oscillation phenomenon.

Finally, the deadzone compensation can be designed to avoid the deadzone. The algorithm of control voltage with deadzone compensation can be expressed by the following equation:

$$u = \begin{cases} u_c + V_a, & if\ u_c > 0 \\ u_c + V_b, & if\ u_c < 0 \end{cases}, \qquad (10)$$

where u_c is the output signal of controller and load compensator, and V_a and V_b are the compensation values of the dead zone at each side of the center.

EXPERIMANTAL RESULTS OF NANOMETER POSITIONING

The above-described controller design is implemented in the microcomputer to control the position of the pneumatic servo table. The air supply pressure is set to

be 5 bar, the sampling time and the reference input are chosen to be 20 ms and 10 mm. The experimental results are shown in Figure 11. The position error is within the range of the resolution 20 nm of the pulse scale from the time instant 1.5 sec. In the fine feed experiment, the feed resolution is noticed through the various step feeds. From Figure 12 one can see that the low friction pneumatic servo table can be controlled to move step by step for 20 nm and the position error is about 20 nm.

Although the positioning accuracy less than 20nm is not possible in these positioning experiments owing to the restriction of the resolution of the pulse scale, it can be predicted that this positioning method has the ability of 20nm or even less feed resolution.
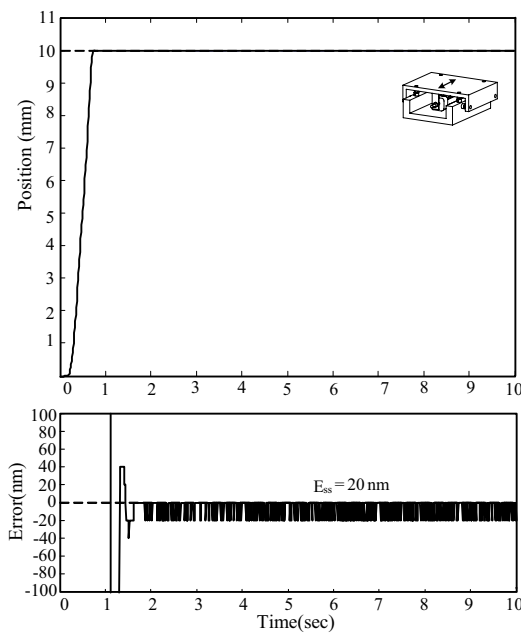
Figure 11 (a) Time response of the pneumatic servo table for a step input 10 mm. (b) Time response of error.
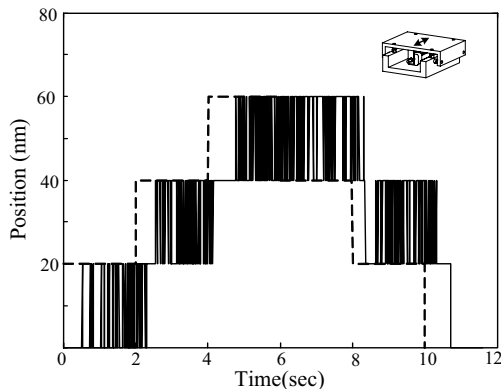
Figure 12 Multi-step responses of the pneumatic table with 20 nm step displacement.

CONCLUSIONS

In the paper, we have fitted the pneumatic cylinder and the low friction driven table with aerostatic bearings, and have designed appropriate devices to measure their corresponding small friction forces. Moreover, this work has designed and implemented a hybrid self-tuning fuzzy sliding mode controller with the dead zone and load compensator for the precision control of the pneumatic table. The experimental results have shown that the pneumatic servo table can be controlled to the nanometer accuracy of 20 nm both with 10 mm step input and 20 nm stepwise input successfully.

REFERENCES
1. Shearer J. J., "The Study of Pneumatic Process in the Continuous Control of Motion with Compressed Air-I", ASME Trans., pp. 233-242 (1956).
2. Moore, P.R., PU, J. and Harrison, R.,"Progression of servo pneumatics forwards advanced applications", in EDGE, K., and BURROWS, C. (Eds.): "Fluid power circuit, component and system design" (Research Studies Press,), ISBN 0863801390, pp.347-365 (1993).
3. Fujita T., Tokashiki R., and Kagawa T., "Stick-slip Motion in Pneumatic Cylinders Driven by Meter-Out Circuit", Proc. of the 4th JHPS International Symposium on Fluid Power, Tokyo, pp.131-136 (1999).
4. Kazama T, and Fujiwara M., "Experiment on Frictional Characteristics of Pneumatic Cylinders", Proc. of the 4th JHPS International Symposium on Fluid Power, Tokyo, pp.453-458 (1999).
5. Ning S., and Bone G.M., " High Steady-State Accuracy Pneumatic Servo Positioning System with PVA/PV Control and Friction Compensation", Proceedings-IEEE International Conference on Robotics and Automation, Vol. 3, pp.2824-2829 (2002).
6. Xiang F., and Wikander J., "Block-oriented approximate feedback linearization for control of pneumatic actuator system", Control Engineering Practice, Vol.12, No. 4, pp.387-399 (2004).
7. Shih M.C., and Pai K.R., "Nanoaccuracy Position Control of A Pneumatic Cylinder Driven Table", International Journal of JSME, Series C, Vol.46, No.3, p.1062-1068, (2003).

P1-01

INVESTIGATION ON CAVITATION BEHAVIOR AND NOISE IN HYDRAULIC VALVES

Xin FU，Liang LU, Xuewen DU and Jun ZOU

State Key Laboratory of Fluid Power Transmission and Control
Zhejiang University
Hangzhou, 310027 China

ABSTRACT

Cavitations inside hydraulic valves were investigated by using high-speed camera technology and noise spectrum analyzing method. The bubble flow's morphological and flowing characteristics were converted into numerical information by the employment of image process, which made the two-phase flow easily identifiable. Based on this, cavitation's distribution and shape characteristics were revealed. Combined with cavitation noise spectrum analyzing, it was found that the shedding process of cavitation had similar high frequency properties with cavitation noise spectrums. Typical noise curves of cavitations were obtained, and the second peak levels were found in low cavitation number conditions. In addition, it assumed that, the shedding frequencies played a good reflection to cavitation noise while using cavitation numbers as the only variable.

KEY WORDS

Hydraulic, Cavitation, Image process, Noise spectrum

NOMENCLATURE

B : the width of groove
Fs : the camera speed
f : the frequency of shedding
h : the depth of groove
L : cavitation bodies' average length
Lp : Cavitation noise level
l : the length of groove
Re : Renault number
s : Cavitation bodies' helical pitch

x : the opening of the valve
σ : the cavitation number

INTRODUCTION

Cavitation phenomena are common in various hydraulic components like pumps, valves and cylinders etc. The reason can be explained by the complex channels and high differential pressure. As we know, cavitation causes undesirable problems, such as vibrations, noise and erosions. Many efforts have been taken on the issue and progresses have been made. Vibrations induced by cavitation were investigated by Guoyu Wang [1]. Cavitation's erosion and flow choking phenomena were revealed in Koivula's papers [2]. Moreover, simulations related were conducted with the code of Fluent by Hong Gao [3]. However, Kiesbauer and Vnucec [4] gave a detailed description about cavitation in control valves with axi-symmetrical characteristics. Special threshold points were indicated within a typical cavitation development process, like incipient cavitation, incipient choked flow, maximum noise and the material damage threshold. A typical cavitation noise curve according to ISA standings was presented. And most experimental dates were gained from the medium of water. In Martin's paper [5], cavitation inception characteristics were investigated in oil by pressure energy spectrum method, which seemed to have similar characteristics with the acoustics noise. Camera vision pictures were presented of cone valves in Kiesbauer's paper, but little information was gained. High-speed photography technology and transparent valve body were employed in our experiments (fig.1, fig.2). With this method, cavitation's distribution and shape characteristics can be easily observed. Furthermore, the relationship between cavitation noise and its morphological characteristics was studied. In Sato and Saito's research on orifice cavitation [6], the similar method was taken. Orifices with different lengths and diameters were studied. From the information supplied by the images, the states of cavitation flow can be identified by its shedding, feed-flow characteristics. Ganippa [7] gave another work in orifices with different flow-in angles. The location of cavitation inception and its no axi-symmetrical changes of flow were illustrated.

Non-circular opening spool valves with U-grooves were studied in our research. Unlike most experimental objects, the U-grooves are not axis-symmetrical. Oil was used as the working media. In most symmetrical flow channels, like cone valves and orifices, cavitation always forms at the position of the inlet edges. However, a new cavitation distribution state was found in the bottom of U grooves. Moreover, the bottom formed cavitation seemed quite calm and made lower noise.

EXPERIMENTAL SET-UP

The experimental set-up includes three parts: throttling valves with turning grooves, high-speed photography

system and noise detecting instrument (fig.1).
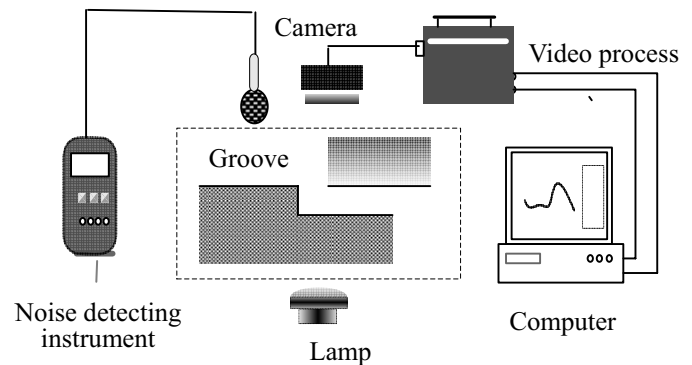
Figure 1 Experiment set-up

The transparent valve body is made of PMMA material (fig.2). All the parameters were the same with the real metallic valve body to keep the original flow state. AWA 6270+ noise detecting instrument was used to gain the noise level and spectrum messages. Cavitation images were taken by FASTCAM-APX 120KC with the maximum speed of 120 000fps. Two photographing direction were used, the front direction and side direction with the angle of 10° (fig.3).

Figure 2 Transparent valve model
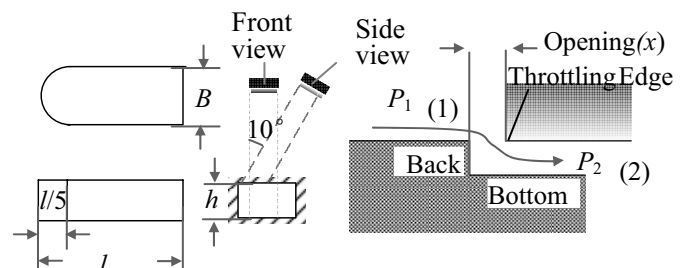
Figure 3 Configurations of the grooves

In this experiment, four types of valve spools of different depths were used. Details of the experimental

body were shown in table 1. The four types of grooves had the same width and length parameters, but different depth with the equal depth interval. Different valve openings of 0.3mm, 0.6m, 0.8mm, 1.0mm, 1.2mm, 1.5mm, 1.8mm, 2.0mm, 3.0mm and 3.5mm were studied.

Table 1 Construct parameters of turning grooves [mm]

Valves		U06	U07	U08	U09
Construct parameter	B	2	2	2	2
	l	5	5	5	5
	h	0.5	1.0	1.5	2.0

DISTRIBUTION AND DEVELOPING TREND OF CAVITATION

As we see in fig.3, the oil flow started from area (1), and entered the turning groove, then flow out by the area (2). P_2 varied in an equal interval in the experiment process while keeping P_1 constant. The changing of flow parameters was denoted by the cavitation numbers. Fig.4 showed us that, cavitation appeared in a threshold cavitation number and its body region extended nearly lineally with the continue decrease of cavitation number. Fig.4-6 showed the inception state of cavitation. As we see, cavitation appeared in one side of the groove, which is coincident with Ganippa's findings.

Frame No.1	σ=0.07
No.2	σ=0.15
No.3	σ=0.25
No.4	σ=0.30
No.5	σ=0.43
No.6	σ=0.58
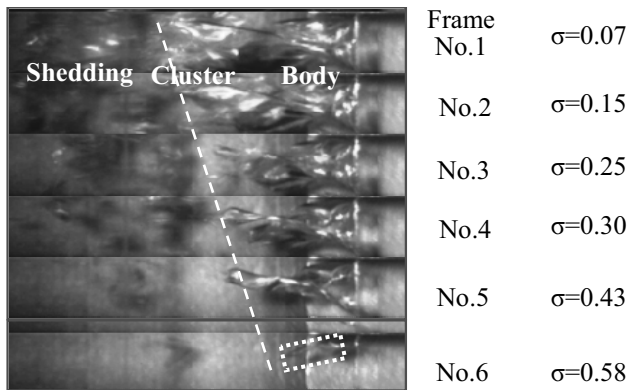
Figure 4 Cavitation's developing Trend

As a typical development process of cavitation, cluster appeared in the body's tail, and then shedding formed, which was referenced from Sato's papers. Cavitation cluster was not quite notable at weak cavitation moments. However, the shedding process always existed in any cases.
As we know, when the local pressure drops down below the liquid's vapor pressure, cavitation incepts. In most cases, cavitation forms near by the entrance edges, like throttling edges of valves and orifices' inlet. At small opening cases in our experiments, cavitation developed under the button of the grooves, which seemed unexplainable by traditional understandings.
The transformation process of cavitation's distribution states were investigated, which seemed regular somehow. Fig. 5-(a) shows cavitation's distribution images in the front view and fig. 5-(b) shows the side view with the angle of 10° in same conditions. The experiment was taken at the cavitation number 0.4 with U07 groove. As we see, in the small opening condition (fig.5-a-3), cavitation developed around the edges formed by the bottom and side faces of the groove looked like the letter of U. As the opening increased, cavitation inception location changed from the bottom of the grooves to the throttling edge. Before the opening reach a threshold value, the letter U distribution state never changed. However, when the threshold reached, the distribution shape transferred from letter U to two radials, and its starting-off location combined with throttling edge. Finally, the two radials hold together to form a single radial (fig.4). As wee in fig.4, the cavitation distribution property didn't change much with the cavitation number as variable. However, the sudden change of distribution state was not found by our ancient studies for the restricting of camera speed.

σ=0.4 x=3.5	
σ=0.4 x=1.0	
σ=0.4 x=0.3	

(a) Front view   (b) Side view
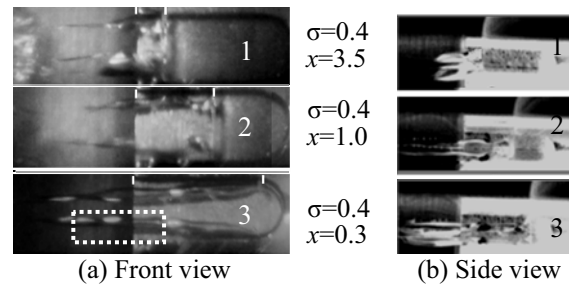
Figure 5 Cavitation distribution states

Many experimental cases were conducted to study cavitation distribution properties and a table was found based on groove's structure parameters. A no dimensional value x/h was used. Since the flow parameters have few influences on the distribution properties, the experiments were conducted in the same cavitation number conditions, σ=0.4. In table 2, the cavitation distribution state-threshold point was remarked with fuscous shadings. In all the U09, U08 and U07 cases, when the value of x/h was less than 1.0, they were cavitation's letter U distribution states, and otherwise were the radial distribution states. It assumed that, the constant value 1.0 of x/h could be used as threshold to distinguish the two distribution states. However, the letter U distribution state never appeared in U06 groove, even the radial distribution state only appeared in sizeable opening cases. When the opening is small, only shedding processes can be found, which

may be explained by its shallow groove property. As the liquid flowed by, the turning trend was unnoticeable in the U type valve, and cavitation formed by the throttling edges.

Table 2 x/h =1.0, the threshold of distribution states

valve opening	U09	U08	U07	U06
0.3	—	0.2	0.3	0.6
0.6	0.3	0.4	—	1.2
0.8	—	—	0.8	—
1.0	—	—	1.0	2.0
1.2	0.6	0.8	—	—
1.5	—	1.0	—	—
1.8	0.9	—	—	—
2.0	1.0	1.3	2.0	4.0
3.0	1.5	—	—	—
3.5	—	—	3.5	7.0

SHAPE AND NOISE CHARACTERISTICS OF CAVITATION

Helix shapes of cavitation body

A typical cavitation development includes three processes, cavitation body, tail cluster and shedding. Most studies emphasized particularly on cluster and shedding characteristics, few researches concerned the cavitation bodies, which seemed to be calm and steady compared with the other two process. However, with the help of the high-speed camera technology, the shape characteristics of the cavitation bodies were made clear.
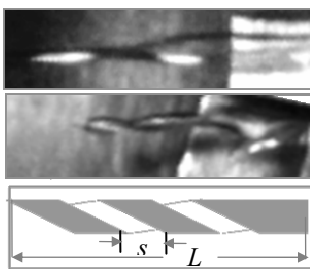
Figure 6
Cavitation bodies' twist shape

Taking parts view from fig.5-a-3 and fig.4-6, it is easy to find that the cavitation bodies present helix shapes. The bodies' average length L and helical pitch s were used to describe the shape characteristics. It is concluded from the experiment dates that, under the same cavitation number conditions, the average length L and helical pitch s were both getting larger with the increasing of groove depths. There were no noticeable cavitation bodies in the U06 groove. Even in certain cavitation number and structural parameter conditions, the screw interval changed slimly with the passing of time. Furthermore, the changing frequency of the helical pitch seemed to have something to do with cavitation's shedding frequency and noise levels, which

will be investigated in our further studies.

Cavitation noise and its periodic shedding process

Typical noise trend with cavitation number as variables was obtained. With the decreasing of cavitation numbers, the noise level raised slowly, however, when cavitation incepted, a sharp rise of the noise level appeared. Until the cavitation number reached its threshold value, the noise came to its maximum and then went down quickly. The similar noise development according to ISA standers was illustrated in Kiesbauer's papers (2006). Second peaks lever (fig.7) were found in the noise curves, and similar trends appeared in Sato's acceleration dates caused by cavitation. As we see in fig.7, the curves of U09 and U08 hold similar characteristics. The average noise level of 0.5mm opening cases in both grooves were quite low than that of larger opening cases, though the opening differences among which were relatively small. However, with the decreasing of grooves' depth, the noise of larger openings weakened, and simultaneously, the smaller ones' get intensified.
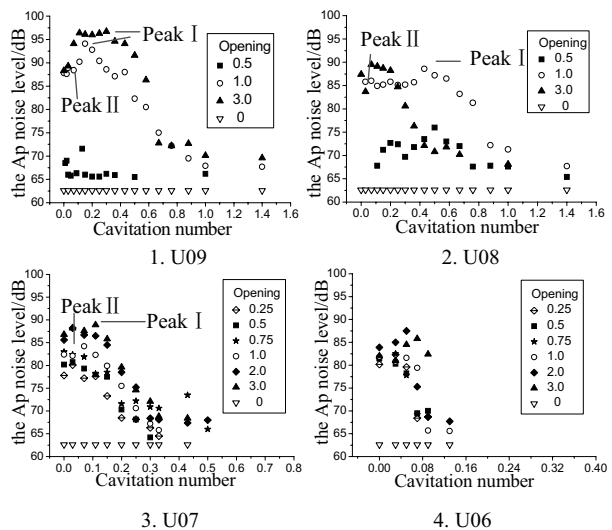
Figure 7 Cavitation noises in different grooves

Periodic shedding processes were studied in Sato's papers, and its relationships with cavitation's re-entrant motion characteristics were revealed. However, the influences of the shedding process on noise were not mentioned. It was concluded from our studies that the shedding frequency reflects cavitation noise to some extent. The shedding periods were obtained by high-speed camera technology and image process. Fig.8 showed the shedding images within one period of three grooves. All the images were taken at their maximum noise condition, while the openings were the same of 1.0mm.

Groove U09   Groove U06

(a) σ=0.15; Fs=40000fps   (b) σ=0.05; Fs=40000fps

Groove U08
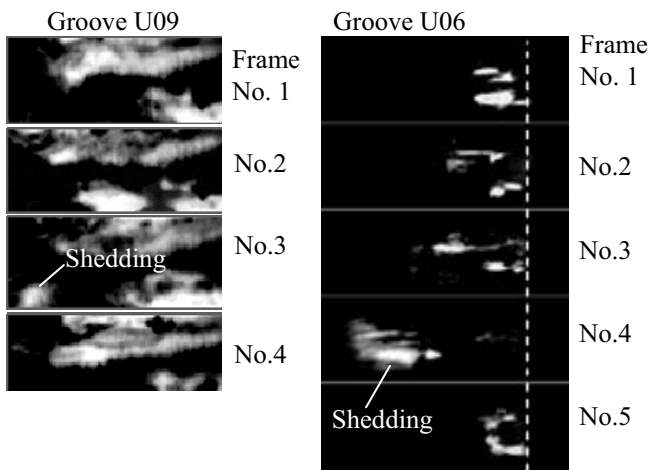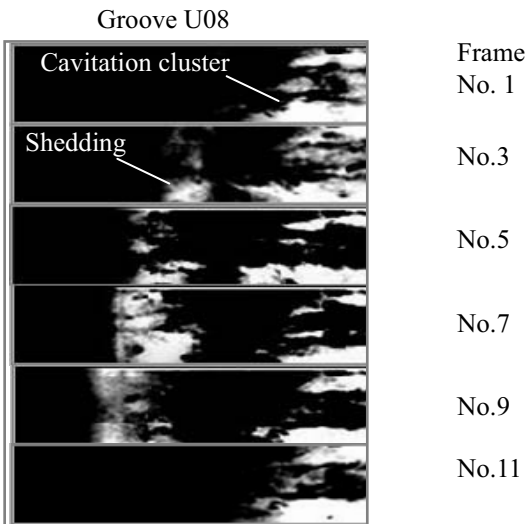
(c) σ=0.11; Fs=40000fps

Figure 8 Cavitation shedding behaviors

Periods can be calculated by the frame number and camera speed. As a result, $f_{09-1.0}$=13.3kHz, $f_{08-1.0}$=4kHz and $f_{06-1.0}$=10kHz. The high frequency characteristics of the shedding processes seemed to be similar with cavitation noise spectrum, as was illustrated in Christopher's book on cavitation [8]. For the purpose of getting a better understanding of the shedding process, an attempt was conducted. As a continual investigation of groove U09 within 1.0mm opening condition, the shedding frequencies based on different cavitation numbers were figured out, as is showed in fig.9.
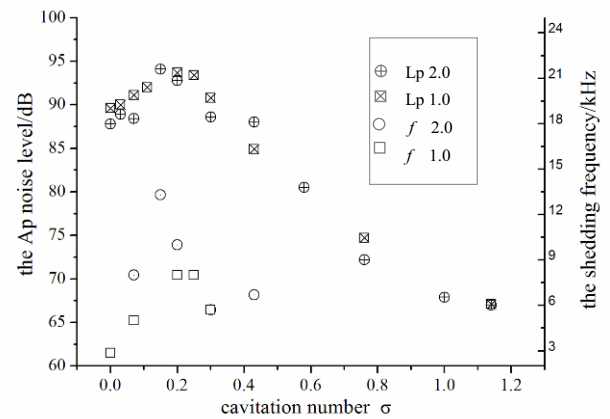
Figure 9 Cavitation noise and shedding frequency

Similar trend of the cavitation noise levels and the shedding frequencies could be seen in this figure. It is reasonable to believe that the shedding frequency could be used as a reflection to cavitation noise. However, with the restriction of camera speed, the frequencies can't be divided detailed, though the highest audible frequency 20kHz can be detected by the current conditions. Moreover, it assumed that the shedding volume also played an important role on cavitation noise, which would be investigated in our further researches.

CONCLUSIONS

(1) Two cavitation distribution states were found in the grooves. And the states' transition threshold point was advanced. It was illustrated that the cavitation distribution characteristics were only effect by structure parameters.

(2) Cavitation's shape characteristics were investigated, the bodies of which exist in liquid environments with helix shapes. The length of bodies extends nearly lineally with the changing of the cavitation numbers. However, no noticeable cavitation bodies, even cluster processes were found in groove U06, though the bodies' average length was getting shorten from groove U09 to U07, which means that there is an appropriate construction for the develops of cavitations.

(3) Cavitation noise was detected in a soundproof room. Typical noise curves were obtained. And moreover, second peck level of noise appeared in the small cavitation number conditions, which is coincident with Sato's acceleration dates on orifice cavitation.

(4) It is illustrated that shedding processes of cavitation exist in any cases, even in groove U06. The shedding frequency was employed to compare with cavitation noise, and similar trends were found within a certain depth and opening condition.

REFERENCES

1. Guoyu Wang and Lei Tao, Characteristics of Vibration Induced by Cavitation, Journal of Beijing Institute of Technology, 2005, 14-4, pp.411-415.
2. Timo Koivula, Proc. of 1st FPNI-PhD Symp., Hamburg, 2000, pp.371-382.
3. Hong Gao, Xin Fu and Yanghua Yong, Numerical Investigation of Cavitating Flow Behind the Cone of A Poppet Valve in Water Hydraulic System, Journal of Zhejiang University Science, 2002, 3-4, pp.395-400.
4. J. Kiesbauer and D. Vnucec, Prediction Cavitation Damage in Control Valves, Hydrocarbon processing, 2006, 85-33, pp.55-61.
5. C. Samuel Martin, H. Medlarz and D. C. Wiggert, Cavitation Inception in Spool Valves, Journal of fluids Engineering, 1981, 103, pp.564-576.
6. Keiichi SATO and Yasuhiro SAITO, Unstable Cavitation Behavior in a Circular-Cylindrical Orifice Flow, JSME International Journal, Series B: Fluids and Thermal Engineering, 2002, pp.638-645.
7. LC. Ganippa, G. Bark and S. Andersson, Cavitation: A Contributory Factor in the Transition from Symmetric to Asymmetric Jets in Cross-flow, Experiments in Fluids, 2004, 36, PP.627-634.
8. Christopher E. B., Fundamentals of Multiphase Flow, 2005, pp.142-149.

P1-02

2D SERVO VALVE WITH A ZERO-OVERLAP OF PILOT STAGE

Sheng LI, Jian RUAN, Xiang PEI, Zheqing YU and Faming ZHU

The MOE Key Laboratory of Mechanical Manufacture and Automation
Zhejiang University of Technology
Hangzhou, 310014, China
(E-mail: li_sheng@mail.hz.zj.cn)

ABSTRACT

A 2D servo valve designed with zero-overlap is proposed. First, the pilot leakage of the 2D servo valve with a zero-overlap of pilot stage is analyzed theoretically. Based on the analysis to the flow field of the clearance between two parallel plates, the overall pilot leakage is calculated through integration. Secondly, the mathematical model of the axial motion of the spool in respect to rotary motion is established and the dynamic response of 2D servo valve is investigated by simulation. Finally, to validate the analysis, the prototype of a 2D valve with flow capacity of 300L/min (at 7Mpa) is fabricated and the pilot leakage and the actual step response are measured. The results of the experiment show that the pilot leakage is about 0.6L/min at 21Mpa and the response time for the step input is 7ms. It is concluded from both theoretic analysis and simulation that the 2D servo valve with a zero-overlap of pilot stage has a fairly fast dynamic response, and its pilot leakage is very small, less than 0.2%.

KEY WORDS

Servo valve, Leakage, step response, two-dimensional control

NOMENCLATURE

α	:	Pitch angle of spiral groove
A	:	End area
A_1	:	Crescent overlap area between the spiral groove and hole 1
A_2	:	Crescent overlap area between the spiral groove and hole 2
B_c	:	Coefficient of viscous frictional force
C_d	:	Coefficient of the flow rate
C_e	:	Modifying coefficient of flow rate
F	:	Coulumb frictional force
h_0	:	Initial overlap size of crescent area
h_1	:	Height of crescent overlap area for the hole 1
h_2	:	Height of crescent overlap area for the hole 2
K	:	Stiffness of the Bernoulli force
L_V	:	depth of left spool chamber
m	:	Mass of spool
p_A	:	Pressure of main valve port A
p_B	:	Pressure of main valve port B
p_c	:	Pressure of the left spool chamber
p_s	:	Pressure of system
q_p	:	pilot leakage flow

Q_1	:	Flow rate entering the left spool chamber
Q_2	:	Flow rate through crescent overlap area of hole 2
Q_{l1}	:	Flow rate entering from hole 1 through spool-sleeve clearance
Q_{l2}	:	Leakage through spool-sleeve from left chamber to hole 2
r_d	:	Radius of the hole 1 (2)
R	:	Radius of spool land
t	:	Time
x_v	:	Displacement of the spool
μ	:	Dynamic viscosity
θ	:	Rotary angle of spool
ρ	:	Density of oil
γ	:	Angle of the small width dl
δ	:	Clearance between spool and sleeve

INTRODUCTION
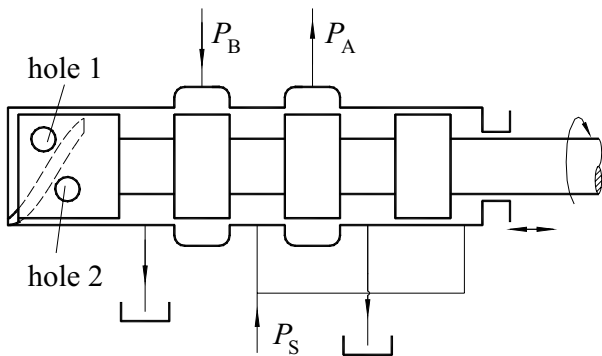
Figure 1 2D servo valve with a zero-overlap of pilot stage

The electrohydraulic servo valve plays a key role in the electrohydraulic servo systems and usually determines the performance of the whole systems to a great extent. The well-known nozzle-flapper servo valve has a fairly fast dynamic response due to the small inertia of its armature-flapper-wire assembly, but it is very sensitive to the contamination of oil media. Moreover, there is always a constant leakage flowing through the gaps between the nozzles and flapper, which results in a substantial power loss in the system, especially when the system is running at high pressure, for the value of the power loss is proportional to the square of the system pressure. As for the jet pipe servo valve, the tolerance to contamination has somewhat been improved, but at the price of even greater pilot leakage and power loss. The 2D servo valve (shown in Figure 1) is designed with two-dimensional structure of a single spool and its dynamic performance is chiefly dominated by the

hydraulic servo mechanism for the rotary-to-linear motion conversion. Because the natural frequency of the hydraulic servo mechanism is extremely high, up to about 10^4 to 10^5 Hz, the 2D servo valve potentially possesses high performances both dynamic and static. In previous studies, its pilot stage is designed with a certain hatch to increase stability. But this results in the leakage of the pilot stage and power loss. Therefore, a 2D valve designed with zero-overlap, hence with tiny pilot leakage, is proposed in this paper.

ANALYSIS OF PILOT LEAKAGE FLOW

2D servo valve with a zero-overlap of pilot stage does not have hatch, the pilot leakage is mainly generated via the clearance between the valve spool and the vale sleeve. Under static conditions, the flow enters the left valve chamber through the clearance via hole 1 (high pressure hole) and then discharges through the clearance via hole 2 (low pressure hole) to tank, so the pilot leakage occurs. As the clearance is very small, the leakage flow is considered to be laminar flow and can be considered the same as that as exists in the clearance formed by two parallel plates. Therefore, based on the model of tiny volume with small width through the clearance between two parallel plates, the leakage flow of 2D servo valve with a zero-overlap of pilot stage can be calculated theoretically.
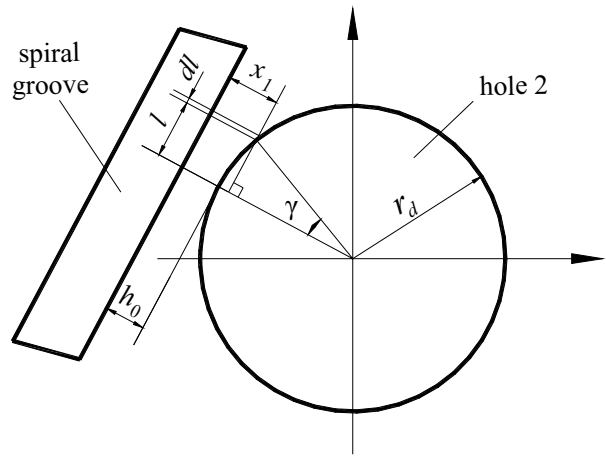
Figure 2 Pilot leakage flow

With reference to Figure 2, the flow of a tiny volume with small width dl through the clearance between two parallel plates can be described as follow

$$dq_p = \frac{\delta^3 \Delta p \, dl}{12 C_e \mu x_1} \qquad (1)$$

Where dq_p is the flow of a tiny volume with width

262

dl through the clearance between two parallel plates; Δp is the pressure difference between the hole and the spiral groove.

For the high pressure hole, $\Delta p = p_s - p_c$; for the low pressure hole, $\Delta p = p_c$; x_1 is the distance from the spiral groove to the hole.

Based on the geometry shown in Figure 2, the following equations can be obtained

$$l = r_d \sin \gamma \qquad (2)$$

$$x_1 = h_0 + r_d (1 - \cos \gamma) \qquad (3)$$

Applying the derivative to Eq. (2), the following equation can be derived

$$dl = r_d \cos \gamma \, d\gamma \qquad (4)$$

Substituting Eq. (3) and Eq. (4) into Eq. (1), the pilot leakage flow q_p is obtained

$$q_p = -\frac{\delta^3 \Delta p \pi}{12 C_e \mu} + \frac{\delta^3 \Delta p}{3 C_e \mu} \frac{h_0 + r_d}{\sqrt{h_0(h_0 + 2r_d)}} arctg \sqrt{\frac{h_0 + 2r_d}{h_0}} \qquad (5)$$

In terms of Eq. (5), the pilot leakage can be calculated at different system pressure, shown in Table 1.

Table 1 Theoretic value of leakage rate

Pressure [MPa]	5	10	15	21
Leakage rate [L/min]	0.1088	0.2175	0.3263	0.4568

ANALYSIS OF DYNAMIC CHARACTERISTIC

To analyze the dynamic response of the 2D servo valve with zero-overlap pilot stage, its mathematical model is established. It can be described through flow rate continuity equation and spool motion equation.

Flow rate continuity equation

In the dynamic process, the flow rate entering the left valve chamber is mainly composed of two parts. One part is the flow rate entering the left chamber through the crescent overlap area of the hole 1, and other part is the flow rate entering from hole 1 through the clearance between the spool and the sleeve. Correspondingly, the flow rate discharging the left chamber is also composed of two parts: the flow rate through the crescent overlap area of the hole 2 and the flow rate from the spiral groove to tank through the spool-sleeve clearance. Therefore, according to the flow rate continuity, the following equation is obtained

$$Q_1 + Q_{l1} - Q_2 - Q_{l2} = A \frac{dx_v}{dt} + \frac{A(L_V + x_v)}{\beta_e} \frac{dp_c}{dt} \qquad (6)$$

The flow rate Q_1 can be calculated by the following equation

$$Q_1 = C_d A_1 \sqrt{\frac{2(p_s - p_c)}{\rho}} \qquad (7)$$

A_1 is the crescent overlap area between the spiral groove and the hole 1. It is dependent upon their relative geometric position. With reference to Figure 2, A_1 can be expressed as:

$$A_1 = \begin{cases} 0 & (h_1 < 0) \\ h_1\sqrt{2r_d h_1 - h_1^2} + r_d^2 \arcsin\frac{\sqrt{2r_d h_1 - h_1^2}}{r_d} - r_d\sqrt{2r_d h_1 - h_1^2} & (0 < h_1 \le r_d) \\ \pi r_d^2 + h_1\sqrt{2r_d h_1 - h_1^2} - r_d^2 \arcsin\frac{\sqrt{2r_d h_1 - h_2^2}}{r_d} - r_d\sqrt{2r_d h_1 - h_1^2} & (r_d < h_1 \le 2r_d) \\ \pi r_d^2 & (h_1 \ge 2r_d) \end{cases} \qquad (8)$$

Where h_1 is the height of the crescent overlap area for the hole 1.

With reference to Figure 2, h_1 can be described as follow

$$h_1 = R\theta \sin\alpha - x_v \cos\alpha - h_0 \qquad (9)$$

Similarly, Q_2、h_2 and A_2 are respectively described as follow

$$Q_2 = C_d A_2 \sqrt{\frac{2p_c}{\rho}} \qquad (10)$$

$$h_2 = -R\theta \sin\alpha + x_v \cos\alpha - h_0 \qquad (11)$$

$$A_2 = \begin{cases} 0 & (h_2 < 0) \\ h_2\sqrt{2r_d h_2 - h_2^2} + r_d^2 \arcsin\dfrac{\sqrt{2r_d h_2 - h_2^2}}{r_d} - r_d\sqrt{2r_d h_2 - h_2^2} & (0 < h_2 \leq r_d) \\ \pi r_d^2 + h_2\sqrt{2r_d h_2 - h_2^2} - r_d^2 \arcsin\dfrac{\sqrt{2r_d h_2 - h_2^2}}{r_d} - r_d\sqrt{2r_d h_2 - h_2^2} & (r_d < h_2 \leq 2r_d) \\ \pi r_d^2 & (h_2 \geq 2r_d) \end{cases} \qquad (12)$$

Spool motion equation
The equation of motion for the spool is given by:

$$p_c A - \frac{1}{2} p_s A = m\frac{d^2 x_v}{dt^2} + B_e \frac{dx_v}{dt} + Kx_v + F \qquad (13)$$

Equation（6）~（13）form the basis of the mathematical model of the 2D serve valve with zero-overlap pilot stage. These equations are nonlinear and solved using numerical computation method. The simulation pattern is shown in Figure 3. From Figure 3, the rising time is about 6 ms.
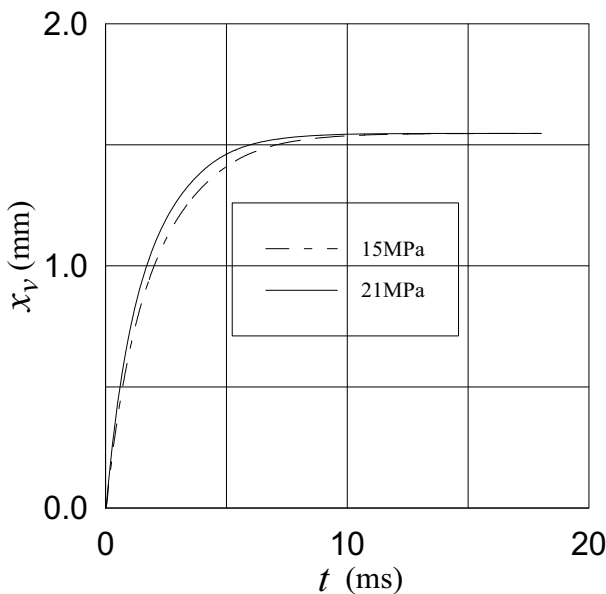
EXPERIMENT

To validate the analysis, the actual test is carried out on an experimental set-up.
Measurement of leakage rate from the pilot
Figure 4 is the experimental set-up of leakage rate of the pilot. The leakage rate was measured using a calibrated glass and a stopwatch. To prevent leakage from the valve port via the spool-sleeve clearance of the central spool land from entering the calibrated glass, port P_B is connected to tank and port P_A blocked off. The measured data is listed in Table 2. It should be noted that the measured leakage flow rate included the leakage through the spool-sleeve clearances. From Table 2, it can be clearly seen that the pilot leakage is 0.6L/min at 21MPa. The data agrees well to the theoretical calculation result and the leakage flow of the pilot is small.

Figure 3 Simulation pattern
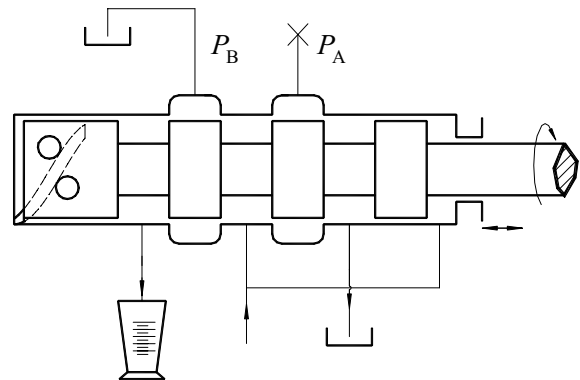
Figure 4 Experimental set-up of leakage rate of the pilot

Table 2 Measurement of leakage rate

Pressure [MPa]	5	10	15	21
Leakage rate [L/min]	0.174	0.316	0.435	0.6

Experiment of step response

Figure 5 is the experimental set-up of the step response. In Figure 5, One end of a steel rob was connected with the spool, and the other end was tied with a steel wire. By pulling the steel wire quickly, the step of spool's rotation was created and the spool also made a linear motion correspondingly in respect to its rotation. The linear motion of the spool was measured with a laser displacement sensor and recorded in an oscilloscope. The measured step response is shown in Figure 6. From Figure 6, it can be clearly seen that the linear motion of the spool in response to its rotation is very fast, and the responding time is about 7ms at 21MPa. This result also proves the correctness of the theoretical analysis.
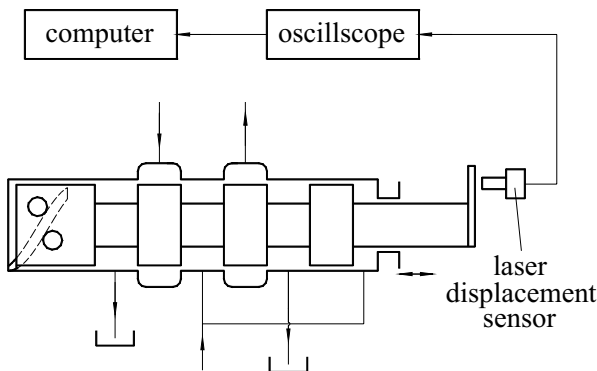
Figure 5 Experimental set-up of step response

CONCLUSION

2D servo valve with zero-overlap is composed of a pilot control valve designed with both rotary and linear motions of a single spool. Because of the extremely large value of the hydraulic natural frequency, the 2D servo valve potentially possesses high performances both dynamic and static. Either simulation analysis of 2D servo valve with zero-overlap or experiment makes it clear that it has fast dynamic response. The step response time is about 7ms. It is also shown its pilot leakage is very small.
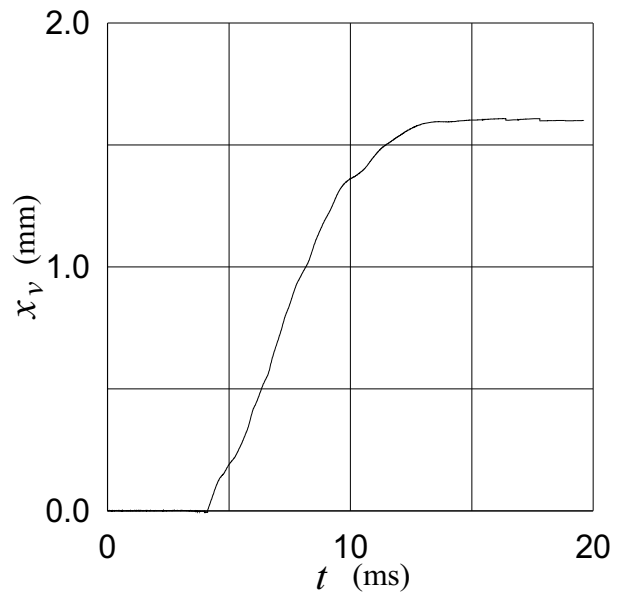
(a) 15MPa
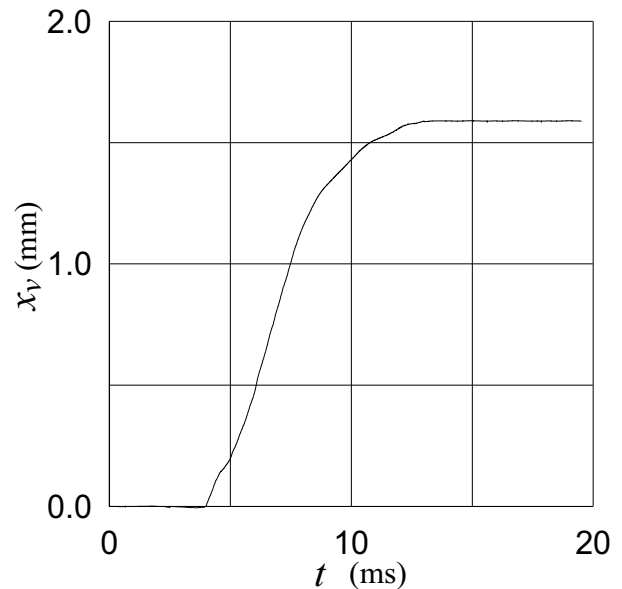
(b) 21MPa

Figure 6 Measured step response

REFERENCES

1. J. Ruan, R. Burton and P. Ukrainetz, An Investigation Into the Characteristics of a Two Dimensional "2D" Flow Control Valve, Journal of Dynamic Systems, Measurement and Control, Transactions of ASME, Vol. 124, March 2002,pp.214~220.
2. Maskrey, R. H.,Thayer, W. J.，Brief History of Electrohydraulic servomechanisms, Journal of Dynamic Systems, Measurement and Control, June 1978.
3. Merritt, H. E., Hydraulic Control Systems, John Wiley & Sons, New York, 1967, pp.67~86
4. Ruan Jian, Electro-hydraulic (pneumatic) Direct Digital Control. Press of Zhejiang University, Hanzhou, 2000, pp.45~48.
5. Li H. R., Electro-hydraulic Control Systems, National Defense Press, 1981.
6. Ruan J., Ukrainetz, P. R. and Burton ,R.,Frequency Domain Modeling and Identification of 2D Digital Servo Valve, International Journal of Fluid Power,2001,1,pp.49~58.
7. Wang Y., et al., Mathematics Handbook, Mass Education Press, 1977,pp.37

P1-03

STUDY ON FAST FORGING PROCESS CHARACTERAISTICS OF 20MN FORGING PRESS

Yao Jing*, Kong Xiangdong*, Gao Yingjie*, He long*, Quan Lingxiao*, Li Nan*

* Department of Mechanical Engineering, Faculty of Electromechanical Engineering
Yanshan University
Qinhuangdao, 066004 China
(E-mail: jyao@ysu.edu.cn)

ABSTRACT

The E/H servo cartridge valve is adopted to control the system of 20MN Forging Hydraulic Press. Its characteristics ,such as short response time, high control accuracy and so on, are extremely fit for forging hydraulic press. As a result the high forging times and accuracy can be achieved. A new saving-energy fast forging press using accumulator is presented for the problem of power waste during forging process. The model of proportional cartridge and accumulator are found, then the mathematical model of the whole fast forging circuit is found and simulated, the results show that it performs perfect for the fast forging press by using accumulator. Finally, base on the fast forging press test with accumulator, the model validity and feasibility of this fast forging circuit are validated.

KEY WORDS

Fast forging, accumulator, forging curve, saving-energy

NOMENCLATURE

A : the cross-sectional area of the accumulator.
A_1 : the plunger piston area of the main cylinder..
A_2 : the plunger piston area of the retracting cylinder..
a : proportional cartridge valve choke area...
B : oil viscous damping coefficient
c_a : gasses coefficient of damping of the accumulator
C_d : proportional cartridge valve flow coefficient
d : proportional cartridge valve choke diameter
K_a : gasses rigidity coefficient of accumulator
K_{vx} : proportional cartridge valve gain
M : the moving part mass
m_a : liquid equivalent mass of accumulator
P_{sa} : the inlet pressure of accumulator
P_1 : the pressure of the main cylinder
P_2 : the pressure of the retracting cylinder
P_s : the pressure of the pump

Q_1 : the flow of the main cylinder
Q_2 : the flow of the retracting cylinder
Q_x : the flow of the accumulator
P_s : the pressure of the pump
V_1 : the initial volume of the main cylinder
V_2 : the initial volume of the retracting cylinder
ω_{vx} : proportional cartridge valve frequency
V_2 : the initial volume of the retracting cylinder

INTRODUCTION

Forging industry is closely linked with national war industry, nuclear energy, airspace, electric power generation, traffic, fossil oil, heavy machinery etc. Forging press capacity tonnage represent a national strength, the advanced forging equipment is also one important symbol for a state industry modernization[1].

With the development of industry modernization, the forging precision and forging velocity are requested more and more high. Because it not only can increase productivity, but also can reduce the loss of the workpiece and economize in raw materials[2]. Due to some characteristics such as high pressure, large flow, heavy moving inertia and so on, the forging hydraulic press often has poor rapidity, large shock during pressure relief and flow relief, low control accuracy and high accident rate. To overcome the negative influence and improve forging press performance, 20MN fast forging hydraulic press have obvious improvement with respect to hydraulic system design, control method and control software.

FAST FORGING PROCESS CONTROL

Fast forging work is mainly used to finishing operation, its forging stroke is not exceed 30mm, the amount of deformation is generally controlled less than 5mm. The simplification schematic diagram of 20MN hydraulic press fast forging system with accumulator is shown in Figure 1.
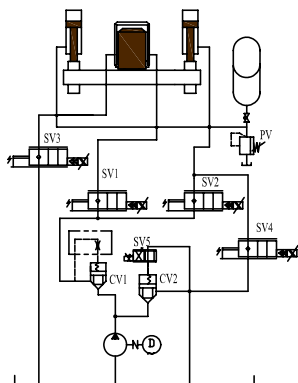
Figure 1 The simplified accumulator fast forging circuit

During fast forging process, SV4 is all along closed, the chamber of return cylinder form close and maintain pressure. Decompression stage，SV1 turns on and high-pressure oil comes into master cylinder, the moving beam go down, oil from return cylinder enter into accumulator and the energy is stored, supporting-valve PV serve for security. During return-stroke hour，SV1 is closed and SV3 is turning on, master cylinder pressure is releasing and SV5 open up instantaneously and main pump unload, at the same time accumulators release, high-pressure oil comes into return cylinder, moving beam is lifted, after running up to upper set point, next working cycle is coming immediately.

FAST FORGING PROCESS MATHEMATIC MODEL

The rapidity and control precision is pursuing goal for hydraulic press, it is important to study on dynamic characteristics of fast forging process.

The E/H proportional cartridge model

20MN fast forging hydraulic press adopts Parker E/H proportional cartridge, its response time is less than 20ms, from Figure 1, SV1，SV3 is this type valve. When hydraulic system natural frequency is less than 50 Hz, the E/H proportional cartridge model can be represented as:

$$\frac{x_v}{I_c} = \frac{K_{vx}}{1 + \dfrac{s}{\omega_{vx}}} \tag{1}$$

The flow equation of the master cylinder's input proportional cartridge valve is：

$$Q_1 = C_d a \sqrt{\frac{2}{\rho}(P_s - P_1)} \tag{2}$$

The flow equation of the master cylinder's pressure relief proportional cartridge valve is：

$$Q_t = C_d a \sqrt{\frac{2}{\rho}(P_1 - P_0)} \tag{3}$$

The throttle area of proportional cartridge valve is：

$$a = x_v \pi d \sin \alpha \tag{4}$$

The accumulator model

Supposing state $0(P_{X0}, V_{X0})$ is the pressure and volume state of initial working point in the air cavity, state $a(P_a, V_a)$ is random working mode of the air cavity. In the fast forging course of hydraulic press, the working frequency of the accumulator is about 1.3Hz，the inflation and deflation time of the accumulator is less than 1min, it can be regard as adiabatic condition, so $k = 1.4$.

Accumulator is a gasses spring-damp model[4], Accumulator motion equation:

$$(P_{sa} - P_a) = \frac{m_a \ddot{V}_a + B\dot{V}_a + c_a \dot{V}_a + k_a V_a}{A^2} \tag{5}$$

According to gas equation, where is

$$p_{x0}V_{x0}^k = p_a V_a^k \tag{6}$$

from above Eq.(6) :

$$p_a = p_{x0} V_{x0}^k V_a^{-k} \qquad (7)$$

Then accumulator from state 0 to state a, pressure increment is :

$$\Delta P = P_a - P_{x0} = p_{x0} V_{x0}^k V_a^{-k} - P_{x0} \qquad (8)$$

The accumulator state of pressure equation is:

$$\dot{P}_a = \frac{\Delta P}{\Delta t} = -\frac{k p_{x0} V_{x0}^k}{V_a^{k+1}} \dot{V}_a \qquad (9)$$

The cylinder model
The controlled actuator of the E/H servo system consists of one main cylinder and two return cylinders in 20MN fast forging hydraulic press. Those cylinders work together to realize forging press framework motion. To model such system, the reciprocating motion cylinders are regarded as a double-acting cylinder with a noticeable difference that is the reciprocating motion cylinders have no internal leakage.
The flow continuous equation in main cylinder:

$$Q_1 = \frac{V_1}{\beta_e} \dot{P}_1 + A_1 \dot{y} - Q_x \qquad (10)$$

The flow continuous equation in return cylinder:

$$Q_2 = -\frac{V_2}{\beta_e} \dot{P}_2 + A_2 \dot{y} \qquad (11)$$

Owing to oil condensability smallness, hydraulic spring stiffness which is caused by the oil condensability is much larger than accumulator loading system [5], so the syntheses spring stiffness of forging system is mostly decided by accumulator.
Neglecting pipeline influence, the flow variation of return cylinder is equal to accumulators', the pressure change of return cylinder is correspondence with the accumulators'.
so

$$Q_2 = A_2 \dot{y} = \dot{V}_1 \qquad (12)$$

$$P_2 = P_{sa} \qquad (13)$$

The moving framework model
Ignoring friction force, the framework motion equation is expressed as follows:

$$P_1 A_1 - P_2 A_2 - B\dot{y} - F_z + G = M\ddot{y} \qquad (14)$$

SIMULATION ANALYSIS

simulation parameter
Master cylinder diameter of 20MN fast forging press is 820mm, return cylinder diameter is 250mm, the weight of moving beam is 200t, balancing deadweight needs for 14.5MPa system pressure, the max flow of compression is 3600L/min, the frequency of fast forging is 80 times/min, stroke is 30mm, gauge reduction is 5mm, accuracy of displacement is ±1mm. Supposing maximum external load is 10MN, practical external load has certain relation with deformation of forging workpiece. Setting the basic parameters of accumulator is very important, selected V_{x0}=40L, P_{x0}=14.5MPa.
simulation analysis
The simulation model is found and simulated by Matlab/Simulink®. Figure 2 shows the fast process pressure and displacement curve of the forging press without load. The displacement curve is smooth and no overshot, and the forging press has high position precision, during compression course, pressure of main cylinder P_1 rises, the pressure P_2 of accumulator also goes up because of absorbing energy. There is one slowdown process near lower-most point, both master cylinder and return cylinder pressure appear wave trough; during upstroke course, main cylinder releases through SV3, pressure decreases to zero, accumulator releases energy, pressure gradually reduces. The pressure fluctuation of main cylinder is due to moving beam quality, hydraulic spring and damping effect together.
The forging press with external load fast process pressure and displacement curves are shown in Figure 3, loaded instant, the moving beam is at once slowdown and displacement curve appears fluctuation, but control accuracy is not affected, the pressure of main cylinder rapidly rises, the pressure of accumulator are also higher than that of no-load. Figure 4 shows the external load input curve.

CONCLUSION

a) 20MN fast forging press adopts advanced electro-hydraulic control system, the simulation results approve that its forging curve is approaching to sine curve.

b) The accumulator fast forging circuit is a new energy saving mode, if only the accumulator parameters are rationally designed and selected, the simulation results
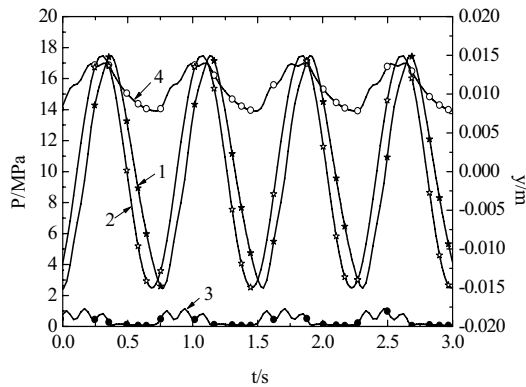
1. forging press displacement 2.input displacement
3. main cylinder pressure 4.return cylinder pressure
Figure 2 The displacement and pressure curve without Load
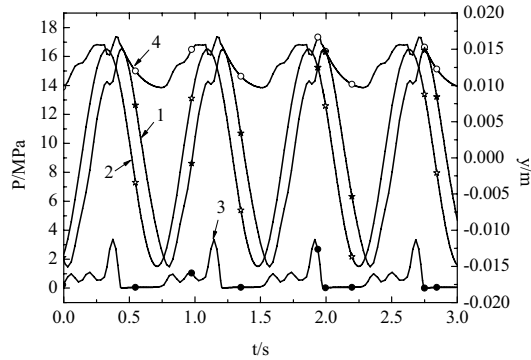
1. forging press displacement 2.input displacement
3. main cylinder pressure 4.return cylinder pressure
Figure 3 The displacement and pressure curve with load
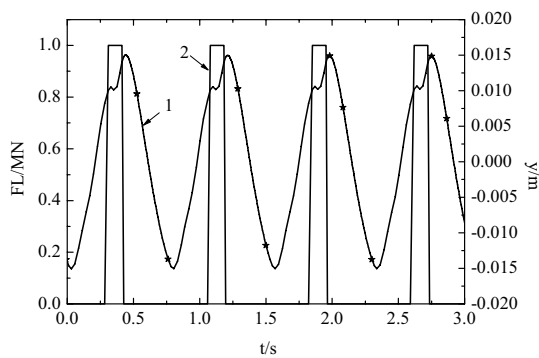
1. external load 2.displacement
Figure 4. The external load curve

prove that it is feasible to use accumulator to realize fast forging.

c)Establishing kinematic equation of accumulator, and supply the gist of fast forging circuit design and accumulator select.

d)Establishing mathematic model of fast forging circuit with accumulator, hydraulic press dynamic characteristics is researched by simulation, which provides theoretical foundation for fast forging press design and application.

ACKNOWLEDGEMENT

REFERENCES

1. G.H.Zhang, Study of 80MN isothermal forging hydraulic press control system.(Master degree dissertation),Tianjin University,2005,pp.1-5
2. F.R.Biglari. Optimum design of forging dies using fuzzy logic in conjunction with backward deformation method. International Journal of Machine Tools&Manufacture, 1998,38,pp.981-1000
3. X.L.Yue, "Hydraulic Press", China Mechanical Press, 1982,pp.
4. L.X.Quan. the Therory and Experiment study on Accumulator Absorbing Pressure Pulsation without Entrance.[J].Chinese Journal of Mechanical Engineering ,2007,43-9,pp.28_32
5 N.L.Wu,.Accumulator Loading System Stiffness Analysis.[J].Engineering mechanie.2003,10,pp.20~23

P1-04

IMPROVEMENT OF TOTAL EFFICIENCY OF HYDROSTATIC TRANSMISSION BY USING OPTIMIZED CONTROL

Mika IJAS and Esa MÄKINEN

Tampere University of Technology

Department of Intelligent Hydraulics and Automation

IHA - Rauma Research Unit

P.O.Box 236

26101 Rauma, Finland

Phone +358 2 823 4970, Fax +358 2 823 4974

E-mail: mika.ijas@tut.fi

E-mail: esa.makinen@tut.fi

ABSTRACT

A basic hydrostatic transmission consists of a variable hydraulic pump and variable hydraulic motor. The most popular strategy is to control the units in sequence. From standstill up to a speed limit set by the maximum pump displacement, the output speed is controlled by the pump. Further increase of the output speed is achieved by decreasing the motor displacement. This way to control of HST is not best thinking of total efficiency. Efficiency of the hydraulic pump and the hydraulic motor are function of pressure, rotating speed and control angle. If it is possible to control independently the hydraulic motor and the hydraulic pump, it can be optimized total efficiency for every operating point (torque and rotating speed of the hydraulic motor). In this study control settings of the hydraulic pump and the hydraulic motor are optimized for each operating point so that the total efficiency should be as good as possible. These optimized efficiencies are compared to efficiencies from traditional control. The entire operating band was studied (rotating speed and torque of the motor) using simulation. Exactly verified simulation models of the HST were used. The base of simulation models was measured data from earlier studies. The results show that efficiency can be improved when the load is low. Power loss decreased maximum about 1.5kW.

KEY WORDS

Key words, Hydrostatic transmission, control, optimization

INTRODUCTION

The closed circuit hydrostatic transmission generally comprises three components: a prime mover (for example electric motor), the hydraulic pump, which converts mechanical power into fluid power and the hydraulic motor, which converts fluid power back into mechanical power.

The ideal hydraulic pump and motor is defined as having efficiency of 100% with no power losses due to leakages or friction. This is no not possible in practice. Variables in hydrostatic transmission which significantly affect the behavior of a system are:

• The operation variables: the rotational speed of the pump, motor and prime mover and the pressure difference across the hydraulic pump and motor

• The hydraulic pump and motor parameters: the volumetric displacement and displacement setting of a unit

• Fluid parameters: the dynamic viscosity, density and effective bulk modulus.

The traditional control of HST (pump and motor) operates as follows: The volumetric displacement of the hydraulic pump is first increased from zero to 1 (the volumetric displacement of the hydraulic motor is at value one). If there is a need to increase the speed of the hydraulic motor, the volumetric displacement of the motor has to be reduced from one to its minimum value (in this study to 1/3 from maximum value).

The total efficiency of the whole system is not very high. The low efficiency of the hydraulic pump and motor increases the temperature of the hydraulic oil. The oil reservoir is typically quite small and it is quite difficult to cool the oil especially in the summer time. The efficiency of the hydraulic components is varying a lot in the HST so the total efficiency is a function of many parameter and variable.

SIMULATION MODEL OF HST [1], [2]

Several different steady-state loss models for hydraulic pumps and motors can be found in the literature. One category of such models (the most common ones) is coefficient models. In most cases the coefficients can be defined by the data given by manufacturer. Another group of loss models is based on measurement. In these models the losses of hydraulic pump and motor are described on the basis of measured data.

The simulation model of efficiency bases on two-line principle in this work. Instead of modeling different loss sources, the two-line principle is based on describing the change in losses as a function of the system variables such as pressure, displacement and rotational speed. The loss model is based on measured data of hydraulic unit. With these measurements two curves are obtained by using polynomial fitting according to two lines [1]. All models have been evaluated and tested in the fluid power laboratory at Tampere University of Technology [1], [2], [3].

The model of hydraulic pump and hydraulic motor used take into consideration also the power loss of the boost pump and minor losses of hydraulic lines. The variables in the simulation model of the hydraulic pump are the following: the pressure difference over the pump, the rotational speed and the displacement control of the pump. The constants are the volumetric displacement, the lowest and highest pressure and the lowest and highest speed of the hydraulic pump. Maximum ratings are needed for the calculation of efficiency. With these parameters the capacity, torque and efficiency of the pump are calculated with the help of the two-line principle. The functions are fitted into the measured data.

The inputs of the model are rotational speed, displacement setting, displacement and working pressure. The outputs of the model are load torque to the prime mover, volumetric flow and total efficiency of the hydraulic pump. These output signals can be connected as inputs to the other blocks of the simulation model of the hydrostatic transmission system. The hydraulic motor is modeled with the same principle as the hydraulic pump. The model used in this study includes submodels for the feed pump, pressure relief valve and hydraulic pipes.

Figure 1 show a simulated example of total efficiency of HST when the size of the pump was 125 cm^3 and the nominal size of the motor was 160cm^3. The system is protected against overloads by pressure relief valves. Therefore there is a huge dropping of efficiency in area of high torque and high rotating speed. The total efficiency of the HST is not very high at the starting point. The reason for this is the poor efficiency of the motor at low running speeds. The efficiency increases rapidly and the maximum point is achieved just after the control has been changed from the pump to the motor. After that the efficiency reduces, when the running speed of the motor increases.

272
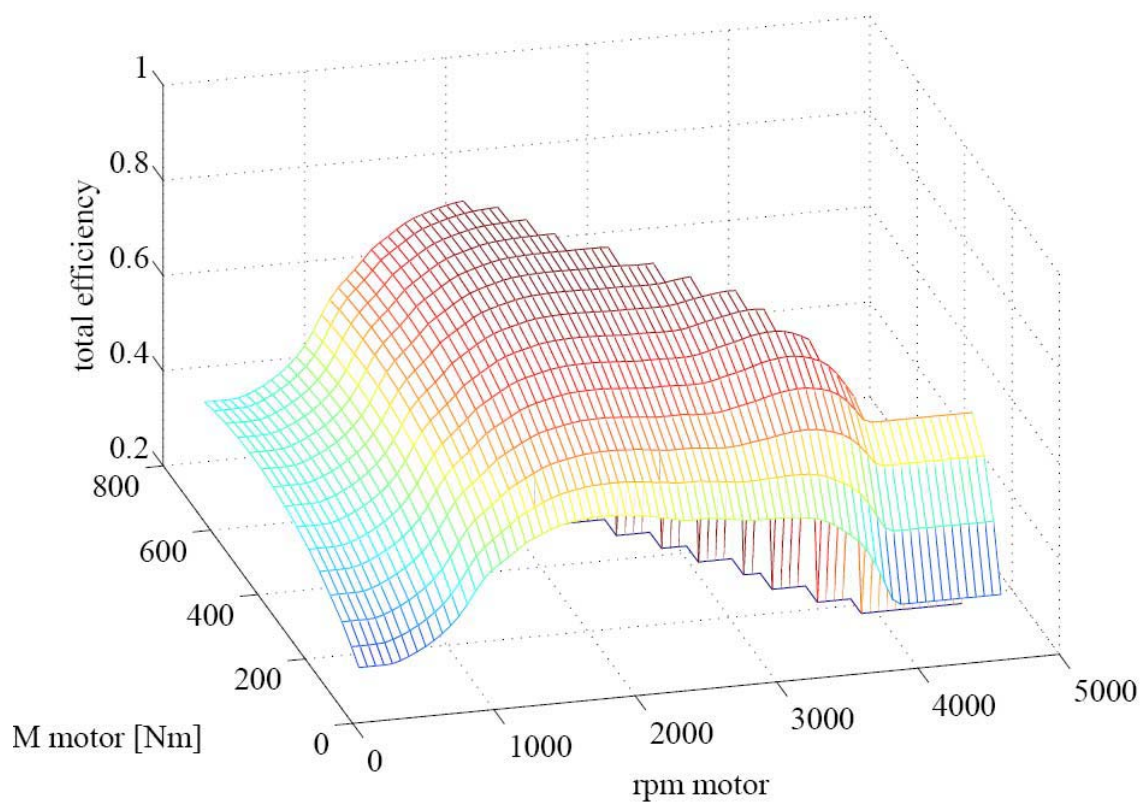
Figure 1. Total efficiency of HST.
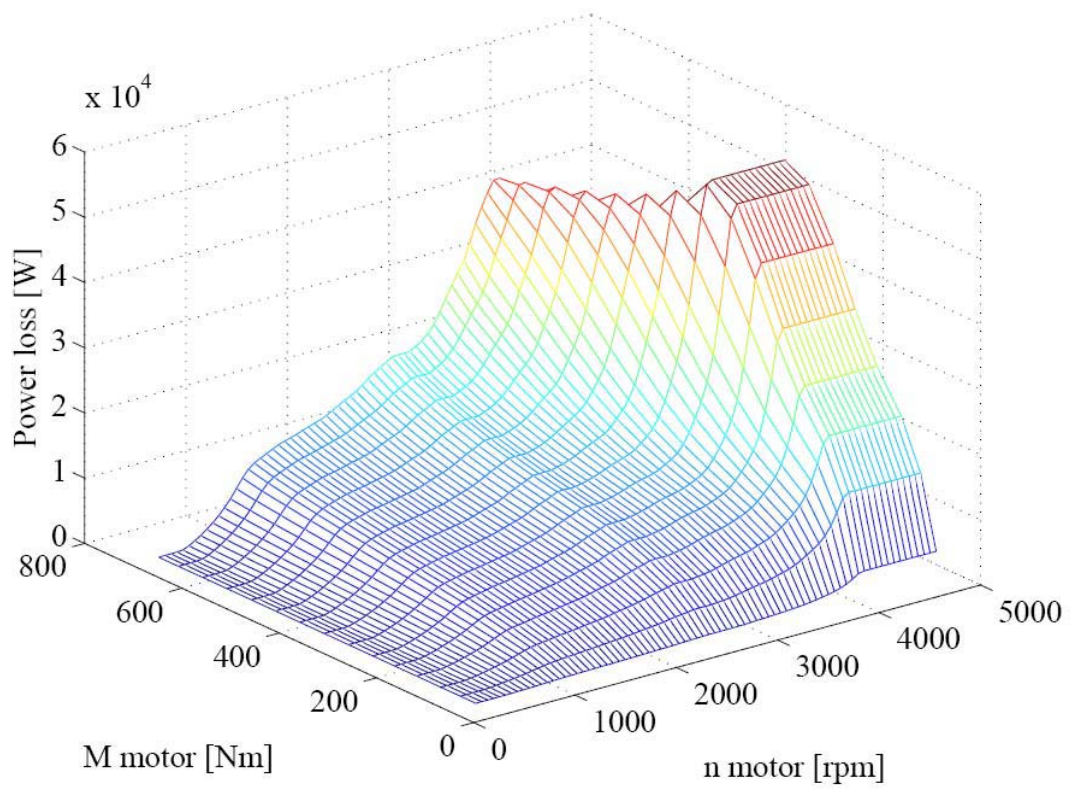
Figure 2. Power loss of HST.

However, the total efficiency is low when the rotating speed and torque are low. Total efficiency is maximum 90% but decrease rapidly when the operational point goes to an edge area. The best efficiency is when the rotating speed is about 1/3 of maximum and torque is about ½ of maximum.

Figure 2 shows simulated power loss of HST when sizes of components were same as in Figure 1. Even if the total efficiency is poor in low rotating speed, the power loss isn't high because the power level is also low. When the power level is high (high rotating speed and high torque) the total efficiency is quite good.

OPTIMIZED HST CONTROL

The main idea of optimized control is that the best settings values of pump and motor control is founded for every operation point. The total efficiency becomes as good as possible. There is not this kind of controller system on the market but the optimization has been made "manually" in this study.

In the figure 3 rotating speed was 1000 1/min and the torque of the motor was 100Nm. The size of the pump was 125cm^3 and size of the motor was 160cm^3.
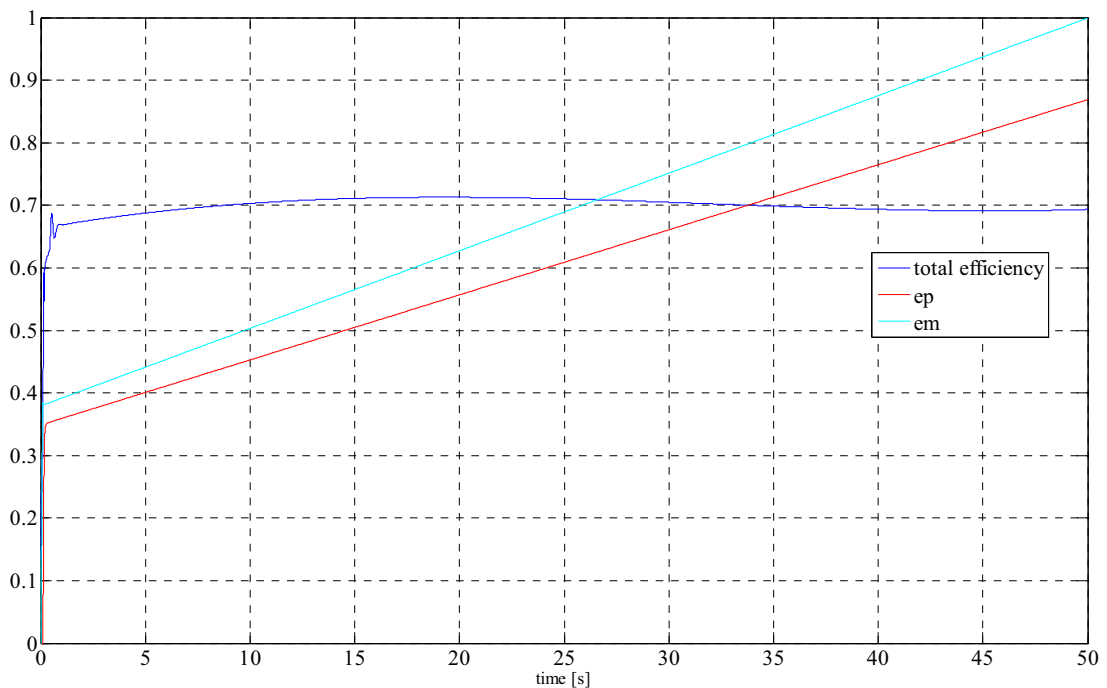
Figure 3. Total efficiency and control angles of HST during simulation.
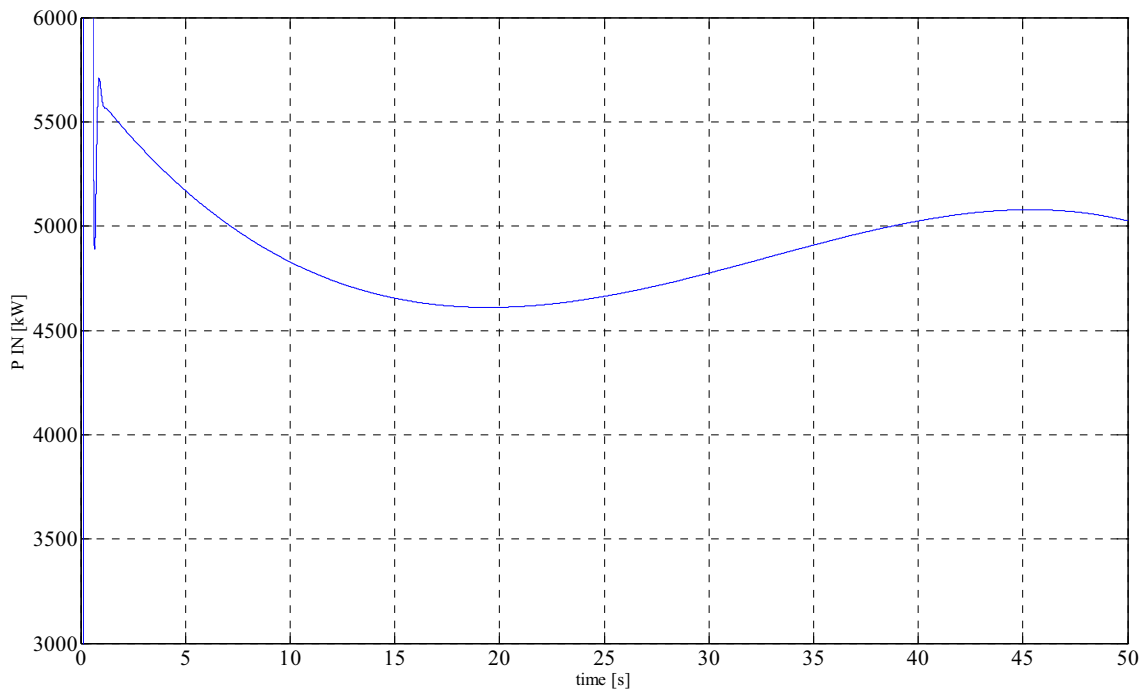
Figure 4. INPUT power of HST during simulation.

The best efficiency is at time 20,8s when input power of HST is 4635W (Figure 4). In the traditional control of HST pump setting 0,87 and motor setting 1,00 result in 1000 1/min rotating speed but the INPUT power of HST was 5118W. In this case the save was 483W when using the optimized control.

This study is done manually step by step. Every operation point (rotating speed and torque of hydraulic motor) needs one simulation as earlier was depicted. This needs a numerous simulations that sufficient cover of operation points were reached.

Figure 5 shows achievable improvements of power save. If the improvement is 0 it refers that traditional control of HST operates on its best efficiency.

The optimized control causes highest improvements when the load is low (<500Nm). The best improvement is about 1.5kW, when rotating speed is 1000 1/min and torque 100Nm. If the torque is high (>500 Nm) the traditional control of HST operates at its best way.

275
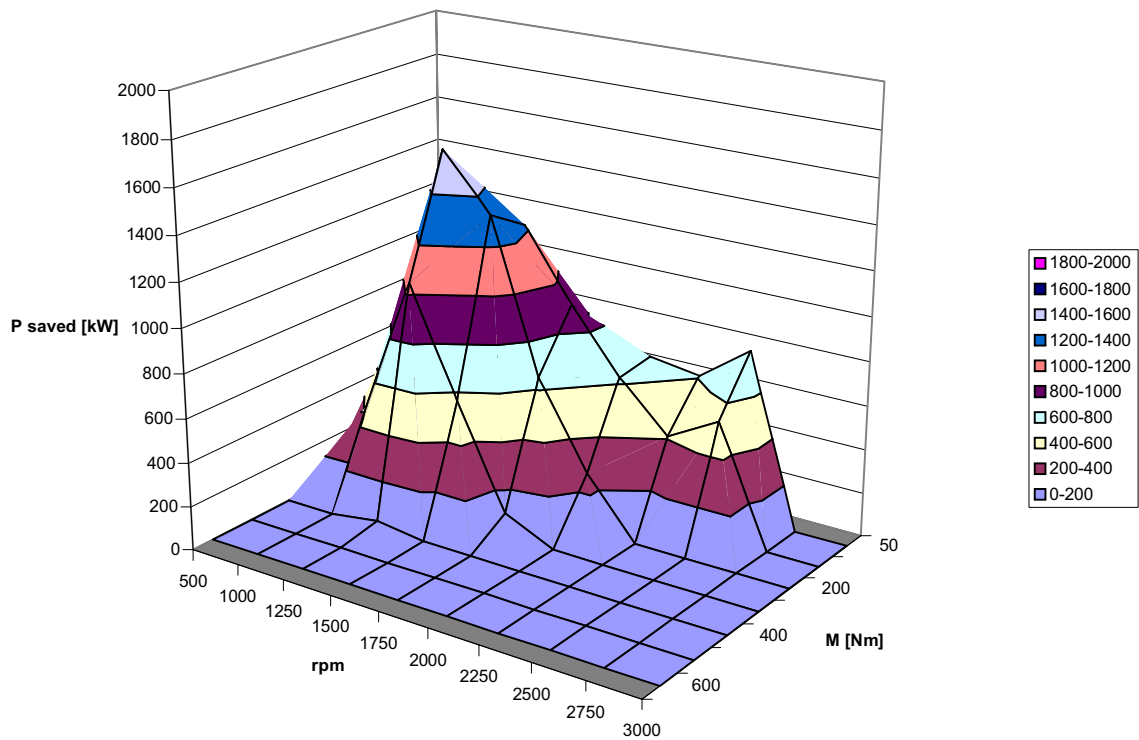
Figure 5. Simulated achievable improvements of power save of HST.

CONCLUSIONS AND DISCUSSION

According to this study the best improvements of power save was about 1.5kW HST size like this. The best accessible improvements are at low torques. If the operating point is continuously at bad operating point area, 1.5kW saving would affect to rising time of temperature notably. However, the traditional control operates well on most operating points. Advantages of optimized control disappear if the operating point varies much. Optimized control is more complex compared to traditional control because it needs separate control system to the hydraulic pump and to the hydraulic motor. It needs also the high level control, which optimizes total efficiency continuously. In this time there is not this kind of control system on the market.

The optimized control improves to total efficiency of the HST but there are also other ways to improve the efficiency balance. For example smart control, which stops prime mover when HST idling, saves energy much. Long idle running of HST is avoidable operation. Power lost of idling HST is about 5kW.
The other case to save power is reducing a flushing loss of HST. There is continues flushing flow through flushing valves which decreases the total efficiency of

HST. It should be study can power level decreases by reducing flushing pressure level in some circumstances.

REFERENCES

1. Huhtala, K. 1996. Modelling of Hydrostatic Transmission- Steady State, Linear and Non- Linear Models, Acta Polytychina Scandinavica Me 123, dissertation
2. Fonselius, J. 2001. Comparing Different Control Strategies of Hydrostatic Transmission System. Acta Polytychina Scandinavica Me 151, dissertation
3. Erkkilä. M. 2007. Dynamic Model of CVT Power Train. The Tenth Scandinavian International Conference on Fluid Power, SICFP'07, May 21-23, Tampere Finland

P1-05

OPTIMIZATION OF RELEVANT DESIGN PARAMETERS OF

EXTERNAL GEAR PUMPS

Casoli P., Vacca A., Berta G. L.

Department of Industrial Engineering, University of Parma
Viale G. P. Usberti 181/A, 43100 Parma, Italy
(paolo.casoli@unipr.it, andrea.vacca@unipr.it)

ABSTRACT

This paper describes a numerical procedure for the analysis and the optimization of external gear pumps. The Fluid Power group of the University of Parma has implemented a numerical code for the simulation of external gear pumps and motors; the code is named HYGESim and it is based on a lumped parameter approach implemented in AMESim, writing proper submodels in C language. This work is focused on the optimization of the pump design with particular reference to the geometry of the recesses machined on the bushings. The procedure is based on a path search method known as *Steepest Descent* and optimizes the considered parameters starting from a design taken as initial reference. The objective functions defined for the optimization permit to account for the volumetric efficiency, the delivery pressure ripple, the maximum and minimum pressure peaks during the meshing process. An optimal design of the recesses has been proposed and a prototype of a pump, equipped with the proposed geometry of bearing blocks, was tested. Measured data and the comparisons with the experimental results obtained for the stock pump taken as reference are presented in the paper, confirming the potentials of the developed optimization methodology.

KEY WORDS

Gear pump, pressure ripple, design of experiments, response surface methodology.

NOMENCLATURE

A…E	Bushing design parameters	V	Volume
$\hat{y}$	Fitting model	w, z	Weight
f	Frequency	θ	Gear angular position
$\vec{g}$	Gradient function	x	Vector of input variable
n	Angular velocity	X	Coded factor
p	Pressure	η_v	Volumetric efficiency
Q	Volume flow rate		
s	Minimum distance between delivery recess and shaft hole	*Subscripts*	
		av	Average
T	Time	D	Delivery
$\bar{u}$	Unit vector	Φ	Objective function

i	Index
max	Maximum
min	Minimum

Superscripts
| *g1* | Driver gear |
| *g2* | Driven gear |

Abbreviations
CV	Control volume
OF	Objective function
TSV	Tooth space volume

INTRODUCTION

The external gear pumps are the most common positive displacement machines in fluid power applications, owing to their simplicity and reliability, despite their unsuitability for variable displacement [1].
Many works, e.g. [2-6], in the open literature are focused on a detailed description of the processes characterizing the machine operation, while others, e.g. [7,8], propose numerical models for the prediction of the gear machine operation. About the application of optimization procedures to hydraulic components, only a few examples appear in the literature as to valves [9], but none has been found for external gear pumps.
The authors have chosen to model the complete machine operation developing a code that provides a detailed evaluation of the flow through the gear machine, allowing, at the same time, the simulation of a complete hydraulic system. The model, named HYGESim (HYdraulic GEar machines Simulator), is based on a discrete parameter approach, and permits the analysis of the flow under a precise characterization of the shape of the teeth profiles, of the recesses and of the axial (gear sides) and radial (between tooth tip and housing) gaps.
This paper reports only a brief description of the HYGESim structure, referring for details to previous works [10-12], being this paper focused on the optimization of the pump design with particular reference to the geometry of the recesses machined on the bushings; as a matter of fact the geometry of the bearing blocks have significant effects on the minimum and maximum pressure peaks during the meshing process, the delivery pressure transients and the volumetric efficiency. The optimization procedure adopted combines Response Surface Methodology and Design Of Experiment (DOE) algorithms, it has been efficiently applied for the optimization of other hydraulic components, as reported in [13,14]. In the present study few objective functions have been considered for the optimization, that permit to account for the main parameters affected by the recesses geometry as previously described.
However this procedure provides reliable results whenever the simulation code evaluates correctly the responses related to all the configurations considered by the optimization process. For this reason the reliability of the HYGESim's results was verified on the basis of experimental data for different prototypes of gear pumps, with particular attention to the parameters that play a

relevant role in the optimization problem, such as the flow oscillations at pump delivery (quantified by the measurement of the pressure ripple) and the volumetric efficiency [15]. The target of this work is to propose a new design of the recesses and to test the prototype pump performance comparatively with that of the stock versions of the same pump.

THE SIMULATION CODE (HYGESim)

The structure of the model includes three different parts: 1) the fluid dynamic model; 2) the model for the evaluation of the geometrical features; 3) the module for the evaluation of the actual position of gear's centres. The HYGESim code has been implemented in the AMESim® environment through the development of many submodels written in C language.
The first version of the code was presented in [10], focusing on a description of the fluid dynamic approach; subsequently, improvements of the code are described in [11]. The actual stage of development is reported in [12] where an integrated procedure is presented that permits the user to utilize the CAD 3D drawings directly as an input for the geometrical description of the machine, thus followed by the fluid dynamic simulations in the AMESim® environment. The code permits to consider a variable position of the axes of rotation of both gears during the simulation, as a consequence of the radial forces and torques generated both by the fluid pressure and by the contact between the teeth in the meshing zone. The model also evaluates the eccentricity of the gear shafts respect to the bearings on the basis of either the Ocvirk or the Warner-Sommerfeld models. The fluid dynamic model is the fundamental component of HYGESim, being the other parts developed in accordance with its specifications. It is based on a lumped parameter approach in that the flow through the machine is simulated by subdividing the domain into a number of control volumes (CVs), as displayed in Figure 1; the complete connection framework regarding each CV is quite complex and can be found in [11].
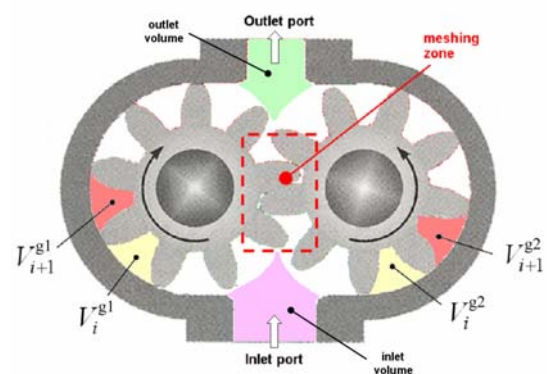
Figure 1 - *Control volumes defined in the fluid dynamic model of the HYGESim*

The actual volume and the connections between adjacent CVs of the framework displayed in Figure 1 are related to the angular position of the gears. For this purpose, a CAD model evaluates all the geometrical

data over a complete revolution of the shaft. Flow rates between different CVs and pressures inside each CV are evaluated according to the Filling & Emptying equations, assuming an isothermal flow. The model accounts for the effects of both gaseous (air release) and vapor cavitation in a simplified manner, by means of a proper relationship between the fluid density and pressure [16]. As concerns the calculation of the leakages (at the tip of each tooth and at gear's lateral surfaces), these are calculated with the modified Poiseuille equation (considering the effect of the shaft speed); in details, the gap between each tooth tip and the casing is determined considering the actual position of the gear centre as a function of the operating conditions. Thanks to its implementation in the commercial platform AMESim®, HYGESim can be used not only to provide detailed insights into the operation of the machine, but also to simulate the behaviour of the external gear unit in a generic hydraulic system.

OPTIMIZATION PROCEDURE
USING DOE AND RSM

The optimization process is based on a numerical procedure implemented in Matlab®, that automatically performs the simulation using the HYGESim code according to the workflow represented in Figure 2.
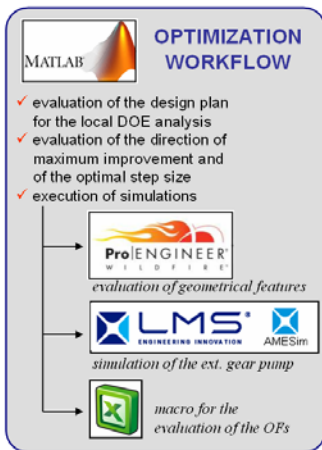
Figure 2 – *The workflow used for the optimization*

The algorithm selected for the optimization is the RSM-*Steepest Descent* method [13]. In particular, the optimization is based on a sequence of line searches in the direction of maximum improvement. The search sequence is continued until there is evidence that the direction chosen does not result in further improvements. The evaluations of the directions of movement and of the proper step sizes are based on the calculations of the value of the defined OF, for each considered geometry. The procedure approximates the OF using a RMS model, with fitting coefficients that are calculated using DOE technique at each new search sequence. Thus, the shape of the OF is reproduced iteratively with continuous changes in the coefficients of the fitting equations used by the RSM model. This is in contrast to the classic RSM approach conceived for fixed and given functions [17].
The procedure evaluates the coefficients for a fitting

model that approximates the OF in a small region around each point considered according to a first order polynomial. A test of adequacy is carried out before moving to a new direction, to determine if the estimated first-order model adequately describes the behaviour of response in the region of factors considered [13]; otherwise a second-order polynomial is considered to approximate the OF near the point considered:

$$\hat{y} = b_0 + x'b + x'Bx \qquad (1)$$

where: x indicates the input variables vector (x' its transpose), b_0 the mean value of responses, b the first-order fitting coefficient vector, and B the 2nd-order fitting coefficient matrix (all terms in matrix B are null for the first order polynomial).
The estimation of the fitting coefficients of Eq. (1) is based on the Ordinary Least Squares method, using the results of a fractional two-level resolution-3 *design* [17]. The gradient of the fitted model is used to determine each new *Steepest Descent* directions. For a single response system, the direction of maximum improvement is determined by the negative of the gradient of $\hat{y}$, Eq. (2) :

$$\vec{g} = \left(\frac{\partial \hat{y}}{\partial X_1}, \frac{\partial \hat{y}}{\partial X_2}, ..., \frac{\partial \hat{y}}{\partial X_n} \right) \qquad (2)$$

where X_i represents the dimensionless coded factor related to each input parameter; for example, X_1 is obtained from data of factor A, according to the Eq. (3) :

$$X_1 = \frac{A_i - (A_{min} + A_{max})/2}{(A_{min} - A_{max})/2} \qquad (3)$$

The coding convention of Eq. (3) has been adopted in order to obtain scale-independent parameter estimates, leading to a more reliable search direction process.
The optimization problem considered in this work is multi-objective: more than one objective function needs to be minimized simultaneously. For this purpose, the procedure follows a weighted priority approach, calculating each search direction by applying assigned weights to the unit vectors provided by the gradients, Eq.(4):

$$\vec{u} = w_{\Phi_1} \cdot \vec{u}_{\Phi_1} + w_{\Phi_1} \cdot \vec{u}_{\Phi_2} + ... \qquad (4)$$

where $\vec{u}_{\Phi i} = \dfrac{\vec{g}_{\Phi i}}{|\vec{g}_{\Phi i}|}$.

Using Eq. (4), the possible differences in the order of magnitude among the typical values of the considered OFs do not affect the effective evaluation of the direction of maximum improvement.

OBJECTIVE FUNCTIONS AND PARAMETERS
CONSIDERED IN THE ANALYSIS

The optimization procedure of Figure 2 has been utilized in order to individuate the best geometry of the recesses machined on the bushings. In detail, the input parameters of the optimization problem are represented

in Figure 3. The figure represents a typical design of the recesses for a external gear pump and the parameters A, B, C, D, E define a wide range of possible solutions. The region of interest is defined by a proper interval (maximum and minimum values) assigned to each input factor of Figure 3. Obviously, few constraints are required in order to avoid unfeasible configurations. These constraints can be expressed as analytical relationships between the input parameters, and are taken into account by the optimization procedure during the path search process.
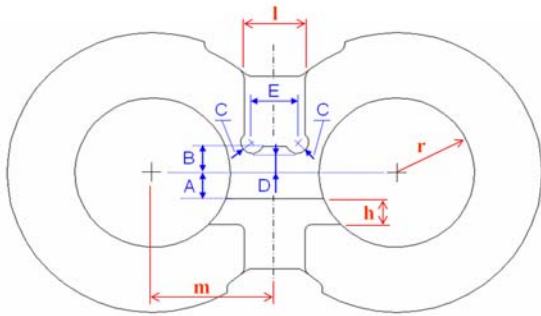
Figure 3 - *Recesses machined on the bushing. Capital letters are used to represent the design parameters of the optimization problem. Other quotes represent the considered constraints*

Specifically, the optimization problem considered in this work requires few geometrical constraints; Table 1 reports the more significant ones.

Table 1 - *Constraints between the factors of Figure 3*

	Constraint
1	$A + D > 0$ (This constraint avoid the contact between the recesses)
2	$D \leq B$
3	$E + C \geq l$
4	$\sqrt{\left(m - \dfrac{E}{2}\right)^2 + \left(D + \dfrac{C}{2}\right)^2} - r - \dfrac{C}{2} \geq s$ (This constraint avoid the contact between the delivery recess and the shaft hole)

As concerns the definition of the objective functions, authors propose a formulations properly to quantify the performance of the considered unit related to the ideal case. As a matter of fact, despite their simple principle of operation, external gear unit are far to be ideal, due to effects mainly related to the displacing action realized by the meshing process. In particular, four different aspects play a crucial role:
1) the amount of transferred flow rate is always lower than the ideal case. This can be quantified by the volumetric efficiency;
2) the reduction of tooth space volume during the first part of the meshing process is responsible of pressure peaks (Figure 4), that can have influence on the flow pulsation at the delivery port. Moreover, they have to

be limited to avoid high loading of the gears, mechanical losses and erosion;
3) the geometrical features that characterizes the meshing process (i.e. the course of each TSV, Figure 4) cause oscillations of the flow at pump delivery. This can be quantified by the measurement of the pressure ripple, and it has to be limited as much as possible in order to reduce noise emissions and to enhance the system stability;
4) as pointed out in the detail of Figure 4, the increment of volume that characterizes the second part of the meshing process leads to pressure levels below the suction value, this reduction can cause gas and/or vapour cavitation onset. This phenomenon should be avoided in order to limit mechanical damages and to increase the transferred flow rate.
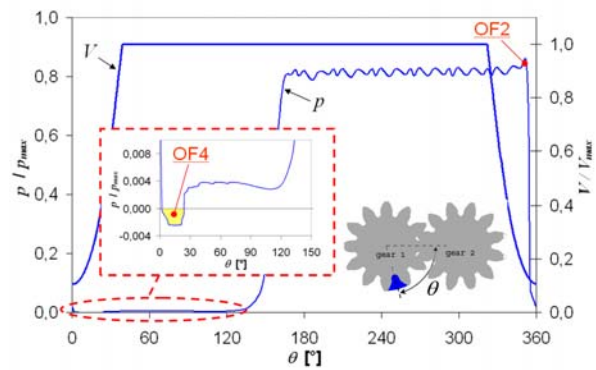
Figure 4 - *Simulated pressure inside TSV; in evidence the first and third objective function*

The optimization problem has been formulated on the basis of the abovementioned effects, in particular an analytical function has been defined to quantify each described aspect. In order to use these functions as OFs for the optimization problem, each function become null in the ideal case. For example, OF_1, related to the volumetric efficiency, is defined as follows:

$$OF_1 = 1 - \eta_v \qquad (5)$$

The definition of OF_2 and OF_4 can be described by means of Figure 4: OF_2 is defined considering the peak reached during the meshing process (Figure 4) related to the average delivery pressure level, while OF_4 considers the angular area of the region where the fluid pressure inside the TSV is below the saturation value. In this way instantaneous pressure peaks below the saturation value are not considered directly. This assumption is coherent with the characteristic of the physical phenomenon involved, as a matter of fact both the air release and phase changes are not instantaneous processes.
As concerns the OF_3 its definition is based on the course of the delivery pressure and it takes advantages of the studies [15]. These studies identify the equivalent amplitude of each fundamental term of the FFT course as a parameter suitable for comparisons between different flow ripples. As described in [15] these parameters are calculated on the basis of the Parseval's theorem, summing the amplitude squared of the spectrum. As highlighted by Figure 2, the evaluation of the OFs required a proper post processing of data after

each simulation performed using HYGESim. This calculation is carried out using macros written in VisualBasic for Excel®. Moreover, as described in [12], before executing the AMESim® model, HYGESim requires the calculation of the geometrical data using a CAD 2D model (in this case implemented with ProE®). The optimization has been carried out on function OF_{tot}, Eq. (6), in which, the weights z_i have been properly assumed.

$$OF_{tot} = z_1 \cdot OF_1 + z_2 \cdot OF_2 + z_3 \cdot OF_3 + z_4 \cdot OF_4 \qquad (6)$$

RESULTS

The optimization procedure is based on the workflow of Figure 2 using the OF_{tot} defined by Eq. (6). However, in order to define an optimal design of the recesses (Figure 3) for all the typical range of operation of the considered pump, at each step the optimization procedure evaluates the average value of the OF_{tot} obtained for four defined operating conditions, that are displayed in Table 3. The path search algorithm was executed changing the starting point, in this way it has been possible to confirm that the final point correspond to a global minimum in the considered region of interest.

Table 2 – *Operating conditions assumed for the calculation of OF_{tot} at each step of the optimization procedure*

Operating condition	Delivery pressure (bar)	Shaft speed (r/min)
1	100	1000
2	250	1000
3	100	2000
4	250	2000
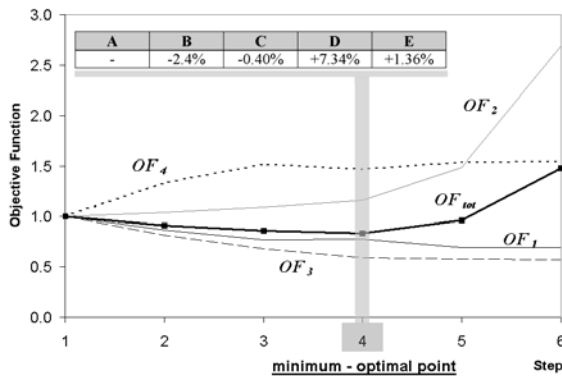
Figure 5 –*Path search sequence for the optimization performed assuming the reference pump as initial point*

Figure 5 reports the details of the path followed by the procedure starting from the configuration of the stock pump taken as reference (Casappa PLP20,11.2 pump). The same figure shows also the dimensionless increment/decrement (as percentage of the reference value) resulting at the end of the procedure, when the final point is reached. From Figure 5 it is possible to notice how the procedure confirms the good design

pertinent to the stock pump taken as reference: as a matter of fact starting from its configuration the optimum is reached after only four steps. However, a slight improvement of the performance is achieved considering the new design, as reported by the simulated data provided in Table 3.

Table 3 – *Simulated pump performance: the values are reported as percentage of the reference values (pertinent to the stock pump)*

Operating condition	1	2	3	4
η_v	+1.60	+2.50	+0.70	+0.20
Pressure peaks (g1)	+0.90	+0.23	+5.00	+4.40
Pressure peaks (g2)	+0.14	+0.13	+0.83	+0.76
Pressure ripple	-28.2	-29.9	-13.3	-20.1

Table 3, in accordance with Figure 5, points out how the proposed configuration, respect to the reference pump, improves the volumetric efficiency and reduces the pressure ripple, while a slight (but tolerable) increase of the pressure peak inside the TSVs of both gears is obtained. This also depends on the values of weights z_i assigned for the calculation of OF_{tot}, Eq. (6).

In order to verify the improvement obtained with the new design, a prototype has been realized and tested, and its performance have been compared with the ones pertinent to the stock version of the pump taken as reference. Tests were performed at the Labs. of the Industrial Engineering Dept. of the Univ. of Parma (IED). Figure 6 reports the measured steady-state characteristics, while Figure 7 displays the obtained volumetric efficiencies. The results confirm the numerical predictions: the new pump shows a slight increment of performance respect to reference pump.
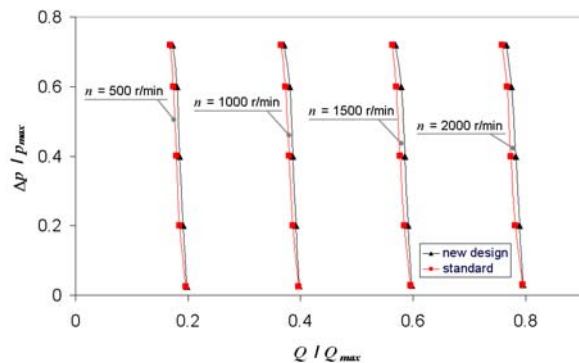
Figure 6 - *Measured steady-state characteristics*

Improvement are more evident observing the course of the delivery pressure ripple, that was measured using the system described in [15]. For all the considered operating conditions a reduction of the oscillations has been observed, as reported in Figure 8 in the time domain. Figure 8 pertain to defined operating condition, but similar improvement were noticed for all the conditions taken into account.
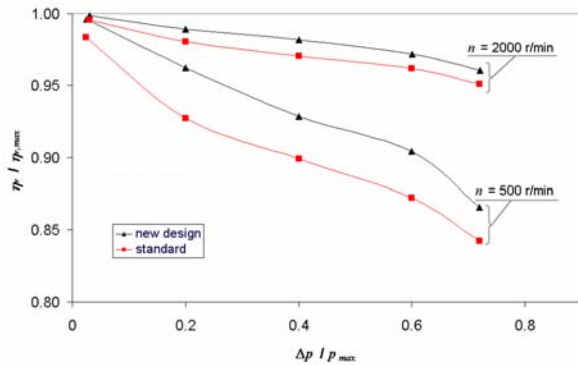
Figure 7 - *Measured volumetric efficiencies*
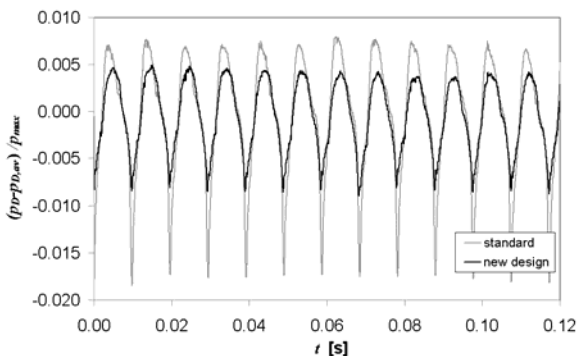
Figure 8 - *Experimental delivery pressure ripple*
(n=500 r/min $p_{D,av}$ = 100 bar)

CONCLUSIONS

This work falls in the ambit of the research activity carried out on external gear machines at the IED. In particular this paper presents the numerical optimization of the design of the recesses machined on the bushings. The procedure is based on a path search method known as *Steepest Descent*, it optimizes few defined parameters starting from a design taken as initial reference. The objective functions considered for the optimization permit to account for the volumetric efficiency, the delivery pressure ripple, the cavitation onset and the maximum pressure peak during the meshing process. Considering a stock pump as reference a new design of the recesses has been proposed. Subsequently, a prototype was realized and tested. Measured data, in terms of volumetric efficiency and delivery pressure ripple, confirm the expected improvement of the performance, respect to the stock version of the pump taken as reference.

ACKNOWLEDGEMENTS

REFERENCES

1. Ivantysyn J., Ivantysynova M., *Hydrostatic Pumps and Motors*, Tech Books Int., 2003, New Delhi, India
2. Mancò S., Nervegna N., *Pressure Transient in an External Gear Hydraulic Pump,* Second JHPS International Symposium on Fluid Power, 2003, Tokyo, Japan.
3. Poy Ferrer M., Codina E., *Suction Capability of Gear Pumps*, 2nd Int. FPNI PhD Symposium, Italy, July 2002.
4. Manring N. D., Kasaragadda S., *The Theoretical Flow Ripple of an External Gear Pump*, ASME Journal of Dynamic Systems, Measurement, and Control., 2003,Vol. 125.
5. Eaton M., Edge K., *Modelling and Simulation of Pressures within the Meshing Teeth of Gear Pumps*, Int. Conf. on Recent Advantages in Aerospace Actuation Systems and Components, June 13-15, 2001, Toulouse, France.
6. Borghi M., Milani M., Zardin B., Paltrinieri F., *The influence of cavitation and aeration on gear pump and motors meshing volume pressures*, Asme-Imece 2006, November 5-10, Chicago, IL (USA).
7. Eaton, M., Keogh, P.S., Edge, K.A., *The modeling, prediction, and experimental evaluation of gear pump meshing pressure with particular reference to aero-engine fuel pumps,* Proc. IMechE Vol.220 Part I: J. System and Control Engineering 2006, pp. 365-379.
8. Wustmann W., Helduser S., Wimmer W. *CFD simulation of the reversing process in external gear pumps,* 6th International Fluid Power Conference, Dresden 31/03-02/04, 2008.
9. Vesely F.., *Design of Pilot Operated Relief Valve by Use of the Simulation*, The 18th Int. Conference on Hydraulics and Pneumatics, 2003, Prague, Czech Republic.
10. Casoli P., Vacca A., Franzoni G., *A numerical model for the simulation of external gear pumps,* The sixth JFPS International Symposium on Fluid Power, Tsukuba, Japan, Novembre 07-11 2005.
11. Casoli P., Vacca A., Berta G.L., *A Numerical Model for the Simulation of Flow in Hydraulic External Gear Machines*, Power Transmission and Motion Control, 13-15 September 2006, University of Bath (GB).
12. Casoli, P., Vacca, A., Berta, G.L., *Potentials of a Numerical Tool for the Simulation of Flow in External Gear Machines,* The Tenth Scandinavian International Conference on Fluid Power, May 21-23, 2007, Tampere, Finland
13. Vacca, A., Cerutti, M., *Analysis and Optimization of a Two-Way Valve Using Response Surface Methodology,* Int. Journal of Fluid Power, Vol. 8, n. 3, November 2007, pp. 43-59.
14. Vacca A., Greco M. Fornaciari A., *A Methodology for the Development of a Relief, Anti-Shock and Anti-Cavitation Cartridge Valve,* 6th International Fluid Power Conference, Dresden 31/03-02/04 2008.
15. Casoli P., Vacca A., Franzoni G., Guidetti M., *Effects of Some Relevant Design Parameters on External Gear Pumps Operating: Numerical Predictions and Experimental Investigations,* 6th International Fluid Power Conference (pp. 469-483 vol. 2), Dresden, 31/03-02/04 2008.
16. Casoli P., Vacca A. Franzoni G., Berta G.L., *Modelling of fluid properties in hydraulic positive displacement machines,* Simulation Modelling Practice and Theory 14, 2006, pp. 1059–1072, Elsevier.
17. Montgomery D.C., *Design and Analysis of Experiments.* 1997, J. Wiley & Sons

P1-06

A STUDY OF A MULTI-STEP POLE TYPE ELECTRO-MAGNETIC ACTUATOR FOR CONTROLLING PROPORTIONAL HYDRAULIC VALVE

Hisao KONDO* and Akira HIBI**

* Department of Mechanical Engineering
Toyota National College of Technology
2-1 Eiseicho, Toyota, Aichi, 471-8525 Japan
(E-mail: hkondo@toyota-ct.ac.jp)
** Department of Mechanical Engineering
Toyohashi University of Technology
1-1 Hibarigaoka, Tenpaku, Toyohashi, Aichi, 441-8580 Japan

ABSTRACT

In this study, a new electro-magnetic proportional actuator composed of an armature and stator with multi convex teeth to control oil hydraulic valves was designed and examined. Each of the convex teeth forms a magnetic pole, and when multiple magnetic poles produce a force simultaneously, a large thrust force is generated in the actuator. The shape of the teeth was varied and influence on the thrust force was examined. As a result, the interval between the convex teeth could be reduced. A 10-step pole type actuator was designed, and its thrust force was estimated. When the dimensions of this actuator are 52mm height, 68mm width, by 102mm length, its thrust force is constant within 2mm of the armature stroke, producing about 300N at an electric power consumption of 15W, and it generates the thrust force in proportion to the coil current. The thrust force of this actuator is about 2.5 times as large as tha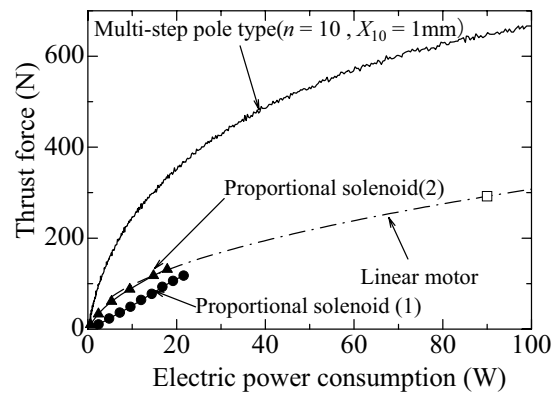t of conventional proportional solenoids and linear motors of the same installation area to the valve body, length and power consumption.

KEY WORDS

Fluid power, Electro-magnetic proportional valve, Valve actuator, Multi-step pole, High force density

INTRODUCTION

There are 4 types of conventional electro-magnetic proportional actuators which can directly operate oil hydraulic valves in proportion to input signal; proportional solenoids, force motors, torque motors and linear motors [1]. A permanent magnet is built in these actuators except for proportional solenoids, therefore their structures are complex and the cost is higher. As well, proportional solenoids cannot generate a very large force in comparison with their dimensions.
In this paper, in order to control oil hydraulic valves, a new electro-magnetic proportional actuator composed of an armature and stator with multi convex teeth was designed and its thrust force characteristics were examined. The principle of the producing force in this actuator is based on the changing reluctance when the overlap between the armature and the stator convex teeth changes. Since this actuator does not use a permanent magnet, there is a possibility of cheaper actuator production. As well, the multi convex teeth of the armature and the stator of the newly designed actuator becomes a multi-step pole, each of the poles producing a force simultaneously. Therefore a large thrust force is generated in the actuator.
Furthermore, an electro-magnetic proportional actuator

composed of an armature and a stator with 10-step convex teeth of triangular groove shape was designed, and its thrust force was estimated and compared with conventional actuators.

STRUCTURE AND BASIC ELECTRO-MAGNETIC CHARACTERISTICS OF THE ACTUATOR

The principle of producing force in a newly designed actuator is based on the principle of producing force in a variable reluctance (VR) type stepping motor. A stator and an armature of the stepping motor are shown in Figure 1. Figure 1 (a) shows a front view of the stepping motor, and Figure 1 (b) shows the relation between the stator and rotor position in side view. In these Figures, there are 6 teeth on the stator and 4 teeth on the rotor. In this stator, a couple of coils are wound on the opposed convex teeth as shown in Figure 1 (a) (the other two couples of coils are omitted). When the electric current flows in the coil, magnetic flux is generated and it flows from upper convex tooth to the lower one through the outside of the stator, and then returns to the upper tooth. Hence, a couple of convex teeth, one on the stator and one on the rotor, in which magnetic flux flows, become a magnetic pole, and then magnetic force acts on these teeth. As illustrated in Figure 1 (a), if a couple of opposed convex teeth of the stator and the rotor are not in line with each other, the force acts on the teeth until the opposed teeth are in line. By this force, a torque is generated in the direction of the arrow illustrated in Figure 1 (a), and a rotating shaft as shown in Figure 1 (b) is turned, and the torque is transferred.

The principle of generating this torque is due to the change of reluctance of the magnetic circuit in this stepping motor as the convex teeth position of the rotor changes. Therefore, the magnetic energy in the air gap between the stator and the rotor convex teeth is transformed to mechanical energy, and then the force is generated between the teeth.

Figure 2 shows the principle of producing force in the multi-step pole type actuator [2]. The armature in Figure 2 (a) does not turn in the rotating direction from this position. The armature fits with the shaft and can slide on the shaft along the axis direction. Then, as shown in Figure 2 (b), the armature and the stator with multi convex teeth are opposed to each other. Now, as illustrated in Figure 2 (b), each of the opposed convex teeth are not positioned in a lap. When the current flows through the coil in this state, magnetic flux flows between the armature and the stator around the outside of the stator as shown in Figure 2 (a). On the other hand, in Figure 2 (b), the magnetic flux produced by the winding coil on the lower stator flows in the armature convex teeth, and it flows from the armature to the upper stator. Also, as shown in Figure 2 (a), the magnetic flux flows through the outside of the stator, and then returns to the lower stator. This magnetic flux flow causes the convex teeth of the armature and stator to become magnetic poles, and a large force is generated in the axis direction by producing a traction force from each tooth simultaneously.

Figure 2 (c) shows the solid shape of the armature with multi convex teeth. First, the convex teeth shape was made rectangular of the same teeth shape as the stepping motor.

(a)   (b)

(c)
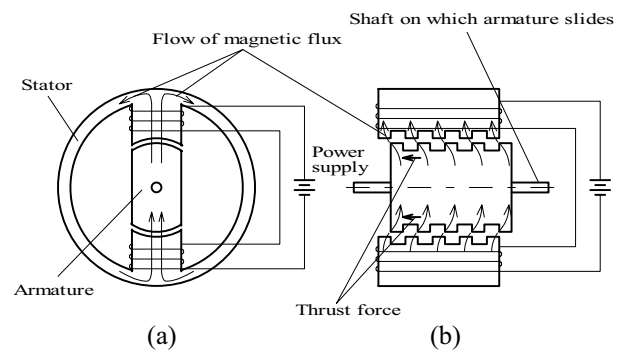
Figure 2 Principle of multi-step pole type electro-magnetic actuator

(a)   (b)

Figure 1 Principle of VR-type stepping motor

284

Figure 3 shows the measured result of the relationship between X/w_1 and F_a. In order to examine the basic force characteristics of the multi-step pole type actuator, an armature with a single rectangular tooth was used. Thickness w_1 of the armature with a single tooth is 5mm, X is an overlap between the tooth of the armature and stator, and F_a is the force acting on the front edge of the armature tooth. As shown in Figure 3, F_a decreases to less than 70% of the maximum force when X/w_1 is larger than 0.5.
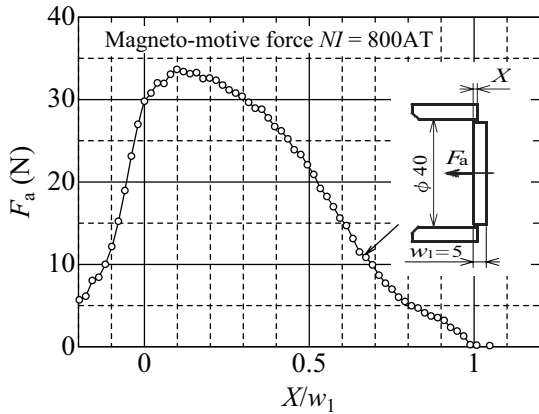
Figure 3 Relationship between X/w_1 and F_a

Figure 4 shows the convex tooth shape of the actuator in Figure 2. The convex tooth shape in Figure 4 is rectangular, the thickness w_1 is 5mm, and the interval p_1 between the teeth is 11mm. If the convex tooth thickness w_1 becomes smaller, magnetic saturation occurs easily at the root of the convex tooth, and it is necessary to make the groove width larger than the tooth thickness. Therefore, it is difficult to make shorter intervals p_1 between the teeth.

An actuator does not need to move both directions like the stepping motor as shown in Figure 1, it only moves in one direction. Furthermore, as shown in Figure 3, force F_a remarkably decreases when overlap X exceeds half of the tooth thickness w_1. For these reasons, as shown on the dotted line in Figure 4, the rear edge of
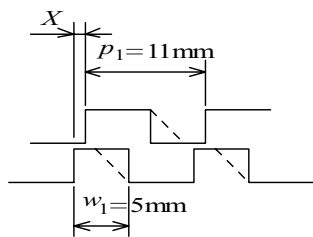
Figure 4 A rectangular tooth shape

the rectangular tooth was cut slanted, and then the intervals of the teeth could be reduced [3].

Figure 5 shows the tooth shape of the slanted rear edge. In order to shorten intervals between the teeth as much as possible, the intervals p_2 and the root dimension w_2 of the teeth were equated. As shown in Figure 5, it is possible to make shorter intervals between the teeth, even though the root dimension w_2 of the teeth is the same as the root dimension w_1 of the teeth in Figure 4.

Figure 6 shows the solid shape of the armature with the convex teeth of the slanting rear edge, in other words, the armature with triangular groove shape teeth.
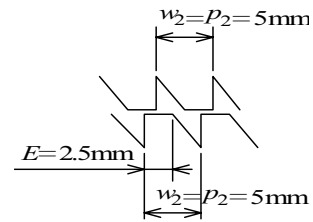
Figure 5 Triangular groove shape
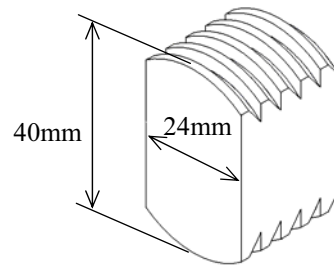
Figure 6 Armature with triangular groove shape teeth
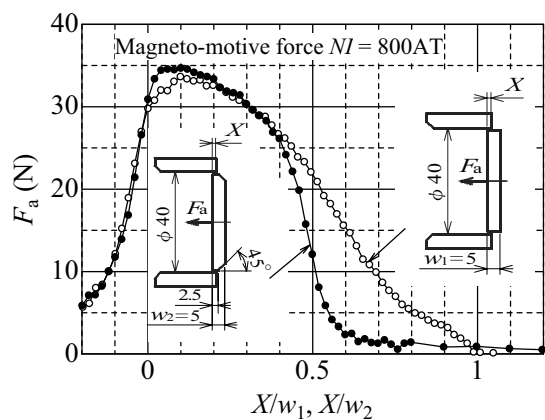
Figure 7 Comparison of relations between X/w_1, X/w_2 and F_a

285

Figure 7 shows the comparison of relations between X/w_1, X/w_2 and F_a when the convex tooth shapes differ as shown in Figure 4 and Figure 5. Force F_a was measured using the armature with a single tooth. In Figure 7, both curves overlap when X/w_1, X/w_2 is less than 0.4, and both maximum forces of F_a are the same. Therefore, the convex tooth shape as shown in Figure 5 can be used on a multi-step pole type actuator, if X/w_2 is in the range of 0 to 0.4.

Figure 8 shows the experimental results of relationship between X_1 and F_a in the case of the armature with a single tooth. In these experiments, armature dimensions are as follows: the thickness w_2 of the armature is 5mm, the length E (shown in Figure 5) of the top land of the tooth is 2.5mm, and the radial clearance between the armature and the stator is 0.05mm. Magneto-motive force NI (coil winding number N, current I) was varied from 400AT(Ampere Turn) to 2000AT at intervals of 400AT, and then force F_a was measured. As shown in Figure 8, force F_a is proportional to magneto-motive

force NI when X_1 is less than 2mm and NI is less than 1200AT.

Figure 9 shows the relationship between distance Y_1 and force F_b (the inverse working direction of F_a), in the case of the armature with a single tooth, same the armature as in Figure 8. As shown in Figure 9, force F_b increases with increasing magneto-motive force NI, and F_b is relatively large even if distance Y_1 is 1mm.

In the multi-step pole type electro-magnetic actuator, force F_a and F_b can be used to calculate the thrust force F_n of n-step as follows [3].

$$F_n = nF_a - (n-1)F_b \qquad (1)$$

Figure 10 shows characteristics of a 10-step ($n=10$) pole type actuator in the case of varying teeth thickness w_2 from 5mm to 8mm. Forces F_a and F_b were measured using the armature with a single tooth as in Figure 8 and Figure 9. Then, F_{10} was calculated by using Eq. (1). When the length E of the top land is 2.5mm, the more the teeth thickness w_2 thickens, the more the interval of the teeth extends and F_b decreases. Therefore, as shown in Figure 10, F_{10} increases with increasing teeth thickness w_2, and the range of X_{10} in which thrust force F_{10} becomes constant is spread. However, the curve of $w_2 = 7$mm is similar to the curve of $w_2=8$mm. The length of the actuator in the case of $w_2=7$mm can be made shorter than that of the case of $w_2=8$mm. Therefore, the actuator with the teeth thickness $w_2=7$mm was selected for designing the actuator as follows.

Figure 8 Relationship between X_1 and F_a

Figure 9 Relationship between Y_1 and F_b
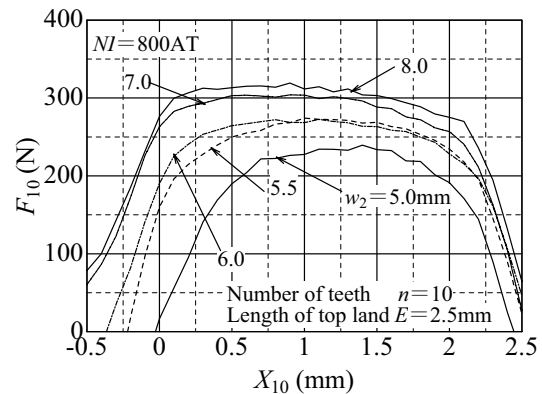
Figure 10 Relationship between X_{10} and F_{10} in the case of varying w_2

EXAMINATIONS OF 10-STEP POLE TYPE ACTUATOR

Figure 11 shows a structure of the designed 10-setp pole type actuator. In this actuator, the length E of the top land of the convex teeth is 2.5mm and the teeth
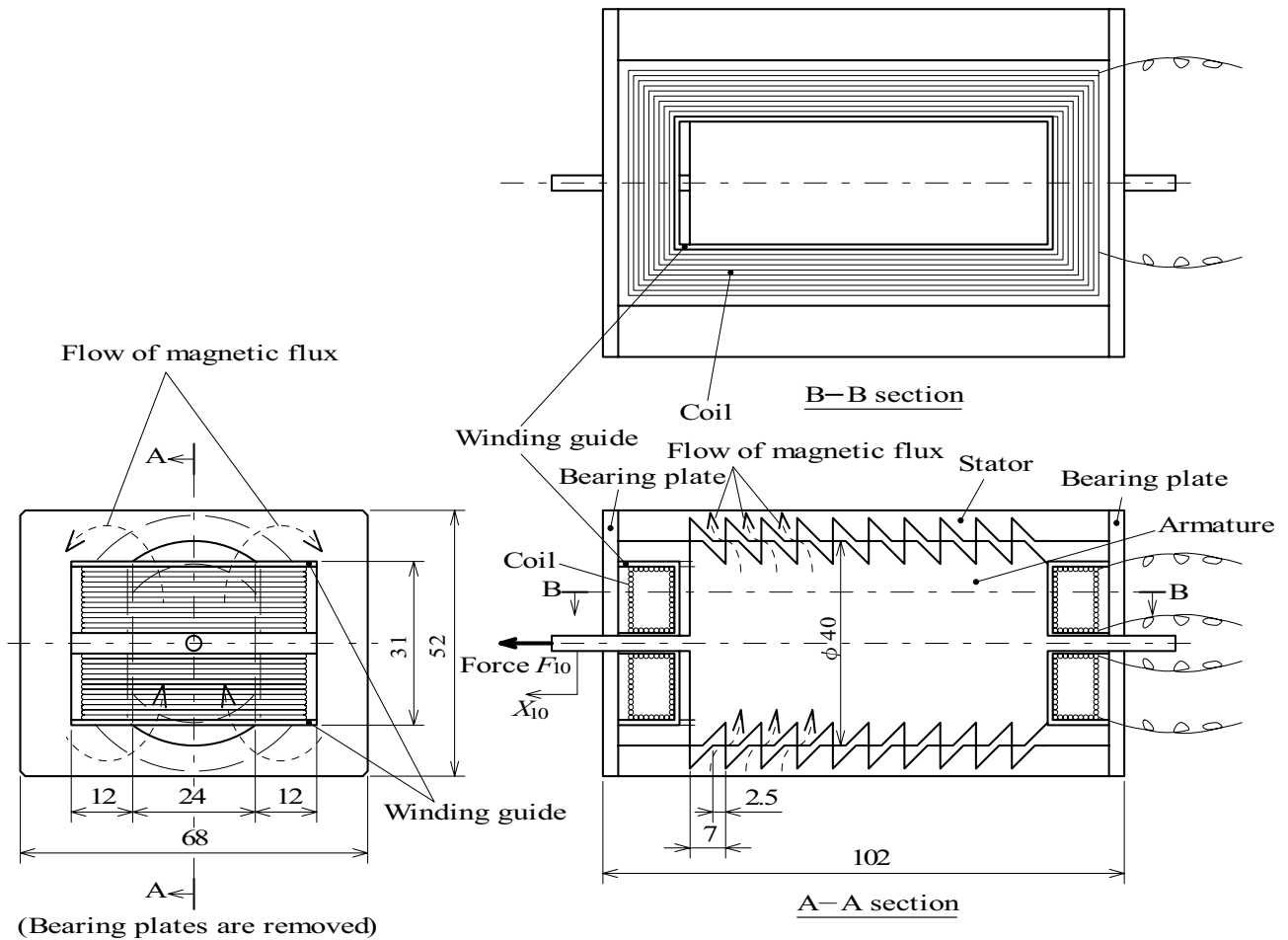
Figure 11 Structure of a 10-step pole type actuator

thickness w_2 is 7mm. This actuator is composed of an armature with a shaft, stator and coil. The coil is wound N turns on the winding guide around four side of the armature as shown in Figure 11 upper view (B-B section). This winding guide is fixed to the stator by bearing plates. The bearing plates (non-magnetic material) are installed and fixed at both ends of the stator. The shaft of the armature is supported by those plates. When the current I flows through the coil, magneto-motive force NI is about 800AT (Ampere Turn) at an electric power consumption of 15W in the 10-step pole type actuator.

Now, the armature position is indicated as X_{10}, and the position when front edges of the convex teeth of the armature and the stator are just encountering each other is defined as $X_{10}=0$mm in Figure 11 (lower right view). The thrust force F_{10} is generated and the armature moves to the left when the current flows through the coil.

Figure 12 shows the relationship between NI and F_{10} in the 10-step pole type actuator. Here, the value of F_{10} is calculated using Eq. (1) by using the measured value F_a

and F_b of the actuator with a single tooth armature. Figure 12 shows the curve when X_{10} is 1mm. As shown in Figure 12, the thrust force F_{10} is in proportion to the
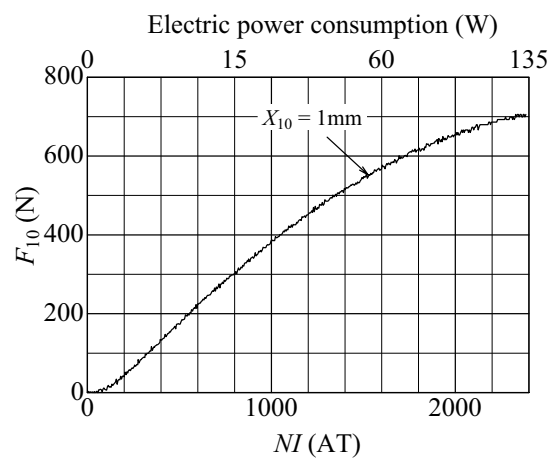
Figure 12 Relationship between NI and F_{10}

magneto-motive force NI in the range of 100AT to 1200AT. Furthermore, the thrust force F_{10} increases with the increasing magneto-motive force NI until electric power consumption of 60W, and F_{10} does not tend to saturate remarkably.

Figure 13 shows the relationship between X_{10} and F_{10}. The calculated value of F_{10} is similar to the calculated value of F_{10} in Figure 12. As shown in Figure 13, the variety of thrust force F_{10} curves is small, in the range of 0 to 2mm of X_{10}. In this range, the thrust force F_{10} is about 300N at an electric power consumption of 15W (magneto-motive force of 800AT). Furthermore, a larger thrust force can be gained by increasing the electric power consumption more than 15W.

Figure 14 Comparison thrust force characteristics of electro-magnetic proportional actuators

Figure 13 Relationship between X_{10} and F_{10}

COMPARISON OF THRUST FORCE CHARACTERISTICS WITH THE OTHER ACTUATORS

Figure 14 shows a comparison of the thrust force characteristics of the 10-step pole type actuator with conventional proportional solenoids and linear motors of the same installation area to the valve body, and length. In Figure 14, the axis of abscissa shows electric power consumption at room temperature. Plotting points are indicated at the catalogue value of A company for the linear motor, the catalogue value of B company for the proportional solenoid (1) and the measured value for the proportional solenoid (2). As well, the thrust force values on the curve of linear motor were calculated as the force is proportional to current of coil. When current flows through the coil in the actuator, the coil temperature rises. In this designed actuator, a rated electric power consumption of 15W at room temperature is proper for the allowable temperature of the coil [2]. As shown in Figure 14, the thrust force of the actuator is about 2.5 times as large as that of conventional proportional solenoids and linear motors at 15W.

CONCLUSIONS

In this study, an electro-magnetic proportional actuator composed of an armature and a stator with multi convex teeth to control the oil hydraulic valves was newly designed. A rectangular shape and a shape that is cut slanted to the rear edge of the rectangular convex teeth were examined. A 10-step pole type actuator with convex teeth was newly designed. Length E of the top land of the convex teeth of the armature and the stator is 2.5mm, teeth thickness w_2 is 7mm. The dimensions of this designed actuator are 52mm height, 68mm width and by 102mm length. As results of estimation of the thrust force of this designed actuator, it became clear that its thrust force was constant within 2mm of the armature stroke, producing about 300N at an electric power consumption of 15W.

The thrust force of this actuator is about 2.5 times as large as that of conventional proportional solenoids and linear motors of the same installation area to the valve body, length and electric power consumption.

REFERENCES

1. W. Backe, Grundlagen und Entwicklungstendenzen in der Ventiltechnik, O+P, 1990, 34-7, pp.496-505.
2. Hisao Kondo and Akira Hibi, A Study of an Electro-magnetic Proportional Actuator of Multi Step Pole Type, Transactions of the Japan Fluid Power System Society, 2005, 36-4, pp.96-101.
3. Hisao Kondo and Akira Hibi, A Study of a Multi-step Pole Type Electro-magnetic Proportional Actuator -2nd Report: Influences of the cross sectional area of a magnetic path and the tooth shape-, Transactions of the Japan Fluid Power System Society, 2007, 38-1, pp.7-12.

P1-07

BUBBLE ELIMINATION FOR ENVIRONMENTALLY FRIENDLY DESIGN OF HYDRAULIC SYSTEMS

Koichi NAGAISHI*, Ryushi SUZUKI**, Yutaka TANAKA*

* Graduate School of Engineering and Design, Hosei University
2-17-1 Fujimi, Chiyodaku, Tokyo 102-8160, JAPAN
(E-mail: y_tanaka@hosei.ac.jp)

** Opus System Inc.
3-18-7 Asagayaminami, Suginamiku, Tokyo 166-0004, JAPAN
(E-mail: rsuzuki@oppssystem.com)

ABSTRACT

Air entrainment in working fluids has great detrimental effects on function and lifetime of the fluid power components and systems. It is important to eliminate the air bubbles from the working oil to preserve oil quality, system performance, and to avoid possible damage of the components. In view point of environmental compatibility, energy saving, cost saving, and high efficiency, one trend in fluid power systems is for them to be designed in a more compact fashion, requiring less fluid in the reservoir and long lifetime of the working oil. A new device using swirl flow for bubble elimination capable of eliminating bubbles and of decreasing dissolved gases has been developed. In this paper we focus on the technical issue for the air bubbles and aging behavior of the hydraulic oil. In order to investigate the effectiveness of the developed bubble elimination device, changes of oil degradation were experimentally measured on our laboratory test bench under the pump operating conditions during 456 hours of continuous running. Oil specimens are sampled and change of a total acid number and a color is investigated as a function of the working time.

KEY WORDS

Bubble elimination, Environmental compatibility, Long lifetime of oil, Total acid number

NOMENCLATURE

P_1 : atmospheric pressure
P_2 : supplied pressure
T_1 : ambient temperature
T_2 : temperature of compressed bubble
κ : specific heat ratio of air

INTRODUCTION

In the 21st century, prevention of global warming and consideration for environmental compatibility are the most important problems for sustainable development of human beings. Recent energy prices and raw material costs are soaring into the stratosphere. Status of fluid power components and systems is becoming an increasingly severe situation. Improvement in efficiency of current uses of fluid power in industries saves energy costs. Meanwhile the advantage of fluid power is to be a compact, portable and powerful actuation.

In view point of environmental compatibility, energy saving, cost saving, and high efficiency, one trend in fluid power systems is to design in a more compact fashion, requiring less oil in the reservoir and long

lifetime of the working oil.

All hydraulic fluids contain an amount of dissolved air, which can be released when the pressure is decreased rapidly from the high pressure to the atmospheric pressure conditions. A cavitation occurrs and bubbles can be created under these conditions. This can occur at valves and orifices, as well as where the fluid returns to the reservoir. Moreover, in mobile hydraulic systems, hydraulic fluids are accumulated, splashed and agitated in the reservoirs. Under these conditions air is sucked into the hydraulic fluid. To overcome air entrainment in hydraulic fluids, the overall dimensions should enclose a sufficient volume of oil to permit air bubbles to escape passively during the stationary time of the fluid in the reservoir. These design policies turn the clock back to more compact design of fluid power systems.

Air entrainment in working fluids has great detrimental effects on function and lifetime of the hydraulic fluids or the fluid power components and systems. The entrained air may cause major problems [4], such as bulk modulus change, cavitation and aeration, noise generation, oil temperature rise [2], and deterioration of oil quality [1]. Especially, when bubbles in oil are adiabatically compressed at high pressure in piston chambers of pump, the temperature of the bubble rises sharply, the surrounding fluid temperature also rises, and the oil degradation is accelerated. Thus, it is important to eliminate the air bubbles from the oil to preserve oil quality, system performance, and to avoid possible damage of the components.

One of the authors has developed a new device that could effectively eliminate air bubbles from working oils [5]. This device is called a bubble eliminator.

In this paper we focus on the technical issue for the air bubbles and aging behavior of the hydraulic oil. In order to investigate the effectiveness of the developed bubble elimination device, changes of oil degradation are experimentally measured on our laboratory test bench under the pump operating conditions during 456 hours of continuous running. Oil specimens are sampled and change of a total acid number is investigated as a function of the working time. It is experimentally confirmed that the bubble elimination prevents the degradation of hydraulic oils.

BUBBLE ELIMINATOR

Figure 1 illustrates the structure and principle of the bubble eliminator. It consists of an inlet tube having two inlet ports, a tapered tube chamber and a straight tube. When the oil with bubbles flows tangentially into the inlet tube, a spiral flow generates in the inlet tube and the tapered tube chamber. The air bubble is separated from the working oil and trapped near the central axis by a swirling flow, because the weight of the air bubble is lighter than the oil. The pressure along the central axis diminish toward the end of the tapered tube chamber and recovers gradually along the straight tube. The trapped bubbles gather together and form an air column. Figure 2 shows an experimental result of flow visualization using a transparent bubble eliminator. When backpressure is applied and a vent port is opened, all collected bubbles are pushed out and ejected from a vent port. The vent port is normally leaved open and the collected bubbles are continuously ejected and returned to a reservoir with a small amount of oil.

The bubble eliminator has a simple structure and direct connection of in-line installation of hydraulic circuits. In addition, it is an energy saving device, because it can remove air bubbles efficiently with only flow energy through the hydraulic circuit without a supplementary power source. The bubble eliminator has a good performance of eliminating bubbles from the working oil [3].

Figure 2 Flow visualization of trapped bubble
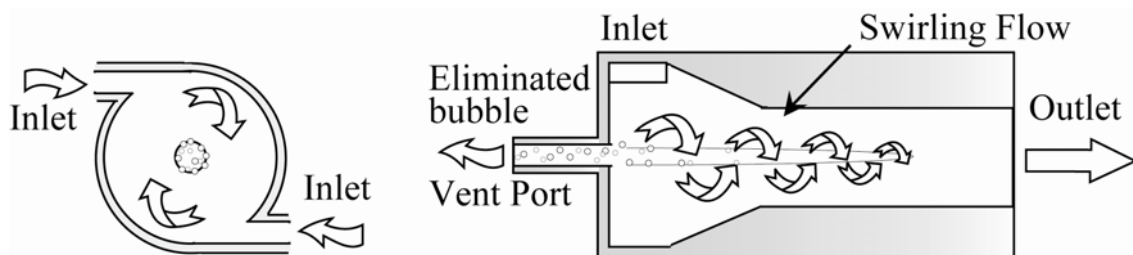
Figure 1 Principle of bubble eliminator
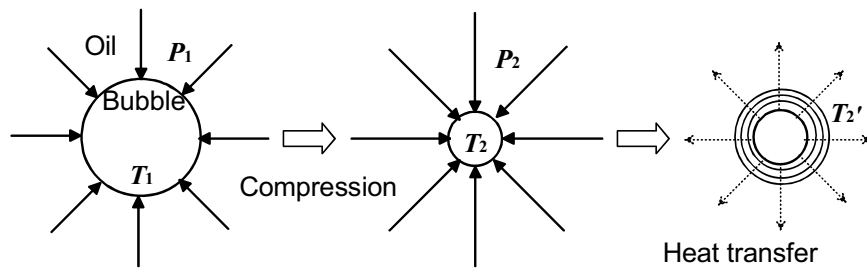
Figure 3 Heat generation model of air bubble

DETERIORATION OF OIL

The main cause of the deterioration of hydraulic fluids is oxidation with oxygen under high pressure and high temperature conditions. A typical solution to improve the oxidation stability of the hydraulic oil is to use additives to the oil. In more compact, high pressure and high performance of fluid power systems, the oxidation stability of commercial hydraulic oils is becoming insufficient for hydraulic designers.

Figure 3 illustrates a heat generation process of a compressed air bubble in oil. When air bubbles in oil are compressed quickly at high pressure in chambers of a pump, the temperature of the bubble rises sharply, and the surrounding oil temperature also rises. If the compressed process is accomplished quickly by the pump at high pressures, the change of process is assumed to be adiabatically. The assumption of the adiabatic compressed process of the air leads to a relationship between a temperature ratio T_2/T_1 and a pressure ratio P_2/P_1 as following Eq. (1).

$$\left(\frac{T_2}{T_1}\right) = \left(\frac{P_2}{P_1}\right)^{\frac{\kappa-1}{\kappa}} \qquad (1)$$

where T_1 is an initial temperature or ambient temperature of the air bubble, T_2 is the temperature of the compressed air bubble, P_1 is initial or atmospheric pressure, P_2 is a supplied pressure by the pump and κ (=1.4) is a specific heat ratio of air.

Relationship between the supplied pressure P_2 and the temperature ratio T_2/T_1 is plotted in Fig.4. The initial pressure P_1 is fixed at atmospheric pressure of 100 kPa. When the oil with bubbles is compressed at 28 MPa in the pump, the temperature of the compressed air bubble T_2 rises by a factor of five to the ambient temperature T_1. If the ambient temperature, T_1 stands at 300 K (=27 °C), the temperature of the compressed air bubble, T_2 adiabatically rises to 1500 K (=1227 °C).

Under highly pressure conditions, the temperature of the air bubble dramatically rises and the surrounding oil is locally situated under the elevated temperature at the moment. During the compression of air bubbles in the
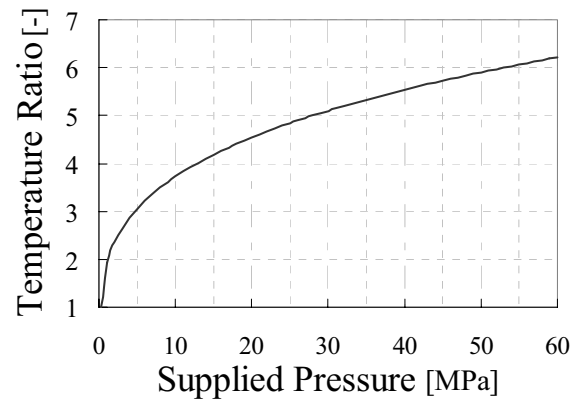
Figure 4 Temperature rise under adiabatic process

oil volume ignition and combustion occur due to the rising temperature on the boundary surface between the bubbles and the oil. The high temperatures, locally caused by compression, affect an accelerated aging of the oils.

EXPERIMENTAL INVESTIGATION FOR INFLUENCE OF BUBBLES

We focus on the technical issue to eliminate the air bubbles entrained in the oil to prevent troubles caused by bubbles. The oil degradation is accelerated with an effective oxygen supply of air, the most influential factor in shortening the life of the oils.

In order to investigate the effectiveness of the developed bubble eliminator experimentally, changes of oil degradation are observed under two different conditions of bubbles for normal pump operating conditions.

Test Bench
An experimental hydraulic circuit of the laboratory's test bench for oil degradation is illustrated in Fig.5. The oil pressurized by an axial piston pump flows through a relief valve and returns to the reservoir. A relief valve is set at a supply pressure of 7 MPa. The downstream line of the relief valve is divided into two lines. One goes

291

through the bubble eliminator and oil cooler to the reservoir. Another goes though the bypass line, in which a stop valve is incorporated and the relief valve to the reservoir.

During the test, the oil temperatures are kept at 60±1.5 °C with the oil cooling system by tap water. The test is performed for base stock of mineral based oil. An oil specimen of 60 cm^3 is sampled once for every 24 hours during continuous running. The changes of the oil properties are investigated as a function of the working times.

Three analytical items and procedures, a visual determination of color regulated by ASTM D1500, a deposit measured by millipore filter methods and a total acid number (TAN) regulated by ASTM D974, are selected to investigate the change of the oil property as an analysis of evaluation for the degradation of oils.

Test-1: Pure Base Stock Oil

In the first experiment, a test is performed for the pure base stock oil having viscosity of 32mm^2/s, having no influence by oxidation inhibitor and anti-wear additive. The pump delivery flow rate is adjusted at a constant value of 9 liter/min. A relief valve is set at a supply pressure of 7 MPa.

The test conditions are tabulated in Table 1. Different parameters such as the bubble eliminator "Unmounted" or "Mounted" are set for the given pump delivery conditions by opening the throttle valves of No.2 or No.3. In cases of air blowing "on", 660cm^3/min air is blowing from the pump suction side.

The changes of the color and the deposit are investigated as a function of the operating time of 96 hours in both cases. Figure 6 and Fig.7 show the change of the analytical data on the deposit and the color plotted as a function of working time, respectively.

Using the bubble eliminator slightly prevents the change of the deposit and the color of the oil. After test running for both cases, much wear debris of the metal in the oil specimen was measured at the end of the test. It should be mentioned that much metal debris is observed in the deposit of the oil in cases A and B. Under poor lubricity caused by supplied air, the wear debris is created on the boundary surface of the pumping elements during pressure build-up.

During 96 hours continuous running, however, no significant difference can be measured in the results of the TAN change in both conditions. In both test conditions, we were not able to keep on carrying out pump running tests, because there was much wear debris in the oil, friction greatly increased and the pumping elements seized.
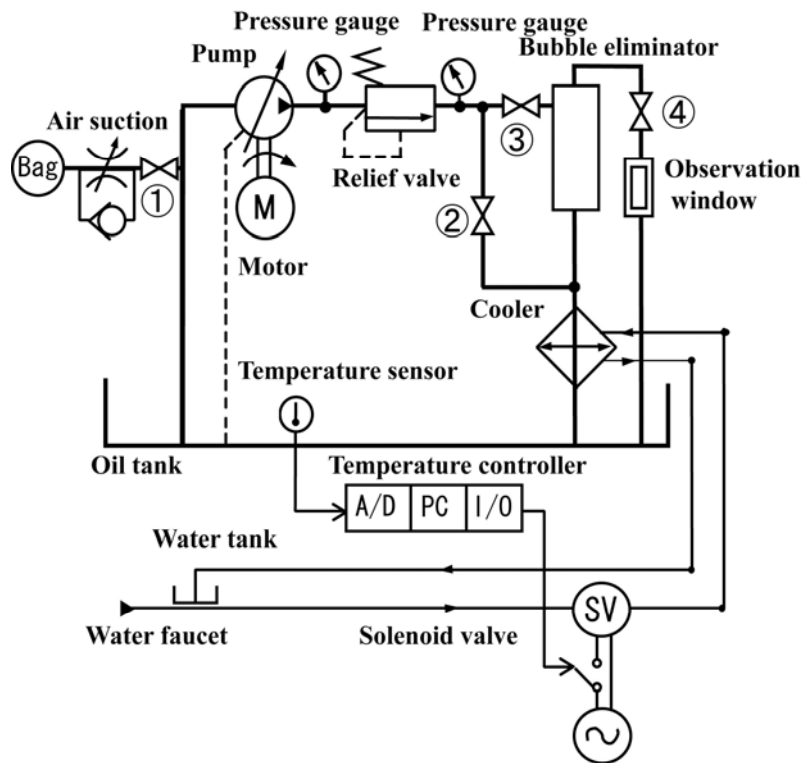
Figure 5 Experimental hydraulic circuit for oil degradation

Test-2: Base Stock Oil with Anti-Wear Additive
The next test is performed for the base stock of mineral based oil with the only anti-wear additive having viscosity of 32 mm^2/s. The newly pump delivery flow rate is adjusted at a constant value of 23 liter/min. The relief valve is set at a supply pressure of 7 MPa. Oil specimen of 60 cm^3 is sampled once for every 24 or 48 hours during continuous running. The changes of the oil property are investigated as a function of the working times of 456 hours for the both data.

The test conditions are tabulated in Table 2. Air is forced to be blowing of 690 cm^3/min, 3% versus the pump delivery flow rate at the suction side of the pump. Figure 8 shows the changes of the total acid number as a function of working times. If the air bubbles in the oil

Table 1 Test-1 conditions

Case	Air blowing	Working time [h]	Bubble eliminator
A	On	96	Unmouted
B	On	96	Mounted

Oil: Base stock without additive
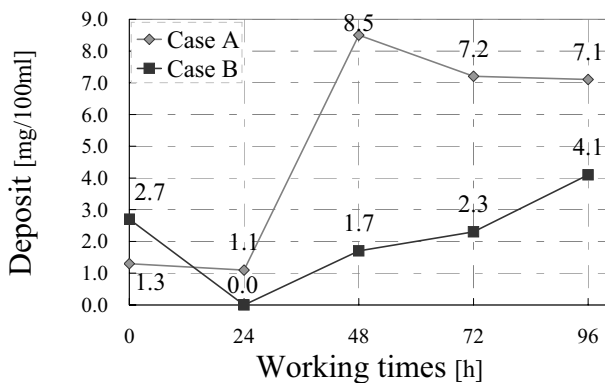
Figure 6 Deposit change in pump test-1
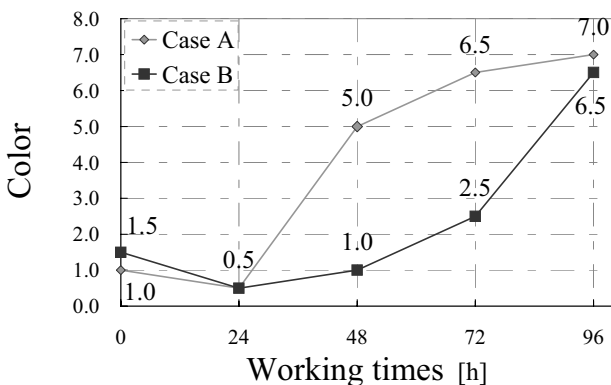
Figure 7 Color change in pump test-1

Table 2 Test-2 conditions

Case	Air blowing	Working time [h]	Bubble eliminator
C	On	456	Unmouted
D	On	456	Mounted

Oil: Base stock with anti-wear additive
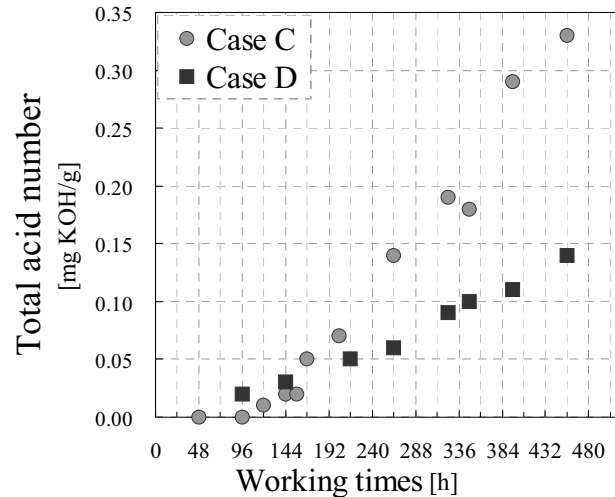
Figure 8 Change of total acid number in pump test-2

are not removed in case C, the oil with the air bubbles compressed adiabatically and the temperature of the air bubbles rose higher. The application limits of the total acid number for hydraulic systems are less than 0.2 mg KOH/g. In case C, the blowing air and cavitation air cause degradation of oil, and the change of TAN increases and exceeds applicable limits on the working times of 350 hours. Judging from the comparison of the plots of C and D, the TAN change becomes steeper when no bubble elimination is use. In case D, the blowing air together with cavitation air are eliminated at the downstream side of the relief valve by the bubble eliminator and the TAN rise can be prevented.

No significant difference can be observed in the results of the color change in both of our experimental conditions. The color change should not be regarded as an obvious indication for an advance degradation of oil. Comparison between the case C and D leads to the conclusion that the bubble eliminator is useful in making oil lifetime longer.

CONCLUSIONS

In this paper we focus on the technical issue for the air bubbles and aging behavior of the hydraulic oil. When

the oil with air bubbles is pressurized, the oil degradation is accelerated. It is experimentally verified that bubble elimination prevents oil degradation. Active removal of air bubbles from the working oil is to realize long lifetime of working oils.

Use of the bubble eliminator may allow the hydraulic designer to reduce the system's reservoir size, extend fluid's useable life and realize environmentally friendly design of fluid power systems.

ACKNOWLEDGEMENTS

REFERENCES

1. Backe,W. and Lipphardt, P., Influence of Dispersed Air on the Pressure Medium, Proc. IMechE.,C97/76, 1976, pp.77-84.
2. Suzuki, R., Tanaka,Y. and Yokota, S., Reduction of Oil Temperature Rise by Use of a Bubble Elimination Device in Hydraulic Systems, Journal of Society of Tribologists and Lubrication Engineers, **54**-3, 1998, pp.23-27.
3. Tanaka, Y. and Suzuki, R, Solution of air entrainment for fluid power systems, SAE 2002 Transactions, Journal of Commercial Vehicles, Section 2, Vol.111, 2002, pp.194-199.
4. Totten, G. E. and Bishop, S., Hydraulic Fluids: Foaming, Air Entrainment, and Air Release –A Review, SAE Technical Paper No.972789, 1997.
5. Suzuki, R., Yokota, S,. Bubble Elimination by Use of Swirl Flow, IFAC Int. Workshop on Trends in Hydraulic and Pneumatic Components and Systems, Poster Paper 2, 1994.

P1-08

GENERATION OF TIME DOMAIN DRIVE SIGNALS IN MIMO RANDOM VIBRATION CONTROL SYSTEM

Guangfeng GUAN*, Wei XIONG*, Haitao WANG* and Junwei HAN**

* Department of Mechanical Engineering
Dalian Maritime University
1 Linghai Road, Dalian, 116026 China
(E-mail: guanguangfeng@yahoo.com.cn)
** School of Mechanical and Electrical Engineering
Harbin Institute of Technology
92 West Da-Zhi Street, Harbin, 150001 China

ABSTRACT

The new generation algorithm of time domain drive signals is presented to reduce the loop time in MIMO(multi input multi output) random vibration control system. The Parks-McClellan method is used to design the FIR (finite impulse response) filter. And then the drive signals in time domain is generated by filtering a series of independent white noise with the designed filter. For avoiding the time domain randomization process in the conventional frequency-to-time transformation, the new method is favorable to improve the real-time property of the control system. Two tests are run in one 6 DOF(degree of freedom) hydraulic shaker with the conventional algorithm and the improved algorithm differently. The results demonstrate the effectiveness of the improved algorithm.

KEY WORDS

Shaker, MIMO random vibration, FIR filter

NOMENCLATURE

f : frequency

$B(f)$: the error PSD between the reference and the control signals

$G_{cc}(f)$: the averaged PSD of control signals

$G_{dd}(f)$: the averaged PSD of drive signals

$G_{cd}(f)$: the averaged cross-spectral density of the control and drive signals

$G_{dd}(f)_j$: the drive signals PSD after j times iterations

$G_{dd}(f)_{j+1}$: the drive signals PSD after $j+1$ times iterations

$H(f)$: frequency response function matrix

$Z(f)$: impedance matrix

α : iteration step size

$\psi(f)$: phase frequency characteristic of the FIR filter

$\theta(f)$: phase frequency characteristic of the drive signals PSD

$\varphi(f)$: linear phase

INTRODUCTION

The shaker is always used for the simulation of actual vibrations to adequately test devices prior to their actual use. The vibrations caused by many natural phenomena and man-made systems are random in nature and are not restricted to specific frequencies. These vibrations are often defined in terms of statistical quantities such as the acceleration spectral density or PSD[1]. In order to adequately test many devices prior to their actual use, it is necessary that the PSD, the devices be subjected in actual usage, are replicated accurately in the shaker. Due to the limit of the frequency bandwidth and the nonlinear of the system, the servo control can't meet the needs of the PSD replication precision. So the vibration control algorithm is used to improve the control precision of PSD replication[2].

FISHER & POSEHN[3] preformed some early work on MIMO random control in 1977. The interactive closed-loop control algorithm of random vibration was presented in their paper. Smallwood and his co-workers[4] significantly contributed to the progress in MISO (multi-input single-output) random control. Stroud & HAMMA[2] generalized the progress of vibration control in 1988 and presented the swept-sine and random vibration algorithms with single shaker and multi shakers. Underwood[5-6] presented the adaptive control method of MIMO swept-sine in 1994.

In the conventional PSD replication algorithm, the drive signals in time domain is generated by frequency domain randomization and time domain randomization. The time domain randomization consists of delay, reversal, windowing and overlapping of the pseudo-random signal generated by frequency domain randomization. For the complexity of time domain randomization, the conventional PSD replication algorithm takes a long time to generate the drive signals in time domain.

The new generation algorithm of time domain drive signals is presented in this paper to reduce the loop time in random vibration test. With the information contained in the drive signals PSD, the Parks-McClellan method is used to design the FIR filter. The white noise filtered by the designed filter is used as the time domain drive signals in the test. The 6 DOF random vibration test are used to verify the validity of the new algorithm.

GENERATION OF TIME DOMAIN DRIVE SIGNALS WITH FIR FILTER

Randomization Method

Figure 1 shows the principle of the conventional method to generate the time domain drive signals.
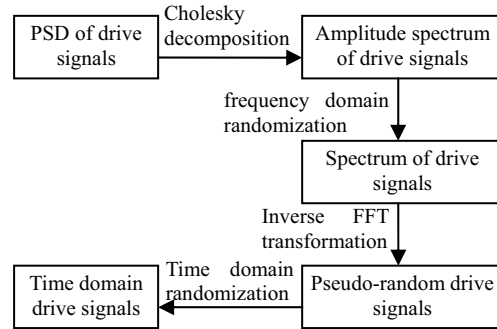
Figure 1   Generation of drive signals with time domain randomization

It can be seen from Figure 1 that the conventional method consists of 4 steps.
(1) Cholesky decomposition: Convert the drive PSD to amplitude spectrum with cholseky decompose.
(2) Frequency domain randomization: Generate the random phase of Gauss distribution and convert the amplitude spectrum to spectrum.
(3) Inverse Fourier transformation: Convert the spectrum to pseudo-random signals with inverse Fourier transformation.
(4) Time domain randomization: Convert the pseudo-random signals to true-random signals through delay, reversal, windowing and overlapping.

For the complexity of time domain randomization, the classical PSD replication algorithm takes a long time to generate the drive signals in time domain.

Filter Method

With the information contained in the drive signals PSD, the Parks-McClellan method is used to design the FIR filter. The drive signals in time domain is generated by filtering a series of independent white noise with the designed filter. Figure 2 shows the principle of the filter method.
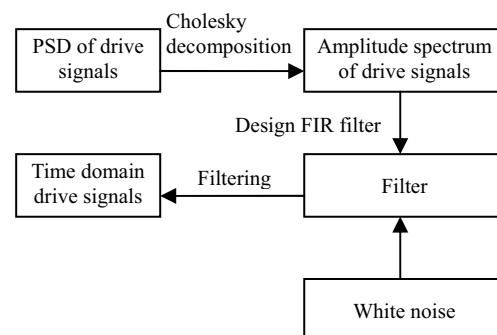
Figure 2   Generation of drive signals with FIR filter

From the filter design theory we know that filters designed using the Parks-McClellan method have equal ripple in their passbands and stopbands. For this reason,

they are often called equiripple filters. They represent the most efficient filter designs for a given specification, meeting the frequency response specification with the lowest order filter[8]. The filters are optimal in the sense that they minimize the maximum error between the desired frequency response and the actual frequency response.

From the stochastic process theory we know that

$$G_{cc}(f) = H(f)G_{dd}(f)H(f)^H \qquad (1)$$

If the drive signal is white noise, the value of $G_{dd}(f)$ is constant. Assuming $G_{dd}(f) = a$, we can get

$$|H(f)| = \sqrt{G_{cc}(f)/a} \qquad (2)$$

$|H(f)|$ is just the amplitude frequency response characteristics of the FIR filter. If the PSD of input white noise signal is a, the PSD $G_{cc}(f)$ of the output signals can be got when the FRF of the system satisfy Eq (2).

Adding the linear phase φ to the phase frequency characteristics of the drive signals PSD, we can get the phase frequency characteristics of the designed FIR filter as

$$\psi(f) = \theta(f) + \varphi(f) \qquad (3)$$

$\varphi(f)$ is given by

$$\varphi(f) = -\frac{Mf}{2} \qquad (4)$$

Where M is the order of the FIR filter.
With the known amplitude and phase frequency response characteristics of the FIR filter, the *remez* function in the signal processing toolbox in *Matlab* can be used to design the FIR filter using the Parks-McClellan method[9].

THE IMPROVED ALGORITHM OF MIMO RANDOM VIBRATION CONTROL

The schematic diagram of the improved random vibration algorithm is shown in Figure 3. The drive signals PSD is corrected by the impedance of the system and the deviation between the reference PSD and the control signals PSD, so that the reference PSD is replicated in high precision in the output of the system.
Figure 3 shows that the random vibration algorithm consists of the FRF estimation, the impedance computation, the correction of drive signals PSD and the generation of the drive signals in time domain.
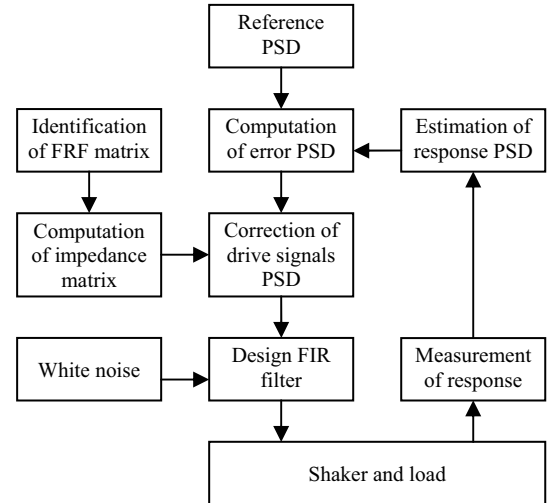
Figure 3　Schematic diagram of MIMO random vibration control algorithm

FRF Estimation and Impedance Computation
Let the drive signals of n in n out system be $\{d_i(t), i = 1, \cdots, n\}$ and the response signals be $\{c_i(t), i = 1, \cdots, n\}$. The FRF H1 estimator is always used in vibration control system[11]. The H1 estimator is given by

$$H(f) = G_{cd}(f)G_{dd}(f)^{-1} \qquad (5)$$

$H(f)$ is a $n \times n$ complex matrix for every frequency. The inverse of FRF is called the impedance. Let $Z(f)$ be the impedance, we can get

$$Z(f) = [H(f)]^{-1} \qquad (6)$$

Correction of Drive Signals PSD
Defining the reference PSD as $R(f)$ and the control signals PSD after j times iterations as $G_{cc}(f)_j$, we can get the error PSD as

$$E(f)_j = R(f) - G_{cc}(f)_j \qquad (7)$$

The drive signals PSD is corrected by

$$G_{dd}(f)_{j+1} = G_{dd}(f)_j + \alpha Z(f)E(f)_j[Z(f)]^H \qquad (8)$$

The value of α needs to be corrected by operator during the tests. Generally speaking, if the estimated FRF matrix matches the true FRF within some acceptable error margin, Eq.(8) is convergent with the α value chosen between 0 and 1. The global convergence property of Eq.(8) is waiting to be proved[5].
Generation of Time Domain Drive Signals

Based on Eq.(2), the *remez* function is used to design the FIR filter with the information contained in the drive signals PSD. And then the drive signals in time domain is generated by filtering a series of independent white noise with the designed filter.

Accuracy Test

The two indexes used to test the precision of random vibration are the RMS value and the frequency domain error between the control and reference PSD. The former is used to test the energy difference of the two PSD. The latter is used to compute the frequency domain errors of the two PSD and is more visualized and specific than the former. So we take the latter index to test the precision of random vibration. The frequency domain error $B(f)$ is given by

$$B(f) = \frac{G_{cc}(f)_j}{R(f)} \qquad (9)$$

The nearer $B(f)$ is to 1, the higher the random vibration precision is. Chinese standard[12] specify that $B(f)$ should be controlled within ±3dB in single axis random vibration test.

TEST AND RESULTS

Two MIMO random vibration tests are run in one 6 DOF hydraulic shaker. The first test is to generate time domain drive signals with time domain randomization. And the second test is to generate time domain drive signals with FIR filter.

The structure of the shaker is shown in Figure 4. The three translation direction is defined as *x, y* and *z*. The three rotation direction is defined as R_x, R_y and R_z.
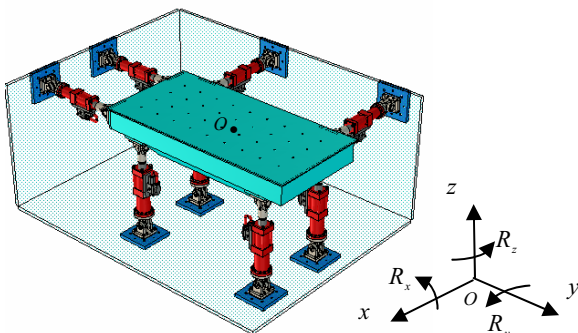
Figure 4   Structure of 6 DOF hydraulic shaker

The reference PSD is generated by MATLAB and the shape is the same in 6 DOF. The reference PSD consists of three segments. The rising spectrum is from 2 to 5Hz. The flat spectrum is from 5 to 60Hz. The ascent spectrum is from 60 to 70Hz. The PSD of flat spectrum is $3\times10^{-4}g^2$/Hz in translation and $2.1\times10^{-3}(rad/s^2)^2$/Hz in rotation.

Figure 5 shows the amplitude frequency response characteristic of the diagonal elements of the measured FRF matrix. Where Hf11 presents the amplitude frequency response characteristic of the element located in first row first column of the FRF matrix. It means the amplitude frequency response characteristic of *x* DOF.
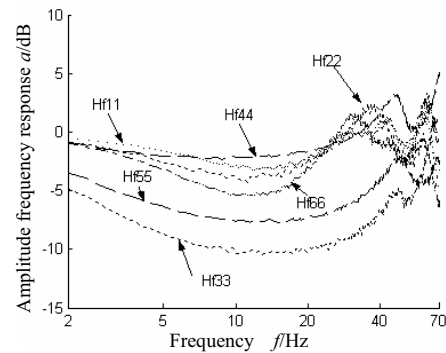
Figure 5   Amplitude frequency response characteristics of FRF matrix diagonal elements

For the amplitude frequency response characteristic of FRF matrix has different deviation to 0 dB in different frequency, we know that the control would has great bias to the reference if with no compensation. So the MIMO random vibration control algorithm is needed to improve the control precision. For the sake of simplify, the test results in *z* and R_z direction are only shown in Figures 6-7.

Figure 6 shows the results after twice iterations in the first test in which the drive signal is generated with time domain randomization. Figure 7 shows the results after twice iterations in the second test in which the time domain drive signals is generated by filtering a series of independent white noise with the filter designed by Parks-McClellan method. It can be seen from Figures 6-7 that the control PSD has been controlled within ± 3dB tolerance of the reference PSD in the whole frequency band. Excellent test result has been achieved in these two tests. But the time spent in the generation of time domain drive signals in second test is less half than that spent in first test. So the loop time is reduced greatly in second test.

a) z

b) R_z
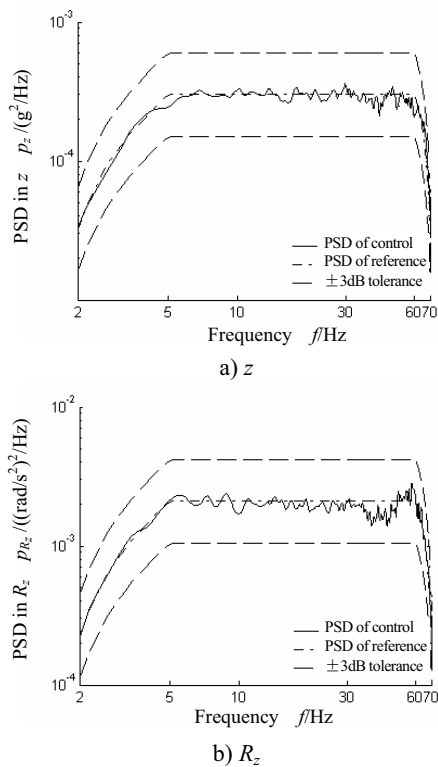
Figure 6   z and Rz test results in first test

a) z

b) R_z
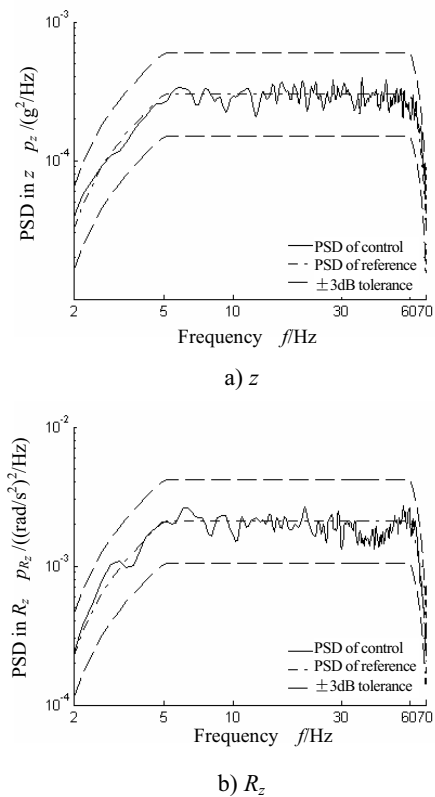
Figure 7   z and Rz test results in second test

From the comparison between Figure 6 and Figure 7 we know that the control PSD in the first test is smoother than that in second test. The drive signals generated by time domain randomization have some pseudo-randomness. The energy of the control signals generated by these drive signals converges in the original frequency certainly. While the drive signals generated by filter is the random signals in true means. The energy of the drive signals is evenly distributed in the whole frequency band of the pass band of the designed filter. This is the main reason of the poor flatness. But the control precision is high enough to satisfy the requirement of MIMO random vibration.

CONCLUSIONS

A new algorithm is presented to generate time domain drive signals. The Parks-McClellan method is used to design the FIR filter and the drive signals in time domain is generated by filtering a series of independent white noise with the designed filter. Test results verify the validity of the new method.

The performance of the improved MIMO random vibration control algorithm is verified by a realistic simulation. The excellent test results indicate that the improved algorithm is favorable to reduce the loop time in MIMO random vibration control system.

REFERENCES

1   Edwin A. Sloane. Vibration Control System. United States: 4989158, 1991.
2   Stroud R.C. and Hamma G.A. Multiexciter and Multiaxis Vibration Exciter Control Systems. Sound and Vibration, 1988, 22-4, pp.18-28.
3   Fisher D K, Posehn M R. Digital Control System for a Multiple-actuator Shaker. 47th Shock and Vibration Bulletin, NM, Albuquerque, 1977, pp.79-96.
4   Smallwood D O. Random Vibration Testing of a Single Test Item with a Multiple Input Control System. Proceedings of the Institute of Environmental Sciences' 28th Annual Technical Meeting, USA, Dallas, TX, 1982, pp.42-49.
5   Underwood M.A. Adaptive Control Method for Multiexciter Sine Tests. United States: 5299459. 1994.
6   Underwood M A. Multi-exciter Testing Applications: Theory and Practice. Proceedings-Institute of Environmental Sciences and Technology, Anaheim, CA, 2002.
7   He xudong, Chen Huaihai. A New Method for the Control of Multi-shakers in Random Vibration Tests. Chinese Journal of vibration engineering. 2004,

299

17-1 , pp.49-52.

8   The MathWorks, Inc. Filter Design Toolbox:
    Designing Advanced Filters: Optimal Filter Design
    Solutions. Matlab Help Document. 2002

9   The MathWorks, Inc. Signal Processing Toolbox:
    remez. Matlab Help Document. 2002

10 Stroud R C, Hamma G A, Underwood M A, et al. A
    Review   of   Multiaxis/multiexciter   Vibration
    Technology. Sound and Vibration, 1996, 30-4 ,

pp.20-27.

11 Underwood M A, Keller T. Recent System
    Developments for Multi-actuator Vibration Control.
    Sound and Vibration, 2001, 246-4 , pp.2-8.

12 China Machinery Industry Federation. GB/T
    8288-2001. Machinery Industry Standard of the
    People's Republic of China. Hydraulically driven
    shaker. 2001.

P1-09

VARIABLE LOAD SENSING AND ANTI-STALL ELECTRONIC CONTROL WITH SLIDING MODE AND ADAPTIVE PID

Massimiliano RUGGERI*, Marco GUIDETTI**

* IMAMOTER, Institute for Agricultural and Earthmoving Machines
National Research Council
Via Canal Bianco 28, 44100 Ferrara, Italy
(E-mail: m.ruggeri@imamoter.cnr.it)
** Technical Director, Casappa S.p.A.
Via Balestrieri 1, 43044 Cavalli di Collecchio, Parma, Italy
(E-mail: guidettim@casappa.com)

ABSTRACT

A variable displacement axial piston pump with Pressure compensator and Load Sensing control is coupled to a diesel engine. The pump is in an open circuit topology for load control in a typical excavator, skid-steer or front loader circuit. The active torque generated by the engine is subject to overloads, due to uncontrolled priority and sum of torque requests from hydrostatic transmission, implements and upper-structure control. In order to avoid engine overload a third 2 ways proportional valve is added to the control circuit. The valve controls the delivery pressure on the load sensing valve port, and the pressure is managed by an electronic system. This circuit architecture allow the designer to use the valve as a variable load sensing system, modifying the load sensing differential pressure depending on working conditions. The control must be in real time and a feed forward control based on the valve characteristic map is useful and helpful but a feedback control is needed to correct the steady state error; a PID and a Sliding mode are superimposed, in order to react to high dynamic transient. The controls runs properly on the bench and the advantages are: more engine efficiency and continuously working capacity, adapting load sensing pressure a more efficient use of power is possible.

KEY WORDS

Load Sensing, Engine Overload, Pressure Control, Proportional Valve, Sliding Mode

NOMENCLATURE

CAN: Controller Area Network
D : Pump Displacement
I : Valve Control Current (mA)
$LVDT$: Linear Voltage Differential Transformer
Q : Pump Flow
P_C : Control Pressure
P_D : Delivery Pressure
P_L : Load Pressure

P_S : Pump Swashplate Piston Control Pressure
P_T : Load Sensing Calibration Pressure
PWM : Pulse Width Modulation Control Signal
β : Pump Swashplate angle (deg)
ω : engine rotational speed (rpm)

INTRODUCTION

The increasing cost of petrol and the increasingly restrictive European and American regulations for

pollution control and reduction make electro-hydraulic solutions for open circuit application in load control in earthmoving machines, attractive and cost effective .s. In the market of compact and mid-size excavators, skid-steer loaders, front and backhoe loaders, the "state of the art" solution for the implements open circuit, is a variable displacement axial piston pump with tandem pressure control and load sensing control hydraulic valves. Manufacturers require new solutions in order to comply with regulations, to reduce machine maintenance costs, to increase reliability and safety. At the same time electronic systems are increasing their role in the hydraulic systems design, and a more strict relation between flexibility, adaptability and electronic systems modifies the market profile in the same way this happened fifteen years ago for passenger cars market.

THE PLANT

The plant designed and realized in a test bench at IMAMOTER Institute is equipped by a mechanically controlled diesel engine   and a driveline that is coupled with a variable displacement axial piston pump with pressure and load sensing control.
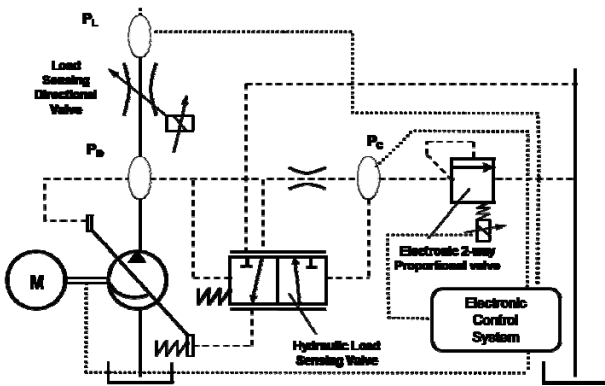
Figure 1 Circuit schematic (Pressure Compensator not shown)

The pump is designed for open circuit, reproducing the actual arrangement for an earthmoving machine. The load pressure is controlled by a servovalve placed in the position marked by P_L in Figure 1. The directional valves flow request is determined by an electronically controlled proportional distributor.
The Axial Piston Pump is a LVP type Casappa 65 cc. variable displacement axial piston pump equipped by a pressure compensator and a load sensing controller. PL is connected to the load sensing port of the LS compensator, while the delivery pressure is connected both to the P port of the pressure compensator and at the P port of the load sensing valve.

THE SOLUTION TARGET

The purpose of the project is to design an electro-hydraulic system that can represent a retrofittable solution for existing systems, capable to add the functionality of anti-stall of the i.c. engine and, if a torque estimate is available, capable to perform a torque control or torque limitation.
The aim is compliance to European regulations, and the target application is torque and speed limitation in mobile application. The implementation of the system is investigated with the purpose to inherit the stability of the hydraulic Load sensing controls, because a complete electronic solution isn't cost effective for mobile applications, yet, due to the higher cost of both a three way proportional valve with high pressure limit and a position feedback (typically an LVDT sensor) and an high-end electronic control system.

THE ELECTRO-IDRAULIC CONTROL SYSTEM

The simplest solution found does not imply the design of new integrated components. The system is equipped by a third electronically controlled two-way pressure regulation proportional valve . The valve characteristic is very attractive because of a good linearity of the regulated pressure as a function of the control current provided to the valve coil (Figure 2).
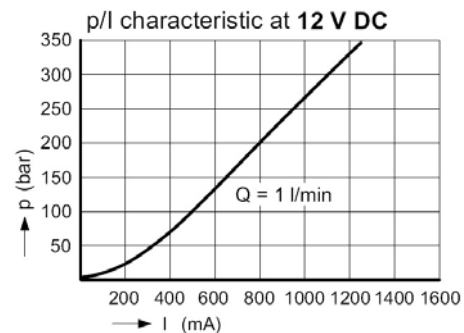
Figure 2 Proportional Valve Characteristic (Current vs. regulated pressure)

The valve P port is connected to the delivery pressure PD of the circuit with a calibrated orifice, the A port is connected to the load sensing port of the pump flow compensator, and the T port is connected to the reservoir.
Two pressure sensors are placed into the system: one at the load port downstream the directional flow request valve in order to acquire the load sensing pressure P_L, and another at the load sensing port of the load sensing valve, in order to sense the controlled pressure P_C (Figure 3).
The first goal of the electronic control system is to copy the load sensing pressure at the A port of the two way

proportional valve in order to reproduce the load sensing control conditions of the hydraulic circuit.

The load sensing control is properly performed by the system only if:

$$P_C = P_L \qquad (1)$$

As a first need the controller and the valve must follow the load pressure with a limited delay, in order to avoid flow loss or pressure transient worse than the original hydraulic solution.

In order to regulate the anti-stall control a third , hall-effect engine speed sensor in the driveline was placed in the system. The only other sensor in the system is the current provided to the valve control feedback in the embedded electronic controller.
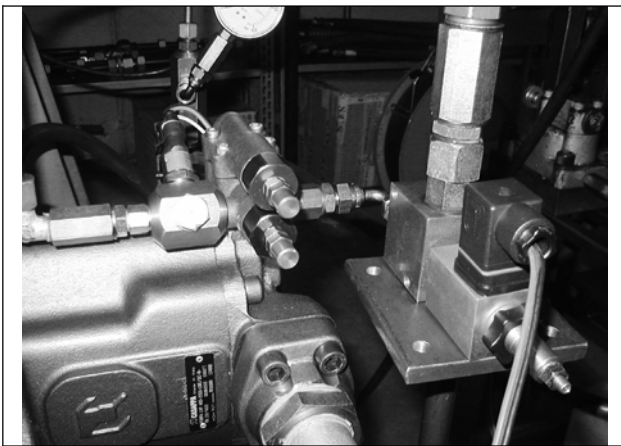
Figure 3 Pump LS and RP valves with the two-ways proportional electro-valve and P_C sensor

As per the system structure, PL and PC are measured by the electronic controller and PD can only be inferred. This control structure allows to control LS both in a traditional and in an adaptive way, simply introducing an offset by the electronic controller. PL is not exactly reproduced but rather an error is added that can be varied depending on the engine working point and/or machine working point, taking into account all the torque request by other hydraulic systems connected to the engine.

The new LS control equation can be written as:

$$P_C = P_L + E_T(\omega, P_L, T_\Sigma) \qquad (2)$$

Where T_Σ is the sum of the Torque requests to the engine and E_T is the Electronic Tuning result as a function of the three variables in brackets.

The load sensing differential pressure at the load sensing hydraulic compensator

$$\Delta P = P_D - P_C = P_D - P_L - E_T(\omega, P_L, T_\Sigma) \qquad (3)$$

allows to modify the ΔP as the implemented controls request. If, for example, an incipient stall condition is recognized, a ΔP greater than the actual (P_D-P_L) can be generated varying the 2-way valve working point, in order to reduce the pump flow and then the torque requested to the engine until the engine speed returns inside the allowable range. In the same way, if an external request is performed, for example by the CAN network, a similar action can take place.

SYSTEM CONSTRAINTS

As in the largest part of industrial and mobile applications, the cost reduction forces some design choices: Casappa called for the usage of a handy electronic control unit used for fan drive application, where real time constraints are less restrictive. A 10 MIPS (theoretical) 8 bit RISC microcontroller was used, optimizing the computational performance, reaching the minimum task repetition time of 3 ms, that we found as being the minimum for a sufficient control stability and performance.

CONTROLLER PERFORMANCE AND LOGGING TOOL CHARACTERISTICS

The control tuning difficulties and the high transient dynamics imposed the use of a functional tool logging not only the test bench physical data (pressure, engine speed and valve current) but also the internal control variables.
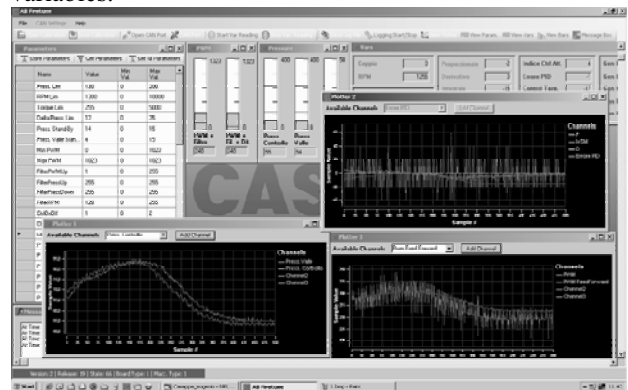
Figure 4 Calibration and logging System via CAN

Traditional communication tools based on a standard serial RS232 communication line were inadequate both for speed and computational resources consumption. A new tool based on intensive usage of CAN network was designed in C# (Figure 4), in order to use a higher communication speed and throughput, and to take advantage of the multi-buffering embedded CAN controller characteristics. This choice allows to manage and send in complete autonomy large amount of

information without lack of performance of the control system.

Even if a low cost 8 bit RISC microcontroller was used, a complete image of the control variables and system data is refreshed for each control task, i.e. every 3 ms, thanks to the presence of 16 message buffer that can be used both in transmission or in reception of the messages by the CAN network.

THE CONTROL STRATEGIES

The system regulates the $\Delta P=P_D-P_L$ in the load sensing valve in order to modify the pump displacement, and consequently both flow rate delivered and torque requested by the pump.
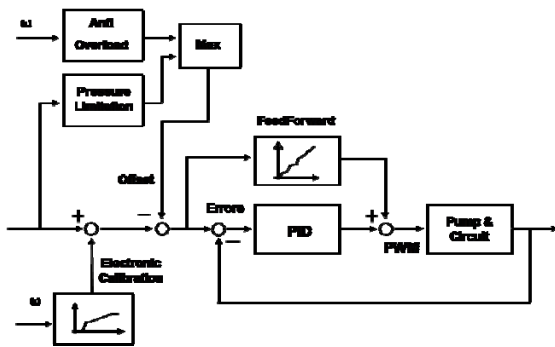
Figure 5 Control System Structure

In order to evaluate whether the system could substitute the traditional pump control structure with RP+LS control valves, a pressure control is added to the variable gain load sensing control and to the anti-stall control. The control system structure and priority is shown in Figure 5, where the electronic calibration is a function of the engine speed (ω). The feed forward function is a 2-way valve characteristic map, that helps to generate the right pressure P_C to be reproduced in real time once the P_L is acquired by the system supplying the exact current that correspond to the pressure target to be reached.

A control system structure based on a classic PID was designed, due to the basic pressure-follower characteristic conceived for the controller, even if tuning of parameters could be difficult, due to nonlinearities of the plant.

THE PID TUNING TECHNIQUE

In order to find the best parameter set for the PID controller, the closed loop Ziegler-Nichols method was applied, carrying the plant and the controller (Figure 6) at the limit cycle instability by a step input, logging the P gain of the PID controller and the oscillation frequency. The data found are significant for the best PID control parameter set definition.

Many test were performed and important differences were found in PID parameters definition as a function of flow rate and pressure; both for P gain (Figure 7) and for oscillation frequency (Figure 8).
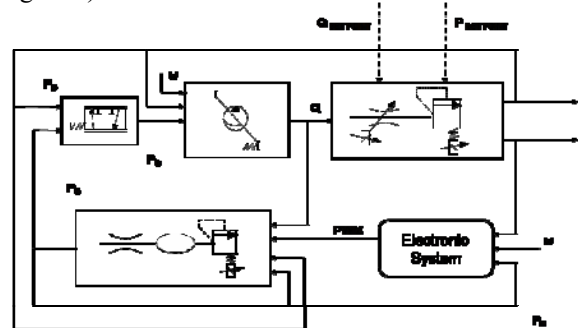
Figure 6 System Model

The parameter definition was thus the minimum set that grant the stability in all working points of the system.
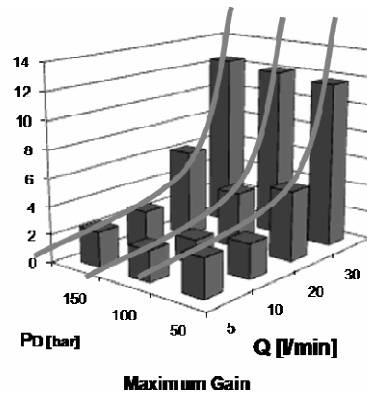
Figure 7 Maximum PID Gain
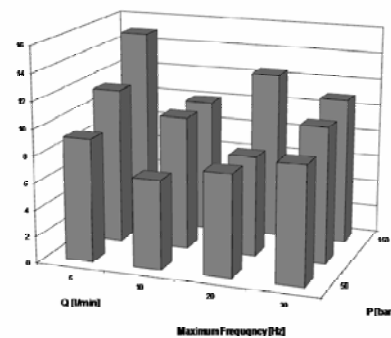
Figure 8 Maximum PID Frequency

A high sensitivity to displacement variation at low flow

rates was found, according to the equation

$$\frac{\partial D}{\partial x} = \frac{D_{max}}{\tan(\beta_{max})} \cdot \frac{R^2_p - 2x^2}{(R^2_p - x^2)^{3/2}} \qquad (4)$$

where R is the swashplate radius and x is the actuator displacement.
The criticality cannot be properly managed without a direct displacement measure being available in the system, therefore the PID parameters were settled based on the most critical working condition.
The forced parameter choice reduces the performance in some condition, and is not sufficient in order to grant the minimum performance requested by Casappa.
Consequently an analytical approach was attempted, and the stability margin was analyzed.
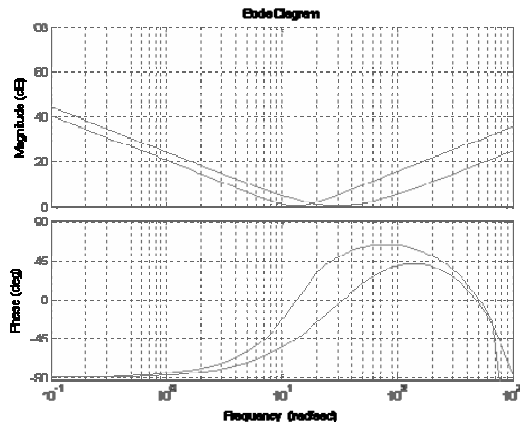
Figure 9 Stability Margin with Increased Derivative

The time domain expression of the controller action is expressed in (5):

$$u(t) = 1,05e(t) + 16,15\int_0^t e(t)dt + 0,017\frac{de(t)}{dt} \qquad (5)$$

The experimental results point out a good precision but slow dynamics due to a limited phase margin. The integral gain was reduced while the derivative gain was increased in order to increase the phase stability margin. The Bode diagrams are shown in Figure 9.
The time domain expression of the modified controller action in expressed as:

$$u(t) = 1,05e(t) + 10,5\int_0^t e(t)dt + 0,06\frac{de(t)}{dt} \qquad (6)$$

While the same expression in the frequency domain is shown in:

$$R(s) = \frac{0,06s^2 + 1,05s + 10,4}{s}e^{-0,0015s} \qquad (7)$$

derived using 3 ms task control repetition rate.
In order to reduce the negative effects of an excessive integral term charge, an anti-windup feature was added in dynamic conditions.

THE ANTI-STALL CONTROL

The PID is the basis to perform all controls implemented in the system. In fact the control system structure allows to supply all the control actions as a Load Sensing calibration offset. The anti-stall control strategy is performed modifying the adaptive load sensing control when the engine speed is under a fixed limit value: a negative offset is added in (2), so a $P_C < P_L$ is reproduced and thus the pump flow is reduced, until the torque reduction is sufficient to reinstate the right engine working point conditions. In anti-stall condition P_C and P_L are different and the difference is function of the engine overload (Figure 10).
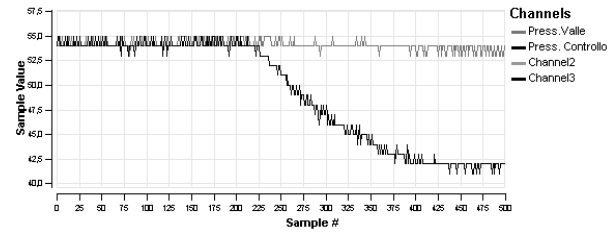
Figure 10 P_L and P_C diagram in anti-stall transient

THE ADAPTIVE LOAD SENSING CONTROL

The same principle was applied in the variable gain load sensing control calibration where a variable ΔP is obtained introducing a degree of freedom of P_C with respect to P_L, adding a positive offset in equation (2).
A variable flow rate target is then obtained in order to fit the torque requests to the engine working point. In Figure 11 an acceleration transient is reported, where the variance of P_C respect to P_L is placed in evidence.

THE SLIDING MODE

Even if the tuned PID demonstrates a good compromise between performance and stability, there are particular conditions where the excessive time delay (due to limited microcontroller performances and the PID controller linearity) evidence some control difficulty. In order to manage high dynamic flow request transient, starting from low or null oil flow, a sliding mode was added acting as a switching control with a dead band in the ΔP, i.e. the pressure error for the electronic LS control, and d(ΔP)/dt surface, its derivative.
The result obtained are shown in Figure 12, where a step transient in flow request is reported.

305
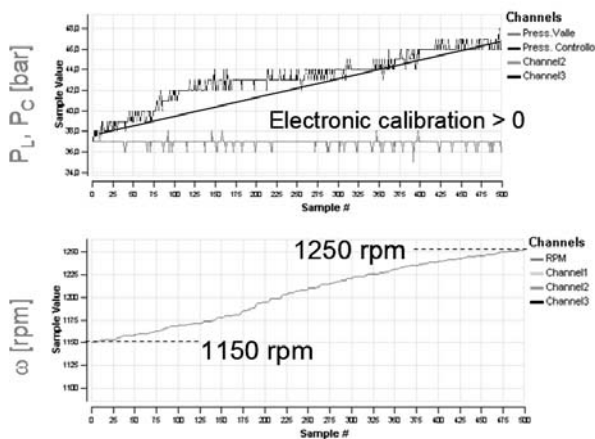
Figure 11 LS with electronic calibration characteristic
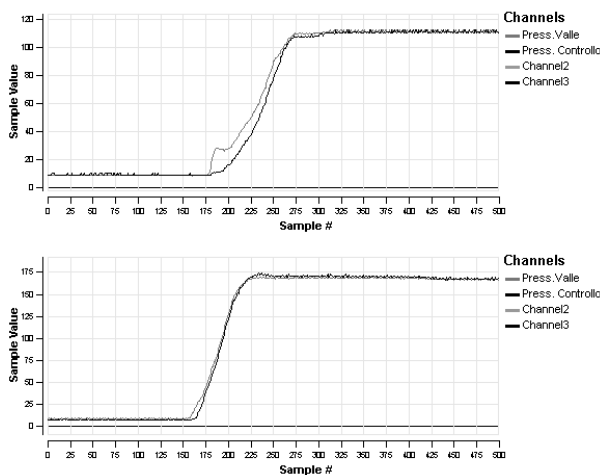
Figure 12 Flow request without and with Sliding Mode

PRESSURE CONTROL AND CONTROLS INTERACTION

An implicit maximum pressure control is obtained simply introducing a condition in pressure reconstruction expression:

$$if\ (P_L + P_{Electronic\ LS\ calibration} < P_{max})\ then\ P_C=P_L$$
$$else\ P_C = P_{max}-P_{Electronic\ LS\ calibration}$$

when the P_D increases beyond a maximum limit, fixed by a set parameter, the increasing ΔP limits the pump displacement and consequently the pressure increases (Figure 13). Experimental results demonstrate that in identical condition the RP hydraulic control operates very rarely and just to reduce the pressure peak, due to the dynamics of the load sensing that is limited by the dynamics of two valves: the 2-way valve and the LS valve.

Figure 14 shows how the system can manage the transition between different control strategies priority:

starting from a load sensing ΔP of 27 bar, at 120 bar (maximum pressure limit in this test) the difference between the two pressure is reversed and the flow rate is resettled to zero.
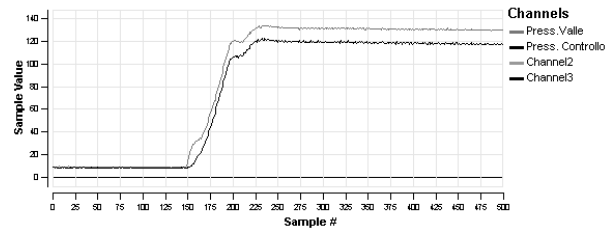
Figure 13 Variable gain LS implicit P_D Control
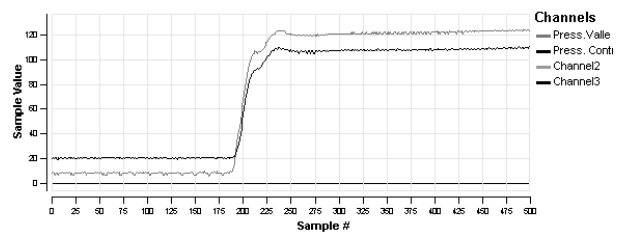
Figure 14 P_L vs. P_C compensator in a transient

CONCLUSIONS

The adaptive load sensing control presented in this paper appears as an interesting option to design flexible control systems. The system nonlinearities are managed exploiting the hydraulic controls layout and available experience. The performance is strongly constrained by the electronic system control computational rate and by the sensors placed in the plant. The lack of Swashplate position sensor is a practical limit in real flow evaluation and limits the maximum controller performance. Despite all these limits the application gave good results on test bench and will be proven on a real excavators, in order to increase experience and to design a commercial application.

REFERENCES

1. Christoph Latour, Electrohydraulic Flow Matching (EFM) – The next generation of Load Sensing Controls. Bosch Rexroth AG, Mobile Conference 2006.
2. Liberzon, D. & Morse, A.S. 1999. Basic Problems in Stability and Design of Switched Systems. IEEE Journal of Control Systems, Vol.25, No.2, October 1999.
3. Slotine, J.E. & Li, W. 1991. Applied Nonlinear Control, Prentice Hall, Inc., Englewood Cliffs, N.J., 1991.

P1-10

HYDRAULIC SERVO SYSTEM USING A FEEDBACK LINEARIZATION CONTROLLER AND DISTURBANCE OBSERVER
- SENSITIVITY OF SYSTEM PARAMETERS -

Ill-yeong LEE*, Tae-hyung KIM** and Sae-ryung CHOI**

* Department of Mechanical Engineering, Pukyong National University
San 100, Yongdang-Dong, Nam-Gu, Busan, 608-739 Korea
(E-mail: iylee@pknu.ac.kr)
** Graduate School, Pukyong National University

ABSTRACT

In this study, the control performance of a hydraulic servo system with a feedback linearization compensator is investigated. The focus of this study is set on the quantitative investigation of the effects(sensitivities) of disturbances and system parameters' variation on control performances of the hydraulic control system. Finally, verifies the efficacy of a disturbance observer to overcome the control performances deterioration due to system parameters' variations, disturbances in the control system.

KEY WORDS

Hydraulic Servo System, Feedback Linearization, Disturbance Observer, Parameters Sensitivity

INTRODUCTION

There are many nonlinearities in hydraulic servo systems like nonlinear pressure-flow characteristics in valves, hysteresis and null point drift in valves, nonlinear driving force from asymmetric cylinder. If hydraulic servo systems are controlled using linear controllers, which are most common so far, it is not easy to achieve satisfactory control performances, as the linear controllers have to be dimensioned conservatively to ensure stability.

As a countermeasure to overcome this difficulty due to hydraulic systems' nonlinearities, applications of feedback linearization controllers to hydraulic control systems has been tried[1-4]. But the research works with the controllers were not fully satisfactory in most cases, because the researchers did not consider the effects of disturbances and parameters' variations in systems.

This study applies state feedback controllers incorporating a feedback linearization compensator to a hydraulic servo system. This study focuses on the effects of system parameters' variations, disturbances on the control performances of the hydraulic servo system with a feedback linearization compensator. Finally, considers the applicability of a disturbance observer to overcome the control performances deterioration due to system parameters' variations, disturbances in the control system with a feedback linearization compensator.

MODELING THE OBJECT HYDRAULIC SYSTEM

System description
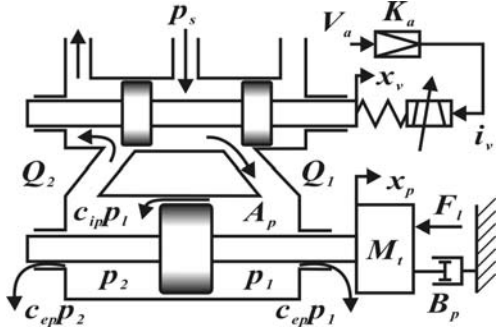
Figure 1 Overview of the hydraulic system considered

Fig. 1 represents the object hydraulic servo system in this study. The main parts of the system are an electro-hydraulic servo-valve, a servo-cylinder and a mass(an inertia load). In the figure, p_s : supply pressure, p_1 and p_2: pressure inside the cylinder, Q_1 and Q_2: flowrate in the servo valve, i_v: electric current in the servo valve.

Basic equations

Flowrate Q_1 in the servo valve is described as

$$Q_1 = K_{sv} i_v \sqrt{p_s - \frac{i_v}{|i_v|} p_l} \qquad (1)$$

where $K_{sv} \left(= Q_{ro} / \left(i_{vr} \sqrt{p_s} \right) \right)$ is a proportional constant, Q_{ro} is flowrate when $i_v = i_{vr}$ and $p_l = 0$, that is the rated current under no load condition. Eq. (1) is effective when the flow in the valve is in steady state. Considering the piston staying in the mid point of the symmetric cylinder, the continuity equation in the cylinder is given by:

$$Q_1 = A_p \frac{dx_p}{dt} + C_{tp} pl + \frac{V_t}{4\beta_c} \frac{dp_l}{dt} \qquad (2)$$

where A_p : piston area, x_p ; piston displacement, C_{tp} : leakage coefficient in the cylinder, β_e : effective bulk modulus of oil in the cylinder, V_t : total volume of oil in both chamber of the cylinder.
The equation of motion of the combined body of the piston and the load is shown as

$$A_p p_l = M_t \frac{d^2 x_p}{dt^2} + B_p \frac{dx_p}{dt} + F_l \qquad (3)$$

where M_t : mass of the combined body, B_p : viscous frictional coefficient, F_l : external force to the piston.
The spool position in the servo valve is described as

$$x_v \cong k_v\, i_v \qquad (4)$$

FEEDBACK LINEARIZATION - STATE FEEDBACK CONTROLLER (FL-SFC)

This section describes the design procedure applying a feedback linearization technique to the object system to overcome the nonlinerities of the system. Differentiating the Eq. (3) with respect to time yields:

$$\frac{d^3 x_p}{dt^3} = \frac{A_p}{M_t} \frac{dp_l}{dt} - \frac{B_p}{M_t} \frac{d^2 x_p}{dt^2} \qquad (5)$$

By substituting Eq. (2) and (3) to Eq. (5), we obtain the following equation.

$$\frac{d^3 x_p}{dt^3} = \frac{4 A_p \beta_e}{M_t V_t} Q_1 - \left(\frac{4 A_p^2 \beta_e}{M_t V_t} - \left(\frac{B_p}{M_t} \right)^2 \right) \frac{dx_p}{dt} \qquad (6)$$

$$- \left(\frac{4 A_p C_{tp} \beta_e}{M_t V_t} + \frac{A_p B_p}{M_t^2} \right) p_l + \frac{B_p}{M_t^2} F_l$$

Eq. (6) is rearranged as Eq. (7), by separating terms including Q_1 and terms having no relation with Q_1.

$$\frac{d^3 x_p}{dt^3} = f\left(\frac{dx_p}{dt}, p_l, F_l \right) + B\, Q_1 \qquad (7)$$

with

$$f\left(\frac{dx_p}{dt}, p_l, F_l \right) = -\left(\frac{4 A_p^2 \beta_e}{M_t V_t} - \left(\frac{B_p}{M_t} \right)^2 \right) \frac{dx_p}{dt} \qquad (8)$$

$$- \left(\frac{4 A_p C_{tp} \beta_e}{M_t V_t} + \frac{A_p B_p}{M_t^2} \right) p_l + \frac{B_p}{M_t^2} F_l$$

$$B = \frac{4 A_p \beta_e}{M_t V_t} \qquad (9)$$

The non-linearities can be canceled out by using the following equation with regard to $\hat{Q}_l$.

$$\hat{Q}_l = \left\{ \phi - f\left(\frac{dx_p}{dt}, p_l, F_l \right) \right\} \Big/ B \qquad (10)$$

where, $\hat{Q}_l$: calculated flowrate, ϕ : control input of feedback linearized system.
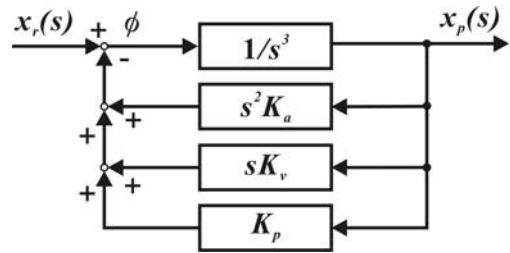
Figure 2 Block diagram for the linearized system using FL-SFC
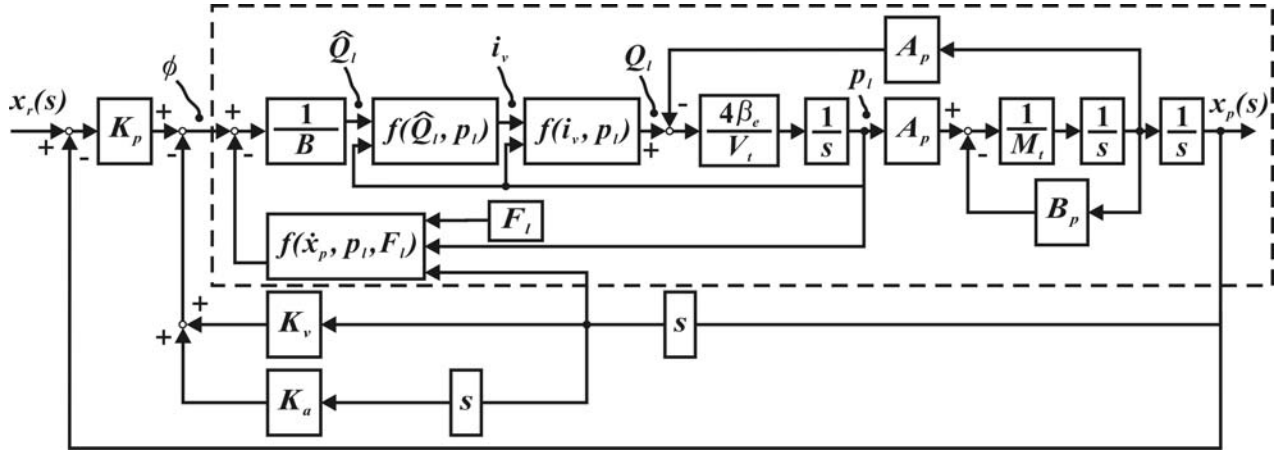
Figure 3 Block diagram of the hydraulic control system using the FL-SFC [the block surrounded with dashed line can be simplified as by the feedback linearization]

Thus, if the flowrate computed by the Eq. (10) is supplied to the system continuously, the condition $d^3x_p/dt^3 = \phi$ can be satisfied. Thereby, a linerized relationship between ϕ and x_p is obtained. Then, a state feedback controller can be applied to the system, as shown in Fig. 2. And also the representative poles in the control system can be placed at the predetermined positions by adjusting the closed loop control gains.

From Fig. 2, a transfer function shown as Eq. (11) is obtained, which is the nominal model of the control system with the feedback linearization compensator.

$$\frac{x_p(s)}{x_r(s)} = H_n(s) = \frac{K_p}{s^3 + K_a s^2 + K_v s + K_p} \quad (11)$$

Fig. 3 shows the block diagram of the control system with the FL-SFC. The state feedback control gains **K** are computed by placing the representative poles at $-38 \pm 24i$ ($\omega_n \doteq 45\,\mathrm{rad/s}$, $\zeta \doteq 0.85$), and other pole is placed at -38×5 on the real axis.

SENSITIVITY ANALYSIS OF THE SYSTEM WITH THE FEEDBACK LINEARIZATION COMPENSATOR

The object hydraulic control system
Fig. 4 shows the photo of the object hydraulic control system. Physical parameters values are listed in Table 1.

Sensitivity of the compensated system
Fig. 5 shows a simplified block diagram of the block surrounded with dashed line in Fig. 3. $G_p(s)$ and $G_c(s)$ in the figure are the control object and the feedback linearization compensator part respectively. Also, ① and ② depict null point drift in the control valve, and external disturbances.

Fig. 6 shows the frequency response characteristics of the subsystem described in Fig. 5 under two different

physical situations; one situation is when external force of 1000 N is applied, the other is when null point drift of the control valve of +2% is applied. Data in Fig. 6 were obtained from simulations by the help of the Control Design™, MATLAB/SIMULINK®. Results in Fig. 6 shows that the linearized model ($1/s^3$) can be affected in a large scale by the external force and valve null point drift.

Table 2 shows the variation of poles of the object system in Fig. 3 under the variation of system parameters β_e, B_p and M_t. The data were given from simulations using MATLAB/SIMULINK®, and
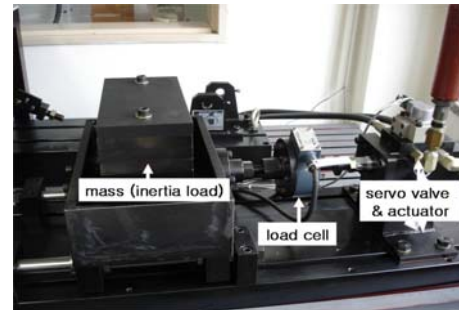
Figure 4 Photo. of the experimental equipment

Table 1 Pysical parameters values in the object system

$A_p\,[\mathrm{m}^2]: 0.00094$, $C_{tp}\left[\dfrac{\mathrm{m}^3/s}{\mathrm{N/m}^2}\right]: 0$, $B_t\left[\dfrac{\mathrm{N}}{\mathrm{m/s}}\right]: 15000$,

$\beta_e\left[\dfrac{\mathrm{N}}{\mathrm{m}^2}\right]: 1.4\times10^9$, $F_l\,[\mathrm{N}]: 0$, $V_t\,[\mathrm{m}^3]: 6\times10^{-4}$,

$K_a\left[\dfrac{\mathrm{mA}}{\mathrm{V}}\right]: 6$, $K_{LT}\left[\dfrac{\mathrm{V}}{\mathrm{m}}\right]: 200$, $M_t\,[\mathrm{kg}]: 118$, $i_{vr}\,[\mathrm{mA}]: 15$,

$K_{sv}\left[\dfrac{\mathrm{m}^3/s}{\mathrm{mA}\sqrt{\mathrm{N/m}^2}}\right]: 8.0\times10^{-9}$, $\zeta_v: 0.84$, $\omega_v\,[\mathrm{rad/s}]: 760$,

$p_s\,[\mathrm{bar}]: 35$
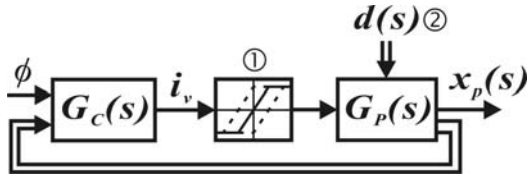
Figure 5 Simplified block diagram of the block surrounded with dashed line in Fig. 3
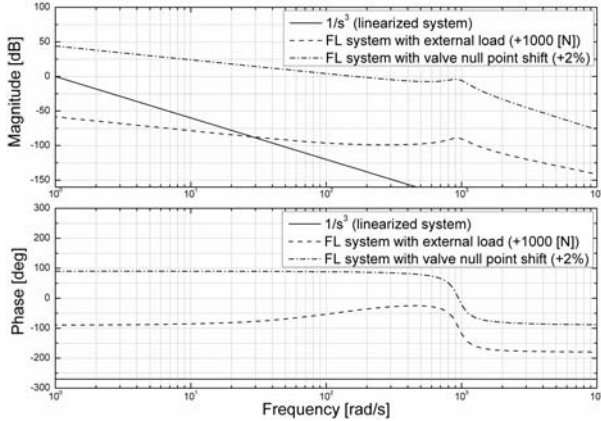
Figure 6 Frequency characteristics of the block surrounded with dashed line in Fig. 3 with external force, with valve null point shift

Table 2 Poles of the object system shown in Fig. 3 under the variation of system parameters

	Pole 1	Pole 2	Pole 3
No Variation	-38+24i	-38-24i	-191
β_e : -50%	-31+30i	-31-30i	-104
β_e : +50%	-40+21i	-40-21i	-290
B_p : -50%	-102+43i	-102-43i	-32
B_p : +50%	-26+30i	-26-30i	-247
M_t : -90%	-21+23i	-21-23i	-3990
M_t : +90%	-22+85i	-22-85i	-27

the transfer functions between Q_l and i_v, and between i_v and Q_l were substituted as '1'. We can have a hint from the data in Table 2 on the fact that the control performances of the system shown in Fig. 3 might be affected severely under the variation of system parameters β_e, B_p and M_t.

DESIGNING A DISTURBANCE OBSERVER

In this section, we will design a Feedback Linearization – State Feedback Controller with Disturbance Observer (FL-SFC-DOB) for the hydraulic servo system. Fig. 7 shows a system with the disturbance observer. $H(s)$ in the figure shows the control system including FL-SFC,
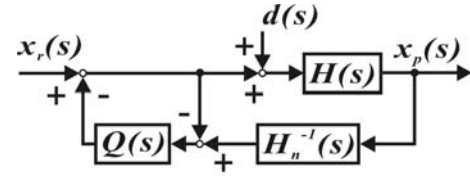
Figure 7 Application of a disturbance observer to the control system shown in Fig. 3

and $H_n(s)$ is the nominal model described by Eq. (11). $Q(s)$ is a filter for disturbance compensation, and $d(s)$ describes external disturbances or disturbance equivalence of system parameters' variation.

In this study, Umeno's method[5] was applied to design $Q(s)$. $Q(s)$ for the system was obtained as Eq. (12) considering that the relative order between the numerator and the denominator of the system transfer function is 3.

$$Q(s) = \frac{\alpha^3}{(s+\alpha)^3} \quad (12)$$

where α is a cut-off frequency.

RESULTS OF EXPERIMENT AND SIMULATION

Experiments were done using the experimental system shown in Fig. 4. The parameters values of the experimental system are given in Table 1. In all the experiments of this study, p_s is set to be 35 bar. For realizing digital control and signal measurements, a PC and MATLAB/RTWT[6] were used.

The results when「FL-SFC」applied
Fig. 8 shows the experimental and simulated results when a step input signal(0→10 mm) is given to the system with FL-SFC. In addition, responses of C-SFC(the Conventional State Feedback Controller applied to the hydraulic servo system) were included in the same figure to evaluate the results of FL-SFC objectively.
In designing C-SFC, a flow equation linearized in the operating point of the servo valve was used. Controller gains for C-SFC were obtained from pole placement method. The representative poles for the
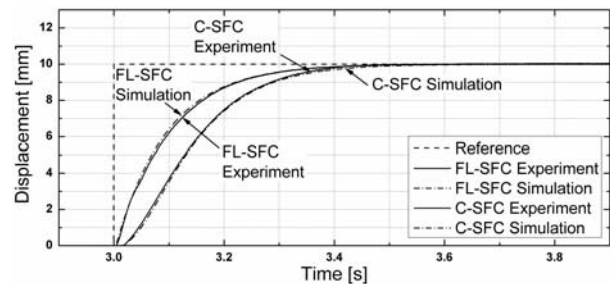
Figure 8 Experimental and simulated results of the object system with C-SFC or with FL-SFC

C-SFC were placed at same positions as ones for FL-SFC(designed in section 3) so as to enable an objective comparison of control performances of the systems with the FL-SFC and the C-SFC. And other poles were placed at -38×5 on the real axis.

Fig. 8 shows the validity of the mathematical model of the control systems used in this study. In this figure, FL-SFC shows better response compared to C-SFC by reducing 17.1% in settling time(±2% basis).

The results when「FL-SFC-DOB」applied

Under external load

Fig. 10 shows the step responses of the control system under external load(Fig. 9), 1000N. When FL-SFC was applied(Fig. 10 (a)), 0.4 mm steady state error and undershoot response appeared. But, with FL-SFC-DOB application, the effects of the external load could be rejected clearly.

Under null point drift in the control valve

In general, allowable limit of null point drift in servo valves is said to be ±2%. With the allowable limit value of null point drift, the control performances of the control system were investigated. The null point drift in
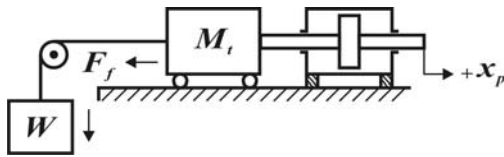
Figure 9 Simplified schematic diagram of the load system in the object system
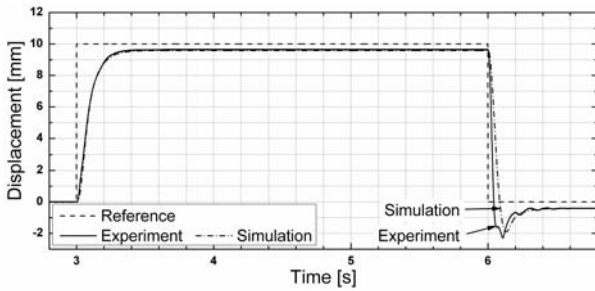
(a) when FL-SFC applied
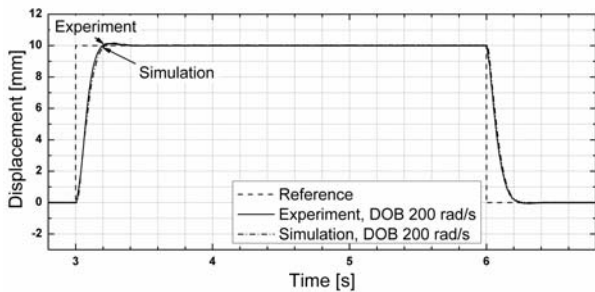
(b) when FL-SFC-DOB applied

Figure 10 Experimental and simulated results of the object system with external load, 1000 N

the servo valve was realized equivalently by shifting null point of the servo amplifier output.

Fig. 11 shows the step responses of the control system under null drift, ±2%. When FL-SFC was applied(Fig. 11 (a)), great steady state errors appeared, which was anticipated result by referring to Fig. 5. But,
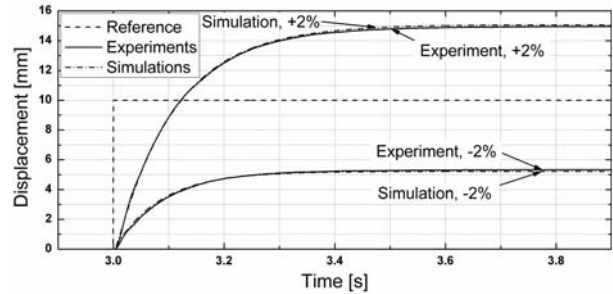
(a) when FL-SFC applied
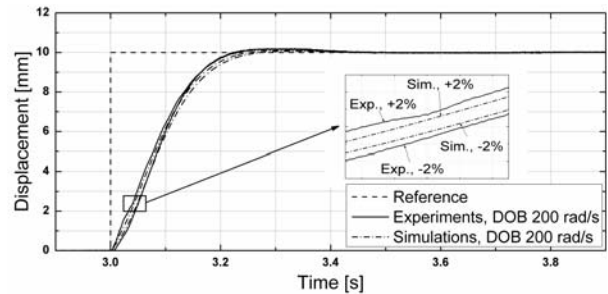
(b) when FL-SFC-DOB applied

Figure 11 Experimental and Simulated results of the object system under valve null point shift with +2%, -2%
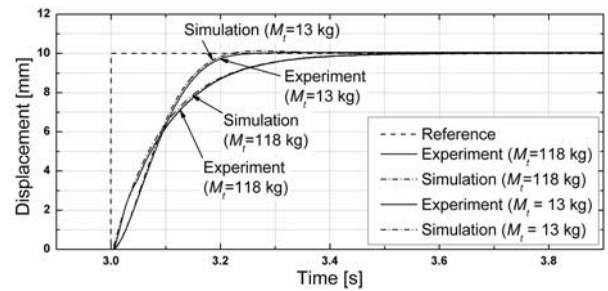
(a) when FL-SFC applied
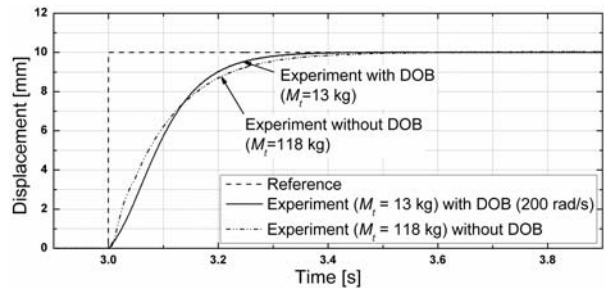
(b) when FL-SFC-DOB applied

Figure 12 Experimental and simulated results of the object system under M_t variation
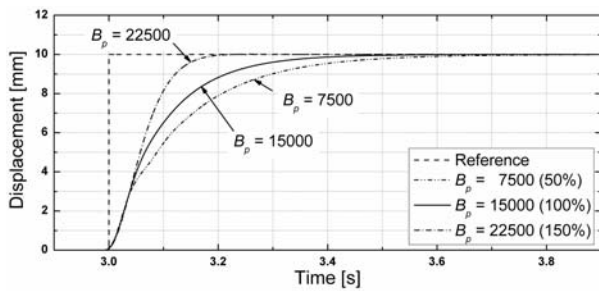
(a) when FL-SFC applied
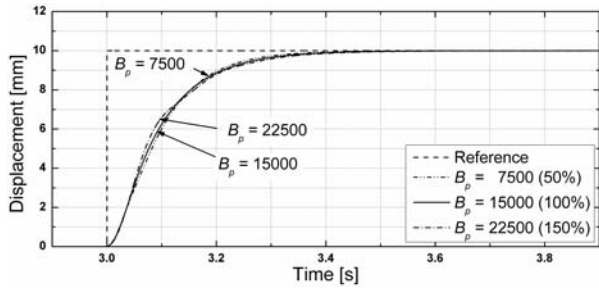
(b) when FL-SFC-DOB applied

Figure 13 Simulated results of the object system under B_p variation
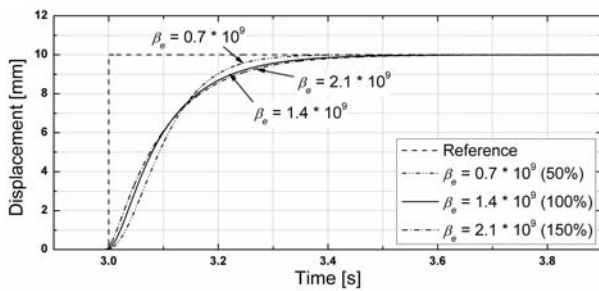
(a) when FL-SFC applied
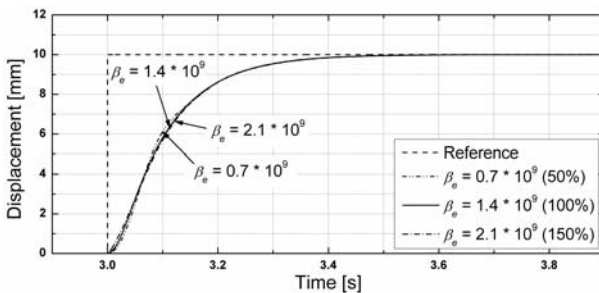
(b) when FL-SFC-DOB applied

Figure 14 Simulated results of the object system under β_e variation

with FL-SFC-DOB application, the effects of the null point drift could be removed and zero steady state error realized.

Under the variations of M_t, B_p and β_e

The effects of the variations of the representative physical parameters M_t, B_p and β_e on the control performances of the control system were investigated. Step responses of the control system under the variation of M_t, B_p and β_e were shown in Fig. 12, 13 and 15. When FL-SFC was applied, change in control performances appeared according to the variation of M_t, B_p and β_e. And, it was ascertained that, with FL-SFC-DOB application, the change in the control performances under the variation of M_t, B_p and β_e could be moderated in a great deal.

CONCLUSIONS

In this study, the control performance of a hydraulic servo system with a feedback linearization compensator was investigated. The focus of this study was set on thequantitative investigation of the effects(sensitivities) of disturbances and system parameters' variation on control performances of the hydraulic control system. Finally, verified the efficacy of a disturbance observer to overcome the control performances deteriorations due to system parameters' variations, disturbances in the control system.

REFERENCES

1. Hahn, H., Piepenbrink, A. and Leimbach, K. D., Input/Output Linearization Control of an Electro Servo-Hydraulic Actuator, Proc. 3rd IEEE Confer. Control Application, Glasgow, UK, 1994, pp. 995~1000.
2. Sohl, G. A. and Borrow, J. E., Experiments and Simulations on the Nonlinear Control of a Hydraulic Servosystem, IEEE Trans. on Control Sys. Tech., Vol. 7, No. 2, 1999, pp. 238~247.
3. Tunay, I., Rodin, E. T. and Beck, A. A., Modeling and Robust Control Design for Aircraft Brake Hydraulics, IEEE Trans. on Control Sys. Tech., Vol. 9, No. 2, 2001, pp. 319~329.
4. Re, L. D. and Isidori, A., Performance Enhancement of Nonlinear Drives by Feedback Linearization of Linear-Bilinear Cascade Models, IEEE Trans. on Control Sys. Tech., Vol. 3, No. 3, 1995, pp. 299~308.
5. Umeno, T. Kaneki, T. and Hori, Y., Robust Servo system Design with two Degrees of Freedom and its Application to Novel Motion Control of Robot Manipulators, IEEE Trans. Ind. Electron., 1993, Vol. 40, No. 5, pp.473-485.
6. Real-Time Windows Target[TM] User's Guide, The MathWorks, Inc., 2008.

P1-11

SYSTEM SIMULATION FOR HYDRAULIC EXCAVATOR

Kazuhide MAEHATA

Development Sect., New Products Development Dept., Hydraulic Components Operations
KYB Corporation
1-12-1 Asamizodai, Sagamihara-shi, Kanagawa-ken, 228-0828 Japan

ABSTRACT

The various hydraulic components for excavator have been developed in KYB Corporation. In early stage of the product development, we usually use calculation of static characteristics, but we do not use calculation of dynamic characteristics for the system. The dynamic characteristics of the system are tuned using actual system in middle stage of the product development. Therefore it is often necessary to extend the product development time. In order to decrease the development time, we developed a simulation model of excavator system for dynamic characteristics calculation. This paper shows case studies of the system simulation for hydraulic excavator applied to the digging-turning-loading cycle analysis.

KEY WORDS

Simulation, Excavator, SIMULINK, ADAMS

SIMULATION MODEL

Figure 1 shows the structure of the simulation model.
The simulation model consists of body model for calculating motion of excavator, and hydraulic circuit model for calculating behaviors of hydraulic circuit.
The actuator force is transmitted from the hydraulic circuit to the body.
The actuator speed and length of the body are fed back to the hydraulic circuit.
In this case, the hydraulic circuit model is modeled on SIMULINK, a control system analysis software, and the body model is represented on ADAMS, a mechanical system analysis software.
Figure 2 shows the body model.

The body model on ADAMS consists of moving parts and constraints (joints). Each moving part has polygon-based geometry to allow easier and quicker modeling. All parameters, such as geometry dimensions and mass properties, can be obtained via actual measurements, relevant technical papers and 3D CAD data.
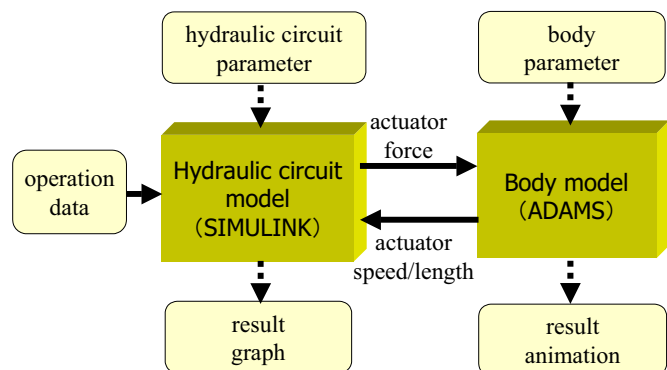
Figure 1 Structure of the simulation model
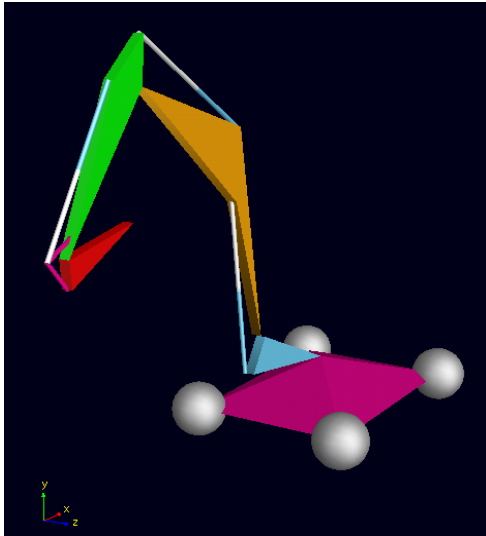
Figure 2 Body model

DIGGING-TURNING-LOADING CYCLE ANALYSIS

Figure 3 shows the block diagram of the simulation model.

In this simulation, the simulation model takes various characteristics into account, such as volumetric and mechanical efficiency of pump and motor, friction of cylinder, pressure loss of control valve inside passage and engine fuel consumption characteristic.

Figure 4(a)-4(f) shows simulation results.

Figure 4(a) shows results for the boom, namely (a1) pilot pressure for boom operation, (a2) pressure of boom cylinder bottom side, (a3) pressure of boom cylinder rod side, and (a4) length of boom cylinder.

Figure 4(b) shows results for the arm, namely (b1) pilot pressure for arm operation, (b2) pressure of arm cylinder bottom side, (b3) pressure of arm cylinder rod side, and (b4) length of arm cylinder.

Figure 4(c) shows results for the bucket, namely (c1) pilot pressure for bucket operation, (c2) pressure of bucket cylinder bottom side, (c3) pressure of bucket cylinder rod side, and (c4) length of bucket cylinder.

Figure 4(d) shows results for the swing, namely (d1) pilot pressure for swing operation, (d2) pressure of swing motor right side, (d3) pressure of swing motor left side, (d4) rotational speed of swing motor.

Figure 4(e) shows results for the pump, namely (e1) discharge pressure of pump-1, and (e2) discharge pressure of pump-2.

Figure 4(f) shows results for the engine, namely (f1) rotational speed of engine, and (f2) flow rate of fuel.

In these figures, the blue lines show experiment results whereas the red lines are simulation results.

The simulation result matches the experimental one with reasonable accuracy.

However, there are a few differences that are remarkable enough to notice at some parts of the results.
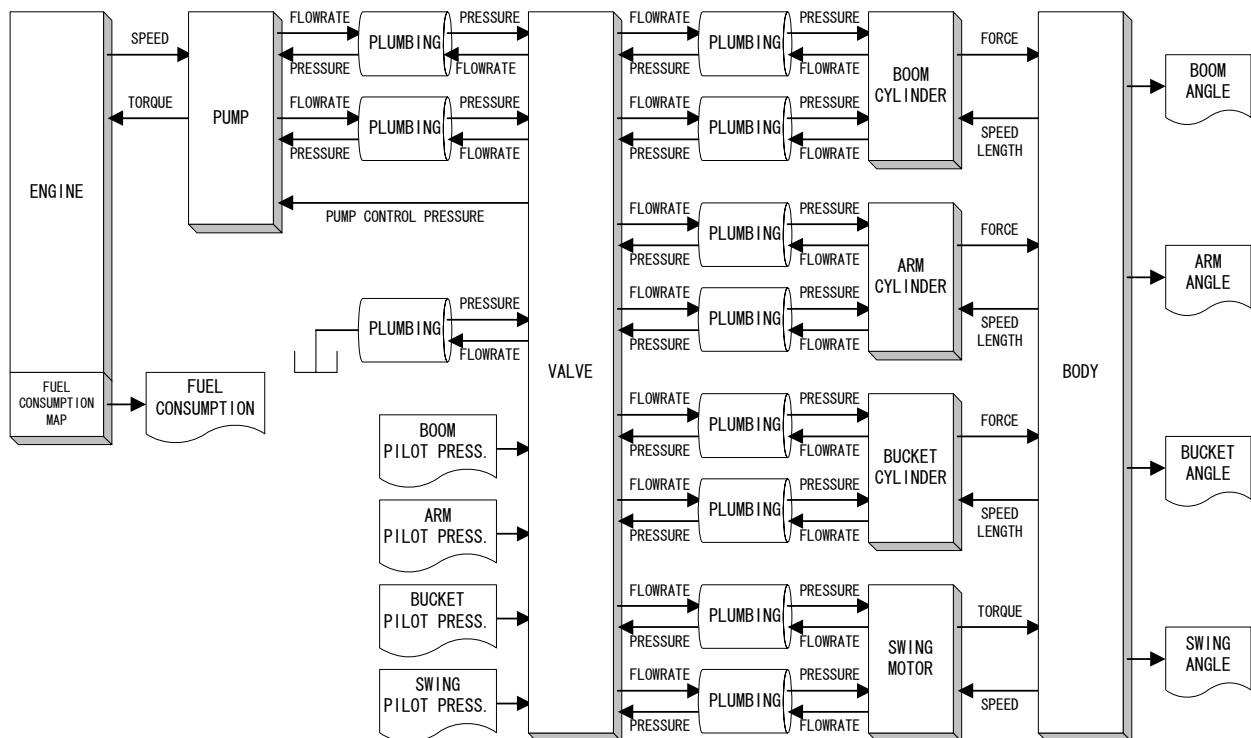
Figure 3 Block diagram of the simulation model
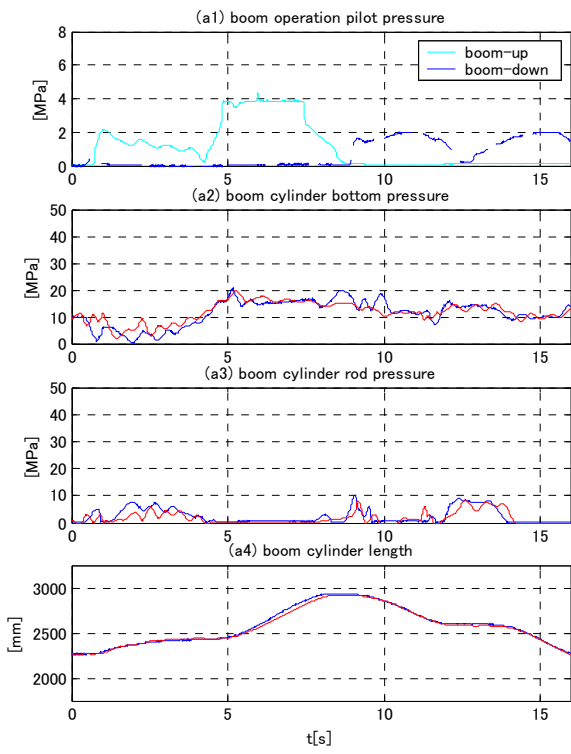
Figure 4(a) Simulation result (boom)
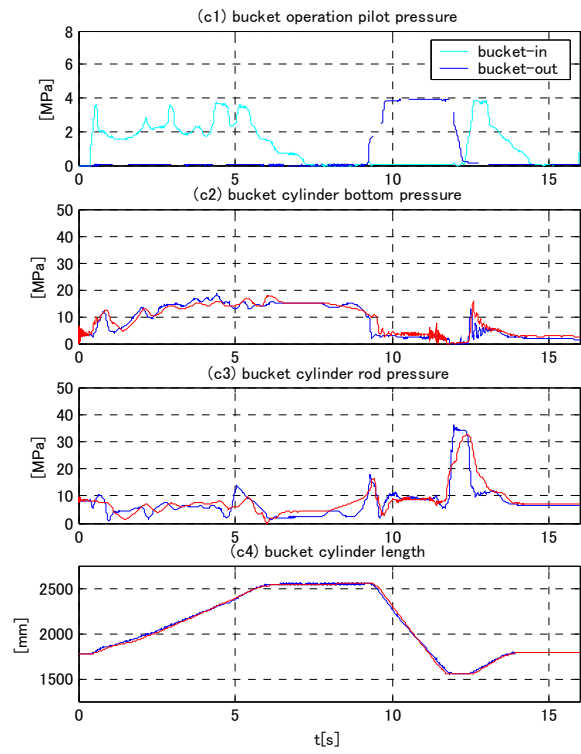
Figure 4(c) Simulation result (bucket)
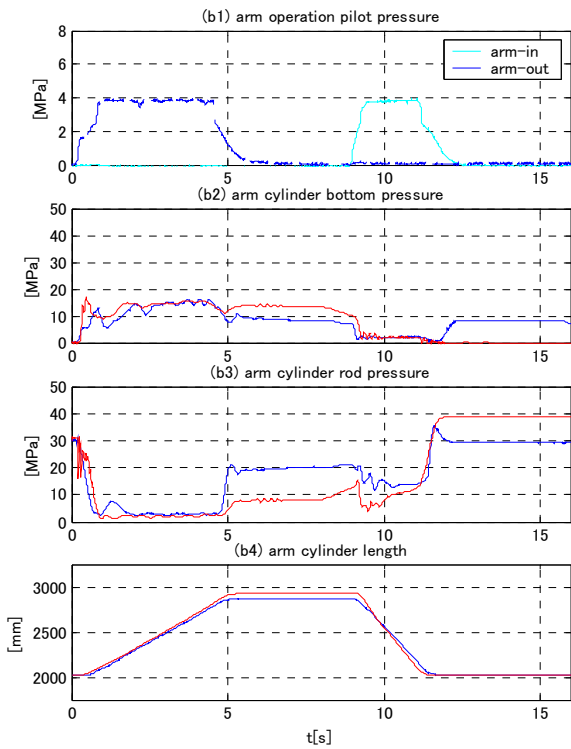
Figure 4(b) Simulation result (arm)
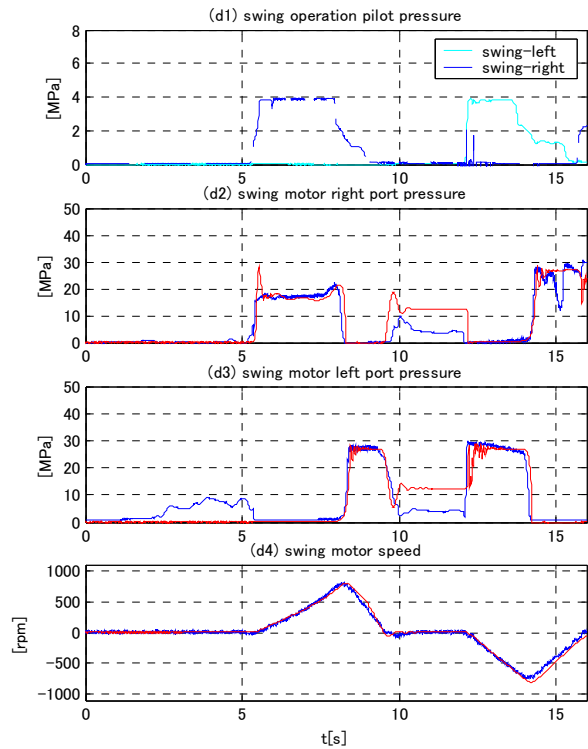
Figure 4(d) Simulation result (swing)

315
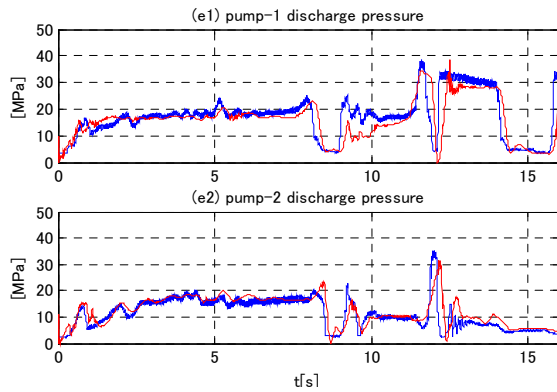
Figure 4(e) Simulation result (pump)
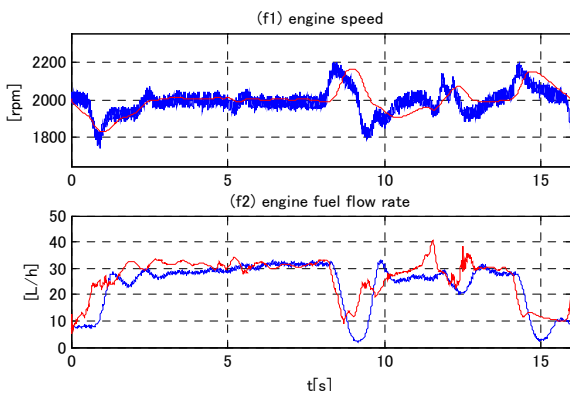
Figure 4(f) Simulation result (engine)
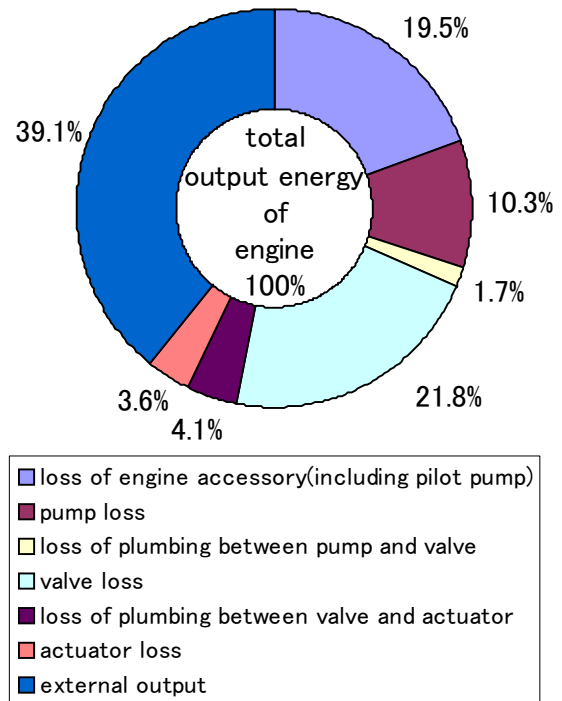
Figure 5 Result of energy analysis

At first, differences are seen for time=5-9 seconds in (b2) pressure of arm cylinder bottom side and (b3) pressure of arm cylinder rod side, are known to be cause by error of (b4) length of arm cylinder. The error then affects body posture, and as a consequence, changes pressure to sustain gravity moments of the body.

Secondly, for the error for time=12-16 seconds, it is caused by relief pressure in the cylinder stroke end.

Thirdly, an error in (d3) pressure of swing motor left side, in time = approximately 2.5-5 seconds, is due to digging reaction force acts on the side face of bucket, which in fact is not considered nor modeled in this simulation.

Finally, for the errors found in (d2) pressure of swing motor right side and (d3) pressure of swing motor left side for time = 10-12.5 seconds, they are known to be cause by a leak in the spool clearance when the valve is in its neutral position.

Using the simulation result, we calculate energy consumption during digging-turning-loading operation. Figure 5 shows the result of the analysis, where total output energy is 100%.

In the figure, a term "external output" means sum of output required to dig and output required to drive the body.

From the figure, it is cleared that valve internal loss is the largest contributor to the total energy consumed by the hydraulic components, and pump internal loss is the second.

By reducing internal loss of valve and pump, the total energy consumption could be saved.

CONCLUSION

Example of the system simulation for hydraulic excavator considering hydraulic circuit and a body movement was introduced.

We will use this simulation model for the product development effectively.

REFERENCE

1. Maehata K., System Simulation for Hydraulic Excavator, KYB TECHNICAL REVIEW, 2006, No.32, pp.4-9.

P1-12

A STUDY ON ENERGY SAVING POTENTIAL OF HYDRAULIC CONTROL SYSTEM USING SWITCHING TYPE CLOSED LOOP CONSTANT PRESSURE SYSTEM

Kyoung Kwan AHN*, Triet Hung HO**, and Quang Truong DINH**

* School of Mechanical and Automotive Engineering
University of Ulsan
Ulsan, South Korea
(E-mail:kkahn@ulsan.ac.kr)
** Graduated School of Mechanical and Automotive Engineering,
University of Ulsan
Ulsan, South Korea
(E-mail:hotriethung@yahoo.com)

ABSTRACT

Up to now, several types of hybrid systems have been developed to deduce energy consumption. Switching type closed loop constant pressure system (SCL-CPS) was proposed as one of feasible hybrid systems. SCL-CPS also uses flywheel, hydraulic accumulator and hydraulic power transmission as a traditional CPS but it has two alternatively high pressure lines. At a same time, one is used as the high pressure line and the other is the low one. Switching between them to overcome large hydraulic shock and noise considered as serious problems in traditional CPS. In this paper, energy saving potential of system is evaluated by considering effect of component efficiencies in system. Recovery efficiency during deceleration the wheel is estimated by simulation. The results indicate that proper determination of recovery time and operating pressure improves significantly energy recovery potential of the system.

KEY WORDS

Constant Pressure System (CPS), Flywheel Switching, Energy saving, Secondary Control

NOMENCLATURE

C	: Viscous friction coefficient	$T_{ac,br}$	: Acceleration, braking torque
D_{max}	: Wheel moment of inertia	T_{in1}	: Torque at pump shaft
J_1	: Flywheel moment of inertia	T_{out2}	: Torque at motor shaft
J_2	: Different pressure	$u_{1,2}$	: Control signal
p_{pre}	: Accumulator pre-charge pressure	μ	: Oil viscosity
$Q_{1,2}$	: Flow rate	μ_V	: Volumetric loss
		μ_M	: Mechanical loss

INTRODUCTION

Recently, hybrid systems equipped an energy recovery and a secondary energy store system have been attractive systems from the viewpoint of energy saving. Several hybrid systems have been developed in literature such as CVT-flywheel system, Flywheel battery system, Electro-chemical batteries system or hydraulic hybrid system. Among them, hybrid systems using flywheel have been considered to be advantageous for some applications because of their high specific power. They have not been applied widely due to some inherit disadvantages for instances CVT-flywheel systems have many problems about controlling the CVT (Continuously Variable Transmissions) or flywheel battery systems need flywheel to work at very high velocity. CPS has been proposed and considered as one of the feasible solutions of low flywheel velocity hybrid systems. In former researches [1], the effectiveness of the CPS hybrid vehicle was verified by simulation. However, the pressure peak generated by the abrupt change of the displacement of pump/motors to change their functions is one of the most obstacles that restrict applicability of this system.

Switching type closed loop CPS (SCL-CPS) is proposed as a good solution to overcome those drawbacks. Energy saving of SCL-CPS can be achieved by saving primary power source and recovering energy during deceleration time. The later is investigated here because it always contributes a considerable part in total saving potential of the system. Many studies on recovery strategies of SCL-CPS have been taken place by using relief valve [4] or changing two pump/motor displacements in a small range [2]. These researches indicate that about 50% energy of the wheel can be recovered but neither flywheel nor wheel is controlled. So they are not used in real applications where the wheel velocity or position must be controlled.

In this paper, influences of wheel deceleration methods, operating pressure of system and pump/motor operating situation are studied. Results of this analysis are use to determine a proper control strategy for the system. Recovery strategy based on constant pressure is chosen. High energy recovery efficiency and controllability of the wheel are dominations of the study when comparing with existences.

SWITCHING TYPE CLOSED LOOP CPS

Proposed Switching Type Closed Loop CPS

A schematic diagram of proposed SCL-CPS is shown in Figure 1. It is a hydrostatic transmission system which consists of a flywheel, two variable displacement pump/motors and three electric clutches. Two hydraulic accumulators and two controllable relief valves play an important role in this system. Especially, the drive pump/motor is only work from 0 to +100% of

maximum displacement and there are two constant pressure lines for driving and energy recovery phase. Pressure in the driving line is high during the driving time, while pressure in the other line is high during recovery one. In mobile applications, system performance, refreshing oil and size of total system are issues need to be considered of a hydraulic circuit. The SCL-CPS using only two pump/motors in a closed loop circuit is a feasible solution of these issues.

Operation modes

The SCL-CPS works as a series hydraulic hybrid system with two different power sources that are the engine and the flywheel. Because of it configuration SCL-CPS is able to work in one of three modes that are on/off the engine, SCL-CPS and energy recovery mode at instantaneous time.
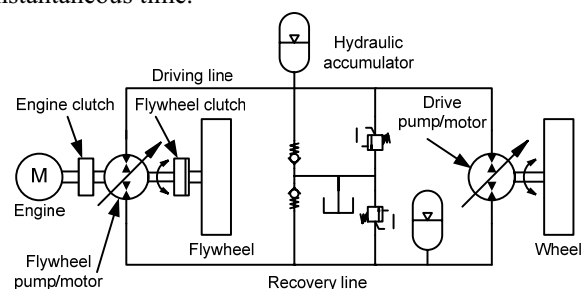
Figure 1 Schematic diagram of newly proposed CPS

On/off the engine mode

In this mode, the flywheel pump/motor functions as a hydraulic pump and the drive pump/motor functions as a hydraulic motor. The engine is turned on or off periodically and a cycle is described as follows. First, both clutches are engaged and the engine is turned on to drive the flywheel from the lower velocity to the upper velocity. Next, the engine clutch is disengaged and the engine is turned off. After that, only the flywheel functions as a power source to drive the wheel so its velocity begin decreasing. When the flywheel velocity gets value of the lower limit a cycle on/off is finished. Finally, the engine is turned on again and the engine clutch is engaged for next cycle.

SCL-CPS mode

The flywheel clutch is always disengaged and the engine is always turned on. Because two variable pump/motor displacements are used to control the wheel velocity so there is a redundant degree of freedom. Therefore, the operation of engine can be uncoupled from the speed and torque of drive wheels. It allows the engine to be operated in the optimum operation efficiency point. Generally, operation point of the engine is controlled to lie on the e-line of the engine at each calculated power of the system.

Energy recovery mode

This mode is depicted in Figure 2, the engine is turned off and the engine clutch is disengaged while the flywheel clutch is engaged during recovery period. The drive pump/motor functions as a pump while the

flywheel pump/motor functions as a motor. The recovery line becomes high pressure line while the driving line becomes low one. Wheel kinetic transform into hydraulic energy via the pump then continuously transforms into flywheel kinetic energy via the motor.
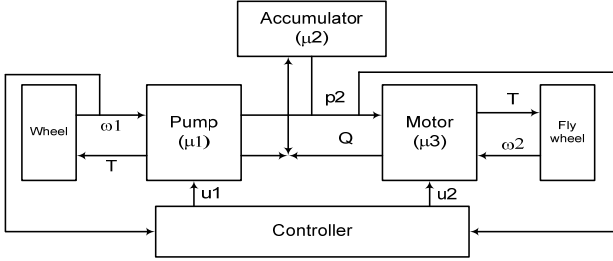
Figure 2 Energy recovery mode of SCL-CPS

Mathematical Model of SCL-CPS components

Hydraulic Pump

$$Q_{out1} = u_1.\omega_1.\mu_{pV}.D_{max,p} \quad (1)$$

$$T_{in1} = u_1.D_{max,p}.\frac{\Delta p}{\mu_{pM}} \quad (2)$$

$$\mu_{pV} = 1 - C_s.\frac{\Delta p.D_{max}}{\mu.\omega_1 D} \quad (3)$$

$$\mu_{pM} = \frac{1}{1 + \left(C_f + C_d.\frac{\mu.\omega_1}{\Delta p}\right).\frac{D_{max}}{D}} \quad (4)$$

Hydraulic Motor

$$Q_{in2} = u_2.\omega_m.\frac{D_{max,m}}{2.\pi\mu_{mV}} \quad (5)$$

$$T_{out2} = u_2.D_{max,m}.\Delta p.\mu_{mM} \quad (6)$$

$$\mu_{mV} = \frac{1}{1 + \left(C_s.\frac{\Delta p}{\mu.\omega_2}\right).\frac{D_{max}}{D}} \quad (7)$$

$$\mu_{mM} = 1 - \left(C_f + C_d.\frac{\mu.\omega_2}{\Delta p}\right)\frac{D_{max}}{D} \quad (8)$$

Hydraulic Accumulator

$$\frac{V_{gas}}{V_{ac}} = \left(\frac{p_{pre}}{p_{gas}}\right)^{\frac{1}{\gamma}} \quad (9)$$

$$p_{gas} dt = \gamma.\left(\frac{p_{gas} + 10^5}{V_{ac}}\right).q_{out} \quad (10)$$

The Wheel and Flywheel

$$T_{br} = J_1 \frac{d\omega}{dt} + C.\omega \quad (11)$$

$$T_{ac} = J_2 \frac{d\omega}{dt} + C.\omega \quad (12)$$

INFLUENCES ON ENERGY RECOVERY POTENTIAL OF SCL-CPS

Wheel deceleration and flywheel acceleration

To estimate this influence three types of decelerations are considered. Parabolic wheel velocity -1st, constant deceleration - 2nd and constant torque - 3rd method are chosen because of their natural characteristics. Parabolic wheel trajectory minimizing friction loss L in Eq. (13) during deceleration the wheel from initial velocity to zero in a given recovery time is chosen to estimate wheel efficiency. Wheel and flywheel trajectories are shown in table 1.

$$L = \int_0^{t_r} C.\omega(t)^2 .dt \quad (13)$$

Wheel and flywheel efficiencies versus time and deceleration and acceleration methods are depicted in Figure 3 and 4. Generally, maximum wheel or flywheel efficiency is inversely proportional to deceleration or acceleration time. Maximum value is reached about 96.67% for first method within 2s deceleration time. Second method is less efficiency than the last, which is inverted during acceleration time. Recovery time more than 16s is not efficiency for energy saving purpose.
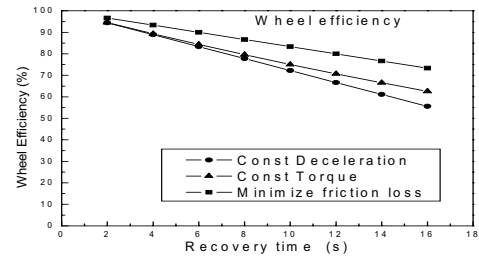
Figure 3 Wheel efficiency

Pump and motor efficiency

Overall CPS recovery efficiency is product of all component efficiencies. Figure 5 shows value of maximum system efficiency when that average value of pump/motor varies from 25-90% and wheel/flywheel efficiency come from previous section.
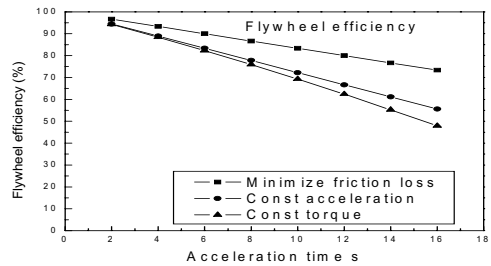
Figure 4 Flywheel efficiency

This value is proportional pump/motor efficiency. If maximum pump motor efficiency is 50% that value of system will be 22.6 % for 2s and 8% for 16s recovery time. It is smaller than 50% system efficiency is very small. It implies that finding out economical operating situation of pump and motor contributes to improvement saving potential of the system.

319
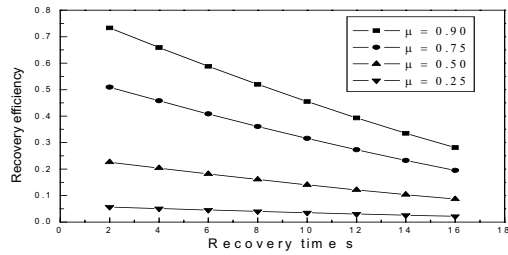
Fig 5 influence of pump/motor efficiency

Figure 6 and 7 describe pump/motor efficiency versus operating pressure, velocity and displacement. The results can be used to estimate pump/motor efficiency in operating situations. In the same working condition, the operating pressure and velocity, pump/motor operates in higher efficiency with higher displacement.
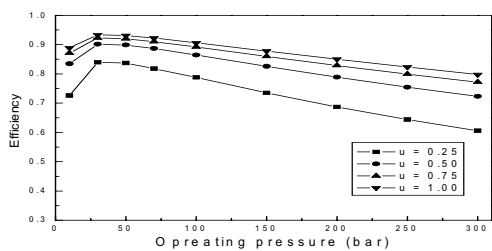
Figure 6 Pump/motor efficiency versus pressure
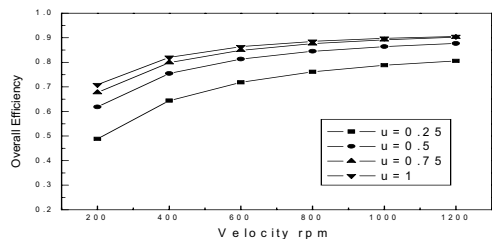
Figure 7 Pump/motor efficiency versus velocity

Operating pressure

In CPS operating pressure and desired torque is directly relative via Eq. (2). System is said to be controlled when it can generate any desired torque depending on deceleration method. The max/min torque depends not only recovery time but also deceleration method. In general that value is inversely proportional to deceleration time. Torque value changes significantly from maximum value to zero in the first method, which differs from the others. Desired torque increases lightly from beginning to the end for 2nd method and be constant for the last. Value of this torque is described in Table 2. Eq. (2) implies that operating pressure is inversely proportional to pump displacement and product of control input and pressure depends on deceleration method. So it should be chosen properly to force pump operate with large displacement, otherwise pump efficiency is small. Range of operating pressure is limited by volume and pre-charge pressure of the hydraulic accumulator. Operating pressure versus recovery time and deceleration methods is described in

Figure 8. Figure shows that system pressure in 1st method must be reached 262 or 534bar with maximum u(t) = 1 and u(t) = 0.5 respectively for 2s recovery time. However, maximum value of pressure for 3rth method needs only 132bar when using maximum displacement and 264 for 50% of that value. The figure also shows that maximum pressure changes significantly when recovery time changes from 2 to 4s. Moreover, maximum operating pressure in 1st method is always considerably higher than that of other methods.
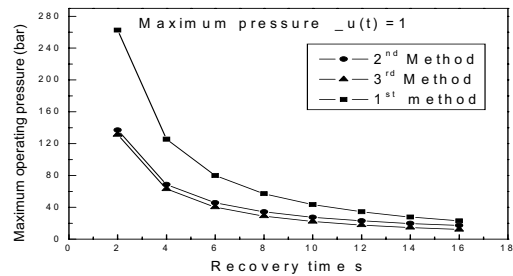
Figure 8 Operating pressure

Control strategies

Eq. (2) implies that the wheel is controlled by changing pressure or pump displacement. In other word, there are three possible strategies as follows.

i. Pressure is controlled as constant and pump displacement is controlled to mach desired torque
ii. Pump displacement is kept as constant and pressure is controlled to mach desired torque
iii. Pressure and pump displacement are variable

In order to estimate effect of control strategy on system saving energy potential a feed-forward controller is used. Secondary control, which includes two sub-controllers one for wheel control the other for pressure control, is used for simulation. Obviously, high working pressure forces pump/motor work in low efficiency but too low value is not able to control the wheel. Beside, efficiency of wheel and flywheel only depend on deceleration or acceleration method. Therefore, pressure is chosen at the possible lowest value for each method. Variable displacement and pressure control strategy is not necessary. Results of two control strategies with 2s recovery time are shown in Figure 9 and 10. Figure 10 and 11 indicate that if wheel is decelerated rapidly then flywheel is fast accelerated without influence of control strategy. If friction loss of the wheel is reduced by using parabolic trajectory that loss of the flywheel is increased during acceleration. Therefore, efficiency of CPS depends strongly on pump/motor one.

In constant pressure control displacement of pump and motor vary to mach desired torque and pressure. Pump and motor displacement vary little and get high value in 2nd and 3rd deceleration method. Motor displacement changes a lot and has lower value in the first method. From the figures, it is also realized that 2nd and 3rth deceleration method are quite similar.

320
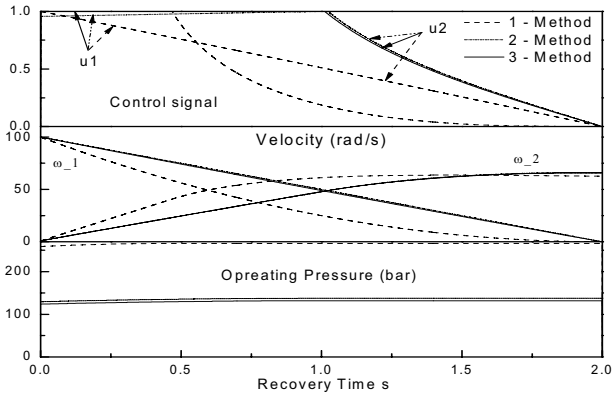
Figure 9 Constant pressure control
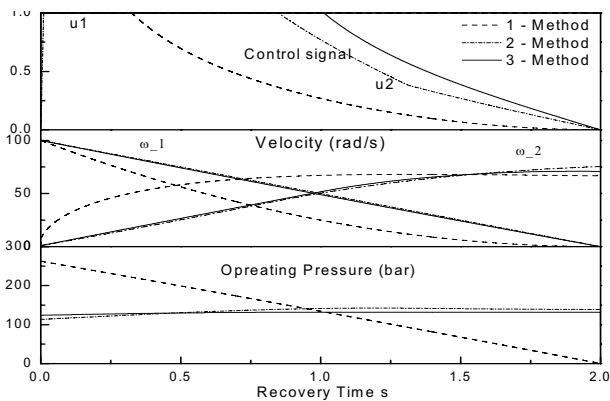
Figure 10 Variable pressure control

For variable pressure control, pump displacement is kept at maximum value. Pressure decreases from maximum to zeros in first method but increases from minimum to maximum value in second method.

Finally, simulation results show that pump or motor efficiency is always low in parabolic deceleration for both control strategies. Control strategy has an insignificant effect on recovery efficiency of the system.

SIMULATION

Simulation is verified by using AMESim software for recovery time changing from 2 to 16s. The value of pressure is minimum for each method corresponding to a given recovery time. Figure 12 and 13 depict overall recovery efficiency of the system in two control strategies and three deceleration methods. The efficiency is calculated in Eq. (14).

$$\mu_{CPS} = \frac{J_2\left(\omega_{2,tr}^2 - \omega_{2,0}^2\right)}{J_1\left(\omega_{1,0}^2 - \omega_{1,tr}^2\right)} \tag{14}$$

A particular situation of 4s recovery time, constant torque deceleration method, operating pressure of 63 bar with constant pressure control is investigated. Overall recovery efficiency of system is about 61%. Figure 13 indicates component efficiency in CPS. To evaluate

pump/motor efficiency during deceleration and acceleration some parameters are defined as follows.
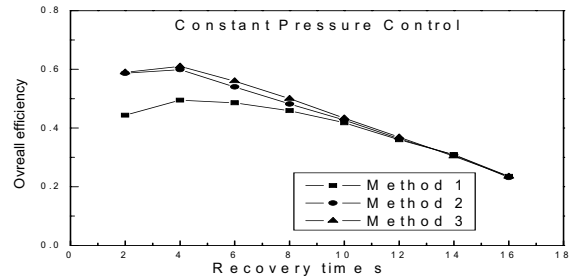
Figure 11 CPS efficiency in constant pressure control
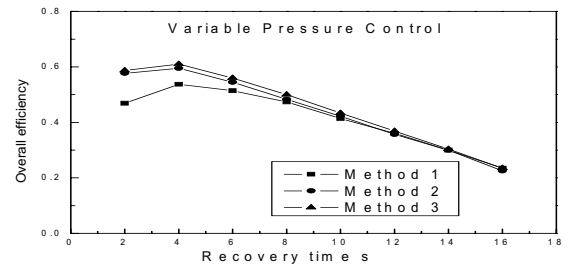
Figure 12 CPS efficiency in variable pressure control
Fig 14 describes relation between overall efficiency and operating pressure. It implies that the efficiency decreases when operating pressure over needed value.
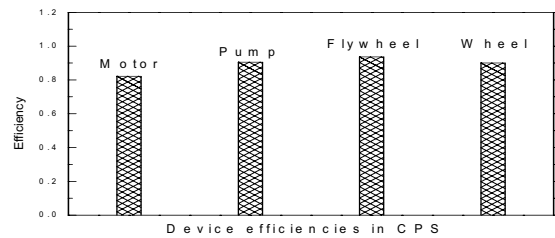
Fig 13 Component efficiency in CPS
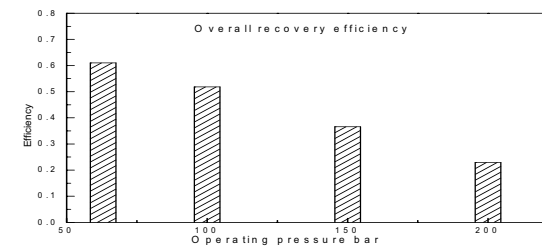
Fig 14 overall efficiency versus operating pressure

CONCLUSIONS

CPS recovery efficiency is analyzed from view point of investigation on operating condition of devices in the system. Pump/motor efficiency influences considerably on overall recovery one. Recovery time and operating pressure must be determined properly to get high energy

saving potential. Good conditions for this system are recover time from 2 to 6s, constant pressure control and constant torque deceleration. The study also indicates that CPS is able to recover about 61% energy of the wheel.

Table 1 Wheel and flywheel velocity trajectory

Deceleration methods	Parameters	Wheel – Deceleration	Flywheel – Acceleration
Minimize friction loss	Velocity	$\omega(t)=\dfrac{\omega_0}{t_r^2}.t^2-2.\dfrac{\omega_0}{t_r}.t+\omega_0$	$\omega(t)=\dfrac{\omega_{max}}{t_a^2}.t^2$
	Friction Loss	$L=\int_0^{t_a}C.\omega(t)^2.dt \quad L_{min}=\dfrac{1}{5}.\omega_0^2.C.t_r$	$L=\int_0^{t_a}C.\omega(t)^2.dt \quad L_{min}=\dfrac{1}{5}.\omega_0^2.C.t_r$
	Valuated Efficiency	$\mu_{reco}=\dfrac{\frac{1}{2}J.\omega_0^2-E_{loss}}{\frac{1}{2}J.\omega_0^2}.100$	$\mu_{reco}=\dfrac{\frac{1}{2}J.\omega_{max}^2-E_{loss}}{\frac{1}{2}J.\omega_{max}^2}.100$
Constant Deceleration/ Acceleration	Velocity	$\omega(t)=\omega_0\left(1-\dfrac{1}{t_r}t\right)$	$\omega(t)=\dfrac{1}{t_r}t$
Constant torque	Velocity	$\omega(t)=-10T+K.e^{-0.04166t}$ $K=\dfrac{\omega_0}{1-e^{-0.041.t_r}}$ $T=\dfrac{K-\omega_0}{10}$	$\omega(t)=T+K.e^{-0.04166t}$ $K=-\dfrac{\omega_0}{1-e^{-0.041.t_r}}$ $T=-K$

Table 2 Desired torque

Deceleration methods	Desired torque	Max value	Min value
Minimized Friction Loss	$T_d(t)=-\omega_0\left[\left(\dfrac{C}{t_r^2}\right).t^2+\dfrac{2}{t_r^2}(J-Ct_r)t+\left(\dfrac{Ct_r-2J}{t_r}\right)\right]$ $0\le t\le t_r$	$T_{max}=-\omega_0\left(\dfrac{Ct_r-2J}{t_r}\right)$ $t=0$	$T_{min}=0,\quad t=t_r$
Constant Deceleration	$T_d(t)=-\dfrac{\omega_0}{t_r}(C(t_r-t)-J)$ $0\le t\le t_r$	$T_{max}=\dfrac{\omega_0 J}{t_r},\quad t=t_r$	$T_{min}=-\dfrac{\omega_0(Ct_r-J)}{t_r}$ $t=0$
Constant Torque	$T_d(t)=\omega_0\left(\dfrac{e^{-0.04166t_r}}{\left(1-e^{-0.04166t_r}\right)}C\right)$ $0\le t\le t_r$	$T_{const}=\omega_0\left(\dfrac{e^{-0.04166t_r}}{\left(1-e^{-0.04166t_r}\right)}C\right)\quad 0\le t\le t_r$	

REFERENCES

1. Shinichi, Y., Takeo, N., Yutaka, K., Yasuo, K., Flywheel Hybrid Vehicle Making Use of Constant Pressure System. Fabrication of Stationary Test Facility and Experiment of Urban Driving Schedule, Transactions of the Japan Society of Mechanical Engineers, 2002, **68**-671, pp.2127-2132.
2. Cho, Y.R., AHN, K.K., A Study on The Energy Saving Hydraulic System Using Constant Pressure System, KFPS, 2007, **4**-1, pp.7-12.
3. Akers, A., Hydraulic Power System Analysis, CRC press, 2006, pp.221-240.
4. Ahn, K.K., and Oh, B.S., An experimental Investigation of Energy Saving Hydraulic Control System using Switching Type Closed Loop CPS, ICFP, 2005, pp.153-157.
5. Ivantysyn, J., Ivantysynova, M., Hydrostatic Pumps and Motors, ABI, New Delhi, 2001, pp. 47-99.

P1-13

PUMP MODE PREDICTION FOR FOUR-QUADRANT VELOCITY CONTROL OF VALVELESS HYDRAULIC ACTUATORS

Christopher WILLIAMSON, Prof. Monika IVANTYSYNOVA

Maha Fluid Power Research Center
Department of Agricultural and Biological Engineering, Purdue University
225 S. University Street, West Lafayette IN 47907, USA
Email: mivantys@purdue.edu

ABSTRACT

Displacement-controlled actuation offers energy savings by eliminating the metering losses associated with hydraulic valves and allowing energy recovery. In a closed-circuit configuration, four-quadrant pump operation can be achieved. This paper considers displacement-controlled boom lift cylinders on a skid-steer loader. Undesirable pump mode oscillation is observed while rapidly lowering small loads. Avoiding this oscillation requires actuator pressure control, which cannot be directly achieved due to insufficient pump dynamic response. The authors propose a predictive observer to provide sufficient lead time for feedforward control of actuator pressure. Design and analysis are presented for a discrete time linear observer which predicts future system states by delaying the input signal. Successful state prediction is demonstrated through simulation and experiment.

KEY WORDS

Displacement control, Valveless, Pump control, Velocity control

NOMENCLATURE

A_p	cylinder piston area	[m²]
A_r	cylinder rod area	[m²]
C_H	hydraulic capacitance	[m/N]
F_f	cylinder friction force	[N]
F_L	cylinder static load force	[N]
H	cylinder stroke	[m]
J_D	mass moment of inertia about boom axis of rotation	[kg·m²]
K_{oil}	fluid bulk modulus	[Pa]
Q	flow rate	[m³/s]
T	digital sampling time	[s]
V	pump displacement volume	[cc/rev]
V_{line}	actuator line volume	[m³]
c_v	coefficient of viscous friction	[kg/s]
k_{Li}	coefficient of internal leakage	[m³/Pa·s]
m_{eq}	actuator inertial load	[kg]
n	pump rotational speed	[rev/min]
p	fluid pressure	[Pa]
v	cylinder velocity	[m/s]
w	cylinder force due to boom weight	[N]
α	cylinder piston area ratio	[-]
Δp	actuator differential pressure	[Pa]
φ	boom angle	[rad]
τ_p	time constant of closed-loop pump displacement control	[s]

INTRODUCTION

Energy-efficient hydraulic systems and controls for mobile machinery has become a major research topic in recent years. Since a large percentage of power loss is due to metering flow through directional control valves, alternative circuit designs that reduce or eliminate these losses offer significant energy savings. One proposed solution is displacement-controlled actuation, in which a variable displacement pump controls the motion of a single or double-rod cylinder. This "valveless" or "pump-controlled" concept offers several advantages over traditional valve control, including higher energy efficiency and linear dynamic characteristics.

DISPLACEMENT-CONTROLLED ACTUATION

DC Concept

The closed circuit design shown in Figure 1 was proposed by Ivantysynova in 1998 and has been developed by her team since that time [1]. A similar concept was proposed independently by researchers in British Columbia in the early 1990s [2-3]. An open-circuit configuration may also be used for displacement control [4]. Displacement-controlled actuation (DCA) is based on the same operating principle as a hydrostatic transmission. Actuator position and velocity are controlled by adjusting the flow rate through a variable displacement pump. The differential flow rate produced by the movement of a single-rod cylinder is compensated by a low-pressure line (supplied by a charge pump and accumulator) via pilot-operated check valves.
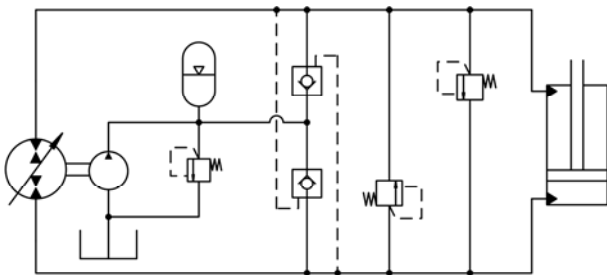
Figure 1 Displacement control circuit

DCA reduces power losses and allows energy recovery. Measurements of fuel consumption on displacement-controlled wheel loaders have shown savings of 15-25% [5]. Recent simulations of displacement- controlled excavators indicate reductions of up to 40% in total energy consumption [6].

Four-Quadrant Operation

The hydraulic pumps used for DCA must operate over center (reversible flow direction) in both pumping and motoring modes. Assuming that the direction of shaft rotation remains constant, these pumps operate in four quadrants of a pressure-flow plane, as defined in Figure 2. This characteristic allows flexible flow control and power recovery. However, it also causes undesirable performance for certain operating conditions.
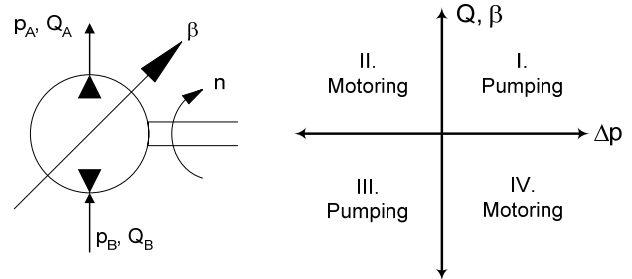
Figure 2 Definition of pump operating plane

$$\text{I. } v = \frac{Q_A}{A_p} \quad \text{II. } v = \frac{Q_B}{\alpha A_p} \quad \text{III. } v = \frac{Q_B}{\alpha A_p} \quad \text{IV. } v = \frac{Q_A}{A_p} \quad (1)$$

$$\alpha = \frac{A_p - A_r}{A_p} \quad (2)$$

Referring to Figure 1, the check valves connect the low-pressure side of the circuit to the charge line. If the net force on the cylinder changes direction, the pressure will also change to accommodate the load and the check valves switch accordingly. The problem that this presents is that the actuator velocity is a discontinuous function of the operating quadrant (Eq. 1). The area ratio α is typically between 0.5 and 0.75 (see Figure 4). If the pump changes operating modes while the cylinder is moving, the cylinder velocity will suddenly increase or decrease by a factor of $1/\alpha$.

Pump Mode Oscillation

Changing modes may be encountered in practice while lowering a light load at a high velocity. When the speed increases to the point where the friction force on the cylinder is higher than the load, the check valves switch, the pump shifts from motoring mode (quadrant IV) to pumping mode (quadrant III), and the cylinder velocity increases. Due to flow resistance and pressure resonance in the cylinder and lines, p_A may then rise above p_B and the pump shifts back to quadrant IV. This sequence then repeats itself, creating a limit cycle between pumping and motoring modes until the pump displacement is reduced enough to slow the actuator. An example of this phenomenon is shown in Figure 3 while rapidly lowering the boom of a displacement-controlled skid-steer loader with no load in the bucket.

Clearly, large oscillations in actuator velocity are undesirable and may be dangerous. From a hydraulic system design perspective, pump mode oscillation may be avoided or ameliorated by reducing cylinder velocity

324

and/or seal friction, increasing static cylinder loads, and increasing the α ratio. Where these solutions are not practical, feedback control may prevent oscillation. Several ideas for eliminating this effect by pressure and velocity control have been considered. As will be discussed in more detail later, the main difficulty in implementing an effective control law is excessive phase lag. The system dynamics are such that the time delay between control input and output measurement is too long for feedback control of the mode switching oscillations. What is needed is a way to anticipate an impending change in the pump's operating quadrant with sufficient time to change the pump displacement and avoid the transition. The goal of this paper is to develop a predictive pump mode observer that provides sufficient phase lead to allow four-quadrant control of actuator velocity.
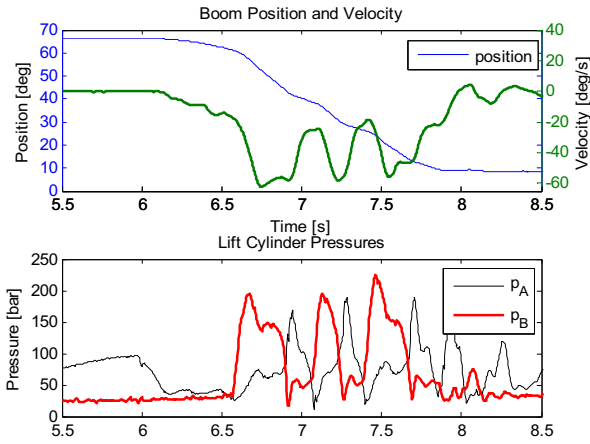
Figure 3 Measured pump mode oscillation

DYNAMIC MODEL

Pump Model

The DC skid-steer loader uses two variable dispalacement, axial piston swash plate type pump/motor units, one each for the boom lift and bucket tilt functions. Pump displacement is controlled by a hydraulic valve operating at a supply pressure of 15 -30 bar. Pump dynamic response for small displacements depends on the bandwidth of the valve [7]. When a larger displacement is demanded, the swash plate velocity is limited by the maximum flow rate through the valve. There may also be signal transmission delay associated with the D/A amplifier between the microcontroller and the valve.

DC actuation requires closed-loop control of the pump displacement. Simple proportional feedback is typical. Position/velocity control of the DC cylinders are arranged in a cascaded structure, with the pump displacement feedback as an inner loop [7]. The closed-loop pump dynamic response can reasonably be approximated by a linear first-order system with a time constant of τ_p.

Actuator Model

The loader's lift cylinders are single-rod linear actuators, as shown in Figure 4.
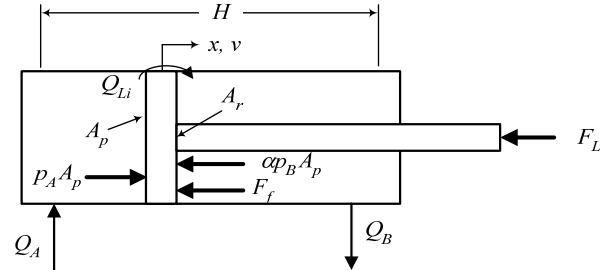
Figure 4 Single rod linear actuator

The actuator's equation of motion, assuming viscous friction only, is given by Eq. 3. Since the boom motion is actually rotational, the combined inertia of the boom and bucket must be expressed in terms of the actuator's linear motion as an equivalent mass in Eq. 4. Pressure build-up in the cylinder chambers is a function of flow rate and piston velocity, as in Eq. 6 and 7. Internal leakage across the piston seals is assumed to be only pressure dependent and external leakage is neglected.

$$m_{\text{eq}}\dot{v} = A_{\text{p}}\left(p_{\text{A}} - \alpha p_{\text{B}}\right) - c_v v - F_L \qquad (3)$$

$$m_{\text{eq}} = J_{\text{D}}\left(\frac{\partial \varphi}{\partial x_{\text{cyl}}}\right)^2 \qquad (4)$$

$$\dot{p}_{\text{A}} = \frac{1}{C_{\text{H}_{\text{A}}}}\left[Q_{\text{A}} - A_{\text{p}}v - k_{\text{Li}}(p_{\text{A}} - p_{\text{B}})\right] \qquad (5)$$

$$\dot{p}_{\text{B}} = \frac{1}{C_{\text{H}_{\text{B}}}}\left[-Q_{\text{B}} + \alpha A_{\text{p}}v + k_{\text{Li}}(p_{\text{A}} - p_{\text{B}})\right] \qquad (6)$$

$$C_{HA} = \frac{1}{K_{\text{oil}}}\left(V_{\text{line}} + A_{\text{p}}\frac{H}{2}\right) \qquad (7)$$

$$C_{HB} = \frac{1}{K_{\text{oil}}}\left(V_{\text{line}} + \alpha A_{\text{p}}\frac{H}{2}\right) \qquad (8)$$

$$Q_{\text{A}} = nV \qquad Q_{\text{B}} = \alpha nV \qquad (9)$$

Constant hydraulic capacitances (Eq. 7-8) is assumed, which is defined at the center of the piston stroke. The flow rate to the cylinder is the product of pump speed n and displacement volume V, neglecting volumetric losses. Further, the rates of fluid flow entering and leaving the cylinder are assumed to be proportional.

State Space System Model

The state equations derived in the previous subsections can now be assembled into a single dynamic model in linear state space form. The state vector consists of the pump displacement V and cylinder position, velocity and pressure. The outputs are the measurable states, which are pump displacement (swash plate angle), cylinder position and pressure. The control input u is the desired pump displacement V_d.

$$\dot{x} = \mathbf{F}x + \mathbf{G}u + d$$
$$y = \mathbf{C}x \tag{10}$$

$$x = \begin{pmatrix} V & v & p_A & p_B \end{pmatrix}^T \tag{11}$$

$$y = \begin{pmatrix} V & p_A & p_B \end{pmatrix}^T \tag{12}$$

$$\mathbf{F} = \begin{pmatrix} \dfrac{-1}{\tau_p} & 0 & 0 & 0 \\[2ex] 0 & \dfrac{-c_v}{m_{eq}} & \dfrac{A_p}{m_{eq}} & \dfrac{-\alpha A_p}{m_{eq}} \\[2ex] \dfrac{n}{C_{HA}} & \dfrac{-A_p}{C_{HA}} & \dfrac{-K_{Li}}{C_{HA}} & \dfrac{K_{Li}}{C_{HA}} \\[2ex] \dfrac{-\alpha n}{C_{HB}} & \dfrac{\alpha A_p}{C_{HB}} & \dfrac{K_{Li}}{C_{HB}} & \dfrac{-K_{Li}}{C_{HB}} \end{pmatrix} \tag{13}$$

$$\mathbf{G} = \begin{pmatrix} \dfrac{1}{\tau_p} & 0 & 0 & 0 \end{pmatrix}^T \tag{14}$$

$$d = \begin{pmatrix} 0 & -F_L & 0 & 0 \end{pmatrix}^T \tag{15}$$

$$G_p(s) = \frac{p_A(s) - p_B(s)}{V_d(s)} \tag{16}$$

The output disturbance d is the gravitational force on the cylinder due to the weight of the boom and bucket, which varies with bucket load and boom angle. It is essential that the model include this disturbance, since the pump's operating mode depends on static pressure, which is directly related to the weight of the boom and bucket.

System Analysis
In order to avoid pump mode oscillation, the cylinder pressure must be controlled. Consequently, the first topic for analysis is the pressure dynamics and the relationship between control input (pump displacement volume) and measured pressure outputs. Define a transfer function from u to y_2-y_3, as in Eq. 16. Roots of its characteristic equation for nominal parameter values are listed in Table 1.
For feedback control of system pressure, the pump bandwidth should be several times faster than the

pressure dynamics. It is clear from Table 1 that this is not the case. Direct pressure feedback is not an option, but feedforward pressure control may be possible. Feedforward control requires that the control input be applied with sufficient phase lead to produce the desired output. Since the cylinder pressure is not periodic, the controller must anticipate future outputs. This state prediction problem will be addressed in section 3.

Table 1: Nominal pole locations of $G_p(s)$

Mode	Frequency (Hz)	Damping (-)
Integrator	0	1
Pump dynamics	5.3	1
Pressure resonance	6.5	0.05

Many of the parameters in the system model are unknown, uncertain and/or slowly varying. Estimated maximum and minimum parameter values were obtained from machine specifications and model identification measurements. Figure 5 illustrates the pressure frequency response with respect to pump flow rate considering model uncertainty.
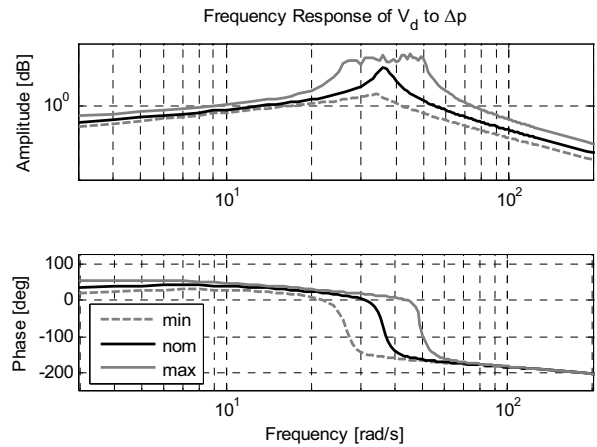
Figure 5 Frequency response of $G_p(s)$

From Figure 5, the maximum crossover frequency of the magnitude ratio is about 73 rad/s (11.6 Hz) and the minimum value is 41 rad/s (6.5 Hz), at which the phase lag is 173° and 161°, respectively. This corresponds to a time delay of 0.041 to 0.069 seconds between input and output.

PREDICTIVE OBSERVER

Observer Design

This section describes the design of an observer (estimator) that predicts future system states with sufficient lead time to allow feedforward pressure control. Analysis of **F**, **G** and **C** from Eq. 10 indicates that all system modes are stable, controllable and observable. The observer will ultimately be implemented with a mobile digital microprocessor. Conducting design and analysis directly in the discrete time domain makes sense in order to avoid the faster sampling times required for a discretized continuous time design. To proceed with the observer design, the plant state-space model derived previously is converted to discrete time with a zero-order hold approximation.

The basic design of a predictive observer is a direct result of the recursive form of the vector state equation, Eq. 17. Given the input vector u for all time, any future state can be calculated from Eq. 18. For notational convenience, the load force disturbance d is treated as an additional input.

$$x(k+1) = \mathbf{A}x(k) + \mathbf{B}u(k) \qquad (17)$$

$$x(k+n) = \mathbf{A}^n x(k) + \sum_{i=0}^{n-1} \mathbf{A}^{n-i-1} \mathbf{B}u(k+i) \quad (18)$$

$$\hat{x}(k+1) = (\mathbf{A} - \mathbf{LC})x(k) + \mathbf{L}y(k) + \mathbf{B}u(k) \qquad (19)$$

$$\overline{x}(k+n) = \mathbf{A}^{n-1}\hat{x}(k+1) + \sum_{i=1}^{n-1} \mathbf{A}^{n-i-1} \mathbf{B}u(k+i) \qquad (20)$$

$$\tilde{F}_L = C_d\left(y - C\hat{x}\right) \qquad (21)$$

$$C_d = \begin{pmatrix} 0 & A_p & -\alpha A_p \end{pmatrix} \qquad (22)$$

$$\hat{F}_L(k+1) = K_p \tilde{F}_L(k) + K_I\left(T\sum_{j=0}^{k} \tilde{F}_L(j) - \frac{T}{2}\tilde{F}_L(k)\right)(23)$$

Of course, future inputs are unknown. It may be possible to predict states by assuming constant future inputs or by extrapolating from past inputs if u is smooth and varies slowly compared to the prediction time. Unfortunately, neither assumption is valid in the current application. The pump mode transition which the observer should detect occurs when the pump displacement is increasing and may occur rapidly, on the order of 50 ms. Assuming constant inputs fails to predict the event by underestimating the rate of pressure change, and extrapolating from previous inputs is too sensitive to noise. Since it is difficult to predict the future, another option is to delay the present. That is, by delaying the application of the control input to the plant, the future reference trajectory is known for a short time in advance. This may not be feasible for some applications, but may work for a skid-steer loader if the time delay is short enough. It is unlikely that a human operator will notice a lag time of less than 0.1 seconds.

The traditional design of a Luenberger observer takes the form of Eq. 19, where the estimated states are denoted with a carat. The predictive observer (Eq. 20) uses output feedback for the current state, but estimates future states (x-bar) up to n steps ahead based solely on the input u.

For accurate state estimation, the observer must also consider the effect of the static load on the cylinder. The payload mass in the loader's bucket is unknown and variable, so an adaptive parameter estimation method is proposed. Estimation error may be calculated from the measured and estimated pressures, as in Eq. 21-22. The current disturbance estimate is adjusted with PI feedback on the estimate error (Eq. 23). A bilinear approximation serves as the integral term [8]. For estimation of future states in Eq. 23, constant load force disturbance is assumed.

Observer Analysis

Observer stability depends on the output feedback gains. The output injection matrix **L** is chosen so as to place the observer poles around 40 Hz. This frequency is fast enough to provide rapid convergence while avoiding amplification of noise at higher frequencies. Feedback gains for the load force disturbance estimate are tuned empirically according to traditional PID rules. As this is a direct digital design, observer accuracy at the sample instances is independent of sampling time. Error due to intersample behavior may be avoided by sampling at least 10 times faster than the pressure frequencies [9], which is not a difficult requirement for the present application.

Observer robustness with respect to model uncertainty may be analyzed in the state space time domain. In Eq. 24, Δ_A represents the maximum singular error value of the **A** matrix in the expected uncertainty range, where **A₀** represents the nominal model. A similar error value can be defined for **B**, leading to a bound on the maximum state prediction error for n time steps in Eq. 25. Conversely, Eq. 25 could be used to find the maximum prediction time interval for a given error tolerance.

$$\Delta_{\mathbf{A}} = \left\|\mathbf{A} - \mathbf{A}_0\right\|_2 \qquad (24)$$

$$\tilde{x}(k+n) = \left(\Delta_{\mathbf{A}}\mathbf{A}\right)^n \tilde{x}(k)$$
$$+ \sum_{i=0}^{n-1}\left[\left(\Delta_{\mathbf{A}}\mathbf{A}\right)^{n-i-1}\left(\Delta_{\mathbf{B}}\mathbf{B}u(k+i)\right)\right] \qquad (25)$$

VALIDATION

The predictive observer was demonstrated first in simulation with a nonlinear model of the skid-steer loader in Matlab/Simulink. This detailed model includes multi-body mechanics, pump displacement

dynamics, and loss models of various hydraulic components [10]. An observer sampling time of 5 ms and prediction time of 30 ms was used for both simulation and experiment. The duty cycle simulated with the nonlinear model consists of raising the boom and then lowering it quickly. As the boom drops, the lift pump oscillates between pumping and motoring modes. Simulation of the predictive observer with this model is shown in Figure 6. The observer successfully predicts that Δ*p* is about to cross zero with >50 ms of anticipation.
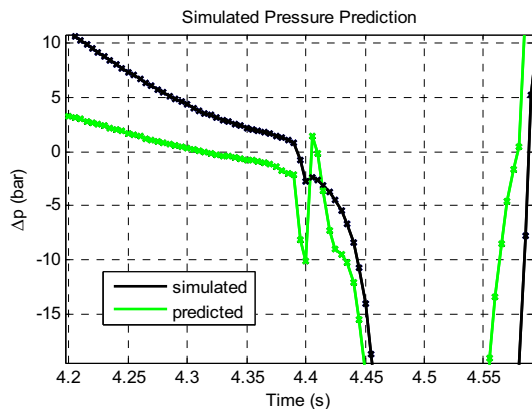
Figure 6   Results with simulated data

The same process was repeated experimentally. Observer pressure predictions with measured data are plotted in Figure 7. Again, the observer successfully predicts the zero crossing with about 60 ms of lead time.
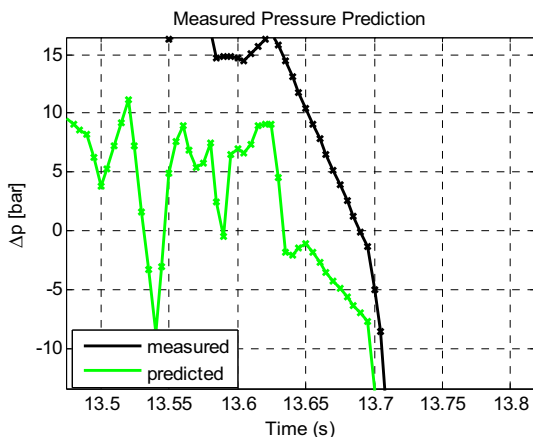
Figure 7 Results with measured data

A few limitations become apparent in the experiment. The state prediction is fairly sensitive to noise in the input command signal. Also, the load force disturbance estimate can negatively affect the pressure state prediction. Higher gains (and faster convergence) for the disturbance estimate tend to reduce the phase lead of the pressure prediction. A model-based method

for load disturbance estimation (such as considering boom kinematics) may reduce the necessity of high feedback gains. Efforts to reduce sensitivity to model uncertainty would also improve the observer's accuracy in practice.

CONCLUSION

Modeling and analysis of the DC hydraulic system indicate that 40 ms or more of lead time is required for feedforward control of actuator pressure and velocity. The intended skid-steer loader application allows a reference input delay of this duration. A discrete time observer is proposed to predict future changes in system pressure. Successful observer operation was shown with simulated and measured data. In future work, the proposed observer will be combined with a pressure and velocity control algorithm for pump-controlled actuation in four operating quadrants.

REFERENCES

1. Ivantysynova, M., 1998. "Energy saving hydraulic actuators for mobile machines", Proc. of 1st Bratislavian Fluid Power Symposium, pp. 47-58.
2. Lawrence, P.D. ; Salcudean, S.E. ; Sepehri, N., et al. 1995. Coordinated and Force-Feedback Control of Hydraulic Excavators. *4th Internat'l Symposium on Experimental Robotics, ISER '95.*
3. Hewett, Allan J. 1994. *Hydraulic Circuit Flow Control.* US Patent No. 5,329,767. July 19, 1994.
4. Heybroek, K., Larsson, J., and Palmberg, J.O., 2006. "Open Circuit Solution for Pump Controlled Actuators," *Proc. of 4th FPNI PhD Symp.,* pp. 27-40.
5. Rahmfeld, R. 2002. *Development and Control of Energy Saving Hydraulic Servo Drives for Mobile Systems.* PhD Thesis, VDI Fortschritt-Berichte. Reihe 12 Nr. 527. Düsseldorf: VDI.
6. Williamson, C., Zimmerman, J. and Ivantysynova, M., 2008. "Efficiency Study of an Excavator Hydraulic System Based on Displacement-Controlled Actuators", *Bath/ASME Symposium on Fluid Power and Motion Control.*
7. Grabbel, J. and Ivantysynova, M., 2005, "An Investigation of Swash Plate Control Concepts for Displacement Controlled Actuators," *Internat'l Journal of Fluid Power*, Vol. 6, No. 2, pp. 19-36.
8. Chiu, G. and Peng, H., 2007. *Digital Control Systems.* www.lulu.com/content/551583.
9. Goodwin, G., Graebe, S. and Salgado, M., 2001. *Control System Design.* Prentice Hall, pp. 381.
10. Williamson, C. and Ivantysynova, M., 2007, "The Effect of Pump Efficiency on Displacement-Controlled Actuator Systems," *Proc. of the Tenth Scandinavian International Conf. on Fluid Power (SICFP '07),* Tampere, Finland, Vol. 2, pp. 301-326.

P1-14

DEVELOPMENT OF OILY HIGH BULK MODULUS FLUID

Toshiyuki TSUBOUCHI*, Hideto KAMIMURA** and Jitsuo SHINODA**

* Advanced Technology Research Laboratories, Idemitsu Kosan Co., Ltd.
1280 Kami-izumi, Sodegaura, Chiba, 299-0293, Japan
(E-mail: toshiyuki.tsubouchi@si.idemitsu.co.jp)
** Lubricants Research Laboratory, Idemitsu Kosan Co., Ltd.
24-4 Anesaki-kaigan, Ichihara, Chiba, 299-0107, Japan

ABSTRACT

The most important role of a hydraulic fluid is transmission of power among various roles. A bulk modulus of the fluid is crucial for hydraulic systems, particularly for high-pressure hydraulics. In theory, compression energy losses are in diverse proportional to the effective bulk modulus of the fluid, and response speed and stability depend directly on the square root of it. Conventional mineral oils have pretty low bulk modulus, compared to water-based hydraulic fluid. On the other hand, the water-based fluids are disadvantageous in lubricity and evaporation. Under the circumstances, we've searched for available oily high bulk modulus fluid, and found organic compounds with water-level bulk modulus.

KEY WORDS

bulk modulus, hydraulic fluid, compression energy, response speed, stability

NOMENCLATURE

d   : Pipe inside diameter

D   : Damping coefficient

K   : Bulk modulus

K_{oil} : Bulk modulus of pure oil

K_{pipe} : Bulk modulus of pipe wall material

s   : Pipe wall thickness

ΔP   : Pressure change

ω_0 : Natural angular frequency

INTRODUCTION

Through the development of traction fluid for cars, we have realized great influence of the molecular structure of base oil on the machine performance, that is, the power of the "Fluid Power", and have been cultivated a molecular design and novel synthetic lubricant developing technology [1]. This time we have paid attention to the hydraulic fluid, and studied its possibility of evolution into a vital machine element.

In recent years, stationary hydraulic drive systems have been changed to electric drives in various uses owing to response speed, control stability, design flexibility and cleanliness. Since hydraulic drives have an advantage of power density, electro-hydraulic drives increase in high performance area such as injection molding machine. So improvement of disadvantages of hydraulic fluid, i.e. response speed and stability, could strengthen its competitiveness (Figure 1).

The most important role of the hydraulic fluid is transmission of the power among various roles, such as lubrication in pumps, seals, and rust prevention. The performance of power transmission depends on bulk modulus   and air bubbles release ability of the

fluids. And base fluids have important roles in both properties. On the other hand, corresponding to energy saving in recent years, hydraulic fluids tend to be lower viscosity and higher viscosity index in order to decrease flow resistance. In general, lowering base fluid viscosity means lowering bulk modulus of the fluid, which means spoiling the primary performance of the hydraulic fluid (Figure 2).
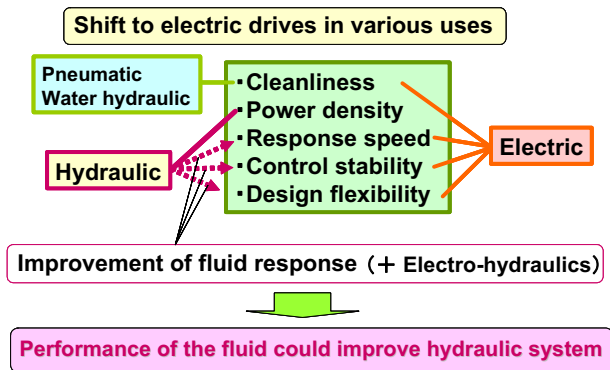
Figure 1 Present circumstances of stationary hydraulics

Figure 2 Primary performance of hydraulic fluid

In this paper effects of hydraulic fluids' bulk modulus upon less compression energy loss, rapid response and precise controllability in hydraulic systems were reviewed, and developmental possibility of a practical oily high bulk modulus fluid which contributes to them was investigated.

BULK MODULUS OF CONVENTIONAL LUBRICANTS

Klaus et al. measured isothermal secant bulk modulus

of various lubricants [2]. Read values from the literature at 37.8 ℃ and 50MPa are 2.68GPa of polyphenyl ether (5P4E) and 2.48GPa of water, compared to 1.65GPa of mineral oil, on the other hand silicone oil has low value of 1.15GPa. Goldman et al. measured isothermal tangential bulk modulus of several kinds of synthetic fluids and mineral oils, and revealed that polyglycol, diester, and tributyl phosphate have lower bulk modulus than that of mineral oil has [3].

5P4E has disadvantages in too high viscosity and poor low temperature fluidity, and water based fluids have disadvantages in poor lubricity and easy evaporation to use for practical hydraulic system. In this way, any available high bulk modulus fluids have not been developed yet.

EFFECTS OF BULK MODULUS ON HYDRAULIC PERFORMANCE [4]

Summaries of the report about theoretical calculation on effects of a high bulk modulus fluid upon improving hydraulic system performances are as follows.
1) In low pressure hydraulics less than about 20MPa, advantages in using high bulk modulus fluid are small. Because effective bulk modulus of the fluid is largely decreased by great influence of extrinsic factors (air bubbles and pipe wall expansion). However, enough pipe wall thickness and less air bubbles make it advantageous.
2) On the other hand, in high pressure hydraulics more than about 20MPa, advantages in using high bulk modulus fluid are great. Because the influence of extrinsic factors becomes less due to thick pipe wall and small air bubble size.
Table 1 shows effective bulk modulus ratio calculated from pipe wall thickness ratio s/d. It says that the lower available pressure is, namely thinner pipe wall, the larger decline of effective bulk modulus ratio with increasing of oil bulk modulus is.

Table 1 Effective bulk modulus ratio calculated from pipe wall thickness ratio

	s/d	0.01	0.05	0.10	0.15	0.20	0.25
	Pmax [MPa]	2.8	14.0	28.0	42.0	56.0	70.0
Koil [MPa]							
1,400		0.60	0.88	0.94	0.96	0.97	0.97
1,600		0.57	0.87	0.93	0.95	0.96	0.97
1,800		0.54	0.85	0.92	0.95	0.96	0.97
2,000		0.51	0.84	0.91	0.94	0.95	0.96

Kpipe = 210,000 MPa for St 35.4 steel pipe
SigmaMax = 140 MPa for St 35.4 steel pipe

A volumetric shrinkage rate of oil by compression is expressed with $\Delta P/K$ and a compression energy loss of oil by volumetric shrinkage is expressed with $\Delta P/(2K)$. For instance, when the mineral oil having bulk modulus of 1.4GPa is used under pressure of 28MPa, it is compressed by 2% and consequently elastic energy of 1% is preserved in oil, but the energy becomes loss without recovery.

Practically the loss is larger than that, in case of axial piston pumps with hollow pistons to reduce inertial weight, which often have the same dead volume as volume of the displacement has, their energy loss becomes 2%. Many pumps with adjustable stroke, especially when controlled in a constant pressure or constant power configuration, operate most of the time at high pressure and low stroke. In this case, the displacement volume is reduced, while the dead volume even increases. That means the compression energy losses easily reach levels of several times of the maximum input power rating. Theoretically compression energy contained in the dead volume in pumps can be recovered. In design practice, however, this can only be achieved to a very minor degree, as output pressures vary in a wide range, making exact fine-tuning is impossible.

In servo-hydraulic control circuits, performance is largely determined by two parameters: speed and stability. The technical equivalents for these are natural angular frequency ω_0 of a system's open control loop, and the damping factor D. For most applications, higher values of both are an advantage. As both ω_0 and D depend directly on the square root of the effective bulk modulus, increasing the bulk modulus of a fluid also increases servo performance, but three times faster servo valve is required. For instance, when the mineral oil having bulk modulus of 1.4GPa is replaced with the synthetic fluid having bulk modulus of 2.0GPa, speed and stability of the system are improved by 20% respectively.

As mentioned above, in theory, it is confirmed that favorable usage for high bulk modulus fluid can bring various improvement of hydraulic system performance in terms of energy saving, high response speed and precise controllability.

RESEARCH INTO HIGH BULK MODULUS FLUID

Measurement of bulk modulus [5]

Bulk modulus was calculated from measured high-pressure density data, as an isothermal tangential bulk modulus at 10, 20, 35 and 50MPa. A high-pressure density was measured by means of the plunger type high-pressure dilatometer (Figure 3) , the fluid was gradually pressurized from ambient pressure

to 200MPa at 40℃. The outer cylinder, with an outer diameter of 80.0mm and inner diameter of 30.0mm, is made of Ni-Cr-Mo steel. The plunger and plug are made of Cr-Mo steel. The plunger and plug each have a high pressure seal. It is comprised of an O ring, a back up ring and an anti-extrusion ring made of beryllium copper. The volume of the tested fluid at ambient pressure was 2ml. The volume of fluid in the chamber correspondent to the pressure is determined from the displacement of the plunger by using a linear gauge.
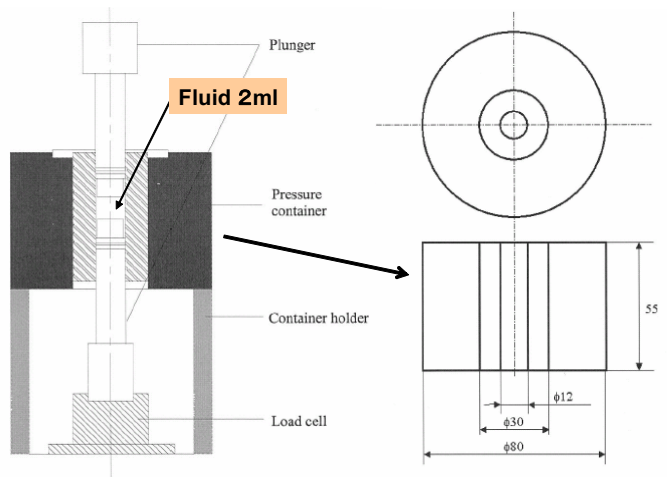
Figure 3 Apparatus for the measurement of fluid's bulk modulus

Figure 4, 5, 6 and 7 show bulk modulus of the conventional base oil (poly butene, mineral oil, 5P4E, and water-glycol type hydraulic fluid) measured by this method at 10, 20, 35 and 50MPa versus kinematic viscosity at 40℃ respectively. They agree with preceding literature data.

Candidate fluids synthesis

Before synthesizing the candidate fluids, following interim criteria which were bare requirements for base fluids were fixed.

Kinematic viscosity at 40℃ : less than 100mm²/s
Pour point : less than -20℃
Flash point : more than 200℃
Elements in molecule : C, H, O, N
(Containing no harmful elements)

Figure 4, 5, 6 and 7 show bulk modulus at 10, 20, 35 and 50 MPa versus kinematic viscosity at 40℃ of newly synthesized candidate fluids together with conventional oils respectively. It is proved that organic compounds having high bulk modulus as water level and also low viscosity do exist. We also have confirmed that fluids with high bulk modulus can be endowed with biodegradability.
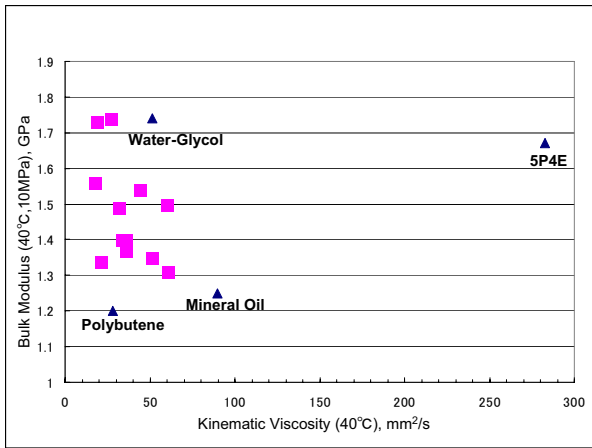
Figure 4 Bulk modulus at 10MPa
versus kinematic viscosity of conventional oil
and newly synthesized fluid

Figure 5 Bulk modulus at 20MPa
versus kinematic viscosity of conventional oil
and newly synthesized fluid
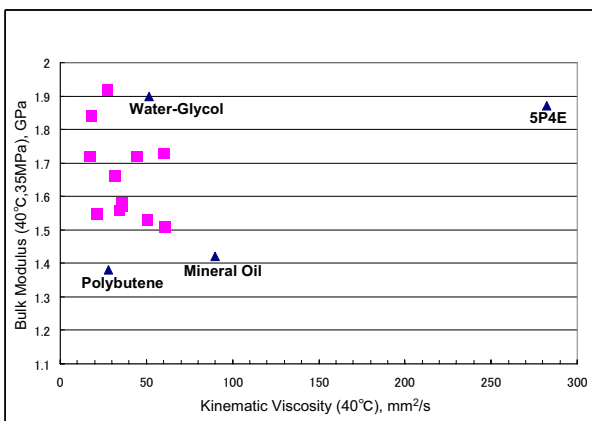
Figure 6 Bulk modulus at 35MPa
versus kinematic viscosity of conventional oil
and newly synthesized fluid

Figure 7 Bulk modulus at 50MPa
versus kinematic viscosity of conventional oil
and newly synthesized fluid

GAS SOLUBILITY OF HIGH BULK MODULUS FLUID

Measurement of gas solubility

As high bulk modulus fluids have small free volume of the molecules, gas solubility is expected to be low, and so nitrogen gas solubility was measured by means of the diffusion type gas-solubility apparatus at 23.5℃ (Figure 8) [6] [7].
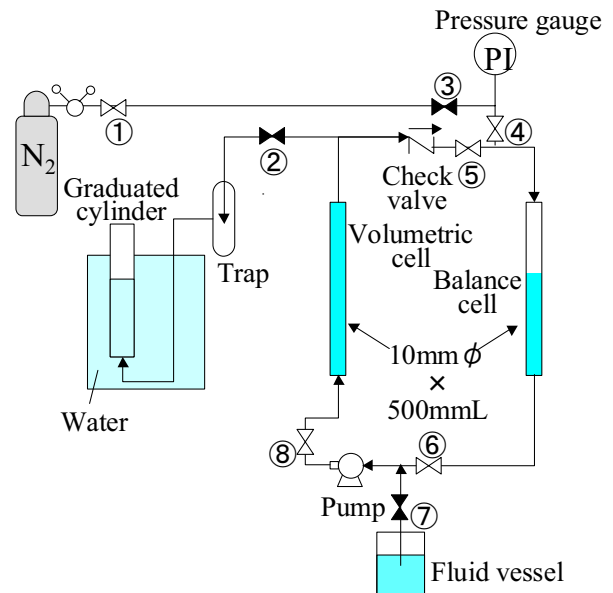
Figure 8 Diffusion type gas-solubility apparatus

After full volume of volumetric cell and half volume of balance cell were filled with test fluid by pump, nitrogen gas was introduced into the balance cell up to

2.5MPa or 4.5MPa. Then fluid was circulated through volumetric cell and balance cell until pressure became stable. After valve⑤ and valve⑧ were closed, valve② was opened gradually, and diffused gas volume was measured with graduated cylinder. Figure 9 shows measured nitrogen gas solubility of high bulk modulus fluids and mineral oil versus pressure.
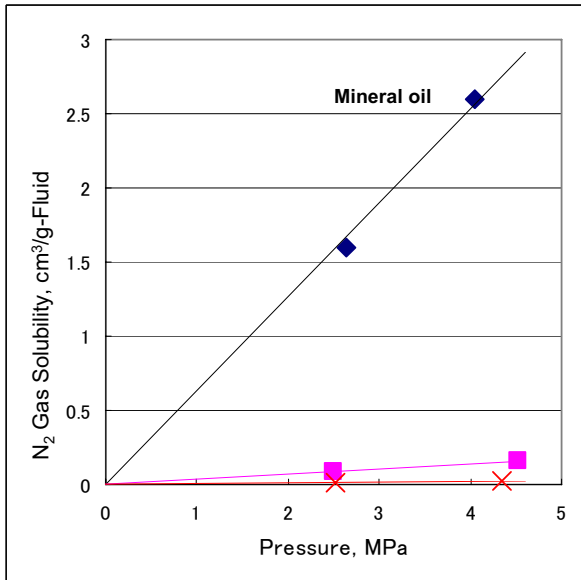
Figure 9 N_2 gas solubility versus pressure

Figure 10 shows bulk modulus at 50MPa of the fluids versus N_2 gas solubility at 0.1MPa, 20MPa and 50MPa calculated under the Henry's law.
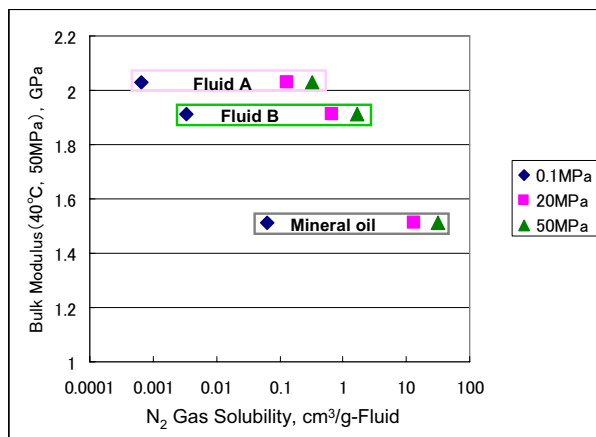
Figure 10 Bulk modulus versus N_2 gas solubility

As shown in Figure 10, high bulk modulus fluids have extremely lower gas solubility than that of mineral oil has.

That is to say, high bulk modulus fluids tend not to generate cavitation and tend not to generate air bubbles caused by gas solubility difference under high pressure and ambient pressure. In addition, generated air bubbles tend to separate from the fluids easily due to high density of the fluids.

High bulk modulus fluids are expected to have an excellent hydraulic performance under low pressure as well.

EXPERIMENTALLY FORMULATED FLUID

Table 2 shows an example of test result of experimentally formulated fluids which consist of two of candidates shown in Figure 4-7. Although there is room for improvements, it has enough performance compared to conventional biodegradable hydraulic fluid.

SUMMARY

1) There is a possibility that energy saving, response speed and precise controllability of the hydraulic system can be improved by using the high bulk modulus hydraulic fluid.
2) The organic compounds having high bulk modulus as nearly water level and also low viscosity with no harmful elements have been found.
3) Biodegradability and high bulk modulus can be compatible.
4) As high bulk modulus fluids have very low gas solubility and high density, they are expected to have an excellent hydraulic performance under low pressure as well.
5) Newly synthesized oily high bulk modulus fluids are expected to be base oils of new concept hydraulic fluids.

PLANS FOR THE NEXT STAGE

1) Optimization of base fluid compound
2) Verification of the effects on energy saving, response speed and precise controllability.
3) Study of possible applications which make the most of oily high bulk modulus fluids.

We sincerely hope that the development contributes toward upgrade of hydraulic systems.

REFERENCES

1. T.Tsubouchi, H.Hata, Y.Yoshida, "Optimization of Molecular Structure for Traction Fluid", Lubrication Science, 16(4), 393-403(2004)
2. E.E.Klaus,J.A.O'brien, "Precise Measurement and Prediction of Bulk-Modulus Values for Fluids and Lubricants", Transactions of the ASME, ser,D,86,469-474(1964)
3. I.B.Goldman, N.Ahmed, P.S.Venkatesan, J.S.Cartwright, "The compressibility of selected fluids at pressures up to 230,000 PSI", Lubrication Engineering, 27(10), 334-341(1971)
4. H.Theissen, H.Murrenhoff, "Determination of Effects of a High Bulk Modulus Fluid", IFAS/RWTH Aachen undisclosed report (2006)
5. N.Ohno,R.Mukai,M.Z.Rahman,K.Shibata, "Bulk Modulus and Poisson's Ratio of Traction Fluids", Proceedings of the 2001 International Symposium on the Tribology of Vehicle Transmissions, 9-12(2001)
6. Erwin Brunner, "Solubility of Hydrogen in Organic Solvents at 298.15, 323.15 and 373.15 K", J. Chem. Eng. Data, 30(3), 269-273(1985)
7. K.Kumanaga, S.Miyamoto, "Method for gas solubility measurement", Idemitsu Technical Report, 45(2), 182-189(2002)　(in Japanese)

Table 2 Test results of experimentally formulated fluid

General Properties	Unit	Test Fluid A	Test Fluid B (Biodegradable)	Conventional Biodegradable Fluid
Kinematic Viscosity(40℃)	mm^2/s	47.26	29.83	45.69
Kinematic Viscosity(100℃)	mm^2/s	7.128	7.208	8.767
Viscosity Index		109	220	175
Acid Number (Indicator Method)	mgKOH/g	0.03	0.22	0.84
Base Number (HCl Method)	mgKOH/g	–	0.29	0.06
Density(15℃)	g/cm3	1.0596	1.0594	0.932
Flash Point(COC)	℃	254	272	312
Pour Point	℃	−47.5	−50.0>	−50.0>
Foaming Test （1）	ml−ml	0−0	–	0−0
Foaming Test （2）	ml−ml	0−0	–	0−0
Foaming Test （3）	ml−ml	0−0	–	0−0
Copper Corrosion Test 100℃×3h		1(1b)	1(1b)	1(1b)
Tone		Brown	Yellow	Yellow
Form		Transparent Liquid	Transparent Liquid	Transparent Liquid
Color(ASTM)		–	–	L1.0
RBOT(1.75kg/cm2)	min	927	1030	123
Rust Preventing Test (Distilled Water) 60℃,24hr		No Rust	–	No Rust
ISOT 165.5℃×72h Properties After 72hrs				
Kinematic Viscosity(40℃)	mm^2/s	47.43	—	99.19
Acid Number	mgKOH/g	3.02	—	10.9
Viscosity Change Ratio	%	0.36	—	117.09
Increase of Acid Number	mgKOH/g	2.99	—	10.06

P1-15

ANALYSES OF ELECTRIC AND FLOW FIELDS IN CHARGE INJECTION TYPE OF ELECTROSTATIC OIL FILTER

Khanh Duong TRAN*, Yu KOJIMA**, Yoshimasa TERASHITA*** and Hideki YANADA****

* Department of Mechanical & Structural System Engineering
Toyohashi University of Technology
** Panasonic Storage Battery Co.,Ltd.
555 Sakaijyuku, Kosai, 430-0452 Japan
*** Fuji Machine Mfg. Co., Ltd.
19 Chausuyama, Yamamachi, Chiryu, 472-8686 Japan
**** Department of Mechanical Engineering
Toyohashi University of Technology
1-1, Hibarigaoka, Tempaku-cho, Toyohashi, 441-8580 Japan
(E-mail: yanada@mech.tut.ac.jp)

ABSTRACT

This paper presents experimental and numerical simulation results of the electric and flow fields in a charge injection type of electrostatic oil filter. A previous work has shown that flow is generated from the tips of the projections of the emitter electrode towards the smooth electrodes because of ion drag phenomenon and that the flow may detach part of the contaminant particles captured on the smooth electrodes and may be the principal cause of the saturation of the filtration speed at higher applied voltages and oil temperatures. In order to minimize the bad influence of the ion drag flow on the filter performance, it is important to be able to predict the flow in filters of various configurations by numerical simulation. Experimental results of the flow field are compared to numerical simulation results. In addition, electric potential distribution is measured and is compared between experiment and simulation. It is shown that the magnitude of the ion drag flow is increased with increasing applied voltage, is decreased with decreasing electrode spacing and is larger for negative charge injection than for positive charge injection. Similar results can be obtained by numerical simulations but the improvement of simulation accuracy is necessary.

KEY WORDS

Electrostatic oil filter, Charge injection, Ion drag flow, EHD simulation,

NOMENCLATURE

D_i : ion diffusivity

$\vec{E}$: electric field

f_x, f_y : Coulomb force

h : height of projection

$\vec{j}$: current density

p : pressure

q : charge density

s : electrode spacing

T : oil temperature

$\bar{u}$: magnitude of ion drag flow

V : applied voltage
$\vec{V}$: velocity
x, y : x and y coordinates
ε : permittivity
μ : viscosity
μ_i : ionic mobility
ϕ : electric potential
ρ : mass density
σ : conductivity

INTRODUCTION

An electrostatic oil filter can remove submicrometer-sized contaminants such as the oxidation products of additives from oils. By virtue of this characteristic, it has contributed to lengthening the lives of lubricating oils and to decreasing waste oil as well as failures of machines including hydraulic systems [1,2]. However, the filtration speed of electrostatic oil filters is slow and it usually takes a long time for a contaminated oil to be purified.

Yanada and his coworkers [3,4] have proposed a new type of electrostatic oil filter, named charge injection type of electrostatic oil filter. The new filter uses one or more set(s) of an emitter electrode with many sharp projections and two smooth plate electrodes. The application of a high DC voltage between the emitter and smooth electrodes enables electric charges with the same polarity as that of the emitter electrode to be injected from the tips of the sharp projections into oils. If the electric charges injected can be adsorbed on the surfaces of the contaminants, the magnitude of Coulomb force exerted on them becomes larger and the contaminants may be easily removed from oils. It has been demonstrated using many types of oil that the filtration speed is increased to a great or some degree [3,4].

Previous investigation [5] has made clear the effects of mechanical factors such as the applied voltage, electrode spacing on the filtration speed. In addition, it has been shown that the filtration speed is apt to be saturated at higher applied voltages and oil temperatures. Observation of particle motion using a two-dimensional filter model has shown that oil flow caused from the tips of the sharp projections by the ion drag phenomenon may detach the contaminant particles from the surface of the smooth electrodes and that the ion drag flow is the primary cause of the saturation of the filtration speed [5]. In addition, in the previous investigation, only electrostatic field simulations were made to discuss the effect of the mechanical factors. If the flow field as well as the electric field in a filter can be predicted by numerical simulation, it will be helpful to design a filter with a better performance.

The ion drag phenomenon has been applied to ion drag pumps, heat transfer enhancement, etc. Numerical simulations of ion drag flow have been made but comparison between measured and simulated flow fields has hardly been done so far.

In this paper, using a two-dimensional filter model, the flow field and electric field are measured. In addition, numerical simulations are conducted and simulation results are compared with measured ones.

EXPERIMENTAL APPARATUS AND METHOD

Test oils

Two types of hydraulic fluids and a multipurpose oil were used for flow field observation. In Table 1, the values of the conductivity and viscosity of the test oils at 313K (40°C) are shown. Porous plastic particles, of which specific gravity is 1.02 and of which size ranges from 75 to 150 μm, were mixed into the test oils to visualize the ion drag flow. It was confirmed that the plastic particles were hardly charged in all the test oils and that the particle motion represented the motion of oil.

Table 1 Physical properties of test oils at 313K
(σ : conductivity, μ : viscosity)

Oil no.	σ (S/m)	μ (mPa•s)
1	1.24×10^{-10}	39.4
2	4.71×10^{-13}	27.1
3	2.48×10^{-9}	36.48

Observation of flow pattern

A schematic of the experimental apparatus used is shown in Figure 1. A test oil in reservoir ① is fed into the filter model ⑤ by a gear pump ③ and then returns to the reservoir. The oil in the reservoir is stirred by a magnetic stirrer ② to avoid the gravitational sedimentation of the plastic particles. A DC voltage is applied by a high DC power supply ⑥. The magnitude of the applied voltage was changed from 8kV up to 14kV in order to evaluate the effect of the applied voltage. The polarity of the applied DC voltage can be changed. The flow rate was adjusted to 2.19×10^{-6} m³/s by an inverter ④. The temperature of the oil is controlled during the experiment by using a heater ⑦ and a thermoregulator ⑧. The motions of the particles were observed by a CCD camera ⑩ and the flow field was analyzed by a PIV technique using computer ⑪. In order to make the observation easy, approximately two-dimensional emitter electrodes were used as shown in Figure 2. The emitter electrodes are made of stainless steel and the rectangular projections were machined by laser beam. A transparent electrode was used as the smooth electrode for a plane light ⑨ to be penetrated

into the filter model, and is made of glass of which surface is coated by a conductive material (SnO_2). Emitter electrodes with different heights, h=5.5, 4.5 and 3.5mm, of the projection were made and the heights correspond to the electrode spacing of s=4, 5 and 6mm, respectively.

The magnitude of the applied voltage was varied from 8kV to 14kV while the electrode spacing was kept at s=4mm in order to investigate the effect of the applied voltage. When the ion drag flow was observed under different electrode spacings, the magnitude of the voltage was kept at 10kV. The oil temperature was kept at T= 313K.

① Reservoir	⑦ Heater
② Stirrer	⑧ Thermoregulator
③ Gear pump	⑨ Light source
④ Inverter	⑩ CCD camera
⑤ Filter model	⑪ Computer
⑥ High DC power supply	
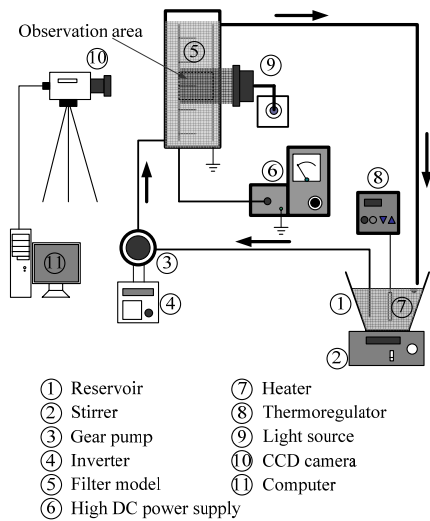
Figure 1 Schematic of apparatus used to observe ion drag flow

(Unit: mm)　Flow
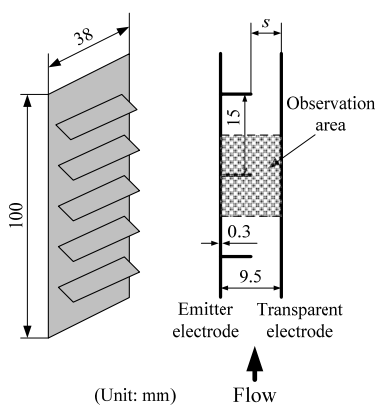
Figure 2 Schematic of two-dimensional emitter electrode

Measurement of electric potential distribution
In order to make clear the electric field between the electrodes, it is important to measure the electric potential distribution. Figure 3 shows a schematic of the apparatus used to measure the electric potential distribution. Because it takes a long time for the measured value at one point to be settled, the potential was measured only along the projection center line. A probe ⑥, which is made of stainless steel wire of 0.3 mm in diameter and is covered by a ceramic hollow tube of 1mm in outer diameter, is inserted between the electrodes and can be moved along the center line. The steel wire sticks out of the ceramic tube by 0.3mm as shown in Figure 3. The probe is connected to a circular plate ⑤ made of stainless steel. The electric potential of the circular plate is measured by using a surface potential meter ③ through a non-contacting probe ④. A DC voltage is supplied by a high voltage power supply ②.

In order to measure the electric potential distribution under different applied voltages, the electrode spacing was kept at s=5mm and the applied voltage was varied from 8kV to 14kV. The applied voltage was kept at V=10kV and electrode spacing was changed from 4 to 6 mm when examining the effect of the electrode spacing on the electric potential distribution.

① Oil tank
② High voltage DC power supply
③ Surface potential meter
④ Non-contacting probe
⑤ Circle plate
⑥ Probe
⑦ Probe tip
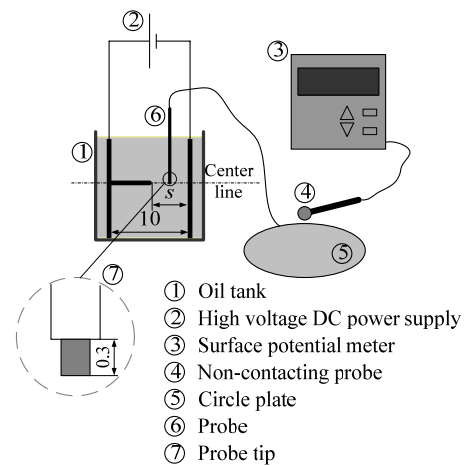
Figure 3 Schematic of apparatus used to measure electric potential distribution

NUMERICAL SIMULATION

In the simulations, two-dimensional, incompressible, steady, laminar flows are assumed. Because of relatively high viscosities of oils and relatively low flow velocities, the assumption of laminar flow is appropriate. Figure 4 shows the unit area to be analyzed. Taking the symmetry of the configuration into account, only a half of the observation area shown in Figure 2 was used for simulation. Followings are the basic equations that describe the flow field and electric field:

337

Continuity equation:

$$\frac{\partial u}{\partial x} + \frac{\partial v}{\partial y} = 0 \qquad (1)$$

Navier-Stokes' equation:

$$u\frac{\partial u}{\partial x} + v\frac{\partial u}{\partial y} = -\frac{1}{\rho}\frac{\partial p}{\partial x} + \frac{\mu}{\rho}\left(\frac{\partial^2 u}{\partial x^2} + \frac{\partial^2 u}{\partial y^2}\right) + f_x \qquad (2)$$

$$u\frac{\partial v}{\partial x} + v\frac{\partial v}{\partial y} = -\frac{1}{\rho}\frac{\partial p}{\partial y} + \frac{\mu}{\rho}\left(\frac{\partial^2 v}{\partial x^2} + \frac{\partial^2 v}{\partial y^2}\right) + f_y \qquad (3)$$

Charge conservation law:

$$\nabla \cdot \vec{j} = 0 \qquad (4)$$

Current density:

$$\vec{j} = q\mu_i \vec{E} + q\vec{V} - D_i \operatorname{grad} q \qquad (5)$$

Gauss' law:

$$\frac{\partial^2 \phi}{\partial x^2} + \frac{\partial^2 \phi}{\partial y^2} = -\frac{q}{\varepsilon} \qquad (6)$$

Coulomb force:

$$f_x = \frac{q}{\rho}E_x = -\frac{q}{\rho}\frac{\partial \phi}{\partial x} \qquad (7)$$

$$f_y = \frac{q}{\rho}E_y = -\frac{q}{\rho}\frac{\partial \phi}{\partial y} \qquad (8)$$

All the equations were discretized by a finite volume method and SIMPLE algorithm was used to solve the discretized equations.

In the numerical simulation of the ion drag flow, the injected charge density has to be given as a boundary condition but it cannot be theoretically known. In addition, it is known that at high electric fields, the ionic mobility does not obey the Walden's law and becomes significantly larger than that predicted by the Walden's law [6]. However, it has not been known how the ionic mobility depends on the electric field. In the simulations, the values of the injected charge density and the ionic mobility are found by trial and error for each test oil. It is assumed that charges are injected only from the surface of the projection tip (Figure 4) and that the amount of injected charges is proportional to the maximum electric field strength at the projection tip of electrostatic field.

RESULTS AND DISCUSSION

Examples of flow field obtained from experiment and simulation are shown in Figures 5 and 6, respectively. As can be seen from both figures, vortices are formed above and below the projection. The forms of the vortices are different to some degree between simulation and experiment but are relatively similar.
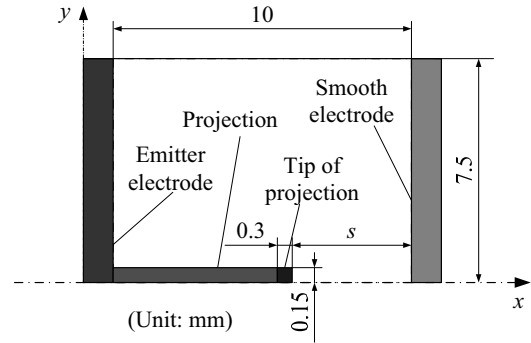
Figure 4 Example of unit area for numerical simulation

In order to evaluate the agreement between simulation and experiment, the velocity distribution in a slender rectangular region, shown in Figures 5 and 6, 0.5 mm above the projection is compared in Figure 7. It can be seen form Figure 7 that the maximum velocity is almost the same but that the velocity distribution in the simulation is not similar to that obtained by the experiment. The ion drag flow pattern is sometimes fluctuated with time and the electrode configuration is not exactly two-dimensional. In addition, the values of the injected charge density and the ionic mobility might not be necessarily appropriate. It is considered that those may be the causes of the difference between the experimental and simulation results.

Figure 8 and 9 show the effects of the applied voltage and the electrode spacing on the magnitude of the ion drag flow, respectively. In addition, comparisons between the experimental and simulation results are made. As described above, the flow is sometimes fluctuated and the measurement along or near the projection line was not easy. Therefore, the average magnitude of the velocity in the rectangular area shown in Figures 5 and 6 was used.

Figure 8 shows that the magnitude of the flow velocity increases with the increase in the magnitude of the applied voltage. The magnitude of the flow velocity increases almost linearly in the simulation. This is because the amount of the injected charge density was assumed to be proportional to the maximum electric field strength at the projection tip for electrostatic field.

Figure 9 shows that the increase in the electrode spacing brings about a larger ion drag flow velocity. The increasing tendency of the velocity in the simulation is the same as the experiment, but the magnitude is lower.
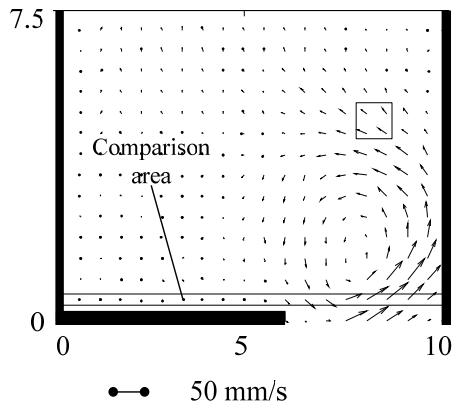
Figure 5 Example of measured flow field
(Oil 1, V=+10kV, s = 4mm, T=313K)
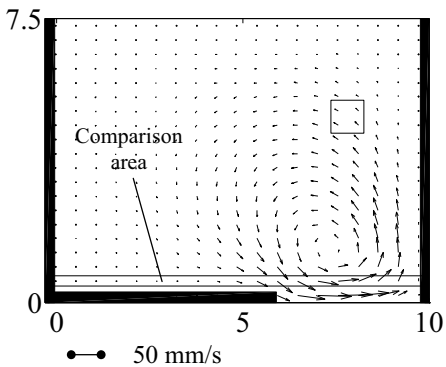
Figure 6 Example of computed flow field
(Oil 1, V= 10kV, s = 4mm, T=313K)
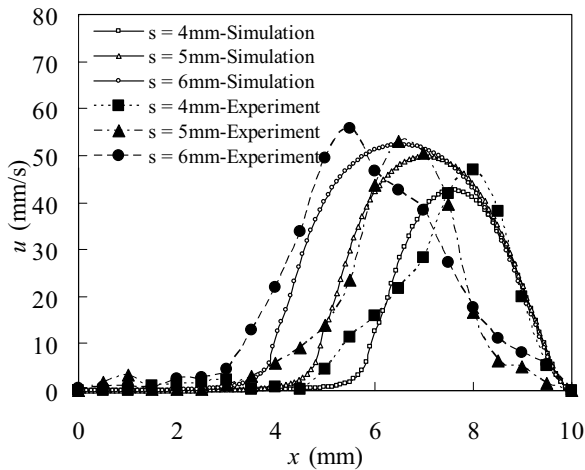
Figure 7 Comparison of velocity distribution between
experiment and simulation for oil 1
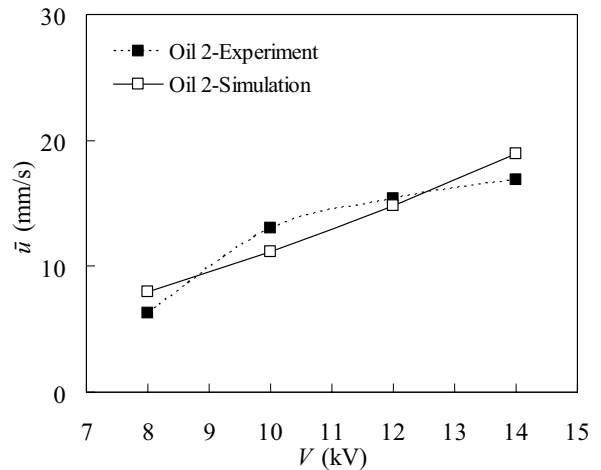
Figure 8 Effect of applied voltage on ion drag flow
(s=5mm, T=313K)
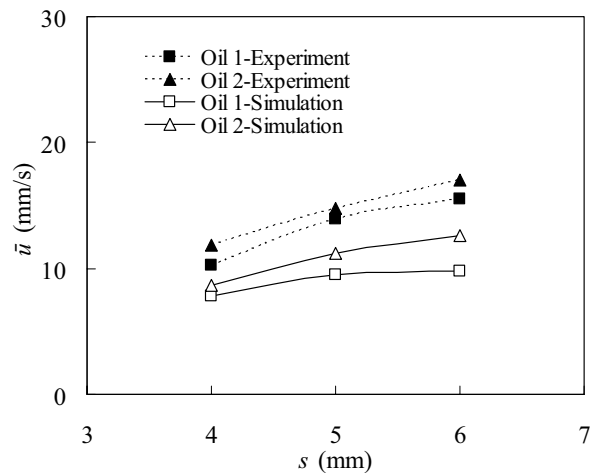
Figure 9 Effect of electrode spacing on ion drag flow
(V=+10kV; T= 313K)

The polarity of the charge injection also affects the ion drag flow as shown in Figure 10. The magnitude of the flow velocity increases with increasing applied voltage more strongly for the negative charge injection than for the positive one. It has been shown that negative charges are more easily injected than positive ones [4]. It has been pointed out that the ion drag flow may prevent contaminant particles from being captured on the smooth electrodes [5]. Therefore, when in particular injecting negative charges, some measures to minimize the bad influence of the ion drag flow have to be taken. This is the subject for a future study.

The results of the measurement and simulation of the electric potential distribution for different applied voltages for oil 2 are shown in Figure 11. The potential

is monotonously decreased from the projection tip to the smooth electrode for the simulation while bumps appear between the electrodes in the measured potential distribution curves. Such difference may arise from inappropriate values of the injected charge density and ionic mobility and the elucidation of the cause of the difference is also the subject for a future study. Similar potential distributions to Figure 11 were obtained for the other test oils.
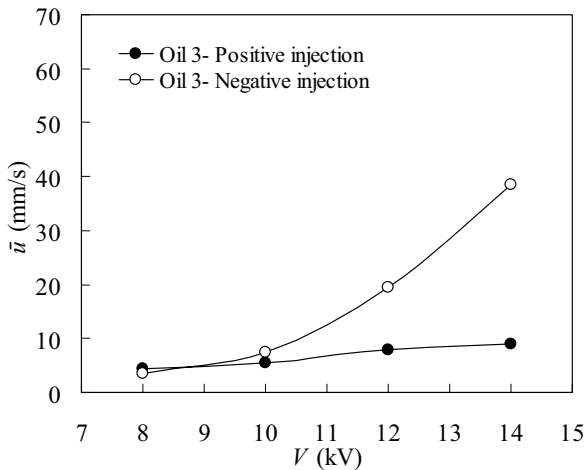
Figure 10 Effect of applied voltage polarity on ion drag flow (oil 3, s=5mm, T=313K)
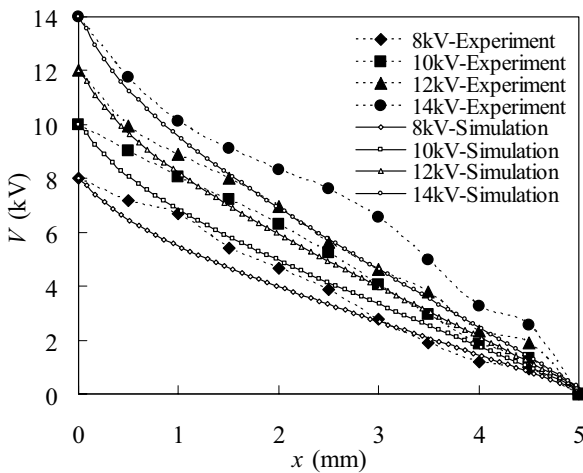
Figure 11 Effect of applied voltage on electric potential distribution (oil 2, s=5mm)

CONCLUSIONS

In this paper, ion drag flow field and electric field in a charge injection type of electrostatic oil filter were examined by experiment and numerical simulation. It was shown that the magnitude of the ion drag flow is increased with increasing applied voltage and decreased with decreasing electrode spacing and that those results can be obtained also by numerical simulation, though the simulation accuracy is not very good. In order to improve the simulation accuracy, the dependences of the injected charge density and the ionic mobility on the electric field strength need to be found out.

REFERENCES

1. Tobisu, T., Separation technology---electrostatic oil cleaner (in Japanese), J. Japan Soc. Lubric. Engrs., 1984, **29**-12, pp.881-884.(in Japanese)

2. Sasaki, A., Sasaoka, M., Tobisu, T., Uchiyama, S., and Sasaki, T., The use of electrostatic liquid cleaning for contamination control of hydraulic oil, Lubric. Engng, 1988, **44**-3, pp.251-256.

3. Yanada, H., Masuoka, T. and Yoshida, Y., Fundamental investigation of charge-injection type of electrostatic oil filter, The 1st Int. Conf. Manufacturing, Machine Design and Tribology 2005, Seoul, Korea (2005), CD-ROM.

4. Yanada, H. and Tran, K. D., Fundamental investigation of charge injection type of electrostatic oil filter, J. Advanced Mechanical Design, Systems, and Manufacturing, 2008, **2**-1, pp.119-132.

5. Tran, K. D. and Yanada, H., Fundamental Investigation of Charge Injection Type of Electrostatic Oil Filter (Effects of Mechanical Factors on Filtration Speed), J. Advanced Mechanical Design, Systems, and Manufacturing (2008), (submitted)

6. Felici, N. J., D.C. conduction in liquid dielectrics - A survey of recent progress (part I), Direct Current, 1972, **2**-3, pp.90-99.

P1-16

TEMPERATURE MEASUREMENT OF TRIBOLOGICAL PARTS IN SWASH-PLATE TYPE AXIAL PISTON PUMPS

Toshiharu KAZAMA*, Tadamasa TSURUNO**, Hayato SASAKI*

* Department of Mechanical Systems Engineering
Muroran Institute of Technology
27-1, Mizumoto-cho, Muroran, Hokkaido, 050-8585 Japan
(E-mail: kazama@mmm.muroran-it.ac.jp)
** Fuji Techno-Service Co., Ltd.

ABSTRACT

Temperatures of a swash plate, cylinder block, and a valve plate of swash-plate type axial piston pumps with a rotating cylinder block and a rotating swash plate were measured. Thermocouples were embedded underneath these parts. Hydraulic mineral oils with ISO VG22, 32, 46, and 68 and a water–glycol type hydraulic fluid with VG32 were used as test fluids. The maximum discharge pressure was 20 MPa and the maximum rotational speed was 28.3 rps. The inlet oil temperatures were specified as 293–313 K. At the atmospheric pressure to the maximum discharge pressure, the temperatures, flow rates, and the torque were measured. Results support the following conclusions: i) as the discharge pressure increased, the temperatures of the swash plate, cylinder block, and the valve plate increased in almost direct relation; ii) the cylinder block temperature at the bottom dead center of the pistons increased markedly; iii) the temperature increases using the water–glycol fluid were noticeably smaller than the rises using the mineral oils; and iv) the temperature rises became large for higher fluid viscosity and lower inlet oil temperature.

KEY WORDS

Fluid power, Tribology, Axial piston pump, Temperature, Experiment

NOMENCLATURE

N : Rotational speed
p_d : Discharge pressure
Q_d : Discharge flow rate
t : Temperature
t_d : Discharge oil temperature
t_{in} : Inlet oil temperature
Δt : Temperature rise = $t - t_{in}$
η : Total efficiency
η_v : Volumetric efficiency

Subscripts

A, B, C, D, E : Temperature measuring points on the swash plate
a, b, c, d, e : Temperature measuring points in the cylinder block
CB : Cylinder block
m : Average
SP : Swash plate
VP : Valve plate
α, β : Temperature measuring points on the valve plate
0 : Standard

INTRODUCTION

Hydraulic pumps and motors are expected to operate under high pressure and under a wide range of speed conditions to be compact, and to have a long useful life while maintaining high reliability and high efficiency. Higher power density forces severe operation at tribological parts of the pumps and motors, resulting in heat generation and seizure.

The need exists for a tool of optimum design and precise estimation including the influence of heat generation and thermal lubrication. For example, Wilson [1] pointed out that the optimum clearance based on the isothermal theory is insufficient to design displacement pumps.

Swash-plate type axial piston pumps offer high efficiency and high power density. Yamaguchi et al. [2–4] experimentally investigated the effects of operation conditions and working fluids on the performance and temperature of an axial piston type test pump, where the thermocouples were installed in the cylinder block. Ivantysynova [5] and Olems [6] measured the temperature distributions of the cylinder block around the cylinder bores using the test pump with installed thermocouples in the cylinder block. They have been given the temperature distribution of and compared with the thermohydrodynamic lubrication (THL) analysis. Subsequently, Wieczorek and Ivantysynova [7] developed simulation software for the swash-plate type axial piston pump. However, the specification of the test pumps and the condition of the experiment differed from those of actual hydraulic pumps.

On the other hand, for large-scale hydrodynamic bearings, many researchers have tackled the subject theoretically using THL theory [8, 9]. Furthermore, experimental studies of journal bearings have been performed by Mitsui et al. [10], Ferron et al. [11], Gethin and Medwell [12], and Wang et al.[13]; experimental studies of thrust bearings have been performed by Horner et al. [14] and Fillon et al. [15].

Kazama et al. quantitatively examined the thermohydrodynamic performance of circular pad hydrostatic thrust bearings [16] including the effect of the changes in physical properties of fluids as functions of temperature and pressure. Later, the authors experimentally measured the temperature of the swash plate and cylinder block of the piston pumps [17] under actual operating conditions. In this report, the temperatures of the valve plate as well as the swash plate and cylinder block of the piston pumps were measured. The results were compared and discussed in detail.

EXPERIMENTAL APPARATUS AND METHODS

The hydraulic circuit of the test rig [17] consisted of test pumps (a rotating type cylinder block and swash-plate rotating type axial piston pumps, with maximum discharge pressure of 21 MPa, and theoretical displacement of 10 ml/rev), a three phase induction motor (7.5 kW), an electric inverter, a strain-gage type torque sensor (20 N·m), flow-rate meters (4000 and 2000 l/h), a pressure transducer, thermistors, thermocouples, valves, an oil-cooler, and a reservoir. The locations of the thermocouples installed in the swash plate, cylinder block and the valve plate are illustrated respectively in Figs. 1–3. Figures 1 and 3 depict the rotating cylinder block type pump; Fig. 2 is the rotating swash-plate type pump. Pumps of two types were prepared with thermocouples installed in the stationary parts of each pump.
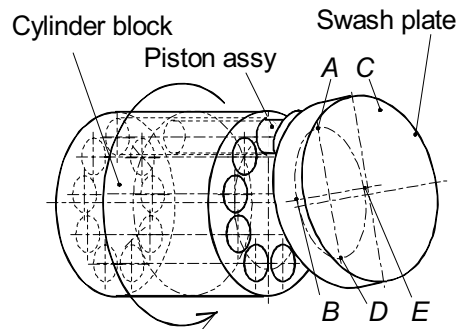
Figure 1 Location of thermo-couples installed in the swash plate (rotating cylinder-block type piston pump)
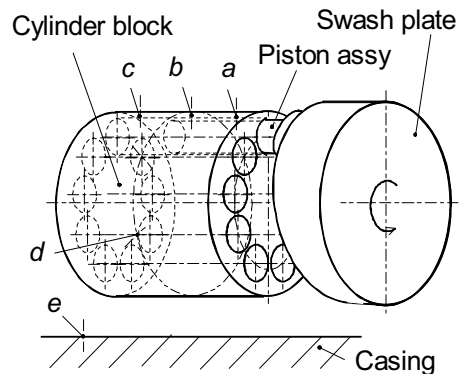
Figure 2 Location of thermo-couples installed in the cylinder block and casing (rotating swash-plate type piston pump)
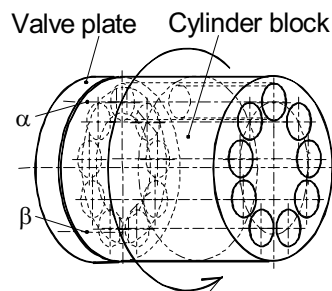
Figure 3 Location of thermo-couples installed in the valve plate (rotating cylinder-block type piston pump)

The induction motor drove the test pump through the torque sensor. Thermistors were placed at the pump inlet and the flow meters were installed in the discharge line and the drain line. The test oils were mineral oil type hydraulic fluids with ISO VG22, 32, 46 and 68 (designated as MO22, MO32, MO46 and MO68 respectively) as well as a water–glycol type hydraulic fluid with ISO VG32 (50% water content, WG32). The fluid densities were 866, 869, 872, 875, and 1069 kg/m^3; the kinematic viscosities at 40/100°C were 23/4.4, 33/5.5, 46/6.9, 68/8.7, 33/7.4 mm^2/s, respectively.

The experiment was conducted as follows: the oil temperature at the test pump inlet and the rotational speed of the pump were set; the discharge pressure was increased from atmospheric pressure to 20 MPa (maximum) by 1 MPa; then decreased from 20 MPa to the atmospheric pressure by 1 MPa. At each setting pressure, the discharge flow-rate, drain flow-rate, torque and temperatures were measured.

RESULTS AND DISCUSSION

Swash plate temperature
Figures 4 and 5 respectively depict the pump performance curve and the swash plate temperature using the rotating cylinder-block type test pump. In the performance curve of Fig. 4, it is readily apparent that the repeatability was good. In Fig. 5 the temperatures t_A through t_E increased in almost direct relation to the discharge pressure p_d. The temperature t_A at the measuring point of the swash plate was highest; it corresponded to the trapping part between the crescent-shaped discharge and suction ports.

Figure 6 depicts effects of oil types on the temperature rise Δt_A of the swash plate at point 'A' [17], where the rise $\Delta t_A = t_A - t_{in}$ was defined. The tendency of the temperature rise Δt_A through Δt_E was similar. For all oils tested, the rise Δt_A increased as the discharge pressure p_d increased. The higher the oil viscosity grade, the higher the rise of Δt_A.
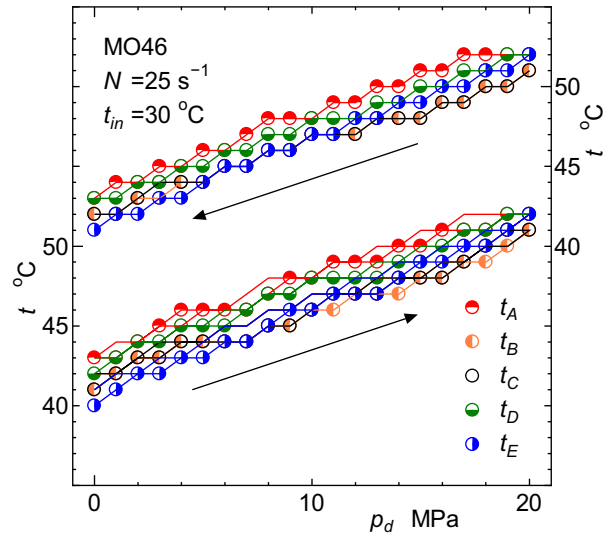
Figure 5 Temperatures of the swash plate (rotating cylinder-block type, MO46, N=25 s^{-1}, t_{in}=30°C)

Figure 4 Pump performance curve (rotating cylinder-block type, MO46, N=25 s^{-1}, t_{in}=30°C)
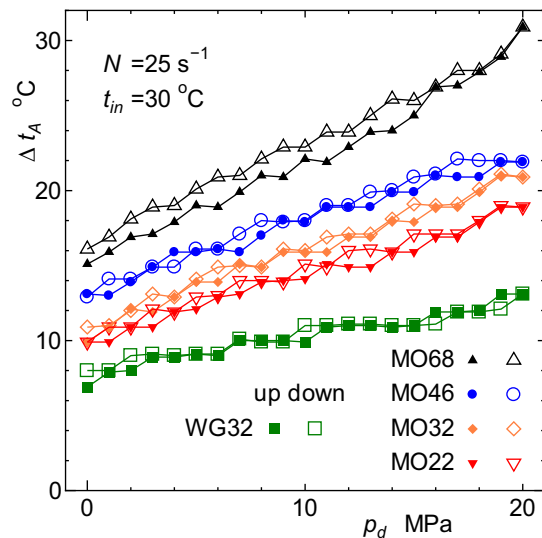
Figure 6 Comparison of swash-plate temperature rise Δt_A for test oils (rotating cylinder-block type, N=25 s^{-1}, t_{in}=30°C)

It is noteworthy that, from the atmospheric pressure to the maximum discharge pressure p_d=20 MPa, the rise Δt_A using the water–glycol hydraulic fluid (WG32) was only 13°C; it was lowest among the oils tested, but the rise Δt_A using MO68 was greater than 30°C.

Figure 7 portrays the effect of the rotational speed N on the swash plate temperature. In that figure, the lines are a guide to the reader's eye. As speed N increased, the temperature rise increased because of the viscous dissipation in the fluid film and frictional heating in metallic contact.

Cylinder block temperature

The rotating swash-plate type axial piston pump was prepared to measure the temperature around the cylinder bores of the cylinder block.

Figure 8 depicts temperatures at points 'a' – 'e' presented in Fig. 2 [17]. Comparing the temperatures t_a, t_b, and t_c on the axial direction of the cylinder bore, t_a was highest and t_c was lowest. Measuring point 'a' was located near the edge of the cylinder bore: the bottom dead-center of the piston. The piston was acted on by the moment-load. Therefore, the piston inclined in the bore and locally contacted at the edge of the bore. The reciprocating action of the piston results in higher solid friction and larger heat generation.

On the other hand, point 'c' was corresponding to the top dead-center of the piston. The part around point 'c' was cooled by suction of the low-temperature fluid and by delivery of the heated fluid.

Figure 9 depicts the effect of the clearance between the piston and the cylinder bore on the mean temperature, which rises $\Delta t_{m\,CB}$ (= (Δt_a + Δt_b + Δt_c) / 3). When the clearance was small (C_p = 19 μm, average) the rise in $\Delta t_{m\,CB}$ was low, most probably because the inclination of the piston in the cylinder bore was suppressed and frictional heating caused by the metallic contact was low.
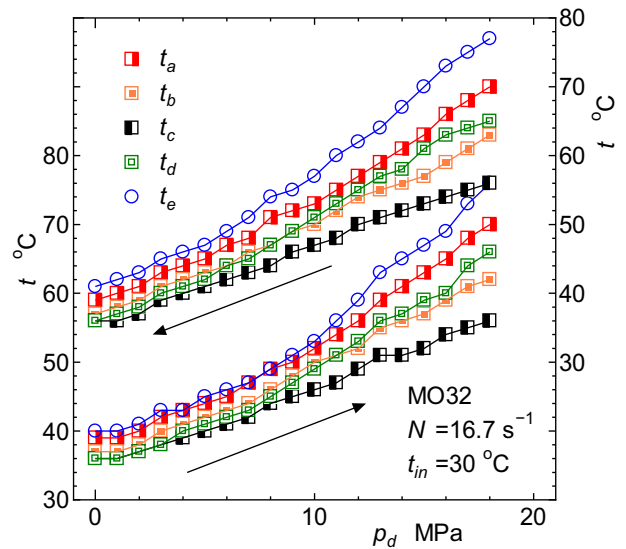
Figure 8 Temperature t of the cylinder block (rotating swash-plate type, MO32, N=16.7 s^{-1}, t_{in}=30°C)

Figure 7 Effect of rotational speed N on swash plate temperature rise Δt_A (MO46, t_{in}=30°C)
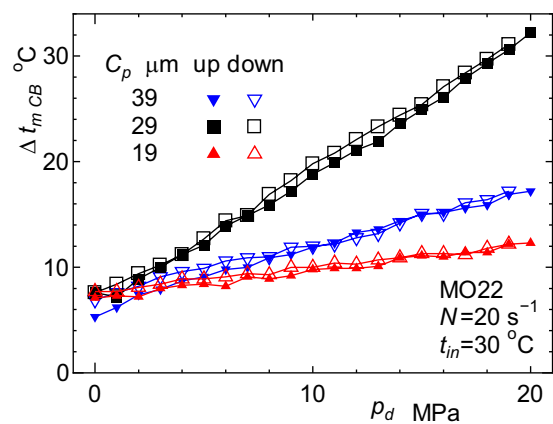
Figure 9 Effect of piston clearance C_p on the mean cylinder block temperature rise $\Delta t_{m\,CB}$ (rotating swash-plate type, MO22, N=20 s^{-1}, t_{in}=30°C)

Valve plate temperature

Temperatures t_α and t_β of the valve plate between the delivery to suction ports and the suction to delivery ports were measured respectively using the rotating cylinder-block type axial piston pump. As presented in Fig. 10, temperatures t_α and t_β increased larger than the discharge temperature t_d. Even if the temperature t_d elevated only 4°C from the inlet temperature t_{in}=30°C, the temperatures t_α and t_β rose higher and became greater than 20°C. The difference in temperatures t_α and t_β was not clearly shown.

Figure 11 shows effects of the inlet temperature t_{in} of the hydraulic fluid on the mean valve plate temperature rise $\Delta t_{m\,VP}$, where $\Delta t_{m\,VP}$ was defined as $\Delta t_m = (t_\alpha + t_\beta)/2 - t_{in}$.

As the temperature t_{in} decreased, the temperature rise $\Delta t_{m\,VP}$ was higher because the viscosity was higher at the lower temperature, which yielded the higher viscous dissipation in the film of the bearing and sealing part.

Figure 12 illustrates the effect of the rotational speed N on the temperature rise $\Delta t_{m\,VP}$ of the valve plate. From comparison to Fig. 7 of the swash-plate temperature rise, it is readily apparent that the speed N less affected the rise $\Delta t_{m\,VP}$ than $\Delta t_{m\,SP}$. The slippers run on the swash plate and would operate in lightly contacting mixed lubrication because the hydrodynamic action and hydrostatic action was able to support the load effectively, while the sliding parts between the valve plate and the cylinder block were strongly contacted and operated perfectly in mixed lubrication.

CONCLUDING REMARKS

Using both the rotating cylinder-block type and rotating swash-plate type axial piston pumps, the temperatures of all three main sliding parts between the swash plate and the slipper, the cylinder block and the pistons, and the valve plate and the cylinder block were measured: the pump performance was evaluated. The viscosity grade of the hydraulic fluids, type of fluid, inlet fluid temperature, discharge pressure, rotational speed, and piston clearance were selected as parameters, and the thermal lubrication characteristics of the pumps were examined experimentally under field operating conditions. The conclusions of this experiment are summarized as the following:

As the discharge pressure increased, the temperature of the swash plate, cylinder block and the valve plate increased almost in direct relation. As the rotational speed increased, the temperature rises were dependent on operating conditions.

The swash plate temperature at the switching parts corresponding to discharge and suction increased greatly. The cylinder block temperature at the bottom dead center of the pistons increased markedly. The valve plate temperatures at both the switching parts were almost the same. The sliding part temperature was higher than the discharge oil temperature.

The temperature rise using the water–glycol fluid was noticeably smaller than the increases achieved using mineral oils. The temperature increases became large as the fluid viscosity increased and the inlet oil temperature decreased.
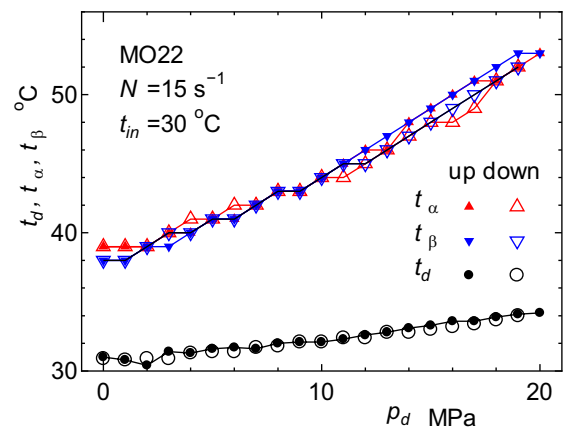
Figure 10 Valve plate temperatures t_α, t_β and discharge oil temperature t_d (rotating cylinder-block type, MO22, N=15 s^{-1}, t_{in}=30°C)
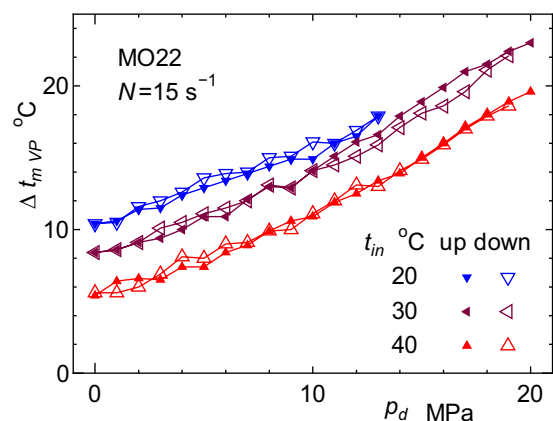
Figure 11 Effect of inlet oil temperature t_{in} on valve-plate temperature rise $\Delta t_{m\,VP}$ (rotating cylinder-block type, MO22, N=15 s^{-1})
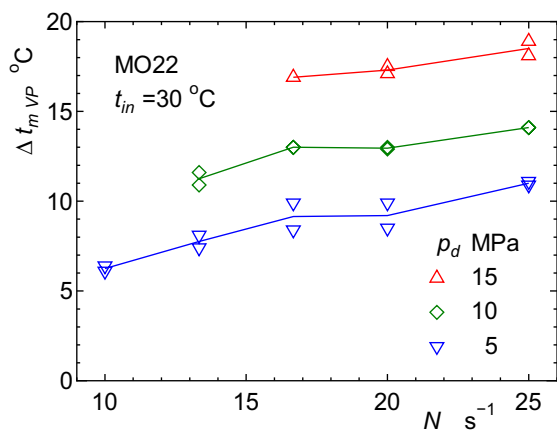
Figure 12 Effect of rotational speed N on valve-plate temperature rise $\Delta t_{m\,VP}$ (rotating cylinder-block type, MO22, t_{in}=30°C)

REFERENCES

1. Wilson, W.E., Design of Optimum Clearances in Positive-Displacement Pumps and Motors, Transactions of American Society of Mechanical Engineers, 1956, pp. 117−122.
2. Yamaguchi, A. and Tsuchimoto, M., Bearing Seal Characteristics of the Oil Film Between a Valve Plate and a Cylinderblock of Axial Piston Pumps (in Japanese), Journal of Japan Hydraulics and Pneumatics Society, 1982, 13−1, pp. 55−60.
3. Yamaguchi, A. and Mizuno, R., Bearing Seal Characteristics of the Film Between a Valve Plate and a Cylinderblock of Axial Piston Pumps, 2nd Report (in Japanese), Journal of Japan Hydraulics and Pneumatics Society, 1983, 14−6, pp. 426−432.
4. Yamaguchi, A., Sekine, H., Shimizu, S. and Ishida, S., Bearing/Seal Characteristics of the Film Between a Valve Plate and a Cylinderblock of Axial Piston Pumps, 3rd Report (in Japanese), Journal of Japan Hydraulics and Pneumatics Society, 1987, 18−7, pp. 543−550.
5. Ivantysynova, M., A New Approach to the Design of Sealing and Bearing Gaps of Displacement Machines, Proc. of 4th JHPS International Symposium on Fluid Power, Tokyo, 1999, pp.45−50.
6. Olems, L., Investigations of the Temperature Behaviour of the Piston Cylinder Assembly in Axial Piston Pumps, International Journal of Fluid Power, 2000, 1−1, pp.27−38.
7. Wieczorek, U. and Ivantysynova, M., Computer Aided Optimization of Bearing and Sealing Gaps in Hydrostatic Machines − The Simulation Tool CASPAR, International Journal of Fluid Power, 2002, 3−1, pp. 7−20.
8. Khonsari, M.M., A Review of Thermal Effects in Hydrodynamic Bearings, Part I: Slider and thrust Bearings, ASLE Transactions, 1986, 30−1, pp.19−25.
9. Khonsari, M.M., A Review of Thermal Effects in Hydrodynamic Bearings, Part II: Journal Bearings, ASLE Transactions, 1986, 30−1, pp. 26−33.
10. Mitsui, J., Hori, Y. and Tanaka, M., An Experimental Investigation on the Temperature Distribution in Circular Journal Bearings, Journal of Tribology, Transactions of American Society of Mechanical Engineers, 1986, 108, pp. 621−627.
11. Ferron, J., Frene, J. and Boncompain, R., A Study of the Thermohydrodynamic Performance of a Plain Journal Bearing Comparison Between Theory and Experiments, Journal of Lubrication Technology, Transactions of American Society of Mechanical Engineers, 1983, 105, pp. 422−428.
12. Gethin, D.T. and Medwell, J.O., An Experimental Investigation into the Thermohydrodynamic Behavior of a High speed Cylindrical Bore Journal Bearing, Journal of Tribology, Transactions of American Society of Mechanical Engineers, 1985, 107, pp. 538−543.
13. Wang, Y., Zhang, C., Wang, Q.J. and Lin, C., A Mixed-TEHD Analysis and Experiment of Journal Bearings Under Severe Operating Conditions, Tribology International, 2002, 35−6, pp. 395−407.
14. Horner, D., Simmons, J.E.L. and Advani, S.D., Measurements of Maximum Temperature in Tilting-Pad Thrust Bearings, Tribology Transactions, 1988, 31−1, pp. 44−53.
15. Fillon M., Bligoud J. and Frene J., Experimental Study of Tilting-pad Journal Bearings—Comparison with Theoretical Thermoelastohydrodynamic Results, Journal of Tribology, Transactions of American Society of Mechanical Engineers, 1992, 114, pp. 579−588.
16. Kazama, T., Yamaguchi, A. and Shimizu, S.: Thermoelastohydrodynamic Behavior of Hydrostatic Thrust Bearings (in Japanese), Journal of Japan Hydraulics and Pneumatics Society, 1990, 21−4, pp. 392−399.
17. Kazama, T. and Tsuruno, T., Thermal Lubrication Characteristics of Swash-Plate Type Axial Piston Pumps (Temperature Measurement of Swash-Plate and Cylinder-Block) (in Japanese), Transactions of Japan Society of Mechanical Engineers, Ser. C, 2004, 74−738, pp. 425−430.
18. Yamaguchi, A., Motion of the Piston in Piston Pumps and Motors (3rd Report, Experiments and Theoretical Discussion) (in Japanese), Transactions of Japan Society of Mechanical Engineers, Ser. B, 1992, 58−547, pp. 785−790.
19. Tanaka, K., Yoshisaki, Y., Nakahara, T. and Kyogoku, K., Relationship between Stiffness of Sliding Part End and Friction Characteristics in Oil Hydraulics Equipment (in Japanese), Transactions of Japan Society of Mechanical Engineers, Ser. C, 2002, 68−666, pp. 601−606.

P1-17

DESIGN AND TEST OF AN INTELLIGENT ENERGY EFFICIENT VALVE TO DECREASE PRESSURE PULSATION IN POWER STEERING SYSTEMS

Torsten VERKOYEN, Hubertus MURRENHOFF

Institute for Fluid Power Drives and Controls (IFAS)
RWTH Aachen University
Steinbachstraße 53, 52074 Aachen, Germany
(E-mail: torsten.verkoyen@ifas.rwth-aachen.de)

ABSTRACT

In a joint research project BMW and IFAS analyzed two well known hydraulic phenomena occurring in power steering systems, in order to reduce noises, that are caused by these phenomena.

The research project was subdivided into three tasks. The first task incorporated the analysis of the power steering system of a BMW 5 series passenger car. During this analysis an impulsive pressure pulsation phenomenon known as rattling as well as a periodic pressure oscillation called shuddering were measured. Both phenomena result in distracting noises within the passenger cabin and occur during certain different driving manoeuvres.

The second task included the construction of two test benches to reproduce rattling and shuddering independent from the car. A comparison of the measured data obtained by driving tests with the collected data from the test benches verified their functionality and accuracy. Another advantage of the test rig is that it provides easy access to the power steering system's components. Modifications can therefore be carried out in a short amount of time.

Finally an intelligent valve was designed and tested at the two test benches. The valve can detect the two different hydraulic phenomena without the need of sensor signals and without causing high pressure drops. In case of rattling the valve softens the return line of the power steering system and in case of shuddering the return line is hardened. A softer return line reduces pressure pulsations while a harder return line is insensitive to periodic pressure oscillations.

This paper describes a solution for two different hydraulic phenomena (rattling and shuddering) occurring in power steering systems. The solution is the integration of an intelligent energy efficient valve into the power steering system's return line, which changes the stiffness of the return line depending on the occurring phenomenon without affecting the sensation of the steering. The functionality of the presented valve is proven by means of the test results obtained from two test rigs designed to reproduce the described phenomena.

KEY WORDS

Power Steering System, Rattling, Shuddering, Pressure Pulsation

NOMENCLATURE

$delta\_phi$	:	angle at pinion gear	$pPst$	:	pressure at pump outlet
C	:	hydraulic Capacity	$pPLv$	:	pressure at steering valve inlet
F	:	external load on steering cylinder	$pTLv$	:	pressure at steering valve outlet
Fkb	:	load an cylinder by hydropulser	tT	:	tank temperature
nP	:	rotation speed of pump	ΔV	:	volume change
Δp	:	pressure change	ykb	:	rack displacement

INTRODUCTION

The reduction of ambient noise has gained great importance in modern automobile design. Following the achievements which have been made in eliminating the engine as a major source of noise, the latest trend in development focuses on ancillary components with a high power density. Among these components, hydraulic power steering systems prove to be a particularly challenging example. The typical design of a hydraulic power steering system is shown in Fig. (1).
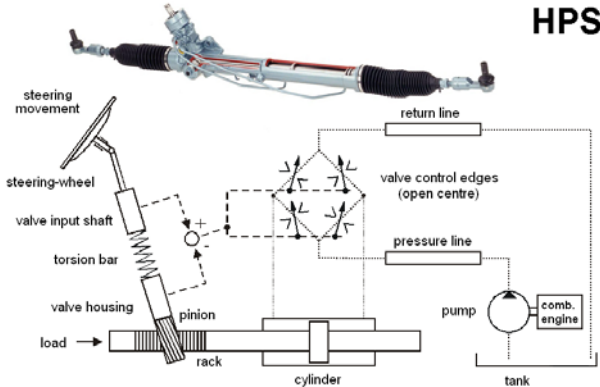
Figure 1 Hydraulic Power Steering System

The steering movements of the driver cause the torsion bar to induce a difference angle between valve input shaft and valve housing. This difference angle leads to twisting out the steering valve, which is designed as a hydraulic full-bridge, so that fluid enters from the pump trough the pressure line and steering valve into the respective cylinder chamber, causing overall movement of the steering cylinder.

The volumetric flow from the second cylinder chamber passes through steering valve and return line into the tank. The valve housing has a gear pinion attached to its end and is joined with the steering cylinder by means of a gear rack. Thus, the difference angle between valve input shaft and valve housing may be compensated by the axial movement of the steering cylinder. If at this point, an external load is applied to the gear rack however, the aforementioned mechanical joint between valve housing and steering cylinder can cause the valve to twist out, leading to increased pressure in the steering system. In this case the steering system is driven by the external load.

Well known accoustic phenomena in hydraulic power steering systems are rattling and shuddering. These are frequently misinterpreted by the driver as a malfunctioning of the steering system. Both accoustic phenomena, rattling as well as shuddering, are brought about by two different driving situations. Rattling, for instance, is caused by driving over an obstacle while moving the steering system at slow vehicle speeds (Figure 2).
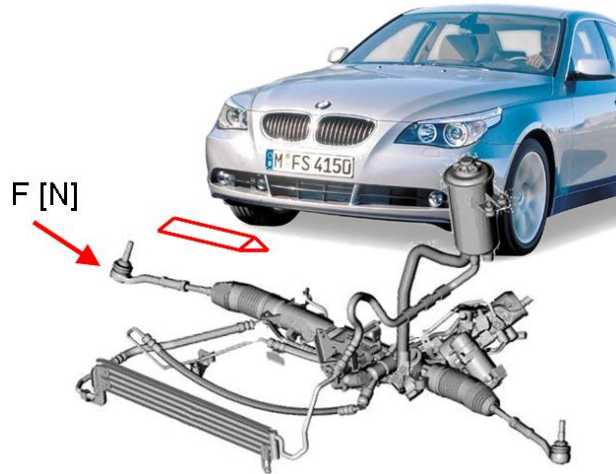
Figure 2 Driving situation for rattling

In daily traffic, kerbstones or floor sills in car parks constitute the most common form of such obstacles. The sudden load induced on the undercarriage by driving over the obstacle is conducted via the steering link onto the steering cylinder.

In the steering system, this incitement of load causes pressure and volumetric flow pulsations, which result in the characteristic oscillating rattling noise.

The phenomenon of shuddering on the other hand, is caused by moving the steering system while the brake system is engaged and the vehicle is at a standstill (Figure 3).

Figure 3 Driving situation for shuddering

Steering on smooth, painted car park floors can lead to a self induced stick-slip effect between tires and surface. As is the case during rattling, this incitement of load is transferred via the steering link onto the steering system. This means for the steering hydraulics, that shuddering causes pressure and volumetric flow pulsations, which are lower in frequency than those observed for the rattling phenomenon. However, next to the disturbing noise, shuddering can also be felt by the driver due to an oscillating torque acting on the steering wheel.

ANALYSIS OF THE ACOUSTIC PHENOMENA

In a joint research project conducted by BMW and IFAS, both accoustic phenomena were examined. One task consisted in the construction of adequate test benches, to reproduce rattling and shuddering in a test environment. Both test benches had to allow for improved accessability to the steering system and should enable an efficient analysis and assessment of possible solutions after the tests had been conducted. In order to realise adequate test benches, the relevant incitement parameters (external load, steering wheel angle, etc.) were determined during road tests.

Figure 4 shows the design of the rattling test bench. Different to the actual vehicle, the steering system's pump is powered by an electric motor. All other components, such as pressure lines, coolers, oil tanks, etc. are arranged corresponding to the test vehicle. The steering system is moved against a spring-mass system from a center position to the left, and thus pressure is induced on the system, which is equal to the pressure that had been measured in the respective cylinder chamber during a road tests, shortly before driving over the obstacle. The steering wheel is fixed in this position. A Hydropulser, consisting of a servo cylinder and a fast control valve, is inducing the same sudden load onto the system, which is equal to the data collected in the road test with the help of strain gauges attached to the steering links. Various sensors are installed on the test bench, which determine the relevant system parameters. The determination of pressures is established by sensors attached to the pump outlet (**pPst**), at the steering valve inlet (**pPLv**) and steering valve outlet (**pTLv**). Next to these, the load on the cylinder by the hydropulser (**Fkb**), the rack displacement (**ykb**) and the tank temperature (**tT**) were plotted. In addition, the angle at pinion gear (**delta_phi**) and the rotation speed of the pump (**nP**) were also monitored.

Because shuddering is determined by the contact between tire and surface, it is imperative that the test bench also includes a front axle corresponding to that of the test vehicle. The shuddering test bench is shown in figure 5. In analogy to the rattling test bench, the pump is also fed by an electric motor. Further components (lines, steering gears, cooler, oil tank, wheel suspension, etc.) corresponded to the design of the test vehicle. A manually adjustable piston served as braking system, in order to carry out steering manoeuvres with enganged front wheel brakes. To simulate the weight of the engine, a clamped-on cylinder is used in simulating the axle load of the test vehicle. The characteristic steering profile is simulated by a position-controlled electric motor, which is shown in the top left corner of figure 5. The profile, which is steered by the electric motor, had been determined beforehand in a road test and assigned on the test bench. A major task of the test bench consists in simulating the stick-slip effect, which occurs during road test, thus shuddering pads are installed between tires and machine base. To determine the various system parameters, the sensors which are applied in the rattling test bench are installed in similar manner. Thus, pressure, rotation speed, displacement and temperature can be measured.

With the help of the pressure readouts from both test benches, an analysis and identification of the accoustic phenomena can be accomplished.

The readouts from the pressure sensors at the rattling test bench are given in figure 6. The pressure curves clearly show an incitement of the steering system through the hydropulser at 0.07 seconds.

This incitement simulates the conditions experienced while driving the vehicle over an obstacle. In the return line of the power steering system, at first an increase of pressure up to ca. 12 bar is evident (**pTLv**), then a sharp drop to 0 bar; which is then followed by sharp pressure peaks. It is this drop to a 0 bar pressure level and the subsequent sharp pressure peaks - caused by a vibrating gear rack that sets the steering valve oscillating - that explains the characteristic rattling noise.

Figure 4 Test bench for rattling
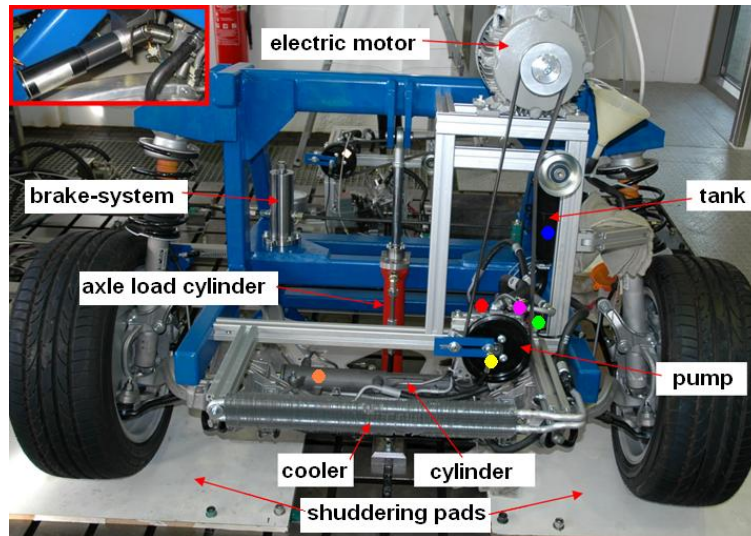
Figure 5 Test bench for shuddering
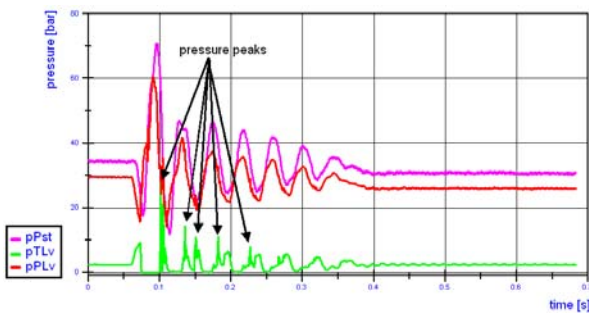
Figure 6 Pressure signals during rattling

The rattling experienced on the test bench constitutes a dampened vibration which fades away after a couple of cycle periods, exactly as found under road test conditions. Thus, next to the measured pressure pulsations, the oscillating steering valve has also to be responsible for the unsteady volumetric flow in the return line. The pressure drop to 0 bar, and the subsequent pressure peaks could even lead one to presume that cavitation is taking place. This initial assumption was confirmed in a test in which a visible section was integrated into the return line [1]. Figure 7 shows the flow channel in the visible section.
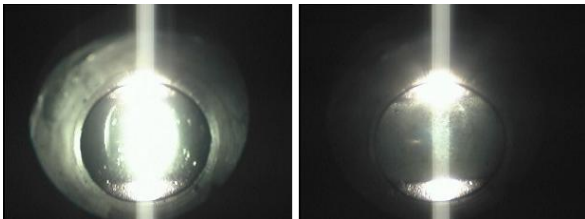
Figure 7 Cavitation bubbles in the return line

The left image shows the normal condition. The flow channel contains a transparent flow, which is illuminated by a source of light beneath the visible section. When the rattling phenomenon commences, the flow channel is temporarily darkened by cavitation

bubbles and the light source will only illuminate the upper and lower margin of the vision panel.

The pressure curves during shuddering are shown in figure 8.
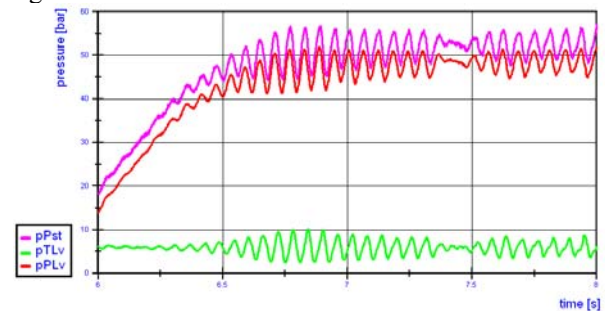
Figure 8 Pressure signals during shuddering

If the steering wheel is moved from its central position, the pressure in the steering system increases up to 40 bar. Next, the linear increase of system pressure is superimposed by a periodic pressure oscillation, which can be measured at the high pressure side of the steering valve (**pPst**, **pPLv**), as well as on the low pressure side (**pTLv**). The pressure pulsations during shuddering are significantly lower in frequency at 20 Hz than during rattling. Steering movements on critical surfaces lead to stick-slip effects on the tires that set the entire steering system pulsating, which is facilitated by an inappropriate front axle geometry and wide tires. Next to the disturbing noise, this periodic pressure oscillation leads to a fluctuation in steering wheel torque, which is experienced as a shuddering sensation by the driver.

TROUBLESHOOTING

To eliminate both noise phenomena - rattling and shuddering - an additional component was to be developed, which can be integrated into the existing steering system According to the results obtained from

the test benches, a reduction of pressure fluctuation in the steering system would correspond to a reduction in noise in the entire system, for rattling as well as for shuddering.

The integration of an additional component into the pressure line was not an option though, because resonators were already installed in the pressure line as a standard measure to reduce pump pulsation.

Possible solutions to reduce pulsation of power steering systems have already been thoroughly treated by [2, 3]. A solution for the return line has to meet the following requirements, set by BMW:

- The additional component is integrateable into the return line of the steering system
- Minimal drop in pressure under normal conditions
- The point of activation must be detected without electronic sensors
- To minimize pressure oscillation no external source of energy is used
- Simple design of the additional component

Prior to developing a new solution, existing production-model solutions were examined and their pros and cons analyzed. There are two orifices integrated into the production-model return line, which produce constant pressure drops. Because of these orifices, a back pressure is building up downstream from the steering valve, which counteracts the 0 bar pressure level in the case of rattling and thus antagonises the formation of cavitation. However, the increased pressure drop also creates an increase in the steering system's energy consumption.

This additional resistance also leads to a shift in the eigenfrequency of the entire system, thus shuddering is – compared to a return line without orifices – reduced but not eliminated. Thus, next to a higher pressure drop in the return line, the orifices are also responsible for a modified line capacity. The hydraulic capacity can be calculated, as shown in Eq. (1):

$$C(p) = \frac{dV}{dp} \qquad (1)$$

An increased pressure drop at a constant tube-chamber volume leads to a lower capacity and thus to a higher stiffness of the return line. In order to determine the consequences of a change in capacity on rattling and shuddering, a simulation model (as shown in figure 9) was built up in DSH*plus*.

In the simulation, the capacity of the individual tubes can be parameterised in the contact points of the hydraulic components, termed volume knots. The simulation results show, that no rattling will occur in a soft return line with a high capacity. In the case of shuddering however, it is imperative that the return line is hard and of little capacity, in order to prevent

self-induced pressure oscillations.
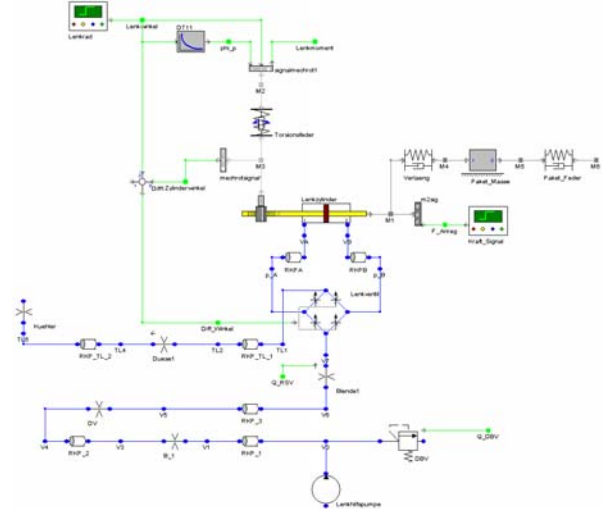
Figure 9 Simulation model of the steering system

This means, that the return line has to be designed with little capacity, which must be increased significantly by a control element if shuddering should occur. In order for the control element to be able to distinguish between rattling and shuddering, the decrease in pressure at the measuring orifice is used as a triggering signal.

Since rattling will cause an impulsive increase of volumetric flow through the system in contrast to shuddering, the decrease of pressure at the measuring orifice will be significantly higher, which also results in an increase of the load acting on the orifice. This increase of load can be used to activate the control element. A decisive advantage over the production-model solution is constituted by the fact, that the diameter of the measuring orifice can be dimensioned a good deal larger than the diameter of the original orifice plate. This is due to the fact that it does not have to function in building up back pressure.

The design of a first prototype is shown in figure 10.
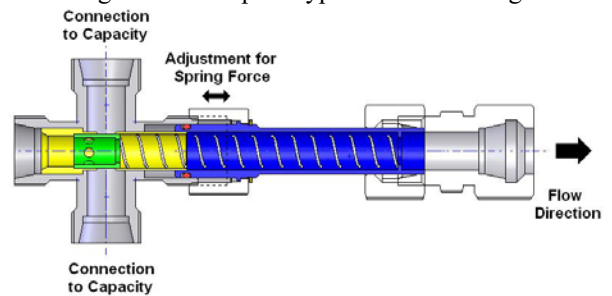
Figure 10 Sectional view of first prototype

The prototype is based on a cross-connection through which the fluid flows from the left side to the right. The top and bottom plugs of the cross-connection are connected with a capacity. The control element is designed as a slider, which generates a pressure drop, dependent on the volumetric flow. If the volumetric

flow rises up to a switch point, the slider moves to the right against the spring force and opens a connection to the capacity through its radial holes. The elasticity can be adjusted with a lock nut.

The capacities used are flat tubes made by ContiTech, which excel in their volumetric expansion ability. Design results for the rattling test bench with an installed prototype are shown in figure 11.
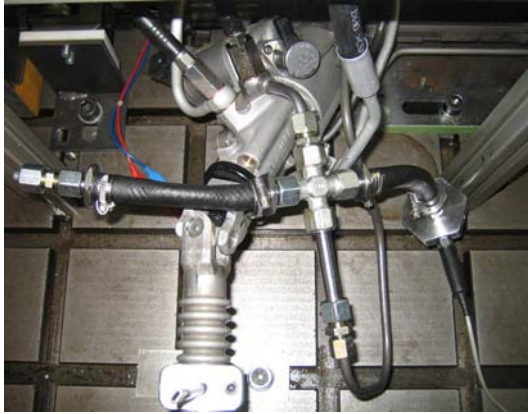
Figure 11 Prototype on the rattling test bench

Both flat tubes were attached as dead ends to the cross-connection. When rattling, there was clear evidence of breathing visible at the flat tubes, which was not the case during shuddering. This fact already indicates the functionality of the prototype valve. The plotted pressure signals verify it.

CONCLUSION

During rattling (see figure 12), there is no evident pressure drop and no pressure peaks caused by cavitation. The additional capacities integrated into the system by means of flat tubes, smooth the pressure curve in the return line.
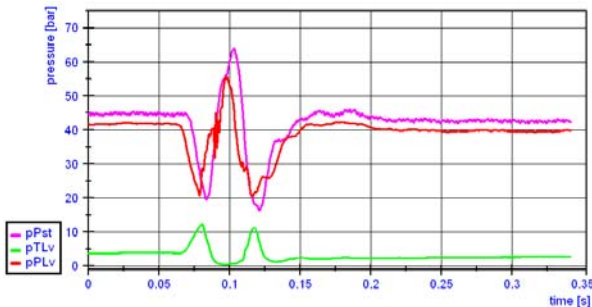
Figure 12 Pressure signals during rattling with integrated protoype

Although the incitement of the steering system by the impact of the hydropulser is clearly visible at 0.075 sec, there is no periodic oscillating pressure, as had been the case before (compare to figure 6). Acoustically, the impact of the hydropulser is now only audible as a dampened noise, which subsides immediately.

The prototype also has a positive effect on system behavior during shuddering (see figure 13). In this loading case, both capacities are shut off from the rest of the system by the closed valve slider. The return line has a lower capacity and thus a higher stiffness.
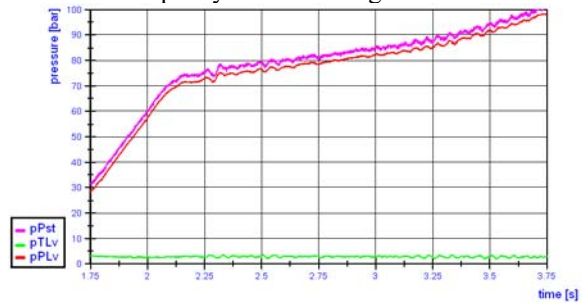
Figure 13 Pressure signals during shuddering with integrated protoype

Compared to the results of measuring shuddering in the standard production-model line (see figure 8), pressure pulsations in the return line could be significantly reduced. At the same time, the pressure amplitude was lowered on the high pressure side, downstream from the steering valve. Thus, a positive effect on steering wheel torque can be sensed by the driver, since no shuddering can be felt on the steering wheel while at a standstill on smooth surfaces.

By means of integrating the valve prototype into the return line of the steering system, a significant reduction of pulsating pressure during rattling as well as shuddering can be achieved. The reduction of pulsation leads to an elimination of the disturbing noise, which is clearly audible when the product-model line is used in the return line. In addition, the integration of the valve prototype leads to the removal of the two orifices of the product model line, thus leading to a reduction of the overall system pressure drop. This leads to increased fuel efficiency for the entire steering system. The radial arrangement of the flat tube around the steel tube would furthermore constitute an improvement in design, saving installation space.

REFERENCES

1. Verkoyen, T., Goenechea E., Goertz H., Bootz A., "Identification and Analysis of Pressure Pulsation to Enhance Driving Comfort in Passenger Cars Power Steering Systems", International Fluid Power Conference, 2006, Aachen, Germany

2. Rösner, J., "Power Demand of Load Adaptive Attenuation of Pressure Pulsation in Automotive Systems", International Fluid Power Conference, 2008, Dresden, Germany

3. Goenechea, E., „Mechatronische Systeme zur Pulsationsminderung hydrostatischer Verdränger-einheiten", PHD Thesis, 2007, RWTH Aachen University

P1-18

STUDY ON THE INSERTION LOSS CHARACTERISTICS OF SIDE BRANCH RESONATOR IN HYDRAULIC LINE

Takayoshi ICHIYANAGI*, Takao NISHIUMI*

* Department of Mechanical Systems Engineering, School of Systems Engineering
National Defense Academy
1-10-20 Hashirimizu, Yokosuka, Kanagawa, 239-8686 Japan
(E-mail: ichiyana@nda.ac.jp)

ABSTRACT

A quarter wavelength side branch resonator has been widely used as a reactive type silencer to attenuate pressure pulsation in hydraulic circuit. The structure of this conventional silencer is very simple and therefore it is a useful device in terms of cost efficiency. However, it is also known as a rather narrow frequency banded resonator that only attenuates the odd order harmonics of the pressure pulsation.
In this study, the attenuation performance of side branch resonator in the hydraulic line is examined numerically by changing the parameters such as the insertion location of side branch and the length of connecting pipe between the side branch and termination load of circuits. The level of attenuation is accessed by insertion loss which is defined as the ratio of overall amplitude harmonics of pressure pulsation with and without the side branch. The paper describes the fundamental principle of side branch and the mathematical model of insertion loss characteristics. Some calculation results for the insertion loss characteristics are carried out to show the influence of even order harmonics and the interaction of pump, termination load and all pulsation propagation characteristics of the circuit including side branch.

KEY WORDS

Hydraulic Silencer, Insertion Loss, Pressure Pulsation, Side Branch

NOMENCLATURE

a : Transfer matrix of upstream line of side branch
b : Transfer matrix of downstream line of side branch
c : Speed of sound
IL : Insertion loss
IL_{OA} : Insertion loss using overall pressure pulsation
L : Length of side branch
L_2 : Length between pump and side branch
L_3 : Length between side branch and termination load
P : Pressure pulsation
P' : Pressure pulsation with side branch
P_d : Discharge mean pressure

Q_m : Mean flow rate
Q_s : Source flow pulsation
r : Radius of pipe
s : Laplace operator
T : Transfer matrix of side branch
TL : Transmission loss
W_i : Incident energy of pulsation into silencer
W_i : Transmitted energy of pulsation through silencer
Z_2 : Impedance of downstream line of side branch
Z_c : Characteristics impedance of side branch pipe
$Z_{c.c}$: Characteristics impedance of connecting pipe
Z_T : Load impedance
Z_s : Source impedance of pump

θ : Pump rotational angle
v : Kinematic viscosity of working fluid
$\xi(s)$: Coefficient which express viscosity resistance
ρ : Density of working fluid

INTRODUCTION

It is well known that all positive displacement pumps generate a flow pulsation, which interacts with the system to produce pressure pulsation. This pressure pulsations are usually the primary source of system noise because they are very easily transmitted throughout the entire system and then excite the mechanical vibrations that generate audible noise. The pressure pulsation is a periodic function of time with a fundamental frequency and higher harmonics. Consequently, if the pump runs relatively constant in the operation cycle such as in a hydraulic excavator, an injection molding machine, etc., the harmonic frequencies of pressure pulsation would be almost constant. For this kind of hydraulic systems, a side branch resonator is often used as a hydraulic silencer [1]. This silencer is only a branch pipe installed in the main flow line. Since its simple structure and low cost, it is known as one of the most effective way to reduce pressure pulsation for an application which operates at a constant speed.

In this report, the attenuation performance of side branch resonator in the hydraulic line is investigated numerically by changing the circuit parameters such as the insertion location of the side branch resonator and the length of connecting pipe between the side branch resonator and termination load of circuits. The level of attenuation is accessed by the insertion loss which is defined as the ratio of the overall amplitude harmonics of pressure pulsation with and without the side branch resonator. The paper describes the fundamental principle of side branch resonator and the mathematical model of insertion loss characteristics. Some calculation results for the insertion loss characteristics are carried out to show the influence of even order harmonics and the interaction of pump, termination load and all pulsation propagation characteristics of the circuit including side branch resonator.

SIDE BRANCH RESONATOR

Figure 1 shows the basic structure of a side branch resonator and the schematic diagram of its resonance mode. Since the termination end of side branch resonator is closed and the connection end to the main line is opened, the standing waves of pressure and flow pulsation become the resonance mode at frequencies correspond to a quarter wave length and its odd number
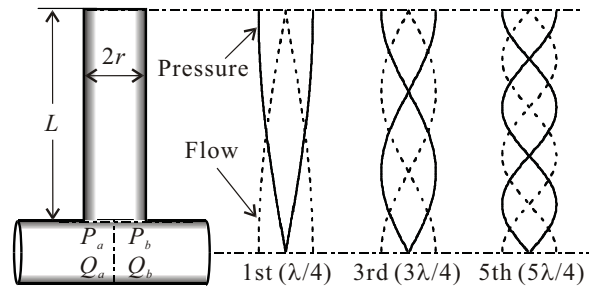
Figure 1 Basic structure of side branch resonator and its resonance mode
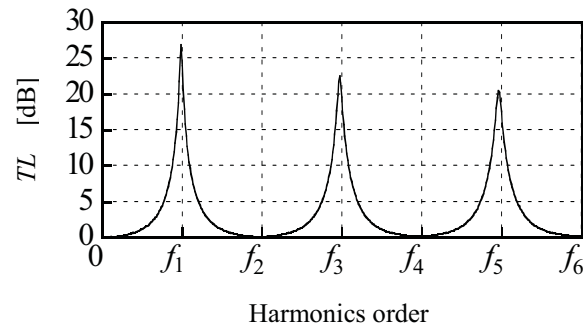
Figure 2 Transmission loss of side branch resonator

multiples. Therefore the pressure pulsation can be attenuated around these frequencies.

The wave propagation characteristics of side branch resonator can be expressed by Eq. (1) as a four pole Laplace transfer matrix, provided that the boundary of inlet and outlet is set by the dotted line in Fig.1.

$$\begin{bmatrix} P_a \\ Q_a \end{bmatrix} = \begin{bmatrix} 1 & 0 \\ \dfrac{1}{Z_c(s)} \tanh\left\{ \dfrac{\xi(s)s}{c} L \right\} & 1 \end{bmatrix} \begin{bmatrix} P_b \\ Q_b \end{bmatrix} \qquad (1)$$

where P_a and Q_a , P_b and Q_b are pressure and flow pulsation at inlet and outlet of side branch resonator respectively. Z_c is the characteristic impedance of the branch pipe and $\xi(s)$ is the complex coefficient for unsteady laminar viscous friction effect [2].

$$Z_c(s) = \frac{\rho c \xi(s)}{\pi r^2} \qquad (2)$$

$$\xi(s) \cong 1 + \sqrt{\frac{v}{r^2 s}} + \frac{v}{r^2 s} \qquad (3)$$

Once the transfer matrix of the side branch resonator is obtained, the transmission loss can be also derived from

354

this transfer matrix [3]. Transmission loss is a measure which express an attenuation performance of hydraulic silence itself and is defined as the ratio of the incident energy W_i to the transmitted energy W_t when there are no reflections in the downstream line of silencer. It is often used to compare the relative performance of silencers. With the transfer matrix elements of a silencer $T_{1.1} \sim T_{2.2}$, the transmission loss is described as the following equation.

$$TL = 10\log_{10}\left(\frac{W_i}{W_t}\right)$$

$$= 20\log_{10}\frac{1}{2}\left|\left\{T_{1.1} + \frac{1}{Z_{c.c}(s)}T_{1.2} + Z_{c.c}(s)T_{2.1} + T_{2.2}\right\}\right| \quad (4)$$

where $Z_{c.c}$ is the characteristic impedance of the connecting pipe (main line) of the side branch resonator. Moreover, the transmission loss of the side branch resonator can be expressed in Eq. (5) by substituting Eq. (1) for Eq. (4).

$$TL = 20\log_{10}\frac{1}{2}\left[\left[2 + \frac{Z_{c.c}(s)}{Z_c(s)}\tanh\left\{\frac{\xi(s)s}{c}L\right\}\right]\right] \quad (5)$$

Figure 2 shows the example transmission loss characteristics of the side branch resonator. It can be seen from this figure that the attenuation peaks are appeared at frequency f_1 that correspond to a quarter wave length resonance mode and its odd multiple frequencies. This indicates that the side branch resonator is only able to attenuate the harmonic components of pressure pulsation around these frequencies.

INSERTION LOSS CHARACTERISTICS

The insertion loss is the difference in amplitude of pressure pulsations in the downstream line with and without a silencer and it is the final criteria that shows how effective a silencer is.

$$IL = 20\log_{10}\frac{P}{P'} \quad (6)$$

where P and P' are the pressure pulsation without and with the silencer.
However the insertion loss involves the complex interaction of the wave propagation characteristics in both the upstream line including the pump pulsation source and the downstream line including the load as well as the silencer itself. Consequently, all these pulsation characteristics of hydraulic circuit have to be
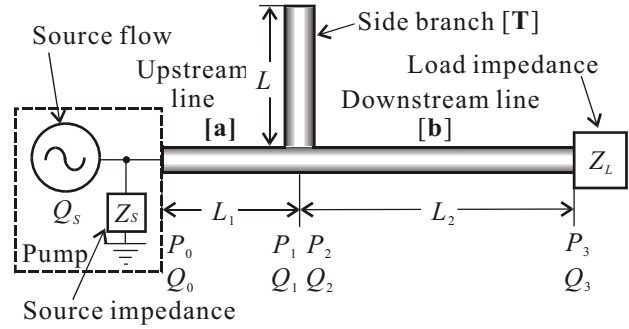
Figure 3 Hydraulic circuit represented by pulsation characteristics

taken into account of the insertion loss calculation. Figure 3 shows the test hydraulic circuit which is parameterized by the pulsation characteristics. Firstly the pulsation source of pump is characterized by the source flow Q_s and source impedance Z_s. In this pump model, the flow pulsation Q_s is generated at an exit of discharge port in parallel with the source impedance Z_s. the pulsation wave propagation characteristics for the upstream line, downstream line and side branch resonator are expressed by the transfer matrix [T], [a], [b]. The load impedance Z_L characterizes the termination of hydraulic circuit such as a control valve. Pressure pulsation at any point of the circuit can be expressed by these pulsation characteristics. For example, P_3, where is the possible highest pulsation point because it is just in front of the load, is obtained by the following equation [4].

$$P_3 = \frac{Z_L Z_S Q_S}{(b_{1.1}Z_L + b_{1.2})\{(a_{1.1} + a_{1.2}Z_S) + (a_{1.2} + a_{2.2}Z_S)\}} \quad (7)$$

where $a_{1.1} \sim a_{2.2}$ and $b_{1.1} \sim b_{2.2}$ are the elements of transfer matrix [a] and [b]. The pressure pulsation at the same point with the side branch resonator P_3' is also expressed by Eq. (8).

$$P_3' = Z_2 Z_L Z_S Q_S / [(b_{1.1}Z_L + b_{1.2})\{(a_{1.1} + a_{2.1}Z_S)$$
$$(T_{1.1}Z_2 + T_{1.2}) + (a_{1.2} + a_{2.2}Z_S)(T_{2.1}Z_2 + T_{2.2})\}] \quad (8)$$

where $T_{1.1} \sim T_{2.2}$ are the transfer matrix element of [T] and Z_2 is the entry impedance of the downstream line of side branch resonator, which is shown as follows

$$Z_2 = \frac{P_2}{Q_2} = \frac{b_{1.1}Z_L + b_{1.2}}{b_{2.1}Z_L + b_{2.2}} \quad (9)$$

It must be borne in mind that these equations for

355

insertion loss refer to only one frequency because they are all dependent on frequency.

As is already shown in Fig.2, the side branch resonator is a relatively narrow banded hydraulic silencer which has the attenuation ability around the fundamental frequency and its odd harmonic frequencies. Therefore, the insertion loss for these interested harmonic frequencies (the fundamental and odd harmonics only) have been focused to evaluate the performance of the side branch resonator. In this report, all harmonic components of pressure pulsation including even number harmonics are taken into consideration of the side branch resonator performance so that a real attenuation performance (i.e. amplitude of a peak to peak pulsation) can be assessed. In order to achieve this, an overall value of pressure pulsation is used in the insertion loss instead of each harmonic component in Eq. (6). The overall pressure pulsation is defined as the square root of the sum of the squares of all the harmonic components and the insertion loss using the overall pressure pulsation can be described in Eq. (10).

$$IL_{OL} = 20\log_{10} \frac{\sqrt{\sum |P|^2}}{\sqrt{\sum |P'|^2}} \qquad (10)$$

SIMULATION AND CONSIDERATIONS

Simulation condition

For the hydraulic circuit such as a construction machine, the side branch resonator is typically installed close to a pump discharge port. Then the flexible hoses or steel pipes are the elements that connect the pump to the termination element such as a control valve of actuators. In this report, the insertion loss characteristics of side branch resonator for this hydraulic circuit are examined by the simulation work. The basic configuration of the hydraulic circuit is already shown in Fig.3. In this simulation, an axial piston pump (displacement: 23 cc/rev., number of piston: 9) is selected as the pulsation source and the steel pipe is used for the pipe element to connect a loading valve to the pump. The side branch resonator is also considered to be the same steel pipe made.

The pulsation source characteristics of the pump used in this simulation are shown in Fig.4 and Fig.5. These results are obtained experimentally from the '2 pressure / 2 systems' method [5]. The running condition of the simulation is set to as follows. The rotational speed of the pump is 1833 min^{-1} (the fundamental frequency of the pump induced pressure pulsation becomes 275 Hz) and the discharge mean pressure P_d is 10MPa. Figure 4 (a) and (b) show the time history waveforms of the source flow pulsation Q_s and its amplitude spectra. It should be noted that this source flow pulsation Q_s is
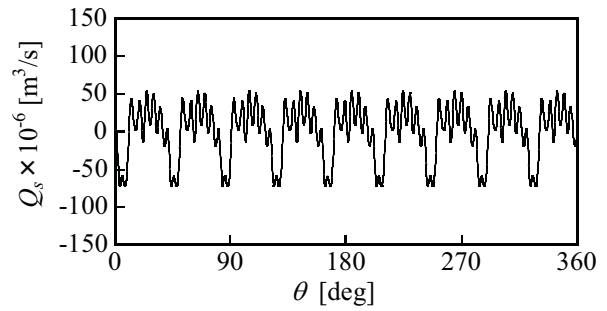
(a) Time history waveforms
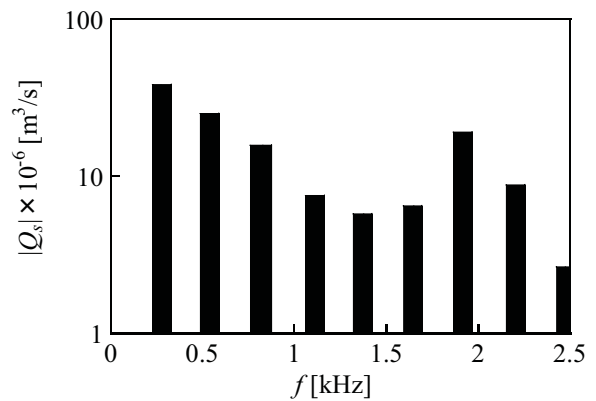
(b) Amplitude spectra

Figure 4 Source flow pulsation of pump
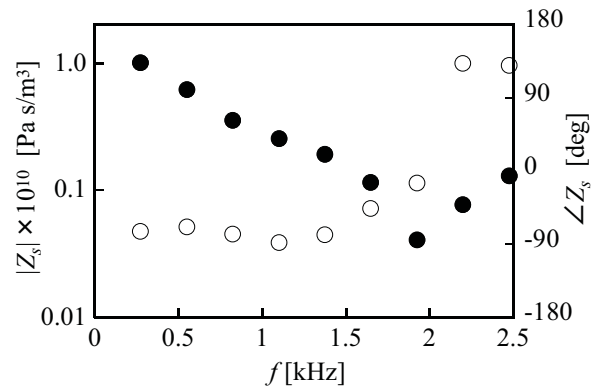
Figure 5 Source impedance of pump

generated at the exit of the pump discharge port. Figure 5 shows the source impedance of the pump. This value characterizes the internal (from the discharge port exit) impedance of the pump. It can be seen that an anti-resonance corresponding to the quarter-wavelength mode of the discharge port, at which the amplitude of the source impedance reaches a minimum and the phase

angle switches from -90 to +90, is apparent at around 2.0 kHz.

In this report, the insertion loss characteristics of the side branch resonator is investigated by changing the insertion location of side branch resonator and the length of the connecting element between the side branch resonator and the termination of circuit. For this reason, the steel pipe are chosen to the connecting elements since the wave propagation characteristics of the pipe is well known theoretically [6]. Provided that the flow in the steel pipe is the two-dimensional, laminar, viscous and compressible, the transfer matrix of the upstream line [**a**] can be described by the following equation.

$$[\mathbf{a}] = \begin{bmatrix} \cosh\left\{\dfrac{\xi(s)s}{c}L_2\right\} & Z_{c.c}(s)\sinh\left\{\dfrac{\xi(s)s}{c}L_2\right\} \\[2em] \dfrac{\sinh\left\{\dfrac{\xi(s)s}{c}L_2\right\}}{Z_{c.c}(s)} & \cosh\left\{\dfrac{\xi(s)s}{c}L_2\right\} \end{bmatrix} \quad (11)$$

The transfer matrix of the downstream line [**b**] can be also expressed in the same equation by substituting L_3 for L_2. The insertion location of the side branch resonator is determined by the length of the upstream line L_2. Generally the side branch resonator is installed near the pump exit or sometimes in the pump casing. In this work, the pipe length L_2 is varied from 0 to 0.5m. The length of the pipe, which connects the termination load element to the pump and is obtained as the sum of L_2 and L_3, is varied from 0.5 to 2.0m so as to examine how this line affects the attenuation performance of side branch resonator as well as the influence of insertion position. The radius of the pipe including the side branch resonator is r=10.5 mm.

Then the termination load of the circuit is assumed to be a load valve, which can be modeled as a resistive impedance load. The load impedance becomes

$$Z_L = \frac{2P_d}{Q_m} \quad (12)$$

where Q_m is the mean flow rate (Q_m=7.03×10⁻⁴m³/s). The working fluid in this simulation is the ISO VG32 hydraulic oil (ρ=875kg/m³, ν=3.2×10⁻⁶Pas, c=1400m/s).

Simulation results
Since the fundamental frequency of the pump induced pressure pulsation is 275Hz, the length of the side branch resonator is designed to L=1.27m in order to match the quarter wavelength resonance mode to the fundamental frequency. For this condition, the insertion loss using the overall pressure pulsation in Eq. (9) was calculated with varying two circuit parameters. Figure 6
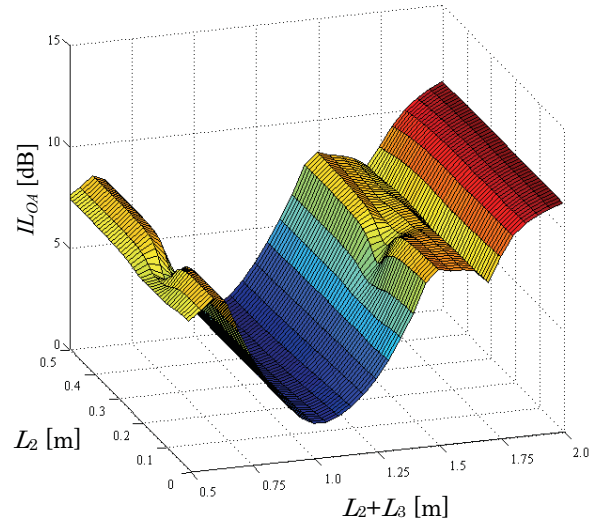
Figure 6 Insertion loss characteristics
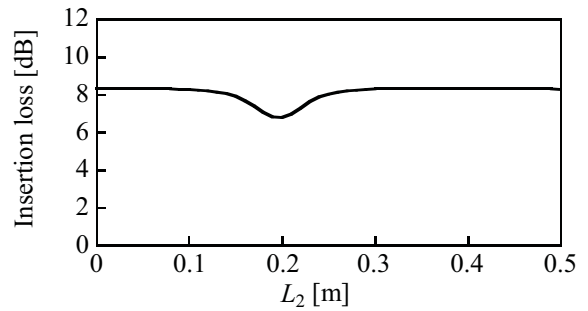
Figure 7 Insertion loss versus insertion location (L_2+L_3=0.6m)
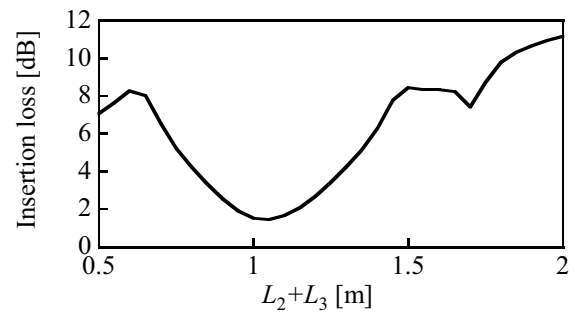
Figure 8 Insertion loss versus length of circuit (L_2=0.1m)

shows the insertion loss characteristics of the side branch resonator. The axis of L_2 is the insertion location of the side branch resonator from the pump exit and the axis of L_2+L_3 is correspond to the total circuit length where is from the pump to the termination loading valve. The typical characteristics of these insertion loss are extracted for each parameter and shown in Fig.7 and Fig.8. From these results, it is obvious that the insertion

357

loss characteristics using the overall pressure pulsation is significantly dependent on the length of the main circuit line, while it is little affected by the insertion location. It can be seen from Fig.8 that the difference in the insertion loss at the length of the circuit L_2+L_3=1m and L_2+L_3=1.5m becomes 6dB. This insertion loss characteristics is mainly due to the standing wave of pressure pulsation generated inside the circuit line.

Figure 9 explains how the standing wave contributes. This figure shows the amplitude of pressure pulsation for the fundamental and the second order harmonic frequency with the side branch resonator. This is so called the standing wave of pressure pulsation. The side branch resonator is installed at the pump exit (L_2=0m) and two circuit length conditions, L_3=1m and L_3=2m, are shown in this figure. It is clear that pressure pulsation of the fundamental frequency component is well attenuated by the side branch resonator for both circuit length conditions. On the contrary, the second order harmonic component remains the same as it is without the side branch resonator. The important thing is that the amplitude of this harmonic frequency is much bigger than the attenuated fundamental harmonic component as well as other harmonic components and this contributes dominantly to the insertion loss using the overall pressure pulsation. This is a reason why the insertion loss characteristics is not affected by the insertion location of the side branch resonator in this report. The harmonic component attenuated by the side branch resonator is rather negligible although the insertion location has a effect on the attenuation performance of the fundamental and the odd harmonic components. It should be mentioned that the insertion location should be close to the pump exit, because these is no attenuation effect on the upstream line of the side branch resonator.

If the second order harmonic frequency is close to the resonance mode of the circuit including the side branch resonator, this harmonic component become large as shown in Fig.9 at L_3=1m. Therefore the insertion loss performance become worse. It can be said that design of the circuit length is very important for the use of the side branch resonator, which is the narrow banded hydraulic silencer.

CONCLUSION

In this report, the attenuation performance of side branch resonator in the hydraulic line is investigated numerically by the insertion loss using the overall pressure pulsation. The following knowledge can be drawn from this work.

The insertion loss defined as the overall pressure pulsation with and without the hydraulic silencer is suitable to access the narrow banded hydraulic silencer such as a side branch resonator because it can express
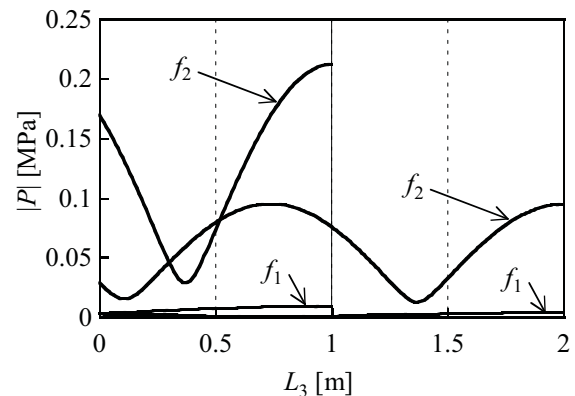
Figure 9 Standing wave of pressure pulsation for fundamental and 2nd order harmonic component (L_2=0.0 m, f_1=275 Hz)

all the harmonic components at once.

The even order harmonic components of pressure pulsation can be dominant since the odd order harmonic components are attenuated by the side branch resonator. Therefore the length of the connecting pipe between the pump and the load should be carefully designed in order to avoid the system resonance mode at the even number harmonic frequencies.

REFERENCES

1. Henderson, R., Quieter Fluid Power Handbook, 1981, BHRA Fluid Engineering.
2. Brown, F. T., Nelson, S. E., Step Response of Liquid Lines with Frequency Dependent Effects of Viscosity, Journal of Basic Engineering, Transactions of ASME, 1965, Series D, **87**-2, pp. 504-510.
3. Kojima, E., Ichiyanagi, T., Generation and Propagation of Fluid-borne Pressure Ripple in Fluid Power Systems Caused a Pump (2nd Report, Experimental Determination of Transfer Matrix Parameters of Hydraulic Silences and Assessment of its Attenuation Performance), Transaction of JSME, 1995, Ser. B, **61**-583, pp. 1014-1022.
4. Kojima, E., Ichiyanagi, T., Research on Pulsation Attenuation Characteristics of Silencer in Practical Fluid Power Systems, International Journal of Fluid Power, 2000, Vol.2, pp.29-38
5. Kojima, E., New Method for Experimental Determination of Hydraulic Pump Fluid-borne Vibration Characteristics (1st Report, Principle of New Method), Journal of Japan Fluid Power System Society, 1993, **42**-2, pp.269-274
6. Japan Society of Hydraulics and Pneumatics, Hydraulic and Pneumatic Handbook, Ohmsha, 1989, pp. 23-31.

P1-19

AUTONOMOUS EXCAVATION USING HYDRAULIC MOBILE MACHINE RETROFITTED WITH ELECTRONIC CONTROL SYSTEM

Otso KARHU, Jarno UUSISALO, Janne HONKAKORPI and Kalevi HUHTALA

Department of Intelligent Hydraulics and Automation
Tampere University of Technology
P.O.Box 589, 33101 Tampere, Finland
(E-mail: otso.karhu@tut.fi)

ABSTRACT

Autonomous functions are a common research topic in robotics. However, the robots typically have limited operating conditions and they can only handle relatively small loads. Many autonomous control concepts are applicable to actual construction machinery. The benefits would be considerable regarding efficiency, safety, and operator comfort. The research projects of this field have often led to systems with cost and complexity too high for most applications. This paper presents an implementation of a cost-effective distributed control system that is retrofitted to a small hydraulic excavator. The system can be used to perform simple operator assisting functions but also to develop autonomous excavation.

The hardware of the system consists of cost-effective joint angle sensors and a flexible microcontroller unit. Control schemes that produce autonomous functions are discussed and tested with the excavator. These include position controllers for conventional mobile proportional hydraulics. The aim is to find computationally simple but flexible algorithms for autonomous excavation. The results of the preliminary tests are presented. Future improvements are discussed.

KEY WORDS

Autonomous machines, Control, Excavator, Mobile hydraulics

NOMENCLATURE

CAN	:	Controller Area Network
MEMS:		Micro Electrical Mechanical System
PWM	:	Pulse Width Modulation
θ_1	:	Angle measured by boom inclinometer
θ_2	:	Angle measured by stick inclinometer
θ_3	:	Angle measured by bucket inclinometer
θ_{bucket}	:	Bucket joint angle
θ_{stick}	:	Stick boom joint angle
e_{tot}	:	Total position error
e_{slew}	:	Relative error in slew position
e_{boom}	:	Relative error in base boom position
e_{stick}	:	Relative error in stick boom position
e_{bucket}	:	Relative error in bucket position

INTRODUCTION

Hydraulic excavators are widely used in earth-moving tasks, for example digging and grading. The working conditions of the machine operator are often uncomfortable because of noise, vibration, and

repetitive nature of the tasks. Because demand for excavator operators is sensitive to economic fluctuations and training takes a lot of time, it is sometimes difficult to find skilled excavator operators for every construction project.

Intelligent control systems could ease all these problems by performing some tasks for the operator or even enabling autonomous excavation. Moreover, as hydraulic excavators are typically very heavy-duty machines, the extra cost of an intelligent sensor and control system is very little in contrast to the total cost of the machine. The recent price development of raw materials and, on the other hand, electronic components makes the ratio even smaller.

A small wheel loader with an excavator attachment is presented as an example in this paper. A cost-effective control system with operator assisting functions is installed and tested. The developed control system enables automatic bucket emptying and return. Preliminary results are presented and future work is discussed.

The basic control concept appears in several patents [5,6]. However, the patented systems are rather expensive and complicated. There has also been significant development in sensor technology since the patents have been published. Therefore, this research presents a more practical approach with modern components.

TEST EQUIPMENT

The test equipment consists of a small commercial wheel loader and an excavator attachment. The machine suits research use well: It is compact and it has mechanical and hydraulic structures similar to larger machines. A photograph of the machine is shown in Figure 1.

Small Wheel Loader
The wheel loader is modified from Avant Tecno 300 series [1]. The machine is skid steered and has a hydrostatic power transmission. The engine is a Kubota diesel with a power output of 15 kW. There is a variety of attachments available for the machine.

The original machine has mechanically operated valves which have been replaced by an electronically controlled stackable mobile proportional valve with six spools. In previous research a CANopen-based distributed control system has been developed. [7] Connecting the attachments is easy: There are quick couplings for hydraulic power and a multipole connector for electric supply and CAN.

Excavator Attachment
The excavator attachment is modified from Avant Backhoe 205. It has four hydraulic cylinders for slew, boom, stick, and bucket movements. The original mechanically operated valves have been replaced like the ones of the wheel loader. An electronic control unit

for the excavator has been designed. The control unit can be configured to compensate typical nonlinear characteristics of proportional valves. [4]
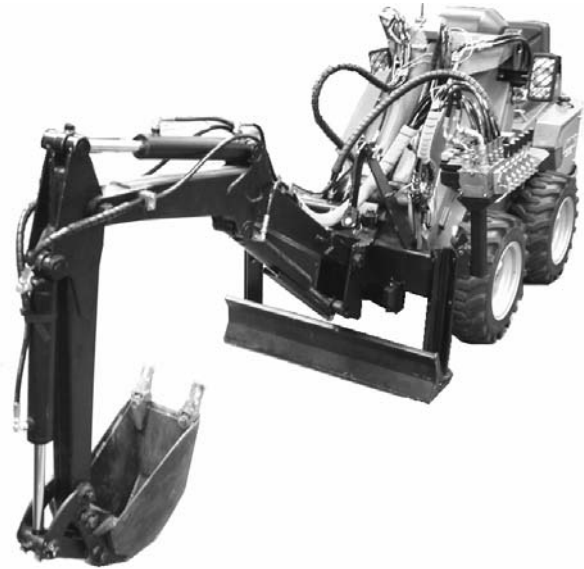
Figure 1 Wheel loader with excavator attachment

In previous research the control unit was programmed to perform simple closed-loop control of the slew cylinder with a linear cylinder position sensor [3]. Because the results were encouraging, more sensors have been added. In addition to the slew cylinder sensor, there are now three inclinometers measuring the absolute positions of the main boom, the stick boom, and the bucket. The arrangement is shown in Figure 2 where the boom, stick, and bucket inclinometers are marked with numbers 1, 2, and 3, respectively. The inclinometer module has been developed at the Department of Intelligent Hydraulics and Automation [2].
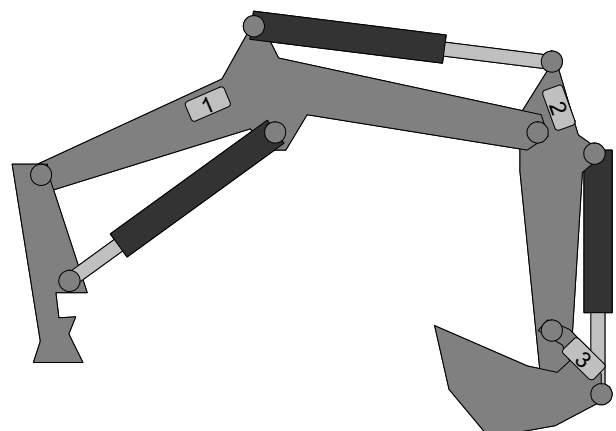
Figure 2 Inclinometer installations on excavator

The inclinometers have MEMS accelerometers which have a limited bandwidth. This should not, however, be a problem with this application. The inclinometers also have MEMS gyroscopes that can be enabled in case the bandwidth has to be extended. The inclinometers have a CAN interface so they are simply connected using 4-pole cables that supply power and communications.

Because there is no inclinometer installed on either the wheel loader or the excavator frame, the actual joint angle of the base boom can not be calculated. This is, however, not a problem in this study as long as the excavator is not pressed against the ground so that the entire machine is lifted.

CONTROLLER DESIGN

As the first step in developing an autonomous control system a simple closed loop controller for slew movement was used. The operator was able to store desired trajectory points and command the slew cylinder to follow them. Now the concept is extended to all four cylinders, which enables automatic emptying and return of the bucket, for example.

A block diagram of the excavator controller is shown in Figure 3. The valve control signals are produced with PWM outputs of the excavator control unit. The valves can be controlled directly with open loop signals. The signals are processed according to parameters that can be set using the CANopen interface.

The controller also approximates the total volume flow that is required from the wheel loader based on the sum of spool control signals of the excavator.
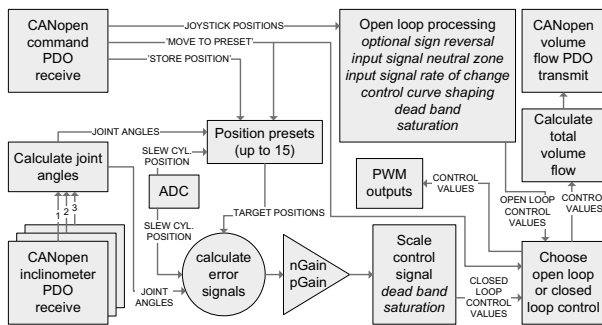
Figure 3 Excavator controller block diagram

Because the inclinometers measure the angle relative to gravity vector, the controller calculates the difference between two inclinometers over a joint to obtain the joint angle according to Eq. (1) and Eq. (2).

$$\theta_{bucket} = \theta_3 - \theta_2 \qquad (1)$$

$$\theta_{stick} = \theta_2 - \theta_1 \qquad (2)$$

Since there are only three inclinometers, the angle of the base boom is obtained directly from the signal of the inclinometer 1. This causes some offset if the wheel loader is not carefully levelled. However, if the wheel loader keeps steady, the offset is not a problem at this stage of the research because the trajectory points have the same offset when they are stored.

Because the inclinometers are based on accelerometers, there is some disturbance in the angle signals as the machine vibrates or the bucket is hit against the ground. Therefore, the maximum angular velocity of the signals is limited to 200 °/s. The effect of the rate limiter on the bucket angle is shown in Figure 4.
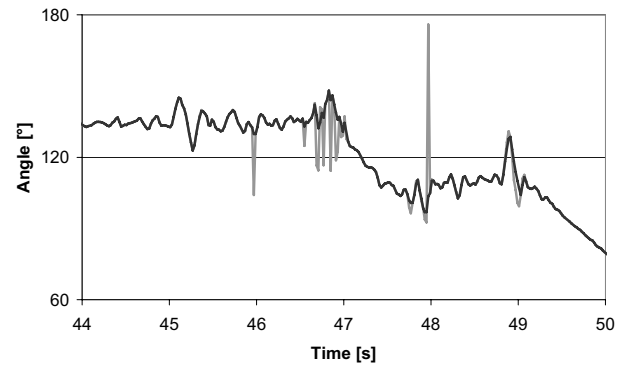
Figure 4 Effect of rate limiter on bucket angle signal

Up to 15 trajectory points can be stored during open loop control. When commanded, the controller will drive the excavator into a desired preset position. The position controller has an individual proportional controller for each cylinder. This typically results in a slightly curved bucket trajectory. There is, however, no path following controller. Therefore, the trajectory points have to be selected so that the order of the joint movements if insignificant. A total error signal is calculated according to Eq. 3.

$$e_{tot} = \sqrt{e_{slew}^2 + e_{boom}^2 + e_{stick}^2 + e_{bucket}^2} \qquad (3)$$

If the total error stays below a set limit a set settling time, the controller will switch back to open loop control. The parameters were set to 3 % total relative positioning error and 500 ms settling time. These limits were experimentally found suitable for the excavation application.

TEST SETUP

The control system of the wheel loader was configured to send a 'store position' command when a button on the user interface is pressed. Another button was configured to send a 'move to preset' command. The number of the

preset was set to cycle from 1 to 3 for both commands, which enabled bucket emptying and return functionality:

1. over digging point, ready to fill bucket
2. soil in bucket, boom over emptying position
3. stick boom and bucket at emptying position

A fourth trajectory point could be introduced if the soil is dug so deep that the base boom has to be lifted before sending the 'move to preset 2' command. Anyway, the three trajectory points are enough to prove that the concept works.

Because the hydraulic system of the wheel loader has a fixed pump, the control system of the wheel loader was also programmed to control the diesel engine according to the volume flow request from the excavator.

The gain parameters of the proportional controllers were tuned experimentally. The main problem is that the excavator frame is not very steadily supported. Therefore, the controller gains have to be quite small to prevent the wheel loader from moving on the ground.

RESULTS

The system was tested by first doing one excavation cycle manually and storing the required trajectory points. Figure 5 shows the joint angle signals during the manual excavation cycle. The vertical dash lines show the three trajectory points that are stored. Note that returning the excavator over the digging point is not shown.
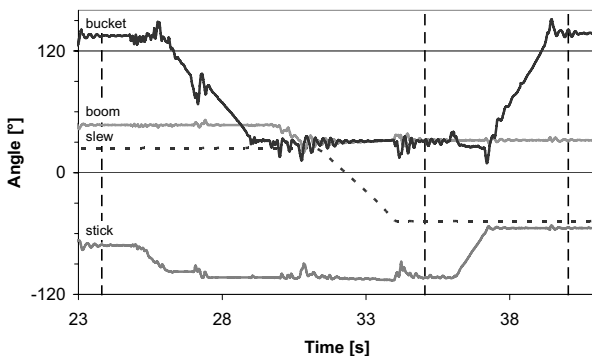
Figure 5 Manual excavation cycle

Between the stored points 1 and 2 the bucket is first filled using the bucket and stick cylinders and then moved over the emptying position using the boom and slew cylinders. Between the stored points 2 and 3 the bucket is emptied using the stick and bucket cylinders. Figure 6 shows an excavation cycle that includes the automatic emptying and return of the bucket. Grey background indicates manual control. The vertical dash lines indicate the instant when a 'move to preset' command is sent and the fixed lines indicate when the preset is reached. The preset number 3 is actually not

reached at all because the operator sends 'move to preset 1' as soon as the bucket has emptied at 80.5 s.
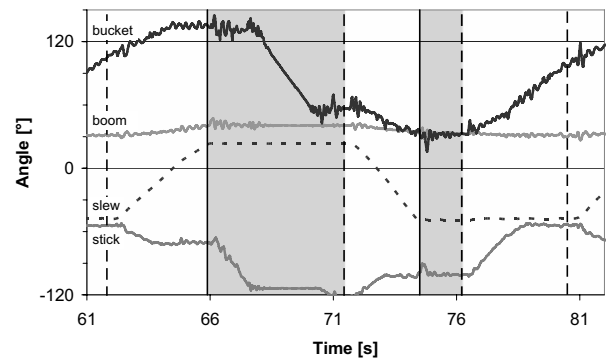
Figure 6 Excavation cycle with automatic emptying

CONCLUSIONS

Conventional mobile proportional valves and low-cost inclinometers can perform closed loop position control. The control software can be quite simple but there are several parameters to configure. The position controller can make excavation work easier and improve the efficiency of novice operators. The preliminary results of this paper could probably be further improved by choosing the controller gains, total error limit, and angular signal rate limits more carefully after thorough testing.

REFERENCES

1. Avant 300 series, 500 series, Avant Tecno Oy, Ylöjärvi, Finland.
2. Honkakorpi, J., CAN-bus based embedded inclinometer, Master's thesis, Tampere, Finland, 2007, 47 p. (in Finnish)
3. Karhu, O., Moya, J., Uusisalo, J. and Huhtala, K., Enabling autonomous functions on hydraulic excavator attachment, Proceedings of the SICFP, Tampere, Finland, 2007, pp. 35-45.
4. Karhu, O., Vilenius, J., Uusisalo, J. and Huhtala, K., Developing intelligent hydraulic excavator, Proceedings of the PTMC, Bath, UK, 2006, pp. 265-274.
5. Sutton, J. O., Computer controlled backhoe, US patent 4288196, 1981, 10 p.
6. Takayasu, I., Kazuo, O., Saburo, N., Michiaki, I., Toshiaki, H. and Kazuhiro, I., (Kabushiki Kaisha Komatsu Seisakusho), Semi-automatic hydraulic excavator, US patent 4377043, 1983, 6 p.
7. Vilenius, J., Raneda, A. and Huhtala, K., Characteristics of teleoperated skid steered mobile machine, Proceedings of the FPNI-PhD Symposium on Fluid Power, Terrassa, Spain, 2004, pp. 587-598.

P1-20

AUTOMOTIVE VARIABLE ENGINE VALVE LIFT MECHANISM CONTROLLED BY A HYDRAULIC 3-STEP ROTARY ACTUATOR

Yasukazu SATO*, Yukinori NISHIMOTO**, Yoshitomo FUKUSHIMA**
and Takuya NAGATAKI**

* Department of Mechanical Engineering, Faculty of Engineering
Yokohama National University
79-5, Tokiwadai, Hodogayaku, Yokohama, Kanagawa, 240-8501 Japan
(E-mail: yasukazu@ynu.ac.jp)
** Research & Development Center, MIKUNI CORPORATION
2480, Kuno, Odawara, Kanagawa, 250-0055 Japan

ABSTRACT

Variable valve lift (VVL) system for automotive engines is one of the key technologies to attain improvement of fuel economy and power output and reduction of emission. This paper presents a highly reliable VVL mechanism controlled by a hydraulic 3-step rotary actuator. 3-step VVL with high-, middle- and low-valve lift, is realized by the pivot shifting of an intermediate cam placed between a camshaft and valve tappet. The hydraulic actuator with no electric device is installed in a cylinder head and its rotary positioning generates 3-step rotation of a specially-designed sprag cam. The actuator can work in low supply pressure of 0.1MPa and control 3-step angles within the interval in which the valve is at rest during camshaft rotation. This paper describes the analytical simulation model of the VVL system, and the experimental evaluation for the developed VVL mechanism and hydraulic 3-step rotary actuator.

KEY WORDS

Hydraulic Rotary Actuator, Variable Valve Lift, Engine Valve Actuation, Cam Mechanism

INTRODUCTION

Variable valve actuation (VVA) is one of the remarkable technologies to attain improvement of fuel economy and power output and reduction of emission, all over the engine rotational speed range.[1]-[5] VVA systems of various mechanisms have been thrown into the market from the second half of the 1980s and have been adopted with many automobile manufacturers' engine. VVA allows some or all of the timing, lift and duration of the intake or exhaust valves, or both, to be changed while the engine is in operation. According to the controlled object, VVA is roughly divided into three types; variable valve timing (VVT) varying the phase of valve actuation, variable valve lift (VVL) varying the stroke of the valve, and variable valve event (VVE)

varying the duration in which the valve is opening.

Although a completely step-less VVA in all the controlled objects is an ideal, even if technically possible, the development of a practical system is worthwhile, which employs one or some features of VVA system efficiently from viewpoints of cost restriction, durability and maintainability.

In this paper, the authors aimed at the development of the simple VVA system, and paid their attention to the VVL mechanism with 3-step lift patterns.

Practical implementation conditions of the VVL mechanism into an engine are settled as follows;

1) Since its fluid power source is an engine oil pump already equipped on an engine, it can operate with the engine oil of the minimum operating pressure of about 0.1-0.2MPa.

2) It has high rigidity for holding valve lift.

3) It can control 3-step lift without any electric sensor.
4) It has satisfying response within 0.3s in the valve lift change as the VVL system for an engine of passenger car.

The VVL mechanism driven by a hydraulic rotary actuator is developed for above purposes. This paper presents the evaluation of its performance by both the simulation and experimental approach.

VVL MECHANISM CONTROLLED BY A HYDRAULIC 3-STEP ROTARY ACTUATOR

Concept of VVL Mechanism with a Shifting Pivot of Intermediate Cam

In the developed VVL mechanism, the valve lift is varied by pivot shift of an intermediate cam placed between a camshaft and valve tappet. Fig.1 shows the principle of the VVL. As the pivot of the intermediate cam moves away from the camshaft, the valve lift becomes shortened. Although Fig.1 shows 6-step VVL characteristics as one example, the developed VVL system was designed to generate 3-step of high-, middle- and low- valve lift which were frequently used in the actual VVL control. Therefore, 3-step positioning of the pivot of the intermediate cam is the key of the developed VVL system.

Combination of a Sprag Cam and Hydraulic Rotary Actuator

In the duration in which the valve is opening due to the camshaft in action, large force is generated at the pivot of the intermediate cam as the reaction force of the camshaft pushing the valve tappet. A component of the reaction force perpendicular to the direction of the pivot shift is borne by the slide guide of the intermediate cam retainer, and a component to the direction of the pivot shift works as a load to the VVL mechanism. From the viewpoint of installing the VVL mechanism into the small and restricted place around the cylinder head, it is unpractical to adopt an actuator which always generates force overcoming this load, because such an actuator is generally large in its body size and needs large power input.

The developed VVL mechanism is characterized by combining the sprag cam with specially designed cam profile, and a hydraulic rotary actuator. For the duration of the valve opening, large reaction force at the pivot of intermediate cam is borne by the sprag cam. Then, the position of the pivot is held with high stiffness. For the duration in which the valve is closing due to the camshaft at rest, the pivot position is controllable by the drive force generated at the hydraulic rotary actuator, because only small initial load acts on the pivot.

Thus, the developed VVL system can keep the pivot position by the sprag cam for the duration of the valve opening, and can operate it by a small hydraulic actuator and low pressure source such an engine oil pump except for that duration.
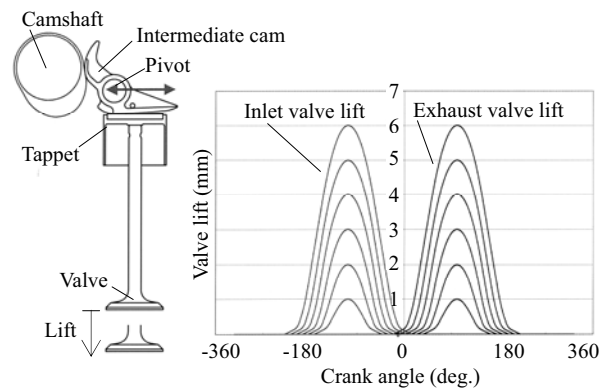
Figure1 Principle of variable valve lift with pivot shifting
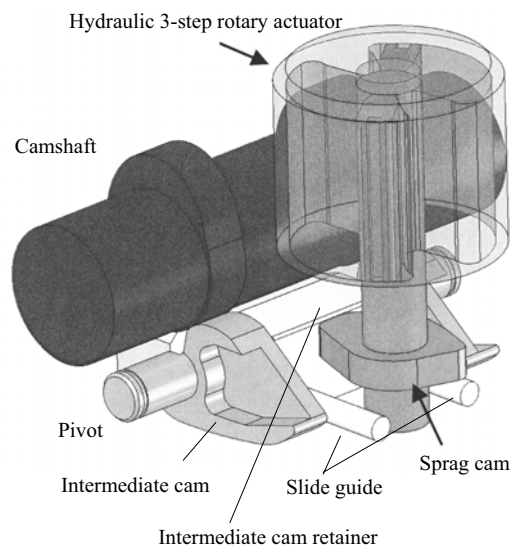
Figure 2 VVL mechanism controlled by the hydraulic 3-step rotary actuator

VVL Mechanism and Hydraulic Rotary Actuator

The schematic view of the VVL mechanism is shown in Fig.2. The hydraulic rotary actuator generates 3-step swing rotation by control of the oil pressure in the chambers inside. The pivot position of the intermediate cam shifts by the rotation of the sprag cam driven by the rotary actuator. The body of the rotary actuator is designed small so that the VVL mechanism could be added on the cylinder head of a conventional engine without complicated arrangement, and be placed between the intake or exhaust valves on each cylinder.

Fig.3 shows the relation between the swing angle of the rotary actuator, the pivot position of the intermediate cam and the valve lift.

The cam profile of the sprag is designed to stabilize its rotation angle by the load force. Therefore the sprag cam has the self-lock function at a certain rotation angle in which no torque from the rotary actuator is required to maintain its angle. As shown in Fig.4, the self-lock

condition is satisfied when the leg of the perpendicular line drawn from the center axis of the rotary actuator to the surface of the intermediate cam retainer exists within the contact surface between the retainer and the sprag cam.

Hydraulic Circuit for Rotary Actuator

The schematic view of the internal structure of the hydraulic rotary actuator is depicted in Fig.5. The chambers **a1** and **a2**, **b1** and **b2** are connected each other by the conduit passing through the center of the rotor shaft. It has a port A, B and C. The port A and B are connected with the chamber **a1**, **b1**, respectively. The port C opens on the lid of the vane housing and the thickness of the vane covers the port C around the swing angle, θ_{middle}, corresponding to a middle valve lift.

Since engine oil is used as working fluid in the hydraulic system of the VVL, the rotary actuator has to work with the minimum operating pressure of about 0.1-0.2MPa.

Sensor-less 3-step swing angle positioning is possible by the operation of the flow direction control valve as follows;

1) *Minimum swing angle positioning for high valve lift*
   The oil is supplied to the port B, and is discharged from the port A. The port C is closed. The swing angle is held with the self-lock of the sprag cam after rotating to the minimum swing angle, θ_{min}, by the driving torque generated by the pressure difference between the chambers.

2) *Middle swing angle positioning for middle valve lift*
   The oil is supplied to both the port A and B, and is discharged from the port C. The rotor finishes swinging when the vane covers the port C completely. Since the thickness of the vane is wider than the width of port C, it has a dead band for vane positioning at the angle around the port C. The final swing angle depends on the initial swing angle from which the rotor started swinging. Since no torque is generated in the region where the vane and the port C fully overlap each other, however, the rotor is positioned at the designed swing angle, θ_{middle}, in that region by the self-lock torque of the sprag cam.

3) *Maximum swing angle positioning for low valve lift*
   The oil is supplied to the port A, and is discharged from the port B. The port C is closed. Positioning to the maximum swing angle, θ_{max}, is the reverse process of the minimum swing angle positioning above-mentioned.

Transition in Pivot Shifting

Since the large reaction force occurs at the pivot of the intermediate cam in the duration of the valve opening, the pivot maintains its position by the self-lock of the sprag cam. However, if that duration starts while the pivot is shifting, the transient behavior appears in the rotary actuator.
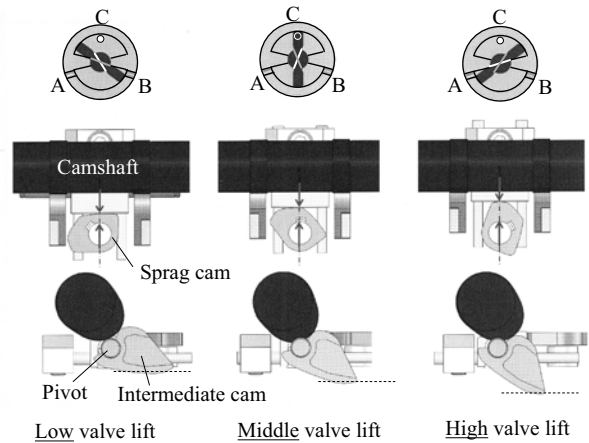
Figure 3 Relation between the swing angle of the rotary actuator, the pivot position of the intermediate cam and the valve lift.
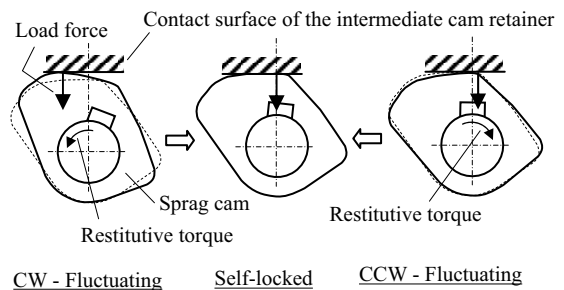
Figure 4 Self-lock function of the sprag cam
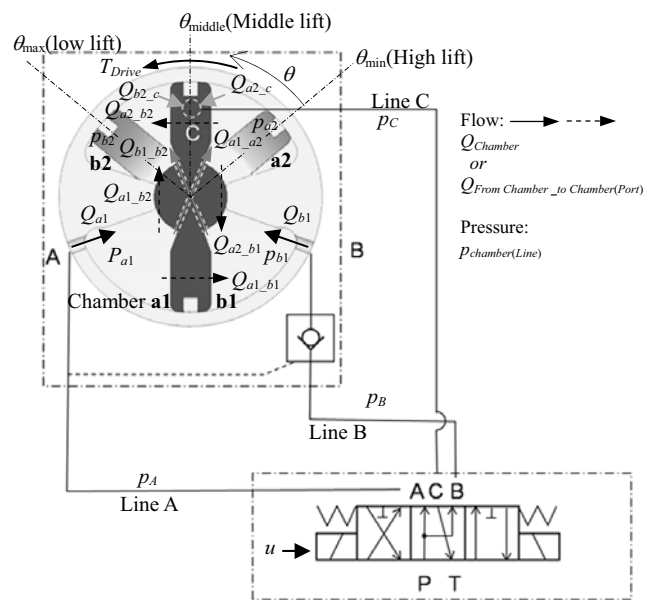
Figure 5 Hydraulic circuit of 3-step rotary actuator

In case that the duration of the valve opening starts while the pivot of the intermediate cam is shifting to the position corresponding to lower valve lift, the rotor

rotates to the angle corresponding to lower valve lift by assistance of the load torque. Consequently, the rotor reaches to the target swing angle, within some cycles of the camshaft rotation.

However, in case that the duration of the valve opening starts while the pivot is shifting to the position corresponding to higher valve lift, the loaded sprag cam generates the load torque to force the rotor to rotate reverse direction. Due to the load torque, the pressure in the chamber **b1** and **b2** easily exceeds the supply pressure of the oil pump. For prevention of the rotor from reverse rotation, as shown in Fig.6, a pilot-operated check valve is installed into the line for the port B. This check valve works as a safety lock and keeps the swing angle in the duration of the valve opening. Then, the rotary actuator restarts and advances its rotation to the target angle corresponding to higher valve lift until next duration of the valve opening starts.

SIMULATION FOR 3-STEP VVL SYSTEM

Purpose of Simulation

In order to grasp the behavior of the VVL system, modeling for the VVL system and evaluation of its performance are carried out. In the simulation, the following points are investigated;

1) Influence of the leakage through the clearance between the vane and housing, on the performance of the rotary actuator,
2) Transient pressure change in the chambers,
3) The behavior of the VVL system in case that the duration of the valve opening starts while the pivot of the intermediate cam is shifting.

The model of the VVL system is described in block diagram form to apply MATLAB/SIMULINK to the simulation. The schematic view of the simulated model and symbols of the parameters used in the simulation have been already mentioned in Fig.5.

Fundamental Equations for VVL System Model

1) *Dynamics of the hydraulic rotary actuator*

$$I_m\ddot{\theta} + B_m\dot{\theta} + K_m\,\theta = T_{Drive} + T_{Load} \qquad (1)$$

where, I_m, B_m, K_m, θ, T_{Drive} and T_{Load} are the inertia of rotating parts of the rotary actuator, viscous friction coefficient, stiffness of rotational limit, drive torque and load torque, respectively. K_m expresses the stiffness equivalent to the contact between the vane and wall of both rotational ends with the nonlinear torsion spring characteristics.

The drive torque T_{Drive} is given by;

$$T_{Drive} = K_T(p_{a1}\text{-}p_{b1}) + K_T(p_{a2}\text{-}p_{b2}) \qquad (2)$$

where, K_T is a coefficient which transforms the pressure difference between the chambers to the rotor drive
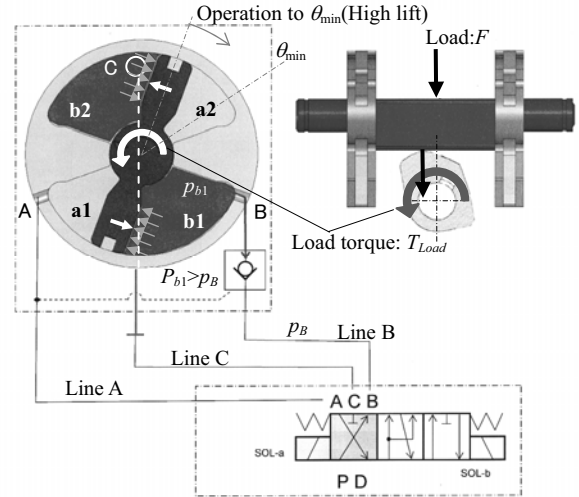
Figure 6 Prevention of the rotor from reverse rotation due to the load torque
(Duration of the valve opening starts while the pivot is sifting to the high valve lift position.)
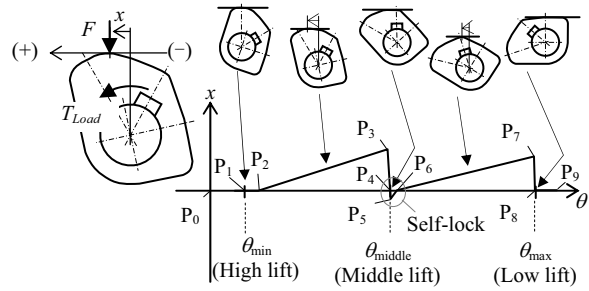
Figure 7 Load torque against every rotor swing angle
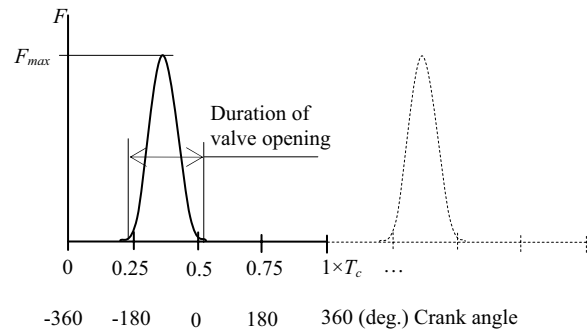
Figure 8 Load force model
(T_c: a cycle of crank shaft rotation as angle of 720 deg.)

torque, and is derived from the dimensions of vane. Referring to Fig.7, the load torque T_{Load} is given by;

$$T_{Load} = Fx \qquad (3).$$

In the simulation, the arm length of the load torque,
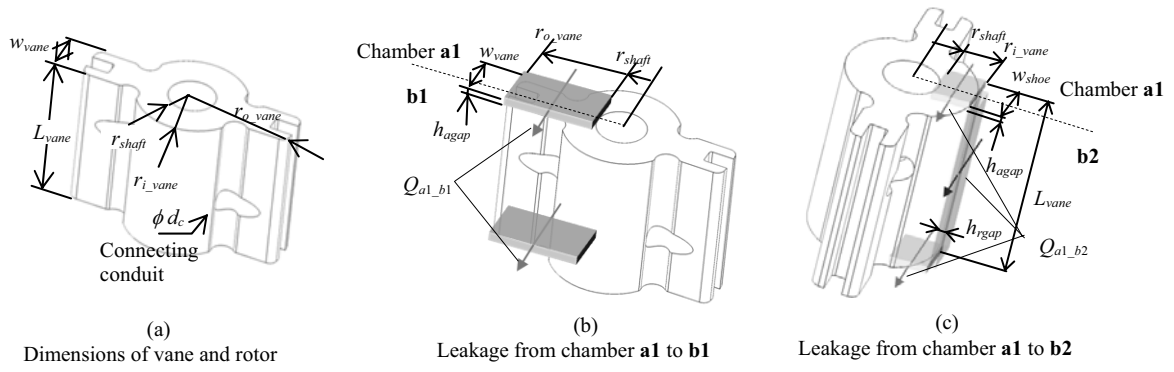
Figure 9 Model of leakage through the clearances at vane and casing wall

namely the offset x on the sprag cam in Fig.7, is assumed to be given as a function of the rotor swing angle θ using SIMULINK LOOKUP TABLE, $x=P(\theta)$, shown in Fig.7.

The load force F acting on the sprag cam is approximated using the form of a periodic function as shown in Fig.8. In Fig.8, F_{max} is the maximum load force acting on the sprag cam. T_c is the period corresponding to a cycle of the crank shaft rotation as angle of 720 deg.

2) *Continuity at the chamber* **a1**

$$\frac{dp_{a1}}{dt}=\frac{K}{V_a}\left(Q_{a1}-Q_{a1\_a2}-Q_{a1\_b1}-Q_{a1\_b2}-K_{Vm}\,\dot{\theta}\right) \quad (4)$$

where, K and V_a are the bulk modulus of the oil, the volume of the chamber **a1**, respectively. K_{Vm} is the change of the chamber volume against a unit swing angle, which is determined by the dimensions of vane.
Continuity at the chamber **a2**, **b1** and **b2** are formulated in similar form to eq.(4), as well.

3) *Flow characteristics at orifice and pipe*
The flow characteristics of each flow resistive element, such as a throttle in a valve and lapped area between the port C and vane width, are approximated using the formula for orifice. The flow characteristics of each piping are approximated using the formula for steady flow through circular pipe.

4) *Leakage flow characteristics between chambers*
Leakage flow between the chamber **a1** and **b1** is estimated by the steady flow between stationary and moving flat, parallel walls as shown in Fig.9 (b). The leakage is given by the following formula using the axial clearance h_{agap};

$$Q_{a1\_b1} = 2\times\frac{\left(r_{o\_vane}-r_{shaft}\right)h_{agap}^3}{12\mu w_{vane}}\left(p_{a1}-p_{b1}\right)$$
$$+\Delta Q_{a1\_b1}\left(U_{vane},p_{a1}-p_{b1}\right) \quad (5)$$

Table 1 Design specifications of prototype rotary actuator

Displacement volume per a chamber	2.5 cm^3
Rotor diameter (outer) r_{o_vane}/(inner) r_{i_vane}	28 / 14 mm
Rotor length L_{vane}	19mm
Swing angle	105 deg
Driving torque at supply pressure of 0.1MPa	0.25 Nm
Response for single step rotation	0.3 s
Pump Supply pressure (typical)/(minimum)	0.27 / 0.1 MPa

where, μ is the viscosity of the oil. The first term represents the leakage flow through the stationary flat, parallel walls, the second represent the flow induced by drag of the vane rotation with the circumferential tip speed of the vane, U_{vane}. No leakage is assumed at the tip of vane due to its seal device. Leakage between the chamber **a2** and **b2** is expressed by the same formula as eq. (5), as well.

Leakage between the chamber **a1** and **b2** is also expressed by the steady flow between stationary and moving flat, parallel walls as shown in Fig.9 (c). Using the axial clearance h_{agap} and clearance between rotor and shoe h_{rgap}, the leakage is given by;

$$Q_{a1\_b2}=\frac{2\left(r_{i\_vane}-r_{shaft}\right)h_{agap}+L_{vane}h_{rgap}^3}{12\mu w_{shoe}}\left(p_{a1}-p_{b2}\right)$$
$$+\Delta Q_{a1\_b2}\left(U_{vane},p_{a1}-p_{b2}\right) \quad (6)$$

The second term also represents the flow induced by drag of the vane rotation. Leakage between the chamber **a2** and **b1** is expressed by the same formula as eq. (6), as well.

5) *Flow characteristics between port C and chambers*
The flow characteristics at the throttle formed by the port C and vane width are approximated using the formula for orifice. The relation between the rotor swing angle and the opening area of the port C is expressed by LOOKUP TABLE in SIMULINK.

6) *Response of control valves*
The response of control valve is approximated using the
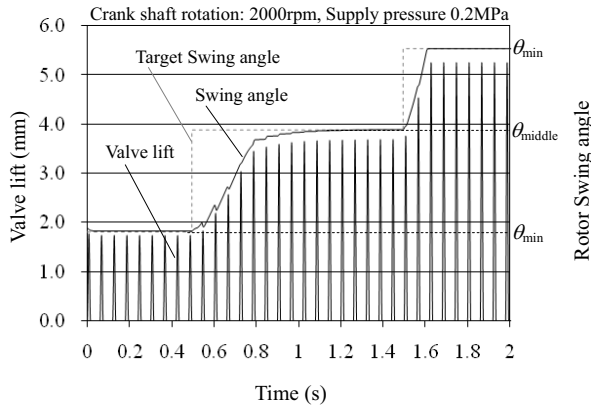
Figure 10 Simulation result for a single step valve lift change from low to middle and from middle to high

first order delay element as a general solenoid valve.

Result of Simulation for 3-Step VVL System

The design specifications of a prototype VVL is listed in Table 1. One of the examples of the simulated result for the prototype VVL is shown in Fig.10. It indicates that the VVL can change the valve lift within 0.3ms at the supply pressure of 0.2MPa even if it changes the lift higher. In case of the supply pressure of 0.1MPa, it takes 0.5s for a single step valve lift change. In case that the axial and radial clearances are 50% larger than the designed value, the VVL cannot work for the lift change from lower to higher, at the supply pressure of 0.1MPa. Since the leakage reduces the pressure difference between the chambers, it is important to design the clearance for securing the sufficient pressure difference for driving the actuator.

EXPERIMENTAL EVALUATION FOR 3-STEP VVL SYSTEM

Figure 11 and 12 show the measured performance of the prototype VVL. It is observed that the actuator keeps its swing angle in the duration of valve opening, withstanding the reverse rotation torque in the transition of valve lift change to higher.

The response time is slight longer than the design target, due to the friction of moving parts and the drop of the drive torque by the leakage.

CONCLUSIONS

This paper has presented the VVL mechanism controlled by the hydraulic 3-step rotary actuator. Simple and reliable VVL system is constituted by a combination of sensor-less drive of the rotary actuator and the specially designed sprag cam. The designed, simulated and measured performances of the developed VVL are listed in Table 2. Optimization of the prototype VVL and development of multi-step mechanism, more than three, with simple structure are starting as a future work.
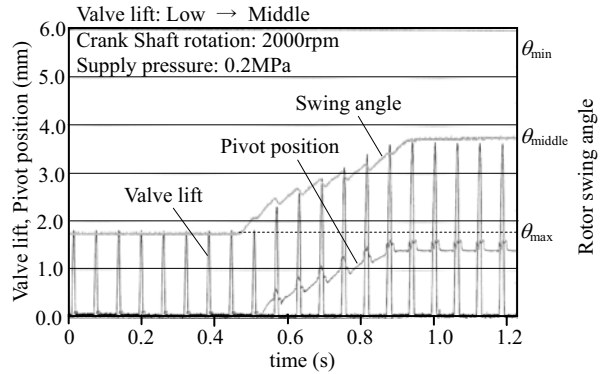
Figure 11 Measured performance of prototype VVL for a step valve lift change from low to middle
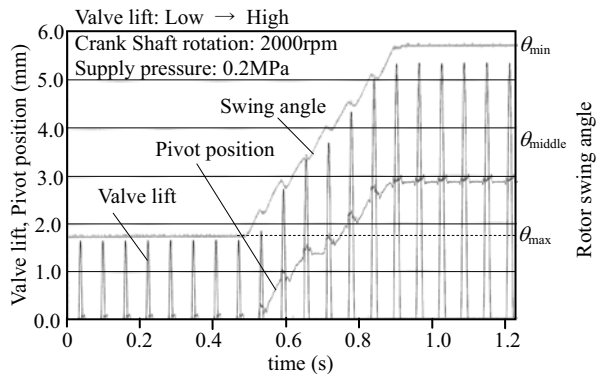
Figure 12 Measured performance of prototype VVL for a step valve lift change from low to high

Table 2 Performance of developed VVL

	Design	Simulation	Prototype
Actuator torque at 0.1MPa	0.25 Nm	0.25 Nm	0.25 Nm
Minimum operating pressure	0.1 MPa	0.2 MPa	0.2 MPa
Lift holding (Self-lock)		Good	Good
Response of a single step lift change	0.3 s	0.3 s	0.4 -0.5 s

REFERENCES

1. Pierik, R., Burkhard, J., Design and Development of a Mechanical Variable Valve Actuation System, SAE Paper 2000-01-1221, SAE International, 2000.
2. Nakamura, M., Hara, S., A Study of a Continuous Variable Valve Event and Lift (VEL) System, SAE Paper 2001-01-243, SAE International, 2001.
3. Flierl, R., Der neue BMW Vierzylinder-Ottomotor mit Valvetronic-Tail1: Konzept und konstruktiver Aufbau (The new BMW Four Cylinder SI Engine with Valvetronic-Part1: Concept, Design and Construction), MTZ, 2001, No.6, pp.450-463.
4. Genise, D., Pierik, R.(Editors), Variable Valve Actuation 2005, SAE Special Publication, SP-1968, SAE International, 2005.
5. Tanaka, H., Toyoda, N., Development of a Sensorless Electrohydraulic Valve Actuator For a Camless Engine, Proceedings of the 6th JFPS International Symposium on Fluid Power TSUKUBA 2005, pp.256-261.

P1-21

DIRECT DRIVE ELECTRO-HYDRAULIC SERVO ROTARY VANE STEERING GEAR

Jihai JIANG*, Wenhai SU* and Qinghe LIU*

* Institute of Fluid Power Transmission and Control, School of Mechatronics Engineering
Harbin Institute of Technology
Harbin 150001, Republic of China
(E-mail:jjhlxw@hit.edu.cn   hitswh@163.com)

ABSTRACT

This paper describes the design and prototype of a new highly reliable rotary vane steering gear of ships which combines the benefits of conventional hydraulic systems and direct drive electrical actuators, namely high torque ratio and modularity. It is referred to as the Direct Drive Electro-Hydraulic (DDEH) servo rotary vane steering gear which results from the fusion of the above mentioned technologies. The DDEH rotary vane steering Gear, including its configuration, controlling principle and specialty, is theoretically analyzed. The mathematical models are built and the simulations of the system are made. The analysis of DDEH rotary vane steering gear is supported by simulation data which explains the extremely high level of performance attained by a prototype of DDEH rotary vane steering gear. Simulation results and its unique advantages show that DDEH rotary vane steering Gear is a prospective equipment for shipping steering which can meet performance requirements.

KEY WORDS

DDEH, Rotary Vane Steering Gear, Economizing, Simulation

INTRODUCTION

A rotary vane steering gear consists of a vane actuator connected directly to the rudder stock. It can control simply the direction of the ship through changing the angle of the moving vane. Rotary vane steering gear operates at lower pressures and has fewer moving parts than a ram steering gear. The rotary vane steering gear has many benefits, such as compact structure, space saving units, easy installation, and low life cycle costs. Furthermore, rotary vane steering gear does make safer navigation through narrow straits, because the vessels increased maneuverability and improved control when docking. Now, the rotary vane steering gear has a proven service record on all types of vessels, especially suit for medium-sized to large ships, including large container vessels and VLCCs [1-3].

The traditional controlling way of steering gear includes using proportional valve or using variable displacement pump. Both kinds of methods require very higher cleanliness of hydraulic system because of adopting precise hydraulic parts. Furthermore, traditional steering gear has complex control system and lots of control components, acting as hidden troubles for failure free operation of steering gear [4-5].To solve these problems, the direct drive electro-hydraulic(DDEH) servo rotary steering gear is designed and constructed by HIT. In this new prototype of steering gear, variable displacement pump and proportional valve are replaced by converter motor and fixed pump, so system needs lower cleanliness. The DDEH servo steering gear is discarded pumping station and pipelines. It has fewer control components and higher reliability and controllability than traditional rotary vane steering gear. Moreover, this steering gear can economize energy efficiently.

CONFIGURATION AND PRINCIPLE OF THE DDEH SERVO ROTARY VANE STEERING GEAR

Figure 1 shows Principle sketch of DDEH servo rotary steering gear. There are four main parts in this DDEH servo system: computer control system, variable frequency speed regulation system, hydraulic power actuator and displacement feedback union. Computer control system incepts input signal and signal by displacement feedback union. The main controller compares two signals and operates, and then translates result to D/A converter. Finally, inverter incepts DC volts and drives asynchronous motor thus control hydraulic power actuator. Motor drives the bidirectional fixed displacement pump and then the pump drives the rotary vane motor directly. Changing the rotating direction, rotating speed and runtime of the motor can control the moving direction, velocity and position of the rudderpost which is fixed with rotary vane motor's stator.

Figure 2 presents the structure of hydraulic power actuator.
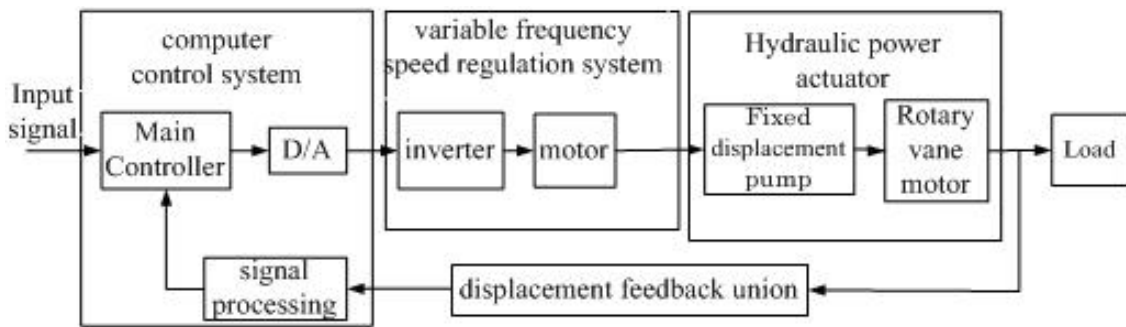
Figure 1 Principle sketch of DDEH servo rotary steering gear
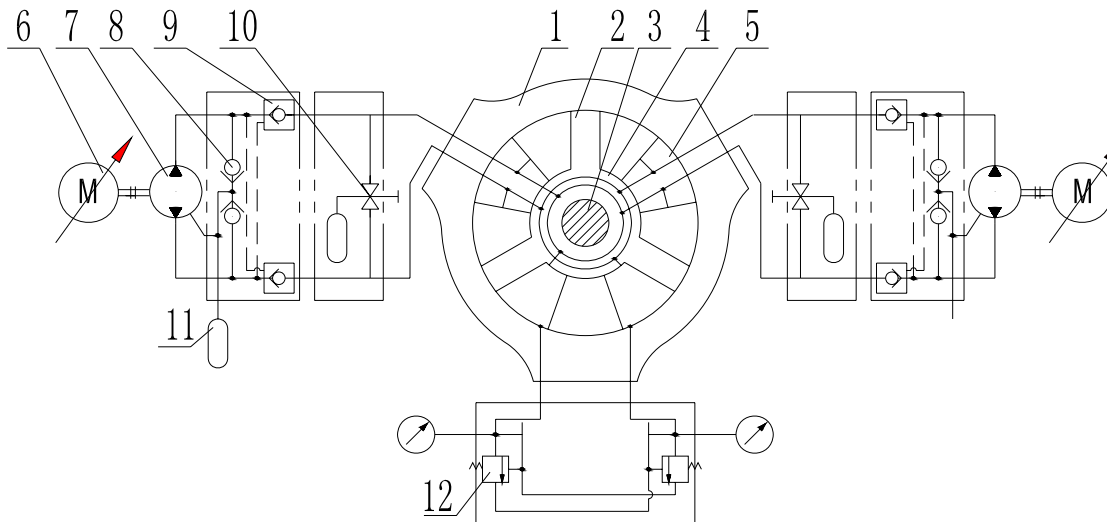
1. housing   2. rotor   3. rudder stock   4. moving vane   5. stator   6. AC motor   7. bidirectional fixed pump
8. filling valve   9. hydraulic operated check valve(hydraulic lock)   10. stop valve   11. oil tank   12. safety valve

Figure 2 Construction drawing of DDEH servo rotary steering gear

In Figure 2, the closed circuit is composed of a fixed displacement pump 7 and rotary vane motor. AC motor 6 drives the bidirectional fixed displacement pump to provide hydraulic power (pressure and flow) to the rotary vane motor. Then through rudderpost, the hydraulic power is transformed into mechanical power (torque and rotating speed). The moving of the rudderpost is carried out through controlling the AC motor according to the input signal. The filling valve 8 composed of two check valves is connected in parallel with the closed circuit to compensate the leak oil. The lock valve 9 is composed of two pilot operated check valves installed in series in the closed circuit. When the ship rudder reaches the right position and the pump

stops working, the lock valve functions as a lock to prevent the oil in the cylinders from moving back because of the action of wave on the ship rudders. Two relief valves are installed in the closed circuit to relieve overload when the ship rudder stops working and the overload is produced by wave acting on the ship rudder. The two relief valves can also be used to relieve overload in the main circuit. If the overloading occurs in the whole system, then the overload relieving is mainly achieved through the inverter's self-restricting torque.

MATHEMATICAL MODEL OF THE DDEH ROTARY VANE STEERING GEAR

The overall mathematical model of the DDEH rotary vane steering gear consists of several subsystems including the inverter-motor system, pump control motor system and actuator load system, et al.

INVERTER AND ASYNCHRONOUS MOTOR

INVERTER

Input of inverter is control voltage while output of inverter are frequency of output and phase voltage of electric machine stator [6]. We have

$$f_1 = K_v \cdot u_c \qquad (1)$$

where K_v = conversion coefficient for translate voltage to frequency

u_c = control voltage, V.

f_1 = frequency of inverter output, Hz.

$$U_1 = \frac{(380 - b)}{100} \cdot f_1 + b \qquad (2)$$

where U_1 = phase voltage of electric machine stator, V.

b = low frequency torque upgrade coefficient,

When b is settled *as zero*, we obtain

$$U_1 = K_f \cdot f_1 \qquad (3)$$

where K_f = conversion coefficient for translate voltage to frequency, K_f =3.8.

ASYNCHRONOUS MOTOR

Asynchronous motor's equilibrium of moments equations is given by

$$\frac{2\pi}{60} \cdot J_T \frac{dn_p}{dt} = T_n - T_{LT} - T_{df} - \frac{2\pi}{60} B_T n_p \qquad (4)$$

where T_n = electromagnetic torque of asynchronous motor, Nm.

T_{LT} = load torque of asynchronous motor, Nm.

T_{df} = nonlinear friction torque of asynchronous motor, Nm.

J_T = moment of inertia referred to motor shaft, kgm^2.

B_T = damping factor of asynchronous motor shaft, Nms/rad.

Electromagnetic torque equilibrium of asynchronous motor

$$T_n = K_{T1}U_1 - K_{T2}n_p \qquad (5)$$

where n_p = real rotary speed of asynchronous motor, rpm.

Load torque of asynchronous motor is input torque of fixed pump. when take loss of mechanical drive, T_{LT} can be given by

$$T_{LT} = \frac{D_p p_p}{\eta} \qquad (6)$$

where D_p = volumetric displacement of pump, m^3/rad

p_p = output pressure, Pa

η = efficiency of mechanical drive , this η =0.95

PUMP CONTROLLED MOTOR

The continuity equation and torque balance equation can be written as

$$\frac{2\pi}{60} n_p D_p = D_m \frac{d\theta_m}{dt} + C_t P_1 + \frac{V_0}{\beta_e} \frac{dP_1}{dt} \qquad (7)$$

$$P_1 D_m = Js \frac{d^2\theta_m}{dt^2} + B_m \frac{d\theta_m}{dt} + G\theta_m + T_L(\theta) \qquad (8)$$

where D_m = volumetric displacement of motor, m^3/rad.

V_0 = Average volume of forward chamber, m^3.

θ_m = angular position of motor shaft, rad.

$C_t = C_{it} + C_{et}$ = total leakage coefficient, m^3/sec/pa.

$C_{it} = C_{ip} + C_{im}$ = total internal leakage coefficient, m^3/sec/pa.

$C_{et} = C_{ep} + C_{em}$ = total leakage coefficient, m^3/sec/pa

C_{ip}, C_{ep} = internal and external leakage coefficient of pump, m^3/sec/pa.

C_{im}, C_{em} = internal and external leakage coefficient of motor, m^3/sec/pa

p_1 = forward chamber pressure, pa

β_e = effective bulk modulus of system, pa

J = total inertia of motor and load, kg·m^2

B_m = total viscous damping coefficient, N·m/(rad/s)

G = spring stiffness of load, N·m/rad

$T_L(\theta)$ = hydrodynamic moment on rudder blade, $= 1/2(C_L \cos\theta_m + C_D \sin\theta_m)\rho A v^2 X_\varepsilon$, N·m

where C_L, C_D is lift coefficient and resistance

coefficient, v is water velocity and v= 1.15-1.2 ship speed, A is unilateral area of wetted surface, ρ is seawater density and $X\varepsilon$ is distance between center of rudder pressure and tiller axes.

MATHEMATICAL MODEL IN TIME DOMAIN

Combines equations being given at last section, mathematical model of DDEH rotary vane steering gear in time domain are described by

$$f_1 = K_v \cdot u_c \qquad (9\text{-}1)$$

$$U_1 = K_f \cdot f_1 \qquad (9\text{-}2)$$

$$\frac{2\pi}{60} \cdot J_T \frac{dn_p}{dt} = T_n - T_{LT} - T_{df} - \frac{2\pi}{60} B_T n_p \qquad (9\text{-}3)$$

$$T_n = K_{T1} U_1 - K_{T2} n_p \qquad (9\text{-}4)$$

$$T_{LT} = \frac{D_p p_p}{\eta} \qquad (9\text{-}5)$$

$$\frac{2\pi}{60} n_p D_p = D_m \frac{d\theta_m}{dt} + C_t P_1 + \frac{V_0}{\beta_e} \frac{dP_1}{dt} \qquad (9\text{-}6)$$

$$P_1 D_m = Js \frac{d^2\theta_m}{dt^2} + B_m \frac{d\theta_m}{dt} + G\theta_m + T_L \qquad (9\text{-}7)$$

$$T_L(\theta) = 1/2(C_T \cos\theta_m + C_D \sin\theta_m)\rho Av^2 X_\varepsilon \qquad (9\text{-}8)$$

SIMULATION OF THE DDEH ROTARY VANE STEERING GEAR

SIMULATION MODEL AND PARAMETERS

System of equations 3.9 can be Laplace transforming and be combined to form the block diagram in Figure 3. θ_0 is steering orders and θ is rudder angle. Based on figure 3, DDEH rotary steering gear simulation model, is implemented in SIMULINK. Bump union is a main subsystem of this model, which is composed of AC converter motor , fixed pump, hydraulic lock and filling valve.
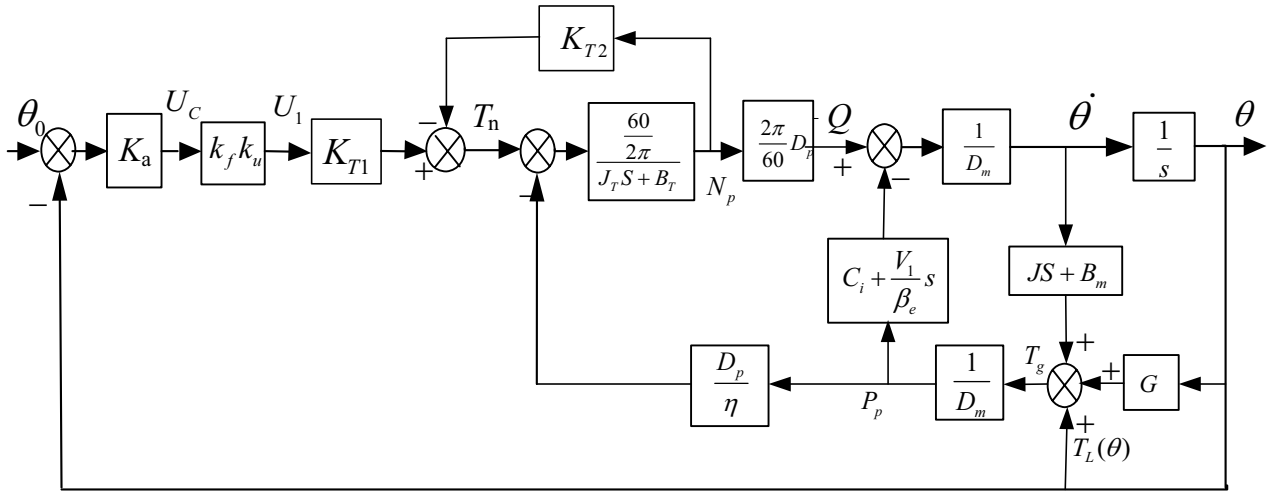
Figure 3 Block diagram of DDEH servo rotary steering gear

Part parameters of the DDEH rotary steering gear selected in this paper are shown in Table 1.

Table 1 parameters for simulation

parameters	value		parameters	value	
K_v	10	Hz/V	D_m	0.04	m^3/rad
K_f	3.8	V/Hz	J_m	3	kgm^2
K_{T1}	26.27		B_m	0.01	Nms/rad
K_{T2}	1.927		C_i	10^{-12}	m^5/Ns
J_T	0.1	kgm^2	β_e	9×10^8	N/m^2
B_T	0.01	Nms/rad	V_0	0.03	m^3
D_p	3.98×10^{-6}	m^3/rad			

SIMULATION RESULTS

Steering gear should meet the requirements for enough torque moment and intensity. SOLAS Regulation I/29.3.2 requires that the main steering gear and rudder stock of vessels shall be capable of putting the rudder over from 35° on one side to 35° on the other side when the ship is at its deepest seagoing draught and running ahead at maximum ahead service speed and, under the same conditions, from 35° on either side to 30° on the other side in no more than 28s[7].

In this paper, a 12,000 DWT crude oil tanker which is running ahead at 13 knot is selected as simulation background. Simulation time is selected as 50 second and original steering angle of vessel is -35°. The steering order changes to 30° since 20 second later. Simulation results are shown in Figure 4 and figure 5. It can be seen in figure 4 that the time of rudder movement is less then 28s. Figure 5 shows that steering gear can output 120KNm torque moment when it turns to 35 degree. Simulation results indicate that DDEH servo rotary vane steering gear meets the requirements of SOLAS.
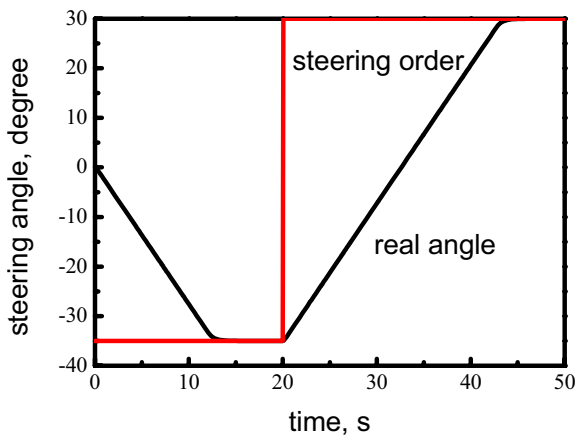
Figure 4 simulation result of steering angle
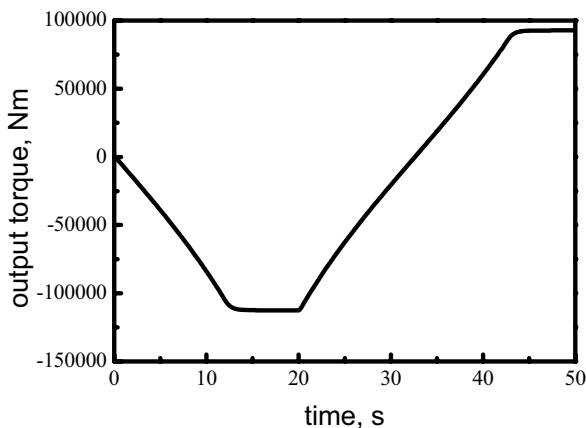
Figure 5 simulation result of torque moment

CONCLUSIONS

A new type steering gear - DDEH servo rotary vane steering gear is designed which is capable both advantages of AC servo system's flexibility and of hydraulic great force. Research results show that DDEH servo rotary vane steering gear measures up SOLAS. Because it has higher efficiency and more compact structure, DDEH servo rotary vane steering gear will have a great prospect in this field.

REFERENCES

1. Wagner Paul, Vail Jeannine A. EVOLUTION OF A MODERN NAVAL STEERING SYSTEM. Naval Engineers Journal, v 99, n 3, May, 1987, p 55-64
2. Anon. Frequency-controlled pumps enhance rotary-vane steering gear. Naval Architect, n, July/August, 2001, p 39
3. Ruosong Cui. Analysis of Some Key Techniques of Rotary Vane Steering Gear, shanghai shipbuilding, February, 2007, p 27-28
4. Changing Chen. Several rivers servo breakdown reason brief analysis. China Water Transport (Academic Version),2006,vol.6 No.7, 19-20
5. Lianzhong Qi. Analysis and control the hydraulic oil contamination of actuator. Journal of Naval Aeronautical Engineering Institute,2006,vol.21 No.6 618-622.
6. Achim Helbig, Injection moulding machine with electric-hydrostatic drives, 3rd international fluid power conference, Aachen, Germany, 2002
7. Protocol of 1978 relating to the international convention for the safety of life at sea, 1974

374

P1-22

DEVELOPMENT OF REMOTE CONTROL SYSTEM FOR FIELD ROBOT

Sung-Min Jin*, Dong-Young Lee**, Sung-Hee Park**, Hyeong-Uk Lee* Chang-Don Lee*** and
Soon-Young Yang**

* Department of Mechatronics/IT, Institute of e-Vehicle Technology, University of Ulsan
Daehakro 102, Nam Gu, Ulsan, 680-749 Korea
(E-mail: elansia@mail.ulsan.ac.kr)
**Department of Mechanical and Automotive Engineering, Faculty of Engineering
University of Ulsan
*** Team of Technical Development for Intelligent Vehicle Parts, Faculty of Engineering
University of Ulsan

ABSTRACT

Hydraulic excavators are the representative of field robot and have been used in various fields of construction. Since the excavator operates in the hazardous working circumstance, operators of excavator exposed in harmful environment. Therefore, hydraulic excavator automation and remote control system has been investigated to protect from the hazardous working environment. Remote control system of hydraulic excavator needs various equipments. In this paper, the method to construct the remote control system is proposed. The remote control system is consisted of a manual and auto mode. Manual mode controls a hydraulic cylinder as open loop control. and auto mode controls the end effecter of excavator using tracking control system. The efficiency of remote control system was evaluated through the field test.

KEY WORDS

Field Robot, Remote control, Excavator, Teleoperated Excavator, End Effecter Control

INTRODUCTION

The hydraulic excavator of field robot has been used in various fields of construction. However, a number of the skilled operator is gradually reduced by the hazardous working environment. Thus, automation and remote control system of excavator have been investigated to protect the operation special situations that present safety or health risk to operators and to operate easily the skilled operator working [1].
We constructed the remote control system with various equipments. Which are remote operator station components and excavator side components, the models of these two parts will be presented to analyze. The simple diagram for the remote control system of excavator is shown in Figure 1

We applied to two control type of Remote control hydraulic excavator system, manual mode and auto mode. Manual mode is control method in the generality of case and auto mode is control of end effecter using inverse kinematics. [3, 4] Also, controller for tracking control system was applied the model reference adaptive controller. [5] The designed controller was implemented by using LabVIEW software.
the structure of the remote control excavator system is described. In the following section, the remote operating system procedure is presented and the efficiency of remote control system was evaluated through the experiments. Finally, concluding remarks are represented in last section.
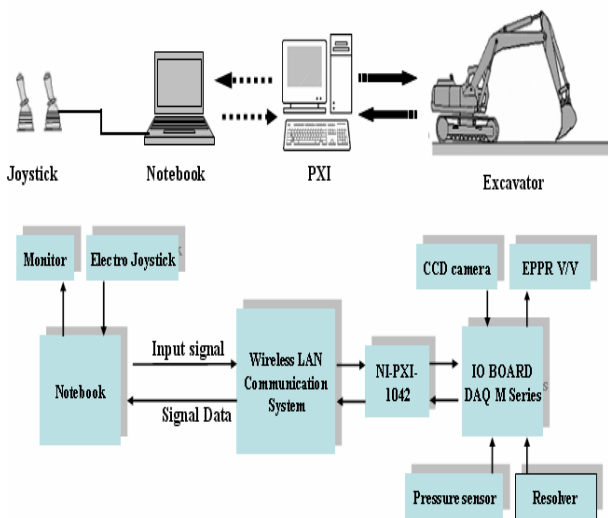
Figure 1 Remote control system

FIELD ROBOT SYSTEM

Since a remote control hydraulic excavator system consists of remote operator station components and excavator side components, the models of these two parts will be presented to analyze.

Excavator side components

Figure 2 Excavator side components

Figure 2 show the excavator side components. As shown in figure, the angle of boom, arm and bucket are measured through the resolver attached in each joint. Pressures of hydraulic cylinder are measured through the pressure sensor attached in each cylinder. Detections of obstacle are measured through the ultra sonic sensor. The environment around excavator displays in CCD camera. The angle of CCD camera is controlled Pan/Tilt motor. Each links of excavator are operated by EPPR

V/V which controls pressure & flow valves of MCV. Using RF (Radio Frequency) communication, receive a joystick signal. The wireless LAN used in communication between remote operation and excavator. The inverter (dc to ac) is used for a source of electric power service. Computer interfacing for control the hydraulic excavator signal is set up using 6704 DAQ equipment manufactured by National Instrument Corp.

In the hydraulic excavator, which was purely mechanically actuated, had to be modified to enable electronic, drive-by-wire control of the various hydraulic circuits. The excavator is conventionally controlled using pressure-controlled joystick. These joystick, operate in the pilot system. These spool valves supply directional control of the main cylinder. For remote control electronic valves were placed in the pilot system. This system should change servo-valve or electro-proportional pressure valve (EPPR V/V) system. In this paper, used by electro-proportional pressure valve system which worked by electronic signal.

Remote operator station components

Figure 3 show the remote operator station components of remote control hydraulic excavator system. As shown in figure, an operator of excavator works using a monitor which displays from a video camera and two electronic joysticks which controls real activity. Using RF communication, send a joystick signal. Using wireless LAN of notebook, receive a sensor signal of excavator and a vision signal. For Computer interfacing for control the remote operator signal is set up using 6036E DAQ equipment manufactured by National Instrument Corp.

Figure 3 Remote operator station components

TRACKING CONTROL SYSTEM DESIGN

376

The Remote controlled hydraulic excavator system is consisted of the manual and auto mode. Manual mode control the cylinder displacement through open loop control and auto mode control the end effect using feed back control system. Figure 4 show the manual mode and Figure 5 show the auto mode. The inverse kinematics coordinates are defined to detect the end effect of the developed excavator is represented in Figure 6
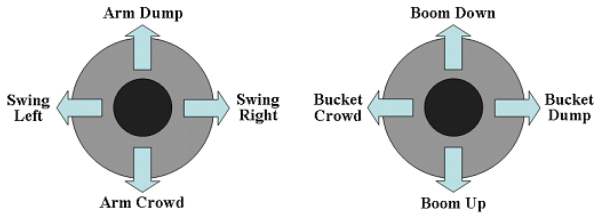
Figure 4 Operate of joysticks in Manual mode
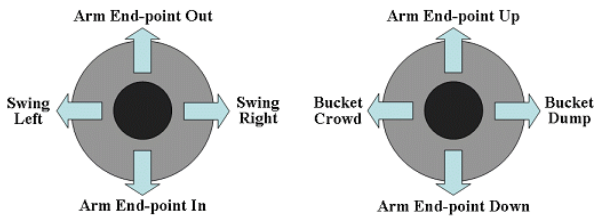
Figure 5 Operate of joysticks in Auto mode
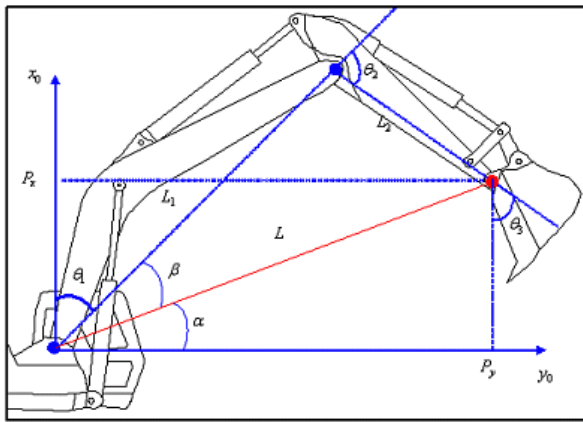
Figure 6 Coordinate of excavator system

The input signal of auto mode is position value of end effect of arm. The derivative of angle of each links using inverse kinematics is induced as

$$\cos\theta_2 = \frac{L_b^2 + L_a^2 - L^2}{2L_bL_a} \tag{1}$$

$$\sin\theta_2 = \sqrt{1 - \cos\theta_2^2} \tag{2}$$

$$\theta_2 = a\tan 2(\sin\theta_2, \cos\theta_2) \tag{3}$$

$$\alpha = \tan^{-1}\left(\frac{P_x}{P_y}\right) \tag{4}$$

$$\beta = \cos^{-1}\left(\frac{L_b^2 + L^2 - L_a^2}{2L_bL}\right) \tag{5}$$

$$\theta_1 = \frac{\pi}{2} - \alpha - \beta \tag{6}$$

$$\gamma = \theta_1 + \theta_2 + \theta_3 \tag{7}$$

$$\theta_3 = \gamma - \theta_1 - \theta_2 \tag{8}$$

EXPERIEMENT

In order to evaluate the tracking performance of the proposed end effecter control system using inverse kinematics. The system is corded Using LabVIEW software of National Instrument Corporation. Figure 7 is response of end effecter of arm for the horizontal signal. Figure 8 is response of boom angel. Figure 9 is response of arm angle. Figure 10 is error response of boom and arm.
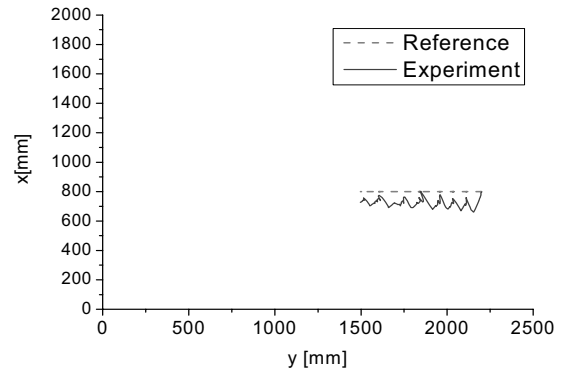
Figure 7 Response of end effecter
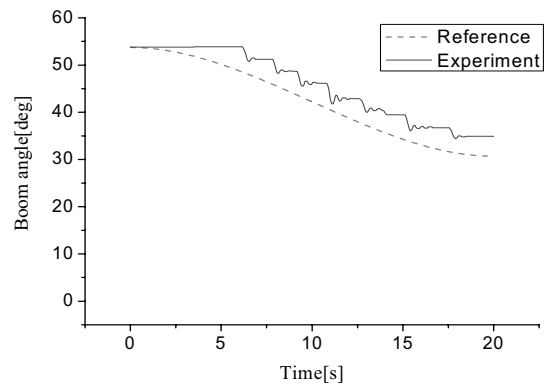
Figure 8 Response of boom angel
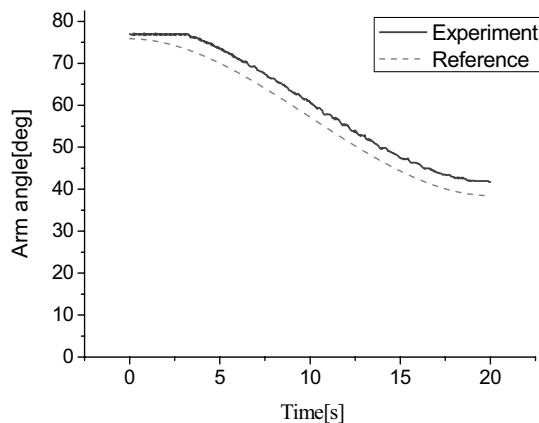
Figure 9 Response of end effect
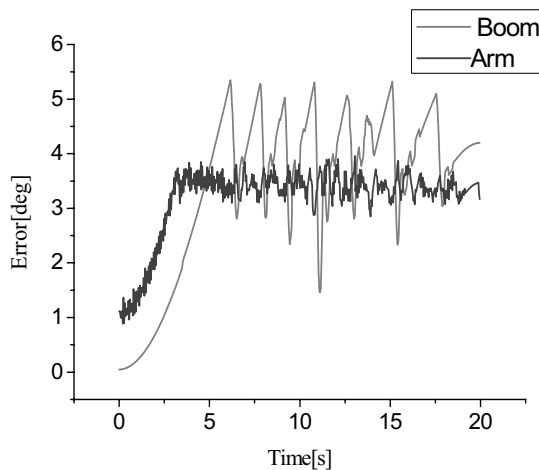
Figure 10 Response of end effect

CONCLUTION

Hydraulic excavator system, i.e. one of famous field robots, can perform various works in the construction fields. We developed the remote control hydraulic exactor system. The developed system is possible to use in harmful working environment without getting on an operator. Therefore, operator of remote control excavator can work safety. Operator of auto mode of joysticks control can work easy. The remote control hydraulic excavator system was manufactured. The efficiency of system has been evaluated through the field test.

ACKNOWLEDGEMENTS

REFERENCES

1. C.H. Lee, S.Y. Jeong, S.S Kim, Development of A Haptic Steering System for a Low Cost Vehicle Simulator using Proving Ground Test Data, The Korean Society of Automotive Engineers Symposium, 2004, pp. 722~727.
2. H. Cho, H.W. Chang, Active Pitch Motion Control of a Hydraulic Excavator, The Korean Society of Automotive Engineers Symposium, 2002, pp. 681-686.
3. J. ballantyne and E. Wong, A virtual environment display for teleoperated excavator, Conference on Intelligent Robots and System, 1998, pp.1894-1899
4. M. Minamoto, K. Matsunaga, Tele-presence information and remote controlled task execution, Conference on Intelligent Robots and System, 1998, pp.1102-1106.
5. S.S. Kim, W.S. Seo, S.Y. Yang, B.R. Lee and K.K.Ahn, Trajectory control of field robot using adaptive control and system identification, Journal of Control Automation and Systems Engineering, 2002, **8**-9, pp.728-735.
6. Xiao, Q., Wang, Q. and Zhang, Y., Control Strategies of Power System in Hybrid Hydraulic excavator, Automation in Contruction, 2007, **16**-5, pp. 1-7.
7. Choopar, T. Yahya, H. Z. Kaspar, A. and Lakmal D. S., On-line Soil Property Estimation for Autonomous Excavator Vehicles, IEEE International Conference Robotics & Automation, Taipei, Taiwan, September, 2003, 14-19.
8. Tafazoli, S., Clarence, W. S. and Peter D. L., Tracking Control of an Electro-hydraulic Manipulator in the Presence of Friction, IEEE Transactions on Control Systems Technology, 1998, **6**-3, pp. 401-411.

P1-23

ELECTROHYDRAULIC VIBRATION EXCITED BY 2D VALVE

Jian RUAN *, R. BURTON**, Sheng LI * and Faming ZHU *

*The MOE Key Laboratory of Mechanical Manufacture and Automation
Zhejiang University of Technology
Hangzhou, 310014, China
(E-mail: wxmin@mail.hz.zj.cn)
**Department of Mechanical Engineering
University of Saskatchewan, Saskatoon, Canada

ABSTRACT

The frequency bandwidth of the electrohydraulic vibrator conventionally constructed by a servo valve and a hydraulic cylinder or a motor is to a large extent limited to fairly narrow range by the dynamic response capability of the servo valve. A 2D electrohydraulic valve is thus developed to enhance the working frequency range to a new high level. In this 2D valve, the continuous rotary motion of the spool is used to create alternated variation of the valve port areas, while the linear motion of the spool is to control the peak value of the valve port areas. The frequency excited by 2D valve is proportional to the rotary speed of the spool and thus the high-frequency can easily be achieved by increasing the rotary speed of the spool well lubricated in hydraulic oil. Experiments have been carried out to the vibrator loaded by an elastic force coming from the deformation of a frame work and the wave forms of the cylinder piston was measured. It is demonstrated that the ascent and descent slopes of the wave form show some inconsistency which alleviates with the reduction of valve linear opening. The phenomenon is explained to be caused by the changing direction of the elastic force. Nevertheless, the wave from is close to a sinusoidal one. It is concluded the development of the 2D valve does point out an access to the high-frequency excitation of the hydraulic vibration.

KEY WORDS

Two-dimensional control valve; Electrohydraulic servo system,Hydraulic vibrator

INTRODUCTION

Vibration is a phenomenon commonly met in mechanical engineering practice. When the frequency of the external excited vibration comes close to the natural frequency of a mechanical structure, resonance occurs, which can be very destructive to the whole mechanical system.

Vibrating test therefore remains an important and objective means to determine the performance of a mechanical system, or part of it, working under vibrating condition[1]. In the vibration tests, the vibrating environment is usually created artificially with a vibrator, which is driven by either mechanical power or electrical power or hydraulic power[2]. In the case of heavy-power

demanded, hydraulic vibrator is commonly used. The conventional hydraulic vibrator is actually a hydraulic actuator, either a cylinder or a motor, controlled by a servo valve. By feeding to the coil of servo valve with a wave form of current in respect to the desired vibrating wave form, the cylinder piston or motor rotor will makes reciprocating motion driven by alternative flow rate into or out of its working chambers created by the servo valve. The reciprocating piston further results in a vibration of loads connected on cylinder rod or motor axis. The bandwidth of the hydraulic vibrator so constructed is greatly restrained by the dynamic performance of the servo valve[3], which is difficult to be enhance to a very high level.

Therefore, searching for a new excitation method for hydraulic vibrator always remains particularly significant in the design of the hydraulic vibrator with wide bandwidth. A promising solution is to apply a new control valve called a two-dimensional or "2D" valve[4]. In the 2D valve, both rotary and linear motions of a single spool are exploited to control the frequency and the amplitude independently. Since the frequency of the vibrator is proportional to the continuous rotary speed of the spool, it can be enhanced to a large extent by increasing the rotary speed of the spool, which is well lubricated in hydraulic oil.

HYDRAULIC VIBRATOR EXCITED BY 2D VALVE

The operating principle of the proposed hydraulic vibrator excited 2D valve is illustrated by Figure 1. It is consists of a symmetrical cylinder and a 2D valve. The spool of the 2D valve is continuously driven by an electric motor. The pressurised oil into and out of the cylinder chambers is achieved using a series of grooves asymmetrically distributed on the spool lands, which create an alternatively varied valve port area between the grooves on the spool lands and the rectangular windows on the sleeve as the spool rotates. This can be clearly seen through the cross-sections of spool lands shown in Figure 1b.

If the central angle between two adjoining grooves is β, then geometrically, the groove of meter-in valve port has an $\beta/2$ angle difference with respect to the meter-out valve port. Such an arrangement will cause a 180° phase angle difference between the wave forms of the meter-in valve port and the meter-out valve port. As a result each of the bi-directional cylinders is a hydraulic bridge with a 180° phase angle difference between the chambers. As the spool of the 2D valve makes a rotary motion the pressure inside the two chambers of the cylinder will change alternatively and the piston is subsequently driven in a reciprocating motion (see Figures 1(a) and (b)). The amplitude of the reciprocating motion or the amplification is controlled by the linear motion of the

spool, through which the area of the valve ports between the grooves on the spool land and the windows on the sleeve can be adjusted. Obviously, the frequency of the reciprocating motion of the cylinder controlled by the 2D valve is proportional to the rotary speed of the spool ω and the number of the grooves on a single spool land Z

$$ f = Z\omega/(2\pi) \qquad (1) $$

(a)

I

II

III

IV)

(b)
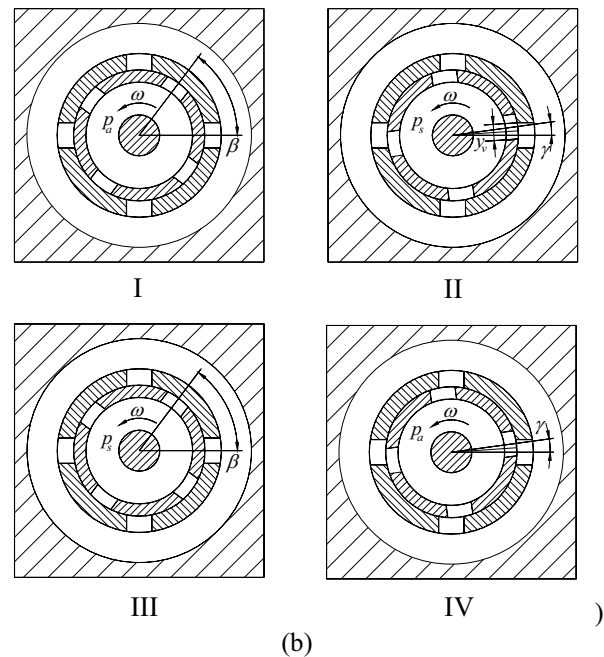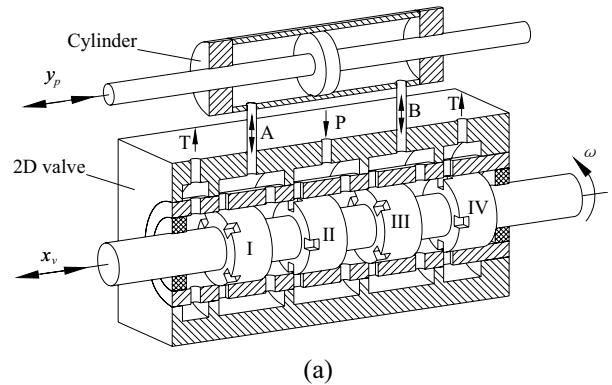
Figure 1 Hydraulic vibrator controlled by a 2D valve

The 2D valve used in the electrohydraulic vibration exciter has a spool with four lands labelled in I, II, III and IV in sequence from left to right in the Figure 1a. These four spool lands are divided into two groups. The spool lands I and II form one group and the spool lands III and IV form the other. On each spool land a number of grooves were asymmetrically distributed in

peripheral direction to coordinate with the windows on the sleeve such that valve ports could be created. The valve ports formed on the spool lands I and II, served as meter-out and meter-in orifices respectively and as a result act as a hydraulic resistance bridge to vary the pressure inside one of the chamber of the double acting cylinder. The valve ports formed on the spool lands III and land IV form another hydraulic resistance bridge to control the pressure inside the other chamber of the cylinder. The numbers of the grooves on these four spool land are the same and the central angle of the adjacent grooves β is equal to four times that of the grooves θ_0, i.e., $\beta = 4\theta_0$. The phase angle of the grooves on each spool land is specially arranged. The phase angle of the grooves on the spool lands I and III are the same and the phase angle of the grooves on the spool lands II and IV are the same; however, the phase angle of the grooves on spool land I (or land III) has a value of 2θ (or $\beta/2$) with respect to the grooves on spool land II (or land IV). The area of the valve port $A_{vI} - A_{vII}$ vs. rotary angle γ is given in Figure 2. It approximates a triangular wave form and its peak value varies with linear valve port opening x_v.

EXPERIMENTAL SYSTEM AND RESULTS

The hydraulic vibrator controlled with 2D valve designed for experiment is shown in Figure 3.
The rotary motion of the spool is driven with a variable AC servo motor while the linear motion of the spool is actuated and positioned the same way of the direct actuated digital valve[6]. In this way, the frequency and the amplitude of the vibration wave output from the cylinder are varied independently via the two independent input signals to the 2D valve controller. The frequency range of the vibrator is to a large degree constrained by the rotary speed of the spool of the 2D valve. The rotation of the AC servo motion is transmitted to the axis of the spool through a gear chain with an effective speed amplification of four. The actual frequency range for the experimental system was 0~800Hz.
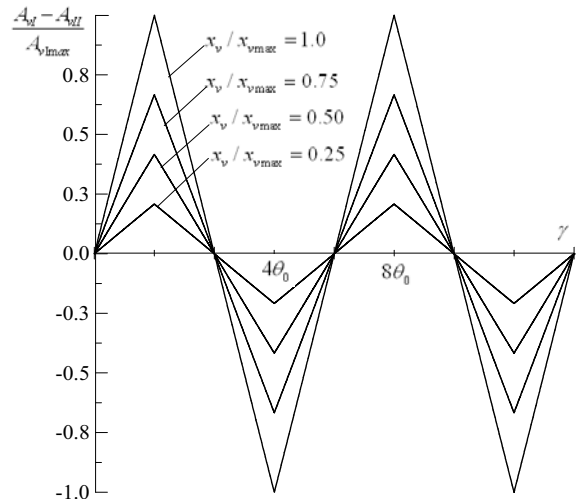
Figure 2 Area of the valve port $A_{vI} - A_{vII}$
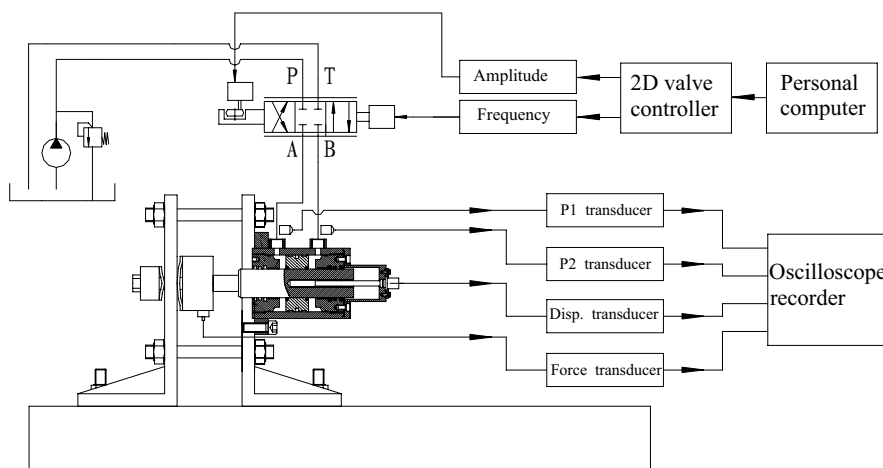
Figure 3   Schematic of the experimental system

Two pressure transducers were used to measure the pressure in each chamber of the cylinder. A force cell was placed between the end of cylinder rod and the rigidly connected frame. The system was therefore a rigid system with a very high spring constant. A displacement transducer was mounted inside of the

cylinder rod to measure the displacement of the piston with respect to the frame in an axial direction of the cylinder. A calibration of the deformation vs. hydrostatic force output by cylinder was carried out using a laser displacement meter (manufactured by Keyance, Japan) with an error less than 0.6 micrometer; the calibration curve is given in Figure 4. It can be observed from the Figure 4 that the relationship between the deformation and the exerted hydrostatic force is fairly linear, which establishes that the deformation of the frame was in elastic range. This ensured that the deformation wave forms of the frame vs. the hydraulic force and piston displacement of the piston were identical. Therefore, the output vibration is presented hereafter as the output force from the force cell.
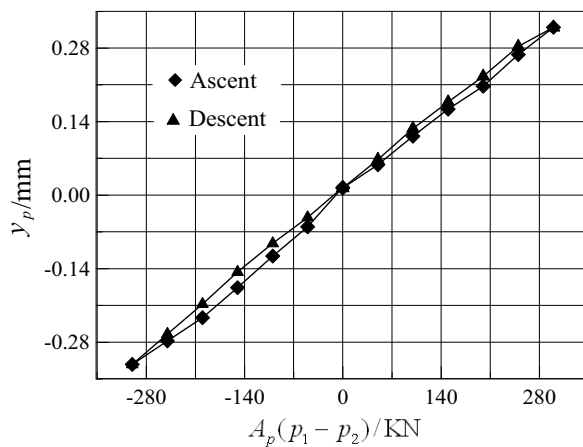
Figure 4 Calibration of deformation of frame work vs. hydrostatic force.

The measured wave forms in the low frequency domain range (10 to 200Hz) are given in Figure 5. It is observed that the measured waves demonstrate the different slopes during ascent and descent which was consistent with the simulation results. The difference was associated with the changing direction of the elastic force of the frame work deformation with respect to the hydrostatic force.

As the spool is rotated, the area of the valve port opening increases and decreases alternatively at the same rate. The process can be approximated as a triangular wave form with the ascent slope being the same as the descent, as shown in Figure 2. This triangular shape is not reflected in the output displacement or force wave form because of the changed direction of the elastic force. With reference to Figures 5 (a), (b), a discussion to the motion of the cylinder piston with the variation of the valve port opening will take an insight into the phenomenon. When the piston is at negative maximum and the speed is zero, the rotary valve ports are all closed at the point, see Figure 2 and the flow rate is at zero). As the spool rotates, the valve port opening area

increases to maximum, pressurized oil is directed to the left cylinder chamber and drained from the right cylinder chamber to tank. This produces a hydrostatic force driving the piston to move in the right hand direction. At this point, the spring force acts as a restoring force, in the same direction as the hydrostatic force. The spring load essentially becomes an "overrunning load. Thus, the curve has a steeper slope. When the valve opening and flow rate reach their maximum and the speed of the piston is at its peak value. As the rotation of the spool continues, the valve port opening area varies from the maximum value to zero, the direction of the hydrostatic remains the same as the proceeding process, but the elastic load turns into a compressed spring, which consumes part of the hydrostatic force. Thus, the curve becomes a smaller slope. When the valve opening and flow rate both drop to zero, the displacement of piston reaches its peak value. A similar reasoning can also be applied to the following process. It should be noted that at the same valve port opening the value of the slope of the positive curve equals to the absolute value of the slope of the negative curve.

The ascent process and descent processes in the wave form of the output displacement y_p or force Ky_p display some inconsistency because of the changing of the elastic load force, which becomes more significant at the critical valve linear opening x_{vc}. As the valve linear opening x_v decreases, the amplitude of the wave form of the output displacement or force will decrease. Concurrently, the load pressure also decreases, but the pressure drop across the valve port will increase since the system pressure p_s is fixed. As a result, the flow rate is less affected by the pressure fluctuation, but is more dependent on the cyclic opening area variation of the rotary valve port. In this case, the change of the flow rate tends to be in the form of a triangular wave and the ascent and descent rates in the wave form of the output displacement or force tend to be identical to each other or to the flow form.

CONCLUSION

A new approach for the excitation of the hydraulic vibration is presented using a 2D valve which extends the frequency range substantially. In 2D valve, the rotary motion of the spool coordinates the grooves of the spool land with the windows on the sleeve and alternates flow into and out of the chambers of the hydraulic cylinder, thus exciting the piston (rotor) to output a vibration. The spool's linear motion is used to adjust the peak flow rate and thus the amplitude of the output vibration. The frequency of the vibration is excited by the 2D valve and is related to the rotary speed of the spool. Thus the potential to extend the frequency of the hydraulic vibrator to even higher levels exists by

increasing the rotary speed of the spool. The experimental results show that in the low frequency domain ascending and descending slopes of the output force waveforms show some differences which become more pronounced at spool displacements above the critical valve linear opening area. As the working frequency passes beyond the low frequency domain, the vibration excited by the 2D valve is mainly influenced by the hydraulic resonance.

It was concluded that the proposed 2D valve and actuator have successfully extended the frequency range of the electrohydraulic vibration exciter.
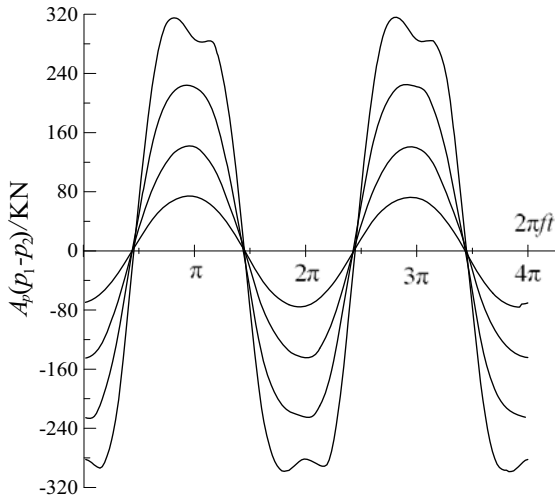
(a) $f = 10$Hz
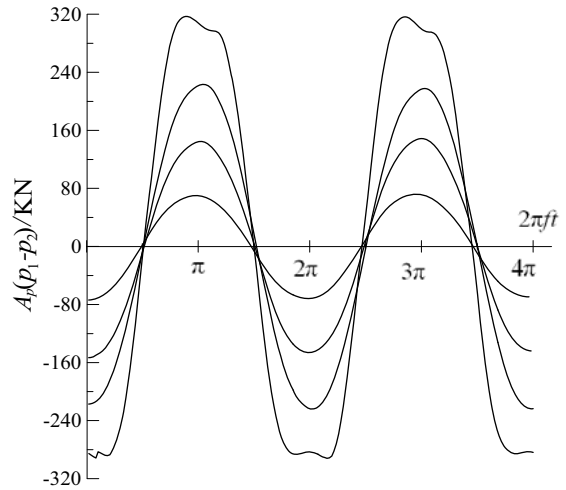
(b) $f = 40$Hz
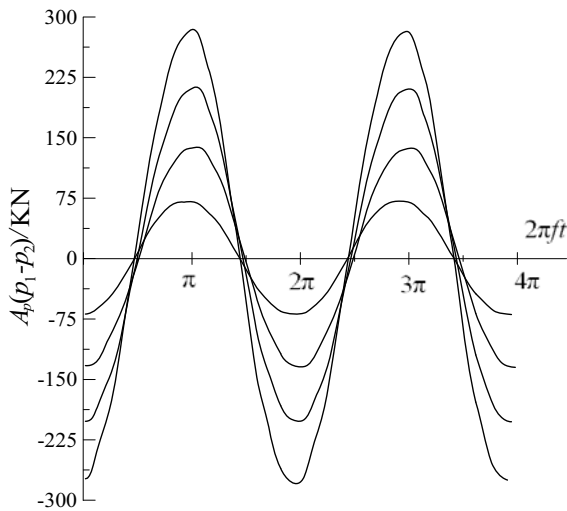
(c) $f = 100$Hz
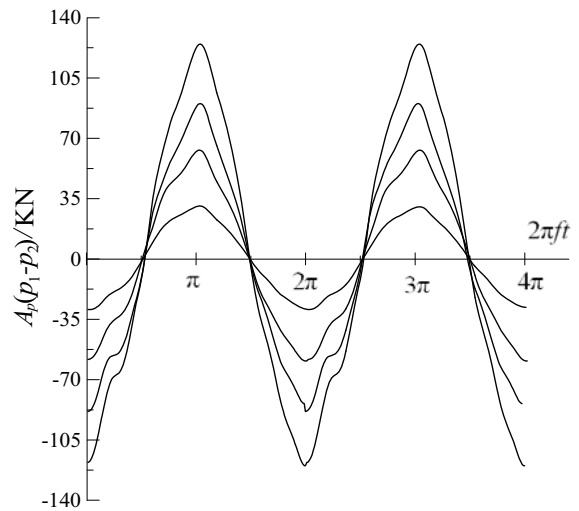
(d) $f = 200$Hz

Figure 5   Wave forms in the lower frequency domain

REFERENCES

2. Lang, Geore Fox, Electrodynamic shaker fundamentals，S V Sound and Vibration, v 31, n 4, Apr, 1997,pp.14~21.
3. SU Donghai, CUI Xiao, WU Xihong，Analysis and Simulation of Dynamic Properties of High Frequency Hydraulic Vibration, 7th International Conference on Progress of Machining Technology, 2004,pp.918~922.
4. Jian Ruan and Richard Burton, Bulk Modulus of Air Content Oil in a Hydraulic Cylinder. ASME,

1. K. G. McConnell, Vibration Testing---Theory and Practice, New York, 1995.
   IMECE2006-15854, Fluid Power Control System Technology, Vol.7, 2006.
5. Merritt, H. E., Hydraulic Control Systems, John Wiley & Sons, New York, 1967,pp.67~86.
6. J. Ruan R. Burton and Ukrainez, Direct Actuated Digital Servo Valve, The Ninth Scandinavian International Conference on Fluid Power, SICF'05, June 1-3, 2005, Linköping ,pp.450-461.

P1-24

STUDY ON THE OPENING FORCE CHARACTER OF WATER PRESS INLET-VALVE

Kong Xiangdong, Zhang Chunyu*, Yao Jing, Zhu Xiaoxia and Tang Xiangjun

* Yanshan University, Qinhuangdao, 066004, PRC
(E-mail: zcy5337@tom.com)

ABSTRACT

In this paper ,base on the operating principle of water press pull-up inlet valve,we model the mathematical model of inlet-valve and made a simulation on computer.By the method of simulation,get the curve of control pressure(up cavity pressure) and opening force in process of pull-up inlet valve opening.Changing the structural parameter of inlet valve and working pressure of water press, gain the relationship between pull-up inlet valve opening force changing tendency and the structural parameter of inlet valve and working pressure.

KEY WORDS

Water press, Inlet-valve, Opening force, Simulation

NOMENCLATURE

B :The damp coefficient of main valve spool

f_b :Cross-sectional area of main valve spool

f_c :End face area of main valve spool in the down cavity

f_s :Area of main valve spool circular bead

F_t :Opening force of main valve

m :Mass of main valve spool

P_a :Pressure at main valve inlet

P_b :Pressure in up cavity

P_c :Pressure at main valve outlet

Q_3 :Flow of main valve port

v_3 :Flow rate at main valve port

y :Offset of main valve spool

θ :Cone angle of main valve spool

ρ :Density of oil water emulsion

INTRODUCTION

The traditional structure of wate press' inlet and outlet valve is pull-up valve,this type valve is opened by using external control organ to pull up the valve plug's middle pole.Without external opening force, the valve plug's middle pole will go back by the force of a spring in the valve's up cavity,then the valve plug closed following the middle pole.

The structure of pull-up inlet valve is shown in Figure1.Its main valve is a cone valve. The pressure relief valve of up cavity pressure is a little cone valve,it is coaxial with main valve and its valve bed is main valve's spool.There are water entrance holes on valve barrel,they can made high pressure water to flow into main valve's up cavity from valve inlet.

The operating principle of water press pull-up inlet valve is so.When pressure relief valve keep shutting, up cavity pressure push main valve spool down on the valve bed.The up cavity pressure begin to drop when pressure relief valve is opened,and when pressure relief valve get its stroke end the main valve spool is pulled up,the inlet valve is opened[1].
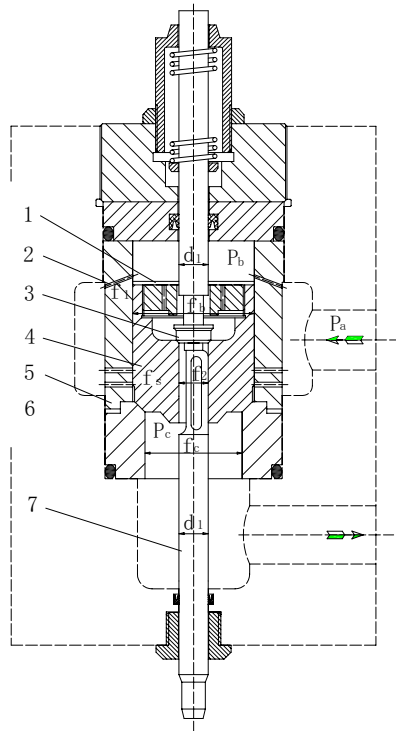
Figure 1 The structure of pull-up inlet valve

Opening pressure relief valve is by the way of pulling up the pull-up pole which under the pressure relief valve,and the valve is shut by the force of a string in the valve's up cavity.While the pressure relief valve is shuting,the valve port area is reduced and the up cavity pressure is rised.The pressure push main valve spool down on the valve bed solidly.

Mechanical Analysis of the Valve's Opening Process

The opening force of pull-up inlet valve is mainly decided by the resultant force acting on the main valve spool.The force acting on the spool when it is opening include up cavity pressure force, down cavity pressure force,rising force of spool circular bead,hydraulic power at valve port and damping force.
The balanced equation of the main valve spool force:

$$P_b f_b = f_c P_c + f_s P_a - Q_3 \rho v_3 \cos\theta + 0.45 P_a \frac{\pi}{4}\left(d_1^{\,2} - d_2^{\,2}\right) + F_t - m\frac{dx^2}{d^2 t} - B\frac{dx}{dt} \tag{1}$$

The item of $0.45 P_a \frac{\pi}{4}\left(d_1^2 - d_2^2\right)$ means the pressure force at cone sealing face of main valve spool.Parameters d_1 and d_2 are outer diameter and inner diameter of the cone sealing face. $0.45 P_a$ means average pressure at cone sealing face of main valve spool[2].

Simulation of the Valve Opening Process

The MATLAB/Simulink model of the pull-up inlet valve is shown in figure 2.
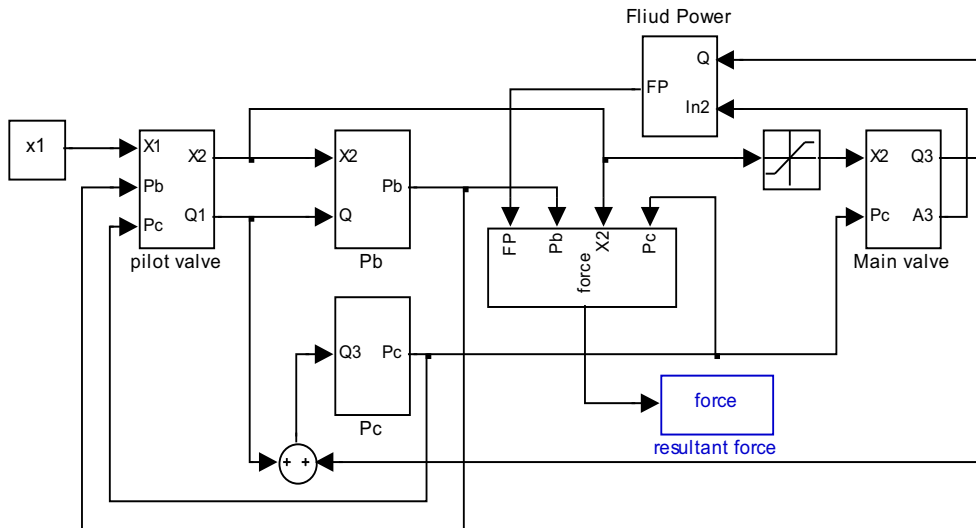
Figure 2 Simulink model of pull-up inlet valve

Changing diameter of water entrance hole and opening stroke of pressure relief valve,we gain the curves of up cavity pressure and main valve spool opening force in the process of inlet valve opening.These curves are shown in figur 3 and figure 4.
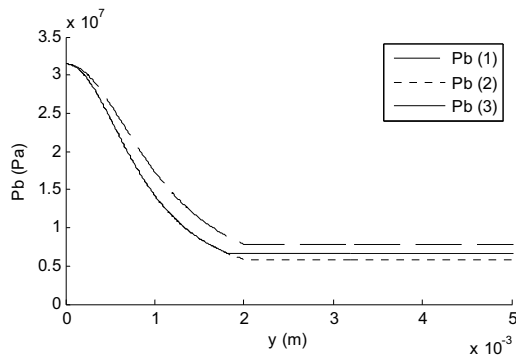
Figure 3 The curves of up cavity pressure
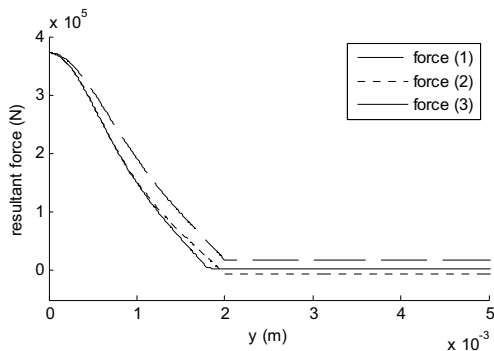
Figure 4 The curves of main valve spool opening force

Structural parameters of curves1,2,3 in figure 3 is below.
Curve1: diameter of water entrance hole is 5mm,opening stroke of pressure relief valve is 2mm.
Curve2: diameter of water entrance hole is 4.5mm,opening stroke of pressure relief valve is 2mm.
Curve1: diameter of water entrance hole is 6.5mm,opening stroke of pressure relief valve is 1.8mm.
Static acting forces on the inlet valve mainly contain up cavity pressure force($f_b P_b$), down cavity pressure force($f_c P_c$),rising force of spool circular bead($f_s P_a$),.and the permeating pressure force at cone sealing face of main valve spool.To make the inlet valve work reliably, need that when pressure relief valve was little opened the main valve spool could be push down on the valve bed solidly,in case of the main valve spool floating with pressure relief valve little opened.The up cavity pressure force is mostly force to keep the main valve spool be push down .Through changing Structural parameters of diameter of water entrance hole and opening stroke of pressure relief valve,we can control the up cavity pressure.The curves in figure 3 and figure 4 show up cavity pressure and opening force of main valve at different structural parameters.The curve 2 in two figures above show the best proper opening force ang pressure .
Working pressure of press have an important influence

on the down cavity pressure of inlet valve. So, following,emulate the opening process of inlet valve under different working pressures.
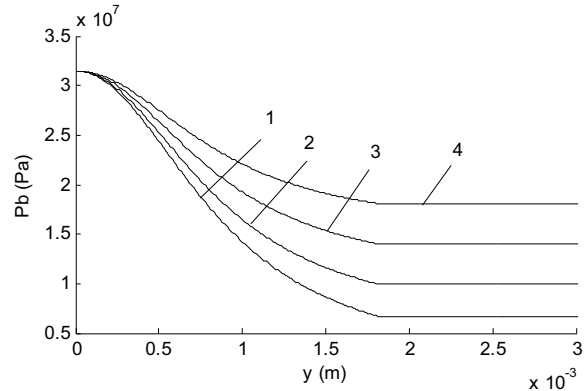
Figure 5 Up cavity pressure under different working pressure
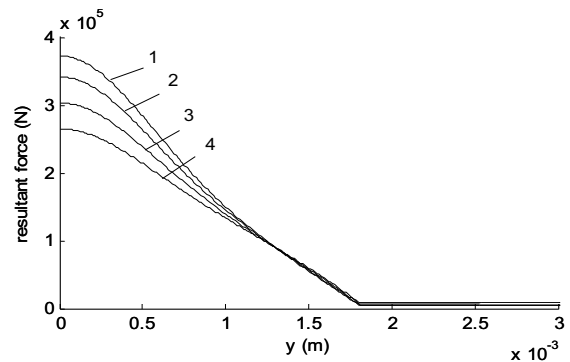
Figure 6 Main valve spool opening force under different working pressure

Curve1,2,3,4 in figure5 and figure 6 ,their working pressure respectively is 1×106Mpa,5×106 Mpa,10×106 Mpa and 15×106 Mpa.From figure5 and figure6,we can know that rising with working pressure going up,but the opening force is little influenced by the working pressure.The reason is that up cavity pressure is stoodoff by down cavity pressure,and the permeating pressure force at cone sealing face have a linear relationship with working pressure,it could farther standoff the influence acted by working pressure.Therefore we have the conclusion that the pull-up inlet valve opening force be influenced by working pressure little,and when supply pressure is given the stabilization of the valve opening force is good.

CONCLUSION

1.The structural parameters of pull-up inlet valve have an important influence on the character of the valve's opening force.
2. When supply pressure is given,the valve opening

force is little influenced by working pressure.

REFERENCES

1. Shen Hong, 120MN Water Forging Press, Machinery Industry Press, 1980, pp. 84-102.
2. T.M.Buster, Plane Hydraulic Drive and Accessory, Defense Industry Press, 1963.

P1-25

DEVELOPMENT OF A ROTARY TYPE

WATER HYDRAULIC PRESSURE INTENSIFIER

Shigeru OSHIMA*, Takuya HIRANO*, Shimpei MIYAKAWA**, and Yoshihiro OHBAYASHI**

* Department of Control & Computer Engineering
Numazu National College of Technology
3600 Ooka, Numazu, Shizuoka, 410-8501 Japan
(E-mail: oshima@numazu-ct.ac.jp)
** Water Hydraulics System Group, Basic Technology R&D Center
KYB Corporation
1-12-1 Asamizodai, Sagamihara, Kanagawa, 228-0828 Japan

ABSTRACT

This study concerns a new rotary type water hydraulic pressure intensifier. The object of this paper is to introduce the structure and the working principle of the pressure intensifier, and to present the fundamental characteristics by experimental results. The basic structure is similar to that of a water hydraulic planetary gear motor. Its main part consists of a stator, a rotor, nine planetary gears and two side plates. The inside of the stator is formed by a curve with 5 lobes and the outside of the rotor is formed by a curve with 4 lobes. Their curved surfaces have teeth like a gear. Nine displacement chambers are formed by the stator, rotor, planetary gears and side plates, and the each chamber's volume varies periodically when the rotor rotates. A side plate has 5 inlet distribute holes and 5 outlet distribute holes alternately located on its surface. Each displacement chamber connects to an inlet distribute hole during the volume is increasing, and it connects to an outlet distribute hole during the volume is decreasing. Now, one of the outlet distribute holes is separated from the other 4, the intensified higher pressure water is discharged from the separated distribute hole. It is found that the critical intensification ratio is about 2.5 by experimental results with a prototype.

KEY WORDS

Water hydraulics, Pressure intensifier, Rotary type, Planetary gear motor, Experimental results

NOMENCLATURE

N : rotational speed of a rotor
n : number of each the inlet distribute holes and the outlet distribute holes
P_e : exhaust pressure
P_i : intensified pressure
P_s : supply pressure
Q : flow rate
T : torque
V_{th} : theoretical displacement volume
η : total efficiency

η_T : torque efficiency
η_V : volumetric efficiency

Subscript
e : concerned with exhaust pressure
i : concerned with intensified pressure
s : concerned with supply pressure

INTRODUCTION

Water hydraulic system which uses tap water as pressure medium has been known as an environmental

friendly new fluid power drive system. It has many advantages; clean, non-toxic, non-flammable, low pressure loss, and so on [1]. It is also a big advantage that the pressure medium is easily obtained and the disposal of the waste is easy, too. They lead to decreasing of management cost.

It is considered that the water hydraulic system has many possible applications in low pressure driving systems as well as in middle and high pressure driving systems. Using the low pressure leads to low cost of the components, and to easy operation and safety driving of the systems. The studies on the low pressure water hydraulic systems have been carried out to aim to get the low price compatible to pneumatic systems while the high power density and good controllability are compatible to oil hydraulic systems [2],[3].

Water hydraulic system has been applied in industries of food processing, beverage bottling and packaging, semiconductor and paper manufacturing, etc. It has also possible applications in welfare equipments, universal house equipments, leisure and amusements park equipments and others [4]. For the many of those applications, the low pressure water hydraulic systems are available. Some of them can be driven directly by the pressure from the civil tap water network or the water supply network for the industries. Otherwise, centrifugal pumps may be often installed as pressure sources. In all the cases, pressure intensifier will be useful when the particular actuators require the higher pressure than the primary pressure from the pressure sources in the systems.

The pressure intensifiers, or boosters, convert high-flow low-pressure fluid power into low-flow high-pressure fluid power. There are many commercial products of oil hydraulic and pneumatic pressure intensifiers. Most of them are cylinder-type and there are a single acting type and a double acting type. The range of their working pressure is very wide; some works at below 0.1 MPa supply pressure and some works with a few hundred MPa intensified output pressure. The intensification ratio is also in variety; 1:2 to 1:80 [5]. Besides the cylinder type, there are a few kinds of rotary type intensifier; one is commonly known as a multiple-section, internal gear flow divider which is appropriately connected into a circuit to make intensification result. Another is a liquid transformer based on a called "radial cylinder motor" [6]. It is designed for oil hydraulic driving with relatively high pressure. It is also expected to be suitable for water hydraulic driving because of its structure with low friction and small leakage. Up to the present, however, the pressure intensifiers available in low pressure water hydraulic systems are very few in market.

In this study, a new rotary type water hydraulic pressure intensifier which is available in low pressure water hydraulic systems is presented. It consists of a small number of parts and simple structure. It is formed with a little modification from a water hydraulic planetary gear motor. Its main part consists of a stator, a rotor, nine planetary gears and two side plates [7]. The object of this paper is to introduce the basic structure and the working principle of the new pressure intensifier, and to present some experimental results on fundamental characteristics of a prototype.

STRUCTURE AND WORKIG PRINCEPL

The basic structure of the pressure intensifier is the same as a water hydraulic planetary gear motor except the location of the distribute holes on the port plate A. The main part of the water hydraulic planetary gear motor consists of a stator, a rotor, nine planetary gears, the port plates A, B and a flange as shown in Figures 1 and 2.
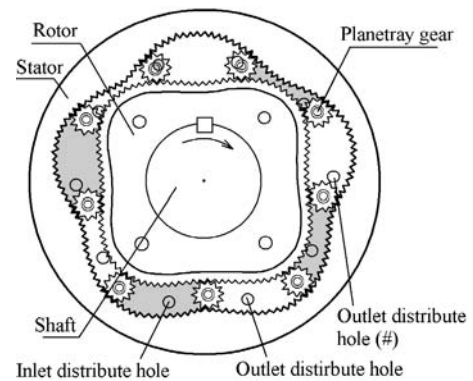
Figure 1 Structure of main part of water hydraulic planetary gear motor
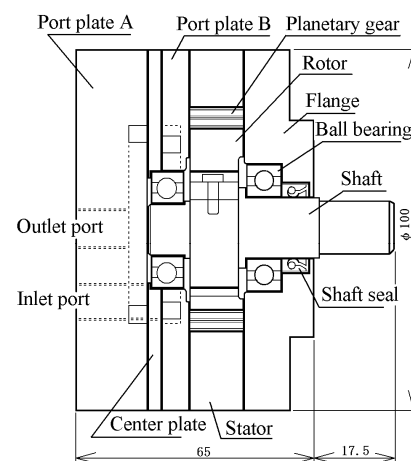
Figure 2 Cross sectional drawing of water hydraulic planetary gear motor

The inside of the stator is formed by a curve with 5 lobes and the outside of the rotor is formed by a curve with 4 lobes. The shape and size of the pitch curves of the both of them and the radius of the planetary gear's pitch circle has a tight connection. They are all determined by numerical calculation of the equation which is derived based on the theorem of friction wheel model [8]. The curved surfaces of the stator and the rotor have teeth which mesh with the planetary gears. Nine displacement chambers enclosed by the stator, rotor, planetary gears, port plate B and flange are formed, and the each chamber's volume varies periodically during the rotor rotates.
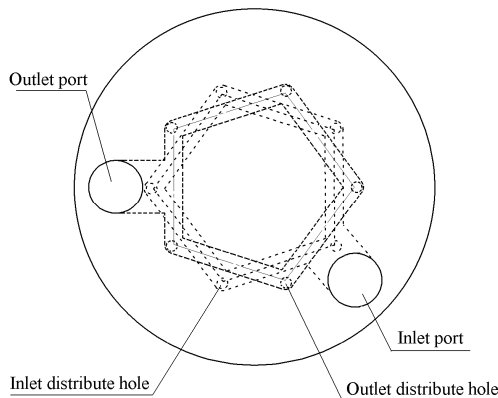
Figure 3 Location of Inlet and Outlet distribute holes on the side plate A and B for the motor

Port plate A has an outlet port and five outlet distribute holes which are all connected with a pentagon groove and port plate B has an inlet port and five inlet distribute holes which are all connected with a pentagon groove such as shown in Figure 3. The inlet port is also drilled through the port plate A to connect the inlet port on the port plate B, and the five outlet distribute holes are also drilled through the port plate B at the same place of each the outlet distribute hole on the port plate A. The inlet distribute holes and the outlet distribute holes are located alternately on the inside surface of the port plate B and open to the displacement chambers as shown in Figure1. Each displacement chamber connects alternately to an inlet distribute hole and an outlet distribute hole during the rotor rotates. The volume of each displacement chamber increases while connecting to the inlet distribute hole and decreases while connecting to the outlet distribute hole. The water from the chamber is exhausted through the outlet distribute holes to the outlet port and to the reservoir.

In the displacement chambers which connect to the inlet distribute holes, the shadowed chambers in Fig.1, the pressure acts on the rotor surface and the planetary gears generates the torque in clockwise. Fig.4 shows the mechanism of torque generation at one of the

displacement chambers. The drawing of (a) shows the generation of torque by the pressure acts on the rotor surface and the drawing of (b) shows that on the planetary gears. Note that there is a distance 'e' between the line of force action and the center of the rotor in (a), and that r_1 is larger than r_2 in (b). The same condition appears at the all displacement chambers when they are connecting to the inlet distribute holes.

(a)   (b)
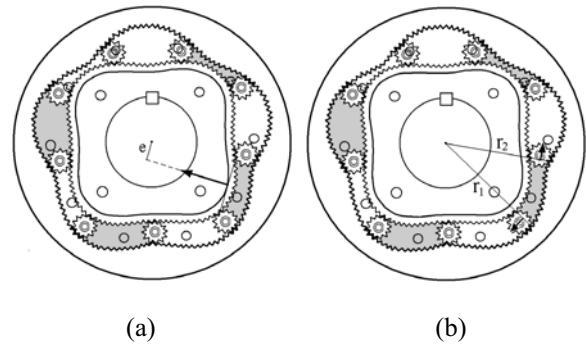
Figure 4 Mechanism of torque generation

As the planetary gears revolve with the rotation of the rotor, the displacement chambers move and switch the connection to the inlet and outlet distribute holes by turns. The rotation of the rotor, therefore, continues while pressurized water is supplied to the inlet port.

The only one modification to get the intensification function is to replace the port plate A by a modified one as shown in Figure 5. On the new port plate A, one of the outlet distribute holes is separated from the other 4 as well as the outlet port. The volume of the displacement chamber decreases while it connects to the separated outlet distribute hole. The displacement chamber works as a pump which is driven by the water hydraulic planetary gear motor, and the chamber therefore discharges intensified higher pressure water to the intensified port in Fig.5, which is equivalent to the outlet distribute hole (#) in Figure 1.
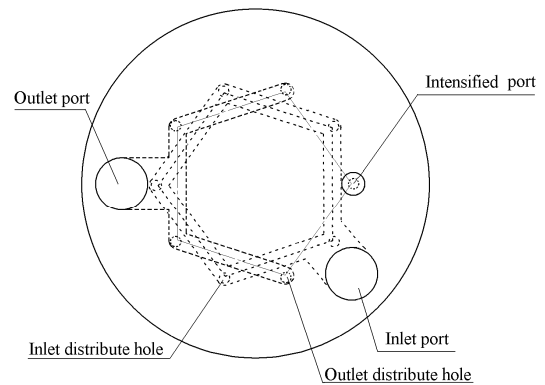
Figure 5 Modified port plate A

BASIC THEORY

The torque T_s generated by the supply pressure P_s, which tends to rotate the rotor, balances with the counter torques T_i and T_e generated by pressures P_i and P_e. The torque balance is presented by Eq.(1).

$$T_s = T_i + T_e \qquad (1)$$

Here, the torques are presented as $T_s = \eta_{Ts} \dfrac{P_s \cdot V_{th}}{2\pi}$,

$T_i = \dfrac{1}{\eta_{Ti}} \dfrac{P_i}{2\pi} \dfrac{V_{th}}{n}$ and $T_e = \dfrac{1}{\eta_{Te}} \dfrac{P_e}{2\pi} \dfrac{(n-1) \cdot V_{th}}{n}$.

Substituting them into Eq.(1), the following equation is derived.

$$P_i = n \cdot \eta_{Ts} \cdot \eta_{Ti} \cdot P_s - \frac{\eta_{Ti}}{\eta_{Te}}(n-1) \cdot P_e \qquad (2)$$

Supposing $P_e = 0$ and putting $\eta_{Ts} \cdot \eta_{Ti} = \eta_T$ in Eq.(2), the intensified pressure is presented by Eq.(3).

$$P_i = \eta_T \cdot n \cdot P_s \qquad (3)$$

Concerning the flow rate, the supply flow rate Q_s, the intensified port flow rate Q_i and the exhausted flow rate from the outlet port Q_e are presented as follows,

$Q_s = \dfrac{N \cdot V_{th}}{\eta_{Vs}}$, $Q_i = \eta_{Vi} \cdot N \cdot \dfrac{V_{th}}{n}$ and $Q_e = Q_s - Q_i$.

Putting $\eta_{Vs} \cdot \eta_{Vi} = \eta_V$, the intensified port flow rate is presented by Eq.(4).

$$Q_i = \eta_V \frac{Q_s}{n} \qquad (4)$$

The total efficiency is defined by Eq.(5).

$$\eta = \frac{P_i \cdot Q_i}{P_s \cdot Q_s} \qquad (5)$$

The following relation is confirmed by substitution of Equations (3) and (4) to the Eq.(5).

$$\eta = \eta_T \cdot \eta_V \qquad (6)$$

SPECIFICATION OF A PROTOTYPE

Basically the prototype is made by a modification of a water hydraulic planetary gear motor, changing the port plate A. The external sizes are shown in Fig.1. The theoretical displacement volume V_{th} is 37.6 cm³/rev. The numbers of lobe are 4 with the rotor and 5 with the

stator, and therefore the numbers of the inlet distribute holes and the outlet distribute holes are 5 respectively. The pitch curve of the rotor is formed by cosine curve of which the maximum radius is 27.524 mm and the minimum radius is 22.552 mm. The width of the rotor, stator and planetary gears are 15 mm. All the main parts are made of stainless steel and the surfaces of the port plate B and the flange are coated with DLC treatment. The tentative specification of the prototype of the water hydraulic planetary gear motor is presented in Table 1. Fig.6 shows the inside view of the motor.

Table 1 Tentative specification of the prototype of the water hydraulic planetary gear motor

Working fluid	tap water
Rated supply pressure	0.25 MPa
Rated supply flow rate	0.008 m³/min
Rated rotational speed	200 rpm
Rated outpet torque	0.9 Nm
Rated output power	20 w

Figure 6 Inside view of the prototype of the water hydraulic planetary gear motor

According to the Eq.(3), the intensification ratio is presented by Eq.(7) for the prototype because the number of the distribute holes n is 5. The intensification ratio will be the maximum 5 when $\eta_T = 1$.

$$\frac{P_i}{P_s} = \eta_T \times 5 \qquad (7)$$

EXPERIMENTAL RESULTS

An experiment is carried out in order to confirm the fundamental function as a pressure intensifier and how large the critical intensification ratio is. Fig.7 shows the circuit of the experimental setup.

Water is supplied from the axial piston pump and the

supply pressure P_s is set at a given value using the relief valve and the throttle valve (1). The intensified pressure P_i is set at an optional value using the throttle valve (2). The pressures P_s, P_i and P_e are measured with Bourdon pressure gauges which contain glycerin as damper oil. The flow rate Q_s and Q_i are measured with turbine flow meters and the rotational speed of the rotor shaft is measured with a digital tachometer.

The flow from the intensified port is discharged periodically and intermittently. The condition is almost the same as in the case of the double acting cylinder type intensifier. There is fluctuation on the intensified port pressure and the fluctuation becomes especially large when the rotational speed is low. An accumulator of 30 cm^3 is installed at the intensified port line to reduce the pressure fluctuation.
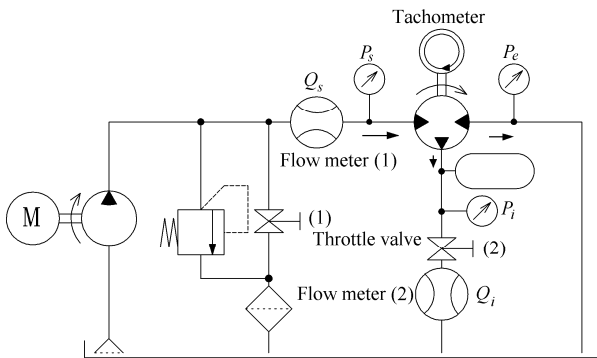
Figure 7 Circuit of the experimental setup

Fig.8 shows the experimental result of the flow rate from the intensified port Q_i versus the intensification ratio P_i/P_s at the five different supply pressures. The maximum values of P_i/P_s are between 2.5 and 2.7 at the each supply pressure. When the ratio P_i/P_s is larger than the maximum values, the rotation of the shaft becomes intermittently and the intensified pressure fluctuates violently. Therefore, there is no plot over the area. The maximum value of P_i/P_s is the critical intensification ratio.

It is confirmed that the new structured intensifier works well as a water hydraulic pressure intensifier even at a low pressure near the pressure of the civil tap water network.

It is found from Fig.8 that Q_i decreases as the ratio P_i/P_s becomes larger under a constant P_s, and Q_i increases as P_s becomes higher under a constant P_i/P_s. This tendency is caused by the change in the rotational speed of the rotor. Fig.9 shows the rotational speed N versus P_i/P_s. The curves are almost the same as in Fig.8.
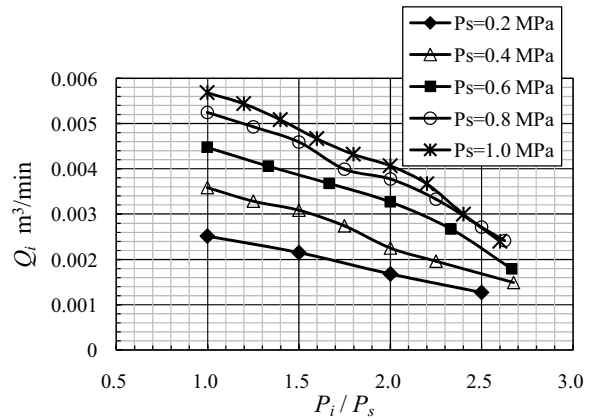
Figure 8 Flow rate from the intensified port Q_i versus the intensification ratio P_i/P_s
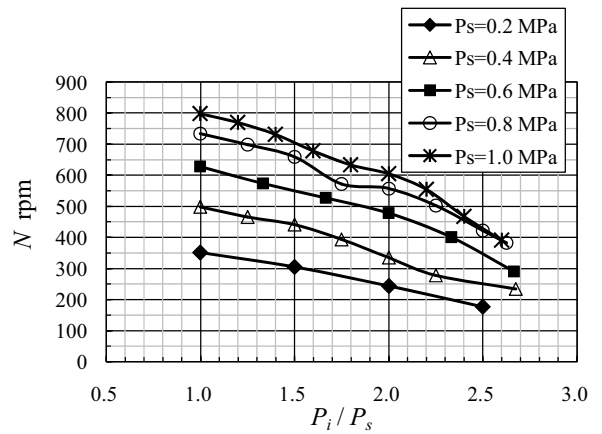
Figure 9 Rotational speed N versus the intensification ratio P_i/P_s
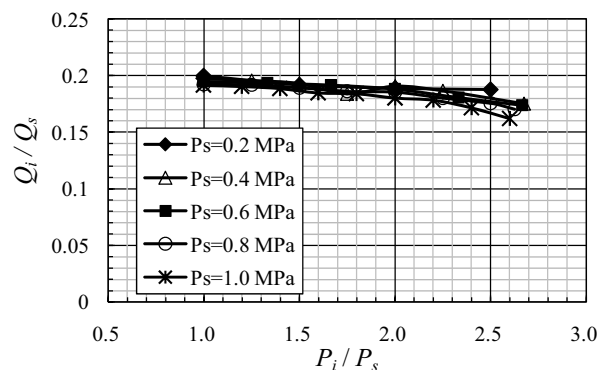
Figure 10 Ratio of Q_i to the supply flow rate Q_s versus the intensification ratio P_i/P_s

The ratio of Q_i to the supply flow rate Q_s versus P_i/P_s is shown in Fig.10. If there is no leakage, that is η_v=1, the ratio Q_i/Q_s becomes 0.2 as shown in Eq.(4). Since the

leakage increases as P_s becomes higher and the ratio P_i/P_s becomes larger, the value of Q_i/Q_s becomes smaller than 0.2. Fig.11 shows the same result by the volumetric efficiency η_v.

Fig.12 shows the torque efficiency η_T versus P_i/P_s. The value of η_T is given by the ratio P_i/P_s as shown in
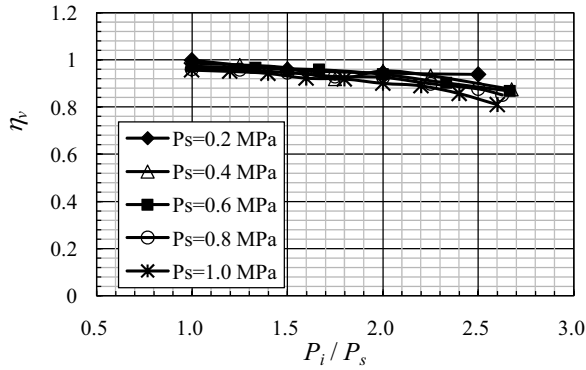
Figure 11 Volumetric efficiency η_v versus the intensification ratio P_i/P_s
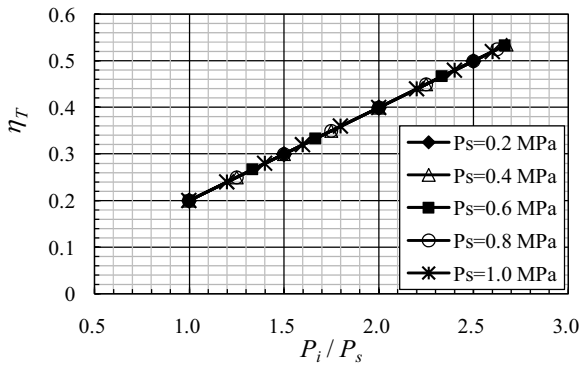
Figure 12 Torque efficiency η_T versus the intensification ratio P_i/P_s
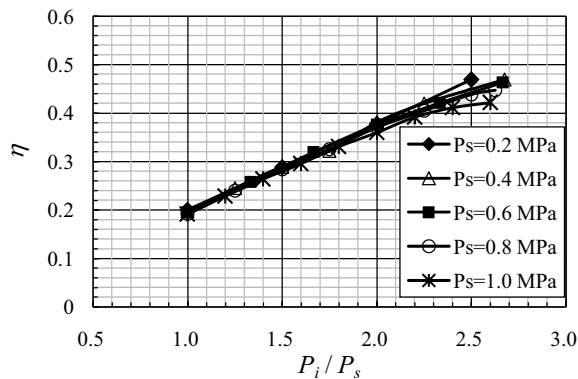
Figure 13 Total efficiency η versus the intensification ratio P_i/P_s

Eq.(7) regardless of the value of P_s. The maximum value of P_i/P_s is obtained when η_T is the maximum. In order to get a larger intensification ratio, to improve the torque efficiency is the key.

Fig.13 shows the total efficiency η versus P_i/P_s. The maximum total efficiency is around 45%. It is found that η becomes higher as P_i/P_s is larger because of increase in torque efficiency η_T. And it is also found that η decreases as the supply pressure P_s becomes higher under the condition of constant P_i/P_s. It is caused by decrease in volumetric efficiency η_v. For the further improvement of the total efficiency and to get a larger intensification ratio, the improvement in torque efficiency is important.

CONCLUSION

It is confirmed that a new rotary type pressure intensifier, which is constructed by a simple modification with a water hydraulic planetary gear motor, works well as a pressure intensifier. It works even in low pressure as same as the pressure in civil tap water network. The critical intensification ratio of the prototype is around 2.5 and the total efficiency is about 45%. The key to increase the total efficiency and to get the larger intensification ration is to improve the torque efficiency.

REFERENCES

1. Modern Water Hydraulics – Your Choice for the Future, Leaflet of Introduction of Water Hydraulics by NFPA, 1995.
2. Aaltonen, J. et al., Experiences On The Low Pressure Water Hydraulic Systems, Proceedings of the Fourth JFPS International Symposium, 1999, pp.357-363.
3. Kunttu, P. et al., Low Pressure Water Hydraulics - Stae of the Art, Proceedings of The Sixth Scandinavian International Conference on Fluid Power, 1999, pp.67-75.
4. Aqua Drive System – A Technical Guide 2, Leaflet of Introduction of Water Hydraulics by JFPA, 2005.
5. A staff report, Intensifiers offer boost from low to high pressure, Hydraulics & Pneumatics, 1999, **52**-7, pp.45-46.
6. Yasuo Kita, Takashi Asami et al., Rotary type liquid pressure transformer, Journal of JFPS Fluid Power System (in Japanese), 2004, **35**-1, pp.67-71.
7. Shigeru Oshima, et at., Development of a Low Pressure Water Hydraulic Planetary Gear Motor, Proceedings of JSME annual conference 2006 (in Japanese), 2006, **2**, pp.327-328.
8. J.W.G.M. Huijbers, Kinematics of the Planetary Gear Motor, Report PGM-T1, Hessels & van Rooij Engineering, 1990.

P1-26

ANALYSIS AND DESIGN OF CRYOGENIC BALL VALVE

Dong-Soo KIM*, Myoung-Sub KIM*

*Roll-to-Roll PEMS Team, Nano Mechanical Systems Research Division
Korea Institute of Machinery & Materials
171, Jang-Dong, Yuseong-Gu, Daejeon, Korea
(E-mail: joseph@kimm.re.kr)

ABSTRACT

Natural gas is being hailed as alternative energy sources for a petroleum, because it is almost no emissions of pollutants in the environment. Use of equipment for liquefied natural gas, along with increased demand for natural gas is also growing. Cryogenic ball valve is used to control the liquified natural gas which temperature is -196℃, supplied pressure is 168kg/cm². To acquire the safety along with durability of cryogenic ball valve, we should consider the structural mechanics such as stress, deformation and dynamic vibration characteristics and identify those important aspects in the stage of preliminary design engineering. For the cryogenic ball valve, the assurance of structural integrity and operability are essential to meet not only normal, abnormal loading conditions but also functionality during a seismic event. In this study, analytical approach and results using finite element analysis and computational method are herein presented to evaluate the aspects of structural integrity along with operability of cryogenic ball valve. Moreover, we have done the optimal design through special processing and heat treatment and so on. Finally, we designed the high pressure cryogenic ball valve that accomplishes zero leakage.

KEY WORDS

LNG, Cryogenic, Ball valve, Analysis, Design

NOMENCLATURE

D : Stiffness matrix
σ : Stress
ε : Strain vector
$\bar{\varepsilon}$: Supposition Strain vector
Γ : Boundary
ku : Elastomer stress vector
u_g : Displacement stress vector
t_b : Boundary stress vector
MPa : Young module coefficient
kg/cm² : Pressure
kg/mm³ : Density
I/℃ : Thermal Expansion coefficient

W/mm℃ : Heat conduction

1. INTRODUCTION

The process of the formation of natural gas (NG) is similar to that of coal. NG can be produced from oil wells as assistant gas; however, most of it is produced as non-assistant gas. 80~85% of NG is methane (CH_4), whose low concentration of hazardous substances makes it a valuable energy resource. However, because NG is difficult to store in large quantities and mass transportation requires a pipeline, technology for NG liquefaction has been developed to solve these problems, enabling mass storage and transportation over long distances. The demand for facilities for the storage, transportation and control of liquefied natural gas

(LNG) is rapidly increasing in line with the rising demand for LNG [1-2].

Most of the high-pressure, cryogenic ball valves are of the side-entry type, the insulation of which has to be cut open to carry out repairs. Therefore, top-entry type cryogenic valves have been adopted recently [3].

Top-entry type, high-pressure, cryogenic ball valves are subject to safety verification to prevent the types of accidents that can be caused by earthquake, fire, or explosion. Their specifications regarding leakage, being very strict, are satisfied by only a few products in the world.

In this study, a numerical analysis is conducted for the structural safety and the distribution of thermal stress and deformation by thermal shock under high pressure and very low temperature conditions, in order to assess the safety and reliability of the ball valves for LNG to provide a basis for the design and manufacturing of products which are safe from leakage under conditions of extreme temperature variance.

Figure 1 Photo of the valves are installed on vessels

2. Finite Element Analysis (FEA) on Ball Valves

2.1. Theoretical Equation for Analysis

Eq. (1) is a finite element equation for 3-dimensional loads[4].

$$\frac{\partial \sigma_{xx}}{\partial x} + \frac{\partial \sigma_{xy}}{\partial y} + \frac{\partial \sigma_{xz}}{\partial \sigma z} = 0$$

$$\frac{\partial \sigma_{yx}}{\partial x} + \frac{\partial \sigma_{yy}}{\partial y} + \frac{\partial \sigma_{yz}}{\partial \sigma z} = 0$$

$$\frac{\partial \sigma_{zx}}{\partial x} + \frac{\partial \sigma_{zy}}{\partial y} + \frac{\partial \sigma_{zz}}{\partial \sigma z} = 0$$

(1)

In order to obtain a variational equation for the numerical analysis of the finite element method (FEM), eq. (1) can be transformed into eq. (2) in a weak form.

$$\int_{\Omega} \overline{u}^T \Delta \sigma d\Omega = 0$$

(2)

Using Green's Theorem, we obtain eq. (3), where $\overline{\varepsilon}$ is a virtual deformation vector and Γ is the boundary.

$$\int_{\Omega} \overline{\varepsilon}^T \sigma d\Omega - \int_{\Gamma} \overline{u}^T t d\Gamma = 0$$

(3)

In order to substitute the boundary condition, the stress vectors can be represented by eq. (4).

$$t = -k(u - u_g) + t_b$$

(4)

Substituting eq. (4) into eq. (3), we obtain eq (5).

$$\int_{\Omega} \overline{\varepsilon}^T D \varepsilon d\Omega - \int_{\Gamma} \overline{u}^T ku d\Gamma = \int_{\Gamma} \overline{u}^T (ku_g + t_b) d\Gamma$$

(5)

Eq. (6) is the finite element equation, and eq. (7) and (8) represent the stiffness matrix K and external force vector f, respectively.

$$Kd = f$$

(6)

$$K = \sum_{i=1}^{e} \left(\int_{\Omega_e} B^T D B d\Omega_e + \int_{\partial \Omega_{e \cap \Gamma}} N^T K N d\Gamma \right)$$

(7)

$$K = \sum_{i=1}^{e} \left(\int_{\Omega_{e \cap \Gamma}} N^T (t_b + ku_g) d\Gamma \right)$$

(8)

2.2. Analyses of Thermal Stress and Resistance against Earthquake

Figure 2 shows the result of the finite element modeling of a 12-inch cryogenic ball valve using HYPERMESH, which is an exclusive item of software for finite element analysis, and ANSYS, which is a commercial FEA software for structural analysis and evaluation. In order to conduct the optimal simulation of a real 12-inch cryogenic ball valve with the FEA model, a tetrahedron solid element was used and the solid45, which is an element for isotropic materials. The solid elements have an average size of 9mm and comprise 609,706 elements and 135,396 nodes. The x, y, and z axes were defined to represent the lateral, longitudinal and vertical

coordinates, respectively.

The material of the valve was stainless steel A351-CF3. One pipe joint was fixed and the other was assumed to be movable in the direction of flow. The internal pressure and temperature were assumed to be $1.68 kg_f/mm^2$ and $-196℃$, respectively. The external temperature was assumed to be $20℃$. Figure 3 shows the result of the thermal analysis at the normal operating temperature, wherein the maximum stress of $23.9 kg_f/mm^2$ appears at the center of the ball.
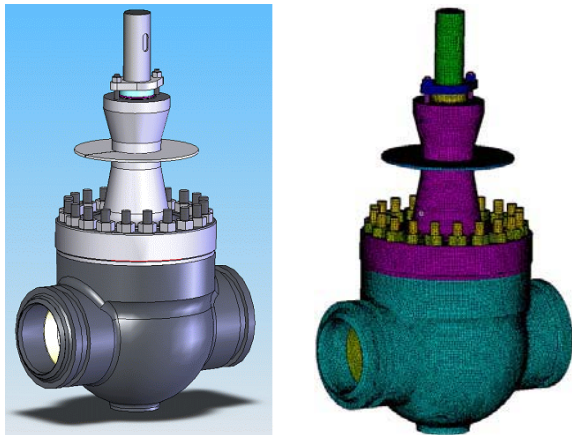
Figure 2 Result of the finite element modeling
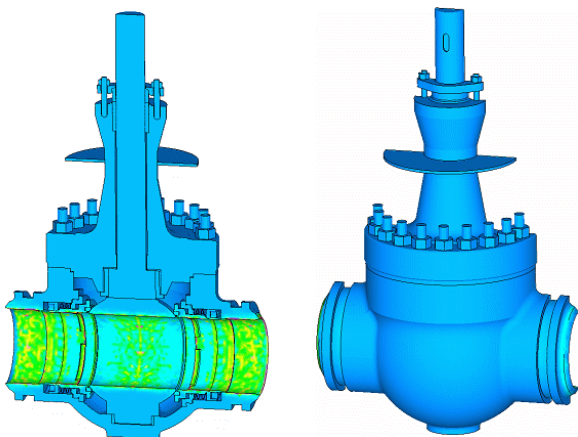
Figure 3 Result of the thermal analysis

2.3 . Earthquake-proof Analysis

The finite element modeling and its boundary conditions were conducted under the same conditions as those established for the thermal stress analysis, added with the conditions for earthquake-proof. The load conditions were classified into the empty weight of the device, internal pressure, temperature, Operating Basis Earthquake (OBE), and Safety Shutdown Earthquake (SSE). The OBE is an earthquake that does not force the

LNG facility to stop operation, on the assumption that it will occur five times during the lifespan of the facilities. Therefore, the maximum stress exerted under an OBE is less than the elastic limit. The SSE, however, is a strong earthquake that may occur once throughout the lifespan of the facility. In this study, the device was applied with maximum acceleration in the x, y, and z directions, as presented in Table 1. The cases of the OBE and SSE include the earthquake accelerations in the vertical and horizontal directions, which are 2.0g, including the device weight, and 1.5g, in the vertical and x-y directions respectively. In this study, the loading conditions of an SSE were applied to obtain a conservative result. Figure 4 shows the results of the earthquake-proof analysis taking an earthquake into consideration. A maximum stress of $25.3 kg_f/mm^2$ was generated at the center of the ball, similar to the figure obtained when the earthquake was not considered.
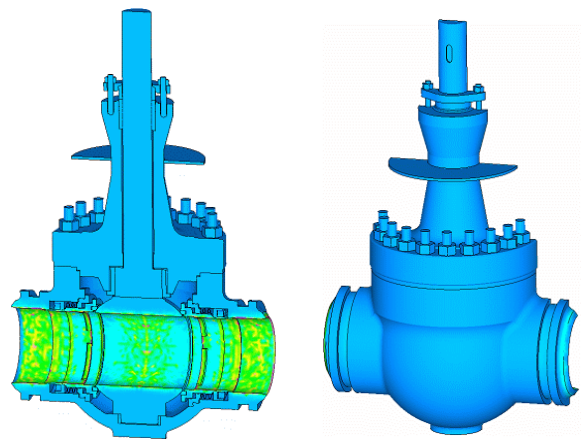
Figure 4 Results of the earthquake-proof analysis

Table 1 Seismic load condition for OBE and SSE

OBE	Vertical	±0.7g (dead weight : 1.0g)
	Horizontal	±1.0g
SSE	Vertical	±1.0g (dead weight : 1.0g)
	Horizontal	±1.5g

2.4. Flow Analysis

The flow analysis on the ball valve was carried out using FLUENT, which is a commercial CFD code with a model that includes 5 times the diameter to the upstream and 10 times the diameter to the downstream. Figure 5 shows the grid system for the numerical analysis. The grid system - a hybrid grid system - was a combination of arranged and non-arranged grids. The grids were allocated densely on the boundary wall to obtain a more precise prediction. The grid's density was made to be higher at the inlet and outlet to analyze eddy flow. The grid had 600,000 nodes for numerical analysis.

The entrance conditions of the analysis model, which were the pressure inlet conditions, were 168kg/cm^2 and 80kg/cm^2, and the exit condition was the atmospheric pressure. The internal temperature was set at -196℃, which is the temperature of LNG. The fluid was assumed to be methane, which accounts for approximately 90% of the composition of LNG (Alaskan). Table 2 presents the physical properties of methane.

Figure 5 Computational grid system of Ball valve

Table 2 Properties of Methane

Properties	Ball Valve	Properties	Ball Valve
Molecular weight	16	Critical pressure	45.8atm
Specific gravity	0.55	Explosion range	5~15% (in Air)
Boiling point	-161.5℃	Ignition point	550℃
Critical temperature	-82.1℃	Melting point	-182.4℃

Figure 6 shows the path lines and velocity distribution vector of the fluid particles. The path lines show relatively uniform velocity distribution, which can be identified by the velocity vector. It can be seen that the speed of the current accelerates after the valve. Figure 7 shows the velocity distribution at a cross-section when in a fully open state. It can be seen that the flow profiles of the cross-sections are similar, and faster, at the center. Figure 8 shows the velocity distribution at the distances of 100cm, 250cm, and 500cm from the valve outlet. On the graph, it can be seen that the velocity is distributed uniformly before and after the valve, and increases as the LNG flows downwards. The velocity profile takes the form of a parabola, which is the typical representation of velocity distribution.

(a) Path lines   (b) Velocity
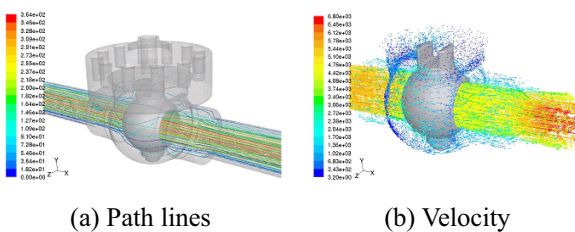
Figure 6 Path lines & Velocity of fully opened state
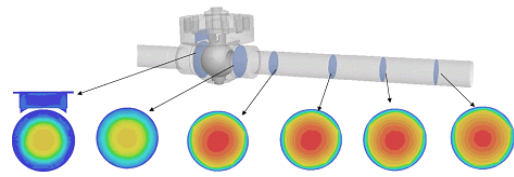
Figure 7 Velocity distributions of cross sectional area
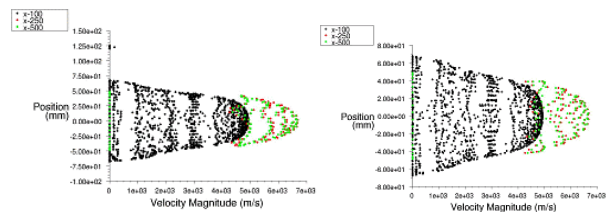
(a) y-direction   (b) z-direction

Figure 8 Velocity distribution graphs

3. Design and Fabrication of Parts

3.1. Body Design

In general, the most important factor to be considered in designing a cryogenic valve is to obtain sufficient strength against internal pressure. This is the most important factor in the design of the pressure vessels; a valve body cannot be designed without careful consideration of the structural strength. In this study, the structural strength, contraction according to the valve configuration, and heat transfer with the extremely low temperature of LNG were analyzed and designed by simulation of the valve body.
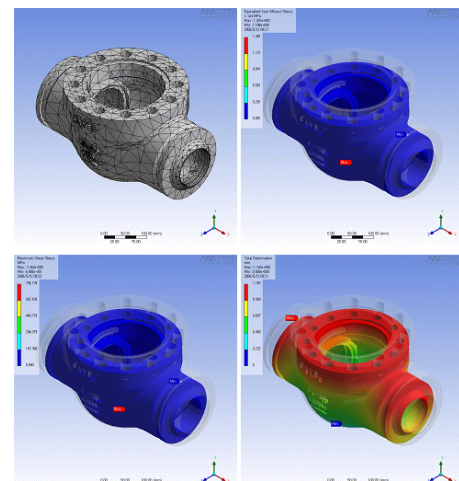
Figure 9 Analysis of Body

3.2. Design and Fabrication of the Seat

In top-entry type cryogenic ball valves, the most important component is the seal, which is very difficult to design and manufacture. Figure 10 shows the structure of a U-cup seal seat, whose test results at very low temperature are presented in Table 3. As the shrinkage rates of a U=cup seal and graphite are lower than that of stainless steel, leakage occurs at the seal at temperatures lower than -196℃. It can be seen that, although leakage under such conditions meets the BS 6364 Standard, it does not meet the specifications of the Korea Gas Corporation and LNG container vessels. Therefore, the seal was modified into a bellows-shape, which is shown in Figure 11.

Internal leakage through the seat was tested after assembling the seat, and there was almost no leakage through the bellows-type seat.
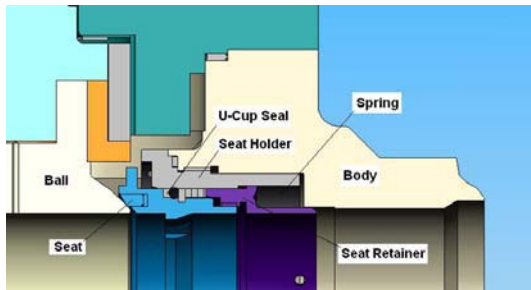
Figure 10 Structure of U-Cup Seal Seat

Table 3 Result of Leakage test

Valve Size	Test Result	Standard		
		BS 6364	KOGAS	LNG vessel
2"	200 cc/min	300 cc/min	10 cc/min	20 cc/min
4"	580 cc/min	600 cc/min	20 cc/min	40 cc/min
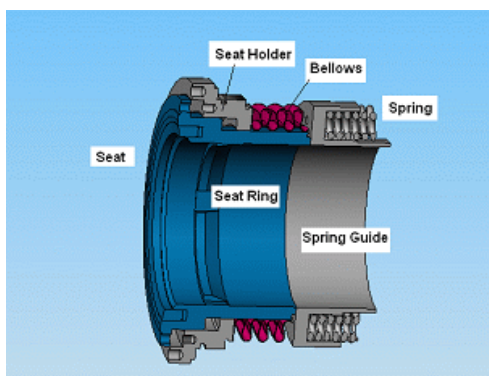
Figure 11 Structure of Bellows Seal Type Seat

3.3. Bonnet Design

A bonnet positioned at the central axis of a valve connects the handle and ball. If icing occurs at the packing, which is located in the upper part, due to low temperature in the lower part, then the LNG may leak. Therefore, a method of preventing icing and a design which can insulate the packing from low temperature in the valve are required. In this study, a heat insulating plate was used and the bonnet length was optimized through analysis and testing. Figure 12 shows the exterior configuration and temperature distribution of the bonnet. Figure 13 shows the measurement of heat transfer to the various parts of the bonnet.
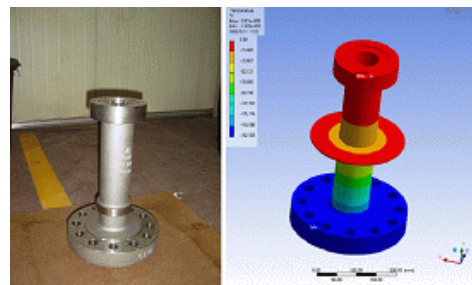
Figure 12 Temperature distributions of Bonnet
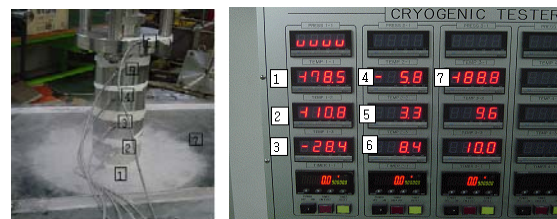
Figure 13 Measuring temperature distribution

3.4. Ball Design

Figure 14 shows the appearance and thermal deformation of the ball. It can be seen that the deformation caused by temperature variance has a constant distribution.
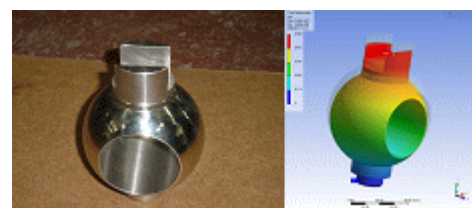
Figure 14 Thermal deformations of Ball

401

3.5. Spring Design

In a bellows-seal type seat, the pressure on surface of the bellows increases as the internal pressure of the valve increases, because the internal pressure is exerted on the effective area of the bellows. However, as the spring force of the bellows is weak at low pressure, a spring is required to press the bellows in order to prevent leakage from the seat during low pressure by maintaining the proper seating force. Table 4 presents the design data of the spring.

Table. 4 Design data of Spring

Item	Dia. (mm)	active coils (turns)	Spring Constant (kg$_f$/mm)	Free length (mm)	Length (mm)	Quantity (es)	Setting Force (kg$_f$)
Value	14.1	5	10.71	33	28	20	1,071

3.6. Fabrication of the Ball Valve

A high-pressure, cryogenic ball valve capable of ensuring zero-leakage was designed, as shown in Figure 15, after analysis the thermal stress, resistance against earthquake, and flow characteristics, and ensuring the optimal design of each part.

Figure 15 Cryogenic ball valve fabricated in this study

4. CONCLUSION

In order to examine the performance characteristics of the parts of high-pressure, cryogenic ball valves, numerical analyses of the strength and thermal shock were conducted and the seat structure was investigated and tested. The following conclusion was obtained.

1. According to the thermal stress analysis conducted at high pressure and very low temperature, a maximum stress of 23.9kg$_f$/mm^2 occurred at the center of the ball.

2. The resistance against earthquake was analyzed at a maximum acceleration of 2.0g in the vertical direction (z axis), including the self-weight, and 1.5g in the x and y axes, at high pressure and very low temperature, to obtain a maximum stress of 25.3kg$_f$/mm^2 at the center of the ball.

3. The flow characteristics of the ball valve were analyzed with inlet and outlet pressures of 168kg/cm^2 and 80kg/cm^2, respectively, to obtain the velocity distribution and eddy flow of LNG according to the valve position.

4. The design of the constituent parts of the ball valve, including the body, seat, bonnet, ball and spring, were optimized.

5. In this study, a high-pressure, cryogenic ball valve that can achieve zero leakage was designed.

REFERENCES

1. Eleftherakis, John G. 1991, "Determining valve contaminant sensitivity effect using two contaminants", SAE TP 910960, pp459～464.
2. Thompson G, Askari, A.R. 1986, "Air leak detection through ball plug valves by vibration monitoring", Noise & Vibration control worldwide, V17, pp140-143.
3. Rouss, Gino james Janna, William S. 2003, "Determination of discharge coefficient for ball valves with calibrated inserts", 2003 ASME Mechanical engineering congress, pp 1~10.
4. Merati, P., Macelt, M.J, 2001, "Flow investigate around a v-sector ball valve", 2001 ASME Fluids engineering, vol.123, no.3, pp662~671.

P1-27

A STUDY ON ULTRA-HIGH PRESSURE WATER JET WALL CLIMBING ROBOT FOR REMOVAL RUST IN VESSELS

Xingru WANG, Yongjun GONG, ZhengyaoYI and Zuwen WANG

Transportation and Logistics Engineering College, Dalian Maritime University
1Linghai Road, Dalian,116026, China
(E-mail:yizhengyao@163.com)

ABSTRACT

In this paper a Ultra-high pressure (UHP) water jetting removal rust cleanout auto-robot is designed, which works with the high-pressure pump units with pressure 250MPa and the vacuum residue displaced system. It is the implement machine for the removal rust system. Three key technique questions are solved in the cleaning automation process. These are wall attaching, wall moving and wall cleaning technique. Experiments showed that the robot both remove rust efficiently and move agility.

KEY WORDS

Removal rust, Wall-climbing robot, UHP water jetting

NOMENCLATURE

d : nozzle diameter
F_f : water jetting kick force
F_m : each permanent magnet adsorption affinity
F_{max} : maximal water jetting kick force
F_{m1} : the first permanent magnet adsorption affinity
F_S : vacuum suction force
G : the total gravity of robot and its load
H : the distance between gravity center and vessel wall
h : the distance between adsorption affinity and holding power in a permanent magnet
l : the distance between first and mid magnet
$l^{'}$: the distance between first and last magnet
M_A : the total tip-back torque of point A
M_f : the total torque from resisting force in a magnet
M_G : the torque from gravity
M_Q : the torque from motor output by reductor
N_i : holding power of each permanent magnet
N_1 : the first permanent magnet holding power

n : the number of permanent magnets attaching wall
P : vacuum pressure
p : jetting pressure
q : flux
r : working radius
a : included angle between vessel wall and gravity
β : water jetting direction change
μ : friction factor between vessel wall and robot
ρ : density of water
v : speed of water jetting

INTRODUCTION

Water hydraulics has advantages of environmental friendly, cleanness, safety, readily available, inexpensive, and easily disposable[1]. Ultra-high pressure (UHP) water jetting has wide apply. As is shown in Figure 1, a UHP water jetting removal rust cleanout system worked by an auto-climbing-robot is designed. In the system three subsystems are established. They are the

high-pressure pump units with pressure 250MPa and power 132kW, the attaching automatically robot system, and the vacuum residue displaced system.

The robot which works as mobile platform and working platform includes two pedrails with some permanent magnets for suction and a combined cleaning device can flush, scrub, scrape the wall surface and collect sewage automatically. It works with water jetting pressure about 250 MPa and can be manipulated by hand-holding control-box remotely.
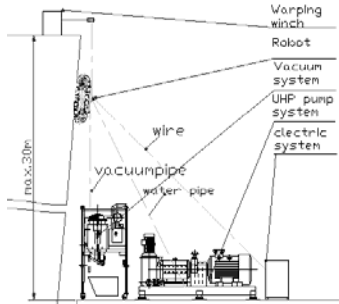
Figure 1 Ultra-high pressure (UHP) water jetting removal rust system

DESIGN INDEX

(1) Max speed : 46.3mm/s
(2) Clambing height : 30m
(3) Rust width : 250mm
(4) Weight : less than 90kg
(5) Degree of vacuum:-0.6bar
(6) Working pressure : 250 MPa
(7) Load ability : 800N

The structure of the attaching robot is design as shown in Figure2. It is driven by two motors that connected with each reductor, and attaching by two pedrails with 72 permanent magnets. A cleaner with nozzles is set in the center of the robot.
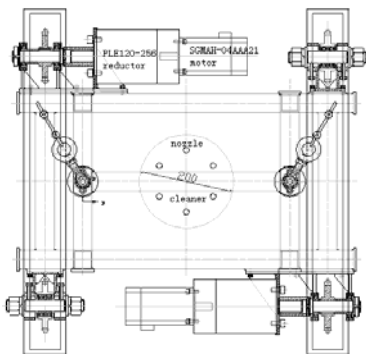
Figure 2 The structure of the robot

THE STATICS ANALYSIS

Considering the operation requires the robot to bear a large load and to be highly reliable, the structure of wall-attaching based on two caterpillar chains with permanent magnets. It is indispensable that the attaching force can overcome the force that arise from robot gravity, load of water canal, air pipe and electric cable, and friction force which arise from vacuum suction[2].

There are water jetting kick force and vacuum suction force act on the robot at work. Their equation are shown in Eq(1) and Eq(2) [3].

$$F_f = 0.745q \cdot \sqrt{p} \qquad (1)$$

$$F_s = \pi \cdot r^2 \cdot P \qquad (2)$$

The robot working platform is not only vertical, even slope. The attaching robot analysis of force in normal vessel wall is shown in Figure 3
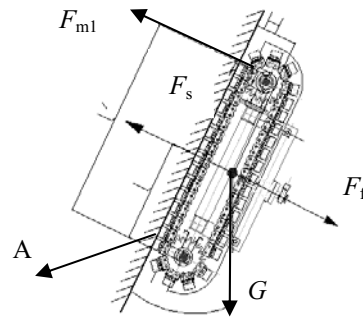
Figure 3 Robot stressed analysis

Gliding analysis
The analysis of force in direction parallel to vessel wall give the no gliding condition in Eq(3):

$$G \cdot \cos \alpha \leq F_f \qquad (3)$$

$$F_f = \sum_{i=1}^{n} N_i \cdot \mu \qquad (4)$$

Considering the water jetting kick force and vacuum suction force, the holding power of each permanent magnet is shown in Eq(5):

$$N_i = F_m - \frac{G \sin \alpha + F_f - F_s}{n} \qquad (5)$$

$$\sum_{i=1}^{n} N_i = n(F_m - \frac{G \sin \alpha + F_f - F_s}{n}) \qquad (6)$$

$$F_f = \mu \cdot (nF_m - G \sin \alpha - F_f + F_s) \qquad (7)$$

By means of analyse the robot with water jetting kick force and vacuum suction force, the condition of no gliding is shown in Eq(8):

$$F_m \geq (\frac{G\cos\alpha}{\mu} + G\sin\alpha + F_f - F_s)/n \quad (8)$$

Set the parameters of Eq(8) ,the no gliding condition is shown in Eq(9).

$$F_m \geq 80\cos\alpha + 40\sin\alpha - 41 \quad (9)$$

The curves between each permanent magnet adsorption force (F_m) and included angle between wall and gravity (a) is shown in Figure 4.
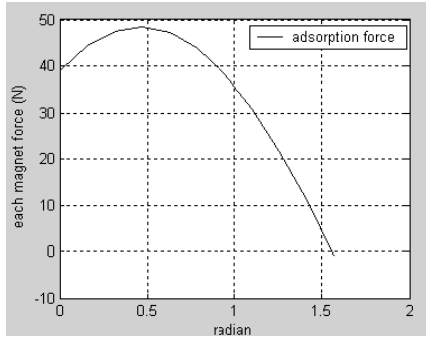
Figure 4 Gliding relation with each magnet adsorption force and angle between vessel wall and gravity

Results

According to the Figure 4, the most dangerous angle (a) is 27.5 degree, and the permanent magnet adsorption force (F_m) approximate 48N.

Tip-back analysis

As shown in Figure 3, tip-back is the robot turn back around point A, the sunction of permanent magnets must overcome the total torque arise from gravity, vacuum suction force and water jetting kick force. The moment balance is shown in Eq(10) and Eq(11) .

$$\sum M_A = (F_m - N_1)l' - \frac{(G\sin a + F_f - F_s)l + GH\cos a}{2} \quad (10)$$

$$\sum M_A = 0 \quad (11)$$

$$F_m = \frac{(G\sin a + F_f - F_s)l + GH\cos a}{2l'} + N_1 \quad (12)$$

According to the Eq(12) ,if the robot work normally, the condition in Eq(13) is indispensable.

$$N_1 \geq 0 \quad (13)$$

Considering the analysis of robot with water jetting kick force and vacuum suction force, the condition of attaching is shown in Eq(14):

$$F_m \geq \frac{(G\sin a + F_f - F_s)l + GH\cos a}{2l'} \quad (14)$$

Set the parameters of Eq(14), the no tip-back condition is shown in Eq(15):

$$F_m \geq 300\cos\alpha + 240\sin\alpha - 307.5 \quad (15)$$

The curves between each permanent magnet adsorption force (F_m) and included angle between vessel wall and gravity (a) is shown in Figure5.
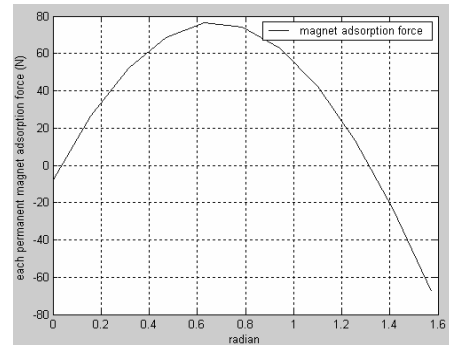
Figure 5 Tip-back relation with each magnet adsorption force and angle between vessel wall and gravity.

Results

According to the Figure 5,the most dangerous angle (a) is 34.9 degree ,and the permanent magnet adsorption force (F_m) approximate 76N.When the angle (a) is 0 to 4.1 degree and 73.4 to 90 degree, the robot will attach the vessel wall all along because of vacuum sunction.

THE DYNAMICS ANALYSIS

The means of moving is two caterpillar chains with two motors. When the robot run up, it is necessary for the output torque of the two motors to overcome the moment of resistance (M_f) which arise from magnets adsorption affinity (F_m) with holding power (N_n), and gravity (M_G). The moment balance is shown in Eq(16):

$$M_Q - M_f - M_G = 0 \quad (16)$$

$$M_f = (F_m + \frac{F_s - F_f}{n}) \cdot h \quad (17)$$

$$M_G = \frac{GH\cos\alpha}{2} \quad (18)$$

By means of the analysis of dynamics, the condition of attaching is shown Eq(19):

$$M_Q \geq (F_m + \frac{F_s - F_f}{n}) \cdot h + \frac{GH\cos\alpha}{2} \qquad (19)$$

THE ANALYSIS OF WALL-CLEANING

Some UHP nozzles is fitted on the robot for bringing the jetting force by high speed water to rusty scale, at the same time the tangential high speed water current brings wedge water, which can expansion the rusty scale crack, and get rid of the rust[3].

The restraint from water jetting nozzle make the speed of water jetting increased. With the jetting enter into air, turbulent flow generates jetting power loss, so the jetting speed reduces that there is no enough energy to remove rust effectively. Therefore, it is necessary to farthest utilize jetting center[4].

Given the water jetting act on the object surface and based on the momentum theorem, the total water jetting kick force is shown in Eq(20):

$$F_f = \rho \upsilon q (1 - \cos\beta) \qquad (20)$$

The simulation of water jetting is shown in Figure6.
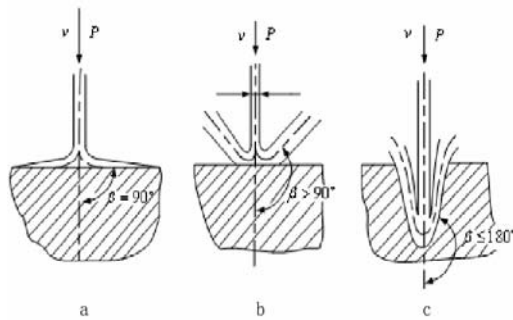
Figure6 Different reflects direction after water jetting acting on the surface of object

According to the Figure6, when the angle is $\beta \approx 180$ degree, the jetting is total reflection, and water jetting kick force is maximal. The distance of robot nozzles from vessel wall is also important. The good distance of the water jetting is shown in Eq (21) and the maximal water jetting kick force is shown in Eq (22):

$$l = 99.7(p/100)^{-0.88} d^{0.9} \qquad (21)$$

$$F_{\max} = 120(p/100)^{1.15} d^{1.75} \qquad (22)$$

EXPERIMENTS

With the pressure is 250 MPa, the number of nozzles is six and the diameter of nozzles is 0.25mm, experiments is did and the data is obtained and shown in Figure 7.
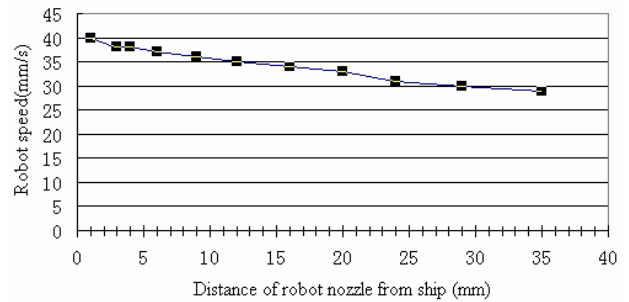
Figure 7 The relation about robot speed and nozzle distance from wall

As illustrated in Figure8, with the distance between nozzle and vessel wall increase gradually, the robot speed of advance must decrease correspondingly, otherwise, the rust will remove ineffectively.

Considering the gravity center of the attaching robot and the agility of robot control, the distance between nozzle and vessel wall was taken as 20mm and the robot speed of advance was taken as 33mm/s.

CONCLUSIONS

(1) Based on statics and dynamics analysis, three empirical equations are obtained, in these equations, the permanent magnet and motor with its redactor can be chosen well.
(2) When the distance of robot nozzles from vessel wall is 20mm and the robot speed of advance is 33mm/s, the robot is in good removing rust working condition.

REFERENCES

1. Kupscznk T. etc., Removal of Non-Skid Coatings From Aircraft Decks, 11th American Water jet Conference, Minneapolis, US, 2001,pp579-588.
2. Hollingum. Jack., Climbing and walking robots gain respectability. An international Journal Vo1.27.No.2, 2000,pp114-119.
3. Tikhomirov R A., High-Pressure Jet Cutting [M].New York, ASME, 1992.
4. Atanov G., The Hydro-Cannon Nozzle Optimization. Proceedings of the 2001 WJTA American Water jet Conference, 2001, pp207-218.

P1-28

DESIGN OF RUNNING-IN AEROSTATIC SPHERICAL BEARING WITH INHERENT COMPENSATION AND LARGE WRAP ANGLE

Wenqi MA, Ang SUN, Zuwen WANG

Transportation and Logistics Engineering college, Dalian Maritime University
1 Linghai Road, Dalian, 116026, China
(E-mail: mawq71@yahoo.com.cn)

ABSTRACT

Aerostatic spherical bearings can operate in places which requiring three degrees of freedom in rotation with a minimum of frictional drag. It is one of the key components of aerocraft motion simulator. With the development of large-scale simulation equipment, the requirement of aerostatic bearing with heavy-duty is widely and imminent. Compared with aerostatic spherical bearing with multi-orifices compensation, the bearing with inherent compensation and integrated socket is newly developed, and it has admirable stability in large scale of supply pressure. A new type of running-in aerostatic spherical bearing with inherent compensation and large wrap angle is designed and optimized. At the same time, the pressure and velocity field distributions in region of gas film are obtained by CFD software. Experimental results are proved that the bearing capacity of the new aerostatic spherical bearing is far improved than conventional one.

KEY WORDS

Aerostatic spherical bearings, Heavy-duty, CFD, Inherent compensation

NOMENCLATURE

e : offset of center point
p : radial pressure
p_s : supply pressure
p_a : ambient pressure
d : diameter of supply hole

θ_0, θ_1 : wrap angle of supply holes
R : diameter of spherical bearings

INTRODUCTION

Gas lubrication is a new technique because of the rapid development of spaceflight and industry since 50 ages. Especially, aerostatic spherical bearings can operate in places which requiring three degrees of freedom in rotation with a minimum of frictional drag, and widely applied by precision bearing on spacecraft simulator, inertial navigation, principal axis of ultra precision machine and so on. The disadvantages such as lower bearing capacity stiffness and stability limit the application, so the research of aerostatic bearings with high-pressure and heavy-load is very necessary.

One key technique of large-space structure is flexibility, the complete physical simulation must be tested to insure the safe of aerocraft, such as the space intersection kinetics and the effect of difficult foundation of precision math model on control system including friction of flywheel on dry condition, 3 axe coupling of twist roller, flexibility of solar panel.

There are special departments to study on physics simulated equipments of large flexibility structure such as Germanic Space Navigation Academe, American Langley Research Center. Especially, Langley Research Center carried the simulation technique, equipments and experiments for space shuttle and manned space station including "Apollo Airship" and "Air Laboratory" since 1960s; they have obtained great achievement by 40 years.

The gas lubrication system is one of the core systems. Chinese some graduate school fetched in a suit of gas lubrication system on condition of high pressure and heavy loading, aerostatic spherical bearings is the main part which can offer lower friction and micro-gravity, the supply pressure is $30 \times 10^5 \text{N/m}^2$, the fact using pressure is $15 \times 10^5 \text{N/m}^2$，carrying capacity is over five tons，the diameter of sphere is only 400mm, the using pressure outclassed that of traditional structure. The working mechanism should be more lucubrated.

There are three common types of aerostatic spherical bearings, one is running-in aerostatic spherical bearing with single orifice which first put forward by Robert[1], the second is aerostatic spherical bearing with multi-orifices and portion spherical socket[2], the third is new aerostatic spherical bearings with inherent compensation having integrated spherical socket. The running-in aerostatic spherical bearing with single orifice was first used, but has been fall into disuse because of instability. The second kind of bearing is often applied on limited structure because of the worse carrying efficiency and flow characteristic. The third type of bearing is a new type of aerostatic bearing developing with the rising of international researching on micro-satellite. This paper designs a new running-in aerostatic spherical bearing with inherent compensation and large wrap angle, and gave the numerical simulation results of static characteristic.

DESIGN OF RUNNING-IN AEROSTATIC SPHERICAL BEARING

Because of air hammer at higher pressure, structure of controlling exhaust including two lines of exhaust holes in spherical socket is applied to keep the air bearing in working order. The air entering into the bearing is divided into three parts: some air outflow through the top gap between the spherical socket and spherical bulb, the two others outflow through the exhaust holes. This kind of structure can avoid the appearance of air hammer and improve the stability of the bearing, shown as Fig.1
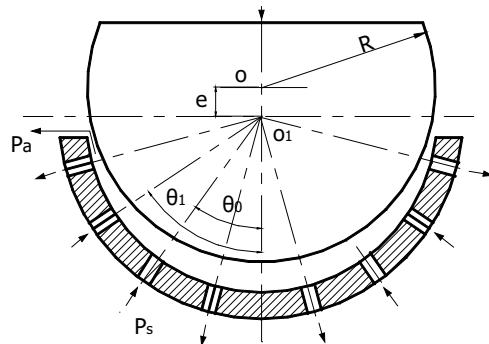
Figure 1 The running-in aerostatic spherical bearing
with inherent compensation and large wrap angle

Spherical bulb and spherical socket has the same radiu R=75mm, the wrap angle of spherical socket is 160°. The wrap angle of supply holes θ_0, θ_1 is separately 36° and 50° which there are 10 uniform holes. The angle of exhaust holes is separately 12° and 70° which there are separately 4 and 12 uniform holes of every　array.

CONTROL EQUATIONS OF SIMULATION

Conventional Reynold control equations are deduced based on neglect of inertia force. But with increasing of the supply pressure and gas film, the effect of inertia force is gradually intensive, the complete N-S equation is adaptive on the working condition[3].

$$\rho \frac{du}{dt} = \rho X - \frac{\partial p}{\partial x} + \eta \nabla^2 u + \eta \frac{1}{3} \frac{\partial}{\partial x}(div\upsilon) \qquad (1)$$

$$\rho \frac{d\upsilon}{dt} = \rho Y - \frac{\partial p}{\partial y} + \eta \nabla^2 \upsilon + \eta \frac{1}{3} \frac{\partial}{\partial y}(div\upsilon) \qquad (2)$$

$$\rho \frac{d\omega}{dt} = \rho Z - \frac{\partial p}{\partial z} + \eta \nabla^2 \omega + \eta \frac{1}{3} \frac{\partial}{\partial z}(div\upsilon) \qquad (3)$$

Steady continuity equation:

$$\frac{\partial}{\partial x_i}(\rho u_i) = 0 \qquad (4)$$

NUMERICAL SIMULATION ANALYSIS

Fluent is general CFD software which the control equations are dispersed and solved with finite volume method. In this paper, explicit coupled solvers linearize the coupled equations of high-speed compressible flows. This method may give it a performance advantage over the segregated solver for the flow on greater inertia force. Pressure equations are solved by linear difference format; density and momentum are solved by second order upwind format. Comparisons of pressure distribution and Mach number are shown as Fig.2.
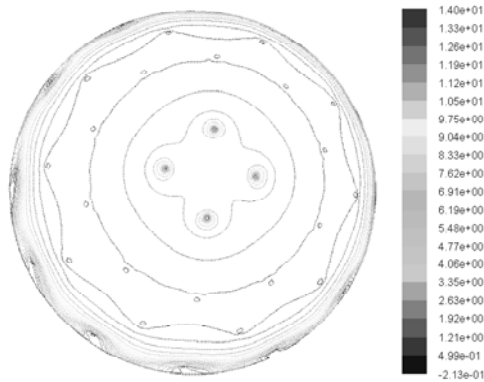
（a） Pressure distribution of gas film
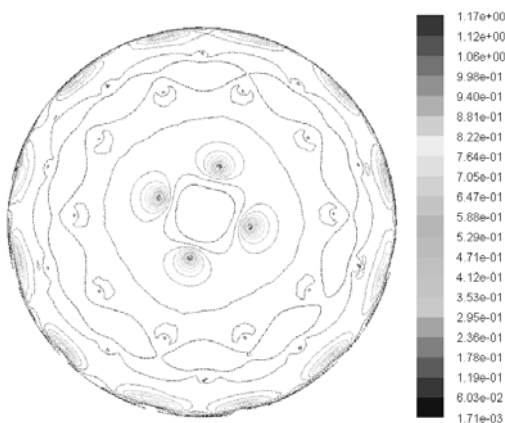
（b） Mach number distribution of gas film
Figure 2 p_s/p_a=14, d=1.2mm, e=40μm

Though the pressure at exhaust holes reduce to ambient pressure, the average pressure value still hold high near the sock, shown as Fig.2(a). The results of Mach number is corresponding as that of pressure, shown as Fig.2(b).

However, when the gas film gets larger to 100μm(shown as Fig.3), pressure depression beyond the supply hole already occurs and the pressure value at 40μm is obviously higher than that at 100μm near ball socket which the maximum difference can reach to 0.5Mpa. Especially, the pressure profile is different, there is a process of falling and recovering near supply hole. The phenomena are caused by interaction between inertia force and viscous force.

In like manner, the tendency of velocity distribution also proved the changes. The velocity at the center of ball socket is zero which forming a stagnant air flow region. The gas at entrance flow into bearing with low velocity, then gradually accelerate along the flow direction which is more obvious at small gas film. The flow velocity reaches to maximum near supersonic flow at exhaust hole because of pressure depression.
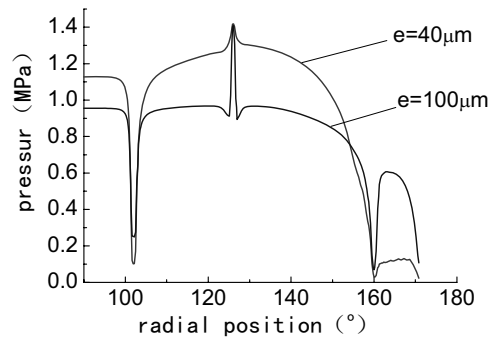
（a） Pressure contrast
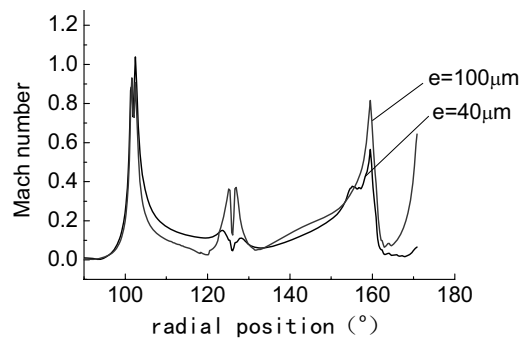
（b） Mach number contrast
Figure 3 Effect of offest e to flow characters

When the diameter of supply hole gets larger (shown as Fig.4), the values of pressure and mach number are very close at the same position. Especially, the mach number profiles are almost superposition. So we should design greater supply hole in favor of machining.
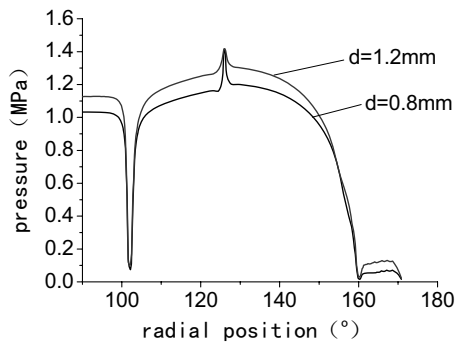
（a）　Pressure contrast
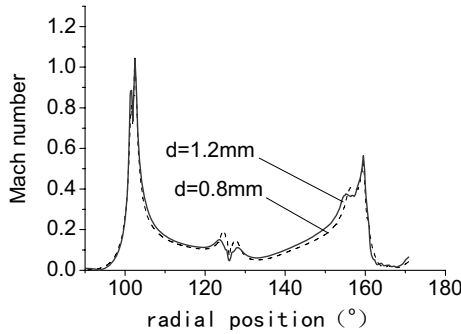
（b）　Mach number contrast

Figure 4 Effect of diameter of supply hole to flow characters

CHARACTERISTICS EXAMINATION

The characteristics examination system mainly includes gas source, filter, loading devices, testing apparatus, etc. (shown as Fig.5)
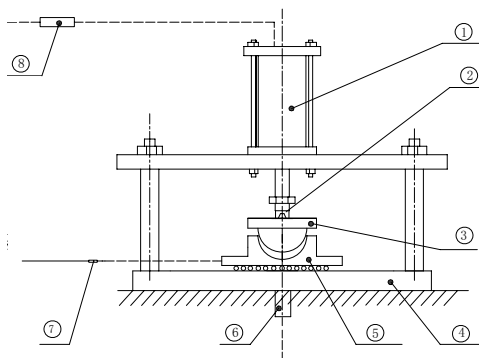
1-Loading system, 2-Force sensor, 3- Spherical bulb, 4-Support plan, 5-Spherical socket, 6-Distance sensor, Figure 5 Sketch map of testing system

The contrastive results of load between numerical simulation and experimental test are shown as Fig.6. Though the tendency of the variety is basically close

agreement each other. The value of carrying force by
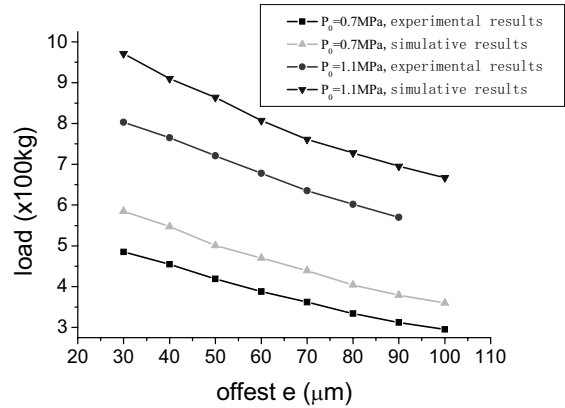
Figure 6 Contract of carrying capacity

simulation is greater 20% than that by testing. The first reason is caused by the simplified flow field as laminar flow; the second reason may be that the beginning offset e is not very precision.

CONCLUSIONS

The new running-in aerostatic spherical bearing has integrated socket, and can offer admirable stability and carrying capacity in large scale of supply pressure. Experimental results are also proved that the bearing capacity of the new aerostatic spherical bearing can steady work at over conventional supply pressure 0.6Mpa. These conclusions give some valuable references for studying on heavy-duty fields.

ACKNOWLEDGMENTS

REFERENCES

1. Grossman R L. Application of flow and stability theory to the design of externally pressurized spherical gas bearings [J].Trans of ASME, Journal of Basic Engineering, 1963, 85 (4):495-502.
2. Liu Dun, Liu Yuhua, Chen Shijie. Externally Pressurized Gas Lubrication [M]. Haerbin, China: Haerbin Institute of Technology Publishing Company, 1990.
3. Dang Genmao. Gas Lubrication Technique [M]. Nanjing：Dongnan Institute Publishing Company, 1990.

P1-29

ESTIMATION OF A CRITICAL PRESSURE RATIO OF A PNEUMATIC PIPE-LINE AND ITS SIMULATION

Katsushi SATOH*, Yukio KAWAKAMI* and Kazuo NAKANO**

*Department of Machinery and Control Systems, College of Systems Engineering
Shibaura Institute of Technology
307 Fukakusa, Minuma-ku, Saitama, 337-8570 JAPAN
(E-mail: i023441@sic.shibaura-it.ac.jp, kawakami@shibaura-it.ac.jp)
**Tokyo Institute of Technology
1-26-28 Izumihon-cho, Komae-shi, Tokyo, 201-0003 JAPAN
(E-mail: nakanokazu@jcom.home.ne.jp)

ABSTRACT

We considered the so-called Fanno flow as a model of flow through pneumatic pipe lines with a constant diameter. The flow is one dimensional, steady and adiabatic. The friction coefficient is constant. We succeeded to express the critical pressure ratio of the flow which is choking at the exit of the pipe line by three parameters, the pipe diameter, the pipe length and the friction coefficient. We compared the theoretically estimated critical pressure ratio to the experimental results. The results showed the good agreements except the case of the short pipe lines less than 10 cm. It was confirmed that our method of determination of the ratio was very useful for the flow calculation using ISO choke equation. With these studies we established the simulation program for the Fanno flow on MATLAB_Simulink and show that the program was easily applied to connected pipelines in series.

KEY WORDS

Pneumatic, Pipeline, Simulation, Friction, Choking

NOMENCLATURE

b : Critical pressure ratio
c : Speed of sound
D : Inner diameter
f : Friction factor
K : Loss coefficient
L : Length of pipe
Q : Volumetric flow rate
q_m : Mass flow rate
R : Gas constant of air
T : Temperature
M : Mach number
p : Static pressure
v : Axial speed of flow
κ : Specific heat ratio
ρ : Density of air

(Subscripts)
1 : Up stream state point
2 : Down stream state point
a : Approximate value
c : Critical condition
e : Exit

INTRODUCTION

It is the one of important problems in the designing pneumatic systems to estimate the pressure drop in pipe lines with losses. Ignoring the compressibility of the air, the estimation becomes simple but the accuracy is not enough for the flow of the large Mach number. The conventional analysis of the Fanno flow[1] ,[2] ,[3],[4] is applicable for the air flow through the uniform adiabatic rigid pipe with losses. But it has the short-coming that the analytical solution to represent the pressure drop as a

function of the mass flow rate is not available and so the numerical method is inevitable in the analysis.

In this paper we introduce the analytical forms of the approximate solutions for Fanno flow and present the simulation programs on MATLAB Simulink[5] for the steady, adiabatic, one dimensional pneumatic flow in uniform pipes with losses.

BASIC EQUATIONS

Generally, the basic equations for a pneumatic pipe line are assigned as follows.

$$\frac{d\rho}{\rho} + \frac{dv}{v} = 0 \tag{1}$$

$$vdv = -\frac{dp}{\rho} - \frac{4f}{D}dx\frac{v^2}{2} = -\frac{dp}{\rho} - dK\frac{v^2}{2} \tag{2}$$

$$vdv + c_p dT = 0 \tag{3}$$

$$\frac{dp}{p} = \frac{d\rho}{\rho} + \frac{dT}{T} \tag{4}$$

Four unknown p, T, v and ρ are determined from these equations for given D, L, f and the boundary conditions.

APPROXIMATIONS FOR THE FANNO FLOW

The friction losses of the flow lead to the pressure drop and the velocity increase along the flow. When the Mach number M_e at the exit of the pipe approaches to the unity, the choking of the flow occurs. The state variables and parameters on the pipe-line are specified as shown in Figure 1. Integrating the basic equations as shown in the references, the loss coefficient K_{12} and the pressure ratio between the state point 1 and 2 is expressed as the function of the Mach numbers as followings.

$$K_{12} = \frac{4fL}{D}$$
$$= \frac{1-\left(\frac{M_1}{M_2}\right)^2}{\kappa M_1^2} + \frac{\kappa+1}{2\kappa}\ln\left\{\frac{M_1^2}{M_2^2}\cdot\frac{2+(\kappa-1)M_2^2}{2+(\kappa-1)M_1^2}\right\} \tag{5}$$

$$\frac{p_2}{p_1} = \frac{M_1}{M_2}\sqrt{\frac{2+(\kappa-1)M_1^2}{2+(\kappa-1)M_2^2}} \tag{6}$$

Define the approximate Mach number ratio $(M_1/M_2)_a$ as shown in the following equation.

$$\frac{\kappa+1}{2+(\kappa-1)(M_1/M_2)_a^2} = \frac{2+(\kappa-1)M_2^2}{2+(\kappa-1)M_1^2} \tag{7}$$
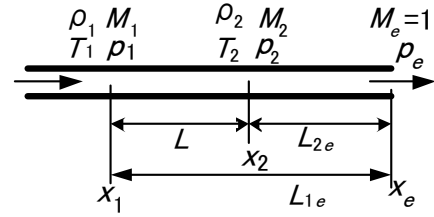
Figure 1   Pipe line and states

This approximation simplifies Eq. (6) as follows,

$$\frac{p_2}{p_1} = \left(\frac{M_1}{M_2}\right)_a\sqrt{\frac{2+(\kappa-1)(M_1/M_2)_a^2}{\kappa+1}} \tag{8}$$

Solving Eq. (8), we get the approximate Mach number ratio as the function of the pressure ratio.

$$\left(\frac{M_1}{M_2}\right)_a = \frac{1}{\sqrt{\kappa-1}}\left\{\sqrt{1+(\kappa^2-1)\left(\frac{p_2}{p_1}\right)^2}-1\right\}^{1/2} \tag{9}$$

Substituting the approximate Mach number ratio $(M_1/M_2)_a$ and Eq. (7) into Eq. (5), the loss coefficient K_{12} is expressed as follows.

$$K_{12} = \frac{1-(M_1/M_2)_a^2}{\kappa M_{1a}^2} + \frac{\kappa+1}{2\kappa}\ln\left(\frac{M_1}{M_2}\right)_a^2$$
$$+ \frac{\kappa+1}{2\kappa}\ln\left\{\frac{\kappa+1}{2+(\kappa-1)(M_1/M_2)_a^2}\right\} \tag{10}$$

M_{1a} is defined as the approximate value of M_1 which fulfils Eq. (10) and expressed by the following.

$$M_{1a} = \frac{\sqrt{\left\{1-(M_1/M_2)_a^2\right\}/\kappa}}{\sqrt{\frac{4fL}{D} - \frac{\kappa+1}{\kappa}\ln\left(\frac{p_1}{p_2}\right) - \frac{2(\kappa+1)}{\kappa}\ln\left(\frac{M_1}{M_2}\right)_a}} \tag{11}$$

From Eq. (9) and Eq. (11) we can get the analytical equation which expresses the approximate Mach number M_{1a} as the function of the pressure ratio p_2/p_1. Solving Eq. (6) and Eq. (11), the approximate Mach number M_{2a} at the state point 2 is obtained.

$$M_{2a} = \left[\frac{\sqrt{1+(\kappa-1)M_{1a}^2\left\{2+(\kappa-1)M_{1a}^2\right\}(p_1/p_2)^2}-1}{\kappa-1}\right]^{1/2} \tag{12}$$

The sound speed at the state point 1 is given by the next.

$$c_1 = \sqrt{\kappa R T_1} \tag{13}$$

414

The mass flow rate is given by the next.

$$q_m = \frac{\pi D^2}{4}\rho_1 v_1 = \frac{\pi D^2}{4}\cdot\sqrt{\frac{\kappa}{R}}\cdot\frac{p_1}{\sqrt{T_1}}M_{1a} \qquad (14)$$

It was presented that the approximate mass flow rate of Fanno flow could be expressed in the analytical form from the given pressure at arbitral two cross sections.

CHOKED FLOW

When the flow is choked at the exit of the pipe, the loss coefficient K between the state point 1 and the exit is obtained from Eq. (1), substituting $M_e=1$ to M_2.

$$K = \frac{1-M_{1c}^2}{\kappa M_{1c}^2} + \frac{\kappa+1}{2\kappa}\ln\left\{\frac{(\kappa+1)M_{1c}^2}{2+(\kappa-1)M_{1c}^2}\right\} \qquad (15)$$

,where M_{1c} is the Mach number at the state point 1 for the flow choked at the exit. The value of the loss coefficient K is shown in Figure 2. The computation of the loss coefficient K for the given the Mach number M_{1c} is straight forward but the inverse has to use a trial and error method. We proposed the functions to compute the approximate Mach number M_{1ca} from the loss coefficient as follows.

In the range of $\quad 0 \leq K \leq 1.3$
$$M_{1ca} \cong 0.95\times\exp\left(-0.728K^{0.415}\right)+0.05 \qquad (16)$$

The M_{1ca} is compared with M_{1c} as shown in Figure 3.

In the range of $\quad 0.5 \leq K \leq 25$
$$M_{1ca} \cong 0.9\times\exp\left(-0.787K^{0.386}\right)+0.1 \qquad (17)$$

Eq. (16) and Eq. (17) coincides at the value $K=0.9335$.

In the range of $\quad 25 \leq K \leq 120$
$$M_{1ca} \cong 0.4\times\exp\left(-0.29K^{0.475}\right)+0.052 \qquad (18)$$

The relative errors $(M_{1ca} - M_{1c})/M_{1c}$ for Eq. (16), Eq. (17) and Eq. (18) are less than 1% in the respective ranges. The pressure ratio p_2/p_1 for the choked flow is defined as the critical pressure ratio b. Substituting M_{1ca} into Eq. (8), the critical pressure ratio b is obtained as shown followings.

$$b = \frac{p_{2c}}{p_{1c}} = M_{1ca}\cdot\sqrt{\frac{2+(\kappa-1)M_{1ca}^2}{\kappa+1}} \qquad (19)$$

From Eq.(15) and Eq. (19), we can plot the b as a function of K as shown in Figure 6.

The critical pressure ratio b is highly affected by the value of the loss coefficient K in the lower range than 20.

The loss coefficient $K=0$ means the non-viscous case and the corresponding critical pressure ratio b is the unity. It shows the Mach number M_1 at the state point 1 is equal to 1.
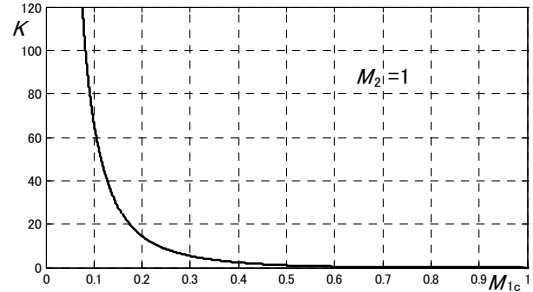
Figure 2   Loss coefficient K
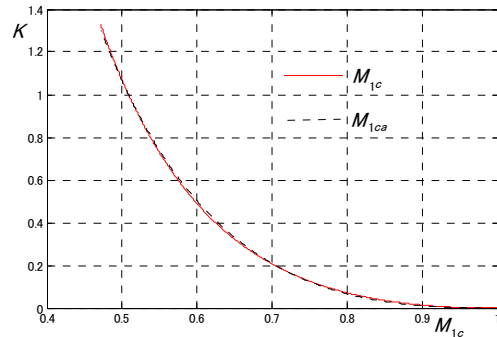
Figure 3 M_{1ca} and M_{1c} ($0 \leq K \leq 1.3$)
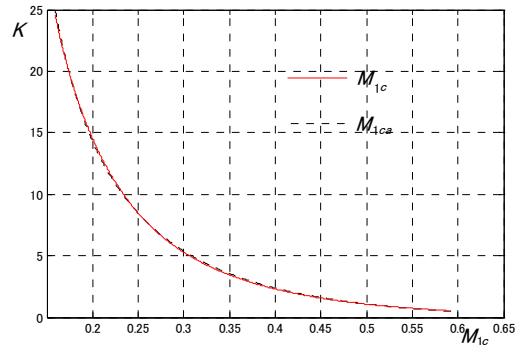
Figure 4 M_{1ca} and M_{1c} ($0.5 \leq K \leq 25$)
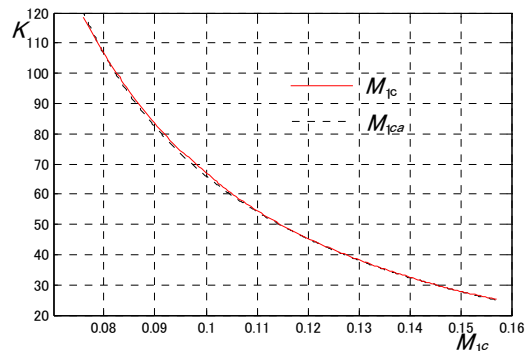
Figure 5 M_{1ca} and M_{1c} ($25 \leq K \leq 120$)
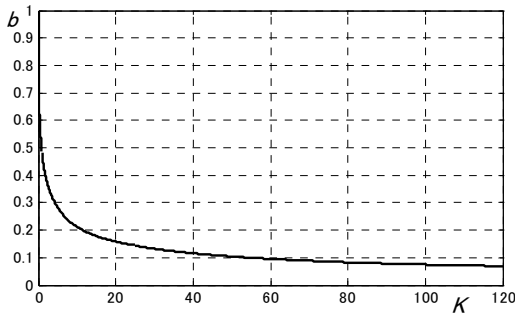
Figure 6　Critical pressure ratio b

SIMULATION PROGRAM ON MATLAB

Now, it became practicable to solve the unknown variables in the Fanno flow by the direct computation of the above mentioned equations under the given conditions. We adopted MATLAB as the one of the simulation tools to simulate the one dimensional steady flow with losses through adiabatic uniform pipes of finite lengths.

As the first step of the simulation, the parameters and the boundary conditions shown in Figure 7 have to be given. The next steps are creating blocks and subsystems to compute equations by making use of the Simulink as shown in Figure 8. The left three ports in Figure 8 are the given states at boundaries and the right five ports give outputs. The details of five subsystems with labels in Figure 8 are shown in Appendix. The subsystem p2/p1 determines p_{2c} at the choking condition by making use of Eq. (16), (17) and (18), and gives the pressure ratio p_2/p_1. The subsystem Mach1 computes Eq. (9), (10) and (11) to get M_{1a} from the obtained the pressure ratio p_2/p_1. The subsystem Mach2 outputs M_{2a} from M_{1a} and p_2/p_1 by computing Eq. (12). The subsystem q2 gives the mass flow rate qm1 by computing Eq. (14). The subsystem T2 computes T_2 from T_1, M_{1a} and M_{2a} by making use of Eq. (20) which is deduced from the fundamental equations for the Fanno flow [1].

$$T_2 = \frac{2+(\kappa-1)M_1^2}{2+(\kappa-1)M_2^2}T_1 \qquad (20)$$

EXPERIMENTS AND SIMULATIONS

The flow rate of the choked flow is given by Eq. (21).

$$q_{mc} = \frac{\pi D^2}{4}\cdot\sqrt{\frac{\kappa}{R}}\cdot\frac{p_1}{\sqrt{T_1}}M_{1ca} \qquad (21)$$

The nondimensional flow rate q_n is defined by Eq. (22).

$$q_n = q_m / q_{mc} \qquad (22)$$

Figure 9 shows the theoretical curves and the marks

of the experimental results [6] which were done at SMC Co. The factor f was chosen to fit the experimental results. The relation between the critical pressure ratio b and the ratio L/D is obtained by our simulation method and it is shown as the one solid line in Figure 10.

Circle marks and asterisk marks are the estimated values of the critical pressure ratio which are based on the results of the numerical flow analysis[7] and the experimental results [6] done at SMC Co. respectively.
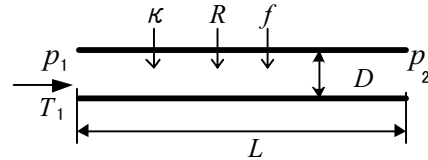
Figure 7　Parameters and boundary conditions of pipe
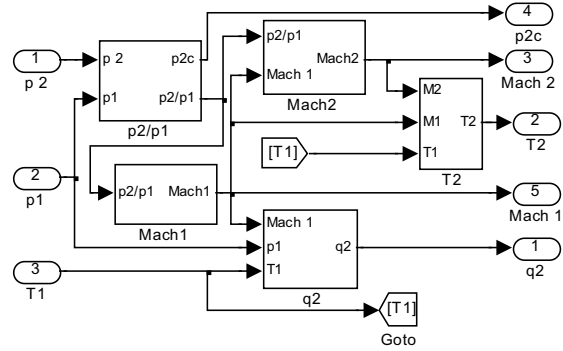
Figure 8　Simulink block diagram of pneumatic lines
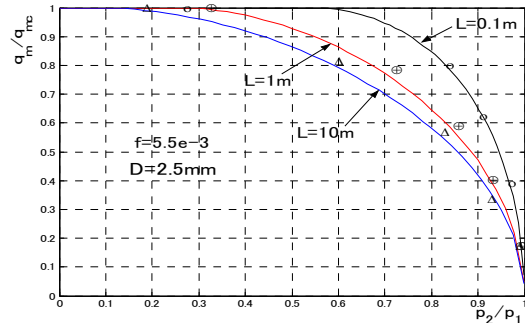
(a) D = 2.5 mm
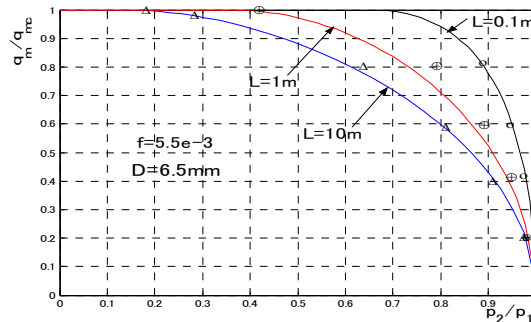
(b) D = 6.5 mm

Figure 9　Nondimensional flow rate
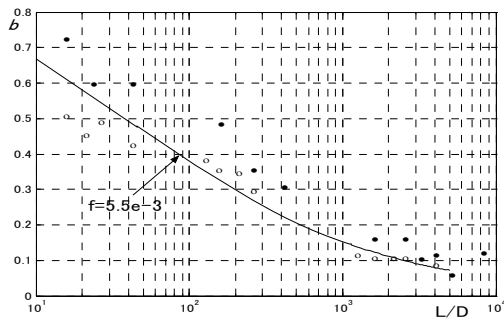
Figure 10   Critical pressure ratio b
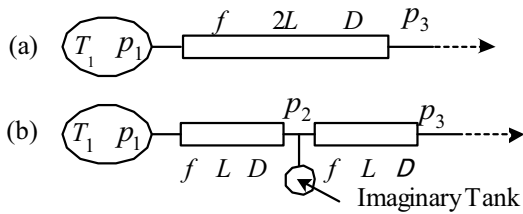
Figure 11   Series connection of pipe lines

The simulation of flows through the series connection of pipes as shown in Figure 11 can be realized by the straight-forward connection of Simulink blocks of each line. In this case we put imaginary tanks at each junction to avoid causal conflicts in computations.

The parameters shown in Figure 11 are f=0.0055, D=4.01mm, L=4.83m. The nondimensional flow rate q_n computed as the single line (a) is shown as the solid curve in Figure12. The same flow rate q_n computed as the connection of two same lines (b) is shown as the diamond marks. The difference between both simulation results is negligible for practical uses. The asterisks and circles shown in Figure 12 are experimental results done at Shibaura Institute of Technology for the single line (a).
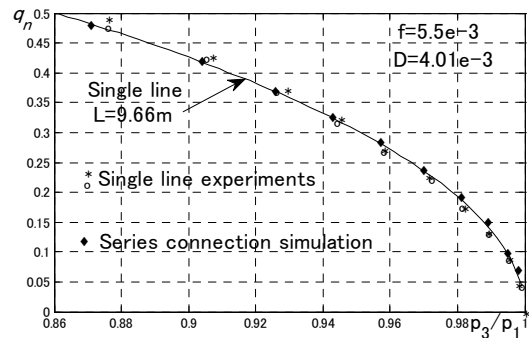
Figure 12   Simulation and experiments

CONCLUSION

It was confirmed that our simulation method was excellent enough to estimate the flow characteristics of pipe lines for designing pneumatic systems. Especially, it is practically useful that the critical pressure ratio b can be expressed by the loss coefficient of the pipe line and the simulation of flow for connected lines in series is straight-forward.

ACKNOWLEDGEMENT

REFERENCES

1. Shapiro, A.H.: The Dynamics and Thermodynamics of Compressible Fluid Flow, Vol. I , Ronald Press, 1954
2. Benedict, R.P. et al: A Generalized Approach to One-Dimensional Gas Dynamics, Trans. ASME, J. E. Power, January ,1962, pp.49-68
3. White, F. M.: Fluid Mechanics, McGraw-Hill, 1979
4. Benedict, R.P.: Fundamentals of Pipe Flow, John Wiley & Sons,1980
5. Trade mark of The MathWork,Inc..
6. Oneyama et al: Research on flow characteristics of pneumatic pipe lines, JHPS Spring Symp., 2003, pp.98-100, in Japanese.
7. Senoo et al: Research on flow characteristics of pneumatic pipelines (Second report), JHPS Spring Symp., 2004, pp.212-214, in Japanese

APPENDIX
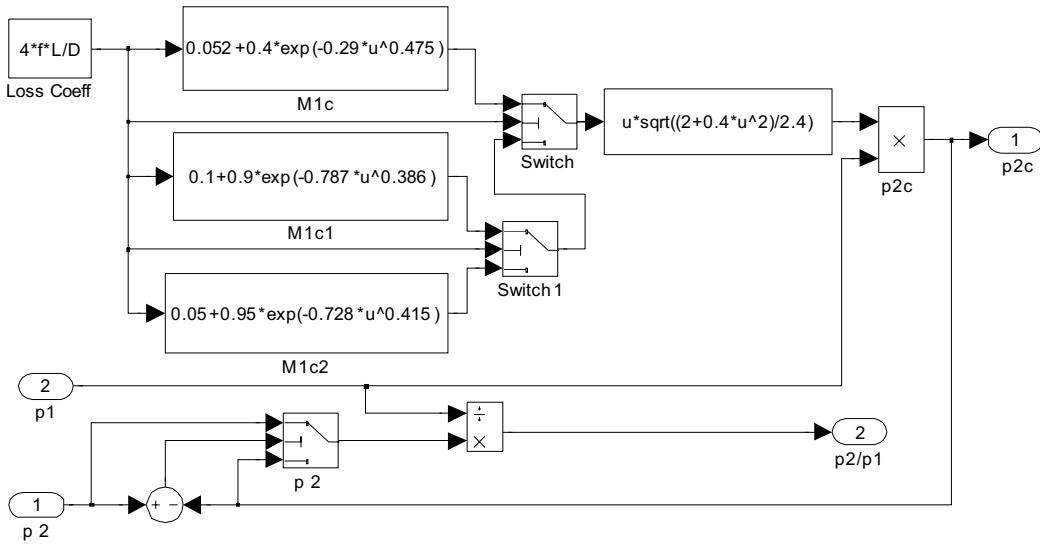
Figure A1   Subsystem p2/p1
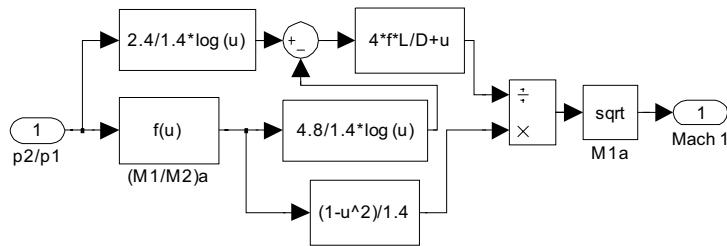
Figure A2   Subsystem Mach1
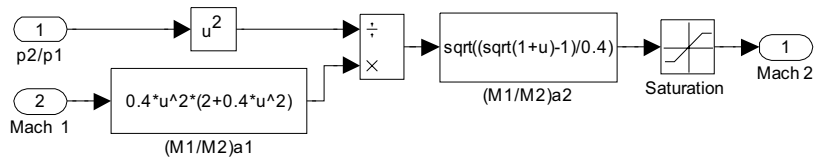
Figure A3   Subsystem Mach2
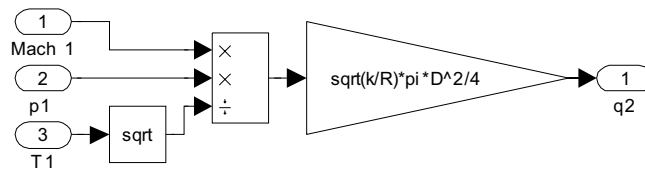
Figure A4   Subsystem q2
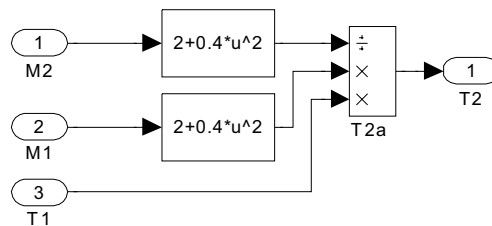
Figure A5   Subsystem T2

P1-30

DYNAMIC SIMULATION AND EXPERIMENTAL RESEARCH ON CHARGE OF GAS BOOSTER

Haitao WANG, Wei XIONG and Zhonghua LI

Transportation and Logistics Engineering College, Dalian Maritime University
1 Linghai Road, Dalian, 116026, China
(E-mail:wht810@vip.sina.com)

ABSTRACT

Based on the analysis of principle and structure of the gas booster, this paper studied on its charging process from low-pressure gas bottle to high-pressure one, considered the effect of some facts, including the changing of inlet and outlet pressure, clearance space, friction, according to the principle of kinematics, gas dynamics and thermodynamics ,established the mathematical and dynamics model of a gas booster system, which includes pressure differential equation of each chamber, flow rate equation, as well as the temperature equation and piston acceleration equation. The system is simulated with M-File of MATLAB software, and we got the pressure change curves, flow characteristic curve and time of charging gas, and the experimental data proved the correctness of simulation result, and provide theoretical basis for model selection and overall design.

KEY WORDS

Gas booster, Mathematical model, MATLAB, Numerical simulation

NOMENCLATURE

A_e : Effective area of pipeline system;
b : Critical pressure ratio;
k : Adiabatic exponent;
M : Mass of the piston;
R : Molar gas constant;
S : Stroke of the piston;
X : Displacement of the piston;
X_{10} : Clearance of chamber 1.

INTRODUCTION

Gas booster is an equipment of compressing low-pressure gas to high-pressure, which has wide applications in gas bottle charging and compression fields. The working principle of gas booster abide by Pascal's Law, if there is a smaller force acting on the big end of piston, there will be a bigger force on the small end. Based on the analysis of principle and structure of gas booster, a mathematical model was set up, and we solved the problem of reciprocating motion of piston in the simulation, the experimental data verified the correctness of this simulation, and provide theoretical basis for model selection and overall design.

MATHEMATICAL MODEL

In the experiment, we use a single acting gas booster to pressurize the gas, whose pressure ratio is up to 30. Aiming at the course of charging, we established the

mathematical model. The model of gas booster system is shown in Figure 1.
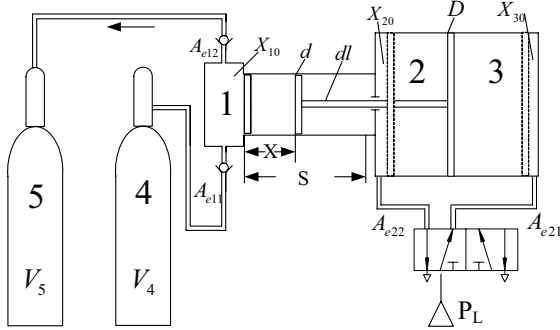
Figure 1 Physical Model of Gas Booster System

For the physical model of gas booster system, we suppose the working media is ideal gas, and there is no leakage in the course of charging; the temperature field and pressure field is uniform in the same chamber, and the state parameters of gas are equal at any point and any time; the gas flowing through a throttle was supposed to be one-dimension adiabatic steady flowing. Take chamber 1 to 5 as control body respectively, and the gas obeys the first law of thermodynamics and the flow rate continuation equation, so we got the pressure equation of each chamber.

Pressure Differential Equation of Chambers
Take five chambers as control body separately, and the volume of gas booster could easily get as shown in Figure.1, according to the first law of thermodynamics, the gas state equation and the flow rate continuation equation, we got the pressure differential equation of each chamber

$$\frac{dp}{dt} = \frac{k \cdot R}{V}(T_{in} \cdot Q_{in} - T \cdot Q_{out}) - \frac{k \cdot p}{V} \cdot \frac{dV}{dt} \quad (1)$$

Temperature Equation
Based on the course of adiabatic inflation for each chamber, suppose its pressure change from P_0 to P, temperature from T_0 to T and volume from V_0 to V, the temperature of gas source is T_s, then the temperature of the chamber after inflation

$$T = \frac{kT_s}{(k+1) + k(\frac{p_0}{p} - 1)\frac{V_0}{V} - \frac{p_0}{p}} \quad (2)$$

Based on the course of adiabatic deflation for a chamber, suppose its pressure change from P_0 to P, temperature from T_0 to T, then the temperature of the chamber after

deflation can be calculated as follows, in which `adiabatic exponent k is 1.4`.

$$T = T_0\left(\frac{P}{P_0}\right)^{\frac{k-1}{k}} \quad (3)$$

Flow Rate Equation
According the study of Sanville F.E., the calculation formula of the mass flow rate for the real pneumatic component can be calculated as follows,

$$Q_m = \frac{A_e p_u \sqrt{1-b}}{\sqrt{RT_u}} \omega(\sigma, b) \quad (4)$$

$$\omega(\sigma,b) = \begin{cases} 0, & \sigma = \frac{p_e}{p_u} > 1 \\ 1, & \sigma = \frac{p_e}{p_u} \leq b \\ \sqrt{1 - \left(\frac{\sigma - b}{1 - b}\right)^2}, & b < \sigma \leq 1 \end{cases} \quad (5)$$

In the equation, A_e is the total effective area of inlet and outlet pipeline system, T_u, P_u, P_e are respectively the upstream temperature, upstream pressure and downstream pressure, according to upper equation, we got the flow rate equation of every chamber of gas booster and gas bottle.

Piston Motion Differential Equation
The reciprocating motion of the piston is mainly due to the gas force of each chamber as well as the friction force between the piston and the cylinder wall. The force diagram of the piston is shown in Figure 2.
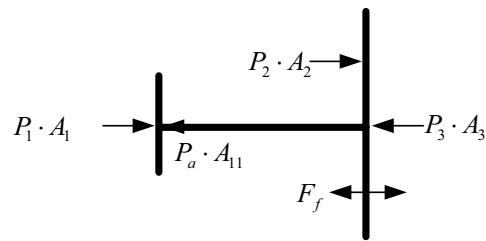
Figure 2 Force diagram of the piston

Take rightward as the positive direction of vector, its value can be calculated as follows:

$$F = P_1A_1 - P_aA_{11} + P_2A_2 - P_3A_3 - F_f \quad (6)$$

In the equation, F_f is the friction between the piston and

the cylinder wall, including the static friction when still and the sliding friction when moving, the direction of which is judged by the velocity or acceleration of the piston, which could be explained as follows

$$F_f = \begin{cases} F_{fs} & v = 0 \\ \left(F_{fc} + B_e|v|\right) \cdot \text{sgn}(v) & v \neq 0 \end{cases} \qquad (7)$$

In the equation, B_e is damping coefficient, F_{fs}, F_{fc} are respectively the maximum static friction and Coulomb friction.

When piston is at the most left and the direction of resultant force is rightward or at the most right and the direction of resultant force is leftward, as well as when piston is in the stroke, the acceleration of piston can be described as follows:

$$\begin{cases} \dfrac{d^2X}{dt^2} = \dfrac{F}{M}, & (X = 0 \cap F > 0) \cup (0 < X < S) \\ & \cup (X = S \cap F < 0) \\ \dfrac{d^2X}{dt^2} = 0 & , (X = 0 \cap F \leq 0) \cup (X = S \cap F \geq 0) \end{cases} \qquad (8)$$

NUMERICAL SIMULATION

The core of the simulation is to solve the differential equations, in Matlab, the type of the solver we used is as follows
[T,Y,TE,YE,IE] = ode45(odefun,tspan,y0,options)
In the mathematical model, the equation of pressure of each booster chamber and flow rate are not the same when piston move rightwards or leftwards, in order to judge the direction of the piston movement, we use the output arguments of the solvers-IE, which is got in the "options" of events. In simulation procedure, the events function is set as follows:
Function [value, isterminal, direction] = events(t, y)
  global S;
  value =[y(1) y(1)-S];   % detect value = 0
  isterminal =[1 1];   % stop integration
  direction =[-1 1];   % direction of value change

SIMULATION RESULTS

Run the simulation procedure in Matlab, simulate the charging process from a low pressure gas bottle of volume and pressure are separately 40L and 7MPa to a high pressure bottle of 30L and 12.9MPa. The driven air pressure p_1 is 0.6MPa, the initial temperature is 20℃. We got the curve of the displacement of the piston and pressure of each chamber. The results are shown in Figure 3 and Figure 4.
Figure 3 indicates that the frequency of piston circle is about 1.4 circles per second, and the displacement of piston in each circle is from zero to maximum stroke

and back to zero. On this basis, the consumption of driven air can be obtained.
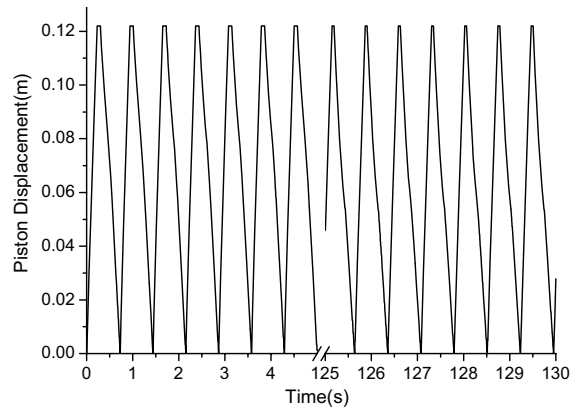
Figure 3 Displacement of piston

Figure 4 shows that the charging time from 12.9MPa to 14MPa is different. The simulation result is 132 seconds, and the experimental result is 140 seconds. There is a good agreement between experimental and simulation results.
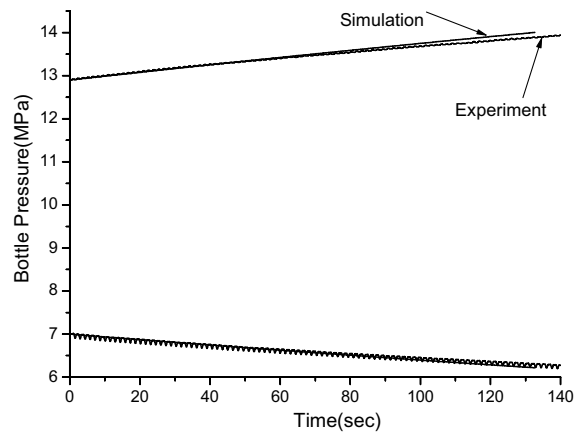
Figure 4 Pressure of two gas bottles

CONCLUSIONS

In this paper, the mathematical model was founded for the course of gas bottle charging, which mainly including the pressure differential equation, piston movement differential equation, as well as temperature and flow rate equation of each chamber. In the simulation process, the problem of reciprocating motion of piston was solved. By comparing with the experiment,

421

the mathematic model was proved to be able to reflect the work process of gas booster correctly. The error of two results is due to the given parameter values. The research provides theoretical basis for model selection, overall design, and for structure optimization.

REFERENCES

1. Li Jianfan. Dynamics of Pneumatic Driving System(Chinese). Publishing House of South China University of Technology,1991.

2. Haskel Gas Booster Catalog. Haskel International, INC.

3. Xue Dingyu,Chen Yangquan. System Simulation and Application Based on MATLAB/ Simulink(Chinese).

4. Chen Weiguo, Ding Xusheng, Guo Xiangfeng. Research of principle and method on fluid pressurization technology. Machine Tool and Hydraulics (Chinese) .2001,pp.13-1

P1-31

THE RESEARCH AND APPLICATION OF HYDRAULICS AND PNEUMATICS IN HUAZHONG UNIVERSITY OF SCIENCE AND TECHNOLOGY

Baoren Li and Jinyun Li

School of Naval Architecture & Ocean Enigineering
Huazhong University of Science and Technology,
Wuhan 430074, China
(E-mail: lbr@mail.hust.edu.cn)

ABSTRCT

The Pneumatic Center in Huazhong University of Science and Technology (HUST) is one of the most active research center in fluid power transmission and control in China. The main fields of Pneumatic Center in HUST are component development and control technology of fluid power. Hydraulics research is the most important part of fluid power in the Pneumatic Center in HUST. Based on several decades of the research on the hydraulics in HUST, the further research and new application in this field are made, include underwater motion platform, automatic buoyancy regulation technology and new type hydraulic valve, etc.. From 1996, the Pneumatic Center in HUST focuses on the combination of electronics, computer technology and pneumatics, and the research achievement play a very important role in some state key engineering projects successively. The pneumatic research and applications have been developed, such as the gas temperature control technology, pressure and vacuum servo control technology, leak-testing technology, pneumatic muscle platform and the high pressure pneumatic valve, etc.. In this paper the main research and application of hydraulics and pneumatic in Pneumatic Center in HUST are introduced. Also some practical examples research projects and subjects in above fields are presented.

KEY WORDS

Pneumatic, Vacuum and Pressure, High Pressure, Hydraulic, Underwater

INTRODUCTION FOR PNEUMATIC CENTER AND RESEARCH FIELD

The Pneumatic Center in Huazhong University of Science and Technology is one of the most active research center in fluid power transmission and control in China. The main fields of Pneumatic Center in HUST are component development and control technology of fluid power.

Hydraulics research is the most important part of fluid power in the Pneumatic Center in HUST. Based on several decades of the research on the hydraulics in HUST, the further research and new application in this field are made, include underwater motion platform, automatic buoyancy regulation technology and new type hydraulic valve, etc..

From 1996, the Pneumatic Center in HUST focuses on the combination of electronics, computer technology and pneumatics, and the research achievement play a very important role in some state key engineering projects successively. The research field pneumatic center includes:

- Study of new type hydraulic and pneumatic component and system

- Electronic hydraulic proportion/servo control technology, including position and force control system
- Electronic pneumatic proportion/servo control technology, including pressure, vacuum, position and force servo control system
- High-pressure pneumatic technology
- Mechanic and electronic integration, computer testing technology
- Study of special equipment applied to the semi-physical simulation system, including air environment simulation technology, load simulator, underwater motion platform etc..

Figure 1 The pneumatic center in Huazhong University of Science and Technology (HUST)

PNEUMATIC TECHNOLOGY RESEARCH AND APPLICATION

Vacuum and Pressure Continuous Control

Research in this sector is aimed to implement semi-physical flight height simulation technology of flight of aircraft. The technology is researched to master the flight condition and characteristics to avoid danger and ensure stable control of flight. In the research, the pressure and vacuum continuous control system is studied, which can implement continuous control of pressure and vacuum with high accuracy and fast response.

Initially, an idea is presented[1-2] to solve the problems mentioned above, that is, making use of pneumatic servo technology to control vacuum, the vacuum servo control system is founded with servo valve and vacuum generator. The research solves the key problem of developing vacuum servo control system with high accuracy and fast response.

The further advances have been made in studies[3-5] the pressure and vacuum continuous control system, which is shown in the Figure 2. The system adopted compressor and vacuum pump as pressure and vacuum source respectively. The research results demonstrated that the system behaved with desirable static and dynamic

characteristics. When absolute pressure in closed chamber declines from 100 kPa to 20 kPa, the transition time is 1.4 s and static error is less than 30 Pa. When system traces sin wave signal (frequency is 1 Hz and amplitude is 0.2 kPa), amplitude frequency error and phase frequency error are 0.37% and 4.939 3° respectively.
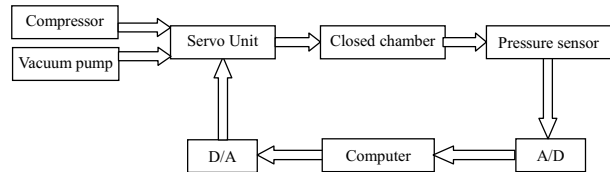
Figure 2 The sketch of the pressure and vacuum continuous control system based on vacuum pump

Based on a decade of theory research, several kinds of simulators for flight height and Mach number are developed with high accuracy and fast response, which are well applied to semi-physical flight height simulation system for aircraft and UAV.

Gas Temperature Control

The growing uses of simulator for total temperature have encouraged research to explore key technology of gas temperature control. For the gas temperature control system being a time-varying, big inertia and non-linear system, it's hard to control the gas temperature accurately, especially gas temperature control of a flowing open system with high degree of accuracy and fast-response signal of gas temperature.

By way of example, Figure 3 describes a principle of high and low temperature control system[6]. The research results show that the system can control gas temperature among the range between 233 K and 393 K. The static error is not more than 0.4 K. The maximal temperature varies rate is 1 K/s.
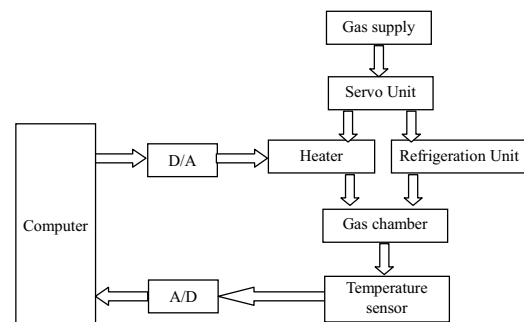
Figure 3 Principle of the temperature control system

Recently, the research in this filed to acquire further development. For the system[7,8] showed in Figure 4, the temperature range been controlled is 293～753 K, the maximal static error is 2 K and The temperature

varies rate can achieve 80 K/s.
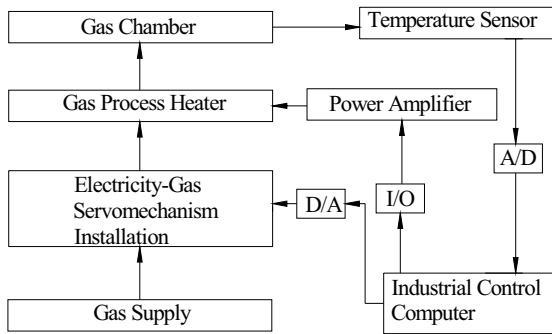
Figure 4 Operating principle of the system

Leak Test
The leak test is another research field of Pneumatic Center. The leak test system[9], which serviced to important device is shown in the Figure 5. When setting pressure in the closed chamber in the system to 50 kPa and 200 kPa respectively, the variety value of pressure is no more than from 20 kPa to 30 kPa.

Figure 5   The leak test system

High Pressure Technology
The research on the high pressure technology firstly focus on simulation of high pressure gas flow. The pressure and flow characterize of high pressure is studied by means of computational fluid dynamics. The simulation result is of benefit to further optimal design of high pressure pneumatic component.
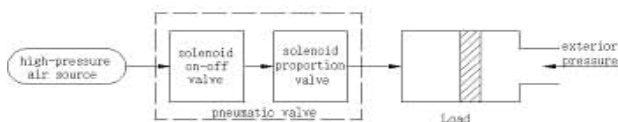
Figure 6 Sketch of high-pressure pneumatic system
Based on theory research, high pressure Pneumatic valves are researched. As shown in the Figure 6, a new type high-pressure Pneumatic solenoid on-off valve[10] is developed, which has the advantages of high work

pressure and large output flow-rate.

HYDRAULIC PRESSURE TECHNOLOGY RESEARCH AND APPLICATION

Hydraulic System
The underwater-simulated device[11] has pure rotational degrees of freedom with rotational range of ±30° with respect to x and y axes and rotational range of ±180° about z axis. It is necessary to design a spatial 3-DOF manipulator according to the requirements of the simulated device. Its architecture is shown in Figure 7. The device consists of a 2-DOF parallel manipulator driven by hydraulic cylinders and a creeper gear with one degree of freedom driven by servo motor. Hence, the kinematic characteristics of the creeper gear are independent of the rotations of parallel manipulator. The characteristics and control of the creeper gear driven by servo motor are simple relative to the parallel manipulator in this project.
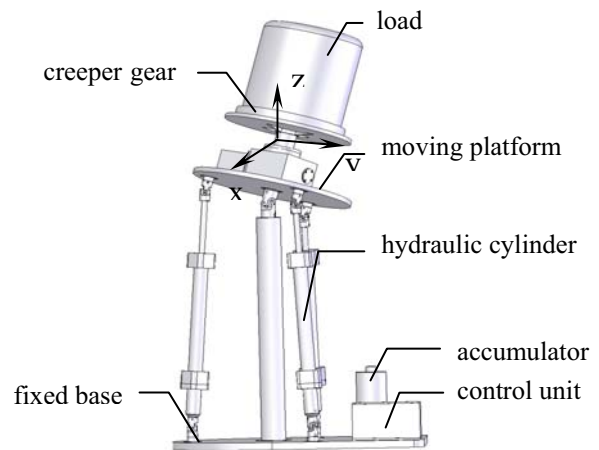
Figure 7 The sketch of the underwater-simulated device

More and More importance is attached to the operating security and reliability of important equipment to which hydraulic system used in such important equipment, fluid flow rate limiting device is developed[12]. Purpose of researching the fluid flow rate limiting device is to improve operating security and reliability of hydraulic system in important equipment.

Hydraulic System for Ocean research
With the development of ocean research, the collection and supervision of observations describing the ocean states are becoming more important. Ocean vertical section plane survey plat roof is a system facing the high technical research plan, which can meet with this demanding in our country. The flotage adjustor[13] exploited is developed to meet with the actual demanding of ocean section plane survey plat roof to realize the purpose of automatic raising or lowering from

425

100m to 150m under the water for the survey plat roof. It is a product with more consideration of light weight, smart volume, low power consumption and high reliability.

Hydraulic Components

With the development of hydraulic technology, hydraulics has been applied widely in many industry fields as an automatic control means. The various valves are also studied with the development of hydraulics. In order to satisfy some special industry requirements, the new types of valves are studied and applied with new material, new structures and new functions. The watering valve presented in this paper is researched for the water supplement of lead-acid batteries[14]. The valve is one kind of autocontrol components, which has sensitive response, accurate control and steady function.

CONCLUSION

Research in the Pneumatic Center in Huazhong University of Science and Technology covers a very wide range. In most research filed in the center, the theory research achievements have been developed to production, which is applied in some important technology area in China. And as the development of center, more complex systems and more precision components in the pneumatic and hydraulic field will be researched to meet demand of important domestic research institution. For Ocean research is the development focus in China in during the next decade, the center will stress pneumatic and hydraulic research which service to ocean technology.

ACKNOWLEDGMENTS

REFERENCES

1. LI Baoren, ZHANG Qingxian, DU Jingmin. Investigations on vacuum servo control system based on fuzzy control[J]. Journal of Huazhong University of Science and Technology, 1999, 27(11): 65-67(In Chinese).
2. ZHU Yuquan, ZHANG Qingxian, DU Jingmin, et al. Research on continuous control of vacuum in closed chamber[C]// Proceeding of the 3rd International Symposium on Fluid Power Transmission and Control, ISFP'99, Harbin, China, 1999: 500-503.
3. LI Jinyun, FU Xiaoyun, DU Jingmin, LI Baoren. Research on pressure and vacuum servo control system based on vacuum pump[J]. Chinese Journal of Mechanical Engineering, 2005, 41(11): 53-57(In Chinese).
4. LI Jinyun, DU Jingmin, FU Xiaoyun, LI Baoren. Pressure and vacuum servo control system based on vacuum pump and study of the system control[C]// The Sixth International Conference on Fluid Power Transmission and Control, ICFP 2005, Hangzhou, China, APR 05-08, 2005: 368-372.
5. Li Jinyun, Du Jingmin, Fu Xiaoyun, Li Baoren, Theoretical and experimental study on the pressure and vacuum continuous control system based on hybrid pump[J], Chinese Journal of Mechanical Engineering, 2007,20(6): 74-78.
6. Du Jingmin, Fu Xiaoyun, Li Baoren. Experimental Research on High Precision Real-time Control of Air Temperature[J]. Chinese Hydraulics and Pneumatic, 2002,12: 19-20(In Chinese).
7. Gao Zeshang, Du Jingmin, Li Baoren. Research on Modelling and Simulation of Gas temperature control system [C]// The Fifth National Symposium on Fluid Power Transmission and Control, Beijing, China, October 15-18, 2008 (In Chinese) (Accepted).
8. Du Jingmin, Zhang Li, Fu Xiaoyun, Li Baoren. Modeling and Simulation of a Gas Temperature Control System[C]// The Sixth International Conference on Fluid Power Transmission and Control, ICFP 2005, Hangzhou, China, APR 05-08, 2005: 459-462
9. FU Xiaoyun, DU Jingmin, LI Baoren. Development on Auto Testing Device for Air-sealing[J]. Chinese Hydraulics and Pneumatic, 2005,5: 35-37(In Chinese).
10. Guo Hao, Yang Gang, Li Baoren. Study on Dynamic Characteristic of a High-Pressure Pneumatic Solenoid On-Off Valve[C]// The Fifth International Symposium on Fluid Power Transmission and Control, ISFP 2005, Beidaihe, China, June 6-8, 2007: 985-988.
11. X.Y. Fu, G. Yang, B.R. Li Analysis and Control of a Parallel Manipulator Applied to an Underwater-simulated Device, Association for the Advancement of Modelling & Simulation Technology in Enterprises journal. (Accepted)
12. Genglang Chen, Zuyao Yu, Baoren Li. Modeling & Simulation Research on New Fluid Flow Rate Limiting Device of High Reliability[C]// The Fifth International Symposium on Fluid Power Transmission and Control, ISFP 2005, Beidaihe, China, June 6-8, 2007: 157-161.
13. Guo Chenbing Yang Gang Li Baoren, Research of Automatic Buoyancy Regulation Device [C]// The Fifth National Symposium on Fluid Power Transmission and Control, Beijing, China, October 15-18, 2008 (In Chinese) (Accepted).
14. QIN Xiaofei , YU Zuyao , GUI Yongsheng , LI baoren. Research and Implementation of the Self-motion Watering System of Lead-acid Storage Batteries[J], Machine Tool & Hydraulics, 2007,5:114-116

P1-32

DEVELOPMENT OF A SKIN DISPLACEMENT SENSOR FOR THE PNEUMATIC POWER ASSISTED SYSTEM

Shujiro DOHTA*, Tetsuya AKAGI* and Hiroaki KUNO*

* Department of Intelligent Mechanical Engineering, Faculty of Engineering
Okayama University of Science
1-1 Ridai-cho, Okayama, 700-0005 Japan
(E-mail: dohta@are.ous.ac.jp)

ABSTRACT

An importance of wearable device in the field of medical treatment has been strongly recognized. Also, the development of the power assisted system has been done to support the nursing care work for the elderly. The purpose of our study is to develop a wearable flexible displacement sensor which can measure the movement of human body by mounting on the skin surface. The tested sensor consists of two fixed electrodes, a slide electrode and a nylon string coated with carbon (NSCC). It works as a flexible potentiometer by sliding the slide electrode along NSCC while keeping the electrical contact. In order to keep a stable electrical contact even if NSCC bends flexibly, the slider is consisted of a brass cylinder filled with carbon black powder. In our previous study, we confirmed that the sensor worked well by carrying out the position control of a McKibben artificial muscle.

In this paper, we proposed and tested a skin displacement sensor using the flexible displacement sensor that can measure the bending angle of the human arm without measuring the joint angle directly. As a result, we confirmed that we can know the human motion indirectly using the tested sensor. We apply the proposed sensor to the control of the power assisted system by using a pneumatic rubber artificial muscle.

KEY WORDS

String type flexible displacement sensor, Skin displacement sensor, Soft sensor, Human interaction

INTRODUCTION

Recently, an importance of wearable devices in the field of medical treatment such as nursing care and rehabilitation has been strongly recognized [1]. In order to support the nursing care task, the power assisted device has to be worn on the human body directly. These wearable devices require the flexible movement to apply a supporting machine for the nursing care work. Also many kinds of wearable device such as a power assisting device and an active rehabilitation device need to realize the flexible and complex movement. The purpose of our study is to develop a flexible, lightweight and simple sensing system for human movement to develop the pneumatic power assisted system and a compact driving system using the flexible pneumatic actuator which can be safe and lightweight enough to be attached to the human body. In this paper, we propose and test a skin displacement sensor using the flexible displacement sensor that can know the movement of the human arm without measuring the human joint angle directly.

STRING TYPE FLEXIBLE DISPLACEMNET SENSOR

Construction and operating principle

Figure 1 shows the construction of a tested string type flexible displacement sensor (we call it "FDS" for short). The sensor consists of two fixed electrodes (that is an anode and a cathode), a slide electrode and a nylon string coated with carbon (we call it "NSCC" for short). It works as a flexible potentiometer by sliding the slide electrode along NSCC while keeping the electrical contact. Therefore, the slider needs the function of keeping a stable electrical contact even if NSCC bends flexibly.
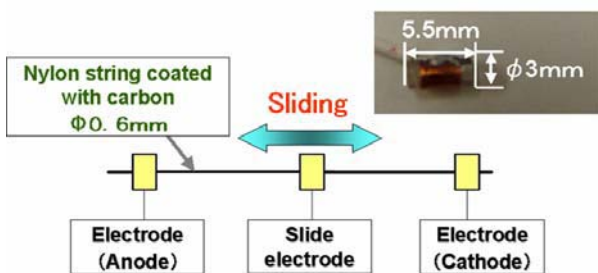
Figure 1 Construction and view of the tested flexible displacement sensor

Figure 2 shows the inner construction of the slide electrode. The slider consists of a brass cylinder that is filled with carbon black powder. The each side of the slider has a rubber sheet, a rubber packing and a plastic cover to keep a sealing. The slider is penetrated with a NSCC. By this construction, the slider can keep a stable electrical contact between the slider and NSCC. The carbon black powder prevents the wear of NSCC because it works as balls of a slide bearing. The tested flexible sensor can realize a longer measurement range than a conductive rubber displacement sensor [2]. The user can easily change a measurement range of the sensor.
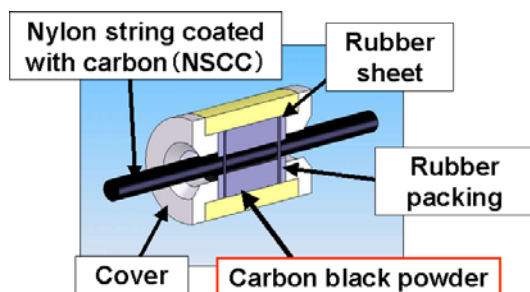
Figure 2 Inner construction of the slide electrode

Characteristics of the tested sensor

Figure 3 shows the relation between displacement and electric resistance of the sensor. We can see that the resistance of the sensor is proportional to the displacement between two electrodes. We also find little hysteresis in experimental results using the tested slide electrode even if one end of NSCC is not fixed on a table. It means that there is less friction between the tested slider and the NSCC.
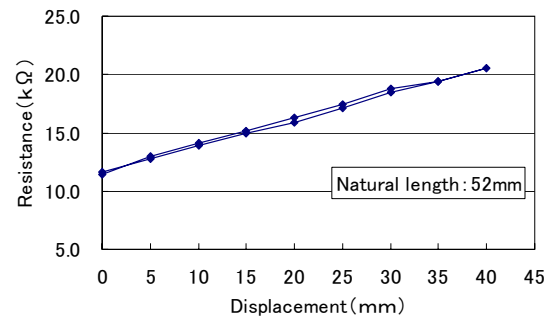
Figure 3 Relation between displacement and resistance of the tested sensor

In such a kind of the slide electrode including the carbon black powder in it, the leakage of the powder from the electrode chamber might become the problem of durability. We investigated the durability of the tested sensor. Figure 4 shows the relation between the number of repetition of sliding and the output voltage of the sensor. In the experiment of endurance test, the slide electrode is driven by the pneumatic cylinder that makes the slide electrode move for the distance of 30 mm within 0.3 seconds. In every 100,000 times sliding, the output voltage from the tested sensor in both points of maximum and minimum stroke of the pneumatic cylinder was measured. In Fig.4, each line shows the average of the measured output voltage of the sensor in each position. The vertical line shows the scatter of the measured data.
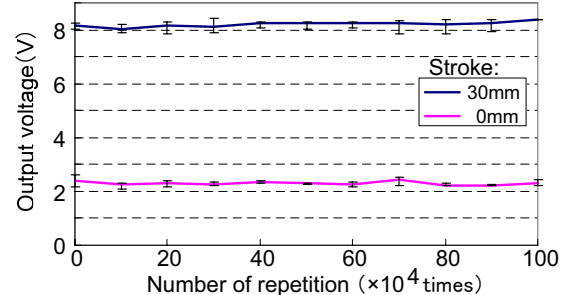
Figure 4 Experimental results for endurance test

We can see that the output voltage of the sensor does not change in the both position even if one million times sliding was applied to the sensor. It means that the tested sensor has good durability. In the experiment, we also found little leakage of carbon black powder from the slide electrode. Through the endurance test, we found that the sensor was able to be used even if the carbon powder was not filled in it.

POSITION CONTROL OF ARTIFICIAL MUSCLE

Position sensing of artificial muscle

As an application of the tested string type flexible displacement sensor to the sensing of robot actuator, we proposed and tested a position sensing system of a McKibben artificial muscle using the tested sensor. Figure 5 shows the relation between the displacement of the McKibben artificial muscle and the output voltage of the attached flexible displacement sensor. In addition, we apply a unique measurement method that the sensor can measure the whole displacement of the actuator by measuring a part of it. The setting position of the sensor in the actuator is parallel to the longitudinal direction of the surface of the actuator. The sensor connected with the actuator is shown in upper photograph in Fig.5. Also, the distance between a fixed electrode and slide electrode was set by 14 mm by considering the movement range of the slider for a supply pressure (from 0 to 500kPa). From Fig. 5, we can see that a linear relationship is established between the displacement of the artificial muscle and sensor output voltage. The correlation coefficient is 0.998. We can confirm that the whole displacement of the actuator is measured by measuring a part of it using the proposed method and the tested sensor.
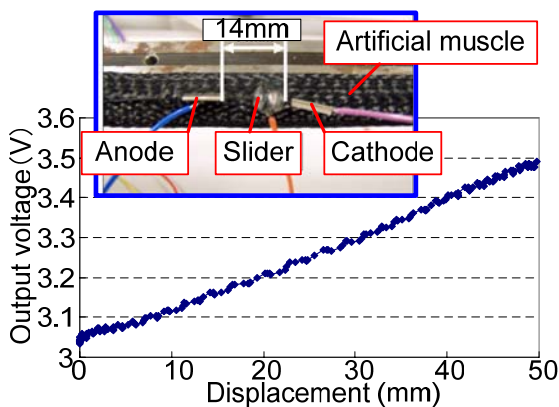
Figure 5 Relation between displacement of artificial muscle and output voltage of sensor

Compact position control system of artificial muscle

Figure 6 (a) and (b) show the construction and the schematic diagram of the position control system of the artificial muscle with the flexible displacement sensor, respectively. In Fig.6 (a), the system consists of a potentiometer to give the desired position, a microcomputer (Renesas Technology Co. Ltd.. H8/3664) , a Mckibben artificial muscle (FESTO Co. Ltd. MAS-10) with the tested flexible sensor and two on/off control valves (KOGANEI Co. Ltd. G010HE-1). The suction and exhaust valves are connected in series as shown in Fig.6. The position control of the actuator is done as follows. First, the microcomputer gets the voltage from the tested sensor and the reference voltage through a 10 bit A/D converter in the microcomputer. In operation, the microcomputer drives the suction or exhaust valves through the transistors according to the deviation from the desired position. When the deviation exists within a certain range, both valves are turned off. In the case when the deviation is larger, the suction valve is turned on and the exhaust valve is turned off. In other cases, both valves are driven so as to become the opposite state of the previous case.
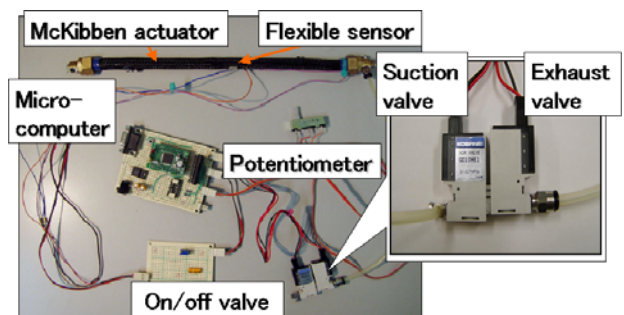
(a) Construction of control system
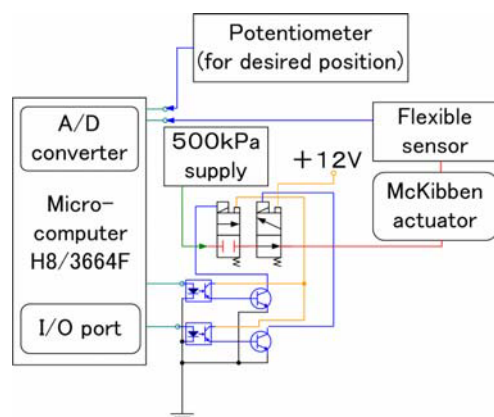
(b) Schematic diagram of control system

Figure 6 Position control system using artificial muscle and skin displacement sensor

Figure 7 shows the transient response of the displacement of McKibben actuator. In Fig.7, each blue and red line show output voltages from potentiometer for desired position and the flexible sensor, respectively. From Fig.7, we can see a vibration of the actuator occurred in the range of smaller displacement because of the control using on/off valves. As a whole, it can be considered that the movement of actuator can trace well the desired position even if a simple control method such as on/off control is used. In addition, we can confirm that the dynamics of tested flexible sensor is very fast so as to measure the vibration of the actuator.
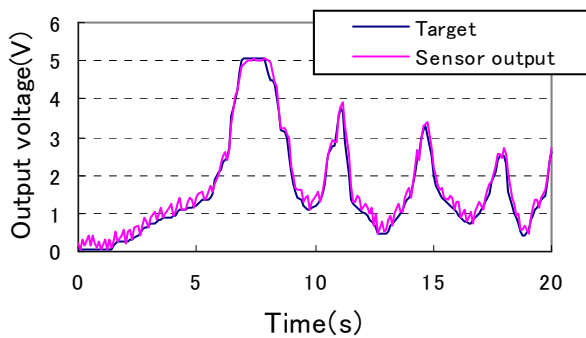
Figure 7 Transient response of displacement of the artificial muscle using tested control system

SKIN DISPLACEMENT SENSOR

Construction and operating principle
It is very useful to measure the movement of human body such as a joint angle indirectly. It is because that such a sensing system does not prevent the human motion and an easy sensor configuration at the point of moving part of human such as a joint. When the human body moves, the muscle also moves. At the same time, the skin covering the muscle moves. Therefore, we propose and test a skin displacement sensor. Figure 8 shows the construction of the skin displacement sensor. The upper photograph in Fig.8 shows the general view of tested sensor. The lower photograph shows the view in the case when the sensor is pasted on the human arm. The sensor consists of the FDS set on a flexible plastic sheet that has bellows and an electric circuit pattern using the conductive paint. The middle figure in Fig.8 shows the electric circuit of the sensor. The electric input and output line are gathered in one end of the sensor. Each end of the FDS is connected with a power supply and GND line. The slide electrode is connected with the sensor output line. The operating principle of the sensor is as follows. First, the both end of the sensor as shown in the lower photograph in Fig.8 are pasted on the human skin as a sticking plaster.

When the body and skin moves, the distance between both pasting points of the sensor is changed. This change causes the pulling and pushing force acted on one end of the FDS. By this method, the sensor measures the displacement of the skin.
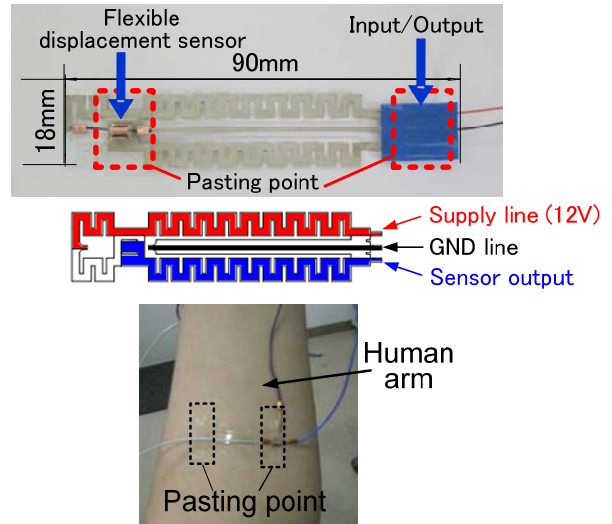
Figure 8 Construction of the skin displacement sensor

Sensing for human motion using skin displacement sensor
Figure 9 shows the experimental setup using the skin displacement senor. The equipment consists of the sensor pasted on the human arm and a voltmeter to measure the output voltage from the sensor. In the experiment, we measure the bending angle of the elbow by taking photographs of the posture of the elbow and the output voltage of the sensor.
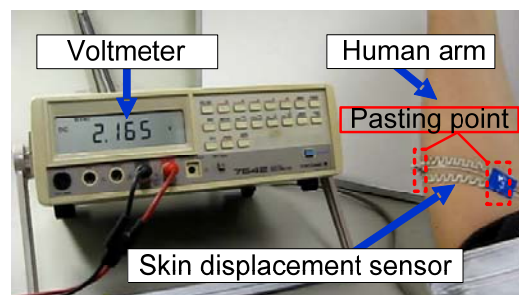
Figure 9 Experimental setup for the tested sensor

As a pasting point of the sensor, we select the skin over the muscle that is related to drive the elbow such as a biceps brachii, a brachialis, a brachioradialis and a triceps brachii as shown in Fig.10.

Biceps brachii   Brachialis   Brachioradialis
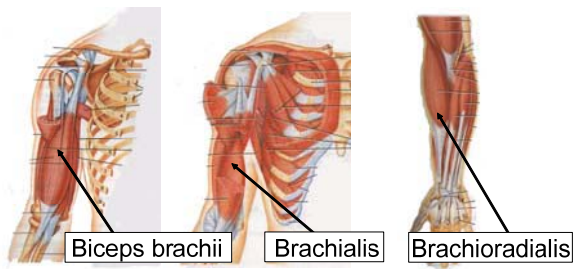
Figure 10 Muscles which are related to
drive the elbow [4]

Figure 11 (a) and (b) show the measuring results when the sensor is pasted on the skin over the biceps muscle parallel and vertically to the muscle, respectively. Figure 11 (c) and (d) show the results when the sensor is pasted over the brachioradialis muscle vertically and parallel to the muscle, respectively. Figure 11 (e) shows the case when the sensor is pasted on the forearm muscle in diagonal direction. Each small illustration in Fig. 11 shows the pasting point of the skin displacement sensor. Each graph in Fig.11 shows the relation between the bending angle of the elbow and the output voltage of the sensor. From Fig.11, we can see that the relation between the bending angle of the elbow and output voltage of the sensor is almost linear in all cases. Each gradient of solid line in the graph shows the sensitivity between the sensor output voltage and the bending angle of the elbow. The increasing and decreasing of the output voltage according to the bending angle in each figure mean that the extended and contracted force are applied to the skin displacement sensor, respectively. As an estimation of the optimal pasting position of the sensor, Table 1 shows the correlation coefficient and the differential output voltage of the sensor when the elbow angle changes from 0 to 90 deg. From Table 1, we can see that the case when the sensor is pasted vertically over the biceps brachii muscle as shown in Fig.11 (a) is superior than other cases because of the higher correlation coefficient (that is -0.957) and the larger output voltage (that is 1.607 volts) for bending. The value of -0.957 in the coefficients of correlation means that the relationship between the skin displacement and bending angle of the elbow measured by the tested skin displacement sensor is almost linear. As a result of these trials, we can say that the tested skin displacement sensor has a possibility of indirect measurement of human motion.
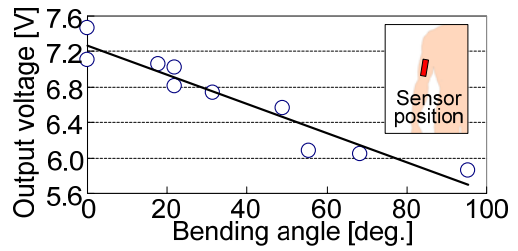
(a) Biceps brachii (parallel direction)
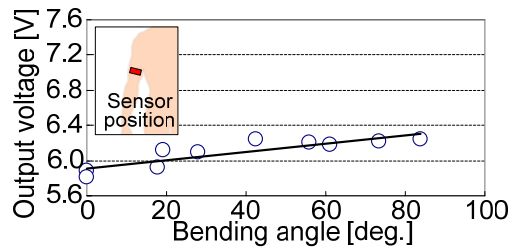
(b) Biceps brachii（vertical direction）
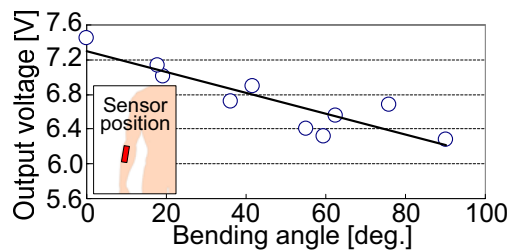
(c) Brachioradialis（parallel direction）
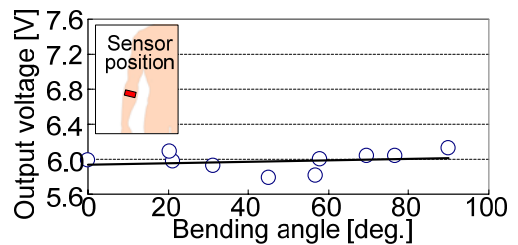
(d) Brachioradialis（vertical direction）
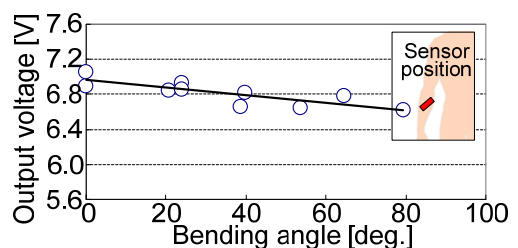
(e)Forearm (diagonal direction）

Figure 11 Relation between bending angle of the elbow
and output voltage of the skin sensor

Table 1 Estimation for pasting point

Pasting point	Correlation coefficient	Differential voltage (V)
Biceps brachii (parallel direction)	-0.9565	1.607
Biceps brachii (vertical direction)	0.8693	0.431
Brachioradialis (parallel direction)	-0.8846	1.167
Brachioradialis (vertical direction)	0.2213	0.341
Forearm (diagonal direction)	-0.8259	0.440

CONCLUSIONS

This study for developing a wearable flexible sensor can be summarized as follows.

1) We proposed and tested a new type of flexible displacement sensor using nylon string coated with carbon. We also proposed and tested a small sized pressure control system to drive a McKibben actuator using on/off valves. As a result, we confirmed that the tested sensor was useful to apply to the position control system using the McKibben actuator because of its compact configuration of sensor and actuator so as not to lose the flexibility of the actuator.

2) We also proposed and tested the skin displacement sensor that can measure the human motion such as a joint movement indirectly. As a result of measuring the elbow angle, we can confirm that the tested skin displacement sensor has a possibility of indirect measurement of human motion.

In our future work, we are going to develop an intelligent skin displacement sensor that has a function of electromyogram as an interface between humans and machines in order to develop the pneumatic power assisted system.

ACKNOWLEDGMENT

REFERENCES

1. M.Ishii et al., Stand-Alone Wearable Power Assist Suit -Development and Availability,Journal of Robotics and Mechatronics,Vol.17, No.5, 2005, pp.575-583.
2. T. Shinohara, S. Dohta and H. Matsushita, Development of a Soft Actuator with a Built-in Flexible Displacement Sensor, Proceedings of 9th International Conference on New Actuator (Actuator 2004), Germany, 2004, pp.383-386.
3. I. Hamamoto et al., Development of Flexible Displacement Sensor Using Nylon String Coated with Carbon and Its Application for McKibben Actuator, Proceedings of SICE-ICASE International Joint Conference 2006, Korea, 2006, pp.1943-1946.
4. G. J. Tortora and S.R. Grabowski, Introduction of the Human Body, 6th edition, The Essentials of Anatomy and Physiology, Japanese translation by Maruzen Co. Ltd., 2004, pp.210-213.

P1-33

A STUDY ON A SOUND OPERATED VALVE
FOR A WEARABLE PNEUMATIC SYSTEM

Ato KITAGAWA, Shuyi JING, Canghai LIU and Hideyuki TSUKAGOSHI

* Department of Mechanical and Control Engineering
Tokyo Institute of Technology
2-12-1 Ookayama, Meguro-ku, Tokyo 152-8550 Japan
(E-mail: kitagawa.a.aa@m.titech.ac.jp)

ABSTRACT

A sound operated directional control valve (SODC-Valve) is proposed which opens and closes in response to the sound of a specific frequency propagated inside the gas supply tube and therefore needs no electric wiring to convey the control signals. By using multi-frequency sound, several valves can be controlled simultaneously and resultantly the pneumatic multi-degree wearable system can be constructed compactly. Firstly, the sound-gas pressure converter is proposed and improved so that self-excited vibration can be suppressed. Secondly, the basic characteristic of the sound-gas pressure converter is investigated to show that the back pressure is different depending on whether the sound of specific frequency is added or not. Furthermore, a pilot valve is developed. Because the pilot pressure change of the pilot valve developed is only 20kPa, a main valve is proposed and developed. Finally, a pneumatic multi-degree-of-freedom wearable power-assist system is constructed by using a Dry Ice Power Cell as the portable gas supply, wearable actuators developed in the previous study, and two sound operated directional control valves developed. Experimental results show that the sound operated directional control valve is feasible and practical in the pneumatic multi-degree-of-freedom wearable system.

KEY WORDS

Pneumatic, wearable, sound-operated, valve, resonance

NOMENCLATURE

p_n : Back pressure of nozzle [kPa]
Δp_n : Change of back pressure of nozzle [kPa]
p_s : Supply pressure [kPa]
x : Space between nozzle and head [mm]
y : Displacement of center of head from center of nozzle [mm]
z : Wave length of sound [mm]

INTRODUCTION

Pneumatic power assist multi-degree-of-freedom wearable system has been developed by many researchers. But in most of the traditional pneumatic systems, their focuses are concentrated on the development of actuators [1] [2]. Few of them are argued about wearable power supply sources or valves. Therefore, there exist the problems when the pneumatic systems are used for wearable power assist. For example, the tubes and electrical cords connected between the actuators and valves are troublesome. In

this paper, a novel valve called Sound Operated Directional Control Valve (SODC-Valve) is developed. The SODC-Valve opens and closes in response to the sound of a specified frequency propagated inside the gas supply tube and therefore needs no electric wiring to convey the control signal for the valve. By using multi-frequency sound, several valves can be controlled simultaneously. Using the previously developed Dry-ice Power Cell [3] as power supply, the SODC-Valve is expected to be used in pneumatic power assist wearable system.

In this paper, firstly, the sound-gas pressure converter is proposed and improved so that self-excited vibration can be suppressed. Secondly, the basic characteristic of the sound-gas pressure converter is investigated to verify that the back pressure is different depending on whether the sound of specific frequency is added or not. Furthermore, a pilot valve of the sound operated directional control valve is developed. Because the pilot pressure change of the pilot valve developed is only 20kPa, a main valve is proposed and developed. Finally, a pneumatic multi-degree-of-freedom wearable system is constructed by using Dry Ice Power Cell as the portable gas supply, wearable actuators developed in the previous study, and two SODC-Valves developed. Experimental results verify that the sound operated directional control valves are feasible and practical in pneumatic multi-degree-of-freedom wearable power assist system.

SOUND-GAS PRESSURE CONVERTER

The SODC-Valve opens and closes in response to the specified frequency sound propagated inside the gas supply tube. If several SODC-Valves are set along the supply tube as shown in figure 1, several actuators can be controlled with the valves simultaneously by adding sound of each valve's resonance frequency into the supply tube.
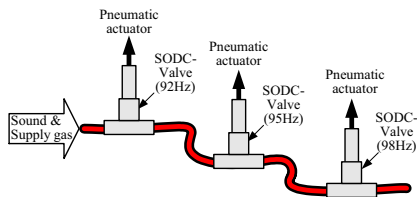
Figure 1 Schematic of multi SODC-Valves system

As the kernel-element of the SODC-Valve, the Sound-Gas Pressure Converter is developed to convert the sound into change of pressure. For convenience, the Sound-Gas Pressure Converter is called S-P Converter. The S-P Converter consists of a nozzle and a vibration element, as shown in figure 2. And the vibration element consists of a mass called head and leaf spring, as shown in figure 3. The head is adjusted to be as close to the nozzle as possible without touching the nozzle.

Resultantly, the leakage from the nozzle is small when the head stands still. If the head of the vibration element responses to the specified frequency sound in the supply tube and resonates near the nozzle in the arrow direction shown in figure 2, the effective area of flow path out from the nozzle to the atmosphere becomes larger and then the flow rate out from the nozzle becomes larger. As a result, the back pressure p_n in figure 2 falls down. In one word, if sound is added to the S-P Converter, the head resonates and the back pressure p_n changes (become smaller). In this paper, the change of the back pressure p_n is used to make the SODC-Valve open and close.
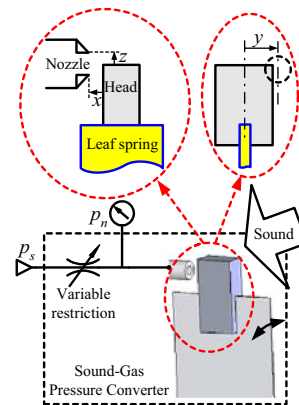
Figure 2 Concept of S-P Converter
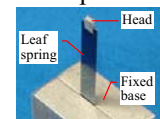
Figure 3 Vibration element

The developed S-P Converter has a resonance frequency of 98Hz. The diameter of the nozzle is 0.5mm, the same with width of the head. The length of the leaf spring is 25mm. The mass of the head is 0.029g. Because the mass is set at the end of the leaf spring, the base mode resonance vibration has larger amplitude and the influence of the higher mode can be neglected.

In order to investigate the vibration characteristics of the vibration element, sound of a specified frequency is added near the vibration element at the atmosphere. As shown in figure 5, when the frequency of the sound is equal to the resonance frequency of 98Hz, the amplitude of the head reaches the maximum of 1.5mm. If the frequency is set apart from 98Hz with over 1Hz, the amplitude becomes half of the maximum. By using this characteristic, several S-P Converters with different resonance frequency can be controlled simultaneously.

SELF-EXCITED VIBRATION

In order to investigate the characteristics of the S-P Converter when supply pressure is added, experiments using circuit shown in figure 2 are conducted. The

434

phenomenon of self-excited vibration arises when the supply pressure is added without any sound. When the supply pressure is raised up to 10~20kPa, self-excited vibration starts even though the sound is not added. Once the self-excited vibration starts, it will not stop until the supply pressure is lowered down to about 0kPa. If measures are not taken to solve the self-excited vibration problem, development of SODC-Valve is impossible.

Two methods are found to prevent the self-excited vibration through trial and error. The first one is introducing the overlap to the head in y direction (i.e. vibration direction) which means that the width of the head is larger than the diameter of the nozzle. The second one is introducing the underlap to the head in z direction (i.e. vertical to vibration direction) which means that the nozzle protrudes from the end of the head. The S-P Converter initially developed is adjusted to be zerolap in y direction which means that the diameter of the nozzle is the same with width of the head in order to obtain a larger effective area change of the nozzle when the head resonates. Because of the self-excited vibration, an overlap in y direction and an underlap in z direction are necessary. In y direction, if width of the head is set with 1.2mm which is larger than the diameter of nozzle 0.5mm, in other words, if overlap of 0.35mm is set on both side of the head as shown in figure 4(b), the self-excited vibration does not arise even though the back pressure is raised up to 100kPa in the experiments. It should be mentioned that the overlap should be adjusted to be the minimum. If the overlap is too large, the change of the effective area of the nozzle will become too small. However, the overlap in y direction is not enough. If the sound or disturbance is added, the self-excited vibration will continue unless the back pressure is lowered down to 0kPa even if the overlap is adjusted to very large.

As regards to z direction, the relative position of the nozzle to the head can be adjusted so that the relationship between the nozzle and the head can be change from overlap to zerolap and underlap as shown in figure 5.

Zerolap   Overlap

(a) y-zerolap   (b) y-overlap

Overlap   Zerolap   Underlap

(c) z-overlap   (d) z-zerolap   (e) z-underlap
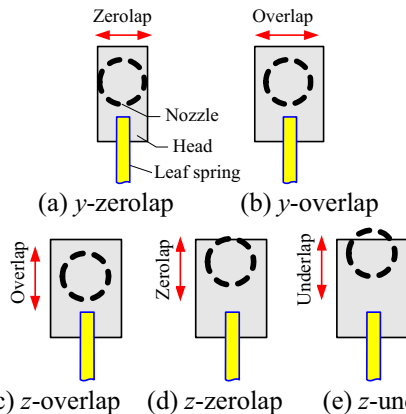
Figure 4 Suppression methods of self-excited vibration
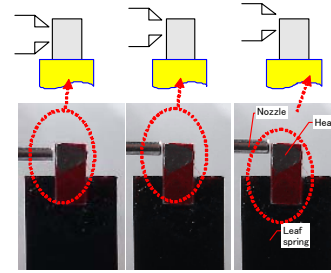
(a) Overlap($z<0$) (b) Zerolap ($z=0$) (c) Underlap ($z>0$)
Figure 5 Photos of relative position of head and nozzle

In case of overlap in z direction as initially adjusted to suppress the leakage, the back pressure falls when the 98Hz sound is added. But the vibration turns into the self-excited vibration even if the sound is stopped. It is interesting that if the nozzle is raised up and reaches the position of underlap, the self-excited vibration stops and again the back pressure jumps up. Under the condition of underlap, the head responses to the 98Hz sound to resonate and stops without any self-excited vibration when the sound is stopped. In one word, the back pressure is controllable by the 98Hz sound.
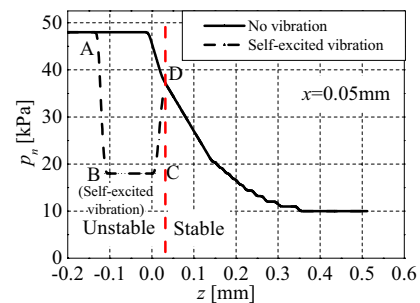
Figure 6 p_n -z characteristic curve
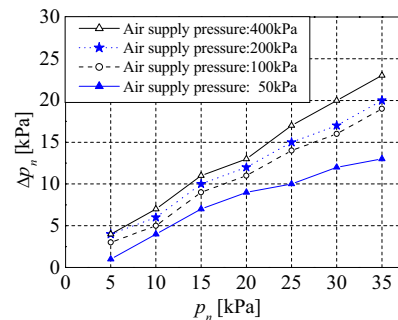
Figure 7 Δp_n of S-P Converter

In order to investigate the best underlap of z direction, experiment is conducted. The vibration of the head is investigated when disturbance (i.e. touching the head) is added or not. The supply pressure is set as 400kPa and the sound is not added. The result is shown in figure 6. The solid line is the result when no disturbance is added. The position of the nozzle is adjusted from overlap to zerolap and underlap. The back pressure falls down from the position of zerolap. The

fall of pressure is due to the increment of the effective area and not due to vibration. On the other hand, the dashline is the result when disturbance is added at the point A. Because at the point A the position of nozzle is overlap, the disturbance triggers the self-excited vibration of the head to start immediately and the back pressure to fall down to B point. If the nozzle is raised continuously, from point C the back pressure jumps up again to reach D where z is 0.3mm (i.e. underlap) and the back pressure is the biggest and the self-excited vibration stops. After point D, the dash line follows the solid line. From the result, it is clear that the position of the nozzle z must be bigger than 0.3mm to ensure that the nozzle is in underlap to suppress the self-excited vibration. On the other hand, it is desired that the underlap of z is set to be as smaller as possible so that change of effective area of nozzle and the back pressure is big. Therefore, z should be adjusted to be as near D point as possible.

Using the S-P Converter as shown in figure 2 with the interval x between nozzle and head adjusted to 0.05mm, overlap on both side of the head in y direction adjusted to 0.35mm and overlap in z direction adjusted to 0.05mm, experiments are conducted. The supply pressure is arranged with 4 conditions and under each condition the back pressure is investigated. In the preparation, the back pressure is tuned using the adjustable orifice shown in Figure 2 without any sound. The change of back pressure before and after the sound of 98Hz is added is shown in figure 7. From the results, it is clear that when the supply pressure is set as 400kPa, the back pressure changes from 35kPa when the head does not resonate to 12kPa when the head resonates. Therefore, it is concluded that the maximum change of back pressure is about 20 kPa in the developed S-P Converter. Absolutely speaking, the change of 20kPa is small, but it is big enough to drive a pilot valve to control an actuator.

PILOT VALVE AND EXPERIMENTS

The developed pilot valve is shown in figure 8. In figure 2, the sound is added to the S-P Converter directly in the air with the sound source placed very close to the head. But in the proposed SODC-Valve, it is required that the sound is conveyed by the supply tube. That means the head in figure 2 must be inserted inside the supply tube. It is clear that the S-P Converter in figure 2 can not be applied directly to a SODC-Valve. This problem is solved by introducing another vibration head. As shown in figure 8(a), the leaf spring stretches to both side of the fixing part with two heads attached at the end to compose two vibration elements. One is called resonance vibration element and the other is called flapped vibration element. Their heads are called resonance head and flapper head. The flapper vibration element is at atmosphere while the resonance vibration element is inserted in the supply tube filled with the sound. The resonance vibration element is adjusted with the vibration direction being along with the sound propagation direction to realize a large resonance vibration amplitude. The resonance vibration of the resonance vibration element is propagated through the leaf spring to the flapper vibration element. The resonance frequencies of the resonance vibration element and flapper vibration element are adjusted to be the same. From figure 8(b), the developed pilot has two parts. The upper part is consisted of flapper vibration element and nozzle, while the lower part is consisted of the resonance vibration element which is inserted into the supply tube with joint.
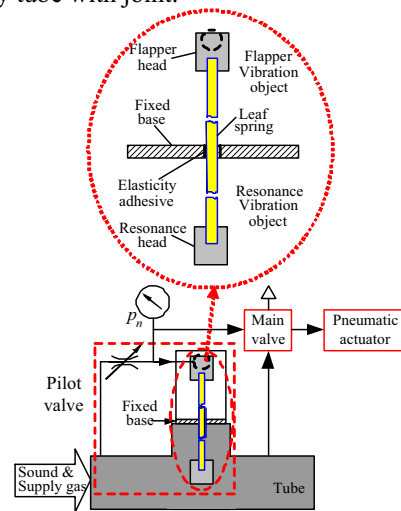
(a) Concept
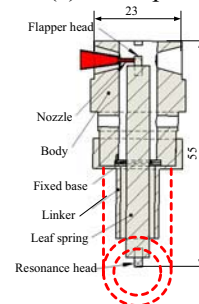
(b) Schematic diagram
Figure 8 Pilot valve

Experiments are conducted to investigate the developed pilot valve using the circuit shown in figure 9. The supply pressure is arranged with 4 conditions and under each condition the back pressure is investigated. Dry-ice Power Cell is used as the power supply. From the results of figure 10, it is clear that when the supply pressure is set as 420kPa, the back pressure has a change of 20 kPa in the developed S-P Converter and is about the same as the results shown in figure 7. By selecting a large area, back pressure change of 20kPa in the pilot valve is able to drive a main valve.
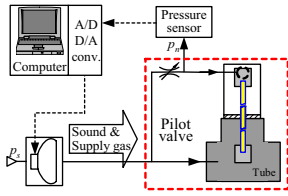
Figure 9 Pilot valve experimental circuit
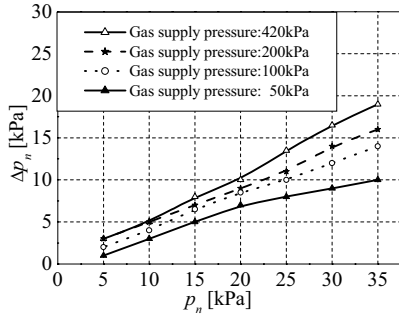
Figure 10 p_n change after pilot valve opens
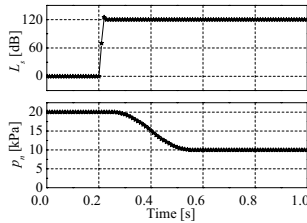
(a) Response of pilot valve turning "ON"
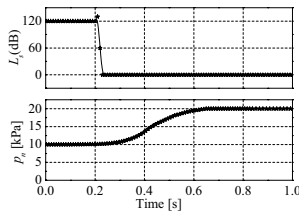
(b) Response of pilot valve turning "OFF"

Figure 11 Step response of pilot valve

The step response of the pilot valve is investigated. From figure 11(a), the time lag of the back pressure is about 200ms, which means the interval from the time sound is added to the time when the back pressure rises to 50% of its maximum value. On the other hand, from figure 11(b), the time lag of the back pressure is 220ms, which means the interval from the time sound is stopped to the time when the back pressure falls to 50% of its maximum value. Two time lags are almost the same.

MAIN VALVE

The pilot pressure is about 20kPa and very small compared with supply pressure. A main valve is developed which can be driven by the 20kPa pilot pressure change. For convenience, a three port main valve is developed in this paper instead of a two port main valve. The schematic of main valve is shown in figure 12 and cross-sectional view is shown in figure 13. The diaphragm is fixed to the poppet so that the pilot pressure can drive the poppet directly. The spring force of the diaphragm is very small and can be neglected. The forces acts on the main valve can be described as the force of pilot pressure, spring force and force of supply pressure. When the pilot valve is OFF, the pilot pressure jumps up to its maximum and the sum of the spring force and the force of pilot pressure becomes bigger than the force of supply pressure. Resultantly, supply pressure port P is closed and port A is opened to the air through port R. When the pilot valve is ON, the pilot pressure falls down to its minimum and the force of supply pressure becomes bigger than the sum of the spring force and the force of pilot pressure. Resultantly, supply pressure port P is opened to port A and port R is closed. The main valve can be controlled by the pilot pressure without any influence of supply pressure.

The room above the diaphragm is the pilot room while the room below the diaphragm is open to the air. The stroke of the main poppet is about 0.5mm. When the O ring attached to the main poppet is pushed down to the valve seat, port A is connected to port R. When the O ring is pushed up to the valve seat, port A is connected to port P.
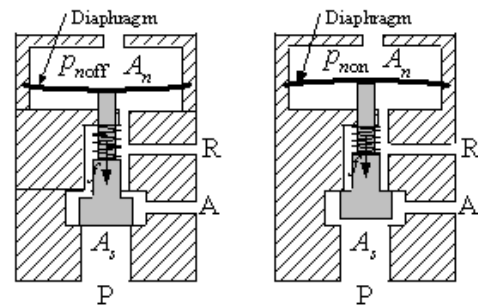
(a) valve OFF   (b) valve ON

Figure 12 Schematic diagram of the main valve
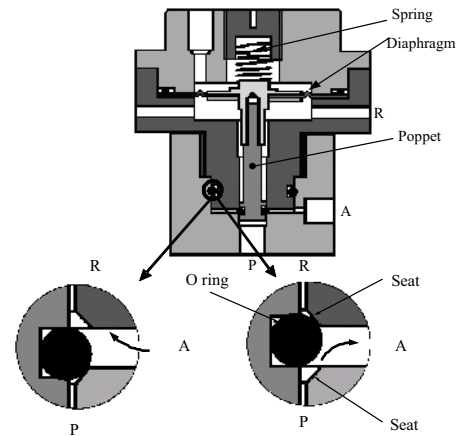
Figure 13 Cross-sectional view of the main valve

SODC VALVE

The SODC valve is shown in figure 14 and is composed of the developed pilot valve and main valve. The goal of this study is to construct a pneumatic multi-degree wearable system. In this study, two SODC valves are developed. The picture of two SDOC valves with resonance frequency of 96Hz and 98Hz are shown in figure 15. Using Dry Ice Power Cell as power supply, wearable actuators developed in previous study and two SODC valves, a novel pneumatic multi-degree wearable system is realized. As shown in figure 16, there is no cord connected to the valves. The actuators used are Tail-Wrist and Fit-band [2].
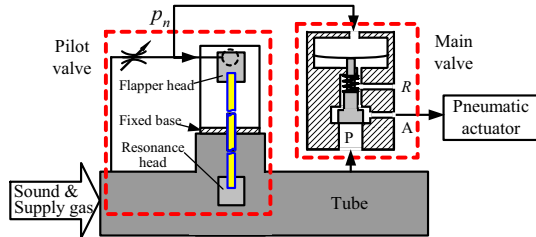
Figure 14 SODC-Valve
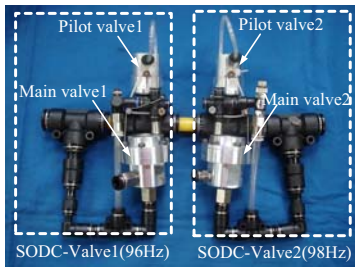
Fig.15 Photo of assembled SODC-Valves
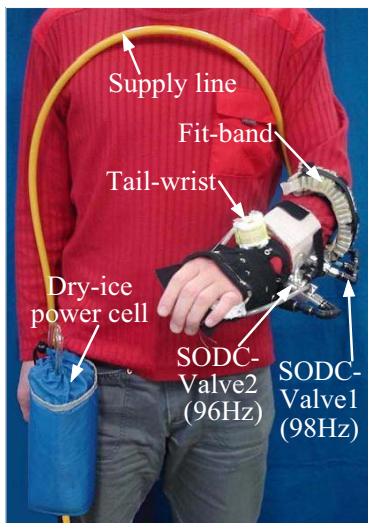
Fig.16 Wearable system driven by SODC-Valves with Dry-ice Power cell
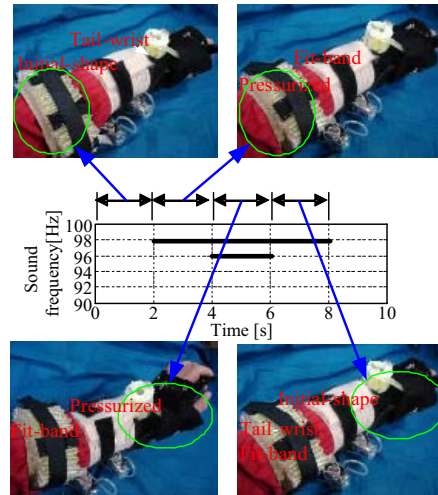
Fig.17 Photos of two wearable actuators driven by SODC valves

In figure 17, the SODC valve with 96 Hz resonance frequency opens from 4s-6s, while the SODC valve with 98 Hz resonance frequency opens from 2s-8s. The two SODC valves can be controlled by sound simultaneously to drive two actuators.

CONCLUSIONS

In this paper, a sound operated directional control valve (SODC-Valve) is proposed which opens and closes in response to the sound of a specific frequency propagated inside the gas supply tube and therefore needs no electric wiring to convey the control signals. By using multi-frequency sound, several valves can be controlled simultaneously and resultantly the pneumatic multi-degree wearable system can be constructed compactly. Experimental results verify that the sound operated directional control valves are feasible and practical in pneumatic multi-degree-of-freedom wearable power assist system.

REFERENCES

1. Yamamoto, K., Ishii, M., Hyodo, K., Yoshimitsu, T. and Matsuo, T. : Development of Power Assisting Suit for Assisting Nurse Labor (Miniaturization of supply system to realize wearable suit), JSME International Journal, Series C, **46**-3, pp.923-930 (2003).
2. Tsukagoshi, H., Kase, S., Kitagawa, A., Fit-band: Development of active installation band with adaption to the human body, JSME Dynamics & Design Conference 2007, pp.289 (2007).
3. Kitagawa, A., Wu, H., Tsukagoshi, H., Park, S.H., Development of a portable pneumatic power source using phase transition at the triple point, Transactions of the Japan Fluid Power System Society, 36-6, pp.158-164(2005).

P1-34

A NEW PNEUMATIC CONTROL SYSTEM

USING MULTIPLEX PNEUMATIC TRANSMISSION

Yasutaka NISHIOKA*, Koichi SUZUMORI*, Takefumi KANDA*, and Shuichi WAKIMOTO*

* Department of Graduate School of Natural Science and Technology
Okayama University
3-1-1 Tsushima-naka, Okayama, Okayama, 700-8530 Japan
(E-mail: yasu@act.sys.okayama-u.ac.jp)

ABSTRACT

The purpose of this research is simplifying and downsizing of pneumatic system consisting of many pneumatic actuators. For this purpose a new method of multiplex pneumatic transmission for multi-pneumatic servo system is proposed. The pneumatic valve for this system has a simple structure consisting of two vibrators supported by springs. The working principle of the valve is based on vibrator resonance caused by multiplex pneumatic vibration in air supply line and this makes the valve work as an ON/OFF valve without electric wire or independent pneumatic tubes. Valve control needs superimposed only an air supply tube for its independent control, making this pneumatic system suitable for the system having many degrees of freedom.

Two prototype valves have been developed to confirm the basic function and adapted to the pneumatic system consisting of two pneumatic cylinders. The prototype valve has been designed based on the result of a dynamic simulation and it was confirmed by basic experiments. In the experiment, the independent control for two pneumatic cylinders with prototype valves has been successfully realized.

KEY WORDS

Actuator, Pneumatic valve, Resonance

INTRODUCTION

A pneumatic actuator has several advantages, which are lightweight, low cost, high compliance, and reliability to humans. However, the system using pneumatic actuators is complicated in general with a compressor, control valves, and air tubes. Researches for downsizing of compressor and control valve have been actively studied [1]-[3]. Solving a lot of control wires to control valves is also studied [4].

The purpose of this research is simplifying pneumatic system having many degrees of freedom. For this purpose we have proposed a new method of multiplex pneumatic transmission for the multi-pneumatic servo system [5]. The pneumatic valve for this system consists of two vibrators and springs. The working principle of the valve is based on vibrator resonance caused by multiplex pneumatic vibration. This valve works as an ON/OFF valve without electric wire but works just through one air supply line. This pneumatic system using the valve realizes independent control of valves with only air tubes. It is effective for the pneumatic system having many degrees of freedom.

The basic working has been confirmed by dynamic simulation and vibration experiment using experimental

model [6]. The experimental model was designed based in the simulation and structure analysis. In this paper, a pneumatic experiment using the experimental model is described.

WORKING

Figure 1 shows the proposed system. This system is configured with multiplex pneumatic transmission, which consists of a PC, and a pressure servo valve. Each proposed valve has a deferent resonant frequency. This valve works as an ON/OFF valve by multiplex pneumatic transmission.

For example, when the actuator 1 is requested to be driven it can be driven by superimposing air vibration of its resonant frequency in the air supply line. The actuator 2 is driven in the same way. When both actuators 1 and 2 will be needed for drive it can be achieved with an air vibration combined with two frequencies.

The representative advantages of this system are follows;

- It can drive many independently actuator without electric wires.
- The structure of the valve is simple.
- This valve in the system can be configured only air tube to actuator.

This system is effective to the system having many degrees of freedom.
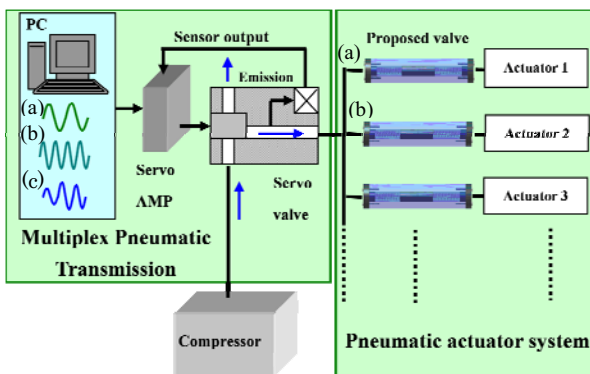
Figure 1 Multiplex pneumatic system

EXPERIMENTS

Valve

Figure 2 shows an outer view of the experimental model for pneumatic valve used in this system. This valve is configured with two vibrators and rubber bellows and linear guide. The rubber bellows is designed using FEM to realize the desired spring constant. The resonant frequency is obtained using the mass and spring constant as shown in Eq. (1).

$$\omega_n = \sqrt{\frac{k}{m}} \qquad (1)$$

Figure 3 shows the working principle of the experimental model. These motions of the vibrators are caused by multiplex pneumatic vibration transmitted from port A. The supply air to the actuator flows through port B to port C. When the driving frequency of pressure from port A is at non-resonance frequency two vibrators move keeping their contact. Thus the pressure from port B is supplied to actuator through port C. When the driving frequency is resonance frequency two vibrators move in different ways to separate. The pressure of Pl_2 from gap between left vibrator and L-shaped angle is increased. The supply pressure to actuator is decreased. In this way model works as an exhaust valve.
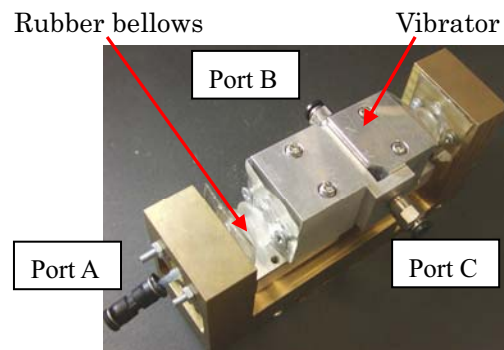
Figure 2 Experimental model
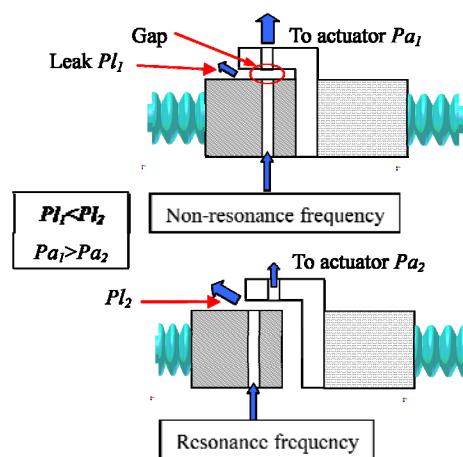
Figure 3 Principle of experimental model

Experimental system

Figure 4 shows the experimental system using two experimental valves. Table 1 shows the parameters of the experimental valves. The real values of resonant frequency are measured through basic experiment.

The experiment is made for the pneumatic system for driving two double-acting cylinders. The supply pressure to double-acting cylinder is about 0.1 [MPa]. Two experiment models have deferent resonant frequency each other. One vibrator in made of stainless steel and the other is made of aluminum. The constant pressure of 50 [kPa] as back forces is supplied to right room of double-acting cylinder.

The input signal to pressure servo system is controlled by a PC and a servo valve. Two experiment models are controlled independently with following four modes;

- ➢ [mode A] for driving cylinder A
- ➢ [mode B] for driving cylinder B
- ➢ [mode C] for non-driving both cylinders
- ➢ [mode D] for driving both cylinders
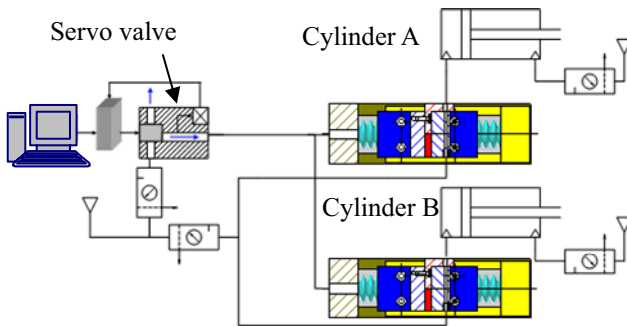
Figure 4 Experiment system

Table 1 Parameters of designed valves

		Valve 1	Valve 2
Vibrator	Material	stainless	aluminum
	Mass	226 [g]	76 [g]
Bellows	Spring constant	0.175 [N/mm]	
Resonance frequency	Theoretical value	4.4 [Hz]	7.6 [Hz]
	Real value	6.2 [Hz]	11.8 [Hz]

Results

Figures 5 show experimental results for driving two pneumatic cylinders. Equations (2), (3), and (4) show input pneumatic signals and motions of cylinders for modes A, B, and D respectively.

$$f_A = 7.0 \times \sin(2\pi \times 6.4 \times t) - 4.0 \tag{2}$$

$$f_B = 7.0 \times \sin(2\pi \times 8.2 \times t) - 4.0 \tag{3}$$

$$f_D = 3.5 \times \{\sin(2\pi \times 8.2 \times t) + \sin(2\pi \times 6.4 \times t)\} - 3.0 \tag{4}$$

The experiment shows that the system works successfully: the cylinder A works independently for modes A and B, as shown in Figures 5 (a) and (b). Both

cylinders work at the same time as shown in Figure 5 (c) for mode D. It shows a great potential of new pneumatic control system.

From the experiment, the response of pneumatic cylinder was confirmed each. The response speed is deferent for mode A and mode B as found in Figure 5 (c). This results from deference of vibration amplitude of the valves.
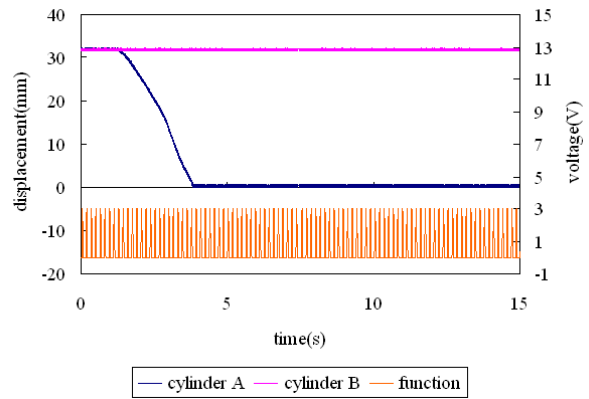
(a) mode A
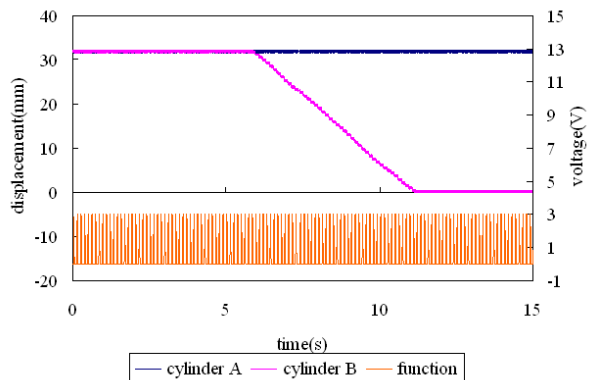
(b) mode B
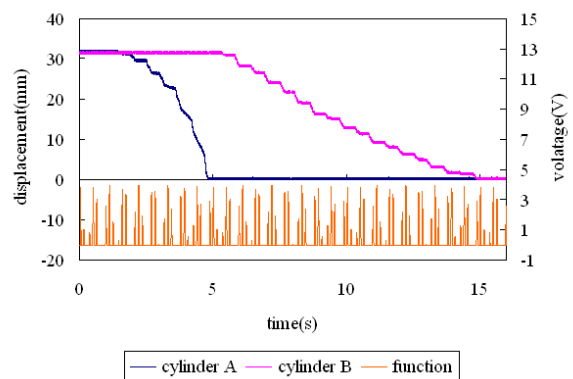
(c) mode D

Figures 5 Experimental results

CONCLUSION

A new method of multiplex -pneumatic transmission has been proposed. This method realized great simplification of pneumatic system consisting of many actuators. A control valve for this pneumatic system is driven only through an air tube without electric wires. In this paper, experimental models was developed and adapted to pneumatic system. In this experiment, the independent driving of two pneumatic cylinders is realized. The principle of the proposed system was shown in this experiment.

REFERENCES

1. A.KITAGAWA, H.WU, H.TSUKAGOSHI, "Sung-Hwan PARK, Development of a Portable Pneumatic Power Source Using Phase Transition at the Triple Point", *Transactions of the Japan Fluid Power system Society*, Vol.36, No.6, (2005), pp.158-164

2. S.UEHARA, S.HIRAI, "Development of Unconstrained Vibrational Pneumatic Valves", *SICE System Integration Division Annual Conference*(2005), pp.817-818

3. S.YUM, K.LEE, H.KIM, H.So, "Development of the pneumatic valve with bimorph type PZT actuator", *Materials Chemistry and Physics* Vol.97, (2006),pp.1-4

4. M.KOSUGI, "Present state of field network about pneumatic devices and technologies wiring-saving (in japanese)", *Transactions of the Japan Fluid Power system Society,* Vol.38, No.3, (2007), pp.153-156

5. Y.NISHIOKA, K.SUZUMORI, T.KANDA, "Pneumatic valve operated multiplex pneumatic transmission", *JSME-KSME Joint International Conference on Manufacturing, Machine Design and Tribology (ICMDT2007)*, B18

6. Y.NISHIOKA, K.SUZUMORI, T.KANDA, S.WAKIMOTO, " Pneumatic Actuator System Operated by Multiplex Pneumatic Transmission (2nd report; application for a pneumatic valve using two pneumatic cylinders) ", *Conference of the Japan Fluid Power system Society,* 31,(2007), pp.109-111

P1-35

REPEATED POSITIONING OF A LONG STROKE PNEUMATIC CYLINDER USING PROXIMITY SWITCHES

Mohammad TAUFIQ MUSTAFFA*, Hidetoshi OHUCHI* and Tasuku OSADA*

* Interdisciplinary Graduate School of Medical and Engineering
University of Yamanashi
4-3-11 Takeda, Kofu, Yamanashi, 400-8511 Japan
(E-mail: g07mm035@yamanashi.ac.jp, ohuchi@yamanashi.ac.jp)

ABSTRACT

This paper deals with a technique of repeated positioning of a long stroke pneumatic cylinder. This system is suitable for a long stroke cylinder when the desired intermediate stop positions are fixed and the same operation may be repeated as in automatic production lines. The basic control algorism is a sequential on-off action of the air valves. For one desired position, three proximity switches are installed to detect the slider passing as well as its velocity. The main experimental result with a rod-less cylinder of 1000 mm stroke is that the control accuracy converged quickly within +/-0.2mm by a learning function.

KEY WORDS

Pneumatic, Cylinder, Positioning, Proximity switch, Learning

INTRODUCTION

This paper deals with a technique of repeated positioning of a long stroke pneumatic cylinder. This system is suitable for a long stroke cylinder when the desired intermediate stop positions are fixed and the same operation may be repeated as in automatic production lines.

The design of an air servo system is not intended. Without constructing a feedback loop, it is possible to maintain the simplicity of the air positioning system.

The basic control algorism is a sequential on-off action of directional air valves. There is a fact that a clear relationship exists between the slider velocity and its braking distance with a strong braking [1]. For one desired position, three proximity switches are installed to detect the slider passing as well as its velocity. After passing the first switch the slider is weakly decelerated, and after passing the second switch it is strongly decelerated. The third switch is installed to detect the final positioning result which is used in the next run by a learning scheme [2]. Another switch is also installed to confirm the slider return to the starting point.

As a matter of course, the positioning accuracy depends strongly on the frictional condition. There is another factor such as the load or the setting direction of the cylinder. In the experiment, the cylinder was set in vertical direction to reveal the effect of the slider load.

A high positioning accuracy can not be expected without a feedback loop. Our final goal is that the stop position converges to the desired region in several operations and that the accuracy can be kept after that.

Figure 1 Experimental circuit

Figure 3 Optimum velocity to start applying the strong braking
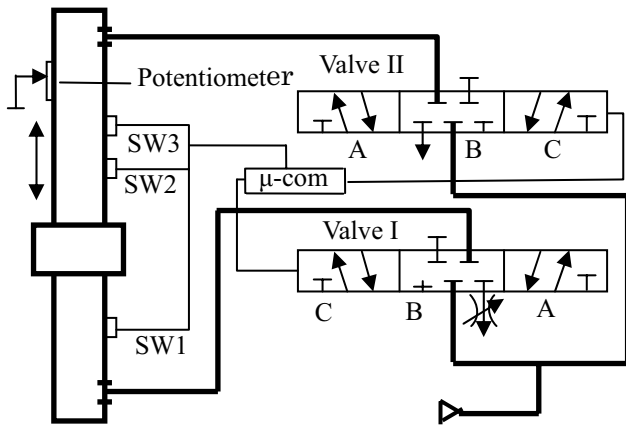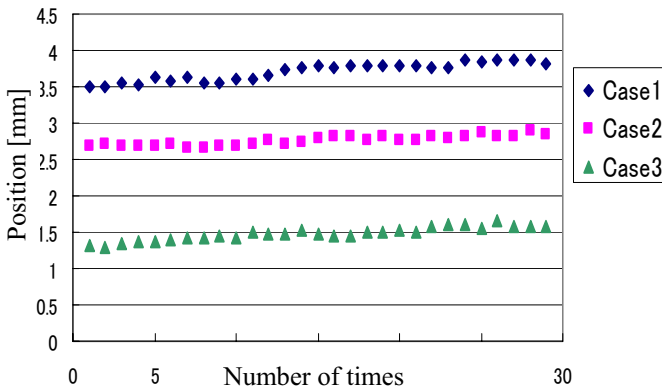
Figure 2 Deviation of the stop position

EXPERIMENTAL APPARATUS AND THE POSITIONING METHOD

Pneumatic circuit

The outline of experimental apparatus is shown in Fig. 1. The cylinder is installed vertically on the wall in a laboratory. The cylinder is of a rod less magnet type and has a stroke of 1000mm in length and a bore of 40mm in diameter.

Four proximity switches are installed. SW1, SW2, SW3 are used for motion control, and SW0 is used only for detecting the return of the slider to the starting point (not shown in the figure).

For the cylinder positioning, we propose a two-stage braking method, which will be described later in detail. In this method, a weak braking and a strong braking are applied in sequence.

At the first stage, weak braking is applied, and strong braking is applied in the second stage. To apply the

weak braking, the valve I is kept on connecting to supply port and only the valve II is closed. To apply strong braking, the valve I is still kept on connecting to the supply port and the valve II is switched to the supply port.

To perform this sequence smoothly, two 3-position 5-port valves are utilized for changing the air flow.

Fluctuations of the stop position

It is a necessary condition for our method that fluctuations of stop position are small even when the two-stage positioning is not applied.

Fig.2 shows the result of the slider stop position in a case that the strong braking was applied simultaneously when it passed through the SW2. The cases of 1, 2, 3 mean that the SW2 passage velocity was changed by the timing of weak braking after passing of the SW1.

The experiments were done continuously 30 times respectively. This figure indicates that during the prolonged operations, the fluctuation in every successive two trials is only about 0.1mm. This amount is small and is not a problem because it can be corrected during the operation. Therefore, the possibility to continuing the operation with maintaining accuracy was confirmed.

Furthermore, Fig.3 shows the relationship between the velocity that the strong braking was started to apply and the deviation of the braking distance. The axis of ordinate is not showing the stop position but the deviation width of the stop positions. One dot indicates deviation width in twenty times operation conducted.

In this experiment, the SW2 passage velocity was also changed due to the weak braking applied at the SW1.

There is an optimal velocity when the braking should be started to apply, and it was about 100mm/s in this case.

Even if it loaded a mass of 3kg, there is no difference in the optimum value.

When the same cylinder was installed in horizontal direction, the value showed 220 - 250 mm/s [1,2].
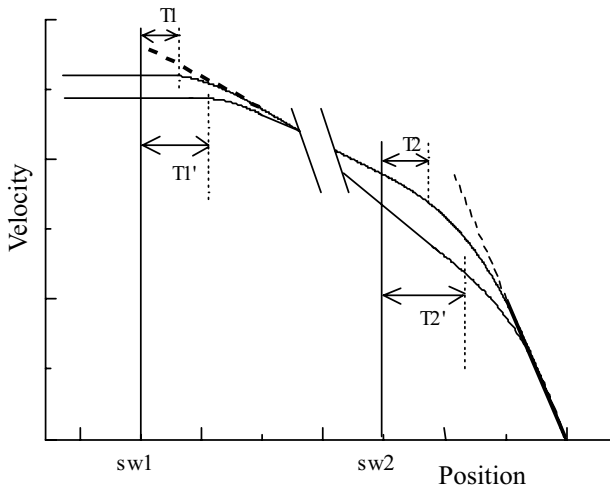
Figure 4 Two-stage braking
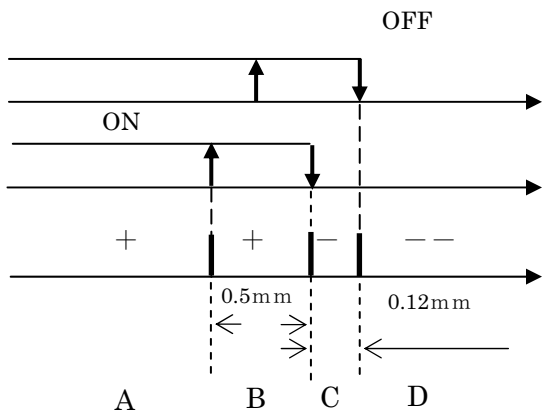
Figure 5 Shifting of the sensing position

Figure 6 Convergence of the stop position

and on, the sensing field is divided into 4 regions, A, B, C, D. The boundary of B and C in the figure was determined as the target position.

In each operation, the detected data are used to update the control parameters of the timer T2 by a learning algorism. In an ideal condition, the slider stops in very narrow region near the boundary of B and C, and every stop position falls into B and C region alternately.

EXPERIMENTS OF REPEATED POSITIONING

Setting of timer T1 and T2
The equations to obtain the timer length $T1$ and $T2$ are as follows;

$$T1 = a1 \cdot (Count\_1 - b1) + c1 \qquad (1)$$
$$T2 = a2 \cdot (Count\_1 - b2) + c2 + \Delta y \qquad (2)$$

where $a1, b1, c1, a2, b2, c2$ are constants, and $Count\_1, Count\_2$ are the counted numbers in the program for the passage time on the SW1 and the SW2, respectively, and Δy is a quantity to be modified for the next operation.

Although $T1$ and $T2$ need to be changed when the cylinder is modified from the horizontal to vertical direction or when another cylinder is used, the minimum change was tried; only the parameter $c2$ was readjusted from our experiences. When the parameter $c2$ was not changed, the controller could not deal with new direction of the cylinder. The value of $c2$ was estimated by preliminary experiments.

For the check of the modifying process, the relation between the stop position and the timer length $T2$ was recorded. The feature of convergence of the stop position is shown in Fig.6. It converged after about 20 times using the data of the position information on the SW3, as well as $Count\_1$ and $Count\_2$.

Positioning method
The outline of the two-stage braking method is shown in Fig. 4. At first, the timer length $T1$ to start applying the weak braking is determined based on the passage velocity on the SW1, so that the slider velocity might become the above-mentioned optimal value at the SW2. Next, the timer length $T2$ to start applying the strong braking is calculated depending on the detected passage velocity on the SW2 so as to stop the slider at the desired position.

Fig. 5 explains the role of the SW3 equipped in order to check the final stop position. It is impossible to detect the stop position in accuracy of 0.1mm because sensing width of an ordinary proximity switch is 3-4mm. Therefore, a small coil was added to the side of the switch to affect the neighboring magnetic field. The sensing position was shifted about 0.12mm as shown in Fig.5. The hysteresis width of the sensor was also used. The hysteresis and sensing positions of the tested proximity switch when the coil current is turned off and on are illustrated in Fig.5. By turning the coil current off

Figure 7 Convergence of the timer length *T*2
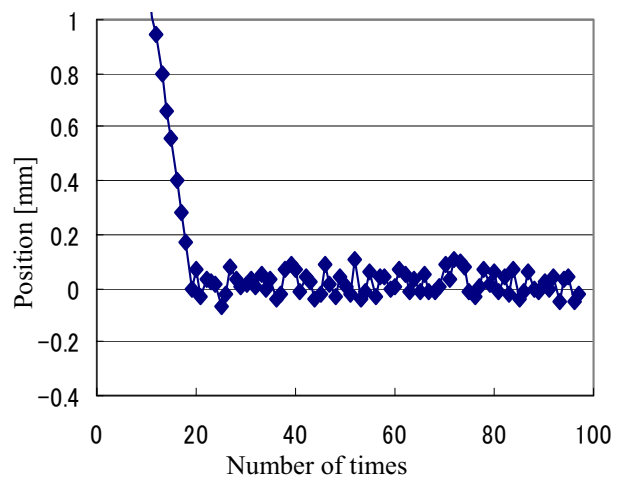
Figure 9 Adjustment of $a2$ and Δy ($a2$=4, Δy=32)
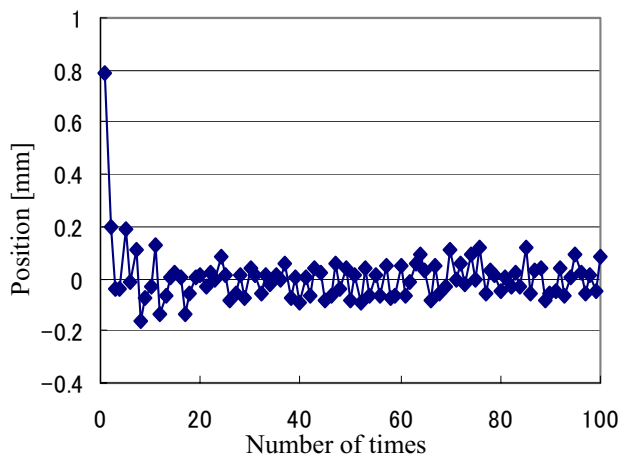
Figure 8 Adjustment of $a2$ and Δy ($a2$=3, Δy=48)
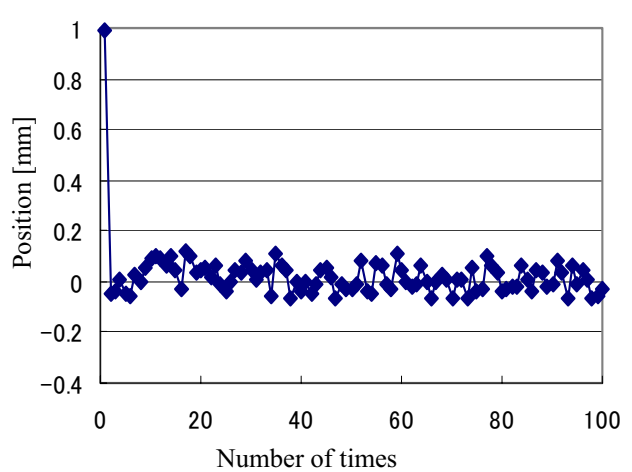
Figure 10 Convergence of the stop position with loading a mass of 3kg

Fig. 7 shows that *T*2 converged after about 50 times using the position information on the SW3. We will discuss later about $a2$ and Δy. There is no necessity to change *b*1 and *b*2 because they are only used in checking if the *Count*_1 or *Count*_2 are too short.

Fine Tuning of Timer T2

Fine tuning of the timer *T*2 rather than *T*1 leads to the improvement in the positioning accuracy. It is because the distance between the SW3 and the stop position is as near as about 30mm. Since approximate values of $a2$ and Δy in equation (1) have been also obtained from preliminary experiments, here we will examine about the constant $a2$. During the usual operation, the value of $a2$ is fixed, while the value of Δy is added or subtracted in every operation.

Fig.8 and Fig.9 are the results of comparing the influence on the values of $a2$ and Δy.

Good results were obtained with the combination of $a2$= 3; Δy=48, or $a2$=4; Δy=32. They were conducted with no load.

When the slider was loaded with a mass of 3kg and the parameters was $a2$=4 and Δy=32, accurate positioning was also good as shown in Fig.10.

REDUCTION OF INITIAL DEVIATION

In this positioning method, the purpose to stop at a target position accurately from the beginning of operation is not expected, and we are satisfied if stop position can converge to the target position after several operations.

However, the less number of operations to converge is the better. Because of it, a means to reduce the initial deviation should be considered.
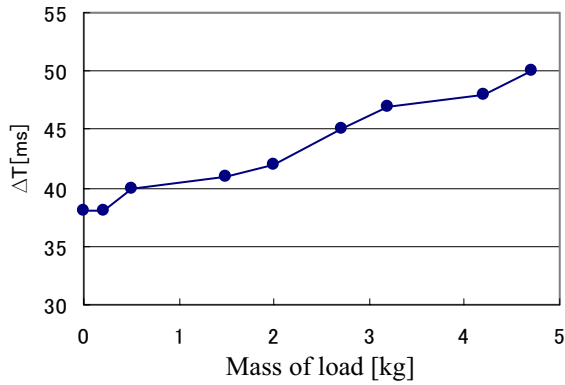
Figure 11 Relation between mass of load and SW2 secession time
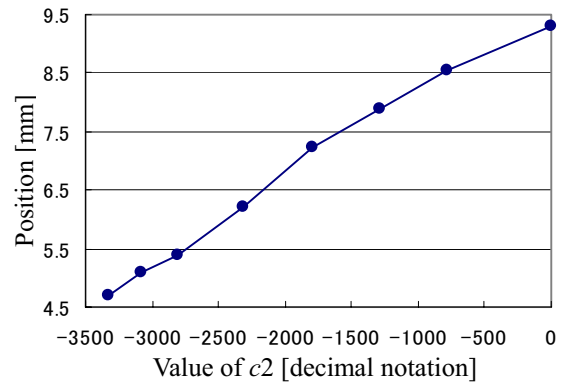
Figure 13 Relation between $c2$ and the stop position
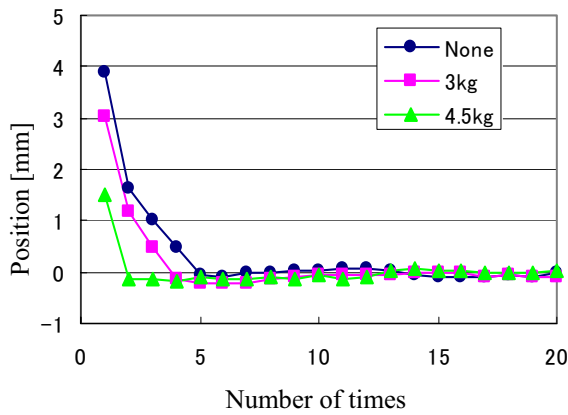
Figure 12 Effects of loaded mass on the stop position

Figure 14 Adjustment of $c2$ with no load

Since the initial deviation is largely caused by the value of $c2$, an automatic adjustment of $c2$ should bring a good result.

SW0 secession time and stop position
As an information factor to be defined, there is a time length between the moments when the slider starts to move upward and when it secedes from the sensing range of SW0. ΔT is determined as this time length. Fig.11 shows the measured ΔT for various mass of loads. Acceleration will take longer time due to the increasing of mass of load. As a result, ΔT becomes larger.

By the difference of magnitude of load the initial stop position was changed as shown in Fig.12. It was predicted that the stop position will be ahead of the target position due to inertia but the result was opposite. This could be explained that the slider velocity became slower caused by the increasing load. After the second time, the stop position converged by this $\Delta T : c2$ adjustment scheme.

Adjustment of T2 by SW0 secession time
The cause of deviation cannot be specified only by the value of ΔT. The change factors are not only the load but also the supply pressure, and they effect in opposite

results on the stop position. In the following, the supply pressure is assumed to be known and a scheme will be investigated to rectify the initial deviation owing to the change of load.

Fig.13 shows the observed result of the initial stop positions. This was obtained by repeated experiments when the value of $c2$ in $T2$ was varied, and only each first positioning was measured and plotted.

Here, using Fig.11 and Fig.13, we consider the approximate first-order equation relating ΔT and $c2$. Our attempt is to adjust $c2$ using ΔT only at the first operation. After the second operation, the stop position will converge by modifying $T2$ with Δy.

Fig.14 indicates the effect of $c2$ adjustment with no load condition. In the figure, "Manual" means that $c2$ was adjusted from experience, and "Self-adjustment" means that it was adjusted automatically using the first value of ΔT. On the other hand, "Fixed" means that $c2$ was set without consideration of the operating condition. Although there is still deviation at the first time even when using the self adjustment, the positioning was improved in number of times to converge as compared to Fig.6-Fig.10.
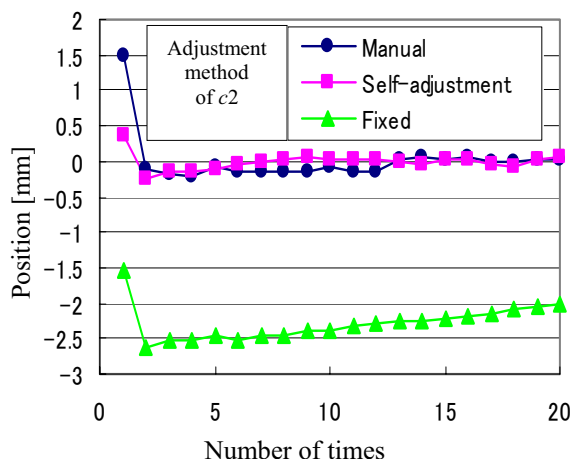
Figure 15 Adjustment of $c2$ with a mass-load of 4kg

Figure 16 Effect of the self-adjustment of $c2$

Fig.15 shows the positioning results when the load was increased to 4.5kg. With the fixed value of $c2$, the initial stop position deviated far away from the desired position. After that, a great number of times were needed to recover to the desired position.

By using "self-adjustment of $c2$", the initial deviation became smaller regardless of the load. After the second operation, fairly good convergence was achieved.

Fig.16 demonstrates the effect of "self-adjustment of $c2$", where the magnitude of load has not been input into the program. Because vertical axes in figures are in different scale, there are difficulties in comparing with others. Nevertheless it can be seen that the positioning accuracy was sufficiently maintained within +/-0.2mm.

CONCLUSIONS

The experimental results on the repeated positioning of a long stroke pneumatic cylinder using proximity switches are summarized as follows.

1) The cylinder was installed in the vertical direction and the positioning accuracy by the existence of load was investigated. With the cylinder stroke of 1000mm, the slider could stop enough in the range of +/-0.2mm, and the accuracy has been maintained also in the following prolonged operation.

2) The timing which finally applies strong braking is the most important, and it turned out that what is necessary is just to perform the timer adjustment according to the operating conditions such as the slider load.

3) The technique of decreasing the initial deviation based on the secession time of the switch installed in the starting point is expected to have sufficient effect when other conditions, for example, the supply pressure, are constant.

Our future work is to improve the system performance to keep a sufficient accuracy from the first operation by automatically adjusting the control timer according to the change of conditions.

ACKNOWLEDGMENTS

REFERENCES

1. Ohuchi, H., Osada, T. and Asai, Y., Positioning of a Pneumatic Cylinder Using Sensor Switches, Proceedings of the fourth International Symposium on Fluid Power Transmission and Control, ISFP2003, pp.374-379.
2. Ohuchi, H., Suzuki, Y. and Osada, T., Repeated Positioning of a Pneumatic Cylinder Using Three Proximity Switches, Proceedings of the ninth International Symposium on Fluid Control, Measurement and Visualization, FLUCOME2007, CD-223.

P1-36

PRESSURE CONTROL CHARACTERISTICS OF ELECTRO-PNEUMATIC REGULATOR WITH TWO MULTILAYERED PZT VALVES

So-Nam Yun*, Young-Bog Ham*, Jung-Ho Park*, Deok-Yong Ham* and Il-Young Lee**

* Korea Institute of Machinery and Materials(KIMM)

104 Shinsung-Rho, Yuseong-Gu, Daejeon, 305-343 KOREA

(E-mail: ysn688@kimm.re.kr)

** Department of Mechanical Engineering, College of Engineering, Pukyung National University

599-1, Daeyeon 3-dong, Nam-gu, Busan, 608-737 Korea

ABSTRACT

This paper presents pressure control method using the electro-pneumatic regulator with two multilayered PZT valves. An electro-pneumatic regulator is a type of pressure control valve that is a combination of a poppet valve for main pressure control, two multilayered PZT valves for pilot pressure control, a microprocessor with a feedback controller and a pressure sensor. The benefits of bender type PZT actuator are faster response times, low energy consumption, and the ability to be used in hazardous environments and field bus systems. Solenoid actuator for electro-pneumatic regulator is widely used but this actuator has a high power consumption characteristics. So PZT actuator is required for the energy saving.

In this study, a multilayered bender type PZT actuator of 27.0 mm(L)×9.0 mm(W)×0.8 (mm) with a constant of 220e-12 m/V and 20 sheets of PZT thin film was fabricated and experimented. The experiments for On-Off control and PID-PWM control of the electro-pneumatic regulator were operated under the input condition of 0.5 MPa. From the experiments, the performance characteristics of the fabricated electro-pneumatic regulator were evaluated. A new control method for precise proportional pressure control using the electro-pneumatic regulator with two PZT valves was suggested. Using this suggested model, all possible operating conditions were analyzed.

KEY WORDS

electro-pneumatic regulator, pressure control, PZT actuator, microvalve, PID-PWM control

INTRODUCTION

The benefits of the pneumatic valve with bimorph type piezoelectric actuator are faster response times, low energy consumption, and the ability to be used in hazardous environments and field bus systems [1]. However, the PZT actuator has hysteresis nonlinearity due to the ferroelectric characteristics of the PZT elements [2, 3]. This causes problems in the pressure control characteristics and deteriorates the performance of the system [4, 5]. In order to overcome the abovementioned problem, the methods of a PZT actuator performance improvement and a electro-pneumatic regulator(E-P regulator) using two PZT microvalves have been studied[6, 7].

In this study, a multilayered bender type PZT actuator of 27.0mm(L)×9.0mm(W)×0.8mm(t) with a constant of 220e-12m/V and 20 sheets of PZT thin film was fabricated and experimented. The maximum operating force of 0.35N and maximum displacement of 80 μm by input condition of 40V were achieved from the fabricated PZT actuator. The rising and the falling time constant of this actuator under the input pressure of

0.5MPa were 0.29s and 0.19s respectively. The experiments for On-off control and PID-PWM control of the E-P regulator were operated under the input condition of 0.5MPa. From the experiments, the performance characteristics of the fabricated E-P regulator were evaluated. The pressure hysteresis of ±2.5% and the time constant of 150ms under the flow input condition of 200lpm were measured through the manufactured experimental setup and it was confirmed that the proposed mechanism has good control characteristics to the response sensitivity and hysteresis.

STRUCTURE AND OPERATING PRINCIPAL OF THE ELECTRO-PNEUMATIC REGULATOR

Fig.1 shows the control flow diagram of the developed E-P regulator. The developed product is a pressure control valve that is a combination of a main poppet valve, two PZT microvalves, a microprocessor and a pressure sensor with a built-in feedback function. The open area of the poppet type output valve is controlled by two PZT microvalves. There is a built-in diaphragm device in the poppet type output valve to receive the pilot pressure. The two PZT microvalves have a multilayered bender type PZT actuator. It is operated in an alternating way by means of PWM signals generated by the controller. A microprocessor is embedded in the controller, which calculates input signals and signals from the pressure sensor in real time. The difference values are then sent to the two PZT microvalves respectively and main output pressure is controlled. The display device turns a voltage into a pressure for a user to easily check the controlled pressure of the system. The pressure sensor is installed on the output unit of the output valve and plays the eventual role of transmitting the pressure information to the controller.

DESIGN AND MANUFACTURING

Fig. 2 shows the appearance and inner structure of a PZT actuator designed to use for a pilot valve. Fig. 3 shows the displacement results, which were calculated using Atila Software. Fig. 4 shows the manufactured PZT actuator. In this study, the manufactured PZT actuator has a 20-layered structure, dimensions of 27.0mm(L)×9.0mm(W) ×0.8mm(t) with a constant of

DESIGN AND MANUFACTURING

220e-12m/V. Fig. 5 indicates the inner structure and assembled appearance of the microvalve using the designed and manufactured PZT actuator. As mentioned previously, two microvalves are used as pilot valves for supply and delivery, respectively. Fig. 6 shows the structure view of the manufactured main body.
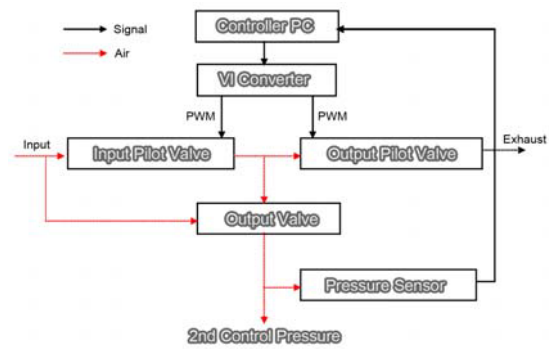
Figure 1 Control flow E-P regulator
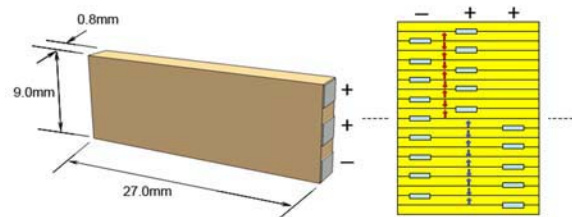
Figure 2 Multilayered bender type PZT actuator
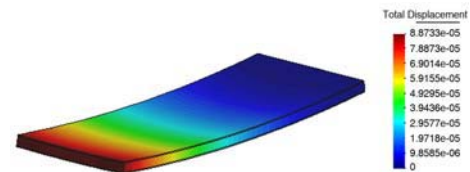
Figure 3 Displacement analysis result
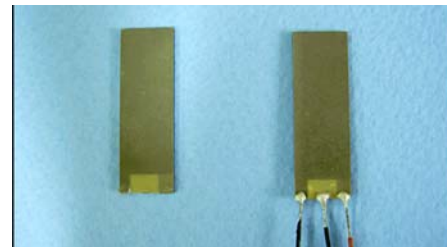
Figure 4 Photo view of manufactured PZT actuator

Figure 5 Photo view of PZT microvalve

450
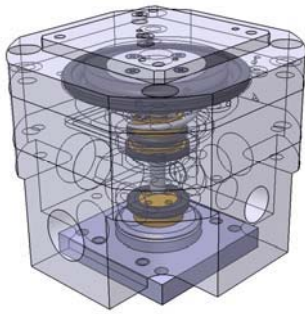
Figure 6 Structure view of main body
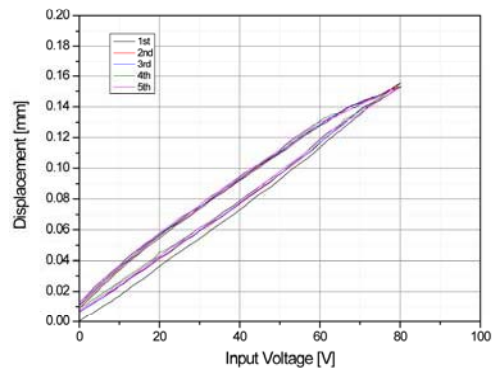
Figure 7 Displacement results of PZT actuator

PERFORMANCE TEST RESULTS

Fig. 7 indicates the test results of the displacement characteristics of the designed and manufactured multilayered bender type PZT actuator. From the results we can get that more than 150 μm of displacement was observed at 80V. In addition, in terms of force characteristics it is verified to be used at a working pressure without any problems. Fig. 8 shows the manufactured experimental setup in order to evaluate the performance of the developed regulator. The developed regulator was compared with the conventional solenoid type, and a control technique to improve the performance of the regulator itself was studied. Tests were performed in three different conditions; one with On/Off control only, another with PID-PWM control, and the other with PID-PWM-Saturation function control. The test conditions were as follows: pressure of 0.4[MPa], sampling time of 0.001[s], PWM signal frequency of 20[Hz], step signal period of 1[s](On)~8[s](OFF), control reference signal of 0[V]~4[V]~0[V], PID gain of k_p=1.1, k_i=0.001 and k_d=0.001. For the data acquisition equipment and software, NI-6062E of NI and Simulink14 of Matlab were used respectively to measure experimental data.

Fig. 9 indicates the Simulink block diagrams for the experiment with PID-PWM control, and PID-PWM-Saturation function control. Here, In the case of (a), the final control signal is turned from a PID control signal into a PWM signal. In the case of (b), the control method is identical to the case of (a), and the system is run smoothly by providing an arbitrary control limit.

Fig. 10 shows the experimental results of applying a PID-PWM control technique to the solenoid method and the PZT one, respectively. PID gain was not optimized, and an identical gain is applied to both regulators. The results of the PZT method were the same as in the solenoid method.

Figure 8 Experimental setup for E-P regulator
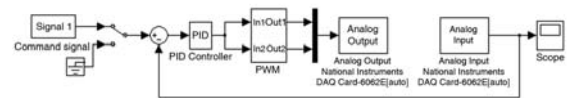
a) PID-PWM control block
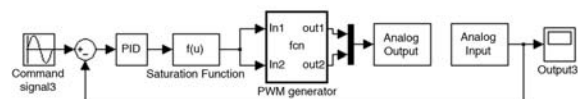
b) PID-PWM-saturation function control block

Figure 9 Pressure control block using Simulink

Fig. 11 indicates the results of the application of the saturating function to the conventional PWM control method in order to improve the hysteresis characteristics of a PZT type regulator. When k=1, linearity improve, but hysteresis deteriorates, while when k=2, both linearity and hysteresis improve. The developed controller makes it possible to adjust this value, depending on the performance of the system.
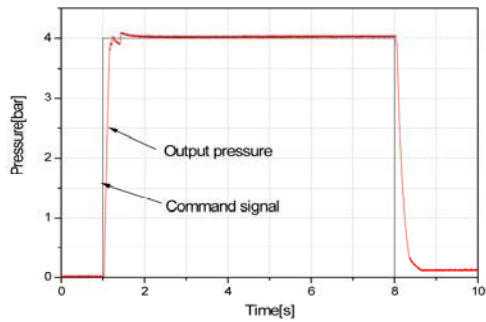
a) solenoid microvalve
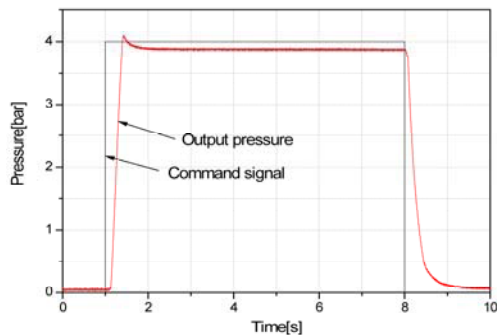
b) PZT microvalve

Figure 10 Pressure control results using PID-PWM method
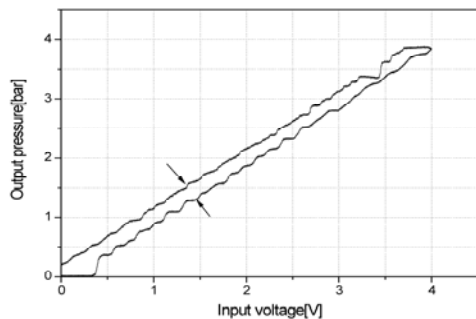
a) Saturation function k = 1
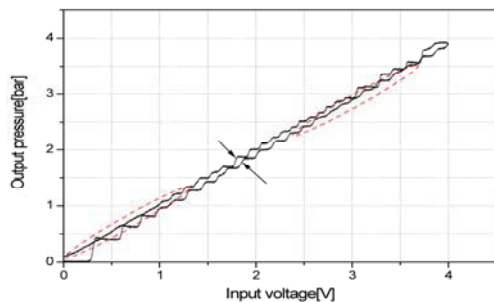
b) Saturation function k = 2

Figure 11 Pressure hysteresis results using PID-PWM-Saturation function method

CONCLUSION

The developed regulator can be used in a wide range of fields, such as semiconductor manufacture, automobile, automation production line, package line, field bus and solar heat energy system. In terms of energy efficiency, it has numerous good characteristics, and for this reason we can anticipate that there will be very high demand for this product, and it will be eventually contribute to energy savings.

However, there are a couple of problems to be solved before it is able to replace the conventional solenoid actuator.

First, the stability of the PZT actuator needs to be ensured. To run at a low voltage and have large displacement and high drivability, a few μm thin film PZT and scores of multilayered process are needed. To achieve this, laminate, polarization and cutting techniques are of great importance, and they should be first solved in order to obtain stability of the PZT actuator.

Second, the PZT actuator is driven at a higher voltage than conventional solenoid actuators. The PZT actuator has condenser characteristics, and in order improve response characteristics, a discharge technique is needed.

Third, durability and reliability also need to be secured. The weakest point of a PZT actuator, which is its brittleness, must be improved, and performance must be raised to a high level of reliability, to the point that there are no problems even after tens of thousands of repetitive operations are performed.

REFERENCES

1. Lou Nohos, NCFP 102-6.7, 2002, pp.179-181.
2. M. Weinmann, M. Muth, M. Giousouf, C. Hanisch and P. Post, State of the art in pneumatic microvalves, Actuator 2002-B 1.0, 2002, pp.217-222.
3. M. Weinmann, A. J. Schmid, M. Fuss, Piezoelectric pneumatic valves, Actuator 2006-A 5.2 ,2006, pp.181-184.
4. P. Mandurino, P.M. Weaver, Electronic domestic gas valve proportionally controlled using piezo actuators, Actuator 2004-A 4.7, 2004, pp.152-155.
5. Hubertus Murrenhoff, Innovative designs and control circuits for proportional valves, NCFP 102-27.2/SAE OH 2002-01-1458, 2002, pp.691-701.
6. So-Nam Yun, Kyung-Woo Lee, Hong-Hee Kim and Hyung-Jong So, Development of the pneumatic valve with bimorph type piezoelectric actuator, Materials chemistry and physics, 2006, pp.1-4.
7. So-Nam Yun, Young-Bog Ham, Jung-Ho Park, Woo-Seok Seo and Kyung-Woo Lee, Electro-pneumatic regulator strategy using two PZT actuator, ATEM'07, 2007, pp. 208.

P1-37

CONSTANT GAP AND MINIMUM ENERGY SUPPLY CONTROL FOR A PROPORTIONAL PNEUMATIC FLOATING VACUUM PAD

Jyh-Chyang Renn *, Chin-Yi Chen ** and Chia-Hua Lu **

* Professor
** Graduate student
Department of Mechanical Engineering
National Yunlin University of Science and Technology
No. 123, University Road Sec. 3, Douliou, 640 Yunlin, Taiwan, R.O.C.
Tel: +886-5-5342601 ext. 4112, 4185
Fax: +886-5-5312062
（E-mail: rennjc@yuntech.edu.tw）

ABSTRACT

In this paper, a new proportional pneumatic floating vacuum pad is developed and constructed. There are two features concerning this new vacuum pad. The first one is the introduced proportional solenoid, which enables the continuously variable control of the suction force output. In addition, the floating mechanism design between the vacuum pad and work-piece is the second feature, which is more preferable in real industries because it can protect the surface of the work-piece from scratching or other damages. Moreover, two control schemes are also proposed in this paper. The first one is the gap control. A pre-set constant gap is input to the controller as the command input which further drives the proportional solenoid to maintain a steady-state gap between the vacuum pad and work-piece. In the second control approach, the gap between the vacuum pad and work-piece is kept as large as possible to minimize the energy consumption. Both control schemes are successfully implemented in this study. It is expected that the newly developed prototype with two different control schemes may find some real applications in the future.

KEY WORDS

Vacuum Pad, Gap Control, Proportional Solenoid, Floating, Vacuum

NOMENCLATURE

$u(k)$: actuating signal
$\Delta u(k)$: actuating signal change
$e(k)$: error signal
K_P : gain of the proportional controller
K_I : gain of the integral controller

K_D : gain of the derivative controller
T_s : sampling time
$V(k)$: velocity signal at kth instant of sampling
$X(k)$: gap signal at kth instant of sampling
$X(k-4)$: gap signal at (k-4)th instant of sampling

INTRODUCTION

Nowadays, applications of pneumatic vacuum pad may be found in many different engineering fields, especially in the field of automatic conveyer system, automatic assembly line, semiconductor industry as well as silicon wafer factory, etc. Traditional vacuum pad generally utilizes a nozzle to produce the effect of vacuum [1, 2]. To adjust the suction force output, it is required to change manually the opening area of the nozzle. In this paper, however, a new proportional pneumatic floating vacuum pad is developed and constructed as shown in Fig. 1 [3, 4]. There are two features concerning this new vacuum pad. The first one is the introduced proportional solenoid, which enables the continuously variable suction force output. The second one is the floating (i.e. non-contacting) mechanism design, which is more preferable in real industries because it can protect the surface of the work-piece from scratching or other damages.

In this paper, two control schemes are also proposed. The first one is the gap control. A pre-set constant gap is input to the controller as the command input which further drives the proportional solenoid to maintain a steady-state gap between the vacuum pad and work-piece. A possible minor fault, however, is that the pre-set gap may not be the optimal setting. It may give rise to larger energy consumption. Therefore, a second control strategy is proposed to minimize the energy consumption. In details, the gap between the vacuum pad and work-piece is no longer a constant. Instead, the gap is kept as large as possible in order to minimize the energy consumption. It is expected that the newly developed prototype with two different control criteria may find some real applications in the future. In the following, the principles of the proportional solenoid as well as the design of the vacuum pad will be illustrated.

VACUUM PAD DESIGN USING PROPORTIONAL SOLENOID

Figure 1 shows the scheme of the developed vacuum pad. The air is guided to flow into the vacuum pad at an eccentric inlet A. After passing through the restrictor C, the air is guided to flow out of the thin film between the vacuum pad and the work-piece denoted by B. The opening area of the restrictor is automatically controlled by the proportional solenoid. The proportional solenoid (Magnet-Schultz, GRF035) is a popular electro-mechanical transducer used in the design of fluid-power proportional valves [4, 5]. It has a quite linear force/stroke relation, which is the key requirement for the design of the proportional vacuum pad. The restrictor poppet, which is subjected to a constant force in the linear working range, reaches a definite position in the vacuum pad according to Hook's law. This definite position of the poppet signifies a definite opening area of the restrictor. Furthermore, it is well-known that the relation between the output force and the input current for the proportional solenoid is linear. Consequently, the opening area of the restrictor is continuously controllable and is proportional to the input excitation current. This is exactly the basic function of the proportional vacuum pad. Other design details can be found in reference [4]. Finally, the picture of the developed prototype equipped with a gap sensor (Keyence, AS440) is shown in Fig. 2.

EXPERIMENTAL RESULTS AND DISCUSSION

Figure 3 shows the gap control block diagram for the proportional floating vacuum pad. In this study, the utilized control scheme is the PID controller, in which the optimal gains are determined by the criterion proposed by Ziegler and Nichols [6]. The discrete-time PID-controller can be formulated as

$$u(k) = u(k-1) + \Delta u(k), \qquad (1)$$

$$\Delta u(k) = K_P[e(k) - e(k-1)] + K_I e(k) + K_D[e(k) - 2e(k-1) + e(k-2)], \qquad (2)$$

For the first control scheme, a constant gap is input to the control system as the command input. In the second control approach, however, the gap input is not a constant. The controller tries to enlarge the gap slowly and continuously after the initial setting in order to minimize the input current to the proportional solenoid as long as the work-piece (a CD-disk) does not fall. However, the oscillation of the gap is inevitable arising from the continuously enlarged gap setting. To prevent the accidentally falling of the work-piece, therefore, the controller must assure that the oscillation of the gap is convergent. To achieve this, an upper limit for the continuously enlarged gap must be found by the controller. Practically, the incremental enlargement of the gap will be stopped by the controller if the obvious oscillation of the gap is detected. Moreover, to detect the gap oscillation precisely, the numerical derived velocity signal after the impact (shown in Fig. 5 and Fig. 6) is employed and expressed as

$$V(k) = \frac{X(k) - X(k-4)}{4T_s}. \qquad (3)$$

If the absolute value of the velocity signal, $V(k)$, exceeds a pre-set bound, it signifies that the obvious oscillation of the gap is detected and the gap should no longer be enlarged by the controller. The most suitable

bound for the velocity signal, however, is obtained by trial-and-error approach

In this study, the picture of the utilized experiment is shown in Fig. 4, where the generated suction force makes successfully a CD-disk adhere to the developed vacuum pad. The supply pressure is adjusted to be 2 bar and the mass of the CD-disk is approximately 16 g.

Figure 5 shows one typical experimental result using the first control scheme. The command gap input is set to be 0.5 mm. The consumed steady-state current input to the proportional solenoid is nearly 0.26 A and the steady-state error of the gap control is 0.01 mm. On the other hand, a comparative experimental result using the second control strategy is shown in Fig. 6. Obviously, the required steady-state current becomes only 0.18 A which is smaller than the aforementioned one. In addition, the gap between the vacuum pad and work-piece is oscillatory at the beginning and settles to 1.14 mm which is larger than the pre-set input gap using the first control scheme. In this case, the percentage of energy-saving is nearly 30%.

From the time response curves of the air gap thickness shown in Fig. 5 and Fig. 6, it is observed as well that the work-piece contacts the vacuum pad at the beginning. After this inevitable impact, however, the thickness of the air gap settles and reaches the steady-state value.

CONCLUSION

In this paper, a new proportional pneumatic floating vacuum pad was successfully developed and constructed. After experimental tests, three conclusions may be drawn from this research.

(1) The most important feature of the developed proportional vacuum pad is the introduction of the proportional solenoid, which can be used to generate automatically the adequate suction force output by closed-loop control technique.

(2) Two control schemes are proposed and successfully implemented in this paper. The first one is the constant gap control, which is proven to be more stable and less oscillatory. On the other hand, in the second control scheme, the gap between the vacuum pad and work-piece is kept as large as possible, which is proven to be more energy-saving but less stable. In this study, the percentage of energy-saving reaches approximately 30%.

(3) During the process of suction force output, it is observed that the work-piece contacts the vacuum pad at the beginning. After this impact, the thickness of the air gap settles and reaches the steady-state value. However, such an impact between the vacuum pad and work-piece is not allowed in some precision applications, such as the silicon wafer industry. In the future, therefore, some advanced closed-loop air gap control

system should be introduced to avoid the direct contact between the vacuum pad and the work-piece.
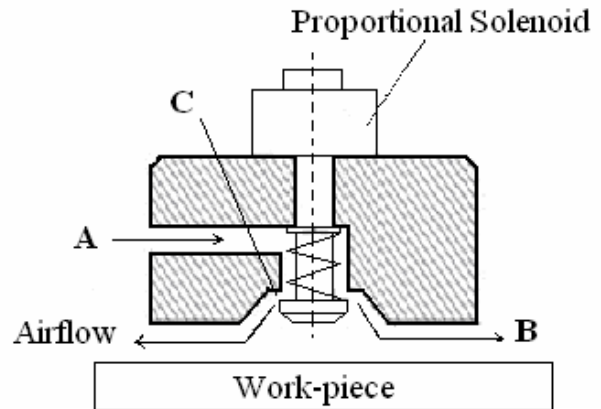
Figure 1 Scheme of the developed proportional floating vacuum pad
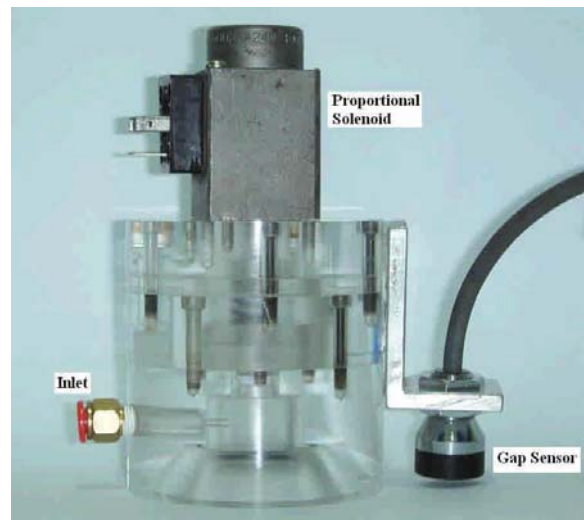
Figure 2 Prototype of the developed proportional floating vacuum pad
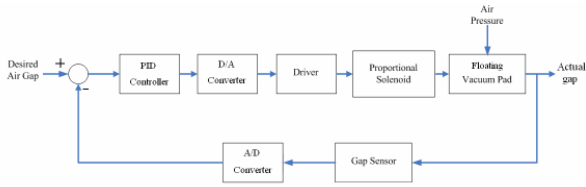
Figure 3 Block diagram of the gap control for the proportional vacuum pad
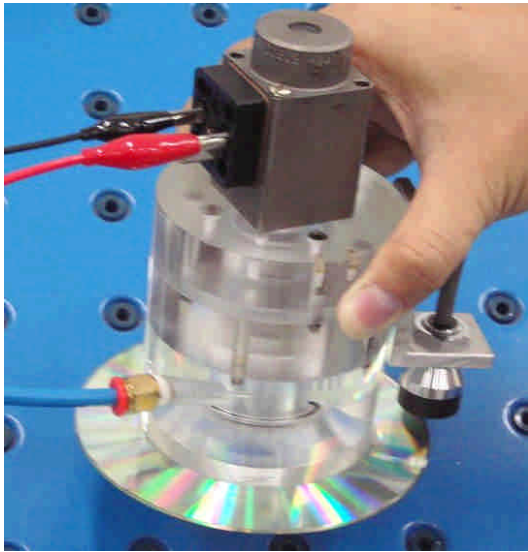
Figure 4 Experimental example showing the developed vacuum pad with a sucked CD-disk

Figure 5 Experimental results using the first control scheme
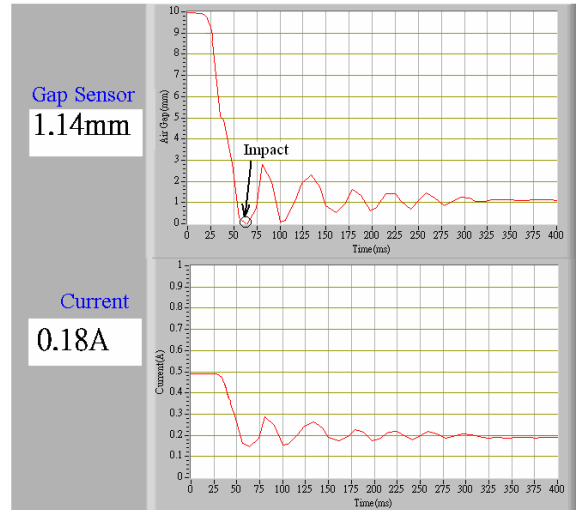
Figure 6 Experimental results using the second control scheme

REFERENCES

1. N. N., SMC-Best Pneumatics, Vol. C003, 2000, Catalogue of SMC Corporation.
2. Renn, J. C. and Jan, D. Y., Application of CFD to the Optimal Design of an Energy-Saving Pneumatic Vacuum Pad, Proceedings of 5th International Conference on Heat Transfer, Fluid Mechanics and Thermodynamics, 2007, Paper No.: **RJ1**, Sun City, South Africa.
3. Renn, J. C. and Jan, D. Y., Designing an Energy-saving Pneumatic Vacuum Pad for Automated Manufacturing System, JMES, Proc. Instn. Mech. Engrs, Part C, 2007, Vol. **221**, No. 12, pp. 1679-1685.
4. Renn, J. C., Jan, D. Y. and Lu, C. H., Development of a New Proportional Non-contacting Pneumatic Vacuum Pad," Proceedings of IFPE 2008 Technical Conference, 2008, Paper No.: **7.2**, Las Vegas, USA.
5. Backe, W., Steuerungs- und Schaltungstechnik II, 1993, Umdruck zur Vorlesung, RWTH Aachen, Germany.
6. Ziegler, J. G. and Nichols, N. B., Optimum Settings for Automatic Controllers, Trans. of ASME **64**, 1942, pp. 759-768.

P1-38

CONTROL SYSTEM DESIGN OF A PNEUMATIC SERVO SYSTEM CONSIDERING THE DYNAMIC CHARACTERISTICS OF THE SERVO VALVE

Masahiro HIRANO*, Kazutoshi SAKAKI**, Toshinori FUJITA***,
Kenji KAWASHIMA**** and Toshiharu KAGAWA****

*Precision Engineering, Tokyo Denki University Graduate School
2-2 Kanda-Nishiki-cho, Chiyoda-ku, Tokyo 101-8457, Japan
(07gmp18@ms.dendai.ac.jp)
**Sumitomo Heavy Industries Mechatronics, Ltd.
19 Natsushima-cho, Yokosuka-city, Kanagawa 237-8555, Japan
***Department of Machinery System Engineering Tokyo Denki University
2-2 Kanda-Nishiki-cho, Chiyoda-ku, Tokyo 101-8457, Japan
****Precision and Intelligence Laboratory, Tokyo Institute of Technology
4259 Nagatsuda-cho, Midori-ku, Yokohama-city, Kanagawa 226-8503, Japan

ABSTRACT

Pneumatic servo systems are applied in several industrial applications and have also been studied extensively for the purposes of compensating the nonlinearity of pneumatic servo systems and improving the controllability with robust control. In their control system design, the transfer function of a pneumatic servo system has been a third-order time lag system, based on the assumption that servo valve dynamics is negligible because it is sufficiently faster than cylinder dynamics. However, the characteristic of a servo valve greatly influences the dynamic characteristic of the pneumatic servo and should be taken into account in the control system design. In this research, a new method of control system design, which deals with the pneumatic servo system as a fifth-order time lag system including a second-order time lag system of a servo valve, has been proposed. The experiment shows that the proposed method is effective. As a result, we can decide all of the control parameters including the proportional gain without trial and error. The obtained proportional gain can be larger, so that the performance of a pneumatic servo has been improved.

KEY WORDS

Pneumatics, Control System Design, Pneumatic Servo System, Servo Valve, Cylinder

NOMENCLATURE

K_{sv}	: Servo valve gain	[m^2/V]
K_n	: Flow gain of servo valve	[m/s/mm^2]
ω_v	: Natural frequency of servo valve	[rad/s]
ω_n	: Natural frequency of pneumatic cylinder	[rad/s]
ζ_v	: Damping coefficient of servo valve	[-]
s	: Laplace operator	[-]
s^*	: Dimensionless Laplace operator	[-]

INTRODUCTION

Since the late '90s, pneumatic servo systems have been used in many fields, such as the active suspension system on the Shinkansen bullet train, molding machines for glass lenses, and amusement robots, because of the numerous advantages of high power, compliant property, and good force controllability. However, the characteristic of a pneumatic servo is nonlinear, which make control difficult. Therefore, control methods of a pneumatic servo, applying advanced control theories such as fuzzy control or robust control, have been investigated [1][2]. In these cases, the transfer function of third-order time lag system derived only from equations on cylinder dynamics is utilized for the control system design, because the pneumatic servo is usually driven by a servo valve that is sufficiently faster than the cylinder dynamics. However, the authors previously clarified

that the dynamic characteristic of a servo valve decides the entire dynamic characteristic of a pneumatic servo. Therefore, the transfer function should be a fifth-order time lag system including the dynamic characteristic of a servo valve in the control system design of a pneumatic servo system. The purpose of research is to establish a new control system design method on a pneumatic servo system considering the dynamic characteristic of a servo valve.

Control system design procedure considering the dynamic characteristic of a servo valve

Mathematical model of a pneumatic servo system [3]
In general, the transfer function of a spool type servo valve is treated as the following second-order transfer function:

$$G_v(s) = \frac{K_{sv}\omega_v^2}{s^2 + 2\zeta_v\omega_v s + \omega_v^2} \tag{1}$$

The mathematical model from the flow rate of a servo valve to the displacement of a pneumatic cylinder, which is an actuator in the pneumatic servo system, is described by the flow rate equation on the servo valve, a gas state equation, and the dynamic equation of the cylinder. By linearizing these equations, where it is assumed that the change in the state of air is an isothermal change and that the friction of a cylinder is negligible, the transfer function is obtained as follows:

$$P_n(s) = \frac{K_n\omega_n^2}{s(s^2 + \omega_n^2)} \tag{2}$$

Conventional control system design method
If the assumption that the dynamics of the servo valve $G_v(s)$ is sufficiently fast compared to the dynamics of the cylinder $P_n(s)$ is true, then the transfer function of the controlled system is a third-order time lag system because $G_v(s)$ is negligible. Therefore, a control method in which the feedback signals are velocity and acceleration, in addition to position, is adopted. A block diagram of this control method is shown in Fig.1, and the non-dimensional transfer function of a closed-loop system transformed by the non-dimensional time $\tau = (K_p K_{sn} K_n \omega_n)^{1/3}$ is given as follows:

$$Gc(s*) = \frac{1}{s*^3 + \alpha' s*^2 + \beta' s* + 1} \tag{3}$$

The velocity or the acceleration feedback gain are then respectively given as follows:

$$K_a = \left(\alpha' K_p^{1/3}\right) / \left(K_{sn} K_n \omega_n^2\right)^{2/3} \tag{4}$$
$$K_v = \left\{\beta'\left(K_{sn} K_n K_p / \omega_n\right)^{2/3} - 1\right\} / \left(K_{sn} K_n\right) \tag{5}$$
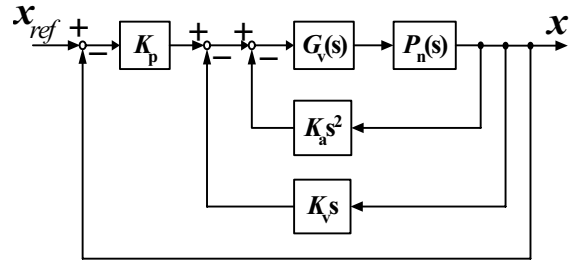
Figure 1 Block diagram of the pneumatic servo system

The transient response of Eq. (3) is determined by the values of α' and β'. These values, usually $\alpha'=2$ and $\beta'=3$, are chosen so as to enable adequate damping in the response. The proportional gain K_p cannot be determined in this conventional method. Consequently, the maximum proportional gain K_p is determined in the stable region by trial and error, because the controllability becomes better as K_p increases. On the servo valve, the control parameters, the natural frequency ω_v, and the damping coefficient ζ_v, are adjusted independently of the pneumatic servo system. The natural frequency ω_v is decided by the maximum force of the actuator driving the valve. In many cases, the damping coefficient of the servo valve ζ_v is set to 0.7 - 0.8 in order to realize a suitable response in second-order time lag system.

Proposed control system design method
In the conventional method, poles of the closed-loop system is bigger and the system response is faster, when the proportional gain K_p becomes large, so that the above assumption that the dynamics of the servo valve $G_v(s)$ is sufficiently fast compared to the dynamics of the cylinder $P_n(s)$, is not true. The closed-loop system should be dealt with as a fifth-order time lag system including the transfer function of the servo valve. In addition, parameters of ω_v and ζ_v on the servo valve should also be included in the adjusted control parameters in the control system design procedure.

The fifth-order time lag system of Eq. (6) is obtained when the closed-loop transfer function of Fig.1 is formed into a non-dimension by the dimensionless time $\tau = (K_c K_p)^{1/5}t$.

$$Gc(s*) = \frac{1}{s*^5 + \alpha s*^4 + \beta s*^3 + \gamma s*^2 + \delta s* + 1} \tag{6}$$

The relationship between α, β, γ, and δ in the above equation and each feedback gain are given by the following equations:

$$K_p = \left\{\left(\omega_{v\max}^2 + \omega_n^2\right)/\beta\right\}^{5/2} / K_c \tag{7}$$
$$\zeta_v = \alpha\left(K_c K_p\right)^{1/5} / \left(2\omega_{v\max}\right) \tag{8}$$
$$K_a = \left\{\gamma\left(K_c K_p\right)^{3/5} - 2\zeta_v\omega_{v\max}\omega_n^2\right\} / K_c \tag{9}$$
$$K_v = \left\{\delta\left(K_c K_p\right)^{4/5} - \omega_{v\max}^2\omega_n^2\right\} / K_c \tag{10}$$

As stated previously, ω_v is decided by the maximum force of the voice coil motor driving a servo valve. That is to say, it can be assumed that this value is known. Then, all of the adjusted control parameters, ω_v and ζ_v, on the servo valve and each feedback gain including a proportional gain K_p can be calculated by giving α, β, γ, and δ in Eqs. (7) - (10). A desired response is obtained when a suitable value of α, β, γ, and δ is selected. There are a number of selection methods, and, for example, the integral of time multiplied by the absolute value of error (ITAE) criterion provides these values.

Effectiveness of the proposed control system design method

Experimental method

The proposed control system design method was tested experimentally using an actual pneumatic servo system, as shown Fig. 2. Figure 3 shows the apparatus of its pneumatic servo system [3]. This pneumatic servo system is general and consists of a pneumatic cylinder, a servo valve, and a controller. However, the pneumatic cylinder is special. An air bearing supports the piston of a pneumatic cylinder and the frictional force is very small. The piston is driven by the supply pressure of 0.4 [MPa]. The cross sectional area of the cylinder is 380 [mm^2], and the stroke of the cylinder is 20 [mm]. The personal computer is used for the controller, and the control algorithm was programmed by xPC-Target of Matlab/Simulink. The cylinder and the servo valve were simultaneously controlled by a single computer. The sampling frequency is 10 [kHz]. The spool position of the servo valve and the cylinder displacement were measured by two digital position sensors and were input to a controller through the I/O-board. The resolution of a position sensor is 0.128 [μm]. The velocity and acceleration signals required for feedback control are obtained from the displacements by using the observer. The observer's poles were set to be sufficiently higher than the pole of the closed-loop system. The output of the controller is output to the servo valve through the D/A-board. Finally, the pneumatic cylinder is positioned.

Validity of a mathematical model

In order to verify the validity of the mathematical model of a pneumatic servo system, a step response test was conducted. The results for the servo valve, where $\omega_v = 140$ [Hz] and $\zeta_v = 1$, are shown in Fig. 4. The origin is the null position of the servo valve. This figure shows that the response of the mathematical model is approximately the same as the experimental response. The response of the closed-loop system is shown in Fig. 5. The step width is 5 [mm], and the one of the stroke ends of the cylinder is the origin point of the cylinder position. The values of ω_v and ζ_v for the servo valve were same as those shown in Fig. 4. The proportional gain $K_p = 0.03$ is chosen, and the feedback gains on velocity and acceleration are calculated from Eqs. (4) and (5) as $\alpha' = 2$ and $\beta' = 3$, respectively. The experimental results show good agreement with the response of the mathematical model shown in Eq. (6), although the pneumatic servo system has some nonlinearity. The mathematical model including the servo valve is therefore valid.

Figure 2   Photograph of the tested pneumatic servo system
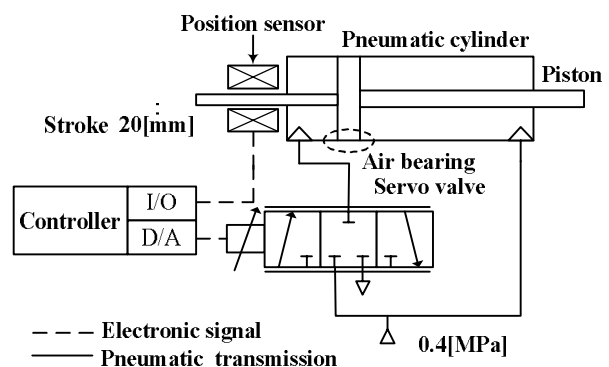
Figure 3 Apparatus of the pneumatic servo system

Effectiveness of the proposed control design method

The step response obtained by the proposed control system design method is shown in Fig. 6. In this design, α, β, γ, and δ are decided by the ITAE criterion, and the natural frequency of the servo valve ω_v is 140 [Hz], considering the validity of the mathematical model. Control parameters, such as the velocity or the acceleration feedback gain, were calculated directly by Eqs. (7) - (9) without the need for a trial-and-error process. The proportional gain then became $K_p = 0.13$ [V/m]. In Fig.5, the dash-dotted line shows the response of Eq. (6) used in the control system design. The experimental results are similar to those of Eq. (6) with respect to the overshoot or undershoot of the response upon settling. This difference may be due to a nonlinearity of the pneumatic system. We concluded that the proposed control design method is effective and that the pneumatic servo system should be dealt with as a fifth-order time lag system.

Comparison with the conventional method

The results of the conventional control system design method are compared with those of the proposed system in Fig. 7. In the conventional method, the servo valve dynamic characteristic of $\omega_v = 140$ [Hz] is the same as that of the proposed method. The damping coefficient of a servo valve was adjusted to $\zeta_v = 0.75$ in a second-order time lag system.

459
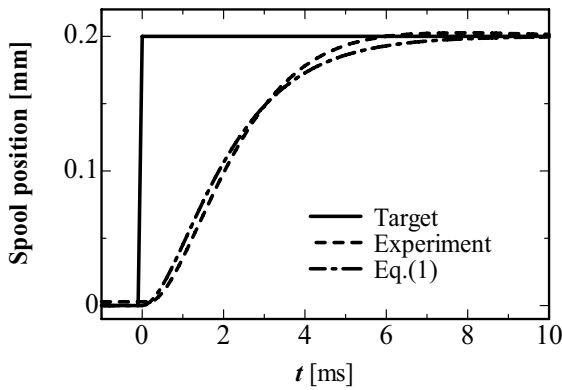
Figure 4 Step response of the mathematical model on the servo valve compared with the experiment

Figure 5 Step response of the mathematical model on the pneumatic servo system compared with the experiment

Figure 6 Step response designed by the proposed method
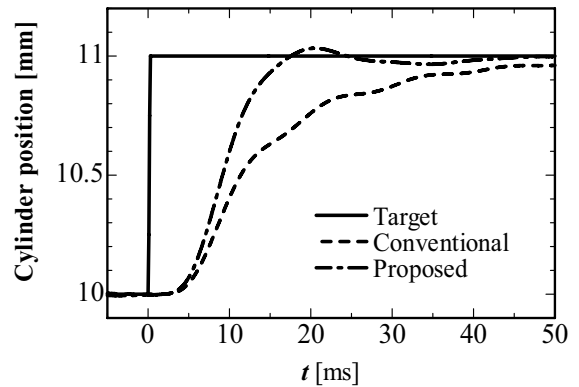
Figure 7 Comparison of the proposed method with the conventional method

The velocity and acceleration gains were calculated from Eqs. (4) and (5) by setting $\alpha = 2$ and $\beta = 3$. The proportional gain K_p was obtained by trial and error, keeping the velocity and the acceleration gains constant, and $K_p = 0.10$ [V/m] was selected. When the proportional gain K_p is set to be greater, a small fluctuation occurred in the response. Consequently, the proportional gain is smaller in the case of the conventional control system design method than in the case of the proposed method. The rise time and the settling time of the proposed method are faster, as compared to the conventional method. Figure 7 reveals the superiority of the proposed technique.

Conclusion

A new control system design method was proposed in which the transfer function of the pneumatic servo system is considered to be a fifth-order time lag system by dealing with the dynamic characteristics of servo valve as a second-order time lag system explicitly. The results of an experiment indicate that the proposed method is very effective. In particular, the proposed

method can be used to decide all of the control parameters without the need for a trial-and-error process. Furthermore, the proportional gain obtained by the proposed method is larger than that obtained by the conventional method through trial and error and is near maximum in the stable region. Therefore, the controllability of the pneumatic servo has been improved.

REFERENCES

1. M.C. Shih, N.L.Luor, Self Tuning Neural Fuzzy Control the Position of a Pneumatic Cylinder UnderVertical Load, International Journal of JSME, 2001, NSC-85-2212-E006-006.
2. M.Chiang, C.Chen, and T.Tsou, Large stroke and high precision pneumatic-piezoelectric hybrid positioning control using adaptive discrete variablestructure control, Mechatronics, 2005, **15**, pp.523-545.
3. Toshinori Fujita, Kenji Kawashima, Takashi Miyajima, Taro Ogiso, and Toshiharu Kagawa, Effect of Servo Valve Dynamic on Precise Position Control of a Pneumatic Servo Table International Journal of Automation Technology, 2008, **2**-1, pp. 43-48.

460

P1-39

RESEARCH ON A NEW TYPE OF ENERGY SAVING PNEUMATIC PISTON VACUUM GENERATOR

Xiaobin PAN* and Xiaoning LI*

*SMC Pneumatic (Nanjing) Technical Center, School of Mechanical Engineering,
Nanjing University of Science & Technology, Nanjing, 210094 China
(xnli2008@jsmail.com.cn)

ABSTRACT

Currently used jet vacuum ejector has a defect of high air consumption due to its requirement of continuous air supply. Focusing on this problem, a new type of piston vacuum generator (PVG for short) has been researched. The PVG has two pairs of pistons. One is for driving and another is for vacuum generating. Besides the maximum vacuum value, the vacuum response time and air consumption are the most concerning performances. Special structural design is made so as to meet all the requirements, in which the unequal diameters of pistons, using directional control valves instead of the check valves and stepped flow rate control scheme are proposed and realized. Experimental results have shown that for the prototype of piston vacuum generator its maximum vacuum is about 93kPa, the response time is about 3.7s and the air consumption is reduced by about 71.3% in time interval of 60s compared to the same level of vacuum ejector.

KEY WORDS

Piston Vacuum Generator(PVG), energy saving, stepped flow rate control

INTRODUCTION

Vacuum pads have been used extensively in vacuum picking operation in pneumatic control systems. Vacuum picking has advantages for moving tiny, easily-deforming or easily-breaking parts[1]. At present, main pneumatic vacuum generating component in industry is still vacuum ejector. According to the working principle of vacuum ejector, compressed air needs to be ejected directly from inlet to outlet and must be maintained for keeping a certain vacuum. Therefore, it has to consume large compressed air and be inefficient in application[2,3]. To solve the problem of high air consumption, a new type of energy-saving vacuum generator called Piston Vacuum Generator(PVG for shot), which works on the principle of generating vacuum by volume expansion, is proposed and researched. It provides a new technical approach for saving energy in pneumatic vacuum system. The structure, key technologies and testing results are introduced in following sections.

STRUCTURE OF PVG

Vacuum could be generated not only by air ejecting, but also by volume expansion[4,5], i.e., by means of piston moving, the piston chamber is enlarged so as to make air expand to decrease the pressure and form vacuum state in the chamber. For applying this principle to generate vacuum and draw air from vacuum pads, a double piston structure of a piston vacuum generator is designed as shown in Figure 1. One of the pistons is in the driving chamber and another is in the vacuum chamber in the PVG. Because of the restriction of structure sizes, the

device can not provide the enough vacuum ability at one stroke of pumping operation. Therefore, the vacuum chamber piston must be reciprocated to generate vacuum continuously and two directional valves, which control piston reciprocating and four check valves, which control vacuum chamber pumping and exhausting, are needed in the structure of PVG.

Due to limited space, the theoretical model is not described in this paper but it can be seen in reference [6]. The working process of PVG can be described as follows. Compressed air is fed into the driving chamber Ⅱ through directional valve and the piston is pushed onto left and the air in driving chamber Ⅰ is exhausted outside the chamber through the directional valve. At the same time, the volume of vacuum chamber Ⅱ is expanded thus to generate a certain vacuum in the vacuum chamber Ⅱ and at vacuum port. Moreover the air in vacuum chamber Ⅰ is also exhausted through a check valve. When the piston moves to the end of stroke, the directional valves are switched and pistons move towards opposite direction. A new vacuum generating process starts and vacuum can be generated continuously.
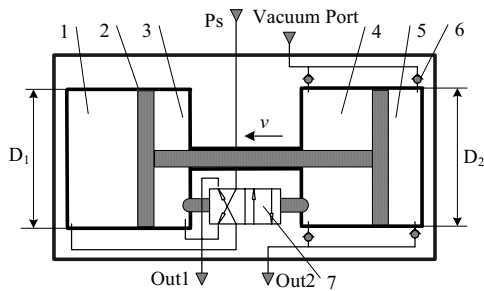
1.driving chamber Ⅰ 2.piston 3. driving chamber Ⅱ
4.vacuum chamber Ⅰ 5. vacuum chamber Ⅱ
6.check valve 7.directional valve
Figure 1 Sketch of PVG structure

The preliminary testing is conducted with the PVG prototype shown in Figure1[6]. It is found that to open pumping check valve some local pressure loss would be taken place in the exhausting process and the effective area of pumping channel would be reduced gradually with increasing vacuum. Therefore, in structure the pumping check valve is not useful for reducing response time. Furthermore, the structure with equal diameters of driving chamber and vacuum chamber is not beneficial to decreasing response time. For overcoming these defects, the generator is improved base on PVG. The improved structure is shown in Figure 2 and is named as PVG-R (Piston Vacuum Generator-Rapid Response).

The main differences between PVG and PVG-R are: 1) The two original check valves are replaced by a pumping directional valve to increase effective area of pumping channel and reduce local pressure lost; 2) A structure with unequal diameters of driving chamber and vacuum

chamber is designed so as to increase piston motion speed; 3) A structural form of pressure balance way is adopted in vacuum chamber to reduce initial expansion pressure in clearance volume. The aim to make these improvements is to reduce the response time of the generator.
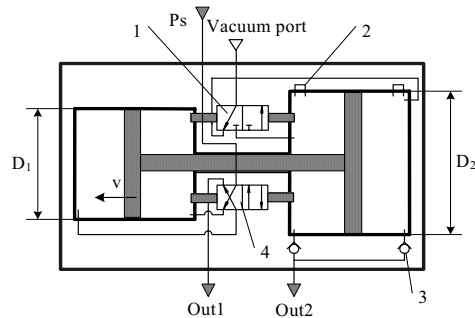
1.pumping directional valve   2.pressure balance way
3.check valve   4.feeding directional valve
Figure 2 Sketch of PVG-R

FUNDEMENTAL CHARACTERISTS EXPERIMENT

The PVG-R prototype is made and tested. The constitution of testing and measuring devices is shown in Figure 3.
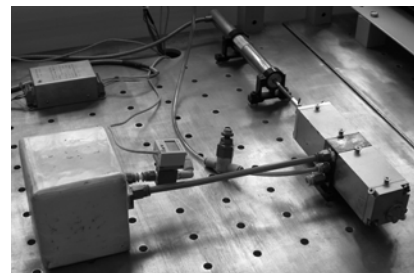
Figure 3 Photo of PVG-R prototype experiment

In the experiment, the main structural parameters of PVG-R prototype are: driving chamber diameter 30mm, vacuum chamber diameter 40mm, piston stroke 60mm, supply pressure 0.21MPa and vacuum vessel 1L. A prototype of PVG-R with above parameters is tested and the supply flow rate and vacuum response time are measured, which are shown in Figure 4 and Figure 5.

The average supply flow rate is near 55L/min and the maximum vacuum is about 93kPa. From the enlarging diagram in the lower right corner of Figure 5, it can be seen that the curve shape of vacuum response of PVG-R is sawtooth and increased gradually up to maximum vacuum. Then the vacuum is kept almost constant.   In addition, from Figure 4 it can be seen that at the initial response stage the supply flow rate is increased rapidly and then decreased a little. But at the vacuum keeping state, the supply flow rate maintains a constant value.
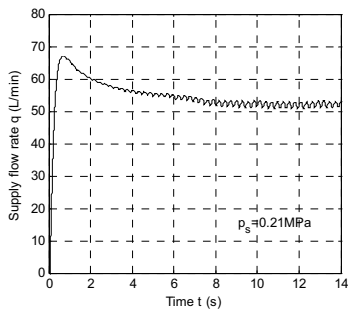
Figure 4 Supply flow rate of PVG-R prototype
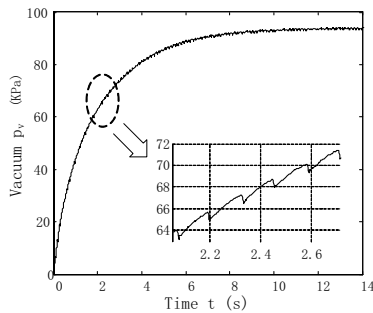
Figure 5 Vacuum response of PVG-R prototype

The average supply flow rate is near 55L/min and the maximum vacuum is about 93kPa. From the enlarging diagram in the lower right corner of Figure 5, it can be seen that the curve shape of vacuum response of PVG-R is sawtooth and increased gradually up to maximum vacuum. Then the vacuum is kept almost constant. In addition, from Figure 4 it can be seen that at the initial response stage the supply flow rate is increased rapidly and then decreased a little. But at the vacuum keeping state, the supply flow rate maintains a constant value.

For comparison of main performances of PVG prototype, PVG-R prototype and other type of vacuum ejector at the same pumping level, in this paper the vacuum response time is defined as the time when the pressure in 1L vessel is decreased from atmosphere to vacuum of 80kPa with supply flow rate 50L/min.
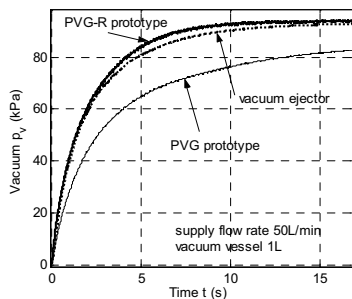
Figure 6 Comparison of vacuum response of two types of vacuum generators with the same pumping level

Comparison of the vacuum response of two types of vacuum generators with the same pumping level is shown in Figure 6. Comparison of the main performances is listed in Table 1. From Table 1, it can be seen that the maximum vacuum of PVG-R prototype is about 93kPa, which is higher than 91kPa of a vacuum ejector at a same level. The response time of PVG-R prototype is about 3.70s, which is less than that of a vacuum ejector at the same level.

Table 1 Comparison of main performances of two types of vacuum generators

Main performances	PVG prototype	PVG-R prototype	Vacuum ejector
Supply flow rate q [L/min]	50		
Supply pressure p_s [MPa]	0.13	0.21	0.40
Response time t [s]	12.60	3.70	4.80
Maximum vacuum p_{vmax} [kPa]	85	93	91

STEPPED FLOW RATE CONTROL

From Figure 4, it can be further analyzed that although the supply flow rate is slightly decreased after vacuum response stage the air supply in vacuum keeping state is still kept at a higher level than the desired.   As we know, if the surface between the vacuum pad and picked part is well sealed, at the vacuum keeping stage only a little air supply is needed to replenish the slight leakage from the contacting surface. Based on this analysis, a technical approach for further decreasing air supply is presented. The idea of the approach is that the large air flow rate is supplied at the initial vacuum response state and then the air flow rate is reduced to a necessary low level enough to replenish the slight leakage and maintain the rated vacuum. This technical approach is called the stepped flow rate control method. In order to implement this stepped flow rate control method, a vacuum detecting and flow rate controlling component is designed and added into the structure of PVG-R, which is named as PVG-RL and is shown in Figure 7.
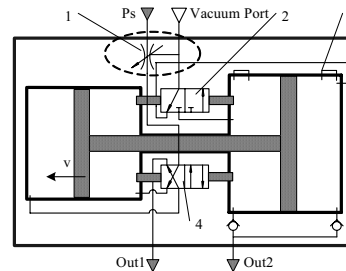
1.stepped flow rate control valve 2.pumping directional valve 3.pressure balance way 4.feeding directional valve
Figure 7 Sketch of PVG-RL

In the structure of PVG-RL, a stepped flow rate control valve which can adjust supply flow rate according to detecting result of the system vacuum is added near the air supply port. The valve can adjust effective area of supply channel to reduce supply flow rate according the preset vacuum.

Through experiments[7], the structural parameters of stepped flow rate control valve are modified and the photo of the modified PVG-RL prototype is shown in Figure 8.
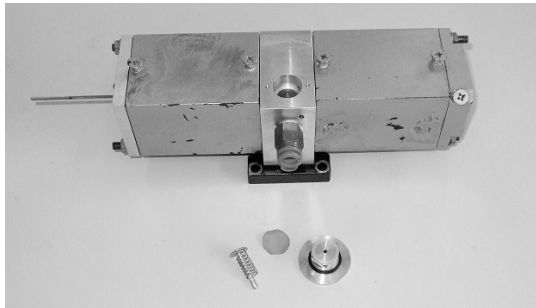
Figure 8 Photo of PVG-RL prototype

Experiments are conducted to measure the response characteristics of PVG-RL prototype. With the condition of supply pressure 0.21MPa, vacuum vessel 1L and preset vacuum 80kPa, the measured response characteristics of PVG-RL prototype is shown in Figure 9.
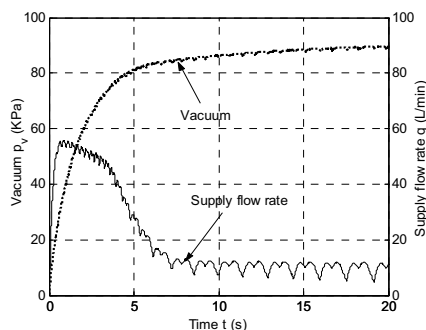
Figure 9 Response characteristics of PVG-RL prototype

From Figure 9, it can be seen that when the vacuum is above preset 80kPa the air flow rate is quickly decreased. This means that the control valve starts after the system vacuum is above the preset vacuum and the supply flow rate falls in a stepped shape. Thus the overall flow rate is obviously decreased.

Experimental results indicate that the minimum supply flow rate of PVG-RL prototype is about 12L/min and the air supply flow rate in vacuum keeping stage is obviously reduced compared with that in vacuum response stage. However, for maintaining a certain vacuum, the normal vacuum ejector has to be supplied with a constant air flow rate at a higher level. For example, a normal vacuum ejector must be supplied with a flow rate of 50L/min to generate and maintain vacuum. But in contrast the PVG-RL prototype only needs an air supply flow rate of 12L/min at vacuum keeping stage, thus reducing a lot of air consumption. Experimental data have figured out that with a quick vacuum response performance the new PVG-RL prototype could reduce the air consumption by 71.5% compared to a normal vacuum ejector at the same level.

CONCLUSIONS

Currently used jet vacuum ejector has a defect of high air consumption due to its requirement of continuous air supply. Focusing on this problem, a new type of piston vacuum generator (PVG for short) has been researched. How to maintain the original performances such as the maximum vacuum value and the vacuum response time that the normal jet vacuum ejector have realized and obviously decrease the air consumption is the key technical problem. For this, special structural design and technical approach are applied such as unequal piston diameters, using directional valves instead of two check valves, adopting pressure balance way and applying stepped flow rate control scheme. Experimental results have shown that for the prototype of piston vacuum generator its maximum vacuum is about 93kPa which a little higher than that of normal jet vacuum ejector, the response time is about 3.7s which is quicker than 4.8s of a normal ejector and the air consumption is reduced by 71.3% in time interval of 60s compared to the same level of vacuum ejector.

REFERENCES

1. SMC. Modern practical pneumatic technology. China Machine Press[M]. Beijing, P. R. China, 2004.
2. Xinrong Zheng. Xian Zhang, Zhangfeng Zhao. Research of Economizing on Energy of Vacuum Ejector[J]. Vacuum & Cryogenics. 2005.3, pp 50-55.
3. Weiqiang Guo, Ruping Pu, Xiujie Han et al. The Analysis Research of the Aspirating Mechanism and Function of Vacuum Generator[J]. VACUUM. 2003.11,pp 54-56.
4. Qingyu Zhang. Hydraulic Reciprocating Vacuum Pump and Compressor[P]. Patent(CN):91219918.0, 1993-7-28.
5. Bin Qu. Special Type of reciprocating Vacuum Pump. 0112181.9[P], 2003-2-5.
6. Xiaobin Pan and Xiaoning Li. Theoretical Study of Pneumatic Vacuum System Consisting of Two Cylinders[J]. MACHINE TOOL & HYDRAULICS. 2008.1,pp 100-103.
7. Xiaobin Pan and Xiaoning Li. Improved Design and Experiments of Pneumatic Vacuum System Consisting of Two Cylinders[J]. VACUUM. 2007.11,pp 69-73.

P1-40

AN APPROACH TO ENERGY CONSERVATION FOR AIR MOTOR

Eisuke SUMIDA*, Masaki GOTO* and Hiroshi MUTOH**

*Department of Applied Mechanics
Graduate School of Fundamental Science and Engineering, Waseda University
3-4-1 Ookubo,Shinjyuku-ku, Tokyo,169-8555 Japan
(E-mail: z-chiyo-add-z@asagi.waseda.jp)
** Department of Applied Mechanics and Aerospace Engineering
School of Fundamental Science and Engineering, Waseda University
3-4-1 Ookubo,Shinjyuku-ku, Tokyo,169-8555 Japan

ABSTRACT

There are many methods to improve actuator efficiency in pneumatic systems. In this research, the authors remodeled rotary valve of radial piston type air motor. During forward rotation, increasing Cut-off ratio of rotary valve which controls supply and exhaust timing can increase expansion process in this motor. As a result, air consumption was reduced, torque was increased and efficiency that we define as the ratio of air consumption to torque was improved. And the authors clarified the existence of an optimum angle in Cut-off ratio.

Considering practical utilizations, performance of this motor is demanded for the same forward rotation as backward rotation. But actually, increasing Cut-off ratio increases compression process and derives efficiency worse.

So the authors have proposed to remodel the casing of this motor in addition to increasing Cut-off ratio. This remodeling makes this motor the same performance forward rotation as backward rotation, but clearance volume expands. So the rate of increasing efficiency under this condition is less than under only remodeling Cut-off ratio. But we directed to possibility of improving efficiency.

KEY WORDS

Key words: Actuator, Rotary valve, Cylinder, Cut-off angle, Expansion energy

NOMENCLATURE

E_I	:	Supplied energy
P_C	:	Cylinder pressure
τ	:	Torque
V_C	:	Cylinder volume
ω	:	Angular velocity
h	:	Efficiency
θ_{ex}	:	Cut-off angle

INTRODUCTION

The characteristic of the pneumatic actuator depends mainly on the compressibility of air as its operating medium. The advantages include the easy storage of energy, the small size and lightweight per output, and the good explosion-proof performance.

The disadvantages include the low energy conversion efficiency, the low controllability caused by the compressibility of air, and the loud exhaust noise, which a variety of researches have been developed to improve. The energy conversion efficiency can be improved by reducing pressure loss or fluid resistance due to air leaks

or restrictions, or by using supplied energy efficiently. This research attempted higher energy conversion efficiency by using the expansion energy of compressed air. The subject is a radial piston type air motor. Remodeling its rotary valve for utilizing the characteristic of air in the cylinder was applied to reduce the supplied and exhaust energy. The problems of the remodeling were shown, which led to the proposal of new remodeling. The validity was examined by simulation.

THE PRINCIPLE

Figure 1 illustrates a radial piston type air motor in section. Supplied air passes through the inside of the rotary valve indicated by the shaded area, pushes the piston down, passes through the inside of the rotary valve again, and then lets out. Figure 2 (a) illustrates a genuine rotary valve in section which is an important part to decide supply and exhaust timing in driving.
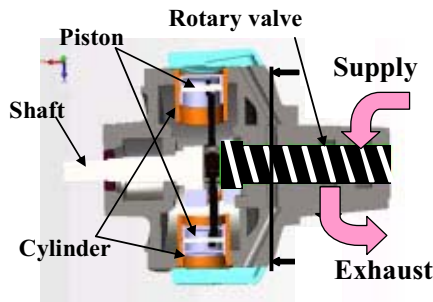
Figure 1   Radial piston type air motor in section

(a)   In section   (b)   Cylinder
Figure 2   Genuine valve
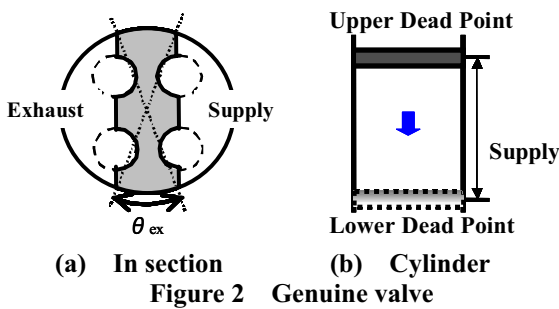
As shown in Figure 2 (b), the genuine valve supplies air during the piston travels from the upper to the lower dead point. This mechanism does not make full use of the expansion energy of air. To improve this, remodeling the rotary valve for using the expansion energy of air was applied. Figure 3 illustrates the remodeled valve in section.
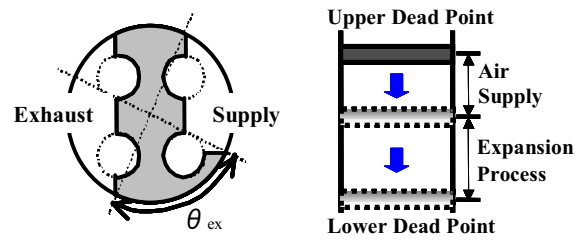
(a)   In section   (b)   Cylinder
Figure 3   Remodeled valve(Forward rotation)

As shown in Figure 3 (a), increasing Cut-off angle θ_{ex} on the supply side cuts air supply off halfway, and the supplied air expands in the rest of its stroke. This may give lower air consumption and higher efficiency. Three remodeled valves were made for the research. Table 1 shows the Cut-off angles and the expansion process rate of the genuine and all remodeled valves. The expansion process rate is defined only for forward rotation. Consideration to backward rotation is in another chapter.

Table 1   Remodeled values of Rotary valves

Valve	Cut-off angle rad	Expansion process rate
Genuine	0.262π	0.001
Remodeled #1	0.479π	0.121
Remodeled #2	0.631π	0.307
Remodeled #3	0.750π	0.487

EXPERIMENTAL SETUP

Figure 4 illustrates the outline of the experimental setup used in this research. The method is to change the angular velocity by controlling the exciting current of the magnetic particle brake at 0.5[MPa] of supplied air pressure.
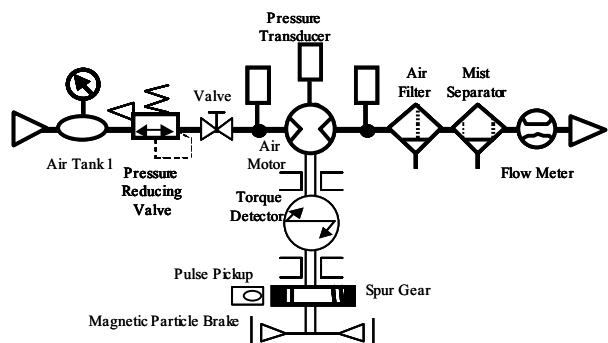
Figure 4   Outline of Experimental setup

EXPERIMENTAL RESULTS AND CONSIDERATIONS

Figure 5 illustrates the *P-V* diagram of the cylinder inside for each valve at 80[rad/s] of angular velocity. Figure 6 illustrates The *P-V* diagram in changing angular velocity for the remodeled #2.
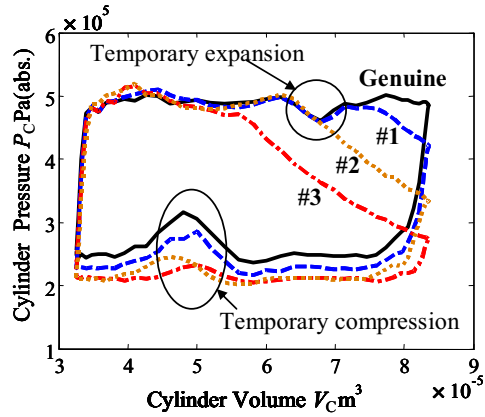
Figure 5   *P-V* diagram (80[rad/s])
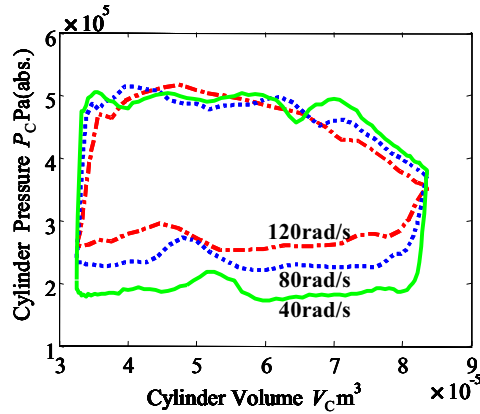
Figure 6   *P-V* diagram(Remodeled #2)

As shown in Figure 5, this process in which the expansion process rate increases as the Cut-off angle increases is categorized into adiabatic expansion. The higher exhaust pressure than atmospheric pressure is caused by the equipment of the air filter, mist separator, and flow meter on the exhaust side.

The lower exhaust pressure of the remodeled valves than the genuine valve appears as the Cut-off angle increases. This is caused by the reduction of air supply at the same revolution. The temporary compression is observed in exhaust. This is considered as the effect of the four cylinders motor in that when the measured cylinder comes at 270[deg] of phase, another cylinder running 90[deg] behind starts exhausting. The temporary expansion in supply is caused by the similar effect. The results of air consumption and output are

shown in Figure 7 and Figure 8.
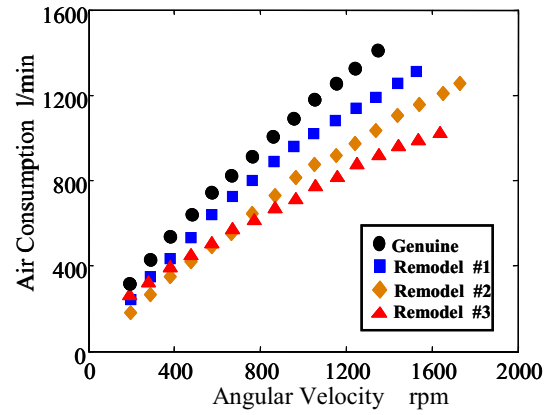
Figure 7   Air consumption
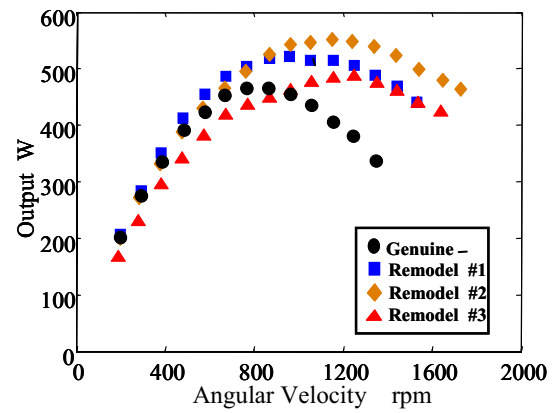
Figure 8   Output

Focusing on the air consumption, it decreases in the high and middle revolution range as the Cut-off angle increases.

The output of all remodeled valves is generated more than the genuine valve. Theoretical torque is represented as the area of *P-V* diagram. In Figure 5, the reduction, in the expansion process, of the *P-V* diagram area for the remodeled valves seems worse than the genuine valve. But the lower exhaust pressure of the remodeled valves than the genuine valves allows the higher torque.

The following equation calculates efficiency. The input is supplied energy and the output is shaft output.

$$\eta = \frac{\tau\omega}{E_1} \times 100 \tag{1}$$

Figure 9 shows the efficiency calculated by this equation. All remodeled valves improve the efficiency in Figure 9. The remodeled #2 which show the highest efficiency improves it by approximately 4[%] in all revolution ranges. The remodeled #1 and #2 show no peaks. This is considered to be caused by the dispersion of revolution on the effect of stick-slip in the low revolution range. The Cut-off angle of each valve

increases as the remodeled number, and the efficiency of #2 is higher than #1 while that of #3 is not the highest. This shows that an optimum Cut-off angle giving a maximum efficiency should exist.
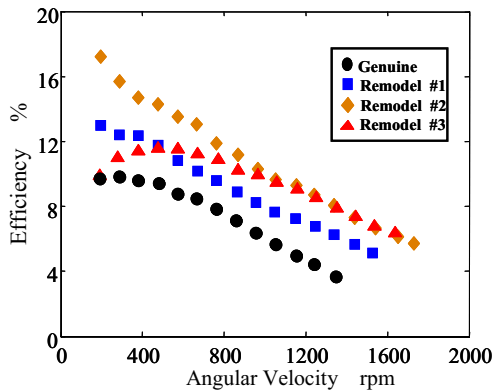
Figure 9   Efficiency

PROBLEMS OF REMODELING

Performance in backward rotation

The improvement of the efficiency in forward rotation was examined in previous chapter. But in backward rotation, the compression process doesn't improve the performance, the expansion process does. Figure 10 and 11 shows the results.
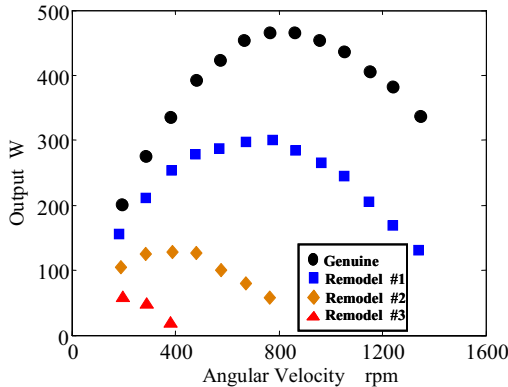
Figure 10   Output(backward rotation)
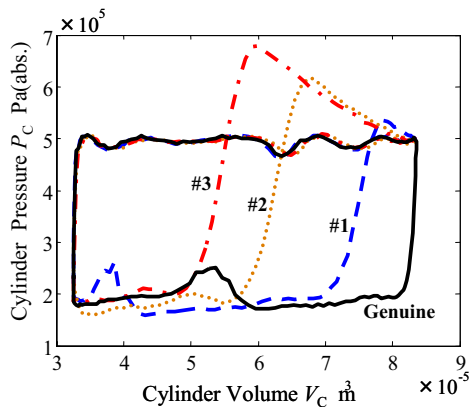
Figure 11   *P-V* diagram(backward rotation 40[rad/s])

Increasing the Cut-off angle expands the compression process to lower the output. The torque output was almost lost at 90[rad/s] for the remodeled #2 and at 40[rad/s] for the #3 of revolution to prevent higher revolution. While the remodeled #1 has much lower torque and output, it can rotate more than at 120[rad/s] of revolution so that it has enough performance to be used even in backward rotation.

Starting torque

Changing the Cut-off angles showed the existence of some specific Cut-off angles at which the upward tendency of starting torque changes into downward or the motor cannot start theoretically.

Figure 12 explains the reason. Air passes through the inside of the rotary valve and the ducts, and is supplied to the cylinder inside. The four ducts connected to each cylinder are used for air supply and exhaust.

In Figure 12(a) air was always supplied to the cylinder, but in (b) air is not supplied. While the experimental estimation of starting torque is difficult on the effect of air leaks, the torque was at approximately 10.5[Nm] in supplying air to two cylinders and 6.8[Nm] in supplying air to one cylinder, at 0.5[MPa] of air supply pressure. The classification of the cut-off angles, the number of cylinders, and the valve types is shown below.
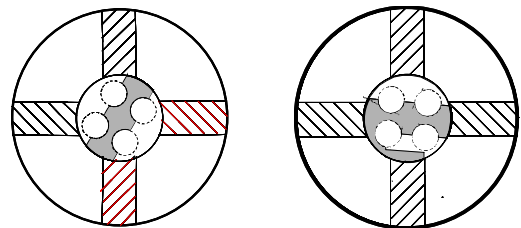
(a)2 cylinders supplied   (b)Not supplied
Figure 12   Starting Torque

(1) $\theta_{ex} < 0.244\pi$ [rad]
  2 cylinders supplied
(2) $0.244\pi < \theta_{ex} < 0.500\pi$ [rad]
  1 or 2 cylinders supplied (genuine, remodeled #1)
(3) $0.500\pi < \theta_{ex} < 0.745\pi$ [rad]
1 cylinder supplied (remodeled #2)
(4) $0.745\pi < \theta_{ex}$ [rad]
0 or 1 cylinder supplied (remodeled #3)

In some cases of the remodeled #3, air was not supplied so that it doesn't rotate theoretically. Actually, the leaked air may come into the cylinder to rotate it. But practical use should be restricted. For the remodeled #1 and #2, air is always supplied to the cylinders, but the starting torque is lower than the genuine valve.

Starting characteristic

Figure 13 shows the experimental results for the starting characteristic of the genuine valve and remodeled #3 applying the step input of air supply pressure.

It shows the genuine valve has the better starting characteristic than the remodeled #3. This is caused by the number of cylinders supplied air. For the genuine valve, two cylinders are usually supplied and for the #3, just one cylinder is. For the other remodeled types, the ducts connected to the cylinders are shut off longer than the genuine valve by increasing the Cut-off angles so that the amount of air supply reduces when step input begins. This makes the starting characteristic worse.
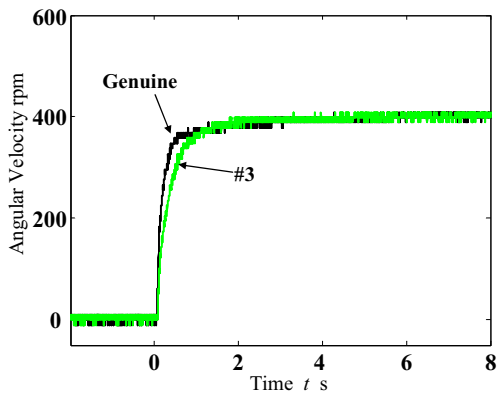
Figure 13   Comparison of Starting Characteristic

PROPOSING NEW REMODELING

The deteriorations due to the remodeling were enumerated in previous chapter. In this chapter, new remodeling for the same level of performance in both rotations is proposed.

Remodeling only rotary valves has limitation for the same level of performance in both rotations. Many practical uses may require the performance of backward rotation so that new design with remodeling casings and rotary valves was developed. The outline is shown in Figure 14 and its casing in section is shown in Figure 15.
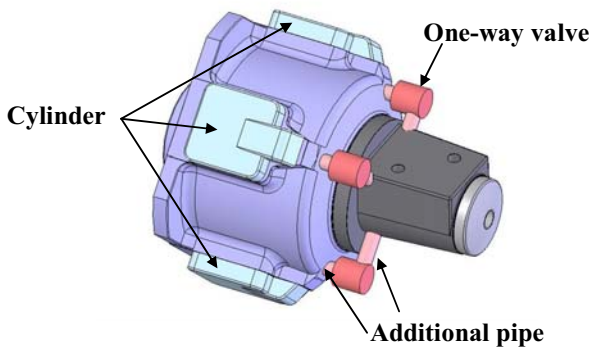
Figure 14   Outline of Casing
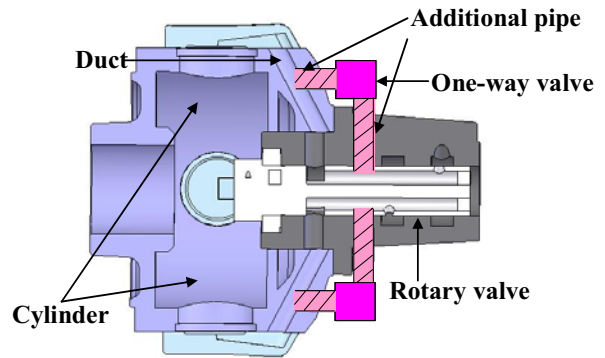
Figure 15   Casing in section

Supplied air usually reaches to cylinders through supply-side pipes inside rotary valves and ducts. After working on pistons, it passes through ducts again and exhaust-side pipes inside rotary valves, and lets out. In backward rotation, however, exhaust grooves do not open immediately so that pistons work on air, which represents the generation of compression process. Additional pipe shown in Figure 15 in section provides another exhaust groove. It is considered that making a hole in the rotary valve along with the phase of the new exhaust groove allows exhaust as compression process occurs. The installation of the one-way valve provides cutting air supply off if expansion process begins during air supply. Without this one-way valve, expansion process may be prevented by supplied pressure air flowing in.

This proposed design is examined by simulation. The two kinds of one-way valve performance used in the simulation are shown in Figure 16. The performance diagrams of the remodeled #2 giving the best efficiency in forward rotation and the specs having the similar Cut-off angle and the one-way valve #1 or #2 are shown.
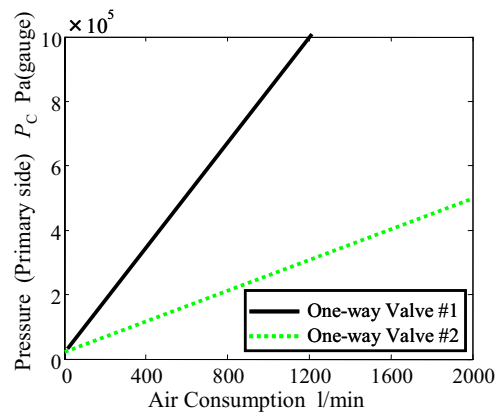
Figure 16   Performance of One-way valves
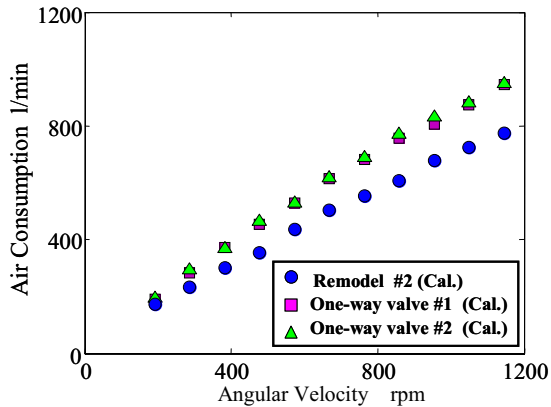
Figure 17 Air consumption(remodeled Casings)
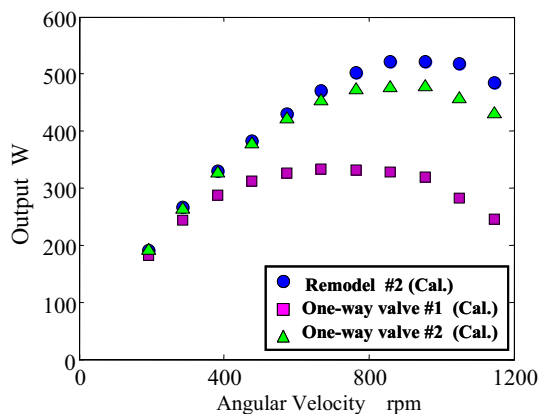
Figure 18 Output (remodeled Casings)

Figure 19 *P-V* diagram (remodeled Casings)

The one-way valve #1 and #2 consumes more air than the remodeled #2. This is caused by increasing the gap volume because of installing the one-way valves and by adding the pipe connecting the one-way valves and the rotary valves. Reducing the additional volume provides the same level of air consumption with the remodeled #2.

The remodeled #2 and the one-way valve #2 have the same level of output in the both low and high revolution ranges. But the one-way valve #1 has much lower output as the revolution increases. Figure 19 shows the *P-V* diagram to explain the reason.

The shift of the diagram toward the right due to the added gap volume is shown. The smaller effective sectional area of the one-way valve #1 than the #2 means no smooth exhaust. When the exhaust route changes from the one-way valve into the original, the higher cylinder pressure keeps the exhaust pressure higher than the remodeled #2 to reduce the output.

CONCLUSION

While the performance tests progressed, no considering the expansion of air characteristic for the existing pneumatic actuators was proved. Therefore this research was planned to improve the characteristic in forward rotation by remodeling the rotary valves working for the supply and exhaust of pneumatic motors. Comparing the remodeled valves with the genuine valve, all remodeled valves improved the output, the amount of air consumption, and the efficiency in forward rotation. The lower exhaust pressure is also supposed to give lower noise. The possibility of an optimal Cut-off angle giving a maximum efficiency was shown.

The remodeling made the problems of the lower performance relating to backward rotation, starting torque, and starting characteristic. A feature of radial piston type pneumatic motors is changing the rotational direction with a low-cost selector valve so that the same level of performance in both directions is required. Therefore the design including the remodeled rotary valve and casing to give the same performance was developed. The simulation of the design showed the added gap volume and installed one-way valve work as the element of pressure loss so that higher efficiency than remodeling only rotary valve is not given. But a guideline was indicated. Reconsidering the shape of the motor and adapting the design for both rotational directions will reduce gap volume to give the same level of efficiency with remodeling only rotary valve.

REFERENCES

1. Goto, Sumida, Mutoh : System control containing pneumatic actuator（Speed control of pneumatic motor）, Journal of Fluid power System Symposium, 2007, pp52-54
2. Sumida, Nakajima, Goto, Mutoh : System control containing pneumatic actuator（Position control of pneumatic motor）, Journal of Fluid power System Symposium, 2007,pp55-57.

P1-41

TORQUE REDUCTION CONTROL FOR AN ELECTRO-PNEUMATIC HYBRID VERTICAL POSITIONING SYSTEM

Hiroshi HIGO*, Yasuo SAKURAI**, Kazuhiro TANAKA*, Takeshi NAKADA***

* Department of Mechanical Information Science and Technology,
Kyushu Institute of Technology
680-4 Kawatsu, Iizuka, Fukuoka, 820-8502 Japan
** Department of Mechanical Engineering,
Ashikaga Institute of Technology
286-1 Oomae, Ashikaga, Tochigi, 326-8558 Japan
*** Department of Environment Integration and design,
Tokyo Denki University
2-1200 Muzaigakuendai, Inzai, Chiba, 270-1382 Japan

ABSTRACT

This paper deals with torque reduction control for an electro-pneumatic hybrid vertical positioning system composed of a servomotor a pneumatic and a mechanical driving sub-system. The servomotor, coupled with a ball screw connected to the load by nut, enables to position a load vertically. The servomotor with small capacity, as well as energy saving, is required for cost down. To realize its small capacity, it is important to reduce the torque of the servomotor in moving the load. In a pneumatic system, a pressure controller generates control signals for the supplied pressure equivalent to the gravitational force of the mass of the load so as to support and move the load smoothly. The torque reduction for the small capacity servomotor needs adequate control pressure supplied to a cylinder. In the present study, a mathematical model of this system has been developed by comparing calculation data with experimental results. The controller designed by this model has succeeded in the torque reduction of the servomotor.

KEY WORDS

Electro-pneumatic hybrid positioning system, Dynamic characteristics, Pressure control, Bondgraphs, Modeling

NOMENCLATURE

A_r	: Area of rod side cylinder	[m^2]
A_h	: Area of head side cylinder	[m^2]
C	: Frictional loss coefficient	[Ns/m]
F	: Force	[N]
g	: Gravity acceleration	[m/s^2]
K	: Rigidity of coupling	[Nm/rad]
Iz	: Momentum of shaft	[kgm^2]
l	: Lead of ball screw	[m]
M	: Inertial mass	[kg]
P	: Pressure	[Pa]
Q	: Flow rate	[m^3/s]
r_0	: Diameter of ball screw	[m]
v	: Velocity	[m/s]
ω	: Rotational speed	[rad/s]
τ	: Torque	[Nm]

INTRODUCTION

A pneumatic cylinder has a difficulty to perform constant-speed drive and intermediate halt such as a hydraulic cylinder due to the compressibility that the air has [1-2]. Therefore, most of pneumatic cylinders are used with full strokes. A pneumatic servomotor to perform highly precise positioning has been developed however its control is complicated and positioning time becomes longer as a disadvantage.

Therefore, in recent years, electro-pneumatic hybrid actuators have been developed to break off this weak point [3]. An atmospherics hybrid actuator has a mechanism in which an AC servomotor is used with a pneumatic cylinder, perform positioning of a cylinder by a servomotor and support loads by air pressure. In the case this actuator is applied to a transport system,
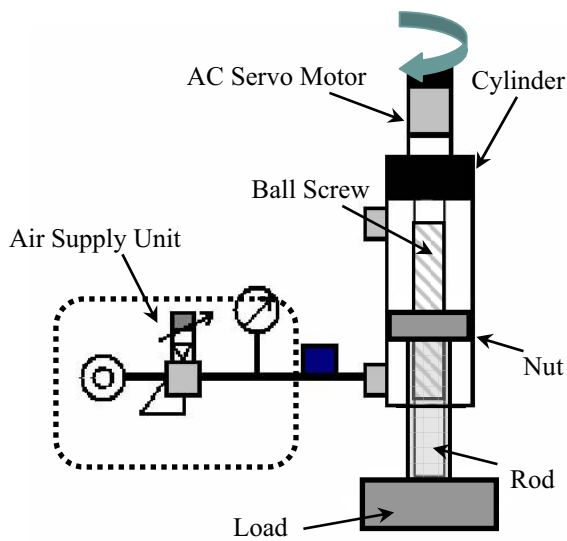
Figure 1 Electro-pneumatic actuator

precise positioning for a heavy load can be performed with a small capacitance motor. Therefore transport systems with low power can be realized with low cost. When an electro-pneumatic hybrid actuator is used under the condition that a load does not vary, it usually works with constant pneumatic pressure. However, when a load varies during an operation, control pneumatic pressure must be controlled depending on loads. At this time, unless the pressure control of a pneumatic cylinder is appropriate, torques more than the allowable value act on a servomotor and the actuator becomes uncontrollable. Furthermore, it may lose its control.

In this study, to solve the above problem, the authors propose a feedback technique to constantly minimize torques acting on a servomotor based on the analytical model [4] of this actuator control system already proposed. Furthermore, we perform control experiment to verify adequacy of this control method and confirm about the torque reduction effect.

EXPERIMENTAL APPARATUS

Electro-pneumatic Hybrid actuator
The electro-pneumatic hybrid actuator used for our experiment consisted of an AC servomotor, a cylinder, ball screw, hollow rod and pneumatic pressure feeding section as shown in Figure 1. The rotating shaft of the ball screw is connected with a servomotor by coupling and a hollow rod is connected with a nut.
When the servomotor runs and ball screw turns, the rod moves up and down. On the other hand, loads are supported by pneumatic pressure supplied from the rod side of the cylinder and even a low volume servomotor can move heavy loads precisely with this mechanism.

Experimental system
Figure 2 shows experimental apparatus used for our experiments. An AD converter, DA converter and motor controller are incorporated in a PC.
The servomotor can rotate with constant angular velocity with control signals from the motor controller. Pressure of the pneumatic cylinder and torques of the servomotor are measured by the AD converter. Operating an electro-pneumatic regulator with the PC, pressure is controlled by the pneumatic regulator. Load Mass 1 is set on the rod of the electro-pneumatic hybrid actuator as shown in the Figure 2. Load Mass 1 is supported by pneumatic pressure and rises in constant speed with the servomotor. When an actuator rises by 20cm, Load Mass 2 on the table is loaded and both
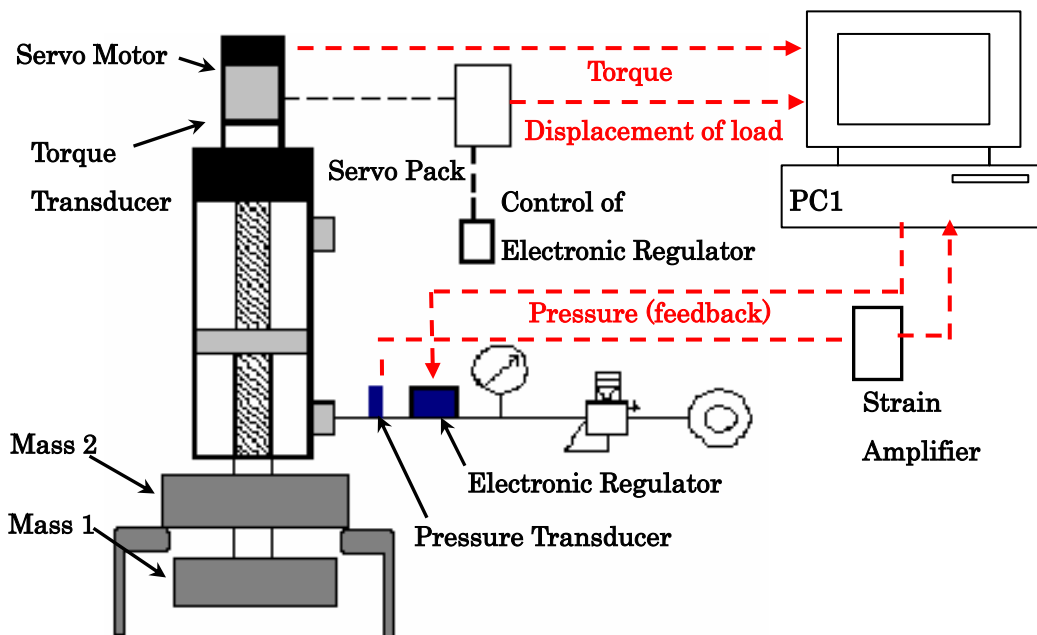
Figure 2 Experimental Equipment
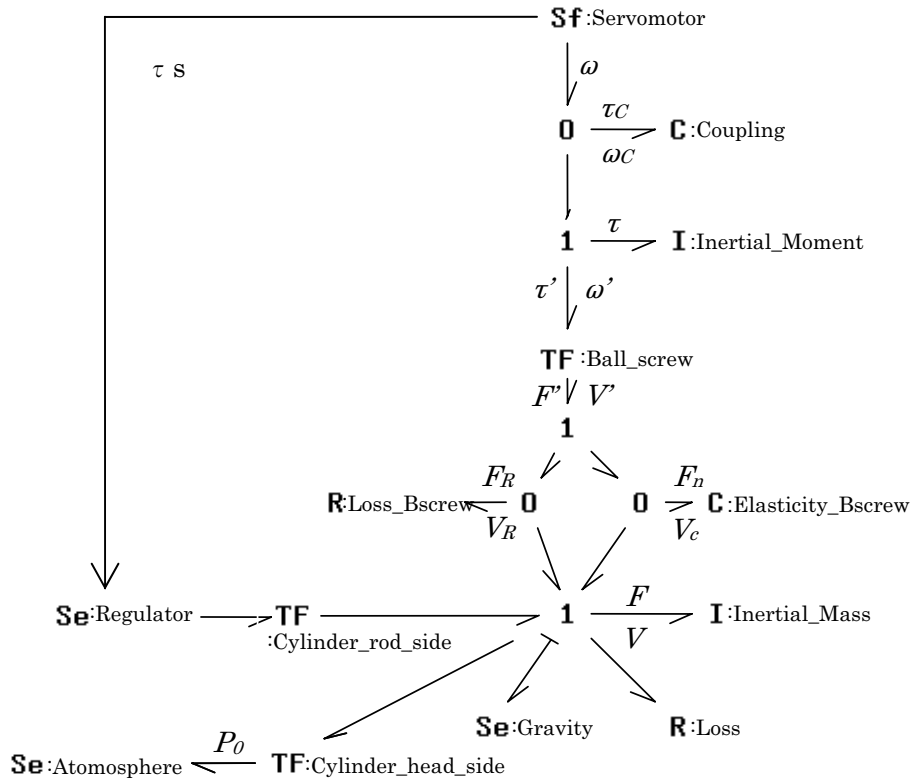
Figure 3 Bond graph model

Mass 1 and Mass 2 act on the actuator.

Feed back control

Torque acting on the servomotor is output as an electrical signal and acquired by a built-in AD converter incorporated in the PC. A pressure value P of the cylinder corresponded to the torque is calculated by Equation (1) and commands are transmitted to an electro-pneumatic regulator through a DA converter to control pressure of the pneumatic cylinder.

$$P = P_0 + \frac{2\pi\tau}{Al} \qquad (1)$$

SIMULATION

Analytical model

We built an analytical model of our actuator control system. We used the bond graph approach as a simulation technique. The bond graph approach is one of the modeling techniques in which flow of power is focused and even a mixed system is expressed integrally as an advantage [5-7].

Figure 3 shows a system model of the electro-pneumatic hybrid actuator for which the experimental apparatus is expressed in the bond graph. A pneumatic cylinder transforms pneumatic pressure into a mechanical force therefore we modeled it by TF: Cylinder_rod_side element. An inertia of load, gravity and friction drag of a cylinder were modeled by I: Mass, Se: Gravity and R:

Loss elements, respectively. The head side of the pneumatic cylinder was opened to the atmospheric pressure therefore it was expressed by Se: Atmosphere element. On the other hand, a servomotor controls revolution speed therefore it was modeled by Sf: Motor element. Power supplied by a motor was affected by torsional rigidity and the rotating shaft's moment of inertia and was transmitted to the ball screw. The ball screw transformed rotary motions into linear motions therefore it was expressed by TF: Ball_Screw element. Effects of friction and an elasticity at the ball screw were modeled by C: Elasticity_Bscrew element and R: Loss_Bscrew element. To perform control, pressure values were calculated by substituting torques consumed in SF: Motor element into Equation (1). The torques were input as pressure values of Se: Regulator element. Pneumatic compressibility was not considered for this model.

Property equation

Property equations of each element used for this study are shown below.

TF: Cylinder_rod_side element,

$$F = AP_2 \qquad (2)$$

$$Q = AV \qquad (3)$$

Se: Gravity element

$$F_g = M_l g \qquad (4)$$

R: Loss element

$(V < -0.01 \quad or \quad 0.01 < V)$

$$F = CV \quad (5)$$

$(-0.01 < V < 0.01)$

$$F = const. \quad (6)$$

It was difficult to theoretically obtain friction coefficient C used for the definitional equation of R: Loss element-type (8) therefore friction coefficient C was determined by the experiment in this study. Moreover, for a threshold value, we used the smallest traveling speed of the cylinder that could be measured in the experiment.

I: Inertia_Mass element

$$V = \frac{1}{M_l} \int F \, dt \quad (7)$$

C: Elasticity_Bscrew element

$$F_n = K_n \int V_c dt \quad (8)$$

R: Loss_Bscrew element

$$F_R = C_B V_R \quad (9)$$

TF: Ball_screw element

$$V' = \frac{l}{2\pi} \omega' = \frac{l}{2\pi} (\omega - \omega_c) \quad (10)$$

$$\tau' = \frac{l}{2\pi} F' \quad (11)$$

I: Inertial Moment element

$$\omega' = \frac{1}{I_z} \int \tau dt \quad (12)$$

$$I_z = \frac{1}{2} M_0 r_0^2 \quad (13)$$

C: Coupling 素子

$$\tau_c = K_c \int \omega_c \, dt \quad (14)$$

Sf: Servomotor element

$$\omega = const \quad (15)$$

Analysis result and verification of adequacy

Table 1 shows parameters analyses and experiments. Analysis and experimental results in the case that feedback control was performed are shown in Figure 4 and analysis and experimental results in the case that control was not performed are shown in Figure 5. Comparing the two figures, it is understood that torques of a servomotor are reduced when feedback control is performed. Similar results have been obtained from the analyses and experiments therefore it is understood that a control system of an electro-pneumatic hybrid actuator can be analyzed by this simulation model.

As a behavior of the servomotor's torques, it has been understood that at first, a large torque acts on a servomotor with a constant load when it begins rising and then it rises with a constant torque. Subsequently, a large torque acts on the servomotor when the load suddenly changes and then the load rises with a constant torque.

Table 1 Simulation parameters

Parameters		Value
Valve effective area [m^2]	A_e	1.2×10^{-5}
Ratio of the specific heat of air [-]	K	1.4
Initial temperature [K]	T_0	293
Gas constant [J/kg K]	R	287.3
Cross sectional area of cyl. [m^2]	A	2.6×10^{-3}
Supplied pressure [MPa]	P_1	0.224
Weight [kg]	M_l	31.7
Elasticity of the nut [Nm/rad]	K_n	1.1×10^{-8}
Lead of the ball screw [m/r]	l	10.0×10^{-3}
Inertial Moment [kgm^2]	I_z	4.06×10^{-5}
Elasticity of coupling [Nm/rad]	K_c	120.9
Rotational Velocity [rpm]	ω	250
Mass 1 [kg]	m_1	10
Mass 2 [kg]	m_2	10
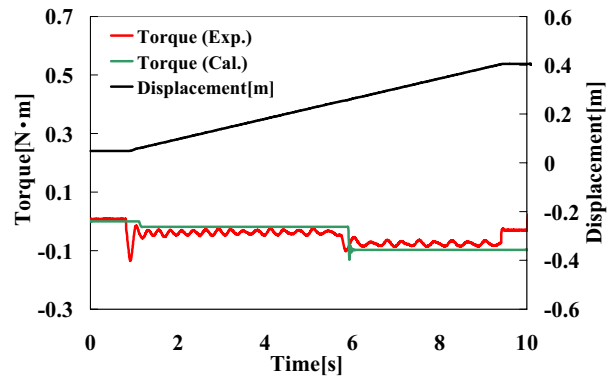
Figure 4 Calculation results (Feedback control)
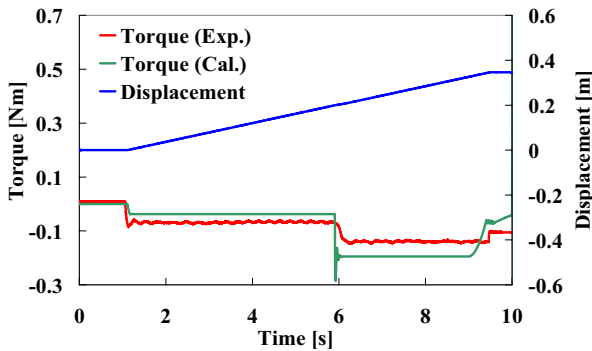
Figure 5 Calculation results (No feedback control)

VERIFICATION OF SERVOMOTOR TORQUE REDUCTION BY EXPERIMENT

Experimental parameters are shown in Table 2. Figures 6, 7 and 8 show the maximum torques that act on the servomotor when feedback control was not performed and Figures 9, 10 and 11 show the maximum torques that act on the servomotor when feedback control was performed.

When feedback control was not performed, the rise of the torques in sudden load variations exceeded the rated torque 0.3[Nm] of the servomotor in almost all cases. However, when feedback control was performed, in the case that Mass 1 was 10kg and 30kg and Mass 2 was 10kg or 20kg, the torque did not exceed the rated torque even when the rotating speed was 1500rpm. Furthermore, even when Mass 1 was 50kg however Mass 2 was 10kg, the servomotor worked within the rated torque even in the case that the rotating speed raised to 1000rpm. Therefore, the feed back control method we have proposed in this study is effective for reduction of torques acting on a servomotor, the authors believe.

Table 2 Experimental Parameters

No.	Mass1 [kg]	Mass2 [kg]	Rotational Vel. [rpm]
1	10	10,20,30	250-2000
2	30	10,20,30	250-2000
3	50	10,20,30	250-2000
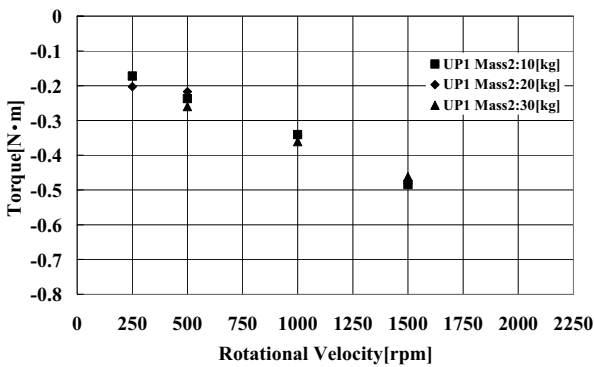
Figure 6 Mass1 10kg (without control)
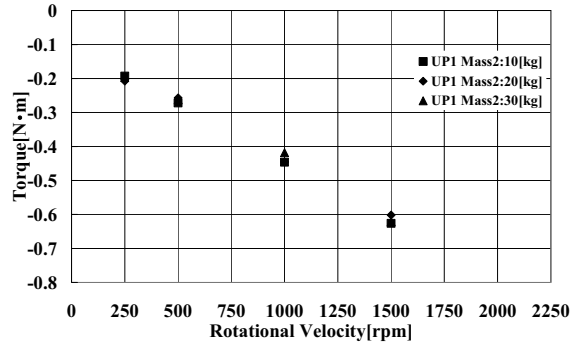
Figure 7 Mass1 30kg (without control)
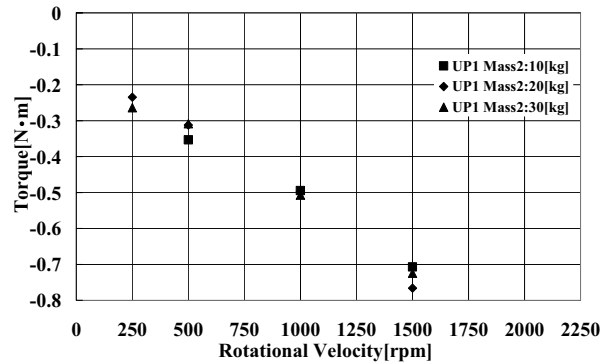
Figure 8 Mass1 50kg (without control)
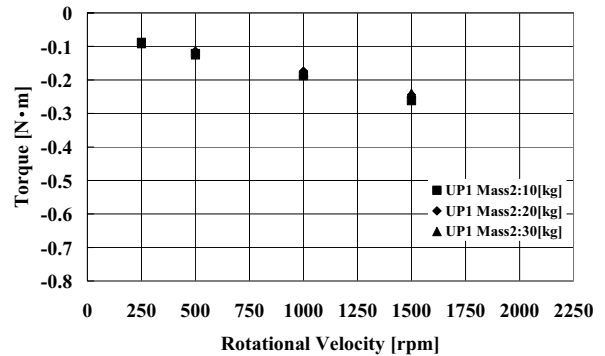
Figure 9 Mass1 10kg (with control)
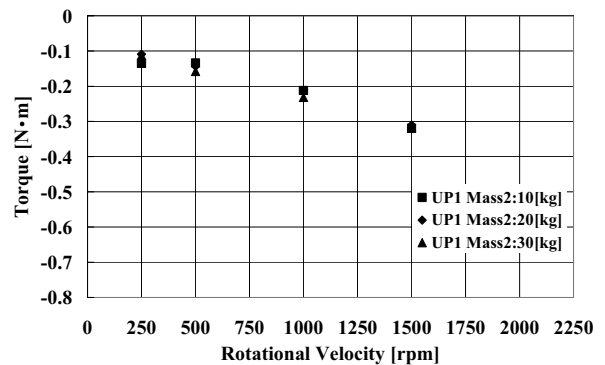
Figure 10 Mass1 30kg (with control)
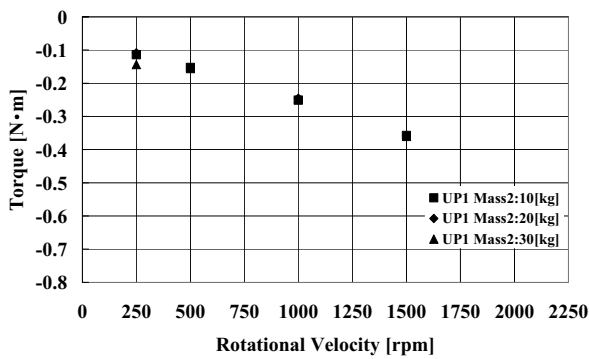
Figure 11 Mass1 50kg (with control)
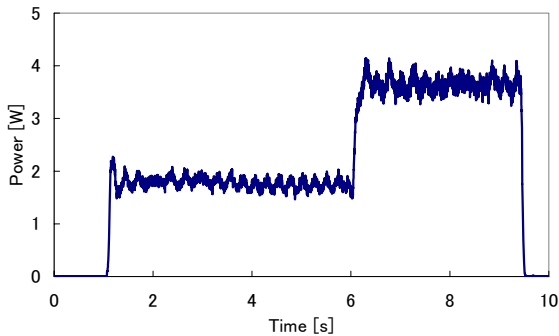
Figure 12 Power consumption (with control)
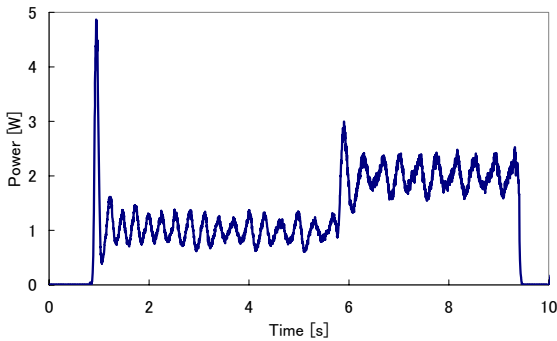
Figure 13 Power consumption (without control)

Table 3 Energy consumption

With control	12.4 [J]
Without control	21.1 [J]

The time dependencies for energy consumption of the servomotor with and without feedback control are shown in Figure 12 and Figure 13, respectively. When the actuator was driven using feedback control, large power is consumed during the starting period and pressure fluctuation becomes large. It is caused by time delay of the pressure control using feedback control.

Compared these two results, smaller amount of power is consumed under the feedback control. Table 3 shows energy consumptions during one stroke. Energy consumption of the servomotor with feedback control is half of that without feedback control. Therefore, it has been found that torques acting on a servomotor can be reduced by this control method.

CONCLUSION

We have proposed a feed back control method for an electro-pneumatic hybrid actuator. An analytical model of an actuator control system was already proposed however we have reverified its adequacy. Furthermore, as a result of the experiment for effects of the feed back control method, it has become able to operate the actuator within the rated torque range of a servomotor. The above result has revealed that it has become able to control a servomotor at the minimum value continuously. Moreover, it has been found that torques acting on a servomotor can be reduced by this control method.

This study has been supported by SMC Co., Ltd. for experimental equipment and so on. We would like to thank here for their cooperation.

REFERENCES

1. Shih, M. and Luor, N., Self-tuning Neural Fuzzy Control the Position of a Pneumatic Cylinder Under Vertical Load. Proc of 6th FLUCOME, Sherbrooke CANADA, CD-ROM, 2000.
2. Zhang, B., Bondgraph Modeling and Simulation of Dynamic Characteristics of a Pneumatic System with an Air Cushion Cylinder, 5th JFPS International Symposium, 2002, pp. 339-342.
3. Sakurai, Y., Tanaka, K. and Nakada, T., Dynamic Characteristic On An Electro-Pneumatic Hybrid Positioning System, 7th Int. Symp. on Fluid Control, Measurement and Visualization, 2004
4. Higo, H., Sakurai, Y., Nakada, T., Tanaka, K. and Nagayama, K., Dynamic Characteristic and Power Consumption on an Electro-Pneumatic Hybrid Positioning System, The 6th JFPS International Symposium on Fluid Power TSUKUBA, CDROM, 2005
5. Wylie E. B. and Streeter V. L., Fluid Transient in Systems, PRENTICE HALL 1993, pp. 2-9.
6. Rosenberg R.C. and Karnopp, D.C., Introduction to Physical System Dynamics, McGraw-Hill, 1983.
7. Thoma J., Simulation by Bondgraphs, Springer-Verlag, 1990.

P1-42

A STUDY OF ON/OFF SOLENOID ACTUATOR WITH POWER SAVING CIRCUIT

Myoung-Sub KIM*, Dong-Soo KIM*

*Roll-to-Roll PEMS Team, Nano Mechanical Systems Research Division
Korea Institute of Machinery & Materials
171, Jang-Dong, Yuseong-Gu, Daejeon, Korea
(E-mail: joseph@kimm.re.kr)

ABSTRACT

The technology of on-off solenoid valves is now considered as a core technology in the fields of the production line of semi-conductor chips and the micro fluid chips for medical applications. And on-off solenoid valves, which operate by compressed air, are characterized by high speed response, great repeatability and that the pressure on the cross sectional area of poppet is kept constant regardless of the fluctuation of the pressure exerted on the ports. The primary objective of this study is to compare the optimally designed solenoid valve with the actually produced one and to design a power saving circuit which can highly improve the efficiency by providing optimal current according to mechanical load. The power saving circuit can be adopted into the 0.35Watt micro valve which has been developed through this study and lower the power consumption of the valve to 0.1Watt. The absorbing force at 0.3mm stroke, the initial stroke of Plunger and Core, is very large. But the absorbing force at 0mm stroke when Plunger and Core are tightly stuck to each other is several newtons lower than that at the initial stroke, the valve still performs stable and flawless though. It means that with lower current consumption, it still performs stable. Based on that, we've designed the power saving circuit.

KEY WORDS

Micro valve, Solenoid, Power saving circuit, Design, High speed response, Great repeatability

INTRODUCTION

Recently, as new computer systems and various controlling technologies are being developed, on-off solenoid valves are able to be more precisely controlled and the application areas, including semi-conductor chip mounter, electronics production line, bearing auto-transmission line, injection molder, fatigue and vibration tester and etc., are getting diverse. Especially, the technology of on-off solenoid valves is now considered as a core technology in the field of technology-intensive process development such as semiconductor industry, and many studies are being conducted to design ones meeting the basic requirements for the improvement in the aspects of high

performance, low price, long life-time, high reliability and ergonomics and the compatibility with the environment[1].

In this study, we carry out the optimal design and modeling of a on-off solenoid valve and analyze it using Maxwell, a commercial analysis program, and then, after actually producing the valve, demonstrate the feasibility of its optimal design by comparing the simulation data of its optimal design with the data of its actual product.

Besides, we design a power saving circuit which can be adopted into the 0.35Watt micro valve which is developed through this study and lower the power consumption of the valve to 0.1Watt.

STRUCTURE & OPERATING MECHANISM

Figure 1 shows a schematic diagram of a micro valve. The major components of a micro valve include poppet which controls the direction of compressed air, plunger, stationary core and spring, o-ring which prevents leakage and gasket.

The basic operating mechanism of micro valves is as follows: when turn on the current in solenoid, poppet moves forward by the electromagnetic power and compressed air starts to flow from supply port to pressure port and when turn off the current in solenoid, poppet moves backward by spring force and supply port closes and the air is then expelled out of exhaust port. Based on this mechanism micro valves perform high speed reciprocating movement.

Table 1 shows the design specification and performance specification of the micro valve designed in this study.
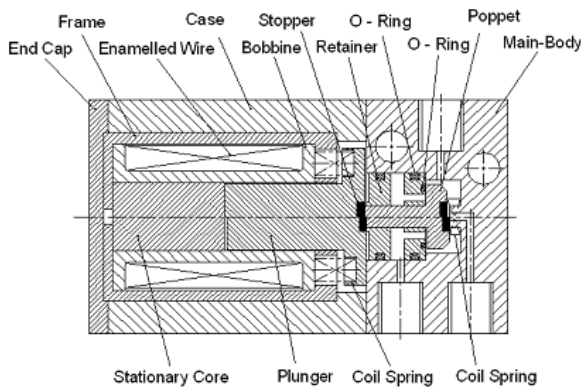
Figure 1 Schematic Diagram of Micro Valve

Table 1 Design Specification

Item	Value	Unit
Supply Pressure	3	bar
Supply Voltage	24	V
Electric Power	0.3	W
Port	3	㎜
Stroke	0.3	㎜
Coil Turn Number	6,500	turn
Coil Diameter	0.04	㎜
Coil Resistance	1.5	kΩ
Response Time	2	ms
Temperature Rise Value	50	℃
Magnetic Force	4.3	N
Spring Constant	0.015	N/㎜

DESIGN THEORY AND MAGNETIC FIELD ANALYSIS OF SOLENOID VALVE

Solenoid Design Theory

The two key technologies for micro valves are solenoid technology and poppet technology. As for solenoid design, a field analysis is the most important factor. The absorbing force(F) induced by solenoid can be obtained from the eq. (1)[2~3].

$$F = \frac{B_g^2 S}{2\mu_0} = \frac{10^7}{8\pi} B_g^2 S [N] \tag{1}$$

where B_g is the air gap flux density by permanent magnets, and μ_0 is the magnetic permeability.

From the eq. (1), the cross-sectional area of the movable element (S) can be expressed as the eq. (2).

$$s = \frac{8\pi \times 10^7 \cdot F}{B_g^2} \quad [\text{m}^2] \tag{2}$$

The radius of the movable element (γ_1) can be calculated by $\gamma_1 = \sqrt{(2\mu_0 F)/\pi B_g^2}$ and the magnetomotive force (U) can be obtained from the eq. (3).

$$U = NI = \frac{B_g l_g}{\mu_0} + \sum H_l l_l \quad [A] \tag{3}$$

The following eq. (4) show the correlations among the value determining the coil space (h), temperature (T), temperature rise values (θ_f and θ_{fi}).

$$\theta_f = (I^2 R)/(2\lambda l_m h) \quad [℃]$$

$$\theta_{fi} = (qp/2\lambda\xi T) \cdot (NI/h)^2 \quad [℃] \tag{4}$$

where θ_f is final temperature rise value, θ_{fi} is continuous certain temperature rise value, and NI is the width of the coil (h/β).

From the eq. (4), the height of the coil (h) can be expressed as the eq. (5).

$$h = 3\sqrt{\frac{q\beta p U^2}{2\lambda\xi\theta_f}} \tag{5}$$

where q is time rating, p is copper wire resistivity, λ is coil's thermal diffusivity coefficient, and ξ is coil's space factor.

The internal and external diameters of the coil ($r_1^{'}, r_2^{'}$) should be determined. Since the internal diameter ($r_1^{'}$) is determined by the external diameter of movable element plus coil's clearance plus Bobbin's thickness, $r_2^{'} = r_1^{'} + T$ and V=IR, then we can derive the eq. (6).

$$V = \frac{4p(r_1^{'} + r_2^{'})NI}{d^2} \quad [V] \qquad (6)$$

Therefore, the wire diameter of the coil (d) can be obtained from the eq. (7).

$$d = \sqrt{4p(r_1^{'} + r_2^{'} \cdot \frac{NI}{V})} \quad [mm] \qquad (7)$$

Thus, the number of coil layers (m) and the coil turn number (N) can be calculated from $m = T / d$ and $N = ((h/d) - 1)m$, respectively.

For temperature rise value, exciting current (I_h) should be previously determined. The mean length (l_m) and the total length (l_t) of the coils can be calculated from the eq. (8).

$$l_m = \pi(2r_1 + T), \quad l_t = Nl_m \qquad (8)$$

The coil resistance at 20 ℃ = $l_t \times$ resistance coefficient, the coil resistance at 100℃ = $1.314 \times R_c$, exciting current $I_h = V / R_h$, and magnetomotive force $U = NI_h$. Therefore, temperature rise value is determined by θ_f.

Solenoid Modeling and Analysis Results
In order to analyze the solenoid part of the micro valve, we conducted the solenoid modeling as shown in Figure 2. Figure 2 ~ Figure 6 shows the analysis results about the static and dynamic characteristics of the micro valve by the solenoid. Figure 2 ~ Figure 6 indicate that it starts to operate at 2ms.

As you can see in Figure 6, the overall changes in the current can be largely divided into 3 sections: A, B and C. In A section, the movement of the plunger is very little and the current is increasing. In B section, the movement of the plunger is getting faster and the current is decreasing. And C section indicates the state after the movement of the plunger is done.
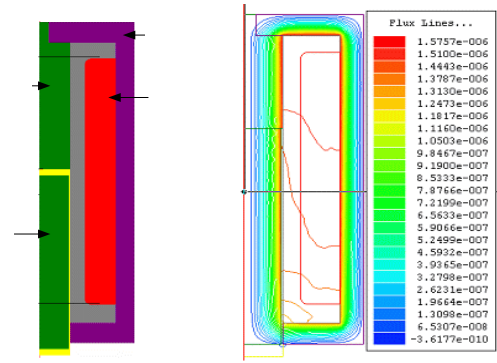
Figure 2 Modeling of Solenoid
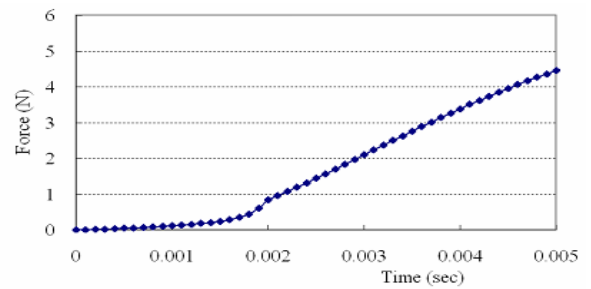
Figure 3 Force vs. Time
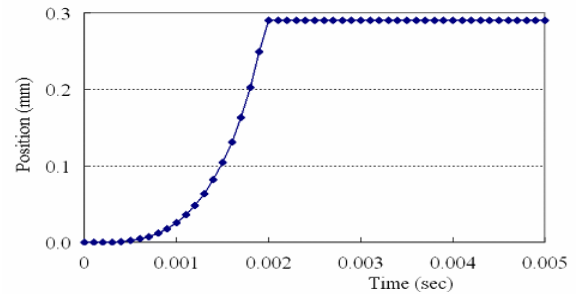
Figure 4 Position vs. Time
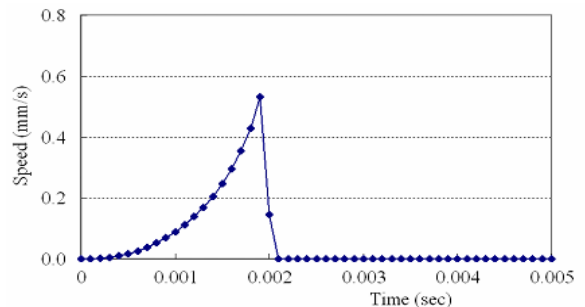
Figure5 Speed vs. Time
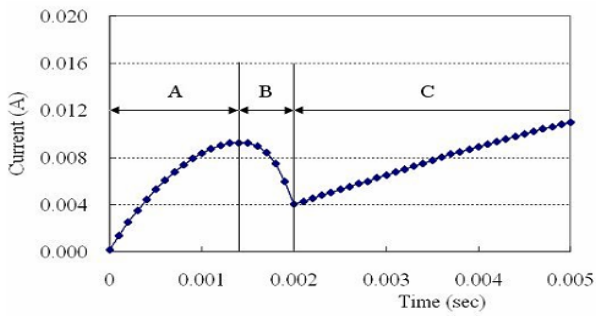
Figure 6 Branch Current

EXPERIMENTATION OF ON-OFF MICRO VALVE

Development of Solenoid Valve

Based on the solenoid modeling above, we produced an actual micro valve as shown in Figure 7. Besides, in order to determine the performance of the actual micro valve, we developed the performance testers as shown in Figure 8.

Figure 7 Micro Valve Parts
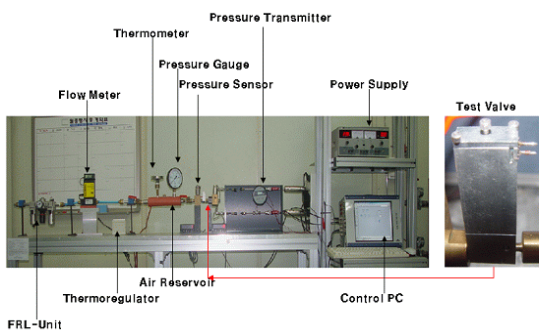
Figure 8 Performance Testers

Micro Valve Tests

Table 2 lists the results of the performance tests of the micro valve that we actually produced in this study and they are found to be similar to the results from the previous Maxwell simulation.

Table 2 Performance Tests

Item	Value	Unit
Supply Pressure	3	bar
Supply Voltage	23	V
Electric Power	0.345	W
Port	3	㎜
Stroke	0.3	㎜
Coil Turn Number	6,700	turn
Coil Diameter	0.04	㎜
Coil Resistance	1.6	kΩ
Response Time	3	㎳
Temperature Rise Value	50	℃
Magnetic Force	3	N
Spring Constant	0.015	N/㎜

Reliability Test of Micro Valve

Figure 9 shows the result of the surge current test and surge current occurs by the effect of different types of load such as voltage and power. If the open-and-close motion due to such mechanical characteristics is repeated several times, the same response concurrently occurs when ON/OFF is repeated. [4]

Figure 10 shows the result of the magnetic force test which was conducted by determining the force on the plunger with load cell after supplying the solenoid DC24V power and moving the plunger downward and upward. As the result, about 3N of absorbing force was observed to be occurring.
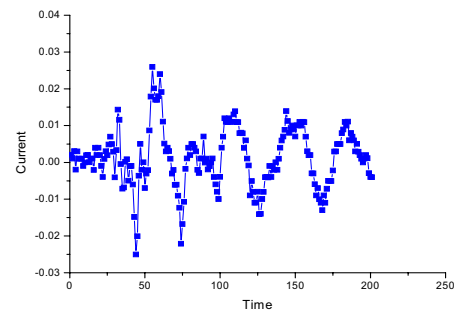
Figure 9 surge current
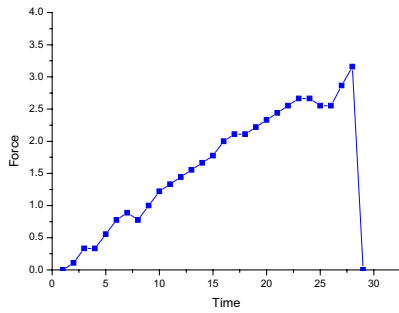
Figure 10 Magnetic Force Test

.
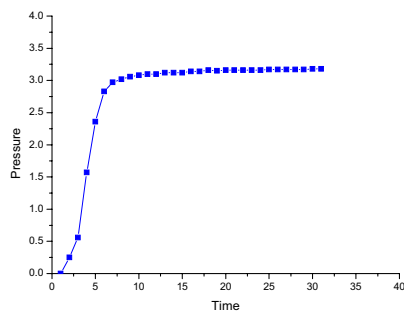
Figure 11 Dynamic Response Test
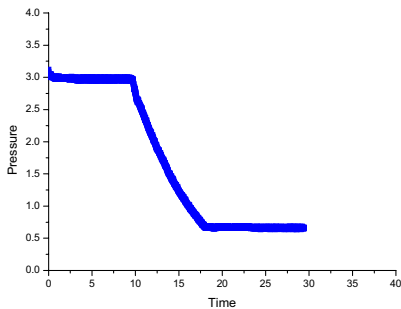
Figure 12 Flow Capability Test

Figure 11 illustrates the graph of the test results of the dynamic response and demonstrates the fast dynamic response by showing that it takes 3m for the pressure on the bottom to lift up to 80% of 3bar after opening the valve.

Figure 12 shows the results of the flow capability test which was performed under the condition of 3kgf/cm2 operating pressure after opening the valve. This graph illustrates that the pressure decreases from 3(bar) at 11.4(s) to 0.62(bar) at 20.16(s). That is to say, it takes

8.76(s) for the pressure to decrease from 3(bar) to 20% of it, 0.62(bar). The effective cross-sectional area(S) is 0.1mm2 and Cv is 0.0059.

MICRO VALVE WITH POWER SAVING CIRCUIT

Power Saving Circuit Design
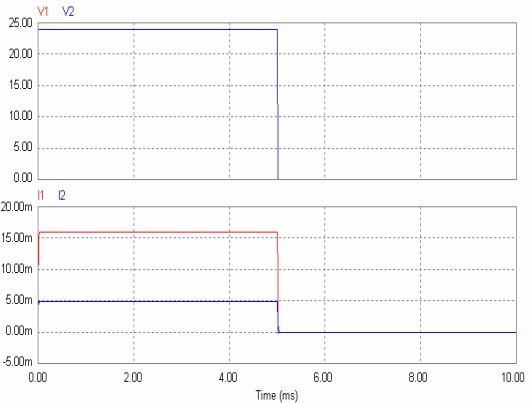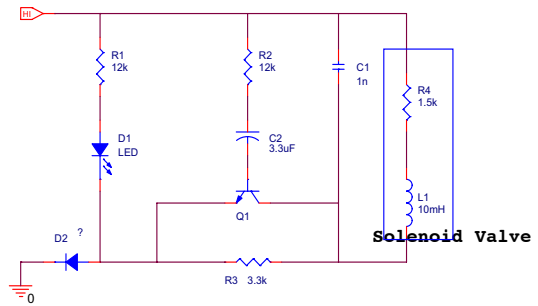
Figure 13 Power Saving Circuit Diagram

This power saving circuit can be adopted into the 0.35Watt micro valve which has been developed through this study and lower the power consumption of the valve to 0.1Watt.

. The absorbing force at 0.3mm stroke, the initial stroke of Plunger and Core, is very large. But the absorbing force at 0mm stroke when Plunger and Core are tightly stuck to each other is several newtons (N) lower than that at the initial stroke, the valve still performs stable and flawless though. It means that with lower current consumption, it still performs stable. Based on that, we've designed the power saving circuit.

For the valve without the power saving circuit (V1, I1), with 24V input, 15mA current flows in the coil. However, for the valve with the power saving circuit (V2, I2), approximately 5mA current flows in the coil and the current can be controlled by adjusting the element values

Power Saving Function Test of Power Saving Circuit
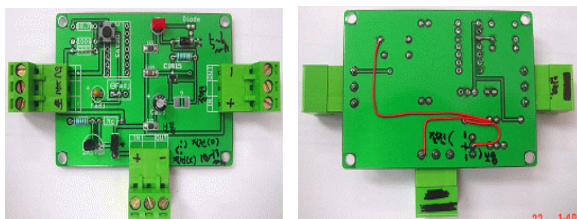
(a) the front side of the power saving circuit

(b) the rear side of the power saving circuit

Figure 14 Power Saving Circuit

Table 3 Comparison between Micro Valves With and Without the Power Saving Circuit

Case	Power (V)	current (A)	Power Consumption (Watt)
24V	23	0.015	0.345
24V with the power saving circuit	23	0.0045	0.1035

The power consumptions in Table 3 were calculated after determining the current when the plunger and the core were close to each other. From Table 3, we can see that the power consumption decreased from 0.345 Watt to 0.103 Watt.

CONCLUSION

In this study, we evaluated the performance of ultra power saving type pneumatic on-off micro valves through characteristic analysis and experiments and obtained the results as follows:

1. We designed a micro valve using the equivalent magnetic circuit method and analyzed it using Maxwell program and then, after actually producing the micro valve, demonstrated the feasibility of its optimal design by comparing the simulation data of its optimal design with the data of its actual product. As the result, the data of its actual product was found to be similar to the data of its optimal design.
2. It was demonstrated that strong enough electromagnetic force (3N) was exerted on the solenoid for the poppet to have the initial stroke (0.3mm) as high speed response (3ms) and any electromagnetic force was not emitted outside by yoke.
3. We equipped the 0.35Watt micro valve that we produced in this study with the power saving circuit and then calculated the power consumption by supplying power and determining the current when the plunger and the core were close to each other (i.e. at 0mm stroke). As the result, it was demonstrated that the power consumption decreased from 0.345 Watt to 0.103 Watt.

REFERENCES

1. B. W. Andersen, 1967, "The Analysis and Design of Pneumatic Systems", John Wiley & Son Inc., pp. 48~61.
2. W. L. Green, 1970, "The Poppet Valve-Flow Force Compensation," Proceedings of Fluid Power International conference, pp. S1~S6.
3. K. Kakano, H. Watanabe and G. Mao-ving, 2000, "Experimental Study for the Compensation of Axial Flow Force in a Spool Valve", Journal of the Japan Fluid Power System Society, Vol. 18, No. 6, pp. 475~482.
4. Herbert C. Roters, Electromagnetic Devices, John Wiley & Sons, USA, 1995.

P1-43

ANGLE MEASUREMENT AND CALIBRATION OF FORCE FEEDBACK DATAGLOVE

Zhongsheng SUN*, Gang BAO**, Xiaoning LI* and Jianping LU*

* SMC Pneumatics (Nanjing) Technical Center, School of Mechanical Engineering
Nanjing University of Science & Technology, Nanjing, 210094 China
(E-mail: Sun19780821@163.com)
** Pneumatics Center, Harbin Institute of Technology, Harbin, 150080 China

ABSTRACT

With the development of virtual reality technology, portable force feedback dataglove plays an important role in virtual assembly and telepresence system. Angle measurement is a basic function of force feedback dataglove, in which the measurement accuracy and calibration are often considered as unsolved problems in previous research. For solving these problems, some work is conducted with an exoskeleton force feedback dataglove using pneumatic artificial muscles as actuators. First, a measurement model of the finger flexion angle based on the theory of four-bar-linkage motion stabilization is built. The effect of structure parameter of linkage on the angle measurement and force feedback is analyzed, which has provided a help for the choice of linkage parameters and improved the accuracy of measuring angle. Then a new calibration method, which is called the "four-posture calibration" based on standard block and genetic algorithm, is proposed. Taking index finger as an example, the process of calibration is introduced in detail. Experiment has shown that with the new calibration method more accurate results can be obtained than that in previous work.

KEY WORDS

Virtual reality, Force feedback, Dataglove, Calibration

INTRODUCTION

Virtual reality can be defined as the user's real-time multimodal interaction with a computer-generated world, which provides a real-time immersive environment that integrated several new communication modalities, such as stereo graphics, three-dimensional sound, force or tactile feedback and even taste and smell, by means of hardware such as head mounted display, stereoglass, dataglove, etc. By providing these sensorial interactions, virtual reality makes the user feel immersed in the simulation or application of the virtual environment. Current applications of virtual reality include virtual assembly, teleoperations and robotic control, etc.

In recent years, haptic interface, especially the portal force feedback dataglove[1~4] has been attracting great attention. Dataglove, measuring directly or indirectly joint angles of human hand and driving a virtual hand, provides a real-time interaction between user and virtual environment in a natural manner. The quality of interaction is much dependent on the accuracy of angle measurement. However, human hands are different in sizes and shape and the glove wearing positions are often changed more or less with different persons or at different time. This will cause measurement errors. In order to decrease the measurement errors caused by the hand sizes and wearing positions, dataglove must be calibrated before use. The structure of dataglove and the

calibration results have much affection on the accuracy of measurement.

For solving problems above-mentioned, some research work is conducted with an exoskeleton force feedback dataglove using pneumatic artificial muscles as actuators. The research work involves designing the whole structure of a dataglove, building a measurement model of the finger flexion angle, suggesting a new calibration method named the "four-posture calibration" and making necessary experiments.

FORCE FEEDBACK DATAGLOVE

The force feedback dataglove shown in Fig.1 can be used to measure the flexion angles of the thumb, index and middle fingers, and provide force feedback with every joint. The work principle of single joint is shown in Fig.2.
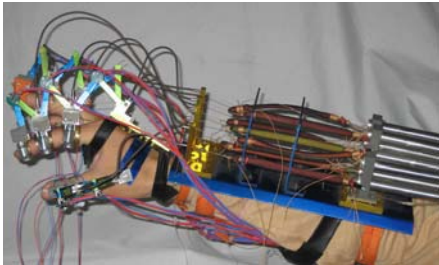
Figure 1 Force feedback dataglove
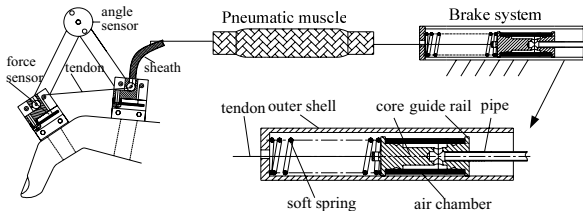
Figure 2 Work principle of single joint

The process can be described as follows. When a hand moves naturally, the angles of links are measured by the angle sensor and the flexion angles of joint are calculated according to the trigonometry of the links. The brake air chambers in deflation condition are not in contact with the outer pipe and only the smooth air chamber slider is in contact with the outer pipe. Therefore the friction is less. A rope drives pneumatic muscle to move with brake air chamber so as to compress the spring. When the hand moves from flexion to extension, the compressed spring makes the muscles and brake air chamber go to the original position. When virtual hand grasps the object in the virtual environment, the inflated air chamber is braked when contacting the outer pipe. Then, the pneumatic muscle is inflated according to the forces calculated from the virtual environment. The user thus feels the force feedback

sensation. The force sensor could measure the value of force and provide the feedback control.

The measurement mechanism and force feedback of single joint are shown in Fig.3. The planar four-bar mechanism is composed of one active joint O_1 and three passive joints. The angle relation between linkages is unique, i.e., if one angle is known, the other angles can be solved according to the trigonometry. The four-bar mechanism consisting of finger phalanx and linkages is equal to the four-bar O_1ABC. The angle α between the linkage AB and BC is measured by a non-contact magnetoresistance sensor. The relation between the joint flexion angle θ and α is indicated in Eq. (1) according to the law of cosines.

$$\theta = \beta_1 + \beta_2 + \beta_3 - 180° \quad (1)$$

Where

$$\beta_2 = \arcsin(h_1 / \sqrt{h_1^2 + h_2^2}) \quad (2)$$

$$\beta_3 = \arcsin(h_3 / \sqrt{h_3^2 + h_4^2}) \quad (3)$$

$$\beta_1 = \arccos(\frac{h_1^2 + h_2^2 + h_3^2 + h_4^2 - (2l_1 \sin(\alpha/2))^2}{2\sqrt{h_1^2 + h_2^2}\sqrt{h_3^2 + h_4^2}}) \quad (4)$$

Where β_2 and β_3 are invariable and determined after the dataglove wearing, h_i ($i = 1, 2, 3, 4$) are the calibrating parameters.

The output force of pneumatic muscle exerts on the finger through the tendon-sheath system. The torque at finger joint is:

$$\tau_m = F_m \sqrt{h_1^2 + h_2^2}\sqrt{h_3^2 + h_4^2} \sin\beta_1 /(2l_1 \sin\frac{\alpha}{2}) \quad (5)$$
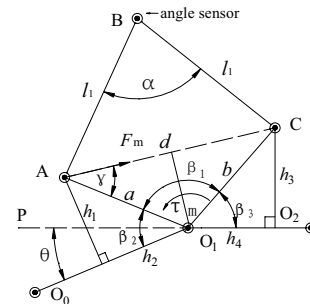
Figure 3 Measurement mechanism and force feedback of single joint

ANALYSIS OF STRUCTURE PARAMETER

From Eq. (1), (5), it can be seen that the measurement of flexion angle and torque are related to the link length. The angle θ is calculated by the angle α according to

the trigonometry. The angle range of finger flexion is definite. At the finger flexion range, the larger the variation of link angle is, the higher the measurement accuracy of α. Eq. (1) can be expressed as the following after derivation and simplification:

$$k = \left| \frac{d\alpha}{d\theta} \right| = \left| \frac{ab(\sin(\theta - \beta_2 - \beta_3))}{l_1^2 \sin \alpha} \right| \qquad (6)$$

The coefficient k denotes the ration of θ to α in unit time. The bigger the coefficient k is, the larger the variation of α corresponding to the unit variation of θ.
The force feedback of dataglove can be realized if the torque at the finger joint caused by contraction force of muscle is equal to the drive torque. When the output force of artificial muscle is definite, the longer the arm of force at the joint is, the bigger the torque and the heavier the grasping object. The effect of structure parameter can be analyzed using the torque at the joint caused by the unit force of muscle.
The structure parameters of four-bar mechanism include l_1, h_1, h_2, h_3, h_4 shown in Fig.3. Taking PIP joint of index finger as an example, the effect of linkage parameter on the coefficient k and the torque of unit contraction force is analyzed as follows.
The value of h_1, h_2, h_3, h_4 is 15,10,15,10mm respectively, and the value of l_1 is 25,30,35mm respectively. The coefficient k shown in Fig.4a) is decreased with the increase of l_1. The torque is shown in Fig.4b). The variation of l_1 has no effect on the torque. In view of angle measurement, the length l_1 of link should be as small as possible.
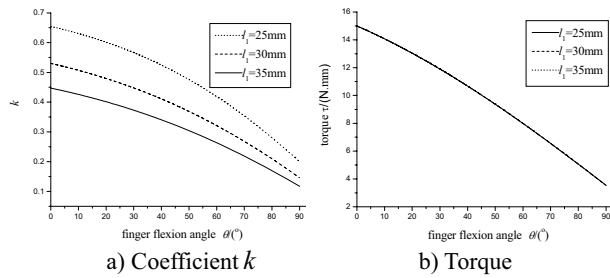
a) Coefficient k b) Torque
Figure 4 Effect of l_1

The value of h_2, h_4, l_1 is 10, 10, 30mm respectively, and the values of h_1, h_3 are 12, 15, 20mm respectively. The coefficient k shown in Fig.5a) is increased with the increase of h_1, h_3. The torque is shown in Fig.5b). The torque is increased with the increase of h_1, h_3. From the analysis above, the length h_1, h_3 of link should be as big as possible.
The value of h_1, h_3, l_1 is 15, 15, 30mm respectively, and the values of h_2, h_4 are 8, 10, 12mm respectively. The coefficient k shown in Fig.6a) is increased with as the increase of h_2, h_4. The torque is shown in Fig.6b). The torque is decreased with the increase of h_2, h_4. From the

analysis above, the length h_2, h_4 of link should be as small as possible, but the variation of h_2, h_4 has less effect on the coefficient k and torque.
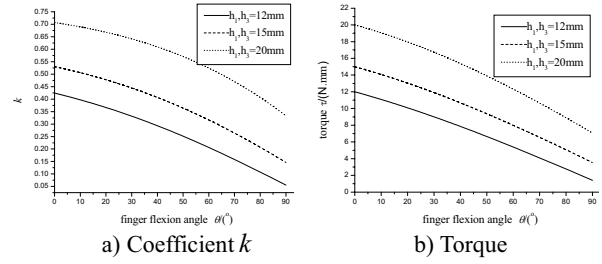
a) Coefficient k b) Torque
Figure 5 Effect of h_1, h_3
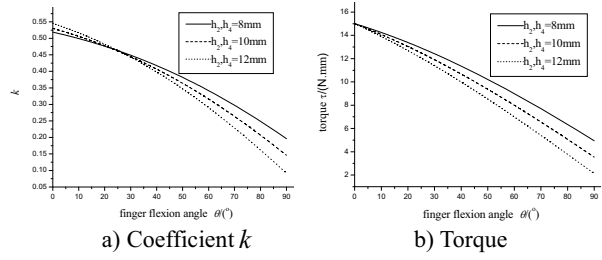
a) Coefficient k b) Torque
Figure 6 Effect of h_2, h_4

From the analysis above, it can be seen that the length l_1 only has effect on the angle measurement and its value should be as small as possible. However the value of h_1, h_3 should be as big as possible. In view of decreasing the whole weight, the values of every link parameter should be as small as possible. In the meantime, every parameter should meet the constraint condition as follows:
1. When the finger flexion angle is 0°, the sum of l_1 should be greater than the sum of h_2 and h_4, that is:

$$2l_1 > h_2 + h_4 \qquad (7)$$

2. When the finger flexion angle is 90°, the following condition should be met:

$$2l_1 > \sqrt{(h_1 + h_4)^2 + (h_2 + h_3)^2} \qquad (8)$$

3. When the finger flexion angle is 90°, the distance from O_1 to AC should be greater than 0. That is:

$$\sqrt{h_1^2 + h_2^2} + \sqrt{h_3^2 + h_4^2} > \sqrt{(h_1 + h_4)^2 + (h_2 + h_3)^2} \quad (9)$$

And

$$h_1 > h_2 \quad \text{or} \quad h_3 > h_4 \qquad (10)$$

Because the diameter of finger and the length of finger phalange are different and their values are not easy to measure accurately, the values of structure parameter

h_1, h_2, h_3, h_4 are only approximately estimated and determined through calibration after wearing the dataglove. The values l_i at DIP, PIP, MP joint of index and middle finger are 25, 30 and 35mm respectively. The values l_i at DIP, PIP joint of thumb finger are 25, 35mm respectively. The distance from point A or C to the surface of finger is 17mm.

CALIBRATION OF DATAGLOVE

Calibration method
Calibration is the initialization of angle measurement, which is indispensable before using the dataglove. The lengths of the linkage AB and BC are known. The mapping relation between θ and α can be calculated as long as the values of h_1, h_2, h_3, h_4 are known. The hand size of a person varies and therefore the relative position of the glove with respect to the hand varies with each wearing. The size and geometry of a hand and the relative position of the glove with respect to the hand together determine the values of h_1, h_2, h_3, h_4. Dataglove should be calibrated to obtain the real values of h_1, h_2, h_3, h_4 before use.
For the exoskeleton dataglove, the two-posture calibration method[3,5] is adopted in the previous research which supposed that the value of h_2 is equal to the value of h_4 or that the values of h_1, h_3 are known. But it is difficult to ensure the complete equality of the value of h_2 and h_4 and measure the length of h_1, h_3 accurately. This causes a bigger calibration error and then affects the measurement accuracy of finger flexion angle.
In order to decrease the calibration error, the dataglove is calibrated using the four postures of hand, which is constrained by the standard block in Fig.7 with four known angles (0°,30°,60°,90°). Then set the finger joint to the known positions respectively, relate the sensor values to those known positions and get four group angles (θ, α). Thus the parameters h_1, h_2, h_3, h_4 are calibrated by the above four group angles.
Eq. (1) can be expressed as the following equation group including the above four group angles. For $i = 1$, 2, 3 and 4

$$h_1{}^2 + h_2{}^2 + h_3{}^2 + h_4{}^2 + 2\cos\theta_i(h_2 h_4 - h_1 h_3) +$$
$$2\sin\theta_i(h_1 h_4 + h_2 h_3) = (2l_1\sin(\alpha_i/2))^2 \quad (11)$$

The solution of the nonlinear equation group (11) can be converted into an optimization problem and solved by the genetic algorithms. Simulation and experiment results demonstrate that more accurate calibration parameters and smaller calibration errors [6] can be obtained by the calibration method based on the genetic algorithms.
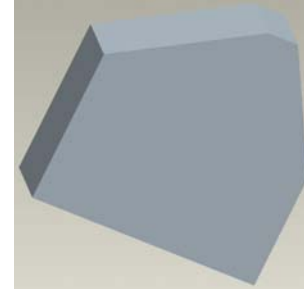
Figure 7 Standard block

Calibration process
Because there is the same structure with the index and middle finger, in this paper it is reasonable to take index and thumb finger as an example for introducing the calibration process and results. Moreover only the calibration of PIP joint of index finger is introduced in detail since the calibration process for every joint is the same. In order to clearly illustrate the calibration process, in Fig.8 only one finger is demonstrated wearing the exoskeleton dataglove. The calibration process of wearing the whole dataglove is identical.
When wearing the dataglove, firstly, the index finger should stretch and put on the side of the standard block shown in Fig.8a). Write down the angle α corresponding to the joint flexion angle θ when it equals to 0 degree. Then bend the joint to the other angle of standard block in turn and write down the angle α respectively shown in Fig.8b), c), d). In this case for Fig.8, the four group angles(θ, α) are (0°,34.43°),(30°,58.34°),(60°, 81.04°), (90°,100.01°).
After obtaining the above four group angles, the next step is to measure the values of every parameter with ruler approximately. The upper and lower limits of parameters are determined according to the measuring values, which are as follows:

$$20 < h_1 < 30; 5 < h_2 < 12; 20 < h_3 < 30; 7 < h_4 < 15 \quad (12)$$

Besides the Eq. (7) ~ (10), the constraint conditions should also include the following conditions according to the wearing position.

$$h_1 < h_3 \,\&\, h_2 < h_4 \quad (13)$$

Solved by the genetic algorithms, the calibration results of PIP joint are shown in Table 1. E_{max} is the maximum error between the finger flexion angle calculated through calibration results and the angle of standard block.
The four group angles(θ, α) of MP joint for index finger are (0°, 60.08°), (30°, 85.41°), (60°, 109.3°), (90°, 128.4°) respectively. Because the value h_3 of PIP joint has been obtained by calculation, the upper and lower limit of h_1 for MP joint can be reduced. The upper and

lower limit of other parameter is determined according to the values measured using ruler. They are as follows:

$$24.99 < h_1 < 26; 20 < h_2 < 25; 25 < h_3 < 30; 10 < h_4 < 16 \quad (14)$$

The constraint conditions should include the following conditions according to the wearing position.

$$h_1 < h_3 \ \& \ h_4 < h_2 \quad (15)$$

The calibration parameters of MP joint are shown in Table 1.
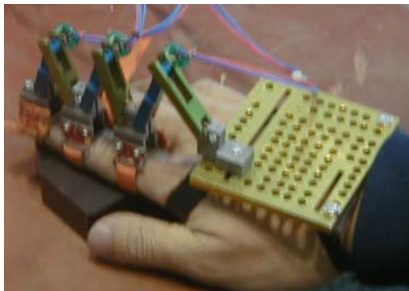
a) 0°
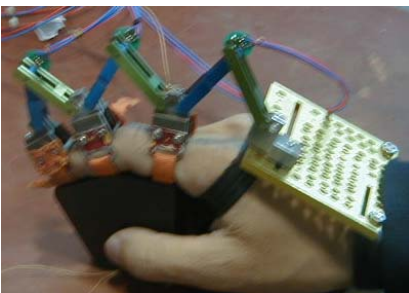
b) 30°
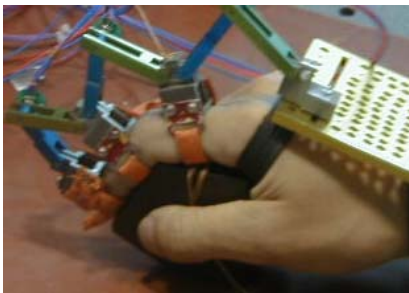
c) 60°
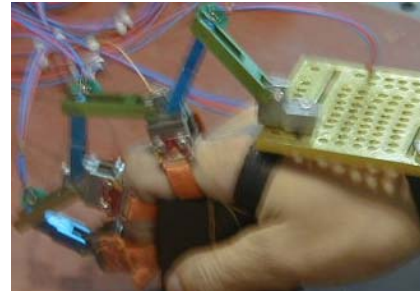
d) 90°

Figure 8 Calibration of PIP joint for index finger

The range of flexion angle for DIP joint (0~70°) is smaller than that for PIP and MP joint and unable to bend to 90°. The angles of DIP joint are not accurate when the finger bends to the standard block. In the research of Lee [7], it is demonstrated that the relation of flexion angle between PIP and DIP joint is described in following formula:

$$\theta_{DIP} = 0.46 \times \theta_{PIP} + 0.083 \times \theta_{PIP}^2 \quad (16)$$

The flexion angle θ of DIP joint can be calculated by the flexion angle of PIP joint according to Eq. (16) and the corresponding link angles α are written down. The upper and lower limit of h_3 for DIP joint can be determined according to that of h_1 for PIP joint. The constraint conditions should include the condition $h_1 < h_3$. The calibration parameters of DIP joint are shown in Table 1.

After finishing the calibration, the length of MP and PIP phalange can be obtained. The distance between the two axes of base is 10mm. The length of MP Phalange, 42.96mm, is the sum of h_4 for PIP joint, h_2 for MP joint and the base length. The length of PIP Phalange, 24.2mm, is the sum of h_4 for DIP joint, h_2 for PIP joint and the base length. The variation of the ratio of every phalange's length to the metacarpal's length is only 1-2%. The length of DIP phalange, 16.72mm, can be calculated according to the length of MP and PIP phalange and the ratio [8]. The accurate value of every phalange is obtained through calibration, so the driving torque can be calculated by the flexion angle and the values of each phalange [9].

Table 1 Calibration results

	h_1	h_2	h_3	h_4	E_{max}(°)
DIP joint of index finger	20.0002	7.1250	22.2694	7.1270	0.6
PIP joint of index finger	22.4364	7.0564	24.9915	10.5156	0.3
MP joint of index finger	24.9985	22.4404	28.6205	11.9180	1

The calibration process of DIP and PIP joint for thumb finger is almost the same to that of index finger. The range of flexion angle for DIP and PIP is 0~75 or 90°. The four-posture calibration is adopted if the finger can bend to 90°. If the finger can't bend to 90°, the three-posture (0°, 30° and 60°) calibration is adopted, but the error would be increased. The maximum error is less than 1.5°, which is a satisfied accuracy to the application of virtual reality (e.g., for telerobotics, virtual assembly).

When the finger bends to the angle of standard block, in order to prevent the difference between the actual flexion angle of finger and standard angle, the method of averaging the multi-measurement values is adopted to decrease the errors.

CONCLUSIONS

Focus on the problems in the measurement accuracy and calibration, an exoskeleton force feedback dataglove is developed using pneumatic artificial muscles as actuators and some theoretical and experimental work are conducted with the dataglove. First, a measurement model of the finger flexion angle based on the theory of four-bar-linkage motion stabilization is built. The effect of structure parameter of linkage on the angle measurement and force feedback is analyzed, which has provided a help for the choice of linkage parameters and improved the accuracy of measuring angle. Then a new calibration method, which is called the "four-posture calibration" based on standard block and genetic algorithm, is proposed. Taking index finger as an example, the process of calibration is introduced in detail. Experiment has shown that with the new calibration method more accurate results can be obtained than that in previous work. In addition, the actual size of each phalange can be obtained as appendix, which can solve the calculation of driving torque of dataglove.

REFERENCES

1. M. Bouzit, G. Burdea. The Rutgers Master II-New Design Force-Feedback Glove. IEEE/ASME Transactions on Mechatronics. 2002, 7(2):256-263
2. Virtual Technologies, 1999. CyberGrasp User's Guide. Virtual Technologies Inc., Palo Alto, CA
3. M. Bouzit. Design, Implementation and Testing of a Dataglove with Force Feedback for Virtual and Real Objects Telemanipulation. Doctor degree dissertation, University of Pierre ET Marie Curie, 1996, pp.12-45
4. Y. Kunii, Y. Nishino, T. Kitada, H. Hashimoto. Development of 20 DOF Glove Type Haptic Interface Device-Sensor Glove II. IEEE/ASME International Conference on Advanced Intelligent Mechatronics. Tokyo, 1997, pp.132-137
5. Wei Jun, Wang Jiashun, Wang Tianmiao, You Song, Li Jianfeng. Design and experiment of a new type data glove orientated to virtual manufacture and assembly. Chinese Journal of Mechanical Engineering. 2000, 36(2), pp.91-94
6. Sun Zhongsheng, Bao Gang, Li Jun, Wang Zuwen. Research of Dataglove Calibration Method Based on Genetic Algorithms. Proceedings of the 6th World Congress on Intelligent Control and Automation. Dalian, 2006, pp.9429-9433
7. J.W. Lee, K. Rim. Maximum Finger Force Prediction Using a Planar Simulation of the Middle Finger. Proceedings of the Institution of Mechanical Engineers. 1990, 204, pp.160-178
8. K. N. An, E. Y. Chao, W. P. Cooney. Normative Model of Human Hand for Biomechanical Analysis. Journal of Biomechanics. 1979, 12, pp.775-788
9. Bao Gang, Sun Zhongsheng, Wang Zuwen. Force Feedback Dataglove Based on Pneumatic Artificial Muscles. Chinese Journal of Mechanical Engineering. 2006, 19(4), pp.588~593

P1-44

MEASURING TRUST OF HUMAN OPERATORS IN NEW GENERATION RESCUE ROBOTS

Eui PARK, Quaneisha JENKINS, and Xiaochun JIANG

Department of Industrial and Systems Engineering
North Carolina A&T State University
1601 E Market Street, Greensboro, NC 27411 U.S.A.
(E-mail: park@ncat.edu)

ABSTRACT

The utilization of mobile rescue robots in dynamic environments decreases the risk to emergency personnel in the field. Recent efforts to improve rescue robot design by using new fluid-power technology provide opportunities of studying the changes in metrics of human-robot interaction (HRI), such as trust. Trust is one of the most critical factors in urban search and rescue missions because it can impact the decisions human make in uncertain conditions. This research is to develop an instrument that can be used to measure trust in human-robotic interaction, which will allow us to collect data for building a quantitative model of trust in HRI. As the first step in this effort, a pilot study was conducted to determine the validity of an instrument to measure the appropriate dimensions of trust in this new human-robot system.

KEY WORDS
Human-Robot Interaction, Rescue Robot

INTRODUCTION

Urban search and rescue (USAR) missions are becoming more and more important in recent years, From the collapse of the World Trade Center towers to Hurricane Katrina, resuce missions are oftern done in hazardous environments. To avoid putting emergency personnel in harm's way, the use of mobile robots is a good alternative. Untethered robots are intelligent and have good maneuverability in conditions and environments that may otherwise be potentially hazardous to humans. Rescue robots are often used to gather and transmit vital information about their location and operational status to their remote operator(s). It may detect victims, check for signs of life using cameras, microphones and sensors, and even provide minor aid if possible. The cooperative relation between operator and robot enhances the coordination of search and rescue efforts and can increase the chances of lives being saved. Although there are many different types of rescue robots used in urban search and rescue, most untethered search and rescue robots are commonly powered by batteries that run out quickly and electric motors that do not provide enough force or power for rescue missions over extended periods of time [1]. Batteries and motors also create extra weight which limits the autonomy of the robot. Furthermore,

human-robot interfaces (HRI) for rescue robots often tend to be hard to use, confusing, and suffer from both information overload and poor situational awareness [2]. With the development of fluid power technology, rescue robots will have a higher power density, weigh less, and will be more flexible than the electric power source robots (Binnard, 1995). For these reasons, a strong interest has recently been shown in fluid-powered rescue robots. Fluid power is the technology that deals with the generation, control, and transmission of pressurized fluids [2]. However, the use of a specific power source for robots certainly impacts the design of the robotic interface. The power source of a robot can affect the interface design of the robot, which will impact how data is relayed from the robot to the operator once it is deployed. Given these changes in design, the human-robot interaction (HRI) may be very different than in previous designs. Thus, opportunities remain for further improvement in the human-robot relationship. As part of the recent efforts in developing and utilizing new fluid power technology, a compact rescue crawler (CRC) is being utilized as an initial test bed at the Center for Compact and Efficient Fluid Power (CCEFP), a National Science Foundation (NSF) funded Engineering Research Center.

ASSESSMENT OF HRI

HRI, within urban search and rescue missions, involves complex systems in dynamic, unstable environments where human and robot must work together, as well as individually. As can be seen in Figure 1, there are various HRI metrics that are influenced by the robot, the human, and the overall human-robot system [3].
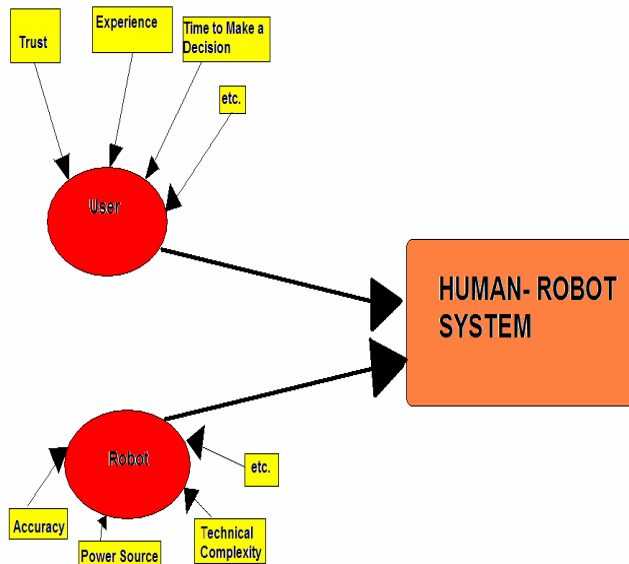
Figure 1: Representation of the Human-Robot System

Those measures include objective measurements, such as performance error of the robot, as well as subjective measurements, such as operator trust in the robot. Trust is one of the significant aspects in HRI urban search and rescue missions because it is influenced by variables within the system and has a significant effect on the output, or performance, of the overall system. The type of missions that the compact rescue crawler robot will be utilized for are characterized by a high degree of uncertainty [4]. Without operator trust in these situations, which involves teamwork between humans and robots, the team's performance can be severely impacted.

Traditionally, trust in human-machine or human-computer interactions is defined as a composite of several dimensions or components. For instance, Muir described trust in automation as "a composite expectation of the persistence of the natural and moral social orders, technical competent performance, and of fiduciary responsibility [5]" in 1994. A decade later, Lee and See, defined trust as "the attitude that an agent will help achieve an individual's goals in a situation characterized by uncertainty and vulnerability [6]." Although there has been research on trust in different human-machine systems since the 1980s, spanning

human-automation relationships and human-computer relationships, little research has been done dealing specifically with human-robot relationships. HRI in urban search and rescue is different from other human-machine systems in that the environments are characterized by a high degree of uncertainty, risk, and the human user is both supervisor and teammate with an artificial intelligence. Therefore, trust in HRI needs to be studied independently. Over the years, researchers have proposed that various dimensions of trust have characterized those dimensions differently. In 1985, Rempel et al. described trust as having three time dependent dimensions of predictability, dependability, and faith [7]. Later in 1992, Lee and Moray identified three dimensions of trust to be performance, process, and purpose [8]. In 2004, Uggirala identified several dimensions of trust to be competence, predictability, reliability, persistence, and overall trust in a system [9]. Some of the dimensions complement each other, are orthogonal to one another, or duplicate other studies; however, those previously mentioned apply to human-human, human-machine, and human-computer interactions. There has been little research on dimensions of trust that apply to human-robot interaction.

The objective of this research is to develop a tool that can effectively be used to measure trust in HRI for the new generation, fluid- powered rescue robot.

METHODOLOGY
Defining Trust Components
The first step in developing a tool to measure trust in human robotic interaction is to identify twelve (12) appropriate trust dimensions which are predictability, dependability, accuracy, helpfulness, power, adaptability, understandability, deceptive, fiduciary responsibility, experience, solidarity, and performance. Definitions of these 12 dimensions are listed in Table 1. Then, a three step procedure will be used to select and define each dimension as it applies to HRI. Subject matter experts will be consulted in this process.

Step 1: Ask each subject matter expert to define each dimension by generating a list of questions that can describe it.

Step 2: Ask each subject matter expert to rank the dimensions along with its questions based on its importance in measuring trust in HRI.

Stewp 3: Select the top eight (8) dimensions as well as the questions for each dimension that is identified and ask the subject matter experts to match the dimension with its defintion (questions). The resulting list will be the dimensions considered most applicable to HRI. A trust measurement instrument will be developed based on this list.

Table 1: List of Proposed Trust Dimensions

Dimensions	Definitions
Predictability	the degree of consistency and desirability of past behavior in a system that enable the user to develop a mental model of future system states [7]
Dependability	the degree of understanding the stable dispositions that guide the system's behavior [7]
Accuracy	the extent to which the system is free of error [9]
Helpfulness	the extent to which the system provides alternative solutions [11]
Power	the extent to which the user is able to control the behavior of the system [4]
Adaptability	the degree to which the system can change according to a situation [10]
Understandability	representing how well the operator perceives what the computer is doing [10]
Deceptive	the extent to which the system explicitly displays or says that it will act in a particular way, but doesn't in future states
Fiduciary responsibility	the degree to which the operator expects that the system will meet its design-based criteria [12]
Experience	based on the specific user's past encounters with the system [13]
Solidarity	the degree to which the user perceives the system shares a similar purpose to himself [4]
Performance	in regards to the overall human-machine system performance [8]

Trust Measurement Instrument Development
Using the list of trust dimensions, a trust measurement instrument will be developed. This instrument will be in a form of questionnaires. Each trust dimension has questions detailing what the dimension means. A Likert scale of 1-5 will be used for each dimension with 1 being strongly disagree and 5 being strongly agree.

Proposed Experiment
To assess the validity of the instrument, an experiment will be conducted as follows:

Subjects: Twenty field experts who have experience operating rescue robot in urban search and rescue (USAR) missions will be recruited to participate in the survey. Demographic information of the subjects as well as their experience and backgrounds will be collected.
Test Materials: A scripted USAR scenario will be given to each subject. They will be asked to complete a questionnaire containing the trust measurement instrument based on the scenario.
Test Procedure: Through email, each subject will be briefed with the purpose of the experiment followed by an informed consent form. Upon agreeing to participate, each subject will be given a USAR scenario and asked to fill out a questionnaire containing the trust measurement instrument. Clarification will be provided whenever necessary. Each subject will spend about half an hour to complete the experiemnt.
Data Collection: Upon collection of the questionnaires, a score of 1-5 will be assigned to each trust dimension from each subject.
Statistical Analysis: Both descriptive statistics such as mean and standard deviation as well as inferential statistics such as correlation analysis will be used. A stepwise regression model will then be used to develop a trust model that can be used to measure operator trust in HRI. Results from this analysis will also reveal the important dimensions of HRI.

DISCUSSION AND CONCLUSION
Possible future research work lies in validating the list of the dimensions, examining any underlying constructs of the dimensions, and determining the relationships between the dimensions themselves and overall trust in the human-robot system.

The purpose of this research is to develop an instrument that can be used to measure trust in human-robotic interaction. A literature review of trust in human-automation and human-computer systems was conducted to build a solid foundation in developing a list of the dimensions of trust most appropriate for HRI in USAR environments. An experiment is proposed to assess the validity of the tool for measuring trust in human-robot interaction for urban search and rescue missions utilizing compact crawler, fluid-powered rescue robots. It is expected that this instrument will contribute to measuring trust in human-robot interaction.

REFERENCES

1. Pachal, P., 2007, "Japanese Rescue Robot Scoops You to Safety," (1 December 2007).

2. Binnard, M. B., 1995. "Design of a Small Pneumatic Walking Robot," Ph.D. dissertation, Massachusetts Institute of Technology, Department of Mechanical Engineering

3. Steinfield, A., Fong, T., Kaber, D., Lewis, M., Scholtz, J., Schultz, A., and Goodrich, M., 2006. "Common Metrics for Human-Robot Interaction," Proceeding of the 1st Association for Computing Machinery (ACM) Special Interest Group on Computer-Human (SIGCHI)/ Special Interest Group on Artificial Intelligence (SIGART) conference on Human-robot interaction, March 2–4, 2006, Salt Lake City, Utah, USA. 33-40.

4. Bickmore, T. and Cassell J., 2001. "Relational Agents: A model and implementation of building user trust," Conference on Human Factors in Computing Systems, Proceedings of the SIGCHI conference on Human factors in computing systems, March 31 – April 5, Seattle, Washington, United States , 3(1), 396-403.

5. Muir, B. M., 1994. "Trust in Automation: Part I. Theoretical issues in the study of trust and human intervention in automated systems," Ergonomics, 37(11), 1905-1922.

6. Lee, John D and See, Katrina A., 2004. "Trust in Automation: Designing for Appropriate Reliance." Human Factors Journal, 46, 50-80.

7. Rempel, J.K., Holmes, J.G, and Zanna, M.P., 1985. "Trust in close relationships," Journal of Personality and Social Psychology, 49, 95-112.

8. Lee, J. & Moray, N., 1992. "Trust, control strategies, and allocation of function in human-machine systems," Ergonomics, 35, 1243-1270.

9. Uggirala, A., Gramopadhye, A. K., Melloy, B.J., Toler, J. E., 2004. "Measurement of Trust

10. Sheridan, T.B., 1995. "Human Centered Automation: Oxymoron or Common Sense?" IEEE International Conference on Systems, Man and Cybernetics, Intelligent Systems for the 21st Century. October 22 - October 25, Vancouver, BC, Canada, 823-828.

11. Lankton, N., and McKnight, H. 2007. "Trust in Technology: Using Expectation-Disconfirmation Theory to Predict Trust and Usage Intentions," MIS Quarterly (under first round)

12. Barber, B. ,1983, The Logic and Limits of Trust. Rutgers University Press, New Brunswick

13. Zuboff, S., 1988, In the Age of the Smart Machine: The Future of Work and Power. Basic Books, New York.

14. Delpish, R. & X. Jiang. 2007, " User-Centered Design for the Rescue Robot with Fluid Power"*Proceedings of Industrial Engineering Research Conference*, Nashville, TN

15. Hoffman, L. J., Lawson-Jenkins, K., & Blum, J. (2006). Trust Beyond Security: An Expanded Trust Model. *COMMUNICATIONS- ACM.* 49 (7), 94-102.

P1-45

WEARABLE MASTER-SLAVE TRANING DEVICE FOR LOWER LIMB CONSTRUCTED WITH PNEUMATIC RUBBER ARTIFICIAL MUSCLES

Daisuke SASAKI*, Toshiro NORITSUGU* and Masahiro TAKAIWA*

*Graduate School of Natural Science of Technology

Okayama University

3-1-1 Tsushimanaka, Okayama, 700-8530 Japan

(E-mail:[daisuke, toshiro, takaiwa]@sys.okayama-u.ac.jp)

ABSTRACT

The purpose of this study is to develop a wearable master-slave lower limb training device for a trainer and a trainee. The developed device is constructed with McKibben type rubber artificial muscles and an appliance, a torque sensor. In addition, to prevent applying an excessive torque to the trainee, a reaction torque from the trainee can be transmitted to the trainer by a bilateral type master-slave control system. In this paper, the structure of the developed device is discussed, and then the validity of the proposed device is evaluated from the experiments assumed a training.

KEY WORDS

Pneumatics , Artificial rubber muscle , Soft mechanism , Wearable robot

INTRODUCTION

Many kinds of power assist device have been developed to assist a hard work, rehabilitate a human body in recent years[1] − [5]. These devices are driven with various actuators such as a electric motor, a hydraulic cylinder and so on. Above all, a pneumatic artificial rubber muscle is effective to drive these device[4][5]. Since these devices used by a human is requried a safty and a light weight. This actuator has a mechanical flexibility by an air compressibility, a rubber material, and has a high power weight ratio. Therefore, this rubber muscle can realize a flexible and a light weight device by a simple mechanism.

The purpose of this study is to develop a master-slave lower limb training device for a trainer and a trainee. The developed master and the slave devices are constructed with McKibben type rubber artificial muscles and an appliance, a torque sensor. McKibben type rubber muscles are installed at the knee and the ankle joints of the appliance, respectively.

In this study, it is assumed that the master and the slave devices are used by the trainer and the trainee respectively, and that the trainer moves the trainee joint angles by moving the trainer's lower limb. To prevent applying an excessive torque to the trainee, a reaction torque from the trainee can be transmitted to the trainer by a bilateral type master-slave control system. In this paper, the structure of the developed device is discussed, and then the validity of the proposed device is evaluated from the experiments assumed a training.

WEARABLE MASTER-SLAVE

TRANING DEVICE

Figure 1, **2** show the structure and the overview of the developed device. McKibben type rubber muscles for a flexion and an extension are installed through a pulley to an appliance in the knee device. For example, when the flexion and the extension rubber muscles are increased and decreased the inner pressures from the balance states, the torque to flex the knee can be generated as shown in **Figure 3**(a). The extension torque can be also generated by decompressing and compressing the flexion and the extension rubber muscles. The weight is about 4.8[kg].

Side view   Front view
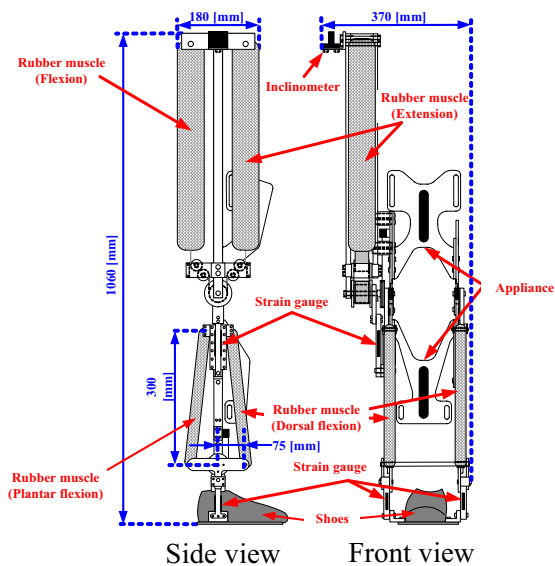
Figure 1 Structure of developed device

In the ankle device, rubber muscles for the dorsal and the plantar flexion are installed respectively. The dorsal and the plantar flexion mean the motions which bend and extend the ankle as shown in **Figure 4**. The movable angles at the knee and the ankle are limited from 0[°] to 100[°] by the knee joint and from -25[°] to 25[°] by the ankle rubber muscles. The generated torque from the rubber muscle is transmitted to the appliance through an aluminium plate, which is mounted a strain gauge. The generated torque can be detected from the strain of the aluminium plate.

McKibben type rubber muscle is constructed with the rubber tube. The rubber muscle is manufactured with a rubber tube and a polyester fiber tube. The fiber tube is the latticed tube weaved with a polyester
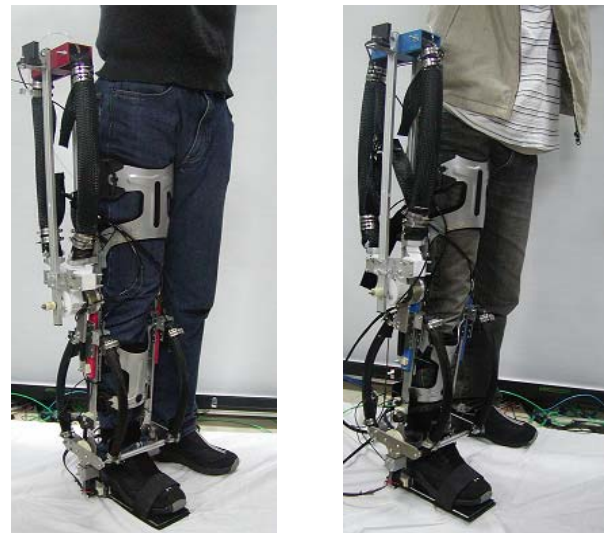
(a) Master device   (b) Slave device

Figure 2 Overview of device

fiber. When a compressed air is supplied into the rubber tube, the rubber tube expands to the radial direction. The radial expansion force of the rubber tube is converted to the axial contraction force as shown in **Figure 5**.
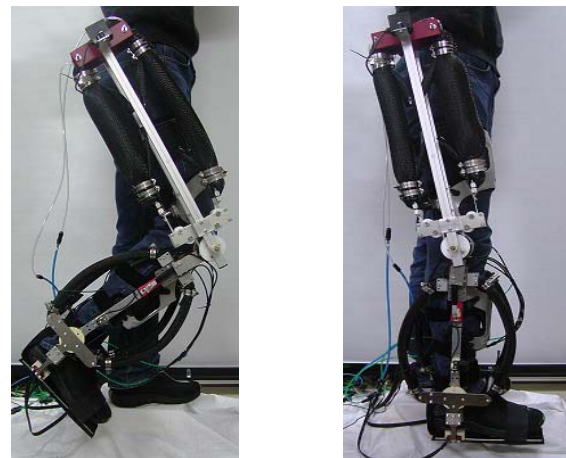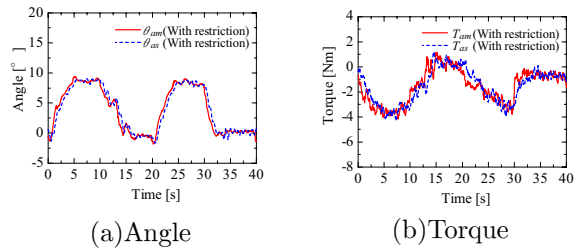

(a) Flexion   (b) Extension

Figure 3 Flexion and extension

In the knee device, the length and the outer and the inner diameter of the rubber tube are 396, 39.3, 30.0[mm], respectively. In the Ankle device, the length and the outer and the inner diameter of the rubber tube are 330, 20.7, 15.0[mm], respectively.

Figure 6 shows characteriscics of rubber muscle using the knee and ankle device. The rubber muscle is fixied with a force sensor and a sensor stage

as shown in **Figure 7**, and the fixed distance L_m is changed in order to measure the force at the each contraction length of rubber muscle. In the expriment, the generated force is measured at the each contraction length in a constant supplied pressure.
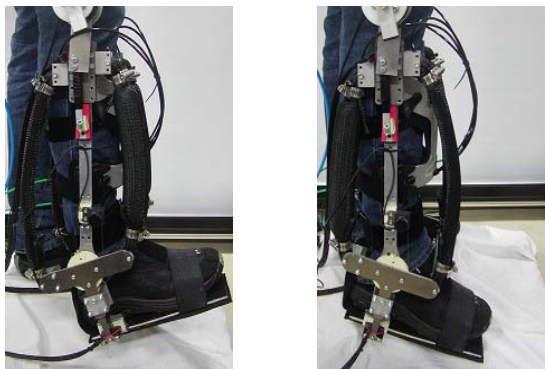
(a) Dorsal flexion   (b) Plantar flexion

Figure 4 Dorsal and plantar flexion
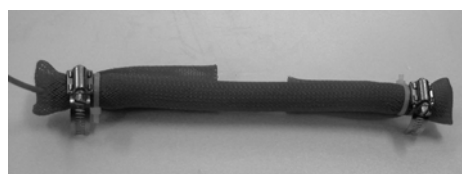
(a) Initial state
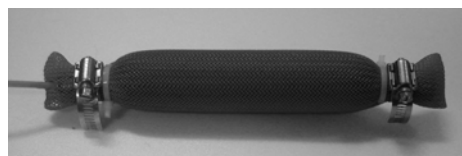
(b) Pressurized state

Figure 5 Overview of rubber muscle

From the force characteristics, the diameter of pulley at the knee is 40[mm], and the ankle rubber muscle is fixed at the distance 75[mm] from the ankle joint.

Figure 8, **9** show torque characteristics of master device. The joint angle of knee and ankle are defined as shown in **Figure 10**. In the figure, subscript m and s represent the master and slave device, and k and a represent the knee and ankle device, respectively. The flexion angle from the standing state is defined as a plus in the knee angles(θ_{km}, θ_{ks}), and the dorsal flexion angle is also defined as a plus in the ankle ones(θ_{am}, θ_{as}). These characteristics in Figure 8, 9 are measured to verify the influence of the

angle upon the torque. In the walking motion, the maximum flexion and extension torques at the knee are about 35, -60[Nm], respectivery. In addition, the maximum dorsal, plantar flexion ones at the ankle are about 10, -120[Nm], respectivery[1]. From the above, this device can assist about 50[%] at the lowest at T_{emk} of the working torque even when the user decreases the muscular power.
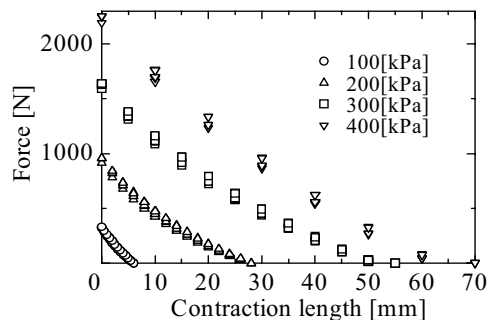
(a) For knee device
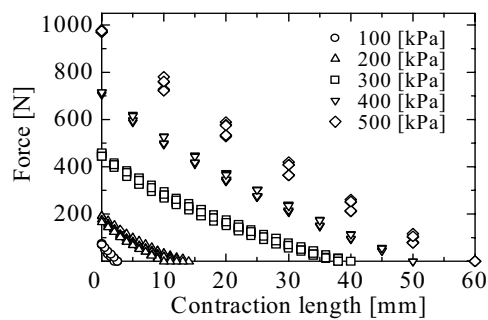
(b) For ankle device

Figure 6 Force characteristics of rubber muscle
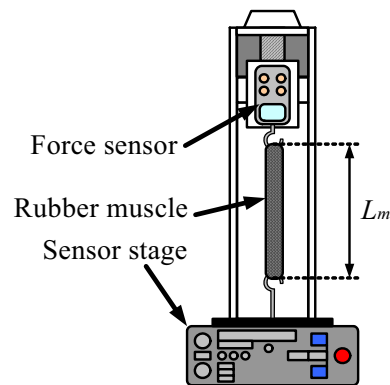
Figure 7 Experimental device

CONTROL SYSTEM

Figure 11 shows a constructed control system,
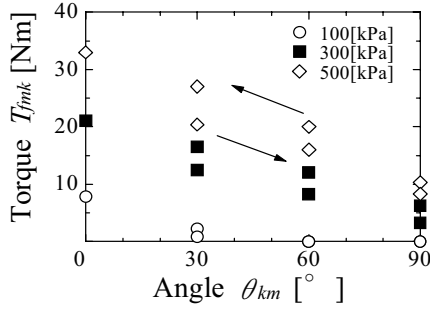
(a) Flexion
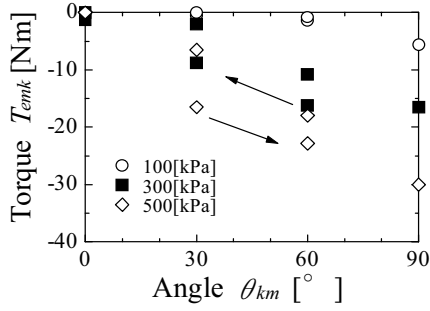
(b) Extension

Figure 8 Torque of knee device (master)
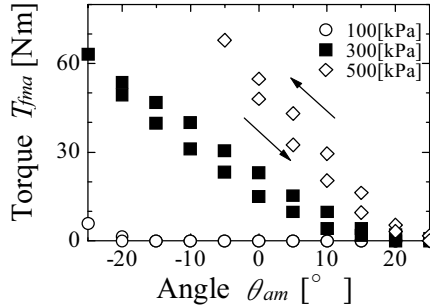
(a) Dorsal flexion
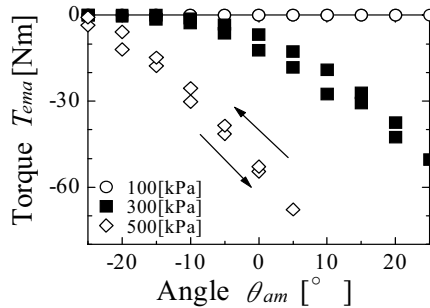
(b) Plantar flexion

Figure 9 Torque of ankle device (master)

which is a force feedback master-slave system to feedback a slave reaction torque to a master user. The main system parameters used in this system are shown in **Table 1**. The torque and the angle control systems are constructed in the master and the slave devices, respectively. The reference angle in the slave control system is the master measured angle $\boldsymbol{\theta}_m(=[\theta_{mk}, \theta_{ma}]^T)$, and the torque control system is inputted the slave reaction torque $\boldsymbol{T}_s(=[T_{sk}, T_{sa}]^T)$, which is obtained by deducting $\boldsymbol{T}_{ws}$ from $\boldsymbol{T}_{Ms}$ and by multiplying a gain $\boldsymbol{K}$.
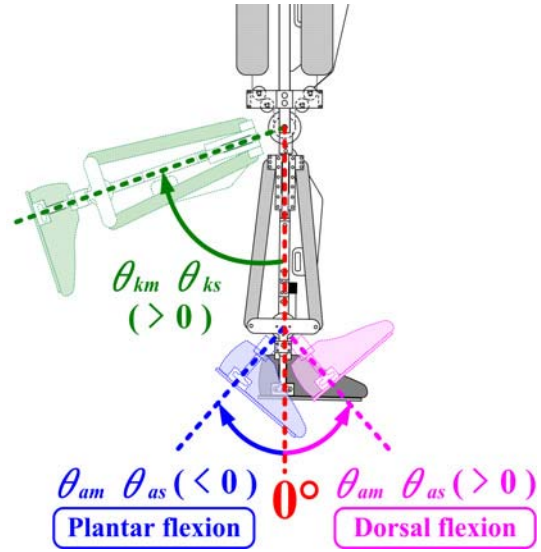
Figure 10 Angle definition

The gain $\boldsymbol{K}$ is introduced in order to generate the master torque in the opposite direction against the slave reaction torque, because the master device must generate the slave reaction torque applied to the slave device by the slave user. $\boldsymbol{K}$ is as follows:

$$\boldsymbol{K} = \begin{bmatrix} -1 & 0 \\ 0 & -1 \end{bmatrix}$$

In this system, the antagonisitic rubber muscles, the flexion and the extension ones at the knee device e.g., are compressed / decompressed from the balance pressure, the flexion and the extension torque $\boldsymbol{T}_{Mm}$, $\boldsymbol{T}_{Ms}$ can be applied to the appliance.

EXPERIMENT

A preriodical step motion assumed a wolk training is experimented in order to verify the proposed device. In this experiment, the slave user is restricted the flexion and the dorsal flexion by a nylon belts as
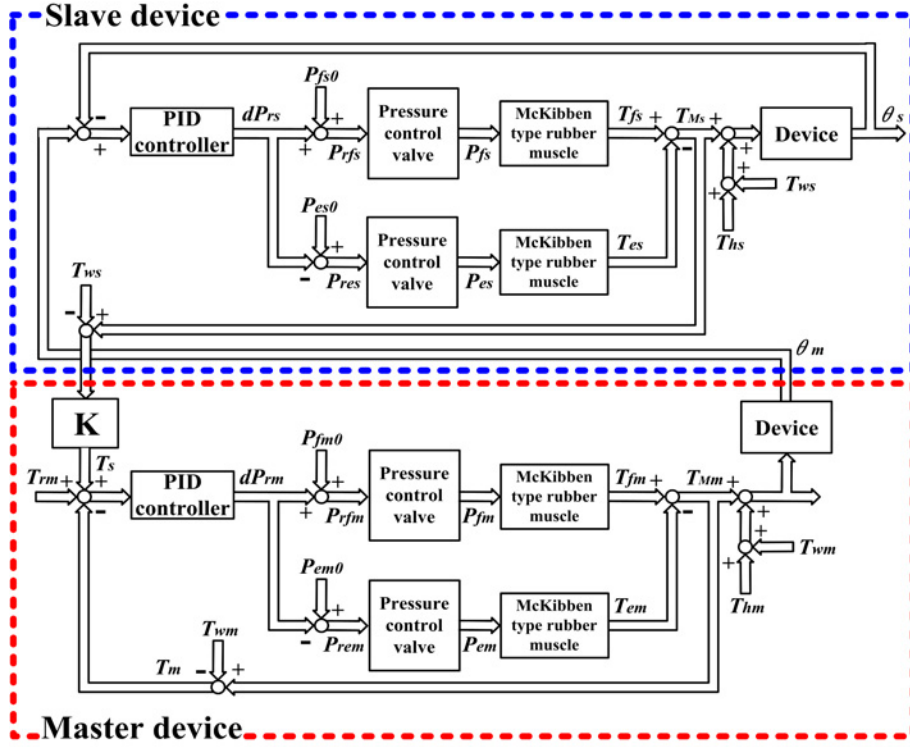
Figure 11 Control system

Table 1 System parameters

Master		
$\boldsymbol{\theta}_m$	Joint angle	[rad]
$\boldsymbol{T}_{Mm}$	Applied torque	[Nm]
$\boldsymbol{T}_{hm}$	Human torque	[Nm]
$\boldsymbol{T}_{wm}$	Weight torque	[Nm]
$\boldsymbol{P}_{rfm}$	Reference pressure Knee:flexion Ankle:dosal flexion	[kPa]
$\boldsymbol{P}_{rem}$	Reference pressure Knee:extension Ankle:plantar flexion	[kPa]
$\boldsymbol{P}_{fm}, \boldsymbol{P}_{em}$	Measured pressure	[kPa]
Slave		
$\boldsymbol{\theta}_s$	Joint angle	[rad]
$\boldsymbol{T}_{Ms}$	Applied torque	[Nm]
$\boldsymbol{T}_{hs}$	Human torque	[Nm]
$\boldsymbol{T}_{ws}$	Weight torque	[Nm]
$\boldsymbol{P}_{rfs}, \boldsymbol{P}_{rem}$	Reference pressure	[kPa]
$\boldsymbol{P}_{fm}, \boldsymbol{P}_{em}$	Measured pressure	[kPa]

shown in **Figure 12**, and the master user periodically steps on the right leg. Nylon belts reproduce contractures on the slave user. The slave user does not apply the torque with the leg, and the master user moves as follows:

$0 \sim 5\,[\mathrm{s}]$
  The master user flexes the knee, and the ankle to the dorsal direction from the standing state.

$5 \sim 10\,[\mathrm{s}]$
  The master user keeps the angles.

$10 \sim 15\,[\mathrm{s}]$
  The master user extends the knee, and flexes the ankle until the standing state.

$15 \sim 20\,[\mathrm{s}]$
  The master user keeps the angles.

$20 \sim 40\,[\mathrm{s}]$
  The master user repeats the above movements.

Figure 13, **14**, **15**, **16** show the experimental results. Figure 13, 15 show the results without the nylon belts, and Figure 14, 16 show the results with the nylon belts. The angle is decreased and the torque is increased on the knee as compared with the results

Figure 12 Experimental condition

(a)Angle   (b)Torque

Figure 15 Without restriction (ankle)

(a)Angle   (b)Torque
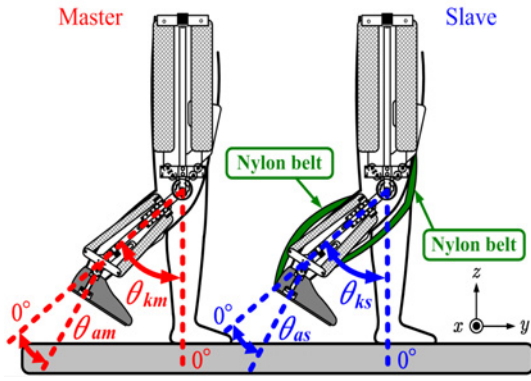
Figure 16 With restriction (ankle)

without the restriction. On the ankle, the torque is also increased as compared with the results without the restriction.

From the above results, the joints stiffnesses of the slave user can be transmitted to the master user even when the joints stiffnesses is increased by the restriction. Because the torque at the knee with the joint restriction is bigger than the torque without the restriction even then the knee angle with the restriction is smaller than the angle without the restriction. In addition, the torque at the ankle with the joint restriction is also bigger than the torque without the restriction.

ture of the developed device has been discussed, and then the validity of the proposed device is evaluated from the experiments assumed the step motion.

From the results, the joints stiffnesses of the slave user increased by the restrictions can be transmitted to the master user by the proposed device.

(a)Angle   (b)Torque
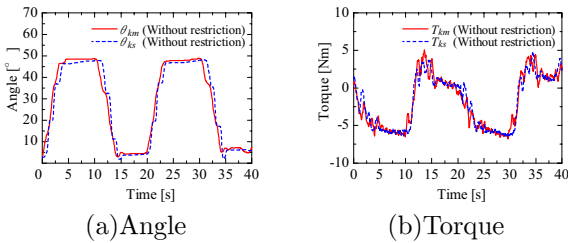
Figure 13 Without restriction (knee)

(a)Angle   (b)Torque
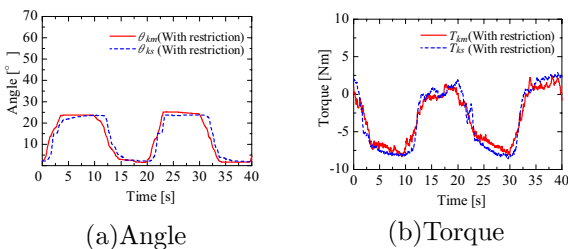
Figure 14 With restriction (knee)

CONCLUSION

In this study, the wearable master-slave lower limb training device which can be used by a trainer and a trainee has been developed. In this paper, the struc-

REFERENCES

1. A.Chu, H.Kazerooni, A.Zoss: "On the Biomimetic Design of the Berkeley Lower Extremity Exoskeleton(BLEEX)", Proc. of the 2005 IEEE International Conference on Robotics and Automation (DVD-ROM), pp.4356-4363, 2005.
2. Y.Mori, K.Takayama, T.Zengo, T.Nakamura: "Development of Straight Style Transfer Equipment for Lower Limbs Disabled: Verification of Basic Motion", Journal of Robotics and Mechatronics, Vol.16, No.5, pp.456-463, 2004.
3. J. Nikitczuk, B. Weinberg, C. Mavroidis: "Rehabilitative Knee Orthosis Driven by Electro-Rheological Fluid Based Actuators", Proc. of the 2005 IEEE International Conference on Robotics and Automation (DVD-ROM), pp.2294-2300, 2005.
4. D.Sasaki, T.Noritsugu, M.Takaiwa: "Development of Pneumatic Power Assist Sprint "AS-SIST" Operated by Human Intention", Journal of Robotics and Mechatronics, Vol.17, No.5, pp.568-574, 2005.
5. H.Kobayashi, T.Siiba, Y.Ishida: "Realization of All 7 Motions for the Upper Limb by a Muscle Suit", Journal of Robotics and Mechatronics, Vol.16, No.5, pp.504-512, 2004.

P1-46

STUDY ON A HIGH PERFORMANCE INSOLE WITH HUMAN COMPATIBILITY

Yasuhiro HAYAKAWA*, Isao HIKITA*, Maisya TUJIOKA* and Naoki NISHIDA*

* Department of Electrical and Control Engineering
Nara National College of Technology
22 Yata-cho, Yamato-Koriyama, Nara, 639-1080 Japan
(E-mail: hayakawa@crtl.nara-k.ac.jp)

ABSTRACT

In recent years, accidents of bone fracture with elderly people increase because of tendency to fall by a little step in a house. As one of this cause, it is considered that a center of gravity position with foot parts of elderly people is changed. Therefore, in order to solve this problem, we propose a new type of insole with high performance by making use of sponge-core-soft rubber actuator (SCSRA). In this study, we apply the actuator to an insole in order to support walking motion. That is to say, a new type of insole to distinguish the foot motion (Pitch or Roll motion) is proposed. To clear the performance of the insole, we develop a test device that is constructed with rotary actuators and a cylinder. In this paper, the mechanism of the proposed insole is explained and basic performances of the proposed mechanism are clarified through some experimental results.

KEY WORDS

Insole, Soft rubber, Stiffness, Stable walk

NOMENCLATURE

F : External force estimation value
P : Pressure
P_0 : Initial pressure
$T_i\ (i=x,y,z)$: Torque
θ : Pitch angle
φ: Roll angle

INTRODUCTION

In Japan, the number of elderly people increases. On the other side, the number of young people decreases. As the result, it is reported that elderly people have to care another elderly person. In order to solve this problem, many kinds of support machines have been developed[1]-[4]. However, with respect to an elderly person who is not physically handicapped, the bone fracture in tendency to fall sometimes becomes a big issue. For example, when the elderly people fail in a little step, some of them sometimes have trouble of bone fracture. Especially, the number of aged person who comes to keep bed increases by reason of the bone fracture of thighbone cervix in the tendency to fall[5]-[8].

With respect to this problem, it is reported that the main cause of tendency to fall is change of gravity position with each foot. That is to say, when elderly people walk on the road, the center of gravity position moves to edge side of the sole as shown in Figure 1. This is because

that the angle between the innominate bone and the thighbone is decreased by the muscle force depression of lower extremities. As the result, the elderly people are easy to stumble over.

Therefore, in order to solve this problem, we propose a new type of insole. The insole is constructed with compound rubber elements that a sponge rubber is covered with silicon rubber[9]-[15]. With respect to the element, since the sponge is coated with silicon rubber, air can be charged into the sponge chamber. As the results, it is possible to control the stiffness of the actuator by controlling pressure in the sponge chamber. Therefore, when some actuators are arranged in parallel, the actuators can estimate the distribution of external force that acts on the actuators. Thus, by making use of control of inner pressure of each actuator, the actuator can adjust torque that acts on the insole.

In this paper, we explain about the structure of insole that is constructed with the elements. Further, a test device to clear the effectiveness of the proposed insole is explained. Moreover, by using the test device an adaptive shape of the insole to distinguish between a roll motion and a pitch motion of the foot part is cleared. From these experimental results, basic characteristics of the proposed insole are clarified.

HIGH PERFORMANCE SHOES

The structure of proposed insole is shown in Figure 2. The insole is constructed with compound rubber elements, a rubber compressor and a tank chamber. When a subject walks on a road with shoes that has the proposed insole, air is compressed by the deformation of rubber compressor according to the motion of heels. Further, the compressed air is charged into the air chamber of the tiptoe part in the insole. Since pressure in the rubber element is measured by a small size pressure sensor, the stiffness of each rubber element can be controlled by pressure in the air chamber. With respect to the control circuit of the insole, a test circuit as shown in Figure 3 is developed. The main MPU is ATmega64 and each valve is controlled by the MPU.
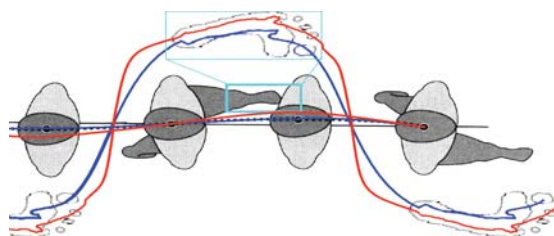
Red Line: Elderly person
Blue Line: Person who is not physically handicapped
Figure 1 Trajectory of center of gravity
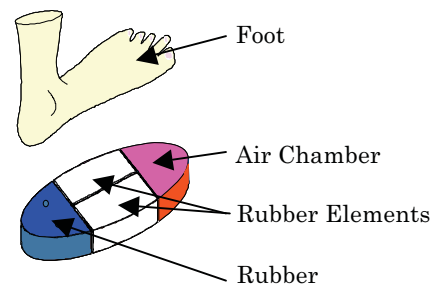
(a) Appearance of the Proposed Insole
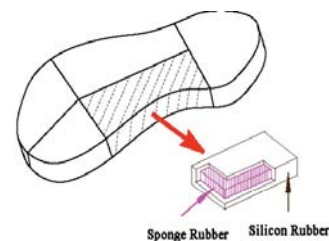
(b) Element of Rubber Actuator
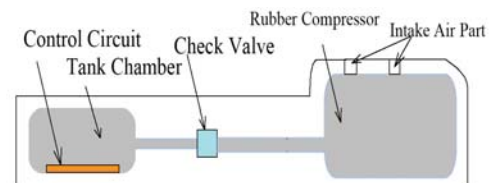
(c)Cross Section of the Proposed Insole

Figure 2 Structure of High Performance Insoles
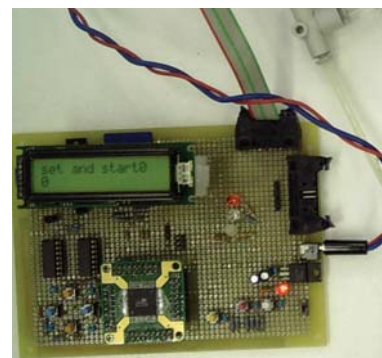
Figure 3 Sample of the Control Device
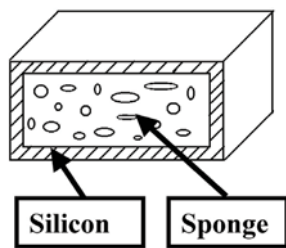
(a)One Layer Structure

(b-1) Initial State

(b-2)Pressurized   State

Figure 4 Schematic View of

Pneumatic Rubber Element

PNEUMATIC RUBBER ELEMENT

In order to develop a new type of insole, we consider a pneumatic rubber element. The structure of the element is shown in Figure 4(a). The actuator is made of two materials. One is silicon rubber and the other is sponge rubber. The sponge is coated with silicon rubber, and air can be charged into the sponge chamber. As the results, it is possible to control the stiffness of the element by controlling pressure in the sponge chamber.

The initial state of the element is shown in Figure 4(b-1). Further, the pressurized structure is shown in Figure 4(b-2). That is to say, since the modification of one layer type element is hardly changed when air is charged into the sponge chamber, the element can maintain safety for users.

INSOLE TEST DEVICE

When a person uses the shoes that has a high performance insole, the shape of the soft rubber element (SCSRA) is changed by external forces to the insole. This is because that the foot consists of a tiptoe, heel and the arch of a foot. Therefore, in order to clear the performance of the proposed insole, we developed a test device for an insole as shown in Figure 5. Figure 5(a) indicates a whole device and Figure 5(b) shows a foot plate (Ground) whose angles (a pitch angle and a roll angle) are controlled by pneumatic rotary actuators. Further, a foot model is attached to the 6 axis force sensor that are set to the tip of the cylinder rod that is driven in the direction of z axis as shown in Figure 6.

In the experiment, two pairs of SCSRA are put on the floor (Figure 5(b):Ground). Further the foot model is put to the elements by using the cylinder as shown in Figure 6. At this time, the floor is driven by each rotary actuator. Thus, the inner pressure in the actuator is measured by a pressure sensor and the both torque and force in the direction of each axis that acts on the ankle part is measured by the 6 axis force sensor (Figure 6).

By using the insole test device, we investigate an adaptive shape of the insole to distinguish the difference between a roll motion and a pitch motion of the foot. This is because that the main motion of falling down is a roll motion of the foot as shown in Figure 1. Therefore, we measure difference pressure between each element by using pressure sensors in the elements. Thus, we clarify the adaptive shape that the difference pressure does not be changed by a pitch motion but the pressure changes just only by a roll motion of the foot part.

SUTABLE SHAPE OF THE ELEMENT

In order to clear the adaptive shape of the element to distinguish between a roll motion and a pitch motion of the foot by value of inner pressure, we investigate the shape of the rubber element that the difference pressure between each rubber element is almost zero when the foot rotates in the direction of pitch motion. In the experiment, we use 2 types of rubber element. Figure 7 shows each shape of the element. Figure 7(a) is a symmetric type and Figure 7(b) is an one side inclination type. By using these elements, we clear variation of the difference pressure between each element with respect to both a pitch angle and a roll angle.

Figure 8 shows the result with the symmetric type and Figure 9 is the result with the one side inclination type. The condition of each experiment is as follows.

[Condition]
    (a): Force(60N), Pitch Angle (θ : -10°～10°)
        Roll Angle(φ : 0°)
    (b): Force(60N), Pitch Angle (θ : 0°)
        Roll Angle(φ : -10°～10°)
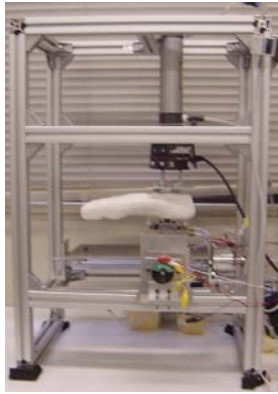
(a-1) Photograph
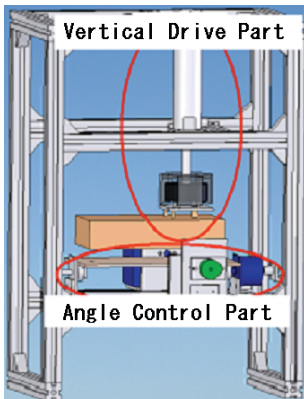
(a-2) Structure

(a)Test Device
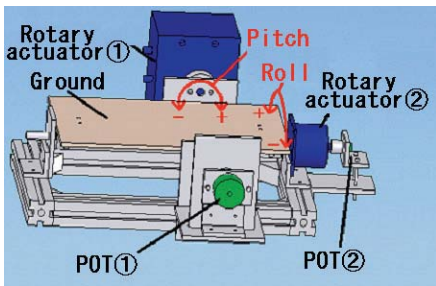
POT: Potentiometer

(b) Mechanism of Foot Plate

Figure 5 Structure of Test Device

From these results, it is cleared that in the case of the symmetric type, the difference pressure changes as the foot rotates in the direction of the pitch angle. On the other hand, in the case of one side inclination type, the value of difference pressure hardly changes when the foot rotates in the direction of pitch angle.

As the result, it is clarified that the one side inclination

type element can distinguish the motion of the foot by the change value of difference pressure between each element.

Further, the torque variation of the ankle part with respect to the one side inclination type element is shown in Figure 10. In this experiment the foot model is rotated in the direction of pitch motion. From this result, it is cleared that the variation of torque in the direction of roll motion is almost zero. Thus, by using the proposed element, the ankle is hardly damaged regardless of the shape of the one side inclination type.
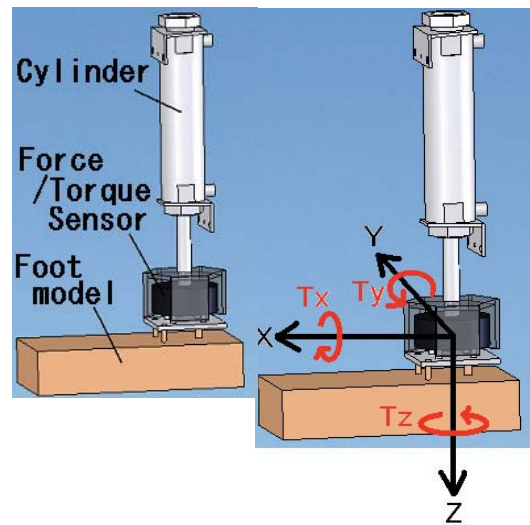
Figure 6 Structure of 6 Axis Sensor Part

CONCLUSIONS

In this paper, we proposed a new type of insole using rubber elements. Further, we cleared the adaptive shape of the element to distinguish the roll motion of the foot by variation of the inner pressure of the element.

ACKNOWLEDGEMENTS

REFERENCES

1. Walking and Fitness Testing in Elderly Women, Fitness for the Aged, Disabled and Industrial Worker, Human Kinetics Publishers, Tokyo, Japan, 1990, pp. 84-89.
2. M.P. Murray, et al., Walking Patterns of Healthy Old men, *J. Gerontology*, **24**, 1969, pp169-178.
3. S. Inoue, K. Saitou, et. al., Influence of Fall Prevention Exercise on Walking Movement and

Body Sway, JSME *Dynamics and Design Conference,* 2003

4. M. Miyamura,Movement physiology studies, Shinkou Trade Co., Ltd., Medical Treatment Publication Department, Tokyo, 1996.

5. S.Oobuchi, Tendency to Fall and Preventation of Elderly People, Journal of Biomechanism, 2005. 27-1, pp.2-5. (Japanese)

6. Ikehara, Tanaka, Tamiya, Hukatani, Development of Walking Assist System of Elderly People, Con ference of Robotics and Mechatronics, 2006, No. 06-4, 1p1-A09. (Japanese)

7. Tanaka, Omata, Ikehara, Nagamura, Ikejyou, Mus culus Activity in Supporting Walk Machine Moun ting to Assist Lower Extremities, Conference of Robotics and Mechatronics, 2006, No.06-4, 2p2-A 07. (Japanese)

8. Y. Hayakawa, H. Mori and R. Tsuda, Basic Study to Develop an Active Supporter with Human Compatibility, *Proc. of the Symposium on Welfare Technology*, 2001.

9. Y. Hayakawa, H. Mori, M. Aichi, T. Kodaka, and S. Higashiura, Study on an Active Supporter Using Pneumatic Foaming Rubber Actuator Coated with Silicone Rubber, *Proc. of the Second European Medical and Biological Engineering Conference, Austria,* 2002.

10. Y. Hayakawa, H. Mori and R. Tsuda, Basic Study to Develop an Active Supporter with Human Compatibility, *Proc. of the Symposium on Welfare Technology*, 2001.

11. Y. Hayakawa, H. Mori, M. Aichi, T. Kodaka, and S. Higashiura, Study on an Active Supporter Using Pneumatic Foaming Rubber Actuator Coated with Silicone Rubber, *Proc. of the Second European Medical and Biological Engineering Conference, Austria*, 2002.

12. Y. Hayakawa, K. Morishita and M. Aichi, Control Performance of a Pneumatic Silicone Outer Fence Mold Actuator, *Proc. SICE Annual Conference*, Fukui, Japan, 2003

13. Y. Hayakawa, K. Morishita and M. Aichi, Study on a New Mechanism of a Silicone Outer Fence Mold Actuator, *Proc. Seventh International Symposium on Fluid Control, Measurement and Visualization*, Italy, 2003.

14. Y. Hayakawa, M. Aichi and K. Morishita, Basic Characteristics of a Silicone Outer Fence Mold Actuator with Human Compatibility, Proc. First International Conference on Computational Methods in Fluid Power Technology, Australia, 2003, PP.595-602.

15. Y. Hayakawa, H. Morishita, M. Aichi and R. Tsuda, Development of a Silicone Outer Fence Mold Actuator, *Journal of JSME*, Series C, **70**, 2004, pp. 433-439.
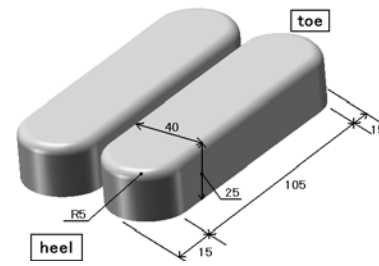
(a) Symmetric Type
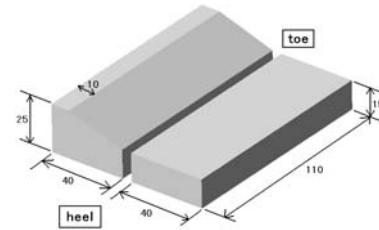
(b) One Side Inclination Type

Figure 7 Rubber Element (Right Side)
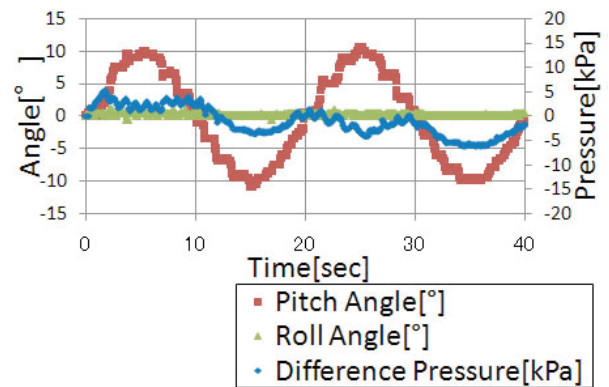
(a) Variation of Pitch Angle
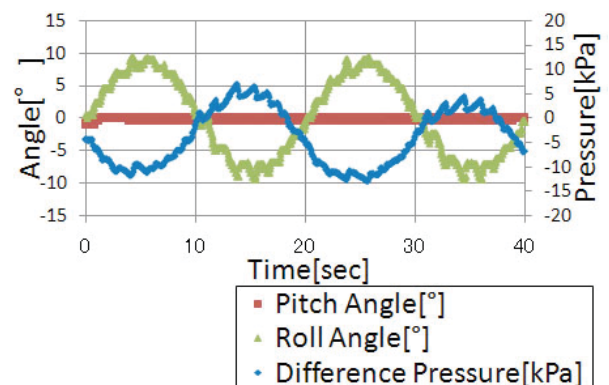
(b) Variation of Roll Angle

Figure 8 Difference Pressure of Symmetric Type

(a) Variation of Pitch Angle

(a) Movement in the direction of Pitch Angle

(b) Variation of Roll Angle

(b) Movement in the direction of Roll Angle
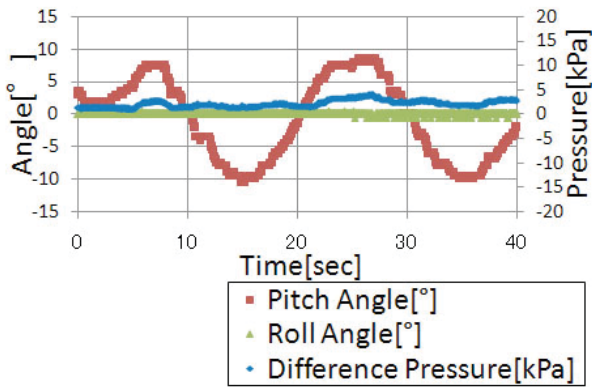
Figure 10 Torque of Ankle Part
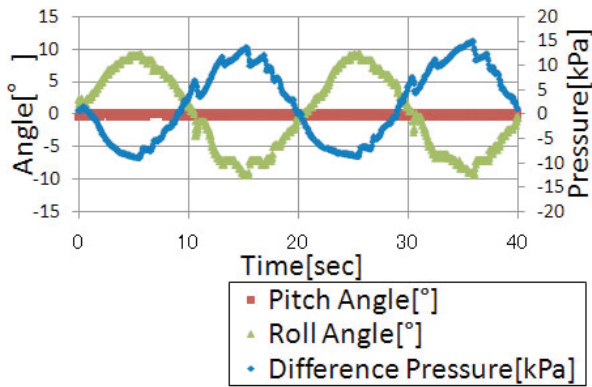
(One Side Inclination Type)

Figure 9 Difference Pressure of

One Side Inclination Type

P1-47

DEVELOPMENT OF GAIT TRAINING SYSTEM USING BI-ARTICULAR MUSCLE MODEL

Yoshiyuki SHIBATA*, Motoki TAKAGI*, Tasuku MIYOSHI*, Ryota AOYAMA*
Shin-ichiroh YAMAMOTO* and Yukio KAWAKAMI*

* Graduate School of Engineering, Functional Control Systems
Shibaura Institute of Technology
307 Fukasaku, Minuma-ku, Saitama-City, Saitama, 337-8570 Japan
(E-mail: shibata@bpe.se.shibaura-it.ac.jp)

ABSTRACT

The purpose of this study was to develop a pneumatic gait training system which was consisted by Mckibben type actuators to achieve the normal gait patterns of lower limb joint angular displacements. These actuators were arranged as human musculoskeletal system; mono- and bi-articular muscles. The system provided a proportional directional control valve which controlled antagonistic actuators, and this system had PID controller and joint angular displacement feedback circuit. In the results, the output of the knee joint movement pattern had well validation for the input signal which was recorded from natural treadmill walking in healthy subjects. This system made the orthosis reproduce like the human natural walking. In conclusion, we structured a fundamental bi-articular muscle type of the gait training system using Mckibben type actuators.

KEY WORDS

Bi-articular muscle, Mckibben Actuator, Gait training system

INTRODUCTION

The value of partial body weight support treadmill training (BWSTT) for disabled individuals has been well established, especially when initiated soon after an injury. Wernig et al. [1] had demonstrated that 25 out of 33 incomplete spinal cord injured persons learned to walk independently at the end of 3-20 weeks (median 10.5) with partial BWSTT. However, this treatment presents special challenges for the therapist. The passive moving of a disabled person's legs is ergonomically difficult since the individual being treated cannot support and/or move his legs by himself. In order to improve this therapy, Colombo et al. [2] developed a driven gait orthosis (DGO) that can be used on patients with varying degrees of paresis or spasticity for up to one-half hour.

Dietz et al. [3] using this gait training system for paraplegic patients, and they suggested the afferent input from hip joints is important for the leg muscle activation during locomotion.

In the previous studies, we had constructed the two types of gait training systems using the Mckibben type of pneumatic actuators to achieve the repetitive physiological gait patterns [4-5]; one was mono-articular muscle model [4], the other was bi-articular muscle model [5]. The Mckibben type actuator had similar mechanism to human muscle contraction for a force generating, and it has high degree of freedom of design and contributes to orthosis lightening. In addition, both of our system has some advantages over the partial BWSTT on land; the system is electrically and mechanically safe since it consists of pneumatic

actuators to prevent short circuits and a burn, and the main frame is an exoskeleton type of the hip-knee-ankle orthosis which is used in general gait training. According to Miyoshi et al. [4], they had developed a robotic gait trainer in water (RGTW) and had demonstrated its efficacy which could reduce the enhanced hip extensor muscle activities, since the water walking needs propulsive forces against the water resistance [6]. In this respect, the bi-articular muscle model could reduce the hip extensor muscle activities [5], since the bi-articular muscles had unique function in force-directing because of their ability to simultaneously regulate or tune adjacent joint torques [7]. The bi-articular muscles are through the two joint, and are arranged in a pair of antagonists; e.g. biceps brachii and triceps brachii, rectus femoris and biceps femoris. The synergistic activities of one antagonistic pair of the bi-articular muscles and two antagonistic pair of the mono-articular muscles might be able to reproduce by single command signal informing force direction via a simple spinal level neural network proposed [8]. To our knowledge, however, there is no gait training system using bi-articular muscle model, because the bi-articular muscle model is redundant and torque shearing problem for two joints is infinite combination.

The purpose of this study was to develop the bi-articular muscle model type of the pneumatic gait training system for achieving the repetitive physiological normal gait patterns of lower limb joint angular displacements, and to design the specific controller for bi-articular muscle model based on PID.

SYSTEM DESIGN

Pneumatic Control
Figure 1 represents the gait training system. The orthosis drives by contraction of the Mckibben type actuators, and we applied antagonistic arrangement of the Mckibben type actuators like human muscles. So, we used proportional directional control valve(servo valve). This valve has 1 input port and 2 output ports which attached to the Mckibben type actuators posterior and anterior. Therefore it's very suitable for control by antagonistic actuators.

Mckibben type actuator
Figure 2 shows the Mckibben type actuator. This actuator generated force by contraction. The outer-tube of mesh texture transformed a radial force into an axial force when inner rubber-tube generated force by expansion. Contraction ratio was 30% on natural length.
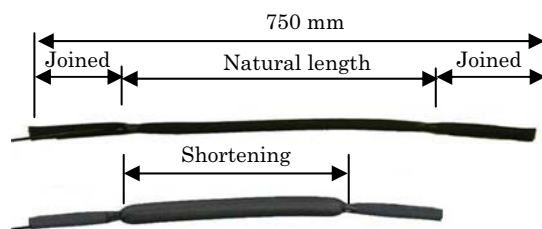
Figure 2 The mechanism of Mckibben type actuator
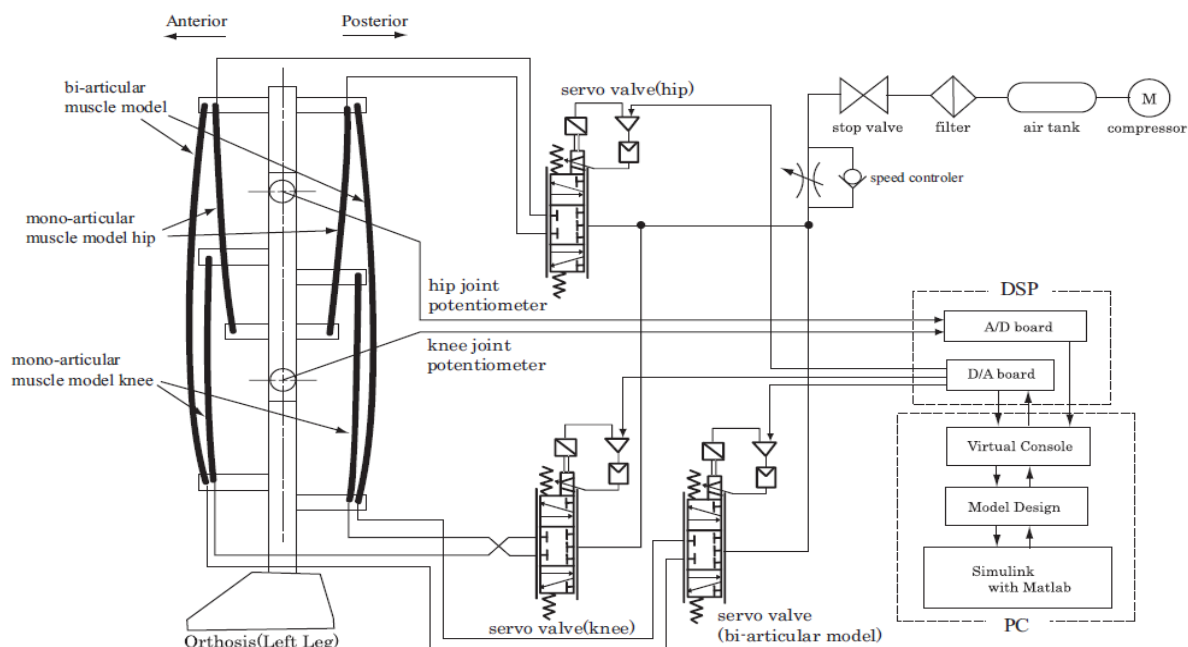
Figure 1 Gait training system schematic diagram

Walking program and control interface

We used a Digital Signal Processor(DSP) for input and output of signals. This equipment has A/D and D/A converter, and control program run the Simulink of Matlab(The MathWorks). Figure 3 shows the block diagram of servo system. Input data was joint angle of gait cycle by healthy people. Hip and knee joint angle of orthosis got feedback which detected by the potentiometer. The PID controller value decided voluntarily from the experiment.

The DSP provides interface function which called Virtual Console. It function is very useful which is able to create one's own GUI, and load parameter from Simulink of Matlab. The user is able to change the parameters without Simulink of Matlab.
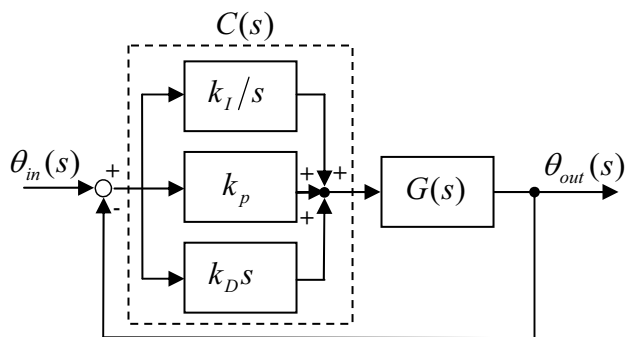
Figure 3 Block diagram of servo system. $\theta_{in}(s)$: Target angle, $\theta_{out}(s)$: Controlled angle, $C(s)$: PID controller, $G(s)$: Servo valve control voltage gain.

The following show equipment list.
 a) Mckibben type actuator: Hitachi Medical Corp.
 b) Servo valve: MPYE-5-1/8-HF-010-B, FESTO Corp.
 c) DSP: ADX5430, A&D Co. Ltd.

Orthosis overview

Figure 4 shows the orthosis overview. The left leg of orthosis fixed to the frame, and suspended. At first, we build up this system only unilateral leg of orthosis on a trial basis. The Mckibben type actuator attached to the anterior and posterior of each joint. The orthosis drove because these actuators contract alternately.

RESULTS

It is possible for proportional directional control valve to control the both agonistic/antagonistic Mckibben type actuators. Thus, it can be decreased the number of control valves to the number of actuators. We achieved simplification of the pneumatic pipe arrangement in this system. This experiment was performed the same parameter between bi-articular muscle model and hip mono-articular muscle model. The PID controller

parameter sets P:1.0, I:0, D:0, to all actuators. The hip joint angle output value was twice as value than the target value, and there were phase shifting(figure 5). The mono-articular muscle model had time-delay, and couldn't reach the maximum target angle.

Figure 4 Left leg of orthosis
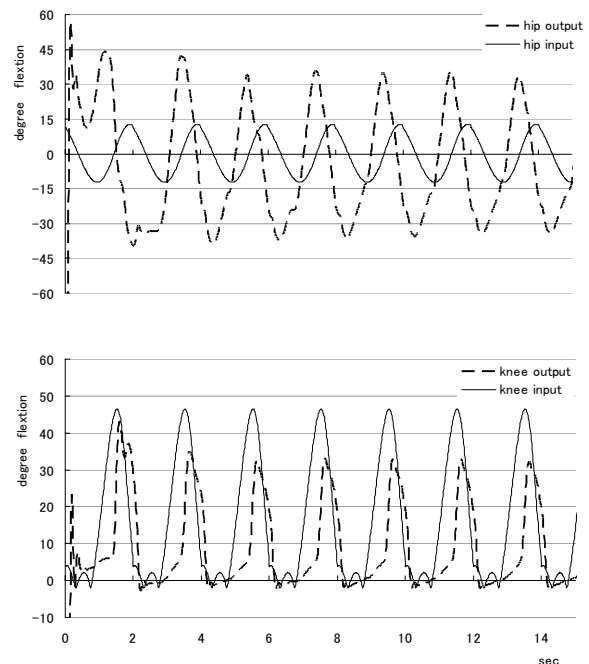
Figure 5 Joint angle variation during orthosis walking. Knee joint angle data(bottom), and hip joint angle data(upper). Target values were hip and knee joint angle for healthy people(one gait cycle:0.5Hz, solid line: target joint angle, break line: controlled angle value).

DISCUSSION

The hip joint angle response was larger than target angle value, it was not appropriate parameter of servo valve control voltage gain. The reason of phase shifts might be overlarge proportional value of PID controller. The bi-articular muscle model was through the two joint, but the angle feedback was performed only hip joint angle. It wasn't optimal follow-up control. The human walking had coinstantaneous rotation knee and hip joint. Hence, we have to determine the PID controller value and feedback parameter for each muscle models.

CONCLUSION

We developed a fundamental gait training system with position feedback and PID controller functions, drove by pneumatic Mckibben type actuator. This system might be possible which reproduce the movement like the human natural walking.

FUTURE WORK

In this study, it was difficult for the bi-articular muscle model to control by hip joint angle feedback. We will determine about the optimal PID controller value of mono-articular muscle model and the appropriate control parameter for the bi-articular muscle model. We have to superstruct control system which mono and bi-articular muscle models will be possible to produce their coordination.

REFERENCES

1. Wernig A, Muller S, Nanassy A, Cagol E. Laufband therapy based on 'rules of spinal locomotion' is effective in spinal cord injured persons. Eur J Neurosci 1995;7:823-9.
2. G. Colombo, M. Joerg, R. Schreier, and V. Dietz, Treadmill training of paraplegic patients using a robotic orthosis, Journal of Rehabilitation Research and Development Vol. 37 No. 6, pp.693-700, 2000.
3. V. Dietz, R. MuÈller and G. Colombo, Locomotor activity in spinal man: significance of afferent input from joint and load receptors, Brain, 125, 2626-2634, 2002.
4. T. Miyoshi, K. Hiramatsu, S. Yamamoto, K. Nakazawa and M. Akai, Robotic gait trainer in water: Development of an underwater gait-training orthosis, Disability and Rehabilitation, 2008; 00(0): 1–7.
5. S. Yamamoto, T. Miyoshi, T. Komeda, K. Hiramatsu, K. Nakazawa, and M. Akai, Development of pneumatic gait assist system, Complex Medical Engineering, 2007. CME 2007. IEEE/ICME International Conference on, 1337 – 1340.
6. T. Miyoshi, T. Shirota, S. Yamamoto, K. Nakazawa and M. Akai, Effect of the walking speed to the lower limb jointangular displacements, joint moments and ground reaction forces during walking in water, Disability and Rehabilitation, 2004;VOL.26, NO.12, 724–732.
7. G. J. Van Ingen Schenau, From rotation to translation: Constraints on multi-joint movements and the unique action of bi-articular muscles, Human Movement Science, Volume 8, Issue 4, August 1989, Pages 301-337.
8. M. Kumamoto, T. Oshima, and T. Fujikawa, Bi-articular muscle as a principle keyword for Biomimetric motor link system, Microtechnologies in Medicine & Biology 2nd Annual International IEEE-EMB Special Topic Conference on, 346-351, 2002.

P1-48

A NOVEL LEAKAGE DETECTION AND LOCALIZATION METHOD BASED ON INFRARED THERMOGRAPHY

Nan GE, Guangzheng PENG

Department of Automatic Control, School of Information Science and Technology
Beijing Institute of Technology
5 South Zhongguancun Street, Beijing, 100081, China
(E-mail: genan@bit.edu.cn)

ABSTRACT

The common ways used to find leak include traditional bubbling test, ultrasonic positioning and helium mass-spectrometer detection, etc. However, each of them has deficiencies of varying degrees, especially low-efficiency in bubbling and mass spectrometry means and poor anti-jamming capability in ultrasonic means. In order to search a better approach to do this job, a new method is introduced in this paper, which is based on infrared thermography. In the experiment, test vessel is firstly aerated with absolute pressure of 0.6-0.7 Mpa and then the temperature field surround the vessel is monitored and acquired by an IR camera. On account of leakiness, compressed air expanses from the leak hole to ambient and heat-absorption effect has taken place around it on the basis of Joule-Thomson Effect, so the temperature difference between the leak area and normal area will be reflected in the thermal images. Moreover, Freon cooler is also set in the pneumatic circuit for the sake of enhancing the phenomenon. During the test, several frames of thermal images in time sequence are transferred to the computer for pre-processing and fusion operating by the use of local entropy difference algorithm. From results, it is shown that the method achieves a good resolution and sensitivity in the application of air-leakage detection and localization. Some modeling and simulating work by finite element analysis is also carried out in this paper.

KEY WORDS

Leak Detection, Leak Localization, Joule-Thomson Effect, Finite Element Analysis, Infrared Image Processing

INTRODUCTION

In most industrial processes, air-leakage detection and localization of vessels is an essential link of manufacturing. With the development of manufacturing technology, more and more requirements about not only leak detection but also leak localization are put forward. Most of current localization researches focus on leakage of petroleum and natural gas pipeline, while little new work was done to vessels' leak. Generally, there are three traditional ways to find tiny leak on the vessels[1]. The first one is air bubbling test which needs the target to soak in water, so it is constrained to be used for objects with immersion forbiddance. The second is mass spectrometry which has the highest precision in detections, but its broad application is hindered by low-efficiency. The third one is ultrasonic positioning which is interfered easily by noise. Due to the disadvantages of low-efficiency and poor anti-jamming capability in traditional vessels' leakage localization

approaches, a novel method was proposed in this paper. Along with the gradual perfection of infrared technology, thermography has been increasingly used in leakage detection and localization field. This paper utilizes a computer based system which contains a specific pneumatic circuit in conjunction with an on-line infrared camera to determine the air-tightness of a test vessel. A mathematical model has been set for subsequent leakage localization processing by analyzing leak throttle and heat transfer process around the leak. Moreover, the finite element analysis (FEA) was used to do some simulations. In order to find the leak point in the thermal images, a set of means based on local entropy difference algorithm has been adopted.

Experiment shows that the simulation fits the result well and verifies that the thermal image based leak detection and localization method is effective and sensitive.

MODELING AND SIMULATION

There are mainly two types of heat transfer process happened when air leak occurred, one is heat absorption caused by air expansion from the leak namely Joule-Thomson effect, the other is heat transfer between air leak flow and leak hole in the vessel if the temperature of them are varied. So, the change in temperature around the leak will be the superposition by the two processes above.

From the aspect of physical quantity, the process of air leak can be considered as steady flow field coupled with two kinds of unsteady heat transfer.

Joule-Thomson Effect

In the course of throttle, gas temperature varies adapted to its pressure, namely Joule-Thomson effect. Normally, in the field of leakage detection with medium of compressed air, the temperature of medium is mostly from 250K to 350K, meantime the test pressure is lower than 1Mpa. Consequently air leak throttle makes positive Joule-Thomson effect according to the isenthalpic inversion curve in the Joule-Thomson T-P diagram. Leak air will have a temperature drop while passing through the leak hole, so it will absorb partial heat from the vessel, and then temperature of leak hole will decrease too. For the sake of calculating the quantitative temperature drop, Joule-Thomson coefficient u_j is introduced as following, which is defined as the temperature change rate in company with pressure during the throttle process (isenthalpic process)[2].

$$u_j = \left(\frac{\partial T}{\partial P}\right)_h = \frac{T\left(\frac{\partial v}{\partial T}\right)_P - v}{C_P} \quad (1)$$

Where, T is thermodynamic temperature of air, K; P is air pressure, Pa; v is specific volume of air, m³/kg; C_p is specific heat at constant pressure, J/K·kg.

Eq(8) shows that, so long as $(\partial v/\partial T)_P$ is worked out from gas state equation and is substituted into Eq(8), u_j will be obtained. Then the temperature difference affected by leak flow will be obvious:

$$\Delta T = \int_{P_1}^{P_2} u_j dP \quad (2)$$

However, for most occasions, it is always computationally expensive to get $(\partial v/\partial T)_P$, therefore direct derivation to real gas state equation which mentioned in reference [3] has been done.

Van Der Waals (VDW) Equation is the primary way to describe real gas, as following:

$$P = \frac{RT}{v-b} - \frac{a}{v^2} \quad (3)$$

u_j will be obtained from simultaneous equations of Eq.(1) and Eq.(3):

$$u_j = \left(\frac{\partial T}{\partial P}\right)_h = \frac{R(v-b)v^3 - RTv^4 - 2av(v-b)^2}{[RTv^3 + 2a(v-b)^2]} \quad (4)$$

Where, R is molar gas constant, 287.1 N·m/(kg·K) for dry air; a and b are Van Der Waals constants, a=135.8×10⁻³Pa·m⁶/K·mol², b=36.4×10⁻³ m³/K·mol.

Though the VDW Equation qualitatively describes the status of real gas, it is not so accurate in quantitative calculation, so compressibility factor Z is applied in the computation of u_j. After v is obtained by substituting the known variable T and P into correction state equation of ideal gas, u_j will be gotten.

Compressibility factor Z is determined by Dranchuk-Purvis-Robinson Correlative Equation[4]:

$$Z = 1 + \left(0.31506 - \frac{1.0467}{T_r} - \frac{0.5783}{T_r^3}\right)\rho_r + \left(0.5353 - \frac{0.6127}{T_r} + \frac{0.6185}{T_r^3}\right)\rho_r^2 \quad (5)$$

Where, ρ_r=0.27(P_r/ZT_r) is relative density of air; T_r=T/T_c is relative temperature of air; T_c is critical temperature, T_c=126K for air; P_r=P/P_c is relative pressure of air; P_c is critical pressure, T_c=3.399 Mpa for air.

Heat Transfer Model

Using the thought of finite element method, the test vessel can be divided into a great deal of infinitesimal

surface elements. Concerning a variety of heat transfer processes among each element, environment, and the compressed air medium with low temperature, the heat transfer model is established. Assuming there is no high-temperature heat source around the test vessel, therefore thermal radiation effect can be ignored. Taking the adjacent infinitesimal element K and K+1 which are far smaller than the leak hole for instance, thermal convection and heat conduction have been considered, sketch is shown as following:
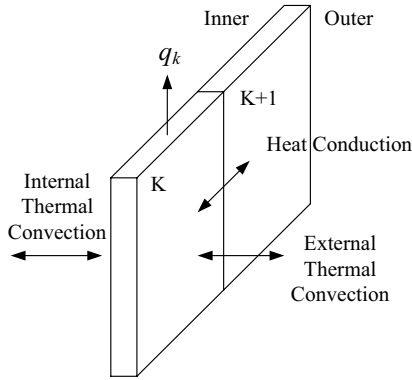
Figure 1 Sketch of heat transfer analysis

If the element K joins with leak hole, q_k is defined as the quantity of heat taken away by leak flow, for the result of forced convection effect.

Assume that λ is thermal conductivity, T_k and T_{K+1} are the temperatures of adjacent elements K and K+1 respectively, $A_{k,k+1}$ is the section area of thermal conduction, $L_{k,K+1}$ is effective length. Then the thermal conduction between element K and element K+1 can be described:

$$Conduction_{k,k+1} = -\frac{\lambda A_{k,k+1}}{L_{k,k+1}}(T_k - T_{k+1}) \qquad (6)$$

As the element K joins with n elements simultaneously, the total quantity of thermal conduction is represented as following:

$$Conduction = -\sum_n \frac{\lambda A_{k,k+n}}{L_{k,k+n}}(T_k - T_{k+n}) \qquad (7)$$

Thermal convection of every single infinitesimal element consists of two parts: the one between external surface and ambient; the other between internal surface and inner compressed air with low temperature. On the basis of Newton Law, assuming the surface area of element K is A_k, the temperature of element K is T_k, then the thermal convection can be conducted:

Interior surface: $Convection_{inside} = A_k \alpha_i (T_k - T_i)$ (8)

Exterior surface: $Convection_{outside} = A_k \alpha_o (T_k - T_o)$ (9)

Where, T_i is the temperature of compressed air inside the test vessel; T_0 is ambient temperature; α is convective heat transfer coefficient.

On the occasion of natural convection, α is a constant, while if there is forced convection, α will be a variable related to flow velocity, and can be conducted by some theoretical and empirical formulas. On account of natural convection happens in both inside and outside of the test vessel, so α_i and α_o are two constants.

From the analysis above, heat balance equation of element K is established as following:

$$\sum_n \frac{-\lambda A_{k,k+n}}{L_{k,k+n}}(T_{k+n} - T_k) + A_k \alpha_i (T_k - T_i) \qquad (10)$$
$$+ A_k \alpha_o (T_k - T_o) + q_k = 0$$

Where, boundary condition $q_k=0$ exists in those elements which are nonadjacent with the leak hole. Setting up the heat balance simultaneous equations of all elements, temperature distribution of the test vessel will be obtained.

Finite Element Analysis
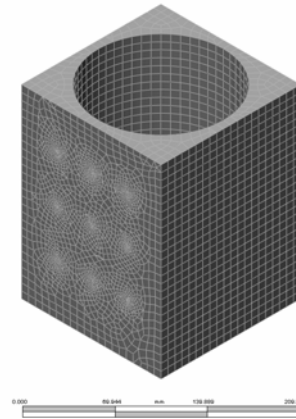
Figure 2 Meshed model

On the theoretical basis of (1) and (2), Simulation work is done below by using ALGOR finite element analysis software[5]. Taking general conditions of vessels' leakage detection for reference, and the material of sample model is chosen as 201.T4 sand cast aluminum. After CAD model is meshed (as shown in Figure2), initial temperatures of nodes are set to 298K, and more boundary conditions are listed in Table 1.

511

Table 1 Boundary conditions for simulation

Parameter	Internal air	Ambient
Type of Convection	Natural	Natural
Abs. Pressure (Mpa)	0.6	0.1
Temperature (K)	263	298
Mass Density (Kg/m^3)	7.94	1.18
Dynamic Viscosity (Pa·s)	1.67×10^{-5}	1.84×10^{-5}
Specific heat (J/kg·K)	1004	718
Thermal Conductivity (J/m·h·K)	84	94
Thermal Expansion Co-efficiency (1/K)	3.80×10^{-3}	3.36×10^{-3}

Dimension of the model is 150mm×150mm×200mm, internal columnar cavity has a radius of 67mm, and its height is 185mm. There are nine via holes composed of 3 rows 3 columns on the facade of the model, holes in each row have a same radius of 0.2mm, 1mm, 0.5mm respectively (from up to down), and holes in each column are in equal depth of 19.74mm，7.92mm，19.74mm respectively (from left to right).
Figure 2 shows the model after meshing with bricks and tetrahedral, because of the great differences in size between the hole and the vessel, some refinement points are defined round the simulated leak hole in order to keep precision.
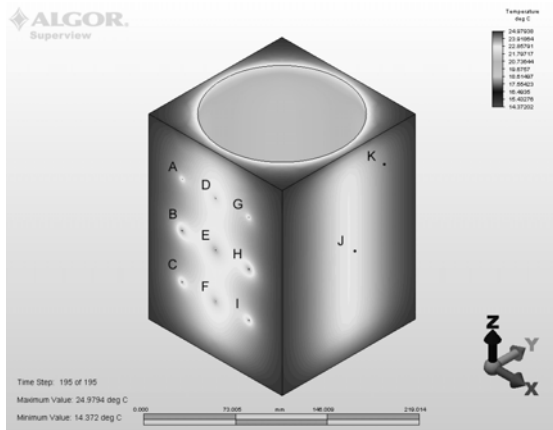
Figure 3 Temperature field of simulation

Figure 3 shows the temperature field of test vessel model when it reaches heat transient equilibrium. For the sake of research on the temperature difference, points A~I near the simulated leak hole and points J~K in no-leak region have been taken as the observational points. In virtue of the both effects of Joule-Thomson and heat exchange, a kind of annular distribution in temperature is presented around the simulated leak hole, and the more the leakage is, the bigger the radius of annular distribution is. Meanwhile, the smaller the depth

of leak hole is, the greater the change in temperature gradient is.
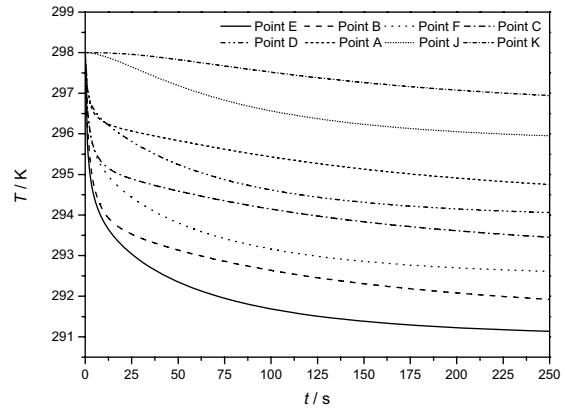
Figure 4 Curves of observational points

Simulation curves of observational points A~F and J~K are shown in Figure 4. From the curves, there is quick drop in temperatures of all the observational points near the leak hole when test starts, while 12 seconds later the tendency of change in temperatures becomes gentle. Since temperatures are steady inclined, the variety in depth of the holes affects the temperature gradient much distinctly. Besides, due to good thermal conductivity of sand cast aluminum, the decrease of temperatures of point J and K is approximate 1 K and 1.7 K respectively, but the changes are still far smaller than those in point A~F.

EXPERIMENT AND RESULTS
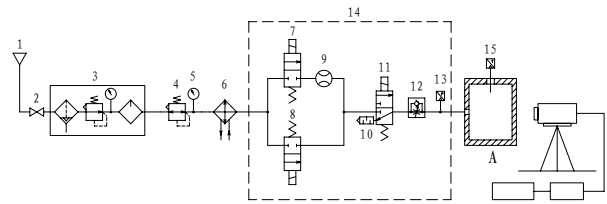
1: Air source 2: Stop valve 3: Pneumatic auxiliary components 4: Precision regulator 5: Pressure gauge 6: Freon based active cooler 7,8: Direct operated switch valve 9: Flow meter 10: Silencer 11: Two-position three-way valve 12: Speed control valve 13: Pressure sensor 14: Insulation material 15: Temperature sensor 16: Infrared camera 17: Computer 18: Image acquisition card A: Test vessel

Fig 5 Experimental pneumatic circuit

The experiment is carried out with the conditions: the test vessel is 500mL air volume with leak which is made of cast aluminum, measured leak flow rate is 20 sccm, inflation pressure is absolute 0.6 Mpa, temperature of compressed air is 263 K, and ambient temperature is

301 K.

Two thermal images are captured utilizing the pneumatic circuit [6] as shown in Figure 5, and Figure 6 (a) shows the temperature field of the air volume before inflation, while Figure 6 (b) shows the temperature field of air volume in the time of 60s after inflation.

(a)Before inflation

(b) 60s after inflation
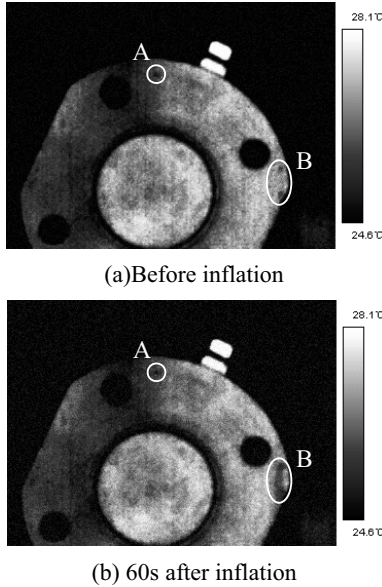
Figure 6 Thermal images of air volume with leak

As the marks shown in Figure6 (a), three obvious singular temperature points can be seen in the regions A and B, among them, the one in region A is visible defect on the surface whereas the ones in region B are not, so all the three points are suspected to be the leak holes if without checking them in Figure6 (b). Comparing both the regions in Figure6 (a) and Figure6 (b), region A is invariant between the two images, while the region B in Figure6 (b) becomes darker than that in Figure6 (a). Hence a preliminary judgment can be made that the point in region A is not a leak hole but defect, nevertheless there are two invisible leak holes in region B. More accurate conclusion will be proposed in the following section by the use of leakage detection and localization method based on local entropy difference algorithm.

LOCAL ENTROPY DIFFERENCE ALGORITHM

Assume that image function has non-negative value, namely $f(x,y)>0$, for a image which size are M×N pixels, define:

$$E = -\sum_{r=1}^{M}\sum_{j=1}^{N} p_{ij} \log_2 p_{ij} \qquad (11)$$

Where
$$p_{ij} = f(i,j)/\sum_{i=1}^{M}\sum_{j=1}^{N} f(i,j) \qquad (12)$$

The appearance probability of a certain gray value is characterized by p_{ij}, and E is named image entropy, furthermore if calculation is only done to one local area of the whole image, then it is called local entropy. According to the definition, entire amount of information contained in the whole or partial image can be reflected by entropy[7]. Because of the existence of negative sign in Eq. 11, so the richer the information is, the smaller the value of entropy is.

In the application of leakage detection and localization based on infrared thermography, leak will be embodied in the images, that is, leak adds some information into thermal images, and it is proved by the experiment shown in Figure 6. Back to the definition, merit is found that even though there is geometric distortion in partial images sometimes, the local entropy is invariant for its statistical characteristics. Moreover, the entropy depends on the computation of whole area, so its robustness may not be influenced by several singular values of isolated pixels. Meanwhile, its anti-noise advantage is ensured by normalization processing of p_{ij}. Due to logarithm involved, sometimes Eq.1 will be simplified as following by taking Taylor Expansion, in order to get real-time performance improvement.

$$E_f = -\sum_{r=1}^{M}\sum_{j=1}^{N} p_{ij}(p_{ij}-1) \qquad (13)$$

Where
$$p_{ij} = f(i,j)/\sum_{i=1}^{M}\sum_{j=1}^{N} f(i,j) \qquad (14)$$

From the perspective of evaluation, entropy, as the characteristic measurement parameter of image information, provides a set of scientific means to evaluate the degree of leakage. Therefore, local entropy difference algorithm is adopted, and its strategies are described below.

For a thermal image F of test vessel captured before inflation, which size are M×N pixels, F will be traversal scanned firstly by an $n_1 \times n_2$ template named A. At the same time, absolute values of every local entropy based on A will be calculated and saved. When the scanning work is done, a matrix $E_F(n_1,n_2)$ is obtained, and all the local entropies are stored in the matrix orderly. Then same calculation will be applied to the thermal image G which is captured in a certain time delay after inflation, and its size are M×N pixels too, similar matrix $E_G(n_1,n_2)$ will be gotten sequentially. Afterward, the difference of local entropy matrix $\Delta E(n_1,n_2)=|E_F-E_G|$ is computed and $\Delta E(n_1,n_2)$ becomes the critical factor for leakage detecting and locating consequently.

(1) If thermal image G matches F well, then the value of ΔE will approach zero, hereby a conclusion can be

made that there is no leak in the test vessel.

(2) Setting the threshold δ as the criteria, if there is a salient region in the local entropy matrix of image, and the value of $\Delta E(n_1,n_2)$ in that region is tenably greater than δ, then leak is confirmed (probably not only one region).

(3) Calculation of reverse mapping is executed to the salient region of local entropy matrix $\Delta E(n_1,n_2)$, so that the coordinates of leakage point can be obtained subsequently.

By using upper strategies, local entropy matrixes with absolute values of the two thermal images shown in Figure 6 are calculated, and are presented in Figure 7 (a) and Figure 7 (b) respectively, finally the difference matrix between them can be easily gotten, as shown in Figure 8 (c).
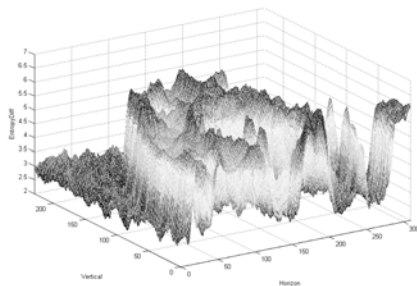
(a) Absolute local entropy matrix of Figure 6 (a)
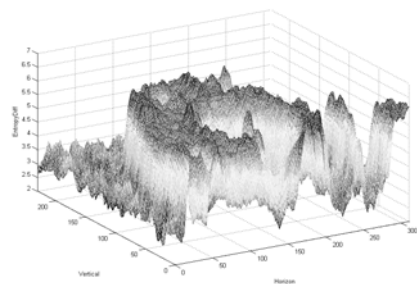
(b) Absolute local entropy matrix of Figure 6 (b)
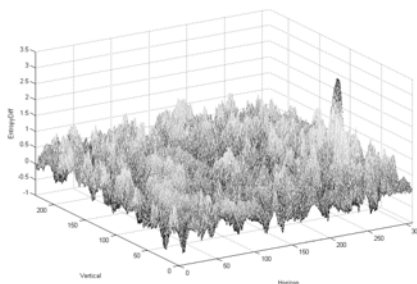
(c) Difference matrix between (a) and (b).

Figure 7 Local entropy matrixes

As shown in Figure 8 (c), the singular value in matrix fits the leakage point well, and the adoption of local entropy difference algorithm eliminates the shape information of test vessel effectively. After operation,

the contrast between leak area and non-leak area gets much more obvious, meanwhile noise and geometric distortion of the thermal images are suppressed evidently.

CONCLUSON

The leakage detection and localization method based on infrared thermography for the vessels is proposed in this paper, and it is proved to be feasible by simulating and experimental results. Mathematical model has been established for heat transfer, and it is evident that the differences in temperature caused by leak are conspicuous enough to be detected, especially by the use of compressed air of low temperature are. Moreover, speed optimization of local entropy difference algorithm should be done in the further study for its computational complexity.

REFERENCES

1. Xiaojian, Wu and Rongxin, Yan, Leak Detection, China Machine Press, Bei Jing, 2005, pp. 49-50, 81-84, 146-148.
2. Maric. I., The Joule-Thomson effect in natural gas flow-rate measurements, Flow Measurement and Instrumentation, 2005, 16-6, pp. 387-395.
3. Shini, Peng and Jianlun Chen, Calculation for Temperature Drop Induced by Adiabatic Throttle of Natural Gas, Gas & Heat, 2006, 26-1, pp. 1-4.
4. ter Brake, H.J.M. and Wiegerinck, G.F.M., Thermodynamic optimization of sorption-based Joule-Thomson coolers, Cryogenics, 2007, 47-3, pp. 143-152.
5. Gonzalez Ulises, Modeling and simulating MEMS devices using finite element analysis, Proceedings of 2001 ASME International Mechanical Engineering Congress and Exposition, New York, NY, United States, pp. 2583-2587.
6. Terumi Inagaki and Yoshizo Okamoto, Diagnosis of the leakage point on a structure surface using infrared thermography in near ambient conditions, NDT&E international, 1997, 30-3, pp. 135-142.
7. Chi Zhang and Hongbin Zhang, Detecting digital image forgeries through weighted local entropy, Proceedings of 2007 IEEE International Symposium on Signal Processing and Information Technology, Piscataway, NJ, USA, pp. 62-67.

P1-49

STUDY OF A GAS THRUST BEARING WITH SUPPLY GROOVES

Guido BELFORTE, Federico COLOMBO, Terenziano RAPARELLI, Andrea TRIVELLA,
Vladimir VIKTOROV

Department of Mechanical Engineering, Politecnico di Torino
Technical University
C.so Duca degli Abruzzi, 24 - 10129 - Torino -Italy
(E-mail: terenziano.raparelli@polito.it)

ABSTRACT

Plane externally pressurized thrust gas bearings for high speed spindles are considered. The behavior of the rotor-bearing system is studied both numerically and experimentally. A numerical model based on Reynolds equation is used to simulate the static and dynamic behavior of the system. Flow rate equation through inlet orifices is coupled with Reynolds equation. The flow rate is calculated by considering an experimentally determined discharge coefficient, that is function of holes diameter and local clearance. To increase stiffness are studied thrust bearings presenting a circumferential groove situated at the same radius of the supply holes. The influence of the groove on stiffness and stability is discussed. Simulations are made to evaluate the influence of supply holes diameter and of axial clearance on bearing characteristics.

Two thrust bearings are studied experimentally. They are composed by a symmetric couple of disks facing the rotor flange. The internal and external diameters of the disks are 52 mm and 110 mm and equipped with 8 holes of diameter 0.35 mm on a circumference of diameter 65 mm. A thrust bearing present a rectangular section circumferential groove, located at the same radius of the orifices, of width 0.7 mm and thickness 10 μm.

Comparisons between simulated and experimental stiffness are presented.

KEY WORDS

Gas, Thrust, Bearing, Grooves

NOMENCLATURE

b	critical ratio = 0.528
C_S	conductance
c_d	discharge coefficient
d_S	supply orifice diameter
F	axial force acting on the rotor (comprehensive of rotor weight)
G	mass flow rate
h	axial clearance
h_0	axial clearance in central position
h_g	groove depth
K	axial stiffness

k_T	temperature coefficient $= \sqrt{293/T^0}$
m	rotor mass
N	number of orifices on each bearing disc
P	absolute pressure
P_S	supply absolute pressure
q	inlet mass flow rate per unit surface
Re	Reynolds number
R^0	gas constant $= 287.6$ m²/s²K
r	radius
r_g	groove radius
r_o	supply holes circumference radius
S	orifice section
T^0	absolute temperature in normal condition
t	time
w_g	groove width
z	axial coordinate
μ	air viscosity
ρ_N	air density in normal condition
ϑ	angular coordinate
ω	rotational frequency

INTRODUCTION

Air bearings are often used in precision systems and high speed spindles for low friction losses and high positioning accuracy. They are applied in linear guideways, thrust bearings and rotating systems. Typical supply systems in case of circular geometries are annular orifices compensated bearings.

The design of such systems is more and more sophisticated and concerns the number and the diameter of supply orifices, the bearing geometry and sometimes the choice of grooves machined on bearing surfaces. The static and dynamic performance of these bearings depend on these parameters. Numerous are the studies on this field intended to optimize either stiffness or air flow rate [1]-[7]. Other works concentrate the study on the micro grooves [8,9] and on the benefits they introduce on the load capacity. It doesn't exist a single procedure that allows to find the best solution, because according to the applications the design requirements are different.

In [10] is presented a theoretical and experimental work on high speed spindle radial air bearings. Figure 1 shows the section of the spindle, composed by the carter 1, the rotor 2 of length 460 mm and diameter 50 mm, the radial bearings 3, the double thrust bearing 4. Each radial bushing presents 16 radial orifices of diameter 0.25 ± 0.01 mm, fabricated with EDM process. Radial clearance is approximately 20 μm.

Air bearings are supplied by ports 5. The rotor is accelerated by the pneumatic turbine 6, supplied by the distributor 7.
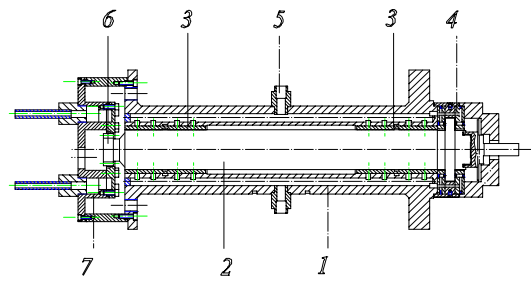
Figure 1 Pneumatic spindle

In this paper is studied the thrust bearing of the above-mentioned spindle with two different thrust geometries. The first solution considers plane disks with supply orifices equispaced, the other one presents a circular groove in correspondence of the supply orifices as well. Are described the geometry of the thrust bearings, the mathematical model, the test rig, the experimental and numerical results in terms of load capacity and stiffness. Then stability is numerically studied.

SCHEME OF THE THRUST BEARING AND NUMERICAL MODEL

Figure 2 shows the principal geometric parameters of the thrust bearing. It is composed by two disks 1 and 2 of inner radius r_i separated by the central ring 3. Between disks 1 and 2 is present the flange 4, of radius r_e, jointed to the rotor of radius R. The difference of thickness between ring 3 and flange 4 defines the axial gap $h_1 + h_2$. On each disc 1 and 2 are symmetrically machined N equispaced axial nozzles of calibrated diameter d_S, positioned on a circumference of radius r_o. In case a of Figure 2 is visible the supply orifices geometry. In case b the disks present a circumferential groove of radius $r_g = r_o$ and rectangular section of width w_g and depth h_g. F is the axial force applied, comprehensive of the rotor weight, z and ϑ are the cylindrical coordinates.

To model the thrust bearing were made the assumptions of isothermal expansion, laminar and viscous flow in the gap. Defining G the air mass flow rate through each supply hole, the time dependent Reynolds' equation (1) [11] in polar coordinates was solved with finite difference method for the two axial gaps.

$$r^2 \frac{\partial}{\partial r}\left(Ph^3 \frac{\partial P}{\partial r}\right) + \frac{\partial}{\partial \vartheta}\left(Ph^3 \frac{\partial P}{\partial \vartheta}\right) + 12\mu R^0 T^0 r^2 q =$$
$$6\mu\omega r^2 \frac{\partial(Ph)}{\partial \theta} + 12\mu r^2 \frac{\partial(Ph)}{\partial t} \qquad (1)$$
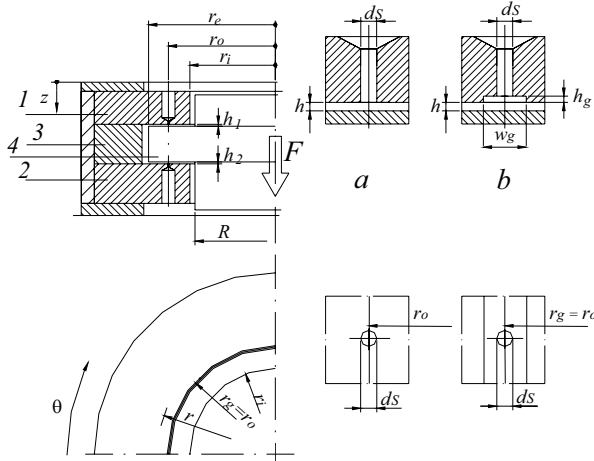
Figure 2 Scheme of thrust bearing

The clearances relative to each bearing disc are:

$$\begin{cases} h_1 = h_0 + z \\ h_2 = h_0 - z \end{cases} \qquad (2)$$

where h_0 is the clearance when the rotor flange is centered between the thrust bearing disks.

Term $q = G /(r\, dr\, d\vartheta)$ is the inlet mass flow rate per unit surface and is calculated only in the nodes that coincide with the supply holes. P_S is the absolute supply pressure. Mass flow rate G is calculated in accordance with ISO 6358, where P_c is the supply hole downstream absolute pressure, see equation. (3).

Conductance C_S appearing in the mass flow rate formula is expressed by equation (4), in which S is the cross-section of the simple orifice and c_d is the discharge orifice coefficient. The former depends on local clearance h, on supply port diameter d_S and on Reynolds number Re , calculated with (5) in correspondence of supply port section. The value of c_d was experimentally determined by measuring G and the pressure distribution under the orifice [13]. The equation extrapolated is (6).

$$G = \begin{cases} C_S k_T \rho_N P_S \quad , & if \quad 0 < \dfrac{P_c}{P_S} < b \\[4mm] C_S k_T \rho_N P_S \sqrt{1 - \left(\dfrac{\dfrac{P_c}{P_S} - b}{1-b} \right)^2} & ,if \quad 0 < \dfrac{P_c}{P_S} < b \end{cases} \qquad (3)$$

$$C_S = 0.686 \frac{c_d S}{\rho_N \sqrt{R^0 T^0}} \qquad (4)$$

$$Re = \frac{4G}{\pi d_S \mu} \qquad (5)$$

$$c_d = 0.85 \left(1 - e^{-8.2 \frac{h+h_g}{d_S}} \right) \cdot \left(1 - e^{-0.005\,Re} \right) \qquad (6)$$

In Figure 3 is shown the pressure distribution (expressed in Pa) in case of eight orifices of diameter d_S, supply pressure P_S =0.7 MPa and clearance h_0 =15 μm.
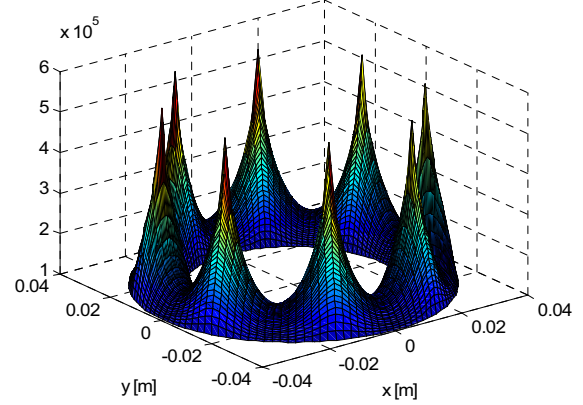
Figure 3 Numerical axial pressure distribution

Static
Calculations were made to obtain the pressure distribution in the thrust bearing at different air clearances h_0 . In this case the program solves equations (1) to (5) numerically in time from initial condition $P = P_a$ everywhere and reaches the steady-state solution after a transient. Mass flow rate through the supply holes is calculated iteratively evaluating the hole downstream pressure level p_c from (1), calculating G from (3-4), Re from (5), c_d from (6) and substituting in (3-4) till convergence.

Dynamic
To analyse the step-jump response of the thrust bearing, equations (1 to 5) were solved in time together with the axial spindle equation of motion (7):

$$m\ddot{z} + F_t(t) = F(t) \qquad (7)$$

in which F_t is the reaction force of the thrust bearing and m is the rotor mass, equal to 7.24 kg. The reaction force is calculated by integrating the pressures P_1 and P_2 present in the axial air gaps h_1 and h_2 over the thrust surfaces:

$$F_t(t) = \int_0^{2\pi} \int_{r_i}^{r_e} (P_2(t) - P_1(t)) r\, dr\, d\theta \qquad (8)$$

EXPERIMENTAL SET UP

Figure 4 shows a scheme of the set up to measure load

capacity and stiffness of the double thrust bearing. The carter *1* is mounted vertically on basement *2*. The load devices *3*, *4* are composed by two hollow cylinders containing a calibrated sphere with a clearance of 40 μm. They are positioned radially and axially and they are facing the nose 5. The load on the rotor is applied by pressurizing the inside of the cylinders; its value is obtained by measuring this pressure. For these tests only axial load was applied and without rotation of the spindle ($\omega = 0$). The axial load device allows to load rotor upwards. To load rotor downwards calibrated masses were laid on its top. In this way it was possible to measure the characteristics in both directions of the external load.

Two are the supply air lines: one is dedicated to the bearings, another to the load devices. In the first one is present a reservoir that assures temporarily supply air also in case of failure of the principal supply line. In both are used two high efficiency filters of class 1 that maintain the air clean from micro particles that could choke some orifices.
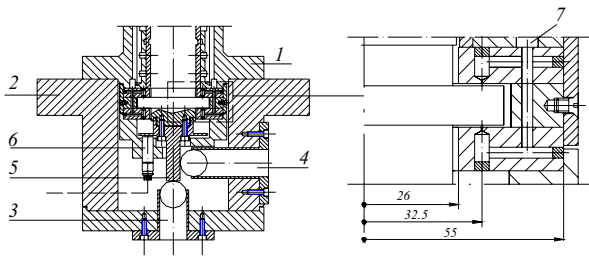
Figure 4 Thrust bearing section

A capacitive displacement transducer *6* with 0.1μm resolution, 500 μm full scale reading and 6 kHz passband was used to measure the axial displacement z. The amplified signal was read on a dedicated conditioning module.

In the same figure is also shown a magnification of the double thrust bearing, where are visible radial and axial supply channels. Supply calibrated holes are fabricated with EDM process. The geometric parameters chosen for the prototypes type *a* and *b* are $N = 8$, $d_S = 0.35 \pm 0.01$ mm, $r_o = 32.5$ mm, $r_i = 26$ mm, $r_e = 38.5$ mm. The nominal axial clearance is $h_0 = 19$ μm. It results measuring axial gap $h_1 + h_2$ like above described using Eq. (2). This value was then compared measuring the axial gap by moving the rotor axially without supply pressure. In this case h_0 is calculated from the rotor axial displacement and it is equal to 13 μm. The difference between the two h_0 values is probably due to geometric tolerance in fabricating the disks of the thrust bearing and on the measure precision.

For the geometry *b* the groove is defined by: $w_g = 0.7$ mm, $h_g = 10$ μm. Figure 5 shows a photo of the

grooved disk and the enlargement of a supply hole.
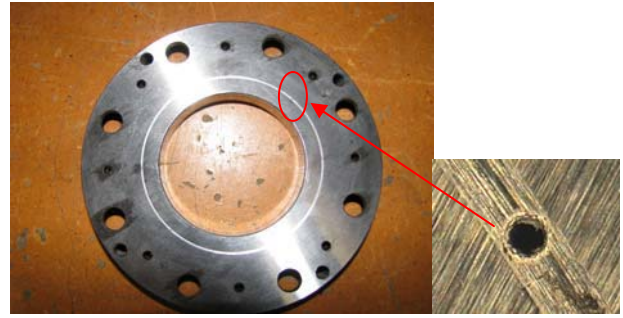
Figure 5 Photo of grooved disk and supply orifice magnification

In Figure 6 are shown the supply air lines of the system: one is dedicated to the bearings, another to the load devices. In the first one is present a reservoir *8* that assures temporarily supply air also in case of failure of the principal supply line. In both are used two high efficiency filters *9* of class 1 that maintain the air clean from micro particles that could choke some orifices.
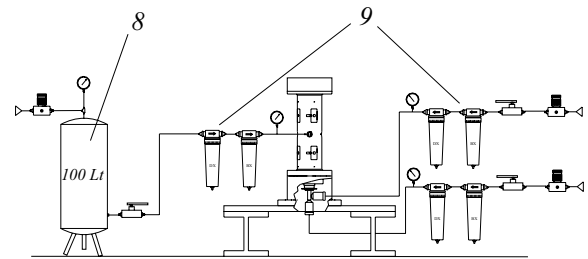
Figure 6 Supply bearing system

RESULTS AND DISCUSSION

Static behavior analysis

Experimental and numerical results are discussed in static behavior considering $d_S = 0.35$ mm, $h_0 = 19$ μm, and different supply pressure P_S (0.3-0.9 MPa) for the two thrust bearings realized ($h_g = 0$ μm, $h_g = 10$ μm). Figures 7 and 8 show the load F v.s. axial displacement experimental diagrams without and with groove.

Positive and negative loads are obtained respectively using the axial load device and applying calibrated mass. The zero displacement point is obtained by applying by the load device an external force opposed to the rotor weight.

Comparing Figures 7 and 8 it is clear that the groove increases stiffness and improves the linearity of the characteristics. It is also verified the simmetry respect the zero.
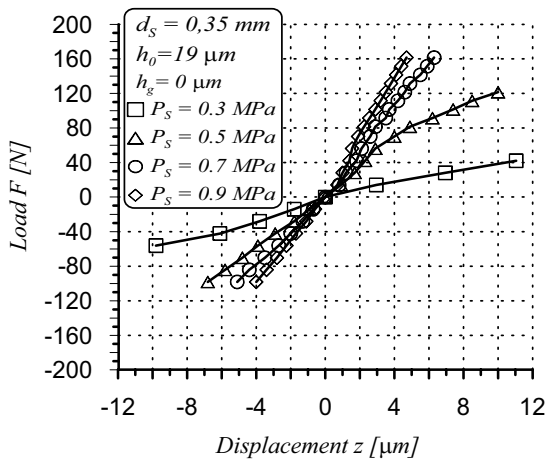
Figure 7 Load v.s. displacement experimental diagram in case of thrust without groove

Figure 8 Load v.s. displacement experimental diagram in case of thrust with groove

Figure 9 Load v.s. displacement with P_S =0.7 MPa
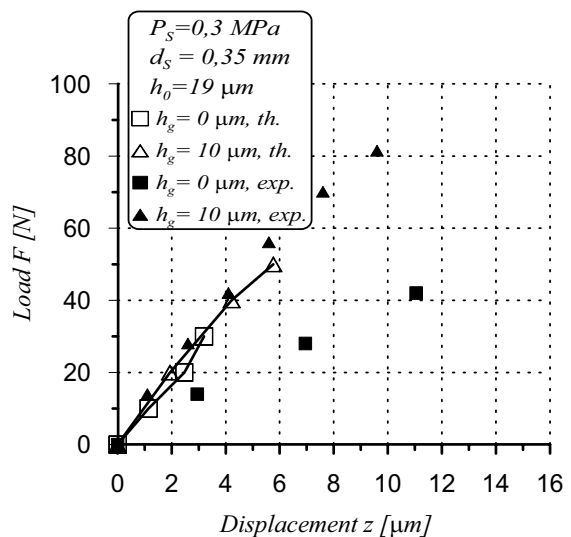
Figure 10 Load v.s. displacement with P_S =0.3 MPa

Figure 11 Stiffness v.s. supply pressure P_S

In Figures 9 and 10 are compared numerical and experimental load carrying capacities respectively at P_S = 0.7 and 0.3 MPa. In particular in Figure 9 calculated stiffness with h_g =10 μm is 40 N/μm, while without groove it is 28 N/μm, that is 30% lower. Numerical results present good linearity in the range $\varepsilon = z / h_0$ =0÷0.4. Experimental stiffness are 6% and 12% lower than numerical ones in case of 10 mm groove and without groove respectively.

In case of P_S =0.3 MPa without groove difference between numerical and experimental results is more evident.

Figure 11 shows a comparison between numerical and experimental stiffness for both thrust bearings at

519   Copyright © 2008 by JFPS, ISBN 4-931070-07-X

different supply pressures.
To evaluate stiffness was considered a 4 μm displacement with respect to central position ($z = 0$).

Step response and stability analysis
In this section are shown the dynamic numerical simulations of thrust bearing considering d_S =0.35 mm, h_0 = 19 μm, and supply pressure P_S = 0.7 MPa. Stability is investigated by analyzing the rotor response to a 100 N force step with different groove depth: h_g =0, 10 and 20 μm. In Figure 12 are compared the responses in the three cases, considering the 7.24 kg rotor mass. It is visible that by increasing the groove depth stiffness increases but motion becomes lower damped till instability for h_g =20 μm.
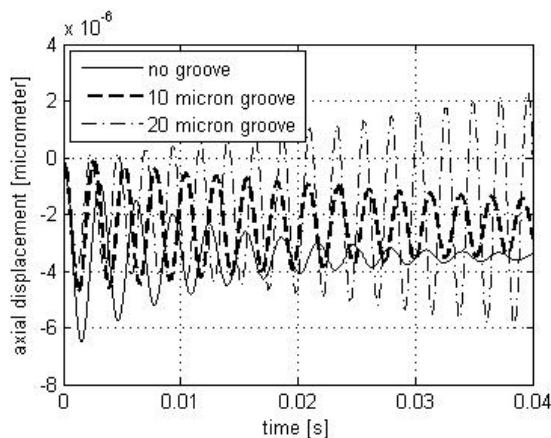
Figure 12 Thrust step response

It was verified that with the 20 μm deep groove the thrust is unstable. So the preferred solution is to adopt a thrust bearing with a groove of 10 μm depth.

CONCLUSIONS

Comparisons between simulated and experimental stiffness and flow rate are shown. Numerical method is suitable to simulate a grooved thrust bearing.
The circular groove increases stiffness, but numerical results show that the groove volume decreases stability.

ACKNOWLEDGEMENTS

REFERENCES

1. Al-Bender, F. and Van Brussel, H., Tilt Characteristics of Circular Centrally Fed Aerostatic Bearings, Tribology International, 1992, **25**-3, pp.189-197.
2. Yoshimoto, S., Tamura, J. and Nakamura, T., Dynamic Tilt Characteristics of Aerostatic Rectangular Double-Pad Thrust Bearings With Compound Restrictors, Tribology International, 1999, **32**, pp.731-738.
3. Bang, K.G. and Lee, D.G., Thrust Bearing Design for High-Speed Composite Air Spindles, Composite Structures, 2002, **57**, pp.149-160.
4. Shigeka, Y., Makoto, Y. and Kazuyuki, T., Numerical Calculations of Pressure Distributionin the Bearing Clearance of Circular Aerostatic Thrust Bearings With a Single Air Supply Inlet, Transactions of the ASME, 2007, **129**-4, pp.384-390.
5. Belforte, G., Raparelli, T. and Viktorov, V., Theoretical Investigations of Fluid Inertia Effects and Stability of Self-Acting Gas Journal Bearings, ASME Journal of Tribology, 1999, **121**-4, pp. 836-843.
6. Belforte, G., Raparelli, T. and Viktorov, V., Modeling and Identification of Gas Journal Bearings: Self-Acting Gas Bearing Results, ASME J. Tribology, 2002, **124**, pp.716-724.
7. Viktorov, V., Belforte, G. and Raparelli T., Modeling and Identification of Gas Journal Bearings: Externally Pressurized Gas Bearing Results, ASME J. Tribology, 2005, **127**, pp.548-556.
8. Nakamura T, Yoshimoto S., Static tilt characteristics of aerostatic rectangular doublecompound restrictors, Tribology Int. 1996; **2**, pp. 145-152.
9. Chen, M.F. and Lin, Y.T., Static Behavior and Dynamic Stability Analysis of Grooved Rectangular Aerostatic Thrust Bearings by Modified Resistance Network Method, Tribology International, 2002, **35**, pp. 329-338.
10. Belforte, G., Raparelli, T., Viktorov, V., Trivella, A., and Colombo, F., An Experimental Study of High-Speed Rotor Supported by Air Bearings: Test rig and First experimental results. Tribology International, 2006, **39**, pp. 839-845.
11. Grassam, N.S. and Powell J.W., Gas Lubricated Bearings, Butterworths, London, 1964, pp. 135-139.
12. Belforte, G., Colombo, F., Raparelli, T., Trivella, A., and Viktorov, V., Study of a High Speed Electrospindle With Air Bearings, European Conference on Tribology ECOTRIB 2007 Ljubliana, June 12-15, 2007, **2**, pp. 969-982.
13. Belforte, G., Raparelli, T., Viktorov, V. and Trivella, A., Discharge Coefficients of Orifice-Type Restrictor for Aerostatic Bearings, Tribology International, 2007, **40**, pp. 512-521.

P1-50

STUDY ON A NEW DEXTEROUS HAND ACTUATED BY PNEUMATIC MUSCLE ACTUATORS

LIU Hao[*], FAN Wei[*], YU Lin[*], PENG Guang-zheng[*], and WANG Tao[*]

[*]Department of Automatic Control, School of Information Science and Technology,
Beijing Institute of Technology, Beijing 100081, China
(fanwei@bit.edu.cn)

ABSTRACT

Research on the robot hand actuated by pneumatic muscle actuators is significative for its complaisance and dexterity. In this paper, a new kind of dexterous hand is designed and produced. The layout of tendon is analyzed and optimized. Furthermore, a single finger is controlled by Fuzz-PID and the good control precision is achieved. And, the master-slave control of the whole dextrous hand is realized simulating the movement of human hand with a cyber-glove.

KEY WORDS

dexterous hand, pneumatic muscle actuator, fuzzy-PID control, master-slave control

INTRODUCTION

Dexterous robot hand is a highly integrated electrical and mechanical system, involving machinery, electronics, computers, control, and other subject areas. Since the 1980s, the technology on the pneumatic muscle actuator (for short, PMA) has been developing. The PMA as a kind of robot actuators attracts more and more attention from researchers.

After a great deal of research on the PMA, the author and colleague of the laboratory design a humanoid dexterous robot hand, driven by PMAs, transited by tendons. The single-finger is controlled by fuzzy PID, and the whole hand planning and master-slave control is based on the cyber glove. It is achieved initial results.

STRUCTURE

System View

The dexterous hand equipment (Figure 1) is constructed from 4 parts. They are dexterous fingers as the controlling object, PMA as the actuator, tendons as the transmission device and proportional pressure valves.

Humanoid dexterous hand is designed into an integrated structural system (hand + arm): the hand and the arm are jointly designed and cannot be conceived as separate subsystems (examples of this approach are the Utah Hand [1], the Robonaut hand [2], the Shadow Hand [3] and the ZAR hand [4]). An integrated system can distribute these actuators in the whole structure, placing them where room is available. Pneumatic muscles which are used to drive fingers are placed in the forearm muscle and the drivers of

the wrist are placed in the upper arm. The power and movement of pneumatic muscles are transited by tendons, which enhance the effectiveness of the bionic, and effectively reduce the size of the palm and fingers.
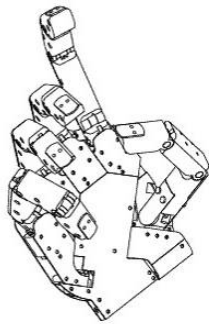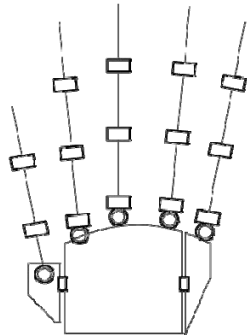
Figure 1 BIT hand　　　　Figure 2 DOF of hand

The PMA of the Shadow company, is 6 mm in diameter, 200 mm in a total length and 10 grams in weight , as Figure 3 shows. It can contract 30 mm, and provide 70N at maximum force. The proportional pressure valve is the ITV0050 from the SMC.

Figure 3 PMA of Shadow Company

Mechanical Profile

As a humanoid dexterous hand, it has 5 fingers. Although the four-fingered dexterous hands, or even three-fingered dexterous hands can make grasp equally well, but the five-fingered dexterous hand, which make control simple, do grasp better. When hold objects in hand, each finger would not have a very clear task demarcation, that control algorithm will be correspondingly simple [5].

Dexterous hand composed by a palm and 5 fingers. The palm is connected with metacarpals of the thumb and the little finger and the near sections of the index finger, the

middle finger and the ring finger (Figure 4).
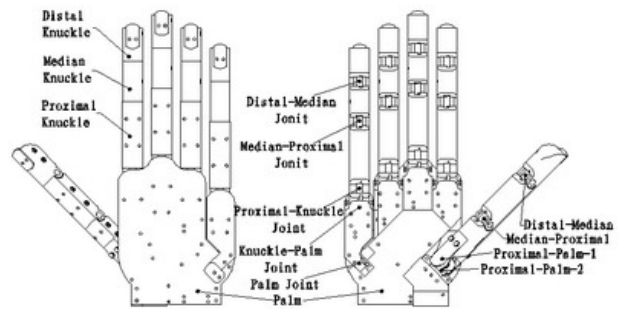
Figure 4 Hand components

The dexterous hand with five fingers, except wrist, has a total of 17 degrees of freedom as shown in Figure 2. The thumb has 4 joints, 4 degrees of freedom; the index finger has 4 joints, 3 degrees of freedom; the middle finger has 4 joints, 3 degrees of freedom; the ring finger has 4 joints, 3 degrees of freedom; the little finger has 5 joint, 4 degrees of freedom. There are 34 PMAs in all. The wrist has 2 joints and 2 degrees of freedom, which driven by 4 PMAs.

Except the thumb, the 2 remote joints of other 4 fingers are coupled by tendons. The coupled joints are combined for a degree of freedom respectively, that is, to reduce the driver number of fingers and to make the movement of fingers more like human fingers as shown in Figure 5.

Each PMA transits the movement and the power through a tendon. The tendon is fixed on the end of knuckle. A couple of PMAs and tendons make up of a degree of freedom shown in Figure 6. The index finger, as an example, has 3 independent degree of freedoms and driven by 6 PMAs.
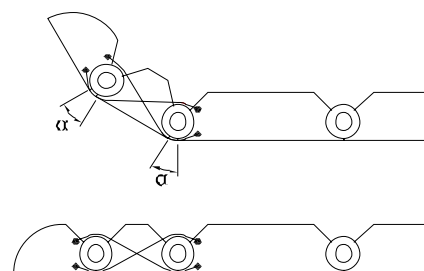
Figure 5 Linkage of joints
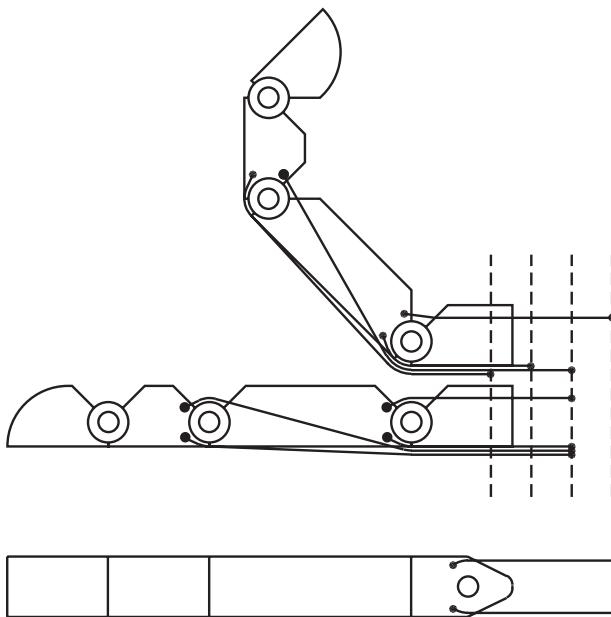
Figure 6 Tendons in a finger

The shape of the dexterous hand has a high imitation of

human nature. It was designed in the size of the scope of the general human hands, and it has the same dimension with real hand (Table 1).

SINGLE FINGER CONTROL

System View

The movement of the dexterous finger in each degree of freedom is actuated by PMAs. Through accommodating the compressed air in pneumatic muscles, we can control the contractile capacity of muscle. Using tendons, the joint movement is towed by muscle contractility.

The control system of dexterous finger, as shown in Figure 7 is comprised by pneumatic muscles, an industrial computer, a PCI-1710 analog input card, a PCL-727 analog output card, SMC ITV-0050 valves and position sensors.

Table 1 Dimension of the hand

Thumb [mm]	Index finger [mm]	Middle finger [mm]	Ring finger [mm]	Little finger [mm]	Palm length [mm]	Palm width [mm]	Palm thickness [mm]
77	105	105	105	105	100	88	17
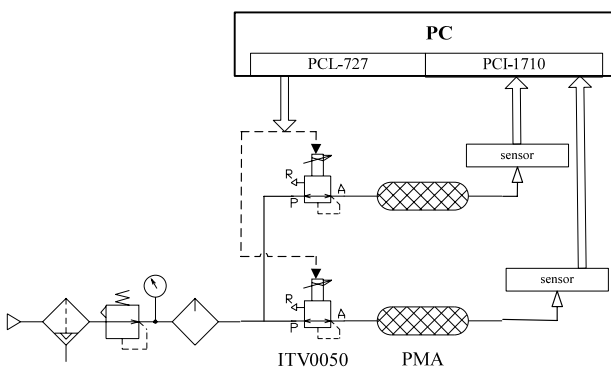
Figure 7 Control system of the dexterous finger
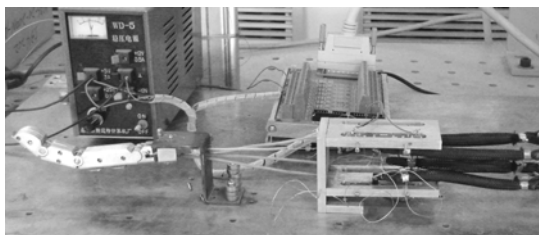
Figure 8 Experiment system of single finger control

In the control system of single finger, we measure the constriction of the PMA in order to calculate the joint angle indirectly. The position sensor adopts the linear potentiometer with 50KΩ.

Fuzzy PID

In the fuzzy-PID controller, PID parameters are adjusted referring to the fuzzy rule and the fuzzy inference. The detail control algorithm is indicated as follow (Figure 9): the inputs are error and the rate of error, noted by e and e_c. According to the fuzzy rule, the PID control parameters K_p, K_i and K_d are adjusted on-line, to meet the performance requests of controller parameters for different errors and different rates of error. After that, the controlled object performs preferable static performance and dynamic performance, according with the demands of control system.
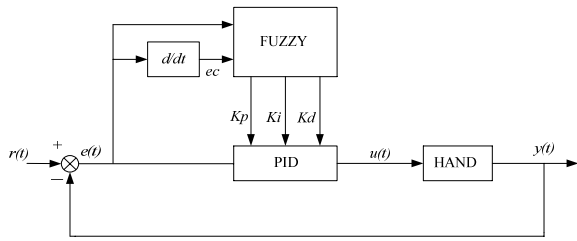
Figure 9 Fuzzy-PID position control system

The algorithm of the integral separation PID position controller is as following:

$$u(k) = K_p e(k) + \beta K_I \sum_{j=0}^{k} e(j)$$
$$+ \frac{K_d}{6}\left[3e(k-1) - 3e(k-2) + e(k) - e(k-3)\right]$$
$$\text{where,} \quad \beta = \begin{cases} 0, & |e(k)| > \zeta \\ 1, & |e(k)| \leq \zeta \end{cases}$$

we program and calculate by Matlab to produce control decision table for K_p, K_i and K_d which is stored in computer. During the control process, using the fetch table method to read the data from control decision table reduces on-line computing time and increases processing velocity of system.

Control result

For the dexterous hand joint actuated by pneumatic muscles, using PID and fuzzy-PID respectively to track the square wave, the contrast experiment result is as Figure 10.

(a) PID   (b) fuzzy-PID
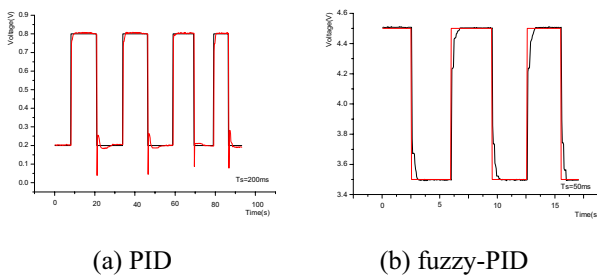
Figure 10 Contrast of PID and fuzzy-PID control effort

In the contrast experiment for tracking the square wave, we can find that by using PID control, there is much more overshoot in the descending portion of the curve. However, fuzzy-PID control performs the faster response and the smoother curve. The system sampling frequency

goes up from 100ms to 50ms. Therefore, it not only can track the signals with higher frequencies, but also increase processing velocity of system

MASTER SLAVE CONTROL

System View

Current control system is comprised as following: a humanoid dexterous hand with five fingers, 34 pneumatic muscles, 34 pressure proportional valves, a cyber-glove, an industrial computer and 3 pieces of PCL-727 analog output cards.
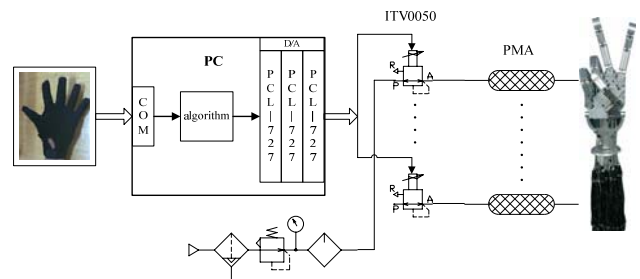
Figure 11 Sketch map of control loop

Cyber-Glove

We need to gather all the real-time information about every joint angle, when any of them is changing. As one of the common equipments in virtual reality system, the cyber-glove is the preferred equipment to gather and output signals (Figure 12). In this cyber-glove, there are 15 flexible sensors fixed on each joint (Figure 13).

Figure 12 Cyber-glove   Figure 13 Sensors on glove
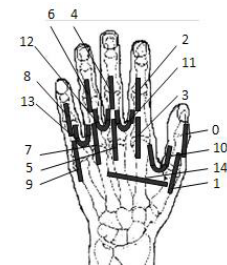
Control Strategy

For representing the control effects of dexterous hand intuitively, each joint of dexterous hand follows the

movements that each joint of human hand performs, as real-time master-slave control. Because of lacking sensors fixed on the dexterous hand, the system control structure is not a closed loop control. Currently, we use the master-slave open loop control strategy, based on the model analysis (Figure 14).
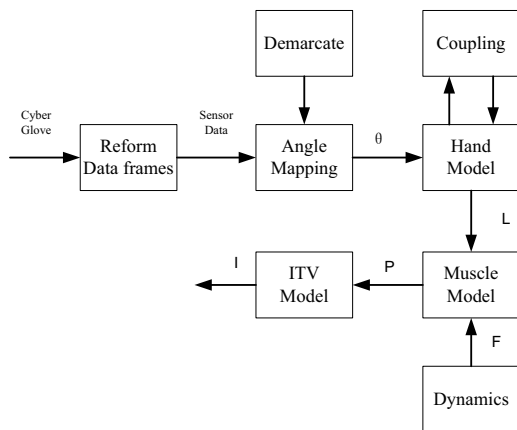
Figure 14 Master-slave control based on model

Control Effect

The actual control effects indicate that the dexterous hand is able to pose common gestures just as the human hand, as shown in Figure 15.

(a)   (b)

(c)   (d)
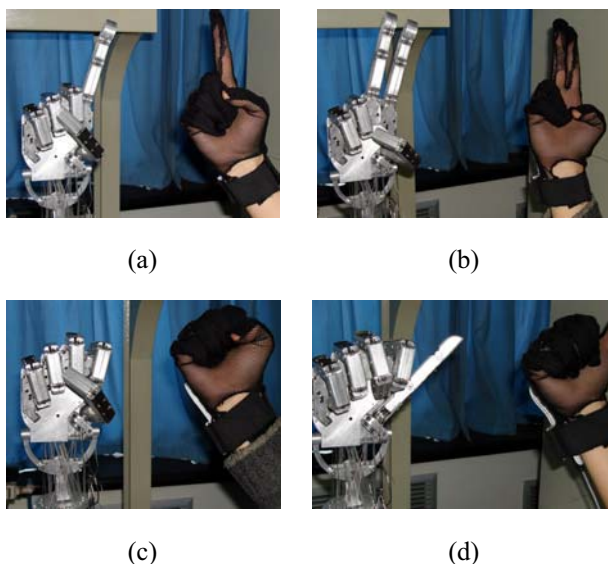
Figure 15 Gestures just as the human hand

The power grasping demonstration (Figure 16) includes grasping a cylinder object (16-a), an angle column object (16-b) and a spherical object (16-c). The cylinder object is a capped bottle. The angle column object is an empty bottle. The spherical object is an orange. The actual control effects indicate that the dexterous hand is able to steadily grasp objects with different shapes, sizes and qualities, by using its five fingers.
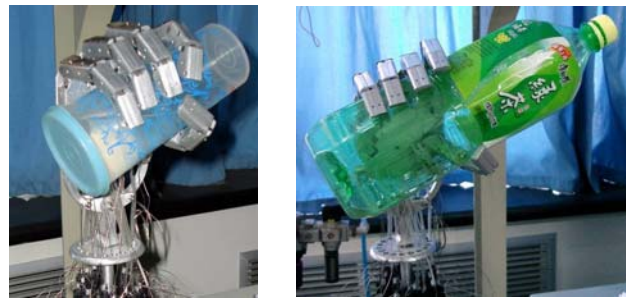
(a)   (b)
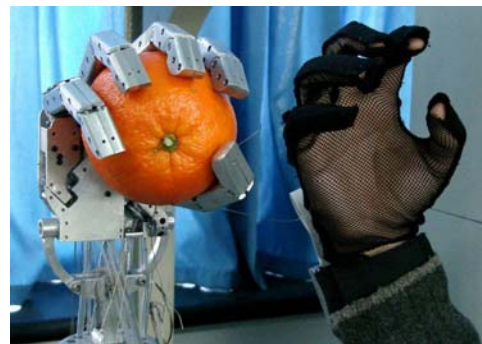
(c)

Figure 16 Power grasping

The precision grasping demonstration (Figure 17) includes seizing an orange with the thumb and the forefinger in Figure 17-a, or seizes a screwdriver with the thumb, the forefinger and the middle finger in Figure 17-b, or grasps a compact disc with the thumb, the forefinger and the middle finger in Figure 17-c. The actual control effects indicate that the above dexterous hand possesses potential abilities for grasping objects and manipulating instruments accurately.

CONCLUSIONS

This paper deals with a new kind of dexterous hand actuated by PMAs. Following conclusions can be summarized:

1. The dexterous hand actuated by PMAs is designed and manufactured.

2. A single finger is controlled by Fuzz-PID and the good control precision is achieved.

3. The master-slave control of the whole dextrous hand is realized simulating the movement of human hand with a cyber-glove. The dexterous hand has the grasp ability as the human does, which can be seen from the master-slave control results.
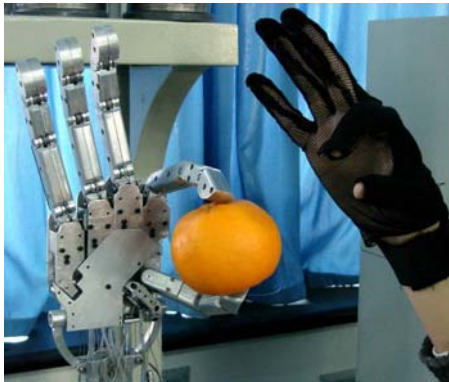
(a)

(b)   (c)

Figure 17 Precision grasping

However, much future work shoud be done. For example, to further improve the system response rate, the process of increasing friction compensation algorithm is needed. The current system of whole hand is still open-loop control system. In the future, to form a position close-loop system, angle sensors are needed; to form a force close-loop system, tactile sensors are needed. And the adoption of distributed signal acquisition and processing can reduce system complexity.

REFERENCES

1. Jacobsen S. C., Wood J. E., Knutti D. G., Biggers K. B., The UTAH/MIT Dextrous Hand: Work in Progress [J]. The International Journal of Robotics Research, 1984, 3(4), pp. 21-50.
2. Lovchik C. S., MDifler M. A., The Robonaut Hand: A Dextrous Robotic Hand for Space [J]. Proceedings for the IEEE International Conference on Robotics and Automation. Detroit, Michigan, 1999, pp. 907-912.
3. Shadow Robot Company. Shadow Dextrous Hand Technical Specification [Z]. 2005,2.
4. Boblan I., Bannasch R., Schwenk H., Miertsch L., Schulz A., "A Human like Robot Hand and Arm with Fluidic Muscles: Biologically Inspired Construction and Functionality", Embodied Artificial Intelligence, Dagstuhl Event 03281, Springer, 2003, pp.160-179.
5. Franca D., Fabrizio S., Supervised term weighting for automated text categorization[C]. Proceedings of the 2003 ACM Symposium on Applied Computing. Melbourne, Florida, USA: ACM, 2003, pp.784-788.
6. Li Haifeng, Jiang Tao, Zhang Keshu. Efficient and robust feature extraction by maximum margin criterion[C]. Pro2ceedingsof the Advances in Neural Information Processing Systems. Vancouver, Canada, MIT, 2003, pp.97- 104.

P1-51

FABRICATION OF AN IN-PIPE MOBILE INSPECTION ROBOT DRIVEN BY PNEUMATIC PRESSURE AND IMITATING MOVING OF A GREEN CATERPILLAR

Yukiya GOTO*, Manabu ONO** and Shigeo KATO*

* Department of System Engineering
Nippon Institute of Technology
Miyashiro, Saitama, 345-8501 Japan
(E-mail: s1034224@stu.nit.ac.jp)
** Department of Mechanical Engineering
Tokyo Metropolitan College of Industrial Technology
Shinagawa, Tokyo, 140-0011 Japan

ABSTRACT

We have many small diameter pipes that are gas or water pipes for individual or corporate houses and boilers or hot water pipes for industries. They must be periodically inspected in order to protect the accident previously. Diameters of these pipes are different at the place where pipes change from the main to the branch and a step comes here. The inspection robot for these pipes must move different diameter and go over the step. We propose a mobile robot that imitates the moving of a green caterpillar. The robot is constructed by the eight parallel rubber bellows and three suction brakes. The fabricated mobile robot was confirmed to move in different diameter pipes whose diameters are more than 70 mm. Its speed was 20 mm/s.

KEY WORDS

A green caterpillar, In-pipe, Robot, Bellows, Suction brake

INTRODUCTION

We have many small diameter pipes that are gas or water pipes for individual or corporate houses and boilers or hot water pipes for industries. These pipes may be occurred to injure or to corrode by their decrepit. The injury or the corrosion of pipes causes the leak of fluid and links to the accident. So, these pipes must be periodically inspected in order to protect the accident previously. They are settled in the ground or in the narrow spaces and some of them are covered by casings or hard heat insulators. So, it is very difficult to inspect from outside of the pipe. If we can insert a mobile inspection robot into the pipe from the suitable position, we are easy to inspect the pipe. In-pipe mobile robots driven by pneumatic actuator have been proposed by

several research groups for same diameter pipes [1], [2]. However, some of these pipes are long and their diameters are different at the place where pipes change from the main to the branch. The diameter of pipes is within 70 mm and 150 mm for example. So, the inspection robot for these pipes must move in different diameter, generating large traction force for the inspection of long distance.

We have fabricated inspection robots applying an earthworm and an inchworm [3], [4]. A braking mechanism which is using cone-shape friction rings for the earthworm type inspection robot is designed for the diameter of 79 mm. Then the inspection robot could not move in pipes whose diameter changes more than 5 mm from 79 mm. The earthworm type inspection robot can not move in pipes that the diameter changes from 70

mm till 150 mm. On the other hand, the inchworm type inspection robot which is using bulging brakes is confirmed to move in pipes whose diameter is 70 mm and 140 mm. However, the traction force of the inchworm type inspection robot changes on the diameter of the pipe. The traction force is 11 N at the 70 mm pipe, but is only 1 N at the 140 mm pipe.

The traction force depends on the friction force of the braking mechanism. So, we propose a suction brake for the braking mechanism. The suction brake can stick on the pipe and hold the pipe by the negative pressure supplied from a vacuum pump. The friction force of the suction brake is so larger than those of another braking mechanism and is predicted easily.

Now, we remark the moving motion of a green caterpillar. The green caterpillar sticks a passage such as the leaf by its prolegs. If we can imitate prolegs by the suction brake, we may obtain large traction force. The green caterpillar moves its prolegs by waving its abdomen. This waving motion is imitated by the action of four parallel rubber bellows actuator driven by pneumatic and vacuum pressure.

The inspection robot that is imitated the green caterpillar can move at the speed of 20 mm/s in the pipe whose diameters are from 70 mm to 150 mm, generating the traction force of as large as 20 N. We may inspect long and different diameter pipes, because we have obtained large traction force. Besides, the green caterpillar type inspection robot has been confirmed to pass the step more than 5 mm.

GREEN CATERPILLAR

We observed moving motion of the green caterpillar. The moving motion is shown in Figure 1. The green caterpillar consists of a head, a thorax and an abdomen. The thorax has six true legs and the abdomen has five pairs of prolegs. Five pairs of prolegs make three groups that are front two pairs, central two pairs and rear one pair of prolegs. The prolegs of the rear one pair are called as claspers. The prolegs are not segmented, but are cylindrical. They are used for walking and clinging as they have microscopic hooks on the base.

The moving of the green caterpillar is as follows.

(a) In the initial condition, the green caterpillar is sticking to the leaf by all of prolegs of the abdomen and is stationary.

(b) The rear abdomen waves and the rear one pair of prolegs (claspers) are taken off.

(c) The central abdomen waves and the central two pairs of prolegs are taken off and the rear one pair of prolegs land on the leaf that is forward direction from the initial condition.

(d) The front abdomen waves and the front two pairs of prolegs are taken off and the central two pairs of prolegs land on the leaf that is forward direction from the initial condition.
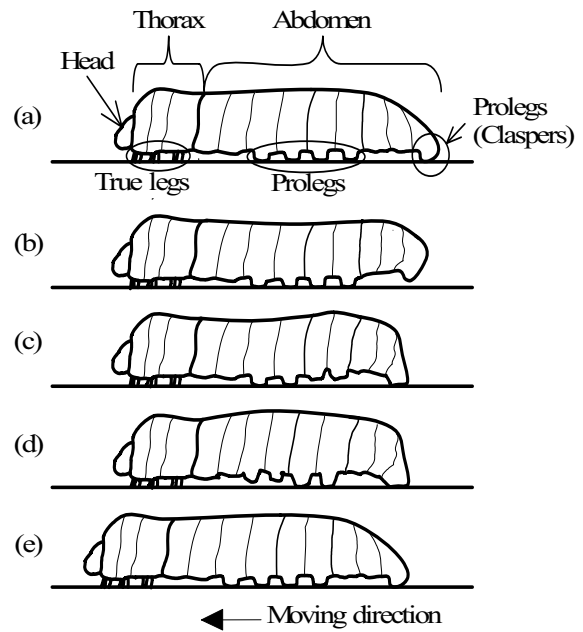
Figure 1   Moving Motion of a green caterpillar
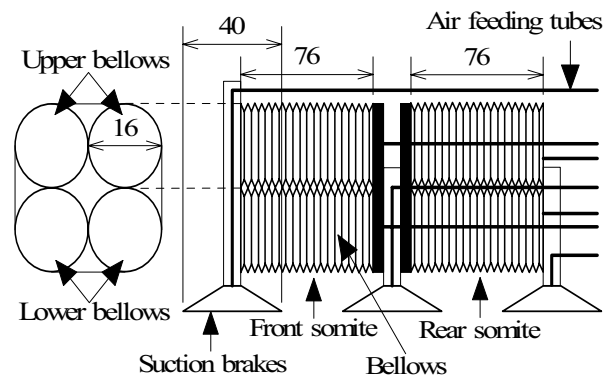
Figure 2   Structure of in-pipe mobile robot

(e) The green caterpillar stops its waving and sticks the all of prolegs to the leaf. Then, the head and the thorax are moved to forward direction. The cycle of moving of the green caterpillar ends.

We understand that the green caterpillar can move to the forward direction by moving of three groups of prolegs in order to the forward direction.

STRUCTURE OF THE ROBOT

A fabricated robot is imitated the abdomen of the green caterpillar. A structure of the robot is shown in Figure 2. The abdomen is imitated by two groups of four parallel rubber bellows actuators which are arranged in the matrix of two rows and two columns. The matrix of two rows and two columns makes a somite of the abdomen.

528

Two parallel rubber bellows in the same row are supplied same pressure by an air feeding tube. The bellows made of Nitrile Butyl Rubber (NBR) is 16 mm in diameter and 76 mm long. A group of prolegs is imitated by a suction brake. The suction brake is a sucker made of NBR and its diameter is 40 mm. The air feeding tube for positive and negative pressure is connected in the center of the suction brake. Three suction brakes are arranged at the front, the center and the rear of the two groups of four parallel rubber bellows actuators.

CONTROL SYSTEM OF THE ROBOT

A control system of the robot is shown in Figure 3. The system is constructed by a robot, seven electromagnetic valves, two different (positive and negative) pressure sources, a computer and a valve controller. The positive pressure source is an air compressor and the negative pressure source is a vacuum pump. The moving sequence of the robot is programmed in the computer. The electromagnetic valves are controlled by the computer through the valve controller. The electromagnetic valve has three ports. The output ports of the four electromagnetic valves are connected to the bellows for the abdomen through the air feeding tubes. The output ports of the three electromagnetic valves are connected to the suction brakes through the air feeding tubes. The ones of input ports are connected to the vacuum pump and the others are connected to the atmospheric pressure.

MOVING MOTION OF THE ROBOT

The robot moves in the pipe by stretching and bending motion of two somites and sticking of the suction brakes using positive and negative pressure.

Moving principle of the somite
Moving principle of the somite is shown in Figure 4. The somite consists of bellows. The bellows stretches when positive pressure is supplied and shrinks when negative pressure is supplied. That is, the somite stretches when positive pressure is supplied to the upper and the lower bellows. The somite shrinks when negative pressure is supplied to the upper and the lower bellows. Besides, the somite can bend when different pressure is supplied to the upper and the lower bellows, for example, the somite bends upward, when positive pressure is supplied to the upper and negative pressure is supplied to the lower bellows. The waving motion of the green caterpillar can be imitated by the stretching, shrinking and bending motion of the somite.

Characteristics of the suction brake
 The robot generates friction force by the suction brake. A model of the suction brake is shown in Figure 5. The suction force N by the suction brake is shown by Eq. (1), where p is the pressure at the radius r from the center of

Figure 3   Control system of in-pipe mobile robot

P : Positive pressure

N : Negative pressure

(i) Stretching

(ii) Shrinking   (iii) Bending
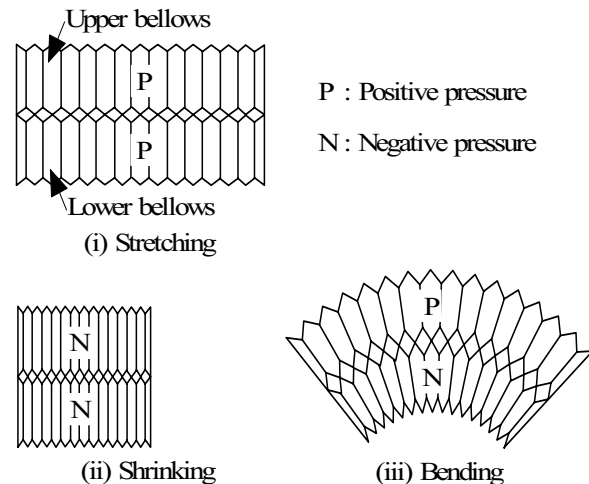
Figure 4   Moving principle of somite
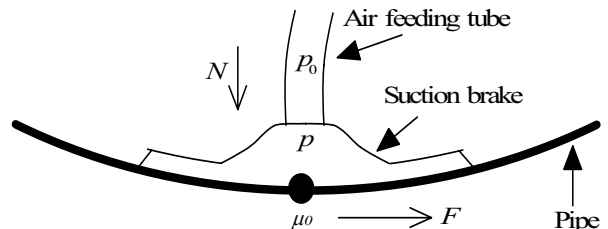
Figure 5   Suction brake model

the suction brake.

$$N = \left| \int p \, 2\pi r \, \mathrm{d}r \right| \qquad (1)$$

An internal pressure distribution in the suction brake is shown in Figure 6. The internal pressure distribution is measured radially from the center of the suction brake put in the pipes whose diameters are 70 mm and 150 mm. Supplied pressure p_0 is -84 kPa. The internal pressure distribution does not depend on the diameter of the pipe. The internal pressure is -84 kPa at the center of the suction brake and less than -80 kPa at the radius within 8 mm. However, the internal pressure is 0 kPa at the radius over 9 mm. The suction force N is obtained as 21.3 N by using Eq. (1) and the internal pressure distribution shown in Figure 6.

The suction force N is represented by Eq. (2), where A is the area of the suction brake and α is the constant.

$$N = \left| \alpha \, p_0 \, A \right| \qquad (2)$$

From comparing of the result of Eq. (1) and Eq. (2), we obtain that the constant α is 0.2. We can predict the suction force N from Eq. (2).

The maximum friction force F is shown by Eq. (3), where μ_0 is the friction factor between the suction brake and the pipe.

$$F = \mu_0 N \qquad (3)$$

The friction factor obtained by an experiment is 1.8 in the case of acrylic pipe and the suction brake.

The maximum friction force $\overline{F}$ is measured by an experiment where negative pressure is -84 kPa. A calculated value F and a measured value $\overline{F}$ of the maximum friction force are shown in Figure 7. We may predict the maximum friction force, because the measured value $\overline{F}$ almost coincides with the calculated value F by Eq. (2) and Eq. (3).

Moving principle of the robot and its confirmation

Internal pressure of the robot is measured when the robot is moving in an acrylic pipe whose diameter is 110 mm. Measured results are shown in Figure 8, 9, and 10. Moving motions by the pressure changes are shown in Figure 11. The robot moves to the forward direction by moving its three suction brakes in order to the forward direction. The robot waves its front and rear somite to push the suction brake to the wall of the pipe and to lift up the suction brake from the wall of the pipe. The suction brake can stick the wall of the pipe by supplying the negative pressure and release the wall of the pipe by supplying the atmospheric pressure. In Figure 11, black colored suction brake shows that the suction brake sticks the wall of the pipe and white colored suction brake shows that the suction brake
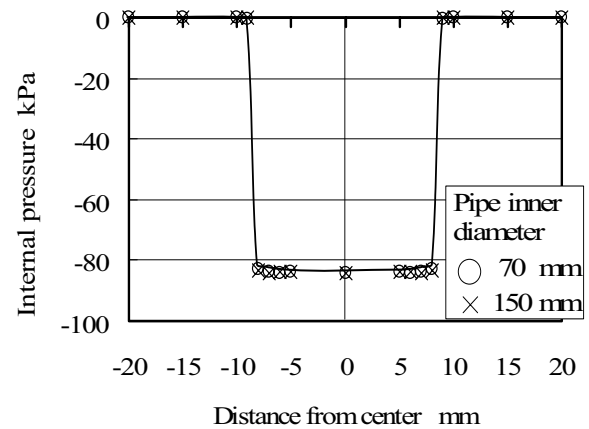
Figure 6   Internal pressure distribution in suction brake
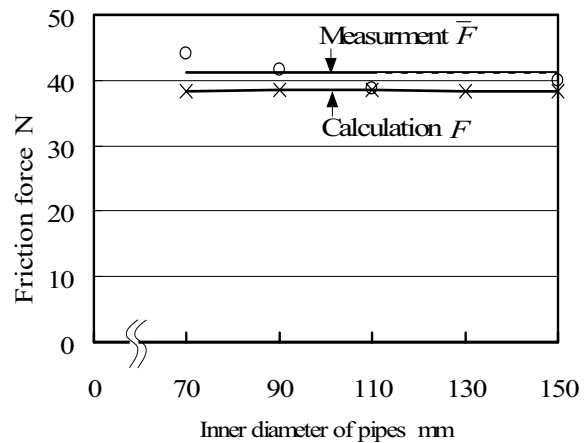
Figure 7   Relationship between diameter of pipes and friction force of suction brake
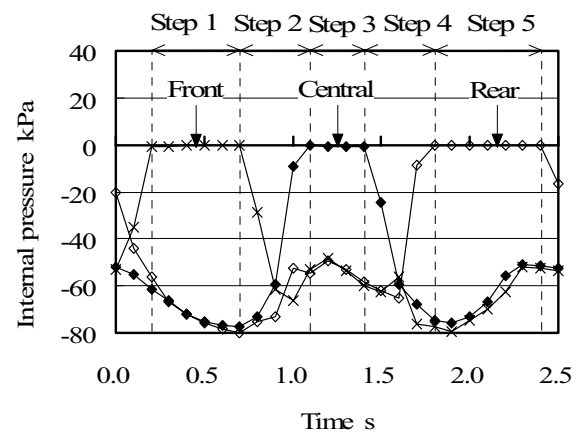
Figure 8   Internal pressure in suction brakes

530
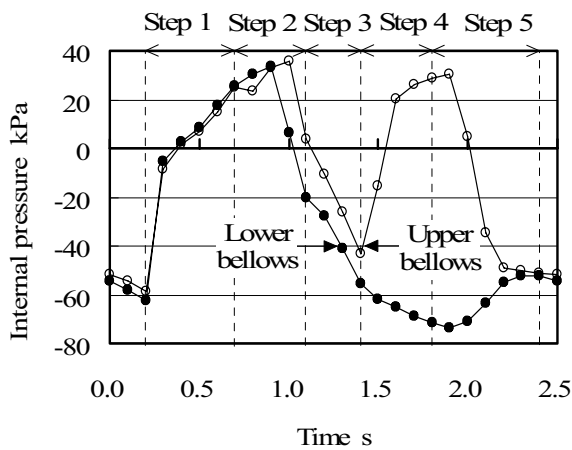
Figure 9   Internal pressure in front somite
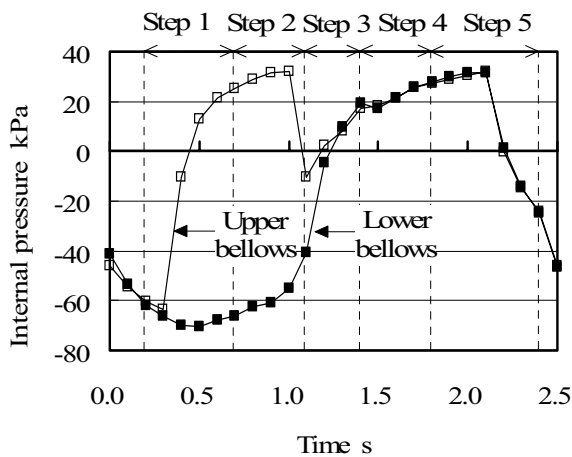
Figure 10   Internal pressure in rear somite

Figure 11   Moving principle of in-pipe mobile robot

releases the wall of the pipe.

In the initial condition, the robot shrinks its front and rear somite and sticks its three suction brakes on the pipe and is in the stationary.

Step 1: After 0.2 seconds of the moving start, the front suction brake releases the wall of the pipe, because the internal pressure of the suction brake goes up to 0 kPa. After the moment, the suction brake keeps the releasing motion in the time of 0.5 seconds. The front somite stretches to the forward direction, because, the internal pressure of the front somite goes up to 25 kPa from -60 kPa in this time. Then, the front suction brake moves to the forward direction.

Step 2: The front suction brake sticks the wall of the pipe, because the internal pressure of the front suction brake goes down from 0 kPa after 0.8 seconds of the moving start.

Step 3: The central suction brake releases the wall of the pipe, because the internal pressure of the central suction

brake goes up to 0 kPa after 1.1 seconds of the moving start. In this time, the front somite shrinks, because the internal pressure of the rear somite goes up over 0 kPa. Then, the central suction brake moves to the forward direction.

Step 4: The central suction brake sticks the wall of the pipe, because the internal pressure of the central suction brake goes down from 0 kPa after 1.5 seconds of the moving start.

Step 5: The rear suction brake releases the wall of the pipe, because the internal pressure of the rear suction brake goes up to 0 kPa after 1.8 seconds of the moving start. The rear somite shrinks because the internal pressure of the rear somite goes down over 0 kPa. Then, the rear suction brake moves to the forward direction.

Step 6: The rear suction brake sticks the wall of the pipe, because the internal pressure of the rear suction brake goes down from 0 kPa after 2.5 seconds of the moving start.

The time required to a series of the moving motion is 2.5 seconds. The robot can move in the pipe by repeating the steps.

MOVING CHARACTERISTICS OF THE ROBOT

The positive pressure of 50 kPa and the negative pressure of -84 kPa are used in the experiment and diameters of pipe made of acrylic are within 70 mm and 150 mm.

Moving speed

Moving speed of the robot is measured in the pipe which is set in horizontal and vertical. The moving speed is shown in Figure 12. Average speed is 20 mm/s in the horizontal case and 23 mm/s in the vertical case. It is confirmed that the moving speed does not depend on the diameters of pipe by the experiment.

Traction force

The experimental traction force is shown in Figure 13. The traction force of 20 N is obtained and does not depend on diameters of the pipe. It is confirmed that the traction force is about half of the maximum friction force.

Confirmation of passing of the step

The robot is confirmed to pass the step of 5 mm that is made by connecting of pipes whose diameters are 110 mm and 120 mm. The robot can pass the step by its waving motion of the somite.

<div align="center">

CONCLUSIONS

</div>

We obtained next conclusions concerning an in-pipe mobile inspection robot which imitates the green caterpillar.

(1) The green caterpillar can move to the forward direction by moving of three groups of prolegs in order to the forward direction. The green caterpillar moves its prolegs by waving its abdomen.

(2) In the fabricated robot, the abdomen of the green caterpillar is imitated by bellows and the prolegs are imitated by the suction brake. The somite structured by four parallel rubber bellows actuators which are arranged in the matrix can imitate the waving motion of the abdomen. The waving motion of the somite could push the suction brake to the wall of the pipe and lift up the suction brake from the wall of the pipe.

(3) The robot that is imitated the motion of the green caterpillar can move pipes whose diameter are more than 70 mm. Average speed is 20 mm/s in the horizontal case and 23 mm/s in the vertical case. The traction force is 20 N and does not depend the diameter of the pipe. This type inspection robot may move long distance, because it has larger traction force. The robot is confirmed to pass the step of 5 mm.

<div align="center">

REFERENCES

</div>

1. Saga, N., Ueda, S. and Nakamura, T., Development of peristaltic Crawling Robot using Artificial Muscle Actuator, Transaction on The Society of Instrument and Control Engineers, 2005, Vol. 41, No. 12, pp.
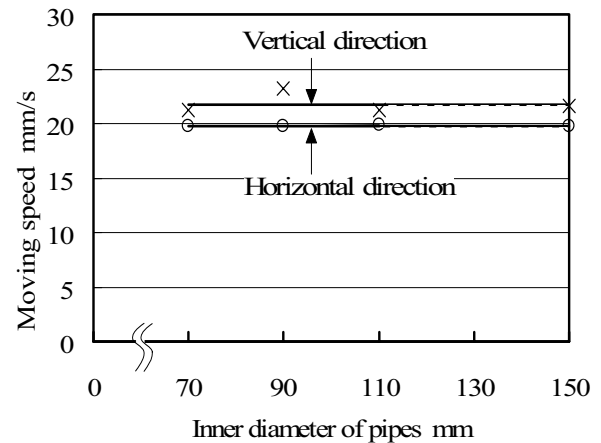
Figure 12   Moving speed of in-pipe mobile robot
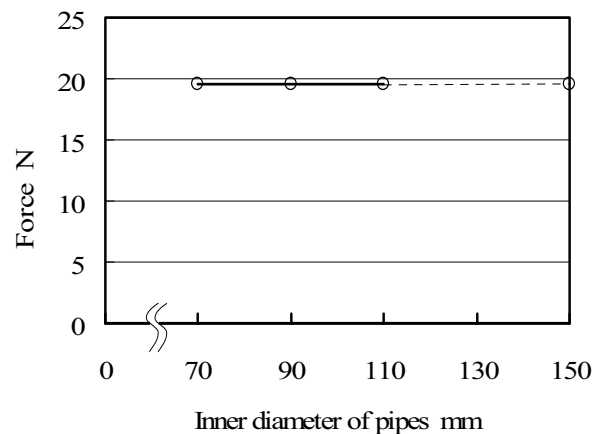
Figure 13   The experimental traction force

1013-1018.
2. Noritsugu, T. and Kubota, M., Development on In-pipe Mobile Robot using Pneumatic Soft-Actuator, Journal of Robotics Society Japan, 2000, Vol. 18, No. 6, pp. 73-80.
3. Ono, M. and Kato, S., A Study of an Earthworm type Inspection Robot Movable in Long and Small Diameter Pipes - Development of a Three Somites type Mobile Robot and its Basic Characteristics -, Journal of the Japan Society for Precision Engineering, 2005, Vol. 71, No. 5, pp. 606-612.
4. Kato, S., Aizawa, Y., Osada, T. and Ono, M., Fabrication of an Inchworm type Mobile Microrobot Movable in Different Diameter Pipes, Proc. of American Society for Precision Engineering 2004 Annual Meeting, pp. 261-264.

P1-52

MAGNETIC BRAKE CYLINDER TO ENHANCE TRAVERSE ABILITY AND ITS APPLICATION TO RESCUE ROBOTS

Eyri WATARI*, Hideyuki TSUKAGOSHI*, Yasuhiro KITAGAWA* and Ato KITAGAWA**

* Department of Mechanical and Control Engineering
Tokyo Institute of Technology
2-12-1-S5-16 O-okayama, Meguro-ku, Tokyo, 152-8552 Japan
(E-mail: eyri.watari@cm.ctrl.titech.ac.jp)

ABSTRACT

In this paper, a novel pneumatic cylinder is proposed, named Magnetic Brake Cylinder. It is composed of a tank, a pneumatic cylinder, and a permanent magnet, and with this, the piston is held by the attractive force of the magnet until the pressure inside the tank is very high, offering a higher driving power than an ordinary cylinder when using the same pressure source. In addition, a control method of its driving power is introduced. The developed actuator is then mounted into two types of rescue inspectors: a rolling and jumping rescue robot, which uses a cylinder to jump over obstacles, and a throw and collect rescue inspector, which deploys with the cylinder a child machine over high obstacles. Both developed prototypes showed higher jumping and throwing height than when using an ordinary cylinder, proving to be an option of effective enhancement of traversing ability for pneumatically powered robots.

KEY WORDS

Pneumatic cylinder, Rescue inspector

INTRODUCTION

In order to enhance the efficiency of searching survivors inside collapsed buildings after an earthquake, several types of rescue robots have being researched among these days. The demanding functions of a rescue robot are mainly three: ability of locomotion through rough terrains by remote control, sensing functions, and human-machine interface. Using existing technologies of sensing and transmitting systems, and having a useful rescue capacity, the enhancement of the obstacle traversing ability and the accessibility to the site of the robot is an important factor.

As for these rescue robots, it is possible to classify them into two major groups. One group is composed of robots which move their center of gravity continuously, and the other is composed of those which move their

center of gravity in scattered pattern. The first group is represented mainly by legged robots, wheeled robots, snake type robots, and the hybrid robots composed of these types. Since their center of gravity moves continuously, it is simpler to increase the weight of the robot without losing much of the efficiency of traversing obstacles, and therefore, it is possible to mount several types of sensors. The second group is composed of robots that kick the ground performing a jump, or robots that deploys part of it or another robot over obstacles. These have not been applied to rescue in large scale as the first group is, but this group holds the possibility of showing high performance and agility which cannot be obtained by continuous locomotion of the center of gravity.

Therefore, this research concentrates on a pneumatic cylinder as the main actuator to realize the locomotion

method based on moving the center of gravity in a scattered pattern. Then, at the same time that it shows limitation of traversing ability when composing with an ordinary cylinder, a new cylinder is proposed to overcome this limit.

In this paper, after showing the target locomotion methods, the limitation of the pneumatic cylinder is presented. Then, the Magnetic Brake Cylinder (MB Cylinder hereafter) is introduced. Its control method is also proposed. Finally, the application of the MB Cylinder to the target locomotion methods is showed.

TARGET LOCOMOTION METHODS

When inspecting inside buildings after disasters, the key issue is the locomotion function of the robot, since it must have ability to traverse obstacles such as furniture and debris. The authors have proposed locomotion methods based on the realization of the traverse action in short interval of time, the possibility of traversing obstacles regardless the shape, and enhancement of traversing height regardless the body size being small.

Roll and Jump Mobile Inspector

One simple locomotion method proposed by the authors is the Roll and Jump Mobile Inspector.[1] It consists of throwing the inspector inside the building, and this inspector uses wheels to efficiently roll on surfaces, it can jump over obstacles larger than its body, and it can also recover its posture from any landing position (Figure 1).
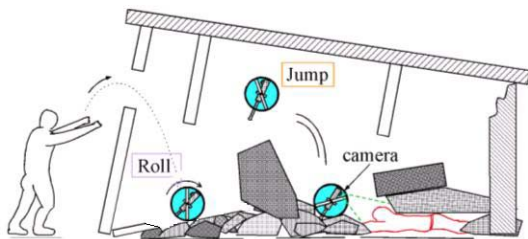
Figure 1 Concept of Roll and Jump Inspector

The rolling motion is driven by an electric motor, while the jump is driven by a pneumatic cylinder (Figure 2), and with this coupled drive the robot is able to traverse obstacles higher than three times its body size. In order to achieve a jumping height of 1m, due to limits of maximum air pressure and flow rate of air, the pneumatic cylinder is analyzed, providing an optimization method of its size.

The developed Roll and Jump Mobile Inspector, named Leg-in-Rotor-V, has 300mm of diameter and 500mm of length, and weights less than 2kg. it is equipped with a wireless microcamera and it is controlled remotely. Figure 3 shows the inspector traversing an obstacle of 1m height.
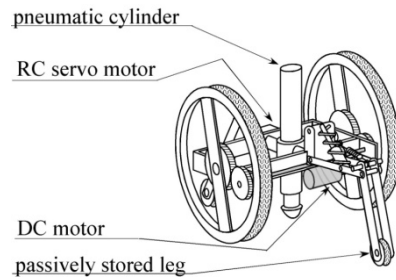
Figure 2 Basic structure of Jump and Roll Inspector

Figure 3 Performance of Leg-in-Rotor-V

However, if the ground conditions are too rough, or if it is soft as a mattress, the robot may not perform the jump as expected. For such situation, the following locomotion method is proposed.

Throw & Collect Type Rescue Inspector

This method consists of the following sequence (Figure 4): after inserting the parent robot (or a pole with the mechanisms) into the site, this throws out a child machine, equipped with camera, and the inspection is performed while this child machine is been drawn back.[2] Using this method, the ground conditions do not affect the throw, which can be done many times into different directions, covering a wide search area.
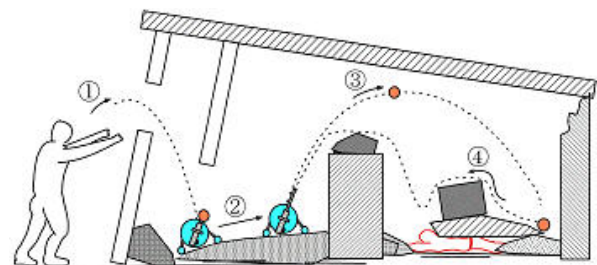
Figure 4 Concept of Throw & Collect Inspector

The basic structure of the Throw & Collect Type Rescue Inspector is shown in Figure 5. The parent robot

534

(or pole) is equipped with a throwing device and a drawing device. In this case, a pneumatic cylinder is used for the throwing device.
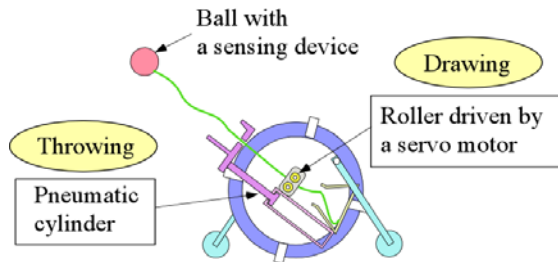
Figure 5 Structure of a Throw & Collect Inspector

Figure 6 shows the drawing device, which consists of a pinch-roller mechanism (Figure 7). The wire which connects the child machine is pinched and pushed by the rollers into a taper case, and this wire is automatically stored in a spiral motion into the case. When performing a throw, the pinch-roller mechanism is opened, and the wire becomes free to be pulled out of the case.
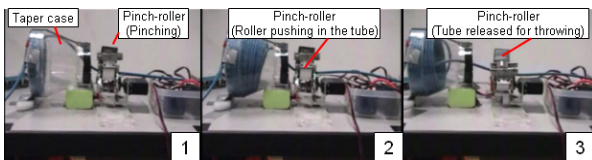
Figure 6 Drawing device
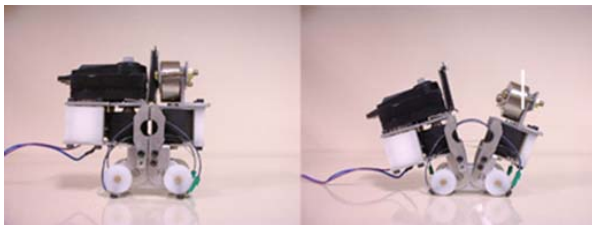
Figure 7 Pinch-roller mechanism

The key issue here is the weight of the child machine and the driving power of the cylinder used to throw the child machine. Since the child machine must be light, the piston of the cylinder starts to move with low pressure, and the flow rate cannot catch up with the internal volume expansion of the cylinder. Therefore, internal pressure fall occurs, and the driving power becomes low. As solution for this problem, a novel actuator is introduced to enhance the driving power of a pneumatic cylinder.

PROPOSAL OF MAGNETIC BRAKE CYLINDER

In order to avoid the problem of internal fall of the pneumatic cylinder and to enhance its driving power, it is necessary to increase the flow rate of air (Figure 8a, Figure 8b). The use of bigger valves, meaning using a larger effective cross-sectional area of the connection to the pneumatic cylinder, is the simplest idea, but the system becomes heavy and bulky.

To increase the flow rate of air, it is possible to use a tank connected directly to the pneumatic cylinder, and this connection can have larger effective cross-sectional area since the distance between the tank and the cylinder is small. In order to realize this method, the piston must be held in its initial position by a triggering device to avoid letting it move with low pressure (Figure 8c).

Therefore, combining the pneumatic cylinder with a tank connected directly to it, and with a triggering device, the problem of internal pressure fall can be suppressed to a minimum. As for the triggering device, a permanent magnet is used (Figure 8d). This way the trigger is passive, without the necessity of using an actuator to hold and release the piston, and it is called magnetic brake cylinder (MB Cylinder). The permanent magnet holds down the piston until the applied force to the piston by the air pressure becomes higher, and when released, it starts moving with high pressure.
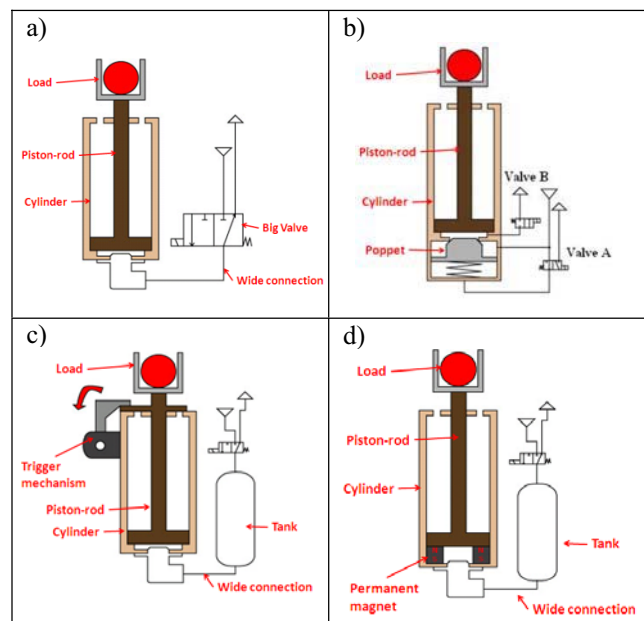
Figure 8 Possible solutions: a) bigger valve, b) poppet valve, c) triggering mechanism, d) magnetic brake cylinder

Figure 9 shows the half-cut model of the MB Cylinder. This MB Cylinder is the developed actuator for the Throw & Collect Inspector, and it also has an additional feature to enable controlling its driving power.
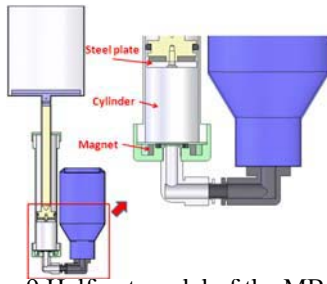
Figure 9 Half-cut model of the MB Cylinder

CONTROL OF THE DRIVING POWER

The driving power of the MB Cylinder can be controlled by two parameters: by altering the attractive force of the permanent magnet; or by altering the force applied to the piston. The first option can be realized by changing the contact area between the piston and the magnet by driving the magnet, or simply use an electromagnet to change the attractive force. However, it would be necessary big actuators, either to drive the position of the magnet or to use large coil to have significant changes to the attractive force, becoming unrealistic.

For the second option, there are two possibilities: changing the applied pressure, and change the area of the piston that receives the pressure. In order to change the applied pressure, it is necessary to use a fast pressure regulating valve, since the control must be performed after the piston detaches from the magnet, and conventional valves do not present the necessary responses for its realization. Therefore, changing the pressurized area of the piston is considered to control the driving power of the MB Cylinder. [3]

To realize this method, the inlet of the cylinder is built in such a way to create two separated chambers when the piston is in its initial position, and each chamber is pressurized by a different valve (Figure 10). The main chamber is pressurized by a main valve (valve 1), and only area A of the piston receives pressure. The control valve (valve 2) is used to pressurize area B of the piston. Since area A is very small, it is necessary elevated pressure to detach the piston from the magnet, while using both areas A and B, the necessary pressure becomes lower.
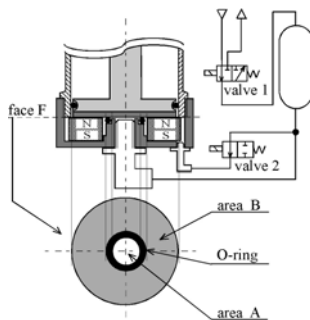
Figure 10 Inlet of cylinder divided into two chambers

Therefore, it is possible to control the driving power by timing the control valve to open in instances delayed from the main valve (Figure 11). Figure 12 shows how the internal pressure changes with different opening times, obtaining different driving powers of the MB Cylinder.
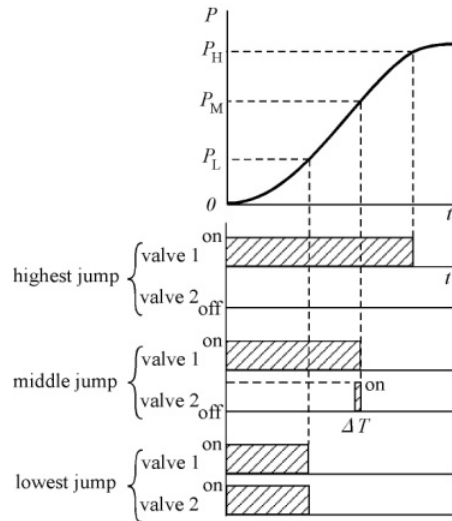
Figure 11 Time triggering of valves to control driving power
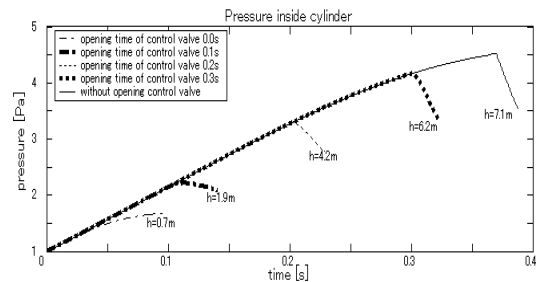
Figure 12 Internal pressure of cylinder with control method

DESIGN METHOD THROUGH NUMERICAL ANALYSIS

In reference [4], the basic equations are presented and the necessary equations to simulate the MB Cylinder regarding unknown variables are derived. Table 1 shows the parameters of the developed MB Cylinder, and in Figure 13, the simulated variables are presented with normalized values.

The simulation was validated by comparing simulated and experimental results. Figure 14 shows the results of simulation and experiment of throwing height of child machines with different masses. As observed, simulated results fit to experimental ones, and therefore, the simulation is validated.

Table 1 System parameters

Cylinder	$A=678.87*10^{-6}$ [m^2] (area of piston) $L=163*10^{-3}$ [m] (length of cylinder) $c=60*(A*\pi)^{1/2}$ [Ns/m] (coulomb friction coefficient) $k_1=220*(A*\pi)^{1/2}$ [N] (viscous friction coefficient) $k_C=100$ [W/K] (product of thermal conductivity and surface area of cylinder tube) $m_r=0.198$ [kg] (mass of rod) $m_c=0.360$ [kg] (mass of child machine)
Experiment Conditions	$g=9.81$ [m/s^2] $P_S=0.46*10^6$ [Pa abs] $P_0=0.1*10^6$ [Pa abs] $T_0=293$ [K]
Air Parameters	$R=287$ [J/kg K] $c_V=716$ [J/kg K] $\kappa=1.402$ $\rho=1.293$ [kg/m^3]
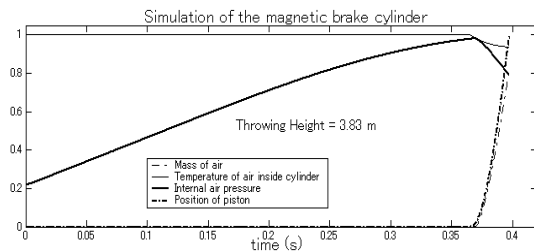
Figure 13 Simulation of MB Cylinder
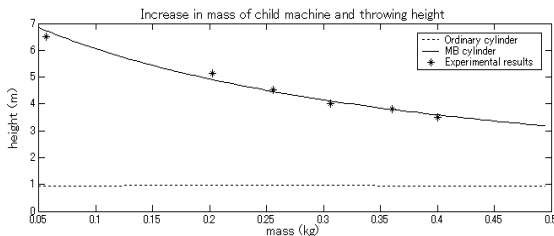
Figure 14 Throwing height of child machines with different masses

Optimization Process

The optimization of the size of the structure of the MB Cylinder is performed regarding the size of the tank and the size of the effective cross-sectional area of the connection between the tank and the cylinder.

First, the size of the tank is analyzed. Using the numerical simulation, the throwing height is observed when the volume of the tank is increased. The optimum tank volume is between 3 to 4 times the volume of the cylinder (Figure 15), and this result is equivalent to any cylinder volume. In this graph, the chosen tank volume is showed, which the volume is closest to the optimum volume, when using commercialized coffee can as the tank for the MB Cylinder.
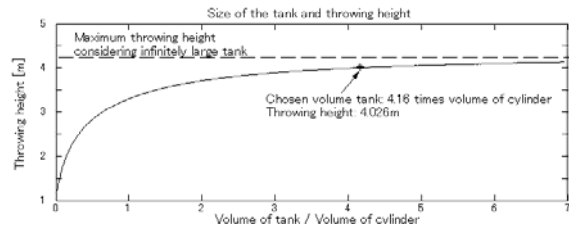
Figure 15 Increase of tank volume and throwing height

Next, the size of the connection is decided with similar process (Figure 16). The throwing height is observed when the effective cross-sectional area of the connection between the tank and the cylinder is increased. Setting 90% of the ideal throwing height, the optimum effective cross-sectional area is defined, and the connection between the tank and the cylinder is built in order to achieve this cross-sectional area.
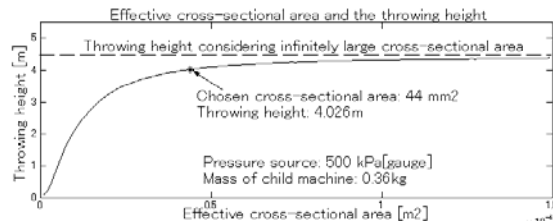
Figure 16 Increase of inlet and throwing height

With this process, the optimum size of the MB Cylinder is obtained.

APPLICATION TO TARGET LOCOMOTION METHODS

Throw & Collect Type Rescue Inspector

With the MB Cylinder, a child machine of 0.35kg is able to be thrown from a mobile inspector, which has the same structure as the Roll and Jump Mobile Inspector. Figure 17 shows the parent robot throwing the child machine over a wall of 2m high, inspecting the area beyond it.
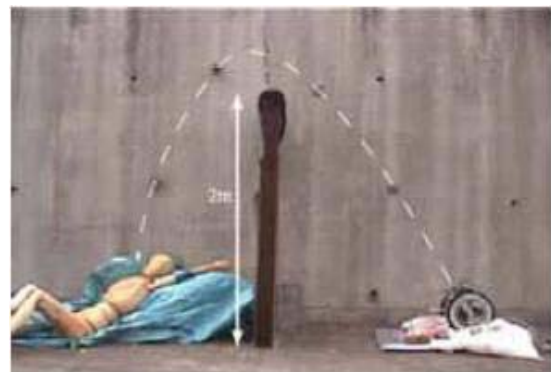
Figure 17 Throw & Collect Mobile Inspector

The developed MB Cylinder is also mounted onto a

pole type Throw & Collect rescue inspector. Figure 18 shows the inspector performing a search inside a train wagon.
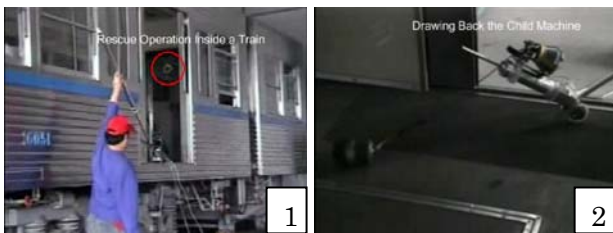
Figure 18 Inspection inside a train wagon

With the controlling method, it is also possible to access difficult places as in Figure 19. The experiment of controlling the throwing distance is showed in Figure 20, performed after using a laser range finder to measure distance and angle of the throw.
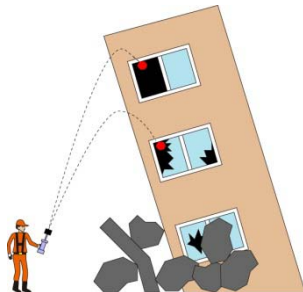
Figure 19 Enhancement of accessibility with the control method

Finally, the MB Cylinder is used to throw a child machine into a window located at the third floor of a building, as proposed in the concept (Figure 21).

Figure 20 Throwing to the target at a distance of 18m
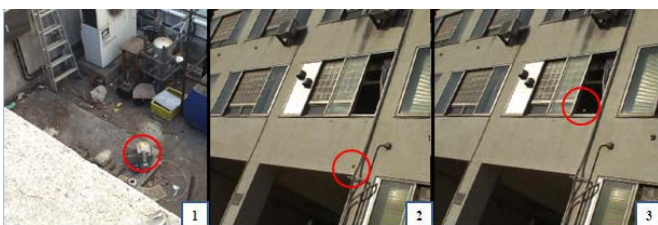
Figure 21 Throw of a child machine to inspect the third floor

Roll and Jump Mobile Rescue Inspector

The previous prototype used an ordinary pneumatic cylinder, and it was able to carry only a microcamera in order to keep the structure as light as possible. Weighting less than 2kg, it performed jumps of 1m high.

The new prototype is smaller and heavier than the past models, being able to carry more types of sensors. It is also protected with cushion material (soft polyurethane sponge), resisting to aggressive landing. If an ordinary cylinder of same size is mounted, the robot is only able to jump 90mm, but changing the actuator to a MB Cylinder, the robot can jump over 1m high (Figure 22).
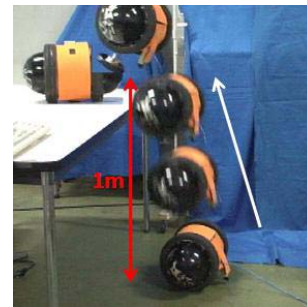
Figure 22 New prototype of the Roll and Jump Mobile Inspector

SUMMARY

A novel pneumatic actuator, the MB Cylinder, is proposed, showing to be an effective enhancement option of obstacle traversing ability. Its control method and structure is also presented. Optimization through numerical simulation is also performed.

The MB Cylinder is mounted into a Throw & Collect rescue inspector, and the control of the throwing height proved to be useful for accessing difficult disaster areas.

The new prototype of Roll and Jump mobile inspector can perform a 1m high jump being heavier than past models.

REFERENCES
1. Tsukagoshi, H., et al, "Development of Jumping & Rolling Inspector to Improve Debris-Traverse Ability," Journal of Robotics and Mechatronics, 2003, **vol.15**, No.5, pp.482-490.
2. Tsukagoshi, H., et al, "Development of a Throwing & Drawing Type Inspector Aimed to Wide-Range Searching Inside Collapsed Buildings," 2005 JSME Conference on Robotics and Mechatronics, 2005, 1P2-S-096.
3. Watari, E., et al, "Development of a Throw & Collect Type Rescue Inspector – 6th Report: Control of the Throwing Distance by a Magnetic Brake Cylinder," SICE-ICASE International Joint Conference 2006, SICE-ICCAS 2006, 2006, SA08-4.
4. Tsukagoshi, H., et al, "Design of a Higher Jumping Rescue Robot With the Optimized Pneumatic Drive," Proceedings of the 2005 IEEE International Conference on Robotics and Automation, 2005, pp. 1288-1295.

P1-53

A STUDY OF MATERIAL RECOGNITION SYSTEM WITH HUMAN TACTILE SENSIBILITY FUNCTION USING PNEUMATIC CYLINDER

Chihiro HAGIWARA*, Osamu OYAMA* and Toshihiro YOSHIMITSU**

* Department of Mechanical Engineering, Faculty of Science and Technology
Meiji University Graduate School
1-1-1 Higasimita, Tama, Kawasaki, Kanagawa, 214-0033 Japan
(E-mail: ce82045@isc.meiji.ac.jp)
** Department of Robotics and Mechatronics, Faculty of Creative Engineering
Kanagawa Institute of Technology
1030 Simoogino, Atsugi, Kanagawa, 243-0292 Japan

ABSTRACT

We have developed an artificial finger which have human tactile sensibility function, such as be desired for some kind of robots. This finger can recognizes some materials pressing and tracing object with the arm actuated by the pneumatic cylinder. There are many factors in recognizing what touched material was. The recognition of materials is run by the neural network system which can be usefully to obscure and complicated control. The sensor in the finger has been used a piezo-electric element and a strain gauge with a thermo-couple respectively before. However only one of these sensors can be installed for one finger and the two or more fingers must be used to recognize one object. Then, the complete recognition is difficult for the reduction of measurement accuracy caused by individual try of many finger and the problem of the setting of output data in the neural network system. Therefore, the purpose in this report is to unify two or more sensors into one finger, and to fulfill the human tactile sensibility function more similar to human than previous subject. In this report, the improvement of the sensor and the device of the neural network are shown.

KEY WORDS

Artificial finger, Material recognition, Neural network system, Action potential

INTRODUCTION

The sense of touch information is necessary when we perform delicate operations such as grasp of objects. The interest rises to welfare and nursing in aging society in recent years, and it is welcome that robots work in such field. In this case, the robot fingers are required to have advanced function equal as human's one.
In this report, the artificial finger touches some materials actuated by pneumatic cylinder, and classifies the information from some sensors into 3 categories.

The first is "hardness" related hardness of surface. The second is "state on surface" related bump of surface. The third is "temperature" related thermal change of surface when the finger touched.
These 3 parameters are used for neural network system.

DEVICE OF EXPERIMENT

The recognition system is shown by Figure 1. The main body is measurement part and is the artificial finger which is moved to axis of x and z using 2 pneumatic

cylinders. The finger implants 4 strain gauges and a thermo-couple inside the imitating skin. The strain gauge is used for measurement of "hardness" and "state on surface" and the thermo-couple is used for measurement of "temperature". "State on surface" can't be obtained directly and then the differentiated value of the signal is used.

The values measured with the sensors are transmitted to the personal computer through the data logger. The datas are converted into the binary data imitating the impulse that simulates the excitement of human nerve. The system recognizes materials through the neural network at the end.

The measureing process is shown below.

1. The target material is fixed to the position on 3mm from an artificial finger and then finger comes in contact with the target.
2. The pneumatic cylinder pushes the finger during 5 seconds and then feeds the finger sliding along the target.
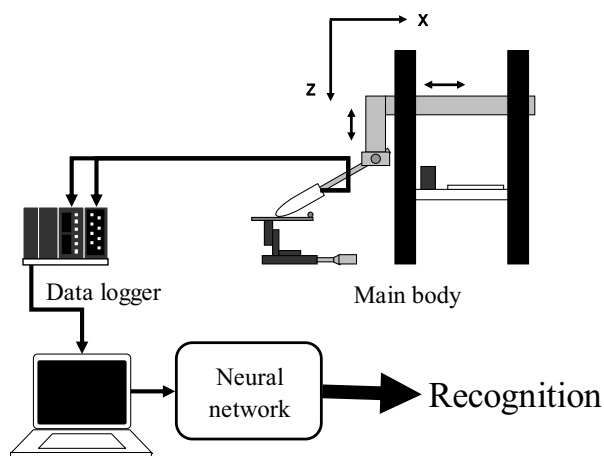
Figure 1 System of material recognition

RESULT OF EXPERIMENT

Figure 2 shows the system operations of learning the neural network based on measurement data. The cyclic calculation is shown on horizontal axis and the learning error is shown on vertical axis. The learning error means the average of square harmony of difference between true value and measurement value (LMS). This grants to know a degree of the learning.

In general, the LMS becomes 0.01 or less and then the system terminates to learn. In figure 2, as the typical case, the LMS becomes 0.002651 in the cyclic calculation of 5000th times. Moreover, the neural network operates stably for unlearned data. As a result,

the recognition rate, which shows the rate of recognized materials correctly, became 33.3%, and the generalization error improved from 0.12 to 0.05 comparing former same condition. The reason of the improvement is mainly a change of teaching data for learning in neural network. The used data had been calculated by SD method since last year, but the proposed neural network uses the elements that respond particular inputs as the parameter, and are named each material name.

However, the correct recognition rate is not high as 33.3%, the neural network sometimes causes not correctly recognition. This reason is that the measurement is not even for a different condition and a performance of the artificial finger is not sufficient. The improvement of hardware is needed for the more accurate recognition.
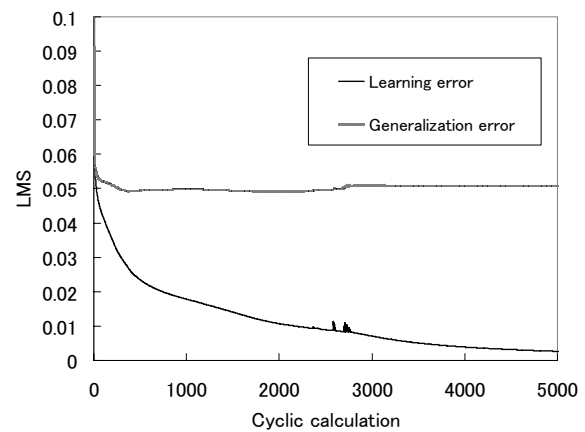
Figure 2 The learning error of neural network

CONCLUSION

We show that the proposed artificial finger is able to recognize some materials by using 3 parameters; "hardness", "state on surface", and "temperature". Moreover, this system deals the compressed binary data imitating the impulse of human nerve. This advantage is that the handling data of each sensor becomes lighter and the calculation becomes faster than ever. By this fact, it is expected that the artificial finger can have a lot of sensors. In addition, it shows to be able to substitute a low-cost microcomputer and FPGA in place of a high-cost personal computer.

The problem is uncertainty on measurement. It is need to improve a structure of the artificial finger, for example changing stuff and process of production.

The artificial finger will have a function similar to human to solve any problems. And the advanced robot hand will flourish in a care case in the future.

P1-54

DEVELOPMENT OF WALKING ASSIST SYSTEM WITH PNEUMATIC ACTUATOR

Tomohiko ARIMA*, Osamu OYAMA*, Toshihiro YOSHIMITSU**

*Mechanical Engineering Major, Science and Engineering Research Course,

Graduate School of Meiji University

**Welfare system Engineering, Kanagawa institute of Technology

*Tamaku higashimita 1-1-1, Kawasaki city, Kanagawa, Japan

**Shimoogino1030, Atsugi city, Kanagawa, Japan

*(Tel : +81-44-934-7907; E-mail: ce82003@isc.meiji.ac.jp)

**(Tel : +81-46-291-3163; E-mail:yosimitu@we.kanagawa-it.ac.jp)

ABSTRACT

The purpose of our study is to develop "Walking Assisting System" that assists the aged and alternative people to walk by themselves, and that can be used as a welfare system to take care of them. Since this system moves by compressed air, no harmful substances are used, and it can apply power as flexibly as human muscles do. Additionally, even in any unexpected situations, the shock and burden to the person using the system are kept to the minimum.

This system not only supports walking on level ground but also assists the movement of the knee joint in walking up and down the stairs, by sensing and acknowledging the walking place of the user and sending compressed air into the pneumatic cylinder at the appropriate timing. In this study, we have installed the acceleration sensors instead of previous inclination sensors, and collected walking data from a wide variety of people with different body sizes and walking speed. Then, we have pursued a control system which can distinguish and assist steady walking in any condition, by generalizing the unique personal factors of various people and determining the discrimination conditions for each of them.

KEY WORDS

Walking Assist System, Air Cylinder, Welfare Care

INTRODUCTION

Today, the aging society is gaining importance in Japan, and one of its reasons, the falling birthrate is also a serious issue. If no changes are made to the current assisting system, the aged or alternative people will not be able to receive sufficient care, therefore being prevented from taking part in society. Thus, in this study, we have made research and development of a walking assisting equipment for those having difficulty in walking by themselves including the aged or alternative people, and have developed a new type of equipment as well.

THE SYSTEM

An outline of walking assist system is shown in Figure 1.This walking assisting system measures the floor reaction force by a pressure-sensitive sensor attached on the sole part, and then amplifies the signal through a sensor amplifier. At the same time, the walking condition of the experiment subject is figured out by measuring the femoral angle with angle sensors and importing the A/D converted data into a H8 micro-computer.
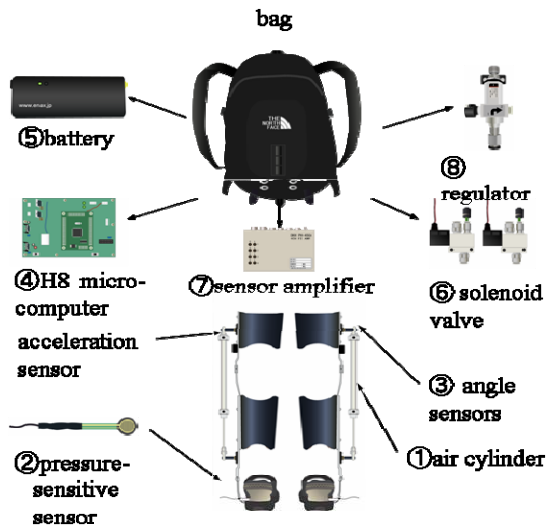
Figure 1 Walking assist system

Then the assist commands are output to the solenoid valve as digital signals. Then the solenoid valve opens, and supplies compressed air. The cylinders are actuated by this compressed air, and start to assist walking. This system had a problem to be improved, that is, the equipment could not be surely fastened to the human leg. This caused inability of grasping the correct walking condition because the measurement accuracies of the sensors are decreased by the equipment's slipping-off phenomenon. Moreover, it became a burden rather than help for the user because it could directly touch the heel or ankle, causing discomfort. We improved this problem by combining the femoral, calf and ankle part all together with shoes, and have succeeded in lessening the user's discomfort and heightening the judgment accuracy of walking condition with this specialized equipment made for the system.

Furthermore, the problem of the inclination sensor still remains. The sensor has liquid as a working medium in it, and the detecting error is seen sometimes caused by liquid waving. So we change the angle sensors into acceleration sensors. The merit to use of acceleration sensor is not only the minimizing size and weight, but also becoming the signal clearly in the change of walking conditions, shown as Figure 2 and Figure 3. As a result, the recognizing of walking condition becomes more correctly, as shown Figure 4.

CONCLUSION

Although we have succeeded in making the current system more useful by this improvement, we still have restrictive conditions such as reduction of the equipment weight and the inability of acknowledging over all specific walking habits of each individual. We seek to develop a more generalized system by verifying use of acceleration sensors more usefully, and evaluating the user's load using muscle electric potential.
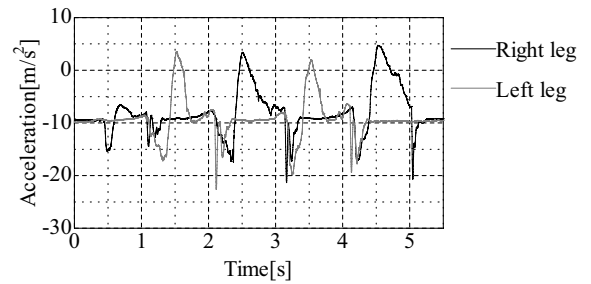
Figure 2 Dynamic wave form change of acceleration

(Flat)
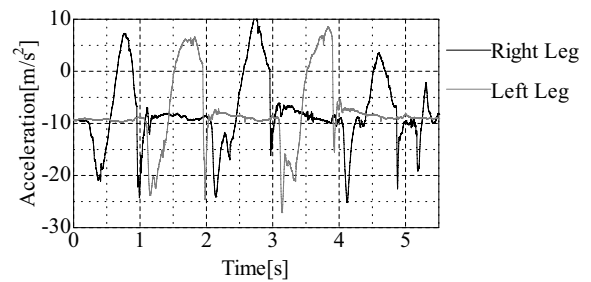
Figure 3 Dynamic wave form change of acceleration

(Up stairs)
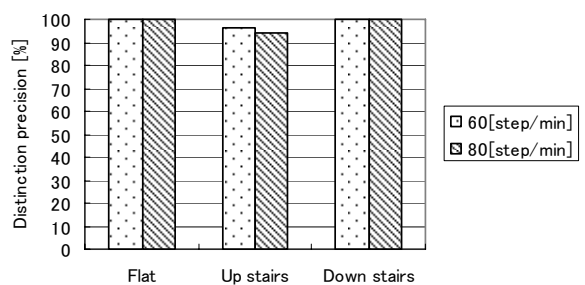
Figure 4 Distinction precision

(new model)

P1-55

BASIC CHARACTERISTICS OF A LIQUID CRYSTAL PUMP

Tetsuhiro TSUKIJI* and Hiroki SATO*

* Faculty of Science and Technology
Sophia University
7-1 Kioi-Cho, Chiyoda-ku, Tokyo, 102-8554 Japan
(E-mail: t-tukiji@sophia.ac.jp)

ABSTRACT

A flow visualization of a liquid crystal was conducted under the application of an electric field in a mini cylinder with electrode strips on the inner surface. Three-phase alternating currents were used as rotation electric fields to generate the rotational flow of the liquid crystal. A pump with a spiral flow channel was designed based on the rotational flow mechanism of the liquid crystal by using the three-phase alternating currents. The pressure-flow rate characteristics of the pump were measured and the characteristics for the length and the shape of the flow channel in the pump were investigated for various amplitudes of electric fields. The pressure increased when we used a liquid crystal with a high dielectric constant and a high kinematic viscosity for the constant voltage. Dimensional analysis was conducted to arrange the characteristics of the present pump simply and the non-dimensional flow rate and pressure were almost on one line. The size of our pump can be decreased by further research. This study contributes to the development of a micro-pump in micro-fabricated systems and our pump eliminates mechanical vibration and noise.

KEY WORDS

Functional Fluid, Pump, Flow Visualization, Pressure, Flow Rate

NOMENCLATURE

D : total length of flow channel, 0.04945m
E : electric field intensity, (=V volt/(0.9×10^{-3})m)
g : acceleration due to gravity, 9.81m/s^2
H : total head, m
p : pressure, Pa
p_m : maximum pressure, Pa
Q : flow rate, mm^3/min
w : channel width, mm
α : angle between the electric rotation direction and the flow direction in a spiral direction
ε_{para} : dielectric constant of the parallel direction to longitudinal direction of the liquid crystal molecule, F/m
ε_{per} : dielectric constant of the vertical direction to longitudinal direction of the liquid crystal molecule, F/m
ε_1 : dielectric constant of insulating part (polyimide film) in the cylinder electrode, Relative permittivity of 3.57 was used (ε_1=3.16×10-11 F/m), F/m
μ : viscosity, Pa・s
ρ : density, kg/m^3

INTRODUCTION

Research has actively been undertaken to provide a better understanding of pump dynamics. Diaphragm- and micro-syringe pumps are typical examples of a mechanical micro-pump [1,2] and the other mechanical micro-pumps are developed recently[3,4].The advantage of these pumps over conventional ones is that they can

be used to pump any liquid or gas. However, they are difficult to micro-fabricate and assemble because they contain many parts, so research is currently being conducted to develop low-noise pumps that use functional fluids and have simplified designs with no sliding parts. Such a micro-pump would have various applications. For example, it could be used in power sources of equipment that supply liquid, cooling systems, micro machines, and supplying fuel to the ultra-micro gas turbine. For this wide range of applications, various micro-pumps are needed to enable its use in any environment and under any conditions. Therefore, various micro-pumps are being designed and are actively being studied. The system with fluid control type would be used widely in micro fields because of the decreased number of parts and the sliding part using the fluid drive by the characteristic of the functional fluid. The properties of functional fluids can be controlled by electric or magnetic fields. Typical fluid pumps use some flow mechanisms, including ion drag [5], electro hydro dynamics (EHD) [6,7], electro-conjugate fluid (ECF) jets[8,9] and electroosmotic flow[10].

In this study, we developed a pump based on the flow of liquid crystals [11] in typical functional fluids by applying an electric field. Rotation electric fields were applied to the electrodes in the pump to add voltage to the fluid, and the flow was induced by the dielectrophoresis[12-16] of liquid crystals. We designed the pump based on the mechanism [17] and subsequently measured the pressure and the flow rate. Especially the effect of the length of the flow channel and the angle between the pump axis and the flow channel direction on the flow rate and the pressure is reported in this paper. Our pump can be also used to transport liquid crystal or to fill a gap of panels for a display with a liquid crystal.

PROPERTIES OF LIQUID CRYSTALS AND

FLOW VISUALIZATION

The characteristics of the liquid crystals used in our study are listed in Table 1. The MLC6650, K15, and MJ0669 were provided by Merck Ltd., Japan. K15 is a nematic liquid crystal. MLC6650 and MJ0669 are liquid crystal mixtures mixed with some nematic liquid

Table 1 Psysical properties of liquid crystals

	MLC6650	K 15	MJ0669
Operating Temperature Region (℃)	-44~99	23.1~35.5	(-10)~45.9
Kinematic viscosity (mm^2/s) (25℃)	59.7	22.4	11.0
Dielectric constant (F/m) (relative permittivity) ε_{per} (20℃)	9.0×10^{-11} (10.2)	5.3×10^{-11} (6.0)	3.5×10^{-11} (3.9)
Dielectric constant (F/m) (relative permittivity) ε_{para} (20℃)	55.6×10^{-11} (62.8)	23.1×10^{-11} (26.1)	9.9×10^{-11} (11.2)
Density (kg/m^3) (25℃)	1099	1020	947

crystals. The value of the kinematic viscosity, the dielectric constant and the density is large in the order of MLC6650, K15, and MJ0669.

As the first stage of our experiment, a flow visualization of the liquid crystal was conducted under the application of the electric field in the cylinder electrode. The purpose of this visualization is to confirm the generation of the rotational flow and the flow direction of the liquid crystal. The cylinder electrode with 9 electrodes was used. The inner diameter of the electrode for flow visualization is about 6mm.

The cylinder electrode for flow visualization is shown in Fig.1. Three-phase alternating current is applied to the cylinder electrode in order to apply the voltage on the liquid crystal. Three-phase alternating current is shown
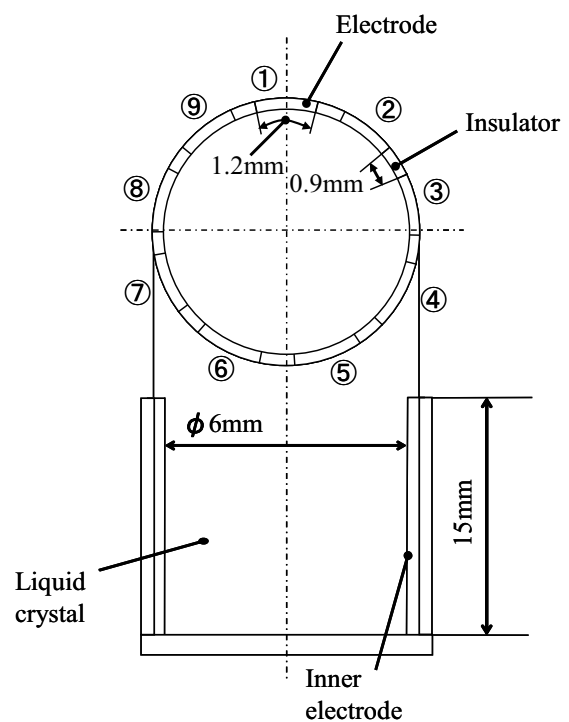
Fig.1 Cylinder electrode

in Fig.2. The voltage curves ①, ② and ③ (④, ⑤ and ⑥ or ⑦, ⑧ and ⑨) come in that order. The voltage is applied in the clockwise direction in Fig.1. Therefore, the electric fields appear to rotate on the cylinder electrode.

The experimental apparatus for flow visualization is shown in Fig.3. In this experiment, the frequency of a voltage wave of three-phase alternating current is 50Hz and the voltage means the effect value. A 50-Hz, 200-V three-phase alternating current is input to a voltage transformer. An output voltage between 0 and 240 V is generated using this voltage transformer. Next, the amplitude of the output voltage is amplified about 15
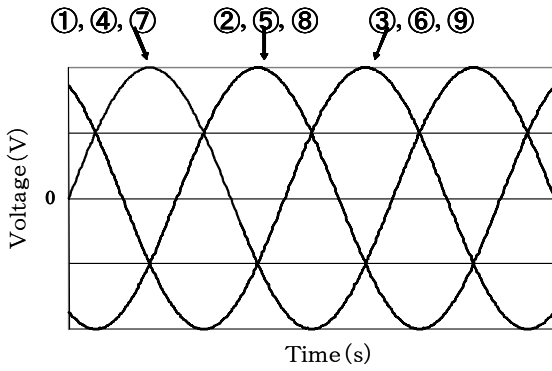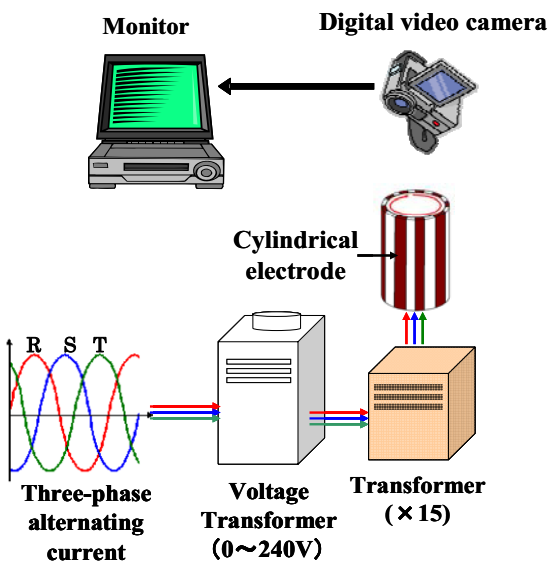
Fig.2 Three-phases alternating voltage

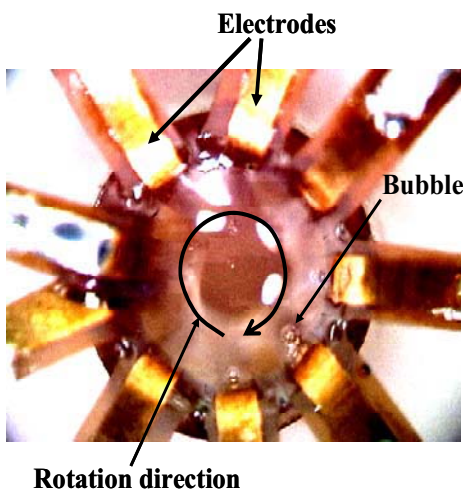Fig.3 Experimental apparatus for visualization

Fig.4 Visualization result for MJ0669

times using the transformer, and the resulting voltage is

applied to the electrodes. The flow of the liquid crystal in the cylinder is observed in the axial direction using a commercially digital video camera. The surface of the liquid crystal is almost flat.

A picture of a liquid crystal flow in cylinder electrode is shown in Fig.4. The voltage is 1000V. A liquid crystal rotated same rotation direction of the electric fields. The
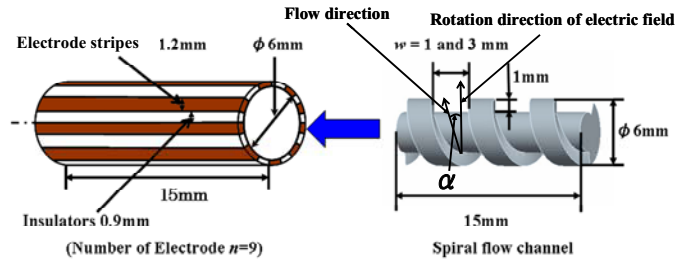
Fig.5 Pump

flow of the liquid crystal is observed by measuring trajectories of bubbles which is indicated by an arrow in the cylinder electrode. The rotational flow and the flow direction of the fluid were confirmed in the present experiment.

EXPERIMENTS FOR PUMP

The electrodes around the flow channel used in the experiment are shown on the left side in Fig. 5. Rotational flow is obtained by applying a three-phase alternating current to the electrodes as described in the previous chapter. The electric fields appear to rotate on the cylinder electrode. The frequency of the voltage wave of the three-phase alternating current is 50 Hz.

The pump consists of a spiral flow channel wrapped inside nine electrodes. The width of the electrodes is 1.2 mm, and the inter electrode distance is 0.9 mm. The
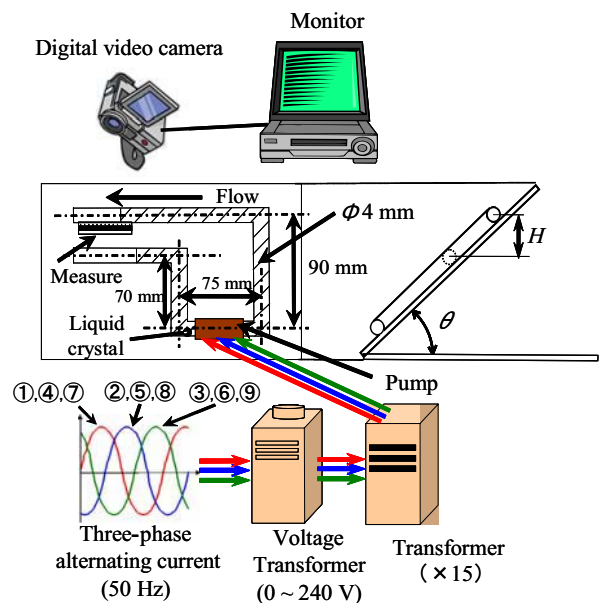
Fig.6 Experimental apparatus for pump

flow channel length in the axial direction is 15 mm, the diameter of the flow channel is 6mm, the channel widths are 1 and 3 mm, and the channel depth is 1 mm. α is the angle between the electric rotation direction and the flow direction. The rotational flow of the liquid crystal is obtained by applying the three-phase alternating current to the electrodes. Therefore, the liquid crystal in the cylinder electrode flows along the flow channel. As a result, the liquid crystal flows in the axial direction of the pump. We designed the pump based on these mechanisms for our study.
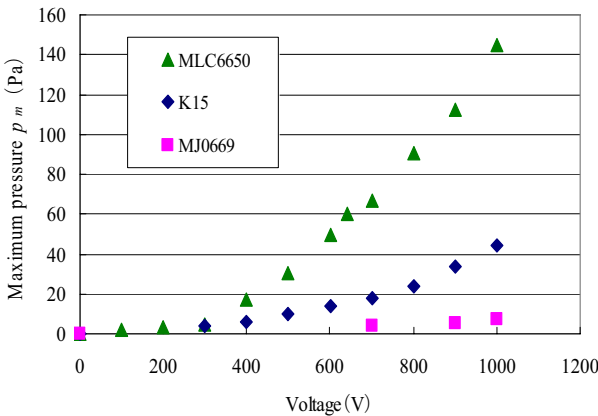
Fig. 7 Relationship between the voltage and the maximum pressure (3turns and w=3mm, α=17.7°)

The experimental apparatus is shown in Fig.6. The
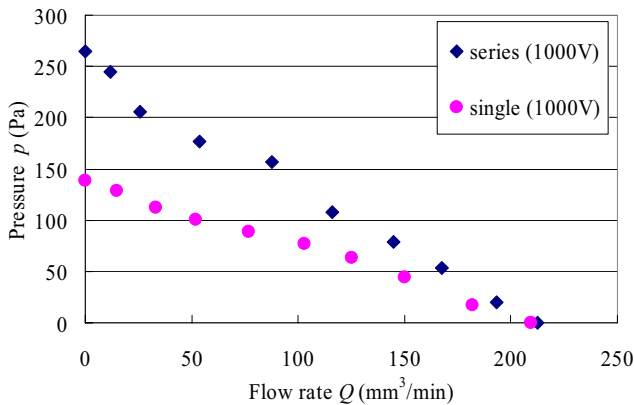
Fig.8 Relationship between the flow rate and pressure (3turns, w=3mm, α=17.7°, MLC6650)

electric circuit is the same as the case of the flow visualization test shown in Fig.3. As a maximum total head is 20mm in this experiment, a maximum pressure is about 200Pa. The voltages between 0 and 1000 V were applied to measure in the above pressure range. A maximum total head is 40mm only for series pump. The flow rate was measured when the total head, H, was changed. To measure the flow rate, we first took a video
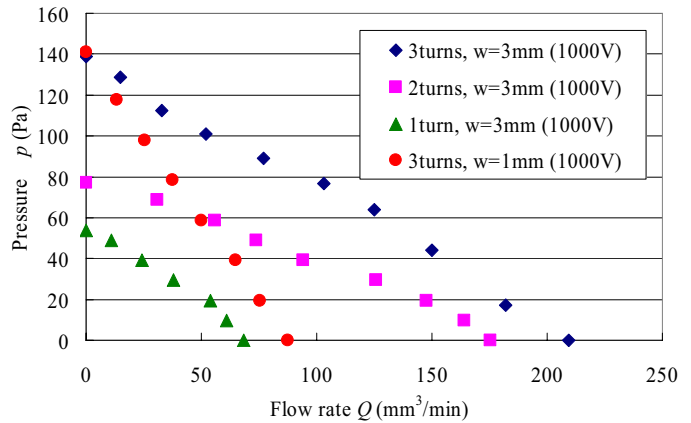
Fig.9 Relationship between the flow rate and pressure (w=1, 3mm, MLC6650)

of the movement of the free surface of the liquid crystal in a pipe whose inner diameter is 4 mm. The video was taken from the direction vertical to the plate. We then enlarged the images in the video to see the flow clearly. The maximum pressure, p_m, is defined without the flow. The maximum pressure is calculated by $p_m = \rho g H$, where ρ is the density, g is the acceleration due to gravity (9.81 m/s^2), and H is the total head.

RESULTS FOR CHARACTERISTICS OF PUMP

The relation between the voltage and the maximum pressure for 3 turn numbers of the spiral flow channel around the axis of the pump and the 3-mm channel width for three liquid crystals is shown in Fig. 7. It is found that the maximum pressure increased when we used a liquid crystal with a high dielectric constant.

The result for two pumps connected in series is shown in Fig. 8. One pump has a 3-mm-wide channel and a three-turn spiral flow channel. Liquid crystal mixture MLC6650 was used because it has highest dielectric
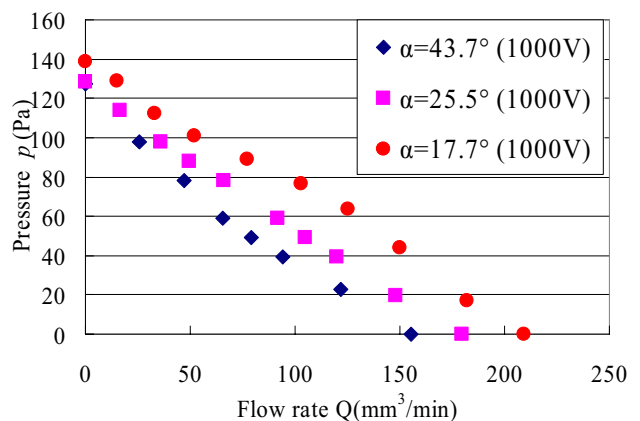
Fig.10 Relationship between the flow rate and pressure (D=49.45mm, w=3mm, MLC6650)
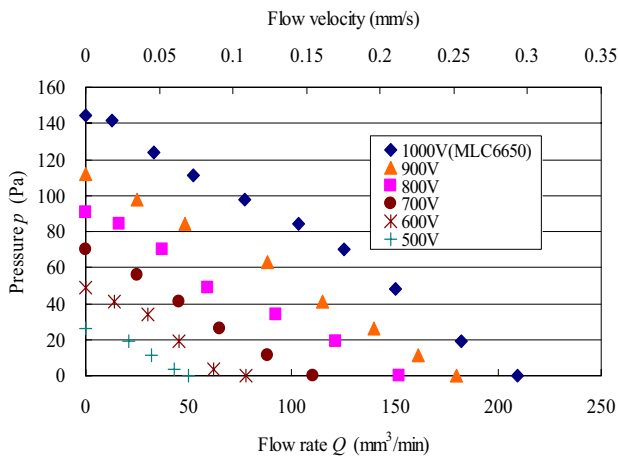
Fig.11 Relationship between the flow rate and
pressure (3turns, w=3mm, MLC6650, α=17.7°)
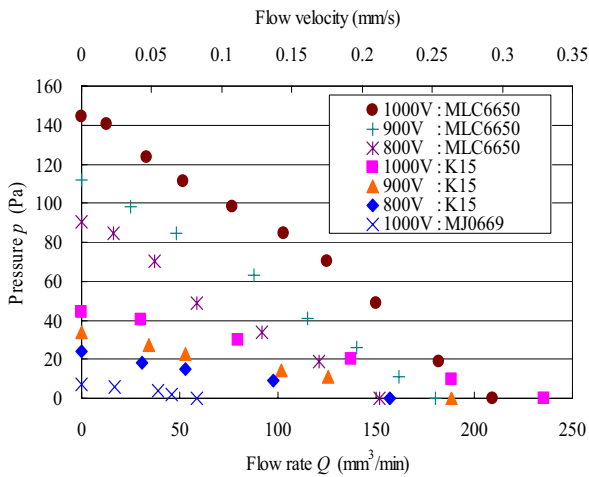
Fig. 12 Relationship between the flow rate and
the pressure (3turns and *w*=3mm, α=17.7°)

decrease of the angle α. Therefore, as the direction of the flow approaches the direction of the electric field, the flow rate increases.

The relation between the flow rate, *Q*, and the pressure, *p*, is shown in Fig. 11 for liquid crystal mixture MLC6650. The pressure is calculated by $p = \rho g H$. The flow rate increased with the voltage when the pressure was the same. Furthermore, the flow rate was a maximum when the pressure was 0, and the pressure dropped off nearly linearly with the flow rate.

The relation between the flow rate and the pressure of each liquid crystal is shown in Fig. 12. The flow rate increased with the voltage for each liquid crystal when the pressure was the same. The flow rate increases with the kinematic viscosity and the dielectric constant except zero pressure for same pressure and voltage. As the flow resistance is high with the kinematic viscosity, the flow rate can be increased using a liquid crystal with high dielectric constant.

The results of the non-dimensional analysis of the pump properties for all liquid crystals are shown in Fig. 13. The pump has a 3-mm-wide channel and 3 turn spiral flow channel.

All relations between $\mu Q / \left\{ D^3 (\varepsilon_{per} - \varepsilon_1) E^2 \right\}$ and $p / \left\{ (\varepsilon_{per} - \varepsilon_1) E^2 \right\}$ derived by the π theorem almost
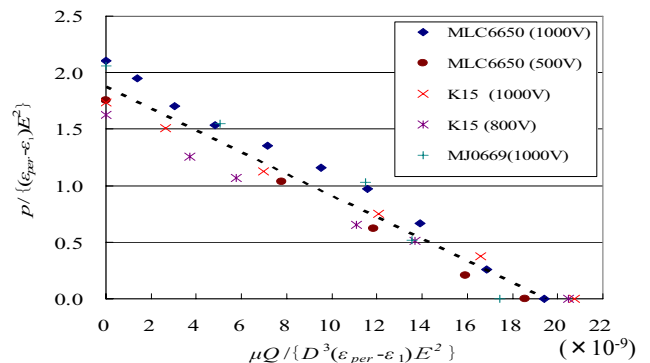
Fig. 13 Nondimensional analysis (3turns,
w=3mm, dielectric constant=ε_{per}, α=17.7°)

constant in this experiment. The maximum pressure increased with the voltage and the maximum pressure for the two pumps connected in series is almost twice that of a single pump.

The relation between the flow rate and the pressure for the number of turns (1 and 3) of the spiral flow channel around the axis of the pump is shown in Fig. 9. The pressure increased with the voltage. Moreover, the pressure increased with the turn number of the spiral flow channel. The flow rate for *w*=3mm is larger than for *w*=1mm because the area of the flow channel is large compared with *w*=1mm.

In Fig.9, both the angle α between the electric rotation direction and the flow direction and the flow channel length D are changed by changing the turn number. So it is not clear that the difference of the results comes from α or D .

The measurement is conducted by keeping the length *D* constant and changing the angle α to investigate the effect of α. From Fig.10, the flow rate increase with

become the same line. The above symbols should be refereed to nomenclature. The pressure-flow rate characteristics of the pump can be guessed from this result when the liquid crystals with different properties are used in the present pump. (ε_{per}—ε_1) means the difference between the dielectric constant of the vertical direction to longitudinal direction of the liquid crystal molecule and the dielectric constant of insulating part. The difference was used for the present non-dimensional analysis because the difference is found to be very important factor, which acts on the characteristics of the liquid crystal under application of the voltage [18].

CONCLUTIONS

In the present study, rotation electric fields were applied to the cylinder electrodes to add the voltage on the liquid crystals, and flow was induced by the property of the liquid crystal. A pump with a spiral flow channel using the above mechanism was designed, and the pressure-flow rate characteristics of the pump were measured. We made the following findings.

1. The maximum pressure increased when we used a liquid crystal with a high dielectric constant and a high kinematic viscosity for the constant voltage.
2. The pressure of two pumps connected in series was almost twice that of a single pump.
3. As the flow direction approaches the direction of the rotational electric field, the flow rate increases.
4. For the dimensionless parameters calculated using the π theorem, all relations between

$$\mu Q \Big/ \big\{ D^3 (\varepsilon_{per} - \varepsilon_1) E^2 \big\} \qquad \text{and} \qquad p \Big/ \big\{ (\varepsilon_{per} - \varepsilon_1) E^2 \big\}$$

almost become the same line.

ACKNOWLEDGMENTS

REFERENCES

1. Enomoto Micropump Co,.Ltd, http://www.emp.co.jp/structure.htm
2. Shinano Kenshi Co.Ltd, http://www.skcj.co.jp/motor/category8.html#02
3. Sakai, Y., Maki, M., Ogata, S. , Sato, K., Yokota, K. and Itoh, M., Influences of Duct Height on Flow Fields and Pressure Performances of a Viscous Micropump Modes Using a Cylindrical Rotor in a Rectangular Duct, Transactions of the Japan Society of Mechanical Engineers, 2006,72-718, pp.1513-1521 (in Japanese).
4. Kilani, M., AI-Salaymeh, A. and AI-Halhouli, A., Effect of Cannel Aspect Ratio on the Flow Performance of a Spiral-Channel Viscous Micropump, Transactions of the ASME J.of Fluids Engineering, 2006, 128, pp.618-627.
5. Yamada, H., Hakama, S., Miyashita, T. and Zhang, N., An Investigation of an Ion Drag Pump Using a Needle-mesh Electrode Configuration, Proc. Instn Mecha. Engrs., 216 Part C, J.Mechanical Engineering Science, 2006, pp.325-335.
6. Feng, Y. and Seyed-Yagoobi, J., Control of Liquid Flow Distribution Utilizing EHD Conduction Pumping Mechanism, IEEE Transactions on Industry Applications, 2006, 42-2, No.2, pp.369-377.
7. Kano, I., Mizuochi, K. and Takahashi, I., Micro-Electro Hydrodynamic Pump by Dielectric Fluid. Improvement for Performance of Pressure Using Cylindrical Electrodes, Proceedings of the Sixth International Symposium on Fluid Power Tsukuba,2005, pp.575-579.
8. Yokota, S., Seo, W., Yoshida, K. and Edamura, K., A Planar Pump Using Electro-Conjugate Fluids (ECF) (Proposition of an ECF Pump for Liquid Cooling of Electronic Chips), Robotics and Mechatronics Division of the Japan Society of Mechanical Engineers, 2004, No.04-4,2P1-L1-61(1-4) (in Japanese).
9. Sakurai, Y., Kadoi, H., Nagata, T. and Edamura, K., Development of Printed Circuit Board Multi-layered Typed ECF-pump and Its Application to Liquid Colling System, Transactions of the Japan Society of Mechanical Engineers,2006, C, 72-715, pp.991-996 (in Japanese).
10. Okazaki, T.,Miyazaki, K. and Tsukamoto, H., Development of an Electroosmotic Flow Driven Liquid Mirco-pump, The preprint of the Mechanical Engineering Congress in Japan(MECJ-06),2006, No.06-1,No.2, pp.291-294 (in Japanese).
11. Tsukiji, T., Koyabu, E., Tsuji, T. and Chono, S., Influence of Electric Fields on the Flow of a Liquid Crystal Mixture in Circular Pipe Electrodes, JSME International Journal, 2005, 48-3, pp.517-523.
12. Tsukiji, T., Murata, Y. and Ito, J., Flow of a Liquid Crystal Mixture in a Mini-Cylinder under Rotating Electric Fields, Proceedings of the Sixth International Symposium on Fluid Power Tsukuba,2005, pp.595-600.
13. Jones, T., Gunji, M., Washizu, M. and Feldman, M., Dielectrophoretic liquid actuation and nanodroplet formation, Journal of Applied Physics,2001, 89-2 ,pp.1441-1448.
14. Jones, T. and Melcher, J., Dynamics of Electromechanical Flow Structure, The Physics of Fluids, 1973, 16-3, pp.393-400.
15. Jones, T., Hydrostatics and steady dynamics of spatially varying Electromechanical Flow Structures, Journal of Applied Physics, 1974, 45-4, pp.1487-1491.
16. Melcher, J. amd Guttman, D., Dielectrophoretic Orientation", AIAA Journal, 1969, 6-1, pp.25-32.
17. Tsukiji, T., Suzuki, K. and Sato, H., Study on Liquid Crystal Pump, Trans. of the Japan Fluid Power System Society, 2008,(in press).
18. Suzuki, K., 2007,"Study on Functional Fluid Pump", Master thesis in Sophia University, Japan.

P1-56

PROPOSITION OF AN ER MICROACTUATOR WITH INHERENT POSITION FEEDBACK MECHANISM

Kazuhiro YOSHIDA*, Kazuhito KAMIYAMA**, Joon-wan KIM* and Shinichi YOKOTA*

* Precision and Intelligence Laboratory
** Graduate School
Tokyo Institute of Technology
R2-42, 4259 Nagatsuta-cho, Midori-ku, Yokohama, 226-8503 Japan
(E-mail: yoshida@pi.titech.ac.jp)

ABSTRACT

The paper proposes and develops a novel smart ER microactuator with inherent position feedback mechanism. The microactuator consists of a pair of movable and fixed parallel plate electrodes with variable gap length and an upstream restrictor, and ERF (electro-rheological fluid) is supplied as a working fluid. By applying voltage to the electrodes, with the increased pressure drop due to ERF viscosity increase, the electrode gap length i.e. the output displacement increases. Also the microactuator can suppress the displacement due to external force by the inherent position feedback mechanism. The mechanism utilizes increase of the flow resistance between the electrodes for decrease of the electrode gap length. In this paper, the structure and working principle are revealed and the mathematical model is derived. Then, a microactuator is fabricated and the characteristics are experimentally clarified. Furthermore, a mechanism to magnify the output displacement is proposed and the validity is confirmed through experiments.

KEY WORDS

Microactuator, ERF (electro-rheological fluid), Functional fluids, Position feedback, ER valve

INTRODUCTION

A smart actuator having built-in position sensor has been required to realize a position control system in compact size without additional sensors [1].

A fluid microactuator connected with an ER microvalve [2]-[4] is one of ER microactuators. By applying electric field to the ERF (electro-rheological fluid) in the ER microvalve, the pressure of the fluid actuator is controlled. Such an ER microactuator features simple and miniaturizable structure. Furthermore, utilizing the functionality of the ERF, a simple and compact smart actuator will be realized as a microactuator.

In this paper, a novel smart ER microactuator is proposed and developed, which can not only control the output displacement / force by the applied voltage but also suppress the displacement due to external force using the inherent position feedback mechanism. First, the structure and working principle are revealed and the

mathematical model is derived. Second, a microactuator is fabricated and the characteristics are experimentally investigated. Furthermore, a mechanism to magnify the output displacement is proposed and tested.

PROPOSITION OF FB TYPE ER MICRACTUATOR

Proposed FB Type ER Microactuator

The proposed microactuator consists of a pair of movable and fixed parallel plate electrodes with variable gap length and an upstream restrictor as shown in Figure 1. The electrodes are disks and the ERF flows from the outside inlet port to the central outlet port on the fixed electrode. The movable electrode is supported by an elastic element such as a bellows. The ERF is supplied at pressure P_s as the working fluid.

When the applied voltage v increases / decreases, the control pressure p_c increases / decreases due to viscosity
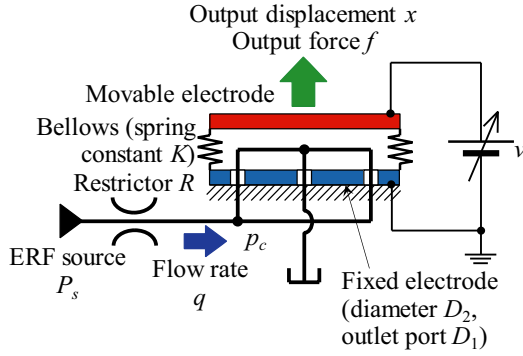
Figure 1 Proposed FB type ER microactuator
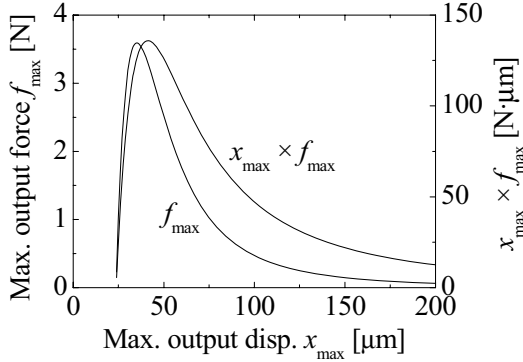
Figure 2 Analyzed characteristics of the FB type
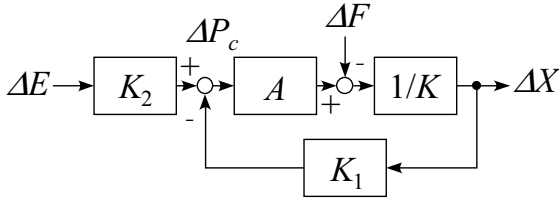ER microactuator

Figure 3 Block diagram of the FB type
ER microactuator

change of the ERF and the output displacement x increases / decreases. Also, with constant applied voltage v, when external force to increase / decrease the gap length is applied, due to decrease / increase of the electric field strength and flow resistance between the electrodes, the control pressure p_c and hence the output force f decreases / increases. As a result, the displacement due to external force is suppressed with the inherent position feedback mechanism.

Mathematical Model

For theoretical investigations, the mathematical model of the microactuator was derived assuming flow between the electrodes to be isotropic flow. Let D_1=1.0 mm, D_2=8.8 mm, the base viscosity without electric field μ_0=24 mPa·s and the ER effect index [3] κ_{ER}=5 of the ERF, P_s=200 kPa and q_{max}=0.1 cm^3/s, the maximum output force f_{max} and $x_{max} \times f_{max}$ were calculated as shown in Figure 2. It is found that $x_{max} \times f_{max}$ becomes maximum at x_{max}=41 μm. With linearization at the driving point, the block diagram can be expressed as in Figure 3. The
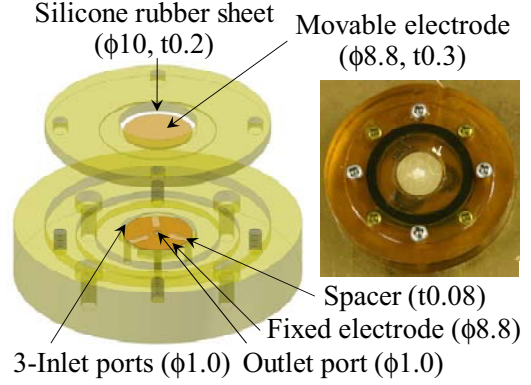
Figure 4 Fabricated electrode part of the FB type
ER microactuator

microactuator is proved to have a feedback loop and the actuator rigidity is derived as follows:

$$K_a = -\frac{\Delta f}{\Delta x} = K + AK_1, \tag{1}$$

which means the microactuator has the actuator rigidity higher than K without additional feedback loop and the microactuator can suppress the displacement due to external force.

FABRICATION AND CHARACTERIZATION OF FB TYPE ER MICRACTUATOR

Fabricated FB Type ER Microactuator
Based on the derived results, a microactuator was designed and fabricated. The fabricated electrode part is shown in Figure 4. The disk electrodes are divided by three parts with independent hydraulic circuits and slant of the movable electrode is suppressed. The movable electrode is supported by a silicone rubber sheet instead of a bellows. The homogeneous ERF used here is a nematic liquid crystal (MLC-6457-000, Merck Ltd., Japan) whose base viscosity μ_0=24 mPa·s and ER effect index κ_{ER}=5.4 [3].

Experiments
The static characteristics were measured with supply pressure P_s=200 kPa. The output displacement x under no load was measured by a laser displacement sensor and the control pressure p_c (average of three pressures) was measured by semiconductor type pressure transducers.
Figure 5 shows the measured results. The origin of the output displacement x is corresponding to the output displacement without supply pressure and voltage. It is found that the output displacement x has nonlinearity, however there is few hystereses. The output displacement range is 52 μm. The output displacement x at v=0 is not zero due to the initial stretched length error of the silicone rubber sheet.
The output force f was measured through the deflection of a brass beam (50×10×1.4 mm^3, spring constant 7.6 kN/m) for the output displacement x to be the value without voltage. Figure 5 shows the measured results. The maximum output force f_{max}=1.5 N was obtained.
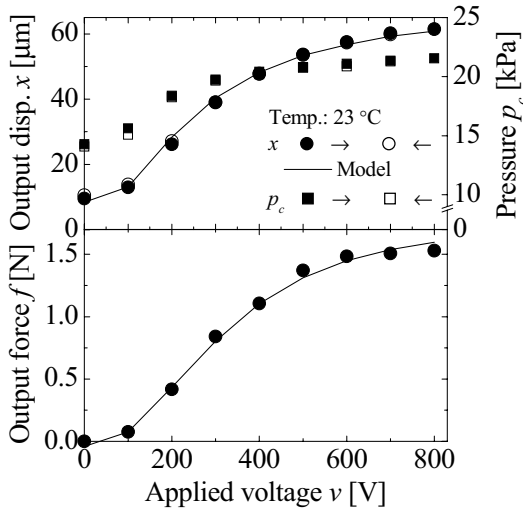Based on the control pressure p_c and the mathematical

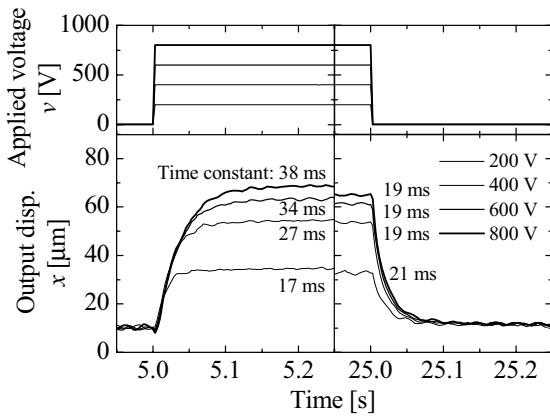Figure 5 Measured static characteristics of the FB type ER microactuator

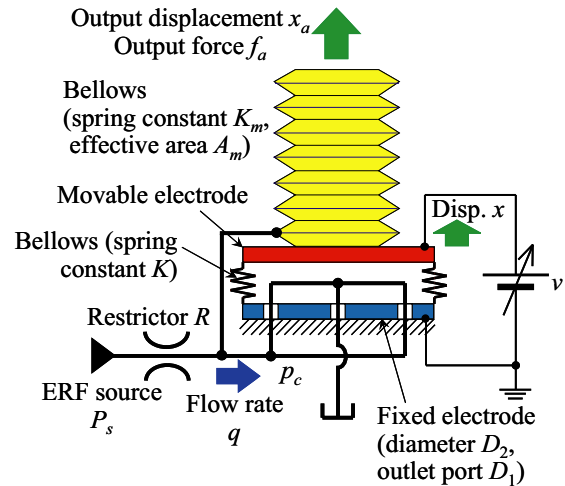Figure 6 Measured step responses of the FB type ER microactuator

Figure 7 Proposed FB type ER microactuator with displacement magnification unit

Figure 8 Block diagram of the FB type ER micro-actuator with displacement magnification unit

model, the parameters were identified. The solid lines in Figure 5 show the results of output displacement x and the output force f. It is ascertained that the results agree well with the measured values. Differences between the identified and the measured parameters are due to different flow from the isotropic flow due to the three inlet ports.

The actuator rigidity at the maximum output displacement was measured using the beam at the applied voltage v=800 V. As a result, K_a=16 kN/m was obtained. The value is 3.7 times higher than the value without feedback loop and the validity was confirmed. The value of the mathematical model is 18 kN/m that agrees well with the measured value.

Figure 6 shows the measured step responses of the microactuator. The step down responses are higher than step up, which is due to the mechanism difference; for step up, the liquid crystal molecules make domains; for step down, the domains collapse by the flow [4]. The identified time constants of the first order lag responses are also shown in Figure 6. As for the effect of the applied voltage amplitude, there are few differences for step down and the step up responses decrease with

higher voltage amplitude, which are the same as the previous ER microactuators [3]. The bandwidth of 4 Hz or more was confirmed.

PROPOSITION OF DISPLASEMENT MAGNIFICATION UNIT

Proposed Displacement Magnification Unit

To extend application fields of the FB type ER microactuators, the output displacement range is required to enlarge. In this paper, a displacement magnification unit utilizing the control pressure p_c is proposed as shown in Figure 7.

The unit is a bellows that is attached on the movable electrode and is connected to the control pressure p_c port in hydraulic circuit. The output displacement x_a is the sum of the movable electrode displacement x and the bellows extension / contraction x_m. When the applied voltage v increases / decreases, the control pressure p_c increases / decreases like the electrode part only. Hence, gap length of the electrodes and length of the bellows of the unit increase / decrease. The output displacement x_a can be controlled by the applied voltage v.

With the constant applied voltage v, when the external force is applied to increase / decrease the output displacement, flow resistance of the electrode unit decreases / increases due to the large / small gap length
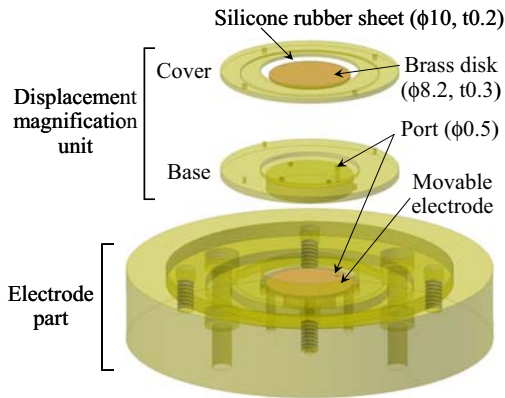
Figure 9 Fabricated FB type ER microactuator with displacement magnification unit
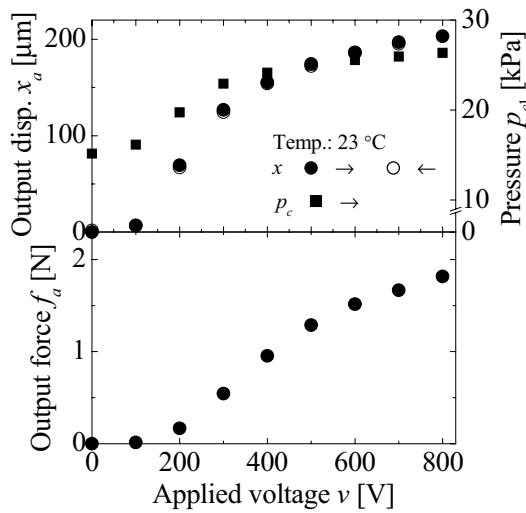

Figure 10 Measured static characteristics of the FB type ER microactuator with displacement magnification unit
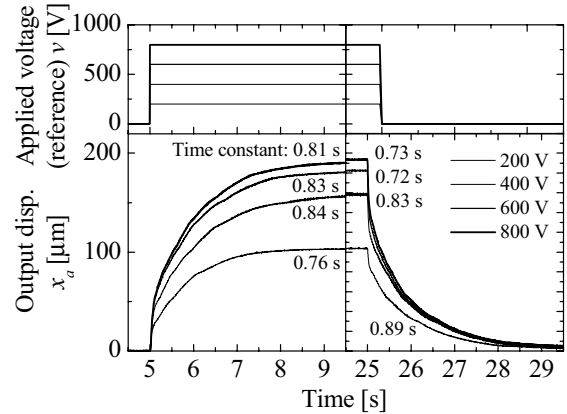

Figure 11 Measured step responses of the FB type ER microactuator with displacement magnification unit

rubber sheet was used.

The static characteristics of the microactuator were measured using the same method as the electrode part. Figure 10 shows the measured results. The output displacement range of 203 μm and the maximum output force of 1.8 N were obtained. The measured actuator rigidity at the maximum output displacement was 6.3 kN/m. Figure 11 shows the measured step responses of the microactuator. Due to flow saturation, the responses were lower than values of the electrode unit. Based on the identified time constant of the first order lag responses, the bandwidth is 0.2 Hz.

CONCLUSIONS

In order to realize a smart microactuator, the FB type ER microactuator was proposed and the basic investigations were conducted. The main results are summarized as follows:
1) The FB type ER microactuator was proposed and the mathematical model was derived.
2) An FB type ER microactuator was fabricated and the validity was confirmed experimentally.
3) A displacement magnification unit was proposed and the basic characteristics were experimentally clarified.

and low / high electric field strength, so the control pressure p_c and hence the output force f_a decreases / increases. The microactuator can suppress the displacement due to external force. As can be seen in Figure 8, the derived block diagram of the microactuator has a feedback loop.

The output displacement x_a under no load, the output force f_a without displacement and the actuator rigidity K_{am} at the maximum output displacement are calculated as follows:

$$x_a = (1 + A_m K / A K_m)x,$$
$$f_a = \begin{cases} \{1 - (A - A_m)K / (K + K_m)\}f & (A \geq A_m) \\ (A_m / A)f & (A < A_m) \end{cases} \quad (2)$$
$$K_{am} = (K + A K_1)K_m / \{K + K_m + (A - A_m)K_1\}.$$

Experiments
The FB type ER microactuator with displacement magnification unit was fabricated as shown in Figure 9. Dimensions of the electrode unit is the same as Figure 4. Instead of the bellows, a diaphragm using silicone

REFERENCES

1. Suzumori, K., et al., Proc. ACTUATOR 2006, 2006, pp. 128-131.
2. Kohl, M., Mechatronics, 2000, **10**-4·5, pp. 583-594.
3. Yoshida, K., et al., Sensors and Materials, 2005, **17**-3, pp. 97-112.
4. De Volder, M., et al., J. of Micromechanics and Microengineering, 2006, **16**-3, pp. 612-619.

P1-57

CHARACTERISTICS AND APPLICATIONS OF AMORPHOUS COMPOUND FLUID

Kunio SHIMADA *, Hitoshi NISHIDA **, Eiichiro YUZE *** and Yaoyang Zheng *

* Department of Symbiotic Systems Sciences, Fukushima University,
Kanayagawa 1, Fukushima 960-1296, Japan
(E-mail: shimadakun@sss.fukushima-u.ac.jp)
** Department of Mechanical Engineering, Toyama National College of Technology,
13 Hongo, Toyama, 939-8630, Japan
*** Akita Prefectural Industrial Technology Center,
9-3, Furudate, Kosaka, Kazuno-gun, 017-0202

ABSTRACT

We proposed an amorphous compound fluid (ACF) as a new intelligent or smart fluid. This fluid contains nm-size magnetite and 1μm-sized amorphous particles in a solvent. This report shows, first, experimental data regarding the viscosity of ACF in a cone-type rotating rheometer under a transverse magnetic field and its magnetization under a DC magnetic field. The experimental results are then compared with those for previous magnetic responsive fluids, magnetic compound fluid (MCF), magneto-rheological fluid (MRF), and magnetic fluid (MF). Those magnetic clusters as aggregated particles were investigated by optical observation. Finally, this report shows the experimental results of engineering applications on polishing that utilize the ACF, and compares the results with polishing that utilizes MCF.

KEY WORDS

Amorphous, Magnetic Compound Fluid (MCF), Magnetic Fluid, Magnetic Field, Magneto-rheological Fluid

NOMENCLATURE

Ra : mean surface roughness
Ry : height of surface roughness between maximum and
     minimum heights

INTRODUCTION

A few intelligent fluids are responsive to magnetic fields, for example, magnetic fluid (MF) and magneto-rheological fluid (MRF). Both fluids have advantages and disadvantages in engineering applications [1]. MF's magnetization and apparent viscosity under a magnetic field is smaller than those of MRF. However, the stability of the particle distribution in an MF solvent is more consistent than that in an MRF solvent. In light of this and for the purpose of producing a new intelligent or smart fluid, one of authors of the present paper, Shimada, has proposed a magnetic compound fluid (MCF) comprised of nm-size magnetite and μm-size iron particles in a solvent, which thereby compounds MF and MRF [2]. He has measured the relation of its shear stress to its shear rate using a rotating rheometer [2, 3] and has also measured its magnetic characteristics [4]. He has also proposed new engineering applications that utilize MCF, for example, in polishing [5, 6] or in a damper [7].
For the same purposes, we propose a magnetic

responsive fluid containing amorphous particles: amorphous compound fluid (ACF) is comprised of 1μm order-sized amorphous particles and MF. In general, the material properties of the amorphous particles are different from those of the magnetite and iron particles regarding stiffness, large magnetization, etc. Therefore, if the amorphous particles are used in a solvent, the possibility of its having engineering applications different from the use of MCF alone can be expected.

In the present paper, we first investigated the magnetic and rheological characteristics of ACF and compared them to those of MCF, MF, and MRF. Secondly, we investigated the potential engineering applications of ACF in polishing.

ACF

We used Co-P amorphous particles (C166) of about 1μm mean diameter that were fabricated and patented in Japan by Yuze [8], one of the present authors. We compounded the kerosene-based MF of HC50 with 1.29g of 50 wt% of 10nm mean diameter Fe_3O_4 produced by Taiho Industry Co. Ltd. in Japan and 2g of amorphous particles (C166) composed of C166 at 60.8 wt%, Fe_3O_4 at 18.0 wt% and kerosene at 21.2 wt%.

MAGNETIC CHARACTERISTICS

We investigated the magnetization of ACF under a DC magnetic field using a VSM (VSM-5S-15, Toei Ind. Co. Ltd., Japan). The experimental results are shown in

(a)
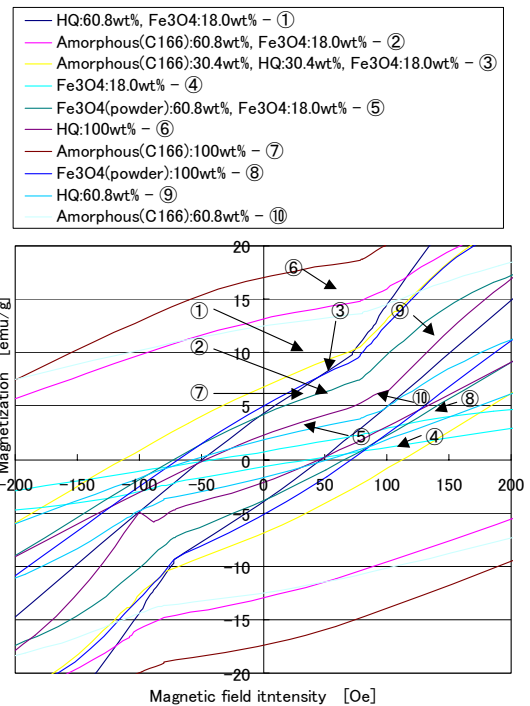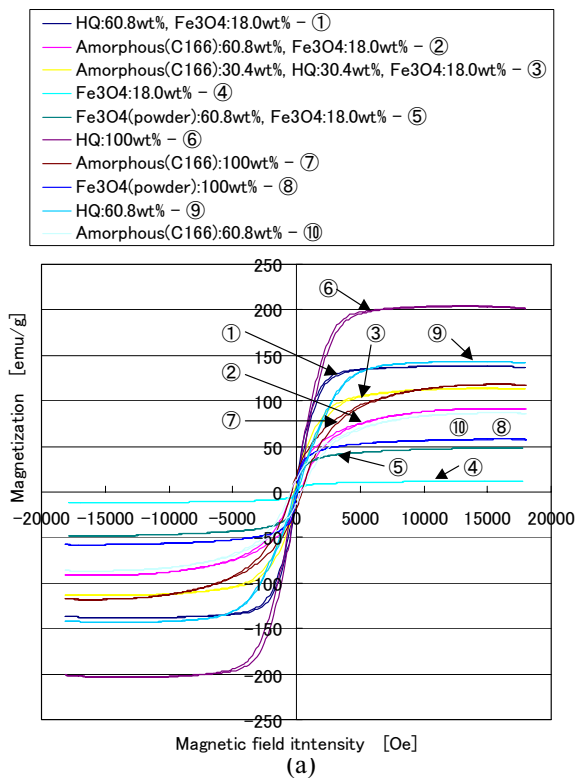
(b)　detail at small magnetic field intensity of (a)

Figure 1 Magnetization of ACF and the others

Table 1 Composite and data of magnetization of ACF, MCF, MRF and MF

Mass concentration (wt%) of testing fluid	Material	Compound	Residual magnetiza-tion [emu/g]
HQ: 60.8, Fe_3O_4: 18.0, other kerosene	MCF	MRF+MF	4.851
C166: 60.8, Fe_3O_4: 18.0, other kerosene	ACF	amorphous particle +MF	13.05
C166: 30.4, HQ: 30.4, Fe_3O_4: 18.0, other kerosene	AMCF	ACF+MCF	7.003
Fe_3O_4: 18.0, other kerosene	MF		1.015
Fe_3O_4 (powder): 60.8, Fe_3O_4 (from the particles of MF): 18.0, other kerosene		powder of Fe_3O_4 +MF	4.394
HQ: 100	powder		2.493
C166: 100	powder		16.74
Fe_3O_4: 100	powder		5.669
HQ: 60.8, other kerosene	MRF		1.827
C166: 60.8, other kerosene	AF		12.48

Fig. 1 and compared to those of MCF, MRF, MF, and powder. The caption in the figure is shown in Table 1 in detail. "Fe_3O_4" in the figure means the magnetite in MF, "powder" the particles only and "HQ" the carbonyl iron having 1.2 μm of mean diameter made by BASF Co. Ltd. AMCF means the compounded fluids of ACF and MCF, which we call "Amorphous Magnetic Compound Fluid". AF means the fluid having only amorphous particles of C166, which we call "Amorphous Fluid".

The magnetic property obtained from Fig. 1 is also shown in Table 1. The saturation magnetization is defined by that of the involved particles. That of ACF is smaller than that of MCF. Therefore, the order of the saturation magnetization is MRF>MCF>AMCF>ACF> MF.

The residual magnetizations and the areas of the hysterisis loops of ACF and amorphous particles are much larger than those of MCF, MRF, Fe_3O_4, and HQ.

HYDRODYNAMIC CHARACTERISTICS

We examined the viscosity using cone-type rotating rheometers under a uniform magnetic field. The magnetic field was applied transversely to the lower plate. Details of the experimental apparatus were
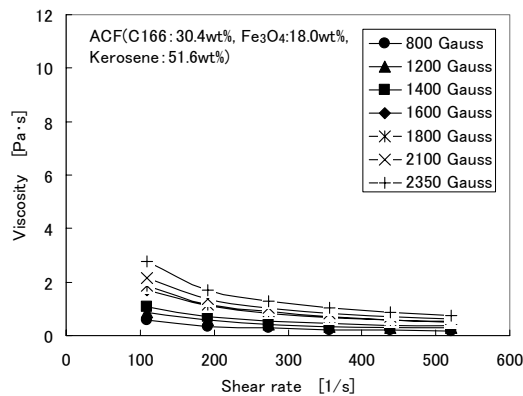
(a)
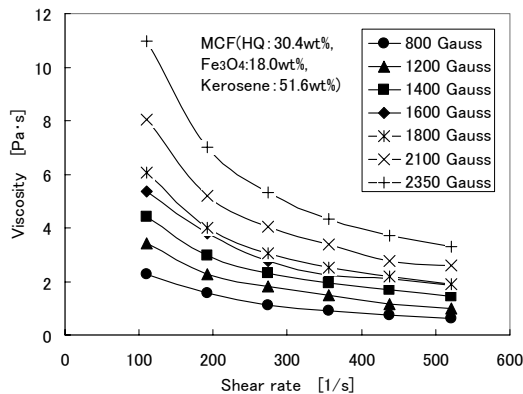
(b)
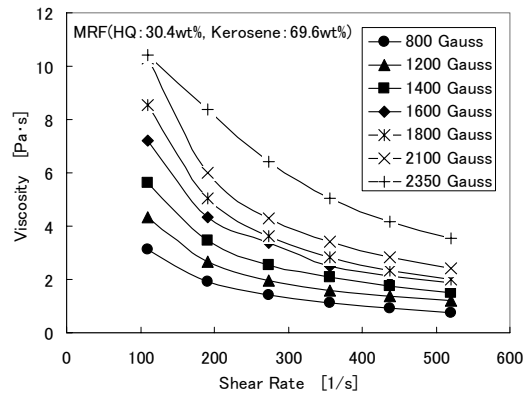
(c)
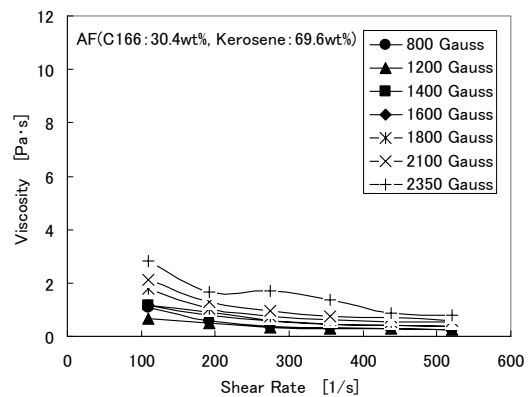
(d)

Figure 2 Viscosity to magnetic field intensity of (a) ACF, (b) MCF, (c) MRF and (d) AF

reported in our other investigation [2, 3]. The experimental results are shown in Fig. 2 and compared to those of MCF, MRF and AF. The viscosity of ACF is less than that of MCF. This is due to the formation of magnetic clusters. As seen in the following section, the "string magnetic cluster" of ACM is weaker than the magnetic cluster of MCF. Therefore, the string-like magnetic cluster can be distributed by a given flow rate, and the viscosity of ACF then becomes less than that of MCF.

CLUSTER

The particles involved in the ACF and other fluids are aggregated as clusters. The clusters can be extracted from ACF as well as from MCF and MRF using the technique proposed by Shimada [9]. A microscope photograph is shown in Fig. 3. The magnetic cluster of ACF differs from that of MCF. The length of the former is much larger than that of the latter, as shown by Fig. 1. In addition, the attractive strength between the particles of the former is much greater than that in the latter in the case when a force is immediately applied to the magnetic clusters in order to distribute each particle uniformly. Therefore, the magnetic cluster in ACF can

557

be called a "string magnetic cluster." However, the force holding the cluster formation in the former is much larger than that in the latter if the applied magnetic field is removed from the magnetic clusters. This is due to the remnant magnetization, as shown in the previous section. After removing the magnetic field, the particles in ACF, AMCF and AF can be held in a string-like cluster formation due to the remnant magnetization of the amorphous particles, as shown in Fig. 3(c-2), (d-2), and (e-2).
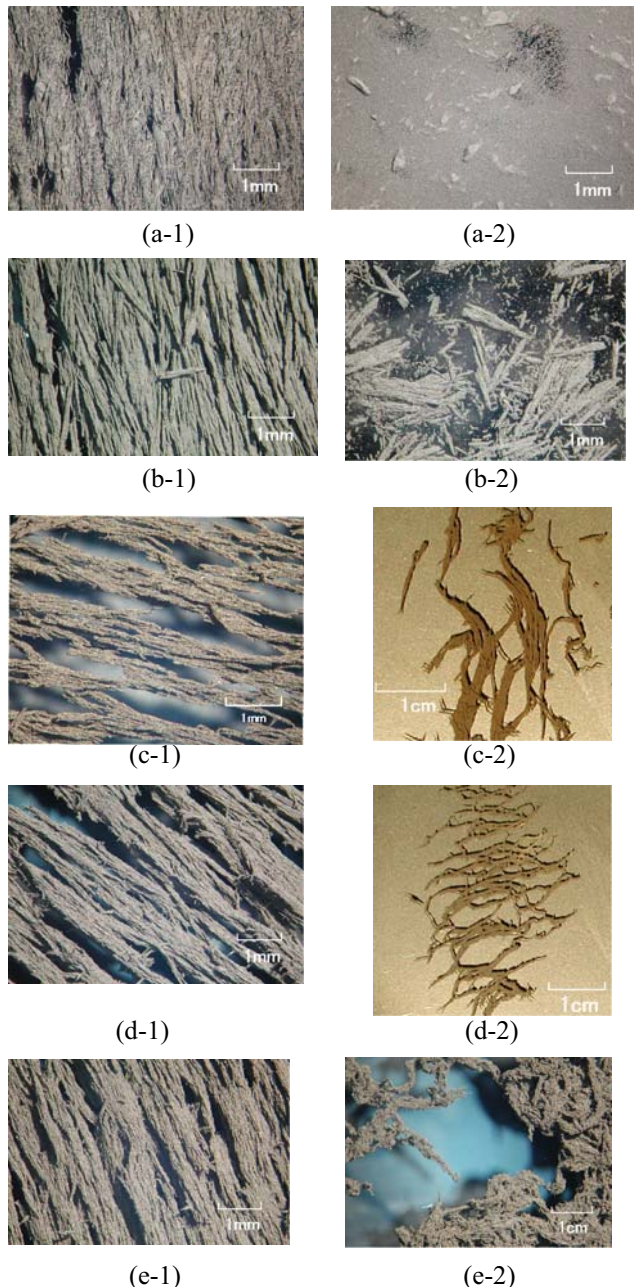

(a-1)	(a-2)
(b-1)	(b-2)
(c-1)	(c-2)
(d-1)	(d-2)
(e-1)	(e-2)

Figure 3 Magnetic clusters of the fluids produced under a magnetic field as seen by a microscope with a multiplying ratio of 60: (a) MCF, (b) MRF, (c) ACF, (d) AMCF, (e) AF; -1 indicates just after being removed

from a magnetic field without any vibration, -2 indicates after being removed from a magnetic field and given a vibration

The particles involved in the ACF were observed by TEM, as shown in Fig. 4. Co and P are in the same position while Fe is in another position. Therefore, the Fe_3O_4 particles are surrounded by the amorphous particles. On the other hand, the amorphous particles are aggregated due to the remnant magnetization.

| (a) | (b) |
| (c) | (d) |
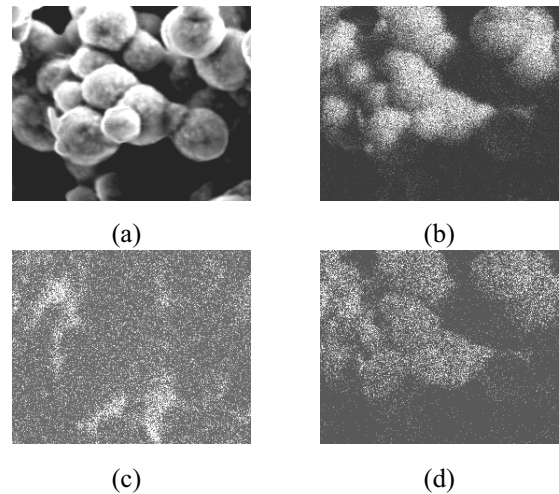
Figure 4 Photographs of ACF by TEM with a multiplying ratio of 10000: (a) all particles, (b) only Co, (c) only Fe, (d) only

APPLICATIONS

We tried to apply the ACF to polishing as one of its engineering applications. We used an experimental apparatus for float polishing, as shown in Fig. 5. A polishing tool having a permanent magnet with a diameter of 8 mm and maximum strength of 4500 Gauss was rotated by a drilling machine having a constant speed of 515 rpm. A disk type testing specimen made of brass having a diameter of 30 mm and thickness of 1 mm was attached to the surface of a lower load cell capsule. A testing fluid was inserted between the test specimen and the polishing tool. The load cell capsule was moved by the vibration machine with two types of motion, rotation and knitted brows rotation, having an amplitude of 10mm and a frequency of 20rpm. The clearance between the test specimen and the polishing tool was adjusted using an attachment to the vibration machine.

Table 2 shows the testing fluids of MCF and ACF used in the present study.

Figure 6 shows the surface roughness after polishing of *Ra* as (a) and of *Ry* as (b). The initial roughness *Ra* was 0.0923 μm and the *Ry* was 0.616 μm. The polishing effect from using the ACF was a mirror-like surface, similar to the case of using the MCF. The cause of this

result was the previously mentioned "string magnetic cluster": for ACF, as shown in Fig. 7(a), "string magnetic clusters" aggregated by amorphous and Fe_3O_4 particles function like a polishing cloth. ACF ca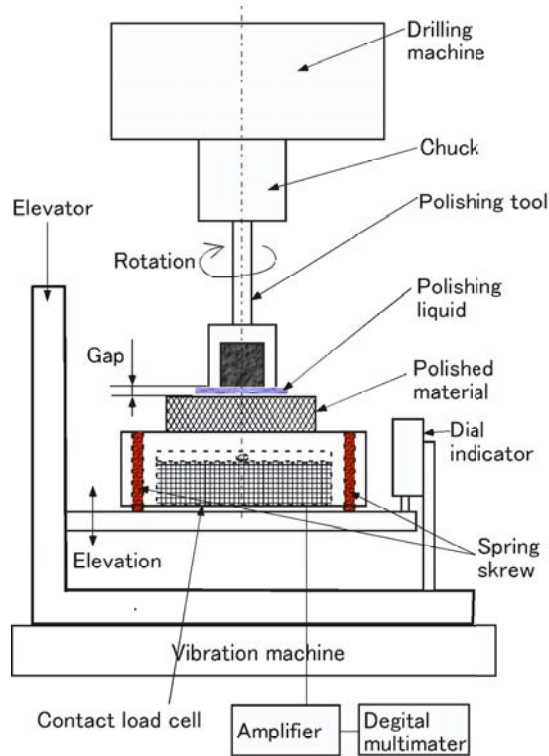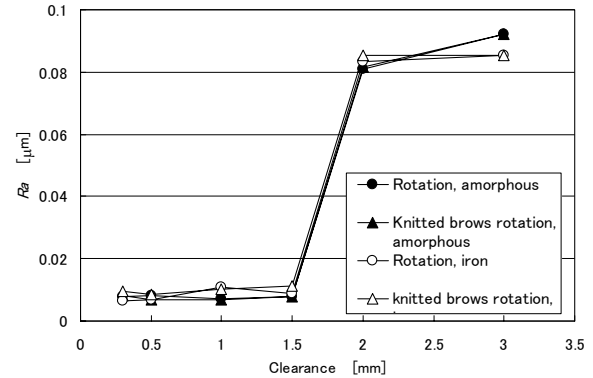n polish more smoothly than MCF. On the other hand, MCF, with needle-like magnetic clusters aggregated by iron and Fe_3O_4 particles, polishes like a toothbrush, as shown in Fig. 7(b). Therefore, a mirror-like polished surface can be obtained by a polishing cloth with the ACF's clusters as well as by a polishing toothbrush with the MCF clusters.

Although the viscosity and saturation magnetization of ACF are smaller than those of MCF, the polishing effect of ACF is the same as that of MCF. The aggregated particle formation is a critical factor in the field of polishing. This result is very typical.

Figure 5 Schematic diagram of float polishing apparatus using the fluids

Table 2 Composite of MCF and ACF in float polishing

Testing fluid	Components	Mass concentration
MCF	・ HQ : 30 g ・kerosene-baseed magnetic fluid （HC50 (50 wt%)） : 38.7 g ・ kerosene : 29 g ・ abbrasive particle (Al_2O_3 (3 μm)) : 19.7 g ・ α-cellurose : 6.3 g	・ HQ : 24.3 wt% ・ Fe_3O_4 : 15.6 wt%
ACF	・ C166 : 30 g ・kerosene-baseed magnetic fluid （HC50 (50 wt%)） : 38.7 g ・ kerosene : 29 g ・ abbrasive particle (Al_2O_3 (3 μm)) : 19.7 g ・ α-cellurose : 6.3 g	・ C166 : 24.3 wt% ・ Fe_3O_4 : 15.6 wt%

(a)

(b)

Figure 6 Surface roughness by float polishing utilizing ACF and MCF.

(a)

(b)
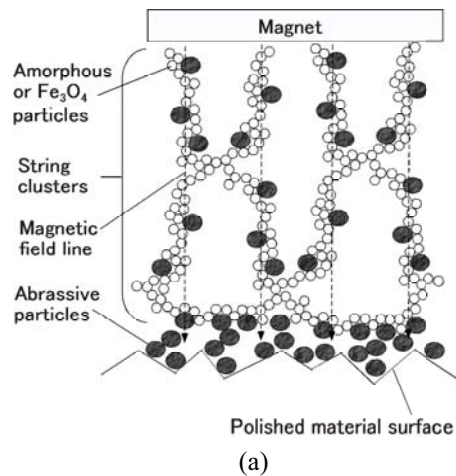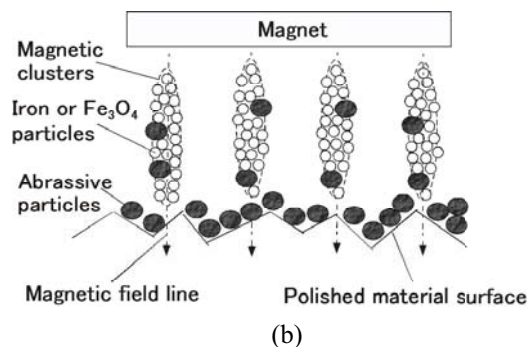
Figure 7 Schematic diagram of polishing model by string clusters in (a) ACF and (b) MCF

CONCLUSION

We proposed an amorphous compound fluid (ACF) as a new intelligent or smart fluid. We investigated the hydrodynamic characteristics of the fluid's viscosity and magnetic characteristics under a DC magnetic field. The viscosity and saturation magnetization of ACF are smaller than those of the previous magnetic responsive fluid, MCF, but its polishing effect is the same. The aggregated particle formation is a critical factor in the field of polishing.

ACKNOWLEDGEMENT

REFERENCES

1. Fujita, T. and Shimada, K., Characteristics and application of magnetorheological fluid, Recent Research Development Magnetism and Magnetic Materials, 2003, **1**, pp.463-479.

2. Shimada, K., Akagami, Y., Fujita, T., Miyazaki, T., Kamiyama, S. and Shibayama, S., Characteristics of MCF (Magnetic Compound Fluid) in a rotating rheometer, J. Magn. Magn. Mat., 2002, **252**, pp.235-237.

3. Shimada, K., Akagami, Y., Kamiyama, S., Fujita, T., Miyazaki, T. and Shibayama, A., New microscopic polishing with magnetic compound fluid (MCF), J. Intel. Mat. Sys. Struc., 2002, **13**-7, pp.405-408.

4. Shimada, K. and Oka, H., Magnetic characteristics of magnetic compound fluid (MCF) under DC and AC magnetic fields, J. Magn. Magn. Mat., 2005, **290/291**, pp. 804-807.

5. Shimada, K., Wu, Y., Wong, Y. C., Fujita, T., Miyazaki, T. and Shibayama, A., Experimental investigation of the effect of the MPL (magnetic polishing liquid) on surface finishing, Proc. SPIE, 2003, **4936**, pp.312-320.

6. Shimada, K., Wu, Y. and Wong, Y. C., Effect of magnetic cluster and magnetic field on polishing using magnetic compound fluid (MCF), J. Magn. Magn. Mat., 2003, **262**-2, pp.242- 247.

7. Shimada, K. Shuchi, S., Kanno, H., Wu., Y. and Kamiyama, S., Magnetic cluster and its applications , J. Magn. Magn. Mat., 2005, **289**, pp.9-12.

8. Yuze, E., Matsuda, M. and Ohtsuka, K., Tokukai2000-87120, 2000, Japanese Patent.

9. Shimada, K., Miyazaki, T., Shibayama, A. and Fujita, T., Extraction of magnetic clusters self-assembled by a magnetic field, Smart Materials and Structures, 2003, **12**-2, pp.297-303.

P1-58

SEMI-ACTIVE VEHICLE CAB SUSPENSION USING MAGNETORHEOLOGICAL (MR) TECHNOLOGY

Albert ACHEN*, James TOSCANO**, Robert MARJORAM**, Ken StCLAIR**,
Bill McMAHON**, Alexander GOELZ***, Shigeru SHUTTO****

* Lord France
11, rue Prieure J. Jenner, F-67500 Marienthal, France
** Lord Corporation
406 Gregson Drive, Cary, NC 27512-8012 USA
***Lord Italy
Via Moscatello, 64, 46040 – Castallaro di Monzambano, Italy
****Lord Far East Inc.
8-11-1 Nishi-Shinjuku, Shinjuku-ku, Tokyo 160-0023 Japan

ABSTRACT

Agricultural vehicle manufacturers are employing new semi-active cab suspensions using Magnetorheological (MR) technology. The use of MR technology in cab suspensions is a logical next step in improving operator safety and comfort. The speed and simplicity of MR technology enables the use of low-stiffness springs without the compromise between ride and stability, and can provide roll, isolation and pitch stability. MR fluids are materials that respond to a magnetic field with a dramatic change in rheological behavior. These fluids can reversibly change instantaneously from a free-flowing liquid to a semi-solid with controllable yield strength when exposed to a magnetic field. MR systems have been developed with a modular, integrated approach that can include a damper containing MR fluid, air spring, automatic electronic leveling, sensors, controller, and CANbus data communication.

KEY WORDS

WBV, whole body vibration, MR Fluid, Magnetorheological, Cabin suspension

INTRODUCTION

The impact of vibration on humans has been studied and reported since the 1930's with first reports on the relation of spinal trauma and truck and tractor driving published in the 50's. RM Stayner has compiled a report [1] with about 230 references on Whole-Body Vibration (WBV), Hand and Arm Vibration (HAV) and shock. WBV describes the vibrations generated by any machine, be it tools or vehicles, transmitted to the human body and which, if above a certain intensity and duration, causes detrimental physical effects (from motion sickness to spine and neck pain). The interest of this study goes to heavy duty vehicles used in agriculture, construction or transport, where WBV is caused by the wheels driving over uneven or rough surface or operating various attachments to excavate the ground or load materials.

Numerous measurements have been taken and compiled by various organizations like Landesamt für Arbeitsschutz (LAS) in Potsdam or in cooperative work under the EU mandated Advisory Committee on Safety

and Health at Work (by HSE, ISVR, HSL, BGIA, INRS) [2]. Vehicles that are often listed to contributing to WBV induced problems involve: forklift trucks, tractors and other agricultural machinery, heavy construction vehicles, like excavators, loaders, overhead (bridge) cranes, high speed boats, not to mention military numerous vehicles.

Vibration is defined by magnitude and frequency. For WBV it is most common to measure and report the vibration magnitude by its root-mean-square weighted acceleration (m/s²). As to the vibration frequencies their effect on health being variable, but the most relevant ones are between 0.5Hz and 80 Hz. To better modulate the effect of frequency, factors are applied (function of absolute frequency as well as for x, y or z directions) in order to obtain frequency weighted vibration values. Figure 1 illustrates the levels of vibration magnitude in common equipment used in Europe [2].
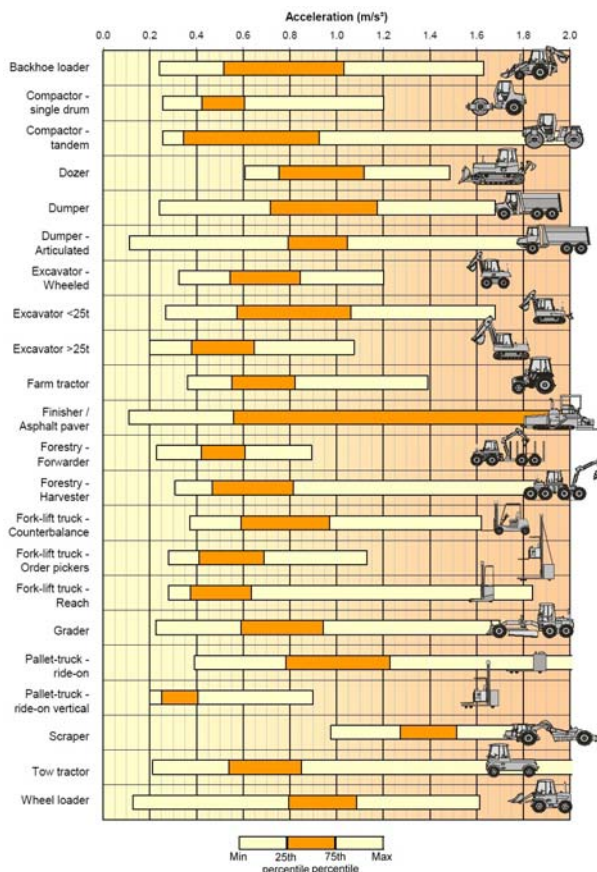
Figure 1: Examples of vibration magnitudes for common equipment on the EU market.

The physical agents Directive (Vibration) 2002/44/EC that came into force in July 2005 defines a WBV exposure action value, above which control measures must be implemented to limit the WBV risks, as well as exposure value limits above which workers must not be exposed to. The daily vibration exposure action value (A(8), the continuous equivalent acceleration, normalised to an 8 hour day) is 0.5 m/s² and the daily exposure limit value is 1.15 m/s².

TRACTOR MR SUSPENSION SYSTEM

Focusing on solutions to WBV in heavy duty vehicles, emphasis was put on agricultural vehicles as they move over all sorts of terrain, use attachments to perform tasks that increase vibrations and shocks, and eventually see their speed increased to the 60 km/h range. The size and weight of cabins continue to increase, and despite very good seat suspensions solutions, shocks, roll, pitch are increasingly difficult to mitigate. The impact on the health of tractor drivers caused by the transmitted vibrations is known and manufacturers have offered various levels of NVH solution to their customers. There are four types of tractor construction when it comes to suspensions:

1) Unsuspended tractor
2) Suspended cabin tractor
3) Suspended front axle & suspended cabin tractor
4) Fully suspended (front & rear axle) tractor

For tractors, the classic "one-piece" engine-transmission-rear axle construction makes integration of axle suspension difficult or expensive, such that many tractor manufacturers mitigate the vibration reduction challenge by installing seats with x,y,z suspensions (dampers and (air) springs). Those systems have been shown to reduce z-axis vibration acceleration by up to 65% [3]. The next step is the incorporation of various cabin suspension systems. In 1987 Renault, now Claas, developed and offered the "Hydrostable" cabin suspension system with four coil-over-damper suspensions at each cabin corner, struts and anti-roll bars. CNH offers a "Comfort Ride" system where the front of the cab is on rubber-metal mounts (or higher performance viscous versions) and the rear cab corners are suspended on coil-over-damper suspensions over the rear axle. This is a typical solution adopted by many manufacturers. Only JCB, towards the end of the 80's, launched the "Fastrac", a front and rear axle suspended chassis for speeds up to 65 km/h. Finally a commonly manufactured tractor suspension system is a front axle suspension system (CNH "Terraglide", John Deere "Triple Link Suspension"), which is combined with a two point cab suspension. Starting from those existing systems and based on the proven Lord magneto-rheological (MR) technology, an integrated adaptive cab suspension system was developed to further reduce WBV and improve ride comfort for

tractors that have larger and heavier cabins and increased driving speeds.

DESCRIPTION OF ADAPTIVE MR SUSPNESION

The Lord Smart Fluids based on magneto-rheological (MR) formulations are widely used in automotive suspensions technology [4][5][6]. They are proven in GM, Honda, Audi, Ferrari car models and in development for adaptive engine mounts and bushings. MR dampers have wide control range that depends mostly on the applied current which generates a magnetic field which is in turn affecting the rheology of the fluid. As such, the applied magnetic field controls the energy dissipation of the fluid inside the damper. Figure 2 shows the forces obtained with a small MR damper.
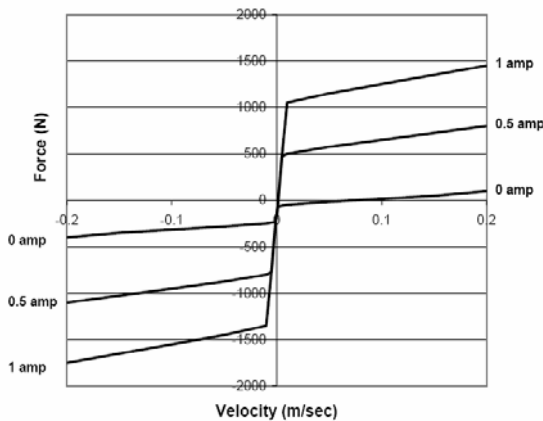
Figure 2 RD1005 MR Damper with 70 cm^3 fluid volume and max 240W dissipation @ 20 cm/s

The suspension unit is based on three components: first a MR damper with +/- 50 mm stroke, a maximum of 350N damping force in OFF (no current) state and up to 3500N in full ON state at 2A in extension or compression. Second, over the damper, an air spring is attached. Finally both parts are operated via a control module with integrated air levelling valves and microprocessor control board.

The control part of the damper locate above the air spring, contains an inlet and outlet for the compressed air used to regulate the air spring which is also used to level the cab.

The valves are controlled from the main electronic board that also contains the microprocessor and memories with the control algorithms and tractor specific tuning parameters. The damper position is determined by a magneto-strictive sensor located inside the damper rod, an xyz accelerometer on the electronics board delivers the data for movement control. The unit

communicates with the other MR suspensions and the tractor ECU via CAN Bus.
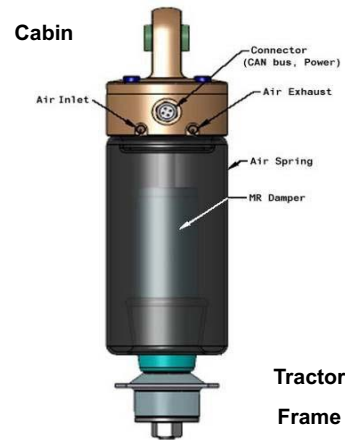
Figure 3: Integrated MR suspension prototype (integrated electronics) schematic view

In terms of mechanical integration on the tractor, the simplest design consists of two hard front rubber mounts which provide roll stability coupled with two MR units at the rear providing isolation and pitch stability. Next one can design a 2-point control with 2 MR suspensions at the rear providing isolation, pitch and roll stability, coupled with two soft front rubber mounts. This solution potentially eliminates the roll bar.
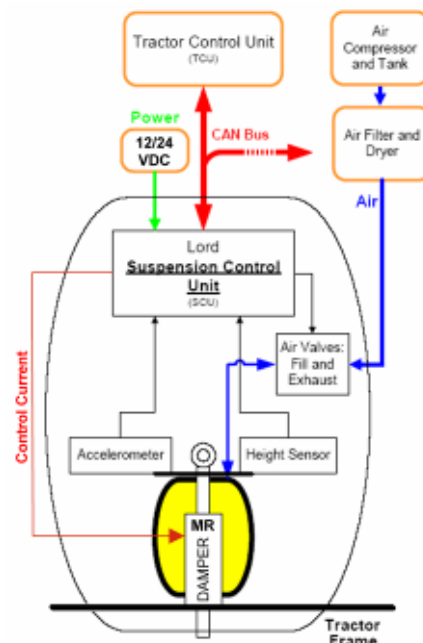

Figure 4: MR cab suspension system layout

Finally four MR suspensions at each corner represent an optimal semi-active control solution.

563

RIDE CONTROL STRATEGY AND PERFORMANCE

Following outputs are being addressed to optimize the ride comfort in view of minimizing WBV: 1) cab levelling control, 2) cab vertical control, 3) cab roll control, 4) cab pitch control, 5) end stop and snubber control. The inputs to the various control algorithms are numerous: right and left damper position and acceleration (lateral and vertical) come from the MR suspension and are used for pitch, roll and vertical skyhook control in order to minimize cab acceleration relative to the earth.

The CANbus also delivers information from the tractor to the suspension control unit. Acceleration (engine rpm), braking and direction (forward or reverse) and gear change are used for pitch control. Steering angle and speed are computed to counteract centrifugal force and control roll. The relative position of each unit and their relative velocity are also used to determine cab levelling and the air flow in or out of the air spring. This relative position is also used by the adaptive rate control algorithm to modulate the current to the MR damper allowing very precise, situation dependent damping control efficiently dealing with WBV.

The control algorithms have default setpoints which can be tuned to specific physical tractor cab configurations and driving situation (soft, medium, hard, field work or drive on public road). This Tractor specific tuning is done via specific software on a portable computer. The chosen gains and parameters are then sent via the CANbus to the MR suspension memory and the system operates independently thereafter.
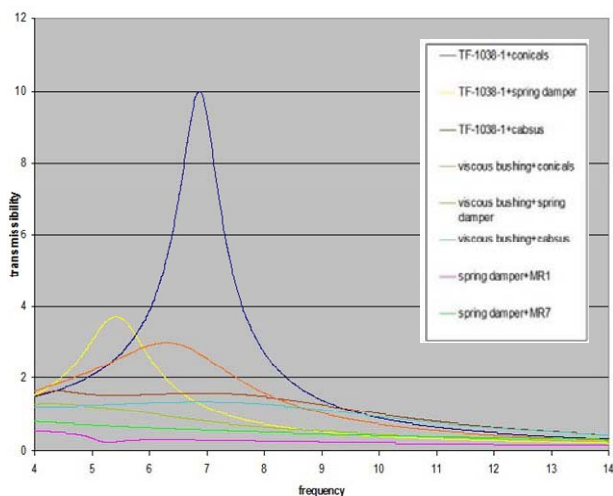
Figure 5: System performance results on test rig

Figure 5 compares the performance of various systems installed in a test rig. The MR based system insulates from vibrations in the entire low frequency range of interest. The two lower curves show the improvements of the MR adaptronic suspension vs. classical cab suspension systems. The implementation of the suspension system on heavy duty vehicles is underway and is detailed in different publications.

CONCLUSIONS

An adaptronic suspension system was developed to reduce or cancel acceleration in the detrimental WBV frequency below 20 Hz. This innovative integration of MR technology, air spring and dedicated control electronics is applicable to cabin suspension of large and heavy driver cabins in trucks, tractors or any heavy duty vehicles known to induce WBV. The MR based cab suspension offers a way to comply with the physical agents Directive (Vibration) 2002/44/EC, but mainly enables operators of heavy equipment to work under improved conditions of comfort, health and safety.

REFERENCES

1. Stayner, R. M., Whole-body vibration and shock: A literature review. Extension of a study of overtravel of seat suspensions, RMS Vibration Test Laboratory for the Health and Safety Executive (HSE Contract Research Report 333/2001), 2001
2. Guide to good practice on Whole-Body Vibration: Non-binding guide to good practice with a view to implementation of Directive 2002/44/EC on the minimum health and safety requirements regarding the exposure of workers to the risks arising from physical agents (vibrations) ISVR, HSL, BGIA, INRS, HSE. 2006
3. Dufner and Schick, John Deere Active Seat[TM]: a new level of seat performance. Proc. VDI Agritechnik Conference 'Agricultural Engineering for Environmental Protection', Martin Luther Universitat, Halle-Wirttenburg, Germany, 2002.
4. http://www.lord.com/tabid/3318/Default.aspx
5. Shutto, S. and Toscano, J. R., Magnetorheological Fluid and its Applications, Proc. The 6th JFPS International Symposium on Fluid Power TSUKUBA 2005, 2005, pp590-594
6. Alexandridis, A. (2006) The MagneRide System, Advanced Suspension Systems, IQPC, Frankfurt am Main

P2-01

STIFF ELECTROHYDRAULIC DRIVES
USING A HYBRID VALVE

Maxim REICHERT, Hubertus MURRENHOFF

Institute for Fluid Power Drives and Controls (IFAS)
RWTH Aachen University
Steinbachstrasse 53, 52074 Aachen, Germany
(E-mail: Maxim.Reichert@ifas.rwth-aachen.de)

ABSTRACT

One of the main problems of electrohydraulic drives is relatively low dynamic load stiffness due to compressibility of oil. Sudden load variations can cause significant deviations of the position of the drive and, consequently, a reduced precision of the controlled process. This has led to a partial substitution of electrohydraulic drives by electromechanical drives in a low power range recently.
One of the approaches to increase dynamic stiffness of a cylinder is to raise valve dynamics. Thus, the system can react to a control deviation and provide the cylinder with a compensating flow faster.
The objective of this paper is to show the development of a stiff cylinder drive using a new high-response servovalve - the hybrid valve. In contrast to a conventional servovalve with an unmovable sleeve, the idea of the hybrid valve is to actuate both the spool and the sleeve simultaneously in opposite directions. Using a piezo-actuator as sleeve drive provides the hybrid valve with very high dynamics in the range of small valve opening, which should be sufficient to increase the disturbance rejection of the cylinder. The performance of the valve prototype and of the cylinder will be shown, and application fields will be discussed in this work.

KEY WORDS

Cylinder Stiffness, Position Control, Servovalve, Hybrid Valve, Piezo-Actuator

INTRODUCTION

An electrohydraulic linear drive which is operated by a control valve and subjected to an external dynamic load deviates from its reference position until the load is balanced by the increased pressure in the counteractive cylinder chamber. The balancing pressure increases due to a compression of oil in the chamber on the one hand and compensating flow provided by the control valve on the other hand. The ratio of the external dynamic load and the deviation of the drive position due to this load is called dynamic load stiffness. The higher is the stiffness, the more precise control of the drive can be achieved in any manufacturing processes.

The dynamic load stiffness of the electrohydraulic linear drive depends on many factors. Some of them are oil compressibility (oil type, dissolved air in oil), dead volume between the drive and the control valve, drive leakage, friction, availability of accumulators, mechanical backlash between the drive and the driven object, strategy and sampling of the controller, resolution and dynamics of the sensors involved in the control loop as well as static and dynamic characteristics of the control valve [1]. The focus of this paper is the improvement of drive performance by use of a novel control valve – the hybrid valve.

CONCEPT AND DESIGN OF THE HYBRID VALVE

The idea of the hybrid valve is to actuate both the spool and the sleeve, whereas in conventional servovalves the sleeve is fixed. Due to a simultaneous actuation of both parts in opposite directions the control orifices can be opened and closed faster [2]. This enables the hybrid valve to provide the cylinder with a compensating flow faster and therefore to reduce the position deviation during dynamic load variation.

Figure 1 shows the concept of the hybrid valve. Here the spool is driven by a relatively slow conventional valve actuator known as a permanent magnet linear force motor with a large stroke (± 0.5 mm), whereas the sleeve is driven by a fast piezo-actuator with a short stroke (approx. 10% of linear force motor stroke).
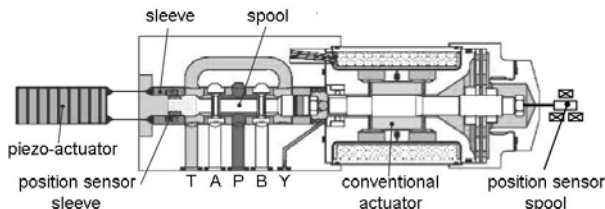
Figure 1 Hybrid valve concept

Spool and sleeve should both be driven in closed position control loops to compensate for the disturbances due to flow and friction forces. Therefore two position sensors should be integrated into the valve measuring spool and sleeve movements.

Besides excellent dynamics, the hybrid valve offers the advantage of high resolution for a small operating signal. Thus, 10% of the valve flow rate can be controlled with a piezo-actuator resolution which is limited by the command signal condition only.

The design of the hybrid valve is based on the modification of a conventional direct drive servovalve D636 by Moog [3] with a nominal flow rate of 37 l/min at a pressure drop of 70 bar over two control orifices.

The piezo-actuator is a low voltage, mechanically prestressed stack actuator (P-843.60) with an integrated position sensor by PI [4]. The position sensor is a Wheatstone bridge of strain gauges bonded to the piezo-ceramics. A membrane sealing has been designed to protect the actuator from oil as this type of piezo is hydrophobic.

The position sensor of the spool is a linear variable differential transformer (LVDT). In contrast to the original design of the valve the sensor has been attached to the armature of the linear force motor directly (s. Figure 1) in order to allow the mounting of the piezo-actuator.

The connection of the spool to the linear force motor remained unmodified as a form-locked join in the conventional valve. The connection of the sleeve to the piezo-actuator has been designed as a force-locked join. The sleeve is pushed by the piezo-actuator in one direction only and retracted by stiff plate springs. The force-locked join compensates possible misalignment of the actuator and the sleeve due to manufacturing inaccuracy.
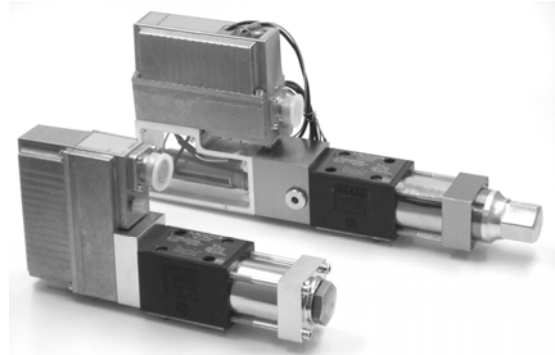
Figure 2 Conventional valve and hybrid valve prototype

Figure 2 shows the conventional valve in front and the hybrid valve prototype in the background. All parts of the prototype except for the original valve parts have been manufactured at IFAS.

PERFORMANCE OF THE HYBRID VALVE

In the following static and dynamic performance of the hybrid valve is shown. All the measurements were been carried out according to ISO 10770-1 [5] with a supply pressure of 140 bar.

Figure 3 presents pressure gain curves of the conventional valve and the hybrid valve. Due to a higher internal leakage of the hybrid valve its pressure gain curve has a slightly smaller slope in the region of hydraulic zero-point.
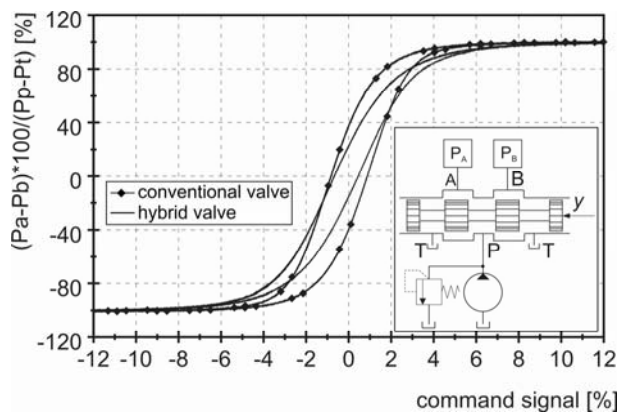

Figure 3 Pressure gain

In order to increase load stiffness of a drive the pressure gain of the valve should be as high as possible. The reduced pressure gain of the hybrid valve will be compensated by its high dynamics.

Figure 4 shows flow gain curves of the conventional valve and the hybrid valve at a constant pressure drop of 70 bar over two control orifices for a command signal of 10%. It can be seen that the slope of the curves is nearly the same in this region of the valve opening. However a smaller hysteresis of the hybrid valve due to an exact control of the piezo-actuator can be clearly recognized in the pressure and flow gain curves. In general the smaller is the hysteresis of a control valve, the higher is the precision of the pressure, velocity and position control of a drive [6].
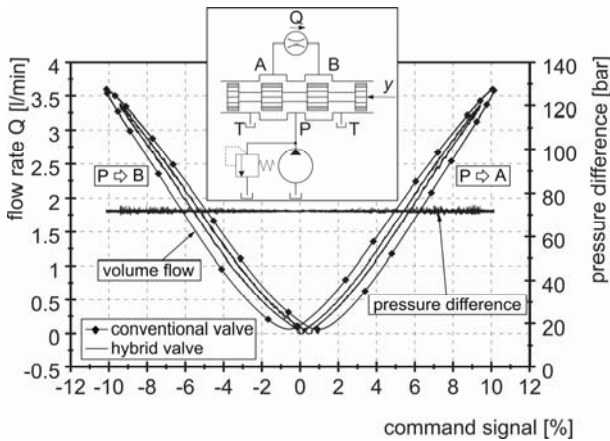
Figure 4 Flow gain

Step responses of both valve actuators are shown in Figure 5. The working ports A and B were blocked during the test. The response time of the piezo-actuator is 10 times faster than that of the linear force motor in the characteristic stroke ranges.
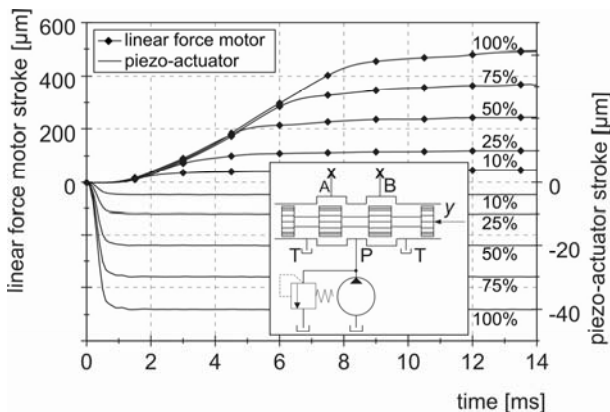
Figure 5 Step responses

Figure 6 and Figure 7 present frequency responses of hybrid valve actuators. Here a continuous sine sweep command signal from 10 Hz to 500 Hz has been applied at different levels. The signal level - 5% and 90% - refers to the nominal stroke amplitude of the actuators (±0.5 mm for linear force motor and ±40 µm for piezo-actuator).
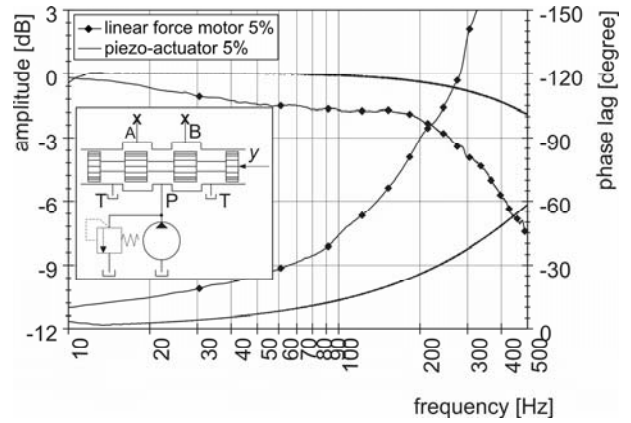
Figure 6 Frequency response of 5%
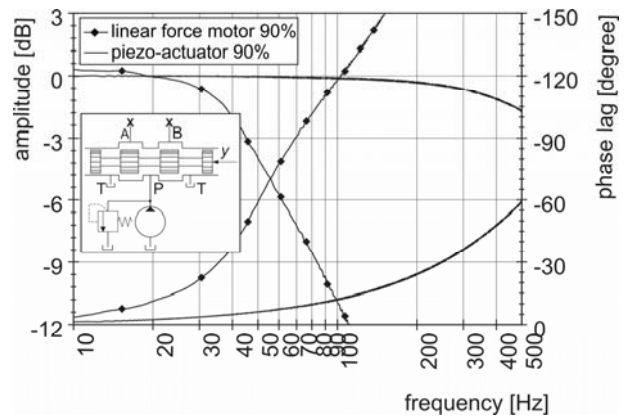
Figure 7 Frequency response of 90%

Whereas the frequency response of the linear force motor decreases with a rising signal level, the piezo-actuator shows nearly the same performance independently of signal level in this frequency range. The high dynamics of the sleeve actuation should raise the response of the valve and increase the load stiffness of the controlled drive.

DRIVE CONTROL STRATEGIES

In this section different position control strategies of an electrohydraulic linear drive are discussed.
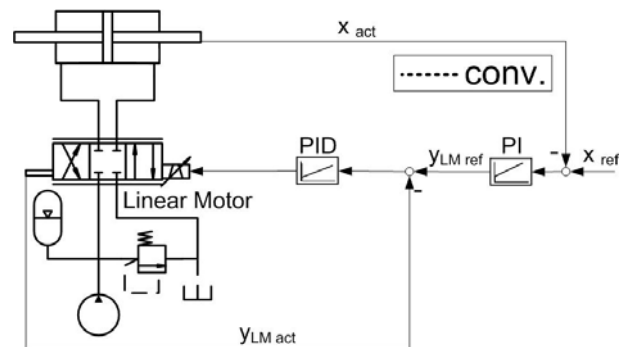
Figure 8 Conventional position control

A simple conventional position control circuit implies a main control loop with a position feedback of the cylinder and a subsidiary position control of a single valve actuator (i.e. linear force motor) (s. Figure 8). The reference signal of the linear force motor $y_{LM\ ref}$ is generated by a PI-controller.

As the hybrid valve has two actuators both of them should be integrated into the drive control loop. The first approach (s. Figure 9) is based on the compensation of a cylinder position error by the piezo-actuator directly. For this reason the reference signal of the piezo-actuator $y_{P\ ref}$ equals the reference signal of the linear force motor $y_{LM\ ref}$ with an opposite sign. There are also subsidiary position control loops of the both valve actuators. The position controller of the piezo-actuator has been implemented as a PI-controller and has been discussed in [7]. This approach is called here "HV cylind.".
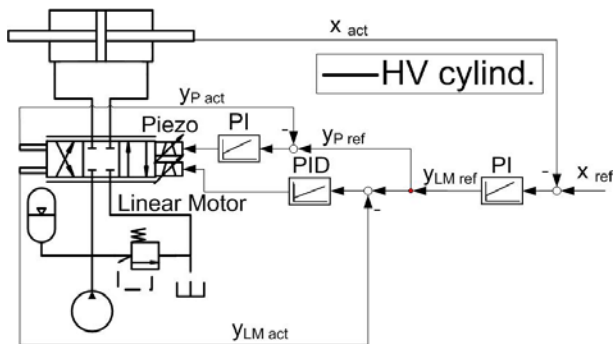
Figure 9 Position control with strategy "HV cylind."

The second approach (s. Figure 10) relies on the compensation of a linear motor position error by the piezo-actuator. Thus the piezo-actuator contributes to the position control of the drive indirectly. Here the reference signal of the piezo-actuator $y_{P\ ref}$ equals the position error of the linear motor ($y_{LM\ ref}$ - $y_{LM\ act}$). The name of this control strategy is "HV linmot.".
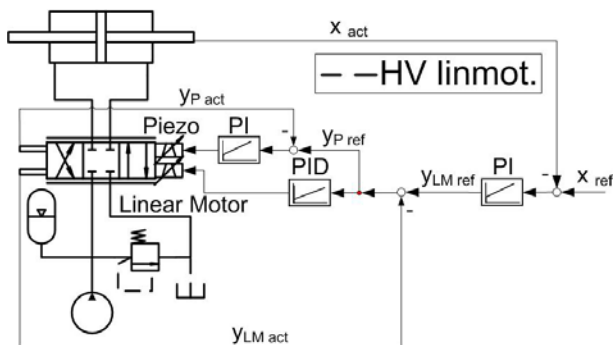
Figure 10 Position control with strategy "HV linmot."

The advantage of the approach "HV cylind." is the fact, that the piezo-actuator keeps the valve open until the cylinder position error is reduced to zero. This provides

the cylinder with a maximum velocity during the whole response time. In contrast to this the approach "HV linmot." brings the piezo-actuator to its zero-point very quickly after the position error of the linear force motor has been compensated. So the time of maximal valve opening in this case is shorter and the drive reaches the desired position later (s. Figure 12).

DRIVE PERFORMANCE

For the investigation of drive performance in terms of reference response and disturbance rejection a test rig (s. Figure 11) was built at IFAS. The cylinder at the bottom is a test cylinder which is investigated and can be controlled by the conventional valve or the hybrid valve. It is a low friction state-of-the-art cylinder with an annular gap sealing by Haenchen [8] for challenging control applications. The test cylinder has a stroke of ±25 mm and possesses an integrated position measurement system (LVDT). The control valve is mounted on the test cylinder directly. There are accumulators on the pressure supply line and tank line to reduce pressure variations in these lines near the drive.
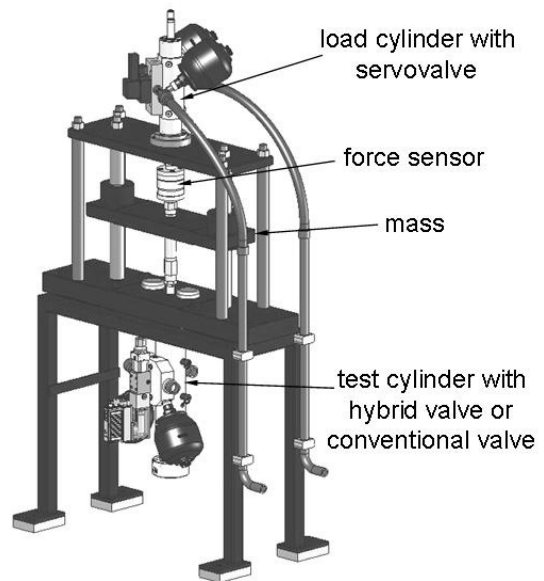

Figure 11 Test rig

The test cylinder is operated in a position control. The disturbance for the test cylinder can by applied by a load cylinder on the top of the test rig. The load cylinder is driven by a high response servovalve D769 by Moog [9] in a force control. The test rig offers a good flexibility in changing the load level and the time constant of the load change. Furthermore it is possible to attach an adjustable mass on the test cylinder and to vary its eigenfrequency. The control circuit has been implemented on a DS1103 PPC controller board by dSPACE [10] and operates at a sampling rate of 10 kHz.

Figure 12 shows the strokes of the valve actuators and the reference response of the test cylinder controlled by the conventional valve and by the hybrid valve with two different control strategies. Here a step reference signal X_{ref} has been applied to the unloaded test cylinder. It can be seen that the cylinder controlled by the hybrid valve with strategy "HV cylind." reaches the reference position faster. The stroke of the linear force motor and the piezo-actuator is approximately in the same range. The improvement of the response compared to the conventional system can be estimated to 30%. Due to the limitation of the piezo-actuator stroke this improvement reduces for higher steps of the reference signal.
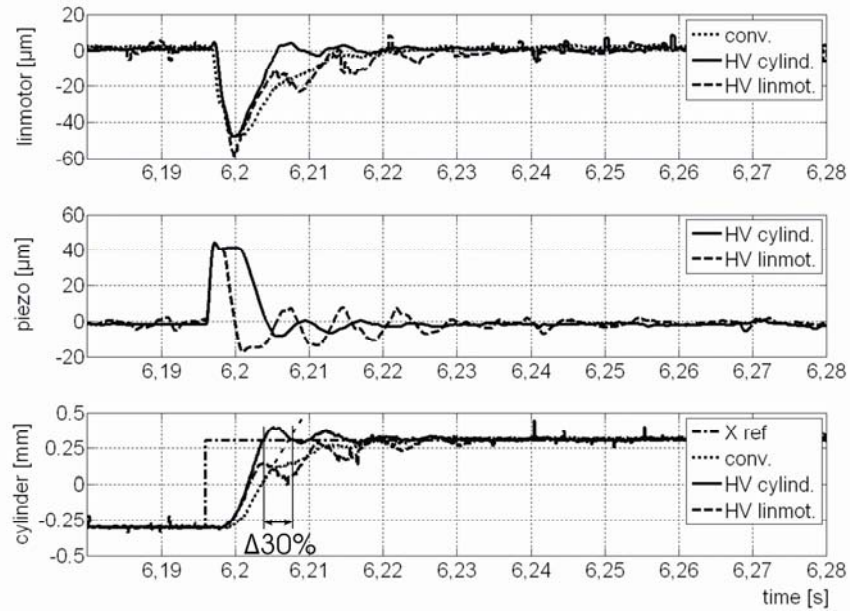
Figure 12 Reference response of the test cylinder

The disturbance rejection of the test cylinder is presented in Figure 13. Here a dynamic disturbance force of 10 kN, which is 90% of the maximum load force at the given supply pressure of 100 bar, has been applied on the test cylinder by the load cylinder. Two curves in the middle of the figure show the strokes of the valve actuators. The position deviation of the test cylinder is presented at the bottom of the figure. The deviation can be reduced by 26% when the test cylinder is controlled by the hybrid valve with a strategy "HV cylind.". Thus the dynamic load stiffness of the drive has been improved by 26%.
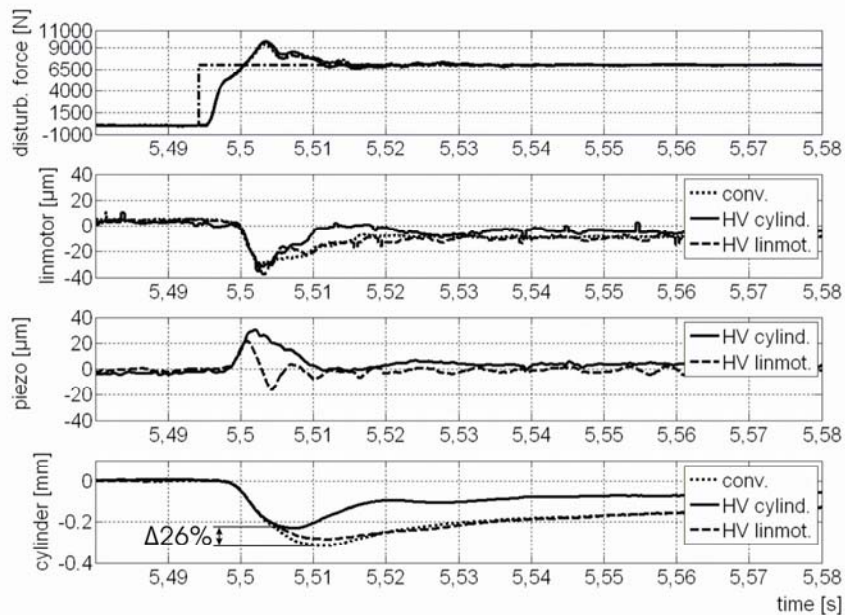
Figure 13 Disturbance rejection of the test cylinder

CONCLUSION AND PERSPECTIVES

Facing the problem of relatively low dynamic load stiffness of electrohydraulic drives the hybrid valve has been developed at IFAS. Its concept combines a conventional electromagnetic actuator and a piezoelectric actuator in an optimal way for direct drive valves. Whereas the relatively slow conventional actuator with a large stroke provides the drive with a good reference response, the fast piezo-actuator with a small stroke results in an outstanding disturbance rejection of the drive. The hybrid valve prototype shown in this paper possesses static characteristics comparable to a conventional valve and dynamic characteristics outmatching that of a state-of-the-art valve.

Even using just relatively simple control strategies with a position feedback of the drive a remarkable improvement in the drive performance has been achieved. The small signal reference response of the drive has been enhanced by 30% using the hybrid valve. However, this effect decreases for large signal reference responses. At the same time the disturbance rejection in terms of dynamic load stiffness of the drive was improved by 26%. This effect has no dependency on the load magnitude as the reaction of the valve to any disturbances of the drive is always in the range of very small valve openings.

The hybrid valve will be able to improve the position, velocity and force control of electrohydraulic drives in machine tools, mills, presses, injection molding machines and testing machines. Further research will focus on implementation of more sophisticated control strategies with a feedback of acceleration or load pressure alteration of the drive.

The development of the hybrid valve has shown that piezo technology can be successfully implemented in industrial hydraulic valves. This technology has already proved itself in the automobile industry, where piezo-actuators, similar to the one presented in this paper, have been used in fuel injectors since 2002. Taking into account falling costs of the piezo-actuators due to mass production for the automobile industry they become a very attractive alternative or supplement for hydraulic valve technology.

ACKNOWLEDGMENTS

REFERENCES

1. Murrenhoff, H., Servohydraulik - Geregelte hydraulische Antriebe, lecture notes, IFAS, Shaker Verlag, ISBN 978-3-8322-7067-4, Aachen, 2008.
2. Patent US2007079879, Highly Dynamic Valve Servocontrol Device, 04.12.2007.
3. http://www.moog.com/media/1/d636_d38seriesvalves.pdf.
4. http://www.physikinstrumente.com/en/pdf/P842_843_Datasheet.pdf.
5. International Standard ISO 10770-1:1998(E), Hydraulic fluid power – Electrically modulated hydraulic control valves – Part 1: Test methods for four-way directional flow control valves.
6. Götz, W., Haack, S., Mertlik, R., Elektrohydraulische Proportional- und Regelungssysteme, Robert Bosch GmbH, ISBN 3-933698-00-6, 1999.
7. Reichert, M., Murrenhoff, H., Increasing the Dynamic Load Stiffness of Electrohydraulic Linear Drives, 6th International Fluid Power Conference (IFK), Dresden, Germany, 2008, 2, pp. 145-157.
8. http://www.haenchen.de/2html_1/download/Prospekt_Ratio_en.pdf.
9. http://www.moog.com/Media/1/D769seriesvalves.pdf.
10. http://www.dspace.de/ww/en/inc/home/products/hw/singbord/ppcconbo.cfm?nv=bbp.

PROPORTIONAL VALVE WITH AXIAL FLOW AND ROTATIONAL METERING

Gabriele ANSALONI*, Pietro MARANI* and Roberto PAOLUZZI*

*IMAMOTER – Institute for Agricultural and Earthmoving Machines,
Italian National Research Council
28, via Canal Bianco, Ferrara, 44100, Italy
(E-mail: info@imamoter.cnr.it)

ABSTRACT

This paper presents a new concept hydraulic valve that tries to overcome a well-known poser affecting the pilot operated proportional valves, the flow forces. Despite of the traditional compensated profile spool valves, the basic idea is to design a valve that has as few mobile surfaces as possible. This assumption modifies the traditional valve design method and opens to new possibilities for the proportional valves. The solution presented in this paper uses an axial flow valve, where the oil gets through the valve across its axis, with two rotating surfaces causing a rotational metering. The result of this new design approach shows several advantages with respect to the common spool valves, such as the extremely compact size and the device versatility. This particular valve can realize the majority of the functions achievable using a two-way two-position proportional valve piloted by two pressure signals (for example a pressure compensated valve); the axial flow and the "built-in" metering edges yield the possibility to produce this valve as a cartridge component, whit all the advantages incidental to this type of devices.
Some Computational Fluid Dynamics Analysis confirm the prediction of a low affection of this valve by flow forces, this attitude makes the axial Flow and Rotational Metering Valve particularly suitable for the local compensation in Flow Sharing Load Sensing distributors.

KEY WORDS

Valve, Flow Forces, Metering, Axial Flow

NOMENCLATURE

A_{flow} : area upon which p_{flow} acts
$A_{flow,A}$: A_{flow} (ARM valve)
$A_{flow,s}$: A_{flow} (spool valve)
A_{pil} : area upon which the pilot pressures act
F_1, F_2 : force of the spring 3, 4 (spool valve)
F_{flow} : flow forces modulus
F' : T_{flow} reduced at R_{coil}
p_1, p_2 : pressure in volume 6, 5 (spool valve)
p_{err} : over-pressure due to flow forces
$p_{err,A}$: p_{err} (ARM valve)
$p_{err,s}$: p_{err} (spool valve)
p_{flow} : mean pressure recovery on spool walls
$p_{flow,A}$: p_{flow} (ARM valve)
$p_{flow,s}$: p_{flow} (spool valve)
p_{LS} : Load Sensing line pressure
p_{m1} : pressure upstream the local compensator
p_{v1} : pressure downstream the local compensator
R_{coil} : mean radius of the coil grooves (ARM valve)
R_{flow} : maximum distance between the valve axis and $A_{flow,A}$
T_{flow} : flow torque (ARM valve)
x : spool stroke (spool valve)
x_r : reducer stroke (ARM valve)
α : coil angle (ARM valve)
ϕ : rotor angular stroke (ARM valve)

INTRODUCTION

The majority of the power control systems can be represented as a block of devices which meter the area connecting two volumes; this devices are variable orifices and can be piloted in several ways such as: manual, pilot-pressure operated, electro-actuated and so on. Whatever the piloting method used, the final configuration of the device is affected by some "secondary effects" caused by the nature of the device itself. One of these secondary effects is that caused by flow forces.

This paper recalls the nature of the flow forces, some well-known method to reduce their impact on the device behavior and a new way to overcome the problem.

A new concept valve will be presented with an extremely low flow forces effect and a brand new axial flow design, some CFD Analysis will show how much this solution is effective in reducing the "over-compensation" of a two-way pilot operated valve .

Finally, some positive secondary aspects will be shown, such as the extreme flexibility of the device, that ensures a reduction of the production costs by the realization of multiple configurations using the same set of components.

THE NATURE OF THE FLOW FORCES

The flow forces

Neglecting the contribution due to changes in flow rate [1], flow forces can be considered a "static" phenomena that occurs every time a fluid is forced to pass through a restriction; due to the continuity equation, whenever a fluid passes through a striction it must increase its velocity, but its total energy is tends to remain constant, neglecting piezometric contribution, the total energy is given by the sum of the kinetic and the hydrostatic part.

The fluid must increase its velocity near the striction, and therefore it must convert some of its hydrostatic energy into the kinetic; this means that near a restriction the fluid accelerates and its static pressure decreases, generating a "local pressure loss". On the other hand, once crossed the striction, the fluid decreases its velocity re-converting the kinetic energetic part into the hydrostatic one, generating a "local pressure recovery".

This phenomena does not cause problems or disturbs hydraulic devices themselves, but is the first cause of the Flow Forces; the local pressure losses or recoveries cause forces when they occur near a surface. If the surface on which the pressure losses and recoveries act is a fixed surface, it doesn't occur cause major troubles, and the behavior of the devices is not affected. But if it occurs on mobile surfaces, which can move along the same direction where the pilot pressure works, their force and the pilot force will sum in ruling the configuration of the device.
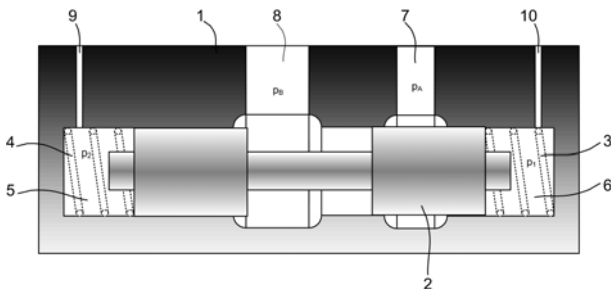
Figure 1 Usual 2 way 2 pilot valve

Let us consider a common spool valve, which has the task to meter the flow area between two volumes (A and B) in function of two pressure signals (p_1 and p_2) and the force of two springs (F_1 and F_2). Referring to Figure 1, this valve is made up by a body (1) with two port (7) and (8) communicating with the volumes A (at pressure p_A) and B (at pressure p_B) respectively. The ports (9) and (10) connect the pilot chambers (5) and (6) with their respective pilot intake (at pressure p_2 and p_1, respectively); the springs (4) and (5) complete the device logic providing the forces F_2 an F_1 respectively.

Linking the volumes (5) and (6) with several pressure intake it is possible to create the majority of the working logic in metering the flow area between two volumes.

The flow area is ruled by the axial position of the spool, and the axial position of the spool is determined by the equilibrium of the forces acting on the spool itself. To understand the relevance of the Flow Forces, an estimate of the spool equilibrium is advisable.

Let's suppose that p_A is greater than p_B and the purpose of this valve is to meter the flow area between volume A and volume B in function of the pressures p_1 and p_2.

At the beginning ($p_1 = p_2$) the spool in the position represented in Figure 1, and upstream the spool the pressure is p_A, while downstream the metering edge the pressure is p_B (even between the spool walls). Increasing p_2 the spool moves right, opening the flow area between A and B; pretending that the flow forces don't exist, the equilibrium equation of the spool is given by Eq. (1):

$$p_1 \cdot A_{pil} + F_1(x) = p_2 \cdot A_{pil} + F_2(x) \qquad (1)$$

Where A_{pil} is the area on which the pilot pressures works (supposed equal on both sides); as it can be seen in Eq. 1, the spool position x is given only by the pressures p_1 and p_2 and the two springs.

If we look more accurately, it is easy to recognize the striction through which the fluid must pass to reach volume B starting from A. The fluid must accelerate near the striction (right wall of the spool) causing a local pressure loss, and it must decrease its velocity near the left wall of the spool, generating a local pressure recovery.

Both the pressure loss and recovery throw off balance the spool with an axial force directed from right to left that tries to close the connection between volume A and B; the correct spool equilibrium equation is given in Eq. 2):

$$p_1 \cdot A_{pil} + F_1(x) + F_{flow} = p_2 \cdot A_{pil} + F_2(x) \quad (2)$$

F_{flow} is function of a large number of parameters [2] [3] such as the flow area, the shape of the area, the jet angle, the pressure gradient, the flow rate and so on; it's very easy to understand that due to the flow forces the spool position is function of several undesired factors that

affect the device logic.

The usual countermeasure is the inlet/outlet profile compensation; adopting this design method we can reach two advantages, first of all it is possible to reduce the momentum variation of the fluid (under-acting the local pressure losses and recoveries), secondary the local pressure variation can be dispatched near a fix wall, cancelling their effect. Unfortunately, the non-linearity of the local pressure variation phenomena makes this approach effective in some device configuration and totally ineffective in others.

Getting rid of flow forces

To show a new way to reduce Flow Forces modulus, it's helpful to express F_{flow} as the ratio between a "mean pressure recovery on spool walls" and the area on which this recovery acts (normalized with respect to the spool displacement), $F_{flow} = p_{flow} * A_{flow}$; the reduction of F_{flow} can be reached by the reduction of its factors.

The first action is to minimize p_{flow} (the mean pressure variation) reducing the fluid momentum variation. This approach implies the minimization of changes in direction of the fluid streamlines in passing through the valve. A spool valve constraints the fluid to perform two variations of direction (from radial to axial and then from axial to radial). The elimination of the direction variation of the fluid velocity suggests the adoption of a valve that makes the fluid to pass through without changing its direction, such as a purely axial flow valve. The increase and the decrease of the fluid velocity across the striction is not removable (until the continuity equation holds), so it's expected that p_{flow} will not drop to zero.

To explain exactly which actions can be undertaken to minimize A_{flow}, it is necessary to focus on A_{flow} definition. The pressure losses and recovery are dangerous when they're near a surface, but this surface must be able to generate a non zero work along the permitted displacement of the device. More precisely, referring to Figure 1, a pressure local variation can be near three type of walls:

- A fixed surface (such as a body wall), in this case the pressure variation doesn't work, because the wall doesn't move
- A cylindrical spool surface (such as the lateral spool surfaces), in this case the pressure variation doesn't work, because the surfaces are always orthogonal whit respect of the permitted displacement
- A plane spool surfaces (such as the vertical spool surfaces), in this case the pressure variation works, because the force generated by itself is directed as the permitted movement.

Reducing A_{flow} means lowering the size of the areas on which the pressure variations act, but means also skewing that surfaces with respect to the displacement direction. Common spool valve sizes are more or less proportional to the maximum flow rate allowed, this

means that trying to reduce A_{flow} in common spool valves is a drudgery; the minimization of A_{flow} is constrained by the need of an edge made up by mobile surface whose sizes are approximately equal to the base of a cylinder housing the spool.

One possible way to minimize A_{flow} is to use edges that move orthogonally with respect to the piloting devices (diaphragms, or rotational meterings) .
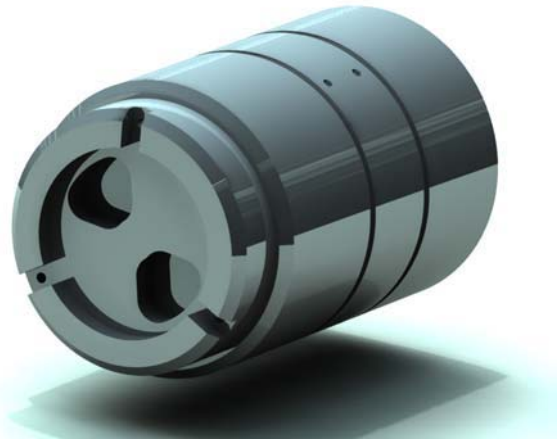

Figure 2 The ARM valve

THE PROPORTIONAL VALVE WITH AXIAL FLOW AND ROTATIONAL METERING

Trying to design a low-flow-forces valve, a new valve was conceived, named Proportional Valve with Axial Flow and Rotational Metering (ARM), and patented as Patent IT TO2007A000518 [4]. This valve almost insensitive to flow forces and allows an axial fluid flow. This latter aspect makes the component particularly suited for cartridge design.

The basic idea is to meter the pass through regulating two areas. The size of these areas is ruled by the relative rotation between two components (a *stator* and a *rotor*) shaped in order to commute from the "fully closed" position to the "fully open" through a relative rotation of a given angle φ. Pilot pressures and possibly springs act on an element called *reducer*. Its position rules the angular displacement between the stator and the rotor.

The ARM valve as a local compensator

Similarly to the common spool valves, the ARM valve can realize a large number of logical operations according as the arrangement of the pilot pressure intakes. For the sake of understanding, suppose that the ARM valve is used as a pressure compensating valve in a Load Sensing Flow Sharing System (LSFS).

Referring to Figure 3, the task of this valve is to keep the pressure in p_{m1} at the Load Sensing value p_{LS}. The volume p_{m1} is connected directly to the supply port of the pump (supposed to be an LS compensated pump), from p_{m1}, the fluid passes through the compensator in

order to decrease the pressure, until it reaches the section load pressure. In order to perform this operation, the compensator meters the passing area until the pressure p_{m1} is kept equal to p_{LS}. Moreover, if p_{m1} is the highest pressure among all the sections, the shuttle valve S opens and the LS line reaches the pressure p_{m1}.

To perform this specific task, the ARM valve is made up by seven elements. Referring to Figure 4, these elements are: the stator (or the cartridge) (1), the rotor (2), a blocking bolt (3), the reducer (4), two spacers (5) and (6) and a spring (7).
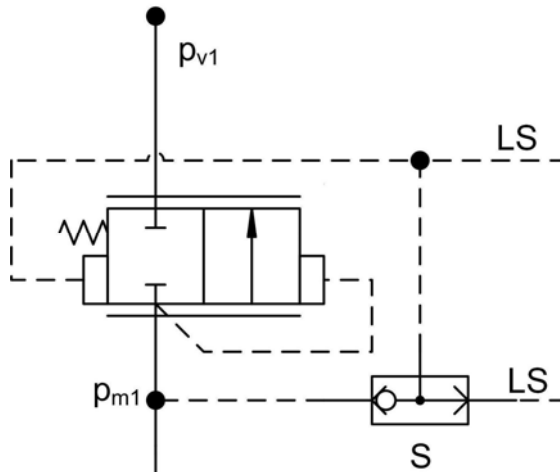
Figure 3 An LSFS local compensator hydraulic scheme

The cartridge (1) has a tubular shape, with a closed base in which two holes are shaped, in order to control a controlled area through which the fluid flows. Three straight grooves are machined inside the cylindrical surface of the cartridge allowing the stator to engage with the reducer (4), creating a prismatic coupling. Some holes are drilled both on the base and on the skin of the cartridge, so that the upstream pressure p_{m1} and the LS pressure p_{LS} can reach their chambers (the volumes from which the holes take the pressure signals are not represented, because they are obtained in the body of the valve housing the ARM). The ARM valve can integrate the function of the shuttle valve, in fact it can select the pressure signal of the highest load and send it on the LS line. This feature is obtained by means of three more holes drilled on the skin of the cartridge connecting the p_{m1} signal chamber to the LS when p_{m1} is higher than p_{LS}.

The rotor (2) is cylindrical as well. It has a closed base where two holes are located, in order to control a controlled area through which the fluid flows. These holes are made so as to meter (together with those on the cartridge) the passing area. The rotor is shaped to enter totally inside the cartridge. Three coil grooves are machined on the external skin of the rotor, thus allowing the rotor and the reducer to engage to each other. Holes and grooves are positioned so as to be in the "fully

closed" configuration when the reducer is at its maximum displacement on the upstream side.

The blocking bolt (3) constrains the rotor to be fixed with respect to the cartridge along its axis, but permits the relative rotation of the two elements.

The reducer (4) is a flat ring that couples the cartridge and the rotor. Since the reducer is positioned between the stator and the rotor, it separates the volumes between the two elements into two chambers where it is possible to bring the two desired pressure signals.

The particular coupling choice of this device ensures that an axial translation of the reducer (with respect to the cartridge) causes an axial rotation of the rotor (with respect to the cartridge as well).

The axial position of the reducer univocally set the angular position of the rotor and, thereby, the metering of the valve. The axial position of the rotor is a function of the two pressures in the pilot chambers and of the spring force.
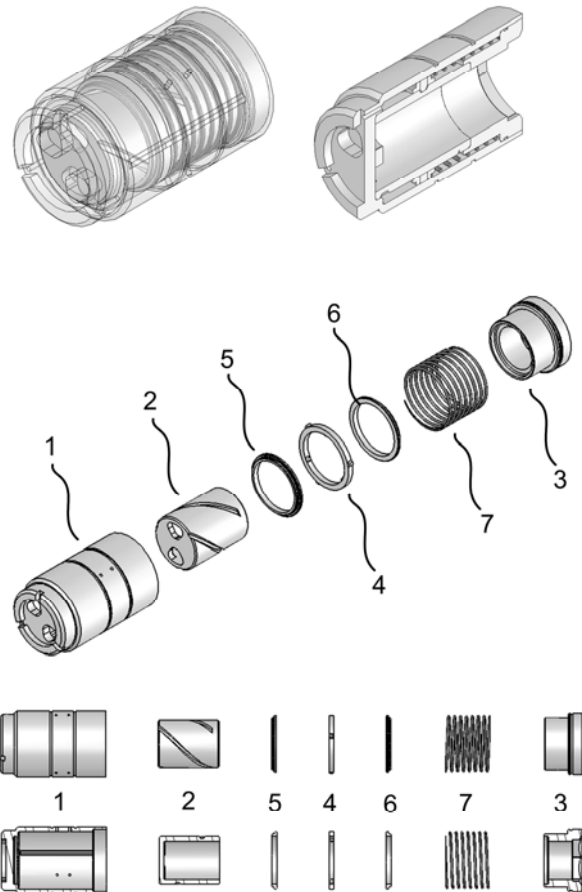

Figure 4 The ARM valve arranged as an LSFS local compensator

The spacers (5) and (6) work as end-stops for the reducer axial displacement and the spring (7) places the reducer against the upstream end-stop, so as to place the

ARM valve in "fully closed" configuration when all pressures are zero (requested feature in local compensator for LSFS valves).

ARM local compensator action

The ARM valve, arranged as previously described and positioned downstream a metering edge, can perform the same identical function of a traditional spool-based local compensator, integrating the selection of the maximum pressure signal (shuttle valve S in Figure 3).

When the section is not activated, the ARM valve is in the "fully closed" configuration (the spring pretension applies a very small threshold pressure). The upstream pilot chamber is subject to the upstream pressure p_{m1}, whilst the downstream chamber is at the LS pressure p_{LS} (the pressure of the highest load of all the active sections). When the section is active, the supply flow finds a closed port (ARM "fully closed"), and then the pressure p_{m1} starts rising. As soon as p_{m1} exceeds p_{LS} the reducer moves backwards (towards the downstream of the valve).

The more the reducer moves towards, the more the rotor rotates. In fact, named α the coil angle, if the reducer moves backwards a stroke x_r, the rotor covers an angle ϕ given by Eq 3:

$$\phi = \frac{x_r}{\tan(\alpha)} \frac{1}{R_{coil}} \qquad (3)$$

The pressure upstream the valve works to gradually line up the holes of the cartridge and of the rotor (opening the valve). The ARM enters its metering condition, and $p_{m1} = p_{LS}$ (neglecting the spring and the flow forces). If p_{m1} is the highest pressure among all sections, p_{LS} can't counterbalance it, therefore the reducer moves totally backwards reaching the downstream end-stop. In this position there is an open link between the upstream pilot chamber and the LS line, inducing $p_{LS} = p_{m1}$.

Further lowering of flow forces

We had already described the straightforward approach to reduce flow forces sensitivity of the valves, namely an action on the mean pressure local variation p_{flow} and the area on which it acts A_{flow}. At this point, since the principles of the ARM valve are known, it is possible to show how this device can reduce further the flow forces sensitivity by a smart kinematic chain that makes flow forces "work badly".

The regulation error introduced by the flow forces can be expressed by the pressure $p_{err} = F_{flow} / A_{pil}$. p_{err} is the pressure that unbalances the system adding itself to the pilot pressure that moves the devices towards the "fully closed" direction. So p_{err} is a significant error indicator that considers the flow forces modulus, but also how them works on the device. Using p_{err}, instead of the usual F_{flow}, we can consider not only the influence of the valve shape on the regulation error, but also the influence of the piloting device of the valve.

In case of a common spool valve $F_{flow} = p_{flow} * A_{flow}$, so

$p_{err,s}$ value is given by Eq. 4:

$$p_{err,s} = (p_{flow,s} A_{flow,s}) / A_{pil,s} \qquad (4)$$

In the ARM valve, some additional considerations must be applied:

- $p_{flow,A}$ acts on walls that rotate, instead of translating
- $p_{flow,A}$, supposed constant, working on A_{flow} causes an axial torque $T_{flow} = p_{flow,A} * A_{flow,A} * (R_{flow} / 2)$, where $(R_{flow} /2)$ is the mean radius on which p_{flow} acts
- named R_{coil} the radius of the coil of the rotor $(R_{coil} > R_{flow})$, the torque T_{flow} is countervailed by a tangential force $F' = T_{flow} / R_{coil}$
- named α the coil angle, the axial force needed to generate a tangential force equal to F' is F_{flow} and its value is $F_{flow} = F' * \tan(\pi/2-\alpha)$

As a consequence, in case of ARM valve, $p_{err,A}$ is given by Eq. 5:

$$p_{err,A} = \left(\frac{p_{flow,A} A_{flow,A} (R_{flow} / 2)}{R_{coil}} \right) \frac{\tan(\frac{\pi}{2} - \alpha)}{A_{pil,A}} \qquad (5)$$

For the sake of comparison between a spool valve and the ARM valve, some hypothesis on the ARM performances must be introduced:

- $R_{coil} = R_{flow}$
- $A_{flow} = 0.6 * A_{pil}$ for both valves
- $\alpha = 45°$, so $\tan(\pi/2-\alpha)=1$
- $p_{flow, s} = p_{flow, A}$

Using these assumption $p_{err,s} = 2 * p_{err,A}$. More realistic hypothesis are: $R_{coil} = 1.3 * R_{flow}$, $A_{flow,A} = 0.2 * A_{pil,A}$, $\alpha = 45°$, $p_{flow, s} = 8 * p_{flow, A}$, these new assumptions show that a common spool compensator is up to ten times more sensitive to flow forces than an ARM valve.

CFD ANALYSIS

A preliminary numerical analysis campaign was performed in order to verify the performance of the ARM valve. It focused on the flow forces and the metering characteristic of the new valve. The analysis shows that the ARM valve is scarcely affected by the flow forces, due to its particular rotating metering edges and its kinematic chain, that dramatically decreases the force that countervail the valve pilot pressure.

The following example allows the reader to benchmark a common spool valve with respect to the ARM valve. In this case the boundary conditions are the upstream and downstream pressures ($p_{m1} = 300$ bar, $p_{v1} = 100$ bar) and the pressure gap is 200 bar. Figure 5 is shows the

pressure contour over the only surfaces that can perform a non-zero work on the pilot system. Some local pressure drops (about 50 to 100 bar) are on these surfaces (blue colored), but it is easy to notice that these zones are very small, inducing a small torque T_{flow} of 0.14 Nm that, thanks to the kinematic coupling, causes only 0.5 bar p_{err}.
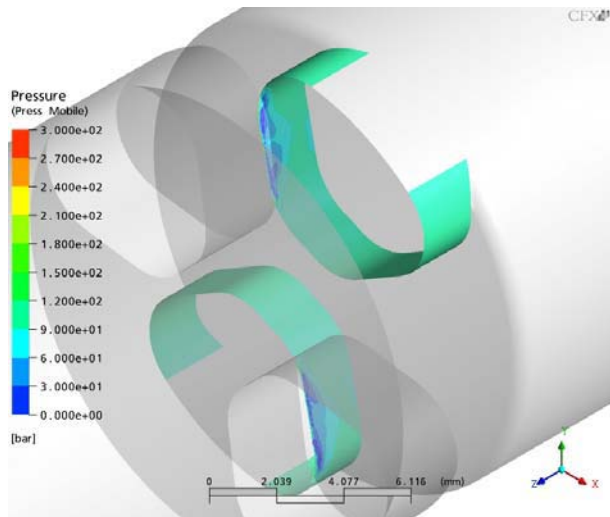

Figure 5 Contour plot of pressures on the ARM valve

Figure 6 shows the results of a spool compensator valve studied in the same boundary conditions (p_{m1} = 300 bar, p_{v1} = 100 bar). It is easy to notice that there are wider pressure recoveries on the mobile surfaces of the spool (red to green colored). These pressure recoveries generate a F_{flow} about 110 N, that means (in the specific case) a p_{err} close to 5 bar.

FURTHER ASPECTS

ARM valve features additional interesting characteristics both on functionality and machining.

It has an extremely compact design (axial dimension about 50 mm, radial dimension 25 mm, with nominal flow of 85 l/min and nominal pressure drop of 3 bar) including all inside components, making the design specially suitable for cartridge valves. The overall dimensions are comparable to those of a fitting and can be integrated in a valve port or hose fitting with almost negligible impact on block size.

Valve dimension allow a very fast reaction. The moving part weights few grams, compared to the usual 50-200 g of conventional spools. This feature keeps inertia effect to a minimum.

The fast action makes the proposed valve suitable also for critical applications where fast reaction is needed.

As to the production features, ARM valve can be easily configured to perform a large part of the conceivable control logic functions usually performed by 2-way valves using the same set of base components. A complete series of valves can be produced from a limited set of common components. For instance, using the same components, two valves with opposite pilot pressure logic can be produced, simply modifying the mounting. This achievement is not trivial, since in traditional valves the exchange of pilot pressure logic forces modifications on valve housing, with additional production costs.

Different functions can be performed simply varying position and number of drilled holes or using different spacers. All results can be achieved with negligible additional costs.

Preliminary numerical investigations, both CFD and dynamic, confirmed the positive advances that the component makes possible. Physical prototype production is being undertaken and will trigger an experimental functional qualification.
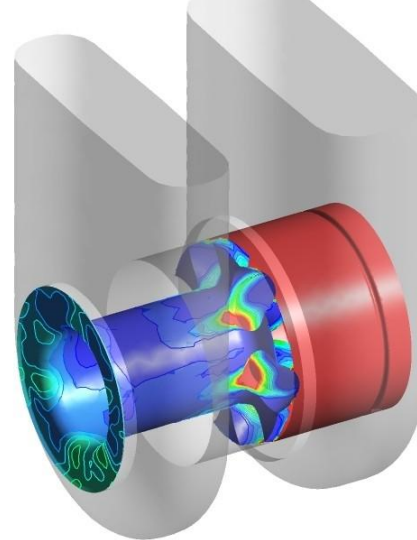
Figure 6 Contour plot of pressures on a spool compensator

REFERENCES

1. Borghi, M., Milani, M., Paoluzzi, R., "Tansient flow force estimation on the pilot stage of an hydraulic valve", Fluid Power Systems and Technology 1998
2. Merritt, H.E., "Hydraulic Control Systems", John Wiley and Sons, 1967
3. Blackburn, J.F., Reethof, G., Sharer, J., "Fluid Power Control", Technology Press of M.I.T and John Wiley and Sons, 1960
4. Ansaloni, G., Paoluzzi, R., Patent IT TO2007A000518, July 2007

P2-03

DYNAMIC CHARACTERISTICS OF PARALLEL LINK MECHANISM WITH SIX DEGREES OF FREEDOM USING ELECTRO-HYDRAULIC SERVO CYLINDERS

Yuuki MIYAMOTO, Masataka KUSAKABE, Katsuya ABE,
Kengo TSUCHIYA, Katsumasa SUZUKI , Sanroku SATO

Department of Mechanical Systems Engineering,
Musashi Institute of Technology
1-28-1 Tamazutsumi Setagaya Tokyo 158-8557 Japan
E-mail: ksuzuki@sc.musashi-tech.ac.jp, Fax: +81-3-5707-1151

ABSTRACT

The Stewart platform type parallel link mechanism with 6 degrees of freedom is a structure which has arranged six single rod hydraulic cylinders parallel between the base platform and the end effecter of the controlled object. The both ends of each link are connected with the base platform and the end effecter using free joints, respectively. The terminal can rotate freely. By controlling the length of each link by the hydraulic cylinder, the position and posture of the end effecter is controlled with 6 degrees of freedom in three-dimensional space.

In this report, the dynamic characteristics between the input and output of one link that comprises the parallel link mechanism is measured. The frequency response is measured for the various center position or attitude of the end effecter. The load mass and the amplitude are also changed.

The interference that each link receives from one link is examined by experiment. The frequency response of the interference that each link received is presented.

KEY WORDS

Parallel Link, Six Degrees of Freedom, Electro-Hydraulic Servo Cylinder

NOMENCLATURE

A: amplitude
C: end effecter center of gravity
L_m: length of link $_m$
M: load mass of end effecter
P_{s1}: supply pressure to cylinder in push side
P_{s2}: supply pressure to servo valve
x, y, z: coordinate of C
$\hat{}$: deviation of variable

INTRODUCTION

The Stewart platform type parallel link mechanism with 6 degrees of freedom is a structure which has arranged six single rod hydraulic cylinders parallel between the base platform and the end effecter of the controlled object as shown by Figure 1 and Photo 1 [1],[2],[3]. The both ends of each link are connected with the base platform and the end effecter using free joints, respectively. The terminal can rotate freely. By controlling the length of each link by the hydraulic cylinder, the position and posture of the end effecter is

controlled with 6 degrees of freedom in three-dimensional space. The parallel link mechanism has high rigidity and high output compared with a serial link mechanism. Since the error is not accumulated, highly precise positioning can be performed. It is widely used for a vibration test machine of many degrees of freedom, a driving simulator for a car, and a flight simulator for an airplane, etc.

In this report, the dynamic characteristics between the input and output of one link that comprises a parallel link mechanism are measured. The frequency

response is measured for the various center position or attitude of the end effecter. The load mass and the amplitude are also changed.

The parallel link mechanism comprises so-called interaction system, where the movement of one link influences those of other links through the end effecter. The interference that each link received from one link is examined by experiment. The frequency response of the interference that each link receives is presented.
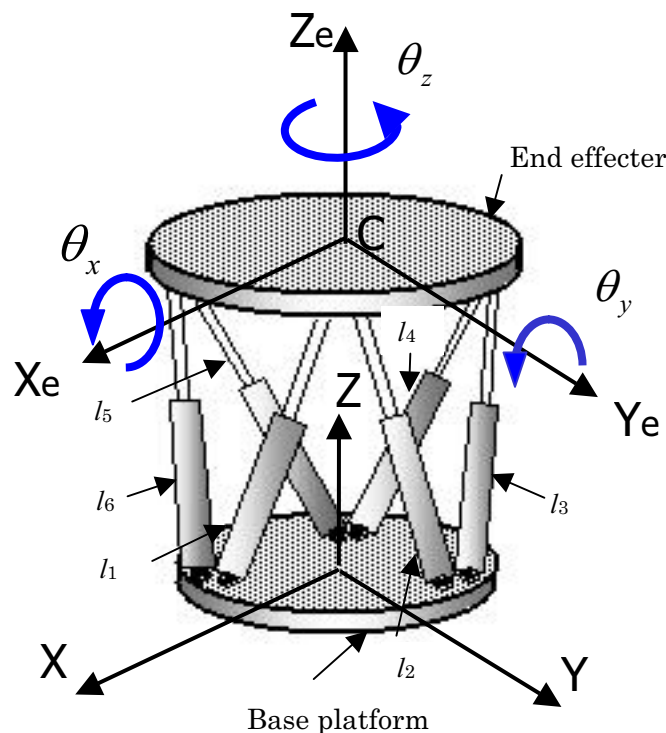
Figure 1 Parallel link mechanism with six degrees of freedom and coordinate system

EXPERIMENTAL DEVICE

A structure of the experimental device is shown by Figure 2.

The desired position and posture of the point C on the end effecter are inputted into PC. The desired length of each cylinder is computed from them with inverse kinematics calculation. The center position of operation is made $(x, y, z) = (0, 0, 0)$. Each link length at this time is all $l_i = 327$ mm equally. The desired signal is outputted to the servo amplifier from PC. The cylinder pressure of the push side, P_{s1} is constant. The cylinder expands and contracts with adjusting the pull side pressure by the servo valve. The cylinder (link) length

is measured by a potentiometer and sent to the servo valve as a feedback signal. The signal is also sent to PC and recorded. The control method is P control.

The gain margin is 10 dB. The supply pressure to the servo valve, P_{s2} is 7.3MPa. The supply pressure to the push side cylinder, P_{s1} is 2.1MPa. The sampling time is 10 ms.
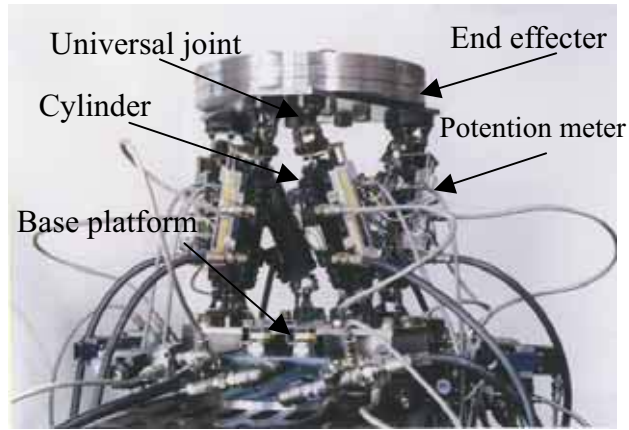
Photo1 Experimental device
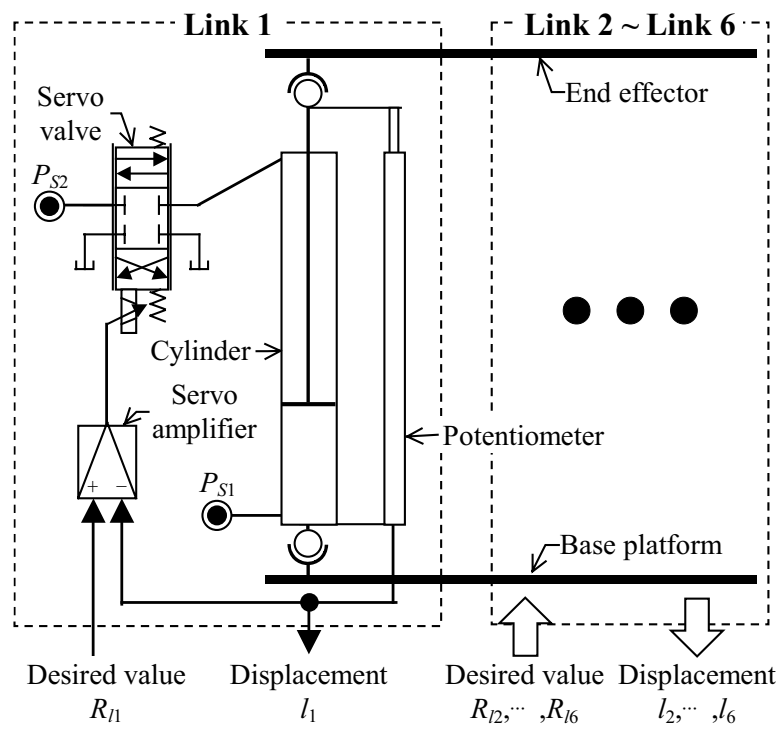
Figure 2 Structure of experimental device
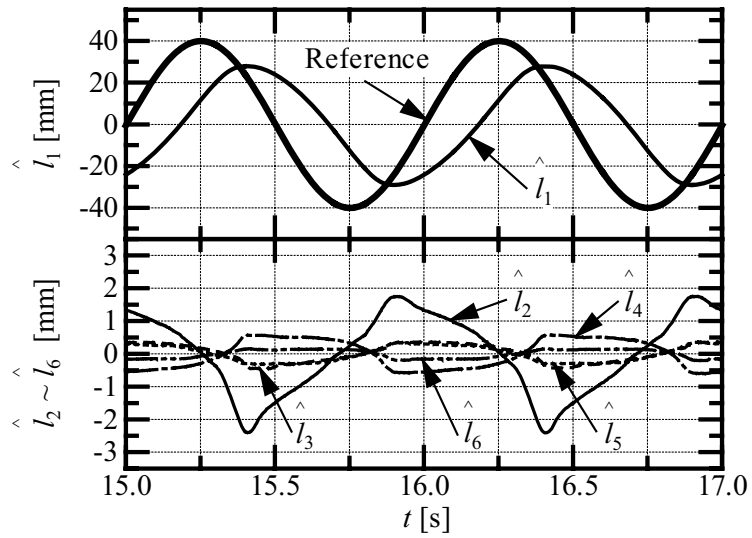
Figure 3 Time response of each link when sinusoidal wave signal is inputted to link1

Table 1 Parameter values

Cross-sectional area of cylinder in push side	A_1=3.14x10^{-4}m^2
Cross-sectional area of cylinder in pull side	A_2=1.37x10^{-4}m^2
Minimum link length	L_{min} = 0.282 m
Maximum link length	L_{max} = 0.377m
Load mass	M = 0, 20, 40, 60 kg
Supply pressure to cylinder in push side	P_{s1} = 2.1 MPa
Supply pressure to servo valve	P_{s2} = 7.3 MPa

Experimental Result
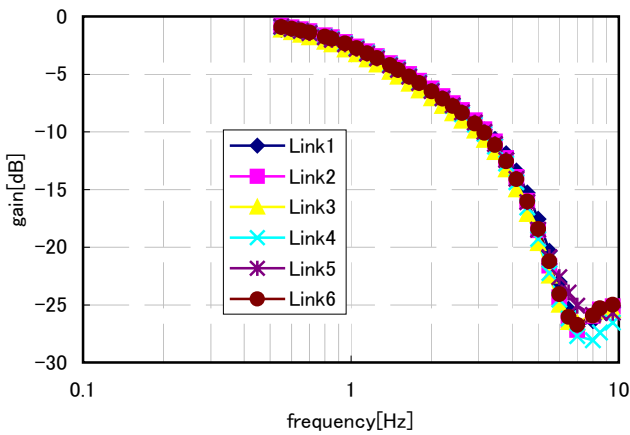
Figure 4 Differences among frequency responses of each link
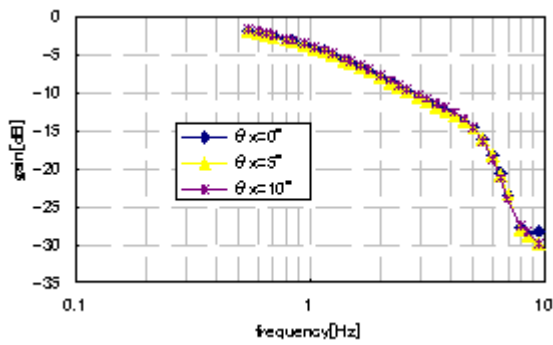
Figure 5 Effect of inclination

Figure 3 shows wave form when the desired value of 1Hz sine wave is inputted into link 1, and the movement of each link is shown. The desired values of the other links are constant (stop signal).

Difference among frequency response of each link

The difference among the characteristics in the drive system of each link was tested. Inputting the desired value of sine wave into one link, and constant value (stop signal) into other links, the frequency response of each link was measured. It turns out that each link has the almost same frequency response characteristics.

Effect of inclination

Inclination was given to the end effecter and the frequency response of link 1 was measured. It turns out that there is almost no difference in frequency responses between $\theta_x = 0$ and 10 degrees.
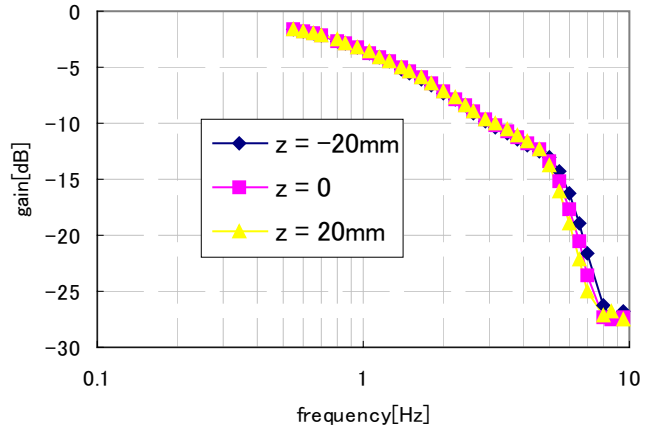
Figure 6 Effect of level z
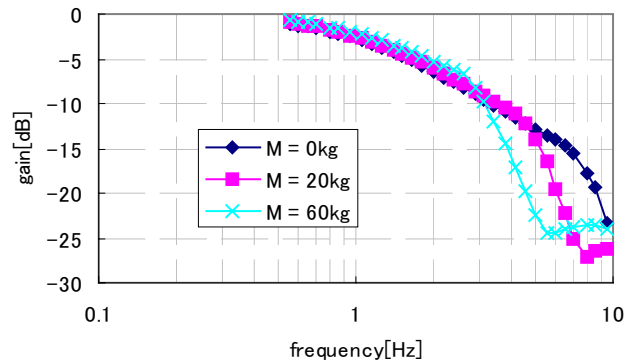
Figure 7 Effect of load mass M

Effect of level

The center position of the end effecter oscillation was moved in vertical direction, and the frequency response of link1 was measured. Some difference appeared with the position.

601

Effect of load mass

The frequency responses were measured for various load mass. When mass is large, the gain fall is large at the frequency more than 3 Hz.

Effect of amplitude

The influence of the amplitude of reference signal was examined. The gain fall is remarkable on the frequency more than 3 Hz, when the amplitude is large.

Interference to each link from link1

When the desired value is inputted into one link, the other links are moved by interference as shown in Figure 3.

When the desired value of the sine wave was inputted into link 1, and constant values (stop signal) were inputted into the other links, the vibration of each link was measured.

The Bode diagram is shown in Figure9 by calculating the ratio of the amplitude of each link to the amplitude of link 1. On low frequency, there is little interference. When frequency becomes high, interference becomes large. Especially the interference to link 2 is large.
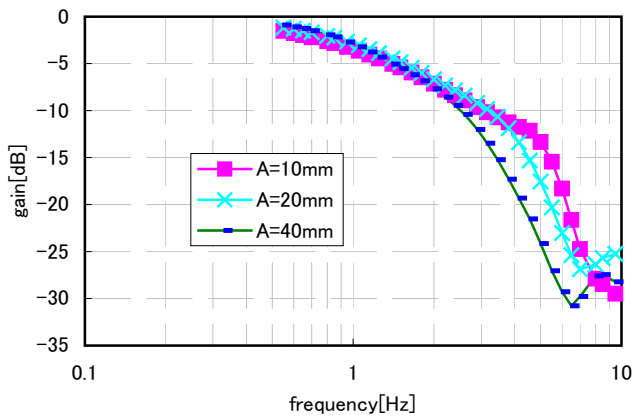
Figure 8 Effect of amplitude *A*
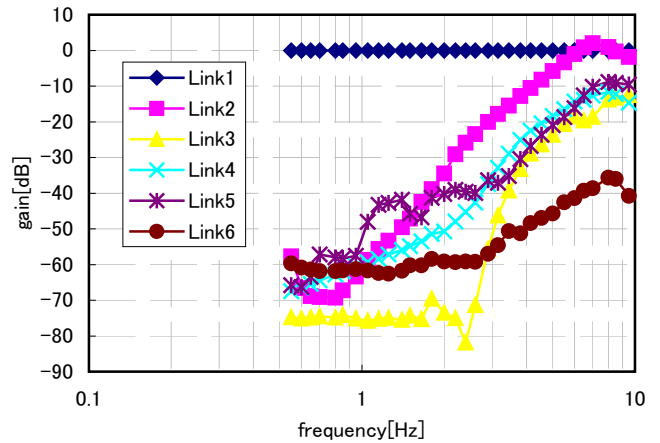
Figure 9 Interference to each link from link1

Conclusion

The frequency response of each link of parallel link mechanism with 6 degrees-of-freedom using electro-hydraulic servo cylinders was investigated in detail.

The influences of the center position, posture of the end effecter, load mass, and the amplitude on the frequency responses were investigated experimentally.

The frequency response hardly changes depending on the center position or the posture of the end effecter.

When load mass or the amplitude is enlarged, the fall of the gain is remarkable on high frequency.

The interference between links was measured. The interference also becomes remarkable with the increase in frequency.

REFERENCE

1. K. Tsuchiya, S. Sato, K. Suzuki; Dynamic characteristics of parallel link mechanism with six degrees of freedom using hydraulic cylinders 1st report; Trans. of JFPS,Vol.37-1, pp1-7 (2006)
2. K. Tsuchiya, K. Suzuki, S. Sato; Dynamic characteristics of parallel link mechanism with six degrees of freedom using hydraulic cylinders 2nd report; Trans. of JFPS,Vol.38-1, pp1-6 (2007)
3. K. Tsuchiya, K. Suzuki, S. Sato; Dynamic characteristics of parallel link mechanism with six degrees of freedom using hydraulic cylinders 3rd report; Trans. of JFPS,Vol.38-1, pp7-12 (2007)

P2-04

STUDY ON A CONTROL SYSTEM OF HYDRAULIC LIFTING AND MOVING RAIL EQUPMENT TEST BENCH

Zhengyao YI , Wei XIONG and Haitao WANG

Transportation and Logistics Engineering College, Dalian Maritime University
1Linghai Road, Dalian,116026, China
(E-mail: wht810@vip.sina.com)

ABSTRACT

A hydraulic lifting-moving-rail equipment test bench is designed, which can lift and move the rail for examining and repairing. The loading system is an electric-hydraulic servo control system. The original control strategy has some disadvantages, such as overshoot and slow response, which severely effect dynamic performance and test precision of system. According to the fuzzy control theory, the fuzzy-PID controller was designed by using ordinarily PID controller method. Experiments show that the performance of fuzzy-PID control system is obviously improved.

KEY WORDS

Hydraulic lifting-moving-rail equipment, Test bench, Electric-hydraulic servo control, Fuzzy-PID controller

INTRODUCTION

In recent years, with the rapid development of rail transportation in China, more high-speed and heavy-load trains are utilized. It is necessary to maintain railway in a good condition. Hydraulic lifting-moving-rail equipment which is used to raise and toggle rail for examination is an important device for railway. Its quality plays a critical role in maintenance and repair of railway. Thus, the functional detection of hydraulic lifting-moving-rail equipment is needed.

The hydraulic test bench is utilized to test output force of hydraulic lifting-moving-rail equipment. The process of pressurizing and maintaining is controlled by an electro-hydraulic servo-controller. With the influence of flow rate, pressure difference of orifices, inertia of oil and piston rod, leak of oil and lag of loop, there are many disadvantage of existing control strategies such as instability of system, large overshoot and slow response, which affects the dynamic performance and detection precision of system seriously [1-2]. So, it is necessary to find optimized control strategies. However, it is difficult to get good experimental results by using traditional PID control methods. Fuzzy control is used to adapt the change of system parameters in order to control the system steadily and accurately. But fuzzy control fails to make upper precision for its own features [3]. Therefore, fuzzy -PID control strategy which combines the merits of fuzzy control and PID control is adopted in this paper.

STRUCTURE AND CONTROL PRINCIPLE OF THE BENCH

Hydraulic Lifting-moving-rail Equipment

A model of hydraulic lifting-moving-rail equipment is shown in Figure 1. With the piston rod of cylinder extension by loading oil tank which connected with cylinder, the lifting wheel can lift and move the rail, and maintain the rail in a certain high for 3 minutes. It is necessary to detect the hydraulic lifting-moving-rail equipment due to its leak and coecibility of the oil and its quality.
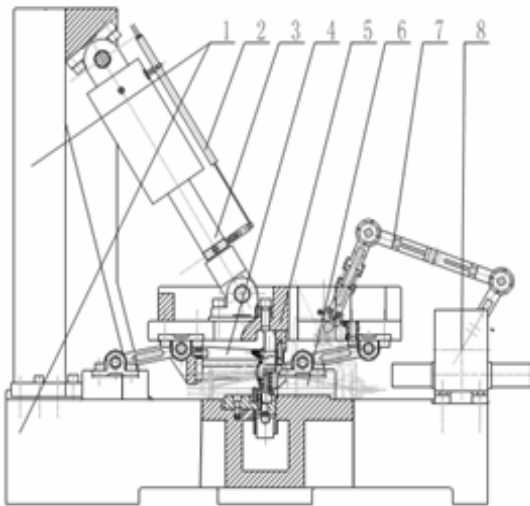
Lifting wheel   Oil tank
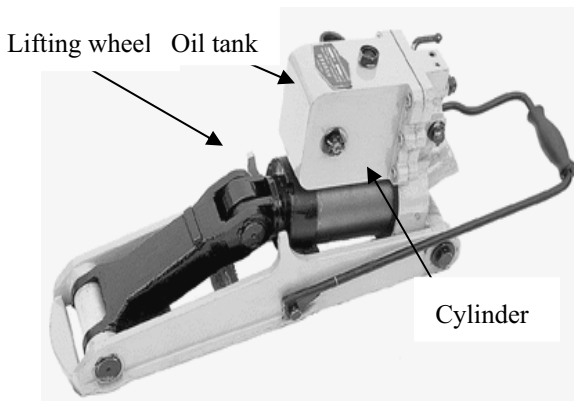
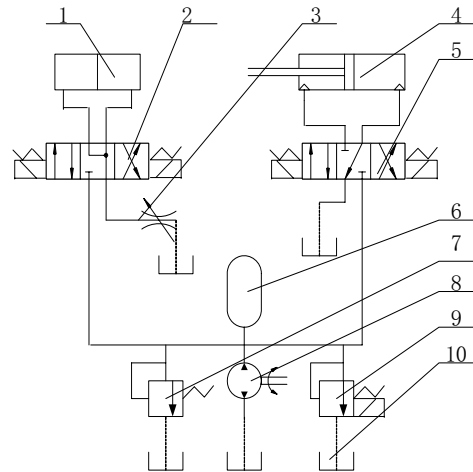Cylinder

Figure 1 Hydraulic lifting-moving-rail equipment

Hydraulic System Principle of the Test Bench

1. Frame 2.Displacement sensor 3.Loading cylinder 4. Press plate 5. Push plate 6.Hydraulic lifting-moving-rail equipment 7.Drive staff 8. Tilting cylinder

Figure 2 Structure of the test bench

The structure of the test bench is shown in Figure 2 and the hydraulic system principle of the test bench is shown in Figure 3. The cylinder piston rod controlled by "J" change valve and detected by displacement sensor is connected with the press plate and push plate , whose function is loading lifting-moving-rail equipment. The tilting cylinder controlled by "Y" change valve is connected with the drive staff, whose function is rising cylinder piston rod of lifting-moving-rail equipment. The electromagnetic relief valve plays a role in adjusting the pressure of system loop.

1. Tilting cylinder2. "Y" change valve 3. Flow regulating valve 4. Loading cylinder 5. "J" change valve 6.Accumulator7.Safety valve8. Hydraulic pump 9.Electromagnetic relief valve10.Oil tank

Figure 3 Hydraulic system principle o f the test bench

Control System Principle of the Bench
Test bench of hydraulic lifting-moving-rail equipment is a control system which tests load actively. It is a closed loop system which is mainly comprised of amplifier, magnetic proportional overflow valve, hydraulic cylinder and pressure sensor, etc. Load control system is shown in Figure4.
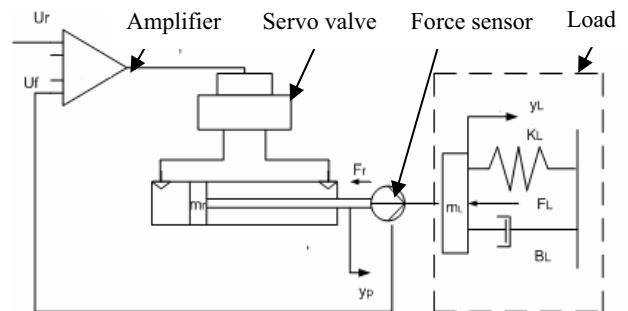
Figure 4 Control system principle of the test bench

DESIGN OF FUZZY CONTROLLER

Principle of Fuzzy PID Control
Traditional PID control is precise and steady. However, it can't adapt the change of parameters. Fuzzy control system is better in dynamic condition, but it can't achieve steady precision; sometimes cause limit cycles oscillations. Thus, fuzzy-PID linear control is proposed to combine the merits of traditional PID and fuzzy

control system [3]. Its principal is illustrated in Figure5.
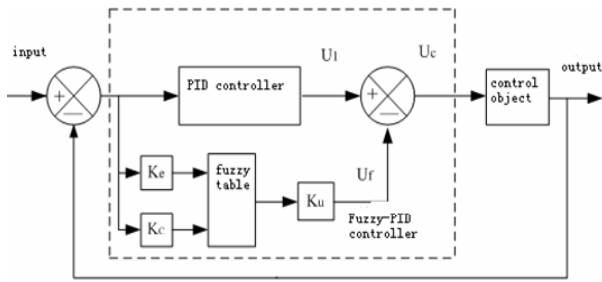
Figure 5 Fuzzy PID complex controller

The main principal of fuzzy PID linear control is explained as following: when system error (e) enter into <0> grade and output (u_f) of fuzzy controller is zero, the output (u_c) of controller is equal to the output (u_1)of linear PID, namely $u_c = u_1$. The system is totally adjusted by linear PID controller. On the other hand, when system error is out of <0> grade, output (u_f) of fuzzy controller is not zero and output (u_c) of controller is the combination of the output (u_f) of fuzzy controller and the output (u_1) of linear PID, namely $u_c=u_f+u_1$. The system is drove more efficiently and obtains better steady dynamic performance [5].

Design of Fuzzy Control Rule Table on the Bench
The control rule is showed in table 1.

Table 1 Fuzzy control rule

Pressure error E	E/CE	The change of pressure error CE						
		NB	NM	NS	0	PS	PM	PB
	NB	PB	PB	PB	PB	PM	0	0
	NM	PB	PB	PB	PB	PM	0	0
	NS	PM	PM	PM	PM	0	NS	NS
	N0	PM	PM	PS	0	NS	NM	NM
	PB	PM	PM	PS	0	NS	NM	NM
	PS	PS	PS	0	NM	NM	NM	NM
	PM	0	0	NM	NB	NB	NB	NB

When system error is big negative and the variation is negative, the trend of error increases. Therefore, the big positive variation of controlled quantity is selected in order to get rid of the big negative error and restrain the trend of error to be big. When system error is negative and the variation is positive, the trend of error decreases. Therefore, the small controlled quantity is selected in order to get rid of the negative error and restrain overshoot. When system error is big negative and the variation is small positive, the mid positive variation of controlled quantity is selected. When system error is big negative and the variation is big positive or mid positive, the increase of controlled quantity is not suitable, or else

it will bring overshoot. Therefore, the <0> grade controlled quantity is selected. Obviously, when system error is mid negative, the choice of controlled quantity is the same as the big negative. Evidently, when system error is small negative, the system is approach steady.

EXPERIMENTS

Interface of Fuzzy PID Controller
Based on fuzzy-PID control strategy and discrete PID control equation, the fuzzy-PID control system is designed by Visual Basic which is shown in Figure6.
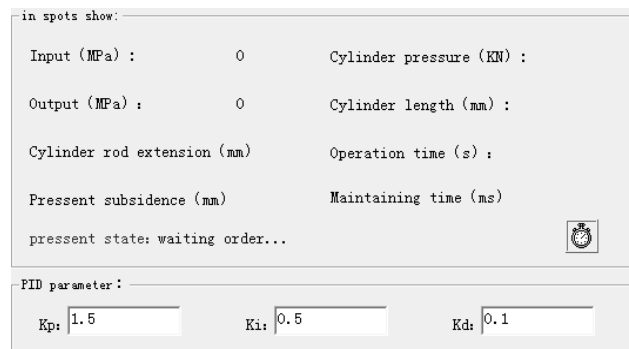
Figure 6 Fuzzy PID control interface

Results
Three response curves which are respectively drawn according to original ratio control, PID control and fuzzy-PID control are shown in the following diagram.
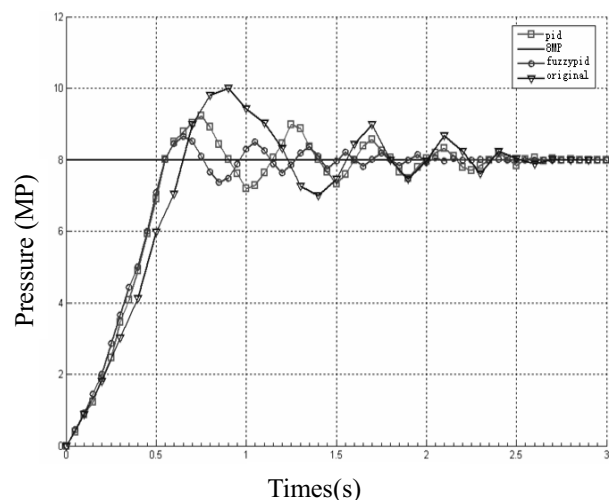

Figure 7 Three time response curves
As illustrated in Figure 7, if the test system of test bench adopts original control, its overshoot is so bigger (25.6%) that it is unstable, and response time exceeds 3 seconds and rise time is 0.9 seconds. The precision of

system is lower. If the test system utilizes PID control, it is relatively stable and its overshoot is 16.4%, and response time is 2.65 seconds and rise time is 0.75 seconds. With the test system of fuzzy-PID control, it is stable and its overshoot is reduced obviously (lower than 8.7%), and response time is 2.25 seconds and rise time is 0.65 seconds. The system precision reaches 1% (lower than 2%), which meets demand of the system.

CONCLUSIONS

(1) The overshoot of fuzzy-PID control system is minimum compared to other two control strategies;

(2) Compared to other two control strategies the response time of fuzzy-PID control is shorter than other two control strategies, but only little difference;

(3) The rise time of fuzzy-PID control is the shortest.

REFERENCES

1. Ke LI, Mannan M.A. and Mingqian XU. Electro-hydraulic Proportional Control of Twin-cylinder Hydraulic Elevators [J]. Control Engineering Practice Volume, 2001, **4**, pp.367-373.
2. Bonchis,A. and Corke, P.I., Variable Structure Methods in Hydraulic Servo Systems Control [J] Automatica, 2001, pp.589-595.
3. Lee S.Y., Fuzzy Controller for an Electro-hydraulic Fin Actuator Using Phase Plane Method [J]. Control Engineering Practice, 2003, **11**, pp.697-708.
4. Voda A., and Landu LD., A Method for the Auto-calibrition of PID Controller [J]. Automatic, 1995, pp.41-53.
5. Sugeno M., and TakahiroY., A Fuzzy Logic-based approach to Aualitative Modeling. IEEE Trans on Fuzzy System, 1993, pp.7-31.

P2-05

IMPROVEMENT OF POSITION TRACKING PERFORMANCE OF ELECTRO HYDRAULIC ACTUATOR SYSTEMS WITH DISTURBANCE

Min Gyu Park*, Sung Hwan Park *, Jong Shik Kim* and Ho Gil Lee**

* School of Mechanical Engineering, Pusan National Univeristy
Jangjeon-dong, Geumjeong-gu, Busan, 609-735, Korea
(E-mail: pmgking@naver.com)
** Dong Jin Co., LTD
10-6 Jukgock-li Jinyoung-up, Kimhea, Kyungnam, 621-801, Korea
(E-mail: hklee1@dongjin.com)

ABSTRACT

Electro hydraulic actuator (EHA) system has inner and outer loops like a cascade system. The inner loop consists of an electric motor, a gear pump, and an angular velocity controller, and the outer loop consists of a hydro-actuator and a position controller. Especially, dead-band nonlinearity that exists between the electric motor and the gear pump and friction that occurs between the cylinder and the piston are considered. The tracking performance of EHA position control systems becomes unsatisfactory due to the dead-band and friction effects. Thus, in order to improve the position tracking performance of EHA systems with disturbance, backstepping control scheme for the desired position tracking is proposed, which is compared with the conventional PID scheme.

KEY WORDS

Electro Hydraulic Actuator, Backstepping control

INTRODUCTION

Hydraulic actuators, in general, have shortcomings such as the leakage of working fluid, environmental pollution due to the leakage, a maintenance load, and limited working space, etc. In addition, conventional hydraulic actuator(CHA) systems have some problems in case of applying to fighting aircrafts, since fighting aircrafts require light weight as well as the improvement their response performance and fault detection for self safety or backup system. Therefore, to overcome these problems, EHA systems have been studied for the integration of components and electric motor control. However, the EHA systems have some merits such as size, energy efficiency, and faster response due to high stiffness compared with CHA systems.

The flow rate and pressure in EHA systems are adjusted directly by the control of the velocity and rotation direction of servo motor connected directly to the bidirectional hydraulic pump. Therefore, the motor control in EHA systems is very important to obtain precise position control performance and velocity control performance of the piston. The servo motor of EHA systems takes an important role for position and velocity controls of the actuator. The position tracking performance of the actuator is greatly influenced by the load pressure due to external load and friction between piston and cylinder. To overcome these problems, Pachter et. al. proposed a robust adaptive control scheme which can guarantee good position tracking control performance, although the system is influenced by disturbance and perturbation of system parameters[1].

Kokotovic et. al. suggested an EHA system with inner loop for the speed control and outer loop for the position control and applied an adaptive control scheme to the inner loop [2]. Although they proposed various control schemes to cope with system uncertainties and disturbance, the establishment of the inner loop controller is technically difficult and it is very expensive to develop it.

In this paper, a bacstepping controller is proposed for the position control of the piston rod with disturbances such as the load exerted on the piston rod and the contact friction between the piston and the cylinder, which affect to the rotation of the servo motor. And the backstepping scheme is compared with a conventional PID scheme for EHA systems with disturbances. Computer simulations are executed in order to verity the effectiveness of the backstepping control scheme for the EHA system with disturbances.

SYSTEM MODELING

Figure 1 shows an EHA system, which consists of the electric servo motor and the bi-directional gear pump. The gear pump is rotated by the servo motor and then the flow rate is generated in the gear pump. The generated pressure by the flow rate makes a position change in the piston rod. And the movement direction of the piston is related to the rotation direction of the servo motor.

As shown in Fig. 1, the servo motor and the bi-directional gear pump are connected directly. Therefore, the servo motor and the gear pump of the EHA position control system can be represented as [3, 4]

$$T_{pm} = J_{pm}\dot{\omega} + B_{pm}\omega_p + T_{DB} + C_p(p_a - p_b) \quad (1)$$

where J_{pm}, B_{pm}, C_p, T_{DB} and ω_p are the equivalent inertia, equivalent viscous friction, volumetric capacity of the pump, torque loss due to static friction, and angular velocity of the pump, respectively.

To derive the dynamics of EHA systems, Newton's second law is applied for the hydraulic piston. Then,

$$\ddot{x}(t) = \frac{1}{M}\left[Ap_l - F_{fric}(\cdot)\right]. \quad (2)$$
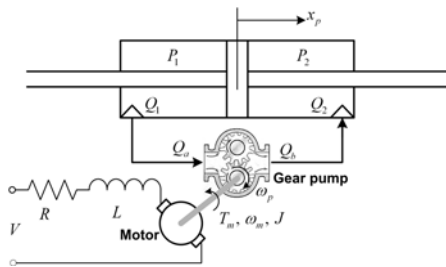
Figure 1 The schematic of an EHA system

where $x(t)$, M, A, p_l, and F_{fric} are the moving position of piston, the piston mass, the cross section area of piston, the load pressure($p_a - p_b$), and LuGre friction, respectively. And the derivatives of pressures p_a and p_b of both the sides on piston can be represented as [5]

$$\dot{p}_a = \frac{\beta_k(q_a - A\dot{x})}{V_a}, \qquad \dot{p}_b = \frac{\beta_k(q_b - A\dot{x})}{V_b} \quad (3)$$

The chamber volumes V_a and V_b depend on the position of the piston $x(t)$ as follows:

$$V_a(t) = V_{0a} + Ax(t), \quad V_b(t) = V_{0b} + Ax(t) \quad (4)$$

The flow rates (q_a, q_b) in the hydraulic pump can be represented with the pressure of the pump (p_a, p_b) and the angular velocity(ω_p) of the pump as follows:

$$q_a = C_p\omega_p - L_f p_l, \quad q_b = -q_a \quad (5)$$

where L_f is the leakage factor of the pump.

By differentiating Eq. (2), we can determine how these pressures can be controlled as follows:

$$\ddot{x} = \frac{1}{M}\left[A\dot{p}_l - \dot{F}_{fric}\right] \quad (6)$$

CONTROLLER DESIGN

Figure 2 shows the block diagram of the EHA position control system. The EHA position control system consists of the inner loop for the speed control of the servo motor and the outer loop for the position control of the piston. For the speed control of the motor in the inner loop, a proportional and derivative (PD) controller is used. In addition, the dynamics of the inner loop is not considered to design a backstepping position controller.

To design the backstepping controller, Eq. (6) is transformed as a general form [6] as follows:

$$\ddot{x} = f + bu \quad (7)$$

where

$$f = -\frac{1}{M}[\beta_k \frac{A^2(V_a + V_b)}{V_a V_b}\dot{x} + \dot{F}_{fric} + L_f p_L],$$

$$b = \frac{\beta_k}{M}\frac{A(V_a + V_b)C_p}{V_a V_b}, \quad u = \omega_p.$$
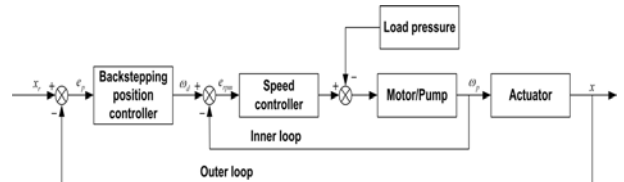

Figure 2 Block diagram of the EHA position control system

Now, let us Eq. (2) represent state equations. Then,

$$\begin{cases} \dot{x}_1 = x_2 \\ \dot{x}_2 = x_3 \\ \dot{x}_3 = f + bu \end{cases} \tag{8}$$

And, in order to design the backstepping controller, a new states are defined as follows:

$$z_1 = x_1 - r(t) \tag{9}$$

$$z_2 = x_2 - \alpha_1(z_1) \tag{10}$$

$$z_3 = x_3 - \alpha_2(z_1, z_2) \tag{11}$$

The design procedure of the backstepping controller is as follows:

Step 1

From Eq. (9), state equation for z_1 can be described as

$$\dot{z}_1 = z_2 + \alpha_1(z_1) - \dot{r}(t). \tag{12}$$

In order to select $\alpha_1(z_1)$ to guarantee stability for error dynamics in Eq. (12), the Lyapunov control function(LCF) is defined as

$$V_1(z_1) = \frac{1}{2} z_1^2. \tag{13}$$

Then,

$$\dot{V}_1(z_1) = z_1 \dot{z}_1 = z_1[\alpha_1(z_1) - \dot{r}] + z_1 z_2. \tag{14}$$

From Eq. (14), if $\alpha_1(z_1) = -k_1 z_1 + \dot{r}$, Eq. (12) can be exponentially stable when $t \to \infty$. And $k_1 > 0$ is a design parameter.

Step2

From Eq. (10), state equation for z_2 can be described as

$$\dot{z}_2 = z_3 + \alpha_2(z_1, z_2) - \dot{\alpha}_1(z_1) \tag{15}$$

where

$$\dot{\alpha}_1(z_1) = \frac{\partial \alpha_1}{\partial z_1} \dot{z}_1 + \frac{\alpha_1}{\partial \ddot{x}_r} \ddot{x}_r$$

$$= -k_1 \dot{z}_1 + \ddot{x}_r = -k_1(z_2 - k_1 z_1) + \ddot{x}_r.$$

Since Eq. (15) includes the information of Eq. (12), the LCF can be selected as

$$V_2(z_1, z_2) = V_1(z_1) + \frac{1}{2} z_2^2. \tag{16}$$

Then,

$$\dot{V}_2(z_1, z_2) = \dot{V}_1(z_1) + \dot{z}_2 z_2$$

$$= -k_1 z_1^2 + z_2 z_3 + z_2[z_1 + \alpha_2(z_1, z_2) - \dot{\alpha}_1(z_1)] \tag{17}$$

If the last term of Eq. (17) is defined as

$$z_1 - \alpha_2(z_1, z_2) + \dot{\alpha}_1(z_1) = -k_2 z_2,$$

Then, α_2 can be obtained as

$$\alpha_2(z_1, z_2) = -(k_1 + k_2) z_2 - (1 - k_1^2) z_1 + \ddot{x}_r \tag{18}$$

where $k_2 > 0$ is a design parameter.

Therefore,

$$\dot{V}_2 = z_2 z_3 - k_1 z_1^2 - k_2 z_2^2. \tag{19}$$

Step 3

From Eq. (11), the state equation for z_3 is described as

$$\dot{z}_3 = \dot{x}_3 - \dot{\alpha}_2(z_1, z_2) = (f + bu) - \dot{\alpha}_2(z_1, z_2) \tag{20}$$

where

$$\dot{\alpha}_2(z_1, z_2) = \frac{\partial \alpha_2}{\partial z_1} \dot{z}_1 + \frac{\partial \alpha_2}{\partial z_2} \dot{z}_2 + \frac{\partial \alpha_2}{\partial \dot{\alpha}_1} \ddot{\alpha}_1 \tag{21}$$

$$= -\dot{z}_1 - k_2 \dot{z}_2 + \ddot{\alpha}_1,$$

and

$$\ddot{\alpha}_1 = \frac{\partial \dot{\alpha}_1}{\partial z} \dot{z}_1 + \frac{\partial \dot{\alpha}_1}{\partial z_2} z_2 + \frac{\partial \dot{\alpha}_2}{\partial \ddot{x}_r} \dddot{x}_r \tag{22}$$

$$= -k_1^2 \dot{z}_1 - k_1 \dot{z}_2 + \dddot{x}_r.$$

Substituting Eqs. (12), (15), and (22) into Eq. (21), Eq. (21) can be rearranged as

$$\dot{\alpha}_2(z_1, z_2) = (k_1^2 - 1)\dot{z}_1 - (k_1 + k_2)\dot{z}_2 + \dddot{x}_r.$$

Since Eq. (20) uses the information of z_1 and z_2, the LCF included Eq. (16) can be described as

$$V_3(z_1, z_2, z_3) = V_2(z_1, z_2) + \frac{1}{2} z_3^2. \tag{23}$$

Then,

$$\dot{V}_3(z_1, z_2, z_3) = \dot{V}_2 + z_3 \dot{z}_3$$

$$= -k_1 z_1^2 - k_2 z_2^2 + z_3(z_2 + f + bu - \dot{\alpha}_2). \tag{24}$$

If the last term of Eq. (24) is defined as

$$-k_3 z_3 = z_2 + f + bu - \dot{\alpha}_2(z_1, z_2), \tag{25}$$

From Eq. (25), the backstepping control law can be obtained as

$$u = \frac{1}{b}(\dot{\alpha}_2 - k_3 z_3 - z_2 - f). \tag{26}$$

Substituting Eq. (25) into Eq. (24), Eq. (24) can be described as

$$\dot{V}_3(z_1, z_2, z_3) = -k_1 z_1^2 - k_2 z_2^2 - k_3 z_3^2 \tag{27}$$

Thus, from Eq. (27), the proposed backstepping control law is exponentially stable, since the time derivative of the LCF about new states is negative.

SIMULATION AND DISCUSSION

To design a backstepping position controller, only actuator dynamics neglected the inner dynamics is considered. And in order to confirm the position tracking performance of the proposed backstepping scheme, a conventional PID position controller is also designed. Figure 3 shows the position command input. The position command input $x_r(t) = 0.05[\sin(0.4\pi t) + \sin(2.4\pi t)]$ has the maximum amplitude of ± 10 [cm] and the variation of velocity during 5 seconds. The load pressure due to the friction between the piston and the cylinder is shown in Fig. 4. This load pressure interrupts the desired rotation of the servo motor and decreases the position tracking performance of the EHA position control systems.

From these simulation conditions, the position error results of the backstepping and PID control schemes are

shown in Fig. 5. In case of the PID position control system, the pattern of the position error is a little irregular. However, that of the backstepping position control system is relatively regular. From this result, the backstepping position control system has desired robustness to the disturbance. Also, the transient response of the backstepping position control system is worse than that of the PID position control system. This result is why backstepping position controller use differential value of the position output state such as the velocity and the acceleration and excessive change of the initial error. The root mean square errors for the backstepping and the PID control systems are 0.019mm and 0.08mm, respectively. Therefore, by using the backstepping scheme in place of the PID scheme, the tracking position performance of EHA system with disturbances can be improved by 4 times.

CONCLUSION

Position tracking performance of EHA systems with disturbances such as friction and dead-band are considered. In order to improve the position tracking performance of EHA with disturbances, backstepping
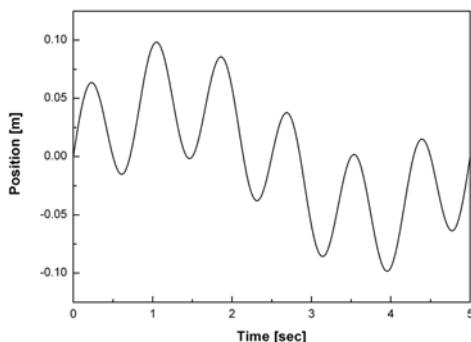
Figure 3 Position command input
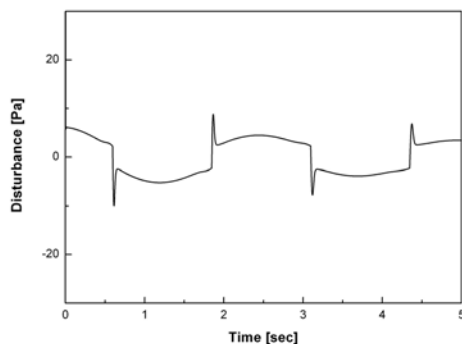
Figure 4 Disturbance input of the EHA system
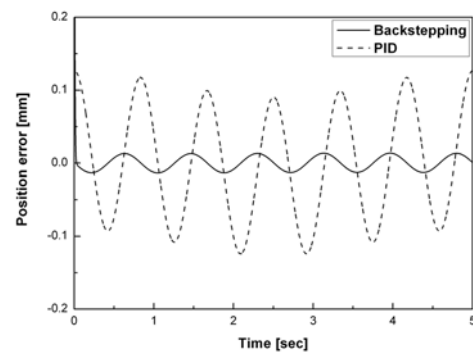
Figure 5 Position error of backstepping and PID control systems

position controller is proposed. It is found that backstepping control scheme based on the system model has robust characteristics for disturbances by computer simulation. The inner loop dynamics, which consist of a servo motor, a servo driver, and a speed controller, are considered as a total EHA systems. And the inner loop dynamics are not considered in a backstepping controller. However, the EHA position control system with the backstepping control scheme has desired position tracking performance and robustness.

REFERENCES

1. M. Pachter, C. H. Houpis, K. Kang, "Modeling and control of an electro-hydrostatic actuator", Int. J. of Robust and Nonlinear Control, 7(6), 591-608, 1997.
2. Vladimir V. Kokotovic, John Grabowski, Viral Amin and John Lee, "Electro Hydraulic Power Steering System", Int. Congress and Exposition Detroit, Michigan March, 1-4, 1999.
3. Watton, J., Fluid Power Systems, Prentice Hall, 1989.
4. Ogata, K., System Dynamics, 3rd edition, Prentice Hall, 1998.
5. Habibi, S. and Goldenberg, A., A Mechatronics Approach for the Design of a New High Performance ElectroHydraulic Actuator, SAE, 1999, pp. 1-8.
6. Krstic, M., Kanellakopoulos, I. and Kokotovic, P., Nonlinear and Adaptive Control Design Wiley Interscience, New York, 1995.

P2-06

A HYDRAULIC SIMULATOR FOR AN EXCAVATOR

Soon-Kwang Kwon*, Jae-Jun Kim*, Young-Man Jung*, Chan-Se Jung*
Chang-Don Lee** and Soon-Young Yang*

* Department of Mechanical and Automotive Engineering, Faculty of Engineering
University of Ulsan
Daehakro 102, Nam Gu, Ulsan, 680-749 Korea
(E-mail: kwang5024@hotmail.com)
** Team of Technical Development for Intelligent Vehicle Parts, Faculty of Engineering
University of Ulsan
Daehakro 102, Nam Gu, Ulsan, 680-749 Korea

ABSTRACT

An excavator consists of several hydraulic components which include pumps, a main control valve and cylinders etc. It operates by the linkage of the components. This paper is concerned with development of a hydraulic simulator for an excavator. The simulator has been developed using AMESim based on specifications of a 1.5 ton excavator. The excavator has been installed additional components to investigate an automated field robot; Electro proportional pressure reducing valve, electronic joysticks, angle sensors and a controller was installed at the excavator. The developed hydraulic simulator has the ability to represent with animation. The modeled MCV has been applied non-linear open area of spools.

KEY WORDS

Excavator, Simulation, AMESim, MCV

INTRODUCTION

The Hydraulic excavator has been the best popular construction equipment because of its multi-working ability in the construction field [1-2]. However its energy efficiency and prevention of environmental crisis are still need to improve.

The capabilities of controllers and components have been tested at the excavator directly. However, these tests accompany with lots of time, risk, resources. In order to develop efficiently, simulation is necessary before the test.

This paper describes the hydraulic simulation of excavators. Components and hydraulic system are built using the AMESim.

MODELING OF COMPONENTS

In order to develop the hydraulic simulator, first each component was modeled. MCV, Joysticks, attachment were newly modeled in this paper. These component modeling are based on 1.5 ton hydraulic excavator.

Main Control valve
The MCV consists of various valves for boom, arm, bucket, travel motor, dozer and swing etc. Only the valves of boom, arm and bucket are considered in this paper.

These valves are 6 ports 3 position types including bypass circuits. The Fig.1 is shown a circuit diagram of a boom valve. When spool is in neutral, the bypass line

is completely open. If pilot pressure act to one side of a valve selectively, spool is moved in accordance with the pressure. Then the open-area shows a non-linear relation with spool displacement as same to the Fig.2.
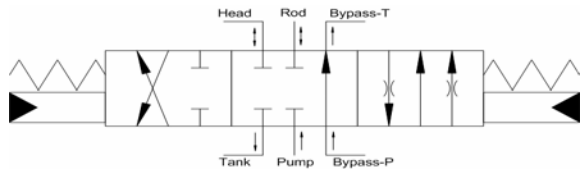
Figure 1 Circuit diagram of the boom valve
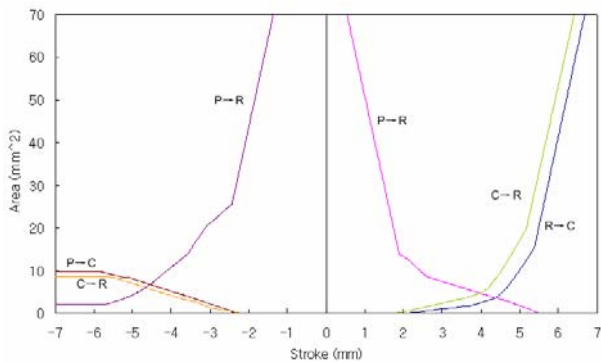
Figure 2 Stroke-Open area characteristics of boom valve

The boom valve was designed in order to include the direction of spool and non-linear open-area using the AMESim as shown in Fig. 3.
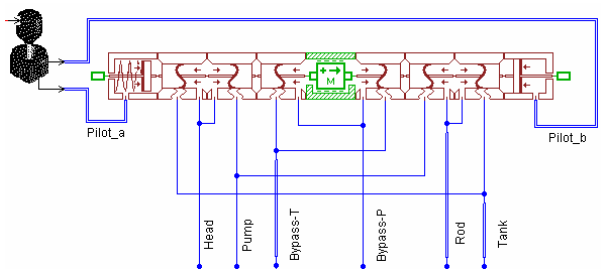
Figure 3 Modeling of the boom valve using the AMESim

Joystick
As for most movements of excavator, it is acted with operations of joysticks. The operations decide on pilot pressure and direction. The pilot pressure having range of 0kg/cm² to 20kg/cm² are used. These pressure and direction move spools of the MCV, then hydraulic oil pass through open-area which are generated by the movement of spools.
In this paper, operating of joysticks is assumed to signal between -1 to 1 and pilot pressure to A, B port is directly proportional to signal. The models of joysticks are same to Fig. 4.
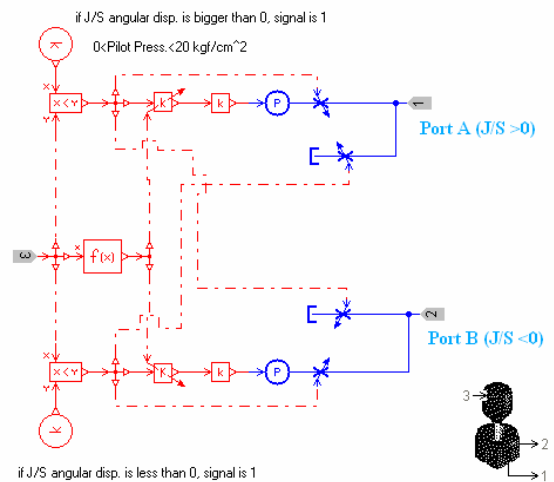
Figure 4 AMESim model of the joystick

Attachment
The size and weight of attachment was obtained by making an actual survey.
In order to start the simulation at wanted shape of the attachment, the initial angular position of boom, arm and bucket had to be decided. It needed to obtain the geometry modeling.
A coordinate system was determined with 3 degrees of freedom as shown in Fig. 5. Although the relative angular position of each component has used generally to study about an excavator [3-5], the absolute angular position which is suitable for the modeling using the AMESim has been used in this paper.
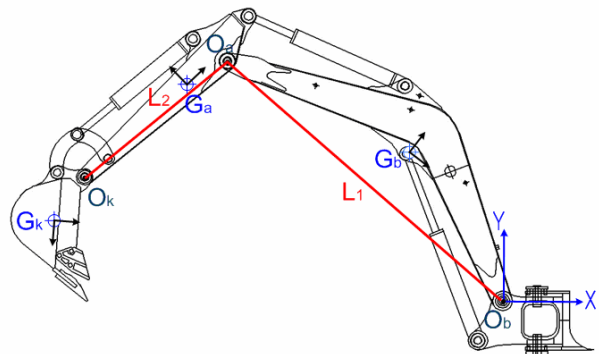
Figure 5 Coordinate system of the attachment

The joints of boom, arm and bucket are denoted as $O_b(x_b, y_b)$, $O_a(x_a, y_a)$ and $O_k(x_k, y_k)$. Their points are obtained using Eqs. (1) ~ (3).

$$x_b = 0,$$
$$y_b = 0, \tag{1}$$

$$x_a = -L_1 \times \cos\theta_b,$$
$$y_a = -L_1 \times \sin\theta_b, \qquad (2)$$

$$x_k = -L_1 \times \cos\theta_b - L_2 \times \cos\theta_a,$$
$$y_k = -L_1 \times \sin\theta_b - L_2 \times \sin\theta_a. \qquad (3)$$

where θ_b, θ_a are the absolute angular positions of boom and arm.
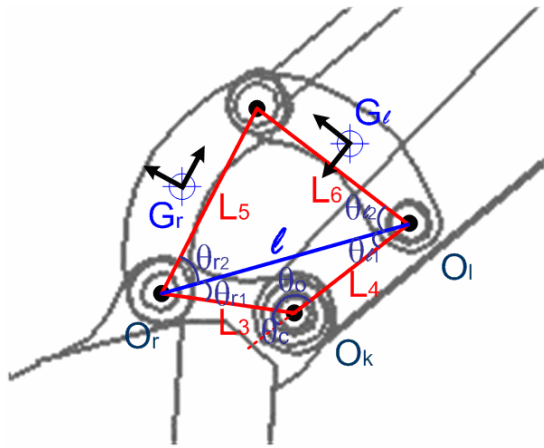
Figure 6 Four-bar linkages system

Fig. 6 shows the four-bar linkages which contain arm, bucket, control link and control rod. Eq. (4) is shown the coordinate point of a joint which connect arm and control link, and Eq. (5) is represented a joint which connects bucket and control rod.

$$x_l = -L_1 \times \cos\theta_b - (L_2 - L_4) \times \cos\theta_a,$$
$$y_l = -L_1 \times \sin\theta_b - (L_2 - L_4) \times \sin\theta_a, \qquad (4)$$

$$x_r = -L_1 \times \cos\theta_b - L_2 \times \cos\theta_a - L_3 \times \sin(\theta_c - \theta_k),$$
$$y_r = -L_1 \times \sin\theta_b - L_2 \times \sin\theta_a - L_3 \times \cos(\theta_c - \theta_k). \qquad (5)$$

where θ_k is the absolute angular position of bucket.
The distance l of O_l and O_r is same to Eq. (6).

$$l = \sqrt{(x_l - x_r)^2 + (y_l - y_r)^2}. \qquad (6)$$

The initial angular position of the control link and control rod can be calculated using the second law of cosines as shown in Eqs. (7) ~ (8).

$$\theta_{l1} = \cos^{-1}\left(\frac{l^2 + L_4^2 - L_3^2}{2 \times l \times L_4} \right),$$

$$\theta_{l2} = \cos^{-1}\left(\frac{l^2 + L_6^2 - L_5^2}{2 \times l \times L_3} \right),$$

$$\theta_{r1} = \cos^{-1}\left(\frac{l^2 + L_3^2 - L_4^2}{2 \times l \times L_3} \right),$$

$$\theta_{r2} = \cos^{-1}\left(\frac{l^2 + L_5^2 - L_6^2}{2 \times l \times L_5} \right),$$

$$\theta_o = \cos^{-1}\left(\frac{L_4^2 + L_3^2 - l^2}{2 \times L_4 \times L_3} \right),$$

$$\theta_l = -\{(180 - \theta_a) + \theta_{l1} + \theta_{l2}\}, \qquad (7)$$
$$\theta_r = \theta_a + \theta_o - (180 - \theta_{r1} - \theta_{r2}). \qquad (8)$$

The attachment was modeled using these equations and measuring data as shown in Fig. 7. This model includes contour data of boom, arm and bucket, so we can confirm the virtual movement of the attachment through simulation result.
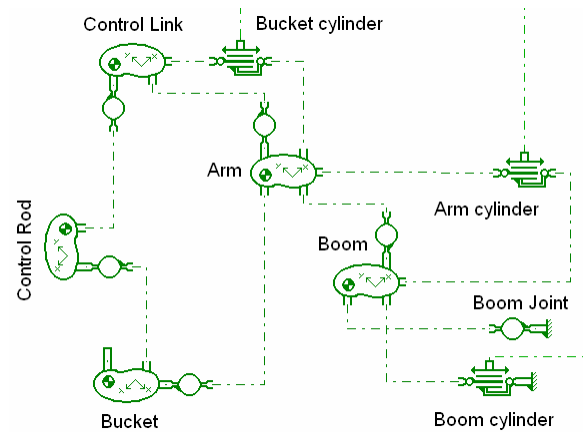
Figure 7 Attachment model using AMESim

Pump
An applied excavator has got three hydraulic pumps. One pump was already shown in Fig 4. The pump is used to control pilot pressure. The orders are fixed capacity type each flowing out 5.1cc/rev. A pump1 mainly take charge of the movement of the arm. And a pump2 usually concern with motion of boom and bucket. When the cylinder need much flow rate, pump2 can concern with the operation through a check valve.

Cylinder

Attachment is moved by stroke variation of three cylinders. The specification of cylinders is the same to Table 1. In this study, the weight of cylinders has been ignored.

Table 1 specification of cylinders

	Boom	Arm	Bucket
Piston diameter	55mm	55mm	55mm
Rod diameter	30mm	30mm	30mm
Length of stroke	0.38m	0.39m	0.3m
Free length	0.62m	0.62m	0.52m

MODELING OF SYSTEM

The hydraulic simulator system for the excavator was completed by assembly of each component. The models of the attachment and valves are setting up to each separate subcomponent.

This simulator system works according to input signals having range of -1 to 1 which they move valve spools. Relief valves set up the maximum pressure in the system to 210 kg/cm^2. Fig.8 shows the hydraulic simulator system using the AMESim. Two pumps turn to the same speed because they are connected with the only engine. And the flow rates are also same.
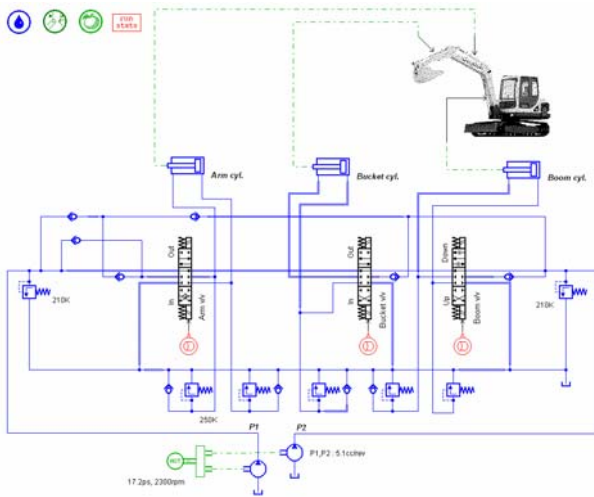
Figure 8 Circuit diagram of simulator using the AMESim

EXPERIMENT

We assumed to work excavation and then the signals were inputted to each valve. An engine speed was supposed to 2300rpm. Then the input signals are same to Fig. 9.
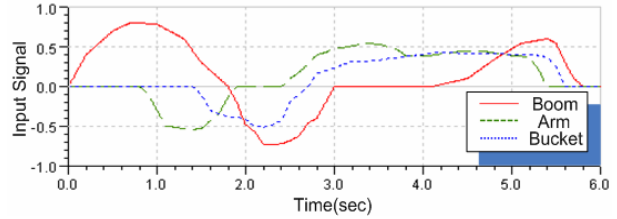
Figure 9 Joystick signals

The moving direction of attachment according to input signal was decided the same to Table 2.

Table 2 Input signal-moving direction characteristics

	Boom	Arm	Bucket
+ (positive)	up	crowd	crowd
- (negative)	down	dump	dump

When input signals are the same to Fig. 9, each cylinder stroke is appeared as shown in Fig. 10.
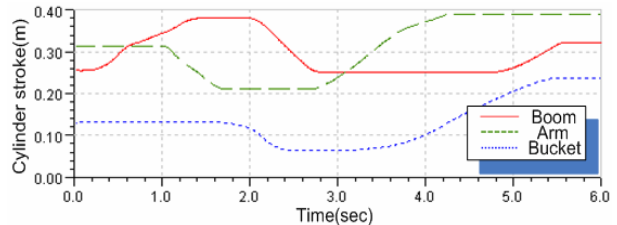
Figure 10 Cylinder strokes

Fig. 11 shows the relative angular positions and Fig. 12 shows the absolute angular positions of the attachment.
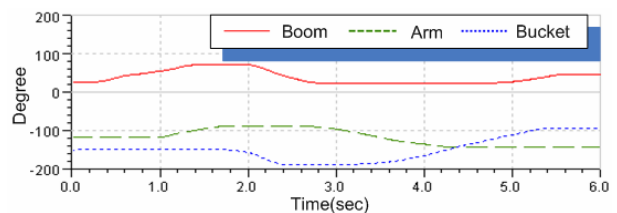
Figure 11 Relative angular positions
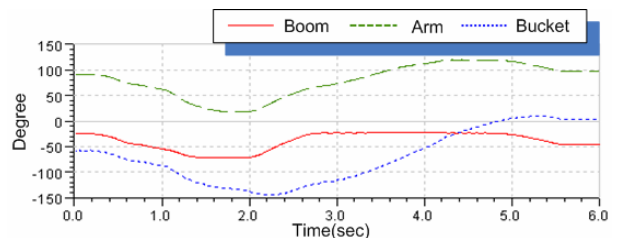
Figure 12 Absolute angular positions

The pressure at both ends of cylinders is also obtained by this simulation as shown Fig. 13.
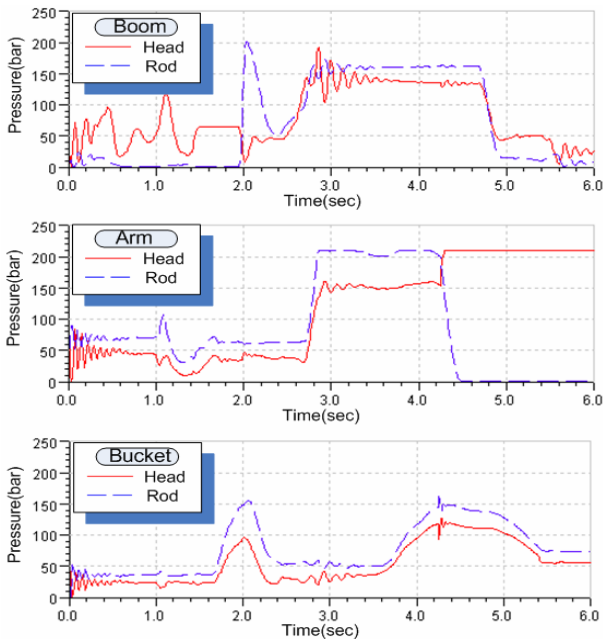
Figure 13 Cylinder Pressure

This hydraulic simulator calculates not only above-mentioned things, but also many other thing, trajectory, flow rate, shaft torque etc. Fig. 14 shows the flow rates at both ends of cylinders in the same simulation.
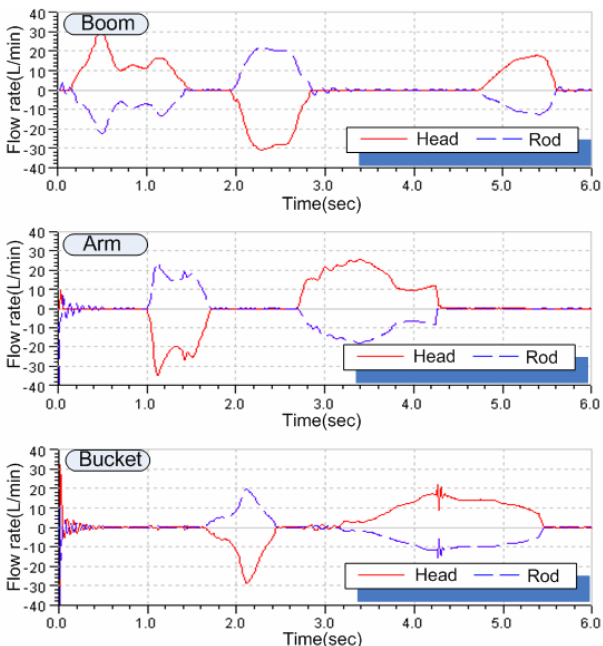

Figure 14 Flow rate at ports of cylinders

The simulation was operated and we obtained the results of that. We can confirm the results more quickly and easily by an animation function. Fig. 15 is a scene of the animation based on the results of the excavation work.
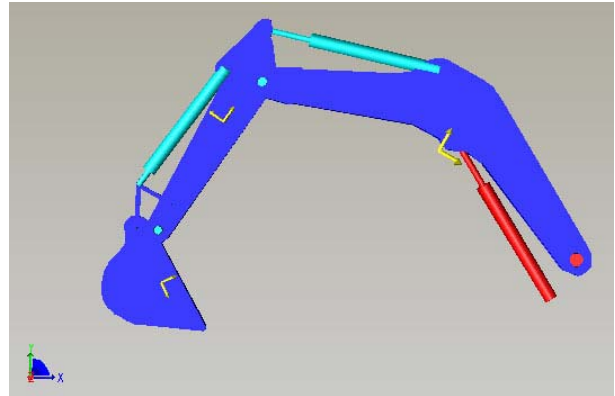
Figure 15 A scene of animation
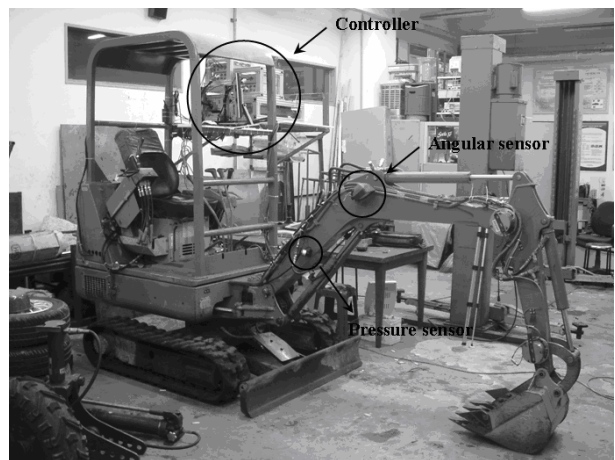
Figure 16 A photo of the applicatory excavator

CONCLUSIONS

In this study, the hydraulic simulator is developed for the excavator. The mechanicals have been modeled in accordance with the specifics and measuring of the excavator. The input signal into the MCV can be controlled in the simulator. Because the MCV model includes a characteristic of non-linear open-area in accordance with displacement of spools, it is more effective than other studies which use feed-back system with linear open-area valve.

Various results are obtained by the virtual excavation work.. We are going to measure the pressure and angular positions using the excavator as shown in Fig. 16. The measuring data and results of simulation will be compared each other to evaluate the simulator.

After rectification and supplementation, it is expected that this hydraulic simulation program are applied automation study, performance test of component etc.

REFERENCES

1. Jong-Hwan Choi, Sung-Su Kim, Soon-Yong Yang and Jin-Gul Lee, Robust Trajectory Control of a Hydraulic Excavator using Disturbance Observer in H_∞ Framework, Journal of the Korean Society of Precision Engineering, 2003, **20**-10, pp.130-140.
2. Sung-Su Kim, Woo-Suk Seo, Soon-Yong Yang, Byung-Ryong Lee and Kyung-Kwan Ahn, Trajectory Control of Field Robot Using Adaptive Control and System Identification, Journal of Control, Automation and Systems Engineering, 2002, **8**-9, pp.728-735.
3. Tomi Makkonen, Kelervo Nevala and Rauno Heikkilä, A 3D model based control of an excavator, Automation in Construction 15, 2006, pp.571-577.
4. P. K. Vähä and M. J. Skibniewski, Dynamic model of excavator, Journal of Aerospace Engineering, 1993, **6**-2, pp.148-158.
5. Seung Ho Cho, A Simulation on the Hydraulic Control Characteristics of Excavator Using Load Sensing System, Journal of the Korean Society of Precision Engineering, 1998, **15**-2, pp.134-145.
6. AMESim user Manual, IMAGINE, 2000.
7. John Watton, Fluid Power System, Prentice Hall, 1989.

P2-07

LOAD SENSING WITH ACTIVE REGENERATION SYSTEM

Pietro MARANI*, Gabriele ANSALONI* and Roberto PAOLUZZI*

* Institute for Agricultural and Earthmoving Machines (IMAMOTER-CNR)
National Research Council of Italy
Via Canal Bianco 28, 44100, Ferrara, Italy
(E-mail: p.marani@imamoter.cnr.it)

ABSTRACT

The paper introduces a novel system design of fluid power systems which improves the control and energy use for multiple actuators systems with particular focus on mobile applications such excavators, loaders, tractors. The system hereinafter described is based on a new patented technology [1], the "Load Sensing with Active Regeneration System". The main idea is to overcome one of the main drawbacks of multiple actuators conventional Load Sensing Systems: while the higher actuator load drives the pump delivery pressure the other active actuators are controlled by the local compensators in a dissipative mode. The goal of the novel architecture is to actively use pressure drops usually wasted in the local compensators and, in case of assistive or overrunning loads, dissipated over control valves.

KEY WORDS

Load Sensing , Active Regeneration, Energy Recovery, Control Valves

NOMENCLATURE

A_i :   Cylinder Active Area at generic section i
F_i :   External Force on Cylinder at generic section i
Q_d :   Flow Rate at *Acceptor* Section **a**
Q_d :   Flow Rate at *Donor* Section **d**
Q_i :   Flow Rate at generic section i
Q_M :   Flow Rate at *Dominant* Section **M**
Q_P :   Flow Rate Supplied by the Pump
Q_R :   Flow Rate Regenerated
T_i :   External Torque on Motor at generic section i
V_i :   Motor Displacement at generic section i
f_a :   Load at *Acceptor* Section **a**
f_d :   Load at *Donor* Section **d**
f_i :   Load at generic Section i
f_M :   Load at *Dominant* Section **M**
Δ :   Effective Pressure Margin
ε_i :   Linear Actuator Area Ratio at generic section i
ε_d :   Linear Actuator Area Ratio at *Donor* section **d**

STATE OF ART

Nowadays the Load Sensing technology can be considered mature in many fields of application: Earth Moving Machinery (Excavators, Backhoe Loaders, Dozers…), Industrial and Road Construction machinery (Telehandlers, Compactors…), Agricultural and Forestry Machinery (Feller Bounchers, Tractors…).

Long time has passed since the appearance of Load Sensing Directional Valves, and in this period this technology has gained more and more importance on the market of mobile applications for two main reasons: the first is because of the control friendliness since the load movement is independent from the external load, and the second because of a better power management, in particular an outstanding energy saving is achieved in comparison with traditional open centre architectures.

A basic version of Conventional LS System is shown in figure 1. A single variable displacement pump supply the oil to a block of parallel directional valves. The pump "senses" the maximum actuators load (*Dominant Load*) through a chain of shuttle valves and sets the delivery pressure at a fixed level equal to the dominant load pressure plus a constant margin, the pressure drop that must be kept across the metering orifices (*Effective Pressure Margin*).
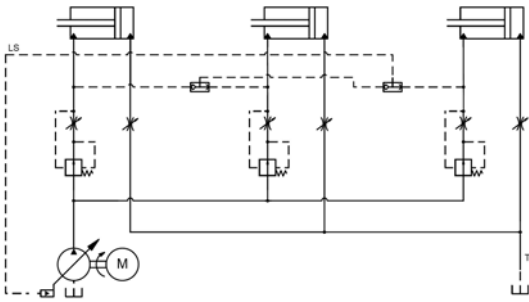
Figure 1 Conventional LS Architecture

Figure 2 The ARLS Architecture

The pressure drop across the metering orifice at the *non-dominant* (*Dependant*) sections is controlled by throttling through the local compensators.

It is trivial to observe that, if the pressure difference between the loads is high a large amount of energy would be wasted through the local compensators (figure 3). At the same time it is evident that control strategy isn't favourable for assistive and overrunning loads as the system is intended for the meter in control.

A NOVEL ARCHITECTURE

One of the possible schemes of the architecture is shown in figure 2. Multiple hydraulic actuators are controlled by a valve block connected to a load sensing pump through the *P rail*. The LS signal is generated by means of cascade shuttle valves selecting the dominant load.

The valve *Discharge Flow Compensator* adjusts the pressure of the hydraulic actuator's outflow according to an electronic external command, rising the pressure on a secondary line called Regeneration rail or *R rail*.

The P rail and the R rail are connected to the inlet of *Upstream Compensator* adjusting the pressure drop across the metering to the effective pressure margin, the outlet of the valve feeds the hydraulic actuator.

The Upstream Compensator is a normally open three-position three-way valve. In the closed extreme position it disconnects the P and R rails from the Actuator; in the middle position connects the R rail but not the P, to the actuator regulating the flow from the R line; in the third position the connection of the R line is saturated open while the flow from the P line is regulated. Basically the actuator is fed so that R rail has priority on P line, in other words the actuator is fed by P line in case the R line has not enough flow rate or pressure to meet the required flow.

A unidirectional valve prevents the reverse flow from the actuator inlet to the R line; a second check valve prevents the reverse flow from the R line to the actuator outlet.
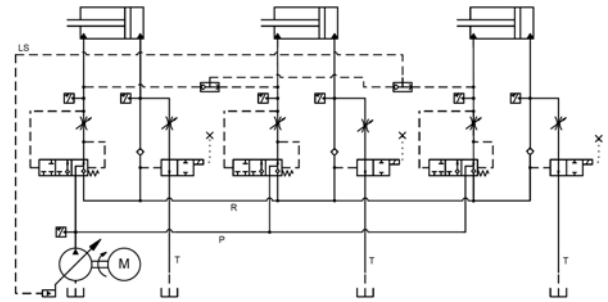
The control strategy is decided by means of the pressure transducers placed on inlets and outlets of hydraulic actuators that strategy consist on the decision of which Discharge Flow Compensator must be regulated or closed to rise the outlet pressure and direct the Outflow of the Actuator to the R rail. The pressure of oil flowing on the R rail must be enough to feed a second actuator. It must be noted that differently from other systems in which the outlet of some actuator is directly connected to a second actuator inlet, though without regulation, in the Active Regeneration Load Sensing System the flow delivered to each actuator is controlled in LS logic by the Upstream Compensator so that the flow always matches the request.

ENERGY CONSIDERATIONS

In Multi Actuator Hydraulic Systems two basic patterns can connect the supply to actuators and actuators to the tank: the first is a parallel architecture, the second is a series architecture.

The second architecture has the general drawback that the flow rate of actuators outlet must match the requested flow rate of the connected actuators inlet. It is trivial to note that if the flow rates always match Energy Management would be optimal: The pump delivers only the flow requested by the first actuator at the sum of loads pressures. Apart from hydraulic losses in pipes and valves, the energy requested exactly matches the energy delivered. It must be noted however that's very unlikely that the request of a actuator matches with the outflow of another in a machine work cycle.

On the other hand the parallel architecture can manage different flow requests by the actuators but, as discussed in many papers, has the drawback that the control of different loads connected to a single source is dissipative since the delivery pressure must be reduced to the level of the lower loads. It is easy to conclude that the if the loads are all equals the power management would be optimal because again apart from hydraulic losses in pipes and valves the energy requested matches exactly the energy delivered. In fact

ideally the pump delivers the sum of flow requested by the actuators at the actuator's pressure (figure 3).

The Active Regeneration Load Sensing System combines the benefits of the two mentioned architectures, as it can work as a parallel Load Sensing System, but can also connect in series the actuators or realize a hybrid pattern in which a Actuator is fed both by the supply and by a Second Actuator Outflow. An important remark is that the control would always be optimal as the pressure drop across the metering orifices is fixed as in conventional LS systems (figure 4).

Some coarse Energetic Considerations can be drawn introducing some hypothesis and nomenclature.

i) The pressure drop on each metering orifice is fixed at the effective pressure margin Δ by the Upstream Compensator

ii) Maximum load (dominant load) section is labelled by letter **M**

iii) Donor section is labelled by letter **d** and its Actuator Outlet delivers flow to rail **R**

iv) Acceptor section is labelled by letter **a** and receives flow from rail **R**

v) The section **d** Discharge Flow Compensator is commanded to rise the Outflow from Actuator **d** pressure until the pressure on rail **R** reaches value $f_\mathbf{a} + \Delta$ implying that the **R** line can supply fluid to Section **a**

vi) Flow rate at a generic section is $Q_\mathbf{i}$, load at a generic section is $f_\mathbf{i}$ being $F_\mathbf{i}$ is the external force, $T_\mathbf{i}$ the external torque; $A_\mathbf{i}$ and $V_\mathbf{i}$, respectively, Cylinder Active Area and Motor Displacement.

$$f_i = F_i / A_i \qquad \text{or} \qquad f_i = T_i / V_i \qquad (1)$$

vii) Linear Actuator's Area Ratio is $\varepsilon_\mathbf{i}$

viii) Oil flow rate in R rail is $Q_\mathbf{R}$

The hypothesis lead to two possible cases:

CASE 1) $\qquad Q_a > \varepsilon_d Q_d \longrightarrow Q_R = \varepsilon_d Q_d \qquad (2)$

The oil flowing out from Actuator **d** is less than the Flow Request at section **a**: section **a** is fed at the same time by supply **P** and by regeneration rail **R**.

The flow $Q_\mathbf{P}$ supplied by the pump will be the sum of all requests minus the regenerated flow Q_R.

$$Q_P = \Sigma Q_i - Q_R = Q_M + Q_a + (1 - \varepsilon_d)Q_d \qquad (3)$$

In this case, see figure 5, the flow pattern is a hybrid beetween series and parallel configuration. The Discharge Flow Compensator at section **d** is completely closed.

CASE 2) $\qquad Q_a < \varepsilon_d Q_d \longrightarrow Q_R = Q_a \qquad (4)$

The flow out from actuator **d** is more than flow rate requested from section **a**: section **a** is completely fed from section **d**.

The flow $Q_\mathbf{P}$ supplied by the pump will be the sum of all requests minus the regenerated flow (equal to flow to section a).

$$Q_P = \Sigma Q_i - Q_R = Q_M + Q_d \qquad (5)$$

In this case, see figure 6, the flow pattern of sections **d** and **a** is a series configuration. The Discharge Flow Compensator at section **d** is active, making some flow rate to be discharged to tank.

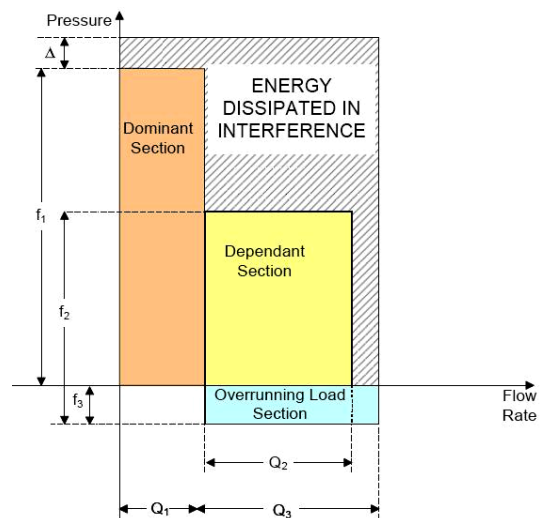Figure 3 Conventional LS Architecture Energy Map
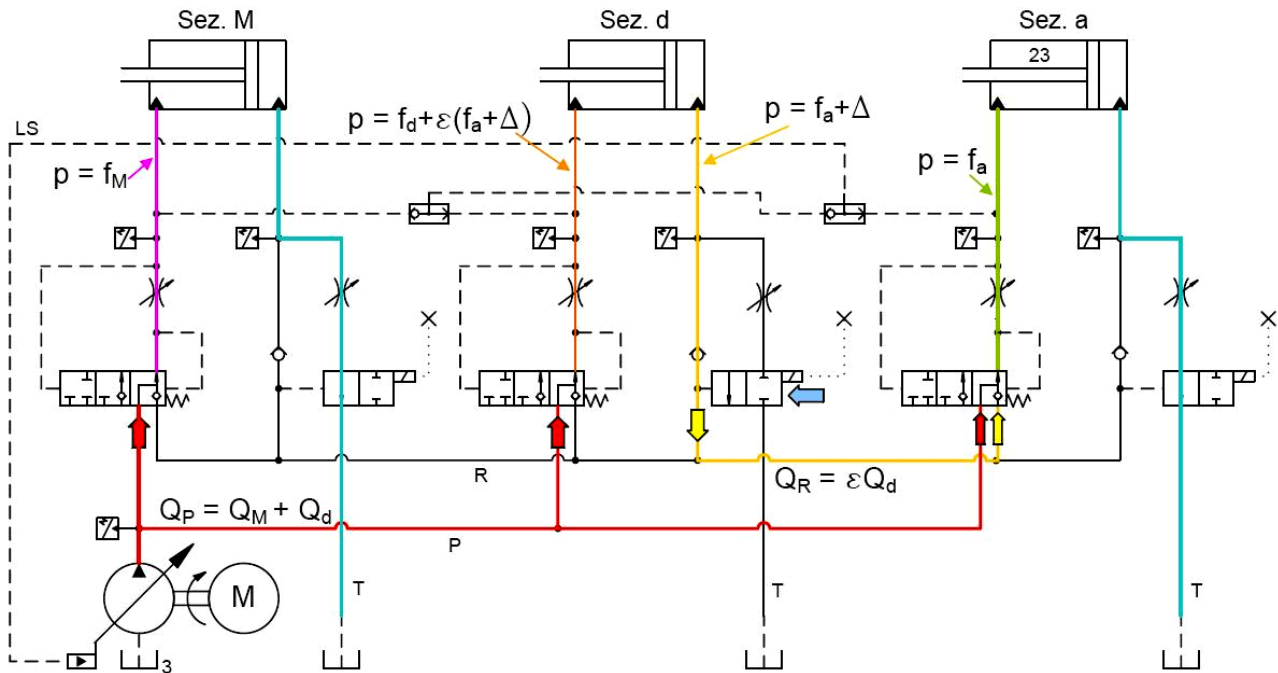

Figure 4   ARLS Architecture Energy Map

Figure 5 Active Regeneration Load Sensing System: Case 1 Flow Path

The touchstone for ARLS System is the conventional compensated LS system (figure 1). In this paper the approach is to make a comparison between the two; mainly as energy balance is concerned. Using equation (3), (5) it is possible to define the energy spent in a ARLS System (6). Similarly it is possible to write the Equation for the Energy spent in LS Systems (7).

$$W_{ARLS} = \left(\max\{f_d + \varepsilon(f_a + \Delta));\ f_M\} + \Delta\right)\cdot$$

$$\cdot \max\{[Q_M + Q_a + (1-\varepsilon)Q_d];\ (Q_d + Q_M)\} \quad (6)$$

$$W_{LS} = (f_M + \Delta)(Q_M + Q_d + Q_a) \quad (7)$$

$$W_{ARLS} < W_{LS} \quad (8)$$

Appling the equations (6), (7) to the Cases 1 and 2 it is possible to obtain two inequalities expressing the condition (8).

CASE 1) $\qquad Q_a > \varepsilon_d Q_d \longrightarrow Q_R = \varepsilon_d Q_d$

$$[f_M - (1-\varepsilon)f_d + (\varepsilon_d{}^2 - \varepsilon_d)f_a + \varepsilon^2\Delta]Q_d >$$

$$> [f_d - f_M + \varepsilon_d(f_a + \Delta)](\Sigma Q_i - Q_d) \quad (9)$$

CASE 2) $\qquad Q_a < \varepsilon_d Q_d \longrightarrow Q_R = Q_a$

$$(f_M + \Delta)Q_a > [f_d - f_M + \varepsilon(f_a + \Delta)](\Sigma Q_i - Q_a) \quad (10)$$

In order to better understand the meaning of the energy balance above the concept is applied to three cases:

One featuring a single section regenerating on itself;

Two sections exchanging flow each other through regenerative rail R;

Three sections with two exchanging flow through the regenerative rail and the third working normally.

First Example Pattern: One Section Regenerating on Itself

Attention is focused on comparison between the two systems, obtaining two cases the first is that the Ratio Area is less than one, the second is that the Area Ratio is bigger than one. Suppose that a section is regenerating while other sections are working normally.

Case 1: Regeneration on section **d**, $\qquad \varepsilon_d < 1$

$$(f_d - f_M)Q_d < [f_M - \frac{f_d + \varepsilon\Delta}{1-\varepsilon}](\Sigma Q_i - Q_d) \quad (11)$$

Observe that this inequality is always verified if the pressure induced by the Regenerated flow pattern is lower than the maximum load.

Case 2: Regeneration on section **d**, $\qquad \varepsilon > 1$

$$f_d < -\varepsilon\Delta \quad (12)$$

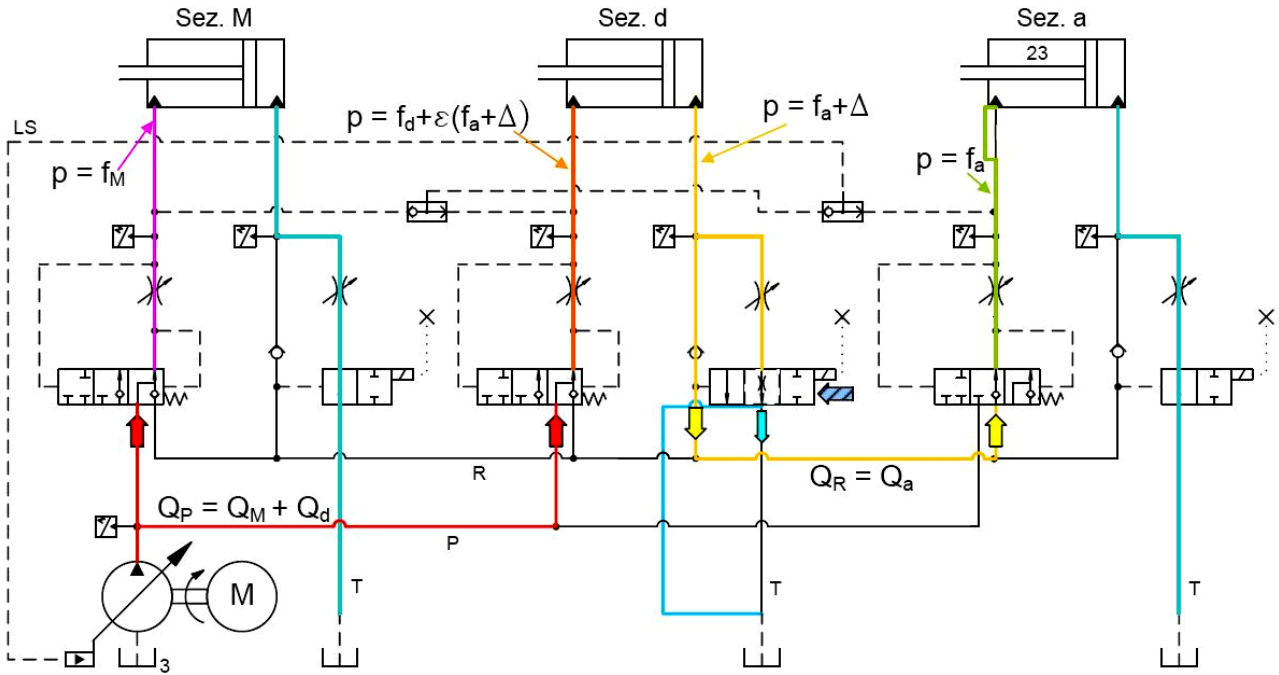This condition is verified only for high negative loads.

Figure 6 Active Regeneration Load Sensing System: Case 2 Flow Path

<u>**Second Example Pattern: Two Active Sections Regenerating**</u>

Applying the equations (9) and (10) to the case of two active sections with section **d** regenerating the flow to section **a** and supposing that the section at maximum load is the donor section **d** (assuming that the area ratio of actuator **d** is unitary) it is possible to obtain the following equations.

Case 1: $Q_a < Q_d$

$$(f_d + \Delta)Q_d > (f_a + \Delta)(Q_a) \tag{13}$$

$$\frac{f_d + \Delta}{f_a + \Delta} > \frac{Q_a}{Q_d} \tag{14}$$

Case 2: $Q_d < Q_a$

$$\frac{f_d + \Delta}{f_a + \Delta} < \frac{Q_a}{Q_d} \tag{15}$$

The two equations can be written simplified

$$\frac{f_d + \Delta}{f_a + \Delta} < \frac{Q_{max}}{Q_{min}} \tag{16}$$

where Q_{max} and Q_{min} are the higher flow rate and lower flow rate respectively.

Significant energy benefits of the ARLS architecture can be observed especially when the flow rates are close to each other and the loads significantly different.

<u>**Third Example Pattern: Three Active Sections, Two Regenerating**</u>

A fairly more complex, yet more significant example, includes three sections: one working normally, one donor and the third acceptor. We again consider unitary Area Ratio for sake of simplicity.

Case 1: $Q_a < Q_d$

$$[f_M + \Delta]Q_d > [f_d - f_M + (f_a + \Delta)](\Sigma Q_i - Q_d)$$

Some considerations can be drawn: if the dominant load exceeds the sum of other two loads plus effective pressure margin energy benefits are always obtained because the second term of equation becomes negative. It can be noted also that the greater the flow rate to the donor section the greater the energy saving is.

Case 2: $Q_d < Q_a$

$$(f_M + \Delta)Q_a > [f_d - f_M + (f_a + \Delta)](\Sigma Q_i - Q_a)$$

As in former Case it is favourable that the dominant

load exceeds the sum of the other two loads plus the effective pressure margin. It can be noted at last that the greater the flow demand at acceptor section, the greater the energy saving is.

OTHER FEATURES

The Active Regeneration Load Sensing System has manifold assets. The feature discussed in the previous paragraphs is to have a flexible flow pattern to optimize the energy consumption, but many other possibilities arise.

The first is the possibility to use assistive or overrunning loads to aid the movement of other actuators without loosing Load Sensing control of actuators. It is widely recognized that a large amount of energy is nowadays wasted in operations such as lowering loads; the ARLS architecture makes possible the recovery of potential energy redirecting the Outflow from Overrunning Load Sections to other active sections.

The second is to have a regenerative function in Load sensing control. In traditional systems the regenerative function is an on off function unfitting the load sensing logic based on proportional control. In the ARLS system it is possible to activate a regenerative function as discussed in the first example pattern throttling the Discharge Flow Compensator while the pressure drop across the metering orifice is kept constant by the Upstream Compensator.

The third is to improve the control of assistive and overrunning loads: the load sensing system are designed for meter-in control, a positive load on the Outlet of the Actuator is better controlled in meter-out control. The Assistive load can cause in LS systems losing of load sensing control (i.e. control proportional to meter-in command) or Cavitation as the load sensing throttles the actuator inlet line to maintain the effective pressure margin on meter-in orifice. In the ARLS architecture the Discharge Flow Compensators can be used to control the Actuator's Outlet Pressure assuring an optimal controllability and preventing the Cavitation phenomena.

Another improvement with respect to traditional systems is that the meter-in function can be disjointed to the meter-out. In fact the distributor spool can be designed so that the supply to actuator connections has proportional feature and the actuator to tank has just directional feature and made all meter out regulations to be performed by the Discharged Flow Compensator.

An important feature is to move the saturation point of the system as the flow request is lower than or (as a worst case) equal to that occurring in traditional systems. In fact every time a regenerative path is activated the flow supplied by the pump reduces by the regenerated flow. Considering a stochastic distribution of flow requests configurations it is trivial that the use of regenerative paths can dodge the Flow Saturation Event.

One of the possible drawbacks of the system is that instability could arise since the hydraulic variables vary during the working cycles and consequently the control parameters and outputs change in time. Possible effects of discontinuities at the endstops of cylinders, flow and pressure saturations are also points which will need further attention. Fortunately first simulations show quite encouraging results on this side.

CONCLUSIONS

A novel Architecture the Active Regeneration Load Sensing System was presented demonstrating that it improves the control and energy use for multiple actuator systems. An energy comparison with respect to traditional LS systems was carried out stressing the energy benefits of the ARLS Architecture.

Additional work is needed to develop a prototype and to work out the control strategy to be embedded in an electronic controller and will be subject of further research in the field.

REFERENCES

1. Marani, Paoluzzi, Patent IT TO2007A000516, July 2007
2. Rivolier, Patent US 5,305,789 , 26/04/94
3. Satoru et ali, Patent JP 7,324,355 , 12/12/95
4. P. Marani, G. Ansaloni, R. Paoluzzi, A. Fornaciari, "Test Methods for Flow Sharing Directional Valves". PTMC Symposium 2006, Bath, UK 2006
5. T. Virvalo, J. Seppälä, "Cross Utilizing degree Of Freedoms of Boom in Energy Saving Concept". PTMC Symposium 2006, Bath, UK 2006
6. R. Rahmfeld, M. Ivantisinova, "Energy Saving Hydraulic Displacement Controlled Linear Actuators in Industry Applications and Mobile Machine Systems". The Fourth International Symposium on Linear Drives for Industry Applications (LDIA03), Birmingham, UK 2003
7. G.L. Zarotti, N. Nervegna, "Saturation Problems in Load-sensing architectures". Proc. of the 43rd National Conference on Fluid Power , IIT Center, Chicago, USA 1988

P2-08

PERFORMANCE OF AC SERVOMOTOR CONTROL ELECTRO-HYDRAULIC VALVE-LESS SERVOMECHANISM

Kenichi HIRANO, Hirohisa TANAKA

Graduate School of Engineering
Division of Mechanical Engineering
Yokohama National University
79-5 Tokiwadai, Hodogaya, Yokohama, Kanagawa, 240-8501 Japan
(E-mail : kehirano@ynu.ac.jp)

ABSTRACT

Valve-less control is a new trend of electro-hydraulic servomechanism. It is possible to position the servo-cylinder directly by controlling the fluid volume discharged from an AC-servomotor drive pump. This paper discusses performance of this system on the point of preciseness, responsibility and stability. It shows efficiency of the system at low power.

KEYWORDS

AC servomotor, Electro-hydraulic control, Valve-less servomechanism, Saving energy

NOMENCLATURE

A_H, A_R	:Area of cylinder
α	:Ratio of cylinder area $\dfrac{A_R}{A_H}$
C_{lp}	:Inside leakage of pump
D_m	:Discharge volume of pump
e	:Deviation of control system
K_{ce}	:Inside leakage of cylinder
K	:Bulk modulus of oil
K_a	:Amp gain
K_s	:Servo amp constant
M	:Mass
$\dfrac{d\phi}{dt}, N$	:Pump revolution
p_1, p_2	:Circuit pressure
p_l	:Equivalent pressure difference

q_1, q_2, q_3, q_4	:Circuit flow
V_H, V_R, V	:Cylinder chamber volume
y	:Cylinder displacement

INTRODUCTION

A servo-valve control system has features of high-speed responsibility and accuracy, but low efficiency of the system. Recent progress of both AC-servomotor and power electronic devices promote valve-less control of the hydraulic servomechanism for saving energy. This paper examines first the steady state position-control preciseness, step- and sinusoidal- responsibilities and next evaluates the power waste of a valve-less servomechanism energized by 1.3kW AC-servomotor driven pump. And a linear mathematical model of the mechanism is expressed.

HYDRAULIC CIRCUIT IN OPERATION

Figure1 shows a hydraulic circuit of the AC-Servomotor drive servomechanism, named as AC servo-pump.
The AC servo-pump discharges fluid to the cylinder in proportion to the electric command signal.
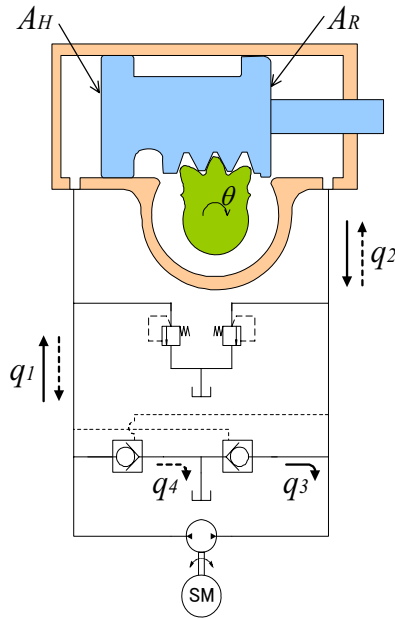
Figure 1   A schematic view of the servo cylinder with hydraulic circuit using AC servomotor

The hydraulic piston actuates a rotary-shaft through the sector gear.
This cylinder is a single-rod type and it is necessary to compensate discharged flow volume. When the cylinder piston moves right direction, flow rate q_2 is discharged from the rod-side chamber. On this case, the pump has to breathe the shortage flow-rate q_3 from reservoir.   On the other hand, when the cylinder piston moves left, oil from piston head side chamber returns to the pump suction port, and then excessive flow rate q_4 discharge to reservoir.   The rotary angle is measured by a potentiometer and its signal is feed-backed to the controller.

MODELING OF THE SYSTEM

The servo cylinder is a single-rod type, and then the displacement volume of the piston is different in right or left motion.
Flow continuity in the cylinder head chamber is

$$q_1 - C_{lp}(p_1 - p_2) = A_H \frac{dy}{dt} + \frac{V_H}{K}\frac{dp_1}{dt} \qquad (1)$$

Excessive flow rate q4 has to be discharged to reservoir.

$$C_{lp}(p_1 - p_2) + A_R \frac{dy}{dt} = q_2 + \frac{V_R}{K}\frac{dp_2}{dt} \qquad (2)$$

$$q_1 = \frac{D_m}{2\pi}\frac{d\phi}{dt} - K_{ce}(|p_1 - p_2|) \qquad (3)$$

$$q_3 = C_3 A \sqrt{p_2} \qquad (4)$$

When high pressure oil from pump flows into the cylinder-rod chamber, the return flow rate from the cylinder head excesses to the pump flow rate, which is discharged to the reservoir through the pilot operated valve.

$$C_{lp}(p_1 - p_2) + A_R \frac{dy}{dt} = q_2 + \frac{V_R}{K}\frac{dp_2}{dt} \qquad (5)$$

$$(q_1 - q_4) - C_{lp}(p_1 - p_2) = A_H \frac{dy}{dt} + \frac{V_H}{K}\frac{dp_1}{dt} \qquad (6)$$

$$q_4 = C_4 A \sqrt{p_1} \qquad (7)$$

$$q_4 = C_4 A \sqrt{p_1} \qquad (8)$$

where C_{lp} is leakage coefficient of the cylinder, K is bulk modulus of oil, V_H, V_R are cylinder chamber volume with piping inner volume.
A motion equation of the actuator is expressed as follows.

$$A_H P_1 - A_R P_2 = M \frac{d^2 y}{dt^2} + C\frac{dy}{dt} + F_D \qquad (9)$$

The cylinder displacement y is transformed output angle θ through by sector gear.

$$\theta = Ly \qquad (10)$$

Motion equations of AC servomotor and hydraulic pump describe as follows.

$$\frac{d\phi}{dt} = K_s e_i \qquad (11)$$

$$e = \theta_0 - \theta \qquad (12)$$

$$e_i = K_a e \qquad (13)$$

$$J_m \frac{d^2\phi}{dt^2} + B_1 \frac{d\phi}{dt} = \tau \qquad (14)$$

$$\tau = Jp\frac{d^2\phi}{dt^2} + B2\frac{d\phi}{dt} + \frac{Dm}{2\pi}(p1 - p2) + F_P \quad (15)$$

where Ks is servomotor constant, Jm, JP are moment of inertia servomotor and pump respectively, Dm is discharge volume of pump.

This system is not a linear system because hydraulic oil paths differ from by depending on the movement direction of the cylinder. Assuming to ignore terms of a little influence in the equations, we can get a linear system as shown next chapter.

A LINEAR MODELING OF THE SYSTEM

Both sides of the cylinder piston area are not the same, so that it cannot generally apply using usual pressure difference to simplify equations of the system. Substituting 'equivalent pressure difference pl' into the relevant equations, as a result, we can simplify the equations as follows.

$$\alpha = \frac{AR}{AH} \quad (16)$$

$$pl = p1 - \alpha p2 \quad (17)$$

$$AH(pl) = M\frac{d^2y}{dt^2} + C\frac{dy}{dt} + FD \quad (18)$$

Assuming $ql = q1 \cong q2$ at Eq. (5),(6)

Substituting Eq. (17) into Eq. (5) and (6), we obtain equations as follows.

$$ql - Clp(pl) = AH\frac{dy}{dt} + \frac{V}{2K}\frac{dpl}{dt} \quad (20)$$

$$ql = \frac{Dm}{2\pi}\frac{d\phi}{dt} - Kce(|pl|) \quad (21)$$

$$\frac{d\phi}{dt} = Ksei \quad (22)$$

$$e = \theta_0 - \theta \quad (23)$$

$$ei = Kae \quad (24)$$

Block diagram of angle control system shows in Figure 2.
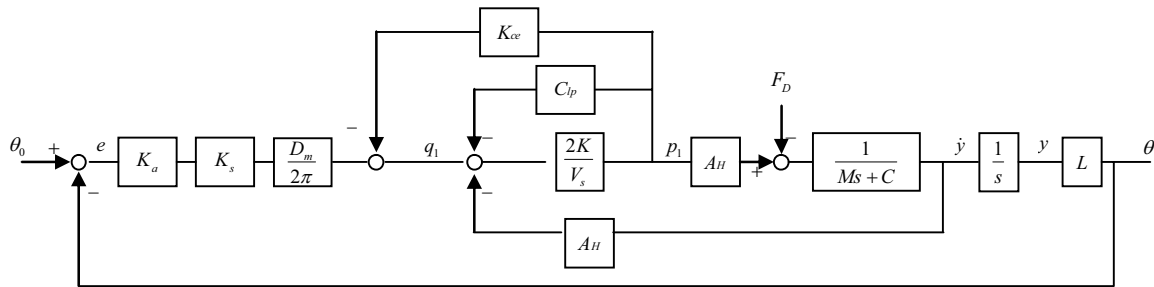
Figure 2   Block diagram of the angle control system using the valve-less servomechanism

We can obtain Eq. (25) by rearranging the block diagram shown in Figure 2.

$$\theta = \frac{KaKs\dfrac{Dm}{2\pi}AH}{\dfrac{VM}{2K}s^2 + (KcM + \dfrac{VC}{2K})s + KcC + AH2}\frac{1}{s}L \cdot e \quad (25)$$

A block diagram of Eq. (25) is shown in Figure 3.
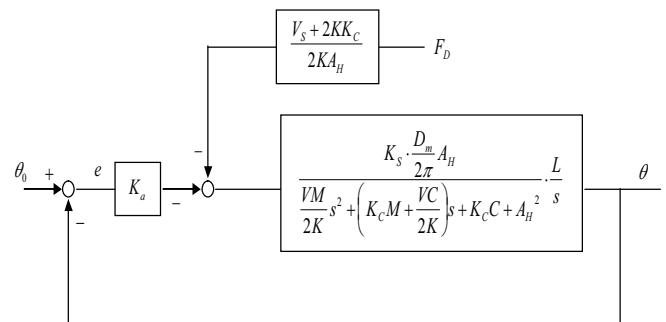
Figure 3   Block diagram of the valve-less servomechanism expressed by using Eq. (25)

Replacing new variables into each term of a fraction in Eq. (25), we can get simplified equation as shown in Eq. (26).

$$G(s) = \frac{\theta(s)}{e(s)} = \frac{kp}{(\frac{s^2}{\omega^2} + 2\varsigma \frac{s}{\omega} + 1)} \frac{1}{s} \qquad (26)$$

where

$$\omega = \sqrt{\frac{2KA_H{}^2}{VM}} \quad , \quad \varsigma = \frac{Kc}{A_H}\sqrt{\frac{KM}{2V}} + \frac{C}{A_H}\sqrt{\frac{V}{2KM}} \quad ,$$

$$kp = \frac{KaKsD_m}{2\pi A_H} L$$

We evaluate the system stability of Eq. (26) by applying in Hurwitz criterion.

$$\frac{kp}{\omega} \langle 2\varsigma \qquad (27)$$

Characteristic equation of the system has 3 orders of polynomial in s. We can get stability condition as shown in Eq. (27). The system has stability, if proper figures setting into K_a satisfy the condition of Eq. (27).

Evaluating of eq. (27), it is shown in $\omega = 1,890$ **rad/s**, and $\frac{kp}{\omega} = 0.016$. It means that the system is stable if ς is more than 0.08.

EXPERIMENTAL RESULTS

A gain tuning of the system has only adjusted proportional gain. Test result of a static characteristics is shown in Figure 4, which has a good linearity without hysteresis.
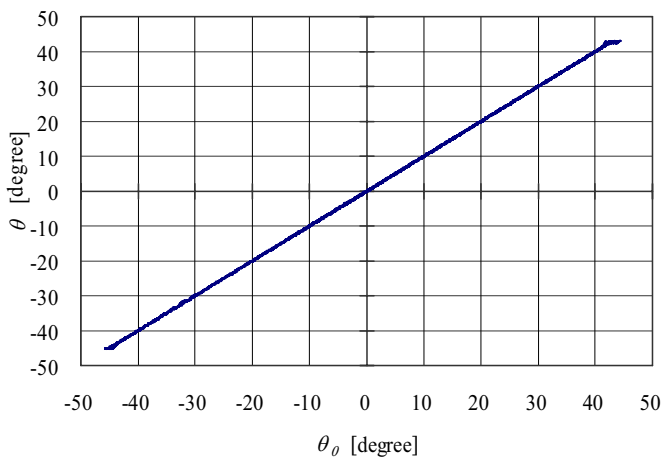
Figure 4 Static characteristic of command vs. output shaft angle
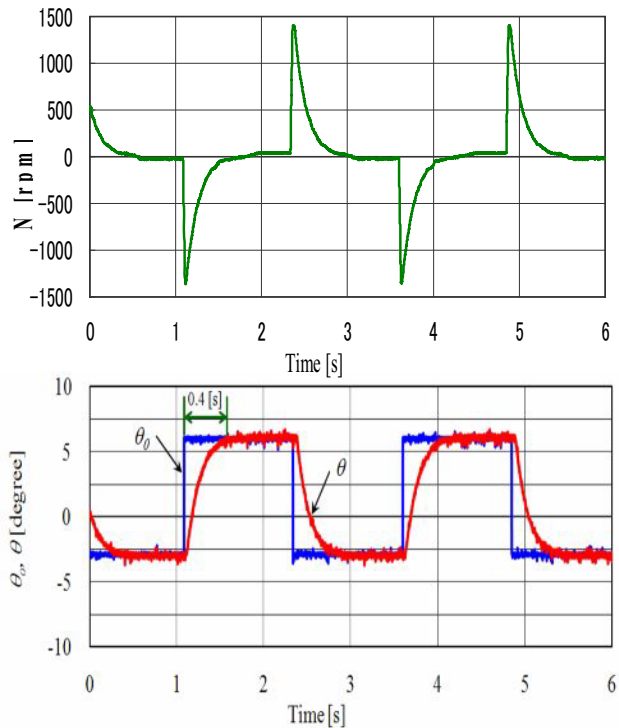
Figure 5 Step response of 10% command signal
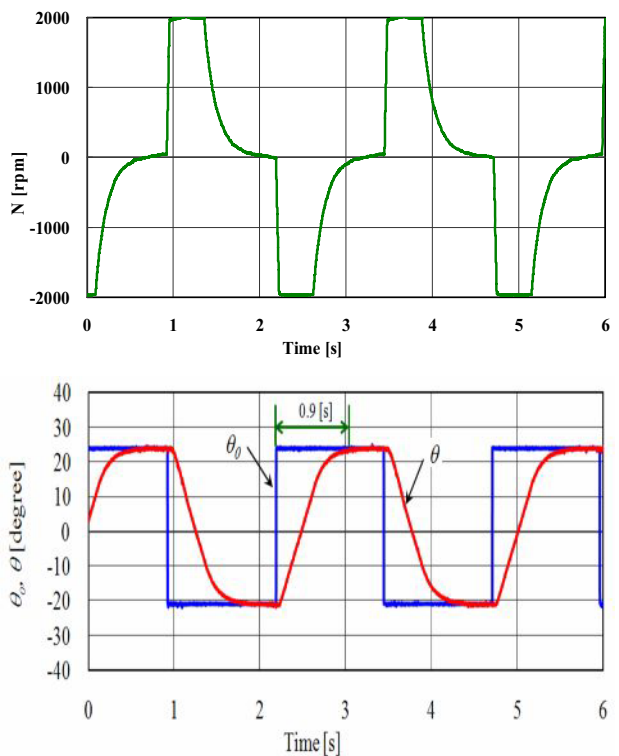
Figure 6 Step response of 50% command signal

Figure 5 and 6 show step responses of rotary angle θ and servo-motor rotational speed N at 10% and 50% amplitude, respectively. We can see that the delay at 10% amplitude is only 0.4s, while it is 0.9s at 50% due to the saturation of motor-speed at Nmax=2000rpm.

Bode diagram of the system is shown in Figure 7. The frequency response is expressed 1.2 Hz at -3dB.
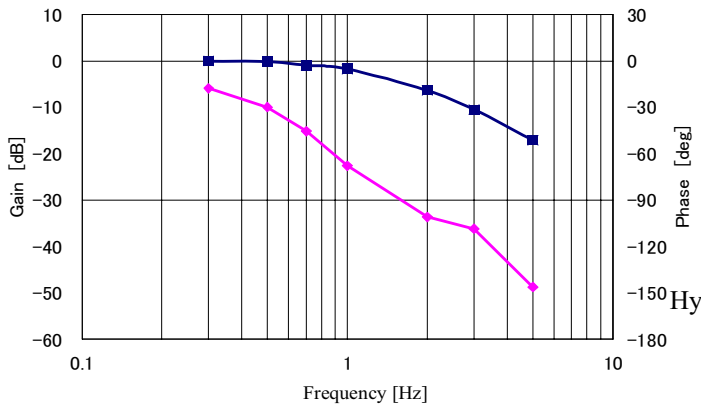
Figure 7 Bode diagram at 10% amplitude command

Experiments of efficiency have conducted under low inertia load, that sinusoidal command signal provides the system. Electric power consumption is measured by a wattmeter in supply line of AC 200V connecting with AC servo amp. The hydraulic output power are also measured.
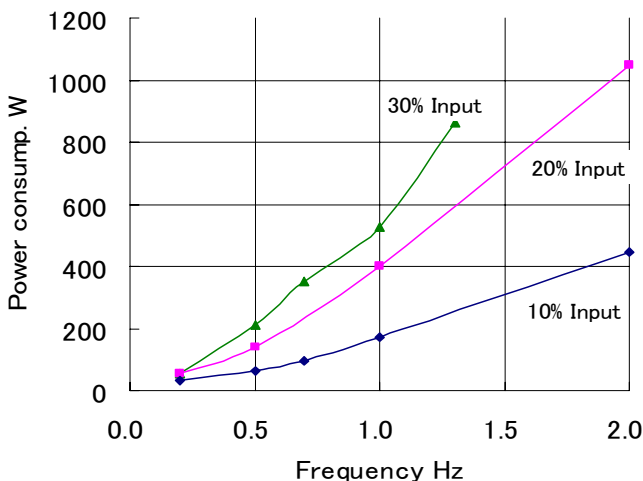
Figure 8 Measured electric power of the AC servo pump in sinusoidal motion of the piston with 10 to 30% amplitude
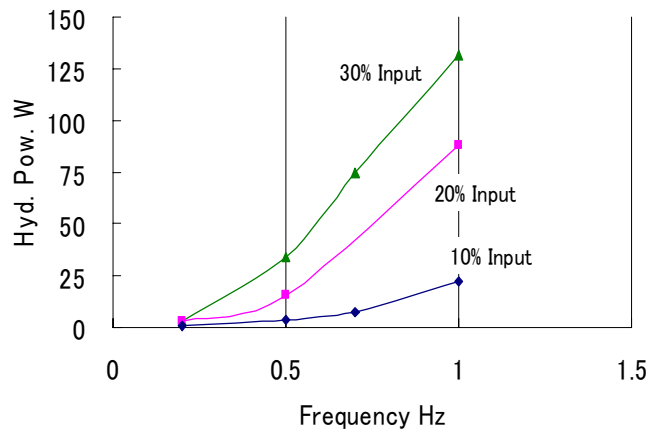
Figure 9 Measured hydraulic power of the AC servo pump in sinusoidal motion of the piston with 10 to 30% amplitude

Mass of the system assesses only 16.6kg. And force of mass inertia is low because of within a few Hz, it can neglect. Servo amp for 1.3kW AC servomotor consume about 40W in case of no operation.

We can realize that electric power consumptions increase in proportion to the frequency as shown in Figure 8.

Hydraulic output power shows in Figure 9 on measuring under the same condition of Figure 8, evaluate average hydraulic power from test results. Figure 10 shows efficiency η of the valve-less servo system, which is ratio of hydraulic output power and electric power consumption.
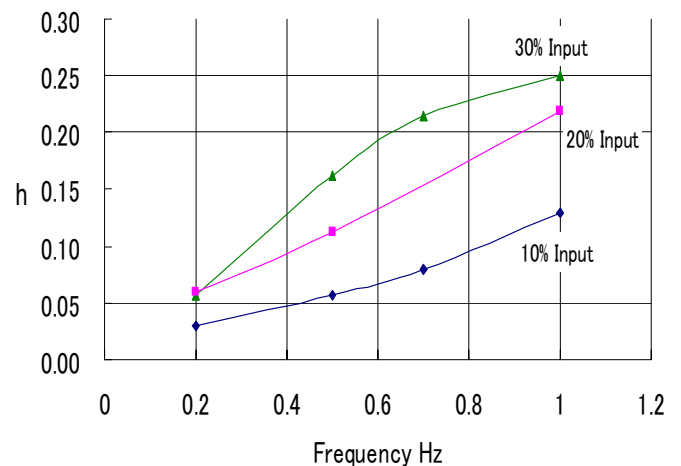
Figure 10 Efficiency of the valve-less servomechanism at low inertia load

On the other hand, we evaluate efficiency of ordinary servo system.
Assuming generating the same output hydraulic power shown in Figure 9, hydraulic power supply for ordinary servo system needs at least 2.4kW, which means flow rate 12l/min and 12MPa. Calculated efficiency ηs of the ordinary servo system, is shown in Figure 11.
Efficiency ηs of ordinary servo system attains only up to 5% under 30% amplitude at 1Hz, as a result.
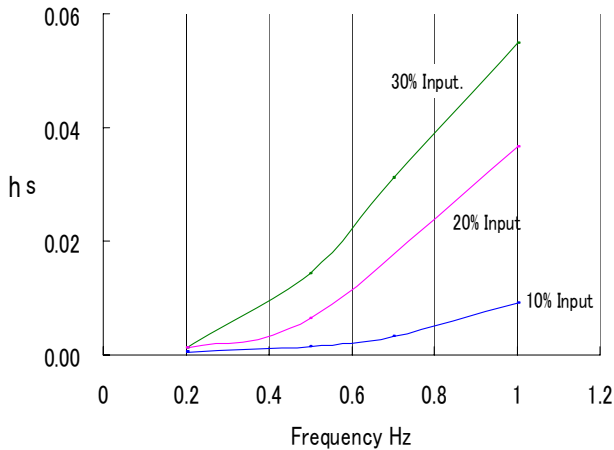
Figure 11 Efficiency of the valve-less servomechanism at low inertia load and *Ps*=12MPa

On the contrary, efficiency of the valve-less servomechanism is about 25% under 30% amplitude at 1Hz.
The efficiency of the valve-less servomechanism is obviously superior to ordinary servo system.
It shows that features of valve-less servomechanism and hydraulic rotational speed control.

CONCLUSION

This paper examines the control preciseness and response speed of the valve less servo actuator driven by a 1.3kW AC servo-pump. It controls a rack and pinion cylinder piston with adequate linearity and low hysteresis as shown in Figure 4, and positions the rotary actuator with 17kg mass within a short lag time of 0.4s under the range of maximum rotational speed of 2000rpm of the AC servo motor as shown in Figure 5. The efficiency of the valve-less control system at a 1Hz sinusoidal oscillation of the mass is about 25%, while the current valve control system is estimated only 5.5% as shown in Figures 10 and 11. The valve-less control system has potential to be applied not only to injection molding machinery but also to construction machinery, automobile auxiliary control systems and train suspensions.

REFERENCES

1. Yamaguti, Tanaka, Hydraulics and Pneumatics Engineering, Corona pub., 1986 (in Japanese)
2. Tanaka, Digital control and its application for Hydraulics and Pneumatics, Kindai-tosho pub., 1987 (in Japanese)
3. Hirano, Oba, Recent trend of hydraulic power saving systems, Vol.32-4, 2001, p225/230 (in Japanese)

P2-09

A COMPARISON OF AN AC-SERVO MOTOR DRIVING VARIABLE ROTATIONAL SPEED AND A VARIABLE DISPLACEMENT PUMP-CONTROLLED SYSTEMS FOR VELOCITY CONTROL

Mao-Hsiung CHIANG[1], Yih-Nan CHEN[1,3] and Chung-Chieh CHEN[2]

[1] Department of Engineering Science and Ocean Engineering,
National Taiwan University
106 Taipei, Taiwan
(E-mail: mhchiang@ntu.edu.tw)

[2] Graduate Institute of Automation and Control,
National Taiwan University of Science and Technology,
106 Taipei, Taiwan

[3] Department of Mechanical Engineering,
Tatung University
Taipei, Taiwan

ABSTRACT

In the hydraulic servo control applications, hydraulic valve-controlled systems, which have a problem of low energy efficiency, are used mostly because of the high response characteristics. Hydraulic pump-controlled servo systems have high energy-efficiency. However, the conventional pump-controlled systems, which are altered by displacement via variable displacement pumps, have lower response. This paper aims to investigate the servo performance of the high response and high energy efficiency electro-hydraulic pump-controlled system driven by a variable rotational speed AC servo motor in comparison with the conventional pump-controlled systems which are altered by displacement via variable displacement pumps. For that, the control strategy, adaptive fuzzy sliding-mode controller (AFSMC) is introduced. The AFSMC can not only simplify the fuzzy rule base but also estimate the equivalent control force and online self-tune the rule base through the adaptive strategy. The developed high response variable rotational speed electro-hydraulic pump-controlled system controlled by AFSMC and the conventional variable displacement pump-controlled system (VDPCS) are implemented and verified experimentally for velocity control with various velocity targets and external loading conditions. Furthermore, the energy efficiencies of different experiments are analyzed and compared precisely by the power quality recorder used to measure the electrical power consumed by the AC servo motor.

KEY WORDS

AC servo motor, Variable rotational speed, Variable displacement pump, Velocity control

INTRODUCTION

The present hydraulic systems are requested for both high response and high energy-efficiency. In view of the hydraulic circuits, two different hydraulic systems are classified, such as hydraulic valve-controlled system

and hydraulic pump-controlled system [1]. The hydraulic valve-controlled systems have high response but low energy-efficiency. Some researches have focused on the improvement of energy-efficiency of the hydraulic-valve-controlled systems [2-6]. However, it is still lower than that of the hydraulic pump-controlled system [5-6]. Hydraulic pump-controlled systems have high energy efficiency. However, the conventional pump-controlled systems that are altered by displacement have lower response. Recently, high response pump-controlled systems driven by AC servo motors are introduced [7-10]. The investigations on high response and high efficiency pump-controlled systems are still in progress.

This paper aims to investigate the servo performance of the high response and high energy efficiency electro-hydraulic pump-controlled system driven by a variable rotational speed AC servo motor in comparison with the conventional pump-controlled systems which are altered by displacement via variable displacement pumps. For that, the control strategy, adaptive fuzzy sliding-mode controller (AFSMC) is introduced. The AFSMC can not only simplify the fuzzy rule base but also estimate the equivalent control force and online self-tune the rule base through the adaptive strategy. The AC servo motor driving variable rotational speed pump-controlled system (VRSPCS) and the variable displacement pump-controlled system (VDPCS) controlled by AFSMC are implemented and verified experimentally for velocity control under external loading condition. Furthermore, the energy efficiencies of the experiments are analyzed and compared precisely by the power quality recorder used to measure the electrical power consumed by the power supply systems.

THE LAYOUT OF EXPERIMENTAL SYSTEM

The test rig layout of the variable rotational speed pump-controlled system (VRSPCS) and the variable displacement pump-controlled system (VDPCS) shown in Fig.1 is set up for experimentally investigating the dynamic behaviors of the control system in this paper. The test rig can be divided into four subsystems, including the hydraulic servo cylinder system, the hydraulic power supply system, the disturbance system and the PC-based control system. The specifications of the main components are listed in Table 1.
The hydraulic servo cylinder system contains a double-rod symmetrical hydraulic cylinder fitted with a linear encoder with the resolution of 0.1 μm. The hydraulic power supply system of VRSPCS consists of a swash plate axial piston pump with constant displacement of 12 ml/rev and is driven by an AC servo motor. In the velocity control of the VRSPCS, the motion of the controlled cylinder is regulated directly by

the volume flow of the constant displacement pump, i.e. the motion of the controlled cylinder is controlled directly by the rotational speed of the AC servo motor. Thus, the control input signals of the AC servo motor are given from the PC-based controller via a D/A converter and enlarged by a servo amplifier. On the other hand, the hydraulic power supply system of
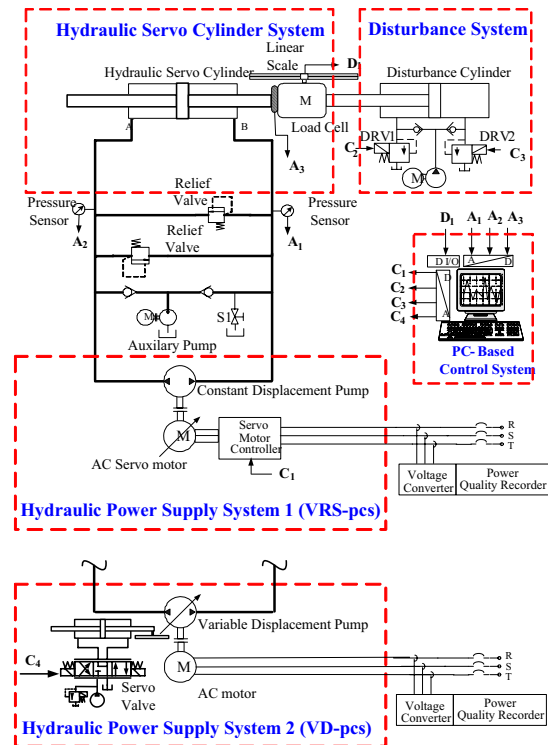

Figure 1 The layout of test rig

Table 1 Main components' specifications

Components	Specifications
AC servo motor	3ψ 220V, 7.0kW Rated rotational speed: 2000 rpm
Hydraulic axial piston pump	Max. pressure: 40 MPa Fixed displacement: 12 ml/rev
Hydraulic servo cylinder	Max. stroke: 400mm Piston /Rod diameter: 80/45mm
Disturance cylinder	Max. stroke: 400mm Piston /Rod diameter: 80/45mm
Optical encoder	Range: 500 mm Resolution: 0,1 μm
Load cell	Range: 111kN/10V
PC-based controller	AMD K6-2 450/512MB
Power quality recorder	Max. sampling rate: 10K/sec A/D resolution: 12bit ±1LSB Freq. response: 25KHz

VDPCS consists of a swash plate axial piston pump with variable displacement, a swash plate control unit and an AC motor. The maximum displacement of the variable displacement pump is 12 ml/rev at rotational speed 1700rpm. The swash plate control unit alters the swash plate's angle for changing the pump's displacement. The swash plate control unit contains a small hydraulic valve-controlled cylinder system for adjusting the swash plate angle. In the velocity control of the VDPCS, the motion of the controlled cylinder is regulated directly by the volume flow of the variable displacement pump. Thus, the control input signals of the motion control are given from the PC-based controller to the servo valve of the swash plate control unit via a D/A converter.

The velocity signals are generated by the digital differential of position signals that are measured by the linear encoder and fed back to the PC-based controller. The force signal is measured by the load cell and fed back to the PC-based controller. The overall electrical power supplied to the electro-hydraulic pump-controlled system is measured by the power quality recorder for energy efficiency analysis and comparison. Besides, the disturbance system, including a disturbance cylinder, two relief valves and a gear pump, is used here to generate external disturbance forces, which can be determined by setting the pressure of the relief valves DRV1 and DRV2, for the different loading conditions of experiments.

CONTROL STRATEGY AND CONTROLLER DESIGN

Fuzzy sliding mode control

Hwang et al. [12] proposed the methods to design the fuzzy sliding-mode controller for a non-linear system with 2nd order where the error and the error change rate were used to synthesize fuzzy reasoning rules. However, the rule number was larger and did not give the mathematical expression. This paper adopts the sliding surface $S = 0$ and extends it to the fuzzy sliding surface $\tilde{S} = \tilde{0}$, and make S be a linguistic description of $\tilde{S}$. The fuzzy rules are given in the following form

$$R^l : \text{IF } S \text{ is } \tilde{F}_s^l \text{ THEN } u_{fs} \text{ is } \tilde{F}_u^{8-l}, \ l = 1, ..., 7. \tag{1}$$

According to the sup-min compositional rule of inference and the defuzzification accomplished by the center-of-area method, the mathematical expression can be derived as

$$u_{fs} = \begin{cases} 1 & , if & z < -1 \\ \dfrac{7.5z^2 + 13.5z + 5}{9z^2 + 15z + 5} & , if & -1 \le z < -\dfrac{2}{3} \\ \dfrac{9z^2 + 11z + 2}{18z^2 + 18z + 2} & , if & -\dfrac{2}{3} \le z < -\dfrac{1}{3} \\ \dfrac{1.5z^2 + 1.5z}{9z^2 + 3z - 1} & , if & -\dfrac{1}{3} \le z < 0 \\ \dfrac{-1.5z^2 + 1.5z}{9z^2 - 3z - 1} & , if & 0 \le z < \dfrac{1}{3} \\ \dfrac{-9z^2 + 11z - 2}{18z^2 - 18z + 2} & , if & \dfrac{1}{3} \le z < \dfrac{2}{3} \\ \dfrac{-7.5z^2 + 13.5z - 5}{9z^2 - 15z + 5} & , if & \dfrac{2}{3} \le z < 1 \\ -1 & , if & z \ge 1 \end{cases} \tag{2}$$

where $z = \dfrac{S}{\Phi}$, and when $|S| \ge \Phi$, it is easy to check

$$u_{fs} = -\text{sgn}(S)$$

Adaptive fuzzy sliding-mode controller

The state equations of the pump-controlled system model can be achieved as follows

$$\begin{aligned} x_1 &= \dot{x}_p(t) \\ \dot{x}_1 &= x_2(t) \\ \dot{x}_2 &= -\sum_1^2 a_i x_i(t) + g(\underline{x})u + d(\underline{x}) = f(\underline{x}) + g(\underline{x})u + d(\underline{x}) \end{aligned} \tag{3}$$

in which $f(\underline{x})$ is the dynamic function of the pump-controlled system, $g(\underline{x})$ is a constant with positive value, and $d(\underline{x})$ is the disturbance function. Define the tracking error $e(t)$ as

$$e(t) = \dot{x}_d(t) - \dot{x}_p(t) \tag{4}$$

where $\dot{x}_p(t)$ indicates the control output and $\dot{x}_d(t)$ is the velocity target. Define a sliding surface as

$$S(t) = \dot{e}(t) + k_1 e(t) \tag{5}$$

Where k_1 is non-zero positive constants. Assume that parameters in Eq. (3) are well known and the external disturbance is measurable, then the control law can be derived as

$$u^* = g^{-1}(\underline{x})[\eta S_\Delta(t) - f(\underline{x}) - d(\underline{x}) + \ddot{x}_d + k_1 \dot{e}(t)] \tag{6}$$

where $S_\Delta(t) = S(t) - \Phi \text{sat}(S(t)/\Phi)$ and Φ is the boundary layer width of sliding surface S. The

properties of the function S_Δ are described as below in the design of adaptive law [11].

Property 1: As $|S| > \Phi, \Rightarrow |S_\Delta| = |S| - \Phi$ and $\dot{S}_\Delta = \dot{S}$.

Property 2: As $|S| \leq \Phi, \Rightarrow S_\Delta = \dot{S}_\Delta = 0$.

Differentiate Eq. (5) as

$$\dot{S}(t) = -f(\underline{x}) - g(\underline{x})u - d(\underline{x}) + \ddot{x}_d + k_1\dot{e}(t) \qquad (7)$$

Substituting Eq. (6) into Eq. (7) gives

$$\dot{S}(t) + \eta S_\Delta(t) = 0, \qquad \eta > 0. \qquad (8)$$

Eq. (8) shows that $\underline{e}(t) = [e(t), \dot{e}(t)]$ will converge to the neighbourhood of zero as $t \to \infty$, and the value of the neighbourhood depends on the value of Φ. However, the system parameters may be unknown or perturbed; the controller u^* cannot be precisely implemented. Therefore, by the universal approximation theorem, for any $\rho^* > 0$, an optimal fuzzy control $\hat{u}_{fz}(S, \underline{\alpha}^*)$ exists that satisfies

$$\left|u^* - \hat{u}_{fz}(S, \underline{\hat{\alpha}}^*)\right| \leq \rho^* \qquad (9)$$

where ρ^* is assumed to be bounded by $|\rho^*| \leq M_\rho$. Utilize a fuzzy controller $\hat{u}_{fz}(S, \underline{\hat{\alpha}})$ to approximate u^* as

$$\hat{u}_{fz}(S, \underline{\hat{\alpha}}) = \underline{\hat{\alpha}}^T \underline{\xi} \qquad (10)$$

where $\underline{\hat{\alpha}}$ is the estimated values of $\underline{\alpha}^*$. The control law for the developed adaptive fuzzy sliding-mode controller (AFSMC) is defined as the following form:

$$u = \hat{u}_{fz}(S, \underline{\hat{\alpha}}) + u_{comp}(S) \qquad (11)$$

where the fuzzy controller $\hat{u}_{fz}$ is designed to approximate the controller u^* and the fuzzy sliding-mode compensation u_{comp} is proposed to compensate the difference between the controller u^* and fuzzy controller $\hat{u}_{fz}(S, \underline{\hat{\alpha}})$. Through Eqs. (6), (7) and (11), the dynamic equation can be derived as:

$$\dot{S}(t) + \eta S_\Delta(t) = g[u^* - \hat{u}_{fz}(S, \underline{\hat{\alpha}}) - u_{comp}(S)] \qquad (12)$$

For ensuring convergence to the boundary layer, the adaptive laws of the AFSMC are chosen as

$$\dot{\underline{\hat{\alpha}}} = \eta_1 \cdot S_\Delta \cdot \xi(S) \qquad (13)$$

$$u_{comp}(S) = -\hat{\rho} \cdot u_{fs} \qquad (14)$$

$$\dot{\hat{\rho}} = \eta_2 \cdot |S_\Delta| \qquad (15)$$

Controller Design
The proposed AFSMC strategy will be implemented experimentally for the velocity control of the pump-controlled system through choosing the suitable control parameters g_s, g_u, the parameters k_1 in the sliding surface and the learning rate parameters (η_1, η_2).

EXPERIMENTS

Velocity control for velocity target 90mm/s
The velocity controls of the VRSPCS and VDPCS are implemented experimentally using AFSMC for velocity target 90mm/s with constant external loading force of 30 kN. Fig.2 indicates the experiment results of the velocity control response and the control error. The rising time of the velocity responses in VRSPC can reach 0.298 sec, and the settling time can be controlled within 0.438 sec. However, the rising time of the velocity responses in VDPCS is 0.375 sec, and the settling time is 0.654 sec. Furthermore, the transient state in VRSPCS is more stable compare to that in VDPCS. Thus, the high response performance in the VRSPCS is verified. Fig.2(b) schematically depicts the zoom in of the steady-state errors that can be controlled within 0.31 mm/s in the VRSPCS and within 0.25 mm/s in the VDPCS respectively. The excellent performance on velocity control accuracy can be clarified in the VRSPCS and VDPCS. The comparison of performance, including the rising time, the settling time and the steady state error is summarized in Table 2.

Energy efficiency in the velocity control
The power consumption in the experiment of velocity control, as shown in the above paragraph, is discussed in this section. The overall electrical power P_{in} supplied to the electro-hydraulic pump-controlled system is directly measured by the power quality recorder. The output power P_{out} of the controlled cylinder can be described as

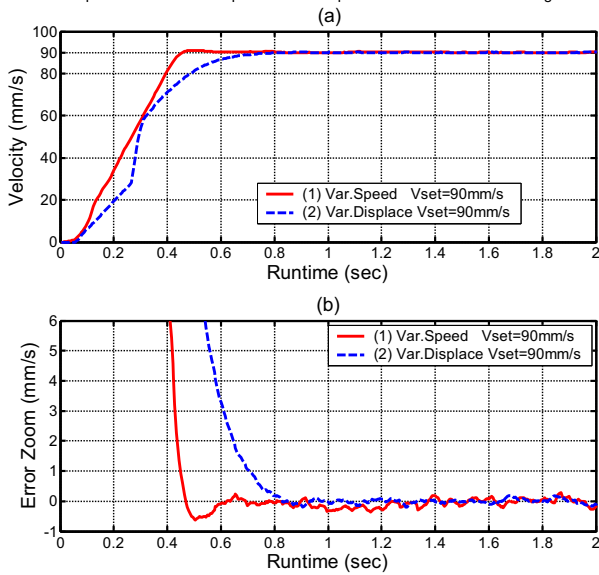$$P_{out} = F \cdot \dot{x} \qquad (16)$$

Figure 2 Experimental results of velocity control for velocity target 90mm/s under loading force 30kN in VRSPCS and VDPCS:(a) velocity control response (b) control error

Table 2 Comparison of velocity control performance for the velocity targets 90mm/s in VRPCS and VDPCS

Targets	VRSPCS	VDPCS
Rising time t_r (10~90%)	0.298 sec	0.375 sec
Settling time t_s (e < 2%)	0.438 sec	0.654 sec
Steady state error e_{ss}	0.31mm/s (0.34%)	0.25mm/s (0.27%)

where F and $\dot{x}$ are the output force and velocity of the controlled cylinder respectively. The output force is directly measured by the load cell, as shown in Fig.3. The feedback velocity signals are generated by the digital differential of position signal measured by the linear encoder. The supply power P_{in} and the output power P_{out} for the velocity control of 90 mm/s in the VRSPCS and VDPCS are shown in Fig.4(a) and Fig.4 (b) respectively. It is clear that the supply power is much less in the VRSPCS than in the VDPCS. The energy efficiency in the stead state can reach over 80% in the VRSPCS and can reach about 55% in the VDPCS, as shown in Fig.5. Consequently, the performance of high energy efficiency of the VRSPCS is evidenced.
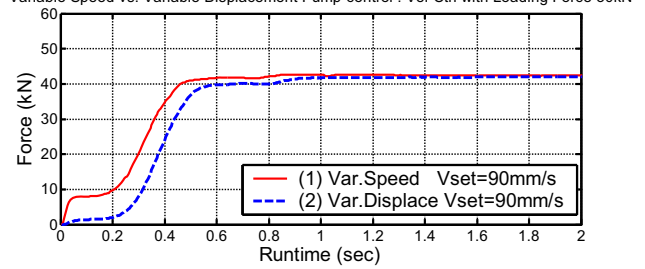
Figure 3 Output forces in the experiments of velocity control for velocity target 90mm/s under loading force 30kN in VRSPCS and VDPCS
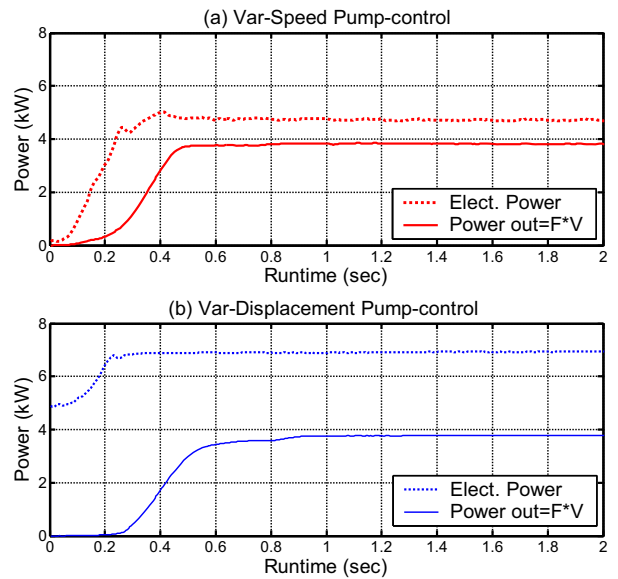
Figure 4 Supply power and output power in the experiments of velocity control for velocity target 90mm/s under loading force 30kN in VRSPCS and VDPCS.
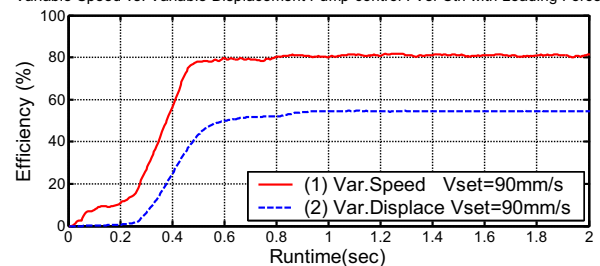
Figure 5 Energy efficiency in the experiments of velocity control for velocity target 90mm/s under loading force 30kN in VRSPCS and VDPCS.

633

CONCLUSIONS

1. This investigation developed a new electro-hydraulic pump-controlled system driven by the AC servo motor and axial piston pump for realizing velocity control with both high response and high energy-efficiency instead of the conventional variable displacement pump-controlled systems. For achieving better velocity control performance, adaptive fuzzy sliding-mode controller is used. The experimental results show that the VRSPCS realizes the performance of high response and little steady-state error.

2. The comparison of the velocity control performance and the energy efficiency measured by the power quality recorder used to measure the electrical power consumed are implemented. The energy efficiency of the VRSPCS in the velocity control for velocity target 90 mm/s under external loading force 30kN can achieves over 80%. It is evident that the VRSPCS realizes the performance of high energy efficiency.

REFERENCES

1. Murrenhoff H, "Servohydrualik" (in German), Lecture notes, RWTH Aachen University, Germany, (1998).

2. Backé, W and Feigel H-J, "Neue Möglichkeiten beim Electro-hydraulischen Load-Sensing" (in German), O+P Ölhydraulik und Pneumatik 34, No.2, (1990), pp. 106-114.

3. Esders H, "Elektrohydraulisches Load-Sensing für Mobile Anwendungen", (in German), O+P Ölhydraulik und Pneumatik 36, Nr.8, (1994), pp.473-480.

4. Kim S-D, Cho H-S and Lee C-O, "Stability Analysis of a Load-Sensing Hydraulic System", Proc. of the Institute of Mechanical Engineers, Part A: Power and Process Engineering, Vol.202, No.A2, (1988), pp.79-88.

5. Chiang M-H and Chien Y-W, "Parallel control of velocity control and energy-saving control on a hydraulic valve controlled system using self-organizing fuzzy sliding mode control", JSME International Journal, Series C, Vol.46, No.1, (2003), pp.224-231.

6. Chiang M-H, Lee L-W, Tsai J-J, "Concurrent implementation of high velocity control performance and high energy-efficiency for hydraulic injection moulding machines", International Journal of Advanced Manufacturing Technology, 23, (2004), pp.256–262.

7. Bildstein A, "Application of electro-hydrostatic actuators (EHA) for future aircraft primary flight control", Proc. of the 1. International Fluid Power Conference (1.IFK), Aachen, Germany, Band 1, (1998), pp.93-105.

8. Helduser S, "Electric-hydrostatic drive – an innovative energy-saving power and motion control system", Proc. of Institution of Mechanical Engineers, Vol. 213, Part I, (1999), pp.427-439.

9. Habibi S and Goldenberg A, "Design of a new high performance electro-hydraulic actuator", Proc. of the 1999 IEEE/ASME International Conference on Advanced Mechatroics, Atlanta, USA, (1999), pp.227-232.

10. Helbig A, "Injection moulding machine with electric-hydrostatic drives", Proc. of the 3. International Fluid Power Conference (3. IFK), Aachen, Germany, Vol.1, (2002), pp.67-82.

11. R. M. Sanner, J. J. Slotine, "Gaussian Network for Direct Adaptive Control", IEEE Trans. Neural Networks., vol. 3, pp. 837-863, 1992.

12. G. C. Hwang, S. Chang, "A Stability Approach to Fuzzy Control Design for Nonlinear System", Fuzzy Sets Syst., vol. 48, pp.279–287, 1992.

P2-10

UNSTEADY FRICTION CHARACTERISTIC OF HYDRAULIC

ACTUATOR AND ITS MATHEMATICAL MODEL

Hideki YANADA*, Yuta SEKIKAWA**, Kazuya TAKAHASHI*** and Akinori MATSUI****

* Department of Mechanical Engineering, Toyohashi University of Technology
1-1 Hibarigaoka, Tempaku-cho, Toyohashi, 441-8580 Japan
(E-mail: yanada@mech.tut.ac.jp)
** Fanuc Ltd. Oshino-mura, 401-0597 Japan
*** Sony Energy Devices Corporation

1-1 Shimosugishita, Takakura, Hiwada-machi, Koriyama, 963-0531 Japan
**** Graduate student, Department of Mechanical Engineering,
Toyohashi University of Technology

ABSTRACT

This paper deals with unsteady-state friction characteristics of a hydraulic actuator. Using a single rod hydraulic cylinder, friction characteristics are experimentally investigated under various conditions of velocity variation at different supply pressures. The friction force of the hydraulic cylinder is measured based on the equation of motion using measured values of the pressures in the cylinder chambers and the acceleration of the hydraulic piston. A method to identify dynamic parameters included in the modified LuGre model, which has been proposed by Yanada and Sekikawa, is proposed. Comparison between measured unsteady-state friction characteristics and those simulated by the modified LuGre model is conducted. It is shown that the unsteady-state friction characteristics simulated using the parameters identified agree with those obtained by experiments with a relatively good accuracy and that the proposed method to identify the dynamic parameters is appropriate. The effect of the supply pressure on the friction characteristics and the dynamic parameters are shown.

KEY WORDS

Hydraulic actuator, Unsteady friction, Mathematical model, Modified LuGre model, Parameter identification

NOMENCLATURE

A_i : piston area (i=1,2)
a : acceleration
F_c : Coulomb friction force
F_r : friction force

F_{rss} : steady-state friction force
F_s : maximum static friction force
$\mathbf{f}$: observer gain vector
g : Stribeck function
h : dimensionless unsteady-state lubricant film thickness

h_{ss} : dimensionless steady-state lubricant film thickness

K_f : proportional constant for lubricant film thickness

m : load mass

n : exponent for Stribeck curve

p_i : pressure (i=1,2)

p_s : supply pressure

t : time

t_d : dwell time

u : control input (servo current)

v : velocity

v_b : upper (for $v>0$) or lower (for $v<0$) limit of velocity range where h_{ss} or h is varied

v_s : Stribeck velocity

x_p : piston position

z : mean deflection of bristles

σ_0 : stiffness of bristles

σ_1 : micro-viscous friction coefficient for bristles

σ_2 : viscous friction coefficient

τ_h : time constant for lubricant film dynamics

τ_{hp} : time constant for acceleration period

τ_{hn} : time constant for deceleration period

τ_{h0} : time constant for dwell period

INTRODUCTION

Accurate modeling of static and dynamic characteristics of each fluid power component is very important to analyze the performance and/or dynamics of or to predict the behaviors of a fluid power system. Friction is always present in fluid power components having sliding parts and especially that of a fluid power actuator may have some undesirable influence on the performance of a fluid power system. Mathematical models to describe the steady-state friction characteristics have been proposed [1-3] and are widely used to analyze the steady-state characteristics of a fluid power actuator. However, those models are useless to predict dynamic behaviors of the actuator especially when the actuator repeats start/stop.

The unsteady-state friction characteristics of a hydraulic motor has been examined by Yanada et al. [4] by varying the rotational speed sinusoidally in one direction in the negative resistance regime. It has been shown that the friction torque traces the steady-state friction torque-velocity curve, i.e., the Stribeck curve, at very low frequencies of the velocity variation, that the negative slope of the friction torque-velocity curve is decreased as the frequency of the velocity variation is increased, and that the negative slope becomes almost null at relatively high frequencies.

Several mathematical models that describe the dynamic behaviors of friction have been proposed [5-9] and among them, the LuGre model [6] is most widely utilized. However, all the models proposed so far cannot simulate well the friction behaviors of a hydraulic motor

in the sliding regime shown in [4]. Yanada and Sekikawa have made a modification to the LuGre model by incorporating lubricant film dynamics into the model and have shown that the proposed model, called the modified LuGre model, can simulate dynamic behaviors of friction observed with a hydraulic cylinder with a relatively good accuracy [10].

However, the dynamic parameters, σ_0, σ_1, τ_h, included in the model were determined by trial and error. Regarding σ_0 and σ_1, methods to identify them have been proposed [11, 12] but those methods utilize some approximation that holds in the presliding regime. It is difficult for a hydraulic actuator to be operated in the presliding regime and, therefore, the methods proposed so far cannot be applied to hydraulic actuators. In addition, for the modified LuGre model, a new parameter, the time constant, τ_h, is added. Some method to identify those parameters needs to be developed.

In this paper, a method to identify the dynamic parameters is proposed. In addition, the effect of the supply pressure on the dynamic parameters is examined.

EXPERIMENTAL APPARATUS AND METHOD

Figure 1 shows a schema of the experimental apparatus used. A single rod hydraulic cylinder, of which stroke, internal diameter and piston rod diameter are 0.2m, 0.032m and 0.018m, respectively, is used. The hydraulic cylinder is fixed horizontally on a surface plate. Sinusoidal or step signals are supplied to the servo amplifier through a 12 bit digital-to-analogue (D/A) converter and then the velocity of the hydraulic piston is varied almost sinusoidally or reaches a constant value corresponding to the input to the servo amplifier. The pressures, p_1, p_2, in the cylinder chambers and the acceleration, a, of the piston are measured using pressure transducers and an accelerometer, respectively and are read into the computer through amplifiers and a 12 bit analogue-to-digital (A/D) converter. The piston velocity is measured using a tachogenerator by converting a linear motion of the piston to a rotational motion through a ball-screw (not shown in Fig.1). The friction force is obtained based on the equation of motion of the hydraulic piston as follows:

$$F_r = p_1 A_1 - p_2 A_2 - ma \qquad (1)$$

Steady-state friction characteristics are obtained by supplying stepwise inputs with different magnitudes to the servo valve and by measuring the steady values of the pressures and velocity. In order to examine the effect of pressure on the friction characteristics, experiments are made at the supply pressures of 3, 5 and 7 MPa. The oil temperature was kept at 303±2 K.
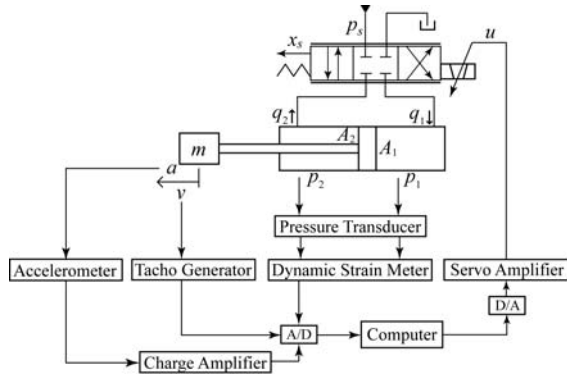
Figure 1 Schema of experimental apparatus

MODIFIED LUGRE MODEL

The Stribeck function, g, was modified by incorporating a dimensionless lubricant film thickness parameter, h. The modified LuGre model is given below.

i) Equations corresponding to the LuGre model

$$\frac{dz}{dt} = v - \frac{\sigma_0 z}{g(v, h)} v \tag{2}$$

$$g(v, h) = F_c + \left[(1 - h)F_s - F_c\right]e^{-(v/v_s)^n} \tag{3}$$

$$F_r = \sigma_0 z + \sigma_1 \frac{dz}{dt} + \sigma_2 v \tag{4}$$

ii) Lubricant film dynamics

$$\frac{dh}{dt} = \frac{1}{\tau_h}(h_{ss} - h) \tag{5}$$

$$\tau_h = \begin{cases} \tau_{hp} & (v \neq 0, \ h \leq h_{ss}) \\ \tau_{hn} & (v \neq 0, \ h > h_{ss}) \\ \tau_{h0} & (v = 0) \end{cases} \tag{6}$$

$$h_{ss} = K_f |v|^{2/3} \quad (|v| \leq |v_b|) \tag{7}$$

$$K_f = \left(1 - F_c/F_s\right)|v_b|^{-2/3} \tag{8}$$

iii) Steady-state friction characteristic

$$F_{rss} = F_c + \left[(1 - h_{ss})F_s - F_c\right]e^{-(v/v_s)^n} + \sigma_2 v \tag{9}$$

In the LuGre model, the absolute value of the velocity is usually used in the second term in Eq.(2). However, when assigning negative values to F_c, F_s and v_s for negative velocity range, the symbol of the absolute

value is not necessary. Letting h in Eq.(3) and h_{ss} in Eq.(9) be null leads to the LuGre model. The time constant shown by Eq.(6) usually takes the relation, $\tau_{hp} < \tau_{hn} < \tau_{h0}$.

All the parameters, except for $\sigma_0, \sigma_1, \tau_h$, included in Eqs.(2) to (9) can be determined from measured steady-state friction characteristics by using the least-squares method. However, the above three parameters were determined by trial and error in [10].

PARAMETER IDENTIFICATION

Identification of time constant, τ_h

In this section, methods to identify the time constant of the lubricant film dynamics are described first. The value of the second term in Eq.(4) becomes almost null except for immediately after the start from rest and for immediately after velocity reversal. Therefore, except for immediately after start and velocity reversal, the relation, $F_r = g(v, h) + \sigma_2 v$, holds and the following equation is derived:

$$h = 1 - \frac{F_r - F_c + F_c e^{-(v/v_s)^n} - \sigma_2 v}{F_s e^{-(v/v_s)^n}} \tag{10}$$

If the values of the friction force, F_r, and velocity, v, can be obtained in real time, the variation of the lubricant film thickness parameter, h, is calculated from Eq.(10). When the velocity is increased or decreased stepwise from a certain velocity, the film thickness parameter, h, is expected to be varied approximately exponentially. The time constants, τ_{hp} and τ_{hn} can be obtained by curve-fitting a calculated variation of h with time using an exponential function.

During dwell period, lubricant film thickness is decreased with time. The break-away force (maximum friction force observed immediately after start) observed at the subsequent start is expected to be larger when the dwell time is longer. Equation (11) is obtained by substituting $v = 0$ into Eq.(10) and holds only for dwell period. However, assuming that Eq.(11) approximately holds also at start after dwell period and substituting the observed break-away force into F_r of Eq.(11), the calculated film thickness can be regarded as the film thickness immediately before the start.

$$h = 1 - \frac{F_r}{F_s} \tag{11}$$

The time constant, τ_{h0}, for the dwell period can be identified by plotting the break-away force against the dwell time before the start.

Identification of σ_0 and σ_1

The stiffness, σ_0, of the bristles strongly affects the

magnitude and rise time of the break-away force. A larger σ_0 yields a larger break-away force and a shorter rise time. The value of σ_0 can be identified by comparing the magnitude and rise time of the break-away force estimated by an observer with those obtained by simulation. The value of σ_1 can be determined by using the relation $\sigma_1 = \sqrt{\sigma_0}$ [6].

Observer for friction force and velocity

The friction force is obtained from Eq.(1). In order to measure unsteady-state friction force accurately, it is necessary to measure the pressures, acceleration and velocity. However, for the purpose of the identification of the parameters included in the modified LuGre model, the accelerometer and tachogenerator are not necessarily needed. The friction force and velocity can be estimated by an observer. A Luenberger type observer can be given by

$$\frac{d}{dt}\begin{bmatrix}\hat{x}_p\\\hat{v}\\\hat{F}_r\end{bmatrix} = \begin{bmatrix}0 & 1 & 0\\0 & 0 & -\frac{1}{m}\\0 & 0 & 0\end{bmatrix}\begin{bmatrix}\hat{x}_p\\\hat{v}\\\hat{F}_r\end{bmatrix}$$
$$+\begin{bmatrix}0\\\frac{1}{m}\\0\end{bmatrix}(A_1 p_1 - A_2 p_2) + \mathbf{f}(x_p - \hat{x}_p) \qquad (12)$$

In practice, Eq.(12) is discretized.

RESULTS AND DISCUSSION

Figure 2 shows the steady-state friction characteristics measured at the supply pressures of 3, 5 and 7 MPa. Positive velocity corresponds to the extending stroke of the piston and negative one to the retracting stroke. The friction force is increased with increasing supply pressure in the extending stroke ($v>0$) but is not varied so much in the retracting stroke ($v<0$). The static parameters, the parameters that describe the steady-state friction characteristics, were determined by the least-squares method.

Figure 3 compares the measured piston velocity and friction force with the ones estimated by the observer, Eq.(12). As can be seen from Fig.3, the velocity and friction force are accurately estimated by the observer. The maximum friction force is observed immediately after the start of the motion and is called the break-away force. Maximum forces observed at and after the second cycle become smaller than the break-away force, as shown in Fig.3(b), because lubricant films are formed between sliding surfaces, which are mainly the piston packing/cylinder inner wall and the rod packing/piston rod.

Figure 4 shows an example of the dimensionless film thickness obtained when the piston velocity was increased stepwise from rest to 0.016 m/s. As shown in Fig.4, the film thickness is increased with time and its variation can well be approximated by a first-order lag element, i.e., by Eq.(5). For the case of Fig.4, the time constant was identified as τ_{hp}=0.29 s.

An example of the variation of the film thickness under a stepwise decrease (from 0.015 to 0.003 m/s at t=3 s) in the velocity is shown in Fig.5. The film thickness is decreased significantly slowly compared with the case of velocity increase (Fig.4). By curve-fitting, the time constant was identified as τ_{hn}=2.0 s for Fig.5.

Such experiments as Figs.4 and 5 were done under various velocities and the time constants were identified in a similar way.
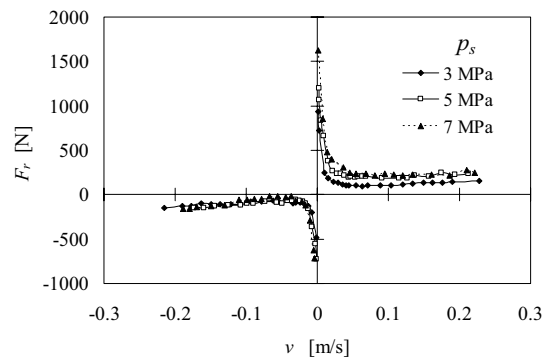
Figure 2 Steady-state friction characteristics
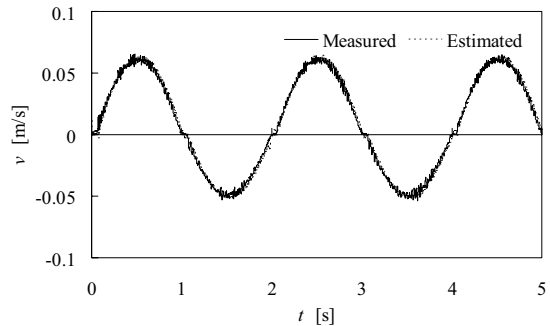
(a) Variation of piston velocity
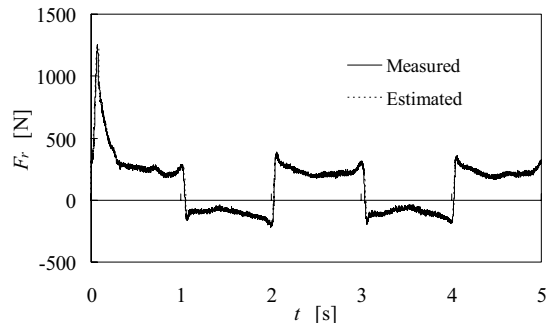
(b) Variation of friction force

Figure 3 Comparison of measured velocity and friction force with estimated ones (p_s=5MPa)
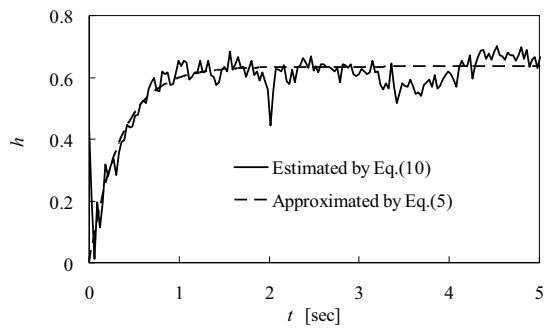
Figure 4 Example of lubricant film thickness variation under stepwise increase in velocity (v=0 to 0.016 m/s, p_s=5MPa)
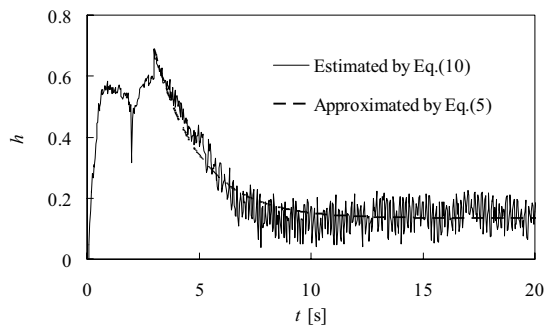
Figure 5 Example of lubricant film thickness variation under stepwise decrease in velocity (v=0.015 to 0.003 m/s, p_s=5MPa)
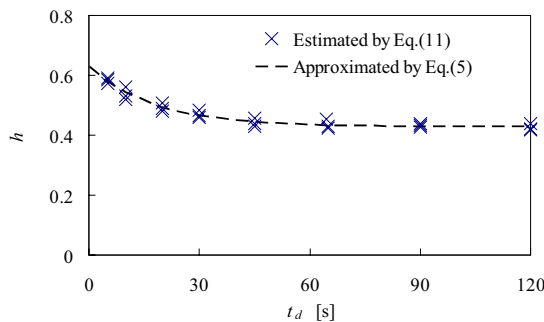

Figure 6 Film thickness variation during dwell period (p_s=5MPa)

Figure 6 shows the relation between the dwell time and the lubricant film thickness estimated by Eq.(11), into which measured break-away forces observed at starting after different dwell times are substituted. The break-away force was increased with the increase in the dwell time before starting and was saturated to a constant value. Therefore, the relation shown in Fig.6 was obtained. Curve-fitting brings a time constant of 17 s for dwell period for the case of Fig.6.

Experiments were conducted at different supply pressures and the average time constants were obtained as shown in Table 1. All the time constants for accelerating, decelerating, and dwell periods are increased with increasing supply pressure. This indicates that the oil is to some degree hard to be taken into and to be squeezed out from the sliding surfaces at higher pressures.

Table 1 Time constants at different supply pressures

p_s [MPa]	τ_{hp} [s]	τ_{hn} [s]	τ_{h0} [s]
3	0.13	1.1	8.1
5	0.28	1.8	17
7	0.32	2.4	43

The stiffness of the bristles was determined by comparing the break-away force and its rise time estimated by the observer with simulated ones. The simulation was done using MATLAB/Simulink and measured velocity wave forms were used as the input to the modified LuGre model. Experiments done under various conditions showed that the value of σ_0=10^8N/m is most appropriate and is not dependent on the supply pressure for the hydraulic cylinder used. The value of σ_1 was determined as the square root of σ_0, i.e., σ_1=10^4 Ns/m.

Figures 7 and 8 show the comparison between measured unsteady-state friction characteristics and simulated ones using the modified LuGre model, in which the identified dynamic parameters as well as the static parameters (not shown) were used. The simulation predicts larger friction force immediately before stop than the experiment (Fig.8). However, comparisons under various conditions including Figs.7 and 8 showed that the simulation results agree relatively well with the measured results. This indicates the proposed method to identify the dynamic parameters is appropriate.

CONCLUSION

In this investigation, a method to identify the dynamic parameters of the modified LuGre model was proposed and was applied to a hydraulic cylinder. In addition, the effect of the supply pressure on the unsteady-state friction characteristics was examined. Simulation results agreed relatively well with measured results. It has been demonstrated that the proposed identification method is appropriate. In addition, it has been shown that the time constant of the lubricant film dynamics is increased with increasing supply pressure and that the stiffness of bristles does not depend on the supply pressure.

REFERENCES

1. Armstrong-Helouvry B. Control of machines with friction, Kluwer Academic Publishers, 1991.
2. Armstrong-Helouvry B, Dupont P, Canudas de Wit C. A survey of models, analysis tools and compensation

methods for the control of machines with friction, Automatica, 1994, **30**-7, pp.1083-1138.

3. Hibi A, Ichikawa T. Mathematical model of the torque characteristics for hydraulic motors, Bull. JSME, 1977, **20**-143, pp.616-621.

4. Yanada H, Inaba T, Ichikawa T. Experimental approach to unsteady friction characteristics of a hydraulic motor in low-speed range, Trans. Japan Soc. Mech. Eng. (Ser. B), 1990, **56**-528, pp.2430-2437. (in Japanese)

5. Haessig D A Jr, Friedland B. On the modeling of friction and simulation, J Dynamic Systems, Measurement and Control, 1991, **113**-3, pp.354-362.

6. Canudas de Wit C, Olsson H, Åström, K J, Linschinsky P. A new model for control of systems with friction, IEEE Trans Automatic Control, 1995, **40**-3, pp.419-425.

7. Dupont P E, Dunlop E P. Friction modeling and PD compensation at very low velocities, J Dynamic Systems, Measurement and Control, 1995, **117**-1, 8-14.

8. Swevers J, Al-Bencer F, Ganseman C G, Prajogo T. An integrated friction model structure with improved presliding behavior for accurate friction compensation, IEEE Trans Automatic Control, 2000, **45**-4, pp.675-686.

9. Dupont P, Hayward V, Armstrong B, Altpeter F. Single state elastoplastic friction models, IEEE Trans Automatic Control, 2002, **47**-5, pp.787-792.

10. Yanada H, Sekikawa Y, Modeling of dynamic behaviors of friction, Mechatronics, 2008, (in press)

11. Hensen R H A, van de Molengraft M J G, Steinbuch M, Frequency domain identification of dynamic friction model parameters, IEEE Trans. Contr. Syst. Tech., 2002, **10**-2, pp.191-196.

12. Madi M S, Khayati K, Bigras P, Parameter estimation for the LuGre friction model using interval analysis and set inversion, IEEE Int. Conf. Syst. Man Cybernetics, 2004, pp.428-433.

(a) Velocity variation

(b) Measured friction force

(c) Simulation using modified LuGre model

Figure 8 Comparison between measured and simulated friction force (with dwell period, p_s=7 MPa)
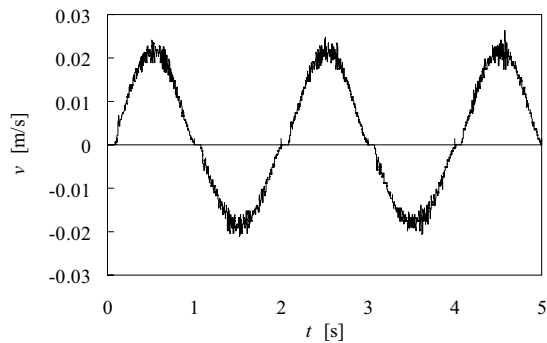
(a) Velocity variation
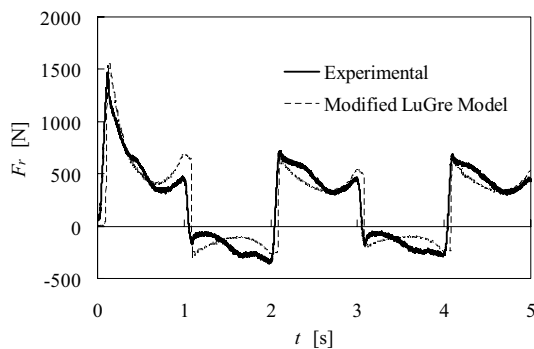
(b) Variation of friction force

Figure7 Comparison between measured and simulated friction force (without dwell period, p_s=7 MPa)

P2-11

A STUDY ON THE STRUCTUREBORNE NOISE OF

HYDRAULIC GEAR PUMPS

Antonino BONANNO, Francesca PEDRIELLI

IMAMOTER – C.N.R.
Institute for Agricultural and Earthmoving Machines of the Italian National Research Center
Via Canal Bianco 28, 44100 Cassana (Ferrara) - Italy
(E-mail: *a.bonanno@imamoter.cnr.it; f.pedrielli@imamoter.cnr.it*)

ABSTRACT

The main source of vibration and noise in hydraulic systems is the flow ripple at the pump output which interacts with the downstream components and generates pressure ripple in the current, structureborne noise in mechanical parts and airborne noise in the environment. The present research was suggested by the observation that some peaks in the airborne noise spectrum of a specific pump family were within a frequency range far from those typically related with the fluidborne or structureborne noise; unfortunately, in that range the human ear does not filter the noise efficiently.

In general, the investigation of the interaction between fluidborne noise and structurebornenoise can be carried through both "macro-analysis" techniques (sound emission analysis, pressure ripple measurement, modal analysis, etc.) and "micro-analysis" techniques (contact mechanics of gears, performance of the bearing system, etc.). The present research started from a "macro" approach inclusive of the modal analysis of a gear pump, the measurement of its pressure ripple and its acoustic mapping though the sound intensity technique. Currently, the focus is on the "micro" approach and specially on the investigation of the elasto-hydrodynamic bearing performance in view of deriving the influence of the bearing geometry on the overall structureborne noise.

KEY WORDS

Journal bearing, Modal analysis, Sound intensity analysis, Structureborne noise.

NOMENCLATURE

a: acceleration

b: adimensional ratio, $b = \dfrac{\Omega}{\omega_0}$

b_{ii}: damping coefficient
B_{ii}: dimensionless damping coefficient
c: radial clearance
$f(t)$: function of time
F_n : generic harmonic function
F_m : mean value of $f(t)$
$F(\Omega)$: Fourier transform of $f(t)$
$G_{xx}(f)$: auto-spectrum of input signal
$G_{yy}(f)$: auto-spectrum of output signal
$G_{xy}(f)$: cross-spectrum of signal

h : damping adimensional ratio, $h = \dfrac{r}{r_c}$

$H(\Omega)$: Harmonic Transfer Function
k_{ii}: stiffness coefficient
K_{ii}: dimensionless stiffness coefficient
m : deflected mass
m_a : shaft mass
M : pump mass
r_c : critical dumping
t : time
v: velocity
$\ddot{x}$: acceleration
$\ddot{X}$: acceleration of pump mass

w_r : resultant load
ϑ_n : phase difference
ω_0 : natural frequency
ω_b : angular velocity
γ_{xy} : coherence function
Φ_l : angle between y axis and resultant load
Ω : angle velocity

INTRODUCTION

The external gear pumps seem to be the assembly of few and relatively simple mechanical parts. In spite of that, the design and analysis of such units is far from being simple, because more functional roles are associated with the individual parts, and consequently the overall behavior is the complex combination of multiple effects. Conversely, the piston units have more mechanical parts, but it's easier to associate a specific issue to a specific pump element, e.g. the pressure ripple to the kidney port or the flexural vibration to the swashplate.

The origin of the present research can be traced back to the analysis of the sound pressure spectrum (Figure 1) of a 12 teeth external gear pump (at different speed and pressure levels): in fact, high noise levels were found in a frequency range (1 – 2 kHz) which is rather distant from the dominant frequencies due to the pressure ripple (i.e. 200 - 600 Hz for a pump running at 1000 rpm). The idea of find the cause of this results brought to investigate the structurebornenoise of the pump and implements two different methods of study:

1) firstly, a number of techniques were applied at the "macro" level, i.e. sound analysis, pressure ripple measurement and modal analysis. The aim was to investigate whether the peaks were originated by a structureborne noise source due to the interaction between pressure ripple and pump structural members;

2) secondly, an analysis at the "micro" level was attempted, focused on a component not much studied by the scholars in this perspective: the journal bearing.

STRUCTUREBORNE NOISE MECHANICS

The pump structureborne noise is important for the same reason why the fluidborne noise is important: it causes other machine structural elements to vibrate and radiate airborne noise [1]. It is caused by all pump structural vibration modes, including those that don't produce sound, and is transmitted by bending or torsional vibrations or by compression or shear waves that travel through solids like sound waves travel through air.

Often the structureborne noise has 1000 times the energy of the pump airborne noise. By converting only a fraction of 1% of the pump structure-born noise into sound, a single responsive part can radiate more airborne noise than the whole pump if such a part is a good sound radiator.
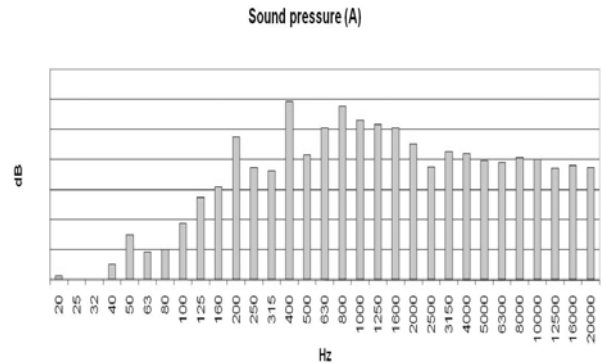
Figure 1 Spectrum of sound pressure level (A weighted) of a 12 teeth external gear pump (1000rpm; 180bar)

Most of the structureborne noise is due to the mechanism shown schematically in Figure 2. The small mass m is a part of the pump subject to the internal pumping forces which cause a movement relative to the rest of the pump mass M (e.g. the oscillation of the shaft in its bearing). The Newton's second law states that the center of the total pump mass must remain stationary unless affected by external forces, the mass M and the mass m must move in opposite directions to compensate and maintain the center of the total mass stationary. Since the center of gravity does not move, the larger mass M moves a fraction of the distance covered by the mass m relative to the center of gravity, as stated in Eq. (1)
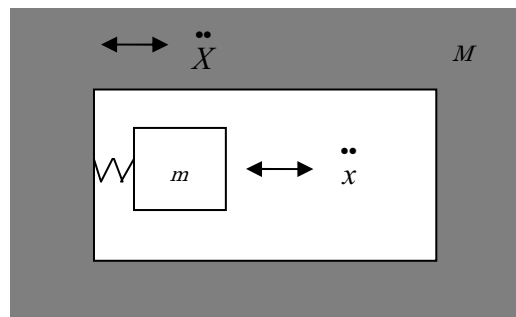
Figure 2 Basic structureborne noise mechanism

$$\ddot{X} = \frac{\ddot{x}\,m}{M} \qquad (1)$$

The imbalance of rotating parts has a similar noise potential. Though most of these parts are fully machined, they can work as sources of structureborne noise because the pressure imbalance works on the pump gears. The structureborne noise is not easy to detect, because

the original vibration can be in one point of the fluid power plant (e.g. the pump) and then propagate through the circuit until it reaches a good emitter which converts the mechanical energy into acoustic energy, i.e. noise. In practice noise occurs when the energy of a vibrating structure is converted into pressure waves which propagate in air. So, vibration and noise are strictly related especially when resonance takes place, i.e. when the exiting forces work at the natural frequencies (or modal frequencies) of a structure.
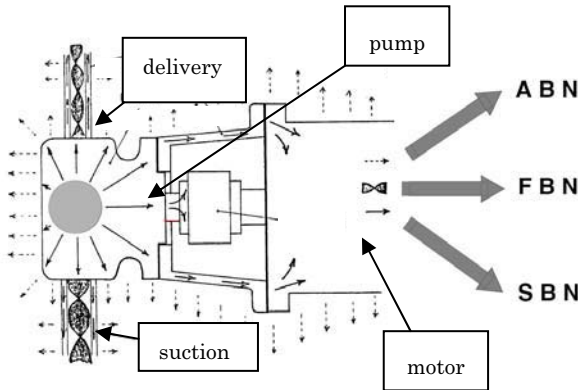
Figure 3 Noise sources in a fluid power pump: ABN (Airborne Noise); FBN (Fluidborne Noise); SBN (Structureborne Noise)

HARMONIC TRANSFER FUNCTION

By mean of the Fourier analysis [3] it is possible to express the cyclic forces as linear combinations of harmonic functions with frequencies that are integer multiples of a fundamental frequency Ω_0

$$f(t) = F_m + \sum_{1}^{\infty} F_{n0} \cos(n\Omega_0 t + \vartheta_n) \qquad (2)$$

Using the linear superimposition principle, the response of a linear system subject to a periodic force can be expressed as the combination of the responses to the harmonic components $F_n(t)$ of the exiting force (the response to a harmonic force is usually defined *harmonic transfer function*). If the force *f(t)* is not periodic, its Fourier transform is to be used, as defined in Eq. (3)

$$F(\Omega) = \frac{1}{2\pi} \int_{-\infty}^{\infty} f(t)e^{-i\Omega t} d\Omega \qquad (3)$$

The behavior of a system subject to a generic force can be described by means of the typical "control" approach. From this point of view the force is the input signal and the vibration is the output signal: the vibrating system is a "black box" that receives a generic force *f(Ω)* as input

and gives the displacement   *x(Ω)* as output (Figure 4).
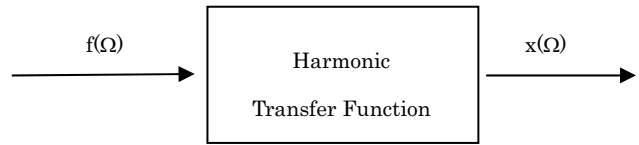
Figure 4 Harmonic Transfer Function definition

The "black box" behavior is fully described by the harmonic transfer function, as shown in Eq. (4)

$$X_p(\Omega) = H(\Omega)F(\Omega) \qquad (4)$$

The results provided by the harmonic transfer function depend on the numerator selected [3] [4]: displacement, velocity or acceleration. Three typical forms of the results provided are:

- Compliance $\dfrac{x}{F} = \dfrac{1}{(k - \omega^2 m) + i(\omega c)}$ (5)

- Mobility $\dfrac{v}{F} = \dfrac{i\omega}{(k - \omega^2 m) + i(\omega c)} = i\omega h(\Omega)$ (6)

- Accelerance $\dfrac{a}{F} = \dfrac{-\omega^2}{(k - \omega^2 m) + i(\omega c)} =$ (7)
  $= -\omega^2 h(\Omega)$

MODAL ANALYSIS OF GEAR PUMPS

The modal analysis of the pump was performed by using an impact hammer as input excitation and the pump body reaction as output response: the complex ratio of the two is the harmonic transfer function. The accelerations were measured in different positions: on the suction, output and upper face, and on the back cover. The accelerometer was kept in a fixed position while the hammer hit the case: (a) firstly in the same position; (b) secondly, in all other positions. Once a series of measurements were completed, the accelerometer was moved and the measurements started again. In Figure 5, the spectrum, phase and acceleration of the pump body in one of the different configuration are shown.
The modal analysis proves the presence of a strong resonance frequency in the range of 5 – 7 kHz, clearly far from the peaks found in the range of 1 – 2 kHz, then, as first partial conclusion it can be state: that the noise produced in this range of frequencies probably is not caused by a pump's body resonance.
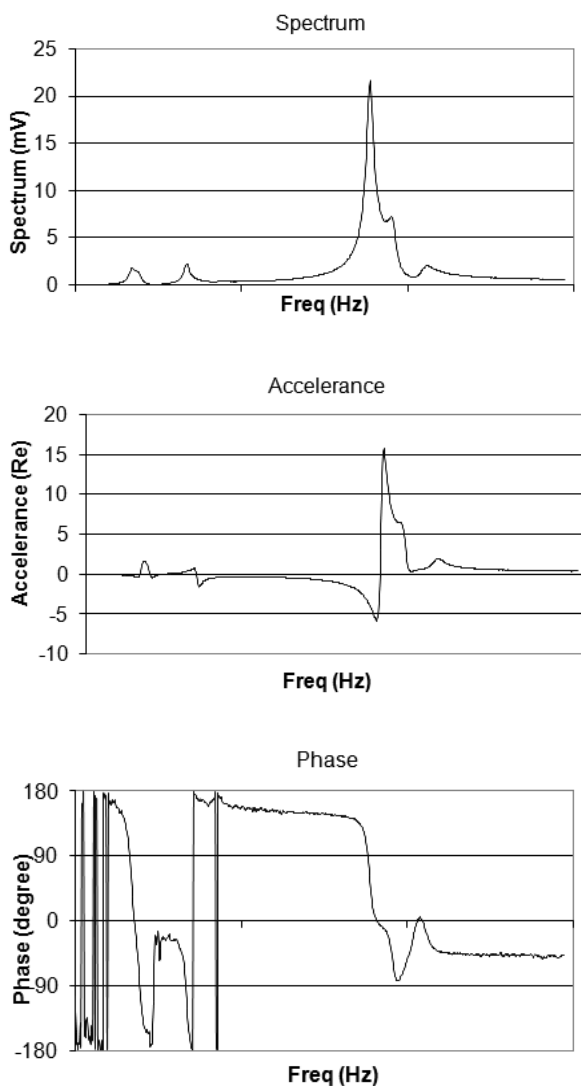
643

$$\gamma^2{}_{xy}(f) = \frac{\left| G_{yx}(f) \right|^2}{G_{xx}(f)G_{yy}(f)} \Rightarrow 0 \leq \gamma^2{}_{xy}(f) \leq 1 \qquad (8)$$

From this point of view, a possible correlation between the airborne, fluidborne and structureborne noise was investigated. A series of measurements of pressure ripple and acceleration were performed at various pressure levels, at various running speed. The coherence function between acceleration and pressure ripple was computed to check the interaction between the fluidborne and the airborne noise. The *mathematical* coherence function proves the absolute deficiency of the *physical* coherence between the two signals in the range 1 – 2 kHz, because the pressure ripple is practically absent above 1kHz, as shown in Figure 6. So, as second partial conclusion, the noise frequency peaks is not due to the interaction between fluidborne and structureborne noise.
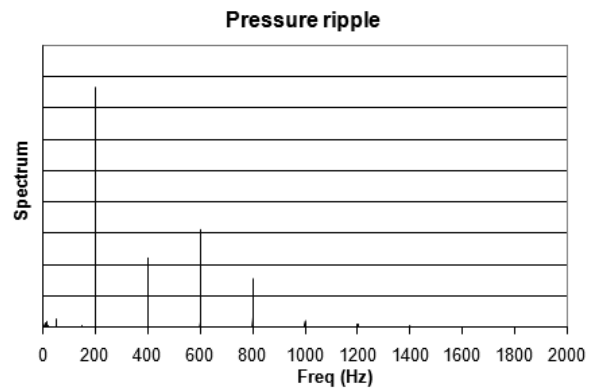
Figure 6 Pressure ripple (1000 rpm, 180 bar)

Figure 5 Harmonic transfer function:
Spectrum, accelerance and phase vs frequency

FLUID- AND AIRBORNE NOISE INTERACTION

By mean of the harmonic transfer function it is possible to investigate the interactions between the fluidborne and the structureborne noise, by using the pressure ripple signal as input and the acceleration of the pump body as output signal. The mathematical tool useful to check the reliability of such a relationship is the *coherence function* defined in Eq. (8). If this function is close to one, the output signal is substantially caused by the input signal; conversely, if the function is close to zero, the two signals are not related or linked by a cause/effect mechanism

JOURNAL BEARING ANALYSIS

Finally, an acoustic analysis was carried out by means of the intensimetry measurement technique – a much more accurate method to describe the acoustic field if compared with the sound pressure measurements - and its results were compared with the acceleration measurements on the pump body.

The sound intensity analysis gave the opportunity to verify that the suction side of the pump body surface emits most of the sound power of the pump. For our purposes, however, the best pieces of information were provided by comparing the acceleration and sound power plots.

The spectrum of Figure 7 confirms the presence of two peaks centered at 315 Hz and 630 Hz, due to pressure ripple, but at the same time the sound power peak in the band centered at 2 kHz is of unknown origin.

In fact Figure 8 shows some peaks of the acceleration plot. A more accurate analysis of the acceleration data,

in the range 1.6 – 2.0 kHz (Figure 9), discovers two lateral bands spaced from the principal one, centered at 1.8 kHz, by a regular interval of 25 Hz, just the same as the shaft revolution frequency.
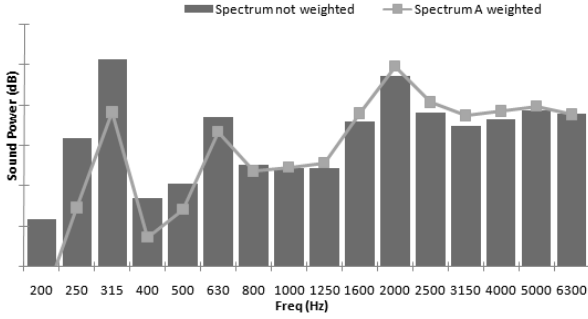
Figure 7 Sound power (1500 rpm, 180 bar)
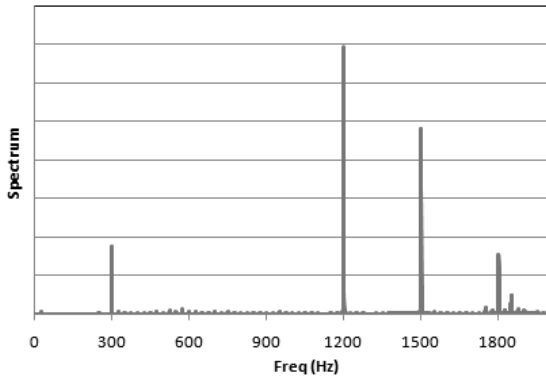
Figure 8 Spectrum of acceleration (1500 rpm, 180 bar)

On the basis of the journal bearing theory [2], it is possible to draw the conclusion that, being the band on the right higher than the other one, an eccentric operation of the shaft could be the origin of the airborne noise peaks.

The eccentricity is a normal operating condition of a shaft supported by a journal bearing (like an external gear pump), but it becomes critical from the structure-borne noise viewpoint if the bearing works in an unstable configuration.

The problem can be studied by applying the fluid film lubrication theory to a shaft of mass $2m_a$ supported by two identical well-aligned journal bearings.

Let the load be stationary, $w_r = w_{x,0}$ and $\Phi_l = 0$; then the linearized equation of the journal bearing is:

$$\begin{Bmatrix} m_a & 0 \\ 0 & m_a \end{Bmatrix} \begin{Bmatrix} \Delta \ddot{x} \\ \Delta \ddot{z} \end{Bmatrix} + \begin{Bmatrix} b_{xx} & b_{xz} \\ b_{zx} & b_{zz} \end{Bmatrix} \begin{Bmatrix} \Delta \dot{x} \\ \Delta \dot{z} \end{Bmatrix} + \begin{Bmatrix} k_{xx} & k_{xz} \\ k_{zx} & k_{zz} \end{Bmatrix} \begin{Bmatrix} \Delta x \\ \Delta z \end{Bmatrix} = \begin{Bmatrix} 0 \\ 0 \end{Bmatrix} \quad (12)$$
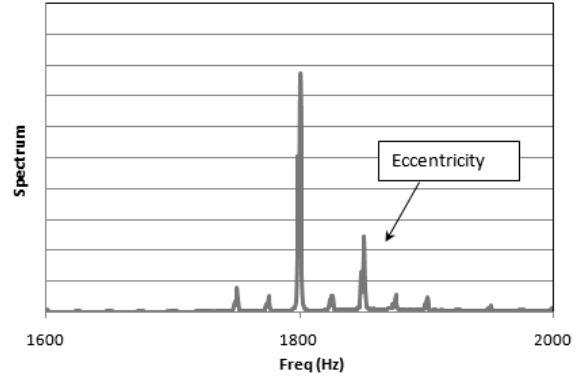
Figure 9 Spectrum of acceleration (1500 rpm, 180 bar)

The stiffness and damping coefficients can be made dimensionless through the following equations:

$$\begin{Bmatrix} K_{xx} & K_{xz} \\ K_{zx} & K_{zz} \end{Bmatrix} = \frac{c}{\omega_r} \begin{pmatrix} k_{xx} & k_{xz} \\ k_{zx} & k_{zz} \end{pmatrix} \quad (13)$$

$$\begin{Bmatrix} B_{xx} & B_{xz} \\ B_{zx} & B_{zz} \end{Bmatrix} = \frac{c\omega_b}{w_r} \begin{pmatrix} b_{xx} & b_{xz} \\ b_{zx} & b_{zz} \end{pmatrix} \quad (14)$$

The substitution the Eqs. (13) and (14) into Eq. (12) gives:

$$\begin{Bmatrix} m_a & 0 \\ 0 & m_a \end{Bmatrix} \begin{Bmatrix} \Delta \ddot{x} \\ \Delta \ddot{z} \end{Bmatrix} + \frac{w_r}{c\omega_b} \begin{Bmatrix} B_{xx} & B_{xz} \\ B_{zx} & B_{zz} \end{Bmatrix} \begin{Bmatrix} \Delta \dot{x} \\ \Delta \dot{z} \end{Bmatrix} +$$

$$+ \frac{\omega_r}{c} \begin{Bmatrix} K_{xx} & K_{xz} \\ K_{zx} & K_{zz} \end{Bmatrix} \begin{Bmatrix} \Delta x \\ \Delta z \end{Bmatrix} = \begin{Bmatrix} 0 \\ 0 \end{Bmatrix} \quad (15)$$

The solution to Eq. (15) is of the form

$$\begin{Bmatrix} \Delta x \\ \Delta z \end{Bmatrix} = \begin{Bmatrix} x_h \\ z_h \end{Bmatrix} \exp\left(\bar{\Omega} t \omega_b \right) \quad (16)$$

The substituting Eq. (16) into Eq. (12) gives

$$\begin{Bmatrix} M_a + \bar{\Omega} B_{xx} + K_{xx} & \bar{\Omega} B_{xz} + K_{xz} \\ \bar{\Omega} B_{zx} + K_{zx} & M_a + \bar{\Omega} B_{zz} + K_{zz} \end{Bmatrix} \begin{Bmatrix} x_h \\ z_h \end{Bmatrix} \exp\left(\bar{\Omega} t \omega_b \right) = \begin{Bmatrix} 0 \\ 0 \end{Bmatrix} \quad (17)$$

where

$$M_a = \frac{c m_a \Omega^2}{w_r} \qquad \text{and} \qquad \bar{\Omega} = \frac{\Omega}{\omega_b} \quad (18)$$

Thus the solution

$$\left(M_a + \bar{\Omega} B_{xx} + K_{xx} \right)\left(M_a + \Omega \bar{B}_{zz} + K_{zz} \right) - \qquad (19)$$

$$- \left(\bar{\Omega} B_{zx} + K_{zx} \right)\left(\bar{\Omega} B_{xz} + K_{xz} \right) = 0$$

is an eigenvalue problem stating that, if the system should dislodge itself from the steady-state position, a transient vibration would result although the external load be constant.

When the load is very high (as in the case of a hydraulic pump) the lubrication's regime (viscous-elastic) could be influenced by two mayor physical effects: the elastic deformation of the walls and the increase in fluid viscosity with pressure. The lubricating regime could be studied by mean of tree dimensionless parameters :

$$\hat{H} = H_e \left(\frac{W}{U} \right)^2 \quad \textit{film thickness parameter} \qquad (20)$$

$$g_v = \frac{GW^3}{U^2} \quad \textit{viscosity parameter} \qquad (21)$$

$$g_E = \frac{W^{8/3}}{U^2} \quad \textit{elasticity parameter} \qquad (22)$$

These parameter could be used to compute the dimensionless minimum film thickness:

$$\hat{H}_{e,\min} = 3.63 U^{0.68} G^{0.49} W^{-0.073} \left(1 - e^{-0.68k} \right) \qquad (23)$$

To reduce the instability, which is found particularly in the cylindrical journal bearing, a lot of efforts have been spent , but a universal solution is still (and far) to come. Since for some applications, new internal profiles have been proposed (Figure 10), some similar design options are under evaluation to check if the journal bearings are the true sources of the anomalous noise levels.
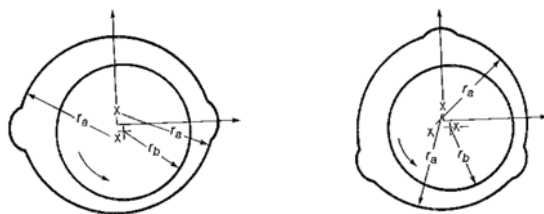
Figure 10 Journal bearings modified to reduce the instability (examples)

CONCLUSIONS

A study on structureborne noise in hydraulic external gear pump was carried out starting from the discovery of a high sound pressure level in a frequency range (1 – 2 kHz) which is far from those typically related with the fluidborne noise. A series of experiments were planned and evaluated:

- a modal analysis was used to derive the resonance frequencies of the pump body. Occurring in the range of 5 – 7 kHz, they are definitely far from the range of interest;
- the interaction between the fluidborne and structureborne noise was checked by applying the standard coherence function. The result was an absolute lack of coherence between the two signals in the range 1 – 2 kHz, because the pressure ripple is practically absent above 1kHz;
- finally the attention was focused on the journal bearings of the wheeled gears. Analyzing the acceleration spectra were find the presence of the two lateral bands spaced from the principal by a regular interval of 25 Hz, equal to the frequency of revolution. The journal bearing theory suggests that an eccentric operation of shaft could be responsible of the noise peaks in the range of 1 – 2 kHz. The same theory is useful to propose alternative bearing configurations to reduce the shaft unbalance.

The work under development now is focused on the experimental analysis – and hopefully validation - of a few newly designed journal bearings.

REFERENCES

1. S. Skaistis, Noise Control of Hydraulic Machinery, Marcel Dekker Inc., New York, 1988.
2. Bernard J. Hamrock, Fundamentals of Fluid Film Lubrication, McGraw Hill, New York, 1994.
3. Meirovitch L., Elements of Vibration Analysis, McGraw Hill, New York.
4. Ewins D. J. , Modal Testing: Teory and Practise, Research Study Press LTD.
5. UNI EN ISO 9614-1/2/3, Determination of sound power levels of noise sources using sound intensity technique.

ACKNOWLEDGEMENT

P2-12

MEASUREMENT OF FREE AIR IN THE OIL CLOSE TO A HYDRAULIC PUMP

Liselott ERICSON and Jan-Ove PALMBERG

Fluid and Mechanical Engineering Systems
Linkoping University
581 83 Linkoping, Sweden
(E-mail: liselott.ericson@liu.se, jan-ove.palmberg@liu.se)

ABSTRACT

Noise is a well-known challenge in hydraulic systems and hydrostatic pumps are one of the largest noise contributors in a hydraulic system. The existing noise reduction features, such as pressure relief groove and pre-compression filter volume, are more or less dependent on the working condition. It is essential to know the amount of free air when designing a quiet pump; however, it is not evident how much free air the oil contains. The free air content is different if the suction port is boost pressured or self-priming. The amount of free air in a well-designed system can be as low as 0.5% while in others up to 10%.

This paper uses the three-transducer method to measure the amount of free air in the oil. The oil's compressibility can be measured for different working conditions and the free air content can then be calculated. The pre-study is performed with an extensive simulation model. Various noise reduction features' sensitivity to free air content is considered.

KEY WORDS

Air release, noise, flow pulsation, hydraulic pump, measurement

NOMENCLATURE

a :	Wave propagation velocity	[m/s]
E :	Modulus of elasticity	[Pa]
i :	Imaginary unit, $\sqrt{-1}$	[-]
J_0 :	Bessel function of order 0	[-]
J_2 :	Bessel function of order 2	[-]
L :	Length	[m]
N :	Viscous friction factor	[-]
n :	Harmonic number	[-]
P:	Pressure	[Pa]
P_0:	Reference pressure	[Pa]
P_l:	Inlet pressure	[Pa]
P_s:	Discharge pressure	[Pa]
P_v:	Pressure at air measurement device	[Pa]
Q :	Flow	[m³/s]
r :	Radius	[m]
s :	Laplace operator, $s=i\omega$	[s⁻¹]
T :	Temperature	[°C]
t :	Wall thickness	[m]
x_0 :	Volume fraction of free air at p_0	[-]
x_l :	Volume fraction of free air at p_l	[-]
Z_C:	Characteristic impedance of the pipe	[Ns/m⁵]
Z :	Impedance	[Ns/m⁵]
β_e :	Effective bulk modulus	[Pa]
β_f :	Effective fluid bulk modulus	[Pa]
β_{oil}:	Fluid bulk modulus	[Pa]

ρ	:	Fluid density	[kg/m^3]
κ	:	Polytrophic exponent	[-]
ω	:	Frequency	[rad/s]
ν	:	Kinematic viscosity	[m^2/s]

Subscripts

| i | : | Downstream of j | [-] |
| j | : | Upstream of i | [-] |

INTRODUCTION

Noise is a well-known challenge in hydraulic systems and hydrostatic pumps are one of the largest noise contributors in a hydraulic system. The existing noise reduction features, such as pressure relief groove and pre-compression filter volume (PCFV), are more or less dependent on the working condition. Rotational speed and pressure variations are the most commonly discussed drive conditions when flow pulsations are considered. Another, less extensively discussed, changing condition is the amount of free air in the oil. The released air from the oil contributes a change in the effective bulk modulus which has an impact on the flow pulsation created in the machine.

A machine works with large pressure differences between the inlet and discharge ports; the fluid properties are therefore not constant. This is principally true of the bulk modulus. In particular, the bulk modulus decreases considerably if the oil contains air bubbles. When the pressure drops below the current saturation pressure level, air is released from the oil and forms air bubbles. The saturation pressure level is not only a fluid parameter but is dependent on the system configuration [1]. Most hydraulic systems are saturated at atmospheric pressure which is at about 1 bar; at this pressure level the oil can dissolve up to 10% volume fraction of air. The air bubbles not only cause a decrease in the bulk modulus, whereby the flow pulsation increases and the efficiency decreases, but also cavitational erosion damage to the surrounding walls when the pressure increases and the released air bubbles collapse. The collapse of the bubbles also causes a broadband spectrum of noise.

The pressure in a hydraulic pump can fall below the saturation pressure level in different ways; when the valve plate is designed with an exaggerated decompression zone or if the inlet kidney closes prematurely, whereby the cylinder tries to suck fluid before it is connected to the inlet port kidney. Another is a result of the jet beam which is created when the valve plate's pre-compression and decompression are insufficient. In this way, substantial high velocity flow pulses are created with and thereby also high dynamic pressure and low static pressure levels. Air bubbles are created and are drawn into the cylinder and have a direct effect on the oil properties at the discharge port.

The third reason for air release in hydraulic pumps is the

suction port design. When the inlet port is self-priming, the pressure may decreases when the speed increases and causes a deficiency in fluid in the suction port. Also, when the pressure falls below the saturation pressure level the effective flow decreases due insufficient filling of the cylinders. If the suction port is boost pressurised the insufficient filling problem does not appears.

It is difficult to predict the amount of free air in a pump, since the inlet pressure can differ from one installation to another. The amount of free air in a well-designed system can be as low as 0.5% while in others up to 10%. It is essential to know the amount of free air when designing a quiet pump; however, it is not evident how much free air the oil contains.

This paper considers different noise reduction features' sensitivity to the quantity of free air right at the entrance to the pump. Moreover, the three-microphone method is used to predict the quantity of free air in the suction port.

SIMULATION MODEL

Rotational speed and pressure variations are the most commonly discussed drive conditions when flow pulsations are considered. However, the amount of air released from the oil is significant when designing a quiet machine.

The most common noise reduction features are more or less air content dependent. The features considered in a simulation model are pre- and decompression angles, pressure relief groove [2], and pre-compression filter volume [3].

Simulation techniques are valuable tools in the early stages of the development process. Different simulation models exist for predicting flow ripple in hydrostatic pumps. In this study, a comprehensive simulation model is created in the simulation program HOPSAN, [4] developed at Linkoping University. HOPSAN is used mainly for hydraulic simulations.

The pump model is composed of the number of cylinders in the pump and every cylinder is connected to two orifices. The orifices represent the opening between the suction port and the discharge port and the logic of the opening of these orifices allows simulation of different noise reduction features as pressure relief groove and pre- and decompression angles. Also, additional orifices and volumes can be added to simulate other features like pre-compression filter volume.

The model includes a large number of different states that express the detailed behaviour of the machine. However, the character that is considered in this study is flow pulsation in discharge port.

The fluid properties are not constant during operation. It is chiefly the bulk modulus that varies due to the large pressure differences between discharge and inlet port and also the amount of free air in the oil. In the

simulation model, the free air content is modelled with the tangent value according to Eq. (1).

$$\beta_e = \frac{\beta_{oil}}{1 + \frac{x_0}{\kappa p}\frac{\beta_{oil}}{1-x_0}\left(\frac{p_0}{p}\right)^{\frac{1}{\kappa}}} \qquad (1)$$

x_0 is the volume fraction of free air in the oil at reference pressure p_0. β_{oil} is the bulk modulus for oil free from air bubbles. The pressure oscillations can be assumed to be an adiabatic process and at normal hydraulic pressure levels, a realistic polytrophic exponent is about 1.8. The model of the free air content is valid for $x_0 \leq 0.1$.

Simulation results are, however, of little practical use before they are experimentally verified. The comprehensive simulation model has been extensively verified on previous occasions with the two-microphone method [5].

MEASUREMENT OF THE BULK MODULUS

There are different methods of measuring the effective bulk modulus in the high pressure line after the pump; see [6] for a comparison of different methods. The three transducer method is used in this paper and is presented in [7]. The method was used in [8] to test different designs of decompression zones.

The method is based on the pressure waves' propagation in a well defined rigid pipe. The pressure waves are created by the pump in this work. The bulk modulus is calculated indirectly by the measured speed of sound in the measurement pipe.

The point impedance can be calculated at all three transducers along the measurement pipe by using the four pole matrix, see for instance [9]. Equations (2) and (3) show the impedance equations where index i is the location upstream of index j.

$$Z_i = \frac{P_i}{Q_i} = \frac{Z_c \sqrt{N} \sinh\left(\frac{Ls\sqrt{N}}{a}\right)}{\cosh\left(\frac{Ls\sqrt{N}}{a}\right) - \frac{P_j}{P_i}} \qquad (2)$$

$$Z_j = \frac{P_j}{Q_j} = \frac{Z_c \sqrt{N} \sinh\left(\frac{Ls\sqrt{N}}{a}\right)}{\cosh\left(\frac{Ls\sqrt{N}}{a}\right) - \frac{P_i}{P_j}} \qquad (3)$$

where

$$Z_c = \frac{\rho a}{\pi r^2} \quad \text{and} \quad N = \frac{J_0\left(ir\sqrt{\frac{s}{\upsilon}}\right)}{J_2\left(ir\sqrt{\frac{s}{\upsilon}}\right)}$$

Using three pressure transducers, index 1-3, separated by lengths L_{12} and L_{23} and with a total length of L_{13}, the point impedance at every transducer can be determined in two ways.

For instance the point impedance at the second

transducer can be determined by using Eq. (2) with pressure P_2 (i=2) and pressure P_3 (j=3) and by using Eq. (3) with pressure P_1 (i=1) and P_2 (j=2). In the same way, point impedance at transducer 1 and 3 can be obtained. If the three point impedance is eliminated and the angle-sum relation of the hyperbolic function is used Eq. (4) - (6) are obtained. A clarifying picture of the notation is shown in Figure 1.

$$-\frac{P_3}{P_1}\sinh\left(\frac{L_{12}s\sqrt{N}}{a}\right) + \frac{P_2}{P_1}\sinh\left(\frac{L_{13}s\sqrt{N}}{a}\right) - \sinh\left(\frac{L_{23}s\sqrt{N}}{a}\right) = 0 \quad (4)$$

$$-\frac{P_3}{P_2}\sinh\left(\frac{L_{12}s\sqrt{N}}{a}\right) + \sinh\left(\frac{L_{13}s\sqrt{N}}{a}\right) - \frac{P_1}{P_2}\sinh\left(\frac{L_{23}s\sqrt{N}}{a}\right) = 0 \quad (5)$$

$$-\sinh\left(\frac{L_{12}s\sqrt{N}}{a}\right) + \frac{P_2}{P_3}\sinh\left(\frac{L_{13}s\sqrt{N}}{a}\right) - \frac{P_1}{P_3}\sinh\left(\frac{L_{23}s\sqrt{N}}{a}\right) = 0 \quad (6)$$
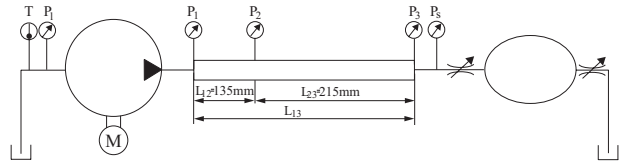
Figure 1 Illustration of the test system.

All three equations ((4)- (6)) are equal and can easily be realised by multiplying Eq (4) with P_1, Eq (5) with P_2, and Eq (6) with P_3 which gives Eq. (7).

$$-P_3\sinh\left(\frac{L_{12}s\sqrt{N}}{a}\right) + P_2\sinh\left(\frac{L_{13}s\sqrt{N}}{a}\right) - P_1\sinh\left(\frac{L_{23}s\sqrt{N}}{a}\right) = 0 \quad (7)$$

Only the pump piston harmonics of the pressure spectra are used and therefore Eq. (7) can not be solved exactly to zero. Instead a numerical optimisation algorithm is used to find the wave propagation speed that minimises the left hand side for every harmonic, ε_n. The objective function is formulated as the least square sum according to Eq. (8).

$$F = \sum_1^n |\varepsilon_n|^2 \qquad (8)$$

The complex algorithm [10] is used to solve the minimisation problem of F; the algorithm is well suited for the problem and gives fast and repeatable convergence.

Normally, the density can be assumed to be constant and together with the measured wave speed the effective bulk modulus is calculated according to Eq. (9).

$$\beta_e = \rho a^2 \qquad (9)$$

The main problem with this technique is considered to be that if not all the frequency spectra of pressure are treated, truncation errors can appear. The measurements carried out in this article are reliable up to about

3000 Hz, which implies that only a few harmonics are considered in high speed measurements. This can be seen as small differences in the speed of sound between different dynamic loads at the same stationary pressure.

CALCULATION OF FREE AIR

The effective bulk modulus includes both the compressibility of the fluid and the wall elasticity. A model for this is considered according to Eq. (10).

$$\beta_e = \frac{1}{\frac{1}{\beta_f} + \frac{r}{2tE}} \qquad (10)$$

where β_e is the effective bulk modulus and β_f is the effective fluid bulk modulus. If free air has been released in the oil, the effective fluid bulk modulus is affected and can be modelled as Eq. (11).

$$\beta_f = \frac{\beta_{oil}}{1 + \frac{x_0}{\kappa p} \frac{\beta_{oil}}{1 - x_0} \left(\frac{p_0}{p}\right)^{\frac{1}{\kappa}}} \qquad (11)$$

x_0 represents the volume fraction of free air at the reference pressure p_0. Equation (11) is actually the same as Eq. (1) considered in the simulation model except that in the measurement the elasticity of the measurement pipe is also considered.

The volume fraction of free air at the pressure level p is determined as

$$x = x_0 \left(\frac{p_0}{p}\right)^{\frac{1}{\kappa}} \qquad (12)$$

The measurement and calculation of the quantity of released air is approximately due to uncertainties regarding how the air is released from the oil. The air release and the re-saturation take some time and it is not obvious how much of the air is resolved back into the oil during the pressurisation in the machine.

TEST SET-UP
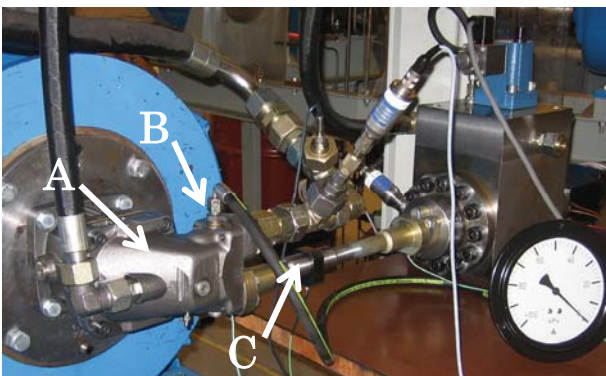
Figure 2 Picture on the test set-up. A is the test pump, B the inlet pressure manometer, and C the measurement pipe with three pressure transducers.

The complete test set-up is shown in Figure 2. The test pump is a 40 cm³/rev bent-axis piston pump with seven

pistons. The tank is located approximately 2 m above the test pump; at very low pump speeds the suction port pressure is therefore about 1.2 bar. The suction port is fairly small and not boost pressured and the pressure is therefore well below atmospheric pressure at higher speeds; see the results section for exact data. The tank volume is about 1 m³ and the fluid's theoretical circulation time is about 15 minutes at 2000 rpm, which is sufficient to dissolve the air bubbles created anywhere in the circuit.

Three dynamic piezoelectric pressure transducers are located at the measurement pipe to enable measurement of the air content and also the pressure pulsation at the discharge port. The static pressure is measured at the suction port and discharge port. The suction port's manometer is placed right at the pump flange. The pump's inlet channel has equal cross section area from the pump flange to the valve plate and should not give any major differences in the pressure level from the measured pressure to the valve plate. The temperature is measured to maintain a constant temperature throughout the measurements.

RESULTS

The simulation results with different features' sensitivity to free air in the oil are presented first, followed by the measurement results.

Simulation results

The amplitude of the flow pulsations is dependent on the fraction of free are and also the inlet pressure. Figure 3 shows how the amplitude of the discharge flow pulsations alter when the fraction of free air varies from 0 to 5.25 % and Figure 4 how the inlet pressure varies from 0.4 bar up to 10 bar. The discharge flow pulsation is calculated according to Eq. (13).

$$q_{frac} = \frac{q_{max} - q_{min}}{q_{mean}} \qquad (13)$$
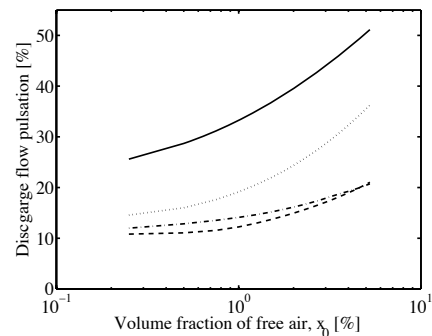
Figure 3 Different noise reduction features' robustness to volume fraction of air, x_0 at inlet pressure 1 bar. The solid line represents simulation for a zero-lapped valve plate, the dotted line pre-compression angle, the dashed line PCFV, and the dashed/dotted line pressure relief groove.
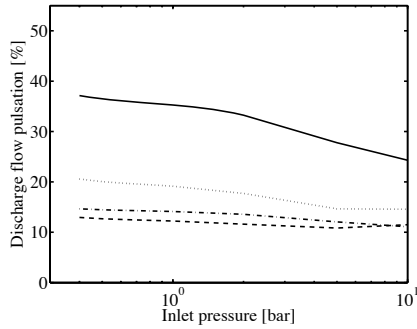
Figure 4 Different noise reduction features' robustness to inlet pressure at x_0=1 %. The solid line represents simulation for a zero-lapped valve plate, the dotted line pre-compression angle, the dashed line PCFV, and the dashed/dotted line pressure relief groove.

The solid line shows a zero-lapped valve plate and as can be seen in Figure 3 an increase in the quantity of free air increases the amplitude of the flow ripple. Boost pressure, Figure 4, also reduces the inlet pressure compared to a self-priming pump.

Figure 3 and Figure 4 show also how robust different common noise reduction features are to variations in air content and inlet pressure in the discharge kidney.

The valve plates with pre-compression filter volume, pressure relief groove, and pre-compression angle are optimised for x_0 = [0, 1, and 5 %] at an inlet pressure of 1 bar. The objective function is the flow pulsation amplitude in the discharge kidney. The pressure is never allowed to fall below 0.3 bar in the optimisation.

The pressure relief groove and pre-compression filter volume is equal sensitive to different volume quantities of free air and inlet pressure. Both pressure relief groove and pre-compression filter volume gives lower amplitude of discharge flow pulsation than pre-compression angle, due the fact that the feature increases the possibilities to avoid cavitation, which is a constraint in the optimisation.

The behaviour of the flow pulsations in the inlet pressure port is the same as for the discharge pressure port.

Measurement results

Speed	p_t [bar]	a [m/s]	β_e [MPa]	x_0 [%]	x_l [%]
900	0.95	1455	1841	1.02	1.05
1100	0.9	1454	1838	1.05	1.11
1200	0.86	1453	1837	1.06	1.16
1400	0.76	1450	1829	1.19	1.36
1500	0.74	1447	1815	1.34	1.59
1600	0.70	1443	1835	1.39	1.69
1700	0.62	1437	1797	1.58	2.06
1800	0.58	1437	1785	1.73	2.33

Table 1 Sound speed measurement with the three-transducer method. The bulk modulus, the fraction of free air at atmospheric pressure, and the suction port pressure are calculated from Eq. (9)-(12).

Measurements of the air content are performed at different rotational speeds at 150 bar and 30°C. Table 1 shows the measurement values when a zero lapped valve plate is used.

The wave propagation velocity, a, is a mean value of two different load cases. The divergence between the load settings measurement is approximately 2 %. However, the results give a reliable trend as can be seen more clearly in Figure 5.
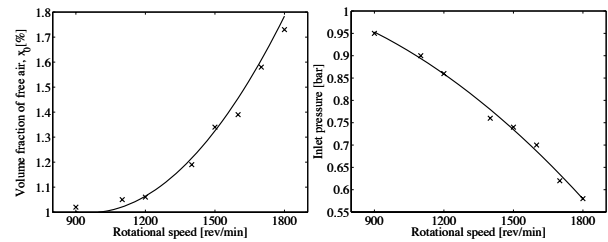
Figure 5 The trend of the volume fraction of released air to the left and inlet pressure to the right when rotational speed increases. Crosses are measurements and solid lines are quadratic equations which are adjusted to the measurements.

The released air increases from 1.02 % to about 1.7 % at atmospheric pressure when the inlet pressure goes from 0.95 bar to 0.58 bar. Provided that no air is created from the inlet port to the measurement pipe the inlet air content can be calculated with Eq. (12) which is shown in very right column of Table 1.

When the pressure varies, the measured fraction of free air also differs. The fraction of free air increases when the pressure increases, as can be seen in Figure 6. The figure shows measurements with two different valve plates. Crosses represent measurements with a zero lapped valve plate and stars a pre-compression angled valve plate. The pre-compression is optimal for a discharge pressure of approximately 60 bar.
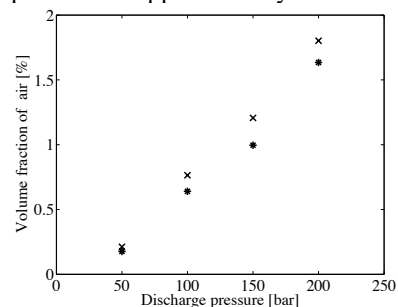
Figure 6 Volume fraction of air at different pressures and valve plate designs. Crosses are with a zero-lapped valve plate while the stars are with a valve plate with pre-compression angle.

DISCUSSION AND CONCLUSION

The simulation results in the paper show some features' robustness to air quantities and inlet pressure.

Implementing a pressure relief groove or a pre-compression filter volume reduces the sensitivity of air content and suction pressure.

The volume fraction of air increases when the speed increases. The main reason for this is probably that the inlet pressure decreases when the speed increases. The filling and emptying speed of the cylinder also increases and the air release can then be delayed which decreases the fraction of air in the oil.

The quantity of released air increases when the discharge pressure increases. The probable cause of this is the jet-beam that is created when the pre-compression is insufficient. The same theory may also be a plausible reason why the pre-compression valve plate creates somewhat less free air than for a zero-lapped valve plate.

All the measurement results show a good picture of the tendency, but the absolute values are less reliable due to uncertainties as regards some parameters.

The paper shows that the valve plate is likely to have an impact on the fraction of free air in the measurement pipe and therefore it is not probable to measure the outlet bulk modulus and predict the fraction of free air in the suction line. The amount of free air should therefore be measured at the inlet to the pump and be compared to the free air content at the discharge port. In this way, the amount of free air created inside the pump can be determined. Further investigation is needed to decide where the air bubbles are created inside the pump, at the discharge port or suction port.

OUTLOOK

Due to the uncertainties as regards the oil properties and the air release behaviour, the results for the quantity of released air are rather approximate. In addition, it is interesting to separate all the air release creating places inside and around the machine. The bulk modulus and thus the volume fraction of air that enters the suction port of the pump should be measured at the suction port. Together with the fraction of free air in the discharge port, the free air created inside the pump can be determined.
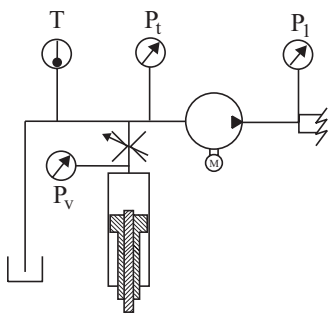
Figure 7 Illustration of the test set-up for measurement of the bulk modulus at the inlet port.

The suction port air content can be measured with a device similar to the piece of equipment used in [11]. A rough illustration of the projected test set-up is shown in Figure 7.

REFERENCES

1. Edge, K.A. and Freitas, F.J.T., A study of pressure fluctuation in the suction lines of positive displacement pumps, Proc. of *the Institution of Mechanical Engineering*, **199**:211-217,1985.
2. Edge, K.A., Designing quieter hydraulic systems - some recent developments and contributions, Proc. of *the Fourth JHPS International Symposium*, Tokyo, Japan, November}, 1999.
3. Pettersson, M., Weddfelt, K., and Palmberg, J-O., Reduction of flow ripple from fluid power piston machines by means of a pre-compression filter volume, Proc. of *Tenth Aachen Colloquium on Fluid Power Technology*, Aachen, Germany, March 17-19, 1992.
4. N.N., *HOPSAN, a simulation package, Users Guide*, Tech Rep. LiTH-IKP-R704, Division of Fluid and Mechanical Engineering Systems, Linkoping University, April, 1998.
5. Weddfelt, K., Measurement of pump source characteristics by the two-microphone method, Proc. of *The Second Tampere International Conference on Fluid Power*, Tampere, Finland, March, 1991.
6. Jinghong, Y. and Kojima, E., Methods for measuring the speed of sound in the fluid transmission pipes, Proc. of *SAE International Off-Highway & Powerplant Congress, Milwaukee*, USA, September, 2000.
7. Johnston, D.N. and Edge, K.A., In-situ measurement of the wavespeed and bulk modulus in hydraulic lines, Proc. of *the Institution of Mechanical Engineering*, **205**:191-197, 1991.
8. Johansson, A. and Palmberg, J-O., The importance of suction port timing in axial piston pumps, *Proc. of The Ninth Scandinavian International Conference on Fluid Power, SICFP'05*, June 1-3, 2005.
9. Viersma, T. J., *Analysis, Synthesis and Design of Hydraulic Servo Systems and Pipelines*, Elsevier scientific publishing company, ISBN 0-444-41869-5, ISSN 0-444-41872-5, 1980.
10. Box, M. J., A New method of constraint optimization and a comparison with other methods, *Computer Journal*, **8**:42-52, 1965
11. Weingarten, F., *Aufbau hydraulischer Zeitglieder und ihr Einsatz im Signalzweig hydraulisch-mechanischer Regelungen*, PhD-thesis, RWTH, Aachen University, Aachen, Germany, 1983

P2-13

ASSISTING FORCE FEEDBACK FUNCTION FOR HAND-HELD REMOTE CONTROL OF EXCAVATOR

Jarno UUSISALO, Otso KARHU and Kalevi HUHTALA

Department of Intelligent Hydraulics and Automation
Tampere University of Technology
P.O.Box 589, 33101 Tampere, Finland
(E-mail: jarno.uusisalo@tut.fi)

ABSTRACT

Remote control of hydraulic mobile machines is often used because of safety issues. In addition to safety, remote control can be used to improve working efficiency and usability of the machine. A prototype of a hand-held remote control is designed to be used as a user interface of a mobile machine with an excavator while the machine is controlled remotely over short-range.

Since the remote control is designed to be used over short-range it provides congruent visual and voice feedback with the ordinary onboard user interface. In order to improve the feel of control an assisting force feedback function is implemented. The load of the machine is measured with a pressure transmitter. When the load tends to certain level information is provided to the operator. The idea is to inform the operator about the high load and possible power limitations, not to provide proportional force feedback.

Implementation of the system is introduced in this paper. The system is tested under real circumstances by using the excavator. Behaviour of the system during an excavation cycle is represented.

KEY WORDS

Remote control, Force feedback, Mobile machine, Excavator

NOMENCLATURE

CAN	:	Controller Area Network
CRC	:	Cyclic Redundancy Check
DSP	:	Digital Signal Processor
FET	:	Field-Effect Transistor
I/O	:	Input/Output
LCD	:	Liquid Crystal Display
LED	:	Light Emitting Diode
LS	:	Load-Sensing
RF	:	Radio Frequency

INTRODUCTION

Hydraulic mobile machines often work in dangerous or uncomfortable conditions. Protecting the operator of the machine against the environment may be difficult or expensive. For instance, damping the vibrations of the cab may increase the costs substantially. In some cases, using short-range remote control of the machine is an easier, better, and more cost effective way to carry out the task. Moreover, in some cases controlling the machine is more effortless for the operator when one can have a different view of the situation, not only the

view from the cabin. [1]

In short-range remote control feedback is based on visual perception. Since expensive cameras are not needed short-range remote control is cost effective to be implemented and it can therefore be used also as an accessory feature with low cost machines. [2]

Several commercial remote controls for hydraulic mobile machines can be found on the market nowadays. In general terms the appearance of those commercial remote controls is quite similar. The enclosure of the remote control is relatively large and it is often supported with a strap behind the neck. The user interface is custom-made. Number of joysticks (usually no more than two), buttons, and switches depend on the application. Feedback for the operator is provided with LEDs and in some cases with an LCD panel. Wireless connection is implemented by exploiting frequency bands which are exempt from licensing.

Figure 1 MC-3-6 remote control by Cavotec
Micro-control [3]

Lack of force feedback is often considered to be the biggest disadvantage of remote control. It is often said that controllability of the machine is getting worse while using remote control since the operator can not feel the load of the machine. However, if the traditional onboard user interface of the hydraulic mobile machine is considered force feedback joysticks are not utilized in the cab. The joysticks are insensitive to the load of the machine. Feedback of the load is actually based on secondary feelings such as the vibrations of the machine and engine sound. On the grounds of these secondary perceptions a human being automatically visualizes the load level. If similar feelings can be provided while using remote control usability and controllability may be improved. Commercial solutions do not provide this feature.

A prototype of a hand-held remote control is developed at the Department of Intelligent Hydraulics and Automation at Tampere University of Technology. The hand-held remote control provides assisting force feedback information for the operator. This paper introduces the idea and implementation of a cost effective assisting force feedback function which is based on eccentric electric motors.

REMOTELY CONTROLLED HYDRAULIC MOBILE MACHINE WITH EXCAVATOR

A prototype of the remotely controlled hydraulic mobile machine (see Fig. 2) which is used as a test platform while testing the hand-held remote control is based on the commercial machine Avant 320+ manufactured by Avant Tecno Oy [4]. The body of the machine is original. Instead, hydraulics and electronics have been re-designed in order to make remote control of the machine possible.
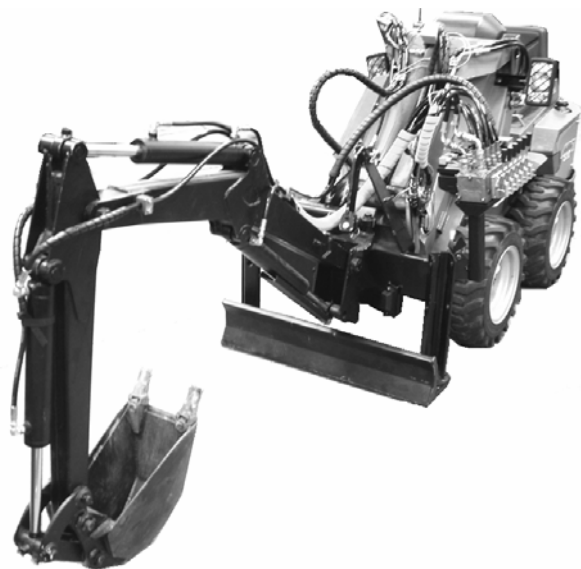
Figure 2 The prototype of the remotely controlled hydraulic mobile machine which is used as a test platform [5]

Various attachments such as different kinds of buckets and brooms can be attached to the basic machine. In this paper the excavator is studied. [4]

Hydraulics of the machine

The power transmission, telescope boom, and bucket of the modified machine are controlled with one valve block. The valve block consists of six electronically actuated proportional spool valves. One of these proportional valves of the block is used for external hydraulics, in this case for the excavator. The proportional valve block includes internal LS line which shows the highest load pressure of the system [6]. The LS pressure is measured by means of a pressure transmitter [7]. The hydraulic diagram of the machine without the excavator is shown in Fig 3.

654
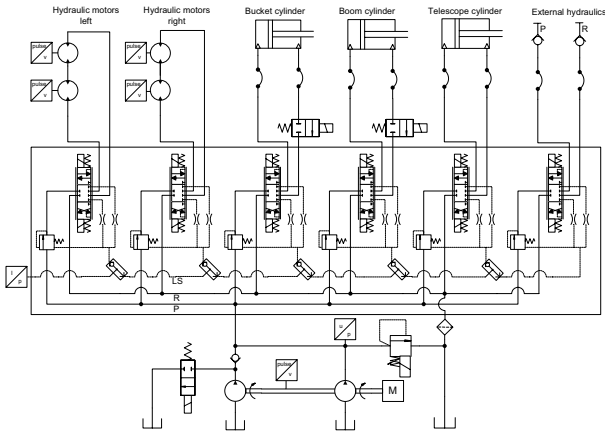
Figure 3 The hydraulic diagram of the machine without the excavator

Similar proportional valve block controls four cylinders of the excavator. The valve is attached to the body of the excavator. Also this valve includes LS line. The pressure and return lines are connected to the external hydraulics valve in the valve block of the basic machine (see Fig. 3). The port is opened when the excavator is used.
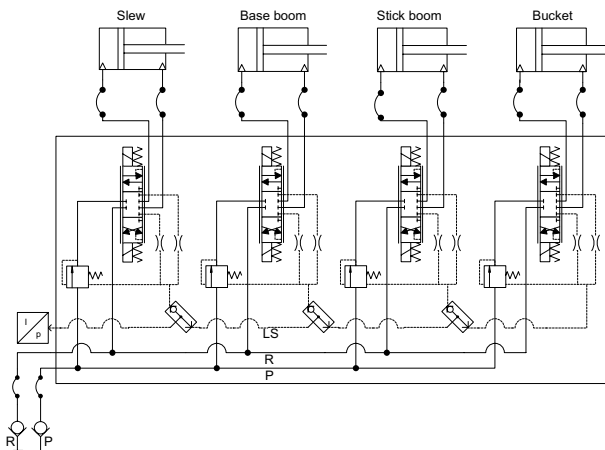
Figure 4 The hydraulic diagram of the excavator

Electronics of the machine
Electronics of the machine is distributed and communication between the modules is carried out via CAN bus. The display module DM586 is the main controller of the machine. It takes care of all high level control tasks of the machine and communicates with the remote control via serial port. Sensor values such as the LS pressure of the machine are read by means of I/O modules. [1, 8]

The excavator is controlled with the excavator control unit [9]. The control unit measures the LS pressure of the excavator with the interval of 1 ms. The pressure is filtered with a moving average filter. The filtered value

is sent to the main controller (DM586) every 10 ms via CAN bus. The algorithm of the moving average filter is represented in Eq. 1. [10]

$$Average_n = Average_{n-1} + \frac{Input\ value - Average_{n-1}}{Filter\ const\,ant} \quad (1)$$

HAND-HELD REMOTE CONTROL

The enclosure of the prototype of the hand-held remote control is from a cordless game controller for Playstation 2, manufactured by Logitech [11]. Instead, electronics and software are totally re-designed and custom-made for this application. Two joysticks of the remote control are used for controlling different actuators depending on the functional mode. Three LEDs provide state information about some important states of the system for the operator. [1, 2]

Figure 5 The prototype of the hand-held remote control

The effect of remote control on working efficiency and usability of the excavator were determined by means of an interview study. 18 testees executed same task with three different user interfaces. Remote control improved both the working efficiency and the usability. In test case, however, processed soil was homogenous and on that account conclusions from actual effect of force feedback can not be drawn. [1]

Data transmission protocol
The wireless connection between the remote control and the machine is implemented by using commercial radio modems. The half duplex data transmission and the baud rate of 38400 bps are used. The data transmission protocol is designed for this application. Nine bytes are sent in every data packet and every byte consists of start bit, eight data bits, and stop bit. New control data is sent every 50 ms. [12]

Contents of the sent and received data packets are

represented in tables 1 and 2. In table 1 the start byte is a constant value which expresses the beginning of the data packet. It also separates similar remote controls from each other if several machines are controlled at the same worksite. The index number byte includes running four-bit number. On the grounds of the index number the receiver can make sure that data is updated. The CRC byte is used for checking if the data is corrupted during the transmission.

Table 1 The sent data packet to the machine

Byte no.	Data
1	Start byte
2	Gas / Base boom of excavator
3	Steering / Bucket of excavator
4	Boom / Stick boom of excavator
5	Bucket / Slew of excavator
6	External hydraulics
7	Button states
8	Index number and button states
9	CRC

Once the main controller of the machine receives correct data packet, it sends the feedback packet to the remote control. The feedback packet includes only one data byte and the CRC byte.

Table 2 The received data packet from the machine

Byte no.	Data
1	Feedback data
2	CRC

ASSISTING FORCE FEEDBACK SYSTEM

Operator's perceptions of the load level of the machine are mostly based on engine sound and the vibrations of the cab. While using short-range remote control the operator is always close to the machine since the machine has to be seen. On that account, the operator will always hear engine sound. Therefore, the only feedback that the operator misses is the sense of vibrations.

Usually the operator is not interested in the load level until it is about to reach the maximum force capacity of the machine. When the maximum capacity is reached the operator either releases or changes the control. Thus, proportional force feedback is not necessary required.

The idea of the assisting force feedback function of the hand-held remote control is to provide for the operator information when the load of the machine increases significantly, close to maximum. Quality force feedback joysticks can not be integrated to a small device such as the hand-held remote control. In this case, the force feedback information is produced by vibrating the device instead of using force feedback joysticks. The vibration is generated by means of two eccentric electric motors (see Fig. 6). Since the motors are of a different size four various strength of vibration can be implemented.
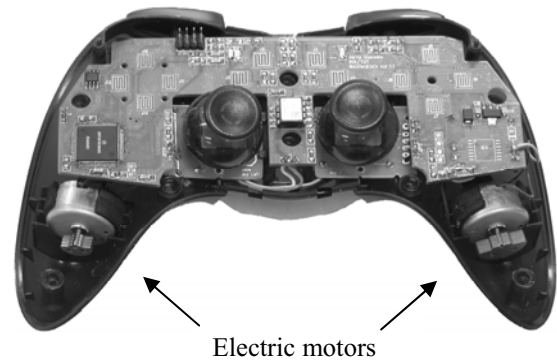
Electric motors

Figure 6 The remote control without the cover. Eccentric electric motors are mounted to the handles

The main controller of the machine (DM586) filters the highest LS pressure of the whole system (LS pressure of the basic machine or LS pressure of the excavator) during the past 50 ms utilizing the moving average filter (see Eq. 1). 50 ms window is used since new control data from the hand-held remote control is received every 50 ms. Depending on the filtered LS pressure one of four load levels is selected. The load levels can be adjusted on-line by tuning parameters in the main controller of the machine.

Information about the current load level is transferred from the machine to the remote control with a two-bit value which is included to the feedback data byte (see Table 2). On the grounds of feedback the eccentric electric motors are controlled.

Control of electric motors

Control of the electric motors is on/off type. Since DSP56F803 which is used as a controller of the remote control can not drive enough current SMART FETs are utilized as amplifier stages. [13, 14]

A disadvantage of the electric motors is electromagnetic interferences. Especially in this case when the motors are close to the processor and RF signals are used interferences have to be taken into account. Passive filtering is utilized in this application. The schematic of the amplifier stage and filtering is shown in Fig. 7.
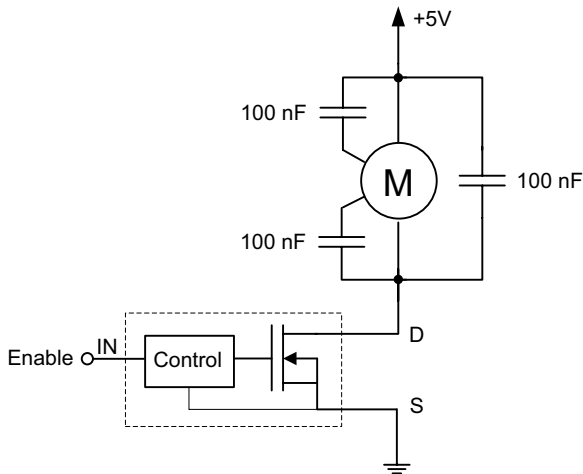
Figure 7 The schematic of the filter and amplifier stage of the electric motors.

BEHAVIOUR OF THE SYSTEM DURING EXCAVATION CYCLE

The system was tested by controlling the excavator remotely. Figs. 8-10 show the behaviour of the system during one excavation cycle. In the test run the bucket of the excavator was filled once by moving all joints. After that the excavator was slewed aside and the bucket was emptied. Finally the excavator was returned back for the next cycle. During the test run the load increased so high that the maximum force capacity of the machine was exceeded. The control values are shown in Fig. 8 and the filtered LS pressure in Fig. 10.
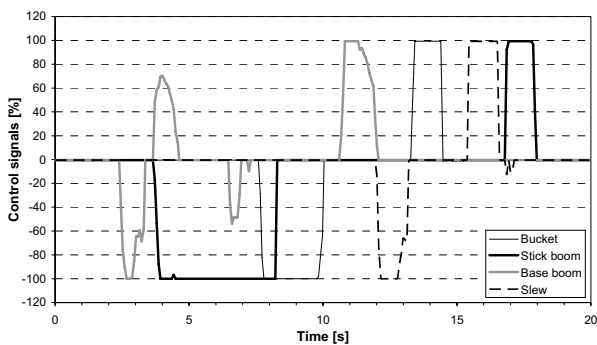
Figure 8 The control values of the excavator during the excavation cycle

The orientation of the excavator was measured by means of a potentiometer and three inclinometers. The potentiometer was utilized for measuring the position of the slew cylinder [5]. The inclinometers (with modified software compared to reference) were attached to the base boom, stick boom, and bucket of the excavator [15]. Approximations of the joint angles were calculated

by subtracting the angle values from each other. The slew angle and the relative joint angles are illustrated in Fig. 9. Some offset have been added to the joint angles to fit curves in one figure. High frequency oscillation and peaks can be noticed in Fig. 9. This oscillation is due to characteristic of the inclinometers utilized in the measurements. In this case peaks and oscillation can be ignored.
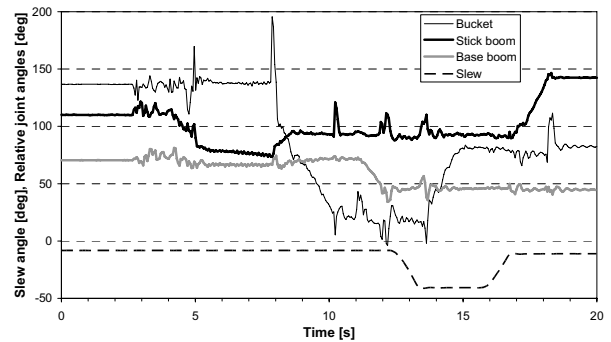
Figure 9 Variation of the angles during the test run. The joint angles are relative values which show the approximation of variation
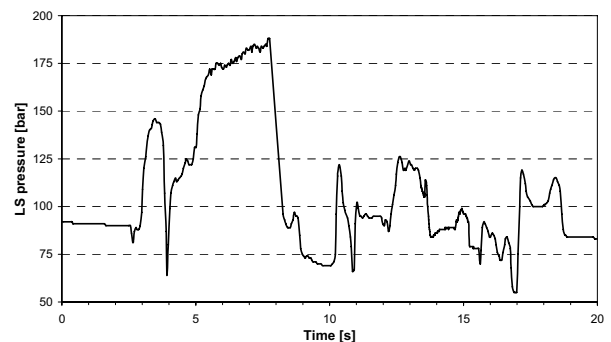
Figure 10 The filtered LS pressure of the excavator

The idea of the assisting force feedback system is to inform the operator when the load tends to the maximum force capacity of the machine. Thus, the pressure behaviour close the maximum pressure is important. In this case the maximum pressure of the system is about 180 bar.

Let us consider more carefully the period from 4 to 9 seconds in Figs. 8-10. After the control of the stick boom is activated (at 4 s), the joint angle of the stick boom starts to change. At the same time the LS pressure increases. During the period from 5 to 7.8 seconds the joint angles of the excavator do not vary significantly even though the stick boom is controlled with the maximum control value. After 5 seconds the LS pressure increases rapidly to 175 bar. The LS pressure

657

remains high until the bucket is controlled at 7.8 seconds. The change in the angle of the bucket decreases the load of the excavator and the LS pressure drops rapidly. In other words, between 5 and 7.8 seconds nothing moves significantly regardless of the controls since the machine does not have enough power to execute the controls. At this time the LS pressure remains almost constant. At other times the machine is able to execute the controls and the LS pressure varies without reaching the maximum value.

If the pressure level which enables force feedback is adjusted to 170 bar the system starts to vibrate the remote control at 5.5 seconds. On the ground of the vibration the operator knows that the maximum force capacity of the machine is achieved. The vibration stops immediately when the operator changes the controls so that the load decreases (in this case controls the bucket).

CONCLUSIONS

Lack of feedback is often considered to be one of the biggest disadvantages of remote control. While using short-range remote control the operator gets good visual feedback including stereoscopic vision. An advantage compared to the traditional onboard user interface is that the angle of view can be changed according to need. Short-range remote control also offers sound feedback. In addition to visual and sound feedbacks the onboard user interface provides force feedback at some level. In real terms the operator composes so called force feedback of the vibrations of the machine and engine sound.

In this paper the idea of the assisting force feedback system for the hand-held remote control is introduced. The load of the machine is measured by means of the LS pressure of the system. The remote control includes two eccentric electric motors which are utilized for vibrating the remote control when the load level of the machine exceeds certain level. Four different strengths of vibrations can be produced.

The system was tested by means of the hydraulic mobile machine with the excavator attachment. Behaviour of the system during one excavation cycle is represented. The goal was to detect the situation when the machine can not execute the control task because of the limited force capacity and inform the operator about the lack of force. According to measurements this phenomenon can be discovered by measuring the LS pressure and the system designed works.

FUTURE WORK

In future more tests have to be carried out to find out how the system works in different conditions. Also a usability test has to be arranged to discover whether the system improves usability of the machine.

REFERENCES

1. Uusisalo, J. R. A., Karhu, O. I., and Huhtala, K. J., A., Hand-Held Remote Control as a User Interface for a Hydraulic Mobile Machine with an Excavator, Proceedings of the 51st National Conference on Fluid Power, Las Vegas, NV, USA, 2008.
2. Uusisalo, J. R. A., Vilenius, J. M., Vuohijoki, A. J., Hirvonen, S.-M., Karhu, O. I., and Huhtala, K. J., Portable Remote Control for Teleoperated Hydraulic Mobile Machine, Proceedings of the Tenth Scandinavian International Conference on Fluid Power, Vol. 3, Tampere, Finland, 2007, pp. 35-45.
3. Radio Remote Control Systems, Brochure, Lugano, Switzerland, 2007, Cavotec Micro-control AS.
4. Avant 300 series, 500 series, Brochure, Ylöjärvi, Finland, 2005, Avant Tecno Oy.
5. Karhu, O. I., Moya, J., Uusisalo, J. R. A., and Huhtala, K. J., Enabling Autonomous Functions on Hydraulic Excavator Attachment, Proceedings of the Tenth Scandinavian International Conference on Fluid Power, Vol. 2, Tampere, Finland, 2007, pp. 35-45.
6. PVG 32 Proportional Valves, Technical Information, Lincolnshire, IL, USA, 2006, Sauer-Danfoss Inc.
7. EXNA250.0A Pressure Transmitter, Data Sheet, Männedorf, Germany, 2006, Trafag AG.
8. Display Module DM586, Technical Data Sheet, Tampere, Finland, 2003, Axiomatic Technologies Oy.
9. Karhu, O. I., Vilenius, J. M., Uusisalo, J. R. A., Moya, J., and Huhtala, K. J., Intelligent Excavator for Hydraulic Mobile Machine, Proceedings of the 22nd International Symposium on Automation and Robotics in Construction, Ferrara, Italy, 2005, 5 pp.
10. CANopen Quad Controller, User Manual UMAX020502, version 1.04, Mississauga, ON, Canada, 2006, Axiomatic Technologies Corp.
11. Logitech Cordless Action Controller for Sony Playstation 2. http://www.logitech.com. (Referred 7.12.2006)
12. Ultracom UC800 Radio Modem, Brochure, Kempele, Finland, 2004, Ultracom Oy.
13. IPS021 SMART POWER MOSFET, Data Sheet, El Segundo, CA, USA, 2001, International Rectifier.
14. DSP56F803, Data Sheet, Austin, TX, 2005, Freescale Semiconductor Inc.
15. Honkakorpi, J., CAN-bus based embedded inclinometer, Master of Science thesis, Tampere, Finland, 2007, 47 p. (in Finnish)

P2-14

CLUTCH-TO-CLUTCH SHIFT CONTROL OF AN AUTOMATIC TRANSMISSION WITH PROPORTIONAL PRESSURE CONTROL VALVES

Bingzhao GAO*, Hong CHEN** and Kazushi SANADA***

* Department of Mechanical Engineering, Yokohama National University, Japan
Jilin University, China;
** Department of Control Science and Engineering, Jilin University
5988 Renmin Str., 130025 Changchun, China
*** Department of Mechanical Engineering, Yokohama National University
79-5, Tokiwadai Hodogaya-Ku, Yokohama, 240-8501, Japan
(E-mail: ksanada@ynu.ac.jp)

ABSTRACT

For a new kind of automatic transmissions using proportional pressure valves to control the clutches directly, a two-degree-of-freedom controller is designed for clutch slip control during the inertia phase of the shift process. The controller is designed based on a low order linear model which is derived from dynamics of the proportional pressure control valve and the vehicle drive line. The feedback gain is calculated by robust pole assignment methods while the feed-forward compensator aims to improve system response. Finally, the designed controller is tested on an AMESim powertrain simulation model. Simulation results show that the rotational speed difference of clutch can track the desired trajectory well, and shift shock can be reduced by designing suitable feed-forward compensator.

KEY WORDS

Automatic Transmission, Proportional Pressure Control Valves, Clutch Control, Clutch-to-Clutch Shift

NOMENCLATURE

A : piston area of clutch B

C_A : a constant coefficient depending on air density, aerodynamic drag coefficient and the front area of the vehicle.

$C(\lambda)$: capacity factor of torque converter

dS_x : longitudinal slip threshold

F_s : force of return spring

F_x : tire longitudinal force

$F_{x\max}$: maximum longitudinal force of the tire

i_b : electric current of pressure control valve B

i_{df} : gear ratio of the differential gear box

$\widetilde{K}_{cv}$: valve gain

$\widetilde{L}_{cv}$: time-lag of valve

N : number of friction plates

p_{cb} : pressure of cylinder B

p_s : input port pressure of the valve

R : effective radius of push force acted on the friction plates

R_w : tire radius

S_x : longitude slip ratio of tires

T_p : torque converter pump torque

T_t : torque converter turbine torque

T_v : resistant torque delivered from tire to drive shaft

T_w : rolling resistant moment of tires

$t(\lambda)$: torque ratio of torque converter

γ : gear ratio of sun gear to ring gear

λ : speed ratio of torque converter

ω_0 : output speed of transmission

ω_e : engine speed

ω_r : rotational speed of ring gear

ω_t : turbine speed

$\Delta\omega$: speed difference of clutch B

μ : friction coefficient of clutch plates

$\tilde{\tau}_{cv}$: time constant

INTRODUCTION

Automotive transmissions transfer the engine torque to the vehicle with desired ratios. To improve fuel economy, reduce emission and enhance driving performance, many new technologies have been introduced in the transmission area in recent years, such as Dual Clutch Transmission (DCT) and new Automatic Transmissions (AT) controlling clutches independently [1]. Furthermore, smart proportional valves with large flow rate are developed for direct clutch pressure control, without using the pilot duty solenoid valve [2]. These valves can be used in new Automatic Transmissions to improve the ability of adapting to different driving conditions, as well as to reduce the cost and to improve packaging.

Clutch-to-clutch shift of this kind of Automatic Transmission involves electronic control of both the oncoming and offgoing clutches, thus guarantee the timing and coordination between them, which are assured by the hydraulic logic circuits in the case of traditional AT. The elimination of some shift valves and accumulators, etc. greatly simplifies the transmission mechanical content, but makes the robust control of clutch-to-clutch shifts a challenge [1, 3]. Furthermore, the sensors for measuring the pressure of clutch cylinder are seldom used because of the cost and durability. If system state feedback is to be used to enhance system control quality, the cylinder pressure needs to be estimated [4, 5].

Two-degree-of-freedom controller design is suitable to many automotive control systems for it can fulfill good tracking performance and robustness simultaneously [6]. In [7], a two-degree-of-freedom controller was designed for the speed control of a braking mechanism, in which the feedback gain was calculated by μ synthesis.

This paper, therefore, use the two-degree-of-freedom controller design method to carry out the clutch engagement control of an Automatic Transmission with proportional pressure control valves. The clutch cylinder pressure, which is necessary for state feedback

control is estimated by a reduced-order state observer. The feedback gain is calculated by robust pole assignment methods while the feedforward compensator aims to improve the system response. Not only the rotational speed can track the desired trajectory well, but also can shift shock be reduced by choosing suitable feedforward compensator. Finally, the designed controller including the pressure estimator is tested on an AMESim powertrain simulation model.

CLUTCH SYSTEM MODELING
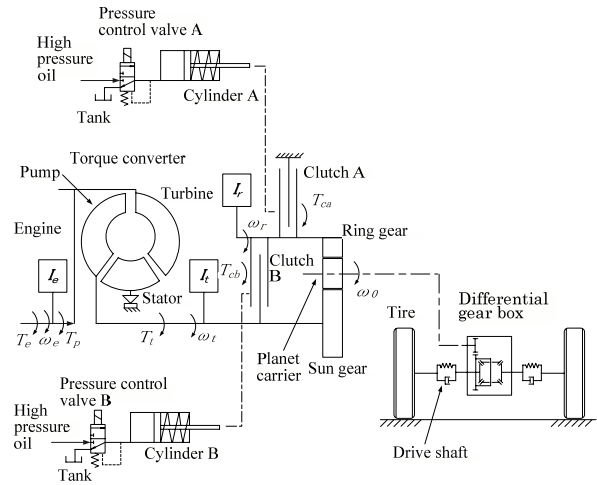
Figure 1 Schematic graph of Automatic Transmission

We consider the powertrain in passenger vehicles with a two-speed automatic transmission, as schematically shown in Figure 1. A planetary gear set is adopted as the shift gear, two clutches are used as the actuators, and two proportional pressure valves are used to control the two clutches respectively. When clutch A is engaged and clutch B disengaged, the powertrain is operating in 1st gear, the speed ratio is

$$i_1 = (1 + 1/\gamma) \qquad (1)$$

While clutch A is disengaged and clutch B engaged, the vehicle is driven in 2nd gear with the speed ratio:

$$i_2 = 1$$

(2)

During the shift process, the oncoming and offgoing clutches are controlled by the proportional pressure control valves independently, thus the shift timing and cooperation of the clutches are guaranteed.

Proportional Pressure Control Valves

The cylinder's pressure is decided by the input electric current of proportional pressure control valve. The dynamics of the proportional valve can be simplified as a first-order system [7]:

$$\tilde{\tau}_{cv}\dot{p}_{cb} = -p_{cb} + \tilde{K}_{cv}\,i_b(t - \tilde{L}_{cv}) \qquad (3)$$

The values of $\tilde{\tau}_{cv}$, $\tilde{K}_{cv}$ and $\tilde{L}_{cv}$ are not constant but

vary according to different operating point.

In order to represent real valve dynamics at different operating points, the parameters $\tilde{\tau}_{cv}$, $\tilde{L}_{cv}$, $\tilde{K}_{cv}$ are given by lookup tables according to different operating points, i.e. valve current i_b and the input port pressure of the valve p_s [8].

The above time-variant model of the valves can be used for system simulation. During controller design stage, however, the parameter variations are ignored, and the dynamics of the valve can be rewritten as

$$\tau_{cv}\dot{p}_{cb} = -p_{cb} + K_{cv}\,i_b \qquad (4)$$

where τ_{cv} and K_{cv} are constants.

Clutch System

The 1st to 2nd up shift is considered here as an example. During the inertia phase, the pressure of cylinder A is already approximately zero, and the pressure of cylinder B is controlled so that clutch B can be engaged smoothly in required time. If the variation of friction coefficient μ is ignored, the speed difference of clutch B can be described by the following equation[9],

$$\Delta\dot{\omega} = (C_{13} - C_{23})\mu\,RNA\,p_{cb} + (C_{11} - C_{21})T_t +$$
$$(C_{14} - C_{24})T_v - (C_{13} - C_{23})\mu\,RNF_s$$

where $\Delta\omega = \omega_t - \omega_r$ and C_{ij} are the constant coefficients decided by inertia moments of vehicle and transmission shafts.

Without considering the transient dynamics of the torque converter, T_t can be calculated by the steady-state characteristics of the torque converter as follows

$$T_t = t(\lambda)C(\lambda)\omega_e^2 \qquad (5)$$

with $\lambda = \dfrac{\omega_t}{\omega_e}$.

Moreover, if the torsion dynamics of drive shaft, tire slip and road grade are ignored, the resistant torque delivered from tire to drive shaft T_v can be calculated as

$$T_v = \frac{T_w}{i_{df}} + \frac{C_A R_w^{\,3}}{i_{df}^{\,3}}\omega_0^2 \qquad (6)$$

Model for Controller Design

By selecting speed difference $\Delta\omega$, and pressure p_{cb} of cylinder B as the state variables $x1$; $x2$ respectively, the inertia phase of 1st to 2nd gear up shift process can be described in the following state space form

$$\dot{x}_1 = (C_{13} - C_{23})\mu\,RNA\,x_2 + T_d \qquad (7a)$$

$$\dot{x}_2 = -\frac{1}{\tau_{cv}}x_2 + \frac{K_{cv}}{\tau_{cv}}u \qquad (7b)$$

where
$u = i_b$, the control input;

$$T_d = (C_{11} - C_{21})T_t + (C_{14} - C_{24})T_v - (C_{13} - C_{23})\mu\,RNF_s \qquad ,$$

regarded as disturbance torque here.

It should be noted that, although T_d is regarded as disturbance torque, it has large effect on the dynamics of speed difference. Our previous study has shown that, when only linear feedback is used to carry out the control problem, it is difficult to get satisfactory control performance. Thus a two-degree-of-freedom controller will be designed and used to improve the control performance.

CONTROLLER DESIGN

The clutch pressure observer [9, 10] design is omitted here, and the clutch pressure is assumed available in the following controller design procedure.

Two-Degree-of-Freedom Controller

Two-degree-of-freedom controller is a control system with a forward compensator besides the feedback controller [11]. Its block diagram is shown in Figure 2.

If the controlled object $P(s)$ is modeled accurately enough, the transfer function from input to output turns to be,

$$\frac{Y(s)}{R(s)} = M(s) \qquad (8)$$

which means that the system transfer function only depends on the dynamics of $M(s)$. Therefore, the quality of output response can be improved by giving suitable $M(s)$. While, on the other hand, the feedback controller $K_b(s)$ can be designed for high stability and robustness.
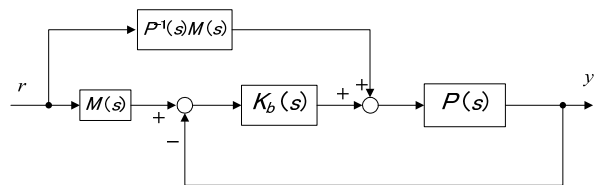
Figure 2 Block diagram of two-degree-of-freedom controller

Two-Degree-of-Freedom Controller Design for Clutch Slip Control

Clutch slip controller will be designed in this section based on equation (7). Rewrite the equation (7) in matrix form:

$$\dot{x} = A\,x + B\,u + E\,d \qquad (9a)$$

and the output equation is:

$$y = C\,x \qquad (9b)$$

where,

$$x = [\Delta\omega \quad p_{cb}]^T, \quad y = \Delta\omega$$

$$A = \begin{bmatrix} 0 & (C_{13} - C_{23})\mu\,RNA \\ 0 & -\dfrac{1}{\tau_{cv}} \end{bmatrix}, \quad B = \begin{bmatrix} 0 & \dfrac{K_{cv}}{\tau_{cv}} \end{bmatrix}^{T}$$

$$E = \begin{bmatrix} 1 & 0 \end{bmatrix}^{T}, \quad C = \begin{bmatrix} 1 & 0 \end{bmatrix}, \quad u = i_b, \quad d = T_d$$

Based on the above linear state equations, the two-degree-of-freedom clutch slip controller is designed. The block diagram is given as Figure 3.
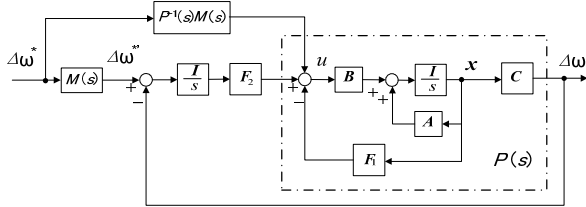
Figure 3 Two-degree-of-freedom clutch slip controller

If no feedforward compensator is included, the gain F_1 and F_2 turns to be the commonly used linear servo system for output tracking control. The robust pole assignment method proposed by [12] is used here to calculate F_1 and F_2, which is also the algorithms of command "*place*" in control toolbox of MATLAB.

After determining the feedback gain F_1 and F_2, the forward compensator can be derived. First the part circled in the dashed line is labeled as $P(s)$. Being different from the $P(s)$ of Figure 2, $P(s)$ defined here includes the state feedback besides the controlled object. This treatment allows for convenient design of the feed forward compensator and the later simulation results show its validity. Thus, $P(s)$ can be calculated by,

$$P(s) = C(s\mathbf{I} - A')^{-1} B = \frac{P_n(s)}{P_d(s)} \quad (10)$$

where

$$A' = A - B\,F_1 \quad (11)$$

$P_n(s)$ is a constant and $P_d(s)$ is a second-order polynomial of the Laplace variable s.

Because $P^{-1}(s)M(s)$ must be a proper transfer function, $M(s)$ is set as a third-order transfer function with the following form,

$$M(s) = \frac{p_0^{\,3}}{(s + p_0)^3} \quad (12)$$

The desired speed difference is given first by the request of shift time, which is shown as $\Delta\omega^*$ in Figure 3. Then it is modified by reference model $M(s)$ and yields $\Delta\omega^{*'}$, the real desired trajectory. The smaller value of p_0 results in smoother shape of $\Delta\omega^{*'}$, which can be seen from Figure 7 in the section "Simulation

results ".

After getting $P(s)$ and $M(s)$, the feed forward compensator $P^{-1}(s)M(s)$ can be calculated by,

$$P^{-1}(s)M(s) = \frac{P_d(s)M(s)}{P_n(s)} \quad (13)$$

SIMULATION RESULTS

Powertrain Simulation Model
The simulation model of the powertrain is established by commercial simulation software AMESim, which supports the Simulink environment by S-Function. The powertrain simulation model can be constructed by combining the different submodels provided by the POWERTRAIN library of AMESim.

a) Engine and torque converter
The function of engine output torque is always given as the map of engine rotational speed and engine throttle angle, which can be fitted as polynomial expression. Figure 4 shows the torque characteristic of the engine used in this study, i.e. a 2000cc injection gasoline engine.
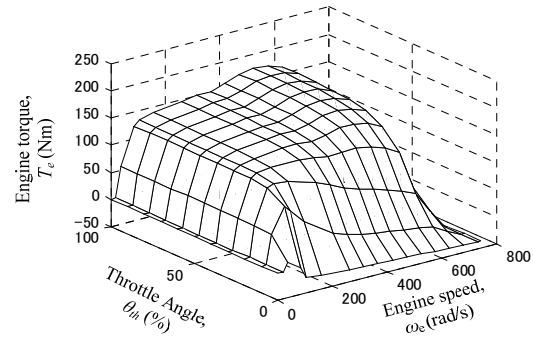
Figure 4 Engine torque map with speed and throttle opening
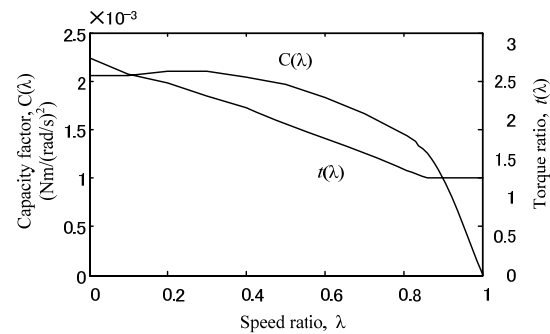
Figure 5 Capacity factor and torque ratio of torque converter

The dynamic properties of torque converter when turbine is driven forward are often characterized as

follows:

$$T_p = C(\lambda)\omega_e^2 \qquad (14a)$$

$$T_t = t(\lambda)T_p \qquad (14b)$$

The capacity factor $C(\lambda)$ and torque ratio $t(\lambda)$ used here are given in Figure 5.

b) Clutches and valves

Different from model for controller design, the friction coefficient of clutch plates μ is not constant but a function of $\Delta\omega$ with the relationship shown in Figure 6.

The dynamic parameters of the proportional valve are also time-variant according to different operating points.
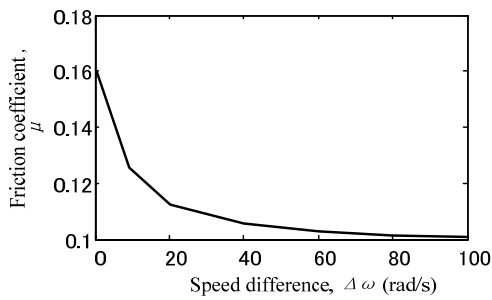
Figure 6 Friction characteristics of clutch plates

c) Driveshaft and tires

The two drive shafts between the differential gear and front wheels are represented as torsion spring with stiffness coefficient K_l and a torsion damping with damping coefficient C_l.

Only the longitudinal force of the tire is considered here. The longitudinal force of the tire F_x is represented as a tanh function of the longitude slip ratio S_x:

$$F_x = F_{x\max} \tanh\left(\frac{2S_x}{dS_x}\right) \qquad (15)$$

Simulation Results

1st to 2nd gear up shift is simulated. During the inertia phase deduced controller works to make speed difference of clutch B tracking desired trajectory.

The feedback gain F_1 and F_2 used here are

$$F_1 = \left[-7.8\times10^{-3} \quad 1.9\times10^{-6}\right]$$

$$F_2 = [-0.081]$$

and the value of p_0 is set to be

$$p_0 = 30.$$

The 1st to 2nd gear up shift simulation results are given by Figure 7. The gear shift process consists of three parts: before 7.94s, the 1st gear torque phase; after 8.24s, the 2nd gear torque phase and between 7.94 s and 8.24s, the inertia phase. During the toque phases the rotational speeds of shafts do not change greatly, while during the

inertia phase, the rotational speeds change intensively because of the clutch slip.

The desired time of the inertia phase is set to be 0.3s. The simulation result of the speed difference of clutch B is shown in Figure 7(b), and $\Delta\omega$ and $\Delta\omega^{*'}$ are also given as well. It can be seen that the speed difference between turbine and ring gear $\Delta\omega$ can track reference value $\Delta\omega^{*'}$ without large error.

The angle of driveshaft θ_l is shown to examine the shift shock. It can be seen that at the time the inertia phase begins and ends, there is no sharp change in the electric current of valve B, which results in smooth change of driveshaft angle. Especially before 8.24s, the time clutch B locked up, the electric current of valve B decreases for a while, which makes the lock up of clutch smooth.

During the shift process, the engine is controlled to cooperate with the transmission shift. The throttle angle θ_{th} decrease and increase respectively when shift start and end, with angle and rotational speed decided in advance.

(a)

(b)
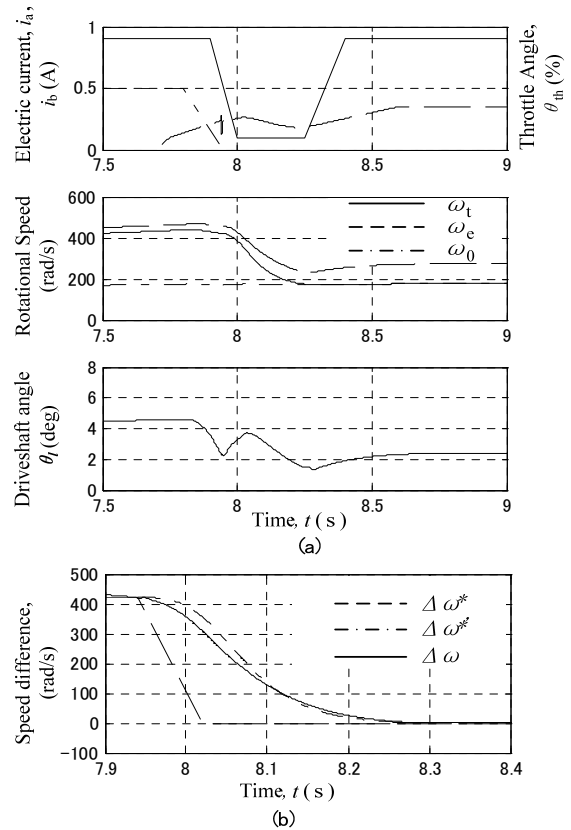
Figure 7 Simulation results of 1st to 2nd gear up shift

CONCLUSIONS

For the automatic transmission using proportional pressure control valves to control the clutches directly, a two-degree-of-freedom clutch slip controller is designed

for the inertia phase of gear shift.

Given required shift time, the controller can be designed and simulation results show that the speed difference can track the desired trajectory well. The feed forward compensator can reduce shift shock as well as improve tracking performance.

REFERENCES

1. Sun, Z., Hebbale, K., Challenges and Opportunities in Automotive Transmission Control. Proceedings of the 2005 American Control Conference, 2005, **5**, pp. 3284-3289.
2. Shioiri, H., Drivetrain. Recent 10 Years of Automotive Engineering. Society of Automotive Engineers of Japan, Tokyo, 2007, pp. 134-137, in Japanese.
3. Morimoto, Y., Mechanism and Control of AT. Grand Prix Publishing, Tokyo, 2006, in Japanese.
4. Yokoyama, M., Sliding mode control for automatic transmission systems, Journal of the Japan Fluid Power System Society, 2008, **39**-1, pp. 34-38, in Japanese.
5. Watechagit, S., Srinivasan, K., Implementation of on-line clutch pressure estimation for stepped automatic transmissions. Proceedings of the 2005 American Control Conference, 2005, **3**, pp.1607-1612.
6. Tsutsumi, J., Higashimata, A., Application of advanced control technologies to the vehicle control. Journal of Society of Automotive Engineers of Japan, 2005, **59**-5, pp.10-15, in Japanese.
7. Sanada, K., Kitagawa, A., A study of two-degree-of-freedom control of rotating speed in an automatic transmission, considering modeling errors of a hydraulic system. Control Engineering Practice, 1998, **6**-9, pp.1125-1132.
8. Gao, B. Z., Sanada, K., Furihata, K., A Study on Modeling Hydraulic-Power-Steering for Heavy Duty Vehicles, Transactions of the Japan Fluid Power System Society, 2008, **39**-2, pp. 19-27, in Japanese
9. Gao, B. Z., Chen, H. and Sanada, K., Two-degree-of-freedom controller design for clutch slip control of automatic transmission, SAE Technical Paper, 2008-01-0537.
10. Gao, B. Z., Chen, H., Zhao, H. Y. and Sanada, K., A reduced-order nonlinear clutch pressure observer for automatic transmission using ISS, submitted to IEEE-CDC 2008.
11. Nonami, K., Nishimura, H., Control Theory Basic Based on MATLAB. Tokyo Denki University Press, Tokyo, 2003, pp. 187, in Japanese.
12. Kautsky, J., Nichols, N. K., Robust pole assignment in linear state feedback. International Journal of Control, 1985, **41**-5, pp. 1129-1155.

P2-15

NONLINEAR MODELING AND CONTROL DESIGN OF ELECTRO-HYDROSTATIC ACTUATOR

Rongjie KANG[*], Jean Charles MARE [**] and Zongxia JIAO[*]

* School of Automation Science and Electrical Engineering
Beihang University, Beijing, 100083, China
(E-mail : kangrongjie@vip.163.com)
** Department of Mechanical Engineering
Institut National des Sciences Appliquees de Toulouse, 31077, France

ABSTRACT

In this paper, a typical architecture of Electro-Hydrostatic Actuator (EHA) is described and modeled by the block diagram based on mathematic equations, which is a nonlinear accuracy model. The single PID, cascade PID and state feedback controllers are respectively designed and applied to this model for comparison analysis that focused on system stability, stiffness and dynamic characteristics. It is proven that the state feedback controller along with dynamic pressure feedback strategy could efficiently improve both static and dynamic performance.

KEY WORDS

EHA, Block diagram model, Single PID, Cascade PID, State feedback

NOMENCLATURE

A : Piston active area [m^2]
B : Oil bulk modulus [N/ m^2]
D : Pump displacement [m^3/rad]
F_c : Coulomb friction [N]
F_s : Maximum static friction of piston [N]
F_{ex} : External load force [N]
J : Total inertia of motor and pump [Kg·m^2]
K_c : Motor speed constant [v/(rad/s)]
K_t : Motor torque constant [N·m/A]
K_{elp} : Pump external leakage coefficient [(m^3/s)/Pa]
K_{ilp} : Pump internal leakage coefficient [(m^3/s)/Pa]
K_{ilj} : Hydraulic jack internal leakage coefficient [(m^3/s)/Pa]
K_{vism}: Motor viscous coefficient [N·m/(rad/s)]
K_{visp}: Piston viscous coefficient [N/(m/s)]
k : Polytropic exponent [-]

L : Motor inductance [H]
M : Total mass of piston and load [Kg]
R : Motor resistance [Ohm]
V_{10} : Initial volume in chamber 1 [m^3]
V_{20} : Initial volume in chamber 2 [m^3]
X_t : Output displacement of actuator [m]
ω : Rotational speed of motor [rad/s]

INTRODUCTION

The demand for conventional hydraulic actuation is gradually decreasing due to its limitations such as: low energy efficiency, leakage, noise, low maintainability. The Power-By-Wire (PBW) technology is becoming an attractive direction of future airborne actuation system. A PBW flight control system would simplify the secondary power generation, eliminate the need for a central hydraulic power supply, and replace the hydraulic pipes by electric power cables. As a result, the reliability,

survivability, efficiency and maintainability of the aircraft would be greatly improved.

The Electro-Hydrostatic Actuator (EHA) is one kind of PBW actuator that uses the hydraulic pump to transfer the rotational motion of electrical motor to the actuator output. EHA is based on the principle of closed-circuit hydrostatic transmission, so that, there are no requirements for oil reservoir or electro-hydraulic servo-valves.

A lot of research papers have modeled the EHA system by transfer functions in the past [1,2,3], however, it is a linear modeling method that has some disadvantages in description of realistic EHA: neglecting the refeeding circuit which contains some nonlinearity; simplifying the friction, especially the static friction; supposing that all the initial conditions are zero. To solve these problems, the block diagram model of EHA is established; furthermore, some different control methods are designed and compared in this paper.

EHA ARCHITECTURE DESIGN

There are several architectures of EHA: EHA with fixed pump displacement and variable motor speed (FPVM), EHA with variable pump displacement and fixed motor speed (VPFM), EHA with variable pump displacement and variable motor speed(VPVM). Nowadays, the FPVM-EHA (Fig.1) is more popular for its simple structure and efficiency. In this system, a bi-directional pump rotates in variable speed and directions given by electric motor. As a result, the oil flow and supply pressure are variable to drive the symmetrical actuator.
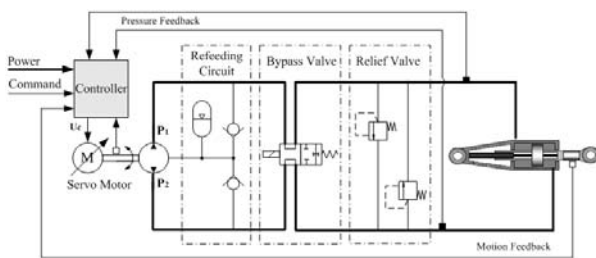
Figure 1 Architecture of FPVM-EHA

EHA MODELING

Modeling of DC Motor
The Brushless DC Motor (BLDCM) is chosen as the EHA driving motor. This is mostly due to its high reliability which is very important for airborne actuation. The mathematic equations of BLDCM are:

$$\begin{cases} U_c = E + L\dfrac{di}{dt} + Ri \\ E = K_c\omega \\ T_e = K_t i \\ T_e = J\dot{\omega} + T_f + T_l \end{cases} \tag{1}$$

According to Eq.(1), a block diagram model of motor is gotten as Fig.2 by Simulink. The part in dashed is current protection that could be realized by software.
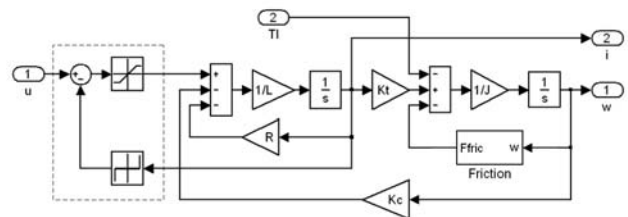
Figure 2 Block diagram model of motor

Modeling of Pump
The flow equation of pump outlet is:

$$Q_1 = D\cdot\omega - K_{ilp}(P_1 - P_2) - K_{elp}(P_1 - P_{ac}) \tag{2}$$

The flow equation of pump entry is:

$$Q_2 = D\cdot\omega - K_{ilp}(P_1 - P_2) + K_{elp}(P_2 - P_{ac}) \tag{3}$$

Where P_{ac} is the pressure of accumulator. The diagram model of pump is shown in Fig. 3.
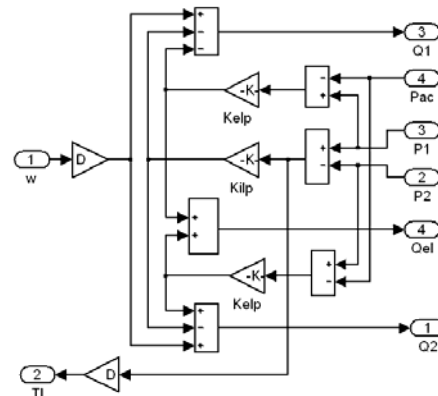
Figure 3 Block diagram model of pump

666

Modeling of Refeeding Circuit

To keep the closed-circuit of EHA, a refeeding circuit composed of accumulator and check valves is necessary. The schematic diagram is shown in Fig. 4.
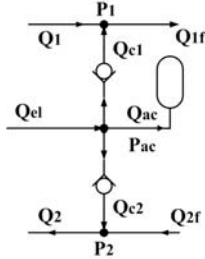
Figure 4 Schematic diagram of refeeding circuit

The flow equations of refeeding circuit are:

$$\begin{cases} Q_{ac} = Q_{el} - Q_{c1} - Q_{c2} \\ Q_{1f} = Q_1 + Q_{c1} \\ Q_{2f} = Q_2 - Q_{c2} \end{cases} \qquad (4)$$

Where Q_{el} is the external leakage of pump, Q_{c1}, Q_{c2} are the flow of check valves depending on $(P_1 - P_{ac})$ and $(P_2 - P_{ac})$. The relationship between Q_{ac} and P_{ac} could be described as follows:

$$P_{ac} = P_{aci} V_{gasi}^k / (V_{gasi} - \int Q_{ac} dt)^k \qquad (5)$$

Where P_{aci} is the initial pressure of accumulator, V_{gasi} is the initial volume of gas, k is the polytropic exponent of gas within the range from 1.0 to 1.4. The block diagram model of refeeding circuit and accumulator are shown in Fig. 5 and Fig. 6.
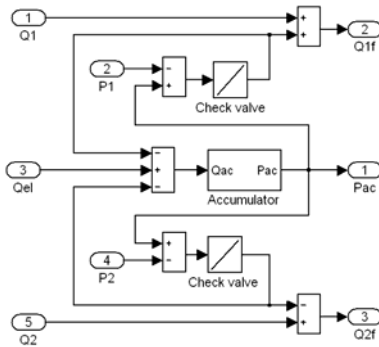
Figure 5 Block diagram model of refeeding circuit
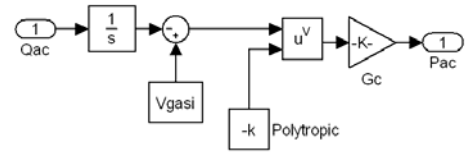
Figure 6 Block diagram model of accumulator

Modeling of Hydraulic actuator

EHA requires a symmetrical actuator in order to ensure flow balance between the actuator and the pump. The hydraulic jack is divided into two working chambers by the piston [4].

The flow of oil-in chamber could be described by the following equation:

$$Q_{1f} = A\dot{x}_t + \frac{V_{10} + Ax_t}{B}\dot{P}_1 + K_{ilj}(P_1 - P_2) \qquad (6)$$

The flow of oil-out chamber could be described by the following equation:

$$Q_{2f} = A\dot{x}_t - \frac{V_{20} - Ax_t}{B}\dot{P}_2 + K_{ilj}(P_1 - P_2) \qquad (7)$$

In such a symmetrical actuator, the initial volume V_{10} and V_{20} are of the same value.

The load force balance equation of the piston is:

$$A(P_1 - P_2) = M\ddot{x}_t + F_{ex} + F_{fric} \qquad (8)$$

Where F_{fric} is the friction which would be described later. The diagram model of hydraulic jack and piston are respectively shown in Fig. 7 and Fig. 8:
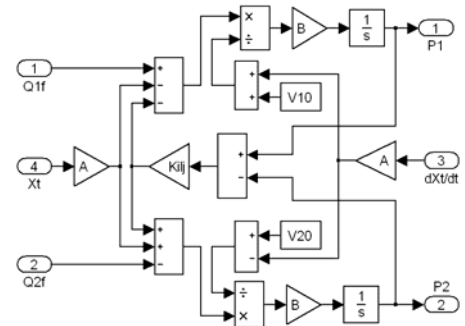
Figure 7 Block diagram model of hydraulic jack
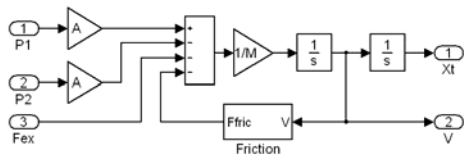
Figure 8 Block diagram model of piston

Modeling of Friction
The friction model is given as follows [5]:

$$F_f(\dot{x}_t) = [F_c + (F_s - F_c) \cdot e^{-|\dot{x}_t|/\alpha} + K_{vis} \, | \, \dot{x}_t \, |] \cdot sign(\dot{x}_t) \quad (9)$$

Where F_c is the Coulomb friction, $(F_s - F_c) \cdot e^{-|\dot{x}_t|/\alpha}$ is the Stribeck friction, and $K_{vis} \, | \, \dot{x}_t \, |$ is the viscous friction. For improvement, $sign(\dot{x}_t)$ could be replaced by $\tanh(\dot{x}_t / \beta)$ to make the model continuous:

$$F_f(\dot{x}_t) = [F_c + (F_s - F_c) \cdot e^{-|\dot{x}_t|/\alpha} + K_{vis} \, | \, \dot{x}_t \, |] \cdot \tanh(\dot{x}_t / \beta) \quad (10)$$

Where α, β are the reference speeds approximately within the range from 0.001m/s to 0.01m/s. The diagram model of the friction is shown in Fig. 9.
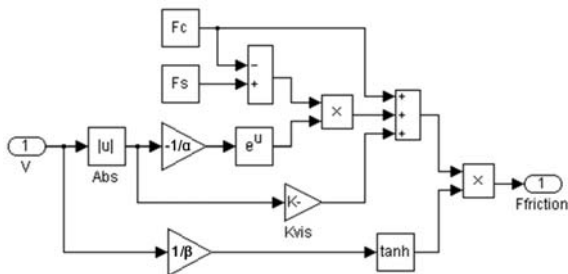
Figure 9 Block diagram of friction

Overall EHA System
Based on the above sub-models, an open-loop FPVM-EHA could be gotten as Fig.10. All the sub-models are enveloped and connected with each other by the defined input and output ports. The EHA parameters are given in Table 1.
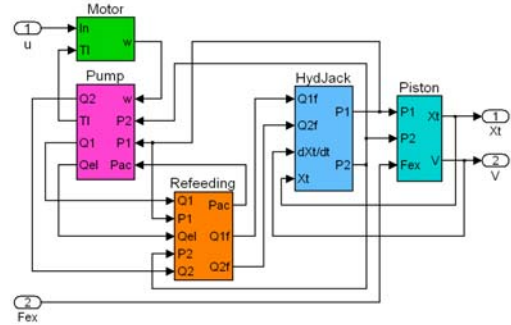
Figure 10 EHA open-loop system

Table 1 EHA Parameters

Symbol	value	Symbol	value
L [H]	2.3e-3	F_s [N]	25
R [Ohm]	1.5	F_c [N]	15
K_t [N·m/A]	0.2	T_s [N·m]	0.5
K_c [v/(rad/s)]	0.2	T_c [N·m]	0.3
J [Kg·m^2]	1.2e-3	V_{10}, V_{20} [ml]	152
K_{vism} [N·m/(rad/s)]	4.2e-4	B [N/m^2]	6.5e8
K_{ilp} [(m^3/s)/Pa]	1e-13	A [cm^2]	19
K_{elp} [(m^3/s)/Pa]	1e-13	M [Kg]	2000
D [ml/r]	1.2	V_{gasi} [ml]	150
K_{ilj} [(m^3/s)/Pa]	1e-13	P_{aci} [MPa]	2.5
K_{visp} [N/(m/s)]	150	V_{oili} [ml]	150
k	1.3		

CONTROL DESIGN AND COMPARISONS

The EHA is a unique device with some complex characteristics due to the combination of electrical and hydraulic components. To obtain desire performance, the single PID, cascade PID, and state feedback control methods are analyzed and estimated.

Single PID Control
Single PID control is popular for its simple structure. Fig.11 gives the position step response, where the input is 20mm and an external force of 20000N is acting on actuator at 2.5s.

The static error caused by the external load indicates the low stiffness of this close-loop system. Moreover, there are some oscillations in pressure response due to the low hydraulic damping. For improvement, the cascade PID control may be a better choice.
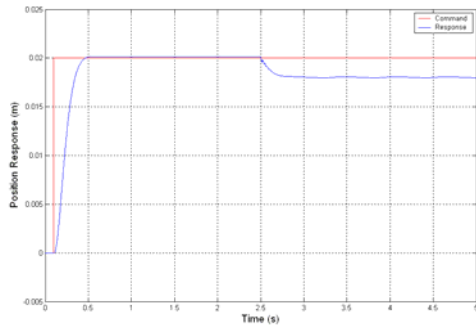
Figure 11 Step response of single PID controlled EHA

Cascade PID Control

The cascade control could detect and compensate the disturbances in the inner loop before they affect the outer variable and speed up the system because the inner loop could use a faster controller [6].

To compose the cascade controller, from inside to outside, there are current loop of motor, speed loop of motor and position loop of EHA. Considering the strong integration in the current loop, the anti-integration saturation method is necessary.

Fig.12 gives the position response. The rise time is reduced to 0.25s, and the static error due to external load is negligible. Compared to single PID control, the cascade control efficiently improves the system's rapidity and stiffness.
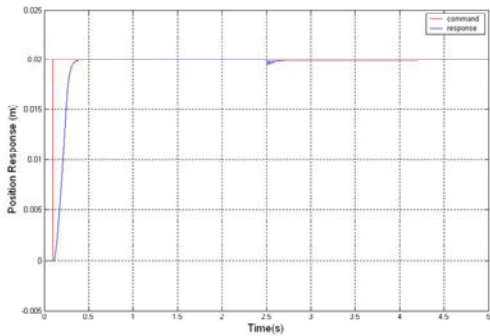
Figure 12 Step response of cascade controlled EHA

However, in view of Fig.13, the pressure oscillations seem to be critical. The frequency is about 36Hz which is close to EHA's natural frequency:

$$f_N = \sqrt{\frac{2 \cdot B \cdot A^2}{M \cdot V_{10}}} = 231.6 rad/s = 36.8 Hz \qquad (11)$$

The usual solution is using the velocity or pressure feedback which means another new loop to the system and becoming difficult to design the parameters in different loops to achieve global high performance.
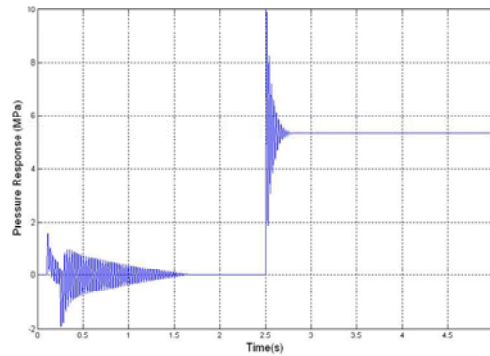
Figure 13 Pressure response of cascade controlled EHA

State Feedback Control

Consider the EHA as a fifth-order system with the following state variables:

$$\boldsymbol{X} = \begin{bmatrix} i & \omega & P_f & x_t & \dot{x}_t \end{bmatrix}^T \qquad (12)$$

All these variables are measurable, which is important for the realization of a full state feedback controller. According to Eq.(1), (2), (3), (6), (7), (8), the state equation of EHA could be described in matrix form:

$$\dot{\boldsymbol{X}} = \begin{bmatrix} -\dfrac{R}{L} & -\dfrac{K_c}{L} & 0 & 0 & 0 \\[2mm] \dfrac{K_t}{J} & -\dfrac{K_{vism}}{J} & -\dfrac{D}{J} & 0 & 0 \\[2mm] 0 & \dfrac{2BD}{V_{10}} & -\dfrac{2BK_l}{V_{10}} & 0 & -\dfrac{2AB}{V_{10}} \\[2mm] 0 & 0 & 0 & 0 & 1 \\[2mm] 0 & 0 & \dfrac{A}{M} & 0 & -\dfrac{K_{visp}}{M} \end{bmatrix} \boldsymbol{X} + \begin{bmatrix} \dfrac{1}{L} & 0 \\[2mm] 0 & 0 \\[2mm] 0 & 0 \\[2mm] 0 & 0 \\[2mm] 0 & -\dfrac{1}{M} \end{bmatrix} \boldsymbol{U} \qquad (13)$$

Input vector: $\boldsymbol{U} = \begin{bmatrix} u & F_{ex} \end{bmatrix}^T$

Output vector: $\boldsymbol{Y} = \begin{bmatrix} 0 & 0 & 0 & 1 & 0 \end{bmatrix} \boldsymbol{X}$

Fig.14, 15 are the position and pressure responses of this system. Compared to cascade PID control, it is a more rapid system and the oscillation is obviously reduced. However, there is an unacceptable static error when loading. The system has to maintain a certain static error to produce enough input to counteract the input loss due to pressure feedback.

To solve this problem, a high-pass filter could be applied

669

to the pressure feedback loop to form the dynamic pressure feedback. This filter keeps the desirable effects of pressure feedback on shaping dynamic response, as well as eliminates the undesirable static error when in static state. It could be realized by electric circuit or software. The cut-off frequency is always chosen as 80%~90% of the system natural frequency.

According to Eq.(11), the cut-off frequency is:

$$f_{cutoff} = 0.85 \cdot f_N = 198 rad/s \qquad (14)$$

So, the transfer function of high-pass filter is:

$$G_{DPF} = \frac{2\pi \cdot s / f_{cutoff}}{2\pi \cdot s / f_{cutoff} + 1} = \frac{0.032s}{0.032s + 1} \qquad (15)$$

Fig.16 gives the new position response. The static and dynamic performances of EHA are both improved.
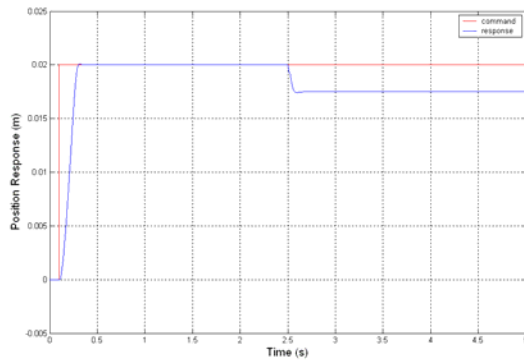
Figure 14 Step response of state feedback controlled EHA
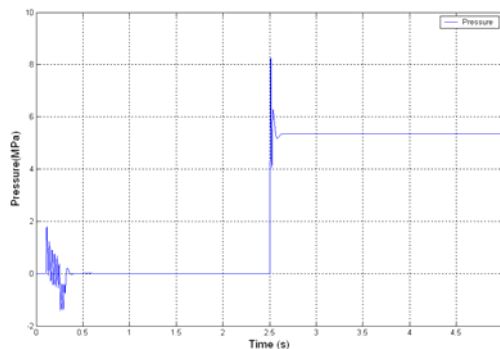
Figure 15 Pressure response of state feedback controlled EHA
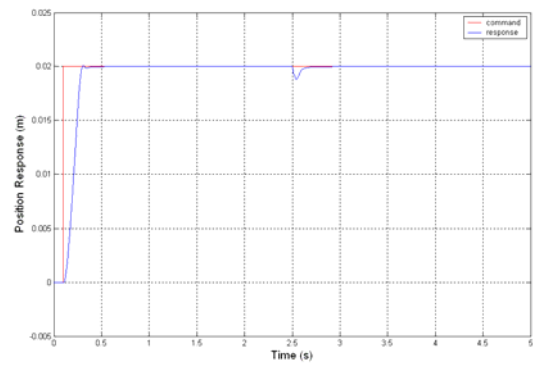
Figure 16 Step response of state feedback controlled EHA along with dynamic pressure feedback

CONCLUSIONS

The block diagram model of FPVM-EHA is established in this paper. It is an accuracy model that contains more information than transfer function model.

The single PID, cascade PID and state feedback controllers are applied to this model for comparison analysis. The single PID control can't satisfy the EHA requirements; the cascade PID control efficiently helps the system to achieve high rapidity and stiffness, but leads to some oscillations; the state feedback control along with dynamic pressure feedback strategy is finally proven to be the best solution for improving both static and dynamic performance of EHA.

REFERENCES

1. Saeid Habibi and Andrew Goldenberg, Design of a new high performance electrohydraulic actuator, Proceeding of the 1999 IEEE/ASME International Conference on Advanced Intelligent Mechatronics Proceedings, Septemper,1999, Atlanta,USA, pp. 227-232.
2. Gao Bo, Fu Yongling, Pei Zhongcai and Ma jiming, Research on dual-variable integrated electro-hydrostatic actuator, Chinese Journal of Aeronautics, 2006, Vol 19(1), pp.77-82.
3. Stephen C J, Flight test experience with an electromechanical actuator on the F-18 systems research aircraft, NASA,1998.
4. Wang Z L, Modern Hydraulic Control. Beijing: China Machine Press, 1997.183-195.(in Chinese)
5. Evangelos G. Papadopoulos and Georgios C. Chasparis, Analysis and model-based control of servomechanisms with friction, Proceedings of the IEEE/RSJ International Conference on Intelligent Robots and Systems, October,2002, Lausanne, Switzerland: 2109-2114
6. Ibrahim Kaya, Nusret Tan and Derk P. Atherton, Improved cascade control structure for enhanced performance, Journal of Process Control, 2007,Vol 17, pp. 2109-2114

P2-16

STUDY OF OPTIMAL DESIGN AND LEG INERTIA EFFECT IN LARGE HYDRAULIC STEWART PLATFORM

Xin FU, Wei WANG, Jun ZOU and Hua-Yong YANG

State Key Laboratory of Fluid Power Transmission and Control, Zhejiang University
No.38, Zhe-Da Road, Hangzhou, 310027, China
(E-mail: xfu@zju.edu.cn)

ABSTRACT

The optimum design of parallel manipulators is an important and challenging problem. Currently, much of optimization work has been done over several criteria related to workspace, stiffness, dexterity and conditioning index. Relatively few papers have taken the control problem into consideration. In this paper, an optimal design method based on generalized natural frequency is proposed, which aims to expand the bandwidth for the control of large hydraulic Stewart platform. A Lagrangian formulation which considers the whole leg inertia is presented to obtain accurate equivalent inertia matrix, based on which, the influence of design parameters on generalized natural frequency is studied. Conclusion drawn from numerical examples, based on more accurate model, demonstrates that the leg inertia especially the piston part plays an important role on the dynamics, and five design parameters (diameters of the moving platform and the base, piston mass, effective driving area and fully retracted leg length) influence the frequency most.

KEY WORDS

Large hydraulic Stewart platform, Optimal design, Control bandwidth, Lagrangian

NOMENCLATURE

A_1 : effective area of the piston side
A_2 : effective area of the rod side
A_{du} : rotation matrix
D : Jacobian matrix
d_i : ith leg length
F : hydraulic driven force vector
f : generalized natural frequency vector
F_{ext} : external generalized force
I_i : ith cylinder inertia of inertia matrix in $\sum$O
$I_i^{b_i}$: ith cylinder mass moment about Bi in $\sum$B$_i$
I_{li} : ith piston inertia matrix
K : total kinetic energy
K_h : stiffness of hydraulic oil spring
K_q : equivalent stiffness matrix
L_{oil1} : equivalent chamber length of the piston side

L_{oil2} : equivalent chamber length of the rod side
l_{pis} : piston length
l_i : length between dli and the ith upper joint
m_{pis} : piston mass
M_p : mass-inertia matrix of moving platform on $\sum$O$_p$
n_{li} : unit vector along the ith leg
P : total potential energy
R : radius of the base
R_i : transformation matrix
q : [x y z ψ θ φ]^T
v_i : unit vector along the ith leg
β : oil bulk modulus
ρ : density of the piston part
ω_i : ith cylinder angular velocity

INTRODUCTION

In 1947 McGough proposed a six-degree-of-freedom platform, which was later used by Stewart (1965) in his flight simulator. In 1978 Hunt suggested using Stewart platform as manipulator.

In the research area of parallel manipulators, the optimum design is an important and challenging problem [1]. Two issues are involved in the optimum design: performance evaluation and synthesis. The latter is to determine the design parameters.

Parallel manipulators' performances depend heavily on their geometry. So much of the research work on parallel manipulators optimization has been done over several criteria related to the workspace [2, 3]. Other authors optimized the structural stiffness of the manipulator [4]. Also, some works may be referred where the optimization criteria used are related with the manipulability, dexterity, payload, conditioning index, or best accuracy . Different methods have been taken to solve the optimum design problems including the cost-function approach, interval analysis, and so on. Relatively few optimization works take the control problem into consideration. Shiller Z [5] used the motion time along the path as the optimization cost function. Khatib O [6] investigated the problem of manipulator design for increased dynamic performance which was characterized by the inertia and acceleration properties of the end-effector. However, the control of hydraulic actuators is more difficult than the control of electrical counterparts especially when manipulators are large.

The purpose of this optimization work is to expand the bandwidth for the control of large hydraulic Stewart platform based on generalized natural frequency. The rest of the paper is organized as follows. Section 2 gives the Lagrangian formulation which considers the whole leg inertia. The optimum method based on generalized natural frequency is introduced in Section 3. Numerical examples are finally carried out to validate and confirm the efficiency of the method in Section 4, in which the influence of design parameters on frequency is studied.

LAGRANGIAN FORMULATION

Several approaches [7] have been proposed for dynamic analysis of Stewart platform. This optimization work is to expand the bandwidth for the control based on generalized natural frequency, and the Lagrangian method is a direct way to get the equivalent mass matrix. To be accurate, the whole leg inertia should be considered. In this paper the legs are decomposed into two parts: the fixed part (to the base) and the moving part (the piston part). The integration method is used to calculate the energy of each part, with this method the energy of particle system includes all the translational and rotational energy.

Kinematics

The Stewart platform is shown in Figure 1.
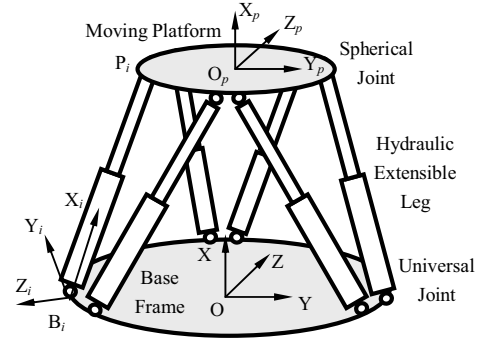
Figure 1   Hydraulic Gough-Stewart platform

The transformation matrix R_i from the leg coordinate to the base coordinate can be obtained as in [8].

Let the rotation matrix be defined by the roll, pitch, and yaw angles, namely, a rotation of φ about the x-axis, followed by a rotation of ψ about the y-axis, and a rotation of θ about the z-axis. Thus, it can be defined as

$$A_{du} = R(y,\psi)R(z,\theta)R(x,\varphi) \qquad (1)$$

The length of the ith leg is given by

$$d_i = f_i\left(x_p, y_p, z_p, \psi, \theta, \varphi\right) \qquad (2)$$

It yields

$$\dot{d} = D\dot{q} \qquad (3)$$

where D is the Jacobian matrix, $\dot{q} = [\dot{x}_p\ \dot{y}_p\ \dot{z}_p\ \dot{\psi}\ \dot{\theta}\ \dot{\varphi}]^T$.

Piston part

The ith leg velocity vector can be written as

$$\begin{bmatrix} \dot{L}_{xi} \\ \dot{L}_{yi} \\ \dot{L}_{zi} \end{bmatrix} = \begin{bmatrix} \dot{x}_p \\ \dot{y}_p \\ \dot{z}_p \end{bmatrix} + \dot{A}_{du} \begin{bmatrix} x_{ui} \\ y_{ui} \\ z_{ui} \end{bmatrix} = \begin{bmatrix} J_{xi} \\ J_{yi} \\ J_{zi} \end{bmatrix} \dot{q} \qquad (4)$$

where $\{x_p\, y_p\, z_p\}$ is the upper platform center coordinate in $\sum O$, and $\{x_{ui}\, y_{ui}\, z_{ui}\}$ is the ith upper joint coordinate in $\sum O_{p}$.

In Figure 2, the coordinate of particle dl_i in $\sum O$ is

$$\begin{bmatrix} x_{li} \\ y_{li} \\ z_{li} \end{bmatrix} = \frac{(d_i - l_i)}{d_i}\left(\begin{bmatrix} x_i \\ y_i \\ z_i \end{bmatrix} - \begin{bmatrix} x_{di} \\ y_{di} \\ z_{di} \end{bmatrix}\right) + \begin{bmatrix} x_{di} \\ y_{di} \\ z_{di} \end{bmatrix} \qquad (5)$$

where l_i is the length between dl_i and the ith upper joint, $\{x_{di}\, y_{di}\, z_{di}\}$ is the ith down joint coordinate in $\sum O$, and $\{x_i\, y_i\, z_i\}$ is the ith upper joint coordinate in $\sum O$.
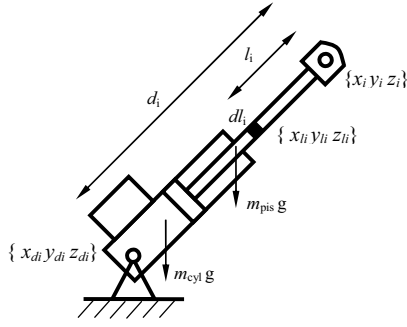
Figure 2　Leg of the Hydraulic Stewart platform

The kinematic energy of dl_i can be written as

$$dT_{li} = \frac{1}{2}\rho dl_i v_{li}^2 \qquad (6)$$

where $\rho = m_{pis}/l_{pis}$, m_{pis} is the piston mass, and l_{pis} is the piston length.

Cylinder part
The velocity of the ith upper joint can be written as

$$v_i = \dot{d}_i \cdot n_{li} + \omega_i \times d_i \qquad (7)$$

No rotation is allowed about the leg axis, so the angular velocity of the cylinder part can be written as

$$\omega_i = n_{li} \times v_i / d_i \qquad (8)$$

It yields

$$\omega_i = \left(\begin{bmatrix} L_{yi}J_{zi} - L_{zi}J_{yi} \\ L_{zi}J_{xi} - L_{xi}J_{zi} \\ L_{xi}J_{yi} - L_{yi}J_{xi} \end{bmatrix} / d_i \right) \dot{q} = J_\omega \dot{q} \qquad (9)$$

Hence the total kinematic energy of the pistons is

$$\sum_{i=1}^{6} \frac{1}{2}\omega_i^T I_i \omega_i = \sum_{i=1}^{6} \frac{1}{2}\dot{q}^T J_\omega^T I_i J_\omega \dot{q} \qquad (10)$$

where $I_i = R_i I_i^{b_i} R_i^T$, $I_i^{b_i}$ is the mass moment inertia of the ith leg about Bi expressed in the leg coordinate.

The lagrangian dynamic formulation
With the principle of virtual work and Lagrange equation, the hydraulic driven force can be written as

$$F = D^{-T}\left(\frac{d}{dt}\frac{\partial K}{\partial \dot{q}} - \frac{\partial K}{\partial q} + \frac{\partial P}{\partial q} - F_{ext} \right) \qquad (11)$$

where K is the total kinetic energy, P is the total potential energy, F_{ext} is the external generalized force.

THE OPTIMUM METHOD

Equivalent inertia matrix
The equivalent inertia matrix is

$$M_q = M_P + \sum_{i=1}^{6} I_{li} + \sum_{i=1}^{6} J_\omega^T I_i J_\omega \qquad (12)$$

where

$$I_{li} = \frac{1}{3}\rho \frac{l_{pis}^3}{d_i^4} D(i,:)^T D(i,:) \begin{bmatrix} x_i \\ y_i \\ z_i \end{bmatrix}^T \begin{bmatrix} x_i \\ y_i \\ z_i \end{bmatrix} + \frac{\rho J_i}{d_i^2}\left(d_i^2 l_{pis} - d_i l_{pis}^2 + \frac{l_{pis}^3}{3} \right) +$$
$$\frac{2\rho}{d_i^3}(\frac{1}{2}d_i l_{pis}^2 - \frac{1}{3}l_{pis}^3) D(i,:)^T \left(\begin{bmatrix} x_i \\ y_i \\ z_i \end{bmatrix}^T - \begin{bmatrix} x_{di} \\ y_{di} \\ z_{di} \end{bmatrix}^T \right) \begin{bmatrix} J_{xi} \\ J_{yi} \\ J_{zi} \end{bmatrix} -$$
$$\frac{2\rho l_{pis}^3}{3d_i^4} D(i,:)^T D(i,:) \begin{bmatrix} x_i \\ y_i \\ z_i \end{bmatrix}^T \begin{bmatrix} x_{di} \\ y_{di} \\ z_{di} \end{bmatrix} + \frac{1}{3}\frac{\rho l_{pis}^3}{d_i^4} R^2 D(i,:)^T D(i,:),$$

$J_i = J_{xi}^T J_{xi} + J_{yi}^T J_{yi} + J_{zi}^T J_{zi}$,
M_p is the mass-inertia matrix of moving platform in $\sum$O.

Generalized natural frequency
It is assumed that the mechanical part is rigid, and the hydraulic oil can be compressed. The stiffness of the hydraulic spring is defined as

$$k_h = \beta \left[\frac{A_1}{L_{oil1}} + \frac{A_2}{L_{oil2}} \right] \qquad (13)$$

$$K_h = \begin{bmatrix} k_h & & \\ & \ddots & \\ & & k_h \end{bmatrix} \qquad (14)$$

where β is the oil bulk modulus, A_1 is the area of piston side, A_2 is the area of rod side, L_{oil1} and L_{oil2} are the two equivalent chamber lengths of the cylinder .
It can be obtained

$$K_q = D^T K_h D \qquad (15)$$

The generalized natural frequency on 6-DOF ($x\ y\ z\ \varphi\ \psi\ \theta$) is given by

$$f_i = \frac{1}{2\pi}\sqrt{\frac{K_q(i,i)}{M_q(i,i)}} \qquad (i=1\sim6) \qquad (16)$$

The optimization scheme
In applications with requirements of high precise positioning and good dynamic performance, e.g. large flight simulators, the control of the platform is complicated and difficult, especially for the hydraulic platform. In general, the control of hydraulic actuators is more challenging than that of their electrical

counterparts when parallel manipulators are large. They exhibit a significant nonlinear behavior. The factors such as nonlinear flow/pressure characteristics, variations in the trapped fluid volume due to piston motion, fluid compressibility, flow forces and their effects on the spool position, and friction, all contributing to this nonlinear behavior. This will influence the actual control bandwidth, and it is less than half of the natural frequency in engineering. To expand the theoretical bandwidth for the control, the natural frequency characteristics must be considered in the optimal design.

For large hydraulic Stewart platform with requirements, the lowest natural frequency in the total workspace and the generalized natural frequency when all the actuators are at their mid stroke are the key frequencies. The aim of the design is to obtain highest frequencies, and the natural frequencies when all actuators are at their mid stroke should be as close as possible.

The optimization work is not based on the cost function. The steps in the optimization are as follows:

Step 1 Choose an initial set of design parameters. It can be roughly determined from the workspace requirement, the desired linear and angular isotropic accelerations at some velocity state.

Step 2 Determine the range of each design parameter, and give the graph results of the influence by the design parameters.

Step 3 Choose a new set of design parameters from step 2, get the task frequencies. If it's not satisfied, change the deign parameters, especially the effective hydraulic driving area and oil bulk modulus (the system oil should be preprocessed if necessary), return to the step 2.

Step 4 Compute the average hydraulic system power as a design reference by the system flow rate and pressure with design parameters.

Step 5 Workspace verifying and other requirements examination.

In the paper, the configuration is representative for a group of nearby or symmetric configurations. Based on the natural frequency, the bandwidth for the control will be determined more appropriate for the designer related to the control of the hydraulic parallel manipulator.

NUMERICAL EXAMPLE

Frequency verifying
The design parameters of the Stewart platform are shown in Table 1.
With the accurate inertia matrix, the generalized natural frequency of the Stewart platform can be obtained as in Eq. (16). With the mathematical model, the generalized natural frequency at the initial pose is:

[19.849 42.180 28.979 41.104 42.180 19.849] Hz

Table 1 Parameters of the Stewart platform

Parameter	Value
Upper Diameter	2.1 (m)
Down Diameter	5.4 (m)
Upper joints angle	21 (°)
Down joints angle	21 (°)
Initial height	2.5 (m)
Length of the piston	2.3 (m)
Length of the cylinder	2.2 (m)
Mass of the moving platform	300 (Kg)
Mass of the piston	200 (Kg)
Mass of the cylinder	350 (Kg)

An ADAMS model is built to validate the mathematical model, and the corresponding frequency is:

[19.848 42.181 28.978 41.103 42.181 19.848] Hz

The effect of leg inertia on the Stewart platform
Comparisons between current model and traditional one are made on the static and dynamic driving forces.
In the simulation of static forces, all the velocities and accelerations remain zero, there is no the external force and torque exerted on the platform, and the moving platform moves horizontally along z-axis between -250mm and 250mm. It's obvious that the inertia of the leg especially the piston part influences a lot on the static driving forces.
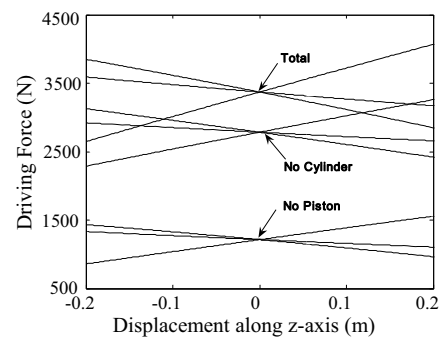
Figure 3 Static driving forces with models considering the whole leg or part of the leg

In figure 4, the moving platform moves horizontally along z-axis with a sinusoidal motion (100sin(πt) mm), while other velocities and accelerations remain zero. The three lines (N_1, N_2, N_3) are the results with current inertia matrix model, and the other three lines (O_1, O_2, O_3) are with traditional one including only the translational part of the leg.
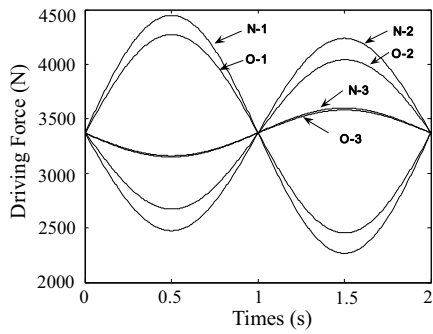
Figure 4 Dynamic driving forces

Figure 7 Influence of down diameter

Influence of design parameters on natural frequency
The influence of design parameters on natural frequency is shown in figure 5-figure 13. Curve 1, curve 2, curve 3, and curve 4 represent the six frequencies when all the actuators are at their mid stroke, and curve 5 represents the lowest frequency in workspace.

With the figures, the influence of parameters can be easily observed. Five design parameters (figure 5 7 9 11 12) influence the frequency most. Especially in figure 7, the frequency lines are highly non-linear, the influence by the down diameter is complicated, which should be paid more attention during the design. If necessary, the oil should be preprocessed, which is effective for increasing the frequencies simultaneously.

Figure 8 Influence of down joints angle

Figure 5 Influence of upper diameter
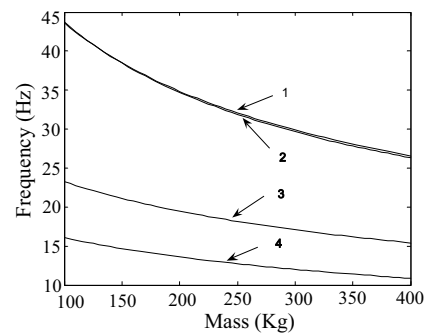
Figure 9 Influence of piston mass

Figure 6 Influence of upper joints angle
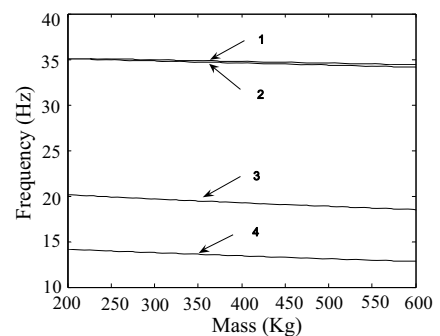
Figure 10 Influence of cylinder mass

675
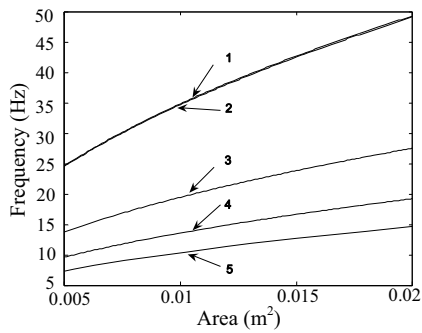
Figure 11 Influence of driving area
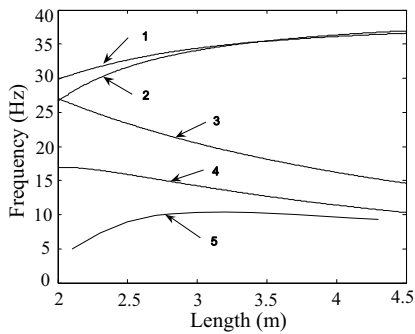
Figure 12 Influence of fully retracted leg length
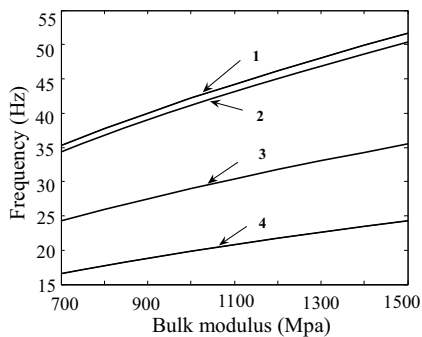
Figure 13 Influence of oil bulk modulus

CONCLUSIONS

This paper presented an optimal design method based on generalized natural frequency, which aims to expand the bandwidth for the control of large hydraulic Stewart platform. The ADAMS model validates and confirms the efficiency of the current model. And numerical examples were carried out and came to the following conclusions:

(1) Current model is more accurate than the traditional one.

(2) The leg inertia especially the piston part plays an important role in the dynamics.

(3) Five design parameters (diameters of the moving platform and the base, piston mass, effective driving area and fully retracted leg length) influence the frequency most.

This optimization method can be used with other requirements. In later work, it will be combined with hydraulic system design (flow rate/pressure, flow power and cooling power). It's an efficiency method to obtain a compact hydraulic Stewart platform with higher bandwidth. It will provide a set of appropriate design parameters for the large hydraulic Stewart platforms. It is suitable for the optimum design of other hydraulic parallel manipulators with higher bandwidth.

REFERENCES

1. Merlet, J. P. Still a long way to go on the road for parallel mechanisms. In ASME 2002 DETC Conference, Montréal, Canada, 2002.
2. Kumar, V. Characterization of workspaces of parallel manipulators. J. Mech. Des., 1992, **114-3**, pp.368-375.
3. Laribi, M. A., Romdhane, L. and Zeghloul, S. Analysis and dimensional synthesis of the DELTA robot for a prescribed workspace. Mech. Mach. Theory, 2007, **42-7**, pp.859-870.
4. Bhattacharya, S., Hatwal, H. and Ghosh, A. On the optimum design of Stewart platform type parallel manipulators. Robotica, 1995, **13-2**, pp.133-140.
5. Shiller, Z. and Sundar, S. Design of robotic manipulators for optimal dynamic performance. In Proceedings of IEEE International Conference on Robotics and Automation, Sacramento, 1991, **1**, pp.334-339.
6. Khatib, O. and Bowling, A. Optimization of the inertial and acceleration characteristics of manipulators. In Proceedings of IEEE International Conference on Robotics and Automation, Minnesota , 1996, **4**, pp. 2883-2889.
7. Khalil, W. and Ibrahim, O. General solution for the dynamic modeling of parallel robots, Journal of intelligent and robotic systems, 2007, **49-1**, pp.19-37.
8. Pang, H. and Shahinpoor, M. Inverse dynamics of a parallel manipulator. J. Robotic Syst., 1994, **11-8**, pp.693-702.

P2-17

AN ANALYTICAL COMPARISON OF HYDRAULIC SYSTEMS BASED ON WATER AND ON OIL

Franc MAJDIC, Jozef PEZDIRNIK, Mitjan KALIN

University of Ljubljana, Faculty of Mechanical Engineering,
Centre for Tribology, Technical Diagnostic and Hydraulics (CTDH)
Askerceva 6, SI-1000 Ljubljana, Slovenia, European Union
(E-mail: franc.majdic@fs.uni-lj.si)

ABSTRACT

Environmental protection regulations are becoming increasingly strict. By using water instead of a hydraulic mineral oil in power-control hydraulic systems we can make a very positive step in complying with these regulations. In this paper we present some preliminary results on twin-type hydraulic experiments, employing equal parts containing water and oil. Our initial findings suggest the need for modifications to the test rig, and a comparison of the behaviour between two similar hydraulic test rigs is shown. The main parameters measured during the investigation were the pressures, the spool displacements and the responses of the piston in the double-acting hydraulic cylinder. However, transient phenomena in the water and oil hydraulic test rig were also analysed and compared. Experiments were performed on systems with and without an applied load. The results reveal very different behaviours for the oil and the water hydraulics.

KEY WORDS

Water, Mineral oil, Power control, Hydraulics, Proportional valve

NOMENCLATURE

I_A	:	input signal at solenoid A (%)
I_B	:	input signal at solenoid B (%)
pA	:	pressure at port A (bar)
pB	:	pressure at port B (bar)
pP	:	pressure at port P (bar)
pT	:	pressure at port T (bar)
$sspool$:		movement of the spool in the valve (%)
$scylinder$:		movement of the piston rod in the hydraulic cylinder (mm)
$t_{A,up}$	:	rising time of the signal for solenoid A (s)
$t_{A,d}$	:	falling time of the signal for solenoid A (s)
t_A	:	total working time of the signal for solenoid A (s)
$t_{B,up}$	:	rising time of the signal for solenoid B (s)
$t_{B,d}$	:	falling time of the signal for solenoid B (s)
t_B	:	total working time of the signal for solenoid B (s)

INTRODUCTION

Unexpected outflows of hydraulic liquids, i.e., mineral oils, into the ground and even into underground drinking-water supplies are a frequent occurrence. One of today's major challenges is to use alternative, natural sources of hydraulic fluid to protect our environment. In power-control hydraulics (PCH) there are two ways in which we can protect the environment. The first solution is to use a biodegradable oil [1-6] instead of a mineral oil. But this is only a partial solution because biodegradable oil has to contain the necessary additives, which are sometimes detrimental to the environment. The second – and better – solution is to use tap water instead of mineral oil. This solution is harmless to the environment, but is very difficult to realise [7-8]. For water hydraulics a relatively simple conventional control valve already exists on the market; however, the continuous control of water hydraulic systems is needed for almost every hydraulic machine. Nowadays, the

market for disposable water-hydraulics components for continuous control is very small. Even if they can be located, they are normally very complicated and with a lot of parts.

Despite many years of water-hydraulics research there is still insufficient understanding of the mechanisms and performance.

In this work we present some preliminary experiments on the design of a new, continuous control 4/3 directional control valve for use with water.

EXPERIMENTAL

Test rig

A dedicated twin test rig for the study of water power-control hydraulics (PCH) was built [9]. The test rig can be used for tests of a water and an oil proportional 4/3 directional control sliding type valve for dynamic-transient and static-long-term life-time tests under the same conditions.

The main parts of the water hydraulic half of the test rig are as shown in Figure 1:

a reservoir, an axial piston pump, a relief valve, a specimen-proportional directional 4/3 control valve, a double-acting hydraulic cylinder with a through rod, a loading mass of 162 kg, four pressure transducers and two linear variable differential transformers (LVDTs). One transformer is for measuring the spool movement and the other is for measuring the rod that moves in the hydraulic cylinder.

The high-pressure hydraulic pump delivers approximately 30 lpm of water flow to the P port of the specimen. It is controlled from a PC using special software.

We observed the pressures, the displacements and the temperatures of the fluid in the reservoir. The pressure relief valve was set to 160 bar.

The water hydraulic test rig (Fig. 2) is assembled from standard, on-market-disposable, water hydraulic components, except for the proportional directional 4/3 control valve and the hydraulic cylinder. These two components were designed and constructed in our laboratory for power-control hydraulics. The tubes for the water and the oil hydraulic cylinders are made from stainless steel and the rod is made from hard-chromium-plated steel. The seals and guide rings for both hydraulic cylinders are the same; they are made from nitrile rubber, polyurethane, and a fabric-based laminate.

The oil hydraulic test rig (Fig. 2) is the same in terms of function, but assembled from standard, on-market-disposable components, except for the hydraulic cylinder. The oil hydraulic cylinder is typical for oil hydraulic applications. It has the same construction, the same dimensions and the same surface

properties as the water cylinder.
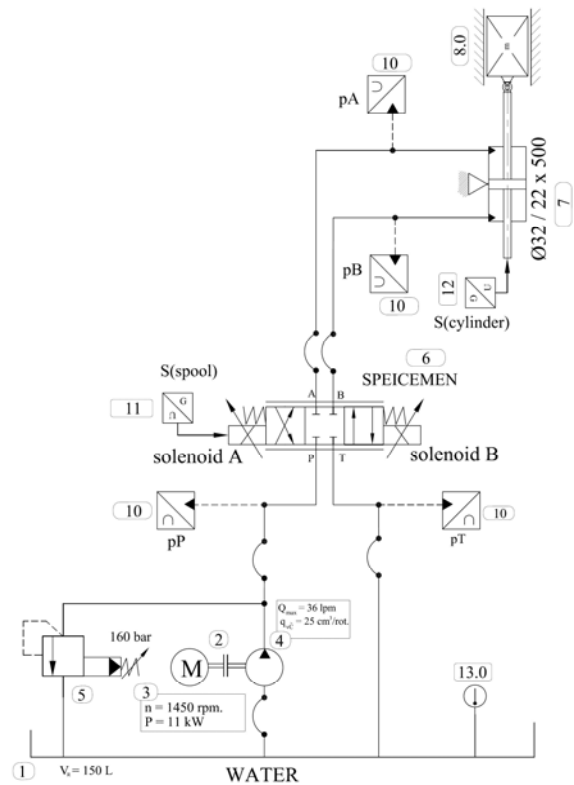
Figure 1 Water hydraulic test rig for dynamic tests

Figure 2 Water (on the left) / oil (on the right) power-control part of the test rig

Samples

The test specimens used in the new, water proportional 4/3 directional control valve were a spool with an outer diameter of 12 mm and a sleeve. The clearance between the spool and the sleeve was less than a few micrometers. In this test the specimens were both made from stainless steel. This material combination, including some other material pairs, was tested in previous tribological experiments [9]. The liquid in the water PCH part of the test rig was distilled water, to ensure a neutral environment that does not reflect the water type from any particular part of the world. The liquid in the oil PCH part of the test rig was the mineral oil ISO VG 46.

Testing procedure

Two types of test were performed: one with a load mass of 162 kg and one without. This load mass was positioned in the vertical direction (Fig. 3).

Figure 3 Water (on the left) and oil (on the right) hydraulic cylinder with load masses

The same experimental procedure was used in both types of test, and the whole testing procedure was fully automated with the PC software.

Fig. 4 shows the loading cycle for each experiment, which is described in more detail in Table 1. The table presents the times for the various stages of the cycle. As shown in Fig. 4, the input signal consists of six phases.

The first phase includes the input signal for moving the spool in the cross-shaped position of the valve. As a consequence, the piston rod of the cylinder starts to move up. This signal increases from 0% to 100% in $t_{A,up}$ seconds. The signal then stays at that level for (t_A - $t_{A,up}$ – $t_{A,d}$) seconds. After that, the third phase of the input signal begins. It lasts for $t_{A,d}$ seconds and causes the spool to return to the zero position. The piston rod in the cylinder then stops moving.

In the fourth phase is the input signal for moving the spool in the parallel-shaped position of the valve. As a consequence, the piston rod of the cylinder starts to move downwards. Increasing the signal from 0% to 100% takes $t_{B,up}$ seconds. This input signal for the parallel-shaped position stays at 100% for (t_B − $t_{B,up}$ − $t_{B,d}$) seconds. In the final phase the input signal falls from 100% to 0% in $t_{B,d}$ seconds.

During the whole set of experiments the signal was a maximum, i.e., 100% for both proportional solenoids, for both the water and the oil proportional 4/3 directional control valve.

RESULTS

Experiments - without mass

Fig. 5.a shows the movement of the spool and the piston rod of the cylinder during the loading cycle without the mass load in the oil PCH. The motion curve of the spool is smooth and without any visible mistakes. The second curve, which represents the response when moving the control spool, is similarly smooth and nearly symmetrical. The downward movement of the oil-cylinder piston rod was approximately 75% of the upward movement for the same, symmetrical input signal.
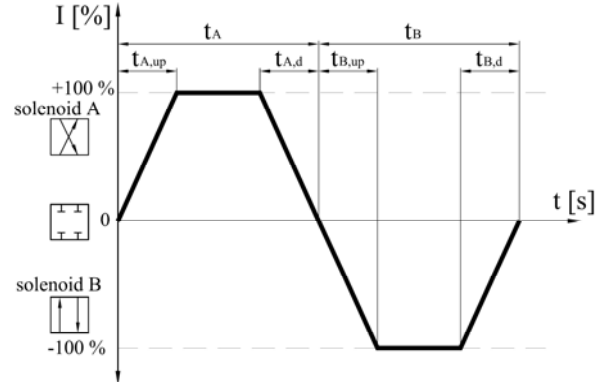
Figure 4 Input signal (time ramp) for specimen

Table 1 Setting the time ramp for the water and oil proportional directional 4/3 control valve

t_A	$t_{A,up}$	$t_{A,d}$	I_A	t_B	$t_{B,up}$	$t_{B,d}$	I_B
0,3 s	0,01 s	0,01 s	100 %	0,3 s	0,01 s	0,01 s	100 %

Fig. 5.b shows the movement of the spool and the piston rod of the cylinder during the loading cycle without any mass load in the water PCH. If we look carefully at the motion curve of the spool we can see the first irregularity, i.e., a peak near to 50% of the signal of the spool moving to the cross-shaped position of the proportional valve. This occurred approximately 0.55 s after the start of the measurement. However, there might be a stick-slip effect or a key-effect because of the small gap, the shape irregularity and the surface roughness. During the de-energizing of the first solenoid for lifting the mass, the movement of the spool from the cross-shaped position of the proportional valve to the zero position showed no irregularity. This part of the curve is smooth. A larger irregularity in the spool's motion occurred at approximately 50% of the negative signal and a time approximately 0.8s after the start of the measurement. Here we were able to see the momentary key-effect of the spool. After that the electrical, closed regulation loop increased the signal to put the spool in the desired position. The spool jumped and the regulation loop subsequently decreased the signal. So there was a strengthening oscillatory movement of the spool using electrical regulation. The cylinder rod's motion curve shows the response of the hydraulic cylinder during the movement of the spool. This curve is quite smooth, but unsymmetrical. The reason for the unsymmetrical shape might lie in the unsymmetrical and irregular input signal, the unsymmetrical movement of the spool or the different friction in the valve and the hydraulic cylinder when

moving up and down the piston rod. In the case of the experiment without any applied mass there was a larger unsymmetrical displacement of the water cylinder in comparison with the oil cylinder. The downward movement of the water cylinder's piston rod was only approximately 33% of the upward movement for the same, symmetrical input signal.
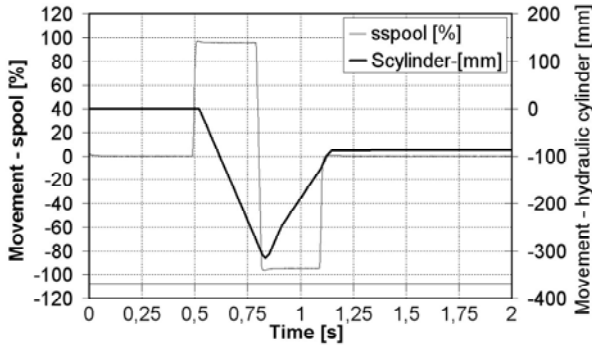
Figure 5.a Movement of the spool and the piston rod of the cylinder without any mass during the loading cycle in the **oil** PCH
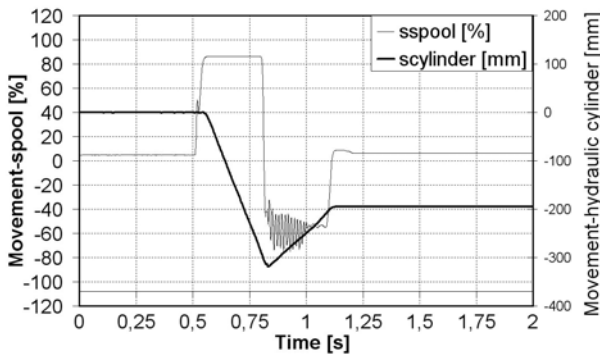
Figure 5.b Movement of the spool and the piston rod of the cylinder without any mass during the loading cycle in the **water** PCH

Fig. 6.a shows the pressure response at port B when moving the control spool in the oil PCH part of the test rig without any loading mass. Port B is on the pressure side of the cylinder piston for lifting the rod up. The pressure curve at the port B shows a pressure peak at the start of the movement of the rod of the cylinder at about 8-bar working pressure. At the end of this phase we observe another, similar, pressure peak. Similar pressure peaks were obtained for the reverse motion of spool (holding the spool in a parallel-shaped position); however, this is not so important, because they are at a very low pressure level. The maximum pressure when moving the piston rod in the oil cylinder was close to 72 bar, at the start of the experiment. Additionally, we observed a water-hammer effect approximately 1.2 s after the start. The effect corresponded to approximately 8% over the static pressure.

Fig. 6.b shows the pressure response at port B when moving the control spool in the water PCH part of the

test rig without any loading mass. The pressure curve of port B shows a pressure peak of around 25 bar above the working pressure, for upward movements of the piston in the water cylinder. The maximum pressure when moving the piston rod in the water cylinder was close to 100 bar at the start of the experiment. This is almost 30 bar more than in the case of the oil. During this transient period the shape of the pressure curve for a constantly increasing pressure was smooth. After obtaining a parallel position of the valve the pressure started to oscillate according to the oscillations of the spool in the proportional 4/3 directional valve. Approximately 1.2 s from the start of the measurement we could see a pressure peak of about 30% over the static pressure, which could be a consequence of the water-hammer effect.
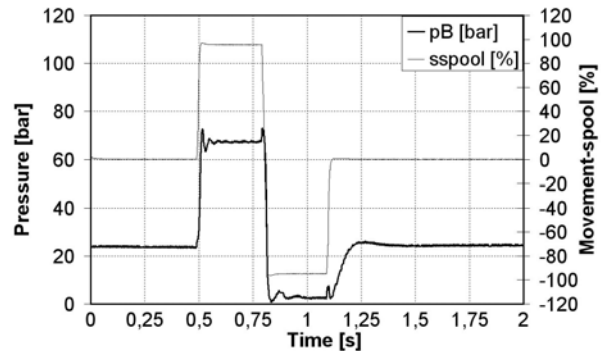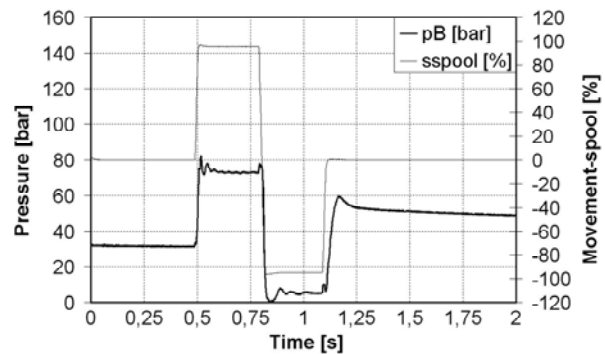

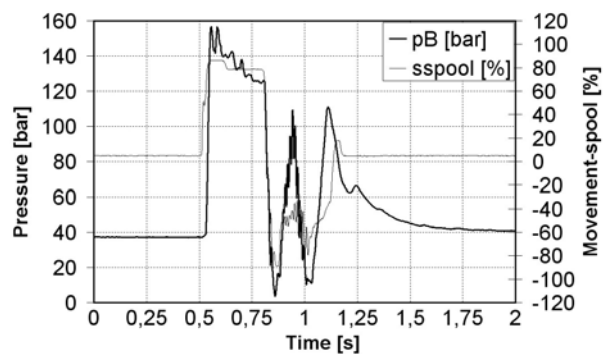Figure 6.a Movement of the spool and pressure changes during the experiment without any mass – cycle in the **oil** PCH
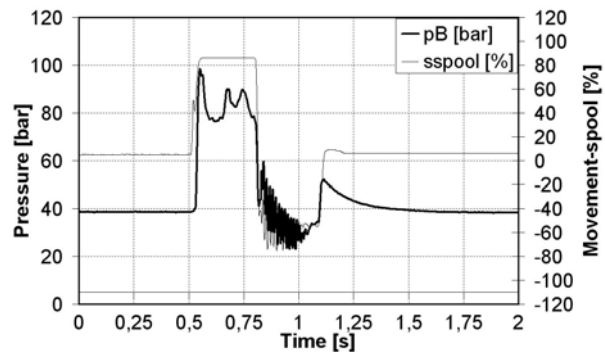
Figure 6.b Movement of the spool and the pressure changes during the experiment without any mass – cycle in the **water** PCH

Experiments – with mass in the vertical position
Fig. 7.a shows the movement of the oil spool and the piston rod of the cylinder during a loading cycle with the mass of 162 kg in the vertical position. It shows a regular, smooth curve when moving the spool. Similar to this curve is the curve for moving the oil cylinder's rod. During the smooth movement of the curve of the piston rod of the oil cylinder we could see distinctive differences in the symmetry between the upward movements and downward movements of the piston rod.

Here we obtained an inverted unsymmetrical curve, in contrast to the case without mass (Fig. 5.a). The upward movement of the piston rod is nearly 56% less than the downward movement.

Fig. 7.b shows the movement of the water spool and the piston rod of the cylinder during the loading cycle with the mass of 162 kg in the vertical position. The curve of the movement of the spool in the direction of the cross-shape position of the proportional water valve was smooth. The second curve, which represents the downward movement of the cylinder rod and the mass, has a major irregularity. The spool first moved regularly to its maximum position, but soon it started to oscillate with a low frequency of about 6 Hz. The reason for this could be the stick-slip effect or the key effect and uncontrolled amplification of the input signal during the regulation of the valve. The water cylinder rod and mass have the expected regular response during the movement of the valve spool.
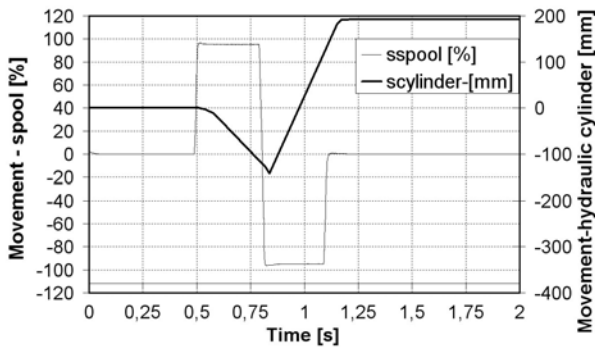
Figure 7.a Movement of the spool and the piston rod of the cylinder with the mass during the loading cycle in the **oil** PCH
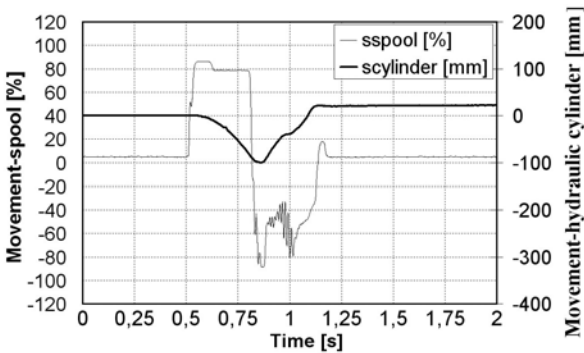
Figure 7.b Movement of the spool and the piston rod of the cylinder with the mass during the loading cycle in the **water** PCH

Fig. 8.a shows the pressure response at port B on the movement of the control spool in the oil PCH part of the test rig with the loading mass of 162 kg. The pressure curve at port B shows a pressure peak at the start of moving the rod of the cylinder by about 10 bar around the working pressure. The maximum pressure when moving the piston rod in the oil cylinder with the mass

was close to 82 bar at start of the experiment. Approximately 1.2 s after the start of the measurement we could see a pressure peak of about 20% more than the static pressure, which could be a consequence of the water-hammer effect. This effect was 12% higher than in the case without any mass.

Fig. 8.b shows the pressure response at port B when moving the control spool in the water PCH part of the test rig with a loading mass of 162 kg. Approximately 20 milliseconds after switching off the solenoid A, the pressure at port B increased up to 160 bar (absolute). After this the pressure decreased and oscillated up to 125 bar. This is almost 80 bar higher than in the similar case with oil. The pressure difference from the start to the end of lifting up the cylinder rod and the mass was 35 bar. In parallel with the oscillating of the movement of the spool was an oscillating pressure with a frequency of approximately 6 Hz and an amplitude of approximately 100 bar. In addition, we observed the water-hammer effect approximately 1.2 s after the start of the measurement. The effect amounted to approximately 190% over the static pressure.

Figure 8.a Movement of the spool and the pressure changes during the experiment with mass – cycle in the **oil** PCH

Figure 8.b Movement of the spool and the pressure changes during the experiment with the mass – cycle in the **water** PCH

DISCUSSION

A new testing device for the study of water hydraulics was developed; this device enables studies with oil and

water in separate, but equivalent, systems under the same conditions. In this work we present some of our preliminary results.

In general, if we compare the behaviour of the proportional 4/3 directional control valve for water (our design – specimen) with the standard proportional valve for oil with a similar gap between the spool and the sleeve we could see that the oil valve worked perfectly, as we would expect, but the water valve has some irregularity in the specific direction of the movement of the spool.

If we compare Fig. 5.a and Fig. 5.b we see that the motion curve for the oil spool is smooth and similar to the input electrical signal (Fig. 4 and Tab. 1). Meanwhile, the motion of the water spool is coincidental. The spool for the water valve obviously blocked in a short time, and most of the time in a parallel-shaped position (downwards moving piston rod). Typically, it is blocked at the side of solenoid B, after approximately 1 second of testing (Fig. 5.b, 6.b, 7.b and 8.b).

These problems are probably linked with the small gap, the shape irregularity, the surface roughness and the poorer lubrication conditions in the water hydraulics compared to the oil system. However, the observed irregularity of the movement of the spool in the water hydraulic valve had almost no influence on the movement of the piston rod of the water cylinder, where the curves are similarly smooth to the case with the oil.

CONCLUSIONS

1. The motion of the spool is regular for oil, but unstable, probably due to stick-slip and/or grab, for water.
2. The unstable motion of the spool in the water system does not result in the unstable motion of the cylinder, which remains similarly smooth and regular to the case with the oil.
3. The pressure in the water system is, however, affected by the irregular motion of the spool, which seems to be influenced through the electric inputs, as well.
4. In the experiments with the mass, the irregularity of the water-spool motion remains, and is even more pronounced than when there is no mass.
5. As expected, the water-hammer effect was much more pronounced with water than with oil.
6. We observed a difference in the motion of the spool towards the cross-shaped position compared to the motion towards the parallel-shaped position. The reason is most probably in the small irregularities of the mechanical parts, rather than with the physical background, which will be investigated in the future.

REFERENCES

1. M. Kalin, F. Majdič, J. Vižintin, J. Pezdirnik, I. Velkavrh, Analyses of the Long-Term Performance And Tribological Bechaviour of an Axial Piston Pump Using Dimond-like-Carbon-Coated piston Shoes and Biodegradable Oil, Journal of Tribology, 2008, vol. 130, pp.11013-1 – 11013-8.
2. M. Kalin, F. Majdič, J. Vižintin, J. Pezdirnik. Performance of axial piston pump using DLC-coated piston shoes and biodegradable oil. in: The 12th Nordic Symposium on Tribology, Helsingor, Denmark, June 7-9, 2006. Nordtrib 2006. (2006), 10 Pgs.
3. M. Kalin, J. Vižintin, A comparison of the tribological behaviour of steel/steel, steel/DLC and DLC/DLC contact when lubricated with mineral and biodegradable oils. Wear 261 [1] (2006) 22-31.
4. J. Barriga, M. Kalin, K. Van Acker, K. Vercammen, A. Ortega, L. Leiaristi. Tribological performance of titanium doped and pure DLC coatings combined with a synthetic bio-lubricant. Wear 261 [1] (2006) 9-14.
5. Kalin, M., Vižintin, J., Vercammen, K., Arnšek, A., Barriga, J., Van Acker, K. Tribological performance of lubricated DLC coatings using biodegradable oils. The coatings in Manufacturing Engineering (2004) 457-465.
6. J. Barriga, M. Kalin, K. Van Acker, K. Vercammen, A. Ortega, L. Leiaristi. Tribological characterisation and validation of carbon based coatings combined with bio-lubricants. Proceedings of the 11th Nordic Symposium on Tribology. Norway, June 2004. Pg. 508-517.
7. Wolfgang Backe, Water- or oil-hydraulics in the future, SICFP'99, May 26-28, 1999, Tampere, Finland, Pg. 51 - 65
8. E. Trostmann: WATER HYDRAULICS CONTROL TECHNOLOGY; Lyngby 1996, Technical University of Denmark; ISBN: 0-8247-9680-2.
9. F. Majdic, J. Pezdirnik, M. Kalin, Comparative tribological investigations of continuous control valves for water hydraulics, SICFP'07, May 21-23, 2007, Tampere, Finland

P2-18

ANALYSIS OF LOAD CHARACTERISTICS AND CONTROL OF WATER HYDRAULIC SYSTEM FOR WAIM

Zengmeng ZHANG, Hua ZHOU

State Key Laboratory of Fluid Power Transmission and Control
Zhejiang University
38 Zheda Road, Hangzhou, 310027 China
(E-mail: zzm.zju@gmail.com)

ABSTRACT

The load characteristics and control of water hydraulic system for water-assisted injection molding (WAIM) are investigated through modeling and simulation. WAIM is an innovative process to mold plastic parts with hollow sections, coming with big advantages: high production efficiency and quality at low cost. The load characteristic is complicated owing to physical properties of polymer, distribution of temperature, flow rate and water channel geometry etc. The load pressure and flow rate are investigated with CFD simulation. An accumulator and a supercharger are applied in the water hydraulic system which is modeled in MATLAB and developed in laboratory. A differential pressure control strategy is provided to regulate the water injection pressure by a proportional relief valve. PI control is used and the steady-state error of step response can be reduced close to zero with integral compensation in closed-loop control. Finally, slope control of injection pressure is studied based on the developed system in simulation. The aim of this study is to improve the control process of WAIM based on the new design and differential pressure control. In addition, this provides an application and practice of water hydraulic proportional control technology.

KEY WORDS

Water hydraulics, Water-assisted injection molding, Load characteristic, Pressure control

NOMENCLATURE

A : Area of piston
A_L : Cross area of internal cavity of mold
B_L : Visco-damping coefficient of load
C_{ip} : Inner leakage coefficient
C_{ep} : Outer leakage coefficient
f : Static friction force of piston
L : Length of the cavity-filling polymer
m : Equivalent mass of load
p : Pressure of chamber in cylinder and load
q : Flow rate
r : Radius of the cavity in mold
T : Temperature of polymer

x : Displacement of piston
β_e : Bulk modulus
η : Coefficient of polymer viscosity
λ : Heat transfer coefficient
ω : Frequency of control link

INTRODUCTION

Water-assisted injection molding (WAIM) is a novel way to mold hollow plastic parts. When the water is injected into the molten regions of a part, cavities are generated and polymer melt is displaced to form a hollow core. It is similar to gas-assisted injection molding (GAIM), but has the advantages such as short

cooling cycle time, high quality of products and low cost, for the reason of the difference between water and gas[1~2]. Especially, WAIM can produce parts with larger void spaces or longer hollow sections than GAIM. It brings the applications of WAIM to a broad field of elongated parts such as automotive industry, office equipment, medical products and building materials [3]. The load characteristic is complicated and coupling with the flow rate and load pressure. The cavity filling process is investigated in a great many researches for GAIM but few in WAIM. The general method used in GAIM simulation is Hele-Shaw model and suitable to thin wall molding perfectly. However there is high Re region in the field of water and the thin-wall model is not suitable to large parts molding. It is necessary to involve turbulent calculation to model the couple relationship between load pressure and flow rate. The load characteristics are the basis of modeling and control of water hydraulic system for WAIM.

In recent years, water hydraulic technology became a hot research area with an increase of concerns for global environment problems and mineral oil. Water hydraulics has some general benefits (e.g., environmental friendliness, non-flammability, easy availability, inexpensiveness) compared to oil hydraulics. The high bulk modulus, constant viscosity and low temperature-induced drift are praised highly in water hydraulic proportional control technique. However, the pressure impact in water hydraulic system increases with the high bulk modulus. Especially, the disturbance of flow fluctuation is serious in process of water injection and causes uncontrollable status frequently. Because of the seal and lubrication in components, the nonlinearity in water hydraulic control systems is much greater than oil systems. The static friction and leakage flow will cause large dead band and hysteresis as disturbance additionally [4, 5]. Hence, the precision of the pressure control of water hydraulic system is lower relatively compared with conventional oil hydraulics. This motivates to apply closed-loop control to improve the performance and capability to resist disturbance. In this paper, load characteristics and water injection process of WAIM are analyzed, based on which a new water hydraulic system with differential proportional pressure control and compound control of pressure and flow rate is developed.

LOAD CHARACTERISTICS

Analysis of Water Injection Process
The whole work cycle in WAIM mainly contains five steps: polymer melt injection, water injection, maintaining pressure, drainage and part ejection, as shown in Fig. 1 [6]. To avoid turbulence in the area of the water injector, the recommendation is to adjust the pressure profile starting with low pressure and then increasing to higher pressure. Large flow is supplied at

the same time. The process of WAIM is intermittent and the injection stage takes very short time, typically only one or two seconds, which is a moment within the whole work cycle. The pressure is maintained after water injection and the flow rate decreases from the total quantity to a very small level to supply the melt shrinkage. The problem about energy saving is how the large-flow injection assorts with the small-flow pressure maintaining in the whole cycle of WAIM.
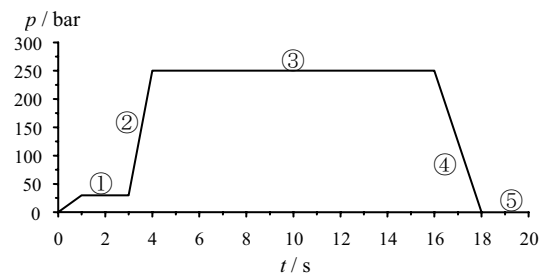
Figure 1 Load pressure profile of WAIM

Certain parameters such as water injection time, pressure profile and temperature of the injected water play an important role in achieving high quality residual wall. The necessary water injection pressure depends on the flow resistance of the plastic material and the part geometry. When injected into the parts, water cools the polymer melt and increases the viscosity. The leading edge of the water forms a solid boundary or highly viscous membrane. The membrane forces molten material forward, instead of the polymer forcing the water to the side [7]. The process of WAIM involves the dynamic interaction of two very different materials (polymer melt and filling water), and strongly depends on the temperature due to viscosity-temperature performance of polymer. The necessary water injection pressure depends on the flow resistance of the plastic material and the part geometry. So the simplification of the cavity filling process is needed to get a linear model of load pressure and flow rate.

CFD Simulation
The viscosity of the load is considered. A Cross-Arrhenius model is suitable to model the viscosity characteristic of polymer melt cavity filling flow in molding injection. The equation is

$$\eta(\dot{\gamma}, T, p) = \frac{\eta_0(T, p)}{1 + \left(\eta_0 \dot{\gamma} / \tau^*\right)^{1-n}} \tag{1}$$

where

$$\eta_0(T, p) = B \exp(T_B / T) \exp(\beta p) \tag{2}$$

Under the condition that temperature drops to a point $T < T_g + 100$ K, The Cross-WLF model shall be used as

686

$$\eta_0(T, p) = \eta_g \exp\frac{-C_1(T-T_g)}{C_2 + T - T_g}\exp(\beta p) \quad (3)$$

Here B, T_B, β, τ^*, C_1 and C_2 are parameters of the Cross model and are quite different between polymers. The apparent viscosity η is influenced by temperature, shear stain rate and pressure in injection. The load pressure p can be given as

$$p = 2L\eta(\dot{\gamma})\dot{\gamma}/r \quad (4)$$
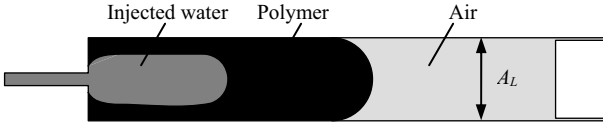
Figure 2 The calculation field of CFD simulation

There are three phases: water, polymer melt and air as shown in Fig. 2. A $k-\omega$ turbulence model is used in the field of water and laminar in polymer melt. The effective heat transfer coefficient λ_{eff} and turbulent viscosity μ_t are written as

$$\lambda_{eff} = \lambda + \frac{C_p\mu_t}{\text{Pr}_t} \quad (5)$$

$$\mu_t = \alpha^*\frac{\rho k}{\omega} \quad (6)$$

where C_p, Pr_t, α^*, k, ω are $k-\omega$ model parameters. The flow front is solved by VOF model and PISO coupling format of velocity and pressure is applied in this unsteady calculation. Results of volume fraction, temperature and ratio of turbulent viscosity are shown in Fig. 3. These show small residual wall gained with simulation close to the experiment results [6, 8, 9]. The maximum of turbulent viscosity ratio $\max(\mu_t/\mu) = 1.38\times10^3$ is in a correct range. Temperature changes greatly on the interface between water and polymer melt. Results of the coupling between load pressure and flow rate are shown in Fig. 4.

(a) Volume fraction of phases (t = 0.2 s)

(b) Static temperature (t = 0.2 s)

(c) Ratio of turbulent viscosity (μ_t / μ) (t = 0.2 s)
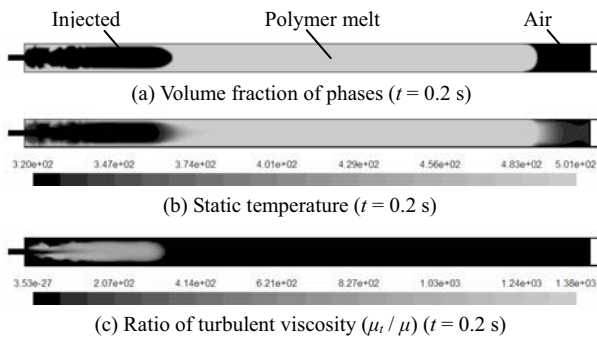
Figure 3 Cavity filling flow simulation for WAIM
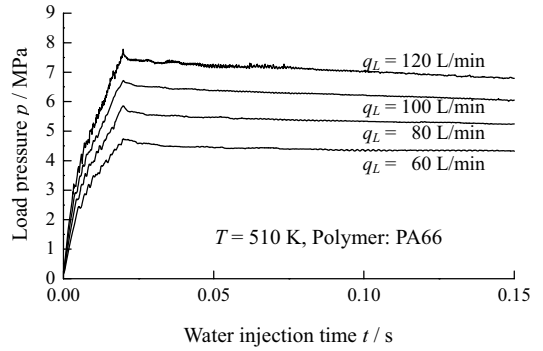
Figure 4 CFD simulation results of load characteristic

Linear Model
The pressure changes according to the flow rate as in Fig. 4 and the approximate equation can be written as

$$p = \frac{B_L}{A_L^2}q_L \quad (7)$$

where B_L is the equivalent visco-damping coefficient of load and can be given from the results of CFD simulation or WAIM experiments.
Considering the load inertia, elasticity and viscosity, the load pressure can be estimated as transfer function

$$G_L(s) = \frac{P}{Q_L} = \frac{m_L s^2 + B_L s + k_L}{A_L^2 s} \quad (8)$$

There are a restrictor of water injector and a throttle valve linearized as

$$Q_L = k_{tL}(P_L - P) \quad (9)$$

where k_{tL} is the pressure gain on flow rate of the throttle valve and injector. By Eq. (8) and (9), we obtain that

$$G_L'(s) = \frac{P_L}{Q_L} = \frac{m_L s^2 + B_L' s + k_L}{A_L^2 s} \quad (10)$$

where $B_L' = B_L + A_L^2/k_{tL}$. The linear control model of the system can be built and simulated with this assumption of visco-elastic load.

PRESSURE CONTROL

The simple water hydraulic system including main components is shown in Fig. 5. The equilibrium point at $\{p_{A0}', p_{A0}, p_{a0}, V_{a0}, q_{A0}, p_{B0}, p_{L0}, p_0, q_{L0}\}$ is investigated linearizing the accumulator, pressure cylinder, relief valve and throttle valves.
Here only discharge process of the accumulator is investigated and this process is fast and suggested as
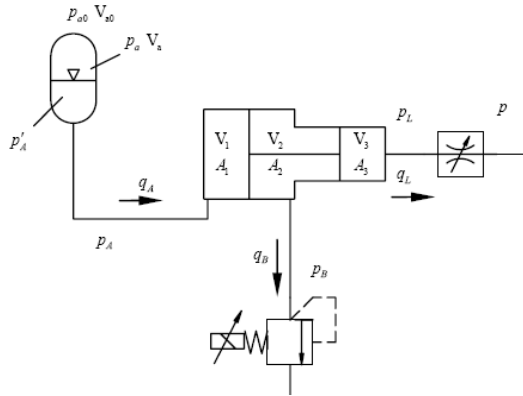
Figure 5 Main components and parameters

adiabatic. Fluid is incompressible in contrast with gas. And no turbulent flow appears in the accumulator [10]. Based on these assumptions and linearization of compressing process of gas, the linear model of accumulator with inlet characteristic can be written as

$$G_A(s) = \frac{P_A}{Q_A} = -\frac{m_a s^2 + B_a s + k_a}{A_a^2 s} \qquad (11)$$

where $k_a = n_a p_{a0} A_a^2 / V_{a0}$ and $B_a = B_{a0} + A_a^2 / k_{tA}$. Here n_a, A_a, B_{a0} and k_{tA} respectively is polytropic exponent, area of cross section, visco-damping coefficient of liquid part and inlet pressure gain on flow rate of the accumulator, as well as p_{a0} and V_{a0} are the initial value of the pre-charge gas. The continuity of water flow and force balance equations for pressure cylinder can be written as

$$p_A A_1 = p_B A_2 + p_L A_3 + m\ddot{x} + B\dot{x} + f \qquad (12)$$

$$q_A = A_1 \dot{x} + C_{ip_1}(p_A - p_B) + C_{ep_1} p_A + \frac{V_1}{\beta_e} \dot{p}_A \qquad (13)$$

$$q_L = A_3 \dot{x} + C_{ip_2}(p_B - p_L) - C_{ep_2} p_L - \frac{V_3}{\beta_e} \dot{p}_L \qquad (14)$$

Non-external leakage consideration and Laplace transformation of these three equations yield

$$P_A A_1 = P_B A_2 + P_L A_3 + ms^2 X + BsX + F \qquad (15)$$

$$Q_A = A_1 sX + C_{ip_1}(P_A - P_B) + \frac{V_1 s}{\beta_e} P_A \qquad (16)$$

$$Q_L = A_3 sX + C_{ip_2}(P_B - P_L) - \frac{V_3 s}{\beta_e} P_L \qquad (17)$$

In general, The transfer function of proportional relief valve can be regarded as a three-order system like

$$\frac{P_B}{U} = \frac{k_r}{\left(\dfrac{s^2}{\omega_{r2}^2} + \dfrac{2\xi_r}{\omega_{r2}} s + 1 \right)\left(\dfrac{s}{\omega_{r1}} + 1 \right)} \qquad (18)$$

This proportional relief valve is the key component of the system. The accuracy is poor and need closed-loop control to improve performance. But the nonlinearity of hysteresis may lead to oscillation and compensation methods will be investigated in the future work.
Let

$$G_1 = \frac{V_1 s}{\beta_e} + C_{ip_1} \qquad (19)$$

$$G_2 = \frac{V_2 s}{\beta_e} + C_{ip_2} \qquad (20)$$

Reduction the equations can yield the control structure of the model of whole system and built in MATLAB. The main parameters set in simulation are shown in Tab. 1 and the Bode diagram is shown in Fig. 6.
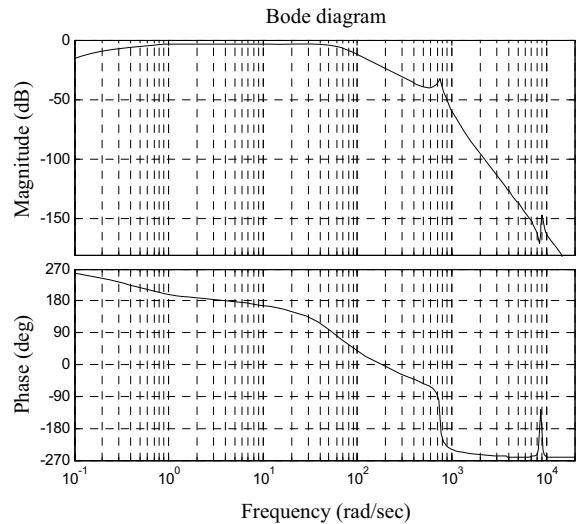
Figure 6 Bode diagram of the system

Table 1 Main parameters for simulation

Parameter	Value	Parameter	Value
k_a	3.8×10^5 N/m	B	39 kg/s
B_a	1422 kg/s	m_L	3.2 kg
A_a	0.015 m^2	f	90 N
β_e	1.6×10^9 Pa	B'_L	6×10^4 kg/s
A_1	0.012 m^2	A_L	0.002 m^2
A_2	0.006 m^2	ω_{r2}	40 rad/s
A_3	0.006 m^2	ξ_r	0.7
m	31 kg	ω_{r1}	320 rad/s

There are two differential links in the open-loop. Furthermore, the load pressure may not follow the input

signal. This is because there is accumulator and the back pressure of cylinder is controlled by relief valve. If no feedback was supplied to the input to tune the back pressure, such a constant command signal set, the accumulator would charge or discharge to change pressure to a new equilibrium point.

Based on the static characteristic of force balance in pressure cylinder, a local feedback strategy for the differential pressure control is defined as

$$U' = \frac{k_{fa}P_A A_1 - UA_3}{A_2} \tag{21}$$

where k_{fa} is the gain of pressure transducer. The pressure of accumulator feedbacks to make the controller response following the pressure decrease and the load pressure be consistent with input. The structure of pressure control is improved and this simple controller is reliable, however, without any other compensation and load pressure feedback, a large error is obvious by reason of the resistance of throttle valves, injector, pipes etc.

A '0-type' system is formed in the open-loop control with correction by Eq. (21). Integral compensation is necessary to be applied in the closed-loop controller. The gain k_I of the integral part is requested as

$$k_I < \omega_{r2} \tag{22}$$

for the reason of the requirement of stability. As shown in Fig. 7, the steady-state error of step response can be reduced close to zero under this closed-loop control in theory.

For slope control of the pressure when water is injected, steady-state error is decreased while k_I is set to a large value as shown in Fig. 8. Nevertheless the stability and the capacity of resisting disturbance become poor.

The load viscosity and elasticity change largely than inertia in WAIM from different polymers. The flow rate is greatly influenced by load characteristics as shown in Fig 9. And the load viscosity has relatively large influence
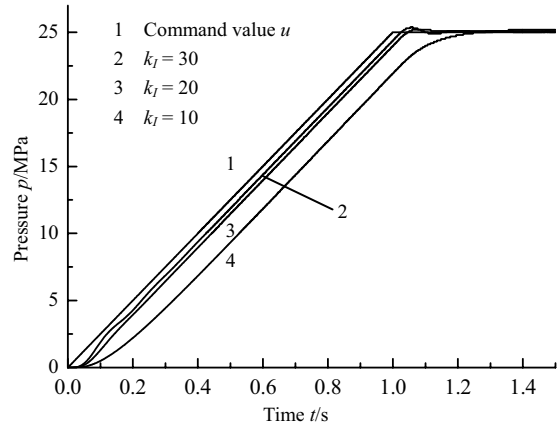
Figure 8 Slope control for various gain of integrator
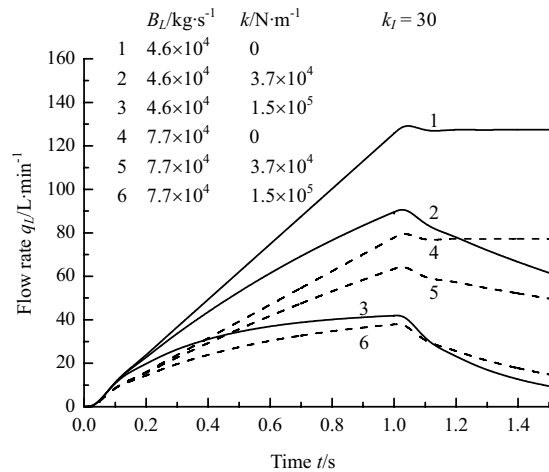
Figure 9 Simulation results of load flow rate

Figure 7 Step-response error with closed-loop control
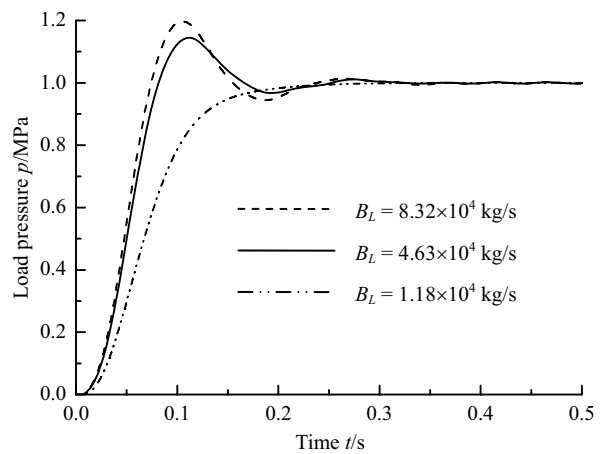
Figure 10 Step responses for different load viscosity

689

on pressure control. Also the slopes tend to be shallow along with the increase of elasticity. The curves may be flat as pressure becomes constant if the elasticity is small. Large elasticity makes flow rate decrease fast when the pressure is maintained. The serials of step responses for closed-loop control with different load viscosity are shown in Fig. 10. The damping ratio of the system increases as the visco-damping coefficient of the load decreases. This illustrates that high viscosity of the polymer melt makes the injection pressure fluctuate when a large input signal change occurs. This shall appear on the start and end of water injection. So a low slope or gentle start should be used to increase injection pressure when molding polymer with high viscosity.

CONCLUSIONS

In this paper, we presented a new control strategy with differential pressure control and energy saving applying accumulator. Through analysis of load characteristic and modeling of the pressure control system, we developed the closed-loop controller.

The differences between polymer melts with load characteristic are great, especially the viscosity and elasticity. The coupling between load pressure and flow rate can be illustrated as linear relationship at aspect of viscosity and an assumption of linear model for WAIM load characteristic is provided. High viscosity leads to large oscillation and instability. The gain of the integrator should be reduced with high-viscosity polymer melt and a low slope or gentle start of command signal should be used to increase injection pressure when molding high-viscosity polymer.

The linear model of the system is built and a '0-type' system is discovered by the feedback of pressure at the accumulator. Based on the closed-loop control with integral compensation, the steady-state error can be reduced close to zero for step response besides the disturbance of nonlinear factors and load fluctuation. Large gain of integrator can be tuned for slope pressure control in WAIM to reduce the error. However, this may result in oscillation of pressure due to nonlinearity of water hydraulic valves. A fitting value of the gain shall be tested in the future experiments. The differential pressure control with pressure piston and accumulator is suitable to the work characteristic of WAIM.

Further research is carried out experimentally. The coupling of load pressure and flow rate and pressure control performance will be measured and investigated.

ACKNOWLEDGMENTS

REFERENCES

1. Mikell, K., Water Injection Molding Makes Hollow Parts Faster, Plastics Technology, 2002, 48-4, pp.42-47
2. Walter, M., Andre, B. and Tim Pohl,. A Comparison of Gas and Water Injection Moulding of Hollow Articles by Fluid-Assisted Injection, Kunststoffe Plast Europe, 1999, 89-9, pp.18-20
3. Walter, M., Tim, J. and Andre, B., WIT-En Route to Series Production: First Industrial Application of the Water Injection Technique, Kunststoffe Plast Europe, 2001, 91-3, pp.37-39
4. TAKAHASHI, H., ITO, K., IKEO, S., Application of Adaptive Controller to Water Hydraulic Servo Cylinder, Proceedings of the 6th JFPS International Symposium on Fluid Power, TSUKUBA, November, 2005, pp.432-436
5. Finn Conrad. Trends in Design of Water Hydraulics – Motion Control and Open-Ended Solutions, Proceedings of the 6th JFPS International Symposium on Fluid Power, 2005, pp.420-431
6. Rainer Protte, Hartmut Bangert, Chris Cooper and Peter Hoeck, Water-Assist Injection Molding – An Innovative Process Technology for Productivity Improvement: Developments in Processing, Equipment and Materials, SPE Antec Proceedings, 2003, pp.404-408
7. Shih-Jung Liu and Shih-Po Lin, Study of 'Fingering' in Water Assisted Injection Molded Composites, Composites Part A: Applied Science and Manufacturing, 2005, 36, pp.1507-1517
8. Shih-Jung Liu and Yen-Shou Chen, The Manufacturing of Thermoplastic Composite Parts by Water-assisted Injection-Molding Technology, Composites Part A: Applied Science and Manufacturing, 2004, 35, pp.171-180
9. LIU, S-J and LIN, C-H., An experimental study of water- assisted injection molding of plastic tubes with dimensional transitions, Journal of Reinforced Plastics and Composites, 2007, 26-14, pp.1441-1454
10. QUAN, LX, and KONG, XD, Theory and Experiment of Accumulator Absorbing Pressure Pulsation without Regard to its Entrance Characteristics. Chinese Journal of Mechanical Engineering, 2007, 43-9, pp.28-32, (In Chinese)

P2-19

COMPARISON OF VIBRATION AND PRESSURE SIGNALS FOR FAULT DETECTION ON WATER HYDRAULIC PROPORTIONAL VALVE

Tomi KROGERUS, Jarno PIETIKÄINEN and Kari T. KOSKINEN

Department of Intelligent Hydraulics and Automation
Tampere University of Technology
P.O.Box 589
33101 Tampere, Finland
(E-mail: tomi.krogerus@tut.fi)

ABSTRACT

The goal of this paper is to detect internal leakages created by seal faults and also identify which seal is damaged from water hydraulic proportional valve using vibration and pressure signals which are analyzed using different data analysis methods. In this study water hydraulic spool valve is studied in a test system during extending and retracting strokes of cylinder while vibration and pressure signals from the valve are measured in normal and different fault situations. Feature extraction is performed using descriptive statistics and wavelet analysis to identify the most influential variables from the measured signals which are then used to classify the state of the system using Self-Organizing Maps (SOM).

KEY WORDS

Water hydraulics, proportional valve, vibration, pressure, condition monitoring

NOMENCLATURE

a : Acceleration [m/s^2]
I : Current [A]
m : Mass [kg]
p : Pressure [bar]
Q : Flow [l/min]
t : Time [s]
T : Temperature [˚C]
U : Voltage [V]
v : Velocity [m/s]
x : Position [m]

INTRODUCTION

Environmental friendliness of hydraulic systems can be increased by using different fluids instead of oil. Despite of its good properties water hydraulics have some challenges which need to be taken into consideration.

The component technology is rather undeveloped when compared to oil hydraulics. In water hydraulic systems there are usually difficulties concerning wear and corrosion of components and also sticking of valves and other components. This requires on-line condition monitoring of the components and fluid as well.

Condition monitoring of hydraulic systems is based on measurements from these systems and especially deviations in these measurement variables. Different measurement variables are more sensitive than others to show early changes in state of the system and components. In this study vibration and pressure signals are used as an indicator of systems health state and the sensitivity of these different measurement variables are compared while final classification result is used as a criterion. Pressure signals are more often used in condition monitoring of control valves than vibration signals. Vibration signals are instead often used to monitor rotating components like a pump or a motor [1,

8, 11]. But there have also been research for monitoring other hydraulic components using vibration measurements. For example in [11] the condition of seals of hydraulic cylinders are studied using vibration measurements.

Neural network research has been very active for several years and there has also been interest in neural network applications to fault diagnosis problems [1, 5, 6, 8, 10]. Neural network is one possible method which is suitable for classifying different system states of the water hydraulic components. Usually all the damages are not known before diagnostics, therefore neural network method Self-Organizing Maps with unsupervised learning are used in this study [2, 6]. Since this type of neural network can perform non-linear functional mapping between sets of variables they can be used to classify raw input data directly [6, 10]. But it is important to preprocess any raw and/or dynamic data before classifying them to improve the performance of the classifier. In this study measurement signals are preprocessed using descriptive statistics and wavelet analysis.

STRUCTURE OF THE TEST SYSTEM

In this study a water hydraulic proportional valve is studied in a test system during extending and retracting strokes of cylinder while vibration and pressure signals are measured in normal and different fault situations. The hydraulic circuit of the test system is presented in Fig. 1.
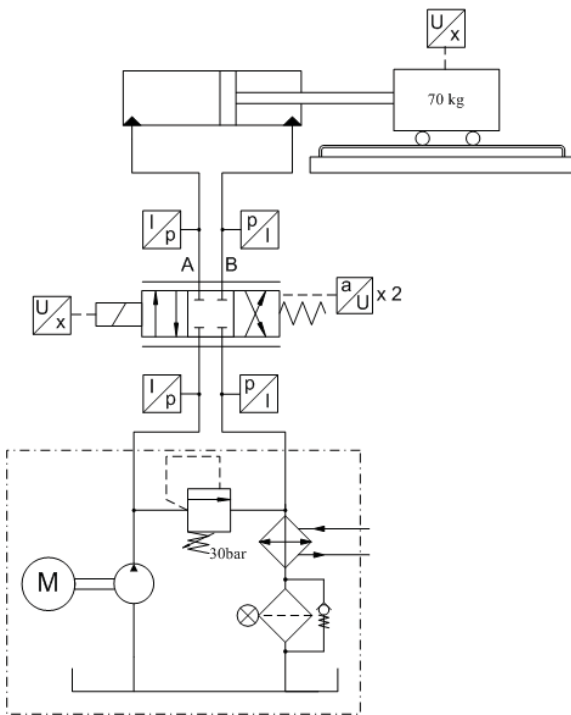
Figure 1 The hydraulic circuit of the test system

The studied water hydraulic proportional valve is 4/3-way spool valve which is modified from a pneumatic on/off valve and it is designed for low-pressure water hydraulics. The position of the spool is measured by a LVDT sensor and the measured signal is used as a feedback signal for a PI-controller. [9]

The dSpace DS1102 controller board was used to control the proportional valve and to measure all variables except the acceleration. It was also used to trigger the acceleration measurements when the control sequence starts. The acceleration signals were measured with IMC Cronos PL measurement device.

An axial displacement pump with maximum delivery of 10 l/min (1500 rpm) is used in the system and the size of the double-acting cylinder is 32/16-500. The supply pressure is 30 bar but also up to 70 bar pressure levels have been tested with this valve. The load used in testing was 70 kg.
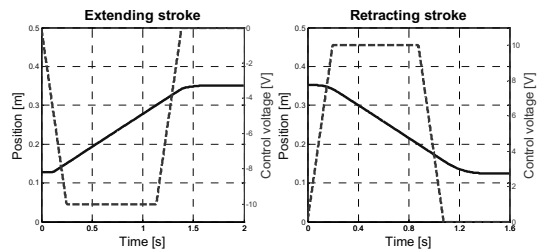
Figure 2 An example of cylinder position and control signal of the control valve from the extending and retracting strokes
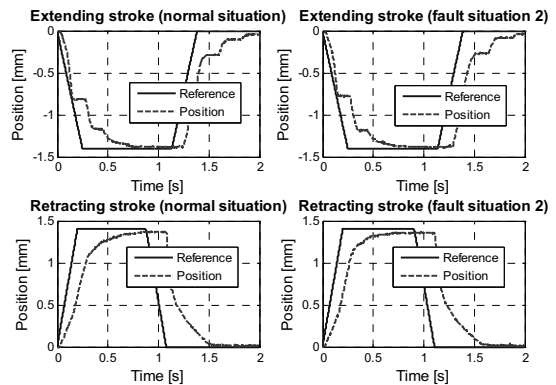
Figure 3 An example of spool position and reference from the extending and retracting strokes

The cylinder is driven in a specified sequence using programmable position limits. After the limit is exceeded the control signal of the control valve is driven to zero using a specified ramp. The upper limit used in the test system is 300mm when the cylinder is extending and the lower limit 200mm when the cylinder is retracting. The starting point of the stroke is where the cylinder has stopped last time. An example of cylinder position and control signal of the control valve in the

extending and retracting strokes of the cylinder are shown in Fig. 2 and spool position and reference signal in Fig.3.

Monitored component and fault type

The potential fault type in the studied proportional valve is increased internal leakage. The construction of the valve is such that the spool is inside a sleeve that is mounted in the body of the valve and between the sleeve and the body are o-ring seals [9]. If these o-rings are damaged the result is increased internal leakage between the ports of the valve. This kind of fault type can be caused by deterioration of the seal material or poor assembling of the spool sleeve into the valve. The used spool sleeve with the seals and an example of a faulty seal are shown in Fig. 4. In Fig. 5 is shown a 50x magnification of a seal fault.
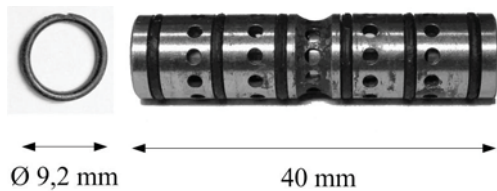
Figure 4 The spool sleeve of the valve and a seal fault
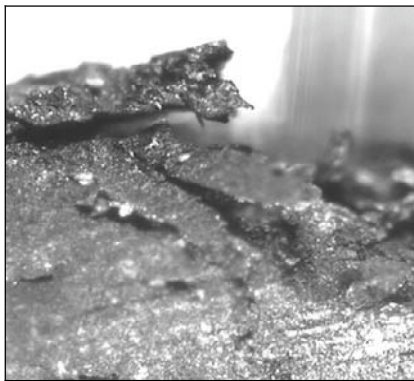
Figure 5 An example of seal fault (50x)

In this study a seal fault in the spool sleeve of the valve has been used as a fault case. The used proportional valve has a spool sleeve with six seals and four of them are of interest in this study. The outermost seals are only for sealing the drain line from the tank line and do not affect the behavior of the system. Therefore, the outermost seals are not used in this study. The effects of the seal faults in these seals are investigated one at a time. The studied seals are numbered 1 to 4 (S1 to S4) starting from the spring end of the valve and the fault situations are 1 to 4 equally. At non-controlled state the cylinder tends to crawl slowly when S2 or S3 is damaged. In the earlier study [4] differences between the velocities of the sequences could be seen between

the normal and the fault situations. A same phenomenon is not possible to see in the present system during the sequence because of a low pressure level, small load and the cylinder is driven horizontally. In [4] the cylinder was driven in vertical direction.

Measurement methods

Acceleration sensors were used to measure the vibrations of the proportional valve during the extending and retracting strokes of the cylinder and pressure sensors were used to measure the pressure from the actuator ports A and B. The locations of the sensors can be seen from Fig. 1.

The model of the pressure sensors is Trafag 8891 NA 100.0A. This type uses a thin film strain gauge technology. The pressures of the cylinder chambers were measured with similar sensors.

The accelerometers exploited were IMI Sensors 603C11 and Kistler 8702B50M1. The frequency range of both sensors is 0.5 Hz to 10 kHz and the resonant frequency 25 kHz and 54 kHz respectively. The signal processing of the measurements was conducted by using a 15th order Chebyshev band-pass filter. The lower and upper cut-off frequencies were 2 Hz and 20 kHz respectively.

The final selection of the two ICP sensors was the IMI Sensors industrial grade accelerometer due to the final classification results compared to the other accelerometer, better mechanical structure, low-cost price and robustness, which are essential in every day use in final applications.

Training and testing data

Training and testing data for use in classification are measured from the test system. The test system is run in normal and four fault situations (four different seal faults) in the extending and retracting strokes. The measured variables are pressures A and B from the actuator ports and acceleration which is measured from the other end of the valve in axial-direction of the spool of the valve (see Fig. 1). The measurement time in the extending stroke is 2.0s and 1.6s in the retracting stroke. The same sequence is measured 10 times in each case for both directions so the total amount of sequences is 100. The measurement frequency with the pressure measurements is 1 kHz and with the acceleration measurements 20 kHz. Multiple sequences are driven because this way it is possible to improve the generalization of the network when new data is presented to the network.

In Fig. 6-7 are shown examples from the pressure measurements. From the figures can be seen how some of the normal and faulty measurement points are very close to each other especially in the middle of the sequence. That is why the whole sequence is classified here as a normal or fault state instead of classifying each measurement point like in [3]. Biggest differences can be seen in the beginning and at the end of the sequence.
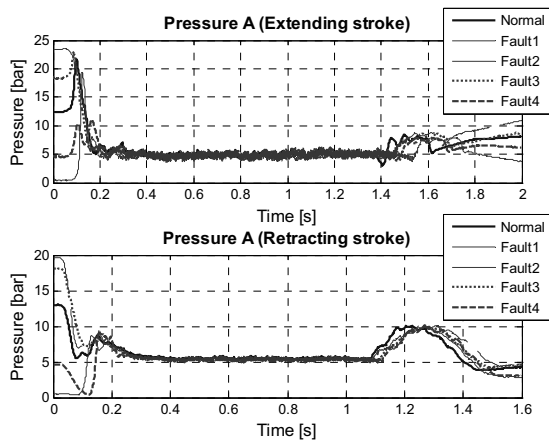
Figure 6 An example of pressure A from the actuator ports from the extending and retracting strokes
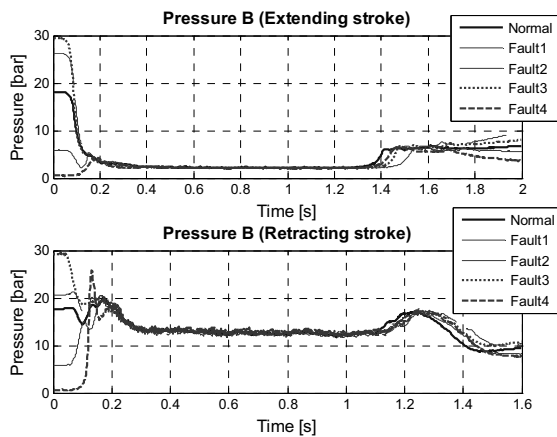
Figure 7 An example of pressure signal B from the actuator ports from the extending and retracting strokes
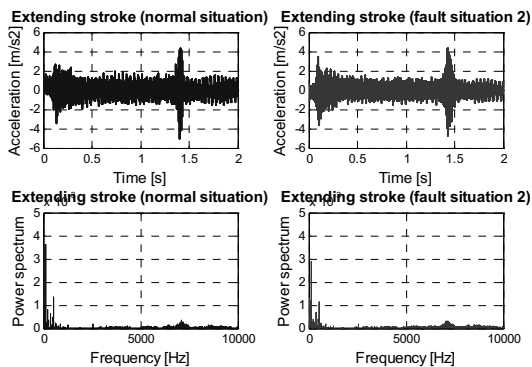
Figure 8 An example of vibration signals from the extending stroke (normal and fault situation 2)

In Fig. 8-9 are shown examples from the vibration measurements in the normal and fault situation 2 in the extending and retracting strokes. In the figures are shown the time and frequency domain of the vibration signal. Deviations from the normal situation are easier

to detect from the frequency domain than from the time domain. In this study the entire measured frequency area 2 Hz - 10 kHz is used in the data analysis. Studying the effect of using different frequency areas in data analysis to improve the classification results are left outside the scope of this paper.
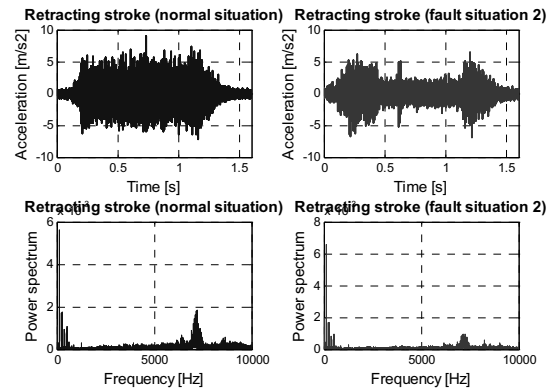
Figure 9 An example of vibration signals from the retracting stroke (normal and fault situation 2)

FEATURE EXTRACTION OF THE MEASUREMENT DATA

Preprocessing of the measurement data usually involves extracting relevant and discriminating information and in so doing reducing data dimensionality. This process is often called feature extraction. [4, 7]

It is important to preprocess any raw and/or dynamic data before classifying them to improve the network performance [4]. Two different type of feature extraction methods are exploited in this study which are descriptive statistics and wavelet analysis.

Descriptive statistics

Descriptive statistics are used to describe the basic statistical features of the data in a study. In this study 11 different statistical values were extracted from both the pressure and the vibration signals to get relevant information for classification. These are: arithmetic mean, median, standard deviation, mean deviation, variance, rms, skewness, kurtosis, maximum, minimum and sum.

Wavelet analysis

The basic idea of wavelet analysis is to adopt a wavelet prototype function, called an analyzing wavelet or mother wavelet. In the wavelet analysis original measured signal is broken up into shifted and scaled versions of the analyzing (or mother) wavelet. In this study analyzing/mother wavelet which was used is Daubenchies (db2). Because the original signal or function can be represented at certain accuracy using only approximation coefficients, data analysis can be performed using just the wavelet coefficients [7].

In the extending stroke 65 coefficients are extracted

from both pressure signals and 315 from the vibration signal. In the retracting stroke 52 coefficients points are extracted from both pressure signals and 252 from the vibration signal.

CLASSIFICATION OF THE EXTRACTED FEATURES

Different system states (normal and four fault states) are classified using Self-Organizing Maps. The extracted information from the pressure and vibration signals is used as inputs to the network.

Self-Organizing Maps
The Self-Organizing Maps (SOM) is a neural network method which can represent any functional relationship between inputs and outputs. The SOM uses unsupervised learning where network learns by evaluating the similarity between the input patterns presented to the network and perform some kind of clustering operation where they categorize the input patterns into a finite number of classes [4]. Training algorithm and more details of the Self-Organizing Maps are presented in the earlier publications [3, 4].

In this study the SOM is first trained to detect the state of the system which is either normal or fault and only the data from the normal situation is used in the training. So the analysis is concentrated on finding the properties of the normal data and the appropriate means to identify the deviations from the normal situation [2, 10]. After the fault states of the system have been identified then the network can be used to identify a specific fault from the measurement data. Here also the data from the fault situations are used in the training.

Classification of the system state
The number of map units in this situation is 4 x 3. The size of the map is quite small but it is not necessary to use a bigger one because it does not make the results any better and it also slows down the calculation [4]. Five sequences from the normal situation are used in the training and five sequences from each system state (normal + 4 x fault) are used in the testing.
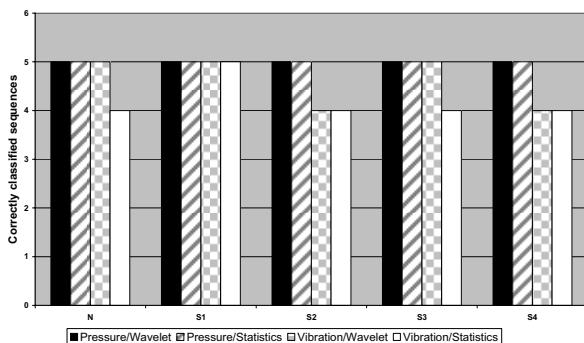
Figure 10 Classification results from extending stroke

In Fig. 10-11 are presented the classification results of the system state. From the results can be seen that almost all the sequences are classified correctly. When the pressure signal is used as an indicator of the system state all the states are correct but when the vibration signal is used there are few wrong classified states in both situations (extending and retracting strokes).
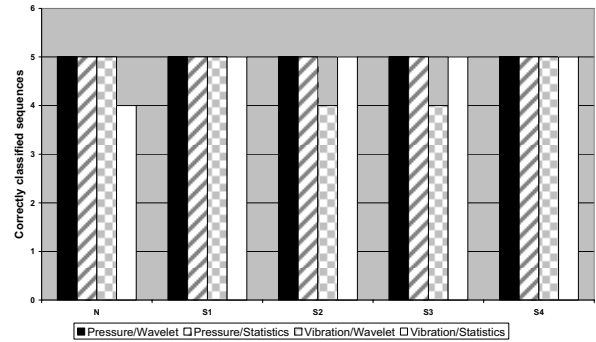
Figure 11 Classification results from retracting stroke

Classification of the fault situations
The number of map units used in this situation is 5 x 2, 4 x 3 or 3 x 3. Five sequences from each system state are used in the training and other five from each system state in the testing. In Fig. 12-13 are presented the classification results of the specific faults situations. Most obvious result is that the pressure signal gives much better classification results than the vibration signal. In extending stroke especially the seal faults S2, S3 and S4 were quite hard to classify regardless of the feature extraction method. For example the classification result for S3 is 0 % when the descriptive statistics were used in feature extraction. The wavelet analysis seems to be a little better feature extraction method in the extending stroke.
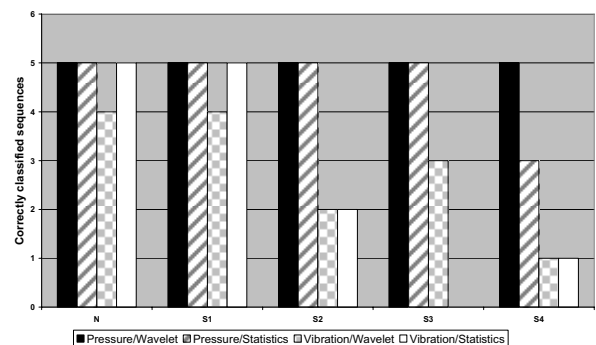
Figure 12 Classification results from extending stroke

In the retracting stroke the difference between the pressure and the vibration is even bigger than in the extending stroke. Only in cases N/statistics and S1/wavelet the vibration signal is as good as the

pressure signal. Again S2, S3 and S4 were hard to classify using the vibration signal. In the retracting stroke the descriptive statistics were overall as good as the wavelet analysis in feature extraction.
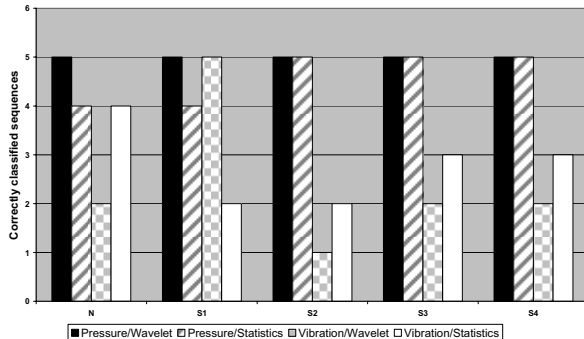
Figure 13 Classification results from retracting stroke

CONCLUSION

The main goal of this research was to detect internal leakages created by seal faults and also to identify which seal is damaged from the water hydraulic proportional valve using the vibration and the pressure signals which were analyzed using different data analysis methods.

Descriptive statistics and wavelet analysis were used to extract information rich features from the pressure and vibration signals which were then used in classification

of the system state.

The SOM is first trained to detect the state of the system. When only normal state was used in classification and state was classified either normal or fault almost all the sequences were classified correctly with pressure and vibration with both feature extraction methods.

After the fault states of the system were identified then it was possible to use the network to identify the specific fault from the measurement data that have not been presented to the network before. In this case also data from the fault situation were used in the training of the network. Here the classification results were much better when the pressure signal was used instead of the vibration signal. The differences between the feature extraction methods are not so high than with the measurement variables.

Preprocessing of the measurement data needs more research so that the best statistical values are found and right amount of wavelet coefficients are extracted. In the measurements there were also changes in the vibration signal in different measurement times when the conditions were the same so more measurements needs to be done so that reliable results can be achieved. Also different frequency areas need to be studied more carefully.

In this study the vibration signal was measured only from one direction. Combining this with two other axial-directions can also give better results. Also effect of different load situations needs to be studied

REFERENCES

1. Chen, H., Chua, P. and Lim, G., Fault Diagnosis of Water Hydraulic Motor by Adaptive Wavelet Analysis Optimized by Genetic Algorithm, International Journal of Applied Mathematics and Mechanics, Vol. 2, pp. 57-78, 2005.
2. Kohonen, T., Self-Organizing Maps, Springer- Verlag Berlin Heidelberg, New York, 3 rd ed., 2001.
3. Krogerus, T., Vilenius, J., Liimatainen, J., and Koskinen, K.T., Self-Organizing Maps with Unsupervised Learning for Condition Monitoring of Fluid Power Systems, SAE 2006 Commercial Vehicle Engineering. Chicago, Illinois, USA, 2006.
4. Krogerus, T., Sairiala, H., and Koskinen, K.T., Fault Classification Based on Self-Organizing Maps in Water Hydraulic Forklift, The Tenth Scandinavian Conference on Fluid Power, SICFP'07, Tampere, Finland, 2007.
5. Kuravsky, L. and Baranov, S., Application of Self-Organizing Feature Maps for Diagnostics of Vibroacoustic Systems. International Conference on Condition Monitoring. St. Catherine's College, Oxford, UK, 2001.
6. Le, T., Watton, J. and Pham, D., Fault classification of fluid power systems using a dynamics feature extraction technique and neural networks. Proc IMechE, Part I, Journal of Systems and Control Engineering, Vol. 212, 87-97, 1998.
7. Mallat, S., A Wavelet Tour of Signal Processing, Academic Press, London, UK, 2 nd ed., 1999.
8. Ramden, T., Condition Monitoring and Fault Diagnosis of Fluid Power Systems – A Approaches with Neural Networks and Parameter Identification, PhD thesis No. 514, Linköping, Sweden, 1998.
9. Sairiala, H., Koskinen K.T., Vilenius, M., Jauhola, P., Jauhola, L., and Selkosmaa, J., Control of a Water Hydraulic Cylinder Drive with New Proportional Valve, The Eighth Scandinavian Conference on Fluid Power, SICFP'03, Tampere, Finland, 2003.
10. Vesanto, J., Data Exploration Process Based on the Self-Organizing Map. PhD thesis, Acta Polytechnica Scandinavica, Mathematics and Computing Series No. 115, Helsinki University of Technology, Finland, 2002.
11. Wue, T.; Chua, P. and Lim, G, On-line Fault Detection and Analysis of Modern Water Hydraulic System. Journal of The Institution of Engineers, Singapore, Vol. 44, Issue 4, 2004.

P2-20

STUDY ON MEASUREMENT OF LIQUID FLOW RATE USING AE SENSOR

Yi Quin ZHENG*, Takeshi NAKADA*, Moritaka OHTA*, Gang WANG* and Yasuo SAKURAI**

*School of Information Environment, Tokyo Denki University,
2-1200 Muzai Gakuenfai, Chiba, 270-1382 Japan
(E-mail: nakada@sie.dendai.ac.jp)
**Department of Mechanical Engineering, Ashikaga Institute of Technology,
268-1 Oomaecho, Ashikaga, Tochigi, 326－8558 Japan

ABSTRACT

This study deals with a computer system for measuring flow rate of tap water flowing in a rigid pipeline in a non-contact method by using an acoustic emission (AE) sensor placed on a surface of a pipeline. The acoustic emission generated by tap water flowing at a constant flow rate in a pipeline is caught by the AE sensor experimentally, and the corresponding output of the AE sensor is converted to a root mean square (RMS) value. It became clear that the relation between flow rate and the corresponding RMS value can be expressed as a quadratic curve with good approximation. This quadratic curve is used as the calibration date for measurement of flow rate.   A prototype of a flow rate measuring system based on a computer was constructed by taking account of the calibration data. It is shown in the experiment that the flow rate more than 3.2 l/min can be measured by using the measuring system proposed in this study.

KEY WORDS

Flow Rate Measurement, Pipeline, AE Sensor, Signal Processing, RMS Value

INTRODUCTION

A measurement of a fluid flow rate is very important to get necessary data for designing or manufacturing a process system and a fluid mechanical system. In this study a method to measure a fluid flow rate in a pipeline using AE sensor is proposed. A measuring system based on this method has advantages to be cheap and be able to measure with noncontact. In this method an AE sensor is installed on the outer wall of a pipeline. The AE sensor detects the acoustic vibration generated by tap water flowing in the pipeline and it outputs the AE signal corresponding to the flow rate of tap water in the pipeline. A signal processing method of the AE signal is developed to measure the flow rate and an automatic measurement system of the flow rate is constructed. The flow rate more than 3.2l/min can be measured in this system. The effectiveness of a prototype flow rate measuring system based on the method proposed in this study is confirmed in the experiment.

PROPOSAL OF MEASUREMENT METHOD USING AE SENSOR

Figure 1 shows a concept of a fluid flow rate measurement method proposed in this study. An AE sensor, which is used to detect acoustic vibration to occur by breaking of materials in general, is installed on

the outer surface of a steel pipe as shown in Figure 2. This AE sensor detects acoustic vibration to occur by tap water flowing in the pipeline, and we use Root-Mean-Square (RMS) method as a signal processing to obtain the corresponding flow rate from the AE output signal.
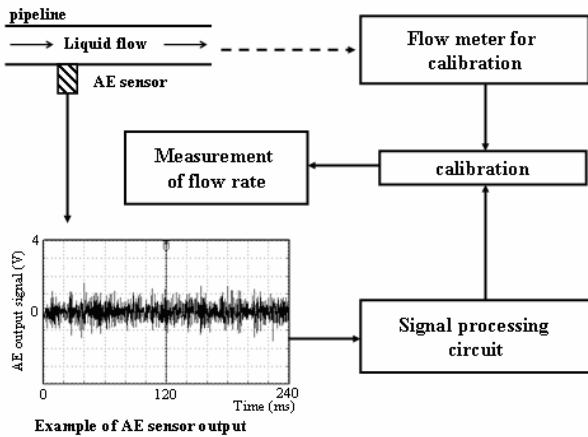
Figure 1 Concept of flow rate measurement

EXPERIMENT

Experimental Apparatus

Figure 3 shows the outline of the experimental apparatus used in this study. This experimental apparatus consists of a fluid source, a steel pipeline, a flowmeter for flow rate calibration, an AE sensor, some amplifiers, a high pass filter, a RMS circuit and a PC for collecting date and a data analysis. The fluid used here is a tap water, and the flow rate is temporally constant. The proposed measurement method can be considered an indirect measurement method, because an AE sensor has an inherent frequency characteristics, and the output signal of the AE sensor are effected by the mounting conditions between the AE sensor and the pipe, and the transmission characteristics of sound. Accordingly, the result of the measurement in our proposed measurement system must be calibrated by a precise flowmeter for flow rate calibration.

Experiment and results

Figure 4 shows an output waveform of the AE sensor at the flow rate Q of 7.3l/min, and it is found that various frequency components are included in it. The output waveform of the RMS circuit is shown in Figure 5, when the output waveform of the AE sensor is given to the RMS circuit, and the RMS value is almost constant during measurement time. This experimental result that a constant RMS value corresponding to a constant flow rate can be gotten shows the possibility of the flow rate measurement by using the AE sensor. Then, the corresponding RMS value was obtained experimentally
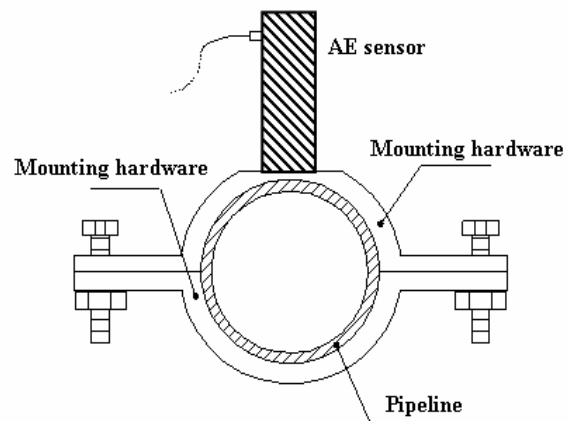
Figure 2 Installation of AE sensor
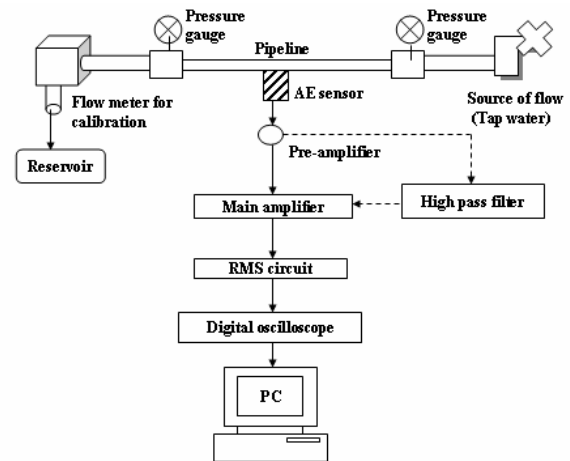
Figure 3 Experimental system of flow rate measurement

at each constant flow rate Q. The high pass filter in Figure 3 is removed in this experiment, and the signal processing system shown in Figure 6 is used. The experimental result is shown in Figure 7, and it is found that the RMS value increases almost in a quadratic function corresponding to the increase of the flow rate in the flow rate $Q>5$l/min. On the other hand the change of the RMS value corresponding to the change of the flow rate can not be found in the flow rate $Q<5$l/min, and it can be considered that the electric noise with the frequency of 50 Hz is this cause. So, the high pass filter with the cut off frequency of 80 Hz was inserted as shown in Figure 8 in order to remove the electric noise, and the gain of the main amplifier was readjusted twice. Under these conditions the relation between the flow rate and the RMS value in the flow rate $Q<5$l/min was obtained experimentally. The experimental result is shown in Figure 9 and its relation shows almost the same tendency as that in Figure 7. The following matters became clear from these experimental results.

(1) The RMS value of the output AE signal increase in a quadratic function, corresponding to the increase of the flow rate in the flow rate $Q>3l/min$, and the possibility that the flow rate can be obtained from the RMS value was found.

(2) The measurement of the flow rate is currently difficult in the flow rate $Q<3l/min$.
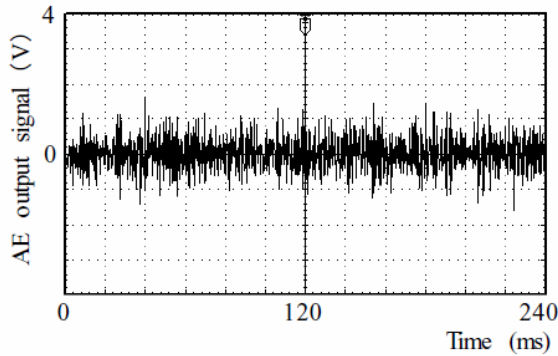
Figure 4 Output signal of AE sensor in $Q=7.3[l/min]$
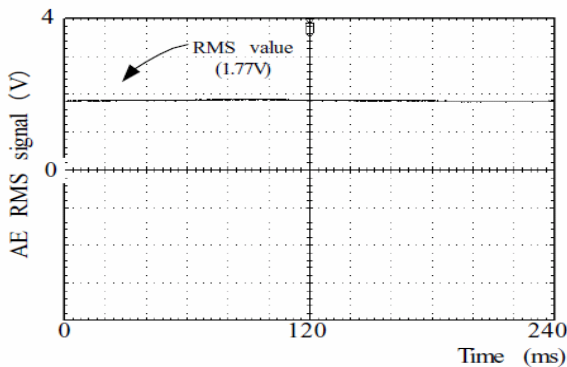
Figure 5 Output signal of RMS circuit in $Q=7.3[l/min]$

Frequency Analysis of AE signal

The frequency analysis of the AE signal caused by the fluid flow in the pipe was performed by using FFT in order to find the possibility of the flow rate measurement in the flow rate $Q<3l/min$. The conditions on the FFT analysis are as follows.

  Frequency range : 20 kHz
  Sampling frequency : 51.25 kHz
  Window function : Rectangular window
  Flow rate Q : 0l/min, 3l/min, 7l/min

Figure 10 shows the analytical results, and it became clear that the frequency components from 1 kHz to 3 kHz centering around 2 kHz are dominant. When focusing on the amplitudes at the frequency of around 2 kHz in the flow rate $Q=3l/min$ and $Q=7l/min$, the
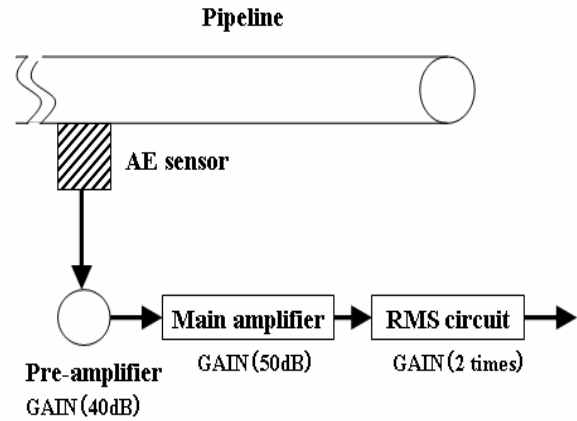
Figure 6 Basic signal processing system of measurement
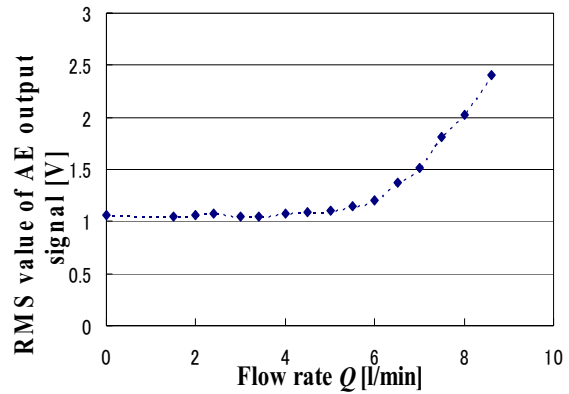
Figure 7 Relation of flow rate and RMS value in use of basic signal processing system
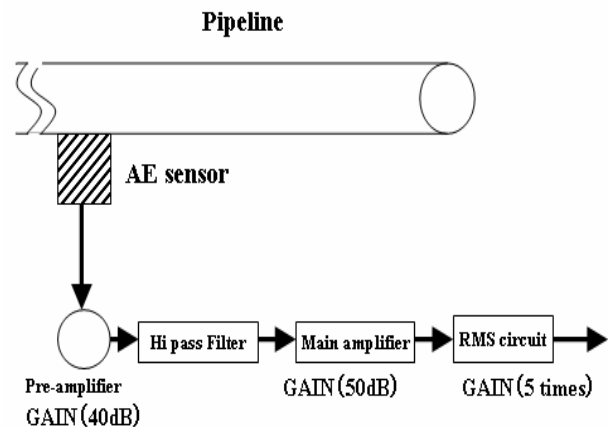
Figure 8 Modified signal processing system (High-pass filter insertion)
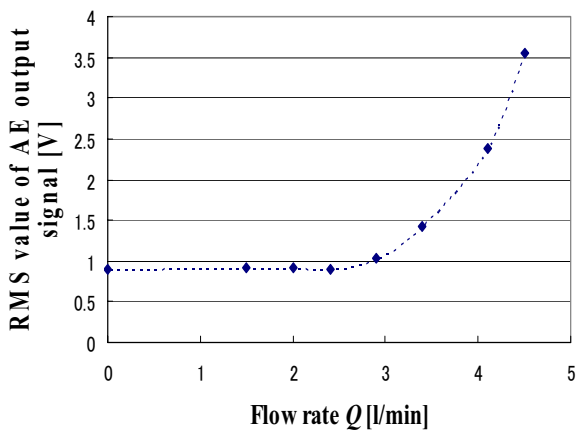
Figure 9 Relation of flow rate and RMS value of
AE output signal in medium flow rate region

focusing on the amplitudes at the frequency of around 2
kHz in the flow rate Q=3l/min and Q=7l/min, the
amplitude in Q=3l/min reduces to 1/10 of the amplitude
in Q=7l/min. Since the amplitude reduces rapidly as the
focusing on the amplitudes at the frequency of around 2
kHz in the flow rate Q=3l/min and Q=7l/min, the
amplitude in Q=3l/min reduces to 1/10 of the amplitude
in Q=7l/min. Since the amplitude reduces rapidly as the
flow rate reduces as stated above, S/N of the AE signal
reduces so small in Q<3l/min, and this makes the
measurement of flow rate in Q<3l/min difficult. A
solution to make the measurement in Q<3l/min possible
may be to reduce the disused frequency components
except 1 kHz to 3 kHz by using band pass filter.

CONSTRUCTION OF FLOW RATE
MEASUREMENT SYSTEM

A flow rate measurement system based on a computer to
measure automatically a flow rate by using the method
proposed in this study was constructed.

Derivation of Calibration Curve of Flow Rate
The flow rate is classified in the large flow rate region
(Q>5l/min), the medium flow rate region
(5l/min>Q>3l/min) and the small flow rate region
(Q<3l/min) in our measurement system. The relation
between flow rate and RMS value in large flow rate
region was shown in Figure7, and the relation in the
medium flow rate region in Figure 9. The flow rate
measurement in the small flow rate region is difficult
presently. For constructing an automatic measurement
system the flow rate has to be determined from the
measured RMS value. In this study the relation between
the RMS values and the corresponding flow rates was
approximated by a quadratic curve, using least square
method. The obtained quadratic curves express as
follows.
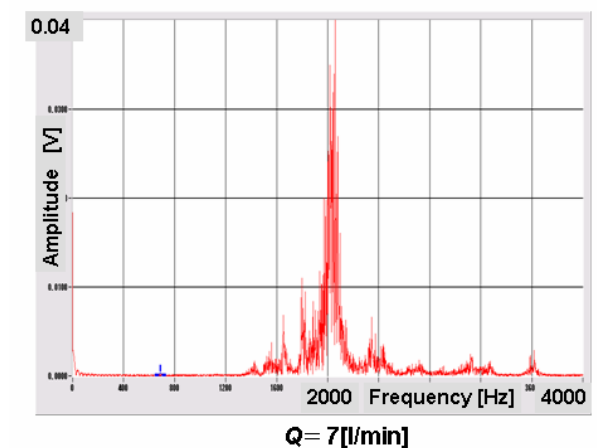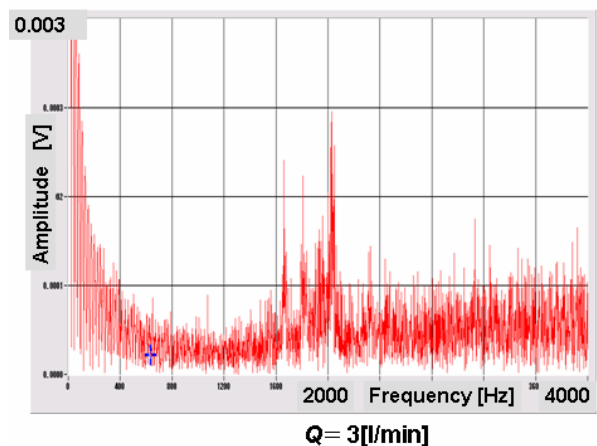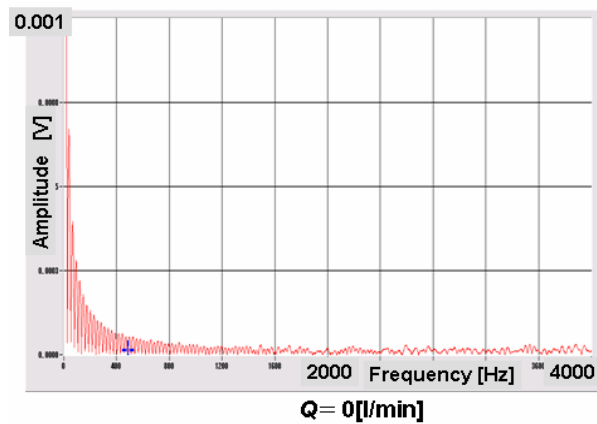
Figure 10 Power spectrum of AE
(Q=0, Q=3, Q=7)

Large flow rate region :

$$V_{RMS} = 0.09Q^2 - 0.86Q + 3.15 \qquad (1)$$

Medium flow rate region :

$$V_{RMS} = 0.69Q^2 - 3.57Q + 5.52 \qquad (2)$$

The experimental results and the quadratic curves in the large flow rate region and the medium flow rate region are shown in Figures 11 and 12, respectively. The quadratic curve in the large flow rate region coincides well in the flow rate ranges more than 5l/min with the experimental results. Similarly, the quadratic curve in the medium flow rate region coincides well in the flow rate ranges more than 3l/min with the experimental results. Therefore, the flow rate can be obtained from the measured RMS value (V_{RMS}) as follows.

Large flow rate region :

$$Q = \frac{\sqrt{0.36(V_{RMS}-3.15)+0.74}}{0.18} + 4.78 \qquad (3)$$

Medium flow rate region :

$$Q = \frac{\sqrt{2.76(V_{RMS}-5.52)+12.74}}{1.38} + 2.59 \qquad (4)$$

Prototype of Flow Rate Measurement System

The flow rate measurement system includes the three kinds of processes as follows. Basically, in our system the flow rate is obtained from the measured V_{RMS} and Eq. (3) or Eq. (4), and the measured V_{RMS} and the flow rate are displayed on a screen.

(1)Process in large flow rate region :

The signal processing system shown in Figure 6 is used, and this process becomes the initial state in this measurement system.

As the flow rate belongs to the large flow rate region, as shown in Figure 11, when V_{RMS} >1.10, the flow rate can be obtained from Eq. (3).

(2) Process in medium flow rate region :

As the flow rate belongs to the medium flow rate region, when V_{RMS} <1.10 in the above process (1),the signal processing system is changed to flow rate in medium flow rate region from Figure 6 to Figure 8 automatically, and the flow rate can be obtained from measured V_{RMS} and Eq. (4).

(3) Process in small flow rate region :

As the flow rate belongs to the small flow rate region, when V_{RMS} <0.91 in the above process (2), the flow rate can not be measured in this state, and "Unmeasurable" is displayed on the screen.

The basic flow chart for the prototype of the flow rate measurement system is shown in Figure 13. Figure 14 shows the signal processing system which switches over from the process of the large flow rate region to the process of the medium flow rate region. The electric relay in Figure 14 is connected to point of contact [1] the initial state for measurement. When the measured V_{RMS} <1.10, the electric relay is connected to point of contact [2] by the operating voltage of 5 V generated from PC, and the process in large flow rate region shifts to process in the medium flow rate. Figure 15 shows an
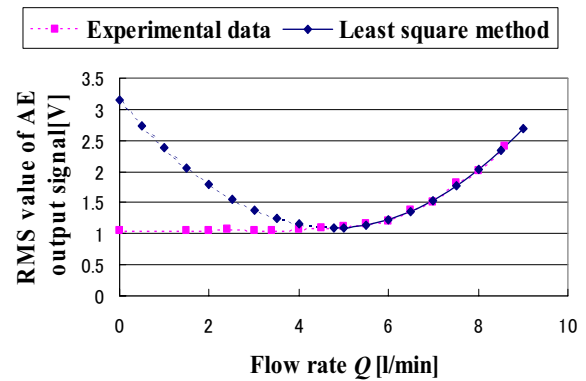
Figure11 Calibration curve of RMS value of AE output to flow rate in large flow rate region
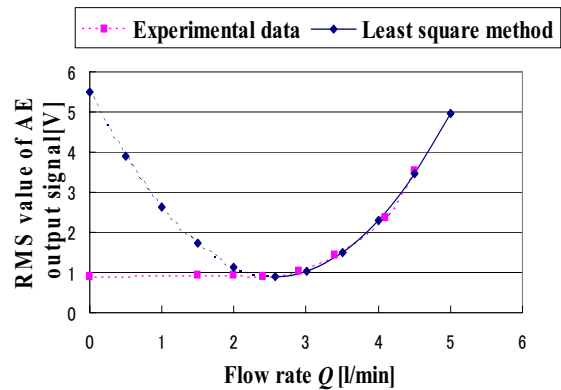
Figure 12 Calibration curve of RMS value of AE output

indication screen of the flow rate in the flow rate measurement system. The measured V_{RMS} is displayed on a part of "Input voltage" on the left of the screen, and the flow rate obtained from V_{RMS} is displayed on a part of "Flow rate" in the lower right of the screen. The insertion state of 80 Hz high –pass filter is displayed on a part of "Filter" of the right side of "Input voltage" by on/off lamp. In case of small flow rate region "Unmeasurable" is displayed on a part of "Error" in the lower left of the screen.

CONCLUSIONS

In this study a flow rate measurement method using AE sensor is proposed and a prototype of the flow rate measuring system based on the method is constructed. It is found that the flow rate measurement is possible in the flow rate region of 3.2l/min～7l/min in this system. However, the improvement of S/N is necessary to measure the flow rate in the small flow rate region less than 3l/min.

Figure 13 Flow chart of AE output and flow rate collation
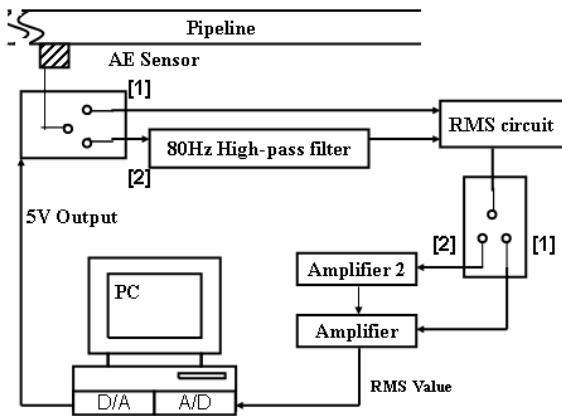
Figure 14 Flow rate process system in stationary flow rate
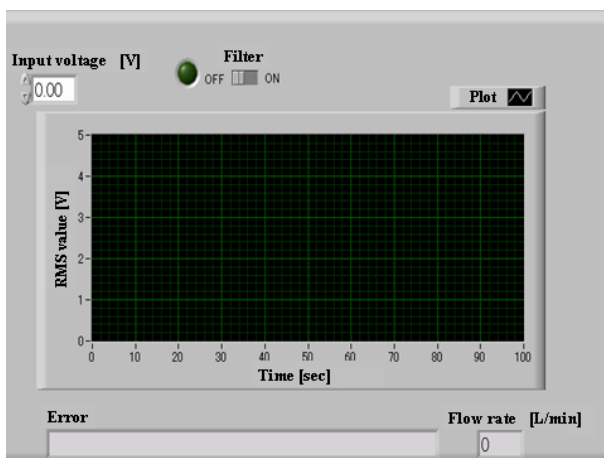
Figure 15 PC screen of flow rate process system

REFERENCES

1. T.Nakada and T.Mitsuoka, Measurement of Acoustic Noize Generated by fluid flow by Using AE Sensor, Transactions of The Japan Society of the Mechanical Engineering, 1985, Series B, 51-470, pp.3155-3164.
2. M.Ohta, T.Nakada, G. Wang, Y.Sakurai, Study on Measurement of Flow Rate using AE Sensor, The proceedings on Autumn Conference of Japan Fluid Power System Society, 2007, pp.206-208

P2-21

PARALLEL CONNECTION MEASURING METHOD FOR GAS LEAKAGE BASED ON STANDARD FLOW

Liang HUANG*, Maolin CAI**

*Graduate School of Automation Science and Electrical Engineering
Beihang University
37 Xueyuan Road, Haidian, Beijing, 100083 China
(E-mail: huang1liang2@hotmail.com)
** School of Automation Science and Electrical Engineering
Beihang University
37 Xueyuan Road, Haidian, Beijing, 100083 China

ABSTRACT

The objective of work described in this paper is to propose a new method of measuring gas leakage for pneumatic industry. The measurement is enabled by employing standard flow. Standard flow is used to determine the internal volume of the measured equipment. An algorithm is formulated to describe, to the extent possible, the relationship between gas leakage and standard flow. This measurement method deviates from the theoretical leakage values by less than 5%, and shows a good precision and scope compared with the traditional flow measurements. In addition, the proposed parallel connection based on standard flow makes easy operation and fast measuring possible, thus promising new area of application for pneumatic equipments.

KEY WORDS

Gas Leakage, Parallel Connection, Standard Flow

NOMENCLATURE

G : Massive flow rate   [kg/s]
k : Kapper
m : Air mass   [kg]
P : Internal pressure in pipeline of equipment   [Pa]
P_a : Atmospheric pressure   [Pa]
P_f : Reference pressure for standard flow   [Pa]
Q : Volumetric flow rate   [l/min(ANR)]
R : Ideal gas constant   [J/(kg • s)]
S_e : Effective area   [m^2]
t : Time   [s]
V : Internal volume   [m^3]

θ : Air temperature   [K]
θ_α : Atmospheric temperature   [K]
ρ : Air density   [kg/m^3]
Suffix:
l : Leakage without Standard flow
s : Standard flow
sl : Leakage with Standard flow

1. INTRODUCTION

Today, compressed air has been widely used in industrialization since 1980s, because of cleanness, low-cost and easy maintenance of compressed air

systems[1]. Compressed air systems are consuming approximate 5 percent of the total supplied electricity in china which reaches to two hundred billion kWh/year. But the consumption of gas leakage takes up to 10-50%[2]. Compared with traditional flow meters, the meter using the proposed new method can be connected parallel to the equipment to detect leakage in the equipment automatically. The relative measurement error can reach to less than 5%. So this method can be largely used for pneumatic equipment.

2. MEASURING PRINCIPLE

The Fig.1 shows the measuring circuit which includes a standard flow circuit.
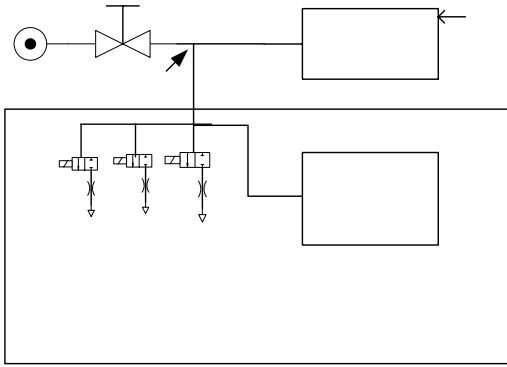
Figure 1 Measuring circuit

Based on thermodynamics, the state equation of compressible air in a chamber can be written as

$$PV = mR\theta \tag{1}$$

When leakage happens, the following equation is derived by differentiating Eq.(1):

$$V \frac{dP_l}{dt} = G_l R\theta + mR \frac{d\theta}{dt} \tag{2}$$

Where G is negative during discharging, and vice versa. To eliminate the temperature effect on the dynamic air pressure, it is necessary to wait until the temperature in equipment become constant after charging[3][4]. So the temperature in equipment can be considered as atmospheric temperature during the measurement. So the equation obtained from Eq. (2) is

$$V \frac{dP_l}{dt} = G_l R\theta_a \tag{3}$$

The volume V varies from different equipments and pipelines. To void the uncertainty of V, we design a standard flow circuit which includes three solenoid valves. For the volume of solenoid valve is far smaller than that of pipeline in equipment, when the standard flow circuit works, Eq. (3) can be written as

$$V \frac{dP_{sl}}{dt} = (G_l + G_s)R\theta_a \tag{4}$$

When leakage happens in the pipeline, compressed air flow through orifice with high speed, the heat can not transfer completely at all.So it can be considered as one-dimensional isentropic flow. For the downstream pressure of leakage passage equals to the atmospheric pressure, the mass flow rate can be expressed as Eq.(5):

$$G = S_e PB \tag{5}$$

Where B are:

$$B = \begin{cases} \sqrt{\dfrac{\kappa}{R \cdot \theta_a}\left(\dfrac{2}{\kappa+1}\right)^{\frac{\kappa+1}{\kappa-1}}} & \dfrac{P_a}{P} \le 0.5283 \\[4ex] \sqrt{\dfrac{2\kappa}{(\kappa-1)}\dfrac{1}{R \cdot \theta_a}\left[\left(\dfrac{P_a}{P}\right)^{\frac{2}{\kappa}} - \left(\dfrac{P_a}{P}\right)^{\frac{\kappa+1}{\kappa-1}}\right]} & \dfrac{P_a}{P} > 0.5283 \end{cases}$$

For $P_a/P < 0.528$, leakage flow rate is proportional to internal pressure, and we can get the Eq.(6):

$$G_l = S_{el}P_l\sqrt{\frac{\kappa}{R \cdot \theta_a}\left(\frac{2}{\kappa+1}\right)^{\frac{\kappa+1}{\kappa-1}}}$$
$$G_s = S_{es}P_f\sqrt{\frac{\kappa}{R \cdot \theta_a}\left(\frac{2}{\kappa+1}\right)^{\frac{\kappa+1}{\kappa-1}}} \tag{6}$$

In Fig.2, the simulation shows how the internal pressure in equipment pipeline changes during leakage, Where R =287, θ=293k,V=20L,P_f =0.5MPa, G_l= -0.987×10⁻³kg/s, G_{s1}=-0.3957×10⁻³kg/s,G_{s2}=-0.987×10⁻³kg/s,G_{s3}= -2.0×10⁻³kg/s.
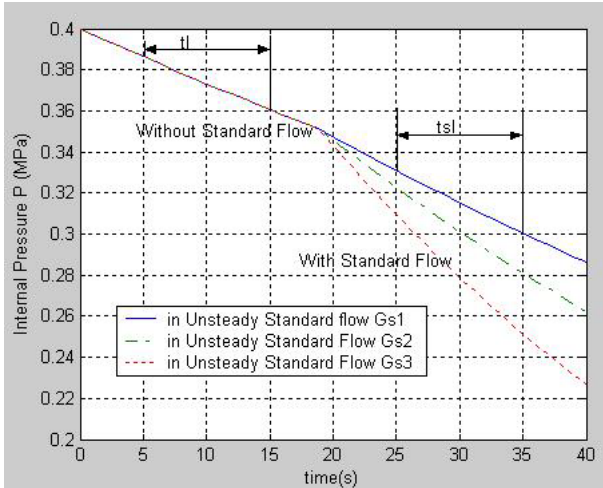
Figure 2 Pressure Change in the Leakage

In the state of leakage, the average internal pressure can be expressed by Eq.(7):

$$V \frac{dP_l}{dt} = S_{el} P_l R \theta_a \sqrt{\frac{\kappa}{R \cdot \theta_a} \left(\frac{2}{\kappa+1} \right)^{\frac{\kappa+1}{\kappa-1}}}$$

$$V \frac{dP_{sl}}{dt} = (S_{el} + S_{es}) P_{sl} R \theta_a \sqrt{\frac{\kappa}{R \cdot \theta_a} \left(\frac{2}{\kappa+1} \right)^{\frac{\kappa+1}{\kappa-1}}} \quad (7)$$

Eq.(7) can be further expressed as Eq.(8) :

$$\ln(P_{ld}/P_{lb}) = S_{el} R \theta_a t_l \sqrt{\frac{\kappa}{R \cdot \theta_a} \left(\frac{2}{\kappa+1} \right)^{\frac{\kappa+1}{\kappa-1}}}$$

$$\ln(P_{sld}/P_{slb}) = (S_{el} + S_{es}) R \theta_a t_{sl} \sqrt{\frac{\kappa}{R \cdot \theta_a} \left(\frac{2}{\kappa+1} \right)^{\frac{\kappa+1}{\kappa-1}}} \quad (8)$$

Based on Eq.(6) and Eq.(8) ,leakage flow rate at P_l can be written as Eq.(9):

$$G_l = \frac{G_s}{P_f} \cdot \frac{P_l}{\left(\frac{t_l}{t_{sl}} \cdot \frac{\ln(P_{sld}/P_{slb})}{\ln(P_{ld}/P_{lb})} - 1 \right)} \quad (9)$$

Where P_{sld}: Internal pressure during leakage with standard flow at the end time, P_{slb}: Internal pressure during leakage with standard flow at the beginning time, P_{ld}: Internal pressure during leakage without standard flow at the end time, P_{lb}: Internal pressure during leakage without standard flow at the beginning time.

3. EXPERIMENT APPARATUS

The measuring circuit is shown in Fig.3. The pilot valve A and standard vale 1, 2 and 3 are all controlled by PC. The orifice of standard valve is 3 mm, and its maximum pressure can reach to 1.0MPa. The volume of chamber is 30L. The maximum measurement pressure of pressure sensor is 1.0 MPa , and the measurement error can reaches to 0.5%. Leakage flow is controlled by a control valve which provides maximum rate 1000l/min(ANR) at 0.6MPa. Real-time pressure signal in the pipeline is gathered by PC. When leakage happens, pressure in equipment will decrease. After standard flow happens, a different differential pressure will occur accordingly. Leakage flow rate can be calculated with two differential pressure changes.
The measuring program is ruled by the following steps:
i) Charge air into the pipeline, and then wait until the temperature recover to the room temperature.
ii) Close the standard flow circuit, then measure the internal pressure in equipment pipeline P_{lb} 、 P_{ld} and leakage period t_l .
iii) The standard flow circuit will work automatically and measure the internal pressure in equipment pipeline P_{slb} 、 P_{sld} and leakage period t_{sl}.
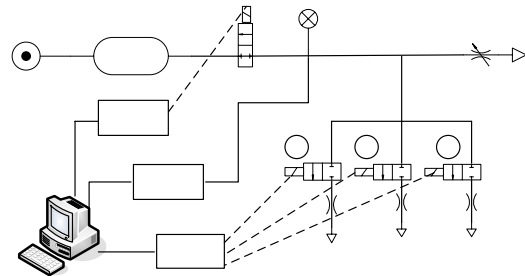
Figure 3 Leakage Flow Measuring Circuit Based on Standard Flow

4. RESULT AND DISCUSSION

Based on the measuring principle and experiment apparatus, experiments have been carried out for the different leakage flow. The measurement result is shown in Table.1. For a pressure wave effect to the pressure sensor when standard flow happens, there will be a sudden drop in the pressure curve in figures below. The internal meter pressure data in experiment with sampling frequency 40 HZ are shown in Fig.4 and Fig.5. The Standard leakage flow rate in Fig.4 equals to -365[l/min(ANR)] at 0.6MPa, and in Fig.5 equals to -114[l/min(ANR)] at 0.6MPa.
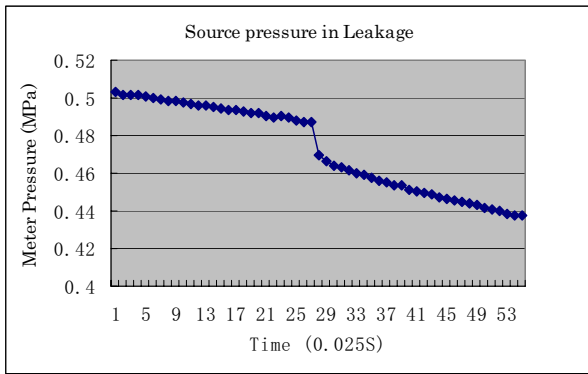
Figure 4 Source pressure in Standard Leakage
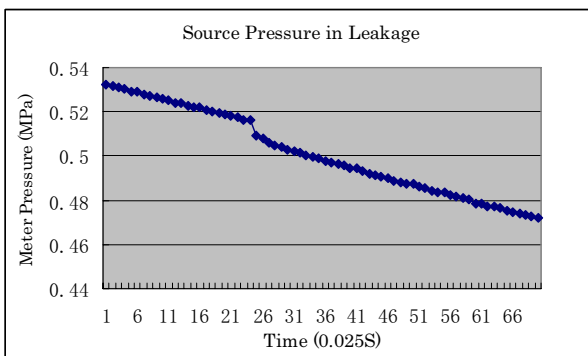
Figure 5 Source pressure in Standard Leakage

5. CONCLUSION

In this paper, a measurement method with parallel connection for gas leakage flow based on standard flow is developed. The relative error has been proved to be less than 5%. Compared with traditional method, it can be connected to equipment pipeline easily which promises the extensive use in pneumatic industry.

REFERENCES

1. Maolin Cai, Toshiharu.Kagawa, kenji Kawashima., Energy Conversation and Power Evaluation of Compressible Fluid in Pneumatic Actuator Systems 37th IECEC, 2002, 19-7, pp.438-443
2. Dutch National Team: Compressed air: Saving of 30% are quite normal, CADDET Energy Efficiency, Newsletter No.3, 1999
3. T.Kato, K.Kawashima, T.Kagawa., Application of Pressure Differential using Isothermal Chamber to Isolation Table, SICE Annual Conference in Sapporo, 2004, 4-8, pp.159-162
4. Ji-Seong Jang , Sang-Won Ji and Bo-Sik kang., Study on the Measurement Method of Leakage Flow-rate for Pnematic Driving Apparatus, SICE-ICASE International Joint Conference in Bexco, Busan, Korea, 2006, 18-10, pp.4116-4120

Table 1 Measurement result Table

Leakage No.	Leakage Flow [l/min(ANR)]	Standard Flow [kg/s]	Measure Flow [l/min(ANR)]	ERROR [%]	P_f [MPa]
N0.1	-460	-365	-440.532	4.23	0.6
N0.2	-210	-365	-217.692	3.66	0.6
No.3	-80	-114	-77.2415	3.44	0.6
No.4	-60	-114	-61.007	1.66	0.6
No.5	-36	-114	-35.347	1.81	0.6
No.6	-20	-114	-19.380	3.10	0.6

P2-22

DEVELOPMENT OF UNSTEADY GAS FLOW GENERATOR WITH HIGHLY PRECISE INLET FLOW RATE CONTROL SYSTEM

Tatsuya FUNAKI *, Tomonori KATO**, Kenji KAWASHIMA*** and Toshiharu KAGAWA***

* Gas Flow Standard Section, Fluid Flow Division, National Metrology Institute of Japan, AIST
AIST Tsukuba Central 3, Umezono 1-1-1, Tsukuba, Ibaraki, 305-8563 Japan
(E-mail: funaki.t@aist.go.jp)
** Department of Monozukuri Engineering, Tokyo Metropolitan College of Industrial Technology
1-10-40 Higashi-oi, Shinagawa, Tokyo, 140-0011 Japan
*** Precision and Intelligence Laboratory, Tokyo Institute of Technology
4259 Nagatsuta-cho, Midori-ku, Yokohama city, Kanagawa, 226-8503 Japan

ABSTRACT

In industry, an unsteady flow rate measurement of gases is becoming important increasingly. Our group has been developed an unsteady flow generator with an isothermal chamber for gases and showed that the calibration of the dynamic characteristics for the tested flow meter was effective. However, not only the measurement of the instantaneous flow rate value but also the evaluation of the time mean value in the unsteady flow becomes important in industry. And it was difficult to control precisely the time mean value of the generated flow rate using the former unsteady flow generator which we developed. In this research, to improve the precision of the generated flow rate with the unsteady flow generator, we suggest the inlet flow rate control method with the sonic nozzle and the high precise pressure control system and apply this method to the developed generator. Moreover, we perform the experiments and uncertainty analysis and confirm the effective of the suggested method.

KEY WORDS

Unsteady Flow Generator, Flow rate control, Precise pressure control, Flow rate measurement

<div style="text-align:center">

NOMENCLATURE

</div>

A:	Area of nozzle throat	[m^2]
b:	Critical pressure ratio	[-]
f:	Frequency	[Hz]
f_d:	Time constant	[s]
G:	Mass flow rate	[g/s]
G_{ref}:	Reference of Generated mass flow rate	[g/s]
K:	Coefficient of unit converter	[-]
K_G:	Gain of flow rate	[kg/(s・mm^2)]

K_p:	Proportional gain of pressure	[-]
K_{dp}:	Proportional gain of pressure differentiate	[-]
P:	Pressure	[Pa]
P_a:	Atmospheric pressure	[Pa]
$\dot{P}$:	Differentiated value of pressure	[Pa/s]
R:	Gas constant number	[J/(kg・K)]
S_e:	Effective area	[m^2]
t:	Time	[s]
T_a:	Control gain	[-]
T_b:	Control gain	[-]

T_p: Integral action time of pressure   [-]
T_{dp}: Integral action time of pressure differentiate   [-]
u: Input voltage to the servo valve   [V]
V: Volume of the chamber   [m^3]
W: Mass of air in the chamber   [kg]
ΔG : Amplitude of mass flow rate   [g/s]
κ : Specific heat ratio   [-]
θ : Temperature of gas   [K]
$\bar{\theta}$: Average temperature   [K]
θ_a: Room temperature   [K]
ρ : Density of air   [kg/m^3]
σ^* : Critical flow coefficient   [-]

Subscripts

c :   chamber
f :   forward
in :   inlet
out :   outlet
s :   supply
up :   upstream

INTRODUCTION

Measurement of an unsteady flow rate of compressible fluids is becoming more important with respect to energy savings, environmental protection, realizations of the technical advantages. Such a measurement provides significant information about the effective performance of engines, pumps, fuel cells and air compressors, and the ability to control the flow rates of gases and fluids in the semiconductor manufacturing process. There is substantial literature dealing with the measurement of unsteady gas flow (see [1]). Mottram et al [2] investigated the influence of pulsating flows on orifice plate flow meters. Hakanson et al [3], Berrebi et al [4] and Dane [5] studied the effects of pulsating flow on ultrasonic gas flow meters. Stone and Wright [6] investigated the dynamics of viscous flow meters both theoretically and experimentally. Uchiyama and Hakomori [7] proposed a method of measuring the instantaneous flow rate by estimating the velocity profiles in pipes. Most of these studies generated unsteady mass flows by using piston cylinders. Clearly, in these studies, substantial efforts must have been required in order to minimize the sensitivity dependence of density fluctuation on pressure and temperature variations. Durst et al [8] developed a mass flow rate controller using a valve and a laminar element that was designed to work up to unsteady oscillatory flow of 125Hz and showed experimental results up to 25Hz. Since the flow passed through a valve becomes a function of temperature, the accuracy could be improved if the temperature change is prevented. Therefore, the unsteady flow measurement of gases is

still a challenging research topic and the method to calibrate the dynamic characteristic of gas flow meters has not been defined yet. To solve these problems, we developed the unsteady gas flow generator using an isothermal chamber in 1997. However, this generator has limitation in time that is only during discharge from the chamber [9,10]. By adding a charging process, Funaki et al [11] developed the newly unsteady mass flow generator for gases that provide a foundation for the effective measurement of the unsteady gaseous mass flow generator and evaluation of the dynamics of gas flow meters in 2006. But it was difficult to control and compensate precisely the time mean value of the generated mass flow rate using the unsteady mass flow generator.

In this study, to solve this problem, we suggest the inlet flow rate control method with a sonic Venturi nozzle [12] and a high precise pressure control system [13,14] and apply this method to the unsteady mass flow generator. Moreover, we perform the experiments and uncertainty analysis and confirm the effective of the suggested method.

UNSTEADY GAS FLOW GENERATOR

Principle

The unsteady mass flow is generated using an isothermal chamber and two spool type servo valves in former research [11]. Here, the state equation for compressible fluids in a chamber can be written as

$$PV = WR\theta \qquad (1)$$

The following equation can be derived by differentiating Eq.(1), if the chamber volume is constant.

$$V\frac{dP_c}{dt} = \left(G_{in} - G_{out}\right)R\bar{\theta} + WR\frac{d\bar{\theta}}{dt} \qquad (2)$$

Here, the mass flow rate G_{in} is charged through the inlet mass flow controller installed in the upstream of the isothermal chamber. The controlled mass flow rate G_{out}, which is the generated flow, is discharged through the servo valve installed in the downstream of the isothermal chamber. The generated flow G_{out} is given by the following equation by transforming equation (2).

$$G_{out} = G_{in} - \frac{V}{R\bar{\theta}}\frac{dP_c}{dt} + \frac{W}{\bar{\theta}}\frac{d\bar{\theta}}{dt} \qquad (3)$$

If the state of air in the chamber during charge or discharge remains isothermal, the generated mass flow rate can be obtained from Eq.(3).

$$G_{out} = G_{in} - \frac{V}{R\bar{\theta}}\frac{dP_c}{dt} = G_{in} - \Delta G \qquad (4)$$

Since the condition remains isothermal, the average

temperature $\bar{\theta}$ in the chamber is equal to the room temperature θ_a. Eq.(4) indicates that if the volume of the chamber V and the room temperature are known, then the generated mass flow rate can be controlled by the pressure difference in the isothermal chamber and the inlet mass flow rate. The flow rate through a pneumatic valve is represented in the following formula for the choked condition [15],

$$G = K S_e (u) P_s \sqrt{\frac{273}{\theta_a}} \quad \left(\frac{P_c}{P_s} < b \right) \tag{5}$$

The case of non-choked flow is given by,

$$G = K S_e (u) P_c \sqrt{\frac{273}{\theta_a}} \sqrt{1 - \left(\frac{P_a / P_c - b}{1 - b} \right)^2} \tag{6}$$

where b is the critical pressure ratio. The critical pressure ratio is defined in ISO6358 [15]. In this paper, the inlet mass flow rate is controlled by the inlet mass flow controller with sonic Venturi nozzle, and the pressure change in the isothermal chamber is controlled by servo valve as shown in Figure 1.

Apparatus

The developed unsteady gas flow generator with highly precise inlet mass flow rate control system is shown in Figure 2. The apparatus consists of an isothermal chamber, a spool type servo valve, an inlet mass flow controller with sonic Venturi nozzle, two pressure sensors, an AD converter, a DA converter and a personal computer. The servo valve has a dynamic response of about 100Hz. The pressure sensor was a semiconductor type with a resolution of 50Pa. The inlet mass flow controller with a sonic Venturi nozzle and a precise pressure regulator controls the charged flow rate to the isothermal chamber, and the servo valve controls the generated unsteady flow from the chamber. The AD converter is used to obtain the supply pressure, the pressure in the chamber and the measured flow rate using the laminar flow meter. The internal volume of the isothermal chamber is 1.0×10^{-4} m^3.
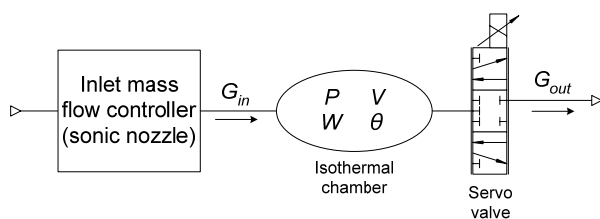
INLET FLOW RATE CONTROL SYSTEM

The sonic Venturi nozzle can realize highly precise flow rate measurement. Therefore, if an inlet flow rate control system consists of a precise pressure regulator with very small fluctuation and a sonic Venturi nozzle, the system can realize highly precise flow rate control.

Arrangement of a precise pressure regulator

The arrangement and the picture of the precise pressure regulator are shown in Figure 3 and Figure 4. The components are a spool type servo valve (FESTO MYPE-5-1/8-HF- 010-B), a laminar flow meter, an isothermal chamber, a pressure differentiator (PD sensor), and a pressure sensor (KEYENCE AP-13S). Though the spool valve has 5 ports, the valve is used as a 3 port type spool type servo valve, having ports of supply, control and exhaust. The unused 2ports are plugged. An 'isothermal chamber' was developed in a previous work. This chamber is filled with copper wool, which allows the state change in the chamber to become nearly isothermal. The isothermal chamber used in this research has a volume of 1.57×10^{-3} m^3. The laminar flow meter [16,17] and the PD sensor [13,14] were also developed in previous research. The laminar flow meter is a differential pressure type flow meter, whose dynamic characteristics are calibrated. The 'PD sensor' is a unique sensor which can directly measure the differentiated value of gas pressure at a high resolution and high response.

Sonic Venturi nozzle

Sonic Venture nozzle is a famous instrument of the precise flow rate measurement. The sonic nozzle is an ISO type toroidal throat Venturi nozzle in which the radius of curvature of the throat is twice the throat diameter and the length of the diffuser with a half angle of 3 degrees is three times of the throat diameter [12,18]. The schematic diagram of the sonic Venturi nozzle used is shown in Figure 5. The throat diameter which we used is 0.594mm. This sonic Venturi nozzle was set up at the nozzle holder as shown in Figure 6.

Figure 1 Schematic diagram of mass flow rate control while charging and discharging
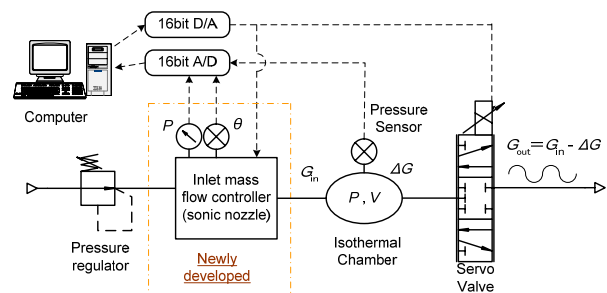
Figure 2 Apparatus of oscillatory gas flow generator

Design of the controller

The purpose of the new pressure regulator is to keep the pressure in the isothermal chamber at a set value, as shown in Figure 3. The objective component, that is the unsteady gas flow generator, is to be connected to the downstream of the isothermal chamber. The very important factor is that, when disturbance of pressure of the flow rate occurs either on the supply or downstream of the pressure regulator, the pressure in the isothermal chamber should be kept stable or immediately recovered. A pressure feed-back loop is the main loop, mean while there are 2 minor loops. One is a flow rate control loop, the other one is to estimate and compensate the output flow rate G_{out}. As a result, we confirmed that the new pressure regulator regulate the fluctuation of the upstream pressure of the sonic nozzle less than 0.9%. Therefore, the inlet mass flow rate G_{in} is controlled precisely and constantly using this inlet mass flow controller, and can be written as Eq.(7).

$$ G_{in} = \frac{P_{up} A}{\sqrt{R\theta_{up}}} \sigma^* = \frac{P_{up} A}{\sqrt{R\theta_{up}}} \sqrt{\kappa \left(\frac{2}{\kappa+1}\right)^{\frac{\kappa+1}{\kappa-1}}} \qquad (7) $$
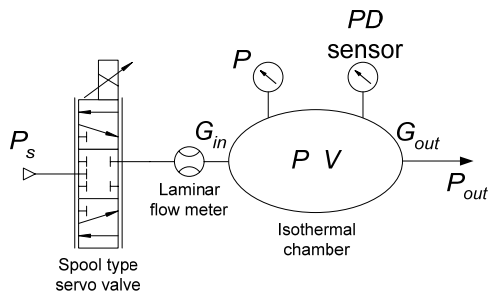
Figure 3 Diagram of precise pressure regulator

Figure 4 Photograph of precise pressure regulator
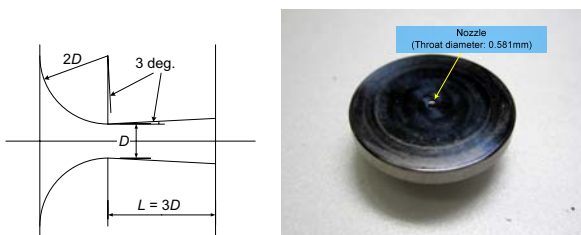
Figure 5 Schematic diagram and photograph of the ISO type toroidal throat sonic Venturi nozzle
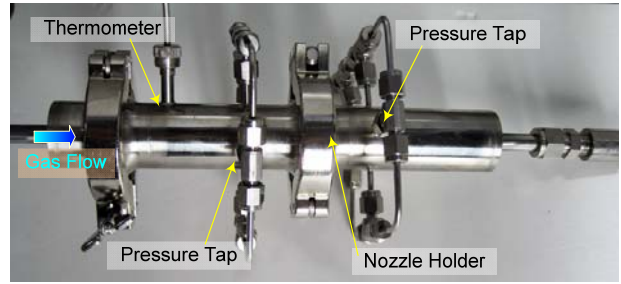
Figure 6 Nozzle Holder
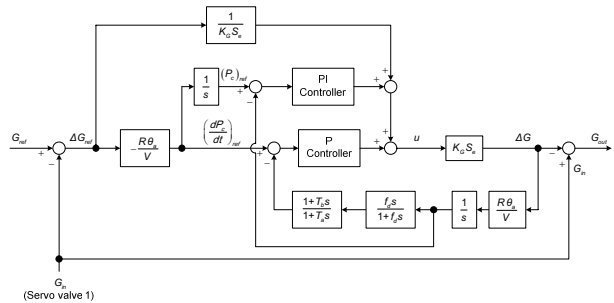
Figure 7 Block diagram of an unsteady gas flow generator

CONTROL METHOD

We controlled the absolute pressure in the isothermal chamber to be the choked flow at the sonic Venturi nozzle of the inlet mass flow rate controller and the non-choked flow at the servo valve. The supply pressure was set up at 600kPa. The precise pressure regulator was set up about 350kPa and the pressure in the isothermal chamber was about 150kPa. Therefore, the pressure ratio is about 0.43. We confirmed that the choked condition is realized at the sonic Venturi nozzle, because the critical pressure ratio of this nozzle was up to 0.6. The manipulated value by the inlet mass flow rate controller is the average value of the generated flow rate. That is, the pressure at the upstream side of the sonic nozzle was constant value. Figure 7 shows the block diagram of the unsteady gas flow generator which we developed in this study. At first, we calculated the reference flow rate using Eq.(4). The control signal to the servo valve is estimated as $G/(K_G S_e)$. This value is given as a feed-forward element to the system. And a PI controller and a P controller were adopted for the pressure control in the isothermal chamber. Therefore, this flow generator can generate the unsteady flow rate continuously, calculating the pressure change in the isothermal chamber and the charged flow rate through the inlet mass flow controller. And the input voltage of servo valve can be written as follows.

$$u = K_p \left(1 + \frac{1}{T_p s} \right) \left\{ \left(P_c \right)_{ref} - P_c \right\}$$

$$+ K_{dp} \left\{ \left(\dot{P}_c \right)_{ref} - \dot{P}_c \right\} + \frac{G_{ref}}{K_G S_e} \qquad (8)$$

EXPERIMENTAL RESULTS AND DISCUSSIONS

Evaluation of inlet flow rate control system

The sonic Venturi nozzle which we used has the uncertainty within $\pm 0.1\%$ [18]. We confirmed that the inlet mass flow rate can be realized the uncertainty within $\pm 0.4\%$ using the inlet mass flow rate control system.

Generation of oscillatory gas flows

At first, the target oscillatory mass flow rate is given as $0.216 + 0.107 \sin(2 \pi f t)$ g/s. The experiment was performed at several frequencies. The low-pass filter was used for the processing of the measured data. The cut-off frequency of the filter was set at five times the frequency of the phenomenon. Figure 8 shows the experimental results at a frequency of 1Hz. In this figure, the black line show the target mass flow rate, the blue line shows the generated mass flow rate using the unsteady gas flow generator and the red line indicates the measured mass flow rate using the laminar flow meter. From this figure, the target flow rate and the generated flow rate is consistent with the measured flow rate using the laminar flow meter to finish the calibration with the former generator. Figure 9 shows the experimental results at a frequency of 10Hz. From this result, it could be confirmed that the target flow rate and the generated flow rate show good agreement.

Moreover, the flow is generated continuously for 60minutes. These results show that the maximum error between the target mass flow rate and the generated mass flow rate is less than approximately 5%.

Evaluation of time mean flow rate

When we examine the dynamic characteristics of the tested flow meter, there are two important factors. One is the responsibility of measured value of tested flow meter in comparison with a standard flow rate wave pattern. Second is the fluctuation of the time mean measured value. In this time, when the generator occurred by various oscillatory flows, we confirmed the fluctuation of the time mean generated value by experiments. As a result, it became clear that the uncertainty is less than $\pm 0.4\%$.
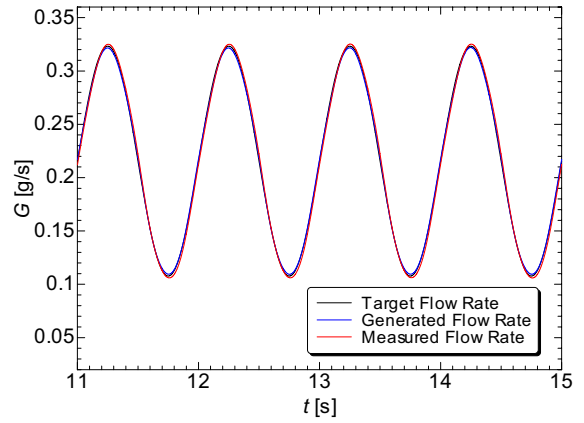
Figure 8 Generation of oscillatory gas flow at the frequency of 1Hz
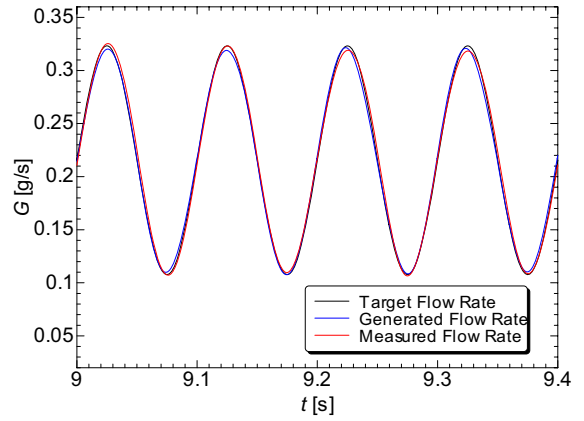
Figure 9 Generation of oscillatory gas flow at the frequency of 10Hz

Analysis of uncertainty

The total uncertainty of the oscillatory gas flow generator is given by the following formula from the propagation of uncertainty as shown in guide by ISO (1993 and 2002) [19,20].

$$\frac{\delta G_f}{G_f} = \sqrt{\left\{ \left(\frac{\delta P_{up}}{P_{up}} \right)^2 + \left(\frac{\delta A}{A} \right)^2 + 0.25 \left(\frac{\delta \theta_{up}}{\theta_{up}} \right)^2 \right\}}$$

$$+ \sqrt{\left\{ \left(\frac{\delta \theta}{\theta} \right)^2 + \left(\frac{\delta V}{V} \right)^2 + \left\{ \frac{\delta (dP/dt)}{(dP/dt)} \right\}^2 \right\}}$$

$$+ \sqrt{\left\{ \left(\frac{\delta \theta}{\theta} \right)^2 + \left\{ \frac{\delta (d\theta/dt)}{(d\theta/dt)} \right\}^2 \right\}} \qquad (9)$$

Where the first term is the uncertainty of the inlet mass flow rate, the second term is the uncertainty of the

pressure change of the isothermal chamber, and the third term is the uncertainty of the temperature change. The uncertainty of the chamber volume measurement is considered to be 0.5[%]. The uncertainty of the effective area is considered to be 0.5[%]. The uncertainty due to the pressure change speed is considered to be 1[%]. The uncertainty of the temperature change is estimated as 3[%] at maximum. The other factors affecting the uncertainty are as mentioned above. From Eq.(15), the generated mass flow rate with only forward direction has a maximum uncertainty of 4.9[%]. Moreover, inlet mass flow rate, that is, the average mass flow rate is within an uncertainty of $\pm$ 0.4%. Therefore, the unsteady mass flow generator for gases has sufficient accuracy for practical use.

CONCLUSIONS

In this paper, the performance of the unsteady gas flow generator with highly precise inlet mass flow rate control system which we developed is investigated experimentally. At first, we developed and manufactured a highly precise inlet mass flow rate control system with the precise pressure regulator and the sonic Venturi nozzle. Secondly, the mean value of the generated oscillatory flow is investigated. It became clear that the uncertainty is within $\pm$ 0.4%. The effectiveness of the generator for calibrating the dynamic characteristics of gaseous flow meters is confirmed.

ACCKNOWLEGMENTS

REFERENCES

1. Miller R W, Flow Measurement Engineering Handbook 3rd edn (New York: McGraw-Hill), 1996
2. Gajan P, Mottram R C, Herbard P, Andriamihafy H and Platet B, The influence of pulsating flows on orifice plate flowmeters Flow Meas. Instrum. 1992, vol.3, pp.118-129
3. Hakansson E and Delsing J, Effects of pulsating flow on an ultrasonic gas flowmeter Flow Meas. Instrum. 1994, vol.5, pp.93-101
4. Berrebi J, Martinsson P-E, Willatzen M and Delsing J, Ultrasonic flow metering errors due to pulsating flow Flow Meas. Instrum. 2004, vol.15, pp.179-185
5. Dane H J, Ultrasonic measurement of unsteady gas flow Flow Meas. Instrum. 1998, vol.8, pp.183-190
6. Stone C R and Wright S D, Non-linear and unsteady flow analysis of flow in a viscous flowmeter Trans. Inst. Meas. Control, 1994, vol.16, pp.128-141
7. Uchiyama M and Hakomori K, Measurement of instantaneous flow rate through estimation of velocity profiles IEEE Trans. Autom. Control, 1983, vol.28, pp.380-388
8. Durst F, Heim U, Unsal B and Kullil G, Mass flow rate control system for time dependent laminar and turbulent flow investigations Meas. Sci. Technol. 2003, vol.14, pp.893-902
9. Kawashima K and Kagawa T, Unsteady flow generator for gases using isothermal chamber Meas. J. Int. Meas. Confed. (IMEKO), 2003, vol. 33-34, pp.333-340
10. Kawashima K, Kagawa T and Fujita T, Instantaneous flow rate measurement of ideal gases ASME J. Dyn. Syst. Meas. Control, 2000, vol.122, pp.174–178
11. Funaki T, Kawashima K, Yamazaki S, Kagawa T, Generator of variable gas flows using an isothermal chamber, Meas. Sci. Technol. 2007, vol.18, pp.835-842
12. ISO9300, Measurement of gas flow by means of critical flow Venturi nozzles, 2005
13. K. Kawashima, T. Kato, Y. Yamazaki, M. Yanagisawa, T. Kagawa, Development of slit type pressure differentiator using an isothermal chamber, Meas. Sci. Technol., 2005, vol.16, pp.1150-1156.
14. T. Kato, T. Funaki, K. Kawashima, T. Kagawa, Active Control of Vibration Isolation Table with Quick Flow Sensor, Proc. of International Fluid Power Conference (IFK2006), 2006, Vol.1, pp.109-120
15. ISO6358, Pneumatic Fluid Power-Components Using Compressible Fluids Determination of Flow-Rate Characteristics, 1989
16. Funaki T, Sengoku K, Kawashima K and Kagawa T, Dynamic calibration of laminar flow sensor for gases SICE Ann. Conf. 2004 (CD-ROM), 2004
17. Funaki T, Kawashima K and Kagawa T, Characteristic analysis of laminar flow meter for gases with high speed response, T. SICE, 2004, vol.40, pp.1008-1013 (in Japanese)
18. Nakao S, Takamoto M, Development of the Calibration Facility for Small Mass Flow Rates of Gases and the Sonic Venturi Nozzle Transfer Standard, JSME International Journal, Series B, 1999, Vol.42, No.4, pp.667-673
19. BIPM, IEC, IFCC, ISO, IUPAC, IUPAP, OIML, Guide to the Expression of Uncertainty in Measurement (Geneva:ISO), 1993
20. ISO/DIS 5168. Measurement of fluid flow -evaluation of uncertainty-, 2002

P2-23

RESEARCH ON THE STATIC CHARACTERISTICS OF AIR DRIVEN GAS BOOSTER

Haitao WANG, Wei XIONG and Xu WANG

Transportation and Logistics Engineering College, Dalian Maritime University
1 Linghai Road, Dalian, 116026, China
(E-mail: wht810@vip.sina.com)

ABSTRACT

The process that the low pressure gas in two gas tanks were reclaimed through air driven gas booster to one empty high pressure tank has been studied in this paper. Calculation formulae of performance parameters of the gas booster such as the inlet pressure, outlet pressure, volume of discharge and intake, air consumption in per cycle were obtained , and the change tendency of these performance parameters during its isothermal quasi-static processes was analyzed and several static characteristics and structural parameters that influences the booster's working performance were found out. The importance of dead volume and the way to raise the booster's efficiency was stated. The results are helpful for model selection, design and application of gas boosters.

KEY WORDS

Air driven gas booster, Static characteristics, Compression ratio, Dead volume

NOMENCLATURE

A :   Area of air driving piston
a :   Area of gas piston
a_0 :   Cross sectional area of piston rod
P_a :   Standard atmosphere pressure
P_D :   Driving air pressure
P_{Ok}:   Outlet air pressure of the k-th cycle
P_{Sk} :   Inlet air pressure of the k-th cycle
S :   Stroke of piston
V_0 :   Dead volume
V_C :   Total volume of high pressure chamber
V_E :   Air consumption volume per cycle
V_{Ok}:   Gas discharge volume of the k-th cycle
V_{Sk}:   Gas suction volume of the k-th cycle
V_{in} :   Total volume before inlet check valve
V_{ou} :   Total volume behind outlet check valve
i :   Pressure ratio
i_{Ck} :   Compressed ratio of the k-th cycle

INTRODUCTION

High pressure compressed air is usually needed in many industrial fields [4]. Air driven gas booster with the advantages of using low pressure air as power, supercharging efficiently, structured compactly, being portable and explosion-proof, reducing the cost and installing spaces to a great extent, has been widely used in many fields such as low pressure gas reclaiming, high-pressure gas injection, gas pressure testing and leak testing [1]. However, the tendency of pneumatic technology to high pressure has raised many new requirements to booster's structure and performance, such as higher pressure ratio and charging efficiency and more compact structure. Based on the working principle and structure of single acting gas booster, this paper has studied parameter factors that influences the booster's working performance and analyzed the booster's static characteristics.

WORKING PRINCIPLE OF AIR DRIVEN GAS BOOSTER

Air driven gas booster works according to PASCAL'S LAW as Figure 1 shows [3]. The large-area air driving piston 5 in the air driving chamber 4 is connected with the piston rod to the small-area gas piston 7 located in the high pressure chamber 6. Thus by using the area difference between the tow pistons, the purpose to compress the gas in the high pressure chamber with the low pressure air as power acting on the large-area piston is realized.
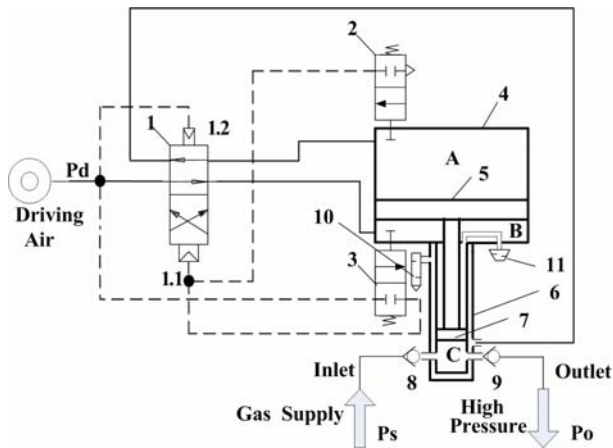
Figure 1 Working principle of air driven gas booster

Based on the static force balance principle,

$$P_O = \frac{A}{a} \cdot P_D = i \cdot P_D \qquad (1)$$

$i = A / a$ is defined as pressure ratio .When $A > a$, $P_O > P_D$ [3]. The larger the area difference is, the more obvious the supercharging effect becomes.

The continuous operation is achieved by the cycling control valve 1 whose spool leads the drive air alternately on the upper and bottom surface of the air piston and is piloted through the upper pilot valve 2 and down pilot valve 3 which are mechanically actuated through the air drive piston in its end positions [1]. The exhaust air from the driving chamber is lead to the peripheral barrel to cool the high pressure gas chamber [2].

PARAMETERS CALCULATION AND ANALYSIS OF STATIC CHARACTERISTICS

The low pressure gas recovery process is studied as shown in Figure 2. At the beginning of recovery, low pressure gas is directly charged to high pressure tank through inlet and outlet check valves as the existence of the pressure difference between the tow tanks, until the pressure of low and high tanks becomes balanced. Then gas booster works. The gas booster works as the sequence of suction, compression and exhaust. Now study on the k-th cycle.
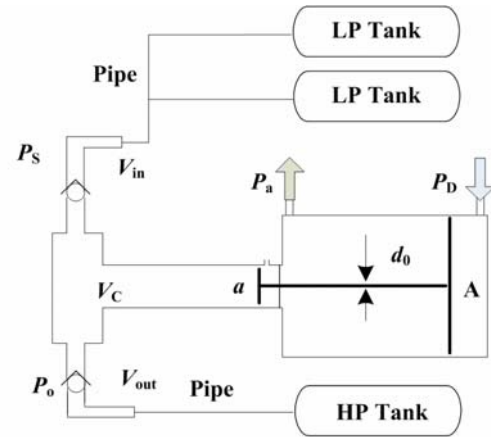
Figure 2 Low pressure gas reclaiming

Inlet and Outlet Pressure P_{Sk} and P_{Ok}

According to law of mass conservation , when the k time cycle ends, there are the equations below:

$$P_{Sk} + V_{out}P_{Ok-1} = \left(V_0 + V_{out}\right)P_{Ok} \qquad (2)$$

$$V_0 P_{Ok-1} + V_{in}P_{Sk-1} = \left(V_{in} + V_C\right)P_{Sk} \qquad (3)$$

The inlet and outlet pressure of the k-th cycle is obtained

$$P_{Ok} = \frac{V_C}{V_0 + V_{out}}P_{Sk} + \frac{V_{out}}{V_0 + V_{out}}P_{Ok-1} \qquad (4)$$

$$P_{Sk} = \frac{V_{in}}{V_{in} + V_C}P_{Sk-1} + \frac{V_0}{V_{in} + V_C}P_{Ok-1} \qquad (5)$$

The change of P_{Ok} and P_{Sk} with the increase of working cycle is obtained recursively as shown in Figure 3. Figure 3 shows that with the increasing of working cycles both curves changes greatly on earlier stage, and change slowly on middle-later stage, and on the later stage when the cycle times reaches up to a certain value, both curves nearly keep stable.

Compressed ratio i_C is defined as follows [1]:

$$i_C = P_O / P_S \qquad (6)$$
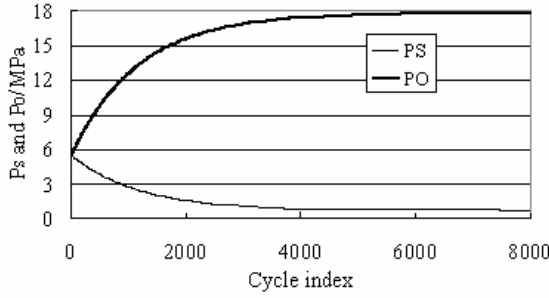
Figure 3 P_O and P_S with the change of cycle

i_C indicates the compressed degree of low gas .It is a variable,while pressure ratio i is a fixed value which shows the maximum ability of compression of the booster. The curve of i_C is shown in Figure 4 below, from which we know that i_C increases gradually , and keeps stable on the later stage.
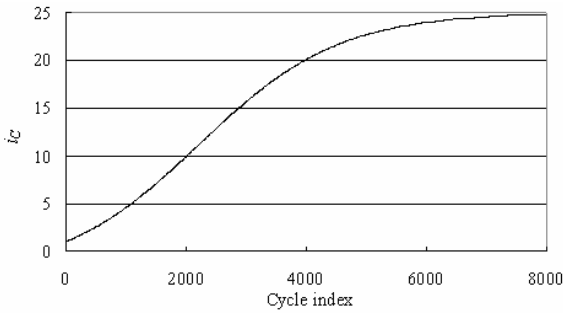
Figure 4 i_C with the change of cycle

Gas Discharge and Intake Volume V_{Ok} and V_{Sk}
Gas discharge volume of the k-th cycle is equal to the standard difference volume of gas in high pressure chamber before and after the compression, so gas discharge volume of the k-th cycle is

$$V_{Ck} = \frac{P_{Sk}}{P_a}V_C - \frac{P_{Ok}}{P_a}V_0 \qquad (7)$$

Formula 7 can also be expressed as follows.

$$V_{Ck} = \frac{P_{Sk}}{P_a}(V_C - i_{Ck}V_0) \qquad (8)$$

The change of V_{Ck} with i_{Ck} is shown in Figure 6. With the increase of i_{Ck}, V_{Ck} reduces gradually, until to zero. And when i_{Ck} gets to a certain value, the discharged gas

becomes very little, and the working efficiency of gas booster is very low.
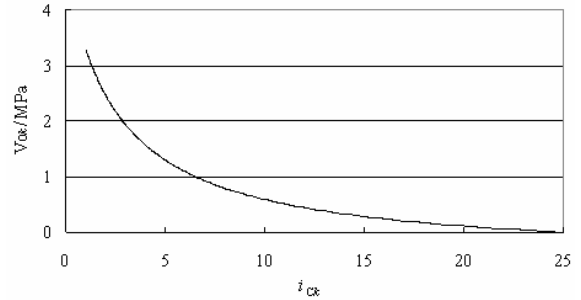
Figure 6 V_{Ck} with the change of i_{Ck}

The i_C when V_C is zero is defined as the maximum compressed ratio i_{Cmax}.

$$i_{Cmax} = \frac{V_C}{V_0} \qquad (9)$$

The dimensions of V_0 and V_C have been decided when the booster was designed, after which the booster's maximum compressed ratio was determined. So when designing, if higher compressed ratio is wanted, reducing V_0 is feasible. For example, if the expected i_{Cmax} is 25:1, V_0 must be less than 4% of V_C.

Intake gas charge volume of the k-th cycle is equal to the standard difference volume of gas in high pressure chamber before and after suction, so intake gas charge volume of the k-th cycle is

$$V_{Sk} = \frac{P_{Sk}}{P_a}V_C - \frac{P_{Ok-1}}{P_a}V_0 \qquad (10)$$

V_{Sk} has similar change law with V_{Ok}.
Air Consumption Volume Per Cycle V_E
The total air consume volume of the k-th cycle is equal to the sum of the air consume volume of the suction and compression stroke. So the air consumption volume of one cycle is

$$V_E = (2A - a_0)\frac{P_D}{P_a} \qquad (11)$$

Formula 11 shows the air consume volume per cycle is a fixed value. On the later stage, the outlet pressure increases very slowly while the piston is still moving under the push of driving air, so lots of driving air is wasted. In addition, when model selecting; the maximum compressed ratio of the booster to be selected

717

should be bigger than the one needed in practical application, in order to save driving air and to limit the charging time to acceptable range.

CONCLUSIONS

Through the calculation and analysis above, the main structural parameters that influence the static characteristics of gas booster, the formulae of boater's performance parameters and its static characteristics combined with lots of graphs were obtained.

The main structural parameters include area of air driving piston A, area of gas piston a, cross sectional area of link rod a_0, stroke of piston S and dead volume V_0. The dead volume V_0 is proved having great influence on the booster's static characteristics, and its dimension should be determined with discretion when designing. In addition, on the process of charging, the outlet pressure increases, inlet pressure reduces, both gas intake and discharge volume decreases, air consumption keeps constant cycle by cycle, and as on the later stage the growth rate of outlet pressure is very low and , it is not recommended to keep the booster working in this case for long time.

REFERENCES

1. MAXIMATOR Sample Manual, USA, 2008, pp.11.
2. HASKEL Sample Manual, USA, 2008, pp.2-4.
3. Jiding Shi, Automatic oil supply air piston pump driven by pneumatic (Chinese), Technology Equipment Department of Second Automobile, 2004, pp.1.
4. Technology of Compressor (Chinese), China, 2006.

P2-24

ANALYSIS OF FLOW BEHAVIOUR AND CHARACTERISTICS OF PNEUMATIC COMPONENTS

Daniel HUBERT *, Sylvie SESMAT**, Rosario De GIORGI**, Didier GAUTIER*** and
Eric BIDEAUX**

* ASCO JOUCOMATIC NUMATIC
32 Avenue Albert 1er, BP 312, 92506 Rueil Malmaison Cedex, France
(E-mail: daniel.hubert@emerson.com)
** Laboratoire AMPERE, INSA-Lyon (UMR CNRS 5005)
25 avenue Jean Capelle, 69621 Villeurbanne Cedex, France
(E-mail: sylvie.sesmat@insa-lyon.fr)
*** CETIM, 52 avenue Félix Louat, BP 80067
60304 Senlis Cedex, France

ABSTRACT

Information concerning the flow characteristics of pneumatic components is essential not only for selecting the right component at the design stage, but also for the simulation and the validation of different performances of a circuit. Recently, some works concerning the revision of the ISO 6358:1989 standard [1] have concerned both the mathematical approximation of the mass flow rate characteristic [2] and the experimental way to obtain the characteristics [3, 4, 5]. This paper proposes to discuss the importance of the upstream and downstream pressures taken as references. Using experimental results, the flow behaviour of two real components is discussed pointing out two different cases, the first being close to a convergent nozzle, the second to a convergent-divergent nozzle.

KEY WORDS

Mass flow rate characterisation, convergent behaviour, convergent-divergent behaviour, pressure measurement

NOMENCLATURE

A	:	geometrical area	[m^2]
C	:	conductance	[m^3/s/Pa]
p	:	pressure	[Pa]
p_b	:	back pressure	[Pa]
p_e	:	exit pressure	[Pa]
q_m	:	mass flow rate	[kg/s]
R	:	gas constant	[J/(kg.K)]
T	:	temperature	[K]
u	:	velocity	[m/s]
γ	:	specific-heat ratio (1.4 for air)	
ρ	:	density	[kg/m^3)]

subscripts

c	:	critical
d	:	port component diameter
D	:	largest diameter D
ISO	:	reference to ISO6358 standard [1]
t	:	total
0	:	stagnation conditions
1	:	upstream conditions
2	:	downstream conditions

INTRODUCTION

ISO6358:1989 standard [1] defines both mathematical approximation of the mass flow rate characteristic and the experimental way to obtain the characteristics. This

standard provides an efficient help to manufacturers to characterise the flow capacity of pneumatic components with a couple of parameters: the sonic conductance C and the critical pressure ratio b. Therefore, this gives very useful information to circuit designers for the component choice. This standard is under revision because it requires some improvements into three directions.

First, the use of two additional parameters has recently extended the range of application of the standard to new components [2]. Second, two new experimental methods for characterizing the components have been proposed. They are based on transient characterisations (discharge method [3, 4] or charge method [5]). But third, whatever the experimental method is, a study has to be carried out in the light of fluid mechanic theory in order to determine the appropriate location of the pressure sensors used for the measurement of the upstream and downstream pressures. This is the purpose of this paper.

After a brief summary of fluid mechanic theory about flow in convergent and convergent-divergent nozzles, different measurement results are discussed according to the way upstream and downstream pressures are measured. For this study two spool valves are characterised. Component 1 has G1/8 connecting ports while component 2 has G1/4.

FLUID MECHANICS MODELING

Up to now, most of pneumatic flow models relies on the theoretical results obtained in fluid dynamics for an ideal convergent nozzle [6, 7]. The case of ideal convergent-divergent nozzle is also interesting. The modelling considers that the flow is one dimensional, isentropic (adiabatic and reversible) and stationary, and that friction forces are negligible [7]. There is an upstream large reservoir with a stagnation pressure p_0 and a stagnation temperature T_0. The flow results from a back pressure p_b (downstream and outside the convergent nozzle) lower than p_0.

The continuity equations (mass and energy) are used to determine theoretically the pressure distributions and the mass flow values according to the pressure conditions (p_0, p_b).

Flow behaviour in a convergent nozzle
Considering the ideal nozzle (Fig.1), the fluid mechanic theory points out two flow behaviours delimited by the critical pressure p_c at which the throat becomes sonic: a subsonic flow and a sonic flow.

Figure 2 shows the corresponding well-known flow representation and the exit pressure evolution p_e/p_0 according to the ratio between the back and upstream stagnation pressure, p_b/p_0.
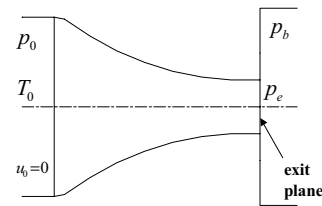
Figure 1: Convergent nozzle and variable definitions.
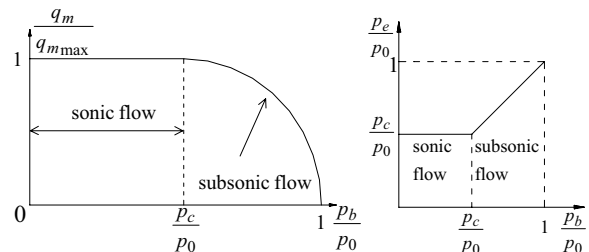
Figure 2: Flow and pressure evolutions for a convergent nozzle.

Flow behaviour in a convergent–divergent nozzle
Similarly, the application of fluid mechanic theory to an ideal convergent-divergent nozzle (Fig.3) leads to four main types of flow behaviours. Figure 4 shows flow and pressure changes according to the pressure ratio p_b/p_0.
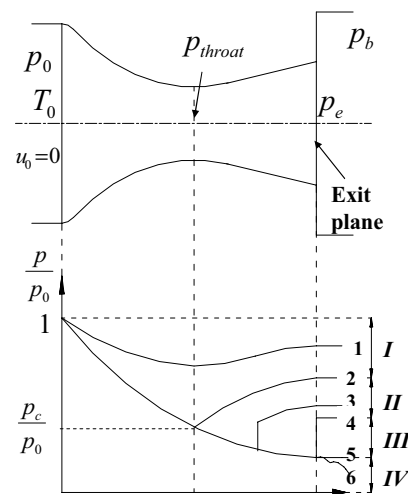
Figure 3: Convergent-divergent nozzle and different pressure distributions according to back pressure value.

The flow curve (Fig.4c) presents two regions corresponding to the subsonic or sonic flow at throat. But downstream the throat, in the divergent part of the nozzle, the flow can be either subsonic or supersonic according to the back pressure value. Furthermore, a normal shock in the divergent section or oblique shocks outside the nozzle outlet can take place. The flow is then no more isentropic downstream to the normal shock in the divergent part of the nozzle.

a – Exit pressure   b – Throat pressure   c – Mass flow rate
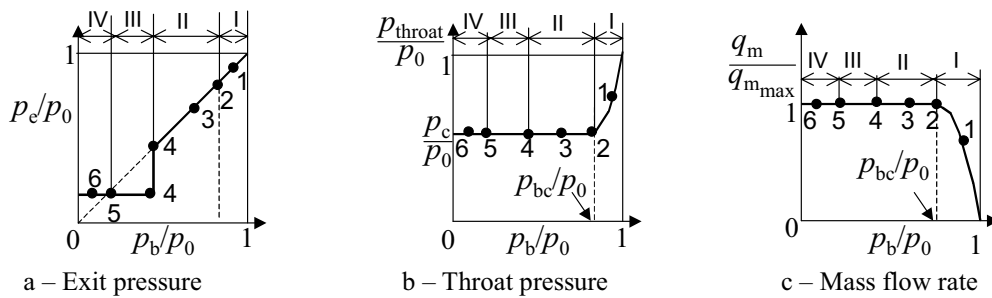
Figure 4: Characteristics of a convergent-divergent nozzle according to the back to stagnation pressure ratio [7].

For point 4, the normal shock is located at the exit plane inducing a discontinuity on the pressure curve (Fig.4a).

FLOW CHARACTERIZATION

Real orifices show some differences with the ideal cases:
- There is a contraction of the stream lines at throat: the effective area is smaller than the geometrical one.
- Friction losses are not negligible.
- According to the rate of kinetic energy recovery, the static pressure is higher downstream than in an ideal nozzle.
- The flow can generally be considered as adiabatic (conservation of the total temperature), but it is not isentropic inducing a loss in total pressure.
Experimental results have shown that however, many components have a flow characteristic that is similar to the one obtained for a convergent nozzle (Fig.2). That is why the ISO 6358 standard proposed a mathematical approximation in which the critical pressure ratio is determined experimentally. The subsonic region is approximated by a quarter of ellipse.
But in the case of a convergent-divergent nozzle, this part of the mass flow rate curve corresponds only to the lower part of a quarter of ellipse. An approximation of this characteristic is however possible using the new formula with four parameters [2].
The flow characterisation consists in the measurement of the mass flow rate, and of the upstream and downstream pressures. However the main question is how and where these pressures have to be measured?
According to fluid mechanics, the total upstream pressure has to be considered as well as the exit and back pressures. But the main difficulty is that the exit pressure can not be measured directly because the internal geometry of components is generally complex and the most limiting section is not always located at outlet but often inside the component itself.
In ISO6358:1989 standard, the pressure sensors are installed on measuring tubes that have the same inner diameter as the port of the component to be characterised. This means that the measured upstream and downstream pressures $p_{1\,\text{ISO}}$ and $p_{2\,\text{ISO}}$ are static pressures. Thus the flow characteristics are depending on the diameter of the connecting tubes because the fluid velocity is not

negligible in these tubes. Measurement methods that allow a better correlation with fluid mechanics theory are now explored.
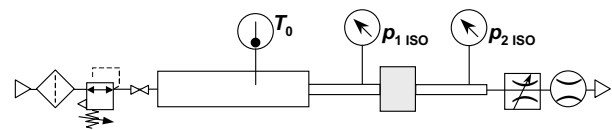
Figure 5 Test bench according to ISO 6358 standard.

UPSTREAM PRESSURE

In order to obtain flow characteristic parameters independent from the upstream velocity, it is necessary to take into account the total pressure. This pressure can be measured directly on a tube of sufficiently large diameter to have a negligible fluid velocity. It can also be obtained by calculation.
By definition, the total pressure is the pressure the flow would reach if brought isentropically to rest [7]. The equivalent total pressure can then be calculated from the static pressure p, with the knowledge of the local geometrical section A:

$$p_t = p \left[\frac{1}{2} + \sqrt{\frac{\gamma-1}{2\gamma} RT_t \left(\frac{q_m}{pA}\right)^2 + \frac{1}{4}} \right]^{\frac{\gamma}{\gamma-1}} \qquad (1)$$

In the following, the total pressures are calculated assuming the flow is adiabatic: the local total temperature equals the upstream stagnation temperature T_0 (Fig.5).
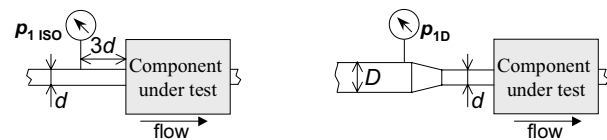
a – ISO 6358:1989.   b – Conical connector.
Figure 6 Upstream pressure connectors used.

In order to measure directly the stagnation pressure, the upstream part of the test bench of ISO 6358 can be modified using the measuring tube shown in Fig.6b.

721
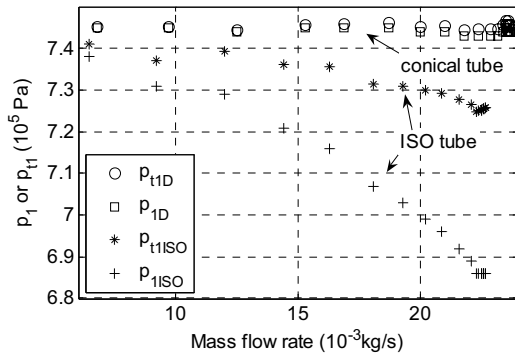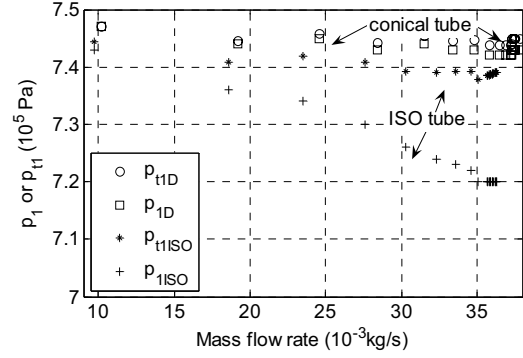
a - Component 1.   b - Component 2.

Figure 7 Comparison of upstream pressures (p_1 measured and p_{t1} calculated).
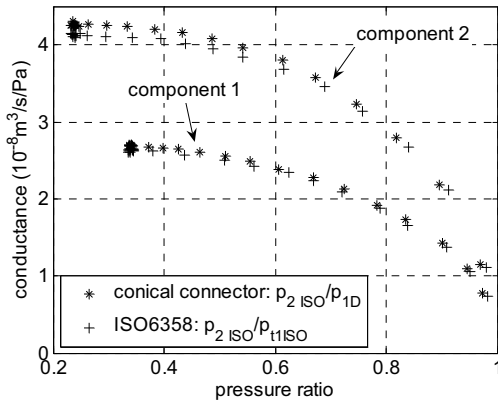
a – Comparison for 2 different total pressures.   b- Comparison between ISO characteristic and the use of p_{1D}.
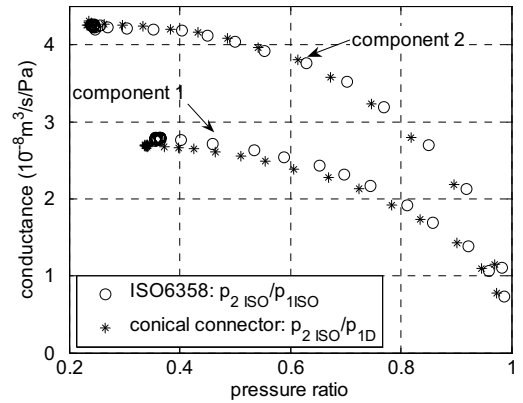
Figure 8 Flow characteristics for different upstream pressures (downstream pressure $p_{2\,\text{ISO}}$ from ISO 6358 tube).

The upstream pressure is measured on a diameter D two sizes larger than the port size of the component under test. The connection to the component is done with a conical part in order to minimise the losses.

In this section, in order to draw comparisons concerning the upstream pressure, experimental results are obtained using an ISO6358 downstream measuring tube.

Figure 7 shows that for both components, the pressure p_{1D} measured on the larger diameter of the conical tube is very close to the corresponding calculated upstream total pressure p_{t1D} because the velocity of the fluid is negligible. It means that this measured pressure p_{1D} can be considered as a total pressure. But in the case of the ISO6358 tube, it is clear that the higher the mass flow is, the larger the difference between the calculated total pressure $p_{t1\text{ISO}}$ and the measured upstream pressure $p_{1\text{ISO}}$.

Figure 8a compares the flow characteristics obtained with the measured total pressure p_{1D} (on conical tube) and with the calculated total pressure $p_{t1\text{ISO}}$ (ISO tube). The conductance is calculated according to ISO6358 standard [1]:

$$C = \frac{q_m}{\rho_0 p_1} \sqrt{\frac{T_0}{T_1}} \qquad (2)$$

For low conductances in the subsonic range, the characteristics are very close, but when the upstream velocity is higher (especially in ISO tubes) the characteristic obtained with the calculated total pressure $p_{t1\text{ISO}}$ is slightly smaller than the one obtained with the direct measurement p_{1D}. It points out the limitation of calculating the total pressure according to (1) due to uncertainties on the effective area A of the flow at the sensor location and on the total temperature T_t. This means that the direct measurement of the upstream total pressure is preferable using a tube of sufficiently large diameter to make velocity negligible.

Figure 8b shows that using this upstream total pressure, the flow characteristic for component 1 is different from the one obtained using the ISO 6358 standard bench (Fig.5). This may seem obvious since the ISO 6358 standard uses a static upstream pressure. However it has to be noticed that for component 2, both curves are close. This can be explained by lower velocities reached in the ISO 6358 upstream tube than for component 1.

DOWNSTREAM PRESSURE

Considering fluid mechanics results, both exit and back pressures seems to be of interest. A conical connector (Fig.9b) can be used to limit the losses (which could appear as a sudden diameter variation) equipped for the measurement of both pressures:

- the pressure p_{2d} on the port diameter d is measured close to the component outlet at a distance equal to $3d$. This pressure corresponds to a static pressure,

- the pressure p_{2D} is measured on the largest diameter D at a distance approximately equal to $13D$ where the flow reaches again a regular shape.

In this section, the flow characterisations use the upstream conical connector (Fig.6b) in order to obtain directly the upstream total pressure p_{1D} which is kept constant. For both components under test, stationary flow characterisation tests are realised with the both downstream tubes shown in Figure 9.
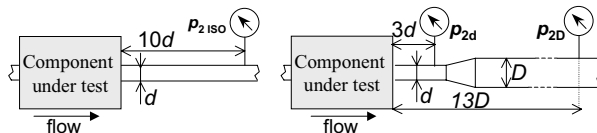
a – ISO 6358:1989.   b – Conical connector.
Figure 9 Downstream pressure connectors.

The use of downstream pressures measured on the component port diameter d either on the ISO6358 tube or on the conical connector leads to the same flow characteristic (Fig.10a). The conical connector presents advantages as it enables lower pressure ratio to be reached during measurement making easier the determination of the characteristic parameters.

The flow characteristic curve is not significantly influenced by the location of pressures measured on the conical connector p_{2d} or p_{2D} (Fig.10b). This can be explained by the low losses in subsonic flow between the two pressure sensors locations (Fig.11 and 12).

However the measure of the pressure on the largest diameter p_{2D} seems preferable because it corresponds to a total pressure (negligible fluid velocity) and thus the complete energy loss is characterised independently of the tubes connected to the component.

The use of the total pressure p_{t2ISO} calculated from the measure of the static pressure p_{2ISO} on the ISO 6358 tube of diameter d leads to a different flow characteristic in the case of component 1 (Fig.10c). This component corresponds to a smaller effective section and accordingly higher velocities are reached. It confirms also that the flow is not really isentropic.

Using both downstream pressures measured with the conical connector, the evolution of the pressure ratio p_{2d}/p_{1D} versus the ratio of p_{2D}/p_{1D} can be plot.
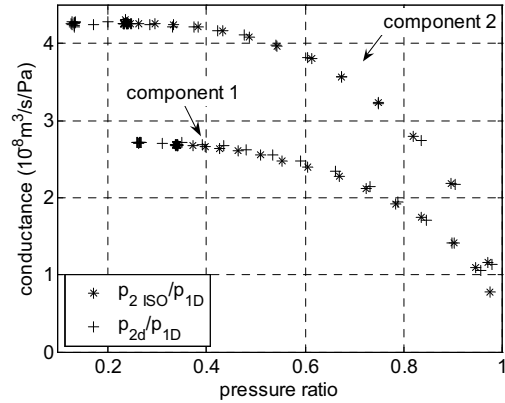
a – Measurements on d: p_{2ISO} (ISO6358) and p_{2d} (conical connector).
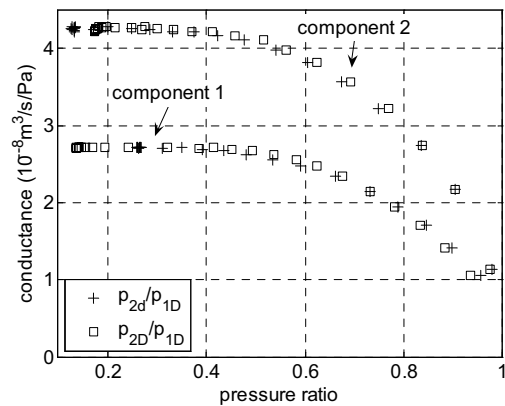
b – On conical connector: p_{2d} on d and p_{2D} on D.
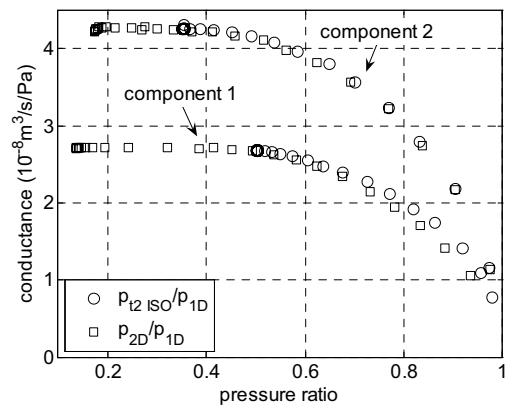
c – p_{t2ISO} from p_{2ISO} on d (ISO6358) and p_{2D} on D (conical connector).

Figure 10 Flow characteristics of both components according to downstream pressures (upstream pressure p_{1D} from conical tube).

For component 1 (Fig.11), the form of the curve is similar to the theoretical curve of an ideal convergent nozzle (Fig.2). However, for component 2 (Fig.12), this evolution presents a sudden variation similarly to the case of a convergent-divergent nozzle (Fig.4).
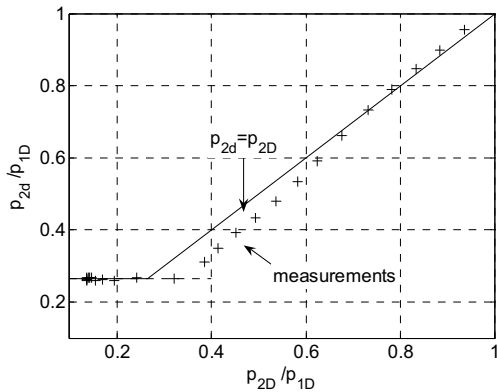
Figure 11 Evolution of pressure ratio for component 1.
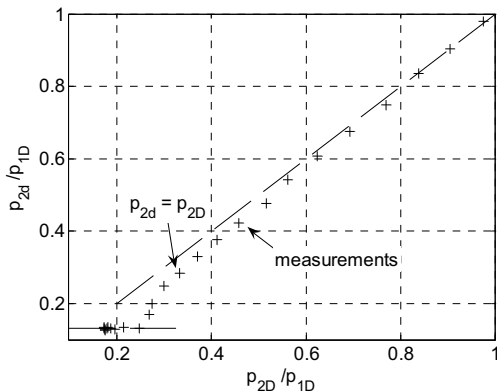
Figure 12 Evolution of pressure ratio for component 2.

In both cases the slope of the oblique line is however different from 1 as in the ideal cases. It shows that there are energy losses between the two downstream pressure sensors. The real flow is not isentropic even with the soft enlargement of the connector. The difference with the ideal cases can come also from the real flow in component which can be tridimensional.

These last remarks mean that the measured pressures can only be considered as an indication respectively of the exit and of the back pressures and not as an accurate measurement of these characteristic pressures.

But it seems sufficient to classify the components under test into two categories according to the similarity of their global flow behaviour with convergent or convergent-divergent ideal nozzles.

CONCLUSION

Keeping in mind that the standard must help users for the choice of the right component, it is necessary to characterise the global losses of the component independently from the functioning conditions: the considered upstream and downstream pressures should be total pressures. The use of conical connectors with the pressure measurements on the largest diameter enables a direct measurement of the necessary total pressures. The use of total pressures presents also the advantage to make easier the calculations of serial association of components [2, 8].

According to fluid mechanics theory, the additional measurement of the pressure close to the component outlet on a diameter corresponding to the component outlet standard connection can give an indication on the global flow behaviour of the component compared to the ideal cases of convergent or convergent-divergent nozzles. This can be useful at the user level since it is well-known that a convergent-divergent nozzle behaviour means that shocks can take place inside the component or downstream.

The analysis proposed here for stationary flows needs naturally to be validated on other types of components and for transient tests to verify that the diverging part of the downstream connector does not change the flow behaviour of the component due to couplings.

ACKNOWLEDGMENT

REFERENCES

1. International Standard ISO6358. Pneumatic Fluid Power - Components using Compressible Fluids - Determination of Flow-rate Characteristics, 1989. 15p.
2. Yan, T., Guo Xiang, M., Huping, Z., Oneyama, N. Study on Composite Flow-rate Characteristics of Pneumatic Components, Spring symposium on fluid power, JFPS, pp. 101-103, 2003.
3. Kawashima, K., Kagawa, T., Fujita, T., Instantaneous flow rate measurement of ideal gases. Trans. of the ASME Journal of Dynamic Systems, Measurement and Control, vol. 1222, pp.174–178, march 2000.
4. De Giorgi, R., Sesmat, S., Bideaux, E., Using Inverse Models for Determining Orifices Mass Flow Rate Characteristics, Proc. of the 6th JFPS Int. Symp. on Fluid Power, Tsukuba 2005, Nov 7-10, 2005
5. Kuroshita, K., Sekigushi, Y., Oshiki, K., Oneyama, N., Development of new test method for flow-rate characteristics of pneumatic components. In Power Transmission and Motion Control, PTMC'2004, Sept. 2004, Bath, England, pp243-256.
6. F.-E. Sanville. New method of specifying the flow capacity of pneumatic fluid power valves. Hydraulic and pneumatic power, n°195, vol. 17, mars 1971.
7. White F., M., Fluid Mechanics, McGraw-Hill, New York, 3rd Ed., 1994, 736p.
8. Sesmat, S., Lecerf, J.-P., Gautier, D., Hubert, D., Bideaux, E., Lallement, J., Calculation method for determining the flow-rate characteristics of a group of pneumatic components, Hydraulics and pneumatics'2007, Wroclaw, 10-12 Oct. 2007, pp.409-419

P2-25

DEVELOPMENT OF SMALL-SIZED FLEXIBLE CONTROL VALVE USING VIBRATION MOTOR

Tetsuya AKAGI*, Shujiro DOHTA* and Shin-ichi KATAYAMA**

* Department of Intelligent Mechanical Engineering, Faculty of Engineering
Okayama University of Science
1-1 Ridai-cho, Okayama, 700-0005 Japan
(E-mail: akagi@are.ous.ac.jp)
** Graduate School of Engineering, Okayama University of Science
1-1 Ridai-cho, Okayama, 700-0005 Japan

ABSTRACT

Recently, due to the ageing in Japanese society and the decreasing birthrate, an important problem of providing nursing care for the elderly has occurred. As a result, it is necessary to develop wearable systems to aid in nursing care. To realize the system, we require not only wearable soft actuators, but also compact and flexible control valve that can drive the soft actuator such as a pneumatic artificial muscle. The purpose of our study is to develop a flexible, lightweight and compact control valve which can be safe enough to be attached to the human body.

In this study, we proposed and tested a new type of control valve. The valve consists of a vibration motor and a check valve that made of a steel ball and an orifice in flexible tube. The operating principle of the valve is as follows. The valve is normally closed as a function of check valve. When the vibration is applied, the inner ball in the check valve moves and the valve opens. By giving continuous vibration, the valve can keep open. As a result, we find that the valve can control the relatively larger flow rate compared to their weight and size.

KEY WORDS

Small-sized control valve, Control using vibration, Flexible control valve, Valve using vibration motor

INTRODUCTION

Recently, force feedback devices in virtual reality and power assisted nursing care systems[1-2] have received much attention and active research. In such a control system, an actuator and a driving device such as a control valve are mounted on the human body[3-5]. To consider the development of wearable control valve that can drive pneumatic actuator so as to support the multi degrees of human motion, the size and weight of the valve become serious problems. The usual electro magnetic solenoid valves drive their spools by using larger solenoid to open the valve. The solenoid valves have complex construction to keep a seal while the spool moving. This complex construction makes the miniaturization of the valve and the fabrication of the low cost valve more difficult. The purpose of our study is to develop a small-sized, lightweight and flexible control valve that can be safe enough to mount on human body with a lower cost. In this study, we proposed and tested a new type of control valve that can make it open by using a vibration motor. In addition, we investigated the output flow characteristics of the tested valve.

CONTROL VALVE USING VIBRATION MOTOR

Concept of the proposed valve

Figure 1 shows a fundamental concept of a proposed control vale. The figure shows the model of the tested valve using the check valve which is composed of a steel ball and orifice. Figure 1 (a) and (b) illustrate the operational image of a usual electro magnetic on/off control valve and a proposed valve, respectively. In the both valves, the supplied pressure is applied from the lower inlets as shown in Fig.1. From Fig.1, the steel ball is always applied by the upper force according to the differential pressure between inlet and outlet of the orifice and the sectional area of the orifice. In the case using the usual on/off valve as shown in Fig.1 (a), to open the valve, it needs a larger longitudinal directional pulling force that can overcome the pushing force of the ball generated by supplied pressure. Therefore, the usual elector-magnetic solenoid valve needs a relatively larger solenoid coil to open the valve surely. It prevents the miniaturization of the valve. In addition, in order to pull the steel ball while keeping the seal between inside and outside of the valve, it needs some complex mechanisms. It prevents to make the cost of the valve lower.

(a) Image of a usual control valve

(b) Image of proposed valve
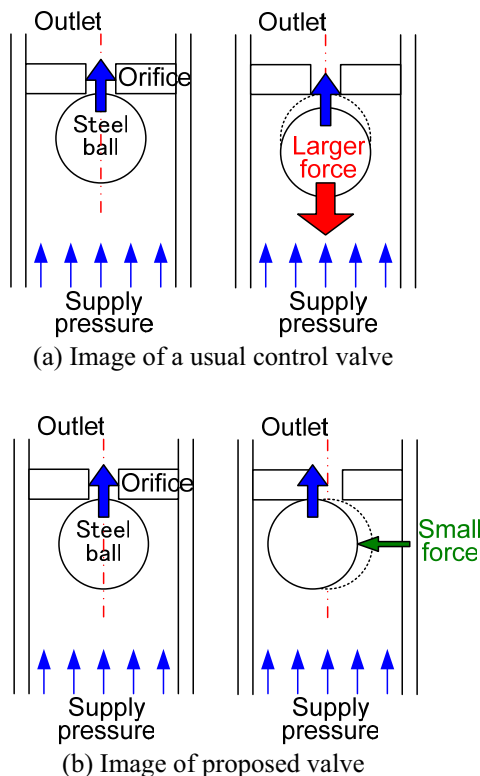
Figure 1 Concept of proposed control valve

In case of the proposed valve as shown in Fig.1 (b), to increase the opening of the valve, we apply the steel ball the horizontal direction force to slide the ball. By using this method, it becomes possible to open the valve using smaller force. In the case of closing, when we stop to apply the horizontal direction force, the inner steel ball automatically moves toward the orifice by the generated force of momentum of the flow such as a check valve. Then, the ball closes the orifice as a stable condition of check valve.

Construction and operating principle

Photo.1 shows the construction of the tested control valve. The tested valve consists of a flexible tube whose inner diameter is 2.5 mm and outer diameter is 4 mm, an acrylic orifice with inner diameter of 0.5 mm, a steel ball with outer diameter of 2 mm and a vibration motor (Shicoh Co.Ltd. SE-4C-1E). The acrylic orifice and the steel ball are inserted into the flexible tube. In the opposite side of the orifice and ball, the ball stopper that has inner bore with diameter of 1.5 mm is inserted into the tube. The vibration motor is set on outer side of flexible tube by an acrylic connector. The orifice and the steel ball are inserted into the tube. There is no mechanical connecting part between the both contents of inner and outer of the tube. It means that the tested valve does not need the special sealing such as a gasket between the inner and outer of tube. In addition, the valve has no mechanical sliding moving part in the tube. The volume of the tested valve including the vibration motor is about 1 cc, that is the valve has the length of 20 mm, the width of 5mm and the height of 10mm. The mass of the tested valve is very lightweight, that is only 2 g. The inner mechanism of the valve is very simple. It means that the valve can be fabricated with a lower cost.
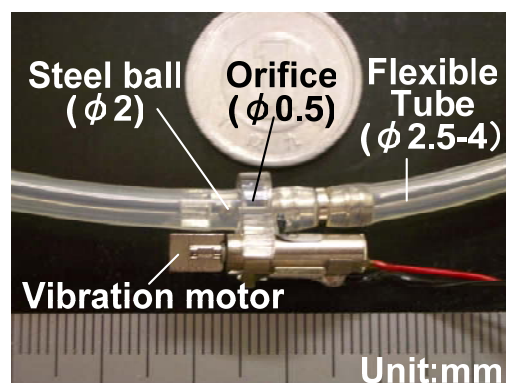
Photo.1 Tested control valve using vibration motor

Figure 2 (a) and (b) show the schematic diagram of the valve and the operation of the valve, respectively. The operating principle of the tested valve is as follows.

When the vibration motor is driven, the tube connected with the vibration motor is oscillated. From the law of inertia, the inner steel ball stays in a certain position of the tube. The inner steel ball contacts to the inner wall of the tube. Then, it gives horizontal direction force to the ball. The inner ball starts to move and rotate along to the inner wall of the tube as shown in Fig. 2(b). By giving the vibration continuously, the ball carries on rotating along to the inner wall of the tube. It is said that the opening of the orifice keeps a certain sectional area while the vibration motor being driven. It means that the tested valve generates the stable flow rate while the valve working. This method is more useful to supply the stable flow rate compared with other way of the valve opening using vibration[6] When the vibration motor is stopped, the steel ball automatically moves toward the orifice by the generated force of momentum of the flow such as a check valve. In the case of giving a large impulse disturbance to the valve such as flipping the valve, the ball moves temporally and a negligibly small leakage occurs. It means that the tested valve does not open when the continuous vibration is applied.

CHARACTERISTICS OF THE TESTED VALVE

In order to investigate the characteristics of the tested valve, we measured the output flow rate from the tested valve when the inlet of the valve is connected with the air supply. Figure 3 shows the experimental setup to investigate the characteristics of the tested valve. The equipment consists of the tested valve, float type flow meter, electric power supply and ammeter. In the measurement of output flow rate, the outlet of the valve is connected to the inlet of a float type flow meter whose outlet is released to the atmosphere. While the valve being driven, the current in the vibration motor was also measured by an ammeter. Figure 4 shows the relation between the supply pressure and output flow rate of the tested valve. In Fig.4, each symbol ●, ▲ and ■ show the results using the tested valve and two

(a) Schematic diagram of the tested valve

(b) Operation of the tested valve

Figure 2 Operating principle of tested valve
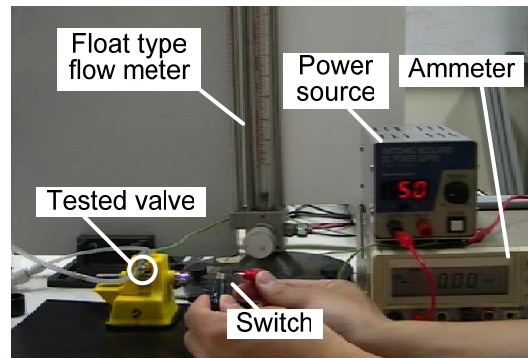
Figure 3 Experimental setup of the tested valve
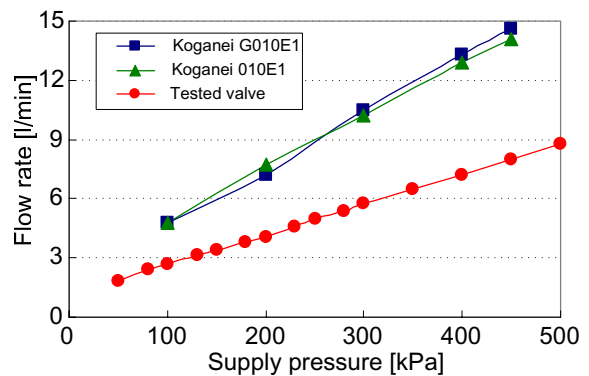
Figure 4 Relation between supply pressure and output flow rate of the tested valve
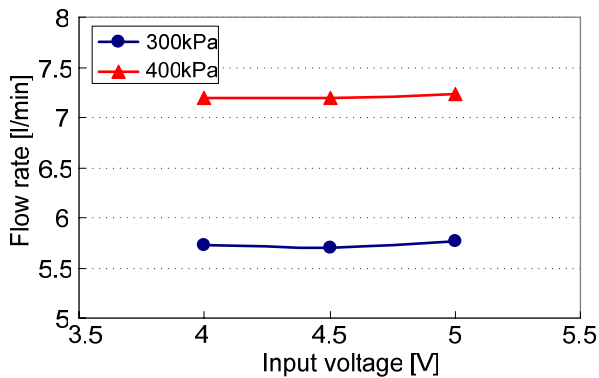
Figure 5 Relation between operating voltage
and output flow rate of the tested valve

types of pneumatic on/off control valve on the market (Koganei Co. Ltd. G010E1 and 010E1), respectively. These commercial pneumatic control valves are relatively small-sized valves on the market. In the experiment, the input voltage of 5 volts was applied to the vibration motor in the tested valve and the input voltage of 12 volts was applied to the commercial on/off valves as an operating input. The supply pressure of these valves was changed from 50 kPa to 500 kPa. From Fig.4, it can be seen that the output flow rate of the tested valve has the linear relationship between the supply pressure and the output flow rate. It can be said that the sectional area of the orifice in the tested valve does not change even if the pushing force acted on the inner ball increases according to the supply pressure.

Figure 5 shows the relation between operating voltage and output flow rate of the tested valve. In Fig. 5, symbols ● and ▲ show the results using supply pressure of 300 and 400 kPa, respectively. The vibration motor in the tested valve can be driven by operating voltage of more than 3 volts. Therefore, the tested valve can be driven by a relatively wide range of the operating voltages, that is from 3 to 6 volts. It means that the tested valve does not need higher operating voltages so as to get the generated magnetic force as large as to drive the solenoid. From Fig.4, we can see that the output flow rate does not change according to operating voltage. These results show that the valve can generate a constant flow rate even if an unstable input voltage is given to the valve.

As a dynamic characteristic of the tested valve, we investigated the response of the float type flow meter connected with the tested valve when the input voltage of the valve was turned ON or OFF. In this experiment, we can see that the response of the tested valve for input voltage is almost same as that of the commercial valve using the solenoid. The response time of the valve for stepwise input voltage looks less than 0.1 s even if the length of the connecting pipe between the valve and the flow meter is about 1m.

In addition, it is necessary to confirm the performance of the valve connected to the closed chamber such as a cylinder chamber. Figure 6 (a) shows the experimental setup for driving the pneumatic cylinder whose inner diameter is 20 mm using the tested valve. The end of the cylinder connected to the weight whose mass is 17.2 kg. Figure 6 (b) shows the transient view of the moment of the cylinder driven by the tested valve. It can be seen that the cylinder can be driven smoothly even if the valve is connected to the closed chamber. The valve can work under the both conditions of pressurizing into the closed chamber and releasing from compressed air chamber. It means that the tested valve can be used as both of supply and exhaust valves.
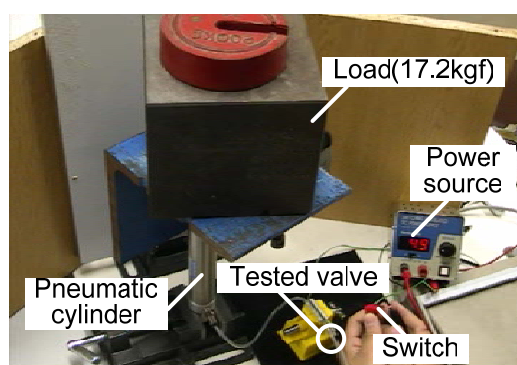
(a) Experimental setup for driving cylinder
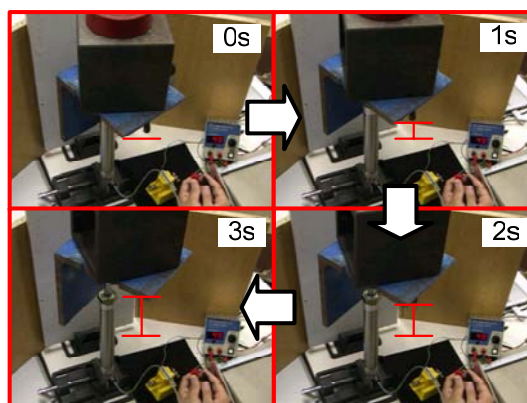
(b) Transient view of movement of cylinder

Figure 6 Experiment for driving cylinder with a load of 17.2 kgf(169N) using the tested valve

COMPARISON TO COMMERCIAL VALVE

Figure 7 shows the comparison of the size and weight of the tested valve with the commercial on/off type pneumatic control valves. The upper bar graph shows the comparison of the size of the valves. The lower graph shows the comparison of the mass. From Fig.7,

728

we can see that the size of tested valve is from one 24th to one 16th, the mass is about one 10th compared with the commercial valves that have almost same output flow rate and same supply pressure range. We can confirm that the tested valve is suitable for the wearable control valve because of small size, lightweight and its flexible property.

Figure 8 shows the relation between the electric power consumption and supply voltage of the tested valve. In Fig.8, symbol ● shows the calculated electrical power using the measured current and supply voltage of the vibration motor. The green and blue lines show the power consumption using the commercial valves that can be driven by the input voltage of 12 volts. From Fig.8, it can be seen that the power consumption of the valve decreases according to the decrease of the input voltage to the vibration motor. The minimum power consumption of the valve is about 0.6 W, that is one second of power consumption using the commercial valve. In addition, the power consumption of the valve can be reduced by changing the construction of the valve so as to generate the resonance phenomenon of the beam-structured tube in the valve using lower electric power. Figure 9 (a) and (b) show the comparison of normalized output flow rate between the tested valve and commercial valves. Figure 9 (a) shows the relation between the supply pressure and the output flow rate normalized by the size of the valves. Figure 9 (b) shows the results of output flow rate normalized by the mass of the valves. In Fig.9, each symbol ●, ▲ and ■ show the result using the tested valve and the commercial valves, respectively. From Fig.9 (a), it can be seen that the normalized flow rate of the tested valve is about 10 times as large as those using the commercial valves. From Fig.9 (b), the normalized flow rate by the mass of the tested valve is about 6 times larger than the commercial valves. The both experimental results prove that the tested valve is suitable as a wearable control valve because of relatively larger output flow rate compared to their weight and size.

Figure 7 Comparison of size and mass between the tested valve and the commercial valves
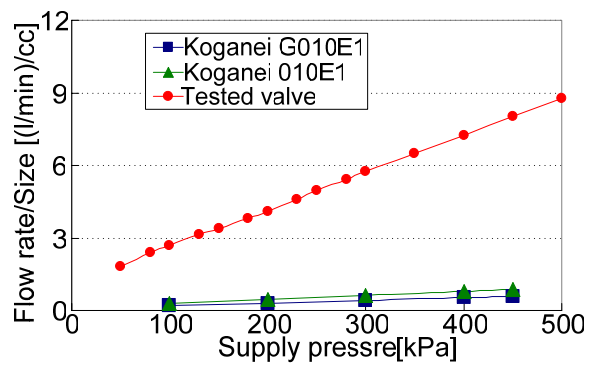
(a) Output flow rate per size of the valve
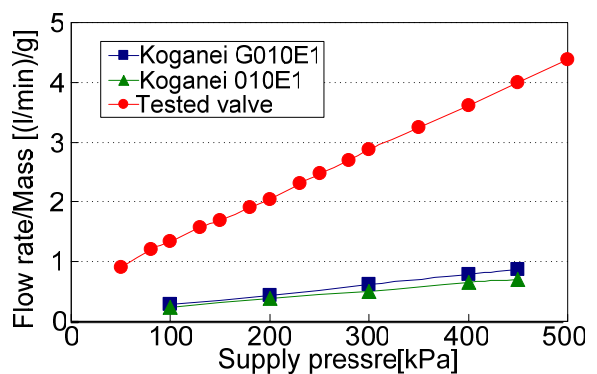
(b) Output flow rate per mass of the valve

Figure 9 Comparison of normalized flow rate between the tested valve and commercial valves

Figure 8 Relation between input voltage and electric power consumption

CONCLUSIONS

This study that we aim to develop the small sized wearable control valve is summarized as follows.

1) We proposed and tested a flexible control valve that consists of a vibration motor and a check valve composed of a steel ball and an orifice in flexible tube. We also investigated the operating principle of the tested valve. As a result, we found that the inner steel ball of the valve rotated along the inner wall of the tube and the constant opening area of the valve could be opened by ball rotating.

2) The output flow rate of the tested valve for various input voltages of the valve was investigated. As a result, it was found that the proposed valve could generate a constant flow rate even if the input voltage of the vibration motor was changed. As a result of experiment for driving the pneumatic cylinder, we can see that tested valve can be used as both of supply and exhaust valves.

3) As comparing the characteristics of the output flow rate of the valve with the commercial valves on the market, the tested valve is suitable as a wearable control valve because of relatively larger output flow rate for their weight and size.

ACKNOWLEDGMENT

REFERENCES

1. Ishii,M., Yamamoto,K. and Hyodo,K. , "Stand-Alone Wearable Power Assist Suit –Development and Avail-ability –", *Journal of Robotics and Mehatronics*, Vol.17, No.5 (2005), pp.575-583.
2. Nagata,Y. ed., Soft Actuators -Forefront of Development -(in Japanese), (2004), pp.291-335, NTS Ltd..
3. Akagi,T. and Dohta,S., "Development of a Rodless Type Flexible Pneumatic Cylinder and Its Application", Transaction of JSME,Series C,Vol.73, No.731 (2007), pp.2108-2114.
4. Akagi,T. and Dohta,S., "Development of McKibben Artifical Muscle with a Long Stroke Motion", Transaction of JSME, Series C, Vol.73, No.735 (2007), pp.2996-3002.
5. Akagi,T. and Dohta,S., "Development of Wearable Pneumatic Actuator and Multiport Pressure Control Valve", Journal of Robotics and Mechatronics, Vol.17, No.5 (2005), pp.529-536.
6. Uehara. S et al.," Unconstrained Vibrational Pneumatic Valves for Miniaturized Proportional Control Devices", Proc.9th International Conference on Mechatronics Technology (ICMT2005).

P2-26

DETERMINATION OF FLOW-RATE CHARACTERISTICS OF PNEUMATIC REGULATORS USING ISOTHERMAL TANK BY PRESSRE RESPONSE

Naotake ONEYAMA[*], Huping ZHANG[*], Mitsuru SENOO[*], Guangzheng PENG[**]
and Jinglong YANG[***]

[*] Technology & Research Division, SMC Corporation Tsukuba Technical Center, 4-2-2, Kinunodai,
Tsukubamirai-shi, Ibaraki-ken, 300-2493 Japan
(E-mail: oneyama@smcjpn.co.jp)
[**] Automatic Control Department, Beijing Institute of Technology, PC 100081 Beijing, China
(E-mail: smcpeng@bit.edu.cn)
[***]Mechanics Department Tsinghua University, PC 100084 Beijing, China
(E-mail: yangjl@tsinghua.edu.cn)

ABSTRACT

ISO 6953:2000 prescribes that forward flow-rate and outlet pressure until maximum flow-rate shall be measured with a constant inlet pressure and two or more outlet set pressures, and their relations shall be indicated by curves on a graph [1][2].   Since this test requires not only a huge air compressor, but also keeping continuous large flow-rate for a long time, enormous energy is consumed. Thus, this paper proposes a method to obtain flow-rate characteristics from pressure response on charging/ discharging compressed air into/from an air tank as an alternative test. This test method requires none of a huge air source, a long testing time, and enormous energy consumption.
In this paper, the above-mentioned alternative test was performed to some pressure regulators which had different constructions and sizes from one another, and it was verified that the results of the alternative test successfully corresponded to the one by ISO 6953 using a flow meter. Examination to optimize the test method was also discussed. The running cost to operate the test, which consists of labor costs based on the test time and energy consumption, was reduced to approximately one-fifth.

KEY WORDS

Pneumatic pressure regulators, Flow-rate characteristics, ISO 6953, Isothermal tank

NOMENCLATURE

G: Mass flow-rate [kg/s]
m: Air mass within the isothermal tank [kg]
p_1: Gauge inlet pressure [MPa]
p_2: Gauge outlet pressure [MPa]
p_3: Gauge pressure within the isothermal tank [MPa]
p_{1abs}: Absolute inlet pressure [MPa]

p_{2abs}: Absolute outlet pressure [MPa]
p_{3abs}: Absolute pressure within the isothermal tank [Pa]
Q_{max}: Maximum outlet flow-rate [dm^3/min (ANR)]
Q_r: Choked relief flow-rate at p_{2abs} [dm^3/min (ANR)]
R: Gas constant 287 [J/(kg•K)]
t: Time [s]
T: Absolute temperature of air within the isothermal tank [K]

T_0: Absolute temperature at the standard conditions, 293 [K]

V: Volume of the isothermal tank [m³]

INTRODUCTION

As shown in Figure 1, ISO 6953:2000 "Pneumatic fluid power – Compressed air pressure regulators and filter-regulators" prescribes that forward flow-rate and outlet pressure shall be measured with a constant inlet pressure and two or more outlet set pressures until the maximum flow-rate and their relations shall be indicated by curves on a graph. Since this test requires not only a huge air compressor, but also maintaining a continuous large flow-rate for a long time, enormous energy is consumed. Thus, this paper proposes a method to obtain flow-rate characteristics from pressure responses by charging/discharging compressed air into/from an air tank as an alternative test. This test method does not require a huge air source, long testing time, or enormous energy consumption.
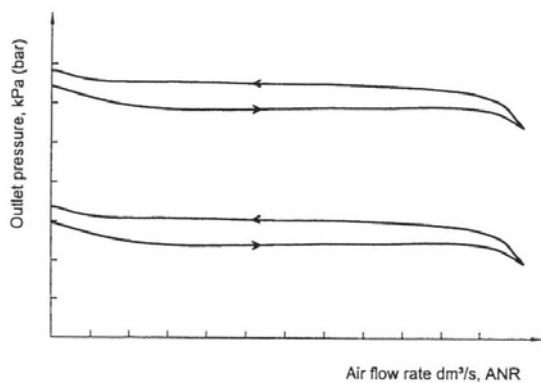
Figure 1 Forward flow characteristics

ISOTHERMAL TANK

The structure of the isothermal tank is shown in Figure 2. The tank consisting of container and the lid, is stuffed with material and has a flow port which connects test component. It also has a source port, with which air is charged or discharged in advance, a pressure measuring port and a drain port. The stuffed material should have a large heating surface area, large capacity, resistant to failure and corrosion-resisting. Thin wire with a diameter of 30μm or 50μm made of a material such as copper or stainless steel is suitable for stuffed material.

Figure 3 shows the temperature drop of each tank with different capacities and ratios of stuffed copper wire having a diameter of 50μm at air discharge. This data was taken when compressed air of 700 kPa was being

discharged from the stuffed tank for approximately 15 seconds, that is, with a maximum pressure-drop rate of 100 kPa/s. If the density of the stuffed material is 0.3 kg/dm³, the temperature drop can be suppressed to 3 K or less. In this case, the volume ratio of the stuffed material is 3.3 %.
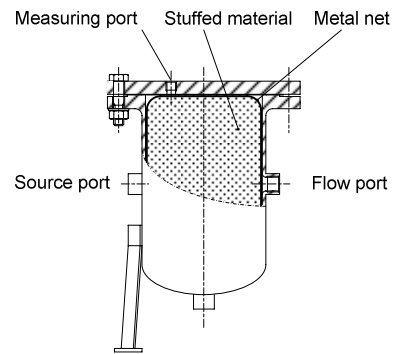
Figure 2 Structure of the isothermal tank
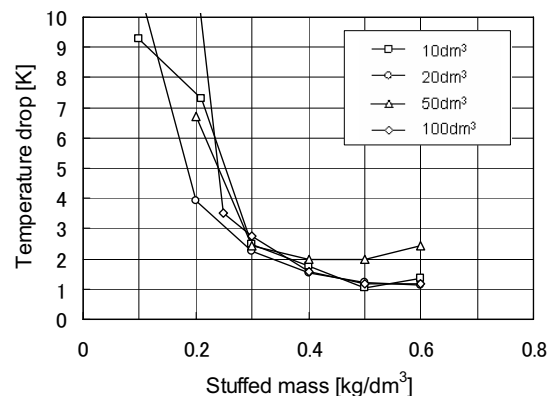
Figure 3 Isothermal performance

TEST INSTALLATION

Figure 4 shows the test equipment. The order of the connection of the test equipment is supply tank (A), regulator for setting inlet pressure (B), regulator under test (C), switching valve (D), and isothermal tank (E). Rectifier (F) and pressure measuring connector (M) are connected before and after the regulator under test. The sizes of the rectifier, regulator for setting inlet pressure, and connecting pipe are twice as large as or more than the size of the regulator under test. A high-pressure supply line (G) for relief test is also provided. If the relief capacity of the regulator under test is very small,

discharge line (H) with a small isothermal tank and switching valve should be used to shorten the testing time.
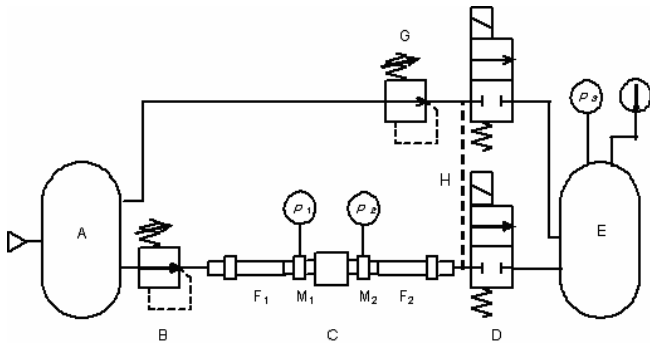
Figure 4 Test installation

TEST PROCEDURES

After inlet pressure is set at, say, 0.63 MPa and the regulator under test is set at, say, 0.4 MPa, charge air to the isothermal tank by opening the switching valve. The flow-rate can be calculated by time-differentiation of the pressure in the isothermal tank. The forward flow-rate characteristics can be obtained by illustrating the relation of the outlet pressure and this flow-rate.

Then, close the switching valve, and supply air to the isothermal tank from the high-pressure supply line up to, say, 0.9 MPa. Open the switching valve, and discharge air to the atmosphere from the relief port of the regulator under test. Calculate the flow-rate by the time differentiation of pressure within the isothermal tank. The relief flow-rate characteristics can be obtained by illustrating the relation of the outlet pressure and this flow-rate.

From the equation of the state of air within the tank,

$$p_{3abs} = \frac{mRT}{V} \qquad (1)$$

Since the capacity of the isothermal tank and the temperature in the tank are constant, the mass flow-rate can be expressed by the following equation:

$$G = \frac{V}{RT} \frac{dp_{3abs}}{dt} \qquad (2)$$

TEST RESULT OF REGULATOR (A)

Figure 5 shows the structure of direct operated regulator (A) of a body size of G1/2 with the relieving mechanism. The test results are as follows.

Figure 6 shows the pressure response when charging air to an isothermal tank of 100 dm^3 by opening the switching valve after inlet pressure at 0.63 MPa and regulated pressure at 0.4 MPa.

Since the regulator (A) had an extremely small relief flow capacity, the circuit was switched to the bypass discharge having an isothermal tank of 10dm^3 at the end of the line to shorten the testing time. The high-pressure supply line for relief was set at 0.9 MPa, and air was supplied to the small tank. The pressure response when discharging air to the atmosphere from the regulator (A) is shown in Figure 7.

Figure 8 shows the flow-rate characteristics obtained both from the pressure response when setting regulator (A) at 0.2, 0.3, 0.4, and 0.5 MPa, and from the test results of the flow-rate measurement based on ISO 6953. The characteristics curve obtained by calculating the measured pressure within the isothermal tank from equation (2) and by smoothing by the method of moving averages are in good agreement with the results of the flow-rate measurement.
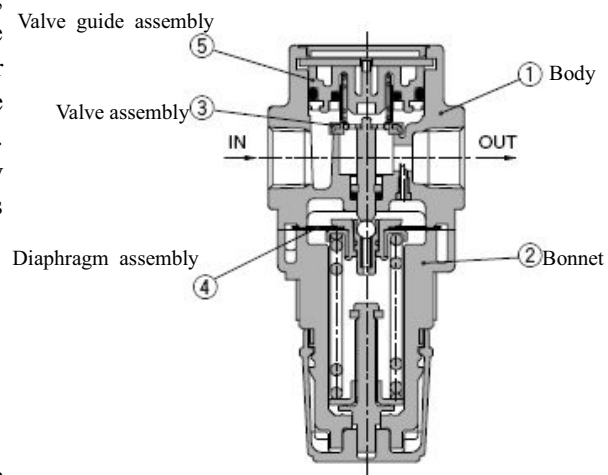
Figure 5 Regulator (A)
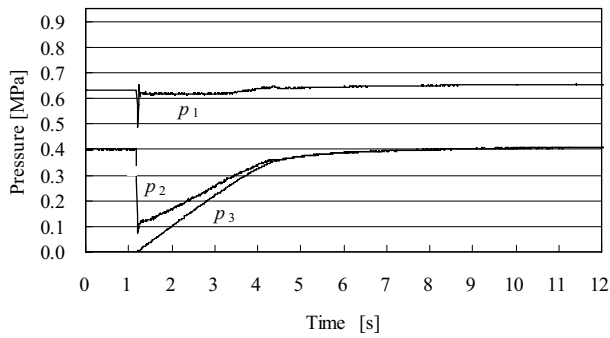
Figure 6 Pressure responses in the tank during charge – regulator (A)
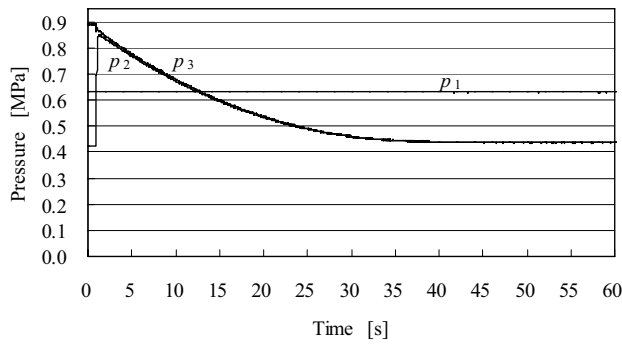
Figure 7 Pressure responses in the tank during discharge – regulator (A)
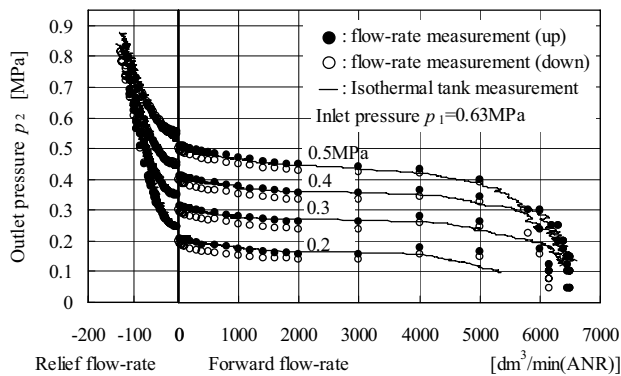
Figure 8 Flow-rate characteristics of regulator (A)

TEST RESULT OF REGULATOR (B)

Figure 9 shows the test structure of the internal pilot type regulator (B) of a body size of G1/4 with a nozzle-flapper type relieving mechanism. The test results are as follows:
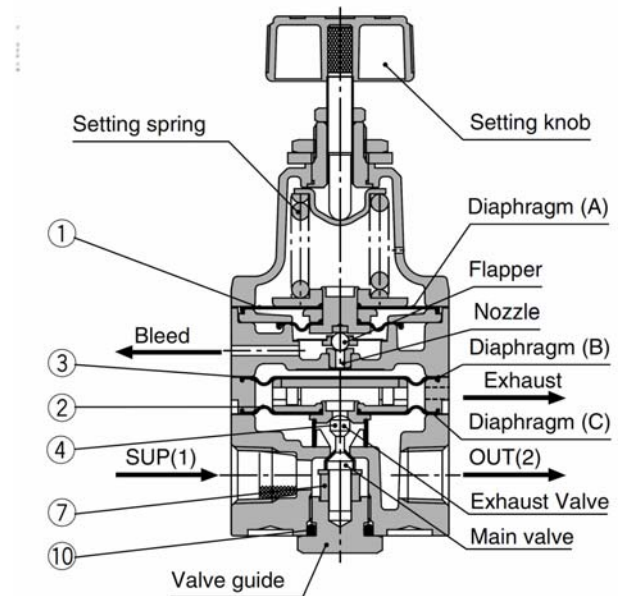
Figure 9 Regulator (B)

Figure 10 shows the pressure response when charging air to an isothermal tank of 10 dm^3 after setting inlet pressure at 0.63 MPa and regulated pressure at 0.4 MPa.

Figure 11 shows the pressure response when air is discharged to the atmosphere from test regulator (B) after the high-pressure supply line for relief is set at 0.9 MPa and air is supplied to an isothermal tank of 10 dm^3.

Figure 12 shows the flow-rate characteristics obtained both from the pressure response with the setting regulator (B) at 0.16, 0.25, 0.4, and 0.5 MPa, and from the results of the flow-rate measurement based on ISO 6953. The characteristics curves for the regulator (B) are also in good agreement with the results of the flow-rate measurement.
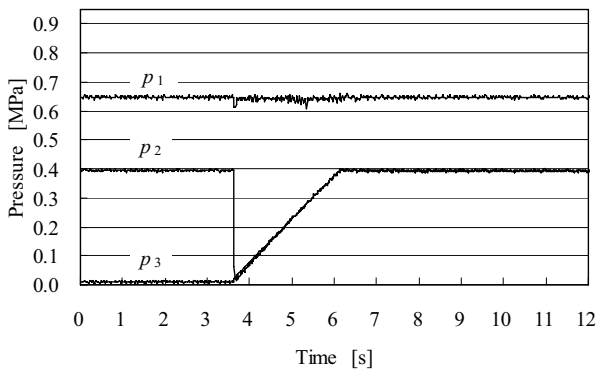
Figure 10 Pressure responses in the tank during charge – regulator (B)
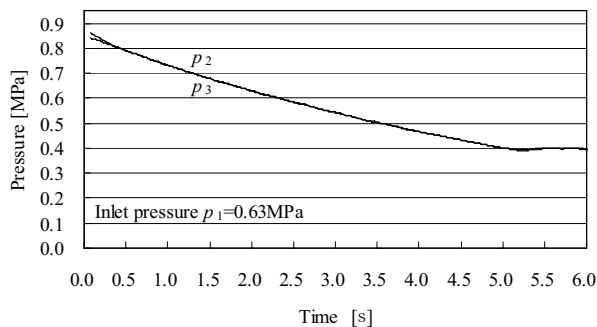
Figure 11 Pressure responses in the tank during discharge – regulator (B)
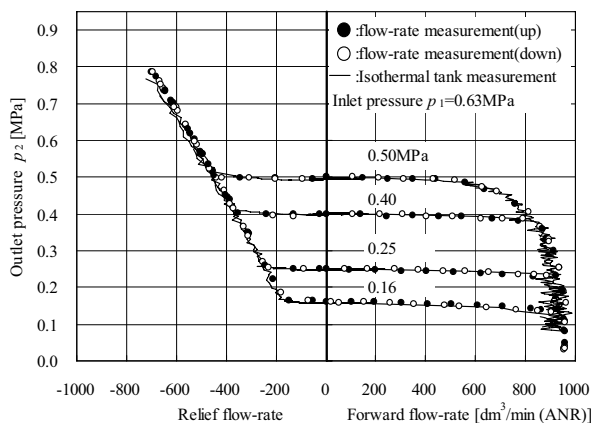
Figure 12 Flow-rate characteristics of regulator (B)

CHARACTERISTIC PARAMETERS

As shown in Figure 13, when the forward flow-rate characteristics of the regulator are approximated to the regression lines L_1 and L_2, and the relief flow-rate characteristics to the regression lines L_3 and L_4, calculated characteristic parameters of the regulator are obtained as shown in Table 1. The forward conductance and relief conductance represent the flow capacity of the regulator. The forward slope and relief slope represent the pressure regulating performance. The dead zone shows the initial pressure difference between the forward flow and relief flow. The regulator (A) is a regulator for general purpose which has extremely small relief flow capacity compared to the forward flow and has a large dead zone. The regulator (B) is a regulator for a precision use which has large relief capacity and extremely small dead zone.

ENERGY SAVING

The total testing time and the energy consumption which covers the mounting of the regulator under test to test installation, three repeated measurements, calculation, plotting, and removal of the regulator from the test installation were measured. Compared to the ISO 6953 flow-rate measurement test, this proposed test takes only 1/10 the amount of time and consumes only 1/30 the amount of air. It proves that this proposal offers a time- and energy-saving test method.
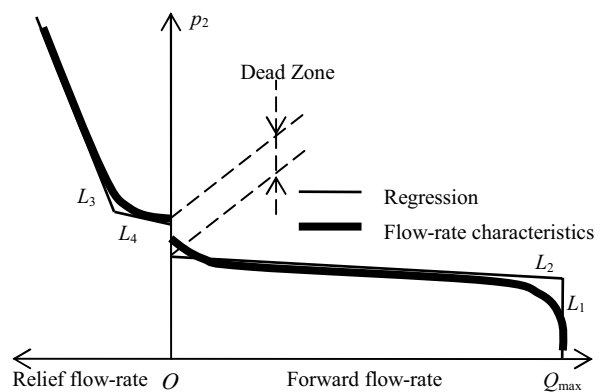
Figure 13 Definitions of the characteristic parameters

735

Table 1. Characteristic parameters of the regulators

Parameters	Calculation methods	Regulator (A)	Regulator (B)
Forward conductance	$C_0 = \dfrac{Q_{\max}}{600\,p_{1abs}}\sqrt{\dfrac{T}{T_0}}$	16.1	2.49
Forward slope K_0	Gradient of regression L_2	-0.00884	-0.0123
Relief conductance	$C_r = \dfrac{Q_r}{600\,p_{2abs}}\sqrt{\dfrac{T}{T_0}}$	0.306	1.46
Relief slope K_r	Gradient of regression L_3	-0.643	-0.0318
Dead zone P_b	Initial pressure difference between L_2 and L_4	30.3	0.00301

CONCLUSIONS

1. This paper describes designed test installation using an isothermal tank, and the results of the charging and discharging tests on two types shows good agreement with the test results based on ISO 6953 on two types of regulators which have different structures and sizes from each other.
2. This test method does not require a huge air pressure source. The testing time and energy consumption are extremely less than that of ISO 6953. This test method can save both time and energy.
3. This test method should be established as an alternative test method by further optimizing the equipment specifications and data processing.

REFERENCES

1. ISO 6953-1:2000, Pneumatic fluid power - Compressed air pressure regulators and filter-regulators - Part 1: Main characteristics to be included in literature from suppliers and product-marking requirements.
2. ISO 6953-2:2000, Pneumatic fluid power - Compressed air pressure regulators and filter-regulators - Part 2: Test methods to determine the main characteristics to be included in literature from suppliers.

P2-27

DEVELOPMENT OF SMALL-SIZED AIR PUMP
USING BALLOON VIBRATOR FOR WEARABLE DEVICES

Yuji MAEDA*, Toshiro NORITSUGU*, Daisuke SASAKI*
Kazukiyo TAKANO**, Takemitsu OKAMOTO*** and Seiji SATO****

* Okayama University
3-1-1, Tsushimanaka, Okayama, 700-8530 Japan
(E-mail: maeda@mcrlab.sys.okayama-u.ac.jp, [toshiro, daisuke]@sys.okayama-u.ac.jp)

** Industrial Technology Center of Okayama Prefecture
5301, Haga, Okayama, 701-1296 Japan

*** Minoru Industrial Co. Ltd.
447, Shimoichi, Akaiwa, Okayama, 709-0892 Japan

**** Chugoku Rubber Industry Co. Ltd.
3-2-20, Higashifurumatsu, Okayama, 700-0921 Japan

ABSTRACT

This study is aimed at developing a small-sized air pump using an originally contrived balloon vibrator for wearable devices. The developed pump can compress air by vibrating a balloon vibrator which is composed of a doughnut-shaped balloon diaphragm fitted with a circular stainless steel plate. The balloon diaphragm is filled with air. This pump has characteristics as an oil-free, doesn't leak air at all, and has a longer stroke than existed diaphragm pumps. Therefore, this pump is expected to have higher discharge performance than existed diaphragm pumps. In addition, it is also expected to develop an output variable air pump by controlling the inner pressure of balloon. In this paper, the structure of the developed pump is described, and then the fundamental characteristics of this pump are evaluated.

KEY WORDS

Pneumatics, Air pump, Wearable device, Small-sized

NOMENCLATURE

P : Discharge pressure [Pa]
Q : Volumetric flow rate [m^3/sec]
W : Input power to the pump [W]

INTRODUCTION

Recently, many types of movement assist devices have been developed because of the falling birthrate and the aging population [1]. In a perspective of affinity for human, wearable devices using pneumatic rubber muscle have been also developed and have been expected to come into practical use.

To drive these devices, air pumps are required. In order to realize the stand-alone wearable system, air pumps require both high discharge performance and portability. However, existed small-sized air pumps don't have enough discharge performance to drive these devices. So, there have been some studies about the several types of air pumps [2][3][4].

This study is aimed at developing a small-sized air pump using an originally contrived balloon vibrator.

The performance targets of the pump are shown as follow.

1. Discharge performance
    - Maximum discharge pressure 350[kPa]
    - Maximum flow rate 12.5[Nl/min]

    Both pressure and flow rate are desired to be higher. However, in consideration of the demanded pressure or the response time of wearable devices and the size of the pump, the target performance is decided as above.

2. Size and weight
    - Less than 1[kg] (include controller, etc.)

    The size is desired to be small so that the pump is not a burden to people when they equip it on the waist, etc.

3. Noise level
    - Less than 60[dB (A)]

    This noise level corresponds to the noise of normal conversation. But, the noise level is desired to be lower.

In this paper, the structure of the developed pump and characteristics of the balloon vibrator are described, and then the fundamental characteristics of this pump are evaluated. In addition, the application to an output variable air pump is suggested.

(a) Intake air

(b) Exhaust compressed air
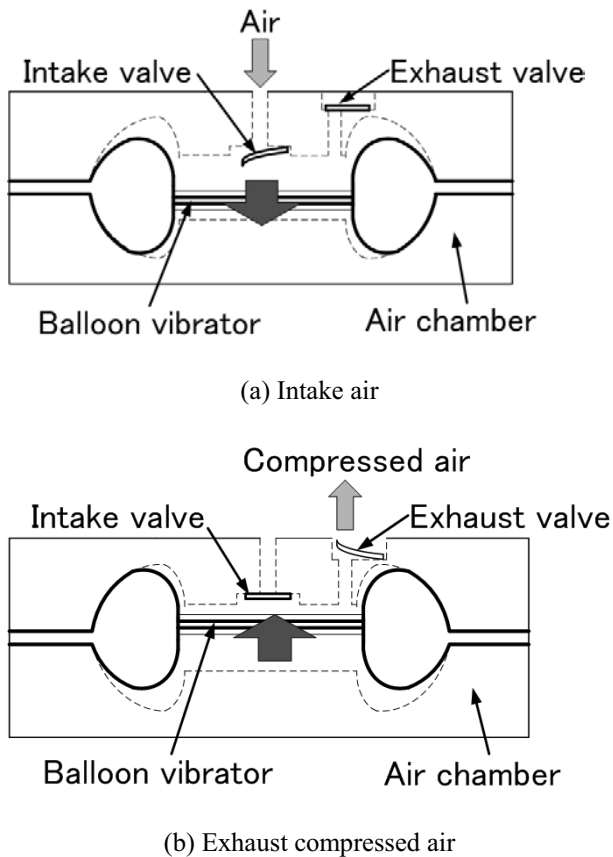
Figure 1 Principle of compression

STRUCTURE OF AIR PUMP

Structure

The developed pump in this study adopts the reciprocating type that is good for reduction in size and weight. And this pump is invented in order to improve defects of piston pumps and diaphragm pumps.

Figure 1 shows the principle of compression of the developed pump. This pump is constructed with an air chamber and a balloon vibrator. The vibrator is composed of a doughnut-shaped balloon diaphragm (shown in Figure 2) fitted with a circular stainless steel plate. The balloon diaphragm is filled with air and serves as a cylinder. By tucking the vibrator with the air chamber and vibrating the vibrator up and down, this pump can compress air.

This pump has characteristics as an oil-free, doesn't leak air at all, and has a longer stroke than existed diaphragm pumps because the vibrator moves using deformation of the balloon diaphragm. In addition, this pump can discharge higher pressure than existed diaphragm pumps because the balloon diaphragm has stiffness by filled with air. Therefore, this pump is expected to have higher discharge performance than existed diaphragm pumps.

Figure 3 shows the structure and the outlook of the prototype pump. This pump lets the balloon vibrator vibrate up and down by an electric motor and compress air. The movable stroke is ± 3.5[mm] from the center of the air chamber. As an intake and exhaust valve, flapper valves are attached. And the weight of this pump is 2.6[kg].

(a) Dimension

(b) Outlook
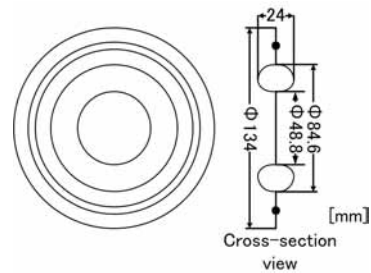
Figure 2 Balloon diaphragm

Characteristics of balloon vibrator

The balloon diaphragm has been originally contrived based on deformation analysis. This diaphragm is made of nitrile rubbers, which are generally used for diaphragms. In order to inhibit expansion of balloon when filled with air, fibers are interweaved inside the diaphragm. A tube with a 2[mm] outer diameter is attached on the side of the diaphragm in order to control the inner pressure of balloon. By controlling the inner pressure, the characteristics of the diaphragm can be changed.

Figure 4 shows the relation between the amount of displacement of the balloon vibrator and the resistance force on each inner pressure of balloon. The measuring condition is shown in Figure 5. The resistance force to move the vibrator ± 3.5[mm] from the center of the air chamber is measured by the force sensor. Figure 4 shows that the resistance force of the vibrator is linearly related to the amount of displacement, and shows that the inner pressure of balloon changes the stiffness of the balloon diaphragm. Figure 6 shows the stiffness on each inner pressure of balloon. Figure 6 shows that the stiffness is linearly related to the inner pressure of balloon.
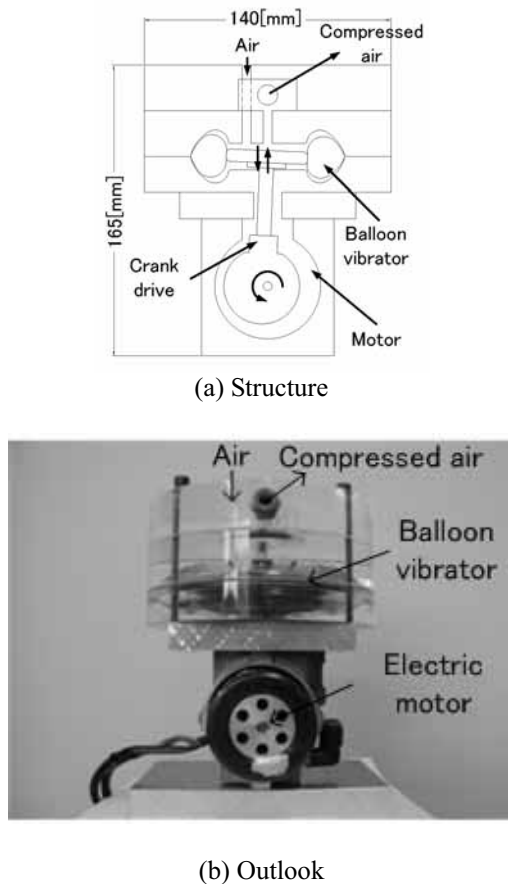
PERFORMANCE EVALUATION

Experimental system

To evaluate the performance of the developed pump, discharge pressure, flow rate and input power are measured. The experimental system is shown in Figure 7. The revolution speed is set at every 500[rpm] from 1000[rpm] to 3000[rpm]. The inner pressure of balloon is set at every 40[kPa] from 0[kPa] to 200[kPa] and controlled by the electro-pneumatic regulator manufactured by CKD. PA-103G manufactured by COPAL as pressure gauges, SEF-52 manufactured by STEC as a flow meter, and WT200 manufactured by Yokogawa Electric as a wattmeter are used for this experiment.
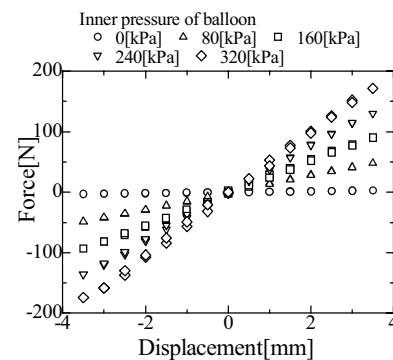
Figure 4 Relation between displacement and force
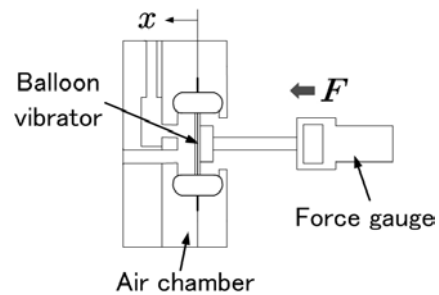
Figure 5 Measuring condition
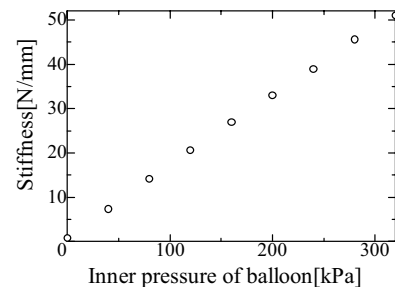
Figure 6 Characteristics of stiffness

(a) Structure

(b) Outlook

Figure 3 Prototype pump

Fundamental characteristics

Figure 8, 9, 10, 11 and 12 show the discharge performance and the pump efficiency of the developed pump on each revolution speed. Each figure shows the measurement result in the normal operation of the motor. The pump efficiency η is calculated using Eq. (1).

$$\eta = \frac{P \times Q}{W} \qquad (1)$$

From the figures, the maximum discharge pressure is about 250[kPa](the revolution speed 2000[rpm], the inner pressure of balloon 200[kPa]), the maximum flow rate is about 57[Nl/min](the revolution speed 3000[rpm], the inner pressure of balloon 200[kPa]), and the maximum efficiency is about 90[%](the revolution speed 2000[rpm], the inner pressure of balloon 200[kPa]). Therefore, the suggested pump mechanism using a balloon vibrator serves as the air pump well.

However, if the discharge pressure becomes higher than the inner pressure of balloon, the discharge performance comes down. When the discharge pressure becomes higher than the inner pressure of balloon, the balloon diaphragm gets dented and the volume of inside of the air chamber increases. The discharge volume by vibrating the vibrator decreases as much as the volume of inside of the air chamber increases. This is the reason why the discharge performance comes down.

In order to compare with the developed pump, the performance of an existed pump for medical use (shown in Figure 13) is evaluated too. The experimental system is the same as the developed pump. Figure 14 shows the discharge performance of the existed pump. From the figures, the maximum discharge pressure is about 280[kPa](the revolution speed 1500[rpm]), the maximum flow rate is about 55[Nl/min](the revolution speed 3000[rpm]), and the maximum efficiency is about 80[%](the revolution speed 2000[rpm]). Though the developed pump is inferior in the discharge pressure, it is comparable in the flow rate and superior in the pump efficiency to the existed pump.

Figure 7 Experimental system
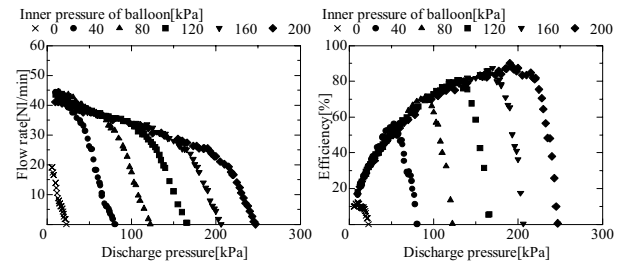
Figure 10 Characteristics of the pump (2000[rpm])

Figure 8 Characteristics of the pump (1000[rpm])
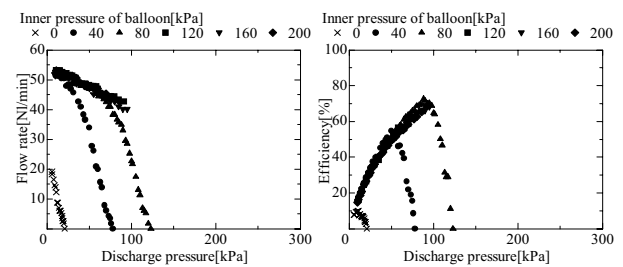
Figure 11 Characteristics of the pump (2500[rpm])

Figure 9 Characteristics of the pump (1500[rpm])
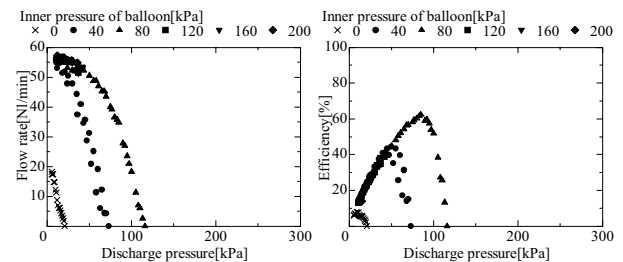
Figure 12 Characteristics of the pump (3000[rpm])

Application to output variable air pump

Figure 15 shows the discharge volume per cycle. Though the maximum volume is about 0.025[Nl/cycle], the volume tends to decrease as the revolution speed increases. It is thought that flapper valves don't work well at the high revolution speed. Therefore, it is needed to consider the size, the configuration, and the mounting location of the valves.

From the figures, the discharge pressure doesn't depend on the revolution speed but the inner pressure of balloon. Therefore, the developed pump can meet various uses only to change the inner pressure of balloon without changing the mechanical structure. In addition, it is expected to apply to an output variable pump that can change the discharge performance continuously by controlling the inner pressure of balloon.

(a) Side view

(b) Top view

Figure 13 Outlook of existed pump
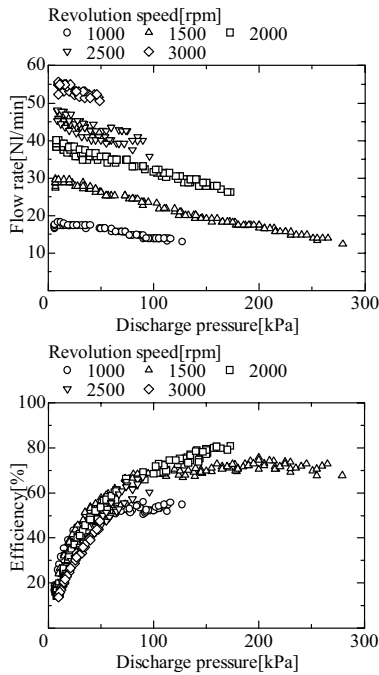
Figure 14 Characteristics of existed pump
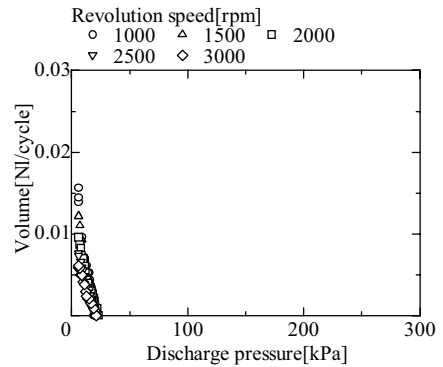
(a) Inner pressure of balloon 0[kPa]
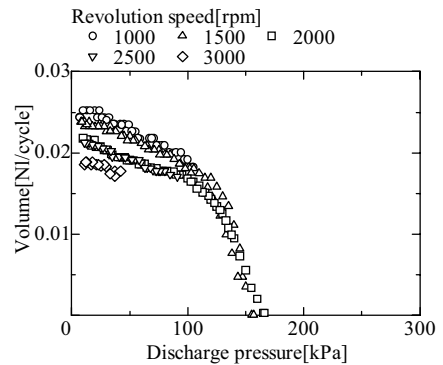
(b) Inner pressure of balloon 120[kPa]
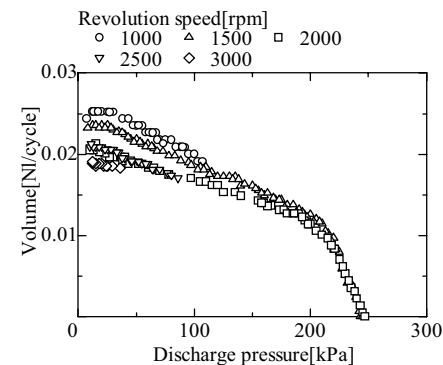
(c) Inner pressure of balloon 200[kPa]

Figure 15 Relation between pressure and volume

741

So, the discharge pressure is measured in setting the revolution speed 2000[rpm], the flow rate 0[Nl/min], and changing the inner pressure of balloon every 40[kPa] in a step from 0[kPa] to 200[kPa]. The discharge pressure is changed continuously by changing the inner pressure of balloon as shown in Figure 16.

In order to realize the output variable pump, it is needed to use compressed air which the developed pump itself discharges to control the inner pressure of balloon. It means the inner pressure of balloon is less or equal to the discharge pressure. Therefore, it is needed to consider the control method, even as to look into the possibility more.
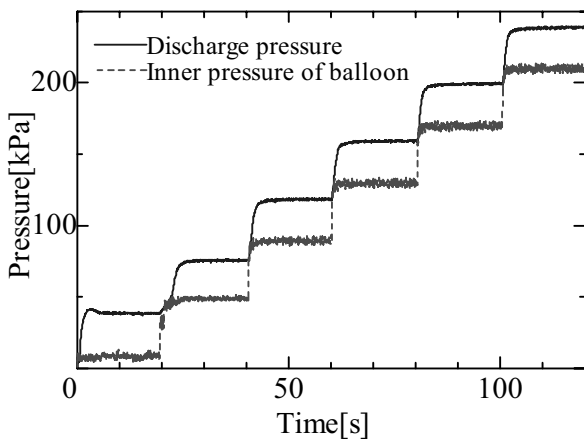
Figure 16 Output variable air pump

CONCLUSION

In this paper, it is described about the air pump using the balloon vibrator for wearable devices and shown that the suggested pump mechanism serves as the air pump well from the performance experimentally evaluated. The balloon diaphragm originally contrived has a linear stiffness and the inner pressure of balloon can control the discharge performance. These characteristics are very useful functions for the design of the air pump.

Issues for the future are shown as follow.

- The design of the most suitable air chamber and the select of the most suitable motor for the reduction in size and weight in order to use for wearable devices.
- The design of the most suitable valves to improve intaking and exhausting air
- The test and improvement of the durability of the balloon diaphragm
- The reduction of noise level and vibration
- The invention of control method for the output variable pump.

REFERENCES

1. Hydraulic and Pneumatics, Vol.45 No.11, 2006 (in Japanese)
2. T. Noritsugu, J. Han, and M. Takaiwa, Development of a Miniature Compressor Driven with a Linear Electromagnetic Actuator, Transactions Of The Japan Fluid Power System Society, Vol.33 No.4, pp.83-90, 2002 (in Japanese)
3. Jose A.Riofrio, Eric J.Barth, Design of a Free Piston Pneumatic Compressor as a Mobile Robot Power Supply, Proceedings of the 2005 IEEE, International Conference on Robotics and Automation (DVD-ROM), pp.236-241, 2005
4. A. Kitagawa, H. WU, H. Tsukagoshi, S. Park, Development of a Portable Pneumatic Power Source Using Phase Transition at the Triple Point, Transactions Of The Japan Fluid Power System Society, Vol.36 No.6, pp.158-164, 2005 (in Japanese)

EXPERIMENTAL EXAMINATION ON THE THRUST ENERGY OF SHOCK ABSORBERS FOR PNEUMATIC CYLINDERS

KeitaroYOSHIDA*, KatushiSATOH*, YukioKAWAKAMI*,
Akiyoshi HORIKAWA**, Yuta OMURA**

* Department of Factory System Engineering, Shibaura Institute of Technology
307 Fukasaku, Minuma-ku, Saitama, 337-5870 Japan
(E-mail: m408064@sic.shibaura-it.ac.jp)
** Koganei Corporation
3-11-28Midorityo, Koganei-shi, Tokyo, 184-8533 Japan

ABSTRACT

Shock absorbers are vital devices for high speed driving with pneumatic cylinders and it is important to select the suitable shock absorbers to use pneumatic systems without trouble. It is commonly believed that the absorbed energy by the shock absorber is the sum of kinetic energy and thrust energy, which are important parameters to set up the pneumatic system. In a typical selecting method of the shock absorber, the value of thrust energy is estimated from the value of only supply pressure. However, the selecting method has been regulated for hydraulic systems and the estimated value of thrust energy in the pneumatic systems is not approximate, because inner pressures in the pneumatic cylinder is not stable and quite different from the supply pressure. Finally there are many bad combinations of the cylinder and shock absorber in the pneumatic system.

In the research, we experimentally investigate the formula for estimation of the thrust energy, which is defined in the selecting method of shock absorbers. Experimental results show that accuracy of the formula to select the shock absorber is inefficient. Additionally we examine on parameters that affect the thrust energy and compensate the formula.

KEY WORDS

Shock absorber, Absorption energy, Evaluation formula, Pneumatics

NOMENCLATURE

E : Collision energy
E_V : Max collision energy with velocity V
E_1 : Kinetic energy
E_2 : Thrust energy
m : Mass of load
P : Differential pressure
F : Thrust of cylinder
E_m : Max absorption energy
V_m : Max velocity of collision
L : Stroke of absorption
V : Velocity of collision
D : Diameter of cylinder
α : Variable of situation
β : Variable of situation

INTRODUCTION

There have been many various systems with pneumatic cylinders in the manufacturing industry. Generally, shock absorbersare used along with the pneumatic cylinders, becauseit is necessary to cushion the impact and vibration when the cylinder is stopped at a stroke end.

To select the appropriate shock absorbers for the cylinder, it is important that the absorbed energy by the shock absorber, which is composed of kinetic energy and thrust energy, is estimated. In a typical selecting method of the shock absorber the value of thrust energy is derived from the supply pressure. It is a problem that the estimated value is not approximate because inner pressure in the pneumatic cylinder is not stable and quite different from the supply pressure. Finally there are many bad combinations of the cylinder and shock absorber in the pneumatic system.

We have experimentally investigated the formula for estimation of the thrust energy, which is defined in the selecting method of shock absorbers. Especially, an influence of the compressible differencebetween hydraulic and pneumaticis considered.

SHOCK ABSOBER

Figure 1 shows typical charactersaboutthree kinds of shock absorbers. These characteristics depend on the inner structure of shock absorbers. Show inner the structure of shock absorbers in figure 2. First, shock absorber is assist device that generate force for frequency and shock at stroke end. Naturally it isn't good thateven if force to generate is too strong and weak. Thus, the selection of shock absorber is very important.
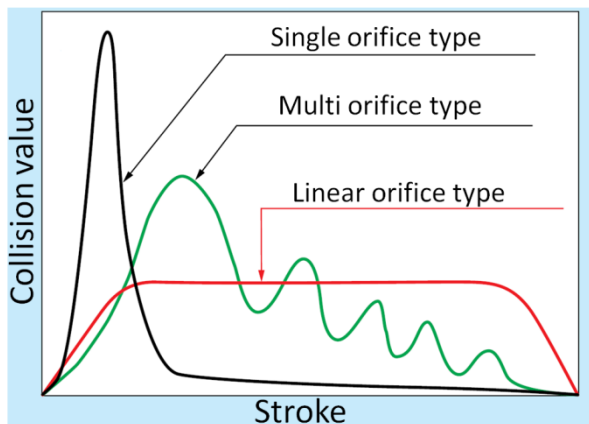
Figure 1   Characters of shock absorbers

(a) Single   (b) Multi   (c) Linear
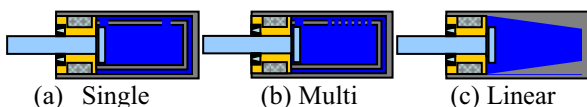
Figure 2   Inner structure of shock absorbers

SELECTED FORMULA

Selected formulas, to use now, are shown in Eq.(1)~(3).

$$E_V = \frac{V \times E_M}{V_M} \qquad (1)$$

$$E = E_1 + E_2 = \frac{mV^2}{2} + F \cdot L \qquad (2)$$

$$F = \frac{\pi D^2}{4} \times P \qquad (3)$$

It is made up two elements: we consider that given energy of shock absorber equal total of kinetic energy and thrust energy, E_1:kinetic energy, E_2:thrust energy. Especially, thrust energy is influenced by compaction property of working fluid. Hence, supply pressure by tank is employed when calculation of thrust,but it is not always true that the value equal actual value.

COLLISION EXPERIMENT

We experimented with device such as figure 3.This device is simply, because, we installed speed controller, load, displacement gauge, pressure gauge on rodless cylinder and connected tank. We let work collide in shock absorber as well as record displacement of work, pressure of supply side and exhaust side. Show the list of changed parameter in experiment for table 1.
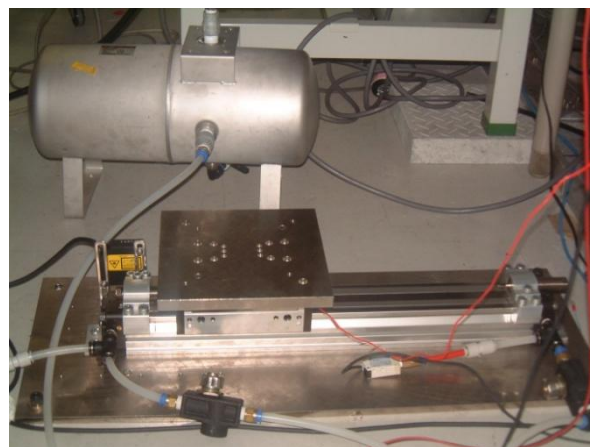
Figure 3   Experimental device

Table 1   Changing parameter

Supply pressure[MPa]
0.3, 0.35, 0.4, 0.45, 0.5
Diameter of cylinder[mm]
16, 25, 40
Load[kg]
2, 4, 9 (D=16)
2, 4, 9, 14, 19, 24, 29 (D=25,40)

RESULT AND DISCUSSION

Result of experiment
First, show an example of the experimental results in figure 4.
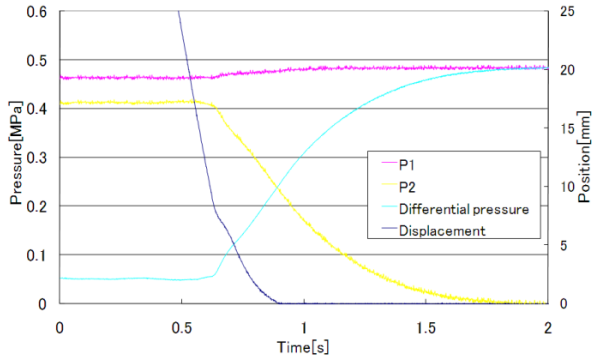
Figure 4   Experimental results (D=16, m=2, P=0.5)

Aqua line of figure 4represents differential pressure in experiment. This value is important to calculate collision energy, because, it yields thrust, Eq.(3). Stroke of shock absorber with experiment device is 10[mm], so we can consider that work was starting to collide in shock absorber when displacement of figure 4 equal 10. So, we assumed differential pressure when stareting to collide in it is reference value for parameter P. On that basis, we calculated theoretical and experimental value of collision energy. Figure 5 shows theoretical and experimental values of collision energy.
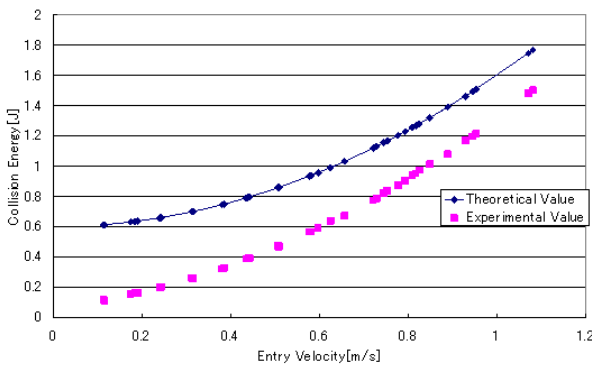
Figure 5   Collision energy (D=16, m=2, P=0.3)

Influence of pressure
We showed collision energy in figure 5, but collision energy encompasses kinetic and thrust energy. Of them, as for value of kinetic energy, both theoretical and experimental are the same. Now, therefore, figure 6 is derived thrust energy from collision energy and plots each velocity.Figure 6 represents that experimental value is generally lower than theoretical value and changed by velocity. So, change of experimental values

by supply pressure is smaller than theoretical values. From Eq. (2),(3) selected formulas don't contain velocity term. Conversely, selected formulas contain pressure term. These things are new items considered by us.
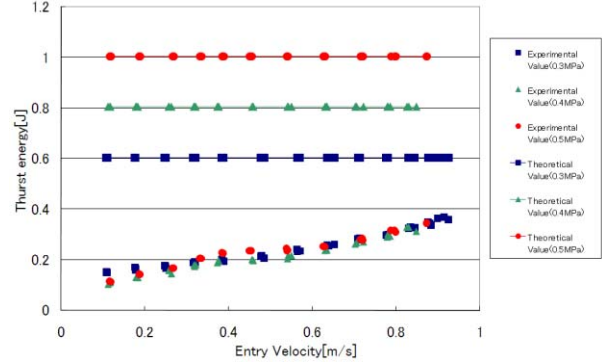
Figure 6   Change of thrust energy (D=16, m=2)

Influence of load
In this section, an influence of loadis considered. Figure 7 shows results of changing load.We can make sure two type that change of thrust energy is effected from load.One is made up two straight lines, another is made up line and curve.
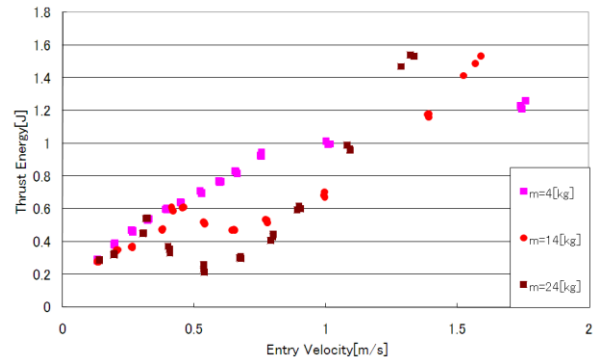
Figure 7   Result of changing load (D=25, P=0.5)
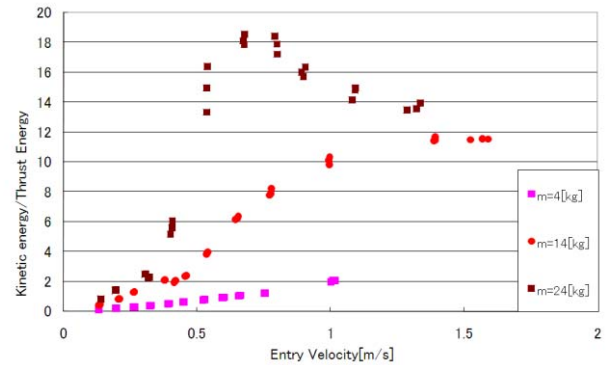
Figure 8 Kinetic energy and thrust energy（D=16, P=0.5）

Straight line is dominant when low load, curve is dominant when heavy load. Thrust energy term of selected formula also doesn't contain load term. However, effect of load isn't only thrust energy. Figure 8 shows ratio of thrust energy to kinetic energy.

If load is heavy, ratio of kinetic energy becomes big and effect of thrust energy is small. By contraries, if load is low, ratio of kinetic energy becomes small and effect of thrust energy is big. So, difference between heavy and low load is a little when velocity is low. Hence, we have to become more chariness to use shock absorber when velocity is not high.

Transition of differential pressure
Transition of the thrust energy is linked withtransition of the differential pressure. The differential pressure is affected by compressibility of pneumatic, and it changes by situation of the experimental device. Figure 9 show example of transition ofthe differential pressure.
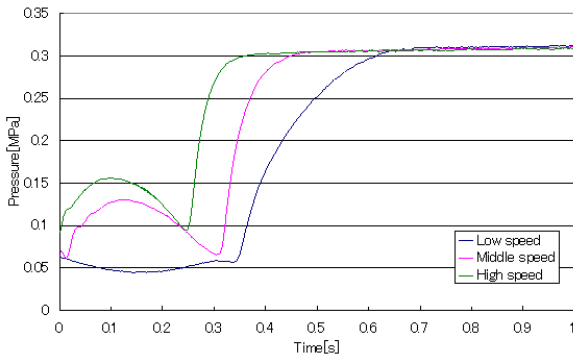
Figure 9　Transition of differential pressure

Approximate equation
If it is assumed that values of the velocity and load are small and the thrust energy is proportional to the velocity, the approximate equation become to Eq. (4).

$$\mathbf{E_2 = \alpha V + \beta} \qquad (4)$$

α and β represent variable of situation. These change upon situation of experimental device. For example, supply pressure, stroke of cylinder, etc. Especially, we consider five points is important from compaction property of pneumatic and experiment.

1. Supply pressure
2. Stroke of cylinder
3. Velocity
4. Diameter of cylinder
5. Load

Figure 10 and 11 show actually appliedEq. (4).If apply Eq. (4), have to fix α and β. In this case, we fixed from many experiment. But, there is a problem in precision

still more. Experimental value is nearly linear when diameter of cylinder is small. However, error becomes large when diameter of cylinder is big. Even so, compensation value is more accurate than theoretical.
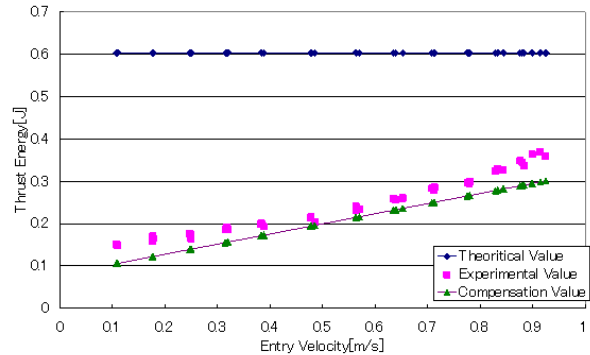
Figure 10Results of compensation (D=16, m=9, P=0.3)
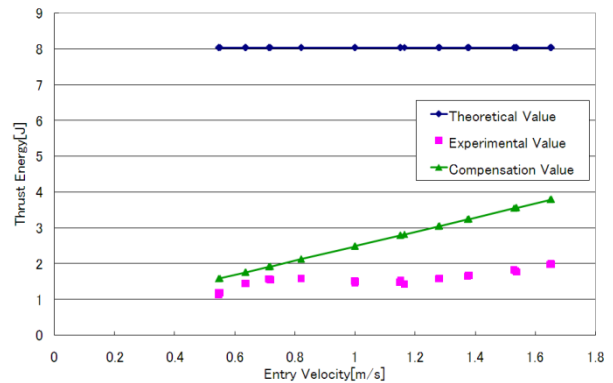
Figure 11Results of compensation (D=40, m=4, P=0.4)

CONCLUSION

Weexperimentally investigate the formula for estimation of the thrust energyin the typical selecting method of the shock absorber.Experimental results show that accuracy of the formula by the supply pressure is inefficient. Additionally we examine on parameters that affect the thrust energy and compensate the formula. The formula with the compensationis as follows.

$$\mathbf{E = E_1 + E_2 = \frac{m \times V^2}{2} + (\alpha V + \beta)} \qquad (5)$$

REFERENCES

1. Koganei corporation HP
   http://www.koganei.co.jp/
2. Japan Fluid Power Association , practical pocketbook of pneumatic, Japan, 1986, pp.285-289.

P2-29

SIMULATION OF DYNAMIC CHARACTERISTICS OF AIR GRIPPER BY A NEW BOND-GRAPH METHOD

Yasuo SAKURAI *, Yoshitaka HANEISHI *, Kazuhiro TANAKA**,
Takeshi NAKADA*** and Takehisa KOHDA ****

* Ashikaga Institute of Technology
268-1 Oomaecho, Ashikaga, Tochigi, 326-8558 Japan
(E-mail: ysakurai@ashitech.ac.jp)
** Kyushu Institute of Technology
680-4 Kawazu, Iizuka, Fukuoka 820-0067, Japan
*** Tokyo Denki University
2-1200 Muzai gakuendai, Innzai City, Chiba, 270-1382 Japan
**** Kyoto University
Yoshida-honmachi, Sakyo-ku, Kyoto 606-8501 Japan

ABSTRACT

This paper deals with the simulation of the dynamic characteristics of an air gripper by a new bond-graph method. Recently, pneumatic systems are widely used with food equipments and wrapping ones, etc. However, the design and the improvement of those pneumatic systems take much time because they depend largely on the experience of designers. In order to make them more effective and systematic, it is necessary and important to predict the dynamic behavior of the system beforehand by computer simulation. An air gripper is often used as an actuator in a pneumatic system. However, there are few reports focused on its dynamic characteristic as authors know. In this paper, to obtain a suitable mathematical model for an air gripper and to show the usefulness of the proposed bond-graph method, both experimental and simulation studies are performed. In modeling for pneumatic field, the new bond-graph method is employed, which had been proposed by some of authors. In the bond-graph method, a pneumatic system can be represented by using conventional 1-port C and 1-port R elements.

KEY WORDS

Pneumatics, Air Gripper, Bond-graph method, Dynamic Characteristics, Simulation

NOMENCLATURE

A : area [m^2]
A_e : effective area [m^2]
M : mass of air in a chamber or a volume [kg]
$\dot{m}$: mass flow rate [kg/s]
P : absolute pressure [Pa]
R : gas constant [J/(kg·K)]

T : absolute temperature [K]
t : time [s]
V : volume [m^3]
v : velocity [m/s]
x : displacement [m]
κ : specific heat ratio
Subscripts
A : atmosphere

E : experiment
F : finger
H : head side of an air gripper
P : piston
R : rod side of an air gripper
S : air supply
Si : simulation
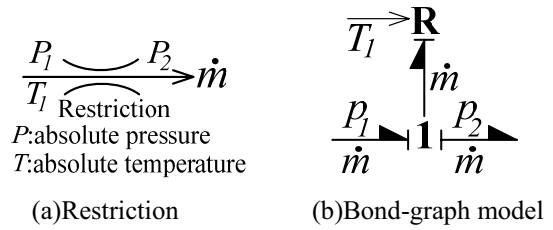
INTRODUCTION

Recently, pneumatic systems are widely used with food equipments and wrapping ones, etc. Generally speaking, the design and the improvement of those pneumatic systems take much time because they depend largely on the experience of designers. In order to make them more effective and systematic, it is necessary and important to predict the dynamic behavior of the system beforehand by computer simulation.

Pneumatic systems have mechanical and pneumatic fields. Pneumatic field has compressible fluid-flow and thermal fields. In constructing the bond-graph model for such a system, true or pseudo bond-graph has so far been employed. Furthermore, in constructing the model for the pneumatic field, two kinds of bonds, which represent both fluid power and thermal power, have been used, and multi-port C and multi-port R elements have been frequently used in the model as well [1-6]. Hence, the resulting bond-graph models are complicated. Then, a new bond-graph method had been proposed [7]. In the bond-graph method, the bond-graph models for pneumatic components are derived by using 1-port C and 1-port R elements. However, the usefulness of the method is not clear because the comparison of the simulated results with the experimental ones has not been shown.

An air gripper is often employed as an actuator in a pneumatic system. However, there are few reports focused on its dynamic characteristic as authors know.

In this study, to obtain a suitable mathematical mode for an air gripper and to confirm the usefulness of the proposed bond-graph method, both experimental and simulation studies are performed. In simulation, Mr.Bond [8] is used, which is a simulation program for bond-graph model.

OUTLINE OF NEW BOND-GRAPH METHOD

In this section, outline of a new bond-graph method [7] is shown, that is, each bond-graph model for restriction, chamber of a pneumatic cylinder and a volume of a pipeline is shown. In constructing the bond-graph model for pneumatic field, pseudo bond-graph is employed, in which effort is absolute pressure and flow is mass flow rate. In mechanical field, true bond-graph is used, in which effort is force and flow is velocity.

P:absolute pressure
T:absolute temperature

(a)Restriction   (b)Bond-graph model

Figure 1 Bond-graph model for restriction

Restrictive element
At a restriction illustrated in Fig. 1(a), the continuity equation yields

$$\dot{m}_1 = \dot{m}_2 = \dot{m} \qquad (1)$$

where $\dot{m}_i$ (i=1,2) is the mass flow rate through cross sections 1 and 2 in Fig. 1(a), respectively.
The mass flow rate through the restriction can be expressed by Eq. (2) and (3).

$$0 \le \frac{P_2}{P_1} < 0.528$$

$$\dot{m} = A_e P_1 \sqrt{\frac{\kappa}{RT_1}\left\{\left(\frac{2}{\kappa+1}\right)^{\frac{\kappa+1}{\kappa-1}}\right\}} \qquad (2)$$

$$0.528 \le \frac{P_2}{P_1} \le 1$$

$$\dot{m} = A_e P_1 \sqrt{\frac{2\kappa}{\kappa-1}\frac{1}{RT_1}\left\{\left(\frac{P_2}{P_1}\right)^{\frac{2}{\kappa}} - \left(\frac{P_2}{P_1}\right)^{\frac{\kappa+1}{\kappa}}\right\}} \qquad (3)$$

As can be seen from Eq. (1), flow $\dot{m}$ is equal at the restriction. And, from Eqs. (2) and (3), flow $\dot{m}$ is expressed as a function of effort P_1 and P_2. Therefore, the restriction can be represented by 1-junction and an R-element as shown in Fig. 1(b). In order to calculate mass flow rate $\dot{m}$ based on Eqs. (2) and (3), temperature T_1 is necessary. Therefore, temperature T_1 is inputted to R-element through the active bond which is denoted by full arrow and transmits a signal.

Capacitive elements
At a head-end chamber of a pneumatic cylinder shown in Fig. 2, the heat transfer through a wall is assumed to be neglected to make the bond-graph structure simple. Then, from the first law of thermodynamics, Eq. (4) can be derived.

$$\frac{dP}{dt} = \frac{\kappa}{V}\left(R\dot{m}T^* - PAv\right) \qquad (4)$$

Assuming that T^* and P in the right-hand side of Eq. (4) can be replaced with the values at one time step before

Figure 2 Head-end chamber of pneumatic cylinder

Figure 4 Rod-end chamber of pneumatic cylinder

Figure 3 Bond-graph model for head-end chamber of
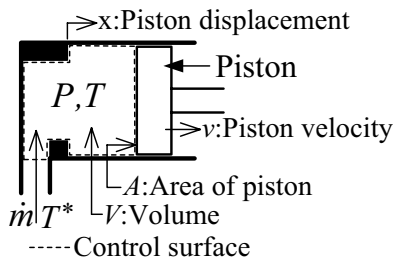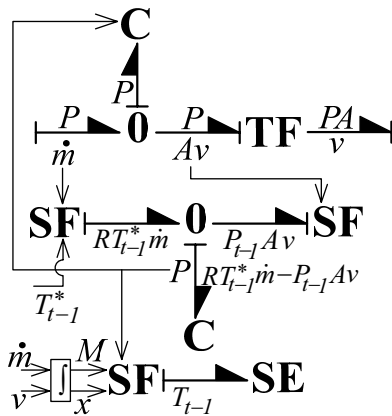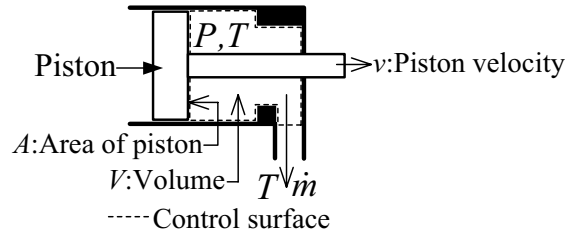pneumatic cylinder
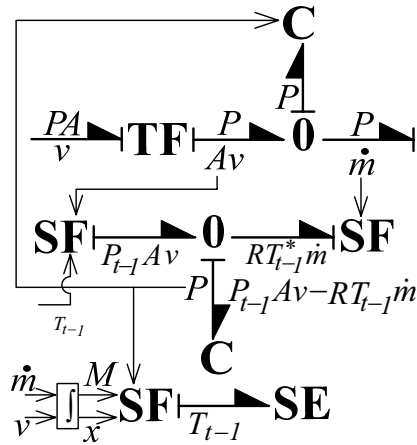
Figure 5 Bond-graph model for rod-end chamber of
pneumatic cylinder

the time, we get Eq. (5):

$$P = \frac{\kappa}{V_{H0} + Ax} \int \left(RT^*_{t-1} \, \dot{m} - P_{t-1} A v \right) dt + P_{H0} \quad (5)$$

where V_{H0} is the head-end chamber dead volume and P_{H0} is the initial pressure at the chamber.

As can be seen from Eq. (5), effort P can be determined by integrating flow $\dot{m}$ and v. And effort P is equal in the head-end chamber of the pneumatic cylinder. Hence, the head-end chamber of pneumatic cylinder shown in Fig. 2 can be modeled by a C-element and 0-junction as shown in Fig. 3. However, in order to calculate effort P from Eq. (5), two SF-elements and a C-element is employed. And then, this C-element is used as a mere integrator. Furthermore, to calculate the temperature of air in the head-end chamber of pneumatic cylinder from Eq. (6), an SF-element and an SE-element are employed as a mere calculator. And then, the flow of the bond between these elements represents the temperature of air in the head-end chamber of pneumatic cylinder at one time step before the time.

$$T = \frac{PV}{MR} \quad , \quad T_{t-1} = T \qquad (6)$$

Similarly, the pressure at the rod-end chamber of a pneumatic cylinder shown in Fig. 4 can be determined by Eq. (7).

$$P = \frac{\kappa}{V_{R0} - Ax} \int \left(-RT_{t-1} \, \dot{m} + P_{t-1} A v \right) dt + P_{R0} \quad (7)$$

In Eq. (7), V_{R0} is the volume of the rod-end chamber when piston displacement x is equal to 0.

As seen from Eq. (7), effort P can be calculated by integrating flow $\dot{m}$ and v. And effort P is equal in the rod-end chamber of the pneumatic cylinder. Therefore, the rod-end chamber of pneumatic cylinder can be represented as shown in Fig. 5. Then, it should be noted that the temperature of air in the rod-end chamber is used in calculating the pressure of air in the chamber by Eq. (7).

Similarly, the pressure in a pipeline shown in Fig. 6 can be represented by Eq. (8).

$$P = \frac{\kappa R}{V} \int \left\{ (T_1)_{t-1} \dot{m}_1 - (T_2)_{t-1} \dot{m}_2 \right\} dt + P_0 \qquad (8)$$

In Eq. (8), P_0 is the initial value of the pressure in the pipeline.

749
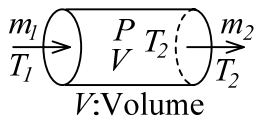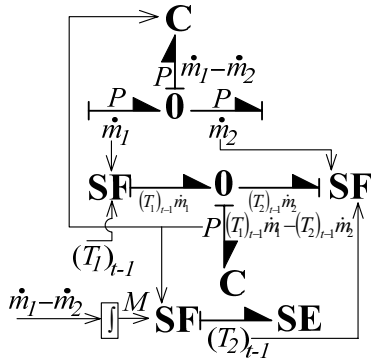
Figure 6 Pipeline

Figure 7 Bond-graph model for pipeline

As seen from Eq.(8), effort P can be calculated by integrating flow $\dot{m}$. And effort P is equal in the pipeline. Therefore, the pipeline can be modeled by bond-graph as shown in Fig. 7. In calculating the pressure of air in the pipeline by Eq. (8), it should be noted that the temperature of air in the pipeline is used.
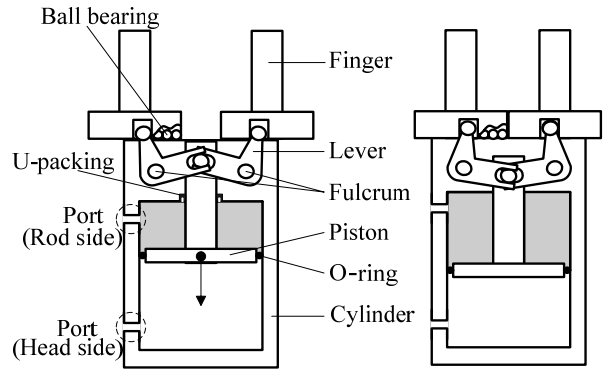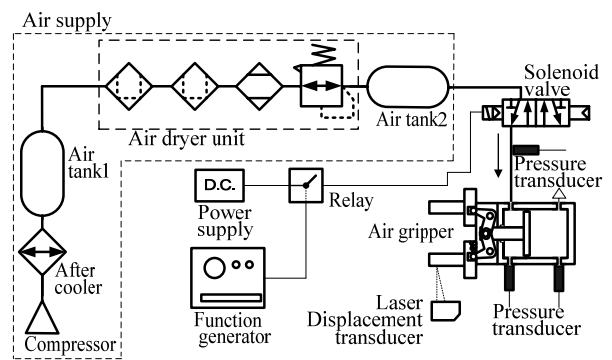
STRUCTURE OF AIR GRIPPER

The structure of an air gripper is shown in Fig.8. When compressed air flows into the rod end chamber of the air gripper through the port, the levers revolve around the fulcrum and the piston moves downward. And then, the fingers close. In the case where compressed air flows into the head end chamber of the air gripper through the other port, the fingers open. In this study, simulation and experiment are carried out for the case where the fingers close.

BOND-GRAPH MODEL FOR AIR GRIPPER

Figure 9 shows the pneumatic system with an air gripper as an actuator. The compressed air through a solenoid valve flows into the rod end chamber of the air gripper. And then, the fingers close.
By using the bond-graph models for restrictive element and capacitive ones mentioned before, the bond-graph model for pneumatic system in Fig. 9 can be derived. The resulting bond-graph model for the pneumatic system is represented in Fig.10. In constructing the bond-graph model, the followings are assumed:
• At the air supply, both pressure P_S and temperature

Figure 8 Structure of air gripper

Figure 9 Pneumatic system

A_R:Area of the head side of the piston
A_H:Area of the rod side of the piston
$\dot{m}_1$:Mass flow rate through solenoid valve
$\dot{m}_2$:Mass flow rate through rod side port
$\dot{m}_3$:Mass flow rate through head side port
P :Pressure at the pipeline between air tank2 and solenoid valve
P_A :Atmospheric pressure
P_H:Pressure (head side)
P_R:Pressure (rod side)
P_S :Air supply pressure
T_1:Temperature of supply air
T_2:Temperature of air in the pipeline between solenoid valve and air gripper
T_3: Temperature of air (rod side)
T_4: Temperature of air (head side)
v_1:Piston velocity
v_2:Finger velocity

Figure 10 Bond-graph model for pneumatic system
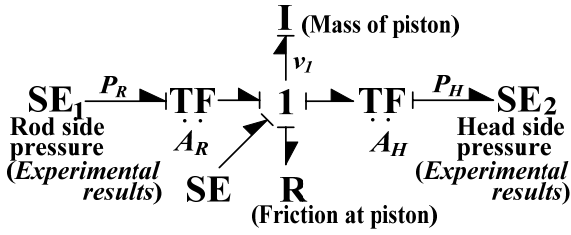
Figure 11 Bong-graph model for air gripper without levers and fingers
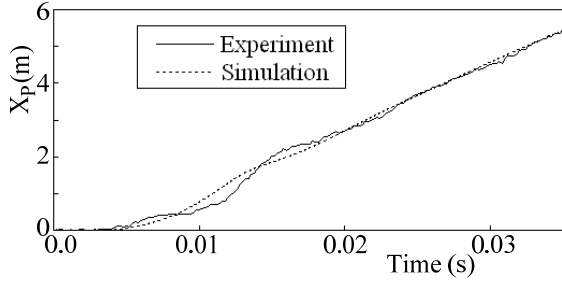
Figure12 Experimental and simulated results for air gripper without levers and fingers

Figure 13 Simulated and experimental results (P_S=0.4MPa abs)

T_1 of air are constant.

- The pressure and temperature of air upstream of the solenoid valve are equal to those at air supply.
- The heat transfer through the wall is neglected at the pipeline between the solenoid valve and the port at the rod end side of the air gripper, at the rod-end chamber and the head-end one of the air gripper.

SIMULATION AND EXPERIMENT

Prior to simulation, it is necessary to predict the friction of the air gripper. Firstly, to predict the friction at the piston of the air gripper, experiments and simulations were carried out for the air gripper without the finger and the lever. The bond-graph model to predict the friction of the piston is illustrated in Fig.11. Based on the bond-graph model, the simulations were carried out varying supply pressure P_S. Then, the effort of the bond connected to SE_1 was pressure P_R in the rod end chamber obtained by the experiment, and the effort of the bond connected to SE_2 was pressure P_H in the head end chamber obtained by the experiment at the same time. And, by comparing the experimental results and the simulated ones, the friction at the piston was predicted. Figure 12 shows an example of a comparison of piston displacement X_P in both the experiment and the simulation.

Consequently, it becomes clear that its stiction is 5.0N and friction F_D in the case where the piston moves can be approximated by Eq. (9) and coefficient of friction K_D in Eq. (9) is 95.0N·s/m.

$$F_D = K_D \cdot v \qquad (9)$$

Secondly, by using air gripper with the levers and fingers, the above mentioned experiments and simulations were carried out. As a result, the friction characteristics became close to ones in the case where the air gripper without the levers and the fingers was employed. Therefore, it is shown that the friction of the air gripper is mainly determined by the friction at the piston.

By using the predicted friction characteristics and the bond-graph model expressed in Fig.10, the simulations were carried out varying supply pressure P_S. The comparison of the simulated results and experimental ones are shown in Fig.13 and Fig.14. The comparison of time t_E and t_{Si} is shown in Table 1. In this table, time t_E and t_S denote the time until the fingers close in the experiment and the simulation respectively. As seen from Figs. 13 and 14, the simulated results agree with experimental ones. Therefore, the proposed new bond-graph method is proved to be valid and useful for the modeling of a pneumatic system. In addition to it, the bond-graph model for an air gripper proposed in this paper is suitable in the prediction of its dynamic characteristics. And from Table 1, by using this bond-graph model, the time until the fingers close can be predicted within 7.0% error.
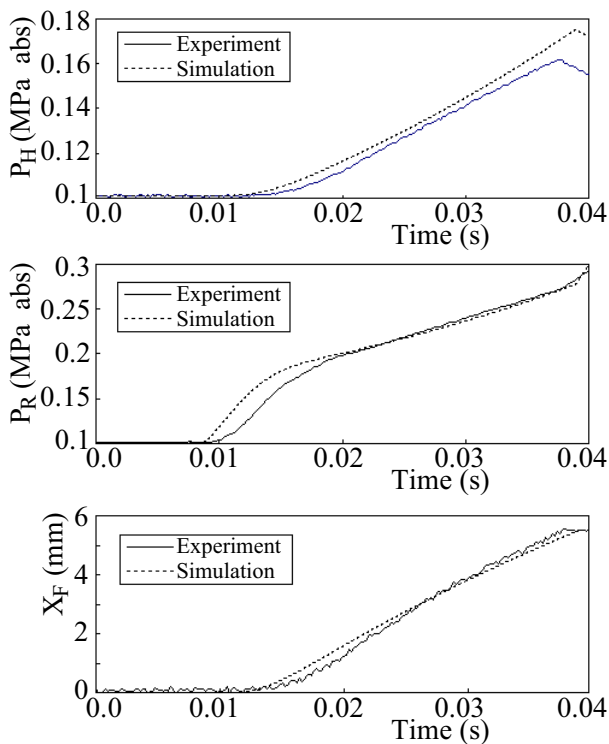
Figure 14 Simulated and experimental results
(P_S=0.6MPa abs)

Table 1 t_S and t_E

P_S (MPa abs)	t_E (ms)	t_S (ms)	$t_E - t_S$ (ms)	$\dfrac{t_E - t_S}{t_E}$ (%)
0.3	52.8	56.5	3.7	7.0
0.4	45.4	47.8	2.4	5.3
0.5	41.0	42.6	1.6	3.9
0.6	37.8	38.8	1.0	2.7

CONCLUSIONS

The bond-graph model for an air gripper is derived by a new bond-graph method. By the use of the bond-graph method, restrictive or capacitive element in pneumatic system can be represented by 1-port R or 1-port C element. To clarify the validity of the bond-graph model for the air gripper and the usefulness of the new bond-graph method, experiments and simulations were carried out.

The simulated results agree with the experimental ones, and the validity of the bond-graph model for the air gripper and the usefulness of the new bond-graph method are shown.

This study has been supported by SMC Co., Ltd.. We would like to thank here for their cooperation.

REFERENCES

1. Rosenberg, R.C. and Karnopp, D.C., Introduction to Physical System Dynamics, McGraw-Hill, 1983.
2. Shoureshi,R. and McLaughlin,K.: Analytical and Experimental Investigation of Flow-Reversible Heat Exchangers Using Temperature-Entropy Bond Graphs, ASME Journal of Dynamic System, Measurement, and Control, 1984, **106**-6, pp.171/175.
3. Shoureshi,R. and McLaughlin,K., Application of Bond Graphs to Thermofluid Processes and Systems, ASME Journal of Dynamic System, Measurement, and Control, 1985, **107**-12, pp.241-245.
4. Thoma, J.U., Simulation by Bondgraphs, Springer-Verlag, 1990.
5. Thoma, J.U. and B. Ould Bouamama, Modelling and Simulation in Thermal and Chemical Engineering, Springer, 2000.
6. Ikeo, S., Zhang, H., Takahashi, K. and Sakurai, Y., Simulation of Pneumatic Systems Using BGSP, Modeling and Simulation, 1994, pp.80/94.
7. Sakurai, Y., Tanaka, T., Nakada, T and Kohda, T, Simulation of the Dynamic Characteristics of a Pneumatic Circuit by OHC-Sim, Proc. of 6th JFPS Symposium on Fluid Power, 2005, pp.346-351.
8. http://sys.tadano.co.jp/frame/frame3_5.html

P2-30

THE HYDRODYNAMICS BEHAVIOUR OF AUTOMATIC EXTINGUISHING SYSTEM

Marijonas BOGDEVICIUS*, Jolanta JANUTENIENE** and Vladimir SUSLAVICIUS*

* Department of Transport Technological Equipment, Faculty of Transport Engineering
Vilnius Gediminas Technical University
27 Plytines, Vilnius, 10105 Lithuania
(E-mail: marius@ti.vgtu.lt)
** Department of Mechanical Engineering, Marine Technical Faculty
Klaipeda University
17 Bijunu, Klaipeda, 91206 Lithuania

ABSTRACT

A simple way to increase the extinguishing water surface area is to atomize water into fine drops. The smaller drops are developed, the better use of water properties can be implemented and less water is consumed in fire fighting. The automatic impulse extinguishing is created. The main aim of the investigation is to develop the approach to investigate the dynamic and hydrodynamic processes in the extinguishing device. The mathematical model of the extinguishing device is presented, where the flow of liquid and gas and the interaction of liquid with the gas are taken into account. The flow of fluid in a hydraulic system is described by a system of equations of a hyperbolic type, which is solved by a characteristics method. An instance of the mathematical simulation of the activity extinguishing device is shown.

KEY WORDS

Extinguishing device, gas, liquid, dynamics, numerical methods

NOMENCLATURE

a_x : acceleration along x axis

a_{gx} : acceleration of gas along x axis

$C(Re, v)$: function

c_g, c : sound velocity in the gas and liquid

d : internal diameter of a pipeline

E : modulus of elasticity of a pipeline

e : thickness of a wall of a pipeline

$\{F(t, p, v)\}$: vector of external forces and moments

F_{aero} : air resistance force

f_{mv} : force

f_{pv} : function

G_{in} : input mass flow

G_{out} : output mass flow of gas (air)

$[J]$: Jacobian matrix,

$K(p)$: bulk modulus of elasticity of liquid

L_2 : length of pipeline (second chamber).

$[M]$: matrix of mass

m_v : mass of fast response valve mechanism

N : number of drops

$p; p_g$: pressure of fluid; pressure of gas

Q : thermal quantum

$\{q\}$	:	vector of displacement
$\{\dot{q}\}; \{\ddot{q}\}$	:	vector of velocity; vector of acceleration
R	:	gas constant
$S(x)$	:	cross section area of a pipeline
S_{v1}	:	cross-section area of the first valve
S_{v2}	:	cross-section area of the second valve
T	:	temperature of fluid
$v; \ v_g$	:	velocity of fluid; velocity of gas
ε	:	ratio of gas volume in the liquid
γ	:	index of adiabatic process
$\varphi(\sigma)$	:	piecewise flow function
μ_1	:	orifice discharge coefficient
$\rho; \ \rho_g$	:	density of fluid; density of gas
σ_{cr}	:	critical pressure ratio
τ	:	tangential liquid stress
$\Pi(x)$	:	perimeter
$\{\Psi\}$	:	vector of Lagrange multipliers
$\{\Phi\}$	:	vector of constraints

INTRODUCTION

The extinguishing systems comprise systems designed for the supply of the extinguishing materials (extinguish-ants) to fight fires. Water has been the most available and the most frequently used extinguishing material since times remembered. Water is distinguished for its distinctive physical and chemical qualities. For instance, it is noted for its heat absorption characteristics that the majority of the natural substances lack. For many years people have been trying to find better ways of delivering water to the scene of an accident and using it in the most effective way in fire fighting. It is not infrequent that damages resulting from inefficient application of water exceed those done by fire to the burned down property and other valuables. Water used in fire fighting tends to leak out and pollute the environment and severely deteriorate the ecological conditions in general. Although various up-to-date pumps, hoses, nozzles and sprayers are used to extinguish fires, water-based fire extinguishing technologies have not reached the top level of performance. Even using the modern centrifugal pumps, it is not possible to prevent water spillage on the scene of a fire accident. In fact, this leaking water is not involved in fire extinction but is being contaminated and wasted.

This is due to the fact that part of this water fails to absorb the entire possible heat and tends to evaporate. This is also explained by the high tension of the water surface, which does not allow it to penetrate into the burning substances. It is evident that the more we will atomize the water, the more of the surface area we will be able to obtain from the same volume of water, which

will directly contact with the fire heat and thus water properties will be used more efficiently. For instance, if water were poured as if from the bucket, its features would be used only at 5 % efficiency. Thus, the increase of the surface area of the extinguishing water augments the efficiency of the water consumption as well. The simple way to increase the extinguishing water surface area is to atomize water into fine drops. The smaller drops are developed, the better use of water properties can be implemented and less water is consumed in fire fighting. The pressure energy of the pressurized and out-flowing water through the opening (i.e. fire nozzle) is transformed into a jet kinetic energy. If we use the energy of the compressed air or other gases to eject water through the nozzle (instead of the compressed water energy) the jet speeds could be much faster. The water droplet speed within the jet sprayed out in an ordinary way reaches tens m/s, while using the compressed air energy the water droplet speed can reach hundreds m/s. Furthermore, because of such speeds, water spray is atomized into fine droplets due to the air resistance (even up to 2 microns in diameter). Consequently, the extinguishing water cover area enlarges as well as the water efficiency. The devices with such properties can be usable in portable version. This is very important to extinguishing small fires. Small fires by statistics reach more than 50% of all fires. When water is supplied in fine droplets, it is possible to reach the use of all of its properties as close as 100%. In addition, the factor of the possible damage of the property and other valuables by water flooding is eliminated completely: facilities that are not within the extinguishing area remain safe from being flooded. The majority of fires could be addressed while using portable effective extinguishing devices.

Scheme of an automatic hydraulic and pneumatic nozzle is presented in Figure 1 [1,2].
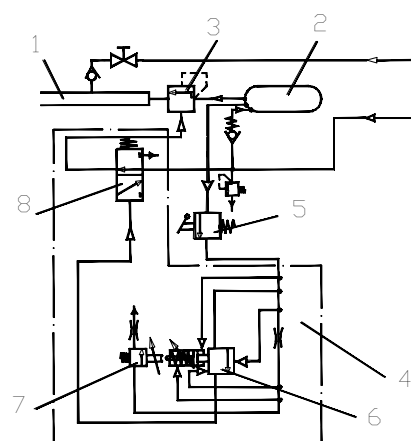

Figure 1 Scheme of automatic hydraulic and pneumatic nozzle

An automatic hydraulic and pneumatic nozzle consists of a water chamber (1), a compressed air chamber (2), a fast response valve (3), a fast response valve automatic control mechanism (4), and compressed air and water sources. The water chamber (1) is supplied from water source or reservoir; the compressed air chamber (2) is supplied from the compressed air source or reservoir. The expanding air expels water from the water chamber (1) due to that water jet is divided into fine droplets. After having activated the fast response valve automatic control mechanism (4) process is repeated constantly and water jets are ejected in series. The fast response valve automatic control mechanism (4) has three valves (6,7 and 8).

The water drops move with the velocity V_1, absorb the environment heat with temperature T_a and steam in the same breath (Figure 2).
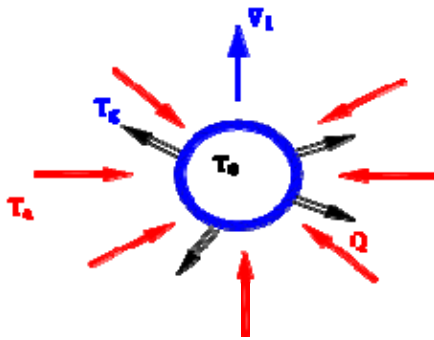
Figure 2 Scheme of drop thermal interchange

The change of thermal flow is directly proportional for the number of drops:

$$\frac{dQ}{dt} = C(Re, v)N^{5/3} \qquad (1)$$

The dependence surface area of one litre water drops from the drops diameter in Figure 3 is presented.
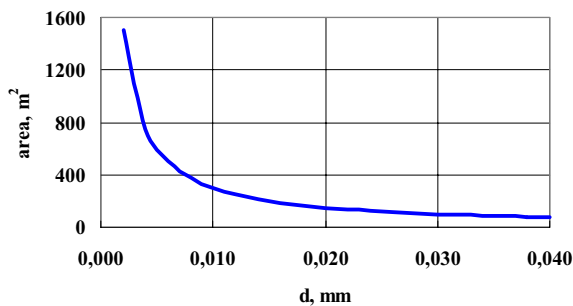
Figure 3 Dependence between surface area of drop and its diameter

II. MATHEMATICAL MODEL OF EXTINGUISHING DEVICE

The extinguishing device consists of two chambers (air container and water compartment) and two valves. The first valve is the fast reaction valve. The second valve opens when the pressure reaches particular pressure. When the fast reaction valve begins to open, the second chamber divides in two volumes. In the first volume there is a high pressure of air and in the second volume there is a high pressure of water.

The dynamic model of the extinguishing device is shown in the Figure 4. Cross-section area S_{v1} of the first valve is the function of time. Cross-section area S_{v2} of the second valve depends on the pressure $p(t, x = L_2)$ (Figure 5). The second air volume and water the compartment is separated by the surface G (Figure 4).
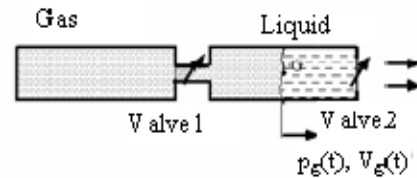
Figure 4 Scheme of extinguishing device

According to the first law of thermodynamics, the whole thermal energy moved with gas is spent for the change of the internal energy and for the work of the expansion of gas in a volume.
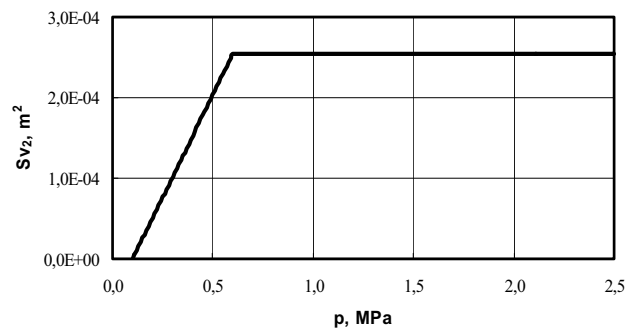
Figure 5 Dependence of cross-section area of second valve on pressure

The continuity and movement equations of viscous and compressible fluid in pressure pipe have the following form [3-7]:

755

$$\frac{\partial}{\partial t}[S(x)\rho] + \frac{\partial}{\partial x}[S(x)\rho v] = 0 \qquad (2)$$

$$\frac{\partial}{\partial t}[S(x)\rho v] + \frac{\partial}{\partial x}[S(x)(p + \rho v^2)] + \Pi(x)\tau +$$
$$+ \rho S(x)a_x + \rho g S(x)\sin(\theta) - p\frac{\partial S(x)}{\partial x} = 0. \qquad (3)$$

An equation of one-dimensional movement of gas and liquid can be written as the system quasi-linear differential equations:

$$\frac{\partial u_g}{\partial t} + B_g \frac{\partial u_g}{\partial x} = f_g, \qquad (4)$$

$$\frac{\partial u}{\partial t} + B \frac{\partial u}{\partial t} = f \qquad (5)$$

where $\quad B_g = \begin{bmatrix} v_g & c_g^2 \rho_g \\ \dfrac{1}{\rho_g} & v_g \end{bmatrix}; \quad U_g^T = [p_g, v_g];$

$$f_g^T = \left\{ \begin{array}{c} -\dfrac{c_g^2 \rho_g v_g}{S(x)} \dfrac{\partial S(x)}{\partial x} \\ -g\sin(\theta) - \dfrac{\lambda(Re,\Delta)|v_g|v_g}{2D} - a_{gx}(t) + \dfrac{p_g}{\rho_g S(x)} \dfrac{\partial S(x)}{\partial x} \end{array} \right\}$$

$$f^T = \left\{ \begin{array}{c} -\dfrac{c^2 \rho v}{S(x)} \dfrac{\partial S(x)}{\partial x} \\ -g\sin(\theta) - \dfrac{\lambda(Re)|v|v}{2D} - a_x(t) + \dfrac{p}{\rho S(x)} \dfrac{\partial S(x)}{\partial x} \end{array} \right\};$$

sound velocities c_g and c is equal to:

$$c_g = \sqrt{\gamma R T}; \qquad c = \sqrt{\frac{K(p)/\rho}{1 + \dfrac{K(p)\cdot d}{E\cdot e} + \dfrac{\varepsilon}{\gamma}\left[\dfrac{K(p)}{\gamma p} - 1\right]}}.$$

The change of pressure of the volume is determined from the following equation:

$$\frac{dp}{dt} = \frac{\gamma R T}{V}(G_{in}(p, p_{in}) - G_{out}(p, p_{out})) - \frac{\gamma p}{V}\frac{dV}{dt}, \quad (6)$$

G_{out} is determined on the formula Sen-Venan and Vencel [1]:

$$G_{out}(p, p_{out}) =$$
$$= \begin{cases} \mu_1 S_{v1}(t) K_1(T) p\varphi\left(\sigma = \dfrac{p_{out}}{p}\right) & if \ p \geq p_{out} \\ \mu_1 S_{v1}(t) K_1(T) p_{out}\varphi\left(\sigma = \dfrac{p}{p_{out}}\right) & if \ p_{out} > p \end{cases}, \quad (7)$$

$$K_1(T) = \sqrt{\frac{1}{RT}}. \qquad (8)$$

To take account of the subsonic and sonic flow, the piecewise flow function $\varphi(\sigma)$ is defined as follows:

$$\varphi(\sigma) = \begin{cases} \sqrt{\left(\dfrac{2\gamma}{\gamma - 1}\right)\left(\sigma^{\frac{2}{\gamma}} - \sigma^{\frac{\gamma+1}{\gamma}}\right)}, & if \ \sigma_{cr} < \sigma \leq 1 \\ \sqrt{\gamma\left(\dfrac{2}{\gamma + 1}\right)^{\frac{\gamma+1}{\gamma-1}}}, & if \ 0 < \sigma \leq \sigma_{cr} \end{cases} \quad (9)$$

where σ_{cr} is the critical pressure ratio given by

$$\sigma_{cr} = \left(\frac{2}{\gamma + 1}\right)^{\frac{\gamma}{\gamma-1}}.$$

The dynamics model of the fast response valve automatic control mechanism (4) (Figure 1) consists of four masses and eight chambers with variable pressures.. The system of equation of fast response motion valve automatic control mechanism have the following form:

$$m_{vi}\frac{d^2 q_{vi}}{dt^2} = f_{mv,i}(q_v, \dot{q}_v, p_v) \quad (i = 1,...,4), \qquad (10)$$

$$\frac{dp_{vj}}{dt} = f_{pv,j}(q_v, \dot{q}_v, p_v), \quad (j = 1,...,6). \qquad (11)$$

For quality work fireman have forces acting on the extinguishing device when out flowing water through the fire nozzle. The main force is recoil force. The dynamics model of fireman is created. The fireman with the extinguishing device is considered as multi-body system. The dynamics model consists from eleven rigid bodies.

The recoil force acting along the extinguishing device axis is equal:

$$F_x = -S_{v1}(p_1 - p_2) + (S_2 - S_{v2})p_{lyq}(x_G) - F_{aero}, \quad (12)$$

756

$$F_{aero} = \begin{cases} \dfrac{1}{2}\rho S_{v2} v_{2,}^2 & if \quad x_G \le L_2 \\ \dfrac{1}{2}\rho_{gas} S_{v2} v_{2,}^2 & if \quad x_G > L_2 \end{cases} \qquad (13)$$

The system of equations describing the movement of the extinguishing device and fireman is as follows [8]:

$$\begin{bmatrix} [M] & [J]^T \\ [J] & [0] \end{bmatrix} \begin{Bmatrix} \{\ddot{q}\} \\ \{\Psi\} \end{Bmatrix} = \begin{Bmatrix} \{F(q,\dot{q},t)\} \\ \{U(q,\dot{q})\} \end{Bmatrix}. \qquad (14)$$

There:

$$\{U(q,\dot{q})\} = -\frac{\partial}{\partial\{q\}^T}\left(\left[\frac{\partial\{\Phi\}}{\partial\{q\}^T}\right]\{\dot{q}\}\right)\{\dot{q}\} -$$

$$-2\left[\frac{\partial^2\{\Phi\}}{\partial\{q\}^T \partial t}\right]\{\dot{q}\} - \frac{\partial^2\{\Phi\}}{\partial t^2}, \qquad (15)$$

$$[J] = \left[\frac{\partial\{\Phi\}}{\partial\{q\}}\right]. \qquad (16)$$

III. THEORETICAL ANALYSIS

An example of the extinguishing device is considered. The following data of the extinguishing device were used: the length of the water compartment is 0.25 m, the volume of the air container is equal to $V_1 = 1.5 \cdot 10^{-3} \, m^3$, the initial pressure in the air container is 2.0 MPa, the inner diameter of the water compartment is equal to 0,025 m. The time integration step is equal to $2.0 \cdot 10^{-6} s$. Dependences of displacements of fast response valve automatic control mechanism upon time first mass is presented in Figures 7a.
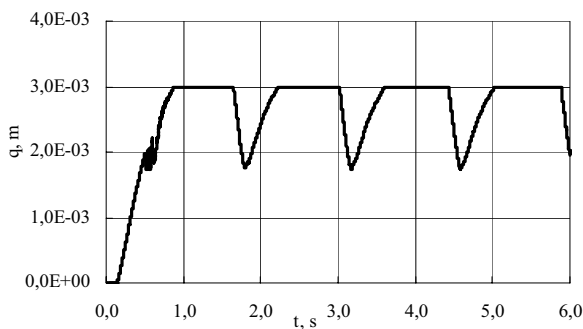
Figure 7a Dependences of displacements: first mass

The displacements of valves of the automatic control mechanism upon time fast response valve (3) are shown in the Figure 7b.
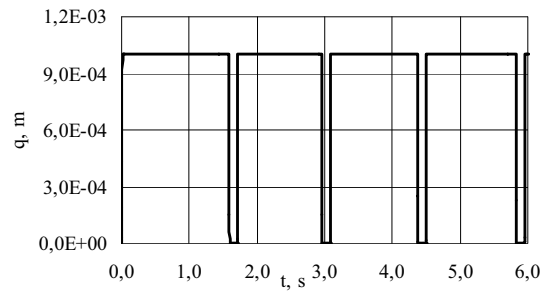
Figure 7b Dependences of displacements: fast response valve 3

The pressures in the chambers of valves of the automatic control mechanism are shown in the Figure 8. The forces acting on the extinguishing device are shown in the Figure 9.
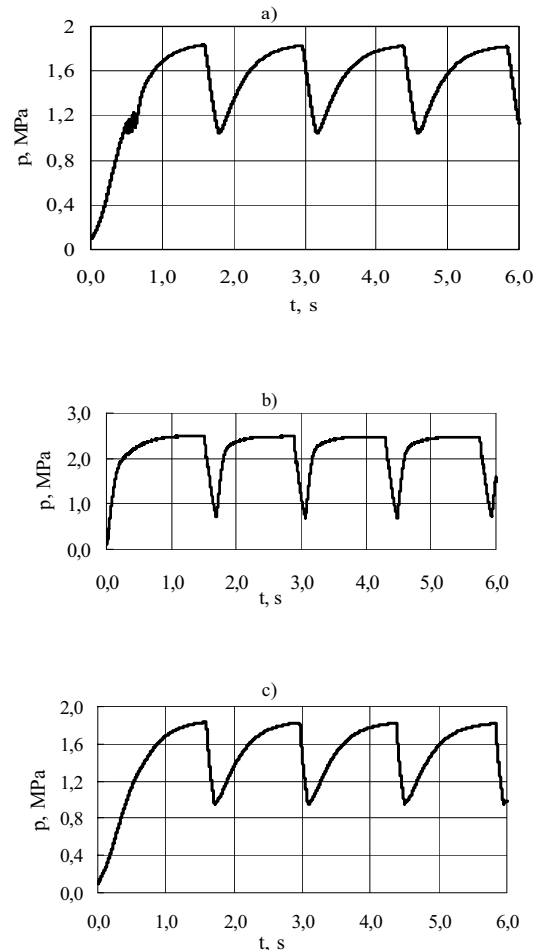
Figure 8 Dependences of pressures: a) first chamber; b) chamber of valve (3) c) compressed air chamber (2)
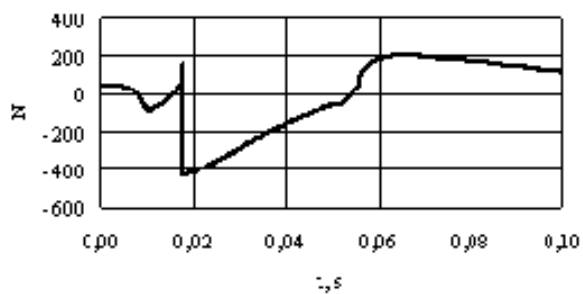
Figure 9 Dependence of recoil force upon time

In the Figure 10 are shown distribution of the cloud of water drops in the different moments of time.

a)

b)

c)
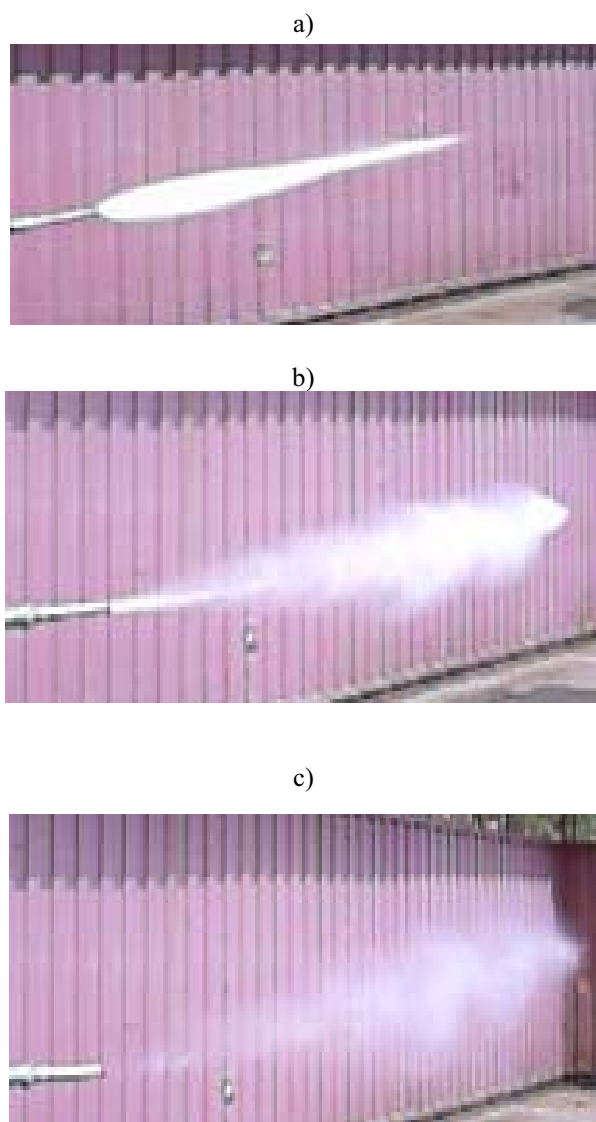
Figure 10 Distribution of the cloud of drops of water

IV. CONCLUSION

A new automatic impulse extinguishing is created. The approach for simulating hydrodynamic processes of the extinguishing device has been developed. The composed mathematical model of the extinguishing device takes into account wave motion of a liquid. The Differential equations, describing hydrodynamic processes inside the extinguishing device, help analyze the movement of liquid and gas better and more precisely. The period of vibration of fast response valve is about 1.4 s and this time can be regulated by changing stiffness of valves. At the end of a pipeline of the extinguishing device the maximum velocity of liquid reaches 60 m/s.

REFERENCES

1. Bogdevičius M., Suslavičius V. Investigation the dynamic process of automatic impulse extinguishing. Proceedings of Twelvtth World Congress on the Theory of Mechines and Mechanisms, Besacon, France, 2008.
2. Bogdevičius M., Matuliauskas A., Mištinas V., Spruogis B., Suslavičius V., Dynamics of pneumatic and hydraulic transport technological equipment system, Transport, 2004, **19**-1, pp.37-42.
3. Bogdevičius M.. Simulation of complex pneumatic system, Transport, 2000, **15**-1, pp.20-28.
4. Bogdevicius M., Pump hydraulic system simulation by the characteristic method, Transport, 1997, **15**-2, pp. 30-37.
5. Bogdevicius M., Calculation of a non-stationary movement of a liquid in elastic-plastic and elastic-viscous-plastic pipeline, University Stuttgart, Institute of Hydraulic Machines, 1991, p.48.
6. Bogdevicius M., Simulation and Interaction of Mechanical and Hydraulic System. Proceedings of Tenth World Congress on the Theory of Mechines and Mechanisms, Oulu, Finland, 1999, pp.2110-2115.
7. Bogdevicius M. Simulation of Dynamic Processes in Hydraulic, Pneumatic and Mechanical Drivers and their Elements. Vilnius, Technika, 2000, p. 96.
8. Aladjev V., Bogdevicius M., Maple 6: Solution of the Mathematical, Statistical and Engineering – Physical Problems, Moscow, 2001.p. 824.

P2-31

RESEARCH ON NEW ENERGY-SAVING VACUUM EJECTOR WITH FLOW SELF-REGULATION

Yan TENG, Xiaoning LI, Jianping LU and Zhongsheng SUN

SMC Pneumatics (Nanjing) Technical Center
School of Mechanical Engineering
Nanjing University of Science and Technology, Nanjing, P.R. China
(E-mail: xnli2008@jsmail.com.cn)

ABSTRACT

Jet vacuum ejectors currently used have a defect of large air consumption due to the need of continuous and constant air supply. To solve this problem, a novel technical structure of the jet vacuum ejector with flow self-regulation by an adjustable cone has been investigated. In this paper, the structure, key technologies and experiment of this new jet vacuum ejector are introduced. In the new ejector, by means of the adjustable cone, the effective cross section at the jet nozzle throat could be adjusted so as to realize the reduction of air supply and achieve energy saving. For this, a key technology for the new structure called chamber-separating pneumatic-magnetic driving is studied, in which a vacuum detecting-differential pressure actuating and non-contacting pneumatic-magnetic driving with a coaxial magnetic ring-axial structure are implemented. Experimental results for the flow self-regulated vacuum ejector have shown that the vacuum response time and maximum vacuum of new ejector are almost equivalent to the constant-area vacuum ejectors with the relative parameters, but the air consumption could save about 14.8%.

KEY WORDS

Vacuum ejector, Vacuum feedback, Magnetic actuating, Air consumption, Energy saving

INTRODUCTION

As a kind of operation form in automation, vacuum attraction technology is widely used in industry [1]. However, as a kind of locally-used vacuum generator, an ordinary jet vacuum ejector must be supplied continuously with constant air when working, so that large air consumption and large corresponding energy consumption are caused. It is an unsolved technology problem how to reduce the energy consumption but to maintain the original working performance in developing a new kind of energy-saving ejector.
Focusing on this problem, much research work has been done recently. For example, there is newly-developed vacuum-generating unit, which integrates vacuum nozzle, check valve and vacuum switch [2] and could control solenoid valve to shut off the air supply when system vacuum reaches at a set vacuum value. When

removing workpieces with this vacuum unit, the air consumption could be decreased to 80% or so [3]. However, due to the increase of flow resistance brought by the check valve and corresponding up to 40% decrease of the exhaust flow, the vacuum response time of this unit would be obviously increased. Another example is a kind of energy-saving parallel-nozzle ejector [4~6]. In this ejector, two parallel nozzles which have different diameter have been used to realize quick vacuum response within the vacuum response stage. Within the vacuum maintaining stage, only the smaller nozzle is switched to work by a solenoid to maintain the vacuum for energy saving. But the parallel-nozzle ejector could not adapt various kinds of complex working conditions because there are only two fixed nozzles and therefore the energy saving effect of the parallel-nozzle ejector is still not so perfect. In this paper, a new energy-saving technology for jet vacuum ejector is presented. The research idea is to adjust the

effective cross section of the nozzle by means of automatic technical operation so as to achieve the result to regulate the air supply and reduce the air consumption. For this, the structure, key technologies and experiments of this new jet vacuum ejector are introduced in following sections.

THE STRUCTURE AND KEY TECHNOLOGIES OF VACUUM EJECTOR WITH FLOW SELF-REGULATION

The Structure of Vacuum Ejector with Flow Self-regulation

The general structure of vacuum ejector with flow self-regulation is shown in Figure 1. (This new ejector with flow self-regulation has applied for China Paten). It is made of two components, one is the vacuum generating component and another is the flow self-regulation component, in which the working principle of the vacuum generating component is as same as that of a normal jet vacuum ejector, i.e., when the ratio of the pressure at the nozzle throat in the Laval duct 9 to the supply pressure exceeds a certain value, the supersonic jet flow could be formed at the outlet of the Laval duct. At the nozzle throat there is a vacuum to be produced. Then the flow from the suction chamber into the mixing chamber is formed and the ejecting gas is brought out of the ejector through the mixing duct. Therefore the local vacuum in the suction chamber could be formed. If the change of the supply temperature could be neglected, the supply flow rate q is in direct proportion to the effective cross section of the nozzle throat A_t [7].

In the flow self-regulation component, the adjustable cone 10 connected with the slave core is in the front of Laval duct and is coaxial with the Laval duct. The
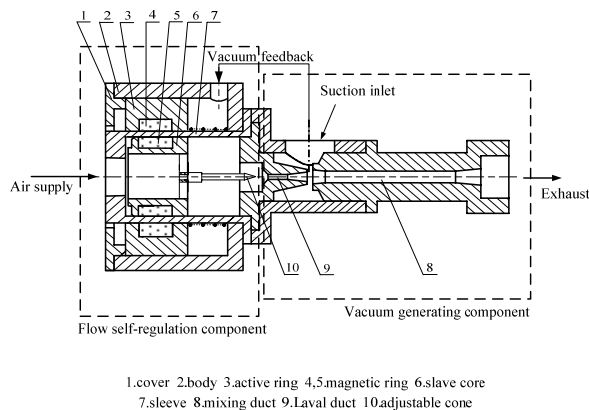
magnetic ring 4 and the magnetic ring 5 are installed on the active ring 3 and the slave core 6 respectively. The left chamber adjacent to the active ring 3 is open to the atmosphere and the right chamber is connected with the vacuum chamber of the ejector. When the ejector ceases working, the active ring, the slave core and the adjustable cone are all on the end of the left position where the adjustable cone keeps a distance away from the Laval duct throat (indicated with the real line in the Figure 2). When vacuum is generated by the ejector, a pressure difference on the two sides of the active ring could be formed and the active ring would be moved to the right. Thus the slave core and the adjustable cone would be driven towards the right and approaches the Laval duct throat by the magnetic force of the two magnetic rings (indicated with the broken line in the Figure 2). Therefore, the effective cross section of the nozzle throat could be adjusted so as to realize the reduction of air supply and achieve energy saving.

Technology of Vacuum Detecting And Differential Pressure Actuating

The driving force of the vacuum ejector with flow self-regulation is one of the key technologies in the structure design of the ejector. A vacuum feedback-differential pressure actuating technology has been presented which is illustrated in Figure 2. In this technical scheme, the working vacuum pressure is fed back directly to the vacuum chamber. The active ring is used to detect and amplify the differential pressure between vacuum and atmosphere pressure and the differential pressure is used for the driving force of the moving components. The merit of the scheme is that it directly utilizes the vacuum pressure to drive the moving components and could meet the work requirements of automatic flow regulation according to the real-time working vacuum. Moreover it has such advantages as rapid response speed, simple structure and good reliability.
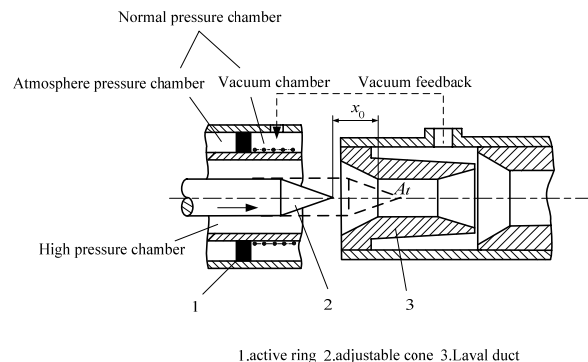

1.cover 2.body 3.active ring 4,5.magnetic ring 6.slave core
7.sleeve 8.mixing duct 9.Laval duct 10.adjustable cone

Figure 1 The structure of vacuum ejector with flow self-regulation

1.active ring 2.adjustable cone 3.Laval duct

Figure 2   Scheme of the vacuum feedback-differential pressure actuating technology

Technology of Pneumatic-Magnetic Driving With Chamber-Separating

As above-mentioned, the driving force of the moving component is produced from the normal pressure chamber constituted of atmosphere pressure chamber and the vacuum chamber, while the adjustable cone acting as a flow regulation part is in the high pressure chamber where the supplied air flows through, so it is another key technology how to use the driving force coming from the normal pressure chamber to drive the adjustable cone in the high pressure chamber, as well as to keep reliable sealing between the two chambers. The normal mechanical transmission-mechanism is difficult to satisfy the sealing requirement between the two chambers. A pneumatic-magnetic driving with chamber-separating and coaxial magnetic ring-axial structure has been presented. As shown in Figure 1, the magnetic force between two magnetic rings which are embedded in the active ring 3 and the slave core 6 respectively could realize the non-contracting driving from the normal pressure chamber to the high pressure chamber. The merit of this technology is that under the condition of effective driving of the adjustable cone it could ensure that the two chambers are not connected through in structure and satisfy radically the sealing requirement between the two chambers.

THEORETICAL MODEL

Dynamic Model of Flow Self-Regulation Component

The force analysis of the flow self-regulation component is shown in Figure 3.

a) active ring   b) slave core
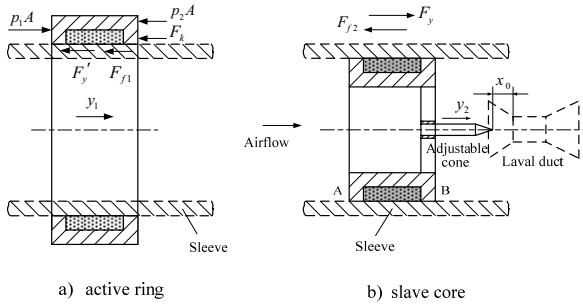
Figure 3   The force analysis of the active ring and the slave core

$$m_1 \frac{\mathrm{d}^2 y_1}{\mathrm{d}t^2} = p_1 A - p_2 A - k_t (y_0 + y_1) - F_{f1} - F_y' \quad (1)$$

$$m_2 \frac{\mathrm{d}^2 y_2}{\mathrm{d}t^2} = F_y - F_{f2} \quad (2)$$

Where magnetic force F_y

$$F_y = \frac{-\sigma^2}{2\pi\mu_0} s[2\Gamma(\Delta y) - \Gamma(\Delta y + L) - \Gamma(\Delta y - L)] \quad (3)$$

In Eq.(3), function $\Gamma(z)$

$$\Gamma(z) = \{(c+h)\mathrm{tg}^{-1}\frac{c+h}{z} - 2c\,\mathrm{tg}^{-1}\frac{c}{z}$$
$$+ (c-h)\mathrm{tg}^{-1}\frac{(c-h)}{z} - \frac{z}{2}[\ln\left((c+h)^2 + z^2\right) \quad (4)$$
$$- 2\ln c^2 + \ln\left((c-h)^2 + z^2\right)]\}$$

In Eq.(1)~Eq.(4), m is mass of moving component,[kg], y is displacement of moving component,[mm], p is pressure,[MPa], A is area of the active ring,[mm^2], k_t is coefficient of resilience,[N/mm], y_0 is initial compressed displacement of spring,[mm], F_f is friction force,[N], F_y is magnetic force,[N], σ is induction density,[T], μ_0 is vacuum magnetic conductivity, s is average circumference of the magnetic ring couple,[mm], Δy is lag displacement with which little magnetic ring moves behind the big one,[mm], L is width of the magnetic ring,[mm], h is thickness of the magnetic ring,[mm], c is radial distance of center of cross section between two magnetic rings,[mm].

Effective Cross Section of Nozzle Throat

When the adjustable cone is not inside the nozzle, the effective cross section of the nozzle throat can be expressed as

$$A_t = \zeta \frac{\pi}{4} d_0^2 \quad (5)$$

When the adjustable cone is inside the nozzle, as shown in Figure 4, the effective cross section of the nozzle throat can be expressed as

$$A_t = \zeta \pi (l - y_2 + x_0)\sin\alpha \times$$
$$[d_0 - (l - y_2 + x_0)\sin\alpha\cos\alpha] \quad (6)$$

1. adjustable cone   2. Laval duct
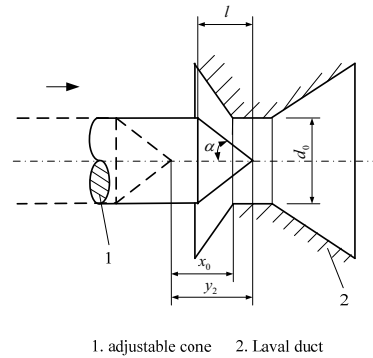
Figure 4   Relative location of adjustable cone and nozzle

In Eq.(5)~Eq.(6), d_0 is diameter of the nozzle

throat,[mm], l is axial length of the cone for the adjustable cone,[mm], x_0 is initial design location of the adjustable cone,[mm], α is half angle of the cone for the adjustable cone,[°], ζ is correcting coefficient.

Air Consumption of Vacuum Ejector

The air consumption of vacuum ejector Q can be expressed as

$$Q = \int_0^t q\,\mathrm{d}t$$
$$= \int_0^t \frac{p_s A_t}{\sqrt{T_s}} \sqrt{\frac{k}{R}\left(\frac{2}{k+1}\right)^{\frac{k+1}{k-1}}} \eta_p \,\mathrm{d}t \qquad (7)$$

In Eq.(7), p_s is supply pressure,[MPa], T_s is supply temperature,[K], k adiabatic coefficient, R is gas constant, η_p correcting coefficient.

REGULATING STRATEGY OF THE ADJUSTABLE CONE

When the adjustable cone is inside the nozzle, the flow field of the vacuum ejector would tend to be bad due to the change of the structure parameter of the duct. If the regulating strategy of the adjustable cone is not reasonable, the performance of the ejector would be dropped greatly and as a result the ejector might not work normally. Therefore it is necessary to find a reasonable regulating strategy of the adjustable cone.

Force on the Adjustable Cone from Airflow

The forces that airflow exerts on the adjustable cone are shown in Figure 5.
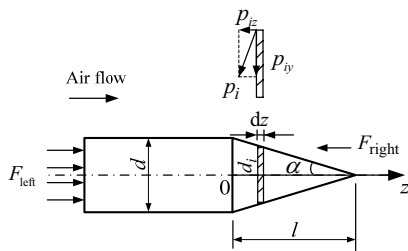
Figure 5   Forces that airflow exerts on the adjustable cone

The resultant force F could be expressed as

$$F = F_{\text{left}} - F_{\text{right}}$$
$$= \frac{\pi}{4} p_s d^2 - \int_0^l 2\pi p_i (l-z)\sin\alpha\tan\alpha\,\mathrm{d}z \qquad (8)$$

In Eq.(8), d is the column diameter of the adjustable cone,[mm], p_i is the airflow pressure distribution on the cone of the adjustable cone,[MPa].

When the distance x with which the adjustable cone enters the nozzle throat is 0 (i.e., the adjustable cone is not inside the nozzle), 0.5mm, 1.0mm, 1.5mm, 2.0mm, 2.5mm respectively, the airflow pressure distribution

p_i on the cone of the adjustable cone obtained from simulation by CFD (Computational Fluid Dynamics) method is shown in Figure 6. It can be clearly seen that the bigger x is the shorter the high pressure range on the cone is and the longer the low pressure range is. Moreover, the gradient from high pressure range is gradually enlarged with the increase of x.
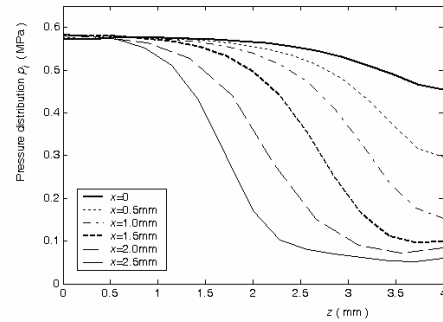
Figure 6   The airflow pressure distribution on the cone of the adjustable cone

The airflow resultant force F exerted on the adjustable cone for different x is shown in Figure 7. It can be seen that the resultant forces are all positive for different x and the bigger x is the larger the airflow resultant force is. Therefore, such conclusion could be drawn that the airflow force tends to push the adjustable cone into the nozzle throat.
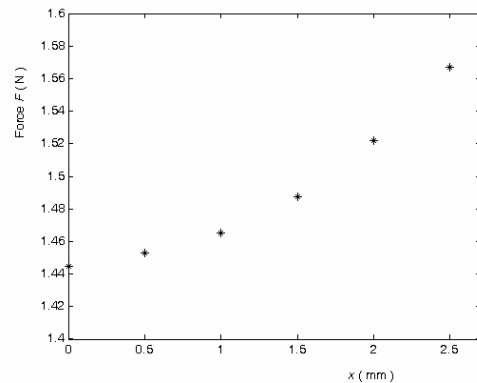
Figure 7   The airflow resultant force on adjustable cone

Study on Regulating Strategy of The Adjustable Cone

When the distance x is 0, 0.5mm, 1.0mm, 1.5mm, 2.0mm, 2.5mm respectively, Mach number and the static pressure along the axis of the 2-D flow field for vacuum ejector obtained from simulation by CFD are shown in Figure 8. It can be seen that Mach number of the nozzle throat is increased with the increase of x, the supersonic field shifts to an earlier position and the oscillation of Mach number is increased. Moreover, the

762
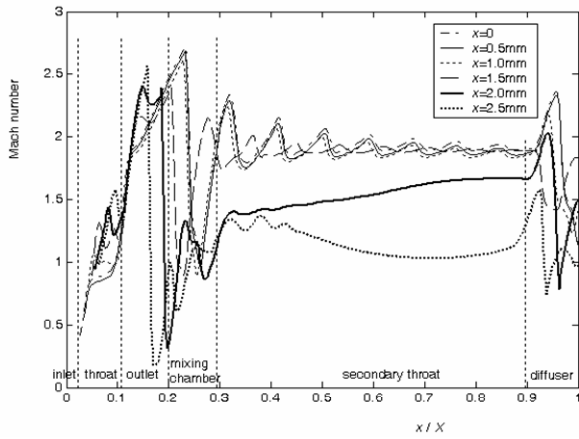
(a) Curves of Mach number
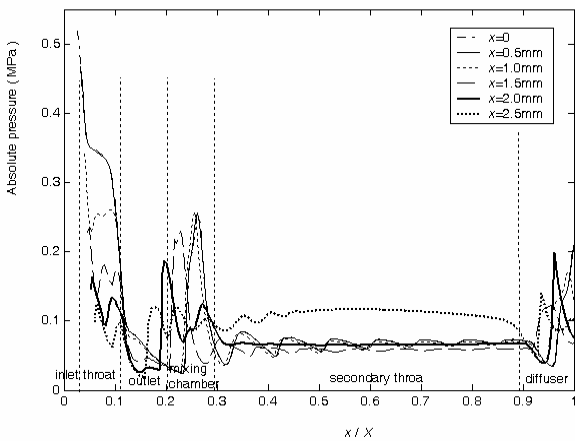
(b) Curves of static pressure along axis

Figure 8   Comparison of flow fields for different x

maximum vacuum field shifts from mixing chamber to the taper exit of the nozzle and the vacuum of the mixing chamber is gradually decreased. In addition, Mach number of the flow field in the secondary throat is also gradually decreased and the absolute pressure tends to increase. In simulation, when $x \leq 2.0$mm, the flow speed in the secondary throat is still sonic. For example, the maximum vacuum in the mixing chamber is about 65kPa when x=2mm. However, Mach number in the secondary throat is smaller than 1, while the absolute pressure is higher than 0.1MPa when x=2.5mm, i.e., the air flow in this field has been decreased to subsonic speed and the vacuum in the mixing chamber has been reduced to 40kPa. This indicates that the vacuum ability of ejector is too weak to maintain normal operation.

Therefore, regulating strategy of the adjustable cone should be suggested that the distance with which the adjustable cone enters the nozzle throat should be controlled within a range which is determined by the required minimum vacuum of the ejector in real operation. For example, when the minimum vacuum required by the real operation of the vacuum system is 65kPa, the distance with which the adjustable cone enters the nozzle throat should be controlled within

2mm under the given condition for tested prototype ejector.

EXPERIMENTAL RESULTS

The experimental studies have been conducted to measure the working performance of the flow self-regulated vacuum ejector (self-regulated ejector in short). For comparison, the vacuum generating component of the flow self-regulated vacuum ejector (constant-area ejector in short) has been measured too. The experimental apparatus is shown in Figure 9. In the experiment, the supply pressure is 0.55 MPa, the volume of the vacuum chamber is 1 L and the diameter of the nozzle throat is 2 mm.
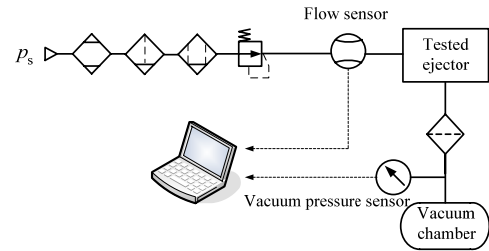
Figure 9   Experimental apparatus

The testing results for the self-regulated ejector and the constant-area ejector are shown in Figure 10.
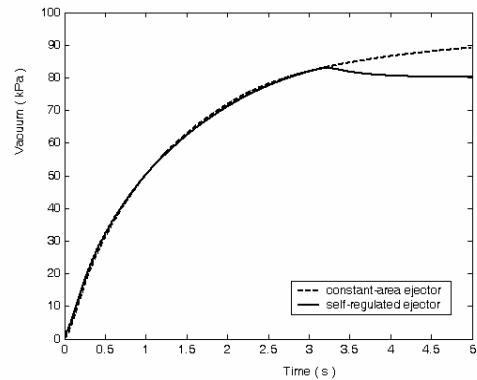
(a) Curves of vacuum
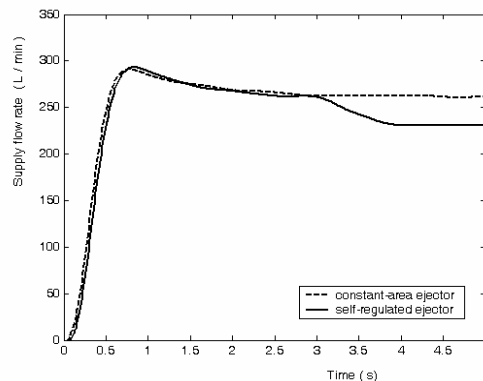
(b) Curves of supply flow rate

Figure 10   Comparison of measured working performances for the self-regulated ejector and the constant-area ejector

763

Usually the normal vacuum range of the vacuum system is from 63% to 95% of the maximum vacuum. The time when the vacuum reaches 63% of the maximum vacuum 90 kPa is defined as the vacuum response time and in this case it is 57 kPa. From Figure 10 (a), it can be seen that the vacuum response times of the self-regulated ejector and the constant-area ejector are almost the same, about 1.25s. This indicates that the quick vacuum response performance of the self-regulated ejector is as good as that of the constant-area ejector. Moreover, although the maximum vacuum of the self-regulated ejector in the vacuum keeping stage is less than that of the constant-area ejector, this vacuum is still kept above 80kPa. This indicates that the vacuum of the self-regulated ejector could still maintain the normal operation. From Figure 10 (b), it can be seen that before 3 s curves of the supply flow rate of the two kinds of ejectors are almost coincident. However, after about 3 s, the supply flow rate of the self-regulated ejector is obviously less than that of the constant-area ejector. The supply flow rate of the constant-area ejector is 270 L/min at the vacuum keeping stage, while that of the self-regulated ejector is 230 L/min. As a result the air supply is reduced by about 14.8%.

The comparison of air consumption of the self-regulated ejector and the constant-area ejector on each time point within 20 s is shown in Figure 11. It can be seen that all the air consumption of the self-regulated ejector on every time point is less than that of the constant-area ejector. If the time of a working cycling is 20 s, the air consumption of the self-regulated ejector within one working cycling could be reduced by about 13.3 L compared to that of the constant-area ejector. It can be roughly figured out that the self-regulated ejector could reduce the air consumption about 12,768 L in every day if the time of a working cycling is 20 s, the time interval is 10 s and the whole working time of everyday is 8 h.
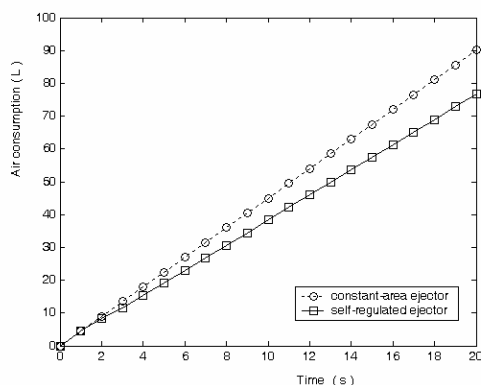
Figure 11   Comparison of the air consumption

CONCLUSION

Jet vacuum ejectors have a defect of large air consumption in use. To solve this problem, in this paper, a novel jet vacuum ejector with flow self-regulation by an adjustable cone has been presented and implemented for the first time. For this, research for the general structure, key technologies and experiment of this new jet vacuum ejector have been conducted. Some conclusions could be drawn as follows.

(1) The structure of the flow self-regulation ejector has been studied and realized. The vacuum feedback-differential pressure actuating technology and the chamber-separating pneumatic-magnetic driving with a coaxial magnetic ring-axial structure have been presented. The technical problem of non-contacting driving resulted from the sealing requirement between the high pressure chamber and the normal pressure chamber has been solved.

(2) The accurate forces that airflow exerts on the adjustable cone in the two-dimension flow field are analyzed. Then the regulating strategy of the adjustable cone has been studied and suggested, i.e., the minimum vacuum required by the normal operation of the vacuum system must be greater than 65kPa, while the distance with which the adjustable cone enters the nozzle throat should be controlled within 2mm under the given condition for tested prototype ejector.

(3) The basic working characteristics of the flow self-regulation ejector have been tested. Experimental results have shown that the vacuum response time and maximum vacuum of new ejector are almost the same compared to the constant-area vacuum ejectors with corresponding parameters, while the air consumption could be reduced by about 14.8%.

REFERENCES

1 SMC(China)Corporation, Modern Pneumatic Technology (In Chinese), 2nd ed, [M], Beijing, China Machine Press, 2004.
2 Convum Corporation, Vacuum Generator (In Japanese), Japan, 2005-180326[P], 2005-07-07.
3 ZHENG X.R., ZHANG X. and ZHAO Z.F., Research of Economizing on Energy of vacuum ejector, [J], Vacuum and Cryogenics, 2005,11-3, pp.50-54.
4 FESTO AG and CO, Vacuum Generator, Europe, DE2000103321220000707, [P], 2002-01-17.
5 SMC Corporation, Vacuum Generator (In Japanese), Japan, 61-55399, [P], 1986-03-19.
6 Zhejiang University of Technology, Energy-saving Parallel-nozzle Ejector (In Chinese), China, 200510050203, [P], 2005-09-14.
7 Tong Bing-gang, Kong Xiang-yan and Deng Guo-hua, Dynamics of pneumatic systems (In Chinese), [M], Beijing, Higher Education Press, 1990.

P2-32

AN APPROACH TO ENERGY CONSERVATION
IN PNEUMATIC SYSTEMS WITH METER OUT CIRCUIT

Hiroshi MUTOH*, Yukio KAWAKAMI**,Yoshinaka HRIATA* and Sunao KAWAI*

*Department of Applied Mechanics and Aerospace Engineering,
School of Fundamental Science and Engineering, Waseda Uiversity
3-4-1Ookubo, Sinjyuku-ku , Tokyo, 169-8555 Japan
(E-mail: hmutoh@waseda.jp.

** Department of Machinery & control Systems, College of System Engineering
Sibaura Institute of Technology
307 Fukasaku, Minuma-ku, Saitama-city, 337-8548 Japan

ABSTRACT

Air cylinders have been used with meter out control.   In these cases, the outlet pressure of air compressors are set at 0.5~0.7[MPa] for consumption air saving, and so downstream pressure of the actuator is low level, such as nearly atmospheric pressure. For pneumatic energy conservation, it is most important that supplying air use effectively. A lot of small cylinders are worked in automatic factory product systems, and air supply lines are longer between compressor and these cylinders.   So, in a plant, energy consumption of pneumatic system is bigger and gets big losses.
In this paper, the authors propose that the exhaust pressure of the cylinder hold middle level (0.2~0.5[MPa]), and so the downstream available for running air blow guns etc. This paper shows the air cylinder dynamics at start and stop, then the parameter are exhaust pressures, cylinder load, supply piping length. Assuming that exhaust flow is used effectively, the proposal method available to prove energy conservation of pneumatic systems. For example, the exhaust pressure setting 0.2[MPa] reduce 15% of pneumatic energy consumption.

KEY WORDS

Eco-System, Cylinder, Meter Out, Modeling

NOMENCLATURE

A	:	receiving pressure area
a	:	heat transfer area
c_P	:	specific heat at constant volume
c_V	:	specific heat at constant pressure
E	:	energy
f_F	:	friction force
G	:	mass flow rate of air
h	:	specific enthalpy
M	:	Mass
α	:	heat transfer coefficient
m	:	moving load

p	:	pressure
Q	:	inlet flow rte
R	:	gas constant
T	:	temperature
t	:	time
V	:	volume
x	:	piston displacement

suffix

1	:	source	2 :	load
S	:	supply		

INTRODUCTION

In many fields, the concrete reduction in CO2 emissions has been required since the Kyoto Protocol came into effect in February 2005. Japan has not yet solved the assignment of the 6% reduction in CO2 emissions. The situation urges also the field of pneumatic power systems to develop any practical measures for reducing CO2 emissions. Despite its application to a wide variety of use, for example auto-assembly machines, pneumatic power systems are estimated to be less energy-efficient comparing with electric or hydraulic power systems. The estimation is, however, based on its energy-efficiency in a steady operating state and doesn't always apply to intermittent operations.

In this situation, the authors have developed the experimental research for reducing CO_2 emissions in pneumatic cylinders which are the typical operational parts of pneumatic power systems. The research
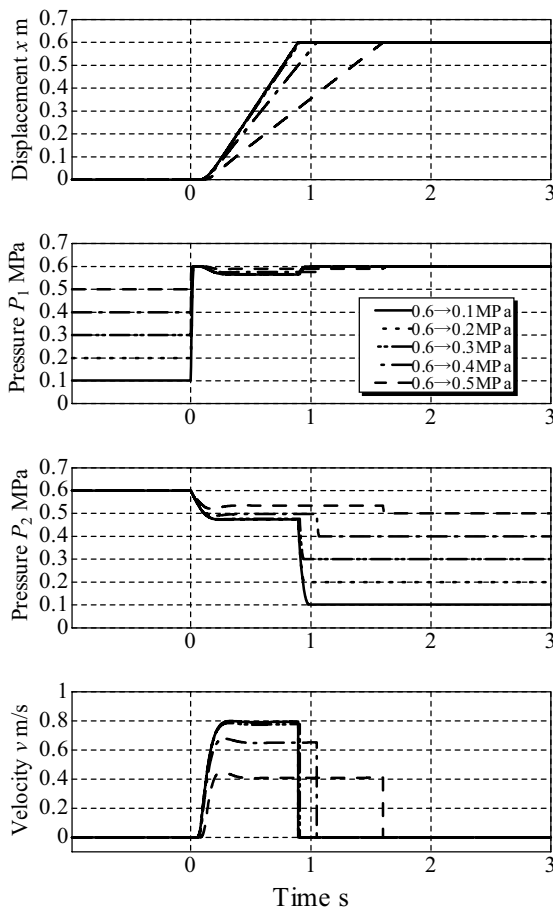
Figure 1 Effects of Exhaust Pressure (Simulation)

proposed the measures to reduce the amount of air consumption in meter-in circuits and showed its effectiveness. Then the measures in meter-out circuits have been considered on the greater use in general. As a method to reduce the amount of air consumption in meter-out circuits, lower air pressure is generally supplied. But this makes bad effects such as the lower sensitivity of response and holding power. Therefore the authors will propose that higher exhaust line pressure than atmospheric pressure should be applied to meter-out circuits to reduce the amount of air consumption as keeping its characteristic. This idea was led by the fact that many plants use their compressed air for air blowing the most and provides efficient use of air supplied from exhaust lines for air blowing.

THE PROPOSED DRIVING METHOD

This proposal comes from the basically unchanged behavior of air cylinders with choked flow on the exhaust side.

As obviously shown in Fig.1, the driving side cylinder pressure is almost unrelated to the exhaust line pressure (i.e. the initial pressure) and the exhaust side cylinder pressure is constant and unrelated to the exhaust line pressure until the piston reaches the end of its stroke.

These show that the cylinder response is almost unrelated to the exhaust lien pressure if choked flow occurs on the exhaust side. This corresponds to the fundamental concept of meter-out circuits in which the stroke speed can be adjusted by supplying compressed air to the driving side cylinder and controlling the exhaust side pressure with speed controller on the exhaust side. From another angle, while meter-in circuits control the amount of supplied energy so that the systems provide energy conservation (reduction of air consumption), meter-out circuits do not directory control the amount of supplied energy so that this method attempts reducing air consumption by the higher exhaust line pressure.

THE OUTLINE OF THE EXPERIMENTAL SETUP

The flow chart of the experimental setup is shown in Fig.2. The air cylinder is set horizontally and drives the

load on the cart with the linier bearings. The exhaust

The experiments for this paper assume that the load should give constant force. The load is connected to the rod of the air cylinder with the wire through the pulley. The load direction same with the driving direction is defined as positive. The load direction opposite to the driving direction is defined as negative. The inlet side of the cylinder is called primary. The exhaust side is called secondary. The air tank supplied the air of constant pressure through the pressure regulator gives a virtual exhaust line.
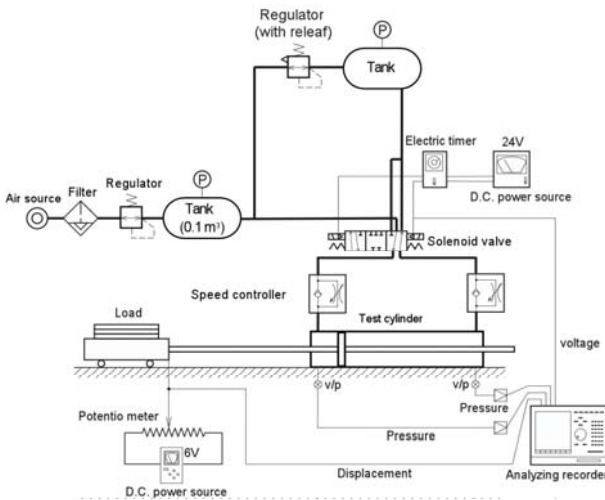
Figure 2 Experimental apparatus

line is represented by the air tank with its inside pressure constant.

The following equation was used for the simulation.

1) Equations of mass conservation

$$\begin{cases} \dfrac{dM_1}{dt} = G_1 \\ \dfrac{dM_2}{dt} = -G_2 \end{cases}$$

2) equations of energy conservation

$$\begin{cases} \dfrac{dE_1}{dt} = G_1 h_s - p_1 \dfrac{dV_1}{dt} + Q_1 \\ \dfrac{dE_2}{dt} = -G_2 h_2 - p_2 \dfrac{dV_2}{dt} + Q_2 \end{cases}$$

3) state equations of ideal gas

$$\begin{cases} p_1 V_1 = M_1 R T_1 \\ p_2 V_2 = M_2 R T_2 \end{cases}$$

4) equation of load mass

$$m \dfrac{d^2 x}{dt^2} = A(p_1 - p_2) - f_f$$

CONSIDERATION BY THE EXPERIMENTS

THE VALIDITY OF THE SIMULATION

Fig.3 illustrates one of the experimental results. It obviously shows that the response of the cylinder is almost unrelated to the exhaust line pressure at 0.6[MPa] of air pressure on the supplying side and 0.3[MPa] or less of exhaust line pressure. This is reasonable in that choked flow on the exhaust side causes the exhaust line pressure to have no effect. Comparing with the simulation result in Fig.1, the similarity which provides the validity of the simulation model appears.
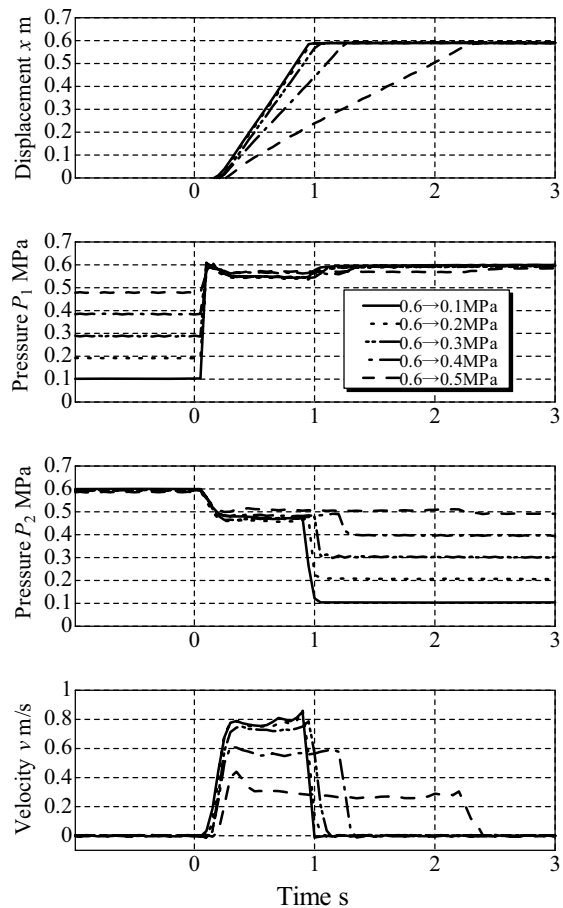
Figure 3 Experimental Results

THE EFFECTS OF THE TUBE VOLUME

Tube volume cannot be ignored for the cylinder volume of smaller pneumatic cylinders. Therefore the higher exhaust line pressure gives more effective

reduction in the amount of air consumption for the tube
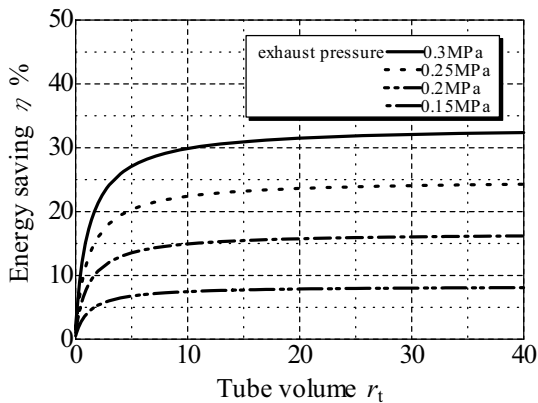
Figure 4   Air Consumption Saving

volume. improves the response slightly and controls the projection speed.

Fig.4 illustrates estimation, the possible amount of reducing air consumption along with tube volume to cylinder volume. As it obviously shows, in the case of larger tube volume for a small pneumatic cylinder, the air consumption reduction rate at 0.6[MPa] of driving pressure and 0.3[MPa] of exhaust line pressure becomes approximately 30%.

Then the effects of exhaust line pressure on response when tube volume cannot be ignored were investigated. One of the experimental results is illustrated in Fig.5.

It is known that a cylinder with its exhaust line pressure set in the range of choked flow can drive as the exhaust line pressure is set at usual atmospheric pressure and that a cylinder can drive normally without choked flow if the cylinder pressure on the exhaust side and the tube pressure give almost the critical pressure ratio. This means, in this case, the higher exhaust line pressure around 0.3[MPa] has almost no effect on the response. Or rather, the higher exhaust line pressure

An increase in the rate of tube volume may also increase the rate of start-up delay to cylinder stroking time. But it is conceivable that higher exhaust line pressure allows tube pressure at a higher level to rise to reduce start-up delay.
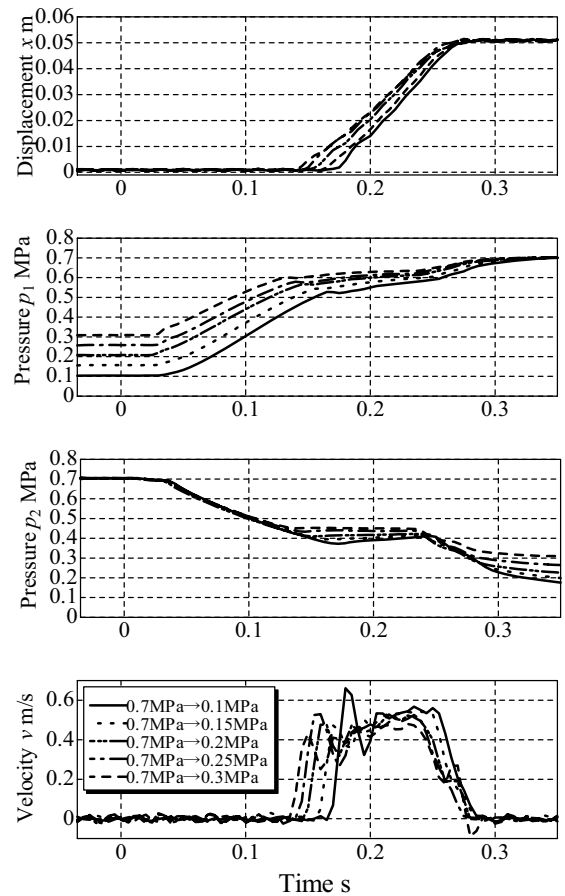
Figure 5 Experimental Results
(Effects of exhaust line pressure at
** % tube volume)
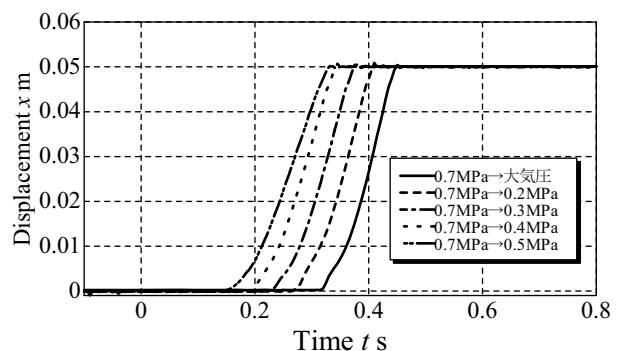
Figure 6 Experimental Results(Tube Volume 20 Times)

THE EFFECTS OF THE LOAD

Fig.7 and Fig.8 illustrate the experimental results. Fig.7 is one of the results when the negative load (the opposite direction to the piston driving direction) was applied. It shows that the higher exhaust line pressure improves the start-up delay. No bad effect of the higher exhaust line pressure can be observed. The improvement is caused by a faster rise in the primary pressure because of the high initial pressure on the primary side (the exhaust line pressure). But the loaded condition requires such higher differential pressure for its start-up that the primary pressure should increase almost up to the supplied pressure and the secondary pressure should decrease. It is considered this decreases the improvement in the start-up delay. The load also requires such higher differential pressure for its driving that the secondary pressure plunges into the range of no
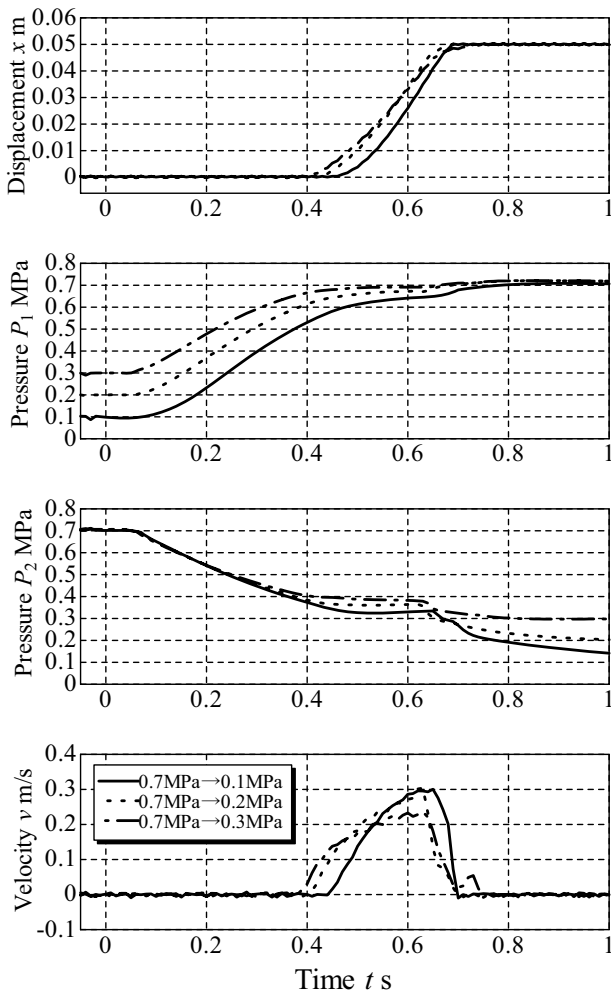
choked flow to decrease the driving speed. These appear obviously as the load rate becomes higher.

Fig.8 illustrates the results when the positive load (the same direction with the piston driving direction) was applied. This shows the improvement in the start-up delay and a rise of the secondary pressure. The differential pressure required for its start-up becomes lower because of the force toward the piston driving direction added by the load and can be reached faster because of the high initial pressure on the primary side (the exhaust line pressure). These improve the start-up delay. In addition, the secondary air is compressed so that the pressure becomes higher to give choked flow even in the range of the exhaust line pressure without choked flow normally.

These give a stable drive. That is to say, higher exhaust line pressure makes no bad effects on driving maximum value tends to be lower as exhaust line

Figure 7 Experimental Results (Load factor -20%)
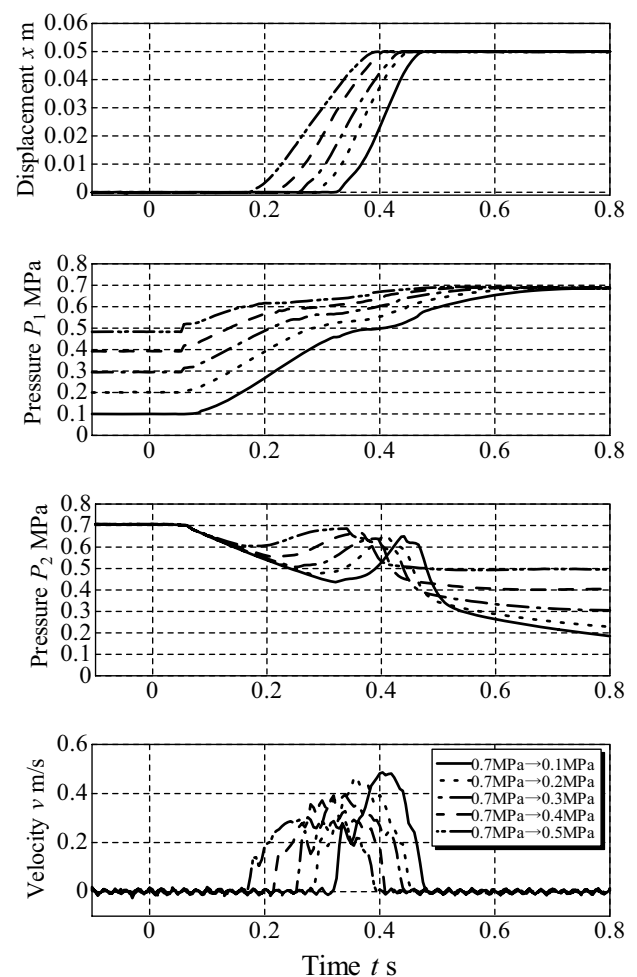
Figure 8 Experimental Results (Load factor +20%)

and improves start-up delay. Focusing on speed, a pressure becomes higher. As described above, however,

start-up delay can be reduced to improve the immediacy of response.

In the condition of actual use, the backward driving of reciprocation is typically without load. For a comprehensive driving-efficiency, the use in the range of choked flow without load is recommended.

Then the experiment on the effect of the load rate with the exhaust line pressure constant was made. Fig.9 illustrates one of the results at 0.2[MPa] of exhaust line pressure. No bad effects of the higher load rate on its driving can be observed. In the result, the load adds the force toward the piston driving direction to improve the response. In addition, no remarkable projection with the higher load rate can be observed. The secondary pressure increases greatly as the load rate becomes higher.

CONCLUSIONS

This paper examined the measures to reduce the amount of air consumption in meter-out circuits with higher exhaust line pressure from the viewpoint of the effect of tube volume and driving load. It was shown the method improves the immediacy of response (caused by higher initial cylinder pressure on the driving side) and reduces the amount of air consumption as long as the condition of choked flow and lower maximum driving force are noted. It was proved that while the characteristic of the method depends on the load direction, it improves the immediacy of response in the both directions and can be applied to actual use even if the effect of load is considered.

REFERENCES

1. Kawakami,Y.,Mutoh,H. and KAWAI,S., An Approach to Energy Saving in Pneumatic Systems with Meter-Out Circuit, Proceedings of the JPSF, 2007-11, pp.112-114.
2.Kawakami, Y. ,Mutoh,H and KAWAI,S., An Approach to Energy Saving in Pneumatic Systems with Meter-Out Circuit (2nd Report), Proceedings of the JPSF, 2007-5, pp.100-102.
3.Kawakami, Y. ,Mutoh,H and KAWAI,S., An Approach to Energy Saving in Pneumatic Systems with Meter-Out Circuit (3rd Report), Proceedings of the JPSF, 2006-11,pp.185-187.

P2-33

ON THE DESIGN OF THE NOVEL PNEUMATIC POWER ASSISTED LOWER LIMB FOR OUTDOOR WALKING

Haifan WU*, Gang FENG* , Tiebing SUN* , Fuzheng QU*, and Wenjun LIU*

* Key laboratory for precision and non-traditional machining technology of ministry of education
Dalian University of Technology, Dalian 116024, China
(e-mail:wuhaifan@dlut.edu.cn)

ABSTRACT

In previous researches, a novel portable pneumatic power source, called a Dry Ice Power Cell, and a novel pneumatic power assisted lower limb for outdoor walking powered by Dry Ice Power Cell, called a DPAL were developed. In this paper, an improvement in design of the DPAL is presented. For those people whose muscle and balance remains in good condition but who have joint pain (hip or knee joint) in their leg and are unable to walk outdoors for long, the developed device can partially lift the patient in a comfortable way by pneumatic cylinder when the affected leg touches the floor, reducing the load to which it is subject as well as the pain joint forces, thus relieving pain during walking. The developed device has the characteristics of a simple structure, low weight, easy to don and doff, and with sufficient capability to bear about 40% of the body weight. In this paper, the structure, function and experiments are described.

KEY WORDS

Walking Assist, Joint Pain, Wearable Fluid Power

NOMENCLATURE

A	:	cross area of cylinder piston
c	:	load threshold
f_a	:	assist force
$f_{a\,ref}$	:	reference assist force
f_b	:	affected leg load
K	:	assist ratio
P_{ref}	:	reference cylinder pressure

INTRODUCTION

Since our society is rapidly aging, there are increasing needs of walking assistance device for the old people. In order to develop a comfort walking assist device with advanced function and liberate the hands, powered assist device is believed an effective way. However,

because all components of such device including actuator, power unit and control system are required to be carried by a person, it is necessary for all the devices made in light weight and compact size.

Many efforts have been put on developing pneumatic powered walking assist devices in the past [1]-[3]. However, the lack of portable pneumatic power source makes them use bulky installed air compressor which will drastically impair the compactness of whole pneumatic system. It is believed that to realize a practical powered outdoor walking assist device, a portable pneumatic power source is necessary.

In the previous researches, a novel portable pneumatic power source, called a Dry Ice Power Cell[4], and a novel pneumatic power assisted lower limb for outdoor walking powered by Dry Ice Power Cell, called a DPAL were developed[5]. In this study, an improvement in design of the DPAL is proposed. It has the characteristics of a simple structure, low in weight, easy to don and doff and with sufficient capability to

bear about 40% of the body weight during about 1000 steps of outdoor walking assist, using the power of the Dry Ice Power Cell.

BASIC CONCEPT

Use of Dry Ice Power Cell

Structure and photo of developed Dry Ice Power Cell is illustrated in Figure 1. Dry Ice Power Cell weighs 600g, and stores 430g dry ice, thus the total weight is about 1kg and can comfortably be carried on a waist belt. 430g dry ice can evaporate to 218NL gas of carbon dioxide and can provide various output flowrate at a constant pressure of 0.42MPa.
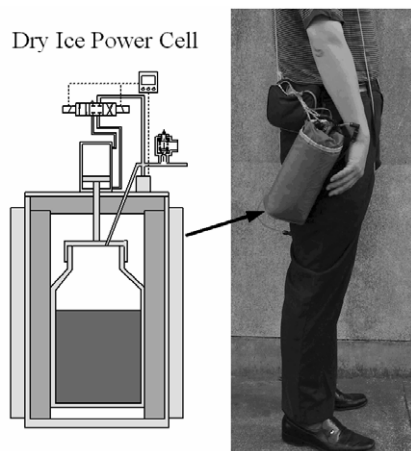
Figure 1 Structure and photo of Dry Ice Power Cell

When the maximum cylinder pressure is, for instance, 0.24MPa (57% of Dry Ice Power Cell's output pressure), a 4cm diameter cylinder can provide 30kgf force so that DPAL can be made in small size. Moreover, assuming the stroke of cylinder needed during one step assist is 3cm, the gas consumption will be 0.13NL which means all the gas evaporated from 430g dry ice can afford 1680 steps of walking assist. Even considering gas leaks at pipe and valve, Dry Ice Power Cell is supposed to drive DPAL for at least 1000 steps.

Proposal of DPAL

The concept of DPAL is illustrated in Figure 2. It comprises a saddle supplied with a hip fastening device (a suspender over the shoulders in this study), an air cylinder, a telescopic pipe with innerpipe lock mechanism inside, and a rubber foot. The lower part of the telescopic pipe is connected to the affected leg side shoe through furniture. When the foot at affected leg side touches the ground and steps the furniture downwards, the innerpipe lock locks, pipe2 is locked in pipe1, the extension force from the air cylinder can be

transmitted from ground to the torso. On the other hand, when the affected foot starts to leg swing, the innerpipe lock unlocks, pipe2 slides inside the pipe1 freely and follow the movement of affected foot, so that DPAL makes no restriction on the swing movement of the affected leg.
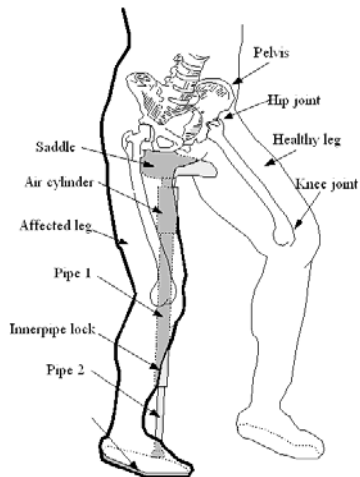
Figure 2 Concept of Pneumatic Power Assisted Lower Limb (DPAL)
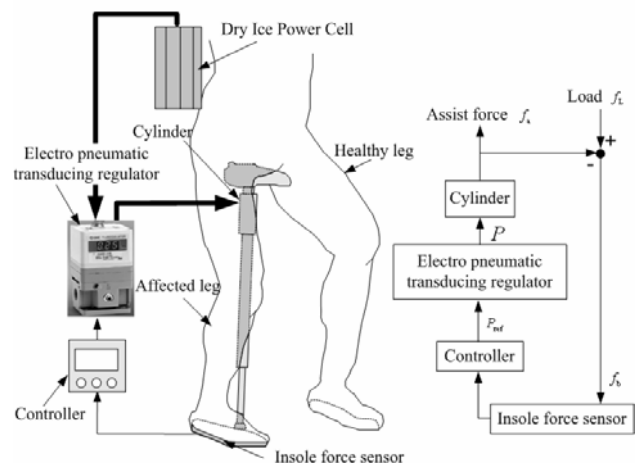
Figure 3 Control system with insole force sensor in ill leg

The concept of DPAL's control system is illustrated in Figure 3. An insole force sensor is set in the shoe to measure the body weight born by the affected leg. Then the measured data is sent to a controller. The controller calculates the control signal and sends it to electro pneumatic transducing regulator thus controls the pressure send to the cylinder. By this way the assist force from DPAL is controlled.

Control algorithm

The relationship between leg force and assist force from DPAL is illustrated in Figure 4.
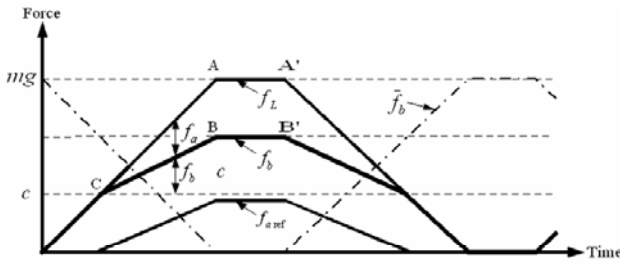
Figure 4 Concept of control rule of pneumatic power assist

When the affected leg is in stance phase, the affected leg load f_b is measured by the insole force sensor inside the affected leg shoe. When the measured data is lager than load threshold c ($c = 20kgf$ in this study), air cylinder starts to extend to provide assist force. When the reference assist force $f_{a\,ref}$ to load increment $(f_b - c)$ ratio is defined as assist ratio, the following equation can be given.

$$f_{a\,ref} = \begin{cases} K(f_b - c) & (f_b > c) \\ 0 & (f_b \leq c) \end{cases} \tag{1}$$

Assuming the retract spring of air cylinder is weak, and slide friction between piston and cylinder can be neglected, the reference pressure of air cylinder can be calculated by equation (2).

$$p_{ref} = \frac{f_{a\,ref}}{A} \tag{2}$$

Such load threshold setting is because when the maximum affected leg load is reduced to a tolerable level, joint pain will be released. As shown in Figure 4, affected leg load is reduced from A-A' to B-B' level, the load incline is also decreased from CA to CB. Only by adjusting two parameters of c and K, even to random human motion, a continuance walking assist control can be achieved. That is another merit for such settings.

DESCRIPTION OF THE STRUCTURE

Construction of the developed DPAL is illustrated in Figure 5. It comprises a saddle, an air cylinder, a telescopic pipe with innerpipe lock mechanism inside, a rubber foot, furniture, and a electro pneumatic transducing regulator.

In order to extremely minimize gas consumption, and prolong the walking assist duration, a innerpipe lock mechanism is used.

The stageless adjustable telescopic pipe with innerpipe lock mechanism inside is a remake of a "Free lock stick" (SUMITA co.). In order to explain the principle of it, the sketch graph is illustrated in Figure 6.
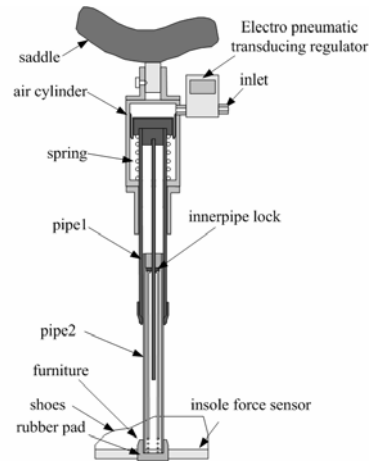
Figure 5 Construction of DPAL
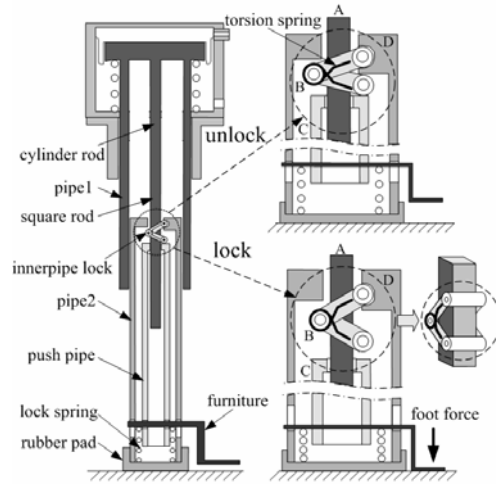
Figure 6 Principle of innerpipe lock mechanism (not to scale)

When the affected leg foot steps on the furniture, pipe C is lowered, the spring beneath it is compressed and C is separated from link B. The B will open wider by the force of a torsion spring thereon and its three shafts closely contact with a square rod A. B has a top end connecting with pipe2 through a pin, while the top end of A is fixed on pipe1. When A is pushed downwards, B will open wider and its three shafts strongly press against A to form a secured lock, thus pipe1 and pipe2 are locked together. On the other hand, when the affected leg is in swing phase, the compressed spring raises C, C push B to make it close narrower, three shafts of B separate from A without pressing it, thus A will pass B freely and pipe 1 and pipe2 are unlocked. By this way, B can lock the telescopic pipe at any position whenever the foot touches the ground and unlock it whenever the foot starts to swing. The telescopic pipe can change its length within 150mm, and can bear more than 100kg bodyweight. By this design, not only the

swing movement is not restricted but also the gas consumption is decreased because the necessary stroke of the air cylinder is reduced to the minimum.

EXPERIMENT

The experimental setup for confirming the function of DPAL is illustrated in Figure 7. In order to examining the relationship between the foot load and the assist force, developed insole force sensor is not used, and a testing stand with three load cell is used to measure the foot force and assist force instead. An 80kg weight person stands on two load cells while DPAL is located on the third load cell. Torso weight is alternately transferred between the left and right legs while DPAL provides assist force simultaneously. The measured data is recorded into the computer. In addition, measured signal by load cell under the affected leg is transferred to the controller. Then the controller generates control signal, and sends it to electro pneumatic transducing regulator, thus controls the pressure of air cylinder according to the reference pressure calculated on equation (2).

Control parameter setting is load threshold $C = 20kgf$ and assist ratio $K = 1$. A sample of experimental results is illustrated in Figure 8 which show the maximum affected leg load is reduced about 30kg. The experimental results confirm the effectiveness of the DPAL. In addition, the experiment confirms that DPAL can assist walking for about 1600 times (about 1hour walking assistance).
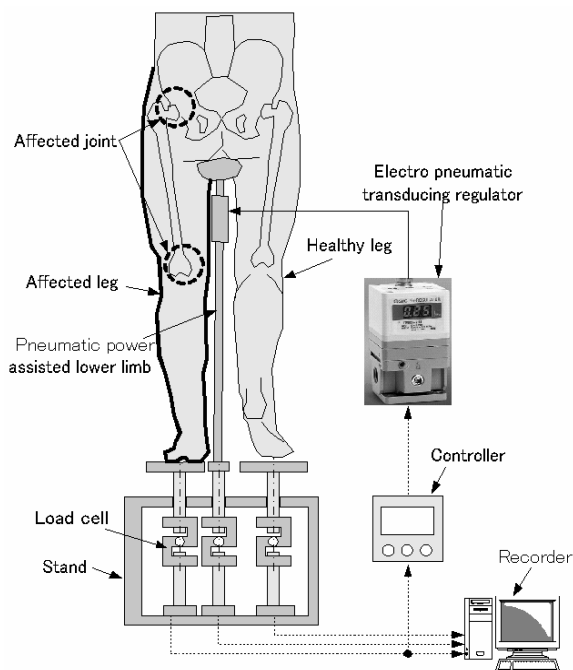
Figure 8 Experimental result sensed by load cell ($K = 1$)

CONCLUSIONS

In this study, a novel pneumatic power assisted lower limb, called a DPAL, is proposed by using Dry Ice Power Cell as its power source. It is confirmed useful for those people whose muscle and balance remains in good condition but who have joint pain (hip or knee joint) in their leg and are unable to walk outdoors for long. It can assist with outdoor walking not only over flat ground but also sloped and stair areas.

REFERENCES

1. Fabio Gazzani, Antonello Fadda, Marina Torre, and Velio Macellari, WARD: A pneumatic system for body weight relief in gait rehabilitation, IEEE Transactions on Rehabilitation Engineering, 2000, 8-4, pp.506-513.
2. Jerry E. Pratt, Benjamin T. Krupp, Christopher J. Morse, The roboknee: an exoskeleton for enhancing strength and endurance during walking, proceedings of the 2004 IEEE International Conference on Robotics & Automation, 2004, pp.2430-2435.
3. H. Yamamoto, K., Ishii, M., Hyodo, K., Yoshimitsu, T. and Matsuo, T., Development of power assisting suit for assisting nurse labor -miniaturization of supply system to realize wearable suit-, JSME International Journal, Series C, 2003, 46-3, pp.923-930.
4. Ato KITAGAWA, Haifan WU, Hideyuki TSUKAGOSHI, Sung-Hwan PARK: Development of a portable pneumatic power source using phase transition at the triple point, Transactions of the Japan Fluid Power System Society, 2005, 36-6, pp.158-164.
5. Haifan WU, Ato KITAGAWA, Hideyuki TSUKAGOSHI, Canghai LIU, Development of a novel pneumatic power assisted lower limb for outdoor walking by the use of a portable pneumatic power source, Transactions of the Japan Fluid Power System Society, 2006, 37-4, pp.43-49.

Figure 7 Experiment setup for testing the response of the DPAL

P2-34

AN INTERNERT-BASED TELE-REHABILITATION SYSTEM WITH SINGLE-MASTER AND MULTI-SLAVES

Zhen XIU*, Ato KITAGAWA*, Canghai LIU*, Hideyuki TSUKAGOSHI*, Kenichiro KONISHI**

* Department of Mechanical and Control Engineering
Tokyo Institute of Technology
S5-16 2-12-1 O-okayama Meguro-ku, Tokyo, 152-8552 Japan
(e-mail: xiuzhen@cm.ctrl.titech.ac.jp)
** Rehabilitation Center
Mo-ka Central Clinic
2-24-5 Kamikoumaza, Mo-ka City, Tochigi, 321-4337 Japan

ABSTRACT

This paper discusses an Internet-based tele-rehabilitation system with Single-Master and Multi-Slaves, which aims to achieve the situation where multiple stay-home patients in scattered places can share rehabilitation instruction from one physical therapist. After the introduction of whole system's concept, 'Passive-Active Shift' rehabilitation is proposed considering the varied symptom of different patients. Then after introduction of master slave system's designing, for passive rehabilitation which is carried through internet-based bilateral teleoperation system by therapist who is necessary, novel control architecture to ensure the stability of tele-rehabilitation system with time delay is proposed. For active rehabilitation, game-based active rehabilitation is proposed to draw the patients' mind into rehabilitation which is important to reestablish neuromuscular control.

KEY WORDS

Tele-rehabilitation, Telerobotics, Time-delay, Bilateral Teleoperation

INTRODUCTION

For patients with neurological impairment, to stimulate neurological system by moving paralyzed limbs will call back brains' potential ability, reestablish neuromuscular control and lead to the function which will make it possible to move their body as the patients wish. Generally, it is supposed to be effective for patients to go to hospital regularly and receive rehabilitation from physical therapists. However, going to the hospital regularly far from their houses actually places a large burden on patients, while it is impossible for a limited number of physical therapists to visit so many patients' houses in the recent aged society of Japan.

To solve this problem, the tele-rehabilitation system is considered to be promising, which offers a sure therapy supervised by skilful therapists to patients in their own houses and brings not so much burden to either patients or therapists. This research aims to build a bilateral master-slave system based on TCP/IP Network to achieve the situation where stay home patients in scattered places can share rehabilitation instruction by one physical therapist.

As the first step to realize the above system, in this paper firstly the concept of the tele-rehabilitation system with single-master and multi-slaves is introduced in

comparison with related previous work. Then the 'Passive-Active Shift' rehabilitation approach is proposed in order to realize that one therapist will implement rehabilitation to multiple patients. For passive rehabilitation done directly by the therapist through internet-based master-slave system, the control architecture for the tele-rehabilitation system with time delay is proposed in section 4. For active rehabilitation, game is used to encourage patients to move their joints by their own mind in order to reestablish their neuromuscular control.

SYSTEM CONCEPT

Internet-based Bilateral Teleoperation System
The task of rehabilitation is not so simple that can be accomplished by an amateur or a robot isolated from physical therapists. Firstly, the rehabilitation should be adjusted adaptively according to the different status of the patients. Secondly communication between patients and therapists is important to relief them and their family. In this research, the master-slave tele-rehabilitation system is built using internet to connect therapist and patients.

Many researches on telemedicine have been studied including tele-rehabilitation. Most were aimed at monitoring, but not include force information into the closed loop of control system. Feedback tele-rehabilitation was also reported as just a brake in case of an emergency [1]. However, according to physical therapists, the force feedback is indispensable in the process of motion rehabilitation in order to enable the therapist to detect the patients' feeling and provide exact rehabilitation.

On the other hand, the study on teleoperation system with time delay is another hot research field recently. Wave-variable method based on scattering theory, event-based method and smith-based method have been proposed [2-4]. In this research, a novel kind of compensator-based control architecture for the bilateral system with time delay will be proposed which considers the operator into whole system and could ensure the system's stability.

Single-Master and Multi-Slaves System
All of the related works mentioned above are systems with single master and single slave. This research, based on the global sharing character of Internet, aims to build a system with single-master and multi-slaves, whose concept is indicated in Figure 1.

In this research the multi-slaves are located in different places to enable the proposed system to achieve the situation where multiple scattered stay home patients can share rehabilitation instruction from a skillful therapist, which is different from the 'multiple slaves' in the work of Dr. Mark W. Spong[5], which means that the multiple cooperative robots in the same place complete one mission by operation of one master.
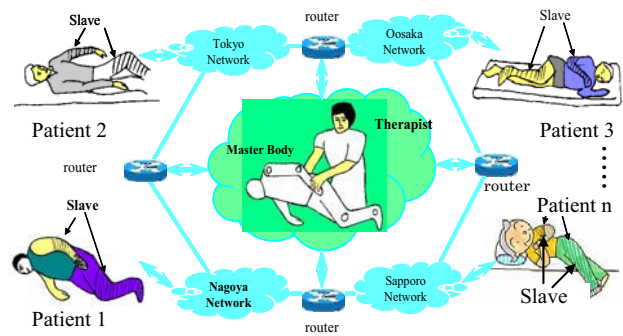
Figure 1 the Concept of Tele-rehabilitation with SMMS

The problem is that the symptom varies from patient to patient and it will be unavailable to share the same instruction among multiple patients. In order to solve this problem, 'Passive-Active Shift' approach is proposed in the following, which will be discussed from rehabilitation approaches.

Aiming Rehabilitation Approaches
According to different situation of the patients, there are passive rehabilitation and active rehabilitation. Passive rehabilitation is usually a preferred method for restoring range of motion (ROM) in the early stages of therapy. This consists of moving the limb with the muscles remaining passive. Active rehabilitation is often using to encourage patients to move their joints by their own mind in order to reestablish neuromuscular control, in the case that the patients have gotten certain recovery from passive rehabilitation. In this stage, according to the different recovery states of the patients, there are active-assistive movement phase, which involves using external assistance to assist the muscles in moving the joins and active-resistive movement phase aiming at returning an individual to normal activities via resistance exercises that are usually focused at regaining muscle strength.

This research is aiming to realize both passive rehabilitation and active rehabilitation for the proposed 'passive-active shift' rehabilitation approach.

Passive-Active Shift Rehabilitation
According to therapist, it will be effective for the patients to do passive rehabilitation and active rehabilitation in shift. Combining with the Single-master and Multi-Slaves system proposed above, 'passive-active shift' rehabilitation approach is proposed in this research. The therapist will do passive rehabilitation to the patient by the master/slave system in turn. And during this period, the other patients will do active rehabilitation such as active-assistive and active-resistive rehabilitation through slave. By the passive rehabilitation, the motion-force relation data will be recorded which will be used as the reference during the active rehabilitation..

At the moment when the therapist implements passive rehabilitation to one of patients through master/slave directly, the therapist/master and slave/patient will

consist of the bilateral teleoperation system; with time delay brought by Internet it will turn to be unstable. So how to build the master-slave system and ensure the system's stability is one of the main tasks in this research. Besides, during the period of active rehabilitation, to build a system which will arouse the patient's mind and provide the proper assistance or resistance force to the patients will be another task of this research. In the following sections, the problems of passive and active rehabilitation will be discussed separately after introduction of master/slave system's designing.

DESIGNING OF MASTER-SLAVE SYSTEM

As the initial step of the proposed system mentioned above, its application to wrist's rehabilitation is examined and the master/slave system is designed.

Advantage of Pneumatic Driving

Pneumatic power is used as the driving power in our design for the following reasons.

The compressibility and flexibility of the air will provide safety for the patients. The movement of device can be stopped when the patients feel pain and give certain resistance force to stop it. Furthermore, by maintaining the position with a pain feeling, the stretching of the muscle will bring effective aspect for the rehabilitation of the patients.

Requirement for the Devices

According to the therapist, dorsal / palmar flexion and radial/ulnar flexion shown in Figure 2 are often used in the wrist's rehabilitation. It will be effective to the rehabilitation if these two kinds of movements can be realized. Besides that the following are also required by therapist: Low cost; Simple and easy to fix the patients' hand in; about 60% movable range of the healthy people; with the property to enable therapist to perceive patient's status; Safe and quiet.

Dorsal / Palmar flexion   Radial/Ulnar flexion
Figure 2 the Required Movement of Wrist

Further more, for most patients with neurological impairment, the palms of their hands will turn to be unable to open themselves as shown in Figure 3 (a).When palm is opened by the therapist during rehabilitation as shown in Figure 3 (b), the muscle around the wrist will be at the stretched state, under

which the patient's neurological system will get most powerful nerve stimulation.
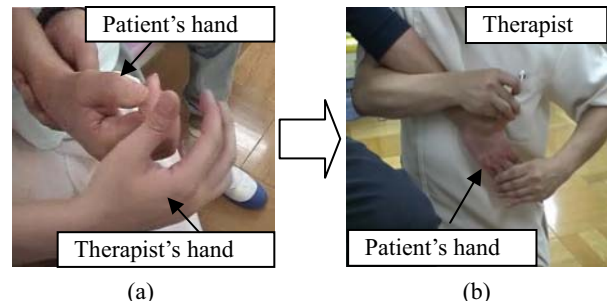
(a)   (b)
Figure 3 On-Site Rehabilitation by Opening the Palm

Mechanism of the Master/Slave

According to the above requirement, the master and slave devices for the wrist's rehabilitation are developed as shown in Figure 4, The slave device which will help the patient do rehabilitation is designed as a desk-top type which will be easy for the patient to put their arm and hand in; the master device which will be operated by the therapist is designed similar with the people's wrist.
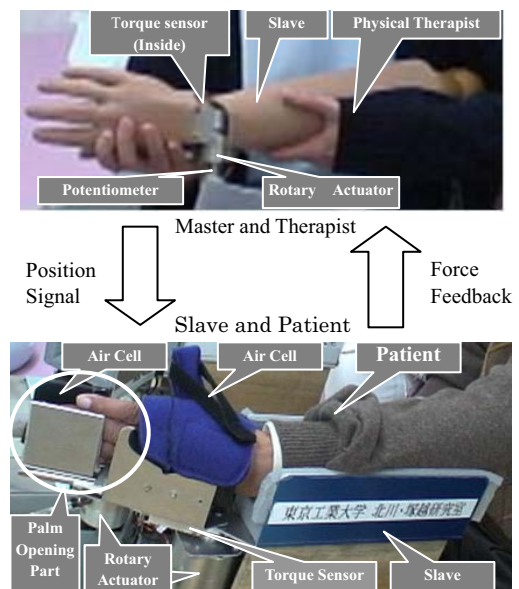
Figure 4 Master and Slave Devices Used in

In order to build bilateral operation system, the pneumatic rotary actuator (KURODA Precision Industries Ltd.) was used in both master and slave devices as the driving power. The slave device used it to realize the rehabilitation motion done by the physical therapist, and the master device used it to enable the therapist to feel the force that the patient feels. The used rotary actuator has two separated rooms in its body and the oscillating motion can be gotten by changing the air pressure in the two rooms. In our designing the pneumatic electronic regulator was used to realize the air pressure control. As shown in Figure 5, by changing the air pressure in the two rooms according to the motion or force feedback to simulate the property of the

extensor and flexor muscle which drive the motion of wrist, the different motion impedance will be gained. The property of such kind system will be similar to the wrist's motion shown in Figure 5.
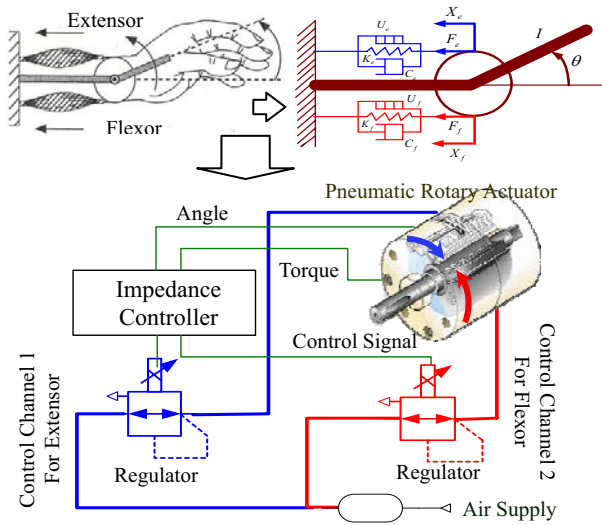
Figure 5 Wrist's Motion Realization by Pneumatic Hi-rotor

Besides, for the part of opening palm, pneumatic rotary actuator with oscillating angle of 180° (KURODA Precision Industries Ltd.) was used to help the patient to open his palm. By this mechanism, during dorsal flexion, the driving force from the rotor will be transferred through the patient's fingers, while during palmar flexion the driving force from the rotor will be transferred through dorsal region of patient's hand, which will be similar to the usual method used by therapist shown in Figure 3 (b).

On-site Experiment Results

Using the designed master/slave system above, the bilateral operation experiment was carried out in the rehabilitation center. In the experiment, the therapist holds the master to do rehabilitation to the patient. Figure 6 shows the position and torque tracing results of one patient, whose profile is shown in table 1.
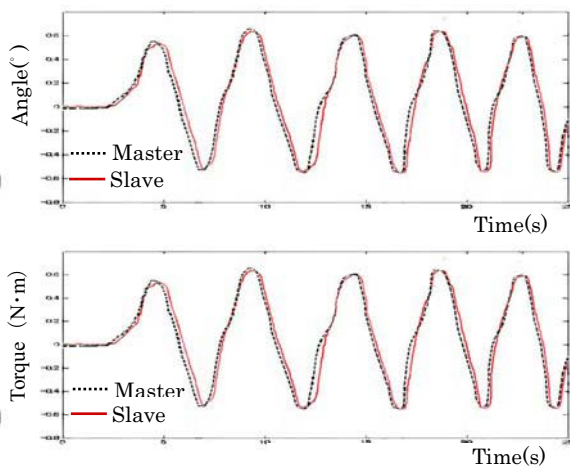
Figure 6 On-site Tracing Experiment Results in Clinic

Table1: Profile of Patient for test shown in Figure 6

Being Left-paralyzed from 2002	
Sex/Age	Male/62
Brunnstrom stage	Left upper limbs(3) Left lower limbs(4) Left finger(3)
ROM	Dorsal(40°) Palmar(60°)
others	Conscious impairment(+) Sense impairment(+) Spastic Muscle

INTERNET-BASED PASSIVE REHABILITATION
When the above system is used for Internet-based tele-rehabilitation, time delay brought by Internet will turn the system to be unstable [6]. In this section, the compensators to ensure system's stability are proposed.

Principle of Compensators

For the convenience of discussion, in this paper $G_M(s)$ is used to represent the whole system of master side and $G_S(s)$ is used to represent the whole system of slave side. The basic idea of compensators control architecture is to design the forward compensator $G_1(s)$ and feedback compensator $G_2(s)$ in forward and feedback path shown in Eq.(1) and Eq.(2) separately, $F_1(s)$ and $F_2(s)$ represent the time-delay section in the forward and feedback path.

$$G_1(s) = F_2(s) \cdot (1 - F_1(s)) \cdot G_S(s) \qquad (1)$$

$$G_2(s) = \frac{1}{1 + G_M(s) \cdot G_S(s) \cdot (1 - F_2(s))} \qquad (2)$$

The working principle of the whole compensator is shown in Figure 7, and the transformation function of the whole system with compensators is shown in Eq. (3).
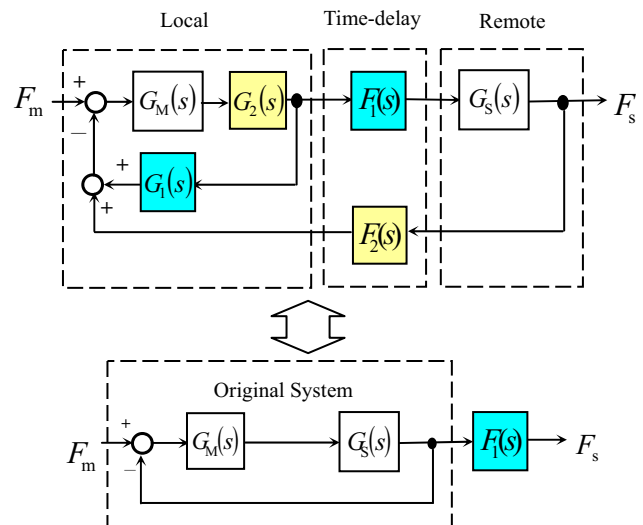
Figure 7 Principle of Compensator

$$G\ (s) = \frac{G_{\mathrm{M}}(s) \cdot G_{\mathrm{S}}(s)}{1 + G_{\mathrm{M}}(s) \cdot G_{\mathrm{S}}(s)} \cdot F_1(s) \qquad (3)$$

From Eq.(3), it can be seen that lag is eliminated and the teleoperation system with compensators is equal to the original system linking with a delay section which can be seen clearly from Figure 7. However, from (1) and (2) it can be seen that there are network time-delay secessions in both of the two compensators. The prediction of the time-delay will be necessary in such kind of compensator.

By writing not only force information of slave but also the according position information to the datagram and feedback to the master side, the time delay sections are replaced by the real network environment shown in Figure 8.Then the prediction of the time-delay turns to be unnecessary. [7]
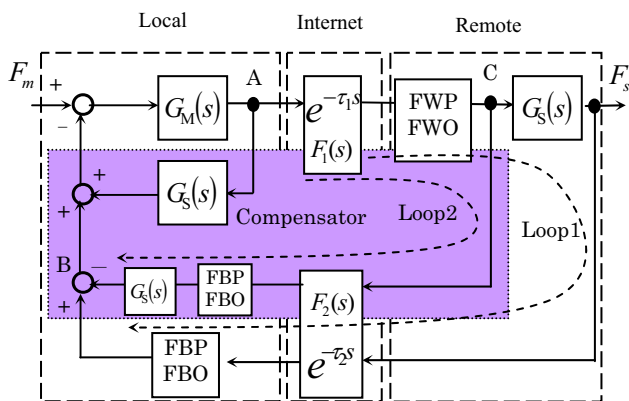
Figure 8 Teleoperation Compensator without Predictor

On-site Experiment Results on Patient

Using the master/slave devices introduced in section 3, the on-site experiment with the compensator mentioned above has been carried on to the same patient shown in Table 1 in rehabilitation center. In the experiment, time-delay shown in Figure 9 was put into the forward and feedback path separately.

(a) Forward Time-delay   (b) Feedback Time-delay
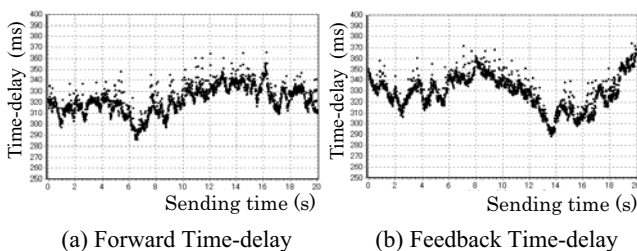
Figure 9 Network Environment in the Experiment

From the result shown in Figure.10, it can be seen that system turned to be stable, and both the position and torque have been traced well, while there was certain lag between the motion of master and slave. According to the therapist who did the experiment, the time lag did bring a sense of incongruity, but still within the endurance, because the rehabilitation is suppose to

be one kind of slow movement. The time delay used in the experiment was measured between Beijing and Tokyo through Internet and with average value of 300ms, it can be supposed that the domestic network will get better situation than that. Further more although it cannot be erased completely, with the development of network technology, the situation of time-delay brought by Internet will expect to be improved.
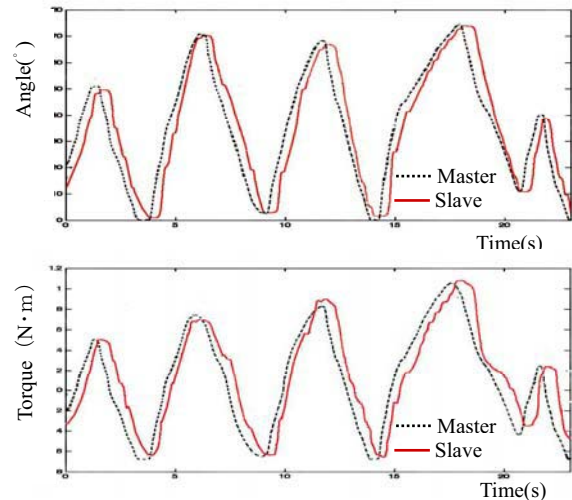
Figure 10 Tracing Experiment Results with Time-delay

GAME-BASED ACTIVE REHABILITATION

By using the motion-force data recorded during the period of passive rehabilitation through internet-based bilateral system described above, the active rehabilitation will be done to the patients other than the one doing passive rehabilitation. As mentioned before, for the patients with neurological impairment, their muscle is normal but the control signal from the neurological system can not reach to the muscle, so active rehabilitation also plays an important role in rehabilitation due to its function of arousing patients' mind which will be effective to reestablish neuromuscular control.

The important task for active rehabilitation is how to draw the patients' mind into the rehabilitation. In this research, game is considered to be utilized, which could also provide the stay-home patients with pleasure during the boring rehabilitation.

Active rehabilitation includes active-resistive rehabilitation, active-free rehabilitation and active-assistive rehabilitation. Here the difference of their engineering realization will be discussed.

Figure 11 shows scence of game-based active rehabilitation carried on by the patient in the clinic.The concept is that the patients move slave device by their imparemented hands which are put in the slave device and use the slave as the input device to move the

779

characters in the game. As a sample, the ball-game shown in Figure 11(a) has been introduced in.The plate in the game is moved.to receive the falling ball. Here the movement of the plate has been endued with power suppier and impidance resistance charactors which is realized by the characters of slave shown in Figure 11(b).
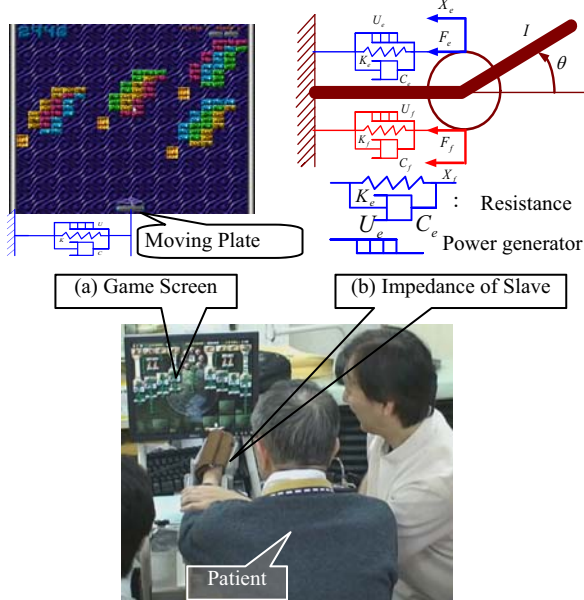
Figure 11 Scene of Game-based Active Rehabilitation in Clinic

For active-resistive rehabilitation, the resistance force with certain impedance character will be added against the movement of the patient's hand. Figure 12 shows results of two sets of experiments for active-resistive rehabilitation with different moving speeds and same resistance impedance (elasticity K:0.007; viscosity B: 0.0056; inertia M :0) following impedance control.

(a) Slower movement   (b) Faster movement
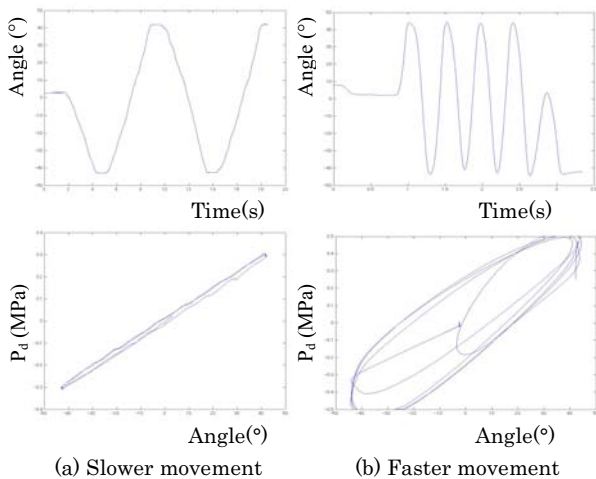
P_d: Deference of Air Pressure between the two rooms

Figure 12 Impedance Control Experiment Result

For active-assistive rehabilitation, the assistive force will be added d by the slave to help the patients whose power is not enough to move to the position they wish. How to get the moving wish of the patients will be important. At this case, it will difficult to measure the force the patients give out by the ordinary torque sensor, because both the power supply and resistance function of the patients muscle around the wrist will be working, which can not be separated by the torque sensor. ElectroMyoGram has been used in some related research, but still be far away from application. In this research, we plan to use game to detect the patients' movement wish and will discussed it in our following work.

CONCLUSION

In this paper, using pneumatic power, the master/slave system for rehabilitation was designed, for passive rehabilitation that needs the bilateral teleoperation of the therapist, novel teleoperation architecture was proposed to ensure the stability of bilateral master-slave system with time-delay, and has been verified by the on-site experiment in rehabilitation center. For active rehabilitation, in order to draw the patient's mind into rehabilitation, game-based active rehabilitation has been proposed and developed.

REFERENCES

1. MinhDuc Duong, Chisato Teraoka, "Teleoperation of Master-Slave Robot System with Haptic Feedback for Rehabilitation," SI2005, Kumamoto Japan, 2005.
2. Anderson, Spong, "Bilateral control of teleoperators with time delay," Proceedings of the 27th Conference on decision and Control, Austin, Texas, 1988.
3. Gunter Niemeyer, Towards Force-Reflecting Teleoperation Over the Internet, Proceedings of the 1998 IEEE International Conference on Robotics and Automation, Leuven, Belgium, 1998
4. Munir.S, Wayne J.Book, Internet-based teleoperation using wave variables with prediction, IEEE/ASME TRANSACTIONS ON MECHATRONICS, VOL. 7, pp.124-133, JUNE 2002.
5. Dongjun Lee, M.W. Spong, Bilateral Teleoperation of Multiple Cooperative Robots over Delayed Communication Networks: Theory, IEEE International Conference on Robotics & Automation, p362-367, 2005
6. XIU Zhen, KITAGAWA Ato, WU Pingdong, A Study on Bilateral Telecontrol of Networked Robot with Variable Time-delay, Proceedings of the 6th JFPS International Symposium on Fluid Power. 652-657,2005.
7. Zhen XIU, Ato KITAGAWA, Internet-based Tele-rehabilitation System -Bilateral Tele-control with Variable Time Delay-, Proceedings of the 2006 IEEE/RSJ International Conference on Intelligent Robots and Systems, 5208-5213,2006.

P2-35

DEVELOPMENT OF PNEUMATIC WALKING SUPPORT SHOES USING POTENTIAL ENERGY OF HUMAN

Masahiro TAKAIWA* , Toshiro NORITSUGU*

* The Graduate School of Natural Science and Technology,
Okayama University
3-1-1 Tsushimanaka, Okayama, 700-8530, JAPAN
E-mail: takaiwa@sys.okayama-u.ac.jp
toshiro@sys.okayama-u.ac.jp

ABSTRACT

Among the elderly person, most of their injuries are reported to be caused by falling down with stumbling. It is due to their shuffling walking style resulted from deterioration of their dorsiflexion muscle force along with aging. Walking plays an important role in their independent day life. In this study   we aim at developing a wearable walking support equipment embedded into shoes for a purpose of fall prevention of elderly person. A commercial product of Ankle Foot Orthosis is introduced and newly developed wire type pneumatic actuator is equipped on to support dorsiflexion motion during swing period at walking motion actively. In generally, these kind of active supporting systems require power source. We propose a driving scheme with no use of electric power, but with only potential energy of the wearer. Required specifications for the equipment are derived and the validity of proposed walking support shoes is verified through some experiments.

KEYWORDS

Walking support, Pneumatic driving system, Energy autonomous

INTRODUCTION

Japan is about to face a super aging society where aged person will occupy 35 % in the total population in 2050[1]. In spite that walking is indispensable for their independent day life, most of their injuries among aged person are reported to be caused by falling down with stumbling. It is supposed to be resulted from their shuffling walking style due to the deterioration of dorsiflexion muscle force along with aging. Once they fall down, they have higher possibility to break bones comparing to younger. Therefore it is significant to develop a walking support equipment to keep their standard QOL.

Some of these kind of equipment have been developed so far, such as, using ER actuator[2] as brake function by regulating viscosity for prevention of drop of foot, using a pneumatic passive element to hold variable stiffness function to support walking[3], using a pneumatic cylinder to support knee joint moment[4][5], using an exoskeletal robot to support gait motion[6][7]. However these equipments generally require energy like an electric power, which may bring problems of cost, total weight and reliability, etc. Therefore we develop a walking support shoes holding a driving mechanism using no electric power at all but just human potential energy.

In this paper, first of all, required specification for the equipment is adjusted and the overview of the equipment is described. After mentioning a driving mechanism of a proposed walking support shoes, the validity of the equipment is verified through some experiments.
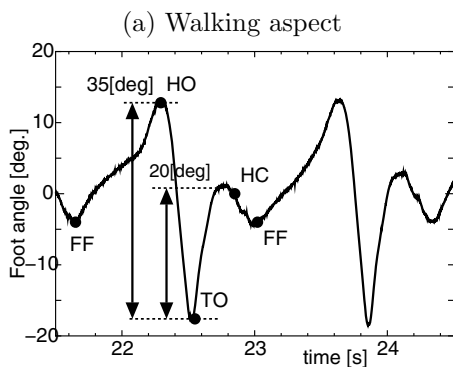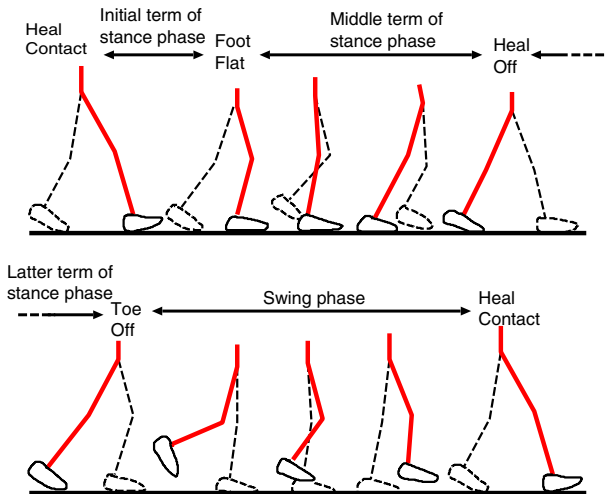
(a) Walking aspect

(b) Foot angle in the walking motion

Figure 1: Foot angle trajectory

REQUIRED SPECIFICATION

Fig.1(a) shows the walking aspect and (b) does the angle of ankle joint during walking. Angle of ankle joint at vertically standing situation is set as standard condition and dorsiflexion direction (direction of rising toe up) is set as positive.

From the state of whole surface of foot contacts with ground (Foot Flat : FF in the figure), the angle of ankle joint is increased along with forward tilting of a body and it reaches at maximum value when a heel leaves ground (Heel Off : HO). After that, the angle is rapidly decreased until toe leaves ground (Toe Off : TO) by the motion of kicking foot backward to obtain thrust forward and then dorsiflexion motion is implemented. In this time, the dorsiflexion angle of aged person is reported to be smaller. The purpose of this study is to raise this dorsiflexion angle by supporting with an equipment. It is confirmed from the figure that about 20 deg. is required for dorsiflexion motion.

In the next, the moment around an ankle joint to attain the 20 deg. of dorsiflexion angle is experimen-

(a) Measurement situation
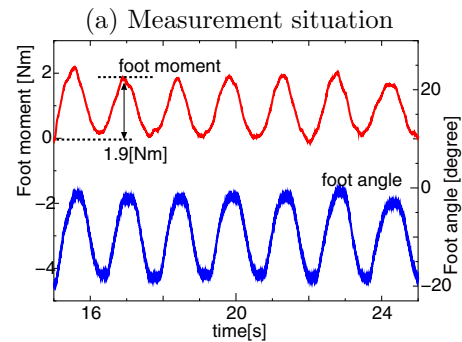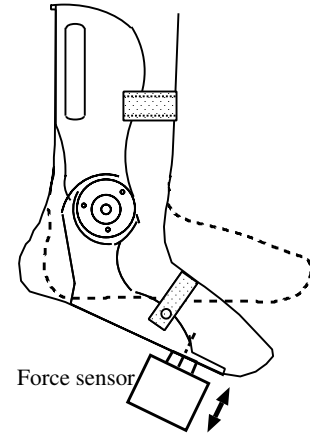
(b) required moment

Figure 2: Measurement foot moment

tally obtained. As shown in Fig.2(a), an ankle joint is forced to move about 20 deg. repeatedly from the angle of TO in Fig.1 through a force sensor. Figure (b) shows the calculated moment around ankle joint and foot angle, which indicate about 2.0 Nm is required to obtain a dorsiflexion angle.

DEVELOPED WALKING SUPPORT SHOES

Fig.3 shows a developed walking support shoes. As shown in (a), newly developed wire type pneumatic cylinder is equipped via a moment arm on the commercial product of ankle foot orthosis (product name : Dream Brace). A foot pump is set under the heel as shown in (b) and an air buffer to accumulate compressed air temporally is also equipped. The air buffer is composed with several balloons, which contribute not only to lower the cost and total weight but to exhaust high pressure air into a cylinder owing to the restitution force due to the elastic property of balloons. In the figure (d), a pilot valve to change flow direction can be seen to be embedded at a middle of a shoe bottom. By utilizing pneumatic power not only

(a) ankle orthosis

(b) shoes with foot pump

(c) Side view

(d) Sole view

(e) Back view
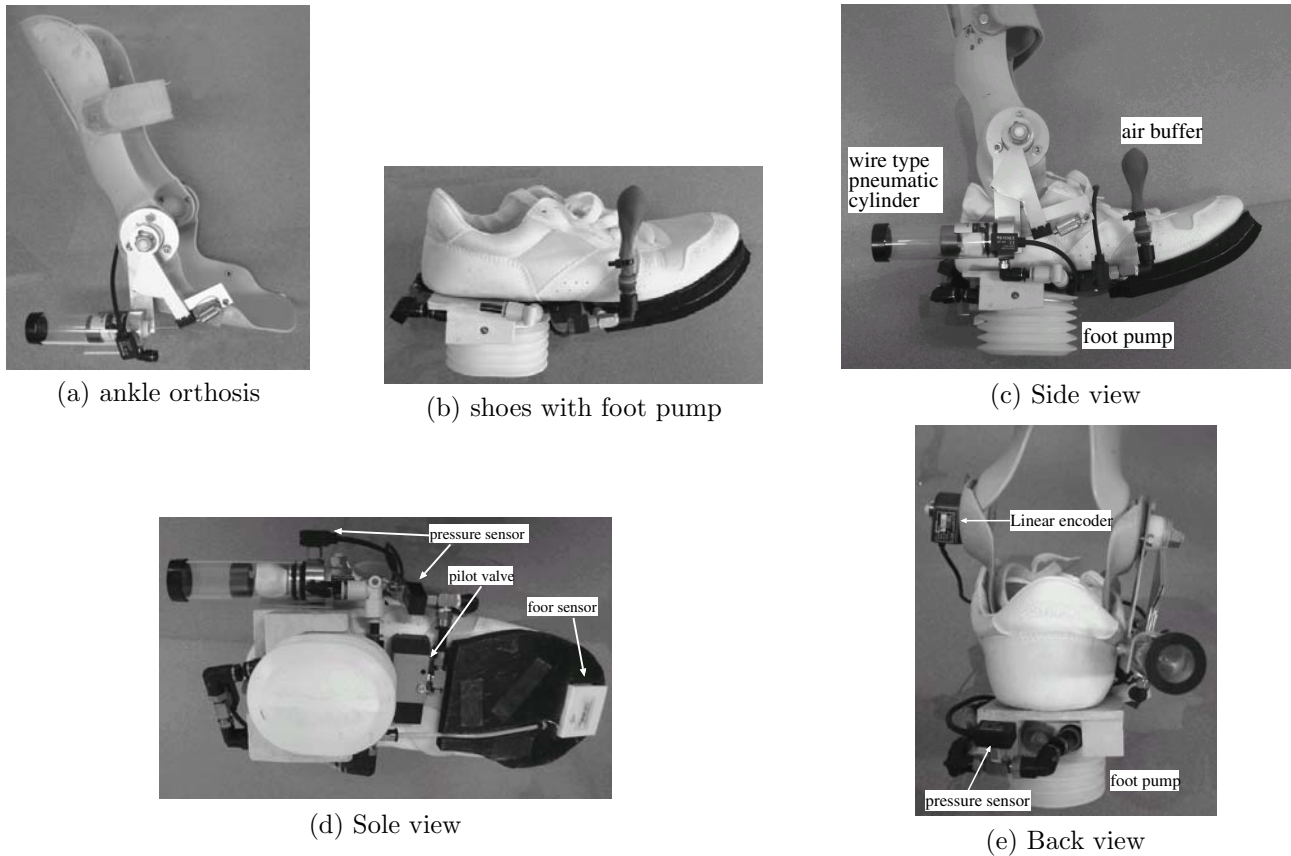
Figure 3: Walking support shoes

as an energy source but as a signal, we accomplish to develop a walking support shoes driven with no use of electrical power entirely. A foot sensor is equipped under the toe by connecting to a pilot valve with tube. The foot sensor is just a spring return type clip, which works as a mechanical switch to change flow direction by lowering pilot pressure.

Pneumatic cylinder (Airpel Co. 25mm diameter) is introduced as a driving actuator from a view point of its high power/weight ratio valid for wearable use. As shown in Fig.4, we improve the pneumatic cylinder mechanically so that it drives by wire instead of piston rod in order to be equipped at a narrow space. Concretely a balloon is inserted into a cylinder and a wire is connected to a piston through inner part of a balloon. The balloon acts as a seal to separate wire side from inner side of cylinder. Applying compressed air into the cylinder chamber, piston pull the tip of a moment arm for the heel side direction to generate dorsiflexion moment around ankle joint.

Table 1 shows the weight of each parts. Total weight is quite light of 860 g. Making further light and smaller is under the current investigation.

Table 1: mass of each part

shoe itself(without bottom part)	135g	15.7 %
ankle foot orthosis	280g	32.6%
wire type pneumatic cylinder	80g	9.3%
bottom part of shoe (pump, pilot valve, foot sensor)	365g	42.4%
total	860g	100%

PNEUMATIC DRIVING CIRCUIT

Fig.5 shows a pneumatic driving circuit. A 5 port type pilot valve is introduced to switch flow direction. At the start state of contact period with walking, a wearer step on a foot pump with their weight. In this study, the compressed air at a foot pump is used as pilot pressure as well for ease. When pilot pressure overtakes certain value(about 60 kPa), compressed air at foot pump starts to flow into the air buffer and it is accumulated until the moment to support dorsiflexion motion. Pilot pressure port is also connected by a tube and its terminal is held by a mechanical

(a) un-pressurized state

(b) pressurized stater
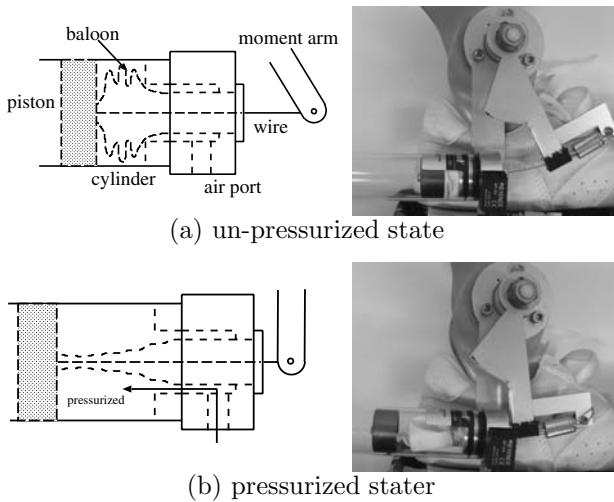
Figure 4: Structure of wire actuator
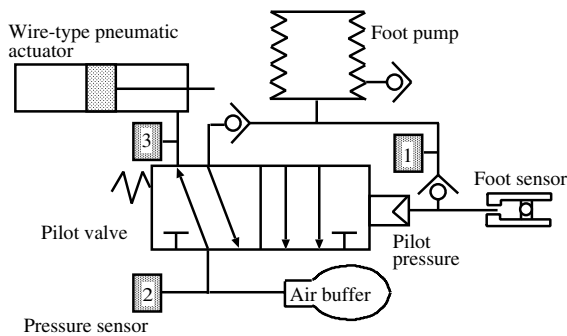
Figure 5: Pneumatic driving circuit

(a) Pressure response

(b) Foot angle

Figure 6: pressure response

clip which is equipped under toe. At the end of contact period, a toe steps on the clip when toe separates from the ground, then a pilot pressure is opened to the atmosphere to let a pilot valve to switch. Consequently the accumulated air at air buffer starts to flow into the air cylinder to generate moment around ankle joint.

Fig.6 shows an aspect of response under the a series of motion mentioned above, where (a) and (b) indicate the pressure response of each part and angle of ankle joint respectively. In figure (a), pressure at foot pump (namely equal to the pilot pressure) shown with red line is rapidly increased as soon as the pump is stepped on at the time marked with HC (Heal Contact) in the figure (b). The blue line shows a pressure at an air buffer, which raises up when the pressure at pump takes over about 60 kPa. At the same time, the air at cylinder drawn by green line is opened for atmosphere to be 0. Consequently the ankle joint is not constrained by cylinder's force. This function is very important not to prevent a foot from implementing kick back motion. Then it is confirmed that the

pressure in a cylinder raises up when toe steps on the clip at the moment of separating from ground at the time marked TO in the figure (b).

Fig.7 shows the effect of air buffer composed with balloons, where (a), (b) and (c) shows the case of using balloons of 5, 3 and 1, respectively. By putting over balloons, higher pressure can be applied to an air buffer and pneumatic cylinder owing to the increase of elastic property of rubber balloons. However a high pressure in a foot pump tends to prevent a wearer from a smooth stepping on a pump. The total number of leaves of balloons must be deiced under these trade-off between support efficiency and stepping feeling of wearer.

EXPERIMENTAL RESULTS

Fig.8 shows the effect of the equipment at simple dorsiflexion motion, where (a) and (b) correspond to the case with and without assist, respectively. EMG of dorsiflexion muscle is introduced to see the support effectiveness[8]. A subject implements a simple dorsiflexion motion repeatedly in order that the angle of ankle joint become the same in both case (a) and (b). In the case of (a), EMG shown with red line is confirmed to be declared comparing with that in figure (b) though the joint angle is almost the same among both cases, which shows the effectiveness of
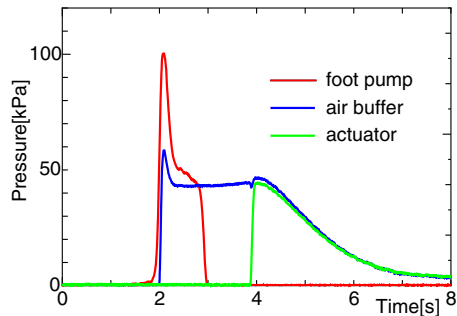
(a) In case of 5 balloons
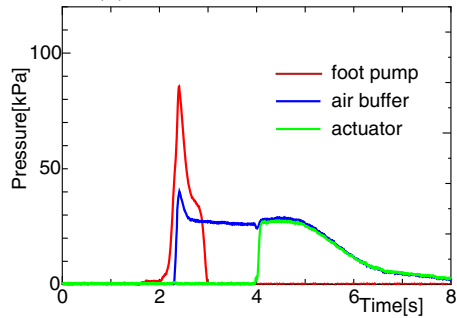
(b) In case of 3 balloons
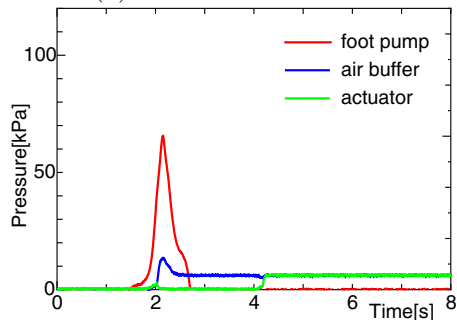
(c) In case of 1 balloon

Figure 7: Effect of the number of balloon at air buffer

(a) With assist

(b) Without assist

Figure 8: Supporting the dorsiflexion

supposing the lowering of dorsiflexion muscle force, an EMG become smaller at dorsiflexion motion in spite the foot angles are kept with almost the same one in both case (a) and (b), which shows possibility of practical use.
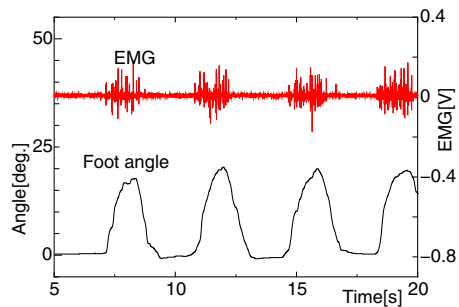
CONCLUSION

In this study, we developed a walking support shoes to prevent aged person from falling down with stumbling. The shoes has a feature to support a dorsiflexion motion using a pneumatic actuator during a swing period in a walking. We also proposed a driving mechanism with no use of electric power but with using only potential energy of wearer.

Concrete pneumatic driving mechanism from a view of flow direction using pilot valve was described.

The validity of the equipment were verified by comparing using EMG of dorsiflexion muscle force under the experiments concerning to a simple dorsiflexion motion and an actual walking one, which showed the effectiveness of the equipment in both cases.

Further improvement of supporting performances and of making smaller and light is under the current investigation.

the equipment.

Fig.9 shows the same experimental results with Fig.8 except that a 0.5 kg of weight is put on the toe by supposing the wearer as aged person. This load equals to 1.0 Nm around ankle joint, which corresponds the half of required moment for dorsiflexion motion during walking. It is also confirmed smaller EMG in case (a) than that in (b).

Fig.10 shows the effectiveness during actual walking. A subject tries to walk in order the angle of ankle joint may be the same regardless of existence of assistance. In the case of actual walking, we can also confirm the deterioration of EMG by being supported with the equipment.

Fig.11 shows the same experimental results with that of Fig.10 except that 0.5 kg of payload is put on the toe like the situation of Fig.9. Even in the case

(a) With assist

(b) Without assist

Figure 9: Support effect in simple dorsiflexion motion
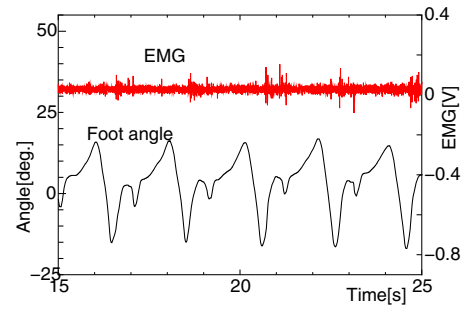
(a) With assist
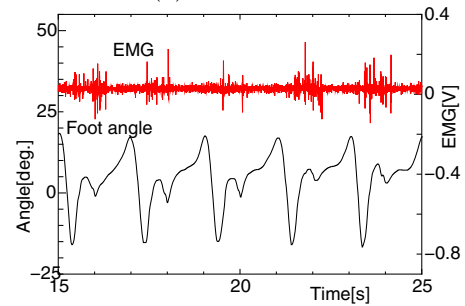
(b) Without assist

Figure 10: Support effect in walking with standard velocity

(a) With assist

(b) Without assist

Figure 11: Support effect in walking with payload

REFERENCES

1 Government of Japan,Annual Report on The Aging Society 2006, Chap.1 Status of population aging

2 Jason Nikitczuk, Brian Weinberg, Constantinos Mavroidis, Rehabilitative Knee Orthosis Driven by Electro-Rheological Fluid Based Actuators, Proc. of ICRA,pp.2294-2300, 2005

3 Hirai H, et.al, Development of an Ankle-foot Orthosis with a Pneumatic Passive Element, Proc. of ROMAN 2006, pp.220-226, 2006

4 Kazuhiro Fujishiro, Tadayuki Ariumi, Osamu Oyama, Toshihiro Yoshimitsu, Development of Pneumatic Assist System for Human Walk, Proc. of SICE Annual Conference, 2003

5 G. Belforte, L.Gastaldi, M. Sorli, Pneumatic Active Gait Orthosis, Mechatronics 11, pp.301-323, 2001

6 S. Lee, Y. Sankai, Virtual Impedance Adjustment in Unconstrained Motion for an Exoskeletal Robot Assisting the Lower Limb, Advanced Robotics, Vol.19, No.7, pp.773-795, 2005

7 J.Hidler, N.Neckel, Inverse-Dynamics Based Assessment of Gait Using a Robotic Orthosis, Proc. of the 28th IEEE EMBS Annual International Conference, pp.185-188, 2006

8 Elain N. Marieb, Essentials of Human Anatomy & Physiology, Igakusyoin, 2000

P2-36

POWER ASSIST WEAR FOR UPPER LIMB
DRIVEN BY SHEET-LIKE PNEUMATIC RUBBER MUSCLE

Masaya ARAGANE*, Toshiro NORITSUGU*, Masahiro TAKAIWA* and Daisuke SASAKI*

* Graduate School of Natural Science and Technology
Okayama University
3-1-1, Tsushimanaka, Okayama, 700-8530 Japan
(E-mail: aragane@mcrlab.sys.okayama-u.ac.jp,[toshiro,takaiwa,daisuke]@sys.okayama-u.ac.jp)

ABSTRACT

Along with declining birthrate and a growing proportion of elderly, to increase the number of people who requires nursing is anticipated. As a result, the shortage of the workers in medical welfare field is serious concerns in Japan. Then, if the wearable power assist device can be developed, many people can live independent life with a slight degree of assist. The purpose of this study is to develop a power assist wear to assist an activity of daily living of aged or disabled person. For the actuator, it is required to have a compact, light-weight and flexibility. Developed sheet-like curved type pneumatic rubber muscle is made of rubber band and has a high affinity for human skin. In this paper, the characteristics of the sheet-like curved type pneumatic rubber muscle and the power assist wear are described.

KEY WORDS

Pneumatics, Power assist, Soft actuator, Wearable device

INTRODUCTION

In Japan, the number of people who requires nursing is anticipated by the reasons below.
1. Declining birthrate and growing proportion of elderly
2. A muscular weakness associated with physical handicap

As a result, the shortage of the workers in medical welfare field is serious concerns. However, people accredit the nursing necessary level 2 or less are accounts for 64[%] of the whole [1]. Then, if the wearable power assist device can be developed, many people can live independent life with a slight degree of assist.

The McKibben type pneumatic rubber muscle is a typical actuator for a power assist device [2] and availability of power assist device such as muscle suit which using this actuator is confirmed [3]. However, it is required to be compact and light as clothes when using in daily life. If the development of power assist device which has soft structure and can be wore as a sense of wearing clothes can achieve, it is useful for the people who only requires slight degree of assistance.

The purpose of this study is to develop a sheet-like curved type pneumatic rubber muscle and the power assist wear to assist an activity of daily living of aged or disabled person [4]. The developed sheet-liked curved type pneumatic rubber muscle is made of rubber band which has anisotropy, and it has a high affinity for human skin. Also, the developed power assist wear using this rubber muscle is composed of clothing fabric and available to wear as clothes.

In this paper, the characteristics of the sheet-liked curved type pneumatic rubber muscle and the developed wrist and elbow power assist wear are described.

MECHANISM OF RUBBER MUSCLE

As shown in Figure 1, sheet-like curved type pneumatic rubber muscle consists of a rubber tube and two sheets. Head of the rubber tube is stopped up by urethane plug to seal-up, and two sheets are sewed to prevent the expansion of rubber tube by pressurization. By using the elastic member for sheet which has anisotropy like a rubber band, the radial expansion of rubber tube is converted to the axial movement.

Figure 2 shows the movement of sheet-like curved type pneumatic rubber muscle. With controlling the amounts of extension of each sheet by changing the number, material, it works out three different movements.

Figure 2(a) is the case when using same number of rubber band for ambilateral sheet. When it is pressurized, the amount of extension is equal, so it makes the movement of extension.

Figure 2(b) is the case when using different number of rubber band for ambilateral sheet. When it is pressurized, the amount of extension is different, so it makes the movement of curve and extension.

Figure 2(c) is the case when one-sided sheet is restricted by using the material which does not extends like nylon band. When it is pressurized, the band only extends, so it makes the movement of curve.

By combining this characteristic, assistance for various body sites can be accomplished.
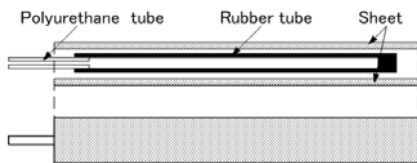
Figure 1 Basement of rubber muscle
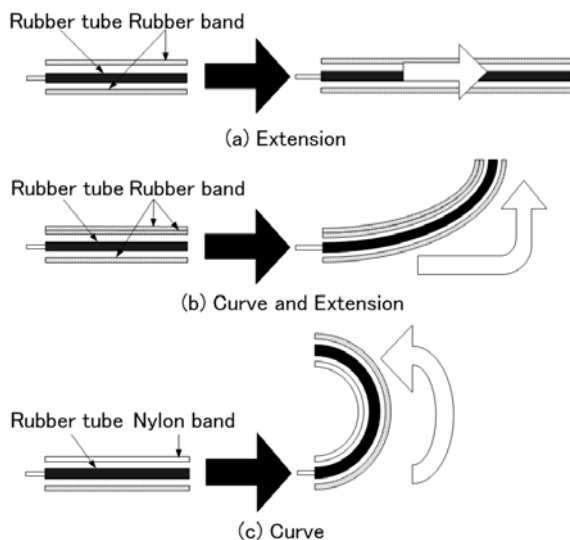
Figure 2 Movement of rubber muscle

WRIST POWER ASSIST WEAR

Structure

As shown in Figure 3, sheet-like curved type pneumatic rubber muscle for wrist power assist wear makes the movement of curve (Figure 2(c)) by sewing the nylon band to the center of the one-sided sheet.

Wrist power assist wear is made of flexible material like clothing fabric and supporter for the interface to transfer the flexion force to wrist. Rubber muscle is unfixed with assist wear, and it moves in length direction by setting the slide mechanism. When the rubber tube is on the surface of the wrist, it can assist the flexion, but it interrupts the movement of dorsal flexion. So in the case when considering the multiple movement of wrist, it requires to be the structure which does not interrupt the movement of wrist. As shown in Figure 4(a), two rubber muscles are set up in both flanks of hand. As shown in Figure 4(b), upper rubber muscle makes the movements of flexion (Figure 5(a)), and rubber muscle below makes dorsal flexion (Figure 5(b)). The weight of one rubber muscle and wrist power assist wear is each 20[g] and 205[g].
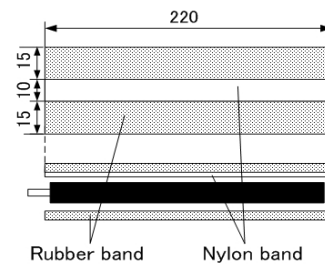
(a) Structure

(b) 0[kPa]   (c) 250[kPa]

Figure 3 Outlook of rubber muscle for wrist
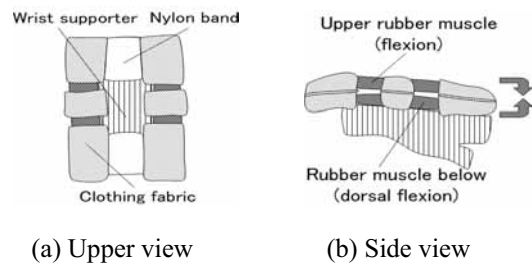
(a) Upper view   (b) Side view

Figure 4 Structure of wrist power assist wear

Torque

Figure 6 shows the torque characteristic of wrist power assist wear. For the measurement, wrist model which only has degree of freedom in flexion and dorsal flexion are used. Torque is calculated from the force generated from the top of power assist wear in each angle. The range of the angle is below.

1. Flexion : 0 to 90[deg] by 15[deg] step
2. Dorsal flexion : 0 to 70[deg] by 10[deg] step

When the gravity center of the hand is assumed to be in the center between fingertips and the joint of wrist, required torque for adult male (height: 1.72[m], weight: 65.58[kg] [5]) to move wrist is about 0.5[Nm] [6]. From Figure 6(c), it is available to assist 90[deg] for wrist flexion and 70[deg] for wrist dorsal flexion by 350[kPa] pressurization. However, in the case of pressuring more than 400[kPa] for flexion in 0[deg], rubber muscle does not move in length direction as shown in Figure 6(b). This is because the seam of the rubber muscle is asymmetry and has different stiffness in both sides.

(a) Flexion   (b) Dorsal flexion
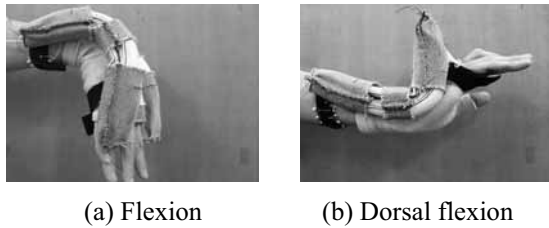
Figure 5 Movement of wrist power assist wear

(a) Experimental condition   (b) Dispersion
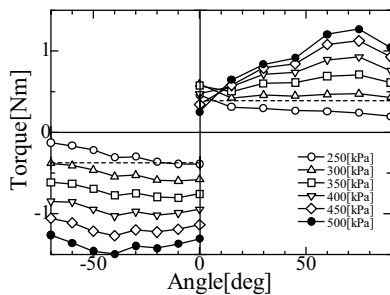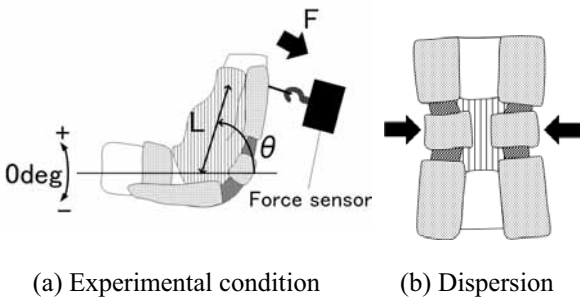
(c) Torque

Figure 6 Torque characteristic for wrist

Effect of assistance

To evaluate the effect of wrist power assist wear, it needs to move without human power. The experiment description is to measure the wrist angle and EMG when the wearer are wearing and not wearing the wrist power assist wear. As shown in Figure 7, the measurement position of EMG is flexor carpi ulnaris for flexion, and extensor carpi radialis longus for dorsal flexion. Considering the daily life, the experiment is held in two positions (Figure 8), and positions depend on the position of human body and upper limb. Experiment is held in the methods below and evaluated by the wrist angle and EMG.

1. 0～5[s]: in condition of weak
2. 5～15[s]: pressurize to 400[kPa] by lamp input
3. 15～20[s]: keep the assist with in condition of weak

Figure 9 and 10 show the result of wrist flexion in both positions. In vertical position, it can assist up to 80[deg] when wearer is in condition of weak. Also, in horizontal position, the relative angle θ of hand and body is 185[deg] (measured angle is 95[deg]). The maximum flexion angle of wearer is 95[deg], and the muscle potential is reduced. From this result, this power assist wear can assist more than 85[%] of the movement.

Figure 11 and 12 show the result of wrist dorsal flexion in both positions. In vertical position, it can assist up to 70[deg] and also in horizontal position, the relative angle θ of hand and body is 155[deg] (measured angle is 65[deg]). The maximum dorsal flexion angle of wearer is 70[deg], and the muscle potential is reduced. From this result, this power assist wear can assist more than 90[%] of the movement.

The assistance over the motion range involves pain, furthermore, it does not have to assist completely when using in daily life. Developed wrist power assist wear is using the flexible material and safe, because it has back-drivability. From these, the wrist power assist wear is available for the assistance of wrist movement.
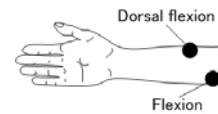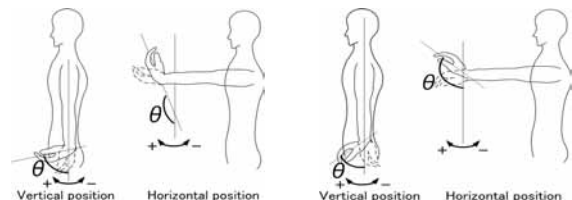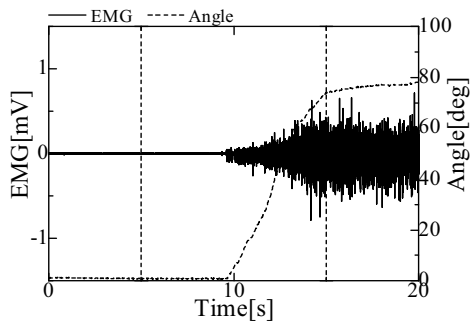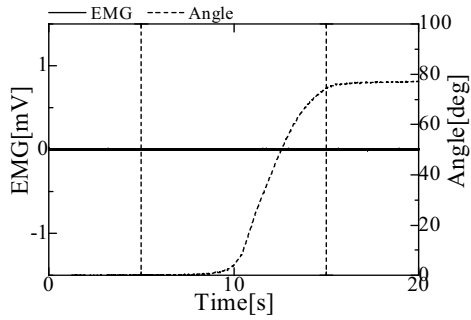

Figure 7 EMG part

(a) Flexion   (b) Dorsal flexion

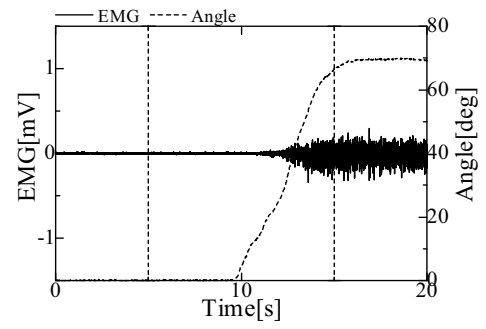Figure 8 Experimental position

(a) Without assist

(b) With assist

Figure 9 Flexion (Vertical position)
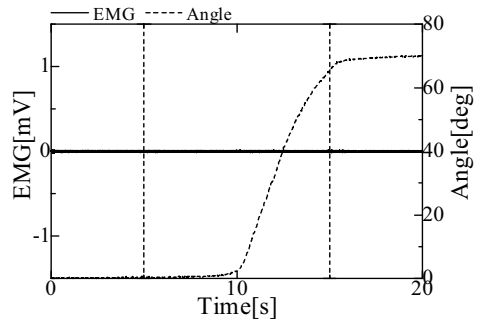

(a) Without assist

(b)With assist

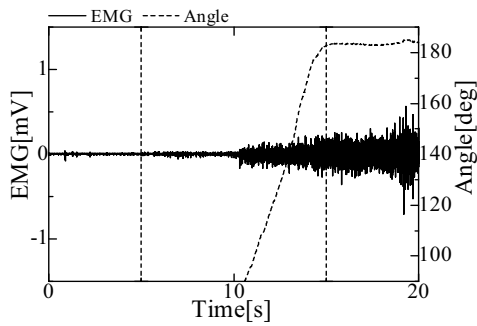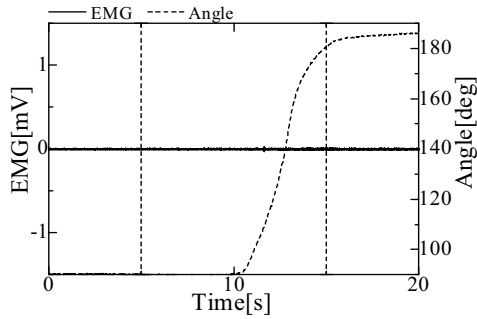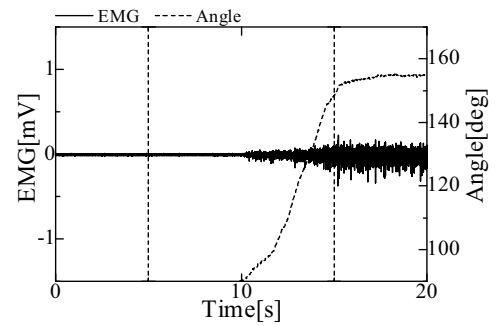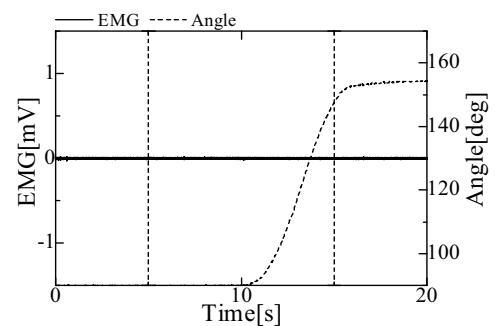Figure 10 Flexion (Horizontal position)

(a) Without assist

(b) With assist

Figure 11 Dorsal flexion (Vertical position)

(a) Without assist

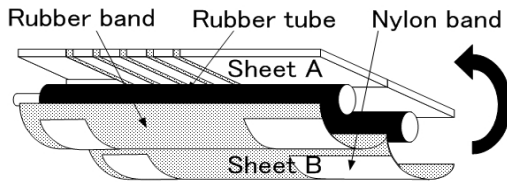(b) With assist

Figure 12 Dorsal flexion (Horizontal position)

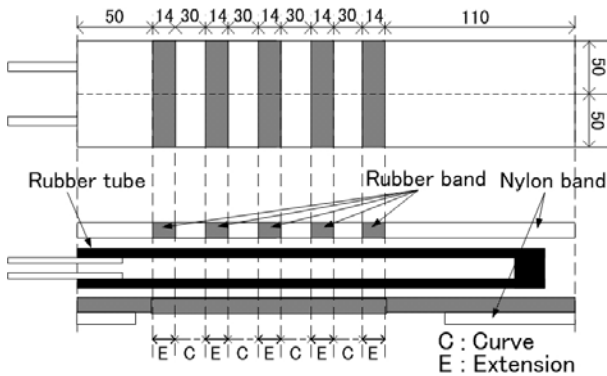## ELBOW POWER ASSIST WEAR

Structure
As shown in Figure 13 and 14, sheet-like curved type pneumatic rubber muscle for elbow power assist wear makes the movement of extension (Figure 2(a)) and curve (Figure 2(c)). Two sheet A are sewed in parallel at the center of sheet B. As shown in Figure 15, elbow power assist wear is made of clothing fabric to transfer the flexion force to elbow.

Torque
Figure 16 shows the torque characteristic of elbow power assist wear. When the gravity center of the arm is assumed to be in the center between fingertips and the joint of elbow, required torque for adult male to move elbow is about 4.0[Nm]. From Figure 16, it is available to assist below 100[deg] for elbow flexion by 320[kPa] pressurization.

Effect of assistance
As well as wrist power assist wear, it needs to be evaluated when considering the use in daily life. As shown in Figure 17, the experiment is held in two positions and the measured part of EMG is biceps brachii. Experiment is held in the methods below and evaluated by the elbow angle and EMG.
1. 0～5[s]: pressurize to 80[kPa]
2. 5～15[s]: pressurize to 320[kPa] by lamp input
3. 15～20[s]: keep the assist with in condition of weak
Figure 18 and 19 show the result of elbow flexion in vertical and horizontal positions. In vertical position, it can assist up to 100[deg] when wearer is in condition of weak. Also, in horizontal position, the relative angle θ of arm and body is 210[deg] (actual measured angle of elbow is 120[deg]). The maximum flexion angle of wearer is 120[deg] and this power assist wear can assist more than 80[%] of the movement.

(a) Structure

(b) Upper view

Figure 13 Structure of rubber muscle for elbow

(a) 0[kPa]　　　　　(b) 250[kPa]

Figure 14 Movement of rubber muscle for elbow
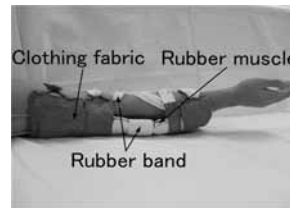
(a) 0[kPa]　　　　　(b) 250[kPa]
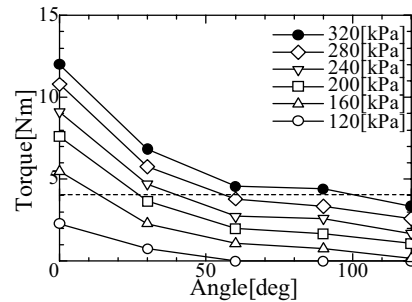
Figure 15 Movement of elbow power assist wear
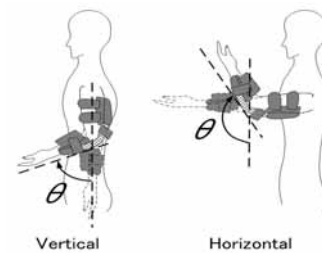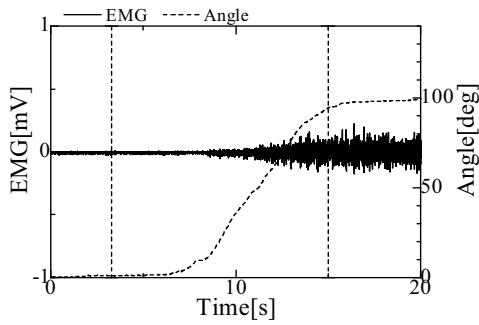

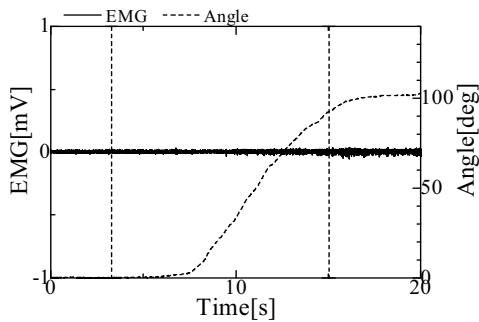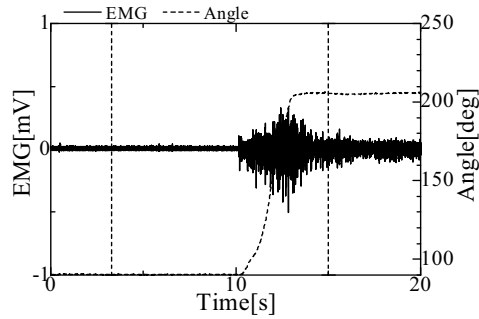Figure 16 Torque characteristic for elbow
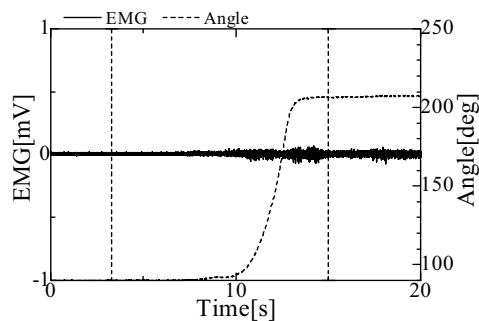

Figure 17 Experimental position

(a) Without assist

(b) With assist

Figure 18 Vertical position

(a) Without assist

(b) With assist

Figure 19 Horizontal position

CONCLUSION

In order to assist the movement of wrist and elbow, power assist wear with sheet-like curved type pneumatic rubber muscle has been developed. Sheet-like curved type pneumatic rubber muscle can make a movement of curve by itself and can transfer the force directly to human body. So the device using this rubber muscle does not need a link mechanism and can make the device light and compact. This power assist wear has the characteristic of light weight and flexible, and it is suitable for the usage in daily life. The assignment for the future is below

1. Improve the structure to transfer the force efficiently
2. Application for the movement of other body site
3. Realization of the movement which is commonly used in daily life

REFERENCE

1. Ministry of Health, Labour and Welfare, Report of the situation of long term care insurance, 2007. (in Japanese)
2. Ching-Ping Chou and Blake Hannaford, Measurement and Modeling of McKibben Pneumatic Artificial Muscles, IEEE Transactions on Robotics and Automation, Vol.12, No.1, 1996.
3. H. Kobayashi, H. Suzuki, and T. Hayashi, A Muscle Suit for Muscular Support – Realization of All Motion for the Upper Limb, 2004 1st IEEE technical Exhibition Based on Robotics and Automation Proceedings, CD-ROM, 2004.
4. M. Aragane, T. Noritsugu, M. Takaiwa and D. Sasaki, Development of Sheet-like Curved Type Pneumatic Rubber Muscle and application of Elbow Power Assist Wear, The 25th Annual Conference of the Robotics Society of Japan, 3I-25, 2007. (in Japanese)
5. Ministry of Education, Culture, Sports, Science and Technology, Research of strength and athletic for 2006, 2007.(in Japanese)
6. J. Kohara et al., Measurement of human body, Japan Publication Service, 1986.(in Japanese)

THE ACTIVE PNEUMATIC-BALANCED CONTROLLED LIFTING POSITIONING SYSTEM FOR THE NEW GENERATION TFT-LCD GLASS SUBSTRATES

Mao-Hsiung CHIANG[*], Yih-Nan CHEN[*,**], Fei-Lung YANG[****], Wei-Chieh CHEN[***] and Hong-Chuen HSIEH[***]

[*] Department of Engineering Science and Ocean Engineering,
National Taiwan University
Taipei 106, Taiwan
(E-mail: mhchiang@ntu.edu.tw)

[**] Department of Mechanical Engineering,
Tatung University
Taipei 104, Taiwan

[***] Graduate Institute of Automation and Control,
National Taiwan University of Science and Technology,
Taipei 106, Taiwan

[****] Department of Mechanical Engineering,
Nanya Institute of Technology,
Taoyuan 320, Taiwan

ABSTRACT

Due to the development of the larger size of FPD, the conveyor system, especially the lifting system, become a significant topic. This paper aims to develop novel lifting system with the AC servo driving and the pneumatic-balanced system for the new generation of LCD glass substrates. Owing to the large variation range of the loading in the new generation lifting system, the pneumatic-balanced system is developed for counterbalanced the weight of the loading for reducing the loading power of the AC servo motor. A PC-Based control system is developed for achieving better response and position accuracy. Adaptive sliding mode control with function approaching technique is used in this paper as the control strategy. In order to improve the jerk problem during the motion process, path control is used. The proposed new lifting system with pneumatic-balanced technique is implemented and verified through simulation and experiment.

KEY WORDS

Pneumatic-balanced control, Path-positioning control, Lifting system, Glass substrate, Flat panel display.

INTRODUCTION

Flat Panel displays (FPD) have become one of the most significant industries in the world. The manufacturers of FPD concentrate especially on the countries in east-Asia, including Taiwan, Japan and Korea. In order to satisfy the fast development of the request of the market that trends toward larger and larger sizes for TV and monitor, the new generations of the glass substrates have been developed almost every three years. However, the weights and the dimensions of the glass substrates also increase such that the manufacturing equipments have to face new process challenge. Table 1 shows the dimension and weight of the different generation of glass substrates. The thickness of the glass substrate is about 0.5 to 0.7 mm.

Table 1 Dimension of different generation of glass substrate

Generation	Size (mm²)	Weight (kgf)
2nd Gen	400×500	0.4
3rd Gen	550×670	0.7
3.5th Gen	600×720	0.8
4th Gen	680×880	1.1
5th Gen	1100×1250	2.5
5.5th Gen	1300×1500	3.5
6th Gen	1500×1850	5
7th Gen	1800×2000	6.5
7.5th Gen	1950×2250	7.5
8th Gen	2160×2460	9.0

The conveyor systems of the glass substrate become more and more complex due to the increase of the dimension and weight of the glass substrate. The conveyor systems of the glass substrate contain horizontal linear conveyor, horizontal rotational conveyor and vertical lifting system. The horizontal linear conveyors are driven by roller generally and can be supported by air bearing in the new generation. The horizontal rotational conveyor rotates the glass substrates. The vertical lifting systems serve to load the glass substrate in and out the cassette, which works as buffer of glass substrate in the process. This paper aims to investigate the lifting positioning system with pneumatic-balanced system. In the new generation of glass substrates, the weight variation between no-load and full-load conditions of the lifting system can reach from 200 kgf to 1000 kgf. The large loading variation results in the demand of larger power of the AC servo motor for positioning. Instead of that, the loading variation can be counter-balanced by the pneumatic cylinders of the pneumatic-balanced system such that the AC servo motor needs only smaller power without adding the inertial mass. Besides, in order to achieve jerk-free motion, path-positioning control, that contains path tracking control in the motion process and positioning control at the target end position, is developed in this paper. For that, adaptive sliding mode control is used to develop the controller.

TESTRIG LAYOUT

The test rig of the active pneumatic-balanced lifting positioning system for the new generation TFT-LCD glass substrate consists of the pneumatic-balanced controlled system, which contains two rodless pneumatic cylinders with pressure control servo valves, and a positioning control system driven by an AC servo motor with belt transmission mechanism that serves as position control of the lifting system. The pneumatic-balanced controlled system serves to balance actively the weight of the loading and the lifting table.
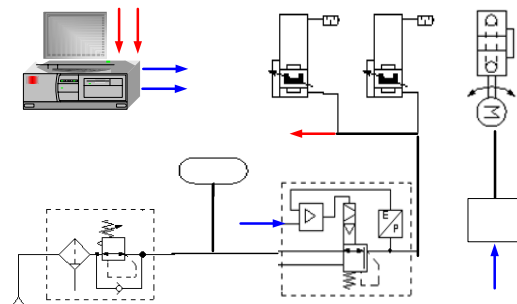

Figure 1 Layout of the test rig

Figure 2 Concept of the test rig

Table 2 Specifications of the test rig

Item	Specifications
Control type	Path-positioning
Glass substrate dimension	1950 X 2250mm
Weight of full loading	1000kg
Weight of no-loading	200kgf
Stroke of Z-axis	1100mm
Velocity	40m/min
Class of clean room	5000
Position accuracy of Z-axis	+/-0.2mm

A PC-based control system is used to implement the positioning control and the pneumatic-balanced control. Figure 1 photographically shows the layout of the test rig. Figure 2 schematically illustrates the concept of the proposed pneumatic-balanced lifting positioning system. The pneumatic balanced control system works firstly to keep the resultant weight constant, which means the weight of loading minus the counter-balanced force form the pneumatic cylinders is constant. Pressure sensors are used to measure the pneumatic pressure p and calculate the pneumatic balanced force F_{pneu} by

$$F_{pneu} = p \cdot A \cdot n \tag{1}$$

where A indicates the effective piston area of pneumatic cylinder; n is the cylinder number. The positioning control system driven by an AC servo motor is measured by a position sensor. Table 2 specifies the required performance.

ADAPTIVE FUZZY SLIDING MODE CONTROL

Designing a SMC needs to know the system models and to find the inverse form of inertia term in system dynamics. However, the accurate mathematical models are always difficult to formulate or even not available. To solve these problems, an AFSMC shown in Fig.3 is proposed.

The state equations of the servo control system model can be achieved as follows

$$\dot{x}_1 = x_2(t)$$
$$\dot{x}_2 = -\sum_1^2 a_i x_i(t) + g(\underline{x})u + d(\underline{x}) = f(\underline{x}) + g(\underline{x})u + d(\underline{x}) \tag{2}$$

Fuzzy Control

Assume that there are n rules in a fuzzy base and each of them has the following form:

$$R^i : \text{IF } S \text{ is } F^i \text{ THEN } u \text{ is } \alpha_i \tag{3}$$

where S is the input variable of the fuzzy system; u is the output variable of the fuzzy system; F^i are the triangular-type membership functions; and α_i are the singleton control actions for $i = 1, 2, ..., n$. The defuzzification of the FC output is accomplished by the method of center-of-gravity (Lee 1990)

$$u = \sum_{i=1}^n \alpha_i \times w_i / \sum_{i=1}^n w_i = \underline{\alpha}^T \xi \tag{4}$$

where w_i is the firing weight of the ith rule, $\underline{\alpha} = [\alpha_1, \alpha_2, ..., \alpha_n]^T$ is the parameter vector and $\underline{\xi} = [\xi_1, \xi_2, ..., \xi_n]^T$ is the vector of fuzzy basis functions

$$\xi_i = w_i / \sum_{i=1}^n w_i \tag{5}$$

For the conventional FC, the control actions α_i should be previously assigned through a lot of trails to achieve satisfactory control performance. In the following, the adaptive algorithm will be proposed to tune these control actions on-line.

Fuzzy Sliding Mode Control

The methods to design the fuzzy sliding-mode controller for a non-linear system with 2nd order where the error and the error change rate were used to synthesize fuzzy reasoning rules was proposed (Palm 1994 and Hwang *et al.* 1992). However, the rule number was larger and did not give the mathematical expression. Thus, it is difficult to analyze the properties of the control system. To overcome this problem, we adopt the sliding surface $S = 0$ of SMC as a variable to compress all the information into one type, extend the sliding surface $S = 0$ to the fuzzy sliding surface $\tilde{S} = \tilde{0}$, and make S be a linguistic description of $\tilde{S}$. In this paper the two triangular-typed functions are used to define the membership functions of IF-part and THEN-part, which are depicted in Figs.4 (a) and 4(b) respectively. The fuzzy rules are given in the following form

$$R^l : \text{IF } S \text{ is } \tilde{F}_s^l \text{ THEN } u_{fs} \text{ is } \tilde{F}_u^{8-l}, \; l = 1, ..., 7. \tag{6}$$

According to the sup-min compositional rule of inference and the defuzzification of the control output accomplished by the method of center-of-area, the mathematical expression can be derived as

$$u_{fs} = \begin{cases} 1 & ,if \quad z < -1 \\ (7.5z^2 + 13.5z + 5)/(9z^2 + 15z + 5) & ,if \quad -1 \le z < -2/3 \\ (9z^2 + 11z + 2)/(18z^2 + 18z + 2) & ,if \quad -2/3 \le z < -1/3 \\ (1.5z^2 + 1.5z)/(9z^2 + 3z - 1) & ,if \quad -1/3 \le z < 0 \\ (-1.5z^2 + 1.5z)/(9z^2 - 3z - 1) & ,if \quad 0 \le z < 1/3 \\ (-9z^2 + 11z - 2)/(18z^2 - 18z + 2) & ,if \quad 1/3 \le z < 2/3 \\ (-7.5z^2 + 13.5z - 5)/(9z^2 - 15z + 5) & ,if \quad 2/3 \le z < 1 \\ -1 & ,if \quad z \ge 1 \end{cases}$$

$$\tag{7}$$

where $z = S/\Phi$ and $\Phi > 0$ is a constant which describes the width of a boundary layer. As $|S| \ge \Phi$, it is easy to check $u_{fs} = -\text{sgn}(S)$.
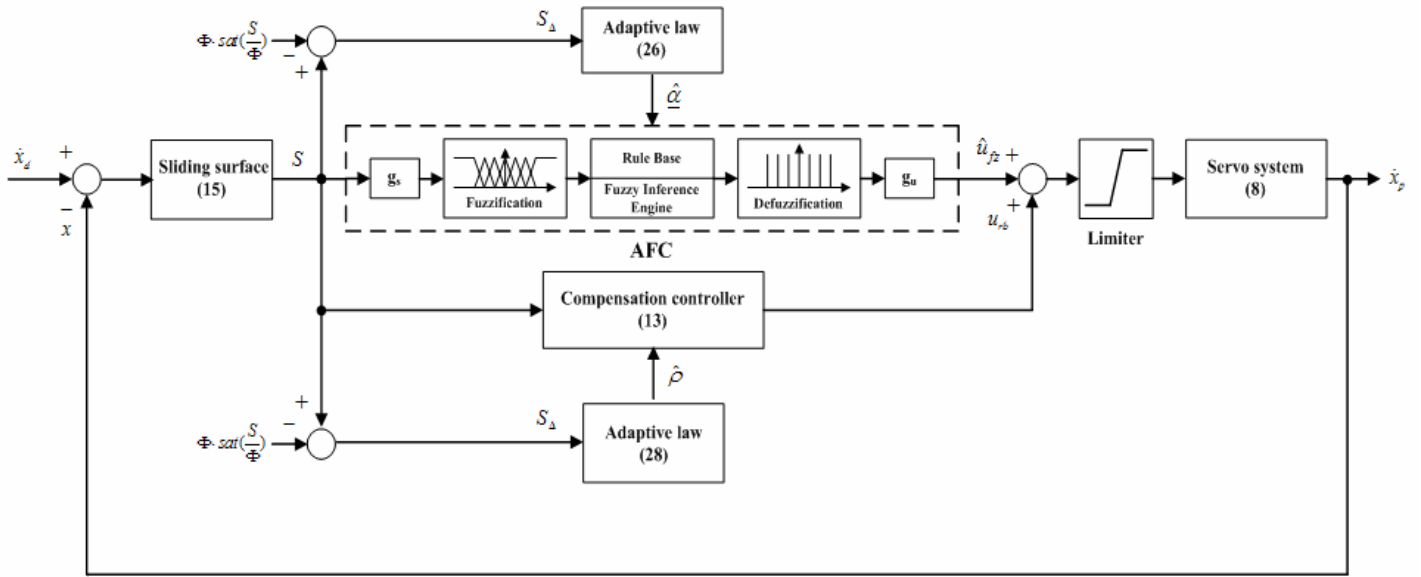
Figure 3 Adaptive fuzzy sliding mode control

Adaptive Fuzzy Sliding Mode Control System

The control objective is to find a control law so that the hydraulic actuator can track the desired velocity $\dot{x}_d(t)$. Define the tracking error $e(t)$ as

$$e(t) = \dot{x}_d(t) - \dot{x}_p(t) \qquad (8)$$

where $\dot{x}_p(t)$ is the control output and $\dot{x}_d(t)$ is the desired velocity. Then define a sliding surface as

$$S(t) = \dot{e}(t) + k_1 e(t) \qquad (9)$$

where k_1 is non-zero positive constants. Assume that parameters of the system in (2) are well known and the external load disturbance is measurable, then we can take the control law as

$$u^* = g^{-1}(\underline{x})[\eta S_\Delta(t) - f(\underline{x}) - d(\underline{x}) + \ddot{x}_d + k_1 \dot{e}(t)] \qquad (10)$$

where $S_\Delta(t) = S(t) - \Phi sat(S(t)/\Phi)$. The function S_Δ has several properties as below that are useful in the design of adaptive law (Sanner *et al.* 1992).

Property1: When $|S| > \Phi$, $|S_\Delta| = |S| - \Phi$ and $\dot{S}_\Delta = \dot{S}$.

Property2: When $|S| \le \Phi$, $S_\Delta = \dot{S}_\Delta = 0$.

The above properties of the boundary layer concept are to be exploited, in the design of AFSMC, our goal being to cease adaptation as soon as the boundary layer is reached. This approach aims to avoid the possibility of unbounded growth. Differentiating (9) along the system trajectories (2), we have

$$\dot{S}(t) = -f(\underline{x}) - g(\underline{x})u - d(\underline{x}) + \ddot{x}_d + k_1 \dot{e}(t) \qquad (11)$$

Substituting (10) into (11) gives

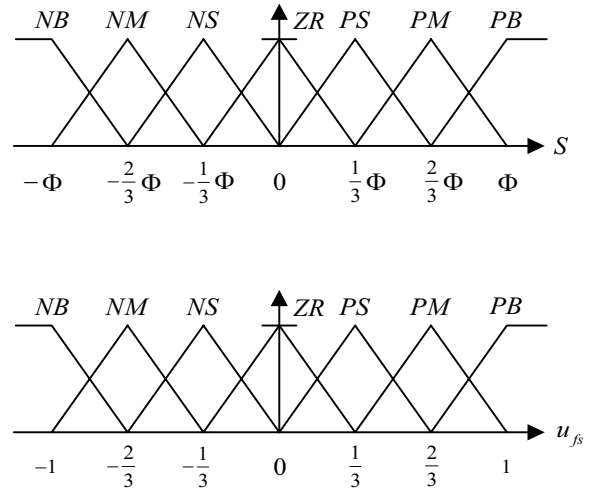$$\dot{S}(t) + \eta S_\Delta(t) = 0, \qquad \eta > 0. \qquad (12)$$

Figure 4 Fuzzy partitions and membership functions of S and u_{fs} in the respective universe of discourse

Equ. (12) shows that $\underline{e}(t)$ will converge to the neighbour of zero as $t \to \infty$ and the value of the neighbourhood are relative to the value of Φ (Slotine *et al.* 1896). However, the system parameters may be unknown or perturbed; the controller u^* cannot be precisely implemented. Therefore, by the universal approximation theorem (Lee *et al.* 2001), an optimal fuzzy control $\hat{u}_{fz}(S, \underline{\alpha}^*)$ in the form of (4) exists such that the approximation error of fuzzy controller can be defined as

$$\left| u^* - \hat{u}_{fz}(S, \underline{\alpha}^*) \right| = \rho^* \qquad (13)$$

where ρ^* is the inherent approximation error and is assumed to be bounded by $|\rho^*| \le M$. Employing a fuzzy controller $\hat{u}_{fz}(S, \hat{\underline{\alpha}})$ to approximate u^* as

$$\hat{u}_{fz}(S, \hat{\underline{\alpha}}) = \hat{\underline{\alpha}}^T \underline{\xi} \qquad (14)$$

where $\hat{\underline{\alpha}}$ is the estimated values of $\underline{\alpha}^*$. The control law for the developed AFSMC is assumed to take the following form:

$$u = \hat{u}_{fz}(S, \hat{\underline{\alpha}}) + u_{rb}(S) \qquad (15)$$

where the fuzzy controller $\hat{u}_{fz}$ is designed to approximate the control u^* and the robust controller $\hat{u}_{rb}$ is designed to compensate the difference between the controller u^* and fuzzy controller $\hat{u}_{fz}(S, \hat{\underline{\alpha}})$. Through (10), (11) and (15) the dynamical equation as follow can be derived:

$$\dot{S}(t) + \eta S_\Delta(t) = g[u^* - \hat{u}_{fz}(S, \hat{\underline{\alpha}}) - u_{rb}(S)] \qquad (16)$$

In order to derive the adaptive laws that ensure convergence to the boundary layer, a candidate Lyapunov function is defined as:

$$V(S_\Delta, \tilde{\underline{\alpha}}, \tilde{\rho}) = \frac{1}{2} \frac{S_\Delta^2}{g} + \frac{1}{2\eta_1} \tilde{\underline{\alpha}}^T \tilde{\underline{\alpha}} + \frac{1}{2\eta_2} \tilde{\rho}^2 \qquad (17)$$

where $\tilde{\underline{\alpha}}^T = \underline{\alpha}^{*T} - \hat{\underline{\alpha}}^T$ and $\tilde{\rho} = \rho^* - \hat{\rho}$ are the approximation error of the parameter vectors $\underline{\alpha}^{*T}$ and ρ^* respectively. In addition, η_1 and η_2 are positive constants. Differentiate (17) with respect to time as

$$\dot{V}(S_\Delta, \tilde{\underline{\alpha}}, \tilde{\rho}) = S_\Delta \dot{S}_\Delta / g + \tilde{\underline{\alpha}}^T \dot{\tilde{\underline{\alpha}}} / \eta_1 + \tilde{\rho}\dot{\tilde{\rho}} / \eta_2. \qquad (18)$$

Thus, if $|S| \le \Phi$, then $S_\Delta = 0$, it follows $\dot{V}(S_\Delta, \tilde{\underline{\alpha}}, \tilde{\rho}) = 0$. If $|S| > \Phi$, then $\dot{S}_\Delta = \dot{S}$. By substituting (16) into (18), (19) can be obtained

$$\dot{V}(S_\Delta, \tilde{\underline{\alpha}}, \tilde{\rho}) = -\eta S_\Delta^2 / g + S_\Delta[u^* - \hat{u}_{fz}(S, \hat{\underline{\alpha}})] - S_\Delta u_{rb}(S) + \tilde{\underline{\alpha}}^T \dot{\tilde{\underline{\alpha}}} / \eta_1 + \tilde{\rho}\dot{\tilde{\rho}}/\eta_2$$
$$= -\eta S_\Delta^2 / g + S_\Delta[u^* - \hat{u}_{fz}(S, \underline{\alpha}^*) + \hat{u}_{fz}(S, \underline{\alpha}^*) - \hat{u}_{fz}(S, \hat{\underline{\alpha}})] - S_\Delta u_{rb}(S) + \tilde{\underline{\alpha}}^T \dot{\tilde{\underline{\alpha}}} / \eta_1 + \tilde{\rho}\dot{\tilde{\rho}}/\eta_2$$
$$\le -\eta S_\Delta^2 / g + |S_\Delta| \|u^* - \hat{u}_{fz}(S, \underline{\alpha}^*)\| + S_\Delta[\hat{u}_{fz}(S, \underline{\alpha}^*) - \hat{u}_{fz}(S, \hat{\underline{\alpha}})] - S_\Delta u_{rb}(S) + \tilde{\underline{\alpha}}^T \dot{\tilde{\underline{\alpha}}} / \eta_1 + \tilde{\rho}\dot{\tilde{\rho}}/\eta_2$$
$$= -\eta S_\Delta^2 / g + [|S_\Delta|\rho^* - S_\Delta u_{rb}(S) - \tilde{\rho}\dot{\hat{\rho}}/\eta_2] + \tilde{\underline{\alpha}}^T(S_\Delta \xi(S) - \dot{\hat{\underline{\alpha}}}/\eta_1)$$
$$\qquad (19)$$

For achieving $\dot{V}(S_\Delta, \tilde{\underline{\alpha}}, \tilde{\rho}) < 0$, the adaptive laws of AFSMC are chosen as

$$\dot{\hat{\underline{\alpha}}} = \eta_1 S_\Delta \xi(S) \qquad (20)$$

$$u_{rb}(S) = -\hat{\rho} u_{fs} \qquad (21)$$

$$\dot{\hat{\rho}} = \eta_2 |S_\Delta| \qquad (22)$$

Then (19) can be rewritten as

$$\dot{V}(S_\Delta, \tilde{\underline{\alpha}}, \tilde{\rho}) \le -\eta S_\Delta^2 / g \qquad (23)$$

Equations (20)-(23) only guarantee that $S_\Delta \in L_\infty$, but do not guarantee convergence. Integrating both sides of (23) and some derivations yields

$$\int_0^\infty S_\Delta^2 dt \le \frac{V(S_\Delta(\infty), \tilde{\underline{\alpha}}, \tilde{\rho}) - \dot{V}(S_\Delta(0), \tilde{\underline{\alpha}}, \tilde{\rho})}{\eta / g} \qquad (24)$$

Since the right side of (24) is bounded, $S_\Delta \in L_2$. Using Barbalat's lemma (Slotine *et al.* 1991) it can be shown that $\lim_{t \to \infty} S_\Delta = 0$. This means that inequality $|S| \le \Phi$ is obtained asymptotically. Thus, the tracking error $e(t)$ converges to a neighbourhood of zero. In summary, the AFSMC system is shown in (15), where $\hat{u}_{fz}$ is given in (20) with the parameters $\hat{\underline{\alpha}}$ adjusted by (20); u_{rb} is given in (21) with the parameter $\hat{\rho}$ adjusted by (22). By applying this estimation law, the AFSMC system can be guaranteed to be stable in the Lyapunov sense.

EXPERIMENTS

In order to verify the new pneumatic-balanced lifting positioning system with the proposed control strategy, experiments with variable motion under different conditions are implemented. Figure 5 shows the experimental results of the multi-step positioning control with 100mm of each stroke within 12 sec in no-loading conditions. The ramp path is given between the positioning points. The pneumatic-balanced pressure is 0.32MPa. Besides, the multi-step positioning control with 200mm of each stroke within 14 sec is also implemented and compared in Table 3.
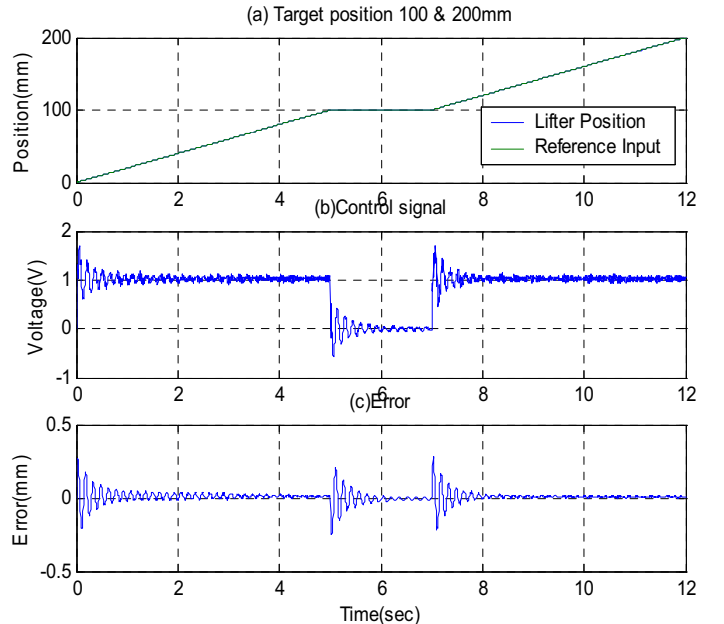

Figure 5 Experimental results of multi-step positioning control

Table 3 Positioning control performance comparison

Multi-step positioning control			
Stroke (mm)	duration (sec)	Max.tracking error(mm)	End point error(mm)
100	0-5	0.279	0.009
200	7-12	0.279	0.006

Figure 6 shows the experimental results of the path-positioning control with 500mm within 5 sec in no-loading conditions. A jerk-free path is given between the positioning points. The pneumatic-balanced pressure is 0.32MPa. Besides that, the path-positioning control experiments with 100 and 300mm within 5 and 10 sec are also implemented and compared in Table 4.

From the comparison of the different experiments, the developed system can satisfy the required specification in Table 2 for the new generation of glass substrates.
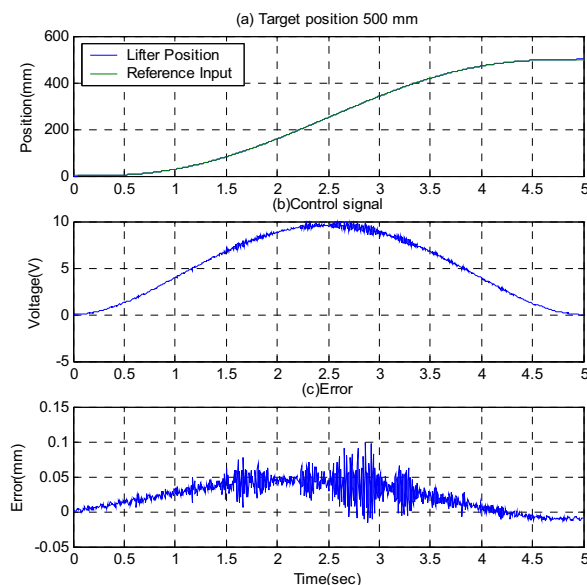
Figure 6 Experimental results of path-positioning control of lifting system

Table 4 Positioning control performance comparison

Path-positioning control			
Stroke (mm)	duration (sec)	Max.tracking error(mm)	End point error(mm)
100	10	0.026	-0.005
300	10	0.101	-0.003
500	10	0.101	-0.006
700	10	0.201	-0.007
100	5	0.026	0.006
300	5	0.065	0.006
500	5	0.099	-0.008

CONCLUSIONS

This paper proposed a novel pneumatic-balanced lifting positioning system for the new generation of flat panel display glass substrates. Through different experiments the feasibility and the repeatability can be confirmed. By means of the pneumatic-balanced control, the lifting positioning system driven by an AC servo motor can almost neglect the wide variation of the loading and achieve high position performance.

REFERENCES

1. TFT LCD Process Equipment Report, Display Search, 2006, U.S.
2. Flat Panel Display 2006, NIKKEI, 2006, Japan.
3. Neumann, R., Göttert, M., Konzepte zur Bahnregelung Servopneumatischer Antriebe, 5. Deutsch-Polnisches Seminar Innovation und Fortschritt in der Fluidtechnik, 2003, Warschau.
4. Hwang, G. C. and Chang, S., A stability approach to fuzzy control design for nonlinear system. *Fuzzy Sets Syst.*, 1992, Vol.48, pp.279-287.
5. Kim, S. W. and Lee, J. J., Design of fuzzy controller with fuzzy sliding surface. *Fuzzy Sets Syst.*, 1995, Vol.71, pp.359-369.
6. Lee, C. C., Fuzzy logic in Control Systems: Fuzzy logic Controller – part I, II. *IEEE Trans. Man, and Cybern.,* 1990, Vol.20, pp.404-435.
7. Lee, H. and Tomizuka, M., Robust adaptive control using a universal approximator for SISO nonlinear systems. *IEEE Trans. Fuzzy Syst.*, 2001, Vol.8, pp.95-106.
8. Maeda, M. and Murakami, S. A self-tuning fuzzy controller. *Fuzzy Sets Syst.*, 1992, Vol.47, pp.13-21.

P2-38

STUDY ON LOW NOISE PRESSURE REDUCING VALVE WITH RADIAL SLIT STRUCTURE

Chongo YOUN*, Yoichi OKAWA**, Kenji KAWASHIMA*, Toshiharu KAGAWA*

* Precision and Intelligence Laboratory
Tokyo Institute of Technology
4259 Nagatsuta, Midori-Ku, Yokohama, 226-8503, Japan
(E-mail: youn.c.aa@m.titech.ac.jp)
** Department of Bioengineering
Tokyo Institute of Technology
4259 Nagatsuta, Midori-Ku, Yokohama, 226-8503, Japan

ABSTRACT

Pressure reducing valves are widely used to maintain the pressure of gas reservoirs to specific values. When highly pressurized air passes through the orifice structure, considerable noise occurs at the downstream side. To solve this problem, we have developed a radial slit structure. The radial slit structure reduces the noise by suppressing the generation of turbulence and shock wave at the downstream. In this paper, we newly develop a pressure reducing valve applied the concept of the slit structure. At the former slit structure, the height of the radial slit was fixed. In the new valve, we proposed an improved slit structure that the height of it is variable. Coned disk springs are installed between the disks and the height of it is controlled from 0 to 50m with a pneumatic cylinder. As a result, the new structure can successfully control the flow rate and control the pressure in a reservoir. The performance of the valve is investigated experimentally and confirmed that noise can be reduced with the radial slit structure.

KEY WORDS

Pressure control valve, Slit structure, Noise

INTRODUCTION

Pneumatic systems are widely used in industrial fields from the viewpoint of low cost and safety. Breather valves are used to maintain the pressure of gas reservoirs to specific values. In a normal valve, supply pressure is depressurized with an orifice plate. When pressurized air passes through the orifice plate, a considerable noise and pressure fluctuation occur at the downstream. Therefore, reduction of noise and pressure fluctuation originating from the valve are required.

These phenomena have been investigated both analytically and experimentally. In addition, several methods, such as the use of diffusers [1], wrapping pipe with sound-damping materials [2], changing the plug structure [3], and the use of silencers [4] have been developed to reduce noise and pressure fluctuation.

However, with these methods, when the flow rate increases, the flow might become turbulent. In some cases, sonic flow occurs even when the pressure ratio is lower than 0.528. Turbulent and sonic flow can generate considerable noise and shock waves.

Therefore, the authors have proposed the slit structure that can reduce noise and pressure fluctuation. This reduces the noise by changing orifice into the slit structure.

The flow of the slit structure reduces the noise by suppressing the generation of turbulence and shock wave. In former research, it was found that the slit structure of height 0.05mm has the silencing effect more than about 40dB in comparison with the orifice [5], and the height of the slit was fixed.

In this paper, we proposed an improved slit structure that the height of it is variable by using coned disk

springs. The structure of variable slit structure and the flow characteristics of the slit are investigated theoretically and experimentally. And, the effect of the noise reduction is investigated experimentally.

VARIABLE SLIT STRUCTURE

Figure 1 shows a schematic drawing of the variable slit structure. The slit structure consists of three elements, a disk, a guiding bar and coned disk springs. The upper part of Fig. 1 shows the cross section of the structure. The upper disk consists of a flow inlet and an upper surface of the radial slit. The inner diameter of upper disk is 8.5mm. The guiding bar guides the movement of the disk. Coned disk springs are installed between the disk structures and the height of them are precisely controlled.

The compressed air enters from the center of the upper disk and is exhausted outward through the radial slit. The lower part of Fig. 1 shows the top view of the lower disk. The lower disk consists of a lower surface of the radial slit and a groove for holding the disc springs. The outer diameter of upper disk is 50mm, and the depth of groove is 0.5mm.

The structure of the coned disk spring and new valve is shown in Fig. 2. The material of it is SUS304, and the spring constant is 619.5N/mm. The diameter of the coned disk spring is 8mm. The thickness is 0.3mm, and height is 0.55mm. It is located on groove of disk. The height difference of groove and coned disk spring makes the 50μm slit. The height of it is precisely controlled with a control force.

In this study, we produced a new valve which has one layer of slit. The compressed air with supply pressure enters from the center of the disks and is exhausted to atmosphere pressure through the slits. The pneumatic cylinder is set up below the disk, and the piston of it is connected with the disk. The control pressure is supplied to the cylinder, and the cylinder moves the disk. Therefore, the height of slits is controlled with the pneumatic cylinder by changing the control pressure.

ANALYSIS OF THE SLIT STRUCTURE

The height of slit is measured by a microscope.
The flow rate characteristics of the slit structure are investigated theoretically under the assumptions that the flow is laminar and passes through the slit under isothermal conditions.
The relationship between the pressure drop and the average flow velocity is given by the next equation

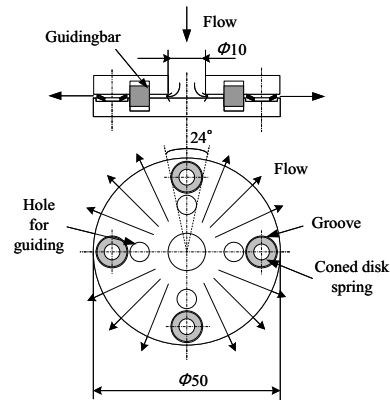$$dP_r = -\frac{12\mu \bar{u}_r}{h^2} dr \tag{1}$$

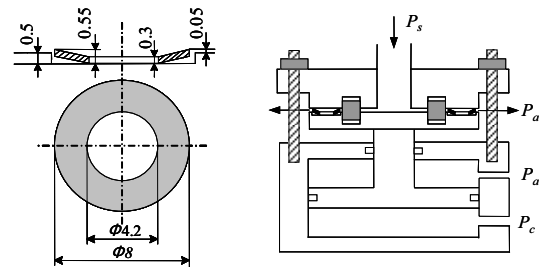Figure 1 Schematic of variable slit structure

Figure 2 Structure of coned disk spring and new valve

which comes from the Navier-Stokes equation of steady state laminar flow between parallel plates . In Eq. (1), stands for the viscosity of the air and h is the height of the parallel slit. The following equation is obtained from the continuity equation:

$$(\bar{u}A\rho)_{r_2} = (\bar{u}A\rho)_r \quad r_1 \leq r \leq r_2 \tag{2}$$

Using the state equation of gases

$$P = \rho R \theta \tag{3}$$

where R and θ are the gas constant and average temperature of air, respectively. The following equation is obtained From Eq. (2) and Eq. (3).

$$\bar{u}_r = \frac{A_{r_2}\rho_{r_2}}{A_r \rho_r} u_{r_2} = \frac{A_{r_2} P_{r_2}}{A_r P_r} u_{r_2} = \frac{r_2 P_{r_2}}{r P_r} u_{r_2} \tag{4}$$

The effective area of the slit A_r at radius r is given by the following equation:

$$A_r = 2\pi r h \frac{264°}{360°} \tag{5}$$

It is assumed that the degree of cross-sectional area is

264°as shown in fig. 2. Substituting Eq. (4) into Eq. (1) yields the following equation:

$$dP_r = -\frac{12\mu r_2 P_{r_2} \overline{u}_{r_2}}{h^2 r P_r} dr \qquad (6)$$

When Eq. (6) is integrated, and the boundary condition of is substituted, the following equation is obtained.

$$P_r = \sqrt{\frac{24\mu \overline{u}_2 r_2 P_2}{h^2} ln\frac{r_2}{r} + P_a^2} \qquad (7)$$

Substituting $\overline{u}_2 = Q / A_{r_2}$ into Eq. (7), the following equation is obtained.

$$P_r = \sqrt{\frac{24\mu Q_{r_2} P_a}{h^2 A_{r_2}} ln\frac{r_2}{r} + P_a^2} \qquad (8)$$

If the flow rate is given, the pressure at r is obtained from Eq. (8). The extra pressure drop must be considered in the inlet region [6]. This is evaluated using the following equation:

$$\Delta P_i = \xi \frac{\rho \overline{u}_{r_1}^2}{2} \qquad (9)$$

where ξ is the friction coefficient.

If the flow rate is given, the inlet average velocity is obtained from the equation. As a result, the supply pressure is given by adding the losses in the slit and the losses in the inlet region.

$$P_s = P_{r_1} + \Delta P_i \qquad (10)$$

FLOW CHARACTERISTICS

The flow characteristics were measured experimentally using the experimental apparatus shown in Fig. 3. Buffer tank and two regulators are set up on the upstream side. Supply and control pressures were regulated by each regulator. The pressure and the flow rate were measured using a bourdon tube pressure gauge and a float-type area flow meter, respectively.

The measured flow characteristic is shown in Fig. 4. The vertical axis is flow rate and the horizontal axis is a radius. The triangular symbols show the experimental result, and the solid line is the theoretical result. The theoretical result is calculated by Eq. 10 using the parameters listed in Table 1. The friction coefficient was chosen to approximately match the experimental results. The supply pressure is set constant at 500kPa. The con-

Table 1 parameters of the slit structure

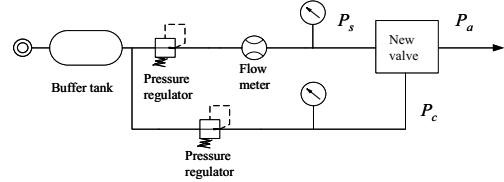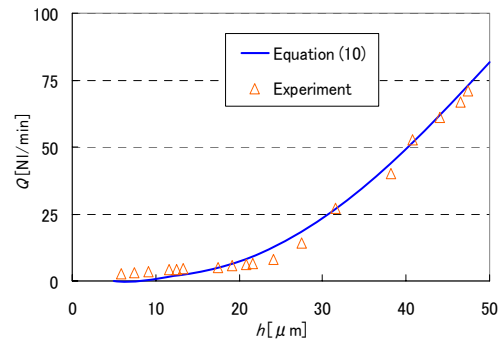| (m)	(m)	(μm)	ξ
0.05	0.025	0 $\sim$ 50	0.45

Figure 3 Experimental apparatus

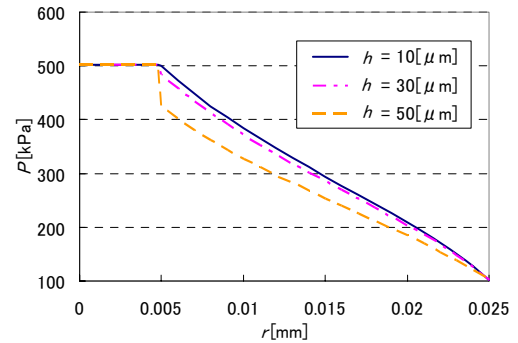Figure 4 Flow characteristics of the slit structure

Figure 5 Pressure distribution along r direction

trol pressure was varied from atmospheric pressure to 580kPa, and the height of slit is varied from 50μm to 0μm. It is thought that from the fact that theoretical analysis and experimental result agree well the flow by the viscosity is dominant.

The pressure distribution along r direction is examined with Eq. 8 and Eq. 9. The result is shown in Fig. 5. The vertical axis is pressure distribution and the horizontal axis is a radius. The pressure loss is almost linear line when the height of slit is 10μm . However, the pressure loss in the inlet region is getting large when the height of slit increases. It means the inlet length effect is greater when the height of slit in-creases.

REYNOLDS NUMBER

The Reynolds number is examined from the result by the theoretical analysis. The Reynolds number is calculated by Eq. (11).

$$Re = \frac{\rho_r \overline{u}_r D_h}{\mu} = \frac{\rho_a Q D_h}{\mu A_r} \qquad (11)$$

Here,

$$D_h = 4 \frac{2\pi rh}{2(2\pi r + h)} \cong 2h \qquad (12)$$

Reynolds number along r direction is shown in Fig. 6. The vertical axis is Reynolds number and the horizontal axis is a radius. When the height of the slit rises, the Reynolds number rises because flow rate increases. Because the Reynolds number is a function of the cross-sectional area, the flow on the radial shape has the effect of reducing the Reynolds number. Because the area ratio of the inlet for the outlet is 0.2, the Reynolds number of the outlet becomes 20% of the inlet. The Reynolds number at the outlet is 2000 or less as a result.
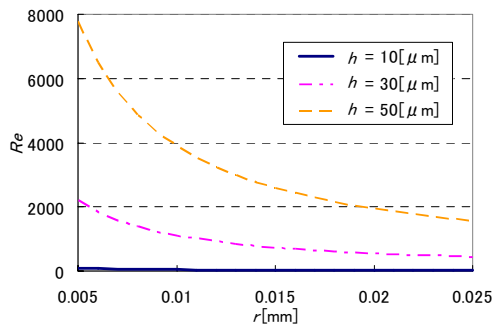
Figure 6 Reynolds number along r direction

NOISE LEVEL

The noise level of the valve was measured using a microphone sensor (Custom corp. ; SL-1370), according to the Japanese Industrial Standards[7]. The background noise level of the room is at 30dB. Microphone was placed in the room at an angle of 45 degree from the center axis of the valve. The distance from the valve to the microphone was 1.0m.

The noise levels of the orifice and the newly developed valve with the variable slit structure were compared. The experimental results are shown in Fig.7. The horizontal axis is flow rate, and the vertical axis is the noise level. We confirmed in advance that the flow characteristics of the orifice and the new valve were approximately the same. The results indicated that the
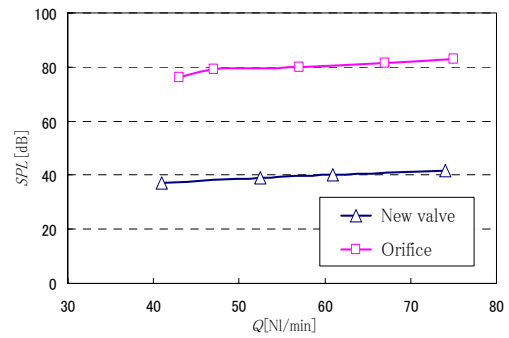

Figure 7 Noise level of orifice and new valve

noise level decreased approximately 40dB in the new valve.

CONCLUSION

This paper proposed variable slit structures instead of orifice structures. The height of slit is variable by using coned disk springs. The coned disk springs, which diameter is 8mm, are installed between the slit structures and the height of them is precisely con-trolled with control pressure.

The flow characteristics of the slit are investigated theoretically and experimentally. The pressure distribution and Reynolds number is examined. The experimental results indicated that the noise level decreased by approximately 40dB.

REFERENCES

1. Boger, H. W., "Designing Valves and Downstream Devices as Low Noise Pack-ages," Heat./Piping/Air Cond. (1971)
2. Bell, L. H., "Industrial Noise Control," Mech. Eng. (Am. Soc. Mech. Eng.), No88, (1993), pp. 417-426.
3. Amini, A., and Owen, I., "A Practical Solution to the Problem of Noise and Fluctua-tion in a Pressure-Reducing Valve," Exp. Therm. Fluid Sci., 10, (1995), pp. 136-141.
4. Davies, P. O. L. A., Harrison, M. F., and Collins, H. J., "Acoustic Modeling of Mul-tiple Path with Experimental Validations," J. Sound Vib., 200(2), (1997), pp. 195-225.
5. Youn, C., Kawashima, K., and Kagawa, T., (2003), "Fundamental Analysis of Super Low Noise Control Restriction for Compressible Fluid," The 18th I.C.H.P., pp. 387-394
6. Stone, C.R., and Wright, S.D., "Nonlinear and Unsteady Flow Analysis of Flow in a Viscous Flowmeter," Trans. Inst. Meas. Control(London), 16(3), (1994), pp.128–141.
7. JIS B8379, The pneumatic silencer, In Japanese, (1995), pp. 653–657

P2-39

STUDY ON THE TWO-STAGE EXPANSION
AIR-POWERED ENGINE

Hao LIU, Guoliang TAO and Ying Chen

The State Key Lab of Fluid Power Transmission and Control, Faculty of Engineering
Zhejiang University
38 Zheda Road, Hangzhou ,310027,China
(E-mail: hliu2000@zju.edu.cn)

ABSTRACT

Air-powered engine is a promising one of the low emission engines, for the advantages of its simple structure and complete zero-pollution. In this paper, the two-stage expansion Air-powered engine (TSEAPE) was studied in theory firstly and then experiments. Based on the model of TSEAPE that has been developed on the thermodynamics and mechanics analysis, the effects of bores ratio on the performance of TSEAPE are investigated by simulation. The results of simulation indicate that the TSEAPE will performance well when its bore ratio is about 1.4, which is a good balance between the power output and the efficiency. Guided by the results of theory analysis, a TSEAPE was developed based on an existing internal-combustion engine. The experiment results of this prototype engine on a test bench show that TSEAPE runs stably on bore ratio 1.4 and has better performance at a low speed.

KEY WORDS

Two-stage expiation air powered engine (TSEAPE), Low emission, Bores ration, Heat transfer

NOMENCLATURE

P_i : Injection air pressure
T_i : Injection air temperature
H_i : Injection air specific enthalpy
M_i : Injection air mass
P_1 : The air pressure in the 1st stage cylinder
T_1 : The air temperature in the 1st stage cylinder
m_1 : The air mass in the 1st stage cylinder
V_1 : The air volume in the 1st stage cylinder
u_1 : Specific internal energy of the air in the 1st stage cylinder
h_1 : Specific enthalpy of the air in the 1st stage cylinder
m_{e1} : Mass of the air out of the 1st stage cylinder
Q_1 : Heat transfer of the 1st stage cylinder
W_1 : Work of the 1st stage cylinder
ϕ : Crank angle
V_h : Volume of the air in the heat-exchanger
Qh : Heat transfer of the heat-exchanger (J)

P_2 : The air pressure in the 2nd stage cylinder
T_2 : The air temperature in the 2nd stage cylinder
M_2 : The air mass in the 2nd stage cylinder
V_2 : Volume of the air in the 2nd stage cylinder
u_2 : Specific internal energy of the air in the 2nd stage cylinder
h_2 : Specific enthalpy of the exhaust air of the 2nd stage cylinder
me_2 : Mass of the exhaust air out of the 2nd stage cylinder
Q_2 : Heat transfer of the 2nd stage cylinder
W_2 : Work of the 2nd stage cylinder
ω : Angular velocity of the crankshaft
U : Gas internal energy
R : The gas constant for air
Ω : Engine speed
A_{w1} : The total surface area of the first cylinder
μ : The coefficient of discharge
A : The opening area of the valve
P_1 : The upstream pressure of the valve

ρ_I :   The density of gas on the upstream

ψ :   The mass flow coefficient

P_II :   The downstream pressure

k   :   The specific heat ratio

a_w :   The coefficient of heat transfer applies to all surfaces of the cylinder

T_w :   The surface temperature of the cylinders

A_{w2} :   The total surface area of the 2nd cylinder

a_{wh} :   The coefficient of heat transfer applies to the surface of the heat exchanger

A_{wh} :   The total surface area of the heat exchanger

P_0 :   Barometric pressure

S_1 :   The projected area of the first piston

β_1 :   The angle between the rod and the axis of the first cylinder

μ :   The coefficient of the sliding friction between piston and the wall of cylinder

A_{b1} :   The contact area of the piston and the wall of the 1st cylinder

m_{i1} :   The reciprocating mass of the 1st cylinder

r :   The radius of the crank

λ :   The ratio of crank radius to connecting rod.

S_2 :   The projected area of the 2nd piston

β_2 :   The angle between the rod and the axis of the 2nd cylinder

A_{b2} :   The contact area of the piston and the wall of the 2nd cylinder

m_{i2} :   The reciprocating mass of the 2nd cylinder

E_i :   The exergy of the high-pressure air injected into the cylinder.

INTRODUCTION

Air-powered engine (APE) uses high-pressure air as energy to operate. Therefore it is of completely zero emission and is becoming a promising candidate for low-emission vehicle propulsion [1].

Generally, two approaches are used to obtain a high efficient APE. One is to sufficiently utilize the energy of the high-pressure air. This goal is achieved by raising the expansion ratio of the air in a single working cycle, which reduces the energy loss with lower air pressure exhaust. The other approach is to obtain extra energy from the ambient. As the air temperature falls greatly in the expansion process which is not isothermal in the cycle, heat can be absorbed from the ambient to enhance the power output. This approach depends mostly on the expansion time and the heat transfer area, but these contributing factors are limited in the single-stage expansion APE. However, the two-stage expansion APE (TSEAPE) integrates the two approaches by expanding the inlet high-pressure air twice in two cascaded cylinders to raise the total expansion ratio which prolongs the time of the air stay in engine and enlarges the total heat transfer area.

With an increasing demand of low-emission vehicles, APE is being studied by many researchers all over the world in recent years and a lot of achievements have been obtained [2-4]. However, most of them are about the single-stage expansion APE except the MDI Company, a French company which has studied Air-powered Vehicle study for over 10 years and has declared a scheme of three-stage expansion APE, but no more details can be found [5]. Yet a lot of factors need to be considered in designing the engine. In this paper, it is of primary importance to make clear the effect of the ratio of expansion volumes on the performance of two-stage expansion APE. As to the reciprocating APE, which is the most common structure because of its reliable structure and nice air tightness, the ratio of expansion volumes is represented by the bores ratio of the cascaded cylinders in deferent stages. Therefore, the effect of bores ratio on the basic multi-stage expansion APE, two-stage expansion APE (TSEAPE), was studied with simulation method, based on the model developed from thermodynamic analysis of the engine. And a prototype TSEAPE was manufactured and experiments were carried out to verify the validity of the model in this paper.

THE MODEL OF TSEAPE

The scheme of reciprocating TSEAPE shows as Figure1. In each cylinder, the operating cycle is finished in two strokes, the intake stroke and exhaust stroke. The deference of pistons' moving phases in the two cylinders is 180° which ensures the two-stage expansion.
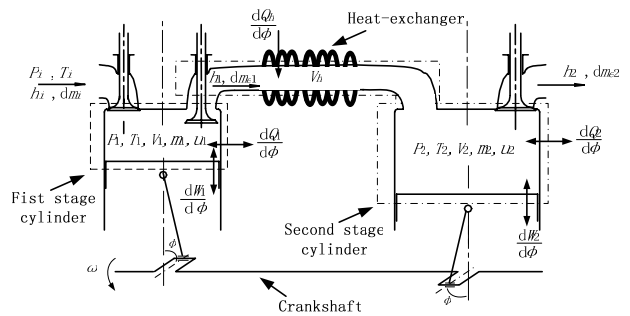

Figure 1 Scheme of TSEAPE

The operating cycle of TSEAPE is a thermodynamic process so that the model of TSEAPE is built on it in this paper. As high-pressure air expands twice in the two cylinders, the model of TSEAPE is composed of two closely linked sub-models. The two sub-models describe the operating processes in the two expansion spaces which are defined as control volumes and marked out with dashed lines. The first control volume is bounded

804

by the piston and walls of the first stage cylinder. Because both the inner spaces of heat-exchanger and second stage cylinder are connected directly by the wide inlet port, the air in the two spaces is considered to be the same state in this paper.

Sub-model of the first expansion stage

The instantaneous state of the high-pressure air in the control volume is determined by energy conservation,

$$dU_1 = dQ_1 + dW_1 + h_i dm_i + h_1 dm_1 \tag{1}$$

The gas internal energy changes accordingly with its instantaneous mass and specific energy, the relation of them is expressed as:

$$dU_1 = d(m_1 \cdot u_1) = u_1 dm_1 + m_1 du_1 \tag{2}$$

As we know, the gas specific energy u is the function of pressure, temperature and component. However, the gas in the control volume is pure air and no component changes in the process, the function can be simplified as:

$$u_1 = u (T_1, P_1) \tag{3}$$

Differential Eq. (3) can be expressed as:

$$du_1 = (\frac{\partial u_1}{\partial T_1})_{P_1} dT_1 + (\frac{\partial u_1}{\partial P_1})_{T_1} dP_1 \tag{4}$$

Because the influence of pressure P applying on the specific energy u is very little, the change of the specific energy u with the pressure can be neglected in our analysis. So when we insert Eq. (4) into Eq. (2), then insert rewritten Eq. (2) into Eq. (1), and for the convenience of analysis in a single cycle, differentiate the equation we obtained to the crank angle Φ and rearrange it, the following differential equation can be obtained as:

$$\frac{dT_1}{d\phi} = \frac{1}{m(\frac{\partial u_1}{\partial T_1})}[\frac{dQ_1}{d\phi} + \frac{dW_1}{d\phi} + h_i \frac{dm_i}{d\phi} + h_1 \frac{dm_{e1}}{d\phi} - u_1 \frac{dm_1}{d\phi}] \tag{5}$$

And considering the specific energy u has the relation with the constant-volume specific heat C_v as follows,

$$\frac{\partial u}{\partial T} = C_v \tag{6}$$

Then Eq. (5) can be rewritten as:

$$\frac{dT_1}{d\phi} = \frac{1}{mC_v}[\frac{dQ_1}{d\phi} + \frac{dW_1}{d\phi} + h_i \frac{dm_i}{d\phi} + h_1 \frac{dm_{e1}}{d\phi} - u_1 \frac{dm_1}{d\phi}] \tag{7}$$

With the differential equation, the relationship between the gas state variable T and the procedure variables is very clear. The items in the right of the equation can be defined in functions that have the crank angle Φ as variable. They are presented as follows.

The heat obtained by the gas in the control volume is mainly the result of the heat transferring between the cylinder surface and the gas. It is determined as:

$$\frac{dQ_1}{d\phi} = \frac{1}{\omega} \alpha_w A_{w1}(T_w - T_1) \tag{8}$$

The output work made by the gas is defined as:

$$\frac{dW_1}{d\phi} = -P \frac{dV_1}{d\phi} , \tag{9}$$

where the cylinder volume V can be obtained from the standard slider-crank relationship.

The changing of mass in the control volume is satisfied the mass conservation deferential equation:

$$\frac{dm}{d\phi} = \frac{dm_i}{d\phi} + \frac{dm_e}{d\phi} . \tag{10}$$

The instantaneous gas mass flow rate $\frac{dm}{dt}$ can be calculated when the differential pressure and the open area of the valve port are determined. It is expressed as:

$$\frac{dm_j}{dt} = \mu A \sqrt{2 P_1 \rho_1} \cdot \psi , \tag{11}$$

where subscript j refers to the injection or exhaust gas property, replacing the subscripts i and e respectively. And the mass flow coefficient ψ is determined by the conditions as follows:

When $\frac{P_{II}}{P_I} > (\frac{2}{k+1})^{\frac{k}{k-1}}$, it is in the sub-sonic flow state and the flow function is:

$$\psi = \sqrt{\frac{k}{k-1}[(\frac{P_{II}}{P_I})^{\frac{2}{k}} - (\frac{P_{II}}{P_I})^{\frac{k+1}{k}}]} , \tag{12}$$

When $\frac{P_{II}}{P_I} \leq (\frac{2}{k+1})^{\frac{k}{k-1}}$, it is in the sonic flow state and the flow function is:

$$\psi = (\frac{2}{k+1})^{\frac{1}{k-1}} \sqrt{\frac{k}{k+1}} . \tag{13}$$

Then, the mass flow rate differencing to the crank angle can be obtained by the equation:

$$\frac{dm_j}{d\phi} = \frac{1}{\omega} \frac{dm_j}{dt} . \tag{14}$$

And the relations between the gas mass m and the state

variables pressure P, temperature T and volume V, are determined by the ideal gas equation of state:

$$PV = mRT \qquad (15)$$

Combining equations Eq. (7), Eq. (10) and Eq. (15), the thermodynamic sub-model of the first expansion stage is obtained.

Sub-model of the second expansion stage

Similarly, the process in the second control volume is analyzed. Here, the energy conservation differential equation can be obtained as:

$$\frac{dT_2}{d\phi} = \frac{1}{mC_v}[\frac{dQ_h}{d\phi} + \frac{dQ_2}{d\phi} + \frac{dW_2}{d\phi}$$
$$+ h_1\frac{dm_{e1}}{d\phi} + h_2\frac{dm_{e2}}{d\phi} - u_2\frac{dm_2}{d\phi}] \qquad (16)$$

The heat exchanges of the second control volume are calculated separately in the above equation, because the heat exchange coefficients are different in the heat exchanger and cylinder chamber. They are expressed as:

$$\frac{dQ_2}{d\phi} = \frac{1}{\omega}\alpha_w A_{w2}(T_w - T_2) \qquad (17)$$

$$\frac{dQ_e}{d\phi} = \frac{1}{\omega}\alpha_{wh} A_{wh}(T_w - T_2) \qquad (18)$$

The output work of the second cylinder is defined as:

$$\frac{dW_2}{d\phi} = -P_2\frac{dV_2}{d\phi} \qquad (19)$$

The changing of mass in the control volume is also satisfied the mass conservation deferential equation:

$$\frac{dm_2}{d\phi} = \frac{dm_{e1}}{d\phi} + \frac{dm_{e2}}{d\phi} \qquad (20)$$

where the mass flow rate of the air injecting into and exhausting out of the second control volume also can be calculated by the equations Eq. (11)~ Eq. (14) separately. For the second control volume which is composed of the inner space of the heat recharge and the inner space of the second expansion stage cylinder, the gas equation of state of the air in the volume is given as:

$$P_2(V_h + V_2) = m_2RT_2 \qquad (21)$$

Combining equations Eq. (16), Eq. (20) and Eq. (21), the thermodynamic sub-model of the second expansion stage is obtained. As the equations show above, the two sub-models are joined by the air which expands in the two stage cylinders successively.

Calculation of torque and efficiency

The instantaneous torqueses of the two cylinders are expressed as follow equations:

$$M_1 = \frac{(P_1 - P_0)S_1 - m_{i1}r\omega^2(\cos\phi + \lambda\cos 2\phi)}{\cos\beta_1 + \mu A_{b1}\sin\beta_1} \cdot \sin(\phi + \beta_1) \cdot r \qquad (22)$$

$$M_2 = \frac{(P_2 - P_0)S_2 - m_{i2}r\omega^2(\cos(\phi + \pi) + \lambda\cos 2\phi)}{\cos\beta_2 + \mu A_{b2}\sin\beta_2}$$
$$\cdot \sin(\phi + \pi + \beta_2) \cdot r \qquad (23)$$

Now the total output torque of the engine M_t goes as:

$$M_t = M_1 + M_2 \qquad (24)$$

Then, the efficiency of the engine η can be obtained by

$$\eta = \frac{\int_0^{2\pi}(M_t \cdot \omega)d\phi}{\int_0^{2\pi}(\frac{dE_i}{d\phi})d\phi} \qquad (25)$$

Because the temperature of the injection air is assumed to be the same of T_0, the E_i can be calculated as

$$\frac{dE_i}{d\phi} = \frac{dm_i}{d\phi}RT_0(\ln\frac{P_i}{P_0} + \frac{P_0}{P_i} - 1) \qquad (26)$$

SIMULATION ANALYSIS OF BORE RATIO

The step-fix 4-order Runge-Kutta method is used to calculate the differential equation sets of the model in the simulation program. The top dead center (TDC) of the first stage expansion cylinder is defined as the start point of the cycle and the simulation step is 0.01°. The main parameters of the engine are defined in table 1.

Table 1 Parameters settings of the APE

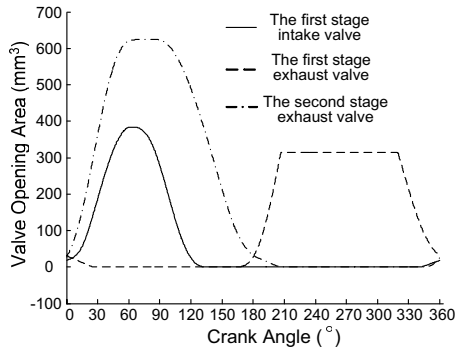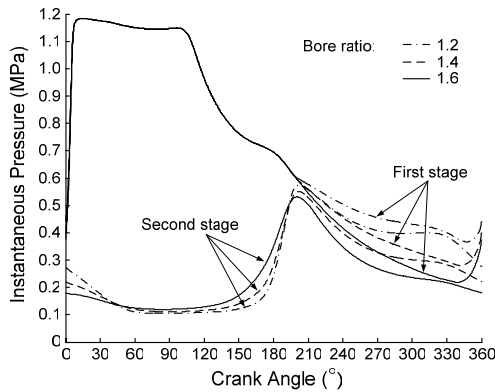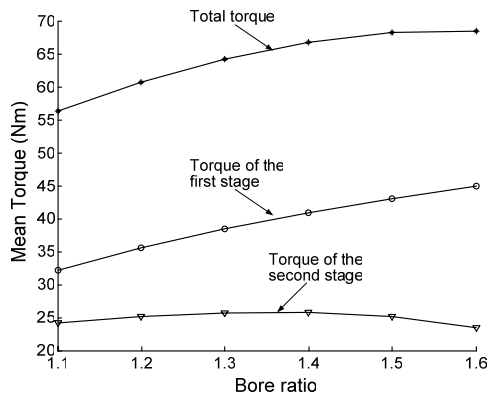| Parameters	Value
Bore of the 1st stage cylinder	50mm
Piston stroke	49.5mm
Length of connecting rod	170 mm
Ambient temperature	20℃
Ambient pressure	0.101 MPa
Injection air pressure	1.2 MPa
Inside diameter of the heat-exchanger	20 mm
Length of the heat-exchanger	200 mm
Speed of the APE	1000 r/min

Figure 2 Valve opening area curves

(c) Air consumption and efficiency
Figure 3 Simulation results under different bore ratio

And the curves of valve opening area in an operating cycle are defined by the port timing as Figure 2 shows. In those curves, the maximum opening area of the second stage exhaust valve is limited by the sectional area of the heat-exchanger.
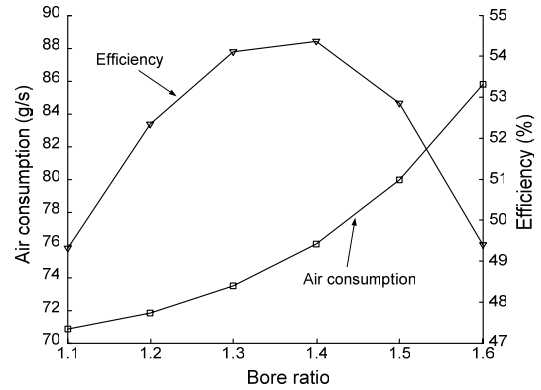
The bore of the first stage cylinder is fixed while the bore of the second stage cylinder is assigned different values to define different bore ratios. Now the bore ratios are changing from 1.1 to 1.6 with the step of 0.1 in the simulation.

The results of simulation come as Figure 3, which show the effect of bore ratio on the performance of TSEAPE. The total torque of the engine appears increasing with the rising bore ratio while its increase rate is dropping. And the efficiency of the engine increases with the rising bore ratio at the beginning but drops too when the bore ratio becomes too big. As figure 3(c) shows, the efficiency will reach the peak near the point that bore ratio is 1.4, where output torque of the engine can express a nice too.

EXPERIMENTS OF TSEAPE

With the indication of the simulation results, experiments were carried out to study the features of the TSEAPE. A production SI engine, which was designed to operate with gasoline, was modified so as to work with high-pressure air in the two-stage expansion mode. After adding lining and reboring, the bore sizes of the four cylinders were changed from originally all of 92mm to two of 72 mm and two of 98 mm. Therefore, the bore ratio of this prototype TSEAPE is 1.36 that comes near the best value appearing in the simulation results.

(a) Instantaneous in-cylinder pressures

(b) Mean Torque

Figure 4 TSEAPE on the test bench

The cylinder end of the engine that contains air distribution system is completely redesigned. From the left end, the first cylinder is cascaded with the third cylinder and the second cylinder is cascaded with the fourth cylinder by heat-exchanges. The engine is installed in a test bench for typical dynamometer experiments, as Figure 4 shows.

Experiments were carried out and the results are exhibited in Figure 5. The prototype TSEAPE under this bores ratio does run stably on air and it appears better power output and efficiency under relatively higher loads. But it is hard to say that its performance is good enough. The main reason is that the prototype TSEAPE is converted from an old combustion engine whose body does not fit the air powered operation mode very much, as carefully analysis after the experiments. The big inertia force and friction force caused by heavy crankshaft and tight bearing waste lots of the power. Those high-strength structures are unnecessary because the pressure in the cylinders is much lower than combustion engine and also the temperature.
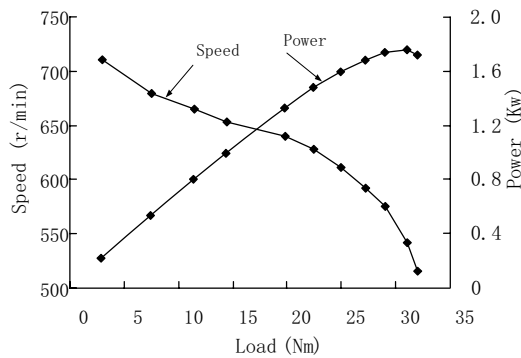
(a) Speed and power
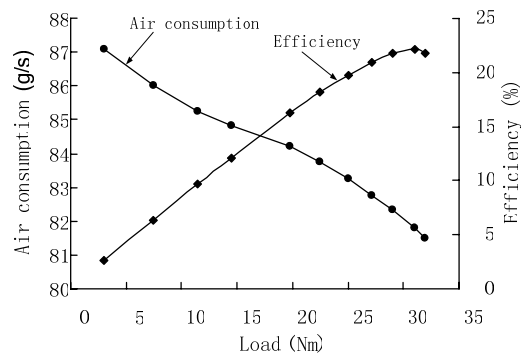
(b) Air consumption and efficiency
Figure 5　Experiment results under different loads

On the other hand, the surface of the heat exchange becomes heavily frosting soon after the engine working, which can be seen in the Figure 5. It shows that the air exhausted from the first stage cylinders is very cold and

does have drastically heat exchange with the ambient when it pass the copper pipes. However, frost that covers the pipes will reduce their heat exchange ability.

Considering the reasons above, the experiment results is not far from the simulation and the analysis based on the model can be approximately approved.

CONCLUSIONS

Bores ratio represents the ratio of expansion volumes of cylinders that cascaded in a TSEAPE and it is a key structure parameter. Based on the model of TSEAPE that has been developed on the thermodynamics and mechanics analysis, the effects of bores ratio on the performance of TSEAPE are investigated by simulation in this paper. The simulation results indicate that the TSEAPE will have a good performance when its bore ratio is about 1.4, which is a good balance between the power output and the efficiency. The experiments carrying out on a prototype TSEAPE with bore ratio 1.4 show that it runs stably on air and appears better power output and efficiency under relatively higher loads. But probably due to the large inertia force and friction force caused by the high-strength structures of the combustion engine body, the energy wasting of the prototype TSEAPE is huge. And thick frost appears and covers the heat exchangers that reduce their heat exchange ability. So the performance of the engine is far from perfect. Considering those disadvantage above, the experiment results go near to the simulation analysis.

It is very important to choose appropriate bores ratio in TSEAPE designing. The method and the result obtained in this paper are of good help for that. And the problems appear in the experiments are some of the key research points that will be solved in the near future.

REFERENCES

1. Chen, Y., Xu, H., Tao, G. L., Wang, X. Y., Liu, H. and Jia, G. Z., Research and progress of the compressed air powered vehicle, Chinese Journal of Mechanical Engineering, 2002, 38-11, pp.7-11 (in Chinese).
2. Liu, L. and Yu, X. l., Optimal design of ideal cycle in air powered engine, Journal of Zhejiang University (Engineering Science) , 2006 ,40-10, pp.1815-1818.
3. Ordonez C A, Plummer M C, Reidy R F., Cryogenic heat engines for powering zero emission vehicles. Proceedings of 2001 ASME International Mechanical Engineering Congress and Exposition, New York: [ASME], 2001.
4. Knowlen, C., Mattick, A. T. and Bruckner, A. P., High efficiency energy conversion systems for liquid nitrogen automobiles, SAE Paper, 1998, No. 981898.
5. Website of MDI Company, http://www.theaircar.com , 2008

P2-40

AN EXPERIENCE ON THE AUTOMATION OF PLANT CUTTING TECHNIQUE FOR PROPAGATING PLANTS

Terenziano RAPARELLI*, Pierluigi BEOMONTE ZOBEL**, Michele ANTONELLI** and Francesco DURANTE**

*Dipartimento di Meccanica, Politecnico di Torino
Corso Duca degli Abruzzi 24, Torino, Italy
(e-mail: raparelli@polito.it)
**DIMEG, Università di L'Aquila
67040 Roio Poggio, L'Aquila, Italy
(E-mail: zobel@ing.univaq.it)

ABSTRACT

Plant cutting is a technique for propagating plants in which a piece of the source plant, called the cutting, is placed in the soil to grow as an indipendent plant. The cutting produces new roots and stems, and thus becomes a new plant. This technique is used in workshops to reproduce plants for selling. In this paper we are presenting a system to automate the plant cutting process of ornamental plants. The process starts with a single stem of the parent plant, with no branches. The system is able to cut the stem for producing the cutting, to remove the leaves from its basal part, and to manipulate it for the hormone subministration and for the insertion in the substrate. The design and the prototype of the automation machine, based on the pneumatic technology, is presented in this paper.

KEY WORDS

Plant cutting technique, pneumatics, automation,design

INTRODUCTION

Plant cutting is a technique for propagating plants in which a piece of the source plant, called the cutting, is placed in the soil to grow as an indipendent plant. The cutting produces new roots and stems, and thus becomes a new plant.
Many ornamental plants can be reproduced by cutting: Ligustrum, Photinia, Viburnum, Callistemon, Spiraea, etc. Many differences exist among these plants to apply this technique (type of cuttings, plant preparation, etc.). The reproduction process by cutting in a workshop follows 5 steps:

1. *The cutting of the parent plant*. Young and vigorous parent plants are used for obtaining branches, eventually with secondary branches, to be used for producing cuttings, Fig. 1. The parent branches have to be fully turgid. They should be irrigated to avoid the loosing of water, and short time has to be spent between the cut of the shoot and the placing of the cutting in the substrate.
2. *The stem cuttings*. The parent branches are cutted to produce cuttings. Each cutting has to include at least one leaf node, at the lower extremity, for the production of the new roots. The cuttings are collected together and mantained wet. If necessary they have to be rehydrated by soaking them in the water.
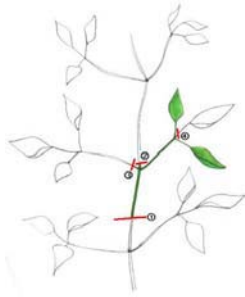
Figure 1 Parent plant used to obtain cuttings
for reproduction

3. *The removal of the leaves*. Each cutting has to be worked to remove the leaves from the stem in the basal part of the cutting. This operation is important to prevent the leaves from being inserted in the substrate that can give problem to the new plant.

4. *The plant hormone subministration*. It consists of the immersion of the basal part of the cutting in a plant growth substance to promote the formation of roots.

5. *The insertion of the cuttings in the substrate*. Each cutting has to be put in a cell of a multi cells tray. The usual trays have 120 or 140 or 160 separate cells. A substrate is used for the cells to promote rooting and to prevent roots from breaking off.

These steps are usually followed in workshops to reproduce plants for selling. The work in these workshops is all handmade and it needs to reduce costs to be competitive on the market.

In this paper a pneumatic system to automate the plant cutting process of ornamental plants is presented. The process starts with a branch of the parent plant, with no secondary branches. The system is able to cut the stem for producing the cutting, to remove the leaves from its basal part, and to manipulate it for the hormone subministration and for the insertion in the substrate. The design and the prototype of this solution, based on the pneumatic technology, is also presented in the paper.

Figure 2 Photos showing the latter 4 steps
in a plant cutting

THE AUTOMATIC SYSTEM FOR PLANT CUTTING

The stem of the branch can be considered like a long cylinder. From this stem starts secondary branches, leaves and, for some species, thorns. Considering only the ornamental plants that are very common in Europe, it is possible to classify them for the purpose of the automation system: plants without leaves, as Forsithia Viridissima, plants with medium size leaves but in small number, as Photinia Red Robin, plants with many leaves of medium size, as Viburnum Tinus Lucidum, plants with many leaves of small size, as Bruxus Sempervirens, and plants with many leaves of small size and with thorns, as Piracantha Moave. In this research the focus was on plants with medium size leaves, so that the extension of the results to plants with small size leaves or without leaves should not be so difficult. The table 1 shows the main characteristics of the branches of Photinia and Viburnum, that were selected for the automation system here proposed.

Table 1 Characteristics of Photinia and
Viburnum branches

MAIN CHARACTERISTICS OF THE BRANCH	Photinia Red Robin	Viburnum Tinus Lucidum
Maximum diameter of the branch in the basal part	5 mm	6 mm
Minimum diameter of the branch in the upper part	4 mm	3 mm
Medium length of the branch	~ 500 mm	~ 400 mm
Maximum distance between stem and tip of the leaf	100 ÷ 105 mm	135 ÷ 140 mm
Minimum distance between stem and tip of the leaf	55 ÷ 65 mm	50 ÷ 60 mm
Maximum width of the leaf	50 mm	55 mm
Minimum width of the leaf	35 mm	40 mm
Length of the leaf-stalk	~ 10 mm	~ 20 mm
Medium distance between two consecutive leaf nodes on the stem	35 ÷ 40 mm	70 ÷ 80 mm
Angle between the stem and the leaf-stalk	≤ 60°	≤ 60°
Curvature of the branch	small or no curvature	small
Consistency of the stem	very high	medium
Compliance of the branch	low	medium
Consistency of leaf and leaf-stalk	very low	very low
Compliance of leaf and leaf-stalk	very high	very high
Resistence of leaf to removal	small	small

The design of the automatic system for plant cutting is started with the description of the 5 steps of the manual procedure that is used in workshops to produce young plants. The deepening of the technical aspects involved in each of these steps, and the discussion about the technical solution for the automation system, suggested us some considerations. The step 1, the cutting of the parent plant, will be skipped because of the range of each attribute of the parent plant: dimension, shape, secondary branches, consistency of the stems in the branch (softwood, semi-hardwood and hardwood), etc. Then a robot was chosen to do the steps 4 and 5 for two reasons. The first one is the final goal of this research project: to validate this system in an experimental greenhouse already equipped with the cartesian robot DEIAFA having a good working volume for our needs (2670x1540x780 mm^3). The second reason is that these steps involve only an handling problem, nothing more!

The main design choices of the automatic system are resumed in the following:

- the step 1 is skipped. The single branch, without secondary branches, of Photinia or Viburnum, is manually loaded into the automatic machine;
- the step 2, the stem cutting, and the step 3, the removal of the leaves, are executed by the automatic machine;
- at the end of the step 3, a gripper of a robot grasp the cutting from the machine and move it for doing the step 4, plant hormone subministration, and the step 5, insertion of cutting in the substrate.

So the operations of the automatic system defined in the steps from 2 to 5 are automatised by two subsystems: an automatic machine for the steps 2 and 3, and the cartesian robot DEIAFA for the steps 4 and 5.

In the following the technical specification of the automatic machine is described. The automatic machine has to:

- start the operations with a branch manually inserted inside the machine;
- sense the presence of the branch;
- feed the machine with the branch, minimising the effect of the curvature;
- move the leaves gently in such a way that the leaf nodes are located by the sensors;
- remove the leaves just in the basal part of the cutting;
- execute the cut of the cutting by a sharp knife to obtain a clean cut and preserving the leaves in the upper side;
- handle the cutting for the immersion in the plant growth substance and, after 5÷7 seconds, for the insertion in a cell of a multi cells tray.

The characteristics of leaf and leaf stalk of Photinia and Viburnum match very well with the needs of the system. For example the compliance is very useful during the movement of the leaves.

The automatic machine proposed consists of:

1. a device to feed the machine with the branch
2. a tool to move the leaves
3. sensors to locate the leaf nodes
4. a device to cut the branch
5. a device to remove the leaves

Following this design idea 3 subsystems can be identified: the device 1, the tool 2 together the sensors 3 and the device 4, the device 5. The Figure 3 shows a sketch of the idea of this automatic machine, where the 3 subsystems can be easily identified.
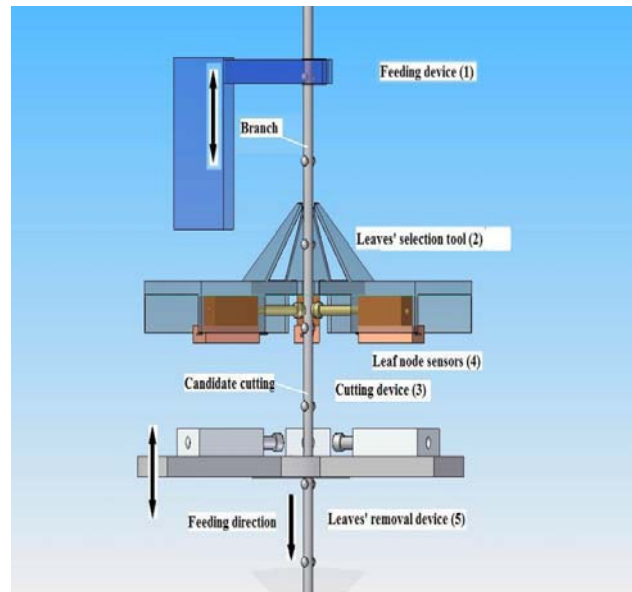
Figure 3 Idea of the automatic machine

Following this design idea a simple sequential functional chart was defined to settle the sequence of the steps involved in the automatic machine and in the robot operations, figure 4.

STEP 1. Feed the branch
    LOOP UNTIL the length of the "candidate cutting" is in the range 9 ÷ 18 cm AND the cutting device is just under a leaf node
STEP 2. Stop the feed
STEP 3. Start the device for the removal of the leaves in the basal part
STEP 4. Move the gripper of the robot just to grasp the "candidate cutting" in the lower side
STEP 5. Cut the stem to obtain the cutting
STEP 6. Immerse the cutting in a plant growth substance
STEP 7. Insert the cutting in a cell with substrate to promote rooting
STEP 8. GOTO step 1

Figure 4 Sequential chart of the automatic system to produce cuttings starting from a branch

In the following the design of the second subsystem, formed by the tool 2, the sensors 3 and the device 4, is explained in detail. The design of the device 1 and 5 is in progress but the technical solution is already defined, figure 3. The device 1, feeding, is formed by a slide and a gripper. The device 5, leaves' removal, is formed by a couple of actuators with a special tool on the rods, that will go in contact with the leaves to be removed, mounted on a plate, and an handling actuator to move this plate along the stem. All the actuators are pneumatically actuated.

The tool 2 to move the leaves is formed by 3 fingers that are very closed each other to have a way through for the branch. Each finger has a compliance structure to adapt itself to different sizes and shapes of the branch. Each fingertip is shaped to move the leaf rigth or leftside during the feeding of the branch. In this way during the feeding the leaves are moved in one of the three simmetric circular sector free of the fixed frame, figure 5b. When the feeding of the branch is running the leaf nodes goes in contact with the contact sensors, so that they are located, figure 5. The contact sensors are rod-shaped mechanical sensors, with an electrical output, and the rod is positioned close to the stem. The tuning of these wires is very important to obtain a positive signal just when a leaf is passing through. Close to them but in the lower side the cut device is located. It has 1 dof (degree of freedom) to move itself frontside (working position) or rearside (rest position). A pneumatic slide is used for this purpose and the driving of the cutter is obtained by a pneumatic cylinder, figure 5. The knifes of the cutter are parts of commercial pruning shears, to be sure of the quality. In the Figure 5a is shown an assonometric view of this subsystem, while in figure 5b a bottom view is reported. All the drivers used in this design are pneumatics based. The choice of the pneumatics technology is motivated because of the agricultural environment. It is very dirty and very extreme as temperature, humidity and sunligth. Another reason is the semplicity of the technical solution that pneumatics technology can offer.

(b)
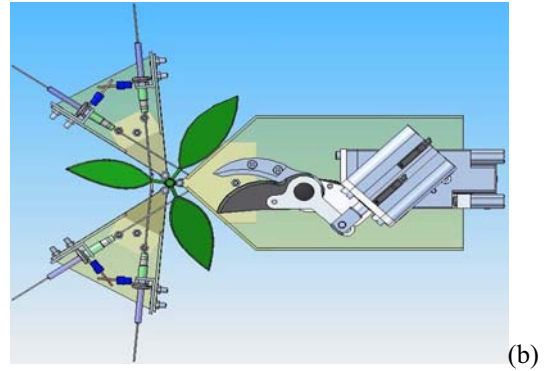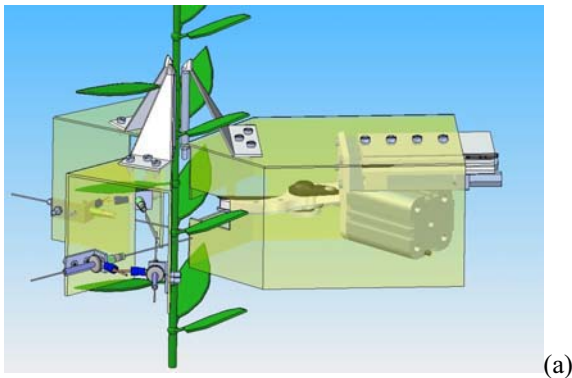
Figure 5 Views of the automatic machine's functional design

The power pneumatic circuit for the automatic machine is shown in the figure 6. It consists of 6 double effects cylinders plus 1 gripper for the feeding device. Each one of these actuators has a 4/2 electropneumatic valve to manage it, except the pneumatic slide for the feeding device. In this case a 4/3 valve is used, that's mean a 3 positions instead of 2 ones valve. This choice permits to obtain the stop of the slide in any position of the stroke, evntually by means of a pneumatic brake too (not shown in the figure 6). The total number of sensors and buttons used in the automatic machine is 22: 3 for start, stop/emergency and reset buttons, 3 sensors to locate the leaf nodes, 1 sensor to state that the branch is loaded and 15 endstroke sensors for cylinders, slides and gripper. All the 22 sensors are feeded with 24 Vdc to be connected to a commercial PLC (Programmable Logic Controller), that is used as controller of the automatic machine: 22 digital inputs and 12 digital outputs, to command the 6 electrovalves, are used.
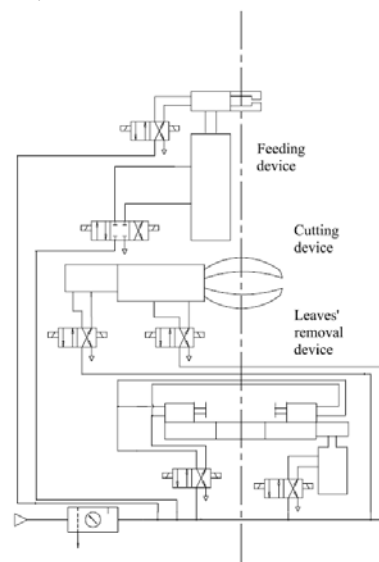

(a)

Figure 6 Power pneumatic circuit of the automatic machine

THE EXPERIMENTAL TESTS AND THE PROTOTYPING

The design procedure, described previously, requires to know the cutting force necessary to cut the branch. This data is necessary because of the importance to obtain a clean cut. For this reason an experimental setup was constructed based on a commercial pruning shears. A pneumatic cylinder was used to apply the cutting force on the shears, modifing the supply pressure with step of 0.05 MPa (0.5 bar). The tests were carried out with 4 different plants (Photinia red robin, Viburnum tinus lucidum, Forsithia viridissima and Bruxus sempervirens) for 3 different sizes of the stem, cutted from a parent branch just a couple of hours before the test. Two different positions of the stem were considered for the tests: stem in contact with the fixed blade and stem between fixed and mobile blade of the shears. The results for Photinia and Viburnum are shown in tables 2 and 3. The criterium adopted to classify the results of the test has 3 scores: B (bad) if the knife doesn't pass through the stem, NG (not good) if the knife pass through the stem, but the cut is not clean, G (good) if the cut is clean.

Table 2 Results of the cutting test on stems of Photinia Red Robin (G = good, NG = no good, B = bad)

Dynamic cutting force [N]		176	235	294	353	411
Stem close to fixed blade: diameter [mm]	6,5	B	B	NG	G	G
	5,5	B	B	G	G	G
	4,5	B	NG	G	G	G
Stem between mobile and fixed blade: diameter [mm]	6,5	B	B	G	G	G
	5,5	B	B	G	G	G
	4,5	B	NG	G	G	G

Table 3 Results of the cutting test on stems of Viburnum Tinus Lucidum (G = good, NG = no good, B = bad)

Dynamic cutting force [N]		176	235	294	353	411
Stem close to fixed blade: diameter [mm]	6	B	B	NG	G	G
	4,5	B	G	G	G	G
	3,5	B	G	G	G	G
Stem between mobile and fixed blade: diameter [mm]	6	B	B	G	G	G
	4,5	B	G	G	G	G
	3,5	NG	G	G	G	G

The results show that:
- the cutting force depends on the dimension of the stem, on the type of plant and on the cutting modality;
- the cut with the stem in contact with the blade gives badder results than the other one;

- appling a dynamic cutting force greater or equal to 353 N than the result is always a clean cut.

Considering that the maximum diameter of the stem is settled to 4 mm, because of the quality of the cutting that requires young branches, the design force of the cutting device was fixed at 235 N. The design calculation of the mechanism to drive the knife was made and a cylinder with a diameter of 32 mm and a stroke of 20 mm was chosen. The prototype of the cutting device was constructed and experimentally tested with good results.

The design of the tool to move the leaves has been already described previously. Here we can add some information more. It was designed on the characteristics of the plants Photinia and Viburnum. The 3 finger are positioned simmetrically with respect to the vertical axis with an angle of 120° on the base plane. The device is formed by 3 fingers, a cilindrical vane with vertical axis and a base frame. The base frame is a case and inside it the cutting device and the sensors for the leaf nodes are fixed. In the prototype each finger has the shape of a thin plate and is made by a rapid prototyping printer. The fingers are fixed at the base frame, in the bottom part. The cilindrical vane is very important to guide the branch inside the machine and to keep the same direction during the feeding. In the prototype this vane is made by 3 steel cilindrical pins positioned at 120° each other. Each pin is fixed in the upper part at the fingertip and in the lower part at the base frame. To verify the correct functionality of this tool many tests were conducted in the lab with good results.
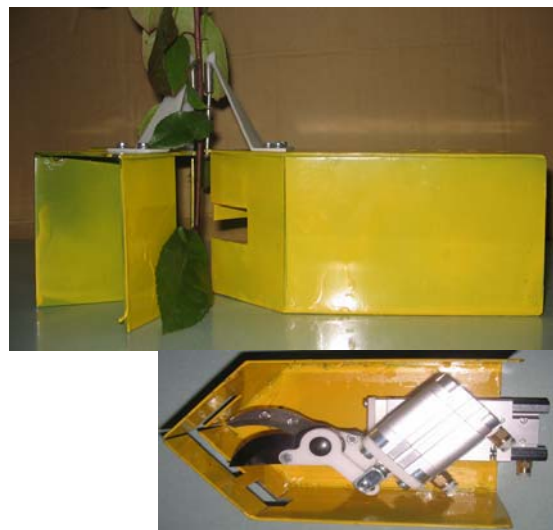

Figure 7 Photos of the prototype

The sensors to locate the leaf nodes are made by a small tube and a small rod inside it. When a contact occurs the rod is pushed against the tube closing an electrical circuit. The sensors were made by ourselves in the laboratory and experimentally tested. The figure 7 shows two photos of the prototype of the subsystem, not completely

assembled, that includes the tool to move the leaves, the sensors to locate the leaf nodes and the device to cut the branch.

CONCLUSIONS

In this paper a system to automate the plant cutting process of an ornamental plant is presented. The process starts with a single branch of the parent plant, with no secondary branches. The system is able to sense the leaf nodes, to cut the stem for producing the cutting, to remove the leaves from its basal part, and to manipulate it for the hormone subministration and for the insertion in the substrate. The technical solution proposed is innovative and the pneumatics technology helps to reach the goal in a simple but reliable way. The functional design and the prototype of the tool to move the leaves, of the sensors to locate the leaf nodes and of the device to cut the branch, are presented in detail. The results of the experimental tests for the cutting device for four different plants are also shown and discussed.

The work is in progress. The design of the last 2 devices, to feed the machine with the branch and to remove the leaves, are completed and the prototyping is the next step. Finally the experimental tests on these devices and on the complete automation machine will be carried out.

ACKNOWLEDGEMENTS

REFERENCES

1. M. Monta, N. Kondo, N. Akiyama and Y. Shibano, Planting system for chrysanthemum cutting , Proceedings of International Symposium on Automation and Robotics in Bio-production and Processing, Vol. 2, 1995, pp. 323-330
2. J. C. Rosier, R. Snel, E. J. Goedvolk, "Automated harvesting of flowers and cuttings", ISBN 0-7803-3280-6/96, 1996, IEEE
3. N. Kondo, M. Monta and Y. Ogawa, Cutting Providing System and Vision Algorithm for Robotic Chrysanthemum Cutting Sticking, International Workshop on Robotics and Automated Machinery for Bio-productions, 1997, pp. 7-12
4. T. Pilarski, M. Happold, H. Pangels, M. Ollis, K. Fitzpatrick, A. Stentz, The Demeter System for Automated Harvesting, Autonomous Robots 13, 2002, pp. 9–20
5. G. M. Acaccia, R. C. Michelini, R. M. Molfino, R. P. Razzoli, Mobile robots in greenhouse cultivation: inspection and treatment of plants, Proceedings ASER 2003, 1st Intern. Workshop on Service Robotics, march 2003, Bardolino, Italy
6. T. Raparelli, M. Antonelli, P. Beomonte Zobel, F. Durante, The automation in plant cutting, Oleodinamica-Pneumatica, ed. Tecniche Nuove, n. 1, january 2008, pp. 78-82 (in italian)

P2-41

GROW-HOSE-I:
A HOSE TYPE RESCUE ROBOT PASSING SMOOTHLY THROUGH NARROW RUBBLE SPACES

Ichiro KIRYU*, Hideyuki TSUKAGOSHI* and Ato KITAGAWA*

* Department of Machine & Control Systems,
Tokyo Institute of Technology
2-12-1-S5-16 Oookayama, Meguro-ku, Tokyo, 152-8552 Japan
(E-mail: ichiro_kiryu@cm.ctrl.titech.ac.jp)

ABSTRACT

This paper presents a hose type rescue robot with new movement abilities, for passing through narrow spaces and searching for victims under debris. At the disaster site, the fiber scope and the pole equipped with a camera on its head were previously used to search for victims. However, there are problems with going into complex curved and rugged spaces due to the friction between the robot body and surface of debris. So in this study, the hose type robot named Grow-hose-I, growing with a rapid motion type hose, is proposed which can move smoothly with no friction between the hose and the ground surface. The hose is composed of flat tubes driven by pneumatics, and it can be actively curved to enable steering.

KEY WORDS

Rescue Systems, Pneumatic Systems, Rubble Space, Grinding Friction, Curving Control

NOMENCLATURE

d : Span between the Tubes
F : Driving Force on the Hose.
p : Air Pressure of the Tube
l_1 : Width of the Flat Tube
l_2 : Thickness of the Flat Tube
R : Driving Resistance on the Bent Part of the Tube.
ρ : Radius of the Bent Part of the Tube

INTRODUCTION

At the disaster site, the fiber scope and the pole equipped with a camera on its head have been previously used to search victims under debris. These tools are available when a straight route can be secured, on the other hand they can't really be used when debris formation is complicated. However, even in such a situation rescue tools are required to be able to be inserted. In addition, the tools are required to have the ability of supplying water, air, and medicine for prolonging the life of survivors.

We have previously developed several types of hose robots which can supply water and medicine from outside the debris [1]. Through these past examples, we can see that technology that moves the hose with decreasing sliding friction as much as possible between

the surface of the hose and the rubble is an indispensable factor. Accordingly, there has been suggested some new types of robots which can move without grinding friction but only have straight motion [2], or can control motion while decreasing the grinding friction by vibrating the thin hair attached to its surface [3]. However it's necessary for the hose to pass through the debris in narrow spaces like Figure 1 while controlling the direction actively.

In this study, we propose an inner body drawn-out type hose "Grow-hose-I" (Figure 2) which can move without grinding friction between the hose surface and the debris. In addition, it can also control the direction on its head part actively by adjusting the air pressure valves.
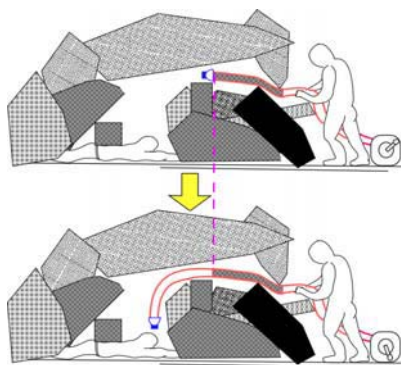
Figure 1 Feature of Complex Debris

Figure 2 Feature of "Grow-hose-I"

DEVICE CONCEPT

It is preferable that the device is a hose type robot that can secure the route between the victims and rescue team members to supply water and medicine for prolonging life.

Some research has previously done on hose robots, and these can be classified into the following types for the most part.

1) Grinding friction decreased type
2) Body crawling type
3) Inner body drawing-out type

1)   Grinding friction decreased type
This kind of robot can move smoothly while decreasing the sliding friction between the robot body and debris environment. During movement, Active Scope Camera [3] decreases sliding friction by vibrating the thin hair around the robot using the vibrating motor.

2)   Body crawling type
This kind of robot can move by using the actuator equipped on the body. Active Curve Hose [1] can crawl into the debris and can control the direction at the head part while using the search camera. Moreover, it can also supply water through the robot body to survivors.

3)   Inner body drawn-out type
This kind of robot moves forward like the growth of a plant stem by drawing out the body at the head part. Pneumatically Controlled Expandable Arm [2] can haul the inner body by using pneumatic power (Figure 3). As a result, the robot can move regardless of the sliding friction between the robot body and the debris.
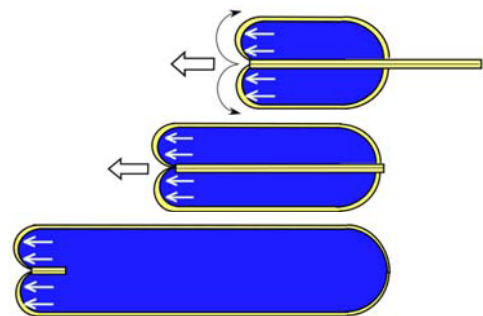
Figure 3 Concept of Grow-hose-at disaster site

SUGGESTED METHOD

We will use type 3. This is because a robot which can move without grinding friction in a complex pebbles environment might be very useful.

Method of Driving
We use the urethane tube flattened by heat-treatment (flat tube, (Figure 4)) to construct the hose. The flat tube has a property that the force is generated on the bent point of the tube when it is bent to 180° and the air pressure is input from one side (Figure 5). We construct the hose with 2 flat tubes and flexible cloth (Figure 6). Then, the hose can drive like the growth of a plant stem as the inner body is being drawn out by inputting the air pressure from the outside tube edge (Figure 7). Therefore it's possible for the hose to go deep into the debris smoothly because the hose surface and the debris don't grind against each other greatly. Moreover, the tubes and the cloth are NOT bonded so that they can slide mutually   to achieve a large curving motion .

Figure 4 Flat Tube

Figure 5 Bent Flat Tube
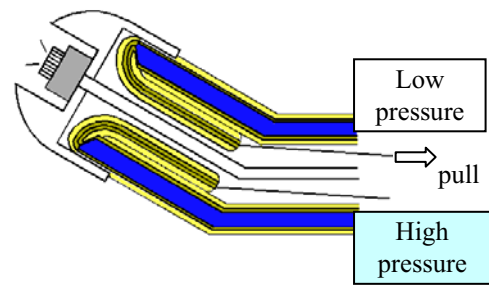
Figure 8 Curving Motion of Hose

(a)Cross View   (b)Side View
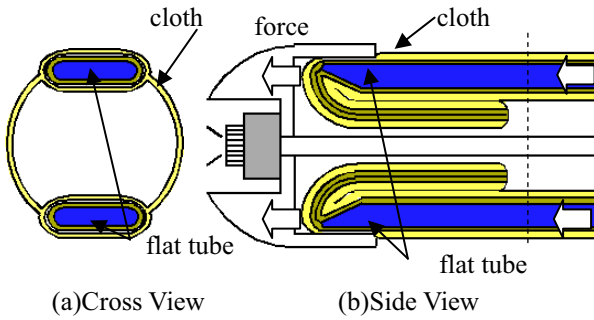
Figure 6 Figure of Hose with Air Pressure Applied
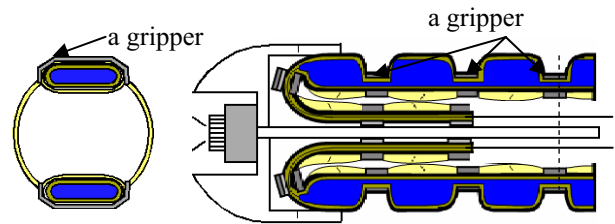
Figure 9 Figure of Hose with Grippers
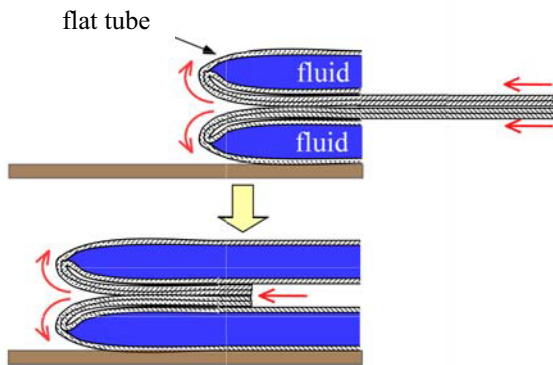
Figure 7 Motion of Hose like Growth of Plant Stem

Figure 10 Figure of Fixed Curve Shape

Curving Motion

The hose curves by adjusting the air pressures of two flat tubes. Moreover, a bigger curving motion can be achieved by pulling the wire installed at the edge of the tube (Figure 8).

Mechanism of Fixed Curving Shape

To keep a hose shape after a curving motion in the assumed environment, a rigid outside body and a flexible inside body might be needed. Therefore, metallic grippers are set over the tube of the hose at constant intervals (Figure 9).

Only the outside tubes of the hose get swollen because the flat tubes seal the air flow at the head point of the hose. Therefore, the grippers are fixed on the tube outside of the hose and are NOT on the inside. As a result, the spans among the grippers are fixed at the moment of curving motion and the hose can keep its curving shape (Figure 10).

CAMERA MODULE

It is preferable that the search camera is set at the head part of the hose for looking through the debris. However, the camera module cannot be fixed on the head part of the hose directly because of the structure of hauling body inside the hose. Therefore, flexible rails are set up on the hose and couples of rollers are set up on the camera module at first, so that the camera module can be fixed on the head part of the hose with the rollers pinching the rails. As a result, the camera module can run while sliding on the rails just like rollers rotating (Figure 12).

(a) side view

A-A' section   B-B' section
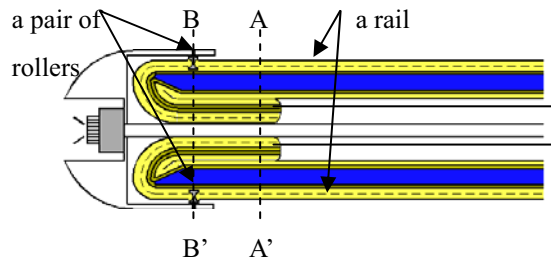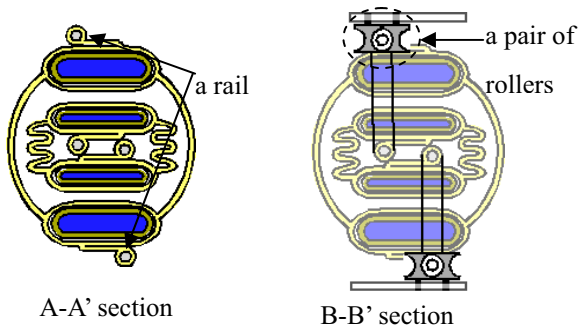
(b) cross section

Figure 11 Camera Module on top of the Hose
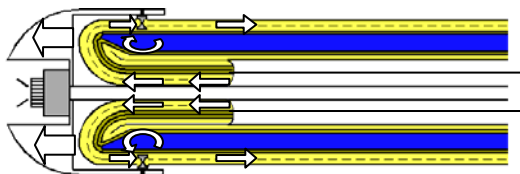
Figure 12 Motion of the Camera Module

PROTOTYPE (GROW-HOSE-I)

The developed hose "Grow-hose-I" and camera module are shown below.

Table 1 Specification of Grow-hose-I

Length of Robot	3.0m
Tube	Flat Tube made of Urethane (width :20mm) ×2 (inside :φ10 outside :φ12)
Gripper Span	25mm-35mm
Hose Body	Spark Satin (Polyester :62%,Nylon :38%)
Tube Span	45mm
Rail	φ2.0

Table 2 Specification of Camera Module

Whole Size	φ62mm×62.5mm
Camera Size	21mm×21mm×16mm
Roller	Stainless steal
Cover	Acrylic fiber

(a) whole view

(b) front view   (c) side view

Figure 13 Figure of Grow-Hose-I
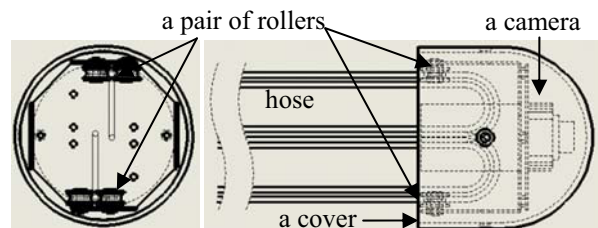
Figure 14 Camera Module

DRIVING FORCE OF HOSE

We measured the driving force of the hose while changing the air pressure p and the tube span d (Table 3)
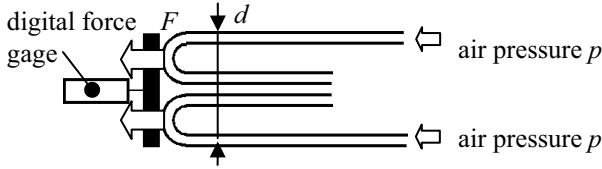
Figure 15 Feature of Driving Force Experiment
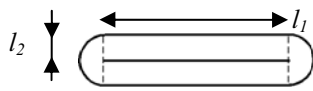
Figure 16 Cross-Section of Tube

Table 3 Experiment conditions

d	40,50,60[mm]
p	0.10, 0.20, 0.30, 0.40, 0.50[MPa]
l_1	16.8[mm]
l_2	1.0[mm]

Result of the Experiment
The result of the experiment is shown in Figure 19. The theoretical value of the driving force used in the figures is that of the ideal condition; where the cross-section of the tube is a perfect circle.

Summary and Discussion
The measured value of the driving force was 80-110% of the theoretical value. In addition, the driving force varied due to the tube span d. Furthermore, the force tended to decrease in the high air pressure range. The reasons are as follows.
(a) There exists a resistance R at the bent part of the flat tube (Figure 17).
(b) The smaller the radius ρ of the bent part, the greater the resistance R becomes.
(c) The R varies due to the air pressure p, because the radius ρ becomes smaller when the air pressure is input and the tubes expand (Figure 18).

Figure 17 Resistance of Bent Tube

(a) Without Air Pressure (b) With Air Pressure
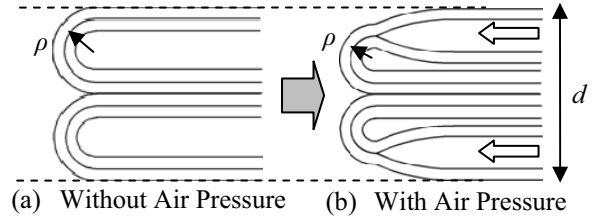
Figure 18 Change of the ρ by the Tubes Expansion
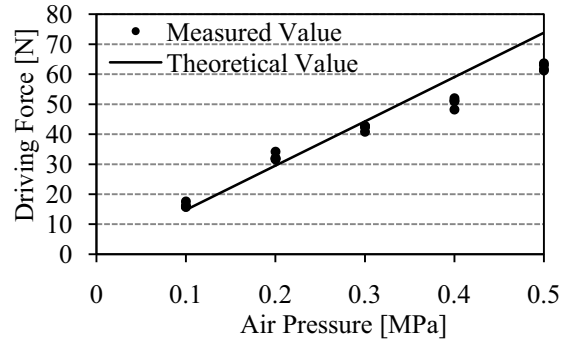
(a) d=40mm
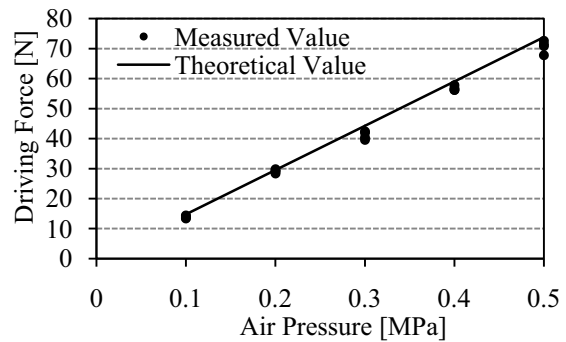
(b) d=50mm
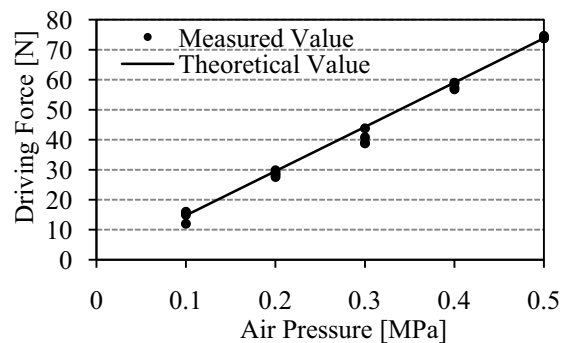
(c) d=60mm

Figure 19 Driving Force of the Hose

819

EXPERIMENT OF GROW-HOSE-I

The appearance of the hose during the driving experiment are shown below while the hose performs (a) a crank drive, (b) a drive inside a pipe and (c) a drive with the camera module (Figure 20). On crank driving, the hose is controlled by inputting the air pressure 0.5 [MPa] to the tube outside of the curve and 0.3 [MPa] to the one inside. Bigger curve curvature can be generated by pulling the wire (inside of curve).
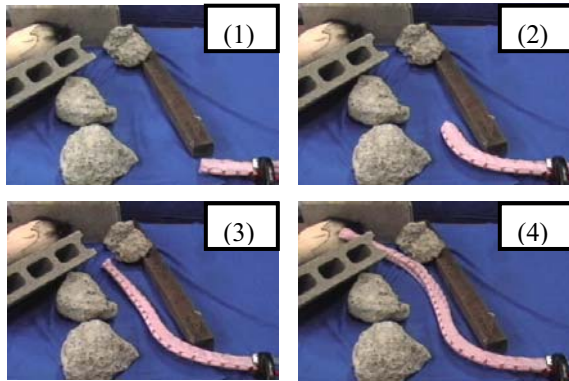
(a) Crank Drive
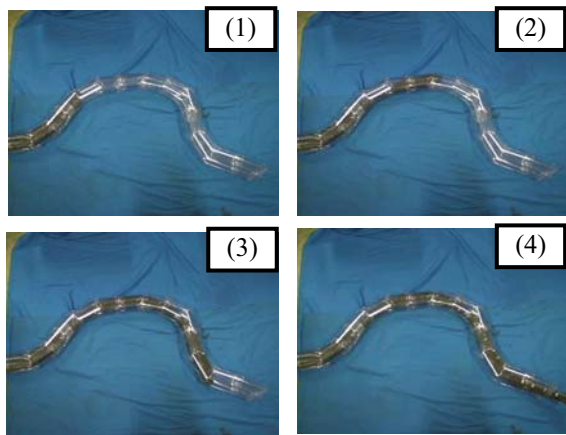
(b) Drive inside Pipe
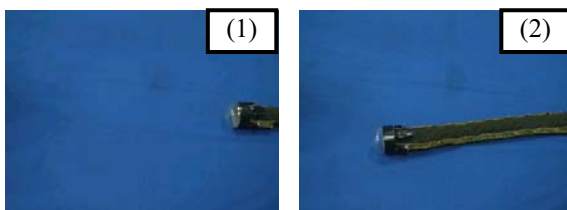
(c) Drive with Camera Module

Figure 20 Experiment of Grow-hose-I

As a result of the experiment, we can see that on a crank drive the direction of the hose can be controlled toward the destination and the curving shape can be kept by the effect of the grippers. In addition, when the camera module was set on the head of the hose, the module was able to move while synchronizing with drawing-out operation of the hose. Moreover, drawing-out motion can be done smoothly in a narrow conduit. Therefore it is thought that this kind of the hose can be applied not only for rescue operation but also for the inspection of piping, etc.

CONCLUSION

In this study, we suggested 'Grow-hose-I' which can pass through the complex debris without grinding friction between the surface of the hose and the debris. The suggested hose can perform a growing motion like a plant stem by drawing-out the inner body. The summary of the results obtained in this study is shown in the following.
1. The hose direction could be controlled by adjusting the air pressure of the flat tubes on the hose.
2. The hose could keep the curving-shape by the effect of the grippers on a crank motion.
3. The camera module equipped on the hose was able to move while synchronizing the drawing-out operation of the hose.

REFERENCES

1. A. Kitagawa, H. Tsukagoshi, M. Igarashi, "Development of Active Hose with a Small Diameter for Search and Life-prolongation of Victims" ,Journal of Robotics and Mechatronics, 15-5, 474/481,2003
2. D. Mishima, T. Aoki, S. Hirose "Development of Pneumatically Controlled Expandable Arm for Search in the Environment with Tight Access", Proc. Int. Conf. on Field and Service Robotics, FSR2003,315-320,2003
3. K. Hatazaki, M. Konyo, S. Tadokoro, "Active Scope Camera for Urban Search and Rescue", Proc. 2007 IEEE/RSJ International Conference on Intelligent Robots and Systems (IROS2007), pp.2596-2602, 2007
4. H. Tsukagoshi, I. Kiryu, N. Arai, H. Onuma, A. Kitagawa, "The Basic Study of Mobile Hose for the Search and the Operation", SICE2006 System Integration Conference, CD-ROM 3A2-7, 2006 (in Japanese)

P2-42

DEVELOPMENT OF ROBOT MANIPULATOR FOR LAPAROSCOPIC SURGERY WITH FORCE DISPLAY USING PNEUMATIC SERVO SYSTEM

Kotaro TADANO*, Kenji KAWASHIMA * and Toshiharu KAGAWA*

* Precision and Intelligence Laboratory
Tokyo Institute of Technology
4259 R2-46 Midori-ku, Nagatsuta, Yokohama, 226-8503 Japan
(E-mail: tadano@k-k.pi.titech.ac.jp)

ABSTRACT

In the teleoperated minimally invasive surgery systems, measurement and display of sense of force to the operator is a problem In this paper, we have developed a master-slave system having 7-DOFs for laparoscopic surgery, which can provide force feedback to the surgeon without using force sensors at the slave manipulator. Pneumatic actuators are used for the slave manipulation because they are effective for haptic devices due to the facility in measurement and control of their driving force. A control method to compensate the effect of the pipeline between the control valves and the actuators is proposed and applied. Then, an impedance control is applied to the slave manipulator and an admittance control is applied for the master manipulator. Finally, a bilateral control is achieved by combining the controllers. Experimental results show that the developed system successfully display the contact force on the slave side to the operator on the master side.

KEY WORDS

Pneumatics, Surgical robot, Laparoscopic surgery, Master-slave system, Bilateral control

INTRODUCTION

As alternative method to open surgery, minimally invasive laparoscopic surgery is an effective method. Robotic manipulators, which have multi-DOFs at their tip, have been reported as alternative to conventional instruments to support the surgery [1][2].
A master-slave type manipulator has advantages that the intuitiveness could be realized. A surgeon is able to teleoperate the forceps at the master side, as if he/she handles the forceps at the slave side in the abdominal cavity[3]. In this type, however, has the problem that the sense of force is lost. In order to realize safer and more precise operation using robotic manipulator especially master-slave system, force measurement and feedback are very important [4].

To realize a precise position control of the manipulator, using electric motors with high reduction gears is effective while the back drivability is small. Sensing the accurate force with such manipulators needs a force sensor at near the tip. However, the sensor at the end of forceps manipulator makes sterilizing and downsizing difficult.
In this research, we have developed a master-slave system with 7-DOFs forceps manipulators that is able to provide a force display to surgeons without a force sensor. To achieve this, we use pneumatic actuators, because they are effective for a haptic device due to the facility in measurement and control of their driving force, and enable the estimation of the external force from the driving force and the impedance. A control method to compensate the effect of the pipeline between

the valves and the actuators is proposed and applied. Then, an impedance control is applied with the compensator to the slave side. For the master manipulator we have developed, an admittance control is used. Finally, a bilateral control is achieved.

DEVELOPED 7DOFs SLAVE MANIPULATOR

Fig.1 shows the developed forceps manipulator that has 7-DOFs. The manipulator consists of a tip and a supporting part. The supporting part was introduced in the former paper, which feature is compact and the pivot point at the trocar cannula is immovable mechanically without direct support [5].

The tip part of the developed manipulator has a roll, two bending joints and a rotating movement can be achieved. The motions are transmitted using wire ropes. The diameter of the manipulator is 10mm that is useful for laparoscope surgery.

The feature of this forceps is that the bending and gripper were realized at the same joint. Therefore, the tip part becam compact. The rotary actuator with low friction (KURODA, PRNAJ1D-90-45) is used. The move angle is more than 73 degree for each joint and the maximum torque is 208 Nm. The driving force of the actuator is given as

$$F_{\mathrm{dr}} = A_1 P_1 - A_2 P_2 \qquad (1)$$

where A and P indicate the pressurized area and the differential pressure and the index 1 and 2 shows the room of the pneumatic cylinder. The supply pressure was set at 500kPa and a pressure sensor having a resolution of 20Pa was used. The actuator was controlled by a five ports servo valve made by FESTO. The servo valve receives the voltage signal and controls the flow rate to the actuator.

Pressures in the actuator were measured with semiconductor type sensors installed at the out port of the servo valve. This is because to make the forceps manipulator as possible as free from sensors to make

Figure.1 Developed slave manipulator

sterilize easy. The measured pressures were used to control the driving force. Position was measured by an encoder having a resolution of 1000Pulse/Rev. We have confirmed in the preliminary experiment that the position error of the actuator is less than 0.1mm using a PID controller.

COMPENSATION FOR PNEUMATIC PIPE LINE

There are 1m length pipelines between the actuators and the servo valves. The inner diameters of the pipelines are 2.5mm. The pipelines might cause the time delays. However, the pressure sensors should not be installed closer to the actuator to make the forceps easy to sterilize. Some compensation should be better applied. Therefore, pressures at two rooms of the actuators P_1 and P_2 and that of at the downstream of the servo valve P_1' and P_2' were measured in advance during force control. Sinusoidal force waves were given to the actuator by fixed the stroke at middle. Three kinds of amplitudes 1, 5 and 10N of force were given with several frequencies.

Fig.2 shows the bode diagrams summarized the experimental results. It became clear that the response between the pressure at the servo valve and that of at the pneumatic actuator could be modeled by a second order delay system given as

$$F = \frac{\omega_n{}^2}{s^2 + 2\zeta\omega_n s + \omega_n{}^2} F'$$
$$\omega_n = 28[\mathrm{Hz}], \quad \zeta = 0.6 \qquad (2).$$

The curves given by Eq.(2) are shown in solid lines in Fig.2. As a result, the driving force at the actuator could be estimated from the pressure difference near the servo valve. As a result, a controller as shown in Fig.3 was proposed and applied to the force control.
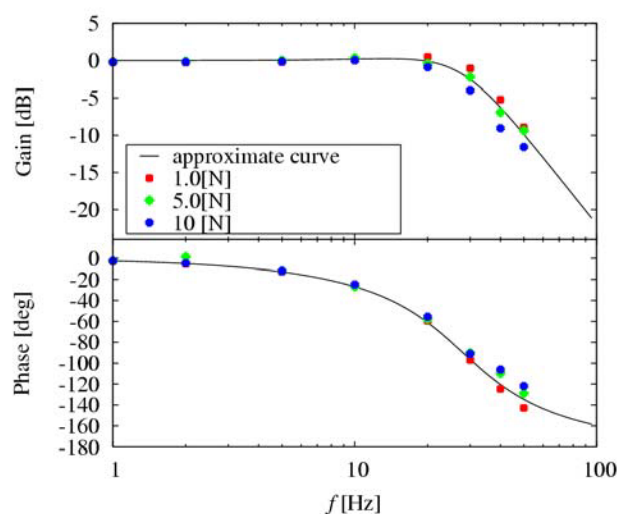

Figure.2 Bode diagram of pressure responses between 1m length pipeline with the diameter of 2.5mm
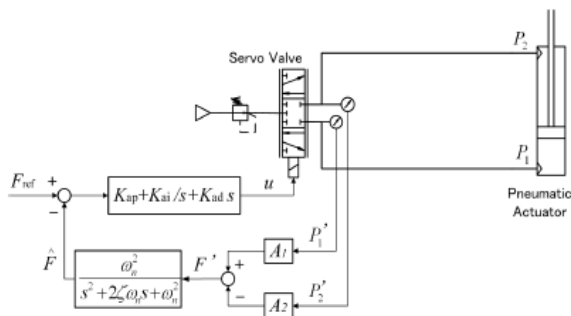
Figure.3 Block diagram of control for driving force

IMPEDANCE CONTROL

The impedance control is classified into force control type and motion control type. For pneumatic manipulators, the impedance control based on force control is considered to be suitable because of high back drivability and flexible characteristics. Therefore, a torque base impedance control without using force sensors is applied. The reference force at the end effector was given as:

$$\mathbf{f}_{\mathrm{ref}} = K(\mathbf{r}_{\mathrm{ref}} - \mathbf{r}) - B\dot{\mathbf{r}} - M\ddot{\mathbf{r}} \tag{3}$$

where,

$\mathbf{r}_{\mathrm{ref}} \in$ R^6 : Reference position at Cartesian coordinate
$\mathbf{r} \in$ R^6 : Slave position at Cartesian coordinate
$K \in$ R : Stiffness of the slave manipulator
$B \in$ R : Viscous coefficient in the slave manipulator
$M \in$ R : Mass

Therefore, the reference torque vector and force vector for joints can be given by

$$\boldsymbol{\tau}_{\mathrm{ref}} = J^T \mathbf{f}_{\mathrm{ref}} + Z(\mathbf{q}, \dot{\mathbf{q}}_{\mathrm{ref}}, \ddot{\mathbf{q}}_{\mathrm{ref}}) \tag{4}$$

$$\mathbf{F}_{\mathrm{ref}} = J \boldsymbol{\tau}_{\mathrm{ref}} \tag{5}$$

where

$\boldsymbol{\tau}_{\mathrm{ref}} \in$ R^6: Reference torque by the actuator at each joint
$Z \in$ R^6: Inverse dynamics function of the manipulator
$\mathbf{q} \in$ R^6 : Displacement of each joint
$J \in$ R$^{6 \times 6}$: Jacobian matrix of the slave manipulator.

The reference velocity and acceleration were obtained from the reference displacement. They were used to calculate the inverse dynamics instead of the velocity and acceleration calculated from the slave position because they include noises. The controller described above can be summarized in a block diagram as shown in the upper part of Fig.4. The compensator for pipeline is implemented at the force controller.

Experiments were conducted with M=0.1kg, B=0.02Ns/mm, and K=0.4N/mm. The experimental scenery is shown in Fig.5. Gripped a 6 axes force sensor

(BL AUTOTEC.LTD., NANO2.5/2) with the forceps to compare the forces.

The experimental results are shown in Fig.6 when the sinusoidal reference position input was given. It is clear as the controlled force given in Eq.(3) agree well with the measured results by the force sensor, the impedance control was successfully performed.
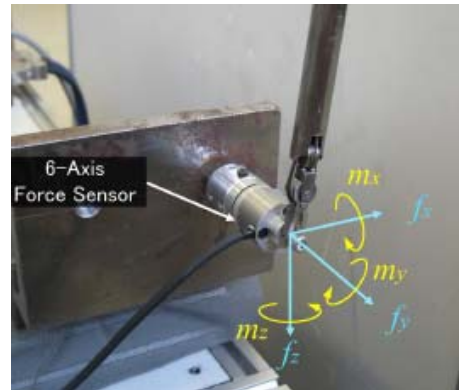

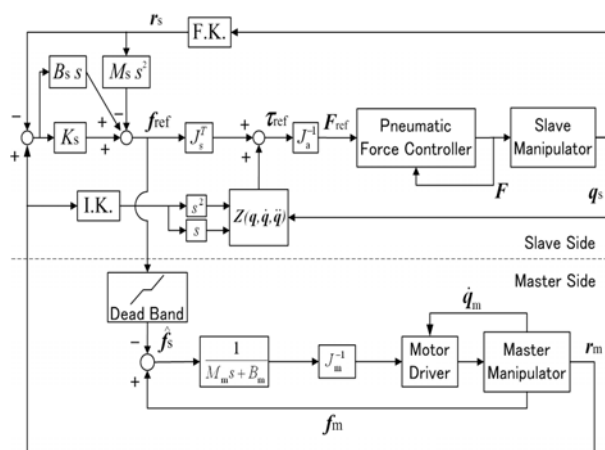Figure.4 Experimental scenery of impedance control
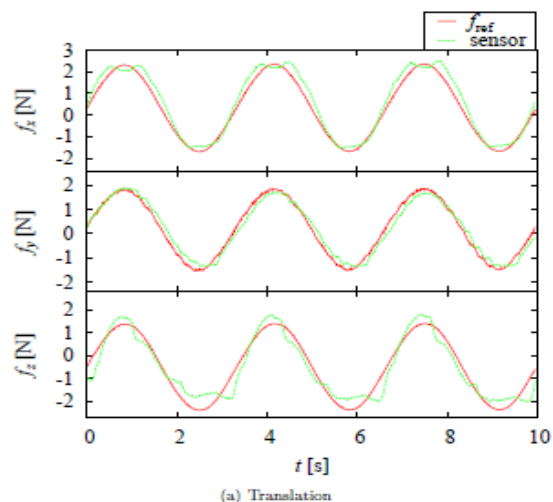

Figure 5 Block diagram

Figure 6 Experimental results of impedance control

BILATERAL CONTROL

Master Manipulator

The master manipulator we have developed used a delta mechanism for translation. In order to realize wide range of the orientation, we mounted a serial gimbal mechanism whose three rotational axes intersect at one point [5][6].

The dynamics of the master manipulator has a high bandwidth with using AC motors with reduction gears. As a result, a motion-based impedance control is suitable, because the dynamics of the manipulator and the effect of the gravity could be compensated by motion control loop and also it is easy to keep the position when the operator released one's hand. Therefore, we applied an admittance control. The block diagram of the controller is summarized in the lower part of Fig.5.

Bilateral Control Experiment

The impedance control at the slave side and the admittance control at the master side shown above were combined for bilateral control (Fig.5). The reference signals become the position and force of the other side. As the force signal from the slave to the master includes some noises, a dead band filter was implemented.

The experimental procedures are as follows: The operator handles the master manipulator to grasp a 6-axes force sensor with the slave manipulator. Then, the operator moves the master manipulator after grasped the sensor as if he or she can feel the force. Experiments were conducted with several impedance and admittance. Experimental results are shown in Fig.7. The impedance at the slave side was given as M=0.1kg, B=0.02Ns/mm, and K=0.4N/mm and M=0.4kg, B=0.005Ns/mm was given for the master side.
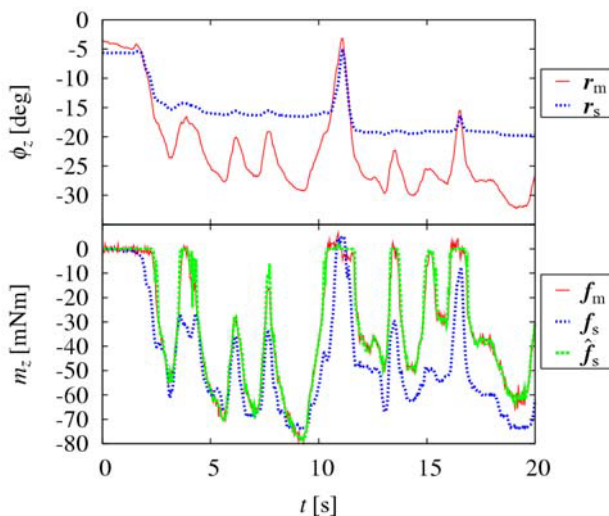
Figure.7 Experimental results of bilateral control

In Fig.7, the horizontal axis shows the time. The upper figure shows the rotational position data around z axis and the lower figures show the force. The dead band filer was selected to cut off less than 3N force and 20mNm torque because noises can be observed within that range.

It is clear that the control is successfully achieved since the lower figure in Fig.7 shows good agreement. To display more small force would be the next study.

CONCLUSIONS

In this paper, we developed a master-slave system having 7-DOFs for laparoscopic surgery, which can provide force feedback to the surgeon without using force sensors at the slave manipulator. Pneumatic actuators were used for the slave manipulation because they are effective for a haptic device due to the facility in measurement and control of their driving force.

A control method to compensate the effect of the pipeline between the control valves and the actuators was proposed and applied. Then, an impedance control was applied to the slave manipulator and an admittance control was applied for the master manipulator we have developed. Finally, a bilateral control was achieved combined the controllers. Experimental results showed that the developed system successfully display the contact force on the slave side to the operator on the master side.

REFERENCES

1. Russell H. Taylor and Dan Stioianovici, Medical Robotics in Computer-Integrated Surgery, IEEE Trans. on Robotics and Automation, 2003, **19**-5,pp.765-780
2. G.H. Ballantyne, J. Marescaux, and P.C.Giulianotti, editors. Primer of Robotic & Telerobotic Surgery. Lipincott Williams & Wilkins, 2004
3. G.S.Guthart and J.K.Salisbury, The intuitive telesurgery system: Overview and application, Proc. of IEEE ICRA, 2000, pp.618-621
4. O. Gerovichev, P. Marayong, A.M. Okamura, The Effect of Visual and Haptic Feedback on Computer-Assisted Needle Insertion, Computer -Aided Surgery, 2004, **9**-6,pp.243-249
5. K.Tadano and K.Kawashima, Development of a Master Slave Manipulator with Force Display using Pneumatic Servo System for Laparoscopic Surgery, International Journal of Assistive Robotics and Mechantronics, 2007, **8**-4,pp.6-13
6. K. Tadano, K. Kawashima and T. Kagawa,Evaluation of a Master Slave System with Force Sensing, Proc. of SICE Annual Conference, 2007, pp.2871-2874

P2-43

ALL IN ONE TYPE FLUID FLOW SERVO SYSTEM USING

SOLENOID VALVE AND ISOTHERMAL PRESSURE VESSEL

Tetsuya UEDA*, Osamu OYAMA*, Toshihiro YOSHIMITSU**, Toshiharu KAGAWA***

* Mechanical Engineering Major, Science and Engineering Research Course
Graduate School of Meiji University
Tamaku higashimita 1-1-1, Kawasaki city, Kanagawa, Japan
(E-mail: ce82007@isc.meiji.ac.jp)
** Welfare system Engineering, Kanagawa institute of Technology
Shimoogino1030, Atsugi city, Kanagawa, Japan
*** Precision engineering laboratory Tokyo Institute of Technology
Midoriku nagatudatyou 4259, Yokohama city, Kanagawa, Japan

ABSTRACT

Abstract-In general, it tends to become a complex and expensive structure in the controlling of flow rate. In this paper, a simple structure and compact flow rate servo system is shown. It is easy to carry by integrating needed element, that is, the solenoid valve, the isothermal pressure vessel, the pressure sensor and one board controller of on-off method, although, the external compressor is needed. The signal measured with the pressure sensor is sent to the controller, and the proper control signal is feedback to the switching transistor according to on-off timing of the solenoid valve. In this method, the small pressure fluctuation caused by switching action of solenoid valve can not be avoided,   however, this pressure fluctuation enables to examine the actual output flow rate by on-line sampling the pressure and calculation using micro processor on controller. So we execute continuous flow rate control by this compact system alone, and are able to change the output flow rate freely according to manual set up or external control signal. For the evaluation of this system, the blowing up device is adopted to confirm the accuracy of flow rate that is constantly controlled ball height apart from seat.

KEY WORDS

Solenoid valve, Isothermal pressure vessel, Flow rate control

INTRODUCTION

For the air pressure servo system, a highly accurate response to change of target value and change of load is requested. In this research, the flow accuracy measured by the small pressure fluctuation caused in the container by using the solenoid valve and the isothermal pressure vessel is shown and it aims at the development of the air pressure flow rate servo that outputs the desired flow rate.

EXPERIMENTAL-APPARATUS

In the device, the supply air pass through the solenoid valve of on-off works, isothermal pressure vessel that suppress the temperature change of the air, and the output flow is delived to devices. The pressure sensor is installed in the pressure vessel, the measured value is sent to microcomputer, and the proper control signal is fed according to the value to the solenoid valve as the timing of the valve open and close

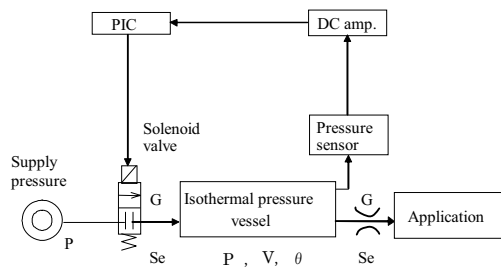Figure 1 shows the experimental apparatus of this research.

Figure 1 Scheme of experimental apparatus

CONTROL METHOD

The pressure fluctuation generated by the opening and closing drive of the solenoid valve depends on the supply pressure and the output flow rate. In a word, the both of output flow rate and the supply pressure fluctuation can be acknowledged from the pressure fluctuation. Therefore, a stable output of the desired flow rate to the target becomes possible. The control of the ripple rate is used as a control method. This control method decides an appropriate rate of the ripple in consideration of the error margin with the target value. The set value upper bound and the lower bound are provided from the rate of the ripple, and the opening and closing timing of the solenoid valve is controlled.

EXPERIMENT RESULT

Figure 2 shows the pressure fluctuation by the control of the ripple rate. Moreover, the error between experiment and desired value and the ripple between experiment and desired value are shown in Table.1 respectively.

The output flow rate as constant desired flow rate of 44L/min is shown in the Figure 2.
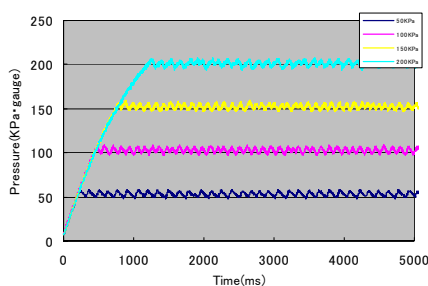
Figure 2   Pressure wave of ripple rate control

	50KPa	100KPa	150KPa	200KPa
The error between experiment and desired value	3.163	2.921	2.450	1.265
The ripple between experiment and desired value	8.214	8.305	7.891	8.735

Unit:[KPa・gauge]
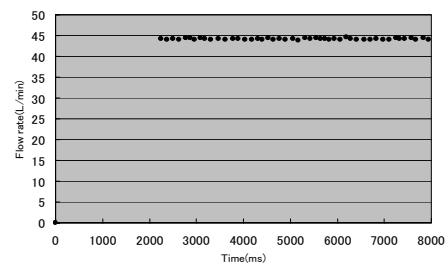
Figure 3   Flow rate by ripple rate

Figure 4 shows the shape of waves of the flow rate when the flow is changed from28L/min to 44L/min by changing load resistance installed in this device. It is understood that the change of the flow rate is stable when the target value is uniformity from the result of Figure 4.
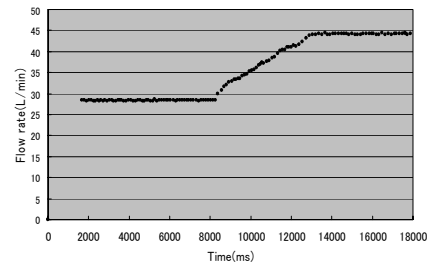
Figure 4   Follow of sample pressure from 100KPa into

200Kpa

CONCLUSION

In this research, the flow rate can be controlled directly with the solenoid valve, by measuring the change of the pressure generated by the opening and closing of the solenoid valve, and the flow rate can meet the desired. The pressure that is an intermediate variable in the system of the flow servo can be used as the control variables. Althogh the effect of changing the unknown supply pressure is not tested, it is expected that the system can adapt change of supply pressure. The error margin of the average flow rate was able to confirm about 2% and highly accurate responses from the result of the experiment.

REFERENCE

1. Toshihiro YOSHIMITSU, Osamu OYAMA, Tosiharu KAGAWA, Flow Rate Servo Using Solenoid Valve and Isothermal Pressure Vessel

P2-44

EXPERIMENTAL AND CFD STUDY ON ONE NEW TYPE OF AEROSTATIC BEARING

Hechun Yu, Wenqi Ma, Zuwen Wang

Transportation and Logistics Engineering College
Dalian Maritime University
Dalian, 116026, China
(E-mail: yuhechun1106@126.com)

ABSTRACT

The pressure depression is usually observed just after the gas supply hole. In order to improve the pressure distribution, a new type of aerostatic bearing (NT) is designed, which has a tapered chamber at the outlet of the gas supply hole. The Fluent software is used to simulate the working conditions of aerostatic bearings. The simulation results show the simulation method can effectively estimate the pressure depression and the pressure distribution of the NT is remarkably improved compared with the traditional annular orifice type(TT). It's found that the characteristics of the Mach Number (MN) distribution of the NT are different from those of the TT and the tapered chamber can effectively reduce the velocity at the bearing clearance entrance. A test rig is built. The pressure distributions are tested and the simulation results of the NT agree well with the experimental results. The simulation method provides a good theoretical method to study the aerostatic bearings and the new design will be helpful to the development of high load capacity aerostatic bearings.

KEY WORDS

aerostatic bearing, pressure depression, Mach Number, Fluent software

NOMENCLATURE

d : gas supply hole diameter
d_1 : tapered chamber outer diameter
D : bearing outer diameter
h : bearing clearance
h_1 : length of gas supply hole
h_2 : height of tapered chamber
P : pressure
P_a : ambient pressure
P_s : gas supply pressure
R : radial coordinate
T : absolute temperature
T_a : ambient temperature
T_s : gas supply temperature

μ : dynamic viscosity

INTRODUCTION

Aerostatic bearings have been widely applied to precision instruments, dental drills, jet engines and computer peripheral devices, because of their substantially low friction loss and heat generation. Recently, the application of aerostatic bearings in micro electro-mechanical system (MEMS) has attracted considerable attention [1]. However, there is a deep pressure depression just after the outlet of the gas supply hole in some cases, which limits the use of

aerostatic bearings [2]. In order to reduce the pressure depression and improve the load capacity of aerostatic bearings, Mori et al first proposed one new type of aerostatic bearing with a tapered chamber at the outlet of the gas supply hole [3]. They found that the pressure distribution of the aerostatic bearing with a tapered chamber is remarkably improved compared with the aerostatic bearing without a chamber. Under some assumptions, they simplified the control equations and calculated the pressure distribution, but the calculating results are not well agreed with experimental results.

In this paper, one of the NT is designed. The Fluent software is used to calculate the flow of aerostatic bearings. A test rig is built, the pressure distributions are tested.

SIMULATION AND EXPERIMENT SYSTEM

Simulation Models

Figure 1 shows the structure of the NT and its parameters are as follow: D=80mm; d=2mm; d_1=20mm; h_1=6mm; h_2=0.4mm. Fig.2 shows the structure of the TT and its parameters are as follow: D=80mm; d=2mm; h_1=6mm. Because of the axis-symmetry, this paper just takes the half of Figure 1 and 2 as the simulation models, which is helpful to densify calculation grids.
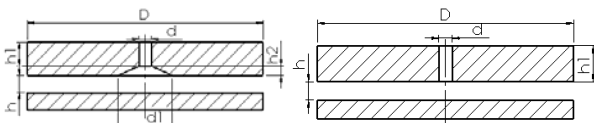
Figure 1 Structure of NT   Figure 2 Structure of TT

Boundary Conditions

The SST k-omega model is used to calculate the flow, and the setting of the boundary conditions are as follow:
(1) P_a =1atm, T_a = 300K.
(2) P_s =6atm (absolute pressure), T_s =300K
(3) In the supersonic flow, the air temperature may change, and the dynamic viscosity of air is usually a function of temperature, so it is estimated using the Sutherland equation as shown below

$$\frac{\mu}{\mu_\infty} = \left(\frac{T}{T_\infty} \right)^{3/2} \frac{1 + S_1 / T_\infty}{T / T_\infty + S_1 / T_\infty}$$

Where μ_∞=1.716-e5; T_∞=273.11; S_1=110.56.

Experiment System

Figure 3 shows the experimental system. The system includes three parts: air source parts, load exertion parts; testing parts.

In the air source parts, the air from the compressor passes through the main filter and dryer and enters into the air tank. The high pressure air from the air tank is reduced by the pressure reducing valves installed in the pipeline and supplied into the bearing clearance.

In the load exertion parts, the load is exerted by an air cylinder. In order to avoid the bearing air supply pressure fluctuation, the air cylinder' air is not supplied by the high pressure air tank but by an independent low pressure air compressor with a 50 L air tank.

In the testing parts, bearing clearance, load and pressure distribution can be tested. The bearing clearance is measured by the inductance micrometer and the load is measured by the weighting sensor. The pressure distribution in the bearing clearance is measured by the multi-channel (16channel) pressure scanning module. During the experiment, the author used two pressure scanning modules to measure the pressure distribution.
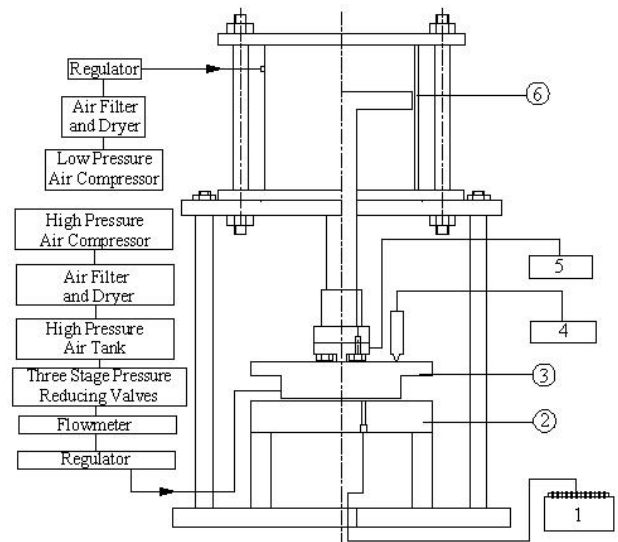

Figure 3 Experiment System
1 pressure scanning module, 2 pressure measuring board, 3 gas bearing, 4 inductance micrometer, 5 weighting sensor, 6 gas cylinder

COMPARISONS AND DISCUSSION

Figure 4~7 shows the pressure distributions obtained from simulations and experiments of the two types of aerostatic bearing under different bearing clearances.
(1) Under four different bearing clearances（Figure 4~7）, both simulation and experiment pressure distributions of the NT are higher than those of the TT. The pressure distributions of the NT are remarkably improved, which are the same to the results of Mori et al [3].
(2) Under 30μm and 40μm bearing clearance（Figure 6~7）, pressure depressions occur in both types of aerostatic bearing. And there are two pressure

depressions occurring in the NT, one occurs just after the outlet of the gas supply hole, which is similar to the pressure depression of the TT after the gas supple hole. The other occurs at the outlet of the tapered chamber. After the first pressure depression, the pressure increases a little, after the second one, no increase occurs. The pressure depression amplitudes of the NT are much smaller than those of the TT, the reason will be explained after.

(3) For the NT, the simulation results are well agreed with the experiment results. For the TT, when the bearing clearance is 10μm, the simulation results are in good accord with the experiment results（Figure 4）, but with the increase of the bearing clearance （Figure 5～7）, the deviation of simulation and experiment results increases, and the experiments are not able to capture the minimum pressure, the experimental pressure distributions are higher than the simulation results. This phenomenon is caused by the arrangements of the pressure testing holes. The arrangements of the pressure testing holes are fixed in the experiment system, but the position of the minimum pressure is changing under different bearing clearances and multi pressure testing holes have influence on the pressure distributions, which increase the pressure distribution under high MN working conditions.
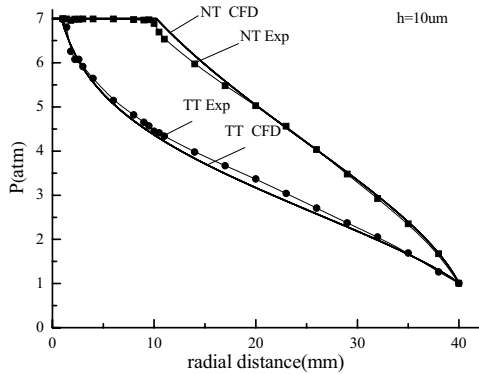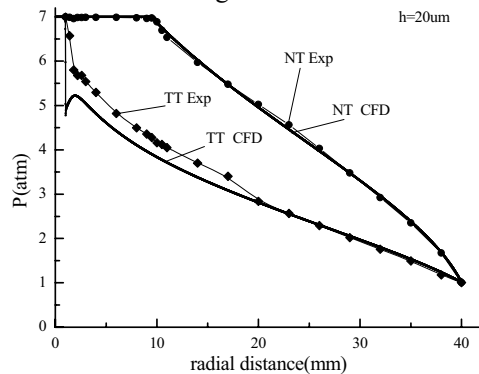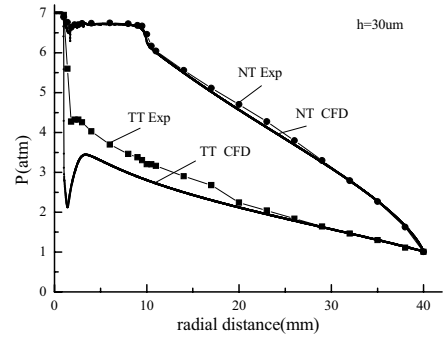
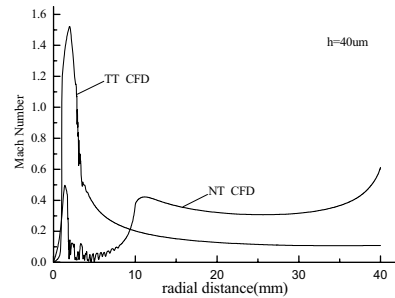

Figure 6
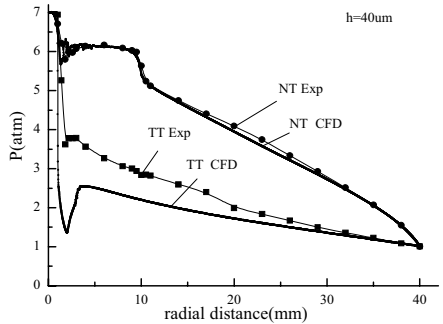
Figure 7

EFFECTS OF CHAMBER ON MN DISTRIBUTION

Figure 8 MN distributions of two types of aerostatic bearing under 40μm bearing clearance

Figure 8 shows the MN distributions of the two types of aerostatic bearing under 40μm bearing clearance, the MN distribution of the NT is quite different from that of the TT.

Before R=10mm, the MN of the NT is smaller than that of the TT; after R=10mm, the MN of the NT is bigger than that of the TT. For the TT, the MN increases first and then decreases. For the NT, generally speaking, there are three increases and two decreases. The first pair of increase and decrease occurs just after the outlet of the supply hole, which is similar to the pair of increase and decrease of the TT, is caused by the change of the flow passage. The second pair of increase and decrease occurs at the entrance of the bearing clearance or the outlet of the tapered chamber. After the second pair of increase and decrease, the MN increases with the

Figure 4

Figure 5

increase of R before the outlet of the bearing clearance. For the TT, the maximum MN occurs just after the gas supply hole and is greater than one. While for the NT, the chamber inhibits the increase of velocity in the chamber, the maximum MN is less than 0.6 and the position of the maximum MN is at the outlet of the bearing clearance. Because the increase of MN in the chamber is inhibited, so the MN of the NT is smaller than that of the TT, and the pressure depression is suppressed. After the gas supply hole, with the increase of R in the chamber, the flow passage area decreases, based on the continuity equation, the velocity must increase. After the bearing clearance entrance, the velocity decrease is caused by the gas viscosity and the increase of flow passage area, but the phenomena that the MN increases with the increase of R before the outlet of the bearing clearance after the second pair of increase and decrease can't be explained now and needs further study.
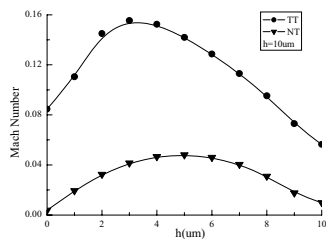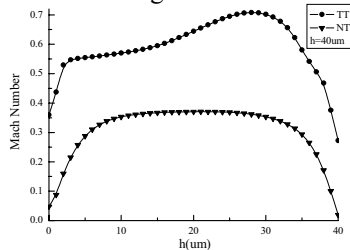

Figure 9
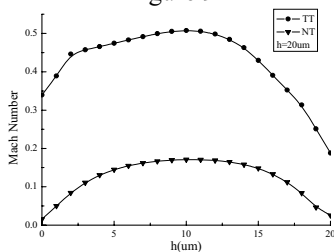
Figure 10
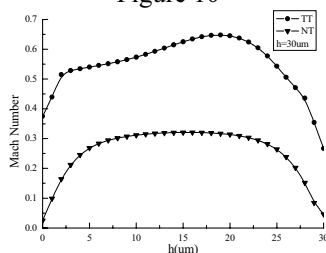
Figure 11

Figure 12

Figure 9～12 shows the MN distributions of the two types at the bearing clearance entrance under four different bearing clearances. It's obvious that the MN distributions of the NT are smaller and more regular than those of the TT because of the tapered chamber. The MN distribution of the NT is less affected by the bearing clearance and accords with the characteristics of laminar flow, it is because in the chamber the flow becomes uniform and the flow passage changes a little before and after the bearing clearance entrance. While in the TT, the flow passage changes abruptly before and after the bearing clearance entrance, the direction of velocity changes much and the maximum MN position move towards the up wall with the increase of bearing clearance. The distribution accords with the characteristics of turbulence flow. Because the MN of the NT is smaller than that of the TT, the effect of inertial force will be less too.

CONCLUSIONS

(a) A tapered chamber at the outlet of the gas supply hole can effectively reduce the pressure depression amplitude and improve the pressure distribution.
(b) A tapered chamber at the outlet of the gas supply hole inhibits the increase of velocity and the appearance of the supersonic velocity after the gas supply hole. It changes the style of MN distribution. It reduces the velocity in the tapered chamber, but it improves the MN distribution after it, the cause of this kind of phenomena needs further study.
(c) The multi-hole pressure testing method can't effectively capture the minimum pressure and has influence on the pressure distributions.
(d) The simulation method can effectively calculate the flow of aerostatic bearings and provides a good theoretical method to study the aerostatic bearings.

ACKNOWLEDGMENTS

REFERENCES

1. Qide Zhang et al. Performance analysis of air bearing in a micro system, Materials Science and Engineering A 423 (2006): pp.225–229.
2. Haruo Mori. A theoretical investigation of pressure depression in externally pressurized gas lubricated circular thrust bearings, Trans of ASME, Journal of Basic Engineer, 1961, 83(2): 201 – 208.
3. Haruo Mori. Research on Externally Pressurized Circular Thrust-Lubricated Bearings, JSME, 1964, 26-7: pp.467-473

P2-45

STUDY ON MOTORS USING LIQUID CRYSTAL FLOW INDUCED BY ELECTRIC FIELD

Liang CHENG *, Tetsuhiro TSUKIJI** , Kazunori HAYAKAWA*
and Xiao dong RUAN ***

*Graduate School of Science and Technology, Sophia University

**Faculty of Science and Technology, Sophia University,

7-1,Kioi-cho, Chiyoda-ku, Tokyo,102-8554 Japan

(E-mail: t-tukiji@sophia.ac.jp)
***Department of Mechanical Engineering, Zhejiang University, China

ABSTRACT

It is well-known from our previous study that LC(liquid crystal) circumrotates in a mini cylinder by a rotating electrical field. The possibility of the development for a motor based on the above idea is investigated in this study. In the experiments, electrodes are located both at the bottom and on the side wall of the cylinder, in which the LC and the rotor are placed. The influence of the viscosity on rotation speed of the rotor is investigated. Moreover, the theoretical study on torque generation is expected too.

KEY WORDS

Liquid Crystal, Relative Permittivity, Functional Fluid, Motor, Unsteady Electric Field

INTRODUCTION

It is known from our previous work that Liquid crystal (LC) flows in a mini cylinder by rotating electric field[1]. The possibility for designing motors driven by the flowing based on the above mechanism is investigated in this study. Many advantages can be obtained in this kind of motors, for example, the structure of the motor is simple and it can be minimized easily.

In the experiments, electrodes are located both at the bottom and on the side wall of a cylinder, in which the LC and the rotor (sampled as a turbine) is placed. The rotating electric field of three-phase alternating current is generated to add it on the electrodes in a motor. Two kinds of LC with different properties, such as viscosity etc. are tested during the experiments. The rotation speed of the rotor is measured under given electric fields with constant frequency [2,3]. One main contribution of this investigation is the comparison in rotation speed when motor is placed under different LC in two cases. One case is that the electrodes are placed just at the bottom of the cylinder. In the other one, the three-phase alternating currant is added on all electrodes in the cylinder. Additionally, the influence of viscosity on rotation speed is also investigated. Moreover, the theoretical study on torque generation is studied too.

TEST BENCH

The test-bench is shown in Fig.1. The height and the diameter of the cylinder are both 4mm. Six electrodes are located at the bottom every 0.2mm (In Fig.1, the

electrodes are equipped both at bottom and the side wall). The faced electrodes as 1 and 4 are the same in voltage level. The 3-phase power supply used in the experiments is same in frequency and the angle is $2/3\pi$ delay in the sequence $1\rightarrow2\rightarrow3$. Theoretically, the liquid crystal should flow in the clockwise way. An impeller with diameter 2.6mm and height 1.5 mm is dipped in the LC (see Figs.1 and 2). The rotating speed is measured by images of the rotor taken using digital camera placed over the cylinder. The input for the equipment A (see Fig.3) is the AC with frequency 50Hz and effective voltage 200V. The output of the transformer A can be adjusted form 0V to 240V. The transformer B is with the transformation ratio 15, which is the final voltage for each electrode. During the experiments, the speed measurement is executed with different voltage level. Furthermore, in experiments, the tests with different dielectric constant of isolation are taken and discussion between two cases is illustrated.

Fig.2 Photo of electrodes and rotor
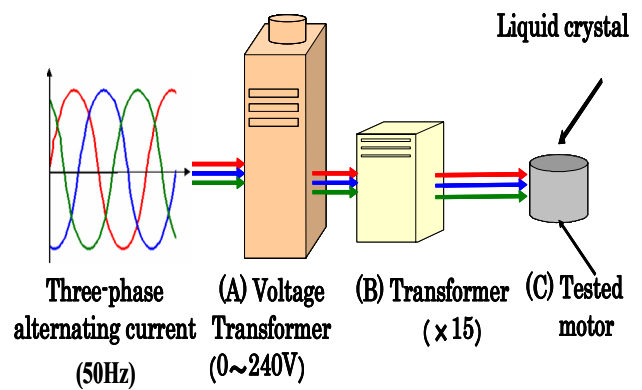(Inner diameter:4mm, Diameter of rotor:2.6mm)

Fig.3 Experimental apparatus using three-phase alternating current

EXPERIMENTAL VALIDATION

The results for experiments A and B are demonstrated as follow.

For experiments A, three kinds of LC (Mixed LC MLC6650, Pure LC K-15 and Mixed LC MJ0669) are tests. Figs.4 and 5 show the curves of speed of rotor with different dielectric constant and voltage level. The average of five measurement of speed is taken for evaluation. The voltage changes from 353V to 1420V in experiments. h is the height of the LC surface.

In Figs.4 and 5, it is clear that in the same frequency, high voltage implies high speed.

Meanwhile, the speed changes with the variation of dielectric constant. In Fig.4   polyamide films   is used with dielectric constant 3.5
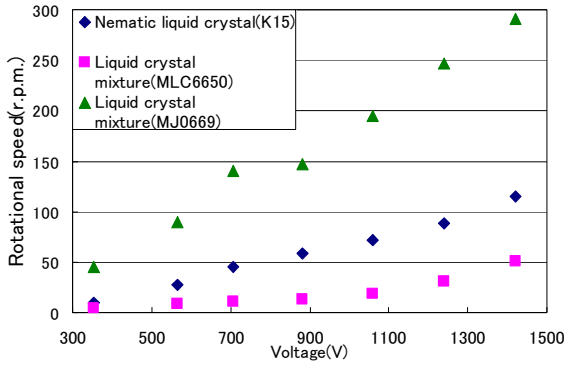

Fig.1 Present motor and rotor

Fig.4 Relationship between rotational speed and voltage for experiment A
(Using polyamide film, specific **permittivity=**3.5, *h*=2mm）

Fig.5 Relationship between rotational speed and voltage for experiment A
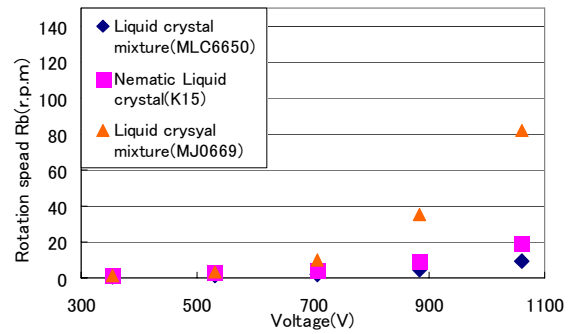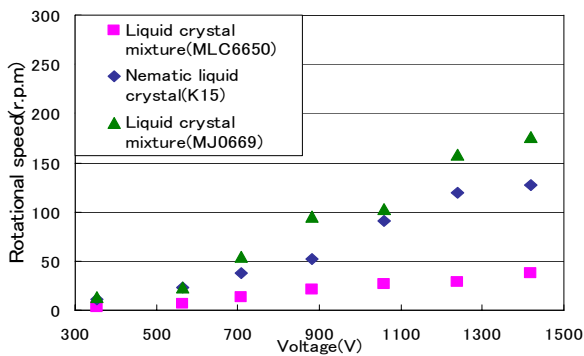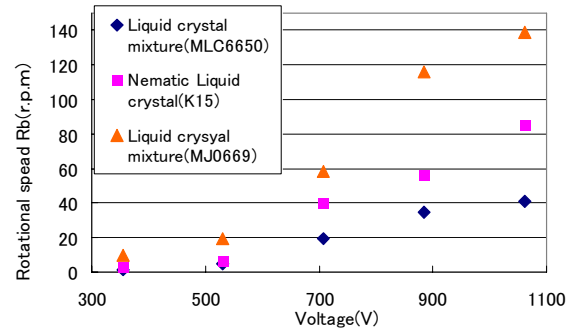(Using glass epoxy board, specific **permittivity=**4.6～4.8, *h*=2mm）

Fig.6 Relationship between rotational speed and voltage for experiment B
(Using polyamide film, on the bottom surface, h=1.8mm）

Fig.7 Relationship between rotational speed and voltage for experiment B
(Using polyamide film, on the bottom surface and side face, h=1.8mm）

In the other way, as the experiment shown in Fig.5, glass epoxy is adopted and the dielectric constant range is from 4.6 to 4.8. According to MJ0669, experiment result shows that small dielectric constant lead to high speed. Furthermore, among these 3 kinds of LC small kinematic viscosity and dielectric constant makes high speed. The highest speed appears in LC MJ0669, then K-15 and finally MLC6650. The kinematic viscosity are 13mm²/s，20 mm²/s，76 mm²/s, respectively. The parameters of dielectric constant are 11.2，26.1，62.8 along the molecule axis and 3.9，6.0，10.2 in the vertical direction.

Figs.6 and 7 illustrate the results for experiment B. The mentioned two cases are compared and the result shows that the speed is high when both the electrodes at bottom and on the side wall are activated. The reason for this phenomenon is that the interface is large in the second case, which provides us the future issue for influencing rotating speed in more effective way.

TORQUE CALCULATION

From Newton secondary law, Eq(1) exists:

$$T = J \frac{d\omega}{dt} \tag{1}$$

where T is the starting torque generated from LC flowing, ω is the angler velocity of the rotor and J $(=1.36 \times 10^{-7} \text{kgm}^2)$ is the rotary inertia.

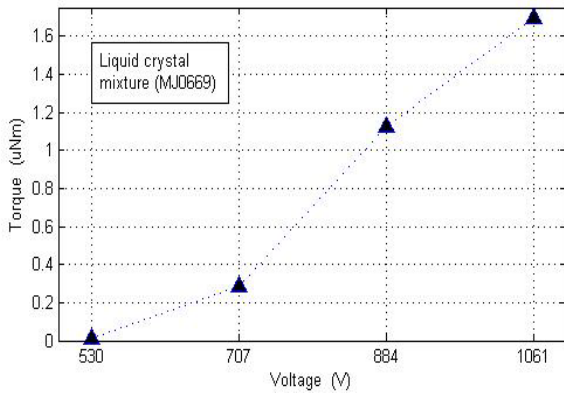The moment of inertia of the gear (J) is obtained from the geometrical calculation.

Fig.8 Relation between torque and voltage
(on the bottom surface and side face，*h*=1.8mm）

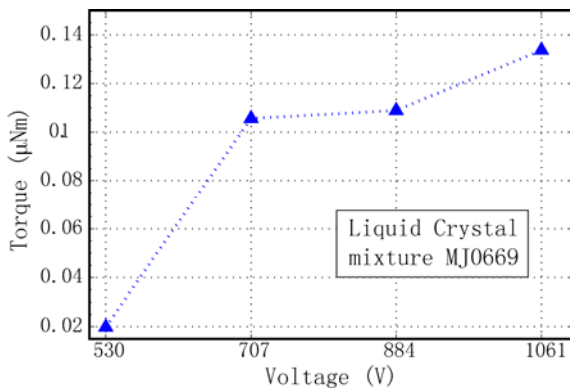Fig.9 Relation between torque and voltage
(Only bottom surface，*h*=1.8mm）

The starting torque *T* is obtained by calculating *dω/dt* from the images of the rotor, taken by video camera. Meanwhile, the rotating angler acceleration (*dω/dt*) is measured through a video recorder. The results of the torque are shown in Figs. 8 and 9. The order of the torque is about *μ*Nm for Fig.9 and 10^{-7}Nm for Fig.10. It is found that the torque for the motor with electrodes both on the bottom surface and side face is greater one order. In fact, since the friction exists, the real torque generation (*T*) from power supply is greater than the values shown in the figure, which is the product of *J* and *dω/dt* .

CONCLUSIONS

In this paper the experimental tests for driving motor with LC is taken. In details, the experiments emphasize the influence of voltage level and dielectric constant on speed. The main result is as follow.

(1) The rotating speed changes when the dielectric constant adjusts, especially with MJ0669, small dielectric constant makes high speed.

(2) The speed of the rotor increases with the electrodes both on the bottom surface and side face compared with only on the bottom surface electrodes and the further development of the electrode situation to produce a large electric field is the future work.

(3) The starting torque is estimated theoretically and its order is 10^{-6} Nm with the electrodes both on the bottom surface and side face

ACKNOWLEDGEMENT

REFERENCES

1. Tsukiji，T., Murata,Y.and Ito,J, Flow of a Liquid Crystal Mixture in a Mini-Cylinder Under Rotating Electric Fields,Proceedings of the Sixth International Symposium on Fluid Power Tsukuba,2005,pp.595-600
2. Tsukiji, T., Suzuki, K., Hayakawa, K., and Murata, U., Developments of Micro-Pump and Motor Using Dielectrophoresis of Liquid, The 11th Annual International Conference of Micro and Nano Systems Conference, St. Petersburg, Florida , August 27-31, 2006.
3. Hayakawa, K. and Tsukiji, T., The Fundamental Research on Micro Motor Driven by Functional Fluid , Preprint of Fluid power system Conference, 2006, Autumn， pp130-132

P2-46

FLUID DYNAMIC INVESTIGATION OF POLISHING THE INNER WALL OF A TUBE UTILIZING A MAGNETIC COMPOUND FLUID (MCF)

Hitoshi NISHIDA*, Kunio SHIMADA** and Yasushi IDO***

* Department of Mechanical Engineering
Toyama National College of Technology
13 Hongo, Toyama, 939-8630, Japan
(E-mail: nishida@toyama-nct.ac.jp)
** Faculty of Symbiotic Systems Science
Fukushima University
1 Kanayagawa, Fukushima, 960-1296, Japan
*** Quality Innovation Techno-Center
Nagoya Institute of Technology
Goki-cho, Showa-ku, Nagoya, 466-8555, Japan

ABSTRACT

In this study, we investigated the mechanism of polishing the inner wall of a tube utilizing a magnetic compound fluid (MCF) from a hydrodynamic viewpoint. We conducted polishing experiments by filling a tube with a MCF consisting of abrasive grains and applying a rotating magnetic field perpendicular to the tube axis. In addition, in order to clarify the polishing mechanism, we performed visualization experiments by observing the behavior of the abrasive grains and measuring the pressure distribution on the inside surface of the tube using a hydrodynamic technique. This study demonstrated that a magnetic field distribution for effective polishing should exist in the region furthest from the centerline between the magnetic poles in the tube. At this position, the abrasive grains are located on the sides of the walls of the inner tube of the clusters formed along the line of magnetic force and the pressure generated is effective for polishing. The pressure distribution has a flat valley profile. Therefore, the radial force of clusters formed near these locations is considered to impart a processing force to the abrasive grains.

KEY WORDS

Magnetic compound fluid, Polishing, Inner tube wall, Visualization, Pressure distribution

INTRODUCTION

The increasing reduction in the size of products and components is making precision polishing essential for the inner walls of capillaries and microtubes having complex shapes. Since conventional methods for

polishing inner tube walls are not effective for polishing such surfaces, it is essential to develop of a new polishing method. Against this background, we have proposed a new polishing method that employs a magnetic compound fluid (MCF), which is a mixture of a magnetic fluid (MF) and iron powder. In this method,

an MCF containing nonmagnetic abrasive grains is allowed to pass through a tube and a rotating magnetic field is applied perpendicular to the tube axis [1]. To clarify the polishing mechanism of this method, we investigated the effect of the composition of fluids containing abrasive grains and the magnetic field distribution on polishing of the inner tube wall with no effect from the fluid. Polishing was found to be greatly affected by the magnetic field distribution and it was possible in the midpoint between the electrodes and in the region furthest from the central axis where the magnetic flux density and the rate of decrease of the magnetic flux density are both large [2].

The goals of this study are to observe the behavior of the abrasive grains in this polishing method and to hydrodynamically investigate the polishing mechanism of this method by measuring the pressure distribution on an inner tube wall. Specifically, a visualization experiment is conducted to observe the arrangement and behavior of the abrasive grains, and a pressure measuring experiment is conducted to check the processing pressure of magnetic clusters and to investigate the characteristics of the pressure distribution in polishing.

PRINCIPLE OF THE POLISHING METHOD

Figure 1 shows a schematic diagram of magnetic clusters and abrasive grains in the cross-section of a tube filled with a MCF when a magnetic field is applied perpendicular to the tube axis. The effect of the applied magnetic field on the MCF is to cause magnetic clusters to form that consist of iron particles and magnetite particles along the lines of magnetic force. The magnetic clusters are concentrated near the magnetic poles and their tips on the inner wall side are considered to retain the abrasive grains. Magnetic clusters are formed even in the center of the tube between the electrodes and in the region furthest away from the central axis. In an earlier report describing our experimental results, we conjectured that this polishing
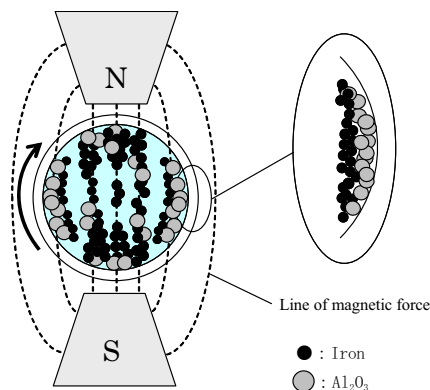

Figure 1 Principle of polishing on an inner capillary wall

method uses abrasive grains retained on the surface of the inner wall of the magnetic clusters in the center of the tube in between the electrodes and in the region furthest away from the central axis, as shown in the figure.

ABRASIVE GRAIN VISUALIZATION EXPERIMENT

Figure 2 shows a photograph of the observation system. The system consists of a turntable on which there is an observation tube filled with a MCF and a magnetic field generator for applying a rotating magnetic field. The MCF used for this experiment was prepared by adding carbonyl iron powder (HQ, Yamaishi Metal) that had an average particle diameter of 1.2 μm to a water-based magnetic fluid (W-40, Taiho Industries). Instead of abrasive grains, 0.4-mm-diameter glass beads were mixed into the solution. Table 1 lists the composition of this fluid called WMCF40G30. The fluid-filled observation tube was a short resin pipe (internal diameter d: 10 mm, external diameter: 16 mm, length: 2 mm) with glass covers bonded to both ends. To generate the magnetic field, permanent magnets ($20\times20\times10$ mm, neodymium magnets, Niroku Seisakusho) were attached to a U-shaped yoke (SS400, cross-section: 20×20 mm) and pole pieces (SS400) having a tip width w of 10 mm were attached. The distance between the magnetic poles δ was fixed at 22 mm. In this experiment, a rotating magnetic field was
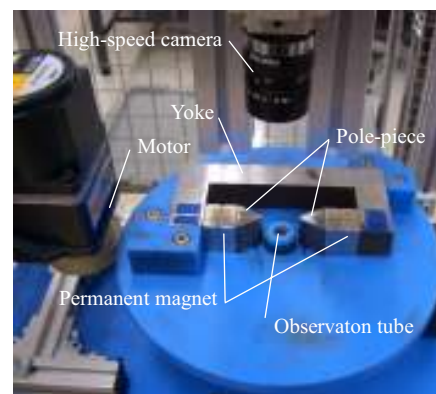

Figure 2 Photograph of the observation system

Table 1 Components of testing fluids

Testing fluids	Volume concentration (Vol.%)		
	Magnetic fluid	Iron	Glass beads
WMCF40G30	62.7	7.3	30.0
WMCF25	94.5	5.5	—

Table 2 Experimental conditions for optical observations

Magnetic flux density at center (w=10 mm)	0.182 T
Revolution rate of magnetic field	7.5 rpm

applied perpendicular to the axis of the observation tube and a halogen light was irradiated through an optical fiber from below the central axis. The behavior of the glass beads in the tube was then observed. Table 2 lists the experimental conditions.

RESULTS OF VISUALIZATION EXPERIMENT AND DISCUSSION

Figure 3 shows a visual image of the glass beads. In the figure the glass beads can be seen to form a strip on the inner wall of the tube in the midpoint between the magnetic poles and in the region furthest away from the central axis. In the experiment, this strip of glass beads was found to rotate synchronously with the rotating magnetic field. This strip may be formed by glass beads ejected from the magnetic clusters in the center of the tube between the magnetic poles and in the region furthest away from the central axis and retained on the sides of the inner tube wall of the magnetic clusters. Therefore, the force of magnetic clusters acting on the glass beads may generate pressure on the inner tube wall. No glass beads were observed near the magnetic poles in this experiment. Judging from this, the tube may be polished by abrasive grains that are retained on the inner tube wall sides of magnetic clusters at the midpoint between the magnetic poles and in the region furthest away from the central axis. However, it is important to note that the glass beads may not exhibit the same behavior as fine abrasive grains since the glass beads are considerably larger than fine abrasive grains.

EXPERIMENT TO MEASURE THE INNER TUBE WALL PRESSURE

The force of the magnetic clusters acting on the abrasive grains, or the polishing force, is considered to be equal to the inner tube wall pressure. Therefore, the distribution of the processing force generated by the
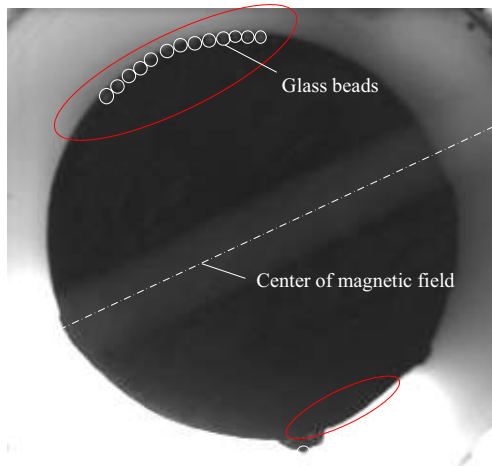

Figure 3 Optical observation of glass beads inner tube

magnetic clusters was investigated by measuring the pressure of the inner tube wall. For this measurement, the observation tube on the observation system was replaced with a circular tube for measuring pressure and a potentiometer makes contact with the turntable to measure the angle of rotation. Figure 4 shows the structure and coordinates of the circular tube for measuring pressure. The circular tube is a cylindrical resin container filled with the test fluid and sealed with a lid (internal diameter d: 10 mm, external diameter: 20 mm, height: 20 mm, internal height: 5 mm). This circular tube had a 0.5-mm-diameter pressure hole. A diaphragm pressure sensor (PSM-1KAB, Kyowa Electronic Instruments) was attached to the pressure chamber. The magnetic field source used was the same as that used for the observation system. The applied magnetic field distribution was varied by installing pole pieces having different tip widths w (=2, 6, 10, and 20 mm). The fluids used in this experiment were W-40 and WMCF25 (see Table 1). A rotating magnetic field was applied perpendicular to the central axis of the pressure measurement circular tube and the output voltages from the pressure sensor and potentiometer were measured. Table 3 lists the experimental conditions.
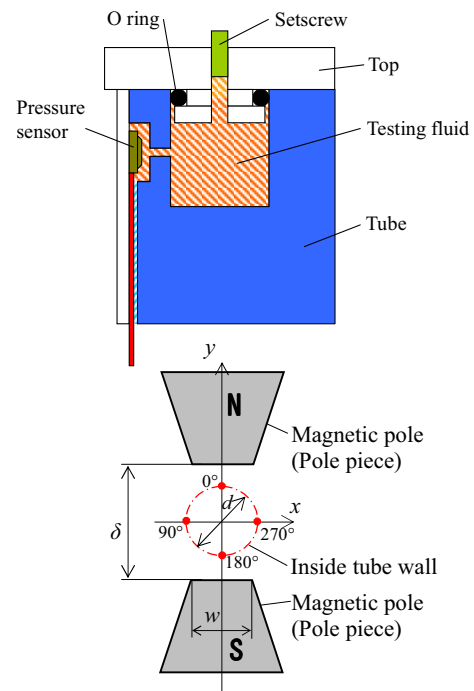

Figure 4 Schematic diagram and co-ordinate system of the experimental apparatus for measuring pressure

Table 3 Experimental conditions for measuring pressure

Magnetic flux density at center (w=2 mm)	0.168 T
Magnetic flux density at center (w=6 mm)	0.180 T
Magnetic flux density at center (w=10 mm)	0.182 T
Magnetic flux density at center (w=20 mm)	0.172 T
Revolution rate of magnetic field	2.5 rpm

PRESSURE MEASUREMENT RESULTS AND DISCUSSION

In the previous report about the results of investigating the influence of magnetic field distribution on polishing, effective polishing was achieved when w = 10 mm [2]. In the current experiment, we investigated the effect of pressure distribution on polishing. Figure 5 shows the results of measuring the inner tube wall pressure distribution about W-40. Theoretically, a magnetic fluid in which the dispersant is dispersed uniformly exhibits a high inner tube wall pressure near the magnetic poles (about 0, 180, and 360°) and becomes zero in the center between the magnetic poles and in the region furthest away from the central axis (about 90 and 270°). According to the experimental results, the inner tube wall pressure is high near the magnetic poles and is low near 90° and 270° being close to zero except when w = 10 mm. When w = 10 mm, the pressure is positive probably because the dispersant aggregates near 90° and 270° and the aggregate generates pressure by acting on the inner tube wall. In the magnetic field distribution when w = 10 mm, the magnetic flux density and the rate of decrease of the magnetic flux density are larger than those for the magnetic poles having different tip widths, so that aggregation occurs easily.

Figure 6 shows the results of measuring inner tube wall pressure with WMCF25 as the MCF. Except when w = 6 mm, the inner wall pressure is higher than with a magnetic fluid. The pressure is high near 90° and 270° when w is 2 and 10 mm. This pressure is attributable to the known anisotropy of the magnetic force generated by nearby magnetic clusters. Compared with the pressure distribution near 90° and 270°, the pressure distribution when w = 2 mm has an almost V-shaped trough. In this case, polishing does not progress because abrasive grains concentrate in confined regions near 90° and 270° where the pressure is low. When w = 10 mm, the pressure distribution shows a trough with a flat bottom. In this case, polishing proceeds because abrasive grains are scattered around 90° and 270°.
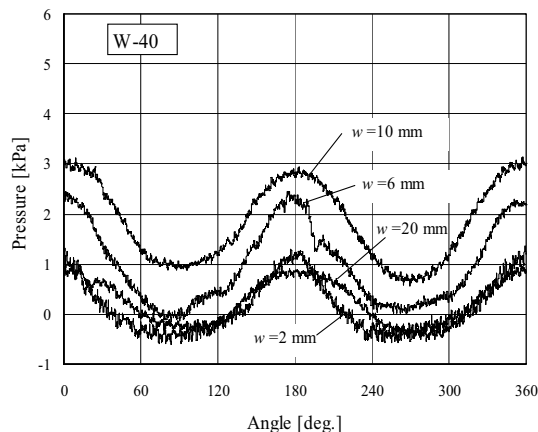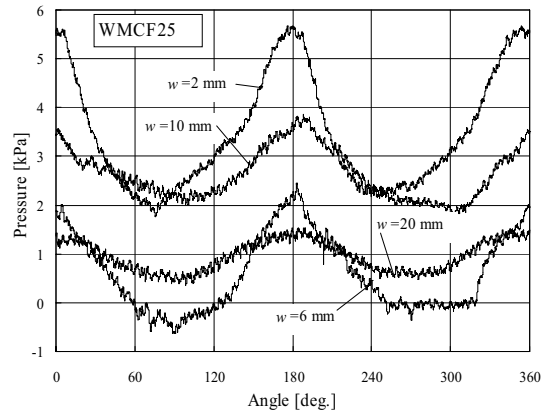

Figure 6 Pressure distribution inner tube wall (WMCF25)

In other words, a polishing effect is obtained when the pressure distribution is flat for the required polishing force near 90° and 270°. This is attributable to the radial force of magnetic cluster strips formed on the inner tube wall near 90° and 270°. Thus, the radial force of magnetic clusters acting on the abrasive grains is considered to produce the force for this polishing.

CONCLUSION

In this study, we clarified the mechanism of inner tube wall polishing using an MCF by observing the behavior of abrasive grains and measuring the pressure distribution on the inner tube wall. The results of this study can be summarized as follows:

(1) Abrasive grains (glass beads) form strips along the tube wall in the center between the magnetic pole and in the region furthest away from the central axis (on the inner tube wall near 90° and 270°).

(2) If the magnetic flux density and the rate of decrease of the magnetic flux density are large on the inner tube wall near 90° and 270°, the pressure distribution exhibits a flat trough in the required polishing force in these regions.

(3) The radial force of magnetic clusters formed near 90° and 270° act on abrasive grains to produce the force for this polishing.

REFERENCES

1. H. Nishida, K. Shimada, M. Goto, Polishing inner capillary walls by a magnetic compound fluid, International Journal of Applied Electromagnetics and Mechanics, 2007, Vol.**25**, No.1-4,pp. 25-29.
2. H. Nishida, K.Shimada ,Y. Ido, Influence of magnetic field distribution on inner tube walls polishing using Magnetic compound fluid, Proceedings of 13th International Symposium on Applied Electromagnetics and Mechanics, 2007, pp.195-196.

Figure 5 Pressure distribution inner tube wall (W-40)

P2-47

SHAPE MEMORY ALLOY ACTUATOR PROTECTED BY ROLLED FILM TUBE FOR ARTIFICIAL MUSCLE

Toshiya ISHIKAWA* and Takeshi NAKADA*

*School of Information Environment, Tokyo Denki University,
2-1200 Muzai Gakuendai Inzai, Chiba, 270-1382 Japan
(E-mail: nakada@sie.dendai.ac.jp)

ABSTRACT

In this study we aim to realize an actuator that is comparable with a natural muscle from a viewpoint of flexibility, the output force and the responses. We constructed the Shape Memory Alloy (SMA) coil actuator protected by "a rolled film tube" with the high heat resistance and the high flexibility, and it is named "the unit cell". The SMA coil in the unit cell is cooled down by inert liquid flowing through the rolled film tube. Then we constructed an actuator named "a motor unit" with the larger output force by bunching up seven unit cells, and the characteristics of the motor unit are investigated by the experiments in which the motor unit is driven in Pulse Frequency Modulation (PFM) found in the bio-motion. The result of the experiments shows that the static characteristics of the output force and the displacement to the input pulse frequency in the motor unit near proportion relations in comparison with the unit cell still more and the output force increases almost seven times as large as the unit cell. Consequently, it is found that these actuators proposed can be employed as applications to a flow control valve and an artificial arm.

KEY WORDS

Shape Memory Alloy, Artificial Muscle, Rolled Film Tube, Motor Unit, Pulse Frequency Modulation

NOMENCLATURE

g	:	gravity acceleration	9.8m/s^2
L	:	output displacement in steady state	m
m	:	mass of weight	kg
P	:	input power	W
T	:	time constant	s
η	:	power efficiency	%

INTRODUCTION

Recently, the necessity for a robot with high affinity for human is increasing. Such a robot needs artificial muscles with the figure and flexibility like those of a human body. Shape Memory Alloy (SMA) actuators with strong output force and large output displacement are researched as artificial muscle actuator in many research institutions. Thin SMA wires with small heat capacity are bunched in parallel at high density in order to get a high response and a strong output force. However, the bunched thin SMA wires are not able to

bend with flexibility. And the heat is accumulated in the space around the bunched thin SMA wires, so the compulsion cooling is necessary. A SMA wire is inserted in a high flexibility tube, and its some tubes are bunched. These SMA wires inserted are cooled by coolant flowing through the tubes. However, there have been no tubes that can fulfill two requirements of high heat resistance and high flexibility so far. For the solution of the above problem in this study [1], firstly, "a rolled film tube" with high heat resistance and high flexibility is proposed as a machine element for SMA actuators. Secondly, "a unit cell" is constructed with a SMA wire inserted in a rolled film tube as a minimum unit of artificial muscle. Thirdly, "a motor unit" like a natural muscle of spindle shape is constructed with a bunch of unit cells. An artificial arm should be driven by natural nerve impulse. The characteristics of the motor unit driven are investigated by the experiment in PFM. The pulse width and pulse frequency band of PFM are the same as a natural nerve impulse. Consequently, the output force and the output displacement are acquired which is almost in proportion to the pulse frequency. It is found in this study that the influence on the time constants of step response against input pulse frequency can be decreased by the pulse width control, and now the power conversion efficiency is several % [1].

CONSTRUCTION OF MOTOR UNIT

On the anatomy, a bunch of muscle cells controlled by one motor nerve is called "a motor unit" [2]-[4]. "A unit cell" corresponds to one natural muscle cell. So in this study, a bunch of unit cells is called "a motor unit". How to make "a unit cell" is shown to the following. A film is cut as shown in Figure 1 (a). "A rolled film tube" is made of the film rolled as shown in Figure 1 (b). A rolled film tube is made of polyimide that has high heat resistance with glass transition point higher than 500℃. And a rolled film tube has a slide structure that can hold efficiently large displacement inner, so it acquires eminently large compliance as shown in Figure 2. Figure 2 shows the characteristics of a rolled film tube, and the characteristics of a silicone rubber tube are shown in this figure for comparison. Two electric wires and two aramid threads are attached on the both ends of a coil spring made of a thin SMA wire, and its SMA coil spring is inserted into the rolled film tube as shown in Figure 1 (c). Figure 1(d) shows that "a motor unit" is bunched by unit cells, and two silicone rubber tubes are attached on the both ends of the motor unit. A SMA coil spring in each unit cell bunched as a motor unit is equally cooled by coolant flowing through a rolled film tube. A photograph of the motor unit is shown in Figure 1 (e). Practically, the flow control valve as shown in Figure 3 (a) and the artificial arm as shown in Figure 3 (b) [1] can be realized by using some motor units.
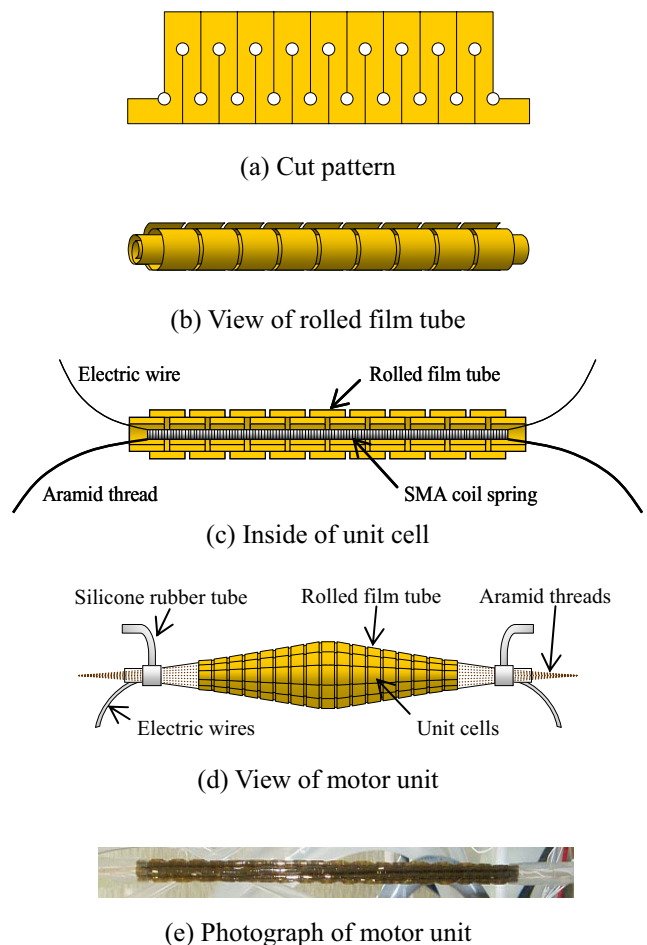

(a) Cut pattern

(b) View of rolled film tube

(c) Inside of unit cell

(d) View of motor unit

(e) Photograph of motor unit
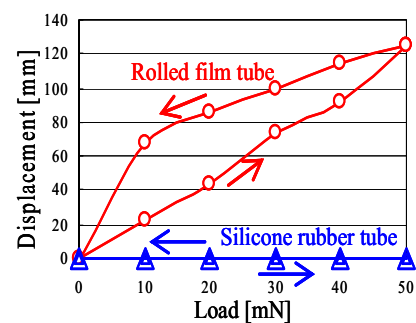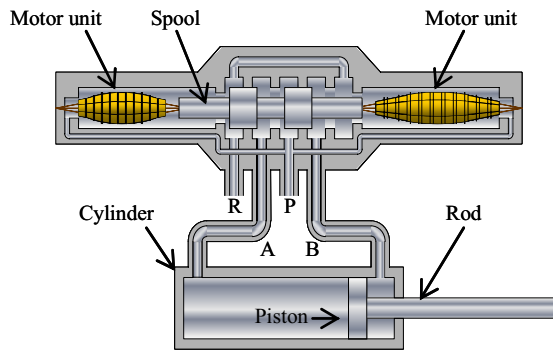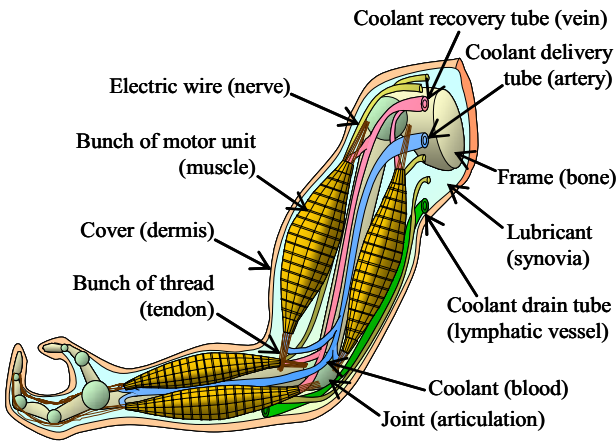
Figure 1 Motor unit

Figure 2 Compliance characteristics

APPARATUS AND METHODS

In this experimental apparatus, Figure 4 (a) shows the front view and Figure 4 (b) shows the side views. The cross section of a motor unit is shown in Figure 5. The specifications of a unit cell are shown in Table 1. For minimizing the volume of a motor unit, 7 unit cells are bunched in a circle with minimum cross section area.
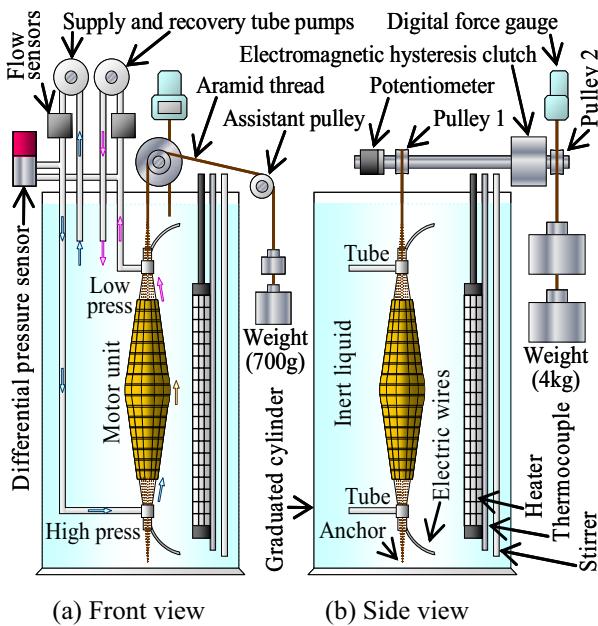
(a) View of flow control valve

(b) View of artificial arm

Figure 3 Applications

(a) Front view   (b) Side view
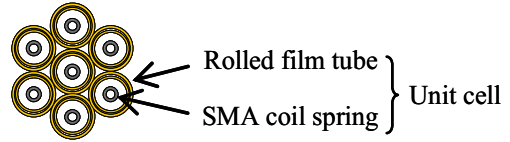
Figure 4 Experimental apparatus

Figure 5 Cross section of motor unit

Table 1 Specifications of unit cell

Rolled film tube	Outer diameter [mm]	ϕ 1.5
	Length [mm]	100
SMA coil spring	Coil outer diameter [mm]	ϕ 0.6
	SMA wire diameter [mm]	ϕ 0.2
	Length [mm]	80
	Phase transformation temperature [℃]	60
Weight [g]		0.15

Table 2 Specifications of inert liquid

Hydrofluoropolyether (HFPE)	
Boiling point [℃]	178
Density [kg/m³]	1720
Specific heat [J/(kg·K)]	1092
Thermal conductivity [W/m·K]	0. 087

Its total weight is 1.05g. The coolant used is an inert liquid with electric high insulation. Its coolant is flowed by the supply and recovery pumps from the bottom of a motor unit to the top, and its temperature is kept to 36℃ by the temperature controller constructed with a heater, a thermocouple and a stirrer. The specifications of an inert liquid as coolant are shown in Table 2. The thread on the top of a motor unit is twisted around the pulley 1 clockwise once, and its end is pulled by the weight of 7N (700g). The output displacement of a motor unit is measured by the angles of the potentiometer. The pulley 1 and 2 are separated or connected by the electromagnetic hysteresis clutch. While, one thick thread is twisted around the pulley 2 clockwise once. The upper end of its thread pulls the digital force gauge and its lower end is pulled by the weight of 40N (4kg). Therefore, the pulley 2 is held by the brake torque of 40Ncm. At this time, the weight of 40N is indicated by the digital force gage. For measurement of the output force, first, the pulley 1 and 2 are separated, then a motor unit is given a bias strain by the weight of 7N (700g) as shown in Figure 4. Next, the pulley 1 and 2 are connected, and then the SMA coil springs in a motor unit are heated by electric heating. Though a motor unit contracts, the pulley 1 is kept initial position by the pulley 2 braked. Then the weight of less than 40N is indicated by the digital force gage. The difference between its weight and 40N is the output force of a motor unit.

843

RESULTS AND DISCUSSION

Output force and output displacement

It is found on the experiments that if the constant frequency pulse voltage is supplied to a motor unit, the static constant output force and the output displacement are generated corresponding with its frequency. Above result is confirmed on the rehearsal experiments [5]. Therefore, the constant frequency voltage pulse trains are supplied to a motor unit. The pulse width (0.5ms) and frequency band (10-70Hz) of its pulse train are same as a natural nerve pulse train. Then the output force and displacement generated is measured about every frequency. The height of pulse voltage is 100V which is the rated voltage of a switch device. The relations of output force and output displacement of motor unit against pulse frequency are shown in Figure 6 (a) and 6 (b), respectively. For comparison, the experimental result of one unit cell is inserted into Figure 6 (a) and 6 (b). Figure 6 shows that the maximum output force of the motor unit is 22.5N, and amounts to 7 times of a unit cell. The maximum output displacement is 40.6mm. Consequently, when a motor unit is made of seven unit cells bunched, its output force is seven times bigger than one unit cell's output force and its output displacement is 85% of one unit cell's output displacement. It is found that the output force of a motor unit increases in proportion with number of the unit cell, and the reduction of the output displacement is due to the friction between the bunched unit cells.
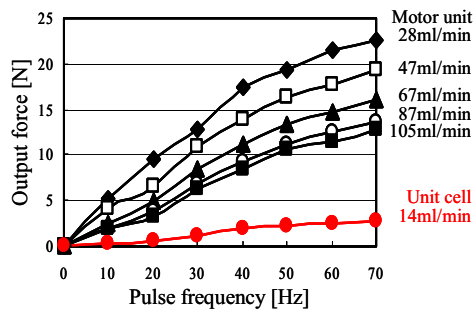
(a) Output force
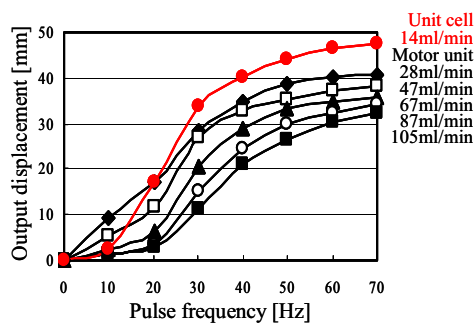
(b) Output displacement

Figure 6 Static characteristics of motor unit
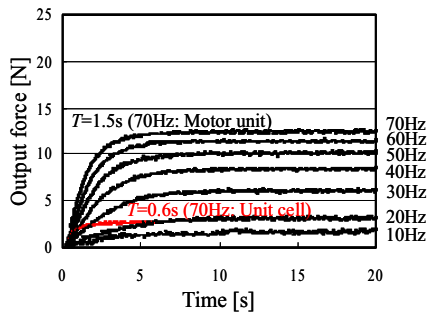
Pulse frequency and step response

The step responses of the motor unit are obtained experimentally on the coolant flow of constant 105ml/min. These results are shown in Figure 7 (a) and 7 (b). For comparison, the results of response of the output force and the output displacement of one unit cell are inserted into Figure 7 (a) and 7 (b). The experimental condition are as follows, (coolant flow: 14ml/min, pulse width: 0.5ms, pulse frequency: 70Hz). When the pulse voltage trains (height: 100V, width: 0.5ms, frequency: 10-70Hz) are inputted to a motor unit and a unit cell at the zero second, Figure 7 (a) and 7 (b) show the temporal responses of output force and output displacement on a motor unit and a unit cell. Figure 7 shows that the time constant T of the output force is 0.6s and the time constant T of the output displacement is 0.4s. However, on the pulse frequency of 70Hz, the minimum time constant T of a motor unit is 1.5s on the output force and is 1.8s on the output displacement. Consequently, the time constants of one motor unit are 2.5 times of the unit cell about output force, and are 4.5 times of the unit cell about output displacement.
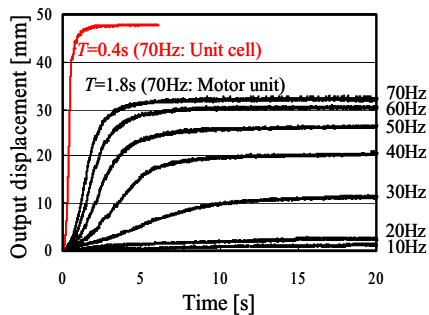
Pulse width and step response

The heat capacity of the motor unit increases, because the dead space volumes of a motor unit increase by bunching unit cells as shown in Figure 5. It is considered that the increase of the time constant depends on the increase of the heat capacitance of the motor unit. At the pulse frequency of 70Hz, the step responses of the output force and the output displacement are shown in Figure 8 (a) and 8 (b), by taking pulse widths as parameter. The pulse width patterns of the pulse trains are shown in Figure 9. The time constant T in the step response about the output force of the motor unit is 1.5s, when the pulse width is 0.5ms. Its time constant is 0.9s longer than the time constant of 0.6s of a unit cell. When the pulse width is extended to 2.0ms, the time constant T is shortened to 0.8sec. Similarly, the time constant T in the step response about the output displacement of a motor unit is 1.8sec, when the pulse width is 0.5ms. Its time constant is 1.4sec longer than the time constant of 0.4sec of a unit cell. When its pulse width is extended to 2.0ms, the time constant T is shortened to 0.5s. Therefore, when the pulse width of a motor unit is extended, its time constant is shortened to the level of a unit cell.

Pulse frequency and time constant

The time constants of the output force and the output displacement against the pulse frequencies are shown in Figure 10 (a) and 10 (b). In Figure 10, the time constants are not mostly influenced by the frequency higher than 40Hz in case of the pulse width more than 1.0ms. Consequently, it is found that the influence of the frequency on the time constant can be made smaller by controlling the pulse width.
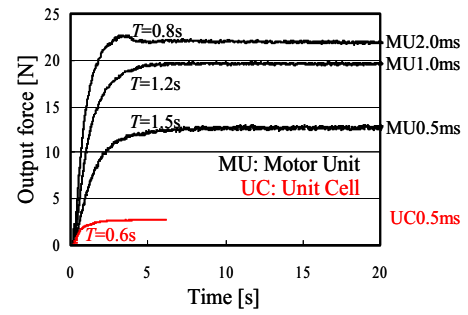
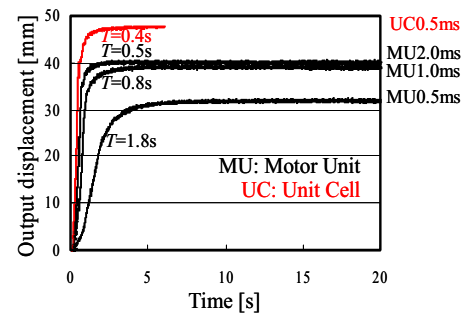844

(a) Output force

(b) Output displacement

Figure 7 Pulse frequency dependency on step response

(a) Output force

(b) Output displacement

Figure 8 Pulse width dependency on step response

Pulse frequency and power efficiency

The power efficiencies of the actuator in this study against the pulse frequencies by the pulse widths as the parameters are shown in Figure 11, by taking the pulse widths as parameter. The power efficiency η [%] can be obtained by the following equation.

$$\eta = \frac{mg \cdot (0.63L / T)}{P} \times 100$$

In this equation, $0.63L/T$ is the average velocity [m/s] of a unit cell or a motor unit. In Figure 11, the power efficiency of a unit cell shows approximately 9% in the frequency region higher than 30Hz. It is well-known that the power efficiency of SMA is approximately 10% [6], and the efficiency of our unit cell attains to this value. However, the power efficiencies of a motor unit show several % in the frequency region higher than 20Hz.

Comparison of natural muscle with motor unit

The main data of a natural muscle and a motor unit are shown in Table 3. The data of a natural muscle are calculated by using the reference [2]-[4]. The size of the natural muscle model is set at the same size with a motor unit.
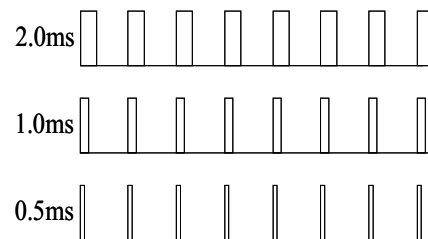

Figure 9 Pulse width pattern

The outer diameter is φ4.5mm, the length is 100mm, and the volume is 1590mm^3. In summary of Table 3, the weight and the density are approximately half on a motor unit against a natural muscle model. The maximum output force and the maximum output pressure are approximately 3 times. The maximum output displacement is approximately same. The maximum output force/self weight and the maximum output pressure/density are approximately 4 times [7]. From these results, it is found that the characteristics of a motor unit in this study are more excellent than a natural muscle. From this study, it is found that the time constant can be improved by controlling the pulse width to some extents.
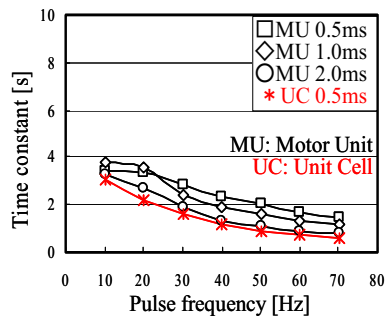
(a) Output force
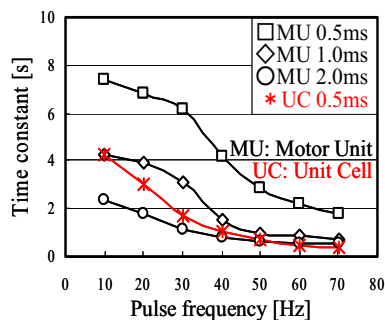
(b) Output displacement
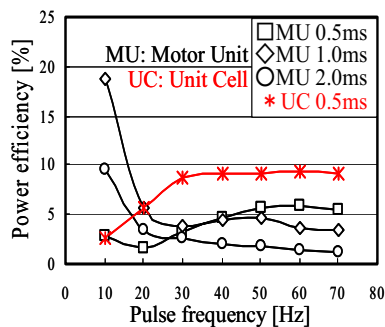
Figure 10 Pulse frequency dependency on time constant

Figure 11 Power efficiency characteristics

Table 3 Comparison of natural muscle with motor unit

Item	Natural muscle	Motor unit
Diameter [mm]	$\phi 4.5$	
Length [mm]	100	
Volume [mm³]	1590	
Blood temperature [℃]	36	
Impulse width [ms]	0.5	2.0
Weight [g]	1.63	1.05
Density [kg/m³]	1020	660
Maximum output force [N]	7.95	21.9
Maximum output displacement [%]	50.0	40.5
Minimum time constant of output force [ms]	40	800
Maximum output pressure [MPa]	0.50	1.38
Maximum output force / weight	497	2127
Maximum output pressure / density [kPa・m³/kg]	0.49	2.09

CONCLUSIONS

"A rolled film tube" with high heat resistance and high flexibility is proposed. "A unit cell" as minimum unit of the artificial muscle is constructed with a rolled film tube and a SMA coil spring. A SMA coil spring inserted into "a unit cell" is cooled by the inert liquid through the rolled film tube. "A motor unit" is constructed with a bunch of 7 unit cells. The characteristics of a motor unit are investigated experimentally. The main results are as follows.

(1) The static characteristics of the output force and the output displacement are approached to the static characteristics of a living body by bunching unit cells.

(2) In the same frequency, the input heat quantity can be controlled by the pulse width.

(3) When the pulse width is expanded, the power efficiency is decreased in the high frequency band.

It is found that a motor unit may be able to drive directly by a natural nerve impulse. The construction of the control system with higher power efficiency and smaller time constant will be an aim of our further study.

REFERENCSES

1. Ishikawa, T. and Nakada, T., Shape Memory Alloy Actuator for Artificial Muscle (Characteristics of Motor Unit), Transactions of the Japan Society of Mechanical Engineers, Series C, Vol.74, No.738, 2008, pp. 359-364.
2. Wirhed, R., Athletic Ability & the Anatomy of Motion, 1996, p.13, Taishukan Publishing Company.
3. Yamamoto, K. and Maruyama, K., Muscle (in Japanese), 1986, p.14, Kagaku-Dojin Publishing Company. INC.
4. Miyamura, S. and Yabe, K., Physical workouts (in Japanese), 1986, p.19, Shinko Trading Co Ltd Publication Department.
5. Ishikawa, T. and Nakada, T., Study on Artificial Muscle Actuator using Shape Memory Alloy (2nd Report, Characteristics of Motor Unit), Proceedings of the 41st JSME Tohoku Branch Autumn Conference, 2005-9, pp.71-72.
6. Hunter, I., Lafontaine, S., Hollerbach, J. and Hunter, P., Fast Reversible NiTi Fibers for Use in MicroRobotics, Proceedings of the 1991 IEEE Micro Electro Mechanical Systems – MEMS'91.Nara.Japan, 1991, pp.166-170.
7. Ashley, S., Artificial Muscles, SCIENTIFIC AMERICAN, OCTOBER 2003, pp.34-41.

P2-48

SIMULATING PRESSURE DISTRIBUTION ON LENS RELEVANT TO FLUID INJECTION FOR IMMERSION LITHOGRAPHY

*Wenyu Chen, **Xin Fu, **Huayong Yang

*The State Key Lab of Fluid Power Transmission and Control
Zhejiang University
Hangzhou, 086-0571-87953395 China
(E-mail: serverlandon@zju.edu.cn)
**The State Key Lab of Fluid Power Transmission and Control
Zhejiang University
Hangzhou, 086-0571-87953395 China

ABSTRACT

Immersion lithography has been proposed as a method for improving optical lithography resolution to 32 nm. The premise behind the concept is to increase the refraction index in the space between the lens and wafer by insertion of a high refractive index liquid in place of the low refractive index air that currently fills the gap. During the scanning and exposure process, immersion liquid is injected into the space between wafer and lens with certain inlet pressure and angle. Because the liquid will act as a lens component during the lithographic process, it must maintain high uniform optical quality. One source of optical degradation may be due to lens distortion caused by the pressure distribution nonuniformity in the fluid flow field. Consequently, any deviations of pressure distribution on flow field boundary in direct contact with lens may damage the uniform optical path.

Three-dimensional computational fluid dynamics models were created to assess the pressure distribution characteristics relevant to flow rates and injecting angles of immersion liquid. Flow field stream patterns were discussed corresponding to dispense port numbers. The numerical simulation results were presented, featuring lens normal and shear pressure and injection flow, considering fluid injecting velocity, dispense ports quantity, and direction angles.

KEYWORDS

Immersion lithography, pressure, fluid flow

INTRODUCTION

For most of the microelectronics industry history, optical lithography has been the backbone for continuing the trend of making features even smaller. However, as the apparent inability of optical lithography for future requirements, technology evolution to next-generation lithography (NGL) was becoming necessary.

Among all of the competing NGL technologies, Immersion lithography has been proposed in the past as a method to improve the resolution of optical lithography, but more recently it has been gaining popularity due its potential for achieving resolution down to 50 nm and below. It has shown promise as a technology extending optical lithography without significant changes to the manufacturing infrastructure used for decades. [1,2]
The intention of immersion lithography is to increase the

index of refraction in the space between the lens and wafer by introducing a high refractive index liquid in place of the low refractive index air that currently fills the gap. Because the liquid acts as a lens component during scan-step process, it must maintain a high and uniform optical quality. Thus, an immersion unit structure must be implemented to keep the flow field from leaking. Also, the immersion liquid within the gap has to be updated as substances unwrapped from chemical reacting may affect the optical quality of the liquid. As a result, the streamline patterns in flow field and velocity distribution have to be predicted, and the spatial distribution and magnitude of pressure distribution on lens have been investigated.
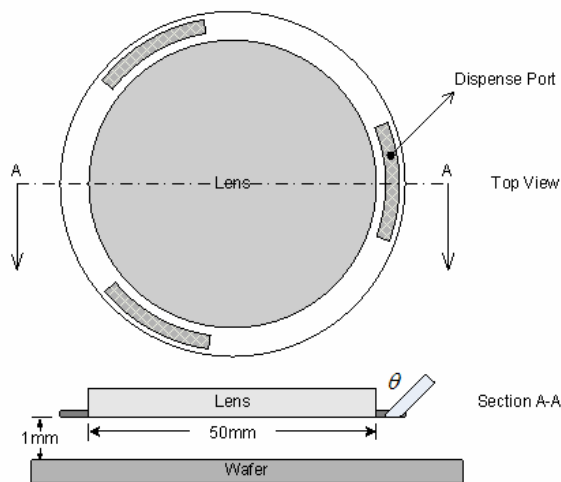
FLOW FIELD MODELING AND BASIC INPUT PARAMETERS

Figure 1. Schematic of the CFD model used to investigate the normal and shear forces on the lens.

A schematic of the model used to study the gap flow field is shown in Figure 1. Top-down and cross-sectional views of the lens/gap/wafer system are shown. To approximate the recovery system, the boundaries at both edges of the model are assumed to have a fixed, negative pressure of 50 Pa. The dispense ports are planar with underneath surface of the lens and the spaces between the lens, dispense port, and liquid collection boundary are enclosed by solid boundaries. The parameter implemented on the above model are listed in Table. 1, and the remaining parameters are discussed in the following context.

Table. 1. Input parameters and material properties for numerical models

Parameters	Value

Fluid density	998.2 kg/m^3
Fluid viscosity	0.001003 kg/ms
Surrounding pressure	101325 Pa
Inject velocity	0.1mm/s
Dispense port total area	55.50 mm^2
Gap Thickness	1mm
Lens area	1963.495mm^2

STREAM PATTERNS IN FLOW FIELD

Through increasing the number of dispense ports, the streamline patterns are listed in Figure 2. Apparently, with asymmetrically ports distribution, the streamline covers entirely and smoothly over the whole lens area, which means better consistency for flow direction. However, taking wafer motion into account, symmetric dispense ports provides much more tolerance of flow change with the course of time due to wafer motion.
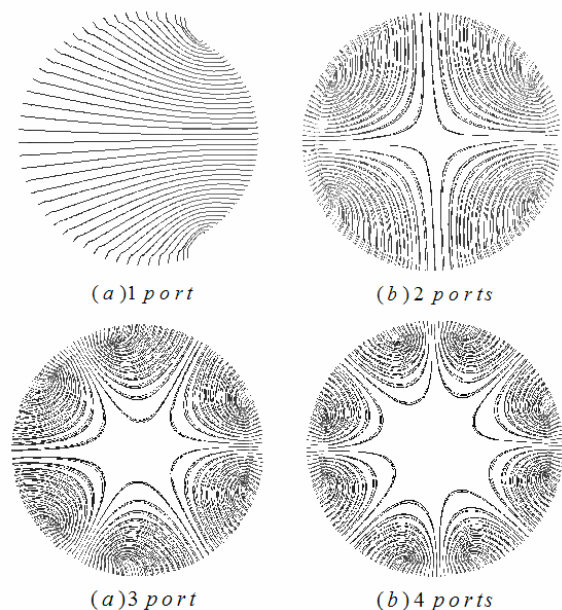

Figure 2. Flow field stream patterns for varying dispense port quantity.

VELOCITY DISTRIBUTION FOR FLOW FIELD FLUID

The velocity distributions along lens diameter in Section A-A (Figure1.) for varying injecting velocity are presented in Figure 3(a), for varying dispense ports quantity in Figure 3(b), and for varying injecting angle in Figure 3(b). As in Figure 3(a), increasing the injecting velocity partially affects the marginal area of the flow field, and the minimum velocity keeps under 10mm/s. As in Figure 3(c), the velocity distribution is left nearly the

same, which indicates that it's probably not necessary to increase the injection angle by altering the immersion unit structure for higher flowing speed in the fluid field. As in Figure 3(b), the cases with symmetric dispensing geometries have the minimum flowing speed near the lens center, while the case of single dispense port with the maximum and the minimum speed located to the lens margin. This indicates the case of single dispense port endorsed with higher general distribution of flow velocity, which means less updating time for gap fluid field.
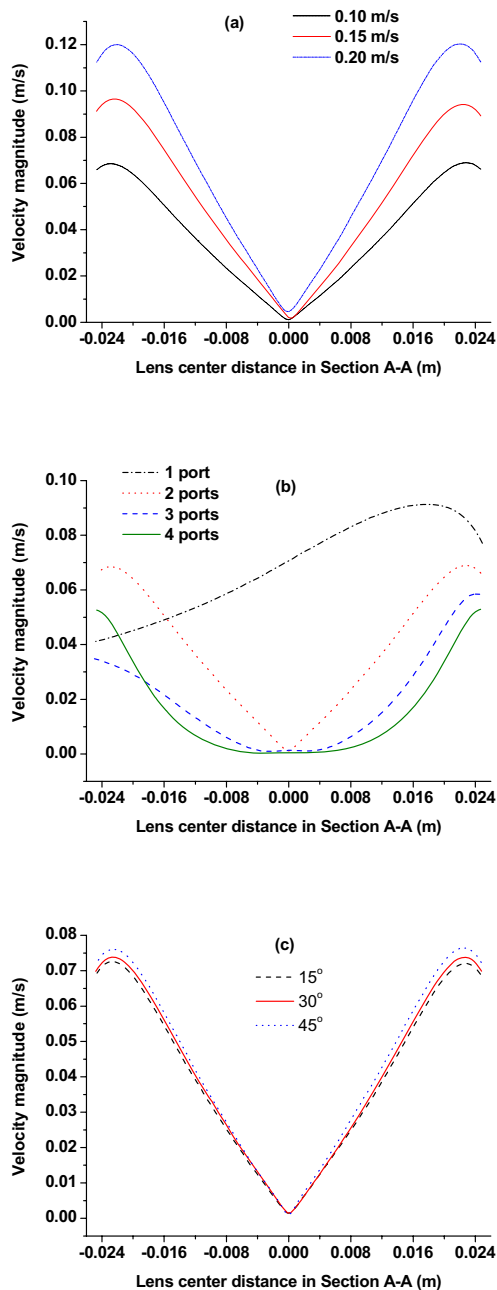

Figure 3. (a) shows the velocity magnitude as a function of lens center distance, for varying injecting velocity. (b) shows the velocity magnitude as a function of lens center distance, for varying dispense ports quantity. (c) shows the velocity magnitude as a function of lens center distance, for varying

injecting angle.

NORMAL PRESSURE ON LENS

With the schematic of the model shown in Figure 1, the shear and normal forces on the lens are studied. Normal forces across the final lens from the immersion flow field are shown in Figure 4, Figure 5, and Figure 6 for various liquid injecting configurations and geometries.

In Figure 4(a), the double dispense ports consist of 60 degree annular sections with a constant velocity at 0.1m/s straight towards the wafer surface, while the velocity has been increased to 0.2m/s. For the models in Figure 5(a) and Figure 5(b), which have the same liquid injecting velocity and injecting angles, the dispense port in Figure 5(b) is divided into four separate parts, symmetrically around the lens area. Since the dispensing ports area remains the same, the total flow rates are equal. The injecting angle has been increased from 15 degree in Figure 6(a) to 45 degree in Figure 6(b), with other parameters being identical.
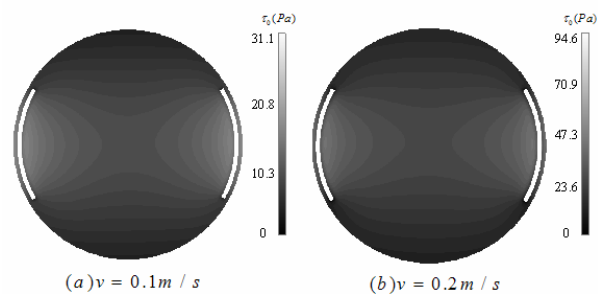

$(a) v = 0.1 m / s$ $(b) v = 0.2 m / s$

Figure 4. Normal pressure distribution on lens for varying injecting velocity.

$(a) 1 \, p o r t$ $(b) 4 \, p o r t s$
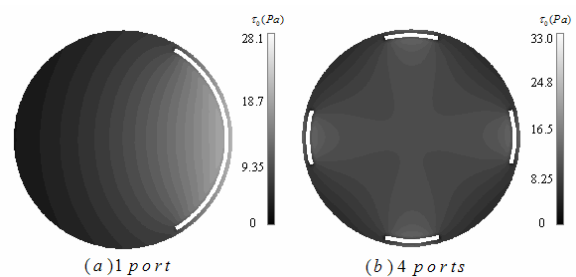
Figure 5. Normal pressure distribution on lens for varying dispense port quantity.
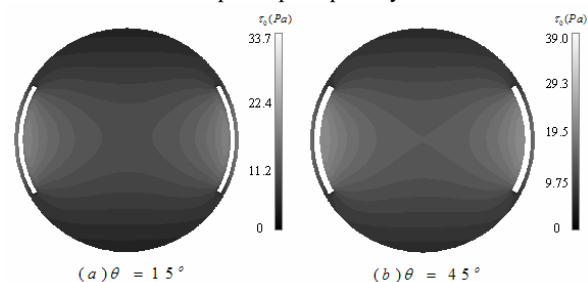

$(a) \theta = 1 5 °$ $(b) \theta = 4 5 °$

Figure 6. Normal pressure distribution on lens for varying injecting angle.

In all eight cases, it can be seen that a pressure gradient exists across the lens. The moment resulting from this pressure gradient will tend to cause the lens to tip away from the higher pressure side, which can be avoided by increasing the dispense port number, resulting in symmetric gradient patterns. Normal pressure distribution deviation on lens exacerbates greatly as injecting velocity increases, while not quite affected by more dispense ports or bigger injecting angles. The overall gradient for the lens normal pressure mostly distributes outboard dispense ports opening, which is far away from the lens. However, these forces will have direct impact on wafers and must be investigated further using a structural model of the overall lens housing in order to determine if changes to the immersion unit structure are necessary.

SHEAR PRESSURE ON LENS

Shear forces across the final lens from the immersion flow field are shown in Figure 7, Figure 8, and Figure 9 for the same liquid injecting configurations and geometries shown in Figure 4, Figure 5, and Figure 6 separately.
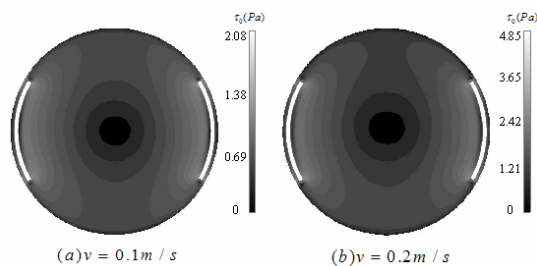

$$(a)v = 0.1m / s \qquad (b)v = 0.2m / s$$

Figure 7. Shear pressure distribution on lens for varying injecting velocity.

$$(a)1 \, port \qquad (b)4 \, ports$$
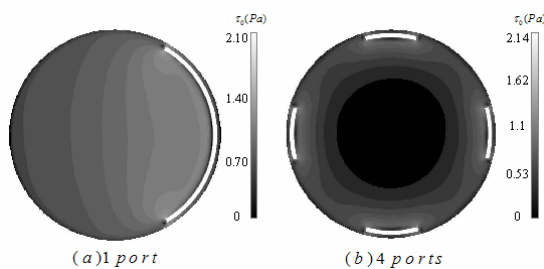
Figure 8. Shear pressure distribution on lens for varying dispense port quantity.
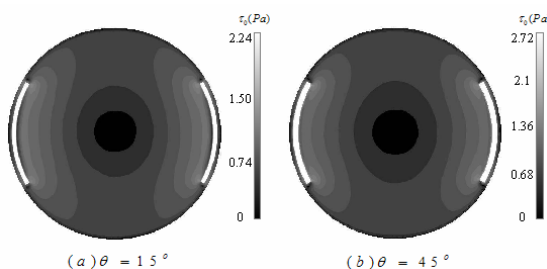

$$(a)\theta = 15° \qquad (b)\theta = 45°$$

Figure 9. Shear pressure distribution on lens for varying injecting angle.

Shear stresses on the lens may cause birefringence. An analysis has been done to estimate the magnitude of the birefringence induced in the lens. So, the largest birefringence estimates in worst situation would be[3]

$$birefringence = 2CR\tau_0 \qquad (1)$$

where C is the birefringence constant, R is the radius of lens, and τ_0 is the shear force. Assuming a birefringence constant of 5 (nm/cm)/(kg/cm2) and using the maximum shear stress obtained from Figure 7(b), the computed birefringence is less than 0.002 nm for a 5.0 cm diameter lens. This is a very small value, meaning that the birefringence introduced by shearing pressure will probably not be a factor in imaging defection, relevant to the above eight sets of liquid injecting configurations and geometries.

SUMMARY AND CONCLUSION

Three-dimensional computational fluid dynamics models have been created to assess the stream patterns in flow field within a range of dispense ports. Velocity distribution for flow field fluid has been discussed with injecting angle, dispense port quantity, and injecting velocity as parameters. The result has indicated that it's probably not necessary to increase the injection angle by altering the immersion unit structure for higher flowing speed in the fluid field and the case of single dispense port is endorsed with higher general distribution of flow velocity, meaning less updating time for gap fluid field. Normal and shear pressure on lens have been presented and discussed. A prediction has been made that the birefringence introduced by shearing pressure will probably not be a factor in imaging defection, relevant to the above eight sets of liquid injecting configurations and geometries simulated.

REFERENCES

1. M. Switkes, M. Rothschild, J. Microlith. Microfab. Microsyst.1 (2002) 225.
2. B. Lin, Microelectron. Eng. 6 (1987) 31.
3. A. Wei, Modeling fluid thermomechanical response for immersion lithography scanning. Microelectronic Engineering 73–74 (2004) 29–34